SELECTIVE WEAKENING AND POST-TENSIONING FOR THE SEISMIC RETROFIT OF NON-DUCTILE RC FRAMES

WENG YUEN, KAM

NOV 2010

VOLUME I: MAIN THESIS

A thesis submitted in partial fulfilment of the requirements
for the Degree of
Doctor of Philosophy in Civil Engineering

Under the supervision of by:
Associate Professor Stefano Pampanin
Professor Athol Carr
Adjunct Professor Des Bull
Dr. Alessandro Palermo

Department of Civil and Natural Resources Engineering
College of Engineering
UNIVERSITY OF CANTERBURY
Christchurch, New Zealand.

ABSTRACT

This research introduces and develops a counter-intuitive seismic retrofit strategy, referred to as "Selective Weakening" (SW), for pre-1970s reinforced concrete (RC) frames with a particular emphasis on the upgrading of exterior beam-column joints. By focusing on increasing the displacement and ductility capacities of the beam-column joints, simple retrofit interventions such as selective weakening of the beam and external post-tensioning of the joint can change the local inelastic mechanism and result in improved global lateral and energy dissipation capacities.

The thesis first presents an extensive review of the seismic vulnerability and assessment of pre-1970s RC frames. Following a review of the concepts of performance-based seismic retrofit and existing seismic retrofit solutions, a thorough conceptual development of the SW retrofit strategy and techniques is presented. A "local-to-global" design procedure for the design of SW retrofit is proposed. Based on the evaluation of the hierarchy of strength at a subassembly level, a capacity-design retrofit outcome can be achieved using various combinations of levels of beam-weakening and joint post-tensioning. Analytical tools for the assessment and design of the SW-retrofitted beam-column joints are developed and compared with the test results.

Nine 2/3-scaled exterior joint subassemblies were tested under quasi-static cyclic loading to demonstrate the feasibility and effectiveness of SW retrofit for non-ductile unreinforced beam-column connections. Parameters considered in the tests included the presence of column lap-splice, slab and transverse beams, levels of post-tensioning forces and location of beam weakening. Extensive instrumentation and a rigorous testing regime allowed for a detailed experimental insight into the seismic behaviour of these as-built and retrofitted joints. Experimental-analytical comparisons highlighted some limitations of existing seismic assessment procedures and helped in developing and validating the SW retrofit design expressions. Interesting insights into the bond behaviour of the plain-round bars, joint shear cracking and post-tensioned joints were made based on the experimental results.

To complement the experimental investigation, refined fracture-mechanic finite-element (FE) modelling of the beam-column joint subassemblies and non-linear dynamic time-history analyses of RC frames were carried out. Both the experimental and numerical results have shown the potential of SW retrofit to be a simple and structurally efficient structural rehabilitation strategy for non-ductile RC frames.

ACKNOWLEDGEMENT

This thesis would not have been possible, without the inspiration and support of my primary supervisor and mentor, Associate Professor Stefano Pampanin. From the first undergraduate lecture on reinforced concrete beam 6 years ago to the very last Skype meeting over the thesis and everything else, Stefano has never stopped inspiring me towards fulfilling my potential as a structural engineer and researcher. *Grazie* Stefano.

I am also grateful to the rest of my supervisory committee: Professor Athol Carr, Adjunct Professor Des Bull and Dr Alessandro Palermo for their kind advice, technical assistance and constant encouragements (and reminders to finish the PhD!).

I would also like to acknowledge the significant financial support provided by the New Zealand Foundation for Research, Science and Technology (FRST), Christchurch Heritage Trust Society, Lee Foundation, University Halls and the University of Canterbury. Without the financial aids from these organisations, my PhD research and experience would not have been possible.

A special thanks needs to go to all the Civil Engineering technicians and staff who have helped on this project. To Mosese Fifita, Tim Perigo, John Maley, Michael Weaver and Richard Newton (now retired)– thanks for saving my projects on countless occasions. Additionally, to Mosese, the huge experimental component of this research would not have been possible within the limited time scale and my atrocious multi-tasking abilities without your dedicated work. Thanks also to Elizabeth Ackerman, Christine McKee - the Engineering Librarian, Sarah Beaven - the ISS staff and Brandon Hutchison for the assistance over the years.

To my fellow postgraduate students, Dr. Dion Marriott, Umut Akguzel, Dr. Brendon Bradley, Dr. Brian Peng, Dr. Alejandro Amaris, Michael Newcombe, Patricio Quintana Gallo, Giovacchino Genesio, Vinod Sadashiva, Tobias Smith, Gregory Cole and numerous others, thank you for your providing insightful comments and suggestions on a range of topics. Thanks for making being a postgraduate student a very enjoyable and satisfying process.

Thanks to the mates who had helped me during the labourious experimental phase of my research, in particular Umut Akguzel, Euving Au and Patricio Quintana Gallo. Special thanks to the friends outside the research environment in keeping my sanity and more importantly humility throughout the doctoral research.

Lastly but most importantly, this dissertation and my whole engineering career would not have been possible without the unwavering support from my family. In the darkest moments, you all were there to sustain me. My deepest gratitude goes to my mom and dad, to my sister, Kam Yuen Chi and to my loveliest soon-to-be fiancée, Sharon Gin and her family. This thesis is dedicated to you all.

While the dissertation is a cumulative of four and half years' worth of research and work, it is the memories and moments along the way that are truly remarkable and defining.

Kam Weng Yuen
23rd Nov 2010
Christchurch, New Zealand

Acknowledgement and thanks to the external PhD examiners: Professor Polat Gülkan of Middle East Technical University of Turkey and Mr Les M. Megget of University of Auckland for the thorough and rigorous examination of the thesis.

While the thesis is being examined, another major earthquake measuring 6.3 M_w has hit Christchurch on 22nd Feb 2011, resulting in severe and widespread structural damage on reinforced concrete (RC) buildings. In particular, two mid-rise RC buildings, including one non-ductile pre-1970s building collapsed, resulting in multiple fatalities. I had the privilege to be involved in the Civil Defence Building Safety Evaluation process, inspecting damaged multi-storey RC buildings within the Christchurch Central Business District. I would like to thank the various individuals and organisations that made this invaluable experience possible, including Dr Stefano Pampanin, Dr Ken Elwood, Dr David Hopkins, Steve McCarthy, Umut Akguzel, Sahin Tasligedik and countless Search and Rescue Teams.

That experience, plus the knowledge gained from this research, further reinforces my conviction that seismic retrofit of vulnerable RC buildings is a key engineering challenge in coming years. I further dedicate my research work and expertise to reducing seismic risks and making safer cities.

Kam Weng Yuen
17th May 2011

MAIN CHAPTERS TABLE OF CONTENT

APPENDICES TABLE OF CONTENT (IN VOLUME II)

Two roads diverged in a yellow wood,
And sorry I could not travel both
And be one traveler, long I stood
And looked down one as far as I could
To where it bent in the undergrowth.

Then took the other, as just as fair,
And having perhaps the better claim,
Because it was grassy and wanted wear;
Though as for that the passing there
Had worn them really about the same.

And both that morning equally lay
In leaves no step had trodden black.
Oh, I kept the first for another day!
Yet knowing how way leads on to way,
I doubted if I should ever come back.

I shall be telling this with a sigh
Somewhere ages and ages hence:
Two roads diverged in a wood, and I--
I took the one less traveled by,
And that has made all the difference.

The Road Not Taken
Robert Frost, 1915

CHAPTER 1. INTRODUCTION

"There are still too many poorly designed and constructed buildings in earthquake-prone areas, and too many people dying because of it."

Salvano Briceño, 16th May 2008
Director, UN Secretariat of the International Strategy for Disaster Reduction ISDR)
In "Poorly constructed buildings kill people during earthquakes"
UN-ISDR Press Release 2008/07 after the 12th May 2008 Wenchuan Earthquake

1.1 BACKGROUND

As Salvano Briceño clearly puts in context, catastrophic losses of human lives and financial resources resulting from large earthquakes near urban population centres remain one of the most daunting challenges in achieving a resilient human society – demographically, socially and economically. In the post-world wars construction booms, hundreds of thousands of reinforced-concrete (RC) structures were built around the world without much or adequate consideration for earthquake forces. In the case of RC structures, the problem is compounded by the fact that this type of construction is widely used for critical public buildings such as schools, emergency services and public administration offices. As such, modern societies in seismically-active regions are dealing with a ubiquitous amount of seismically-at-risk RC buildings. The problem is not limited to developing nations where building codes development, implementation and enforcement are lax but also equally critical in developed nations such as New Zealand as modern seismic building codes for RC structures did not appear until the mid-1970s.

Urbanisation and human population growth mean there are more lives and properties exposed to extreme seismic hazards. In the Twelfth Mallet-Milne Lecture, Bilham [3] estimated future earthquake-related fatalities could exceed one million in a megacity such as Tehran while possible earthquake-related financial losses could be as much as $200 billion in developed nations. With increased seismological and geological knowledge about geophysical behaviour of

faults and realistic earthquake hazard modelling, it is more certain that earthquake risks of these seismically vulnerable structures cannot be neglected as extremely-low probability of occurrence. This is evident in recent large earthquakes such as the 1994 Northridge (blind fault [12]), the 1999 Kocaeli/Izmit (poor construction practice [33]) and the 2008 Wenchuan (large urban population and large number of pre-modern seismic codes buildings [35, 36]).

Simultaneously, our knowledge of the poor structural performance of these pre-1970s non-ductile RC buildings has been augmented by the field observations of the collapsed and damaged RC buildings. Some examples of structural and soft-story collapse, initiated from beam-column joint failures are presented in Figure 1.1. Experimental and theoretical researches have also improved our understandings of the inherent vulnerabilities of these brittle buildings, in particular those funded by long-term national level research programmes such as the USA's National Earthquake Hazards Reduction Program (NEHRP).

Figure 1.1: Structural collapse and damage due to beam-column joint failures a) Kaiser-Permanente Clinic, Northridge 1994 [14], b) Yingxiu school, Wenchuan 2008 [36] c) Femina Hotel, Padang, Indonesia 2009 [25].

In addition, following our increased awareness of the seismic vulnerabilities of existing building stock, much research has been emphasised in developing seismic retrofitting strategies and techniques in the past thirty years. Evidently, the number of technical papers in the past World Conferences on Earthquake Engineering (WCEE) on the area of seismic retrofit and rehabilitation have been increasing steadily since the 6th WCEE in 1977 [34]. In the past decade or so, the design and seismic performance of various 'conventional' seismic retrofit techniques such as seismic isolation, element jacketing, added bracing, supplementary damping, and global strengthening through additional seismic frames or walls, have been refined and widely published. In conjunction with these developments, various technical guidelines [10, 11, 24] and standards

[1, 6, 19] have been published with some emphasis on the seismic assessment techniques and lesser on the seismic retrofitting techniques.

While the political question on whether to ignore the problem, to demolish and to rebuild or to seismically retrofit existing RC structures remains, the sustainability and economics questions are more straightforward. The concept of reducing energy and materials consumption for urban development recently emerges within the sustainability and climate-change debate. It is apparent that seismically-retrofitting and 'recycling' the existing structure can be more sustainable than complete rebuilding [15]. The direct seismic retrofitting costs vary significant among different types of buildings and retrofit solutions, and typically range from 10-40% of the replacement cost of a RC building [8]. However, when the life-cycle costing of a building includes the sustainability and material-related carbon cost, seismic retrofitting becomes more economically-viable.

The selection of retrofit strategies and interventions can be complex; it depends on the cost, existing structural capacities, building typologies, performance objectives, and availability of local material, labour and technology. In particular, the performance targets of seismic retrofit exercise should be well-defined and consistent with the expectation of the stakeholders (i.e. owners, communities and users). In terms of the available retrofit strategies and techniques, in spite of tremendous progress in the past few decades, there is a considerable area for further development.

1.2 NEED FOR RESEARCH

The seismic deficiencies of pre-1970s non-ductile RC moment resisting frames have been widely recognised and well documented in literature (e.g. [1, 6, 10, 19, 24]). In particular, the beam-column joint connections have been shown to be a critical weakness that could lead to structural collapse or irreparable damage in these structures, as observed in the field (e.g.[16, 31, 33, 35, 36]) and in the laboratory simulation (e.g. [2, 5, 30]). The beam-column joint connections have not been given considerable attention by structural engineers prior to the 1970s. This was largely due to the lack of complete understanding on the beam-column joint shear mechanism and the historical development of RC lateral systems in general. While research in recent decades has refined the design of RC beam-column joints, the behaviour of lightly-reinforced joint is still not

fully understood. Hence, the present work would attempt to improve the understanding on the shear and failure mechanisms of these non-ductile joints before and after seismic retrofitting.

The poor behaviour of joints typical of older construction can be attributed to the inadequate shear reinforcement and details in the joint region, the poor bond properties of plain round bar reinforcements, inefficient anchorage into the joint core and, in a wider sense, the lack of capacity design considerations. In resolving these seismic deficiencies of non-ductile RC frames, various seismic retrofit solutions have been considerably developed for RC beam-column joints. In the next two chapters (Chapters 2 and 3), the seismic vulnerabilities and various existing retrofit solutions for non-ductile RC beam-column joints will be presented in considerable depth.

With recent recognition of the importance of displacement-based and performance-based seismic engineering, significant challenges and opportunities arise when seismic retrofit objectives have been shifted from a strength-focused retrofit towards a deformation and acceleration-based retrofit. Whilst this philosophical shift has long been recognised [32] and ductility-enhancement retrofit has been used for many years, conventional retrofit strategies targeting an increase of local-ductility often have unquantifiable strength and stiffness effects on the global structural response. In the context of a “minimalistic” seismic retrofit approach, where minimal cost, disruption and invasiveness are targeted, alternative retrofit solutions can be developed by recognising the inherent displacement capacity and by ‘intelligently’ changing the inelastic mechanisms of the structure. A minimalistic (cost-efficient) retrofit approach yields an economical and simple solution that could be extended to a wide-implementation of seismic rehabilitation of a large building stock.

In New Zealand, acknowledging a general lack of a national platform of knowledge and expertise associated with seismic retrofit for multi-storey buildings as well as practical design and implementation guidelines, a co-jointed multi-year research programme [13] funded by the New Zealand Foundation for Research, Science and Technology (FRST) started in 2004 at the University of Auckland and the University of Canterbury. Building on a New Zealand Earthquake Commission (EQC) funded research project on the seismic behaviour of RC beam-column joints with sub-standard details [30] and a recent European project on seismic vulnerability of RC frames (e.g. [4, 7]), the University of Canterbury group, in which this research is part of, investigated various seismic retrofit solutions for RC structures.

1.3 STATEMENT OF RESEARCH: HYPOTHESIS AND OBJECTIVES

Against this backdrop, this dissertation presents the development and validation of a counter-intuitive, innovative seismic retrofit strategy – termed as *Selective Weakening (SW)* retrofit for non-ductile RC frames. Contrary to the common misconception that seismic retrofit must involve strengthening (under a force-based paradigm), the *Selective Weakening* retrofit relies upon targeted weakening of structural elements in order to achieve a ductile failure mechanism, thus, explicitly enforcing capacity design philosophy within a displacement-based retrofit approach. Similar to the structural weakening concept in FEMA-273 [9], the research at the University of Canterbury [26] developed and tested the *Selective Weakening* retrofit techniques for shear-deficient structural walls [17, 18] and deficient hollowcore floor-seating connections [20, 21].

This dissertation focuses on structural intervention on the exterior beam-column joints of non-ductile RC frames. By selectively weakening the beams through cutting the bottom longitudinal reinforcements and/or adding external prestressing to the beam-column joint, a more desirable inelastic mechanism can be attained, leading to improved global seismic performance.

This research therefore seeks to answer two hypotheses, elaborated as follows by several research questions. The hypotheses and research questions below also form the objectives of this research:

- Hypothesis 1:

  A displacement-based *Selective Weakening* retrofit strategy can enhance the seismic performance of pre-1970s RC frames and beam-column joints with non-ductile structural detailing typically adopted worldwide as well as in the New Zealand context.

  a. What is the seismic vulnerability of pre-1970s RC frames and the associated beam-column joints in terms of international and New Zealand practice as indicated by past earthquake lessons and existing experimental evidences?
  b. What is the current seismic assessment procedure for non-ductile RC frames and joints in terms of assessing the collapse mechanism and damage potential?
  c. What are the state-of-the-art seismic retrofit strategies and techniques for non-ductile RC frames and in particular the exterior beam-column joints?
  d. What retrofit techniques can be implemented to achieve the performance objectives of the *Selective Weakening* retrofit strategy?

e. Can the *Selective Weakening* retrofit be reliably designed though simplified design methodology and equations?

- Hypothesis 2:

  Selective beam weakening and/or post-tensioning retrofit techniques present feasible retrofit solutions for the seismic retrofit of pre-1970s RC exterior beam-column joints, in the context of a more general *Selective Weakening* retrofit strategy.

  a. How do selective beam weakening and/or external prestressing affect the lateral displacement and strength capacities of the exterior RC beam-column joints with non-ductile detailing?
  b. What are the influences of column lap-splice, floor slab and transverse beams on the seismic performance and retrofit of non-ductile RC exterior beam-column joints?
  c. Can the realistic behaviour of the as-built and retrofitted exterior RC beam-column joints be modelled and can such models be used to indicate the design limitations for the *Selective-Weakening* retrofit?
  d. In the theme of *Selective Weakening* retrofit – what is the global seismic performance of the as-built and retrofitted RC frame structures in terms of displacement-capacity and collapse mechanism, under inelastic dynamic analysis?

1.4 SCOPE

To thoroughly test the hypotheses postulated, a broad research approach has been undertaken in terms of research methodology to answer the set of questions above. However, certain research boundaries have to be established in order to expressively qualify the results and conclusions presented in this thesis.

In this research, the seismic vulnerabilities of RC frame structures prior to the introduction of modern seismic codes will be reviewed (in Chapter 2). However, to meaningfully limit the scope of this research, reinforcing details of the prototype RC frames of those representatives of pre-1970s New Zealand construction and the New Zealand construction peculiarities will be considered within the experiment design. Various researchers around the world adopted different sets of as-built configurations based on both geographical and historical influences. It is, however, important to note that those variations were quite minimal as the

findings in Chapter 2 will illustrate. For this research, taking the lessons from literature review and desktop study of seismic vulnerabilities of New Zealand pre-1970s RC frame structures, the following pre-1970s detailing for non-ductile exterior RC beam-column joints are adopted:

- The use of smooth plain round bars with poor concrete-to-reinforcement bond behaviour.
- No consideration of capacity design in the beam and column flexural and shear capacities.
- 180° hook anchorage for beam longitudinal top and bottom reinforcements into the joints.
- No transverse reinforcement or stirrup in the joint core.
- Presence of column lap-splice in two of the test specimen joints.
- Presence of floor slab and transverse beam stubs in two of the test specimen joints.

Next, to adequately define the limitations and to outline the design procedure for the SW retrofit of the exterior beam-column joints, this research considers the following key parameters during the experimental and numerical investigation phases:

- Level and location of beam flexural weakening.
- Level of external prestressing (post-tensioning) of the joint and the beam.
- Influence of bond strength.

Another limitation of this investigation is the assumption that the achievement of a more ductile behaviour and a better hierarchy of strength mechanism only within the retrofitted exterior beam-column joints can lead to a more ductile global behaviour in the retrofitted global frame system. This retrofit strategy has been previously presented in literature and described as partial-retrofit intervention [27, 28]. Retrofit intervention is concentrated only on the exterior beam-column joints whilst some levels of joint damage and column inelastic mechanisms are accepted in interior beam-column connections as long as the global performance targeting collapse prevention, life safety and damage (given by drift or acceleration limitations) are achieved. This assumption would be further qualified by numerical inelastic dynamic analysis of as-built and retrofitted frames (in Chapter 9).

A corollary of this assumption is that the interior beam-column joints will be able to withstand the deformation and ductility demands but the seismic retrofit of the interior beam-column joints is out of the scope of this research. Studies have shown non-ductile interior beam-column joints having substantial residual gravity-carrying capacity despite apparent extensive

damage in the joint panel itself or in the interior columns [2, 22, 23, 29]. For life-safety and no-collapse performance limit states, the focus can be limited to the retrofit of the exterior beam-column joints, while for higher performance objectives such as damage control / immediate occupancy , the interior joints and base columns may require further retrofit treatment.

1.5 RESEARCH METHODOLOGY

The research methodology can be summarised in Figure 1.2 and can be divided into four distinct phases: Theory and Concept → Experiment → Numerical Modelling → Design Procedure.

The Selective Weakening (SW) retrofit will be first conceptualised from desktop studies and literature reviews on the problem, i.e. the seismic vulnerability of non-ductile RC frames and the available retrofit solutions. Drawing from the existing seismic assessment procedures of RC frames and beam-column joints with substandard detailing, the existing analytical framework is extended to provide a preliminary design procedure for the SW retrofit. By understanding the limitations of conventional seismic retrofit techniques – in particular with regards to the effectiveness, constructability and intrusiveness of the intervention, the design and implementation of the SW retrofit techniques for the exterior RC beam-column joints will be adjusted accordingly.

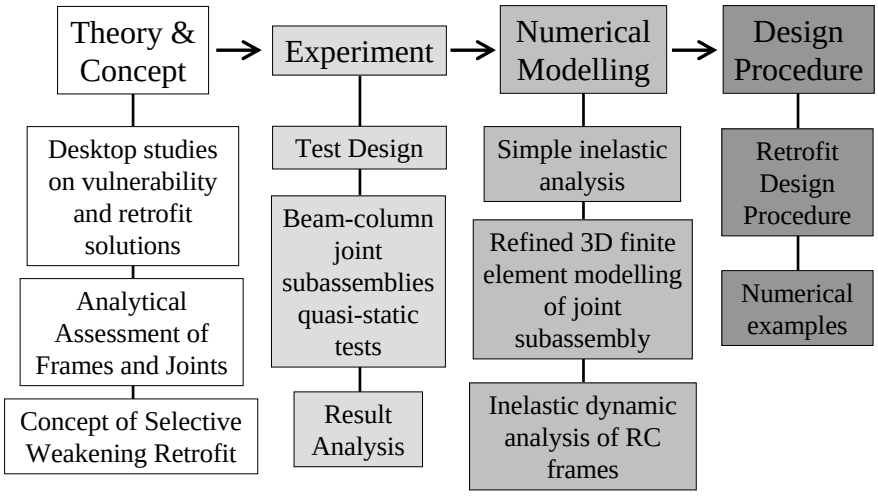

Figure 1.2: Four stages of the research methodology.

Next, the laboratory experiments will be designed and carried out to investigate the feasibility of the SW retrofit. Nine 2/3 scaled RC exterior beam-column joint subassemblies, as-built and retrofitted, will be tested under quasi-static reverse cyclic loading. Differential test matrix will be used in the experiments to provide clearer understanding of the influence of each

parameter: the level of joint external post-tensioning forces, the location of beam weakening, the presence of floor slab-transverse beam and the presence of column lap-splice.

The numerical modelling phase will be based on two levels of refinement: a) refined three-dimensional (3D) finite-element (FE) modelling of the beam-column joints subassembly using an advanced micro-plane fracture-mechanics based approach, and b) macro-level inelastic dynamic modelling using lumped plasticity two-dimensional (2D) models. The refined 3D FE model, calibrated against experimental results, is a powerful tool to conduct a parametric study of the governing retrofit design parameters. Furthermore, due to the inherently complex nature of the RC joints and the even more complicated retrofitted scenario, the use of fracture-mechanics based modelling allows for a more realistic representation of reinforcement-to-concrete bond, unconfined concrete joints and strength degradation. The macro-level inelastic dynamic analysis, on the other hand, is based on experimental and numerical calibrated hysteresis models, giving more practical and manageable insights of the dynamic response and global behaviour of retrofitted frames. However, due to time-limitation, only preliminary investigations will be carried out in the numerical modelling phase.

Lastly, a design procedure for the SW retrofit of the pre-1970s RC frames will be developed and proposed based on the insights and conclusions drawn from previous phases. Within this thesis, a preliminary design procedure would be developed for the design of the test specimen. The preliminary design procedure will then be discussed and refined in light of the lessons from the laboratory results. To facilitate implementation, the design procedure is aimed to be simple and straightforward for daily use of practitioner engineers.

1.6 THESIS ORGANISATION

The thesis is laid out in such a manner that the hypotheses and research questions presented in Section 1.3 are studied, researched and answered in a logical order. The dissertation is divided into ten chapters including this introductory **Chapter 1**.

In **Chapter 2**, the seismic vulnerability and typical structural deficiencies of pre-1970s RC frames and beam-column joints will be established based on desktop studies of RC seismic code development, literature studies and case study of actual pre-1970s buildings. Past field observations and laboratory studies of non-ductile exterior beam-column joints will also be

discussed. A seismic assessment procedure for non-ductile beam-column joints will be presented and extended for seismic evaluation of pre-1970s RC frames.

Chapter 3 will introduce performance-based seismic engineering and will evaluate existing seismic retrofit strategies and techniques for RC frames and beam-column joints. Drawing from existing research, the concept of the Selective Weakening (SW) retrofit for pre-1970s RC frames will be developed and presented. A retrofit design methodology for the SW retrofit of non-ductile RC frame and specifically the exterior beam-column joints is also included in this chapter.

Chapter 4 will describe the experiment design and test programme for the beam-column joint subassemblies quasi-static cyclic loading test. In particular, the specimens' design, details and assumptions will be given in detail. The material properties, testing setup, loading protocol, instrumentations and data processing will also be described to allow for replication of test by other researchers.

The test result of the as-built benchmark beam-column joint specimen (NS-O1) will be presented in detail in **Chapter 5.** Particular emphasis will be given to the influences of the poor bond associated with plain-round reinforcement and of the effects of column axial loads on the seismic performance and the joint shear mechanism of non-ductile joints. Albeit a short chapter, the results of the as-built specimen NS-O1 will serve as the reference-benchmark for all subsequent test results presented in the following Chapters 6, 7 and 8.

In **Chapter 6**, the experimental results of three retrofitted specimens: selective beam-weakening-only (NS-R1), joint post-tensioning only (NS-R2) and selective-weakening and joint post-tensioning (NS-R3 and NS-R4) will be presented. Emphasis will be given to the seismic performance of the retrofitted joints in terms of force-displacement hysteresis, energy dissipation and displacement capacities. The effects of the level of joint post-tensioning forces and location of beam-weakening on the success of the SW retrofit techniques will be discussed. The test results and the analytical-experimental comparisons will be discussed to highlight the limitations of the design procedure presented in Chapter 3.

Chapter 7 and **Chapter 8** will present the experimental findings on as-built and retrofitted beam-column joints with column lap-splice and floor slab-transverse beam stubs respectively. Chapter 7 will focus on the assessment of lap-splice capacity of plain round bars and the effect of lap-splice failure on the seismic behaviour of pre-1970s beam-column joints. In

Chapter 8, the test results will be discussed in light of the influences of floor slab and transverse beams onto the retrofit techniques' constructability, hierarchy of strength and overall seismic behaviour of pre-1970s exterior beam-column joints.

The numerical investigations will be presented in **Chapter 9**, with two distinctive parts. Firstly, the numerical investigation of the as-built (NS-O1) and the beam-weakening only (NS-R1) retrofitted exterior beam-column joints with a fracture mechanics-based continuum FE model will be presented. The numerical simulation focuses on replicating the failure mechanism and joint mechanics of the as-built and retrofitted joints, with particular emphasis on the demonstration of the applications and limitations of FE model on retrofitted joints. Secondly, the global seismic performance of as-built and retrofitted RC frames will be evaluated with non-linear dynamic analyses. The global building drift demands and the deformation/ductility demands of structural elements from the time-history analyses will be discussed in terms of different ground motion types, different SW retrofit techniques and relevance to the retrofit design procedure.

Chapter 10 will summarise the important results and conclusions from each phase of the research. Suggestions for future research will be presented with emphasis on the limitations of this work and potential for further investigations.

A collection of Appendices which provide supplementary experimental and numerical data is included at the end of the thesis:

Appendix A: Evaluation of the variation of axial load and the M-N performance domains of experimental beam-column joint subassemblies.

Appendix B: Appendix to Chapter 5 – experimental data for NS-O1.

Appendix C: Appendix to Chapter 6 – experimental data for NS-R1, NS-R2, NS-R3 and NS-R4.

Appendix D: Results of trial experiments of the SW repair and retrofit of exterior RC joints.

Appendix E: Appendix to Chapter 7 – experimental data for S-O1 and S-R3.

Appendix F: Appendix to Chapter 8 – experimental data for SL-O1 and SL-R3.

Appendix G: Appendix to Chapter 9 – Supplementary data to the numerical analyses.

1.7 CHAPTER 1 REFERENCES

[1] ASCE-SEI-41-06. (2007) *Seismic rehabilitation of existing buildings. ASCE standard ASCE/SEI 41-06*. American Society of Civil Engineers (ASCE), Reston, Va.

[2] Beres A, Pessiki S, White R, Gergely P. (1996) Implications of experimental on the seismic behaviour of gravity load designed RC beam-column connections. *Earthquake Spectra*. **12**(2):185-198.

[3] Bilham R. (2004) Global urban earthquakes: a safer world or worse to come? *Seismological Research Letters*. **75**(6):706-712.
[4] Calvi GM, Magenes G, Pampanin S. (2002) Experimental test on a three storey RC frame designed for gravity only *Proc. of 12th European Conf of Earthquake Eng*, Elsevier, London, UK.Paper No 727.
[5] Calvi GM, Moratti M, Pampanin S. (2002) Relevance of beam-column damage and collapse in RC frame assessment. *J of Earthquake Eng*. **6**(1):75-100.
[6] CEN. (2006) *European Standard EN 1998: Eurocode 8 - Design of structures for earthquake resistance - Part 3: Assessment and retrofitting of buildings*. Comite Europeen de Normalisation, Brussels.
[7] Fardis M, Negro P. (2005) *SPEAR: Seismic performance assessment and rehabilitation of existing buildings. International Workshop, Ispra 4-5 April 2005 Proceedings*. European Laboratory for Structural Assessment (ELSA), Ispra, Italy.
[8] FEMA-156. (1994) *Typical costs of seismic rehabilitation of existing buildings, 2nd ed.: Vol 1 - Summary*. Federal Emergency Management Agency (FEMA), Washington, D.C.
[9] FEMA-273/274. (1997) *NEHRP guidelines for the seismic rehabiliation of buildings (and commentary)*. Federal Emergency Management Agency (FEMA), Washington, D.C.
[10] FEMA-547. (2006) *Techniques for the seismic rehabilitation of existing buildings*. Federal Emergency Management Agency (FEMA), Washington, D.C.
[11] fib. (2003) *Seismic assessment and retrofit of reinforced concrete buildings: State-of-the-art report, fib Bulletin no. 24*. Intl. Fed. for Struct. Concrete (fib), Lausanne, Switzerland.
[12] Finn WDL, Ventura CE, Schuster D. (1994) Ground motions during the 1994 Northridge earthquake. *Canadian Journal of Civil Eng*. **22**(2):300-315.
[13] FRST Retrofit. (2009) Seismic Retrofit Solutions NZ. [Website] [cited 31th Dec 2009]; Available from: http://www.retrofitsolutions.org.nz/index.shtml
[14] Hall JF. (1996) Northridge Earthquake Reconnaissance Report. Supplement C, vol. 1. *Earthquake Spectra*. (11):1-523.
[15] Hamburger RO. (2009) Performance-based seismic upgrade of building structural systems: A 2020 Vision. *Proc. of ATC-SEI Conf, on Improving the Seismic Performance of Existing Buildings and Other Structures*, San Francisco, CA, p. 10-16.Plenary Paper.
[16] Holmes WT, Somers P. (1996) Northridge Earthquake Reconnaissance Report. Supplement C, vol. 2. *Earthquake Spectra*. (11):1-278.
[17] Ireland MG, Pampanin S, Bull DK. (2006) Concept and implementation of a selective weakening approach for the seismic retrofitting of R.C. buildings. *Proc. of 2006 NZSEE Conf*, NZSEE, Napier, NZ,
[18] Ireland MG, Pampanin S, Bull DK. (2007) Experimental investigations of a selective weakening approach for the seismic retrofit of r.c. walls. *Proc. of NZSEE Conf 2007*, NZSEE, Palmerston North, NZ.Paper No. 16.
[19] JBDPA-2001. (2001) *Standard, Guidelines and Technical Manual for seismic evaluation and seismic retrofit of existing reinforced concrete buildings. 1st English Version. Translated by Building Research Institute*. Japan Building Disaster Prevention Assoc. (JBDPA), Tokyo, Japan.
[20] Jensen J, Bull DK, Pampanin S. (2006) Conceptual retrofit strategy for existing hollowcore seating connections. *Proc. of 2006 NZSEE Conf*, NZSEE, Napier, NZ,
[21] Jensen J, Bull DK, Pampanin S. (2007) Experimental investigation of existing hollowcore seating connection: Seismic behaviour pre and post retrofit intervention. *Proc. of NZSEE Conf 2007*, NZSEE, Palmerston North, NZ.Paper No. 12.
[22] Lehman DE, Stanton J, Anderson DL, Alire D, Walker SG. (2004) Seismic performance of older beam-column joints *Proc. of 13th World Conf on Earthquake Eng*, Vancouver, Canada.Paper No 1464.
[23] Leon RT, Jirsa JO. (1986) Bidirectional loading of R.C. beam-column joints. *Earthquake Spectra*. **2**(3):537-564.

[24] NZSEE. (2006) *Assessment and improvement of the structural performance of buildings in earthquakes*. New Zealand Soc. for Earthquake Eng. (NZSEE), Wellington, NZ.
[25] NZSEE. (2010) New Zealand Engineer Mission to Padang, Indonesia. [Website] [cited 23rd Jan 2010]; Available from: http://db.nzsee.org.nz/EqPadang.xml
[26] Pampanin S. (2005) Vulnerability assessment and retrofit strategies for existing under-designed R.C. frame buildings. *Proc. of NZSEE 2005 Conf*, NZSEE, Wairakei, NZ,
[27] Pampanin S. (2006) Controversial aspects in seismic assessment and retrofit of structures in modern times: Understanding and implementing lessons from ancient heritage. *Bull of New Zealand Soc of Earthquake Eng*. **39**(2):120-133.
[28] Pampanin S, Bolognini D, Pavese A, Magenes G, Calvi GM. (2004) Multi-level seismic rehabilitation of existing frames and subassemblies using FRP composites. *Proc. of CICE 2004*, Adelaide, Australia,
[29] Pampanin S, Calvi GM, Moratti M. (2002) Seismic behaviour of RC beam-column joints designed for gravity loads. *Proc. of 12th European Conf on Earthquake Eng*, London, UK.Paper 726.
[30] Park R. (2002) A summary of result of simulated seismic load tests on reinforced concrete beam-column joints, beams and columns with substandard reinforcing details. *J of Earthquake Eng*. **6**(2):147-174.
[31] Park R, Billings IJ, Clifton GC, Cousins J, Filiatrault A, Jennings DN, et al. (1995) The Hyogo-ken Nanbu Earthquake of 17 January 1995. *Bull of New Zealand Soc of Earthquake Eng*. **28**(1):1 -99.
[32] Priestley MJN. (1997) Displacement-based seismic assessment of reinforced concrete buildings. *J of Earthquake Eng*. Jan 1997; **1**(1):157-192.
[33] Sezen H, Elwood K, Whittaker AS, Mosalam KM, Wallace JW, Stanton J. (2000) *Structural engineering reconnaissance of the August 17, 1999, Kocaeli (Izmit), Turkey, Earthquake. PEER Report 2000/09*. Pacific Earthquake Eng. Res. Center (PEER), Berkeley, CA.
[34] Sugano S. (1996) State-of-the-art in techniques for rehabilitation of buildings. *Proc. of 11th World Conf on Earthquake Eng*, Elsevier Science Ltd, Acapulco, Mexico.Paper 2175.
[35] Wang Z. (2008) A preliminary report on the Great Wenchuan Earthquake. *Earthquake Eng & Eng Vibration*. June 2008; **7**(2):225-234.
[36] Wu C-L, Chai J-F, Lin C-CJ, Lin F-R. (2008) Reconnaissance report of 0512 China Wenchuan Earthquake on schools, hospitals and residential buildings. *Proc. of 14th World Conf on Earthquake Eng*, Beijing, China.S31-004.

CHAPTER 2. SEISMIC VULNERABILITY AND ASSESSMENT OF REINFORCED CONCRETE FRAMES

"…making strong walls and buildings is the priority of our profession…"

Tsuneo Katayama, 2008

Opening speech at the 14th World Conference on Earthquake Engineering, Beijing

2.1 INTRODUCTION

A first step in developing any solution is to diagnose the problem properly. In the metaphor of a medical diagnosis of the non-ductile reinforced concrete (RC) buildings under seismic excitation, one must identify the medical records (i.e. historical development and understanding of the RC construction practice and building codes), observed symptoms (i.e. field observations from earthquake reconnaissance) and existing medical textbooks (i.e. existing experimental and analytical studies on non-ductile RC frames). Upon diagnosing the problem, further assessment or diagnostic tests onto identified critical issues are necessary. In the context of the vulnerability of pre-1970s RC frame structures, in-depth evaluation procedures of most probable failure mechanisms of non-ductile RC joints subassemblages are reviewed and summarised within a holistic seismic assessment framework.

The focus of this chapter is therefore divided into three areas:

(1) the seismic vulnerability of pre-1970s RC frames, with a particular attention to the New Zealand context;

(2) the seismic performance of non-ductile beam-column joints and;

(3) the seismic assessment of non-ductile beam-column joints and RC frame structures.

The information reviewed and summarised in this chapter forms the prerequisite knowledge in the development of an economical, non-invasive and effective retrofit solution.

Firstly, the seismic vulnerability of non-ductile RC frames is established with a review of the historical development of the RC building design in New Zealand. Typical structural deficiencies of pre-1970s non-ductile RC frames will be identified and discussed. Distinctions between the New Zealand practice and international practice prior to the 1970s will be highlighted. The scale of seismic vulnerability of the 1970s RC buildings in New Zealand will be discussed in light of existing literature and new database survey for the Christchurch pre-1970s building stock. Lastly, a desktop study on existing New Zealand RC buildings built between 1940s and early 1970s will be carried out to confirm the structural characteristics of the pre-1970s RC buildings in New Zealand.

Secondly, the deficiencies of joints typical of older construction with respect to the pre-1970s construction practice and code requirements will be discussed. The poor behaviour of joints typical of older construction can be attributed to the inadequate shear reinforcement and details in the joint region, the poor bond properties of plain round bars reinforcing, the inefficient anchorage into the joint core and, in a wider sense, the lack of capacity design considerations. Some examples of field observation of beam-column joint failures leading to structural collapse/damage will be reviewed. An extensive account of past experimental evidence of seismic behaviour of non-ductile RC beam-column joints will be presented. The insights on the existing literature gap in terms of as-built beam-column joint tests will be used to assist the design of the experimental research.

The third part of the chapter will present a framework for the seismic assessment of beam-column joint capacities, including the evaluation of the internal hierarchy of strength and expected sequence of events. State-of-the-art assessment tools to determining both the strength *and* the deformation capacities of various structural elements within a beam-column joint connection will be used in conjunction with an equivalent column moment (M_c) versus column axial load (N_c) interaction diagram analysis to identify the inelastic/failure mechanism of the beam-column joints. Some shortcomings of existing assessment tools will be discussed. The retrofit design procedure for Selective Weakening (SW) retrofit (to be presented in Chapter 3) is built on this seismic assessment framework.

2.2 SEISMIC VULNERABILITY OF RC FRAMES

2.2.1 Historical development of RC buildings design in New Zealand

Several years before the deadly Napier Hawke's Bay 1931 earthquake [62] that would dramatically change New Zealand construction practice, the first known New Zealand publication on earthquake design was written by C. Reginald Ford [84]. Ford's description drew heavily from the state-of-knowledge following the Kanto, Japan 1923 and San Francisco 1906 earthquakes as well as the construction practice from Japan and the USA. Legislations imposing lateral load design on buildings were introduced in Japan (1924 Urban Building Law, Revision of Law Enforcement Order) and in the USA (Field Act 1933 on public schools and Riley Act 1933 on non-residential large buildings). The seismic lateral loading imposed was a function of the total building mass, following the equivalent static force approach pioneered in Japan by Toshikata Sano [172].

The early legislations in New Zealand outlining the seismic design were the 1935 New Zealand Standard (NZS) Model Building By-Law [158] and the 1939 NZS Code of Building By-Laws [159]. Both documents specified a seismic coefficient of 0.08g and 0.10g of building weight for ordinary and public buildings respectively, which were consistent with the international practice then. This lateral force was taken to be a continuously applied force up the building height. A maximum seismic coefficient of 0.15g was also imposed in addition to the requirements of tying the building together and induced torsional moment design. For RC structures, the materials' working stresses under combined gravity and lateral loading were allowed to be increased up to 25% of the allowable stresses. The allowable stress for mild steel in bending was 124MPa (18000psi) and for concrete compression in bending section was 5.2-6.7MPa (750-975psi). The 1935 By-law [158] was not compulsory and depended on the adoption by local territorial authorities.

The 1955 revision of the NZS Standard Model Building By-Law (NZS95:1955) [95, 160] introduced an inverted triangular distribution of horizontal load as an alternative loading pattern with seismic coefficients of 0.12g and 0 at the top and bottom of the structure respectively. While this reflected better understanding of the 1st mode dynamic loading on multi-storey structures, NZS95:1955 [160] lacked significant improvement in terms of RC seismic design and detailing. The provision for shear resistance of concrete elements was tightened and the requirement of 135° anchorage for stirrups was included. The contribution of the concrete shear resistance, v_c, at

different levels of shear stress was better defined in the 1955 code. Another notable change was the inclusion of average (as well as maximum) permissible bond stresses and the relaxation of the maximum allowable bond stress limitation of 150psi (1034kPa). Furthermore, explicit definitions of deformed and plain round bars were given with (only) 10% higher allowable bond stresses specified for deformed bars.

The NZS1900:1964 code [163, 164] was a significant evolution from its predecessors, proving increased understanding of seismic hazards and RC seismic design [7, 44]. In particular to the seismic coefficient calculation, three seismic zones with the maximum seismic coefficient ranging from 8% (zone C) to 12% (zone A) were introduced to better represent the regional seismicity of New Zealand. The magnitude of seismic force was formed as a function of the building natural period and the inverted triangular force distribution up the building was modified to account for higher mode dynamic effects. More importantly, the concept of structural ductility was introduced with the stated assumption of 5-10% of damping for structural ductility of four.

However, no provision for ductile RC detailing or modern capacity design considerations was included. NZS1900:1964 was based on the working stress concept for member design despite the introduction of ultimate limit states design in other contemporary international RC codes [7, 44]. These shortcomings led New Zealand engineers to adopt (part of) overseas codes such as the 1966 SEAOC recommendations [214] for the design of ductile structures by the late 1960s. It was noted [78] that the British Standard CP-114 [21] was also widely used in the design of RC buildings in New Zealand prior to the 1970s [142]. Plain-round bars were still extensively used up to the mid-1960s [184].

Due to language and cultural factors, the pre-1970s engineering practice in New Zealand was closer to the USA and British practice, when compared to other seismically active regions such as Japan and Mediterranean nations. However, as shown in the two examples of pre-1970s RC construction practice from Italy and New Zealand in Figure 2.1, the RC construction practice was quite similar and consistent in terms of non-seismic detailing.

A 1950s Italian gravity-designed only RC frame (Figure 2.1a) exemplifies the use of double-180° hook anchorage into the joint and column lap-splice at the plastic-hinge region. In the New Zealand 1960s RC building example (Figure 2.1b), while the anchorage detail was improved with longer development lengths provided and 90° hooks anchorage of beam longitudinal bars, no joint reinforcement was provided and column lap-splices just above floor

levels were used. In both examples, the column transverse reinforcing were inadequate and plain-round bars were used. The use of plain-round bars also led to the use of 180° hook lap splices in both examples.

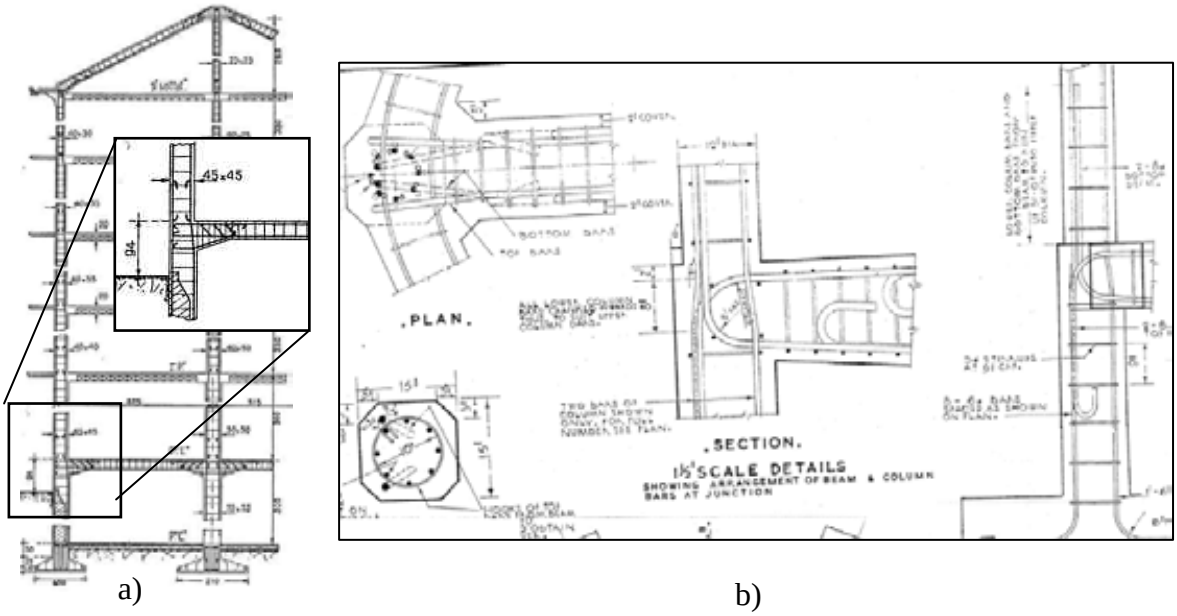

a) b)

Figure 2.1: Pre-1970s RC construction practice: a)Typical Italian 1950s gravity-designed RC frame (taken from [209]); b) RC beam-to-column and column detailing in Christchurch, New Zealand circa 1960s (Uni. Of Canterbury archive).

By the mid-1960s, the concepts of modern seismic RC design and detailing began to take form. The work by Blume, Newmark and Corning in 1961 [33] pioneered the concept of ductile RC buildings and introduced detailing for ductile RC elements. The 1966 SEAOC recommended lateral force requirements [214] was the first codification of the design and detailing of ductile moment-resisting RC frames. Requirements for confinement and anti-buckling reinforcement within the plastic-hinge regions were introduced. Lapping of column bars in potential plastic hinge regions was prohibited. However, in the Blume *et al.* textbook [33], there was conspicuous absence of design and detailing recommendation for beam-column joints.

The importance of beam-column joint design and detailing was first highlighted in the 1966 SEAOC recommendations [214] based on preliminary experimental results [23, 40, 98] from the Portland Cement Association. The lack of experimental studies on the seismic behaviour of the beam-column joint connections led to many significant studies in the late 1960s [58, 99, 106] and early 1970s [97, 100, 113, 143, 147, 185, 193, 205, 220, 227] around the world, cumulating in the ACI-352 Committee report in 1976 [10]. The 1971 ACI-318 code [8] contained

an appendix of special provisions for seismic design, which included some of the aforementioned innovations and provisions for beam-column joint shear design. Figure 2.2 gives some examples of the RC beam-column joint theory and detailing introduced in the 1970s.

However, the 1971 ACI-318 concrete code [8] did not have any capacity design provisions [186]. Neither minimum column-to-beam flexural strength ratio nor over-strengths from plastic actions in the flexural hinges or slab-flange effect on the beam negative moment capacity were considered. Furthermore, the shear design provisions for flexural-hinging elements and beam-column joints were significantly lower than modern design codes. The 1971 ACI-318 [8] and the 1966-1973 SEAOC recommendations [214, 215] also allowed 50% of the beam longitudinal bars to be bent away from the joint core at the exterior beam-column joint. 180° hook was not prohibited though the 90° hook was preferred for longitudinal beam bar anchorage into joint region (as shown in Figure 2.2a). The bend-away 90° hook or 180° hook anchorages were then acceptable as the anchorage of the longitudinal beam bars into the joint was considered primarily as a transfer of beam-bond force, as described in the 1976 ACI-352 [10]. These apparent deficiencies reflected the limitations of the early 'modern' RC seismic design code for buildings constructed prior to the 1980s.

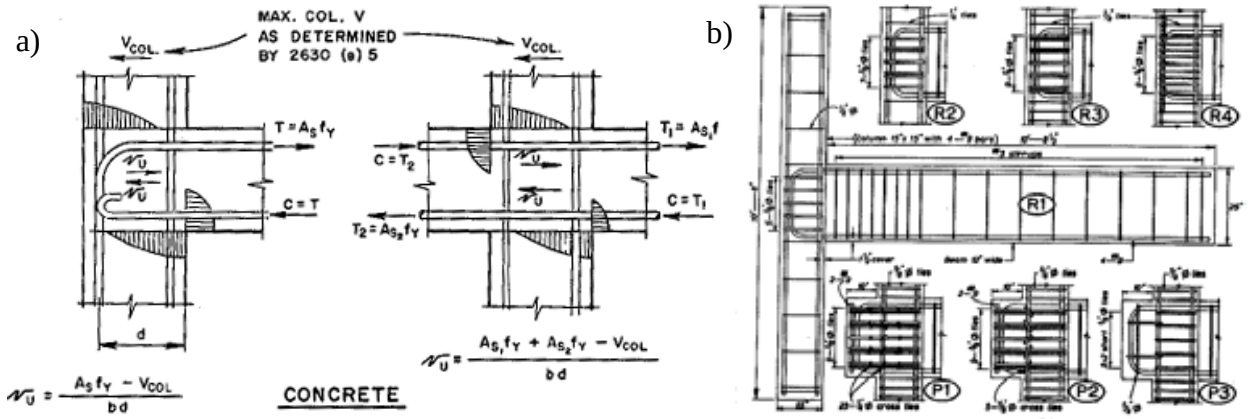

Figure 2.2: Design and detailing of exterior beam-column joints: a) Joint shear model presented in 1973 SEAOC recommendations [215]; b) Various configurations of joint detailing tested in New Zealand[187].

In 1969, JP Hollings [107] introduced a step-by-step design procedure to achieve beam-hinging inelastic mechanism in RC frames under seismic loading, which was the prelude to the concept of capacity design. Recommendations included the use of confining transverse reinforcing and equal top and bottom longitudinal reinforcing for the ductile detailing of the plastic hinges in the beams. The 1970 Ministry of Work's Code of Practice for Design of Public

Buildings [78, 142, 152] adopted many ductile detailing recommendations from the 1966 SEAOC recommendations [214] and the 1971 ACI-318 code [8].

This development encouraged New Zealand researchers to make further experimental studies to validate the recommendations within the 1971 ACI-318 code [8]. Park and Paulay, in their seminal publication in 1975 [187], outlined many concepts of modern seismic RC design and detailing, including a rigorous design procedure of RC frames under the capacity design philosophy originated from New Zealand research. Many innovations, including the use of ultimate strength method in member section design, joint zone reinforcement in beam-column joints, column confinement and anti-buckling transverse reinforcement requirements and capacity design philosophy, were disseminated into the New Zealand engineering practice and building codes [167] from the mid-1970s onwards[186].

The provisional NZS3101 code, published in 1972 [165], also adopted many parts of the 1971 ACI-318 code [8] and some of the recommendations were from the draft version of ref [187]. However, not until the revamp of the New Zealand loading code NZS4203 in 1976 [167], the update of the ACI-318 code in 1977 as well as the various drafts of the 1982 edition of the NZS3101 concrete design standard [166], that modern seismic design for RC buildings was fully codified in New Zealand. In his Hopkins Lecture in 2000, Park [183] gave a critical discussion of the development of seismic engineering in New Zealand in the past fifty years. Others have attempted to outline the historical development of seismic design in New Zealand [142] as well as to compare the current RC design to the past New Zealand provisions [167].

2.2.2 Typical deficiencies of pre-1970s non-ductile RC frames in New Zealand

The preceding review of the development of RC seismic design in New Zealand establishes a clearer understanding of the typical deficiency of pre-1970s non ductile RC frames in New Zealand. The following sub-sections will discuss some of the typical deficiencies of pre-1970s non-ductile RC frames, while §2.3 will look specifically into the deficiencies of pre-1970s beam-column joints. §2.2.4 will provide some illustrative case study of buildings examples of these deficiencies in New Zealand.

2.2.2.1 Inadequate seismic and lateral force design requirement

Without explicit design for lateral-force resistance, for example, buildings constructed prior to NZS95:1955 provisions, pre-1970s RC frames generally have insufficient lateral strength

capacity and inadequate lateral stiffness owing to small columns dimensions. Figure 2.3 shows the evolution of the seismic coefficient for the lateral system design up to the 1976 NZS4203 [168]. Brunsdon [38] has shown that for short period RC frames ($T \leq 0.45$sec), pre-1970s buildings were under-designed by 40% to 60% (depending on the site seismicity) when compared with the NZS4203:1976 [168].

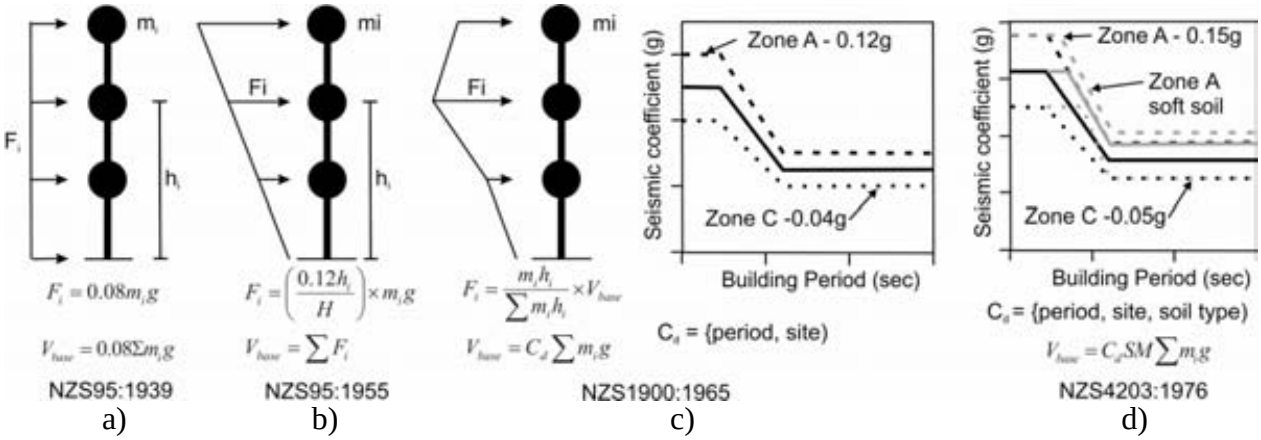

Figure 2.3: Seismic coefficient for the lateral system design: a) NZS95:1939 [159], b) NZS95:1955 [160], c) NZS1900:1965 [163], and d) NZS4203:1976 [168].

In a more recent study, Fenwick and MacRae [78] have shown that the pre-1970s RC frames were generally flexible, with 25%-50% of modern code stiffness requirements. By comparing the pre-1970s design base shear in terms of the current loading standard (NZS1170:5 [161]), the associated structural ductility demands (based on the NZS1170:5) ranged between 2.0 for low seismicity region and long period and 9.8 for high seismicity region and short period.

2.2.2.2 Absence of capacity design philosophy

In capacity design principles [187, 196], specific provisions have been adopted to ensure the formation of the desired beam-sway inelastic mechanism in RC frames under earthquake attacks. As such, brittle shear and anchorage failures in all structural elements and column flexural hinging part from the column at the base are specifically excluded as possible failure mechanisms. Amplifications of demand from dynamic high-mode effects and flexural over-strength effects from plastic hinges in the beams are explicitly considered.

In absence of these capacity design principles in pre-1970s RC frames, unexpected brittle failures or weak-column strong-beam soft-storey collapses are highly probable in the event of a large earthquake. An obvious evidence of the lack of capacity design considerations is the

presence of large beam depths with higher capacities when compared to the columns in the pre-1970s RC frames.

Another consequence of the absence of capacity design principles is the overlook of the flexural over-strengths from various mechanisms such as reinforcement strain-hardening and slab-flange effects. In traditional gravity-load-only design, these are considered additional conservatisms but in modern seismic design, the over-strengths can change the internal hierarchy strength of the beam-column joints leading to undesirable column flexural hinge or shear failures.

Thus, a direct and effective retrofit strategy could aim at modifying the internal hierarchy of strengths of the RC frames such that capacity design principles are respected and beam-sway inelastic mechanism is activated.

2.2.2.3 Inadequate transverse reinforcement

Inadequate transverse reinforcement in the columns is principally consequences of the lack of capacity-design consideration and the lack of specifications of transverse reinforcement in providing confinement and anti-buckling restraints. Consequently, the columns in non-ductile RC frames are susceptible to flexural, shear and axial failures. A column-sway (soft-storey) inelastic mechanism generally has excessive curvature and ductility demands such that collapse is often inevitable. The non-ductile behaviour of columns with inadequate transverse reinforcement is well documented in literature (e.g. [72, 206, 218]).

Based on the historical seismic code development presented in §2.2.1 and the case-studies to be presented in §2.2.4, it is concluded that the columns in pre-1970s New Zealand RC frames, in particularly public buildings designed by the New Zealand Ministry of Works [151], were generally better designed, in comparison to the contemporary construction practice around the world. Some New Zealand designers aptly used larger column dimensions, higher column reinforcement ratio, smaller column stirrups spacing and distributed column bars than required in the building codes of those times. In addition, 135° anchorages for transverse reinforcement, which allowed for improvement confinement and anti-buckling performance, had been specified in the New Zealand codes [95, 160] since the 1950s. In North America and Mediterranean nations, poorly anchored transverse reinforcing (with 90° closed stirrup or unclosed stirrups) were still widely used until the introduction of modern seismic code in the mid 1970s.

In comparison to the columns, shear reinforcement in the beams in pre-1970s RC frame was generally adequate. Prior to the 1955 NZS95 [160], due to the lack of understanding of

shear-transfer mechanism in flexural elements, all shear forces due to gravity loading in the beams were designed to be taken by steel reinforcement. This apparent conservatism was lost in between 1955-1976 New Zealand concrete codes as the shear resistance contribution from concrete was allowed to be accounted for in the plastic hinge region of the beam. Further problems arose from the lack of anti-buckling and confinement requirements for transverse reinforcement that was more critical in terms of ductility capacity.

2.2.2.4 Inadequate beam-column joint design and detailing

While the nascent seismic engineering practice in the early-1960s to early-1970s had started adopting many basic 'good practices' described above, the beam-column joints were still generally neglected and not designed for. Typical pre-1970s 'non-engineered' beam-column joints principally had three major inadequacies: a) absence of horizontal and/or vertical transverse reinforcement; b) non-ductile anchorage of beam longitudinal bars into the joint; and c) lack of reliable joint shear transfer mechanism beyond diagonal cracking. §2.3 will discuss further the seismic vulnerability of these non-ductile beam-column joint detailing.

2.2.2.5 Problems of anchorage, development lengths and splices

The development lengths at anchorage and lap splices were generally inadequate in pre-1970s RC structures. This stemmed from three factors: a) the use of plain-round bars and lap-splices with 180° hooks in New Zealand prior to the mid-1960s [184]; b) the common practice of lapping column longitudinal reinforcing with column starter bars at floor levels, which were potential locations of moment reversal plastic hinges in the columns; and c) scarce experimental data and understanding on cyclic behaviour of bond of reinforcement and concrete. The influence of insufficient anchorage and development lengths on the seismic behaviour of as-built and retrofitted beam-column joints will be further discussed in §2.4.5.

The use of plain round bar reinforcing with poor bond behaviour was typical of the pre-1950s practice in the USA, the pre-1960s in New Zealand/Japan and the pre-1970-80s (mostly) elsewhere around the world [5, 42, 74, 132]. For example, in the 1955 NZS95 [160], a column lapping length of $40d_b$ was specified for straight plain round bars, while 10% increase in allowable working bond stress was specified for deformed bars. Deformed reinforcement was formally introduced in the 1964 NZS1900 concrete code [164] after the publication of the 1962 NZS1693 specifications for deformed reinforcing [162]. Minor increases in allowable stresses for

flexural, shear and anchorages were given in the 1964 NZS1900. In the USA, deformed bars were introduced much earlier due to the introduction of various propriety deformed reinforcement [5]. Only by the mid-1970s the seismic codes for RC specified longer development lengths for plain-round bars, in which the development lengths for plain-round bars were twice of the required values for deformed bars.

2.2.2.6 Other features/deficiencies not considered in this research

Some other deficiencies of pre-1970s RC frames that could potentially lead to non-ductile failure will not be considered in this research. These are generally unique problems that would require further independent studies to quantify their influence on the seismic retrofit of pre-1970s RC frames.

- Presence of masonry infill panels made of clay bricks or concrete block masonry and distributed partially or uniformly up the height could lead to unexpected structural-infill interaction and premature structural failures [59, 137, 219].
- Deep spandrel beams or partial-height infill without separation from the columns could lead to short-column effects. This problem is well recognised and available retrofit techniques are also available in literature [90, 169].
- The influence of material variability on the seismic behaviour of pre-1970s RC frames could be significant. In-situ test [38] and literature [169, 203] suggested that the most probable strength of aged concrete in pre-1970s RC buildings was approximately 1.5 times the specified values and could thus be in the range of 25-30MPa (for specification of 16-20MPa). However, there were other occasions where very low concrete strengths (8-10MPa) were found, due to poor quality of construction (e.g. [216]). For the steel reinforcement, probable yield strength was likely to be the characteristic values of the specified yield strength (227-275MPa for pre-1970s RC construction).

Lastly, it is interesting to note that the aforementioned construction practices are still common in many non-seismic countries. The widely used British BS-8110 concrete code [39, 120], for example, does not explicitly specify the transverse reinforcement requirements for beam-column joints. Figure 2.4 below shows some examples of standard construction practice taken from non-seismic design guidelines [109], confirming the non-ductile detailing discussed in the preceding paragraphs.

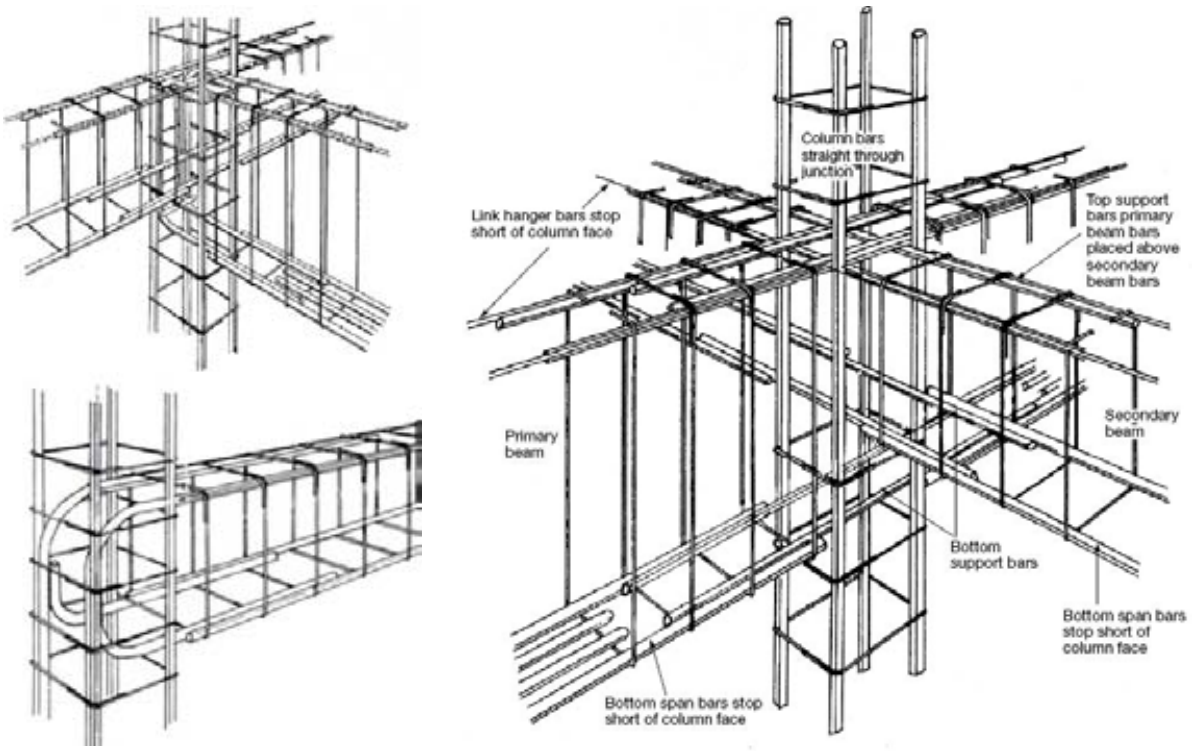

Figure 2.4: Examples of non-ductile detailing in modern non-seismic construction practice (e.g. as per BS-8110:1997 [39]). Illustrations are taken from ref. [109].

2.2.3 Scale of problems of pre-1970s non-ductile RC frames in New Zealand

Limited systematic studies [32, 38] are available in terms of understanding the actual scale of the problems of earthquake-prone RC buildings in New Zealand despite the plethora of information within the database of local territorial authorities from the building consent process.

Brunsdon and Priestley [38] surveyed the existing RC buildings built between 1936-1975 within the three Central Business Districts (CBDs) of Wellington, Christchurch and Lower Hutt. Within the three CBDs, there were 82 buildings with more than 3-storey built between 1936 and 1975. Without adequate assessment and modelling of the beam-column joints, Brunsdon concluded that while inherent conservatism existed in the working-stress design and relevant factor-of-safety, column and joint shear failures were limiting the ductility capacities of the RC frames.

In a more recent study by Blaikie and Spurr [32], a survey of Wellington CBD and the associated seismic risk of RC buildings built between 1935 and 1975 was carried out. 374 multi-storeys RC buildings were surveyed with 48% having four-storey or more. The survey data presented in Figure 2.5 indicate the shifting trend of the dominant structural systems with frames

with perforated wall buildings in the 1950s, wall and dual wall-frame buildings in the 1960s and predominantly frame buildings in the early 1970s. In particular, RC frame system was widely used for tall buildings (with ten storeys or more). The study also confirmed the widespread problem of non-ductile beam-column joints, inadequately confined and reinforced columns and absence of capacity-design criteria to ensure weak-beam/strong-column mechanism. The use of plain-round bars was also noted in buildings constructed in the late 1950s and the early 1960s. The study suggested that RC frame buildings built in the mid 1960s to early 1970s in New Zealand often had closer tie spacing in the columns when compared to international practice of the same period.

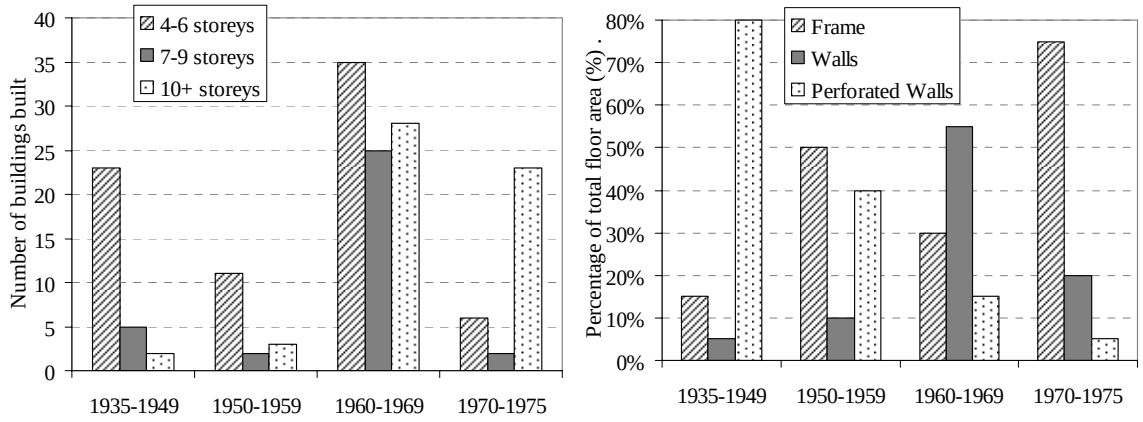

Figure 2.5: Representation of distribution of heights, year of construction and type of lateral-resisting systems for RC buildings with four storeys or more in Wellington CBD (data taken from [32]). The bottom axis is the year of construction.

Christchurch city has a mix of newer RC buildings with modern detailing and older non-ductile reinforced concrete structures. Using the building data provided by Quotable Value New Zealand Ltd and confirmed by visual walk-about survey, Figure 2.6 illustrates the distribution of number of storeys of mid- to high-rise RC buildings categorized by construction age. 126 mid-to high-rise RC building were identified within a set of 736 'concrete' buildings. A recent review [101] of the heritage buildings within the Christchurch City Council (CCC)'s City Plan shows that out of the 490 heritage-listed buildings, 29 are non-ductile RC buildings. Most (21) of these 29 buildings were built in intra-war periods of 1920-1939. This was consistent with Brunsdon and Priestley's study [38] in the 1970s, which indicated about 40 non-ductile RC buildings (both non-heritage and heritage) in Christchurch CBD.

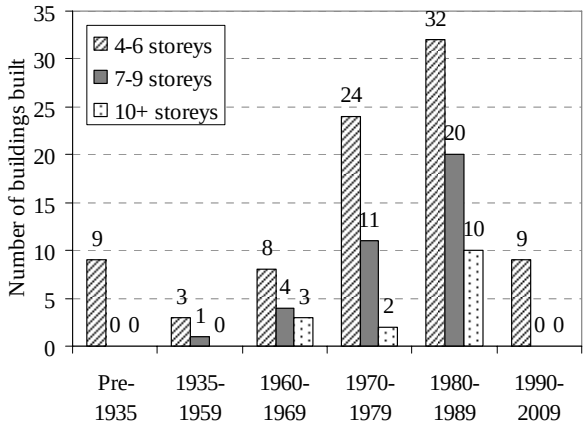

Figure 2.6: Buildings storey distribution for RC buildings within the City Center and above 3-storey. (Source: Quotable Value New Zealand Ltd).

In terms of the scale of implementation of seismic retrofit of non-ductile RC buildings in New Zealand, there is no existing literature despite many seismic retrofit implementations for unreinforced masonry buildings had been carried out since (at least) 1968. A legislation [157] on high-risk buildings was introduced in 1968, where high risk buildings were defined as unreinforced masonry structures that would exceed ultimate capacity under one-half (50%) of the NZS1900:1964 seismic loading [163]. This 1968 legislation was subsequently incorporated in a whole form into the New Zealand building legislations, including the 1991 Building Act [29].

During the revision of the 1991 Building Act, driven by the lessons of Northridge 1994 and Kobe 1995 earthquakes, substantial changes were proposed and adopted in the 2004 Building Act [61]. It redefines earthquake-prone buildings as those which ultimate capacities would be exceeded in moderate earthquakes of one-third as strong as the new seismic loading requirements. In the 2004 definition, Earthquake-Prone Buildings (EPBs) are not limited to any particular structure type. In 2006, the New Zealand Society for Earthquake Engineering (NZSEE) published a set of seismic assessment guidelines [169] for various building types to assist the implementation of the 2004 Building Act. Various examples of implementation of seismic retrofit in New Zealand are available in literature (e.g.[54]).

Section 122 of the 2004 Building Act defines the EPB as a building with its ultimate capacity exceeded in a *moderate earthquake* and would likely to collapse causing injury or death or damage to neighbouring properties. A *moderate earthquake* is defined as an earthquake that would generate shaking with the same duration but that is one-third as strong as the design earthquake shaking for new buildings at that site. The NZSEE guidelines give an interpretation of

the terminologies of the 2004 Building Act and define EPBs as buildings with one-third as strong as the New Building Standard (NBS) or 33%NBS lateral capacity.

Given that non-ductile RC frame can result in brittle, catastrophic collapse in the event of strong seismic shaking that exceeds their lateral strength capacity, in a binary 'elastic or collapsed' response, it could be argued that the 2004 Building Act legal requirement is inadequate to achieve the acceptable likelihood of injuries, death and damage to neighbouring properties. Therefore, a performance-based seismic assessment and retrofit approach, as espoused by this research, is necessary to achieve the desirable ductile collapse mechanism, while still respecting the economics needs to accept some level of risks and damage in a moderate seismic event.

2.2.4 Case study on New Zealand existing buildings

Some tens of buildings constructed between the 1940s and early 1970s were surveyed and studied to confirm the structural characteristics of the pre-1970s RC frame buildings in New Zealand. The initial survey exercise was carried out by the author with two fellow postgraduates - Umut Akguzel and Dion Marriott, with inputs from the Seismic Retrofit Research Board (SRRB) consisting of practicing New Zealand engineers. Building construction drawings were taken from the University of Canterbury's MacMillan Brown Library and Facility Management collections, Christchurch City Council's building consent archives and SRRB members' contributions. In this section, two case studies of non-ductile RC frame buildings are presented and reviewed qualitatively in terms of their seismic deficiencies.

Building A is a four-storey RC office building designed and built in the 1950s by the New Zealand Ministry of Works. On the long direction, it consisted of five-bay RC frames with brick infill and on the short direction, it consisted of three-bay RC frames. In the front elevation, there is a perforated wall with frame reinforcing detailing, as shown in Figure 2.7a and Figure 2.8a. Figure 2.7b shows the structural detailing of the transverse frames. The columns were tapered from 16" (406.4mm) squares at the first two floors to 14" (355.6mm) squares at upper stories. The beams were 24" (609.6mm) deep by 12" (304.8mm) wide. In all the frames, column stirrups were typically ¼" bars at 10-11" spacing (i.e. 6mm diameter at 250-280mm centres) while the beam stirrups were 3/8" bars at 12" spacing (9.5mm diameter at 305mm centres). Beam-column joints were not reinforced with stirrups. The beam longitudinal bars anchored into the joints were using 90° hooks and 180° hooks for the top and bottom beam reinforcing respectively.

Reinforcing details for the exterior and interior beam-column joints are shown in Figure 2.8b & c. Column reinforcing were spliced with 24db lapping length, with probable assumption of compression-only lap design for plain round bars.

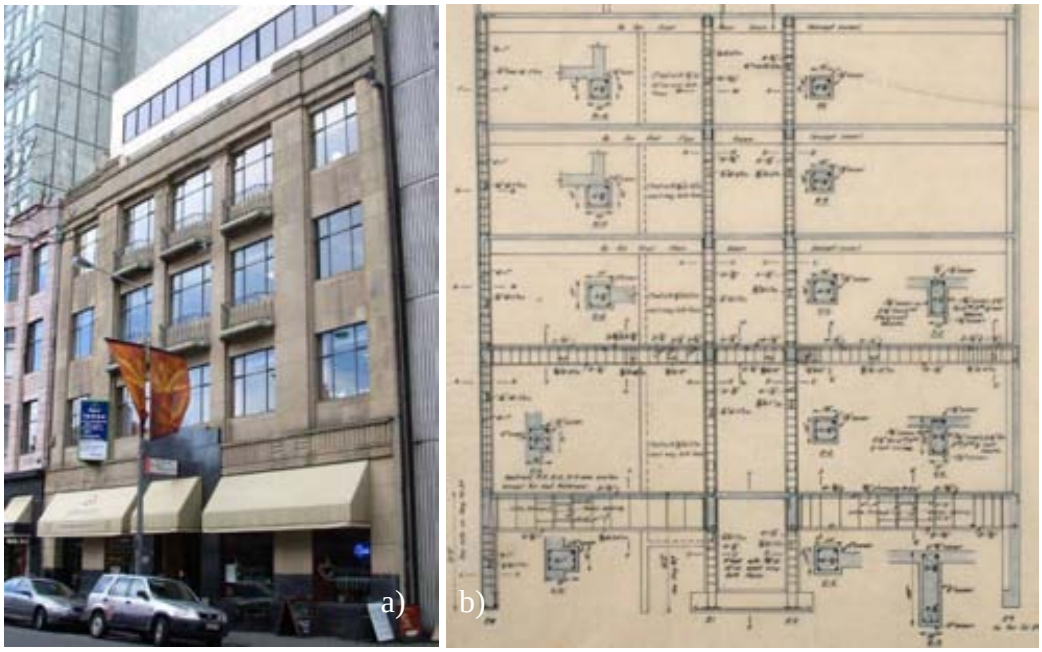

Figure 2.7: Case study building A: a) Front elevation wall with large openings; b) Structural detail of the RC frame in the transverse direction.

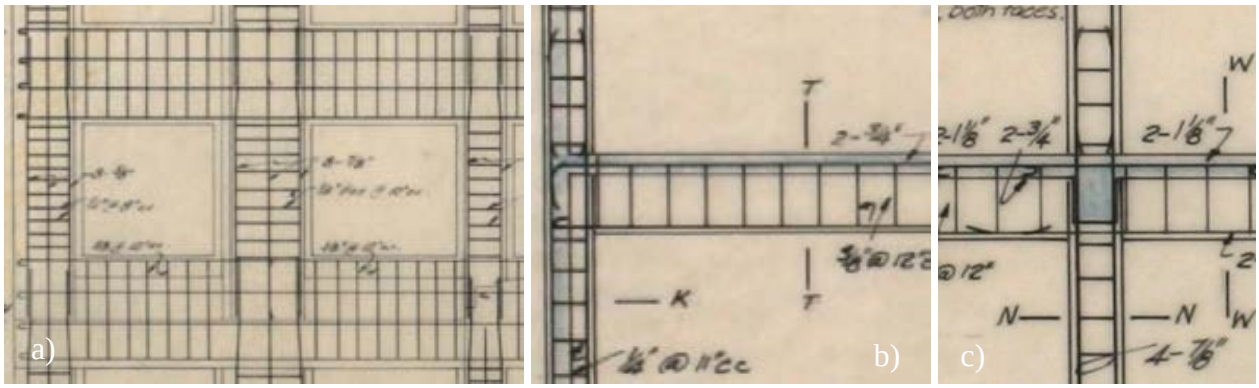

Figure 2.8: Case study building A: a) Reinforcing details of the front elevation perforated wall; b) Reinforcing details of the exterior beam-column joint; c) Reinforcing details of the interior beam-column joint

Building B is a six-storey RC office building designed and built in 1965 by a private engineering firm. It consisted of five-bay front elevation frame, two-bay internal frames and cast-in perforated RC back walls in the transverse direction. In the longitudinal direction, the most probable lateral system was the combination of external perforated-walls and internal irregular multi-bays frames. For the internal frames, the columns were 22”(558.8mm) and the beams were

mostly 30”(762mm) deep by 16”(406.4mm) wide. For the front elevation frame, 4’ (1200mm) deep 9” (228.6mm) wide spandrel beams were used in conjunction with 14” (355.6mm) columns. Reinforcing details of the spandrel beams and the joint connections are given in Figure 2.9b.

The dimensions of the beams and columns within Building B frames were marginally larger for the approximately same tributary areas when compared to Building A. More transverse reinforcing were used in both the columns (3/8” bars at 9” spacing i.e. 9.5mm at 228.6mm) and the beams (3/8” bars at 6” spacing i.e. 9.5mm at 152.4mm at beam ends). Noticeably, in Building B, closer spacing of transverse reinforcement was used in the supposed beam plastic hinge regions (see Figure 2.9c). As with Building A, no joint shear reinforcement was used in Building B. In both buildings, lap-splices were placed in locations of potential plastic hinges. In Building B, longer lapping lengths were used in the columns (36 times bar diameter, d_b), as full tension force was expected to be developed in those lap-splices. From the column lap-length, it could be inferred that deformed bars were used in Building B, as the older NZS codes [160, 164] allowed for 10% reduction in lap-length for deformed bars (compared to $40d_b$ requirement for tensile lapping).

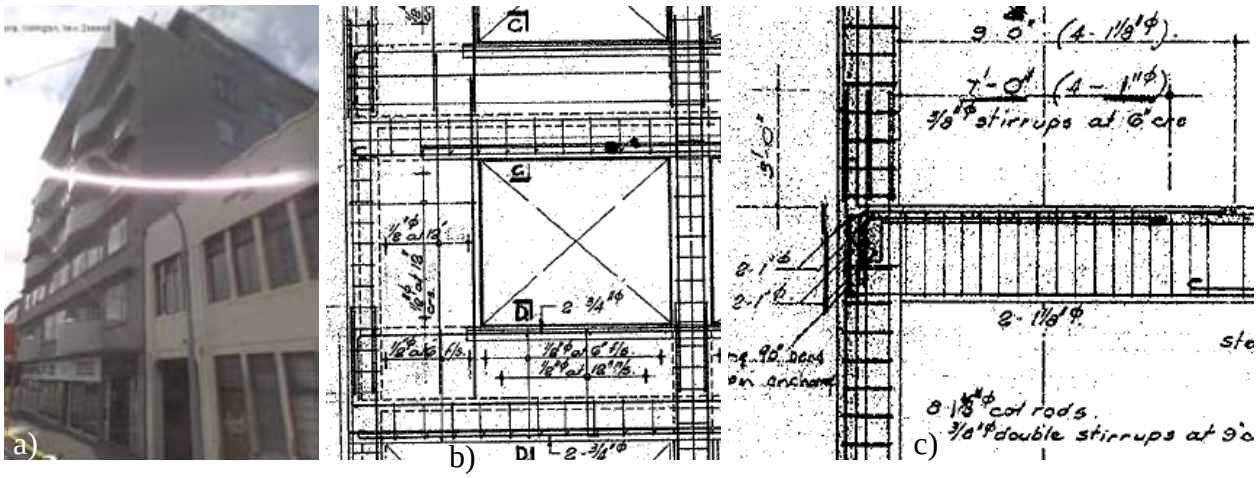

Figure 2.9: Case study building B: a) Front elevation frame and side elevation perforated RC walls; b) Beam-column joint and deep spandrel beam detailing of the front frame; c) Reinforcing detailing of the exterior beam-column joints within the internal frames.

2.3 SEISMIC PERFORMANCE OF NON-DUCTILE RC BEAM-COLUMN JOINTS

2.3.1 Deficiencies of pre-1970s RC beam-column joint connections

The beam-column joint is a critical weak link in pre-1970s RC frame structures because of its complex nature and its conspicuous absence from the early seismic codes as illustrated in §2.2.1. Early attempts [58, 99, 144, 185] of analytical frameworks for beam-column joint shear

mechanism had been controversial, though rationalised modern seismic design of RC beam-column joints had been achieved through multi-national research [9, 112]. However, the nearly-universally accepted joint shear model [4, 9, 99, 167, 195, 196] for modern well-designed beam-column joints, based on the truss mechanism and the diagonal strut mechanism, is not entirely suitable for the assessment of pre-1970s RC exterior beam-column joints with no or limited joint shear reinforcement. Considering the lightly reinforced joint core, an alternative based on principle tensile and compressive stresses may be more suitable for the assessment of these joints [91, 178, 180, 202, 203]. This will be further discussed in §2.4.5.

The primary deficiency of pre-1970s beam-column joints was the inadequate joint shear reinforcement, which was essential for post diagonal cracking shear transfer, joint shear capacity, anti-buckling of the column bars and confinement of the joint core concrete [4, 196]. Prior to the introduction of modern seismic codes, beam-column joints were not properly "engineered", and were treated either as construction joints or as part of the columns [99, 100, 187]. Consequently, these beam-column joints would have none, single or few joint stirrups, as schematically shown in Figure 2.10.

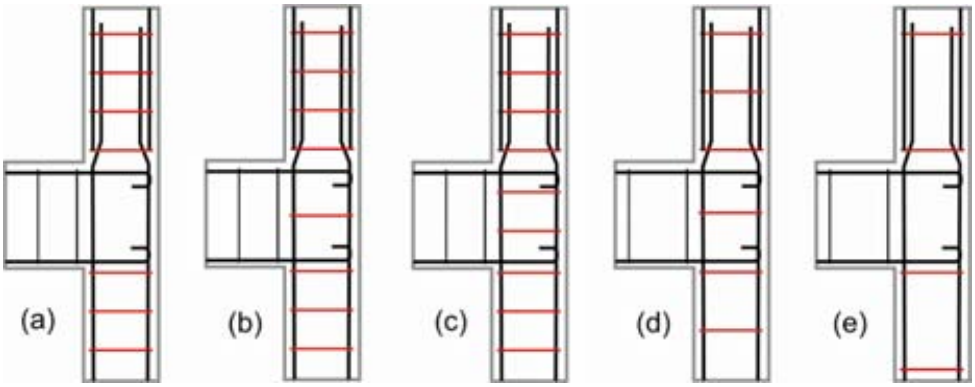

Figure 2.10: Schematic illustrations of joint stirrups in relation to the column stirrups and pre-1970s design assumptions: a-b) Joint neglected or considered as construction joint; c-e) Joints were treated as part of column, therefore quantity of joint stirrups depended on column stirrup spacing and beam depth.

When the beam-column joints were assumed as construction joints, either none or very few stirrups would be arbitrarily included, regardless of the column stirrup spacing as shown in Figure 2.10a and b. When the joints were treated as part of the columns, the quantity of joint stirrups would therefore depend on the column stirrup spacing and beam depth, as illustrated from Figure 2.10c to e. As the maximum allowable column stirrup spacing was large (least of 2/3 h_{col}, 12$d_{b,col}$ and 12'(304.8mm))in the 1955 NZS95 concrete code [160] and was even larger (least

of h_{col}, $16d_{b,col}$ and $48\ d_{b,col\text{-}st}$) in the 1963 ACI-318 code [7], either none, single or double stirrups could be expected within most beam-column joints constructed prior to the 1970s.

Another critical deficiency of the pre-1970s exterior beam-column joints was the ineffective anchorage of beam longitudinal bars into the joint core. In absence of sufficient confinement from the lack of joint transverse reinforcement, the non-ductile anchorage detail resulted in lack of reliable joint shear transfer mechanism beyond diagonal cracking and extremely brittle seismic behaviour. Previous studies [25, 27, 91, 113, 120, 147, 177] have tested a variety of beam bars anchorage details, including a) 180° standard hooks, b) 90° inward bends, c) 90° bends outward, d) early straight length termination (for bottom beam bars only), and e) combination of 90° bends inward for top and 180° standard hooks for bottom beam bars.

Figure 2.11 presents the schematic illustrations of some of the different beam bars anchorage details typically found in RC frames constructed prior to the 1970s. Laboratory tests [120, 147, 177] demonstrated that double 180° standard hooks anchorage (Figure 2.11a) would result in the most significant joint damage and strength degradation under seismic loading attacks. For interest, the U-shaped bars anchorage detail (Figure 2.11f) is still commonly used in gravity-only design of beam-column joints such as those prescribed by the British BS-8110 concrete code [39, 120]. The experimental tests by Megget [140] and Renton [205] have shown the poor bond performance of the U-bar detailing used for the anchorage of beam bars into joints.

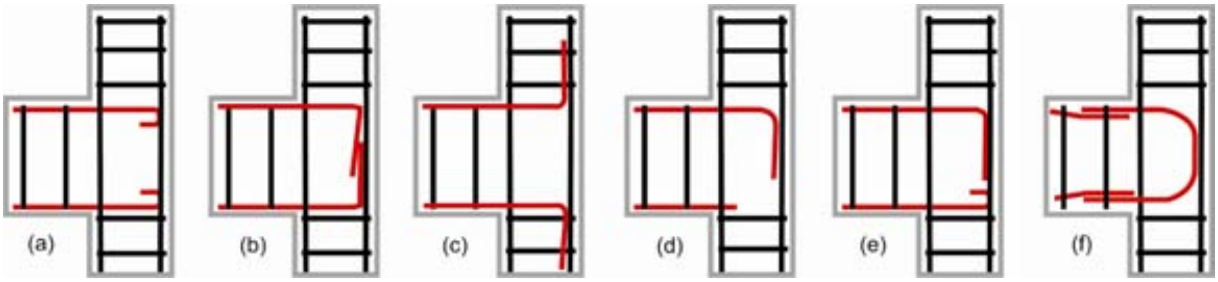

Figure 2.11: Varieties of non-ductile beam-column joint detailing: a) double 180° hooks, b) double 90° inward bends, c) double 90° outwards bends, d) early straight length termination for bottom beam bars, e) combination of 90° and 180° anchorage, and f) U-shaped bar.

In the USA, the anchorage detail with terminated straight bottom reinforcement, as shown in Figure 2.11d, was common and thus such details were more commonly tested in North America as §2.3.3 will show. Instead, in Mediterranean countries, New Zealand and Japan, anchorage details that included tension anchorage in the bottom reinforcing such as Figure 2.11a to c were more common. Unlike the ACI-318 contemporary codes [5-7], New Zealand's

NZS95:1955 [160] required at least one-third of the tension reinforcement of the beams and slabs to be extended into the support in order to develop half the allowable stress of the bars. Figure 2.12 illustrates this difference between the USA and the NZ pre-1970s construction practice for exterior beam-column joints. This difference was rectified in the 1971 ACI-318 [8].

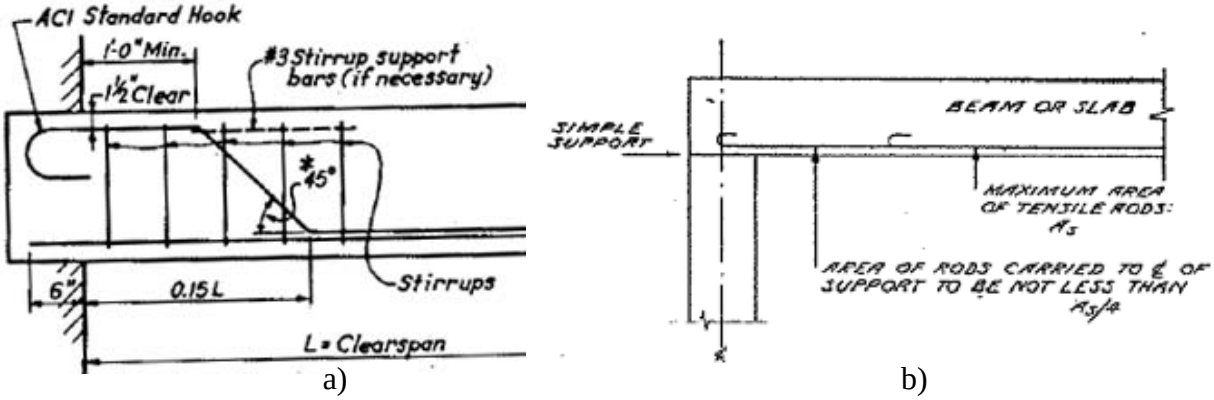

Figure 2.12: a) ACI-318:1963 [7] specification for end-span beam-column joint [3]; b) NZS95:1955 [160] requirement for the tension reinforcement in beams/slabs to be anchored into the support [95].

As discussed in §2.2.2.5, the prevalence of plain round bars prior to 1950-70s was another source of seismic vulnerability of the pre-1970s RC frames. Experimental tests [42, 105, 132, 177] of pre-1970s beam-column joints with plain round bars have shown extremely poor seismic performance due to the premature bond failure, slip and push-out spalling of a concrete wedge. Significant diagonal shear cracking within the joint core reduced the anchorage capacity of plain round bars which relied on adhesive and friction for their bond capacity.

2.3.2 Field observations of beam-column joint relevance to the collapse of RC frames

In the past, it was claimed that importance of beam-column joints in seismic design was overemphasised because little field evidence of major damage or collapse could be attributed to joint failures [196]. Building collapses due to joint failures were hard to be ascertained as joint damage could also lead to subsequent column bar buckling and loss of gravity-carrying capacity. Some of the earliest field observations were from the 1980 El Asnam, Algeria earthquake [28] and the 1985 Mexico City earthquake[207]. However, earthquake reconnaissance missions in recent years have provided ample field evidences of significant damage and critical structural collapses due to beam-column joint failures.

Figure 2.13: a) Damaged RC corner beam-column joint at the Erzincan 1992 earthquake (taken from [34]); b) Collapse of RC frame building in Erzican earthquake 1992 (Photo taken from:[138]);c) Collapse of RC frame due to non-ductile beam-column joint failure, with noticeable plain round bars and double 180° hooks anchorage, Kocaeli 1999 earthquake (photo credit: Uni. of Bogazici website [31]).

The Kaiser Permantente Clinic collapse during the 1994 Northridge earthquake [94], as shown in Figure 1.1a (of Chapter 1), was a well-known example of structural collapses due to joint failures. The end bays collapsed over the full height of the building, with some fallen beams and columns relatively undamaged but with the beam-column joints completely shattered. The 1992 Erzican [138] and 1999 Kocaeli/Izmir [208, 216] earthquakes, both in Turkey, presented more widespread examples of joint failures. In Turkey, poor material quality, non-ductile (e.g. 180° hooks) beam anchorage, plain round bars and unreinforced joint cores were common (see examples in Figure 2.13 and Figure 2.14a). Many of the collapsed buildings were built after the 1970s, but poor enforcement of the modern seismic code and continuing poor construction practice resulted in poor seismic performance of these buildings [208, 216].

More recent earthquakes such as the 2005 Kashmir, Pakistan earthquake [64] and the 2008 Wenchuan, China earthquake [239] also provided many field observations of beam-column joint failures leading to collapses. Figure 1.1b and Figure 2.14b show some examples of the catastrophic RC frame building collapse in the Wenchuan earthquake due to joint failures. Figure 2.14c shows that a moderate earthquake such as the 2009 L'Aquila, Italy earthquake (M_w = 6.3) could induce significant damage in lightly reinforced and inadequately detailed beam-column joints.

The brief discussion above on beam-column joint failures should not over-shadow the other critical weaknesses of weak-column strong-beams, column lap-splice in plastic hinge regions, column shear failure or other possible failure modes of non-ductile RC frames. Figure

2.14a is a good example of different failure mechanisms of non-ductile RC frames. In the experimental and numerical studies in subsequent chapters, realistic considerations are also given to these other inadequacies in pre-1970s RC frame structures.

Figure 2.14: a) Corner non-ductile RC beam-column joint failures, Kocaeli/Izmit 1999 earthquake (photo credit: Halil Sezen, NISEE collection [156]; b) Collapse of RC frame school building in Yingxiu city, Wenchuan 2008 earthquake (Photo taken from:[239]); c) Damaged beam-column joints at moderate L'Aquila Italy earthquake (photo credit: Dr Anna Brignola).

2.3.3 Literature review on the vulnerability of pre-1970s RC beam-column joints

A comprehensive review of existing literature on experimental studies on beam-column joints with non-ductile detailing is carried out to understand the various as-built parameters that would influence the seismic performance of these joints. The focus is on exterior beam-column joints while relevant interior joint test results will be briefly discussed. In the next five sub-sections, the literature review is presented in five categories: a) early tests on exterior beam-column joint s carried out prior to the availability of modern seismic design, b) tests on non-ductile exterior beam-column joints, b) tests on non-ductile interior beam-column joints, d) tests on beam-column joints including floor slab and transverse beams and e) large-scale tests on non-ductile RC frames.

2.3.3.1 Early exterior beam-column joints experimental tests

In the mid-1960s and early 1970s, many exterior beam-column joints were tested to develop a rational seismic design methodology for these connections. Some of these early joint tests are of interest to this research as they have inadequate joint shear reinforcement, inadequate bond resistance and non-ductile beam anchorage details by modern standards.

In the early 1970s, a series of thirteen exterior beam-column joint subassemblies were tested under quasi-static cyclic loading in the University of Canterbury [185]. Megget and Park [143] demonstrated the importance of joint shear reinforcement in preventing joint shear failure. Patton's tests [193] illustrated the importance of proper anchorage of the beam flexural reinforcing by extending them beyond the column face using a beam stub. The University of Canterbury tests [205, 220] also confirmed the beneficial effects of column axial compression force on column in improving the joint seismic behaviour. The positive effects of joint confinement, joint reinforcement and axial column load were also observed in the pioneering exterior beam-column joint tests by Hanson and colleagues [99, 100, 227, 228].

Interestingly, Park and Thompson [188, 189] tested several interior beam-column joints with prestressed and partially-prestressed beams to investigate the effect of axial horizontal compression on the joint behaviour. They observed improved joint behaviour with prestressed joint cores. This research is adopting a similar approach to seismic retrofit exterior joints by adding external unbonded post-tensioning (as to be discussed in Chapter 3).

In a set of comprehensive Japanese experimental studies in the 1980s, summarised by Kurose [123], various RC joint design parameters were tested: concrete strength, beam-to-column width, beam-to-column depth, transverse beam, joint reinforcement, column axial load and column depth-to-beam bar diameter ratios. Of the 84 beam-column joint specimens reviewed, 72 failed either by joint shear failure or by joint shear failure after beam hinging. A large sub-set of the joints had no joint reinforcement and peak shear stresses in these joints observed were in the range of $1.16\sqrt{f'_c}$ to $1.83\sqrt{f'_c}$ MPa. Joint reinforcing were found to increase the joint shear strength (Figure 2.15-left) while the influence of column axial load (Figure 2.15-right) and transverse beam stubs were less apparent.

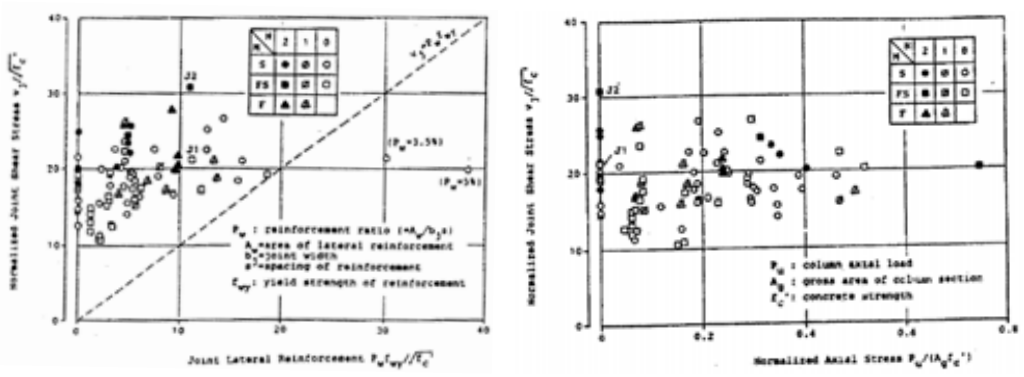

Figure 2.15: Influence of transverse reinforcement and axial column load on joint shear behaviour[123].

2.3.3.2 Non-ductile exterior beam-column joints

In the past two decades, in light of the recognised importance of beam-column joint behaviour in the seismic performance of RC frames, many exterior beam-column joint representatives of pre-1970 construction and/or of gravity-only design have been tested. While a large portion of the studies was focussing on deriving the seismic performance and joint shear models of these non-ductile connections, some tests were carried out as benchmark within seismic retrofit studies and validation of finite element models of these joints.

A large-scale research programme was carried out at the National Center for Earthquake Engineering (NCEER) to investigate the seismic performance of gravity-load-only design RC frame buildings in as-built or retrofitted configurations. These results were published in a series of NCEER reports [17, 25, 27, 35, 36, 53, 197] and journal publications [18, 26, 37, 66, 121, 122].

Beres *et al.* [26, 27] and Pessiki [197] jointly tested 20 interior and 14 exterior full-scale beam-column joints under quasi-static cyclic loading and several as-built parameters. The typical structural details of the tested joints are shown in Figure 2.16. For the interior beam-column joints in general, bottom beam longitudinal bars suffered from pull-out anchorage failure due to limited embedded length and loss of bond beyond joint cracking. For exterior joints, however, failure occurred as a result of a combination of excessive joint diagonal cracking followed by lap-splice failure in the column and push-out of the concrete cover by the 90° bent-down beam top reinforcing. For most of the specimen tested, beam pull-out failure occurred at approximately -0.8% inter-storey drift while joint shear damage resulted in structural failure at approximately +2.0% inter-storey drift. Figure 2.16b shows the typical damage patterns of the exterior and interior joints at the end of the tests. Peak shear stress developed in the joints without joint reinforcement was about $1.1\sqrt{f'_c}$ MPa.

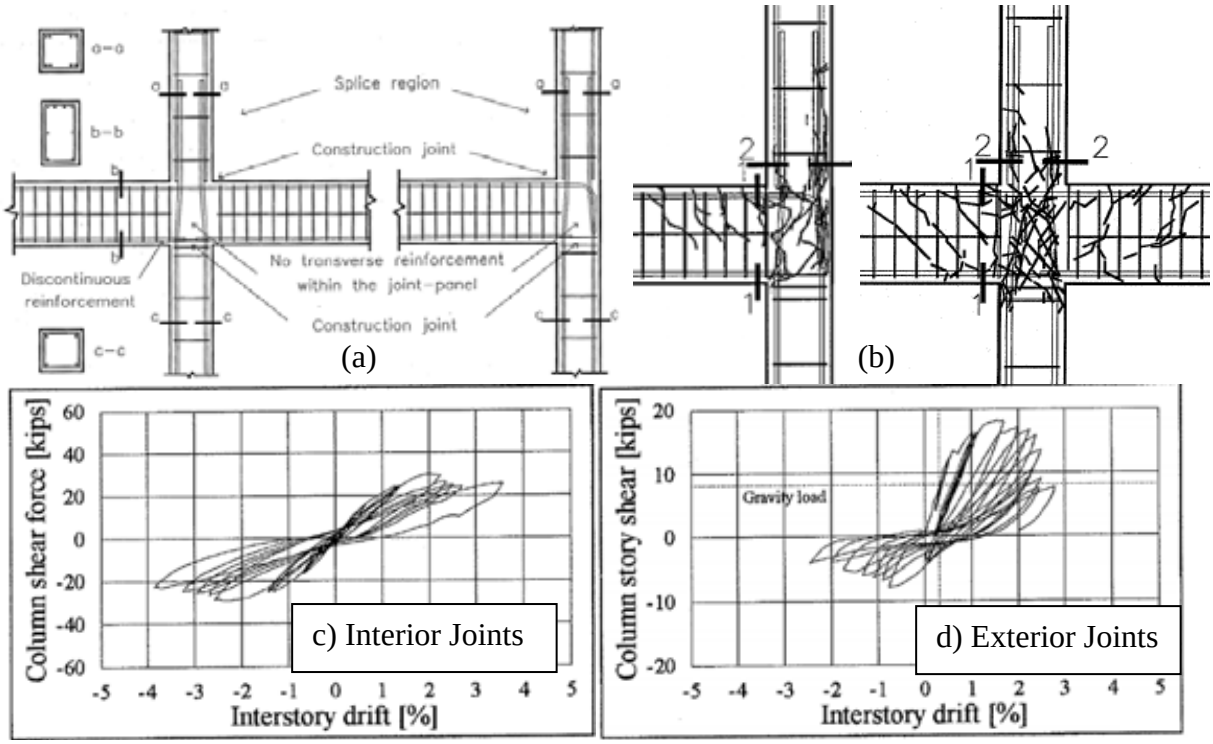

Figure 2.16: Experiment tests on non-ductile beam-column joints: a) Typical deficiencies of the non-ductile joints tested; b) Typical damage patterns at the end of the tests; c) Typical load-displacement plot for interior joints with discontinued beam bottom bars; d) Typical load-displacement plot for exterior joints [27].

The parameters investigated by Beres *et al.* [26, 27] included the quantities of joint and column reinforcing, presence of transverse beam stubs, column axial force levels and diameters of discontinued beam bottom longitudinal bars. Increase in the column axial load resulted in increase in joint shear strength, increase in overall stiffness and reduction in strength degradation in the exterior beam-column joint specimens. Confinement from transverse beam stubs did not prevent joint shear failure and higher lateral capacity, but provided more gradual strength degradations, as indicated by the load-displacement envelopes given in Figure 2.17.

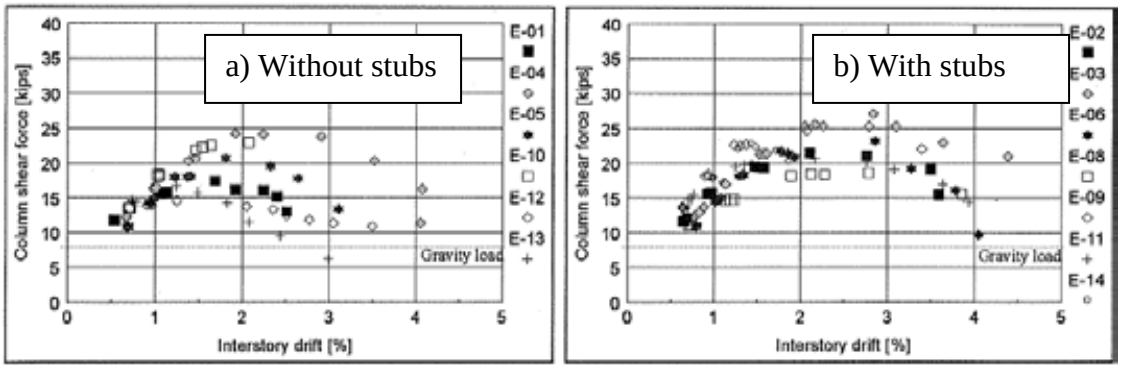

Figure 2.17: Comparison of load-displacement envelopes for exterior beam-column joints with and without transverse beam stubs [27].

Under the same NCEER programme, Aycardi *et al.* [17, 18] tested one exterior and one interior beam-column joint, both representatives of gravity-load-only design without joint stirrup or capacity-design principles, as per detailed by Bracci *et al.* [35]. Floor slabs and transverse beam stubs were included in both specimens, which constrained any direct measurement of joint deformation. For the exterior joint, a varying axial load of $22.24+2F_c$ (in kN) was used, where F_c is the imposed lateral load on the beam-column joints. It was reported that the exterior joint was failing in anchorage pull out of the bottom beam reinforcement while the interior joint had column hinging above the floor slab. A careful review of the test results presented in [17] suggests that the exterior beam-column joint subassembly failed in a mix of joint shear and beam-anchorage failures. The cracking pattern along the beam-joint interface as shown in Figure 2.18 indicates damage within the joint core.

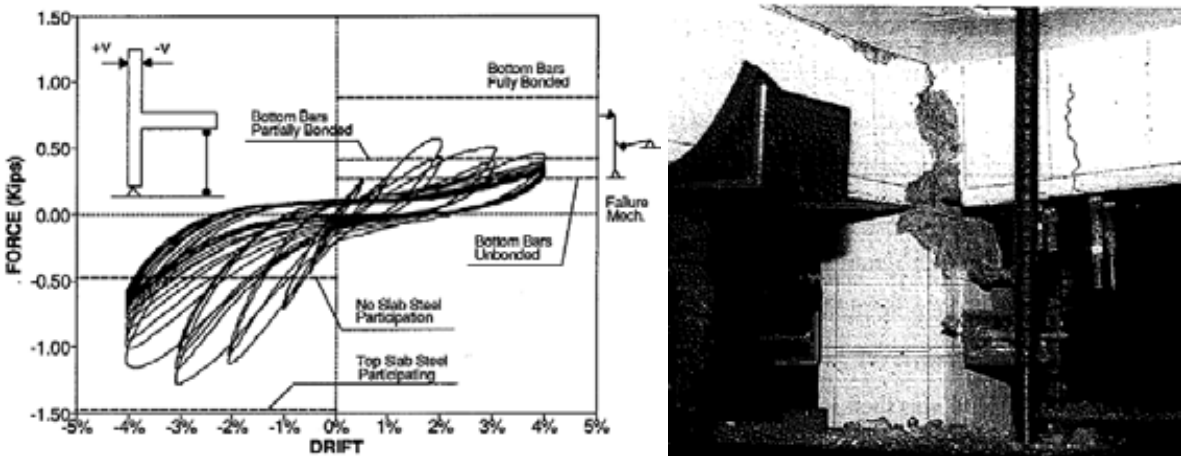

Figure 2.18: Non-ductile RC exterior beam-column joint with transverse beam and floor slab: Load displacement plot and damage pattern indicating joint damage and beam anchorage failure [17].

Hakuto *et al.* [91-93] tested two exterior beam-column joints with two beam anchorage details with one stirrup within the otherwise unreinforced joint (Figure 2.19a). Test specimen O6 had 90° hooks bent into the joint core and specimen O7 had 90° hooks bent away from the joint. Deformed longitudinal reinforcing was used. Figure 2.19b presents the load-displacement hysteresis curves of the two test units. Specimen O6 demonstrated ductile beam hinging response with negligible joint and column cracking while Specimen O7 failed in shear soon after the formation of diagonal tension cracking in the joint. In terms of drift capacity, Specimen O7 failed at the 0.5% and 1.0% drifts in the positive and negative loading directions respectively. While not discussed here, four interior joints tested by Hakuto *et al.* [91-93] highlighted the influence on bond degradation of the reinforcement in compression in terms of the yield curvature, ultimate

curvature and flexural capacity. More significantly, Hakuto *et al.* [91, 92] proposed a joint shear degradation model for non-ductile beam-column joints based on principle stresses analyses.

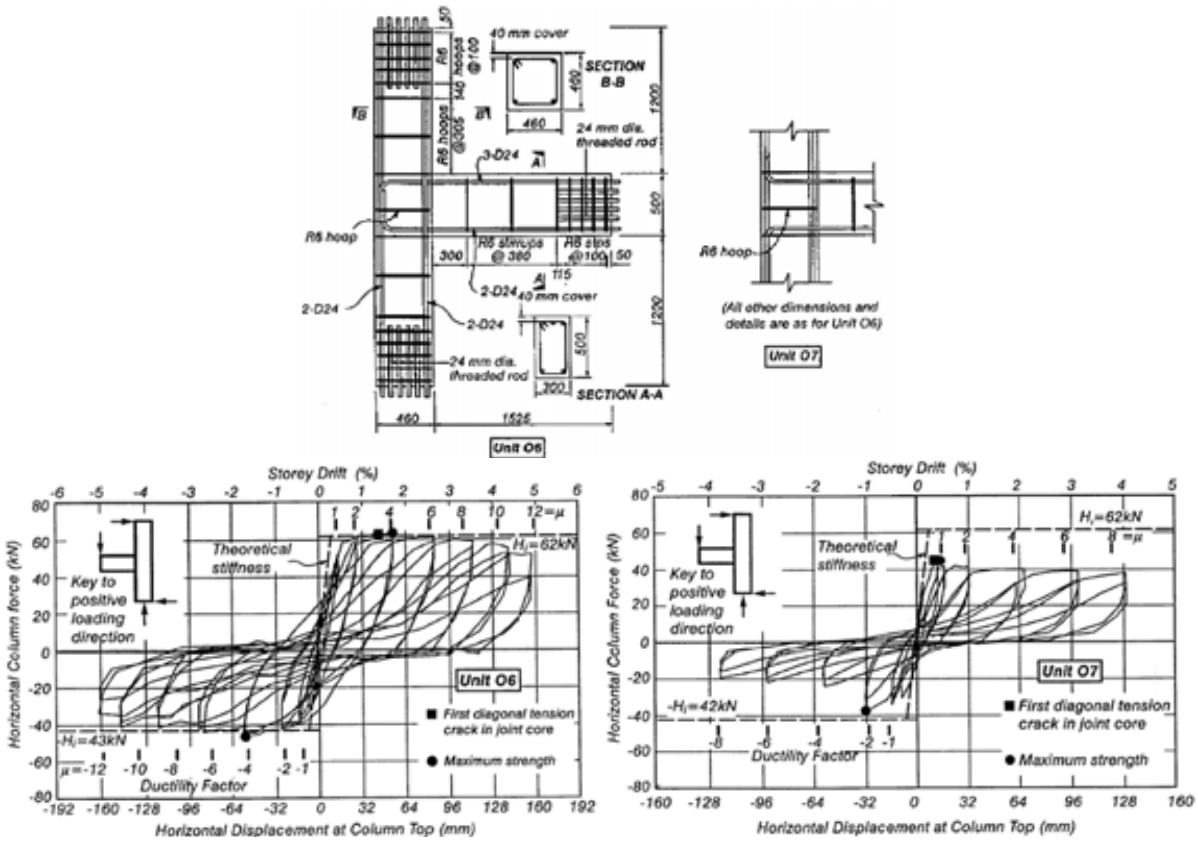

Figure 2.19: Non-ductile exterior beam-column joint with deformed reinforcing: top) Reinforcing detail for test units O6 and O7; bottom) Load-displacement plots for test unit O6 (left) and O7 (right) [91, 93].

Liu and Park [132, 133] repeated Hakuto *et al.* [91-93]'s beam-column joint experiments using plain round bar longitudinal reinforcement. Four exterior beam-column joints were tested, with reinforcing detail identical to Hakuto's specimen O6 and O7 as shown in Figure 2.19a. Two levels of column axial loading (zero axial load and 0.23-0.25$A_g f'_c$) were used for the two different joint anchorage types. Test results indicated the bond failures of plain smooth reinforcement precluded joint shear failure and the fixed-end rotation of the beam components contributed significantly to the inelastic deformation. Large beam-end flexural cracks and steel strain concentration at these cracks were observed in the specimens with plain round bars. The same beam-column joint with plain reinforcement, when compared to the joint with deformed reinforcement, had twice the flexibility and 25% less strength. With a higher compressive axial column load, the non-ductile exterior beam-column joints showed an increase in stiffness and strength, as shown in the hysteresis plots given in Figure 2.20. The summary of the University of

Canterbury test results on the sub-standard RC beam-column joints, beams and columns is given in ref. [184].

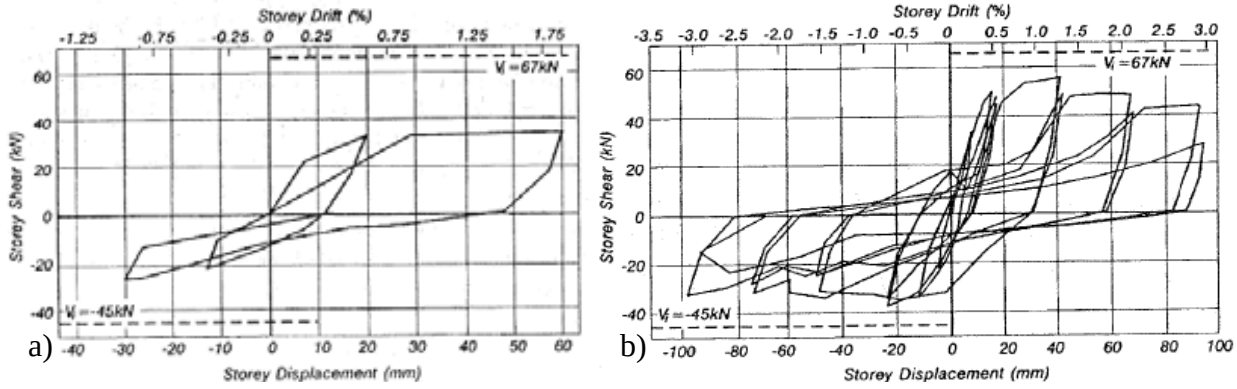

Figure 2.20: Load-displacement plots of non-ductile exterior beam-column joint with plain round bars and 90° hook bend away from joint anchorage: a) EJ1 – no axial load and b) EJ3 – $0.25A_g f'_c$ axial load [132].

Pantelides *et al.* [55, 181, 182] tested four half-scale RC exterior beam-column joints with no joint stirrups and 90° inward bend beam anchorage details. All specimens had joint shear failures with minor variation in peak shear strengths attained. Two levels of axial compressive loads ($0.1A_g f'_c$ and $0.25A_g f'_c$) were used in which the higher axial load led to joint cracking prior to beam reinforcement yielding. The performance limit states of non-ductile exterior joints, (Figure 2.21), showed the positive and negative effects of the higher axial load. While specimens with higher axial load had higher maximum principal tensile and shear stresses in the joint core, the deformation capacities were nominally lower with joint shear cracking and failure occurred at approximately 0.5 and 1.5% drifts, respectively.

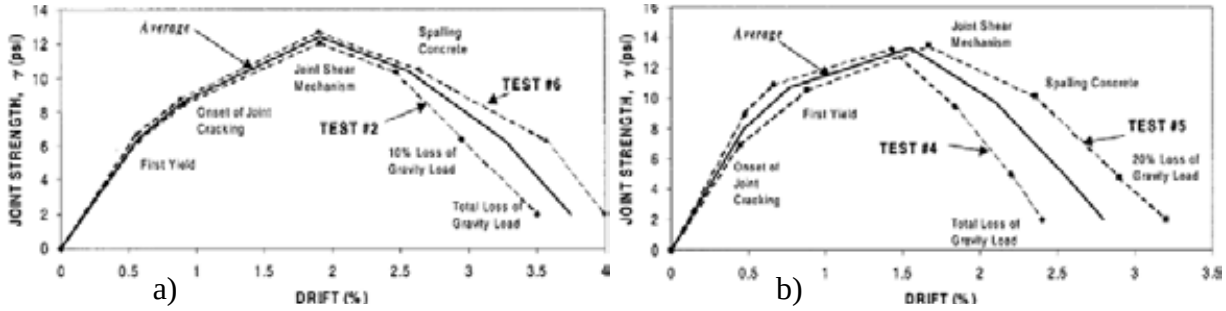

Figure 2.21: Limit states model for exterior beam-column joint with no stirrups and 90° hook bend into joint: a) $0.10A_g f'_c$ axial load and b) $0.25A_g f'_c$ axial load [181].

Pampanin *et al.* [42, 177] tested two exterior, two interior and two knee beam-column joints, all with non-ductile pre-1970s detailing and plain round (smooth) reinforcement with end-hook anchorages, under quasi-static cyclic loading and varying column axial load. Brittle failure

mechanism was observed for the exterior joints with joint diagonal cracking leading to subsequent concrete spalling and buckling of the column longitudinal bars. Figure 2.22-top presents the load-displacement response and damage pattern of one of the exterior joints. The authors attributed the severe concrete-wedge spalling in the joint to the localised push-out force from the hook anchorage due to the bond deterioration and slipping of the plain-round reinforcement, as shown in Figure 2.22-bottom. The test result was extended to evaluate the implications of joint shear hinge mechanism [178] on the seismic response of pre-1970s RC frames [42, 87].

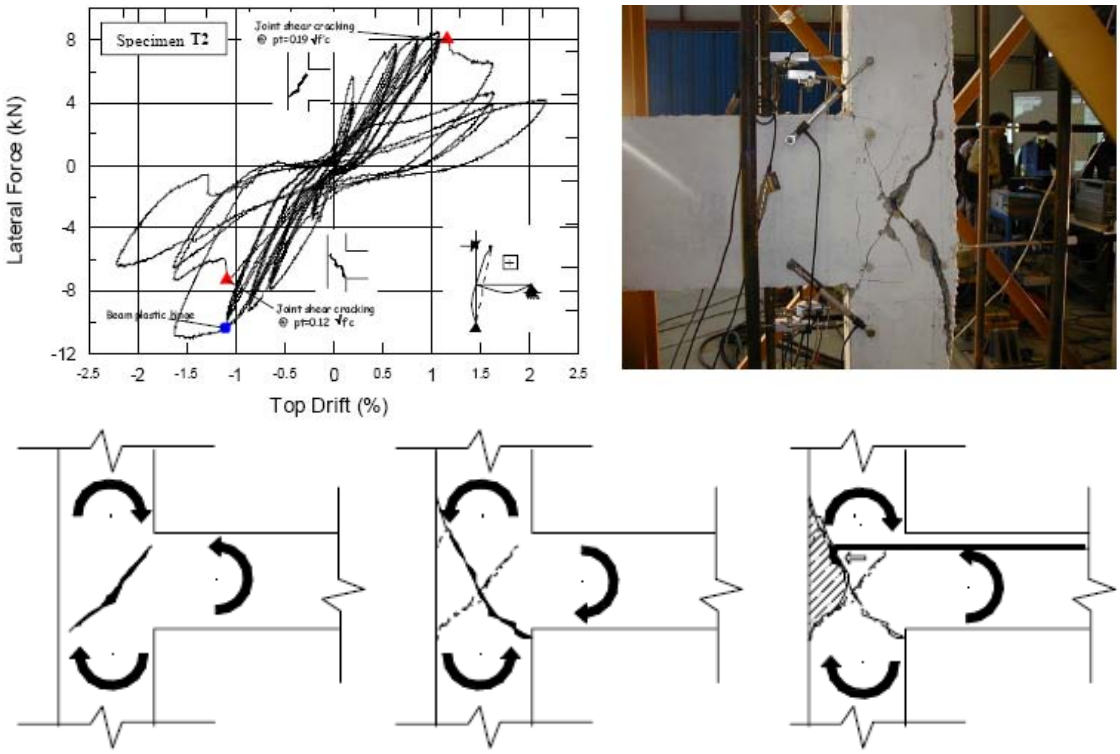

Figure 2.22: Exterior beam-column joints with no stirrups, double-180° beam anchorage and plain round reinforcement: top) Force-displacement plot and final damage pattern for T2 exterior joint; bottom) Progression of damage for 'concrete wedge' failure of exterior beam-column joints [177].

Hertanto [105] tested a total of nine exterior beam-column joints with different typologies, including shallow-beam-to-column connections, deep beam-to-column joints and three-dimensional (3D) corner space joints under quasi-static cyclic loading and varying column axial loads. Other parameters investigated included the effect of plain-round reinforcing and different anchorage detailing (double 180° hooks, 90° bends into the joint). All specimens had one single joint stirrup. Figure 2.23 shows the final damage patterns and force-displacement hystereses of four plane joint specimens tested. Exterior joints with shallow beams were performing relatively

well without any joint shear damage. Pinching-shaped hystereses as a result of plain bar bond failures were evident in all plane specimens. Alternative strength degradation curves corresponding to various joint reinforcement details were provided based on the test results. The variation of axial loading resulted in asymmetric force-displacement hystereses highlighted the influence of column axial load on the joint shear and plain bar bond capacities.

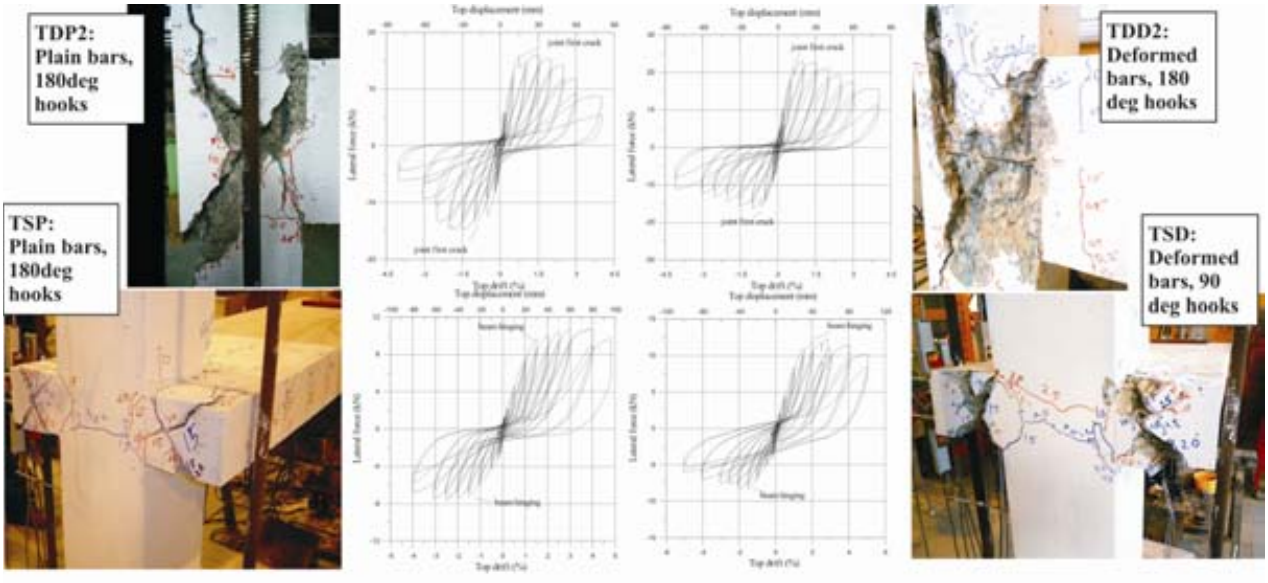

Figure 2.23: Experimental results of four plane beam-column joints with plain and deformed reinforcing, and deep and shallow beams (taken from [105]).

A very recent study by Bedirhanoglu *et al.* [22] tested a series of exterior beam-column joints with plain round bars to investigate the effects of axial load, joint reinforcement, displacement history and transverse beam stubs. Their test results indicated that the plain reinforcement bond slips and joint shear failures governed the inelastic mechanism of these joints. Figure 2.24 summarises the key experimental results from Bedirhanoglu *et al.* tests [22]. While the slab/transverse beam resulted in a 30% strength enhancement for JO1 when compared with the planar exterior joint (JO5), as seen in Figure 2.24a, limited ductility and displacement capacities were attained for both specimens. Higher column axial loads were observed to improve the peak lateral strengths (JO7≥JO1≥JO6); while after the joint shear diagonal cracking, the higher axial load had led to lower displacement capacity and accelerated strength degradation due to the buckling of the column bars. Column bar buckling was more evident in the specimen JO7 than the specimen JO6.

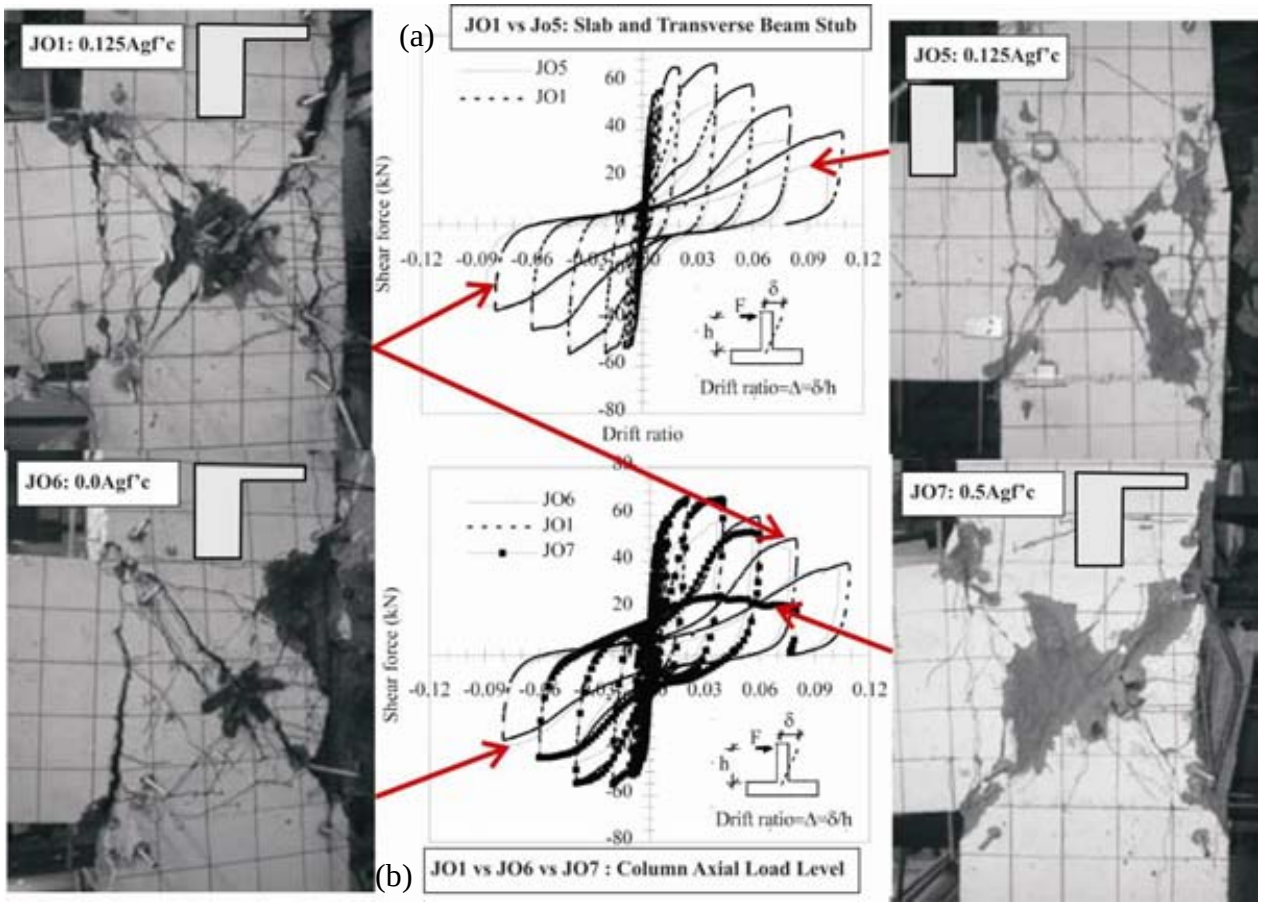

Figure 2.24: Experimental results of beam-column joints with plain reinforcement considering: a) Presence of slab-transverse beam b) Varying levels of column axial load (adopted from [22]).

Some researches on the monotonic and cyclic loadings on gravity-only design beam-column joints as shown in Figure 2.4 are relevant to this research as the joint details tested are consistent with the pre-1970s construction practice. Scott [212, 213] tested 17 BS-8110 [39] designed beam-column joint connections, fifteen of which were subjected to monotonic quasi-static loading and two were subjected to seismic cyclic loading. Three different joint reinforcing details (90° hook bend down, 90° hook bend up and U-bars) were tested. Detailed strain-gages instrumentation gave a clearer picture of the bond and reinforcement steel stresses within the joint regions.

Murty *et al.* [153] tested twelve exterior beam-columns with four different types of beam bar anchorages and three levels of joint shear reinforcing. All joints failed in shear with limited ductility capacities. Peak shear stresses developed in the joints without any joint reinforcement were in the range of $1.25\sqrt{f'_c}$ to $1.32\sqrt{f'_c}$ MPa, while improved anchorage and joint reinforcing details increased the peak shear stresses to the range of $1.40\sqrt{f'_c}$ to $1.79\sqrt{f'_c}$ MPa.

Hegger *et al.* [103, 104] tested eight exterior joints with various non-ductile joint reinforcing detailing under monotonic loading to develop empirical joint shear strength equations and FE model of these joints. There were more similar studies [96, 171, 191, 210] but they were not reviewed as limited test observations were presented. As with Hegger *et al.*, these studies focussed on developing empirical joint shear models and validating numerical FE models.

Kuang and Wong [120, 238] tested seventeen exterior beam-column joints designed according to the BS-8110 [39] under cyclic loading to investigate the influence of different beam-anchorage types, beam-column depth ratios, joint and column reinforcing and axial load levels on the joint shear strengths. All joints failed in shear (as shown in Figure 2.25a). Maximum shear stresses were in the range of $0.43\sqrt{f'_c}$ to $0.68\sqrt{f'_c}$ MPa for various beam anchorage configurations. They confirmed Hakuto *et al.* [91-93]'s conclusion that beam-column joints with 90° hooks bend in anchorage detail performed significantly better than joints with 90° hooks bend away anchorage detail. In addition, Wong [238] developed a modified softened truss shear model for non-seismically reinforced joints.

In addition to the aforementioned results, there were other experimental tests on non-ductile pre-1970s beam-column joints in the literature, in which several benchmark as-built specimens were tested in conjunction with retrofitted specimens. Figure 2.25 illustrates some of the as-built benchmark specimens which predominantly failed in joint shear.

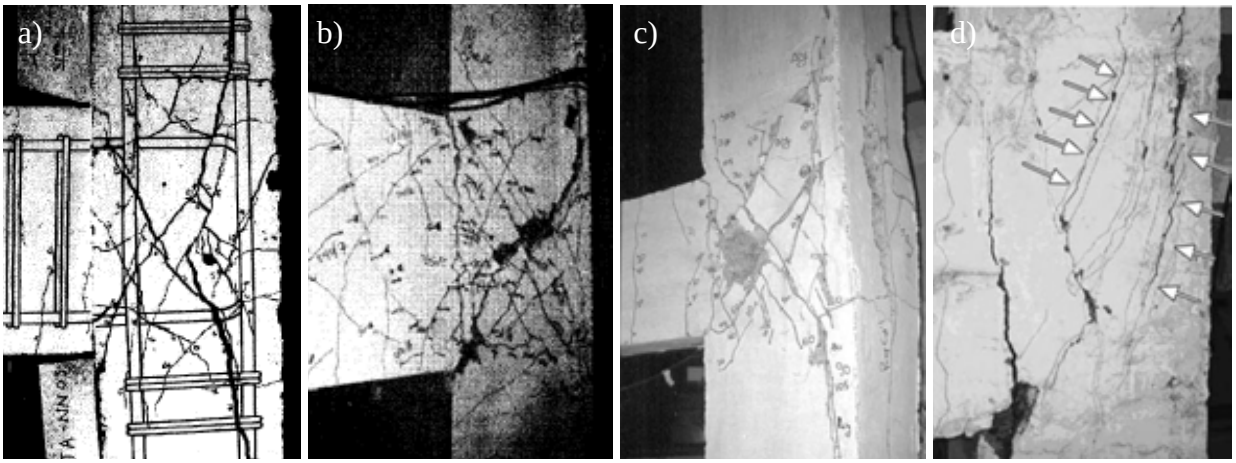

Figure 2.25: Exterior beam-column joint failures: a) Wong (2005) [238]; b) Biddah and Ghobarah (1997) [30]; c) Ghobarah and Said (2002) [88]; d) Parvin *et al.* (2010)[192].

2.3.3.3 Non-ductile interior beam-column joints

While not a focus of this research, studies on interior non-ductile RC beam-column joints highlighted some of the issues and structural deficiencies that are relevant to exterior joints.

While joint shear failures of interior beam-column joints with non-ductile detailing (e.g. no stirrups) were commonly observed, the load-carrying capacities were generally sustained over a few inelastic cycles up to 2% drift (e.g. [63, 91, 125, 133]). Similar observations can be made with interior beam-column joints with insufficient joint stirrups [65, 126, 188].

Considering the improved in-plane confinement from the framing beams, interior joints could maintain the gravity capacities as the axial load demand can be carried by the alternative load paths of concrete compression struts and by column longitudinal reinforcing [125]. For interior joints with plain-round bars, premature bond-slip would limit the joint shear demand and its damage, thus maintaining some ductility capacity within the system [132, 133, 177]. These conclusions are of particular interest to the partial retrofit strategy (to be described in Chapter 3) as a non-ductile RC frame collapse-prevention retrofit could be achieved by targeting only the exterior joints.

Lehman and colleagues [14, 125, 237] tested eleven interior beam-column joints without joint reinforcement, with four displacement-history loading protocols, two concrete compressive strengths and six joint shear stress demands (by changing the beam flexural capacity). The joints performed reasonably well up to 1.5% drift and shear stress demand of less than $0.83\sqrt{f'_c}$ MPa. Displacement histories were found to affect the joint shear strength, cumulative damage and joint stiffness. A stiffness and strength degrading constitutive spring model was proposed to model these non-ductile RC joints [15]. Using existing data set and existing literature on interior beam-column joints that failed in joint shear [65, 114, 115, 144, 197], Pagni and Lowes [173] developed fragility function for non-ductile interior beam-column joints.

Li Bing *et al.* 2002 [130, 131] tested four full-scale interior beam-wide-column joints with non-seismic detailing (designed to the BS-8110), with and without column lap-splice and joint reinforcement. The joint shear model proposed by Hakuto *et al.* [91] was found adequate in predicting the maximum horizontal shear stress and failure mode. More recently, Li Bing *et al.* [127, 128] tested six interior beam-to-wide columns and beam-to-walls specimens, all with non-seismic detailing. These joints were found to be able to sustain damage without losing lateral capacity up to 2.0% drift, suggesting inherent nominal ductility in these non-seismically designed connections. Similarly, Supaviriyakit and Pimanmas [224] tested five half-scaled interior joints with various joint detailing and concluded that with large column dimensions, nominally ductile behaviour can be attained.

2.3.3.4 Exterior beam-column joints with slab and transverse beams

In terms of modern seismic design and seismic assessment of existing structures, the influence of floor slabs, through tension flange effect, on the beam negative flexural over-strength and the internal hierarchy of strength of the beam-column joints, is well understood [4, 16, 167, 169, 196].

However, the actual confinement effect of transverse beams with and without floor slab is more controversial. Transverse beam stubs, acting together under tension membrane action of the floor slab, meanwhile, are expected to improve the joint shear behaviour because the confinement transverse beams on the dilation of the cracked joint concrete core [9]. It has been argued that in bi-directional loading and in presence of bi-directional frames, the possible development of plastic hinge in the transverse beams would reduce the effect of confinement and apparent increase in joint shear strength [50, 196].

Few experimental studies on lightly-reinforced exterior beam-column joints included floor slabs and/or transverse beams as the test parameters. Most tests discussed in the following paragraphs are on conventionally designed joint subassemblies.

Two exterior RC beam-column joints with and without transverse beam stubs tested by Megget [141] indicated beneficial confinement effects from transverse beam stubs. Comprehensive tests on joints designed according to the 1971 ACI-318 [8] by Meinheit and Jirsa [144, 145] confirmed the positive confinement effect of transverse beams on joint shear strength. Their results validated the 1976 ACI-352 guidelines [10] and the basis for the current ACI-318 code [4] provisions to assign higher shear strength for joints with transverse beams.

However, in the tests by Uzumeri *et al.* [229, 230] on unreinforced exterior RC beam-column joints with and without transverse beam stubs, the transverse beam stubs were found ineffective in improving joint shear capacities. For all three specimens, cyclic loading resulted in joint shear cracking, bond and anchorage failures of the beam bars before reaching the ultimate flexural capacity of the beams.

Within a US-Japan-New Zealand-China collaborative project [112] on beam-column joint design, Cheung *et al.* [51] tested three full-scale beam-column joints with floor slabs, designed according to the 1982 NZS3101 [166] requirements. No evidence of joint confinement from the slabs or transverse beams was observed but over-strength of beam negative flexural capacities due to slab flange effect was measured. The transverse beams and floor slab contributions were found to be negligible when seismic-induced ductility demands became dominant in both

principal directions under bi-directional loading. Similarly, under orthogonal (45°) direction earthquake attacks, the floor slabs were found inefficient in resisting forces generated in the joints. Figure 2.26 shows the damage patterns of the specimens tested by Cheung *et al.* [51]. In the same collaborative project, Kurose *et al.* [124] reported results of three beam-column joints with floor slabs, in which all had joint shear failures after beam-yielding and significant loss of stiffness and strength beyond 2.0% drift cycles with ultimate failure at 4.0% drift cycles.

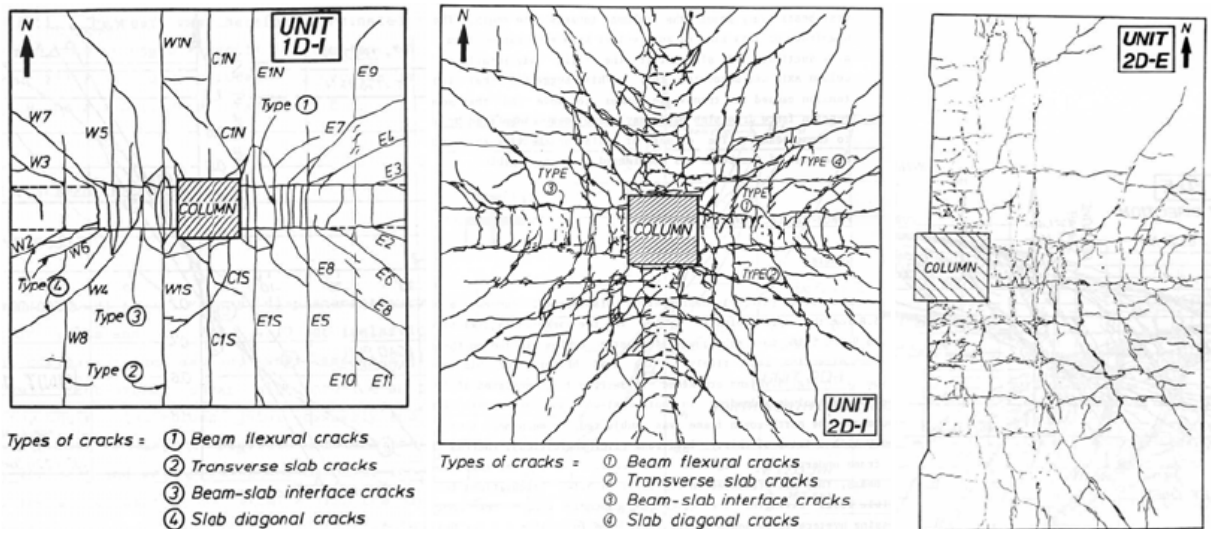

Figure 2.26: Damage patterns of interior and exterior beam-column joints with floor slabs and transverse beams tested under uni-directional and bi-directional loading [51].

More recently, Li Bing *et al.* [129] tested five ¾-scaled interior beam-column joints, investigating the influence of floor slabs and column orientation on the lightly-reinforced concrete beam-column joint behaviour. The performance of all specimens were satisfactory up to 2.0% drift ratio, after which joint shear and beam bar anchorage failures resulted in significant strength and stiffness degradations. Significant pinching in the hysteresis loops was also observed. While floor slabs over-strengthened the interior joints by about 11% to 27%, joint shear failure and gradual loss of lateral load carrying capacity occurred at approximately 1.5-2.0% drift for all unreinforced joints with and without slabs. The 3D FEM model was calibrated and validated in order to investigate the influence of column axial load and slab effective width. The effective width of slab participating in the three specimens with floor slabs was estimated to be 42% of the 2008 ACI318 [4] recommendation (b_w+16t_{slab}). b_w and t_{slab} are the beam web width and floor slab thickness respectively.

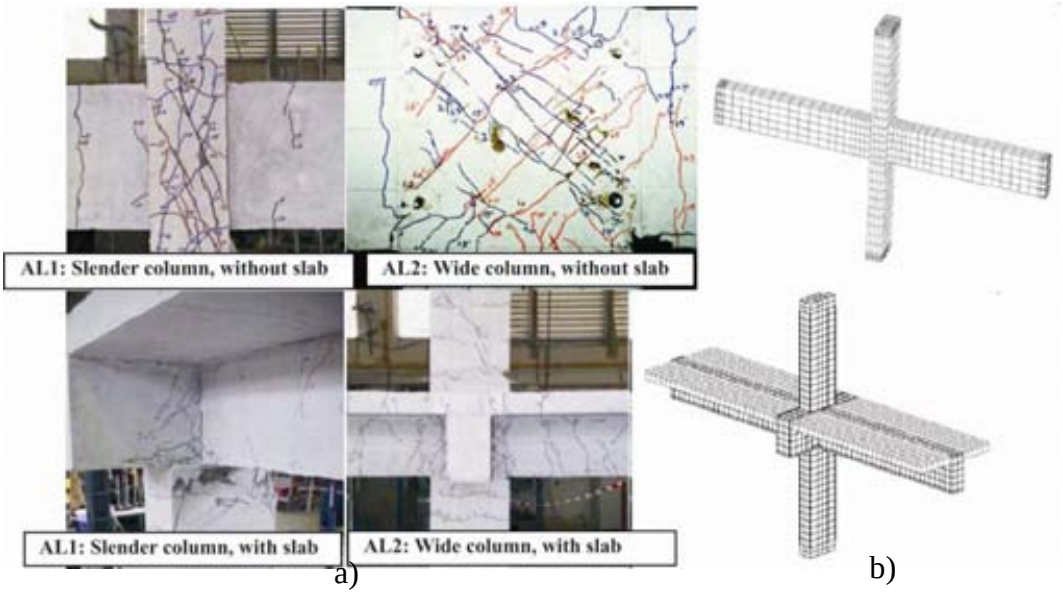

Figure 2.27: Interior beam-column joint with and without floor slabs: a) experimental damage pattern for slender and wide-column joints; b) FEM model of the interior beam-column joints [129].

2.3.3.5 Large-scale non-ductile RC frames testing

While beam-column joint subassembly tests give valuable information on the seismic capacity and the failure mechanisms of these joints, only large-scale testing of the whole structure would give complete information of the interaction between structural elements and dynamic seismic forces. However, these large-scale tests are expensive and complex, in that specific collapse mechanism or vulnerability cannot be studied in detail unless the test model has been designed to fail in such a manner.

Early experimental studies on non-ductile RC frame buildings were done on small-scale model structures. El-Attar *et al.* [66] tested an 1/6-scale two-storey one bay and an 1/8-scale three-storey three-bay building model of non-ductile RC frame using shaking table. Later, an 1/3-scale three-storey three-bay building model of El-Attar *et al.* prototype, was tested with and without retrofit by Bracci *et al.* [35-37]. While test results have highlighted the non-seismic details (e.g. unreinforced joint and lightly reinforced columns) were sources of damage and inelastic deformation, inherent resistance of the frames prevented complete structural collapse under a moderate earthquake excitation (up to 0.3g peak ground acceleration (PGA) ground motions). The review of El-Attar *et al.* [66] results implies that the small scaling factors (1/6 and 1/8) have possibly suppressed shear and/or axial failure of the beam-column joints and columns. In Bracci *et al.* [36, 37] tests, column-sidesway mechanism was observed in the first two storeys but soft-storey collapse was averted under the moderate 0.3g PGA excitation.

Pampanin *et al.* [41] tested a 2/3-scale three-storey three-bay RC frame, a representative of 1950-1970s Italian design, under quasi-static cyclic lateral loading (Figure 2.28a). Plain round reinforcement, column lap-splice and non-ductile detailing of the joints were employed in the test specimen. The frame developed an increasing level of damage within the 1.0-1.6% top drift cycles with significant exterior joint damage at the first storey and partially at the second storey. This was recognised as the development of a "shear hinge mechanism" [42, 178] which allowed the distribution of the drift demand over the first two storeys, avoiding an otherwise predictable full soft-storey collapse. The final damage pattern at 1.6% building top drift with corresponding 2.0% inter-storey drifts for the first two floors is shown in Figure 2.28c.

A full-scale of a four-storey three-bay 1950-70s Italian RC prototype frame was tested at the ISPRA laboratory as part of a research on seismic retrofit solutions [43]. Under pseudodynamic loading simulating a 975-year return period earthquake (0.29g PGA), soft-storey collapse was observed in level 3, with global top drift of 1.08%. Limited ductility of the column plain-round reinforcement lap-splices was the source of the brittle failure of the columns.

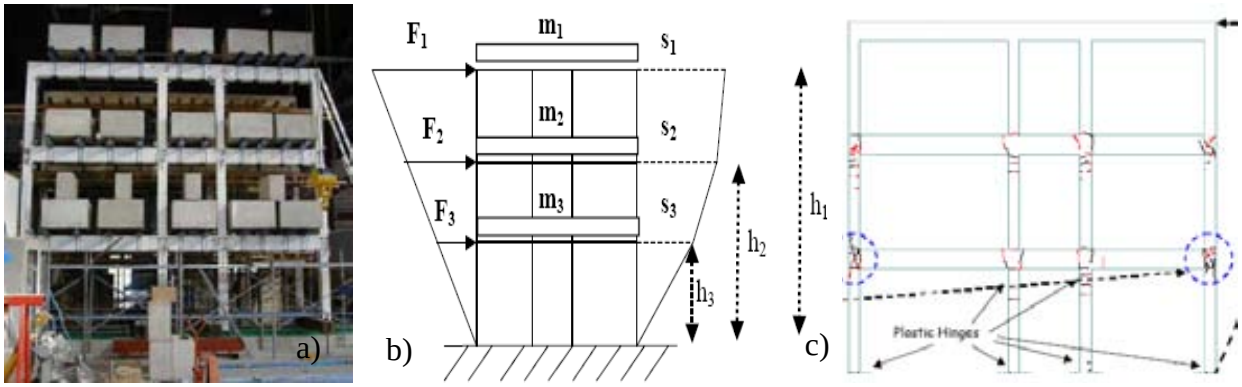

Figure 2.28: Pre-1970s non-ductile RC frame tested under cyclic quasi static loading: a) Test specimen; b) Hybrid force-displacement controlled loading; c) damage pattern at end of test (taken from [41]).

Under the European SPEAR project, a full-scale three-storey gravity-load designed RC frame with torsional asymmetry was tested under bi-directional pseudodynamic loading [149, 155] and an ¼-scale model of the same prototype building was tested under bi-directional shaking table test [56]. In the large-scale test, larger than expected torsional amplification leading to column failure occured and subsequent soft-storey collapse of the second floor was observed. In the ¼-scale test, both joint spalling and column top and bottom hinging were observed without complete soft-storey collapse of the structure.

Ghannoum [86] tested an 1/3-scale three-storey three-bay RC frame with light transverse reinforcing in the columns to severe column shear failure and axial collapse. Half of the columns were detailed to be axial-flexural-shear critical columns as previously tested in column subassemblies [69, 218]. The beam-column joints were well confined with transverse reinforcement and 90° bend in beam anchorage to prevent inelastic joint failures. The non-ductile base columns exhibited brittle shear failures that led to axial collapse. While not highlighted by Ghannoum [86], the first floor exterior joints were extensively damaged.

Wu *et al.* [240] tested the first-storey three-bay sub-frame of Ghannoum's prototype to study the progressive collapse of columns due to the axial-shear failure. The study was coupled with a numerical modelling analysis of progressive collapse [242]. Following these studies, four two-storey two-bay 1/2.25-scale non-ductile RC frames were tested dynamically at the NCREE shaking table facility under moderate and high gravity loadings. [241]. The interaction of multiple vulnerabilities of non-ductile RC frames was investigated as some of the test specimens included both non-ductile unreinforced beam-column joints and axial-shear critical columns. Unconfined joint failures were found to prevent column axial-shear failures, but total structural collapse due to joint failures was also averted as only 'half' joint cracks were formed owing to the nature of the earthquake excitation.

Recently, Reyes *et al.* [85] reported a shaking table test of a two-storey full scale RC frame with deficient beam-column joint detailing. Under moderate input ground motion (PGA = 0.20g), the exterior joints and roof columns were reasonably damaged. At the strongest input ground motion used (PGA=0.4g), soft-storey failure mechanism was triggered at the second storey with the exterior joints and knee joints hinging.

In recent years, several large-scale tests on non-ductile RC frames with unreinforced infills have been carried out [13, 48, 199, 219]. As the behaviour of infilled and non-infilled RC frames are very different owing to the complex interaction between the infills and bare frames [102, 137], these results are not considered herein. Most tested frames exhibited localised column shear brittle failure due to the diagonal compression strut mechanism of the infill walls. In a recent test on 2/3-scaled three-storey two-bay non-ductile RC frames with brick masonry infills by Shing *et al.* [219], exterior joint shear failure was observed under very severe ground motions.

2.4 ASSESSMENT OF BEAM-COLUMN JOINT HIERARCHY OF STRENGTHS

2.4.1 Assessment framework

The framework to evaluate the beam-column joint subassembly capacity and hierarchy of strength is based on the concept of capacity design of RC structures [196, 202]. By identifying the weakest link within the system, the plastic mechanisms can be identified and based on the ductility and deformability of the plastic mechanisms, the collapse and failure mode can be determined. Current practice of seismic assessment often fails to consider the interacting demand-capacity of various structural elements within the beam-column joint. By evaluating various failure mechanisms based on comparable strength and deformation capacities (lateral column force or global inter-storey drift), a more realistic failure mode may be identified.

In assessing its performance, different performance limit states can be defined for each structural element of the beam-column joints. For this study, the primary concern is related to life-safety and collapse prevention limit states, therefore the assessment would focus on critical strength and ductility/displacement ultimate limit states. For serviceability or high performance (e.g. no residual deformation or no structural damage) limit states, the seismic assessment framework can be modified with respect to relevant material, deformability and damage performance levels.

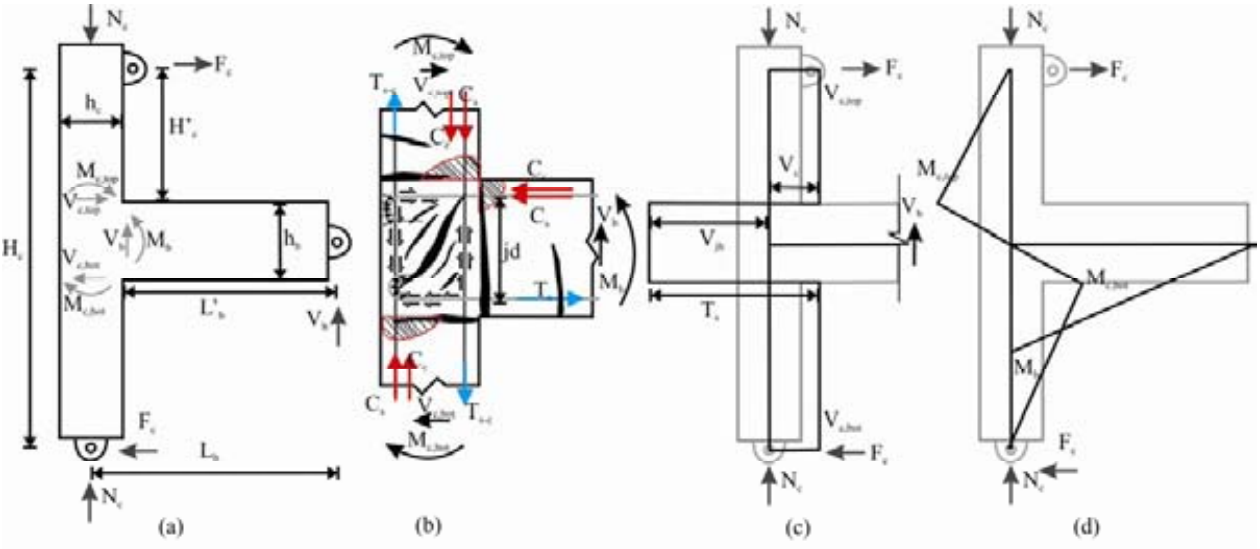

Figure 2.29: Equivalent column moment for various internal actions on exterior beam-column joints subassembly: a) Labelling; b) Internal action of exterior joint; c-d) Corresponding shear force and bending moment diagram of exterior beam-column joint subassembly.

Following the procedure proposed by Pampanin *et al.* [174, 175] the inelastic mechanism of the beam-column joints is determined by comparing the hierarchy of strengths of the beams, columns and beam-column joints using a common denominator unit: *equivalent column moment*, M_c, (also abbreviated as M_{col} in other sections in the thesis). With reference to Figure 2.29 above, Equations 2.1 to 2.6 relate the internal actions (demand or capacity) for the beam and joint to the equivalent column moment, M_c. The capacity of the joint sub-assembly with respect to the applied top column lateral force, F_c, is given by M_c / H'_c.

The equivalent column moments for beam flexural capacity, M_b, and beam shear capacity, V_b, at the beam-to-column interface, $M_{c,bf}$ and $M_{c,bs}$ respectively, are given by:

$$M_b = F_c \frac{H_c}{L_b}(L_b - \frac{h_c}{2}) = F_c \frac{H_c}{L_b} L'_b \qquad \textbf{2.1}$$

$$M_{c,bf} = M_b \frac{L_b}{H_c} \frac{H'_c}{L'_b} \qquad \textbf{2.2}$$

$$M_{c,bs} = V_b \frac{L_b}{H_c} H'_c \qquad \textbf{2.3}$$

where $H'_c = ½ (H_c - h_b)$ and $L'_b = L_b - h_c/2$.

With reference to Figure 2.29, the equivalent column moment for a given joint shear horizontal capacity, V_{jh}, at the joint core, $M_{c,j}$, can be derived using the following equations:

$$V_{jh} = T_s - V_c = \frac{M_b}{jd} - \frac{2M_c}{(H_c - h_b)} \qquad \textbf{2.4}$$

$$M_{c,j} = \frac{V_{jh} H'_c}{\left[\frac{H_c}{jd}(1 - \frac{h_c}{2L_b}) - 1\right]} \qquad \textbf{2.5}$$

where jd is the internal lever arm of the moment couple in the beam critical section, as shown in Figure 2.29b. Equation 2.5 above can be further simplified with the assumption of $M_b \approx 2M_c$:

$$M_{c,j} = \frac{V_{jh} H'_c \; jd}{(H_c - h_b - jd)} \qquad \textbf{2.6}$$

Given a performance limit state (reinforcement yielding, concrete crushing, joint cracking etc.) the capacity of each structural element can be represented with M_c "performance domain" within a column equivalent moment, M_c, versus column axial load, N_c, (M_c-N_c) interaction diagram . As with the conventional *M*-*N* capacity-demand analysis, the beam-column joint's

sequence of failure is determined deterministically by comparing the probable hierarchy of strengths of each connecting structural elements to the seismic demand parameters (M_c*, N_c*, V_c*, M_b*, V_b*). The seismic demands are derived from either a conventional force-based or a displacement-based seismic assessment and the internal forces are derived from the structural analysis of the beam-column joint sub-frames.

A schematic representation of such evaluation of hierarchy of strength and *sequence of events* within a M_c-N_c interaction performance domain is shown in Figure 2.30. In the example below, the inelastic mechanisms predicted were joint shear failure and beam reinforcement bond-slip, followed by flexural beam hinging in the direction with decreasing axial loads. In the direction of increasing axial load, the predicted inelastic mechanisms were beam reinforcement bond-slip followed by joint shear failure. Depending on the deformation / ductility capacities and 'post-yield' strength of the first inelastic mechanism, the second or more inelastic mechanisms may be activated, resulting in a mixed-hybrid failure mechanism. The variation of the axial load due to the loading directions is a representation of the variation of column axial load in exterior beam-column joints due to the frame action under lateral swaying. The effects and evaluation of the variation of the axial load will be further discussed in §4.6.3 and Appendix A.

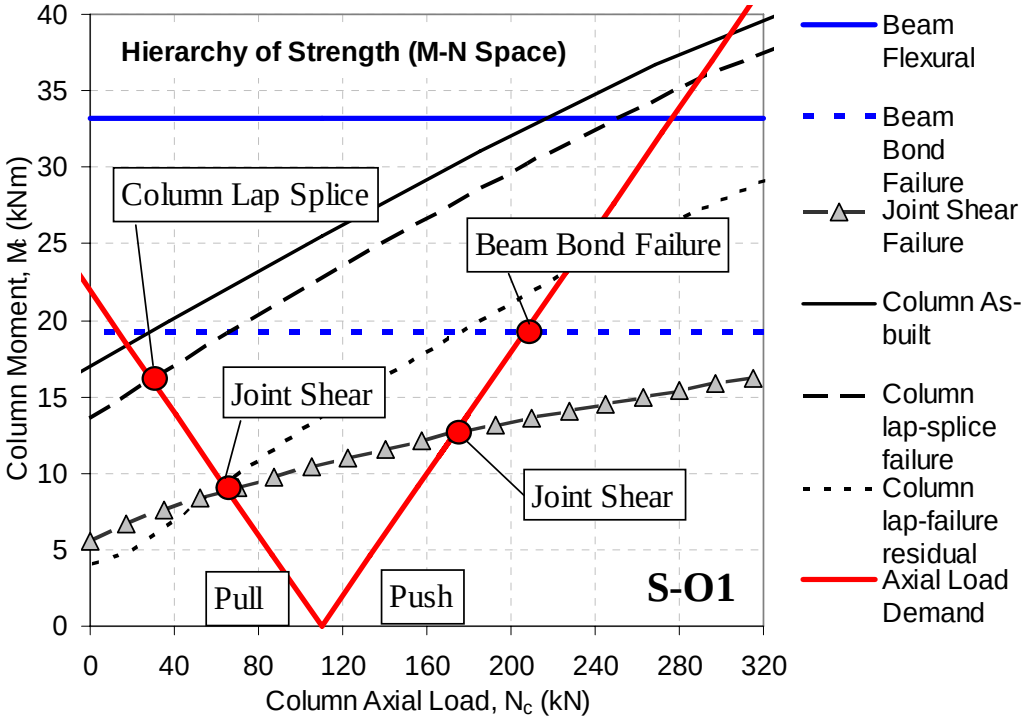

Figure 2.30: Assessment framework for hierarchy of strength of exterior beam-column joints within M_c-N_c (column moment versus axial force) interaction diagram.

Upon establishing the M_c-N_c performance domain of the beam-column joints, depending on the inelastic mechanism, the deformation capacity of the system in terms of inter-storey drift, θ_{drift}, can then be inferred from the available ductility of the inelastic mechanism. For flexural hinging elements, the available ductility and deformation capacities are straight-forward as they can be derived directly from the moment-curvature analysis. For brittle failures such as joint shear, column shear or bond-failure – generally empirical formulas are available and will be used in this study. The following sub-sections will discuss the procedure to calculate the equivalent column moment (M_c) and deformation capacities (e.g. θ_{drift}) for the different inelastic mechanism and failure modes (e.g. beam flexural, joint shear, anchorage and bond failure etc.).

2.4.2 Joint shear capacity evaluation

The evaluation of beam-column joint shear capacity has been traditionally a 'design' question. Depending on the seismic codes, modern joint design would either emphasise on the joint confinement and maximum average joint shear stress without explicit considerations of force transfer within the joint [4, 9] *or* evaluation of the shear force transfer within the diagonal strut and truss mechanisms [47, 167]. In some codes [47, 167], the positive contribution of axial force to joint shear capacity is also recognised. Nevertheless, the design-focussed approach for joint shear capacity based on the truss and the diagonal strut mechanisms may not be entirely suitable for beam-column joints with no or limited joint shear reinforcement and with poor bond behaviour of the reinforcement.

Many past studies have developed various empirical and semi-empirical analytical models for unreinforced or lightly reinforced RC beam-column joints [15, 19, 108, 134, 135, 171, 180, 190, 203, 223, 238]. Further details of the various joint shear models for unreinforced exterior beam-column joint are discussed in ref [190]. In this study, three approaches are considered to assess the joint shear capacity, namely: a) the principal stresses approach [42, 91, 176, 178, 203], b) the ASCE-41 [16]/ACI-318 [4] joint shear stress γ-factor and c) the NZSEE 2006 [169] approach. While the Eurocode 8 (EC8) includes a chapter on seismic assessment of existing structures [46], the joint shear evaluation is based on design expressions for the modern high ductility beam-column joints. Nevertheless, the European fib 2003 bulletin on the Seismic Assessment and Retrofit [80] outlines both the principal stresses and nominal shear stress approach for the assessment of older beam-column joints. Interestingly, joint failures are not included in the Japanese documents on seismic assessment of existing RC buildings [110, 111].

To determine the joint shear demand and capacity, the internal forces within the joint under lateral loading shown in Figure 2.29b are assumed. Given the horizontal shear force, V_{jh}, acting on the joint core (Equation 2.4), the average horizontal shear stress at the mid-depth of the joint core, v_{jh}, therefore can be expressed as:

$$v_{jh} = V_{jh} / b_j h_c \qquad \textbf{2.7}$$

where b_j is the effective width of the joint core as defined by the following equations:

$$b_j = \min of \begin{Bmatrix} b_c \\ b_b \\ b_c + 0.5h_c \\ b_b + 0.5h_c \end{Bmatrix} \qquad \text{NZS3101:2006 [167]} \qquad \textbf{2.8}$$

b_c and b_b are the widths of the column and beam respectively and h_c is the depth of the column. For comparison, the ASCE-41 definition of b_j is shown in Equation 2.9:

$$b_j = \min of \begin{Bmatrix} b_c \\ b_b + h_c \\ b_b + 2x \end{Bmatrix} \qquad \text{ASCE-41 2006 [16]} \qquad \textbf{2.9}$$

where x is the smaller of the perpendicular distance from the longitudinal axis of the beam to the column side.

2.4.2.1 Principal stresses approach for joint shear capacity

In beam-column joints without shear reinforcement, it is reasonable to assume that the joint shear strength is reached at the initiation of the initial diagonal cracking in the joint core [202, 203]. As shown by Vecchio *et al.* [180, 231], the presence of diagonal tensile strain in the joint core will reduce the diagonal compressive strength of the concrete and the maximum joint shear capacity. At the mid-depth of the joint, average shear and axial stresses can be assumed. Given a particular stress state as shown by Mohr's circle in Figure 2.31b, the horizontal joint shear stress, v_{jh}, to induce diagonal joint cracking, is governed by the behaviour of unconfined concrete under bi-directional stresses. Given a limit γ for diagonal principal tensile and compressive strengths of concrete, p'_t and p'_c, the maximum v_{jh} prior to diagonal joint cracking is given by:

$$p'_c, p'_t = \frac{f_v + f_h}{2} \pm \sqrt{\left(\frac{f_v - f_h}{2}\right)^2 + v_{jh}^2} \qquad \textbf{2.10}$$

Note that in Equations 2.10 and 2.11, compression stress is positive as illustrated in the Mohr's circle diagram in Figure 2.31. Considering the vertical average axial stress, f_v is given by P/A_g, the horizontal average axial stress is typically zero (without prestressing) and the principal tensile stress, p'_t can be represented by $\gamma\sqrt{f'_c}$, then Equation 2.10 can be rearranged and simplified for maximum v_{jh} sustained prior to diagonal joint cracking :

$$v_{jh} = \sqrt{p'^2_t - p'_t(f_v + f_h) + 2 f_v f_h} \qquad \textbf{2.11}$$

$$v_{jh} = \gamma\sqrt{f'_c}\sqrt{1 + \frac{P}{\gamma A_g \sqrt{f'_c}}} \qquad \textbf{2.12}$$

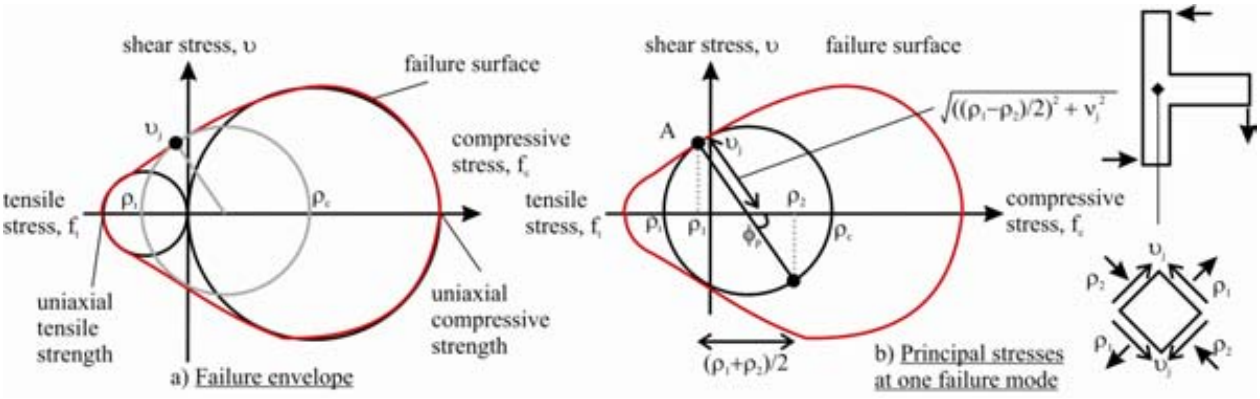

Figure 2.31: Mohr's circle of stress analysis for failure condition of unreinforced beam-column joint.

Based on experimental evidences, various performance limits have been proposed for the principal stresses within the beam-column joints. Priestley *et al.* [202, 203] suggested $p'_t = 0.29\sqrt{f'_c}$ MPa based on the conservative estimation of the concrete direct (uniaxial), typically in the range of $0.33\sqrt{f'_c}$ MPa to $0.5\sqrt{f'_c}$ MPa [57, 196]. In terms of principal compressive stress, p'_c, Priestley *et al.* [203] proposed $p'_c \leq 0.3f'_c$ in order to prevent diagonal compression strut failure. This value was based on the recommendations from Paulay and Priestley [196]. The New Zealand Concrete Standards, NZS3101 [167] also specifies the maximum v_{jh} to be less than 0.20-$0.25f'_c$ in order to prevent brittle diagonal compression failure.

By evaluating empirical data of eighty interior beam-column joints without joint reinforcement, Hakuto *et al.* [91] estimated mean value of $p'_t = 0.17(f'_c)^{2/3}$ and 95% confidence limit value of $p'_t = 0.0867(f'_c)^{2/3}$. From Hakuto *et al.* [91] experiment results, maximum v_{jh}

sustained in interior joints without shear reinforcement was $0.17f'_c$ or $1.0\sqrt{f'_c}$ MPa. For lightly-reinforced exterior joints, the maximum v_{jh} were $0.31\sqrt{f'_c}$ MPa and $0.25\sqrt{f'_c}$ MPa for end hook bent into the joint and out of the joint core respectively [91]. Hakuto *et al.* also proposed a shear degradation curve as a function of ductility of the adjacent beam plastic hinges. Pampanin *et al.* [42, 176, 178] and Hertanto [105] provided further experimental results for several other joint detailing types and reinforcement types.

Figure 2.32 below summarises various proposed degradations of effective p'_t as a function of joint shear deformation, γ_j. The deformation capacity of the system in terms of inter-storey drift, θ_{drift} can be approximately equated to the limiting γ_j. It should be noted that the γ_j value in Figure 2.32 corresponding to the cracked limit state is considerably different (0.0015 instead of 0.015, thus by a factor of 10) from those given in literature [42, 177, 203], as reviews of the experimental results that form the basis of these curves have indicated the possible inaccuracies (if not simply a typo) of such values proposed in literature. Chapter 5 will re-visit these curves in light of the experimental results from this research as well as other tests.

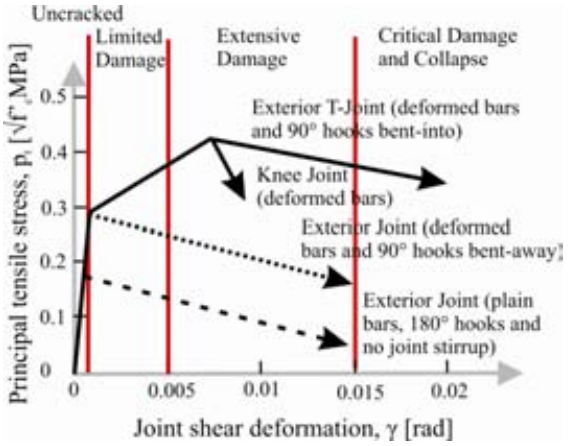

Figure 2.32: Principal tensile stress, p_t degradation curves.

The vertical lines in Figure 2.32 indicate the damage limit states based on joint deformations as suggested by Pampanin *et al.* [178]. These limit states were at that time based on limited experimental data, but other researchers [117, 173, 181] have recently attempted to refine the damage limit states based on larger experimental data set. Pagni and Lowes [173] for example, showed the mean γ_j (as drift ratio) for limited damage, extensive damage and critical damage/collapse to be 0.5%, 1.3-2.4% and 3.0% respectively. However, due to limited experimental data and the diversity in beam-column joint detailing in available test data, these damage limit states are indicative values at best.

In literature, there were several other approaches to the joint shear strength evaluation that were based on the joint principal stresses. Pantazopoulou and Bonacci [180] formulated a shear strength model for interior beam-column joints based on the compatibility of average strain and stress equilibrium, assuming well-confined joints. Two failure mechanisms, the yielding of column longitudinal reinforcement and the diagonal compressive strut failure, were defined. Wong [238] adopted the modified compression field theory (MCFT) [231] with softened truss modelling within an iterative solution for the average shear and principal stresses-strain responses. Others have used strut-and-tie models in conjunction with principal stresses damage limit to assess the joint shear strengths [171, 222, 223, 236].

2.4.2.2 ASCE-41 recommendations

The ASCE-41 seismic assessment guidelines [16] use the same ACI-318 code [4] and ACI-352 recommendation [9] for calculating the joint shear capacity with modified values for joint shear capacity coefficient γ. Lower values of γ are specified in ASCE-41, considering the non-ductile detailing prescribed in pre-1970s beam-column joints. As per ACI-318 code, higher joint shear capacity coefficient γ is assigned to joints with confining transverse beams (as shown in Figure 2.33a). Table 2.1 below summarises the joint shear strength coefficient γ as recommended by various international seismic design and assessment codes. The standard form of equation for joint shear strength is described by Equation 2.13:

$$V_{joint} = \gamma \sqrt{f'_c} b_j h_c \qquad \textbf{2.13}$$

where b_j is the effective width of the joint, as described in Equation 2.9 (ASCE-41 specification).

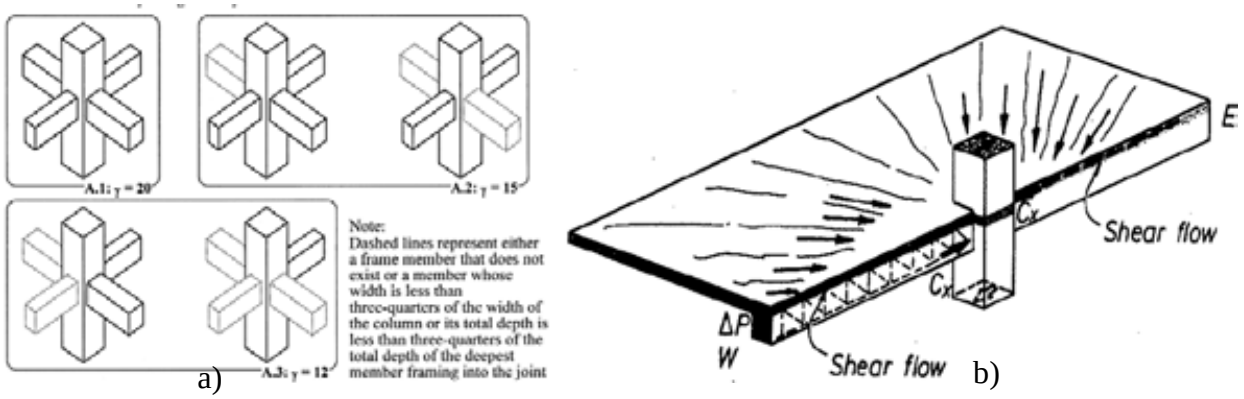

Figure 2.33: a) Values of joint shear strength coefficient γ for various joint topologies given by 2008 ACI-318 [4]; b) Transfer of flange membrane forces into beam-column joint [196] .

In comparison, the equivalent γ factor (named k) in the New Zealand assessment guidelines [169] is not a function of the presence of transverse beams but a function of longitudinal beam anchorage and type of joint (exterior vs. interior). This is consistent with the assumption that confinement effect from tension flange membrane forces (Figure 2.33b) would diminish when plastic hinges developed in the transverse beams [51, 196]. In the EC8-III [46], the joint shear strength is assessed based on similar provisions for the design of new beam-column joints, in which the confinement from transverse beams is neglected. In Chapter 8 of this study, a more thorough treatment of the influence of floor-slabs and transverse beam stubs on exterior beam-column joints will be given, in light of the experimental results of as-built and retrofitted beam-column joints with floor slabs and transverse beams.

Table 2.1: Values of joint shear strength coefficient γ for various joint topologies based on various international codes. A constant column axial load was assumed in the assessment.

Code/Guidelines	knee joint	exterior joint		interior joint	
		unconfined	confined	unconfined	confined
ACI-318-08 / ACI-352-02	1.00	1.00	1.25	1.25	1.66
ASCE-41 / FEMA 356 *	0.33	0.50	0.66	0.83	1.00
NZSEE 2006	-	0.25**	0.50***	1.00	1.00
NZS3101:2006 [+]	1.00	1.00	1.00	1.00	1.00
EC8-III (2004) [++]	2.44	1.95	1.95	2.44	2.44

Notes: Confined joints are joints with two transverse beams framed into the joint.
*for lightly reinforced joints (ρ"<0.003) **Beam bars bent away from joint. ** Beam bars bent into the joint. [+] Maximum joint stress of 0.2f'c or approximately 1√f'c (MPa) in all joint types. [++] based on assumed f'c of 25MPa and normalised axial force of $0.1A_g$f'c.

In the ASCE-41 Supplement 1 [68], the joint transverse reinforcing are categorised into conforming and nonconforming detailing, where joint transverse reinforcement are conforming if stirrups are spaced at $h_c/2$ within the joint. The values given in Table 2.1 are still applicable despite the change in the approach of assessing the conformity of the joint reinforcing. The proposed update for ASCE-41 [68] includes a 50% reduction of the effective stiffness of beam-column joints. ASCE-41 does not specify any method to calculate the deformation capacity of joint but includes a very strict plastic rotation for acceptance criteria, where joints are expected to respond elastically.

2.4.2.3 2006 NZSEE recommendation

The procedure outlined in the 2006 NZSEE guidelines [169] is based on the principal tensile stress approach [91, 201, 202] as it is acknowledged that NZS3101-06 [167] is too conservative

for seismic assessment of existing beam-column joints. The shear strength of beam-column joints without shear reinforcement, V_{pjh}, is calculated as:

$$V_{pjh} = v_{ch} b_j h \quad \text{(in kN)} \tag{2.14}$$

$$v_{ch} = \sqrt{1 + \frac{P}{A_g k \sqrt{f'_c}}} \sqrt{f'_c} \le \frac{1.92}{0.85} \sqrt{f'_c} \quad \text{(in MPa)} \tag{2.15}$$

where k is the factor accounting for different joint typographies and detailing. P is the axial column compression force on the joint. For exterior joints with beam longitudinal bars hooked into the joint core and away from the joint core, k factors are 0.4 and 0.25 respectively and for interior joints, k factor is 1.0. In ref. [202], k factor is given as 0.29 as the lower limit.

To determine the deformation capacities of the joint shear hinges, a shear strength degradation curve as a function of the curvature ductility of the adjacent plastic hinges, as shown in Figure 2.34, is given. The joint shear envelope then is used to determine the available curvature ductility of the adjacent plastic hinge, to determine the global displacement capacity.

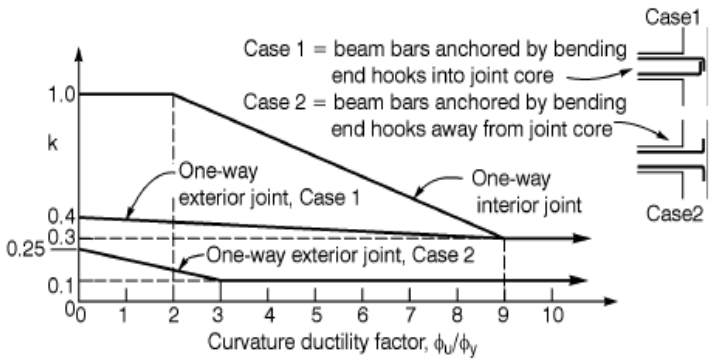

Figure 2.34: Joint shear strength degradation as function of adjacent plastic hinge curvature [169].

2.4.3 Beam and column flexural capacities

The elements' flexural strength capacities are established using moment-curvature analysis based on fibre sectional analysis and fundamental principles of RC [187, 196]. The moment curvature analysis is performed by solving the neutral axis to balance the section equilibrium for increasing levels of section curvature, as shown in Figure 2.35. The Excel spreadsheet section analysis is compared and verified with the section analysis program Response-2000 [24]. Acknowledging the influence of bond failure of the plain round reinforcement on the flexural and ductility capacities, the flexural capacities of the elements are evaluated for both values of steel stress, f_s,

calculated using assuming full bond and bond-slip (limited by the bond stress capacity, $\tau_{b,max}$)(to be expanded in §2.4.5).

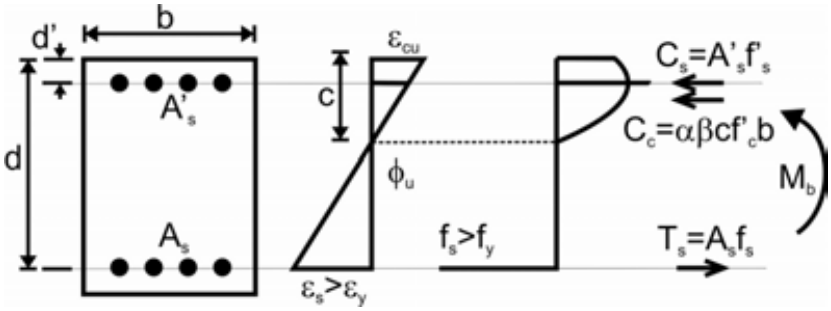

Figure 2.35: Section analysis of flexural capacity for beam.

Concrete compression strain at peak stress, ε'_c, and maximum compression concrete strain, ε_{cu}, of 0.002 and 0.004, are adopted as these are typical design limits [203]. Flexural elements in pre-1970s RC constructions typically have only nominal transverse reinforcing e.g. ¼" bars at 10-11" spacing (6mm diameter at 250-280mm centres) as shown in Building A described in §2.2.4. As such, Popovics unconfined concrete stress-strain relationship [57] as given by the following equations was used for the sectional analysis:

$$\frac{f_c}{f'_c} = \frac{n\left(\varepsilon_c / \varepsilon'_c\right)}{n-1+\left(\varepsilon_c / \varepsilon'_c\right)^{nk}} \text{ (MPa)} \qquad \textbf{2.16}$$

$$k = 0.67 + f'_c / 62 \geq 1.0 \text{ (MPa)} \qquad \textbf{2.17}$$

$$n = \frac{E_c}{\left(E_c - f'_c / \varepsilon'_c\right)} \qquad \textbf{2.18}$$

where f_c is the concrete stress given concrete strain ε_c, f'_c is the peak compressive stress from a cylinder test, ε'_c, is the concrete strain at peak stress f'_c and E_c is the modulus of elastic of concrete. To approximate E_c, the equation recommended by NZS3101[167] is used:

$$E_c = 3320\sqrt{f'_c} + 6900\left(\frac{\rho_c}{2300}\right) \text{(MPa)} \qquad \textbf{2.19}$$

Concrete density, ρ_c, of 2400kg/m^3 is assumed.

For the reinforcing steel, the closed-form stress-strain relationship proposed by King *et al.* [118], as given by the following equations, is used:

$$f_s = E_s \varepsilon_s \qquad \varepsilon_s \le \varepsilon_y \qquad \textbf{2.20}$$

$$f_s = f_y \qquad \varepsilon_y \le \varepsilon_s \le \varepsilon_{sh} \qquad \textbf{2.21}$$

$$f_s = f_y \left[\frac{m(\varepsilon_s - \varepsilon_{sh}) + 2}{60(\varepsilon_s - \varepsilon_{sh}) + 2} + \frac{(\varepsilon_s - \varepsilon_{sh})(60 - m)}{2(30r + 1)^2} \right] \qquad \varepsilon_{sh} \le \varepsilon_s \le \varepsilon_{su} \qquad \textbf{2.22}$$

$$m = \frac{\left(f_{su} / f_y \right)(30r + 1)^2 - 60r - 1}{15r^2} \qquad \textbf{2.23}$$

$$r = \varepsilon_{su} - \varepsilon_{sh} \qquad \textbf{2.24}$$

where ultimate steel strain, ε_{su} = 0.20, yield steel strain, $\varepsilon_y = f_y/E_s$, onset of strain hardening steel strain, ε_{sh} = 0.015, and the yielding and fracture steel stresses, f_y and f_u are taken from steel coupon tensile tests. Figure 2.36 illustrates the stress-strain relationships used.

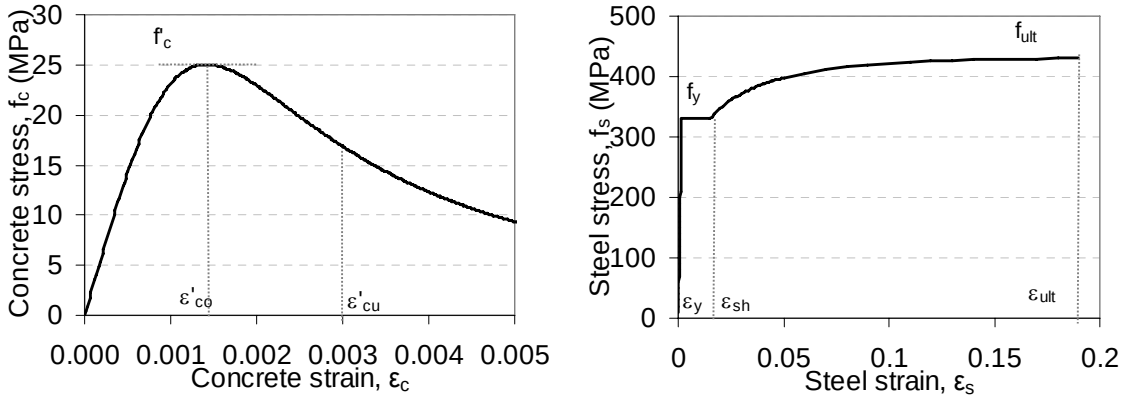

Figure 2.36: Stress-strain relationships for sectional moment-curvature analysis: a) Popovic's unconfined concrete model; b) King and Park reinforcing steel model.

For beams with floor slabs, the slab reinforcement contribution within the effective flange width is assessed in calculating the beam negative moment capacity. Further discussion on the assessment of effective flange width, b_{eff}, of a cast-in-site floor slab in pre-1970s beams will be given in Chapter 8. In the preliminary assessment of the beam-column joint flexural strength with the floor slab flange contribution, the b_{eff} calculation as per prescribed in Cl. 9.3.1.4 of the 2006 NZS3101 [167] and as given by Equation 2.25, is adopted. The equation recommended by the 2006 NZSEE guidelines [169], given in Equation 2.26, is considered non-conservative as it overestimates the b_{eff} significantly. In comparison to other international codes as tabulated in Table 2.2, the 2006 NZSEE calculated b_{eff} is significantly larger.

$$b_{eff} = b + \min of \begin{Bmatrix} h_b \\ 8t_{slab} \\ \frac{1}{8}L_x \\ \left(\frac{h_{b1}}{h_{b1}+h_{b2}}\right)L_y \\ 0.5w_{flange} + h_b \end{Bmatrix} \text{NZS3101 [167]} \qquad \textbf{2.25}$$

$$b_{eff} = b + \min of \begin{Bmatrix} 0.25L_x \\ 0.5L_y \\ 0.25L_{x,tb} \end{Bmatrix} \text{NZSEE 2006 [169]} \qquad \textbf{2.26}$$

where L_x = beam span, L_y = bay width between parallel beams, $L_{x,tb}$ = length of transverse beam along the edge of slab, h_b = beam depth and b = beam width, w_{flange} = width of the provided flange at edge of slab, and t_{slab} = thickness of the slab.

Table 2.2: Values of effective slab tension flange width, b_{eff} based on various international codes.

Code/Guidelines	Effective tension flange width (mm)
NZS3101:2006	890
ASCE-41 / FEMA 356	980
NZSEE 2006	1753
JBDPA-2001 / AIJ-1994	839
EC8-III (2004) [+]	630

All calculations assumed the presence of transverse beam, beam span of 3047mm, bay width of 3047mm, beam and column widths of 230mm, beam depth of 330mm, slab thickness of 100mm and provided clear slab flange width of 375mm.

NZS3101:2006 specifies two sets of expressions to calculate the b_{eff} for the contribution of slab tension flange. Cl. 9.3.1.4 used herein (Equation 2.25) dictates the contribution of the slab reinforcements to the T- and L- beams design flexural strength. These equations are consistent with the Cl. 8.12 of the 2008 ACI318 code [4] and Paulay and Priestley [196] recommendations. These equations are derived from experimental tests of beam-column joint subassemblies.

Cl. 9.4.1.6.2 of NZS3101:2006 dictates the contribution of the slab reinforcements to the beam over-strength capacity for capacity design. This over-strength contribution is generally observed in large frame sub-assemblies tests and is attributed to diaphragm interaction with transverse beams and beam-elongation. Therefore, for beam-column joint subassembly studied in this research, Cl. 9.3.1.4 of NZS3101:2006 gives a more realistic estimation of effective tension flange width.

Figure 2.37 shows the moment-curvature plots for various beam sections with and without the slab flange effects. Notably, for the example presented in Figure 2.37, a realistic 6" (152.4mm) cast-in-situ slab can have significant strength enhancement to the negative flexural capacity of a 13.5" x 19.5" (345 x 495 mm) beam. While ultimate curvature decreases with floor slab strength enhancement (as well as beam section with bond slip failure), curvature ductilities of 8 to 16 were still attained in the example shown in Figure 2.37.

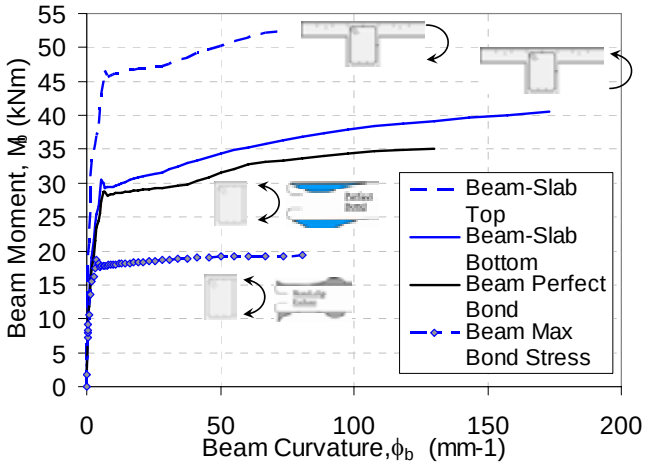

Figure 2.37: Moment-curvature analysis for beams with and without slab and bond effects.

For the generation of column moment-axial force (M-N) interaction diagrams, the section analysis program Response-2000 [24] is used for its accuracy and simplicity. Response-2000 implements the aforementioned Popovic unconfined concrete model and a simple quadratic beyond strain hardening steel stress-strain model [24]. In the assessment of the ultimate limit state, two limiting M-N surfaces for the columns are considered: a) conventional tensile and compressive failures and b) lap-splice failure of the column longitudinal reinforcement. Strain at the end of the yield plateau, ε_{sh} of 0.015, and ultimate steel strain, ε_{su} of 0.15, are adopted. §2.4.6 will give further details on the procedure adopted in evaluating the lap-splice capacity of plain smooth reinforcement. Figure 2.38 illustrates the hierarchy of strength performance domain and the moment-curvature examples for a pre-1970 column section.

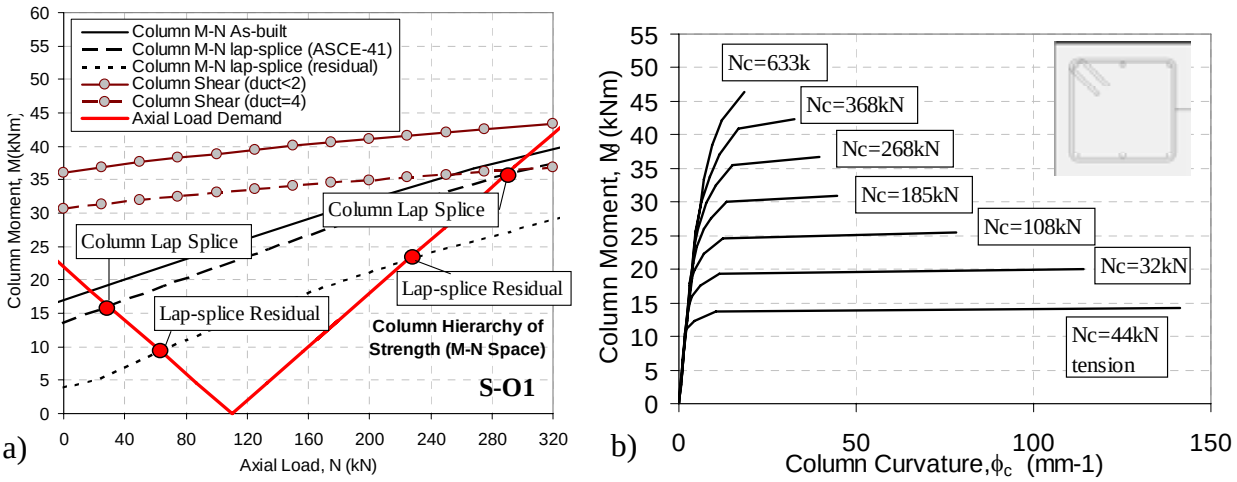

Figure 2.38: a) Hierarchy of strength analysis for column failure modes only; b) Moment-curvature analysis for columns under varying axial column loads.

To calculate the corresponding displacement capacities given the curvature and rotation capacities of the flexural elements, an idealisation of the curvature distribution can be assumed [196]. By considering the strain penetration length, L_{sp}, and the plastic hinge length, L_{ph}, the yield deformation, θ_y, and ultimate flexural deformation, θ_u, can be calculated using following equations:

$$\theta_y = 2\Delta_y / L_x = 2\left(\phi_y \left(H + L_{sp}\right)^2 / 3\right) / L_x \qquad \textbf{2.27}$$

$$\theta_u = 2\Delta_{ult} / L_x = 2\left(\Delta_y + (\phi_u - \phi_y) L_{ph}\right) / L_x \qquad \textbf{2.28}$$

$$L_{sp} = 0.022 f_y d_b \qquad \textbf{2.29}$$

$$L_{ph} = 0.2\left(\frac{f_u}{f_y} - 1\right) H + L_{sp} \le 2L_{sp} \text{ and } 0.2\left(\frac{f_u}{f_y} - 1\right) \le 0.08 \qquad \textbf{2.30}$$

where L_x is the beam span and H is the length from the contra-flexural point to the centroid of the plastic hinge length. It is noted that Equations 2.27 to 2.30 are derived from experimental tests with deformed bar reinforcing. It is thus expected that the use of plain round bars in this research would affect the values of Δ_y and Δ_u While other empirical equations are available to predict the deformation capacities of flexural elements, e.g. ([80, 111, 179]), the lack of comprehensive pre-1970s experimental database limits the accuracy of these empirical equations.

2.4.4 Beam and column shear capacities

The in-depth assessment of the shear strength of beams and columns is a complicated subject that is beyond the scope of this study. Significant progress has been made in recent years pertaining to the accurate evaluation of shear failure before and after the yielding of the flexural elements [119, 204, 217, 231] and more recently the evaluation of shear-axial failure of non-ductile columns [70, 71]. Shear strength degradation is generally a function of structural and curvature ductility. For this study, the strength capacity of the beam and columns are evaluated using the following Equations 2.31 to 2.34, as proposed by Sezen and Moehle [217] for lightly-reinforced concrete columns, which has also been adopted in the ASCE-41 standard [16].

$$V_n = k_\Delta (V_c + V_s) \tag{2.31}$$

$$k_\Delta = \begin{cases} 1.0 & \mu_\Delta \le 2 \\ 1.0 - 0.075(\mu_\Delta - 2) & 2 < \mu_\Delta \le 6 \\ 0.7 & \mu_\Delta > 6 \end{cases} \tag{2.32}$$

$$V_c = \frac{0.5\sqrt{f'_c}}{a/d}\sqrt{1 + \frac{P}{0.5\sqrt{f'_c}A_g}}(0.8A_g) \tag{2.33}$$

$$V_s = \frac{A_{st} f_{yh} d}{s} \tag{2.34}$$

where μ_Δ = displacement ductility, P= axial compression load on the section, a = distance from maximum moment section to point of inflection (typically 0.4-0.6H_c for columns), d = effective depth of the section (=0.8h), A_g = gross area of the section, $A_{st,}$ f_{yh} and s are the reinforcement area, yield strength and spacing of the transverse reinforcement. The ratio a/d must not be less than 2 or greater than 4. The deformation capacity of the flexural elements with and without axial load under shear failure, $\theta_{drift,s}$, can be determined using the following empirical formula[71]:

$$\theta_{drift,s} = \frac{\Delta_s}{L} = \frac{3}{100} + 4\rho'' - \frac{1}{500}\frac{\nu_{jh}}{\sqrt{f'_c}} - \frac{1}{40}\frac{P}{A_g f'_c} \tag{2.35}$$

where ρ'' = transverse reinforcement ratio and v_{jh} = the maximum nominal shear stress.

For comparison, the approach proposed by Priestley *et al.* [203, 204] and adopted in NZSEE 2006 [169] in assessing the shear strength of column is given by the following Equations 2.36 to 2.41. Similar to the Sezen-Moehle model, the shear strength degradation factor is given as a function of column curvature ductility, as shown in Figure 2.39b.

$$V_n = 0.72(V_c + V_s + V_p) \quad \textbf{2.36}$$

$$V_c = \alpha\beta\gamma\sqrt{f'_c}(0.8A_g) \quad \textbf{2.37}$$

$$1 \le \alpha = 3 - \frac{M}{Vd} \le 1.5 \quad \textbf{2.38}$$

$$\beta = 0.5 + 20\rho_{cl} \le 1.5 \quad \textbf{2.39}$$

$$V_s = \frac{A_{st} f_{yh} d}{s}\cot\theta \quad \textbf{2.40}$$

$$V_p = P\tan\varsigma \quad \textbf{2.41}$$

where M/V = the ratio of moment to shear at the section, d= is effective depth of the section, ρ_{cl} = column longitudinal reinforcement ratio, θ = angle of critical flexural shear cracking, taken to be 30° and ς = effective angle of the compressive strut in the column (represented by α in Figure 2.39a below).

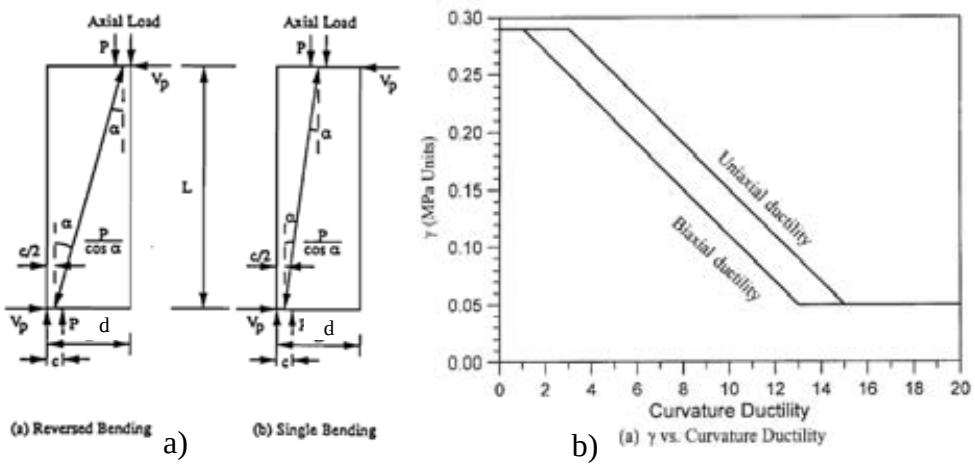

Figure 2.39: Column shear strength assessment based on Priestley *et al.* [119, 204]: a) contribution of axial force to shear strength; b) shear strength degradation factor based on curvature ductility for Eqn. 2.37.

2.4.5 Capacity of anchorage and bond of plain round bars

Anchorage and bond capacities of reinforcing steel can significantly influence the seismic behaviour of reinforced concrete elements, in particular the beam-column joints (e.g.[20, 79]). For pre-1970s beam-column joints with plain round bars, the anchorage and bond failure could be the weakest link that limit the steel stress development within a beam or column flexural hinge [77, 232]. The failure of the beam longitudinal anchorage and subsequent bond degradation

within the joint would also limit the joint shear capacity [42, 92]. Herein, an empirical method to evaluate the influence of bond and anchorage capacity for plain round bars will be presented, after a discussion of existing literature on the bond capacity of plain round bars.

2.4.5.1 Existing tests and literature on the bond and anchorage of plain round bars

As discussed in §2.2.2.5, the use of plain round reinforcing was prevalent around the world prior to the 1950-70s. Much research has been carried out in studying the bond of reinforcing steel-to-concrete as well as the anchorage capacity of straight and hooked anchorages (e.g. [12, 79]). Mylrea [154] gave a good background of the historical development of the 180° hook anchorage of the plain-round bars prior to the 1930s while Fishburn [83] carried out an extensive pull-out test campaign of plain and deformed bar anchorages with various bending angles.

With the introduction of deformed reinforcement in the 1940-50s in the USA [5], most post-1950s bond researches were focussed on deformed bars. Seminal works by Abrams [2], Goto *et al.* [89], Lutz and Gergely [136], Tepfers [225, 226], Popov *et al.* [81, 82, 200] and Eligehausen *et al.* [67] have laid the foundation of the understanding of bond stress-slip behaviour and the bond mechanics of deformed bars. Figure 2.40a shows the cyclic average bond stress-slip model conventionally used for deformed-bar bond modelling [67]. The average bond stress, τ_b, along a reinforcement bar with diameter d_b, cross section area A_s and average steel stress f_s, acting along a development length, l_d, can be calculated using:

$$\tau_b = \frac{f_s A_s}{\pi d_b l_d} \qquad \textbf{2.42}$$

In a more generic form of relationship between the reinforcement steel stress-strain constitutive [f_s =f(ε_s)] and the bond stress-slip [τ_b = f(Δ_{slip})] relationships, Monti *et al.* [150] have illustrated the equilibrium and compatibility conditions that approximate the relationships:

$$f_s = \pi d_b \int_0^{l_{d,prov}} \tau_b dx \qquad \textbf{2.43}$$

$$\varepsilon_s = \int_0^{l_d} \Delta_{slip} dx \qquad \textbf{2.44}$$

where $l_{d,prov}$ is the development length provided or the embedded straight length of the reinforcement.

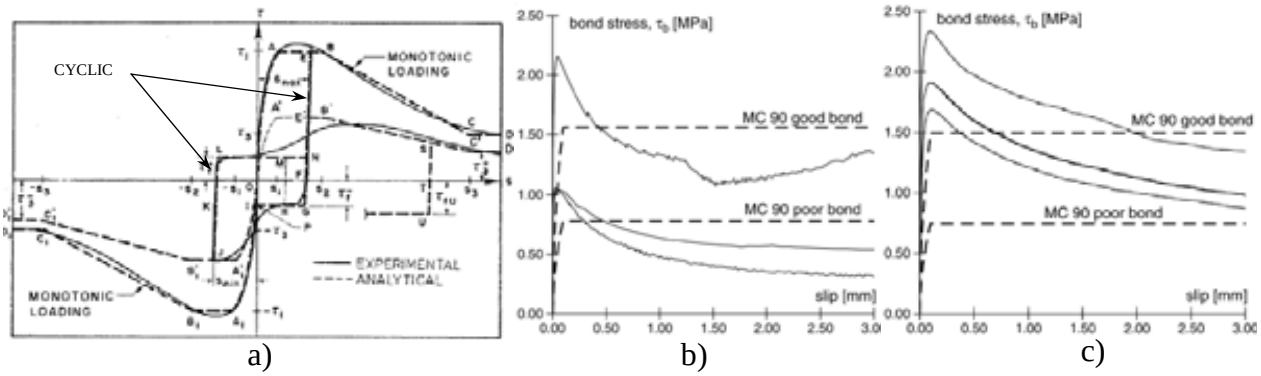

a) b) c)

Figure 2.40: a) Conventional deformed reinforcement-to-concrete cyclic and monotonic bond model [67]; b-c) Bond stress-slip relationship of plain round bars within $10d_b$ straight anchorage length: b) beam bond test [74]; c) pull-out test [74].

In relation to the anchorage capacity of hooked reinforced in beam-column joints, the research at the University of Texas Austin [139, 147, 198] provided the experimental validations for the 1976 ACI-352 recommendations [10]. However, most of their tests are under monotonic loading while in reality, reversal cyclic action is important for hooked anchorage into beam-column joints.

More recently, to better model and evaluate the seismic performance of the pre-1970s non-ductile RC buildings built with plain round bars, various pull-out and beam tests on this type of older smooth reinforcement have been carried out [73-76, 116, 234]. Plain round bars under monotonic loading generally exhibited a bond stress-slip hysteresis as shown in Figure 2.40b-c. The monotonic tests by Fabbrocino *et al.* [74, 75] and Kankam [116] have measured the maximum bond stress capacity, $\tau_{b,max}$, to be 1.0MPa (on average) and residual bond stress capacity (at ~3mm slip), $\tau_{b,res}$, to be 0.5MPa (on average). These results were consistent with the CEB-Fib 1990 Model code [45] recommendation of $\tau_{b,max} = 0.3\sqrt{f'_c}$ MPa and $\tau_{b,res} = 0.15\sqrt{f'_c}$ MPa for plain round bars with good bonds.

Verderame *et al.* [234, 235] tested plain-round bars under monotonic and cyclic loading to verify the local bond degradation. The range of maximum bond stress capacity, $\tau_{b,max}$ measured was 0.6 to 2.15MPa (average of 1.24MPa or $0.31\sqrt{f'_c}$ MPa). The cyclic bond hysteresis and strengths were found dependent on the residual frictional bond strength, $\tau_{b,res}$. Beyond the initial $\tau_{b,max}$ where adhesive micro-interlocking was no longer resisting any bond stress, the bond resistance reduced to a relatively stable (constant energy dissipation) hysteresis loop with maximum residual bond strength of $\tau_{b,res}$, as shown in Figure 2.41 [234, 235].

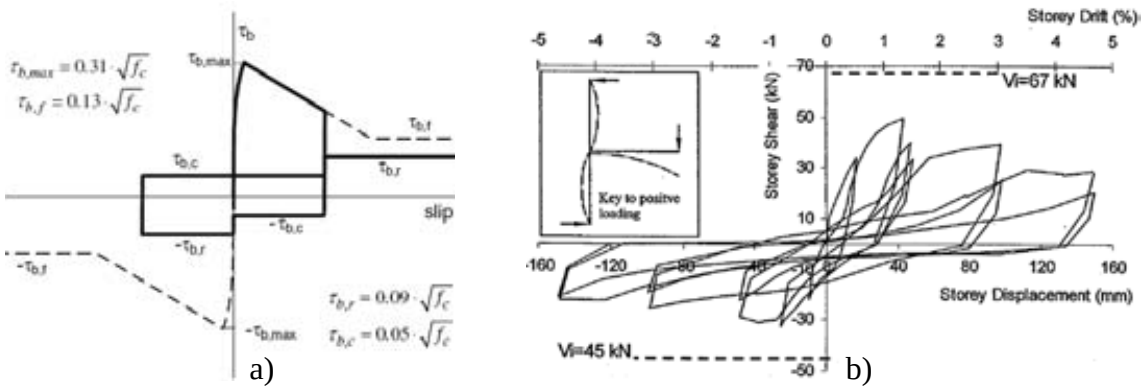

Figure 2.41: a) Cyclic bond model for plain round bars [235] b) Pinching hysteresis on exterior beam-column joint with bond degradation of plain round bar reinforcement[132].

Some trends of bond degradation were observed with increasing loading cycles. Verderame *et al.*'s data gave the range of $\tau_{b,res}$ = 0.25-0.68MPa (average of 0.46MPa or $0.12\sqrt{f'_c}$ MPa) in the first post-$\tau_{b,max}$ cycle. In subsequent cycles, $\tau_{b,res}$ degraded to the 0.20 MPa ($0.05\sqrt{f'_c}$ MPa) in the 2nd cycle and 0.11 MPa ($0.03\sqrt{f'_c}$ MPa) in the 5th cycle. Significant variability attributed to the variability of the adhesion and friction mechanisms of the bond of plain-round bars to concrete was observed in the results. A cyclic bond model was proposed by Verderame *et al.* based on these test results, as shown in Figure 2.41a.

In terms of global hysteresis behaviour, tests on beam-column joints subassemblies [105, 132, 177] with plain round bars have shown significant pinching hysteresis behaviour and reduced energy dissipations due to bond loss from cyclic loading as illustrated in Figure 2.41b. The expected poor bond behaviour of plain round bars within cracked beam-column joint core is almost unavoidable, even in some post-retrofit solutions, unless a whole new load path is provided and joint cracking is prevented in the retrofit scheme. For interior joints where reversal of stresses along the longitudinal bars passed through the joints demand significant bond strength, bond failure was shown to reduce adjacent beam curvature ductility [92] and reduced column flexural capacity [42].

2.4.5.2 ASCE-41 assessment of bond-slip capacity of plain round bars

As mentioned in §2.4.3, in order to calculate the flexural capacities of the beams and columns with plain round bars, the limit of the bond stress capacity, τ_b, on the maximum f_s developed within the longitudinal reinforcement must be assessed. Most existing procedures rely on either the ratio of the provided and required development lengths, l_d, or some semi-empirical formulations that relate the maximum τ_b and force transferred into the steel reinforcement ($A_s f_s$).

For bond capacity of reinforcement anchored within beam-column joints, it is more common to use the latter method [16, 80], as considered herein.

The empirical model proposed by Moehle *et al.* [148] and adopted in the FEMA356/ASCE-41 [16] and the fib report [80] is given by the following equation:

$$f_s = \frac{10\sqrt{f'_c}\,l_{d,prov}}{d_b}(350 - f_{s,col}) \le f_y \qquad \textbf{2.45}$$

where $l_{d,prov}$ is the provided development length and $f_{s,col}$ is the column reinforcement stress obtained from sectional analysis.

Alternative equations for l_d for straight anchorages terminating in exterior joint were available in some older literature from the 1992 ACI-408[12] and the 1985 ACI-352R[11], but no longer available in the 2002 ACI-352 [9]. However, the difficulty to implement these empirical equations such as Equation 2.45 led to a simplified equation in the ASCE-41 standards. For straight, discontinuous bars embedded in beam-column joints, with clear cover over the embedded bars exceeding $3d_b$, the maximum strength developed before bond failure is:

$$f_s = \frac{17.23}{d_b} l_e \le f_y (in \quad MPa) \qquad \textbf{2.46}$$

Where d_b = diameter of embedded bars and l_e = embedded development length within beam-column joint. However, as explained in §2.3.1, such a scenario of straight embedded anchorage terminated within the joint was uncommon in New Zealand's pre-1970s construction practice.

The improved tensile anchorage of 90°/180° hooked anchorages into beam-column joint, while not specified in ASCE-41, is recognised in the 2008 ACI-318 [4]. For example, with 90° hook bend into the joint core with at least $4d_b$ straight extension beyond the bending, the minimum required straight development length into beam-column joint for normal weight concrete is given by:

$$l_d = \frac{f_y d_b}{5.37\sqrt{f_c'}} \ge \max\begin{cases} 8d_b \\ 152.4mm \end{cases} (mm) \qquad \textbf{2.47}$$

In the NZSEE guidelines [169], while qualitative discussion of the influence of bond on the strength and deformation capacities of the beams, columns and joints is given, no quantitative procedure has been given for the assessment of the effect of bond degradation on the lateral capacities of the beam-column joint connections. The NZSEE guidelines refer to the work of Hakuto *et al.* [91, 92], in which bond degradation of the longitudinal beam bars across the

interior joints was found to reduce the adjacent beam's flexural strength by 5-10% and curvature ductility by 50-70%.

2.4.5.3 Semi-empirical formulation for bond failure of plain round bars

The procedure discussed in the preceding section was developed largely based on experimental tests on structures with deformed bars. In light of the bond test data of plain round bars, as discussed in §2.4.5.1, a semi-empirical formulation based on the maximum and residual bond stress capacities, ($\tau_{b,max}$ and $\tau_{b,res}$) can be developed to calculate the maximum f_s within the RC section.

By assuming a simple triangular bond stress-slip relationship and a uniform bond stress, u_b, along a development length, l_d, Equation 2.42 can be expanded and rearranged for the maximum f_s developed in the reinforcement given a u_b capacity:

$$f_s = \frac{\tau_b \pi d_b l_b}{A_s} = \frac{4 l_{d,prov} u_b}{d_b} \le f_y \qquad \textbf{2.48}$$

$$f_s = \frac{4(1.5h_c)(0.3\sqrt{f'_c})}{d_b} \le f_y \text{ for maximum bond capacity} \qquad \textbf{2.49}$$

$$f_s = \frac{4(1.5h_c)(0.15\sqrt{f'_c})}{d_b} \le f_y \text{ for residual/frictional bond capacity} \qquad \textbf{2.50}$$

where $l_{d,prov}$ is the provided development length, d_b is the beam longitudinal beam diameter, f_y is the yield strength of the beam reinforcement.

$l_{d,prov}$ is taken to be 150% the provided straight embedded length (approximately the depth of the column, h_c) to account for added efficiency of the 180 degree hooks. This was derived from the ratio of the required straight development lengths for straight bars and hooked anchored bars from NZS3101 and ACI318. This is given as the ratio Equations 2.56 and 2.58 (to be described in the next section). Numerically, the hooked anchorage is therefore approximately 3.0 more effective in terms of the maximum f_s developed for deformed bars. For plain round bars, a factor of 1.5 (150%) is therefore used, as the required l_d for plain bars is typically double the l_d required for deformed bars.

Considering the range of values of the bond stress peak and residual capacities ($\tau_{b,max}$ and $\tau_{b,res}$) for plain round bars discussed in the preceding section, the CEB-Fib 1990 Model code [45] recommendations for plain round bars good bond were used. That is $\tau_{b,max} = 0.3\sqrt{f'_c}$ MPa and $\tau_{b,res} = 0.15\sqrt{f'_c}$ MPa. Therefore, substituting $u_b = \tau_{b,max}$ and $u_b = \tau_{b,res}$ would yield to simplified

expressions for maximum bond and residual bond capacities for RC flexural elements with plain round bars (Equations 2.49 and 2.50). For example, a typical pre-1970s beam-column joint with h_c=450mm, d_b=15mm and f'_c=20MPa would suggest a maximum and residual f_s of 241.5MPa and 120.7MPa.

2.4.6 Capacity of column lap-splice with plain round bars

Extending the anchorage issue to the columns lap-splice in beam-column joints subassemblages, inadequate lap-splice in columns subassemblages (e.g. [1, 49, 52, 146, 211, 232, 233]) and in beam-column joints subassemblages [27, 197] were found to reduce ductility capacity of the column flexural hinges, resulting in premature column failure. Very limited amount of tests were done on columns or joint subassemblies with plain round bars column lap- splice [211, 232, 233].

Figure 2.42a shows an example of force-displacement hysteresis of column specimens with plain round bars reinforcing and inadequate lap-splice tested by Saunders [211]. Straight lap length, l_d of 45d_b was used. In tests by Verderame *et al.* [232, 233], column subassemblies with lap-splice of 180° hooks plain round bars with l_d = 45d_b were tested. A fixed-end rocking at the column and foundation cold-joint interface prevented total lap-splice failure in Saunders' tests. A comparison of the force-displacement hysteresis is given in Figure 2.42. Nevertheless, the characteristic slipping and pinching hysteresis loop and cyclic strength degradation from lap splice and bond failure were evident from both Saunders and Verderame *et al.* tests.

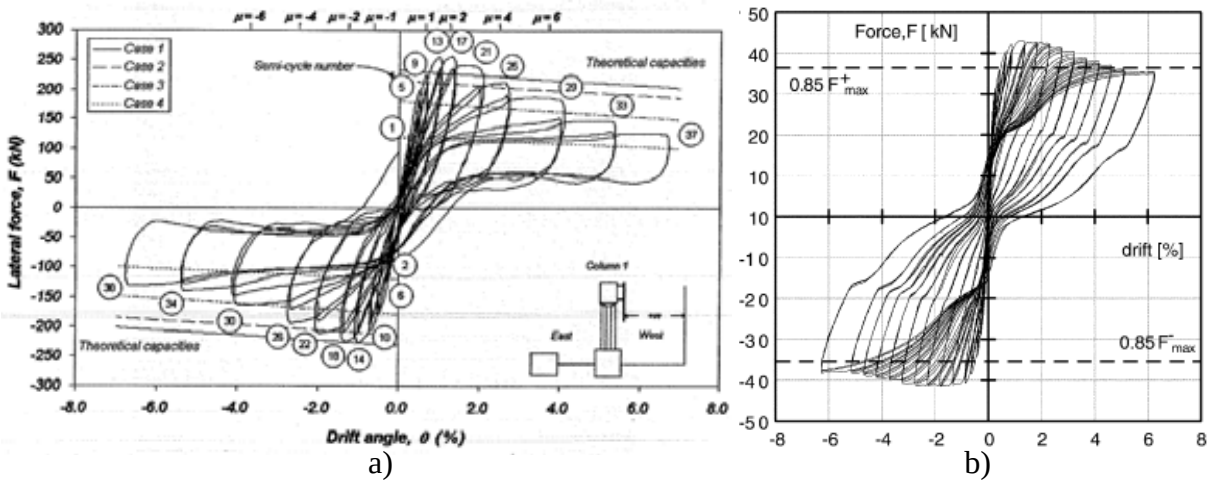

a) b)

Figure 2.42: Cyclic test load-displacement plots for pre-1970s columns with plain round bars: a) lap splice with straight lapping length of 45d_b [211]; b) lap splice with 180° hooked bars with lap-length of 40d_b [232].

In absence of capacity design to prevent flexural hinges in the columns, premature failure of the column lap-splice would limit the column flexural strength and ductility capacities [35, 60,

170, 194, 197]. For the assessment of column lap-splice capacities with plain round bars, two approaches: a) the ASCE-41 [16] and b) the NZSEE seismic evaluation guidelines [169], are discussed. In the Japanese seismic assessment guidelines, JBDPA-2001 [111], column lap-splice has not been explicitly considered or assessed. In the assessment of column lap-splice capacities, as described in the following sub-sections, the required l_d is an important parameter. For plain round bars, the development and splice lengths are often specified to be twice the values calculated for deformed reinforcement in accordance to modern seismic codes [4, 167]. Chapter 7 would revisit the assessment of column lap-splice capacity in relation to the experimental results of as-built and retrofitted beam-column joints.

2.4.6.1 ASCE-SEI 41/ ACI-318 approach for anchorage and lap-splice capacity

The approach adopted in ASCE-SEI 41 [16] in terms of the assessment of anchorage capacity of straight embedded bars and lap-splice is based on the simplified approach first proposed by Kunnath *et al.* [121]. In the ASCE-41 Supplement 1 revision [68], an updated straight lap-splice assessment model is given to account for the strain hardening of reinforcement and inherent conservative of modern seismic codes for anchorage [52]. The maximum stress developed in the reinforcing bars without sufficient development lengths is given by:

$$f_s = 1.25\left(\frac{l_{d,prov}}{l_d}\right)^{2/3} f_y \qquad \textbf{2.51}$$

where f_s = maximum stress developed in the reinforcement without sufficient development lengths or anchorages, $l_{d,prov}$ = development length provided, l_d = development length required, as given by Chapter 12 of ACI-318 [4], f_y = yield strength of reinforcement. f_s from Equation 2.51 is limited to f_y for force-controlled actions (shear, axial) and $1.25f_y$ for deformation-controlled actions (flexural).

ASCE-SEI 41 [16] also allows for full stress development of f_s if confining transverse reinforcing are distributed along the development length with spacing not exceeding one-third of the effective depth of the section. For larger spacing of transverse reinforcement, typical of pre-1970s buildings, the developed f_s is assumed to degrade from $1.0f_s$ at ductility demand μ=1.0 to $0.2f_s$ at ductility demand μ=2.0.

The required development or lap-splice length as specified in ACI-318 [4] is developed empirically [170, 221]. For plain round bars, all development and splice lengths are taken to be

twice the values of ACI-318 [4]. The ACI-318 [4] development length required for tension straight anchorage is given by:

$$l_d = \frac{3}{40}\frac{f_y}{\lambda\sqrt{f_c'}}\frac{\psi_t\psi_e\psi_s}{\left(\frac{c+K_{tr}}{d_b}\right)}d_b(in) \quad \text{OR} \quad l_d = \frac{9}{10}\frac{f_y}{\lambda\sqrt{f_c'}}\frac{\psi_t\psi_e\psi_s}{\left(\frac{c+K_{tr}}{d_b}\right)}d_b(mm) \qquad \textbf{2.52}$$

where c is the smaller of the distance from the center of the bars to concrete surface and one-half of the center-to-center spacing of the bars; λ is to account for lightweight aggregate. Ψ_t , Ψ_e, Ψ_s are modification factors accounting for reinforcement location, coating type and size respectively. For most pre-1970s existing RC frames, these factors (λ, Ψ_t, Ψ_e, and Ψ_s) can be taken to be 1.0. K_{tr} is given by:

$$K_{tr} = \frac{A_{tr} f_{yt}}{10.34sn} \qquad \textbf{2.53}$$

where A_{tr} = area of confining stirrup with yield strength f_{yt}, and spacing s (in mm) and n= number of bars spliced. The term $(c+K_{tr})/d_b$ is limited to 2.5. l_d must be at least 12 inches (304.8mm).

For the assessment of column lap-splice, only tension development length is considered as longitudinal column reinforcement would undergo tension forces under reversal cyclic loading. For existing R.C. buildings where staggering of splices is uncommon and column longitudinal bar stresses generally exceed $0.5f_y$, lap splices will inevitably be Class B splice, and thus required development length, $l_{d,req}$ is 1.3 times l_d calculated in Equation 2.51. NZS3101 [167] has very similar provisions for the development length for tension/compression anchorage, in which as a result, similar l_d required would be calculated.

2.4.6.2 New Zealand NZSEE / NZS3101 approach for lap-splice capacity

The 2006 NZSEE guideline [169] calculates the flexural capacity of columns with inadequate lap-splice length as a function of nominal flexural capacity, M_n, and residual flexural capacity of column assuming lap-splice failure, M_f, as given in Equation 2.54. Two equations for M_f are given, as shown in Equation 2.55, reflection of the linear assumption of available strength in inadequate lap-splice ($l_{d,prov}/l_d$) as well as acknowledgement of contribution of static flexural capacity from column axial forces. The NZSEE calculation of M_f is based on the recommendations from Priestley *et al.* [203]:

$$M_{lap} = M_n - \frac{\theta_p}{0.025}(M_n - M_f) \quad \textbf{2.54}$$

$$M_f = \max\begin{cases} \frac{l_{d,prov}}{l_d} M_n \\ 0.5N(h_c - a) \end{cases} \quad \textbf{2.55}$$

where M_n = nominal flexural strength of the section without lap-splice, $l_{d,prov}$ = provided lap-splice length, l_d = required development length, h_c = gross depth of the column, and a= depth of compression stress block. The difficulty of using these equations is owing to the need to estimate the plastic rotation demand on the column, θ_p, as well as the axial force in the column, N, prior to the frame structural analysis.

As no specific l_d values are given, the 2006 NZS3101 [167] recommendations for basic calculations for l_d in tension and compression should be applicable and plain round bars $l_{d,req}$ is twice the NZS3101 specified l_d. The refined calculations for l_d in NZS3101 are not applicable in pre-1970s columns with inadequate confinement transverse reinforcement. The basic development length in tension is given by:

$$l_d = \frac{0.5\psi_a f_y}{\sqrt{f_c'}} d_b \quad \textbf{2.56}$$

where ψ_a =1.3 for beam top reinforcement with at least 300mm concrete underneath the bars and 1.0 for all other cases. f''_c in Equation 2.56 is limited to 70MPa. The basic development length in compression is given by:

$$l_d = \frac{0.22 f_y}{\sqrt{f_c'}} d_b > 0.04 f_y d_b > 200mm \quad \textbf{2.57}$$

In terms of development length of bars with hook anchorage (as in anchorage of beam longitudinal reinforcing into the beam-column joint), NZS3101 provides a different l_d equation (Cl 8.6.10.3):

$$l_d = 0.24\psi_b\psi_1\psi_2 \frac{f_y d_b}{\sqrt{f_c'}} > 8d_b \quad \textbf{2.58}$$

where $\psi_b = A_{s,req} / A_{s,prov}$ in the column, ψ_1 = 0.7 for 32mm, d_b or smaller with side concrete cover ≥60mm and hook end cover ≥40mm, and ψ_2 = 1.0 for other cases, and ψ_2 = 0.8 for well confined splice (with stirrups spacing < $6d_b$) and ψ_2 = 1.0 for other cases. $A_{s,req}$ and $A_{s,prov}$ are the areas of flexural reinforcing required and provided respectively.

2.5 CONCLUSIONS

This chapter has presented a summary of the state-of-knowledge on seismic vulnerability of non-ductile pre-1970s RC frames and beam-column joints. A seismic assessment procedure of non-ductile beam-column joints based on capacity design philosophy and hierarchy of strength evaluation has been presented with the necessary analytical tools to evaluate the specific failure mechanisms. The following are some unique contributions, insights and conclusions:

1. In the absence of capacity design philosophy, the inadequately designed and detailed pre-1970s RC frames are particularly susceptible. Within the local structural elements, lack of transverse reinforcement for ductility, absence of beam-column joint shear reinforcement and inadequate or non-ductile anchorage of longitudinal reinforcement all result in very poor seismic behaviour of pre-1970s beam-column joints.

2. RC frame buildings built in New Zealand prior to the 1970s have distinctive structural peculiarity but nevertheless have in general the same non-ductile structural deficiencies typical of that construction practice overseas. Among the peculiarities, it is worth noting the use of somewhat stronger columns (larger dimensions with distributed longitudinal bars) and closer transverse stirrup spacing, the use of 135° anchorages for transverse reinforcement, different beam-column joint detailing and replacement of plain round bar reinforcement with deformed bars starting in the mid-1960s.

3. The realistic non-ductile RC deficiencies of pre-1970s RC exterior beam-column joints discussed in §2.3.1 would form the basis of test specimen design for the experimental phase of this research, to be presented in Chapter 4. The prototype exterior beam-column joint would include the use of plain-round bar reinforcement, 180° hook anchorage for beam longitudinal reinforcement, weak-column strong-beam flexural design, no joint shear reinforcement and inadequate transverse reinforcement in columns and beams.

4. Variation of axial load, lap-splice in columns and the presence of floor slab-transverse beams would also play a significant role in the seismic behaviour of non-ductile exterior

joints – as these details were generally ignored in the past experimental studies due to the complexity of multi-source failure.

5. The desktop study of existing buildings confirmed these typical deficiencies for the New Zealand scenario. A lack of complete database of as-built and retrofitted pre-1970s multi-storey buildings stock in New Zealand is notable, despite the availability of such information within local territories, city councils and heritage trusts. It is suggested that future research to complete the relatively sparse database on seismically vulnerable and retrofitted buildings within major New Zealand cities.

6. Current practice of seismic assessment often fails to consider the interacting demand-capacity of various structural elements connecting the beam-column joint. In addition to the possibility of hybrid failure/inelastic mechanisms within the joints, the capacity/demand of beams, columns and joints can be influenced and limited by parameters such as lap-splice failure, bond failure, and floor slab over-strength. Within a seismic assessment framework based on capacity design and hierarchy of strength evaluation, the inelastic mechanism of the beam-column joint is determined by comparing the realistic failure mechanisms (e.g. joint shear failure, beam hinging, bond slip etc.) using a common denominator called *equivalent column moment*.

7. Various interpretations of joint shear capacity are available – from empirical based to semi-mechanistic model. A principal stresses approach is taken for this study for its simplicity in concept and somewhat conservatism. The Mohr's circle stress analysis used within the joint shear assessment is also suitable for the evaluation of the Selective Weakening retrofitted joint, to be explored further in Chapter 3.

8. Existing literature on plain-round bar reinforcing has been briefly summarised. Procedures to evaluate the bond, anchorage and lap-splice capacities of flexural elements with plain round bars have been described. In particular, a semi-empirical formulation to evaluate the maximum stress developed within the reinforcement with bond-slip failure has been proposed. State-of-the-practice procedure to evaluate the column lap-splice capacities with plain round bars has also been discussed.

9. Some comments with regards to the current differences and limitations of the 2006 New Zealand Society for Earthquake Engineering (NZSEE) assessment guidelines [169] to international practice have been made. Possible improvements to the NZSEE guidelines can be made by adopting some of the suggested procedures in §2.4.

2.6 CHAPTER 2: REFERENCES

[1] Aboutaha RS, Engelhardt MD, Jirsa JO, Kreger ME. (1996) Retrofit of concrete columns with inadequate lap splice by the use of rectangular steel jackets. *Earthquake Spectra*. Nov 1996; **12**(4):693-714.

[2] Abrams DP. (1913) *Test of bond between concrete and steel. Bulletin no. 71*. Uni. of Illinois Eng. Experimental Station, Urbana, IL.

[3] ACI315-65. (1970) *Proposed revision of ACI 315-65: manual of standard practice for detailing reinforced concrete structures. 5th ed.* American Concrete Inst. (ACI), Detroit, MI.

[4] ACI318-08. (2008) *Building code requirements for structural concrete and commentary*. American Concrete Inst. (ACI), Farmington Hills, MI.

[5] ACI318-51. (1950) Proposed revision of building code requirements for reinforced concrete (ACI318-47). *ACI Structural Journal*. Dec 1950; **47**(12):269-275.

[6] ACI318-56. (1956) *Building code requirements for reinforced concrete (ACI318-56)*. American Concrete Inst. (ACI), Detroit, MI.

[7] ACI318-63. (1963) *Building code requirements for reinforced concrete (ACI318-63)*. American Concrete Inst. (ACI), Detroit, MI.

[8] ACI318-71. (1971) *Building code requirements for reinforced concrete (ACI318-71)*. American Concrete Inst. (ACI), Detroit, MI.

[9] ACI352R-02. (2002) *Joint ACI-ASCE Committee 352: Recommendations for design of beam column joints in monolithic reinforced concrete structures*. American Concrete Inst. (ACI), Farmington Hills, MI.

[10] ACI352R-76. (1976) Joint ACI-ASCE Committee 352 - Recommendation for design of beam-column joints in monolithic reinforced concrete structures (ACI-352R-76). *ACI Structural Journal*. July 1976; **73**(7):375-393.

[11] ACI352R-85. (1985) Joint ACI-ASCE Committee 352: Recommendations for design of beam column joints in monolithic reinforced concrete structures. *ACI Structural Journal*. **82**(3):266-283.

[12] ACI-408. (1992) *State-of-the-art report on bond under cyclic loads (ACI408.2R-92)*. American Concrete Inst. (ACI), Detroit, MI.

[13] Al-Chaar G, K., Issa MA, Sweeney S. (2002) Behaviour of masonry-infilled nonductile reinforced concrete frames. *ASCE J of Struct Eng*. Aug 2002; **128**(8):1055-1063.

[14] Alire D. (2002) Seismic evaluation of existing unconfined reinforced concrete beam-column joints [M.Sc. thesis]. Uni. of Washington, Seattle, WA.

[15] Anderson M, Lehman DE, Stanton J. (2008) A cyclic shear stress-strain model for joints without transverse reinforcement. *Eng Structures*. **30**:941-954.

[16] ASCE-SEI-41-06. (2007) *Seismic rehabilitation of existing buildings. ASCE standard ASCE/SEI 41-06*. American Society of Civil Engineers (ASCE), Reston, Va.

[17] Aycardi LE, Mander JB, Reinhorn AM. (1992) *Seismic resistance of reinforced concrete frame structures designed only for gravity loads: Part II - Experimental performance of*

subassemblages, NCEER-92-0028. National Center for Earthquake Eng. Research, SUNY at Buffalo, Buffalo, NY.

[18] Aycardi LE, Mander JB, Reinhorn AM. (1994) Seismic resistance of R.C. frame structures designed only for gravity loads: Experimental performance of subassemblages. *ACI Structural Journal*. **91**(5):552-563.

[19] Bakir PG, Boduroglu HM. (2002) A new design equation for predicting joint shear strength of monotonically loaded exterior beam-column joints. *Eng Structures*. **24**:1105-1117.

[20] Balazs GL. (1998) Bond under repeated loading. In: Leon RT, editor. *Bond and development of reinforcement, SP-180*. American Concrete Inst. (ACI), Farmington Hills, MI; p. 125-143.

[21] BC-CP114:1957. (1957) *The structural use of concrete in buildings*. British Standard (BSi), London, UK.

[22] Bedirhanoglu I, Ilki A, Pujol S, Kumbasar N. (2010) Behaviour of deficient joints with plain bars and low-strength concrete. *ACI Structural Journal*. May-June 2010; **107**(3):300-310.

[23] Bennett BW, Parme AL, Hanson NW, Sbarounis JA. (1965) *A laboratory investigation of reinforced concrete beam-column connections under lateral loads*. Portland Cement Association, Skokie, IL.

[24] Bentz EC, Collins MP. (2003) Response-2000. 1.6.8 (beta) ed. Uni. of Toronto, Toronto, Canada; p. Reinforced concrete sectional analysis using the Modified Compression Field Theory.

[25] Beres A, El-Borgi S, White R, Gergely P. (1992) *Experimental results of repaired and retrofitted beam-column joint tests in lightly reinforced concrete frame buildings. Technical Report NCEER-92-0025*. National Center for Earthquake Eng. Research, SUNY, Buffalo, NY.

[26] Beres A, Pessiki S, White R, Gergely P. (1996) Implications of experimental on the seismic behaviour of gravity load designed RC beam-column connections. *Earthquake Spectra*. **12**(2):185-198.

[27] Beres A, White R, Gergely P. (1992) *Seismic behaviour of reinforced concrete frame structures with nonductile details: Part I - Summary of experimental findings of full scale beam-column joint tests. Technical Report NCEER-92-0024*. National Center for Earthquake Eng. Research, SUNY, Buffalo, NY.

[28] Bertero VV, Shadh H. (1983) *El Asnam, Algeria Earthquake, October 10, 1980*. Earthquake Eng. Research Inst. (EERI), Oakland, CA.

[29] BIA. (1991) *Building Act 1991*. Building Industry Authority (BIA), Wellington, NZ.

[30] Biddah A, Ghobarah A, Aziz T. (1999) Upgrading of nonductile reinforced concrete frame connections. *ASCE J of Struct Eng*. **123**(8):1001-1010.

[31] Birgoren G, Tarhan C. (2009) 17 August 1999, Kocaeli earthquake - Turkey. [Website] [cited 31th Dec 2009]; Available from: http://www.koeri.boun.edu.tr/depremmuh/eqspecials/kocaeli/kocaeli_eq.htm

[32] Blaikie E, Spurr DD. (1990) *Earthquake Risk Associated With 1935 - 1975 Reinforced Concrete Buildings In NZ, EQC Research Paper. 207*. New Zealand Earthquake Commission (EQC), Wellington, NZ.

[33] Blume JA, Newmark NM, Corning L. (1961) *Design of multistory reinforced concrete buildings for earthquake motions*. Portland Cement Association, Chicago, IL.

[34] Booth E. (1994) *Concrete structures in earthquake region: Design & analysis*. Longman Scientific and Technical, Essex, UK.

[35] Bracci JM, Reinhorn AM, Mander JB. (1992) *Seismic resistance of reinforced concrete frame structures designed for gravity loads: Part I - Design and properties of a one-third*

scale model structures. Technical Report NCEER-92-0027. National Center for Earthquake Eng. Research, SUNY, Buffalo, NY.

[36] Bracci JM, Reinhorn AM, Mander JB. (1992) *Seismic resistance of reinforced concrete frame structures designed only for gravity loads: Part III - Experimental performance and analytical study of a structural model. Technical Report NCEER-92-0029*. National Center for Earthquake Eng. Research, SUNY, Buffalo, NY.

[37] Bracci JM, Reinhorn AM, Mander JB. (1995) Seismic resistance of reinforced concrete frame structures designed for gravity loads: Performance of structural systems. *ACI Structural Journal*. **92**(5):597-609.

[38] Brunsdon DR, Priestley MJN. (1984) *Seismic performance characteristics of buildings constructed between 1936 and 1975. UC Research Report 84-14*. Dept. of Civil Eng., Uni. of Canterbury Christchurch, NZ.

[39] BS8110-97. (1997) *Structural use of concrete - Part 1: Code of practice for design and construction*. British Standard (BSi), London, UK.

[40] Burns NH, Seiss CP. (1962) *Load-deformation characteristics of beam-column connections in reinforced concrete. Civil Engineering Studies SRS-234 - a report to the Port Cement Association.* . Uni. of Illinois at Urbana-Champaign, Urbana, IL.

[41] Calvi GM, Magenes G, Pampanin S. (2002) Experimental test on a three storey RC frame designed for gravity only *Proc. of 12th European Conf of Earthquake Eng*, Elsevier, London, UK.Paper No 727.

[42] Calvi GM, Moratti M, Pampanin S. (2002) Relevance of beam-column damage and collapse in RC frame assessment. *J of Earthquake Eng*. **6**(1):75-100.

[43] Carvalho EC, Coelho E. (2001) *Seismic assessment, strengthening and repair of structures*. Laboratorio Nacional de Engenharia Civil, Lisbon, Portugal.

[44] CEB-1964. (1964) *Recommendations for an international code of practice for reinforced concrete*. American Concrete Inst. (ACI) & Cement and Concrete Assoc.(CCA), London, UK.

[45] CEB-Fip-MC90. (1993) *CEB-FIP Model Code 90, CEB Bulletin d'Information No. 213/214*. Thomas Telford Ltd., London.

[46] CEN. (2006) *European Standard EN 1998: Eurocode 8 - Design of structures for earthquake resistance - Part 3: Assessment and retrofitting of buildings*. Comite Europeen de Normalisation, Brussels.

[47] CEN. (2006) *European Standard EN 1998: Eurocode 8 (Part 1-5)*. Comite Europeen de Normalisation, Brussels.

[48] Centeno J. (2009) In-plane shake table testing of gravity load designed reinforced concrete frames with unreinforced masonry infill walls [M.App.Sc.]. Uni. of British-Columbia, Vancouver, Canada.

[49] Chai YH, Priestley MJN, Seible F. (1991) Seismic retrofit of circular bridge column for enhanced flexural performance. *ACI Structural Journal*. Sept-Oct 1991; **88**(5):572-584.

[50] Cheung PC, Paulay T, Park R. (1991) Mechanisms of slab contributions in beam-column subassemblages. In: Jirsa JO, editor. *Design of beam-column joints for seismic resistance, SP-123*. American Concrete Inst. (ACI), Detroit, MI; p. 259-290.

[51] Cheung PC, Paulay T, Park R. (1991) *Seismic design of reinforced concrete beam-column joints with floor slab. UC Research Report 91-4*. Dept. of Civil Eng., Uni. of Canterbury, Christchurch, NZ.

[52] Cho J-Y, Pincheira JA. (2006) Inelastic analysis of reinforced concrete columns with short lap splices subjected to reversed cyclid loads. *ACI Structural Journal*. Mar 2006; **103**(2):280-290.

[53] Choudhury D, Mander JB, Reinhorn AM. (1992) *Evaluation of seismic retrofit of reinforced concrete frame structures: Part I - Experimental performance of retrofitted subassemblages, NCEER Report No. NCEER-92-003*. National Center for Earthquake Eng. Research, SUNY, Buffalo, NY, USA.

[54] Clark WD, Mason JE. (2005) Base isolation of an existing 10-storey building to enhance earthquake resistance. *Bull of New Zealand Soc of Earthquake Eng*. Mar 2005; **38**(1):33-40.

[55] Clyde C, Pantelides CP, Reaveley LD. (2000) *Performance-based evaluation of exterior reinforced concrete building joints for seismic excitation. PEER Report 2000/05*. Pacific Earthquake Eng. Res. Center (PEER), Berkeley, CA.

[56] Coelho E, Costa AC, Candeias P, Silva MJF, Mendes L. (2005) Shake table tests of a 3-storey irregular RC structure designed for gravity loads. In: Fardis M, Negro P, editors. *SPEAR: Seismic performance assessment and rehabilitation of existing buildings International Workshop, Ispra 4-5 April 2005 Proceedings*. European Laboratory for Structural Assessment (ELSA), Ispra, Italy; p. 123-138.

[57] Collins MP, Mitchell D. (1997) *Prestressed concrete structures*. Response Publications, Toronto, Canada.

[58] Corley G, Hanson NW. (1969) Design of beam-column joints for seismic resistant reinforced concrete frames. *Proc. of 4th World Conf on Earthquake Eng*, Santiago, Chile,

[59] Crisafulli FJ, Carr A, Park R. (2000) Analytical modelling of infilled frame structures: A general review. *Bull of New Zealand Soc of Earthquake Eng*. **33**(1):30-47.

[60] Darwin D. (2005) Tension development length and lap splice design for reinforced concrete members. *Prog in Struct Eng Material (EESD)*. **7**:210-225.

[61] DBH. (2004) *Building Act 2004*. Dept. of Building and Housing (DBH), Wellington, NZ.

[62] Dewell HD. (1931) The New Zealand Earthquake of February 3, 1931. *Bull of Seismo Soc of America*. Dec 1931; **21**(4):251-260.

[63] Dhakal RP, Pan T-C. (2003) Characteristics of high-speed cyclic test of beam-column joints. *ACI Structural Journal*. **100**(2):188-196.

[64] Durrani AJ, Elnashai AS, Hashash YMA, Kim SJ, Masud A. (2005) *The Kashmir earthquake of October 8. 2005: A quick look report, CD Release 05-04*. Mid-America Earthquake (MAE) Center, Uni. of Illinois at Urbana-Champaign, Urbana, IL.

[65] Durrani AJ, Wight J. (1985) Behaviour of interior beam-to-column connections under earthquake-type loading. *ACI Structural Journal*. May-June 1985; **82**(3):343-349.

[66] El-Attar AG, White R, Gergely P. (1997) Behaviour of gravity load design reinforced concrete buildings subjected to earthquakes. *ACI Structural Journal*. Mar 1997; **94**(2):133-145.

[67] Eligehausen R, Popov EP, Bertero VV. (1983) *Local bond-stress relationships of deformed bars under general excitation, Report No. UCB/EERC:83-23*. Uni. of California, Berkeley, Berkeley, CA.

[68] Elwood K, Matamoros A, Wallace JW, Lehman DE, Heintz JA, Mitchell A, et al. (2007) Update of ASCE/SEI 41 concrete provisions. *Earthquake Spectra*. Aug 2007; **23**(3):493-523.

[69] Elwood K, Moehle JP. (2003) *Shake table tests and analytical studies on the gravity load collapse of reinforced concrete frames. PEER Report 2003/01*. Pacific Earthquake Eng. Res. Center (PEER), Berkeley, CA.

[70] Elwood K, Moehle JP. (2005) Axial capacity model for shear-damaged columns. *ACI Structural Journal*. **102**:578-587.
[71] Elwood K, Moehle JP. (2005) Drift capacity of reinforced concrete columns with light transverse reinforcement. *Earthquake Spectra*. Feb 2005; **21**(1):71-89.
[72] Elwood K, Moehle JP. (2008) Dynamic collapse analysis for a reinforced concrete frame sustaining shear and axial failures. *Earthquake Eng & Struct Dyn*. **37**:991-1012.
[73] Fabbrocino G, Verderame GM, Manfredi G. (2002) Experimental behaviour of straight and hooked smooth bars anchorage in existing r.c. buildings *Proc. of 12th European Conf on Earthquake Eng*, Elsevier, London, UK,
[74] Fabbrocino G, Verderame GM, Manfredi G. (2005) Experimental behaviour of anchored smooth rebars in old type reinforced concrete buildings. *Eng Structures*. **27**(10):1575-1585.
[75] Feldman LR, Bartlett FM. (2005) Bond strength variability in pullout specimens with plain reinforcement. *ACI Structural Journal*. Nov-Dec 2005; **102**(6):860-867.
[76] Feldman LR, Bartlett FM. (2007) Bond stresses along plain steel reinforcing bars in pullout specimens. *ACI Structural Journal*. Nov-Dec 2007; **104**(6):685-692.
[77] Feldman LR, Bartlett FM. (2008) Bond in flexural members with plain steel reinforcement. *ACI Structural Journal*. Sept-Oct 2008; **105**(5):552-560.
[78] Fenwick R, MacRae GA. (2009) Comparison of New Zealand Standards used for seismic design of concrete buildings. *Bull of New Zealand Soc of Earthquake Eng*. Sept 2009; **42**(3):187-203.
[79] fib. (2000) *Bond of reinforcement in concrete: State-of-the-art report, fib Bulletin no. 10*. Intl. Fed. for Struct. Concrete (fib), Lausanne, Switzerland.
[80] fib. (2003) *Seismic assessment and retrofit of reinforced concrete buildings: State-of-the-art report, fib Bulletin no. 24*. Intl. Fed. for Struct. Concrete (fib), Lausanne, Switzerland.
[81] Filippou FC. (1986) A simple model for reinforcing bar anchorages under cyclic excitations. *ASCE J of Struct Eng*. **112**:1639-1659.
[82] Filippou FC, Popov EP, Bertero VV. (1983) *Effect of bond deterioration on hysteretic behaviour of reinforced concrete joints. Report No. UCB/EERC-83-19*. Earthquake Eng. Research Center, Uni. of California, Berkeley, CA.
[83] Fishburn CC. (1947) Strength and slip under load of bent-bar anchorage and straight embedments under haydite concrete. *ACI Structural Journal*. Dec 1947; **44**(4):289-308.
[84] Ford CR. (1926) *Earthquakes and building constructions*. Whitcombe and Tombs Ltd, Auckland, NZ.
[85] Garcia R, Hajirasouliha I, Pilakoutas K. (2010) Seismic behaviour of deficient RC frames strengthened with CFRP. *Eng Structures*. Oct 2010; **32**(10):3075-3085.
[86] Ghannoum WM. (2007) Experimental and analytical dynamic collapse study of reinforced concrete frame with light transverse reinforcement [PhD dissertation]. Uni. of California, Berkeley, Berkeley, CA.
[87] Ghobarah A, Biddah A. (1999) Dynamic analysis of reinforced concrete frames including joint shear deformation. *Eng Structures*. **21**:971-987.
[88] Ghobarah A, Said A. (2002) Shear strengthening of beam-column joints. *Eng Structures*. July 2002; **24**(7):881-888.
[89] Goto Y. (1971) Cracks formed in concrete around deformed tension bars. *ACI Structural Journal*. April 1971; **68**(4).
[90] Guevara LT, Garcia LE. (2005) The captive- and short-column effect. *Earthquake Spectra*. **21**(1):141-160.

[91] Hakuto S, Park R, Tanaka H. (1995) *Retrofitting of reinforced concrete moment resisting frames. UC Research Report 95-4*. Dept. of Civil Eng., Uni. of Canterbury, Christchurch, NZ.

[92] Hakuto S, Park R, Tanaka H. (1999) Effect of deterioration of bond on beam-bars passing through interior beam-column joints on flexural strength and ductility. *ACI Structural Journal*. **96**(5):858-864.

[93] Hakuto S, Park R, Tanaka H. (2000) Seismic load tests on interior and exterior beam-column joints with substandard reinforcing details. *ACI Structural Journal*. Jan-Feb 2000; **97**(1):11-25.

[94] Hall JF. (1996) Northridge Earthquake Reconnaissance Report. Supplement C, vol. 1. *Earthquake Spectra*. (11):1-523.

[95] Hamann CW. (1953) *Commentary on New Zealand Standard Building Code.* . N.Z. Institution of Engineers, Technical Publications LTD, Wellington, NZ.

[96] Hamil SJ. (2000) Reinforced concrete beam-column connection behaviour [PhD dissertation]. Uni. of Durham, Durham, UK.

[97] Hanson NW. (1971) Seismic resistance of concrete frames with grade 60 reinforcement. *ASCE Journal of Structural Division*. **98**(6):1685-1700.

[98] Hanson NW, Conner HW. (1965) *Reinforced concrete beam-column joints for earthquakes*. Portland Cement Association, Skokie, IL.

[99] Hanson NW, Conner HW. (1967) Seismic resistance of reinforced concrete beam-column joints. *ASCE Journal of Structural Division*. **95**(5):533-560.

[100] Hanson NW, Conner HW. (1972) *Tests of reinforced concrete beam-column joints under simulated seismic loading. Report No. RDO12.01D*. Portland Cement Association.

[101] Hare J. (2009) *Heritage earthquake prone building strengthening cost study. Prepared for Christchurch City Council. (Internal report)*. Holmes Consulting Group, Christchurch, NZ.

[102] Hashemi A, Mosalam KM. (2006) Shake-table experiment on reinforced concrete structures containing masonry infill wall. *Earthquake Eng & Struct Dyn*. **35**(14):1827-1852.

[103] Hegger J, Sherif A, Roeser W. (2003) Nonseismic design of beam-column joints. *ACI Structural Journal*. **100**(5):654-664.

[104] Hegger J, Sherif A, Roeser W. (2004) Nonlinear finite element analysis of reinforced concrete beam-column joints. *ACI Structural Journal*. **101**(5):604-614.

[105] Hertanto E. (2006) Seismic assessment of pre-1970s reinforced concrete beam column joint subassemblies. [M.E. dissertation]. Uni. of Canterbury, Christchurch, NZ.

[106] Higashi Y, Ohwada Y. (1969) Failing behaviours of reinforced concrete beam-column connections subjected to lateral load. *Memoirs of Faculty of Technology Tokyo Metropolitan Uni*, Tokyo, Japan; p. 91-101.

[107] Hollings JP. (1969) Reinforced concrete seismic design. *Bull of New Zealand Soc of Earthquake Eng*. **2**(3):217-250.

[108] Hwang SJ, Lee H-J. (1999) Analytical model for predicting shear strengths of exterior reinforced concrete beam-column joints for seismic resistance. *ACI Structural Journal*. Sept-Oct 1999; **96**(5):846-857.

[109] IStruct. (2006) *Standard method of detailing structural concrete. A manual for best practice. (3rd ed.)*. Institution of Structural Engineers, London, UK.

[110] JBDPA-1977. (1977) *Design guidelines for aseismic retrofitting of existing reinforced concrete buildings (in Japanese)*. Japan Building Disaster Prevention Association (JBDPA), Tokyo, Japan.

[111] JBDPA-2001. (2001) *Standard, Guidelines and Technical Manual for seismic evaluation and seismic retrofit of existing reinforced concrete buildings. 1st English Version. Translated by Building Research Institute.* Japan Building Disaster Prevention Assoc. (JBDPA), Tokyo, Japan.

[112] Jirsa JO, (1991) editor.^editors. *SP-123: Design of beam-column joint for seismic resistance*. American Concrete Inst. (ACI), Farmington Hills, MI.

[113] Jirsa JO, Marques JLG. (1972) *A study of hooked bar anchorages in beam-column joints, RCRC Project 33 Final Report*. Dept. of Civil Eng., Uni. of Texas at Austin, Austin,Texas.

[114] Joh O, Goto Y, Shibata T. (1991) Behaviour of reinforced concrete beam-column joints with eccentricity. In: Jirsa JO, editor. *Design of beam-column joints for seismic resistance, SP-123*. American Concrete Inst. (ACI), Detroit, MI; p. 317-357.

[115] Joh O, Goto Y, Shibata T. (1991) Influence of transverse joint and beam reinforcement and relocation of plastic hinge region on beam-column joint stiffness deterioration. In: Jirsa JO, editor. *Design of beam-column joints for seismic resistance, SP-123*. American Concrete Inst. (ACI), Detroit, MI; p. 187-223.

[116] Kankam CK. (1997) Relationship of bond stress, steel stress, and slip in reinforced concrete. *ASCE J of Struct Eng*. **123**(1):79-85.

[117] Kim J, LaFave JM. (2007) Key influence parameters of the joint shear behaviour of RC beam-column connections. *Eng Structures*. **29**:2523-2539.

[118] King DJ, Priestley MJN, Park R. (1986) *Computer programs for concrete column design. UC Research Report 86/12*. Dept of Civil Eng., Uni. of Canterbury, Christchurch, NZ.

[119] Kowalsky MJ, Priestley MJN. (2000) Improved analytical model for shear strength of circular reinforced concrete in seismic regions. *ACI Structural Journal*. May-June 2000; **97**(3):388-396.

[120] Kuang JS, Wong HF. (2006) Effect of beam bar anchorage on shear strength of beam-column joints. *Proc of the ICE - Structures and Buildings*. **159**(2):115-124.

[121] Kunnath SK, Hoffmann GW, Reinhorn AM, Mander JB. (1995) Gravity-load-designed reinforced concrete buildings — Part I: Seismic evaluation of existing construction. *ACI Structural Journal*. **92**(3):343-354.

[122] Kunnath SK, Hoffmann GW, Reinhorn AM, Mander JB. (1995) Gravity-load-designed reinforced concrete buildings — Part II: Evaluation of detailing enhancements. *ACI Structural Journal*. **92**(4):470-478.

[123] Kurose Y. (1987) *Recent studies on reinforced concrete beam-column joints in Japan, PMFSEL Report No. 87-8*. Dept of Civil Eng., Uni. of Texas at Austin., Austix, TX.

[124] Kurose Y, Guimaraes GN, Zuhua L, Kreger ME, Jirsa JO. (1991) Evaluation of slab-beam-column connections subjected to bidirectional loading. In: Jirsa JO, editor. *Design of beam-column joints for seismic resistance, SP-123*. American Concrete Inst. (ACI), Detroit, MI; p. 39-68.

[125] Lehman DE, Stanton J, Anderson DL, Alire D, Walker SG. (2004) Seismic performance of older beam-column joints *Proc. of 13th World Conf on Earthquake Eng*, Vancouver, Canada.Paper No 1464.

[126] Leon RT. (1990) Shear strength and hysteretic behaviour of interior beam-column joints. *ACI Structural Journal*. **87**(1):3-11.

[127] Li B, Pan T-C, Tran CTN. (2009) Effects of axial compression load and eccentricity on seismic behaviour of nonseismically detailed interior beam-wide column joints. *ASCE J of Struct Eng*. **135**(7):774-784.

[128] Li B, Pan T-C, Tran CTN. (2009) Seismic behaviour of nonseismically detailed interior beam-wide column and beam-wall connections. *ACI Structural Journal*. Sept-Oct 2009; **106**(5):591-599.

[129] Li B, Tran CTN, Pan T-C. (2009) Experimental and numerical investigations on the seismic behaviour of lightly reinforced concrete beam-column joints. *ASCE J of Struct Eng*. Sept 2009; **135**(9):1007-1018.

[130] Li B, Wu Y, Pan T-C. (2002) Seismic behaviour of non-seismically detailed interior beam-wide column joints - Part I: Experimental results. *ACI Structural Journal*. Nov-Dec 2002; **99**(6):791-802.

[131] Li B, Wu Y, Pan T-C. (2003) Seismic behaviour of non-seismically detailed interior beam-wide column joints - Part II: Discussion and Theoretical Comparisons. *ACI Structural Journal*. Jan-Feb 2003; **100**(1):56-65.

[132] Liu A. (2001) Seismic assessment and retrofit of pre-1970s reinforced concrete frame structures, PhD Dissertation [PhD]. Uni. of Canterbury, Christchurch, NZ.

[133] Liu A, Park R. (2001) Seismic Behaviour and retrofit of pre-1970s as-built exterior beam-column joints reinforced by plain round bars. *Bull of New Zealand Soc of Earthquake Eng*. **34**(1):68-81.

[134] Lowes LN, Altoontash A. (2003) Modeling reinforced-concrete beam-column joints subjected to cyclic loading. *ASCE J of Struct Eng*. **129**(12):1686-1697.

[135] Lowes LN, Moehle JP. (1999) Evaluation and retrofit of beam-column T-joints in older reinforced concrete bridge structures. *ACI Structural Journal*. **96**(4):519-533.

[136] Lutz LA, Gergely P. (1967) Mechanics of bond and slip of deformed bars in concrete. *ACI Structural Journal*. Nov 1967; **64**(1):711-721.

[137] Magenes G, Pampanin S. (2004) Seismic response of gravity-load design frames with masonary infills. *Proc. of 13th World Conf on Earthquake Eng*, Vancouver, Canada.Paper No. 4004.

[138] Malley JO, Celebi M, Bruneau M, Saatcioglu M, Erdik M, Gulkan P. (1993) Chapter 5. Buildings (of 1992 Erzican earthquake reconnaissance report). *Earthquake Spectra*. July 1993; **9**(S1):49-85.

[139] Marques JLG, Jirsa JO. (1975) A study of hooked bar anchorages in beam-column joints. *ACI Structural Journal*. May 1975; **72**(5):198-209.

[140] Megget LM. (1971) Anchorage of beam reinforcement in seismic resistance reinforced concrete frames. [M.E. thesis]. Uni. of Canterbury, Christchurch, NZ.

[141] Megget LM. (1974) Cyclic behaviour of exterior reinforced concrete beam-column joints. *Bull of New Zealand Soc of Earthquake Eng*. **7**(1):27-47.

[142] Megget LM. (2006) From brittle to ductile: 75 years of seismic design in New Zealand. *Proc. of NZSEE 2006 Conf*, NZSEE, Napier, NZ, p. 15.Keynote Address.

[143] Megget LM, Park R. (1971) Reinforced concrete exterior beam-column joints under seismic loading. *NZ Engineering*. Nov 1971; **26**(11):341-353.

[144] Meinheit DF, Jirsa JO. (1977) *The shear strength of reinforced concrete beam-column joints. CESRL Rep. No. 77-1*. Uni. of Texas, Austin, TX.

[145] Meinheit DF, Jirsa JO. (1981) Shear strength of R/C beam-column connections. *ASCE Journal of Structural Division*. Nov 1981; **107**(11):2227-2244.

[146] Melek M, Wallace JW. (2004) Cyclic behaviour of columns with short lap splices. *ACI Structural Journal*. Nov-Dec 2004; **101**(6):802-811.

[147] Minor J, Jirsa JO. (1971) *A study of bent-bar anchorages, Structural Research at Rice Uni., Report No. 9*. Uni. of Rice, Houston, TX.

[148] Moehle JP, Nicoletti JP, Lehman DE. (1994) *Review of seismic research results of existing buildings. Report No. SSC 94-03*. Seismic Safety Commission, California.
[149] Mola E, Negro P. (2005) Full scale PsD testing of the torsionally unbalanced spear structure in the 'as-built' and retrofitted configurations. In: Fardis M, Negro P, editors. *SPEAR: Seismic performance assessment and rehabilitation of existing buildings International Workshop, Ispra 4-5 April 2005 Proceedings*. European Laboratory for Structural Assessment (ELSA), Ispra, Italy; p. 139-154.
[150] Monti G, Filippou FC, Spacone E. (1997) Finite element for anchored bars under cyclic load reversals. *ASCE J of Struct Eng*. May 1997; **123**(5):614-623.
[151] MOW-NZ. (1950) *Ministry of Works technical memorandum*. Ministry of Works, Wellington, NZ.
[152] MOW-NZ. (1970) *PW81/10/1: Code of Practice, Design of Public Buildings*. Office of Chief Structural Engineer, Ministry of Works, Wellington, NZ.
[153] Murty CVR, Rai DC, Bajpai KK, Jain SK. (2003) Effectiveness of reinforcement details in exterior reinforced concrete beam-column joints for earthquake resistance. *ACI Structural Journal*. **100**(2):149-156.
[154] Mylrea TD. (1928) The carrying capacity of semi-circular hooks. *ACI Structural Journal*. Feb 1928; **24**(2):240-272.
[155] Negro P, Mola E, Molina J, Magonette GE. (2004) Full scale PsD tsting of a torsionally unbalanced three-storey non-seismic RC frame. *Proc. of 13th World Conf on Earthquake Eng*, Vancouver, Canada.Paper No. 968.
[156] NISEE. (2003) Izmit Collection IZT-673. National Information Service for Earthquake Engineering (NISEE). [Website] [cited 31th Dec 2009]; Available from: http://nisee.berkeley.edu
[157] NZ. (1968) *Amendment 301A Local Municipal Corporations Act 1968*. New Zealand Statute, Wellington, NZ.
[158] NZS95:1935. (1935) *New Zealand Standard model buildings by-laws*. New Zealand Standards Inst., Wellington, NZ.
[159] NZS95:1939. (1939) *New Zealand Standard code of buildings by-laws*. New Zealand Standards Inst., Wellington, NZ.
[160] NZS95:1955. (1955) *New Zealand Standard - Model Building By-Laws: Part IV and V*. New Zealand Standard Inst., Wellington, NZ.
[161] NZS1170. (2004) *NZS 1170.5:2004 Structural design actions*. Standards New Zealand, Wellington, NZ.
[162] NZS1693:1962. (1962) *Deformed steel bars of structural grade for reinfroced concrete*. Standards Assoc. of New Zealand, Wellington, NZ.
[163] NZS1900.8-64. (1964) *NZS1900 - Model building bylaw: Chapter 8: Basic Design Loads and Commentary*. . Standards Assoc. of New Zealand, Wellington, NZ.
[164] NZS1900.9-64. (1964) *NZS1900 - Model building bylaw: Chapter 9.3: Design and construction - Concrete*. Standards Assoc. of New Zealand, Wellington, NZ.
[165] NZS3101:1970P. (1970) *Code of practice for the design of concrete structures NZS 3101:1970 (Provisional)*. Standards Assoc. of New Zealand, Wellington, NZ.
[166] NZS3101:1982. (1982) *Code of practice for the design of concrete structures NZS 3101:1982*. Standards Assoc. of New Zealand, Wellington, NZ.
[167] NZS3101:2006. (2006) *NZS 3101:2006 Concrete structures standard*. Standards New Zealand, Wellington, NZ.

[168] NZS4203:1976. (1976) *Code of practice for general structural design and design loading for buildings. NZS 4203:1976*. Standards Assoc. of New Zealand, Wellington, NZ.
[169] NZSEE. (2006) *Assessment and improvement of the structural performance of buildings in earthquakes*. New Zealand Soc. for Earthquake Eng. (NZSEE), Wellington, NZ.
[170] Orangun CO, Jirsa JO, Breen JE. (1977) A reevaluation of test data on development length and splices. *ACI Structural Journal*. Mar 1977; **74**(3):114-122.
[171] Ortiz IR. (1993) Strut-and-tie modeling of reinforced concrete short beams and beam-column joints. Uni. of Westminister, London, UK.
[172] Otani S. (1996) A japanese view of the 1906 San Francisco earthquake disaster. *Earthquake Spectra*. Apr 2006; **22**(S2):S183-S205.
[173] Pagni C, Lowes LN. (2006) Fragility functions for older reinforced concrete beam-column joints. *Earthquake Spectra*. Feb 2006; **22**(1):215-238.
[174] Pampanin S. (2006) Controversial aspects in seismic assessment and retrofit of structures in modern times: Understanding and implementing lessons from ancient heritage. *Bull of New Zealand Soc of Earthquake Eng*. **39**(2):120-133.
[175] Pampanin S, Bolognini D, Pavese A. (2007) Performance-based seismic retrofit strategy for existing reinforced concrete frame systems using fiber-reinforced polymer composites. *ASCE J of Composite Constr*. March/April 2007; **11**(2):211-226.
[176] Pampanin S, Bolognini D, Pavese A, Magenes G, Calvi GM. (2004) Multi-level seismic rehabilitation of existing frames and subassemblies using FRP composites. *Proc. of CICE 2004*, Adelaide, Australia,
[177] Pampanin S, Calvi GM, Moratti M. (2002) Seismic behaviour of RC beam-column joints designed for gravity loads. *Proc. of 12th European Conf on Earthquake Eng*, London, UK.Paper 726.
[178] Pampanin S, Magenes G, Carr A. (2003) Modelling of shear hinge mechanism in poorly detailed RC beam-column joints. *Proc. of Concrete Structures in Seismic Region: fib 2003 Symposium*, Federation International du Beton, Athens,
[179] Panagiotakos TB, Fardis M. (2001) Deformation of R.C. members at yielding and ultimate. *ACI Structural Journal*. Mar 2001; **98**(2):135-148.
[180] Pantazopoulou SJ, Bonacci JF. (1992) Consideration of questions about beam-column joints. *ACI Structural Journal*. **89**(1):27-36.
[181] Pantelides CP, Clyde C, Reaveley LD. (2002) Performance-based evaluation of reinforced concrete exterior joints for seismic excitation. *Earthquake Spectra*. Aug 2002; **18**(3):449-480.
[182] Pantelides CP, Hansen J, Nadauld J, Reaveley LD. (2002) *Assessment of reinforced concrete building exterior joints with substandard details. PEER Report 2002/18*. Pacific Earthquake Eng. Res. Center (PEER), Berkeley, CA.
[183] Park R. (2000) *Improving the resistance of structures to earthquakes, Hopkins Lecture - 16th Aug 2000*. Uni. of Canterbury, Christchurch, NZ.
[184] Park R. (2002) A summary of result of simulated seismic load tests on reinforced concrete beam-column joints, beams and columns with substandard reinforcing details. *J of Earthquake Eng*. **6**(2):147-174.
[185] Park R, Paulay T. (1973) Behaviour of reinforced concrete external beam-column joints under cyclic loading. *Proc. of 5th World Conf on Earthquake Eng*, Rome, Italy, p. 772-781.Paper 88, Vol 1- Session 2D.

[186] Park R, Paulay T. (1975) Ductile reinforced concrete frames - some comments on the special provisions for seismic design of ACI 318-71 and on capacity design. *Bull of New Zealand Soc of Earthquake Eng*. Mar 1975; **8**(1):70-90.

[187] Park R, Paulay T. (1975) *Reinforced concrete structures*. John Wiley & Sons, New York.

[188] Park R, Thompson KJ. (1974) *Behaviour of prestressed, partially prestressdd and reinforced concrete interior beam-column assemblies under cyclic loading: test results of units 1 to 7. UC Research Report 74-9.* Dept. of Civil Eng., Uni. of Canterbury, Christchurch, NZ.

[189] Park R, Thompson KJ. (1977) Cyclic load tests on prestressed and partially prestressed beam-column joints. *PCI Journal*. Sept-Oct 1977; **22**(5):84-100.

[190] Park S, Mosalam KM. (2009) *Shear strength models of exterior beam-column joints without transverse reinforcement. PEER Report 2009/106*. Pacific Earthquake Eng. Res. Center (PEER), Berkeley, CA.

[191] Parker DE, Bullman PJM. (1997) Shear strength within RC beam-column joints. *The Structural Engineer*. Feb 1999; **75**(4):53-57.

[192] Parvin A, Altay S, Yalcin C, Kaya O. (2010) CFRP Rehabilitation of concrete frame joints with inadequate shear and anchorage details. *ASCE J of Composite Constr*. Jan-Feb 2010; **14**(1):72-82.

[193] Patton RN. (1972) Behaviour under seismic loading of reinforced concrete beam-column joints with anchorage blocks [M.E. thesis]. Uni. of Canterbury, Christchurch, NZ.

[194] Paulay T. (1982) Lapped-splice in earthquake-resisting columns. *ACI Structural Journal*. **74**(6):458-469.

[195] Paulay T, Park R, Priestley MJN. (1978) Reinforced concrete beam-column joints under seismic actions. *ACI Structural Journal*. **75**(11):585-593.

[196] Paulay T, Priestley MJN. (1992) *Seismic design of reinforced concrete and masonry buildings*. John Wiley & Sons Inc., Christchurch, NZ.

[197] Pessiki S, Conley C, Gergely P, White R. (1990) *Seismic behaviour of lightly reinforced concrete column and beam-column joint details. Technical Report NCEER-90-0014*. National Center for Earthquake Eng. Research, SUNY, Buffalo, NY.

[198] Pinc RL, Watkins MD, Jirsa JO. (1977) *Strength of hooked bar anchorages in beam-column joints, CESRL Report No. 77-3*. Dept. of Civil Eng., Uni. of Texas at Austin, Austin, TX.

[199] Pinto A, Molina J, Varum H, Verzeletti G, Coelho E, Carvalho EC. (2001) Tests on a full-scale model of existing reinforced concrete frames (infilled and strengthened with shotcrete). In: Carvalho EC, Coelho E, editors. *Seismic assessment, strengthening and repair of structures*. Laboratorio Nacional de Engenharia Civil, Lisbon, Portugal; p. 109-123.

[200] Popov EP. (1984) Bond and anchorage of reinforcing bars under cycling loading. *ACI Structural Journal*. **31**:340-349.

[201] Priestley MJN. (1997) Displacement-based seismic assessment of reinforced concrete buildings. *J of Earthquake Eng*. Jan 1997; **1**(1):157-192.

[202] Priestley MJN, Calvi GM. (1991) Towards a capacity design assessment procedure for reinforced concrete frames. *Earthquake Spectra*. **7**(3):413-437.

[203] Priestley MJN, Seible F, Calvi GM. (1996) *Seismic design and retrofit of bridges*. John Wiley & Sons Inc., NY.

[204] Priestley MJN, Verma R, Xiao Y. (1994) Seismic shear strength of reinforced concrete columns. *ASCE J of Struct Eng*. **120**(8):2310-2329.

[205] Renton GW. (1972) The behaviour of reinforced concrete beam-column joints under seismic loading [M.E. Thesis]. Uni. of Canterbury, Christchurch, NZ.
[206] Rodriquez M, Park R. (1994) Seismic load tests of reinforced concrete columns strengthened by jacketing. *ACI Structural Journal*. **91**(2):150-159.
[207] Rosenblueth E, Meli R. (1986) The 1985 Earthquake: Causes and effects in Mexico City. *Concrete International: Design & Construction*. May 1986; **8**(5):23-34.
[208] Saatcioglu M, Mitchell D, Tinawi R, Gardner NJ, Gillies AG, Ghobarah A, et al. (2001) The August 17, 1999, Kocaeli (Turkey) earthquake - damage to structures. *Canadian Journal of Civil Eng*. **28**:715-737.
[209] Santarella L. (1957) *Il cemento armato. 2nd ed. [in Italian]*. Hoepli, Milan, Italy.
[210] Sarsam KF, Phillips ME. (1985) The shear design of in-situ reinforced concrete beam-column joints subjected to monotonic loading. *Magazine of Concrete Research*. Mar 1985; **37**(130):16-28.
[211] Saunders DB. (2004) Seismic performance of pre 1970's non-ductile reinforced concrete waffle slab frame structures constructed with plain round reinforcing steel [PhD dissertation]. Uni. of Canterbury, Christchurch.
[212] Scott RH. (1992) The effects of detailing on reinforced concrete beam-column connection behaviour. *The Structural Engineer*. Sept 1992; **70**(18):318-324.
[213] Scott RH. (1996) Intrinsic mechanisms in reinforced concrete beam-column connection behaviour. *ACI Structural Journal*. May-June 1996; **93**(3):336-346.
[214] SEAOC. (1966) *Recommended lateral force requirements*. Structural Engineers Association of California (SEAOC), Sacramento, CA.
[215] SEAOC. (1973) *Recommended lateral force requirements and commentary*. Structural Engineers Association of California (SEAOC), Sacramento, CA.
[216] Sezen H, Elwood K, Whittaker AS, Mosalam KM, Wallace JW, Stanton J. (2000) *Structural engineering reconnaissance of the August 17, 1999, Kocaeli (Izmit), Turkey, Earthquake. PEER Report 2000/09*. Pacific Earthquake Eng. Res. Center (PEER), Berkeley, CA.
[217] Sezen H, Moehle JP. (2004) Shear strength model for lightly reinforced columns. *ASCE J of Struct Eng*. **130**(11):1692-1703.
[218] Sezen H, Moehle JP. (2006) Seismic tests of concrete columns with light transverse reinforcement. *ACI Structural Journal*. Nov-Dec 2006; **103**(6):842-849.
[219] Shing B, Stavridis A, Koutromanos I, Willam K, Blackard B, Kyriakides MA, et al. (2009) Seismic performance of non-ductile RC frames with brick infills. *Proc. of ATC-SEI Conf, on Improving the Seismic Performance of Existing Buildings and Other Structures*, San Francisco, CA, p. 1117-1128
[220] Smith BJ. (1972) Exterior reinforced concrete joints with low axial load under seismic loading. Uni. of Canterbury, Christchurch, NZ.
[221] Sozen MA, Moehle JP. (1990) *A study of experimental data on development and lap-splice lengths for deformed reinforcing bars in concrete.* S&M Partnership, Urbana, IL.
[222] Sritharan S. (2005) Strut-and-Tie analysis of bridge tee joints subjected to seismic action. *ASCE J of Struct Eng*. **131**(9):1321-1333.
[223] Sritharan S, Ingham JM. (2003) Application of strut-and-tie concepts to concrete bridge joints in seismic region. *PCI Journal*. **48**(4):66-90.
[224] Supaviriyakit T, Pimanmas A. (2008) Comparative performance of sub-standard interior reinforced concrete beam-column connections with various joint reinforcing details. *Material and Structures (RILEM, Paris)*. **41**(3):543-557.

[225] Tepfers R. (1973) *A theory of bond applied to overlapped tensile reinforcement splices for deformed bars. Publication 73:2*. Div. of Concrete Structures, Chalmers Uni. of Technology, Gotenborg, Sweden.
[226] Tepfers R. (1979) Cracking of concrete cover along anchored deformed reinforcing bars. *Magazine of Concrete Research*. Mar 1979; **31**(106):3-12.
[227] Townsend WH. (1972) The inelastic behaviour of reinforced concrete beam-column connections [PhD Dissertation]. Uni. of Michigan, Ann Arbor, MI.
[228] Townsend WH, Hanson R. (1977) Reinforced concrete connection hysteresis loops. *Reinforced Concrete Structures in Seismic Zones, SP-53*. American Concrete Inst. (ACI), Detroit, MI; p. 351-370.
[229] Uzumeri SM. (1977) Strength and ductility of cast-in-place beam-column joints, SP-53-12. *Reinforced Concrete Structures in Seismic Zone, ACI SP-53*. American Concrete Inst. (ACI), Detroit, MI; p. 293-350.
[230] Uzumeri SM, Seckin M. (1974) *Behaviour of reinforced concrete beam-column joints subjected to slow load reversals. Publication No. 74-05*. Dept. of Civil Eng., Uni. of Toronto, Toronto, Canada.
[231] Vecchio FJ, Collins MP. (1986) The modified compression-field theory for reinforced concrete elements subjected to shear. *ACI Structural Journal*. **83**(22):219-231.
[232] Verderama GM, Fabbrocino G, Manfredi G. (2008) Seismic response of r.c columns with smooth reinforcement. Part II: Cyclic tests. *Eng Structures*. **30**(9):2289-2300.
[233] Verderama GM, Fabbrocino G, Manfredi G. (2008) Seismic response of r.c. columns with smooth reinforcement. Part I: Monotonic tests. *Eng Structures*. **30**(9).
[234] Verderama GM, Ricci P, De Carlo G, Manfredi G. (2009) Cyclic bond behaviour of plain bars. Part I: Experimental investigation. *Construction and Building Materials*. **23**(12):3499-3511.
[235] Verderama GM, Ricci P, De Carlo G, Manfredi G. (2009) Cyclic bond behaviour of plain bars. Part II: Analytical investigation. *Construction and Building Materials*. **23**(12):3512-3522.
[236] Vollum RL, Newman JB. (1999) Strut and Tie models for analysis/design of external beam-column joints. *Magazine of Concrete Research*. Dec 1999; **51**(6):415-425.
[237] Walker SG. (2001) Seismic performance of existing reinforced concrete beam-column joints [M.Sc. thesis]. Uni. of Washington, Seattle, WA.
[238] Wong HF. (2005) Shear strength and seismic performance of non-seismically designed RC beam-column joints [PhD thesis]. Hong Kong Uni. of Science and Tech., Hong Kong.
[239] Wu C-L, Chai J-F, Lin C-CJ, Lin F-R. (2008) Reconnaissance report of 0512 China Wenchuan Earthquake on schools, hospitals and residential buildings. *Proc. of 14th World Conf on Earthquake Eng*, Beijing, China.S31-004.
[240] Wu C-L, Kuo W-W, Yang Y-S, Hwang SJ, Elwood K, Loh CH, et al. (2009) Collapse of a nonductile concrete frame: Shaking table tests. *Earthquake Eng & Struct Dyn*. Feb 2009; **38**(2):205-224.
[241] Yavari S, Elwood K, Lin S-H, Wu C-l, Hwang S-J, Moehle JP. (2009) Experimental study of dynamic behaviour of multi-story reinforced concrete frames with non-seismic detailing. *Proc. of ATC-SEI Conf, on Improving the Seismic Performance of Existing Buildings and Other Structures*, San Francisco, CA, p. 489-499
[242] Yavari S, Elwood K, Wu C-l. (2009) Collapse of a nonductile concrete frame. *Earthquake Eng & Struct Dyn*. Feb 2009; **38**(2):225-241.

CHAPTER 3. CONCEPTUAL DEVELOPMENT OF SELECTIVE WEAKENING RETROFIT FOR RC FRAMES

"In the capacity design of structures for earthquake resistance, distinct elements of the primary lateral force resisting system are chosen and suitably designed and detailed for energy dissipation under severe imposed deformations."

Thomas Paulay and M.J. Nigel Priestley, 1992

(Seismic Design of Reinforced Concrete and Masonry Buildings, Wiley Interscience)

3.1 INTRODUCTION

3.1.1 Philosophy of retrofit strategy

The fundamental philosophy of *modern seismic design* is to activate a suitable inelastic mechanism in a building during a seismic event, so that such inertial forces can be dissipated in a safe, controlled and ductile manner, as clearly summarised by the quotation above. Using rational hierarchy of strength and understanding of the *capacity design principles*, a reinforced concrete (RC) building can be designed to respond under inelastic flexural yielding of plastic hinges detailed for ductility. Similarly, a successful *seismic retrofit strategy* should 'force' the RC structure to respond under a specific inelastic mechanism with substantial ductility and deformation capacities. This fundamental principle is behind the concept of Selective Weakening (SW) retrofit.

As the design philosophy for new buildings evolved from a working-stress approach, to a limit state ultimate strength approach, to a displacement-based approach, the seismic retrofit design philosophy too gradually moved from a force-based to a displacement and performance-based framework [137, 138, 162]. In seismic rehabilitation guidelines such as the FEMA 356 [65] and the ASCE-41 [11] for example, displacement and strain-based limit states for the local structural elements (i.e. columns and joints) as well as for the global structure (inter-storey drift,

θ_{drift}) are outlined. The key recognition that damage is directly related to displacement capacity and demand of a structure is fundamental to the understanding and development of seismic retrofit techniques that aim at improving structural displacement capacities such as the SW retrofit. As such, the proposed SW retrofit strategy in this research requires a paradigm shift towards the performance-based seismic retrofit.

3.1.2 Performance-based seismic retrofit - performance objectives

Much has been developed in terms of qualitative and quantitative descriptions of the performance-based earthquake engineering. In essence, for a particular structure, the building structural and non-structural performance levels (PLs) can be associated with some given levels of seismic intensities associated with specified return periods. These are in turn related to global performance objectives – be it to maintain functionality of the building post-earthquake (Operational PL) or to minimise fatalities (Life Safety PL). This reflects a change from the conventional life-safety-only design requirement with implied minimal damage. Figure 3.1 shows the performance objective matrix for new buildings and for existing structures from the SEAOC Vision 2000 document [178] and the ASCE-41 respectively.

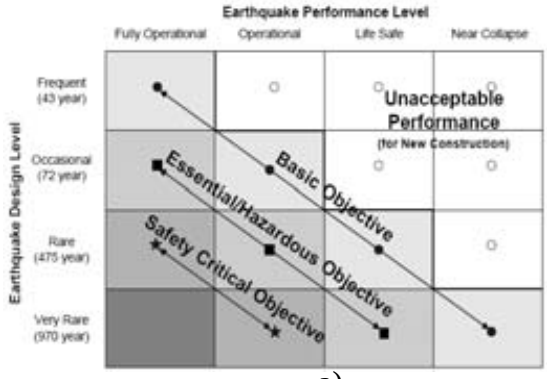

a)

ASCE-41 Table C1-1. Rehabilitation Objectives		Target Building Performance Levels			
		Operational PL	Immediate Occupancy PL	Life Safety PL	Collapse Prevention PL
Earthquake Hazard Level	50% in 50 years	a	b	c	d
	20% in 50 years	e	f	g	h
	10% in 50 years	i	j	k	l
	2% in 50 years (MCE)	m	n	o	p

Notes: Limited Objectives; Basic Safety Objectives (BSO); Enhanced Objectives

PL = Performance Level
MCE = maximum credible earthquake

b)

Figure 3.1: Performance objective matrix a) SEAOC Blue Book seismic performance domain for new buildings; b) ASCE-41 rehabilitation objectives for existing structure.

In the European interpretation [67] of performance-based seismic retrofit and the associated retrofit objectives, building performance and thus building damage are recognised as a function of building components' deformations. As such, different PLs can be achieved using either brittle but strong structures or ductile but weaker retrofitted structures as illustrated by Figure 3.2. Thus, by applying capacity design principles into the seismic retrofit, selective weakening of specific structural elements could induce the weakest links at ductile flexural

hinges, thus achieving the "ductile but weaker" (in some cases, 'weaker' even when compared to the as-built configuration) retrofit objectives without global strengthening.

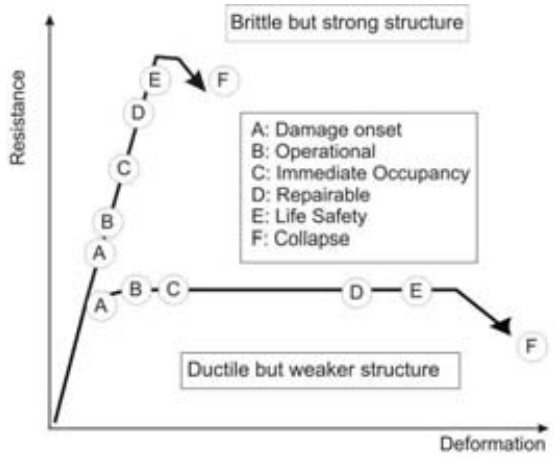

Figure 3.2: Performance levels for two different retrofit approaches/strategies (adopted from fib-24 [67]).

The concept of multi-level performance objective matrix shown in Figure 3.1 could be further extended towards a more comprehensive structural and non-structural 3D performance matrix as illustrated in Figure 3.3 [102]. Figure 3.3 shows the schematic view of considering various performance measures and physical damage indicators such as peak displacement, acceleration and residual deformation for a given level of seismic intensity. Pampanin *et al.* [144] have previously proposed the combined maximum-residual displacement performance matrix for new structures. Adopting the same performance-oriented earthquake engineering for seismic retrofit, it is clear that given the socio-economic limitations of a particular city or community, different performance objectives can be accepted and different retrofit strategies can be adopted to achieve these performance objectives.

Performance-based seismic retrofit allows a greater flexibility in deciding the building performance objectives for seismic retrofit when compared to the design of new buildings. Different post-retrofit targeted PLs can be described qualitatively depending on the following acceptable: a) risks of the owners and users, b) levels of occupants' safety and functionality of the building during and after an earthquake, c) levels of heritage intrusion and invasiveness, d) repairability and reversibility of the retrofit, and, most importantly, e) costs of the seismic retrofit. In brief, performance-based seismic retrofit recognises the crucial socio-economic limitations in the development of retrofit strategies and in the selection of targeted performance objectives. Therefore, recognising larger societal needs for earthquake-resilient buildings and communities,

seismic retrofit strategies can be designed to achieve higher performance levels, with reference to Figure 3.3 and as per ASCE-41 terminology:

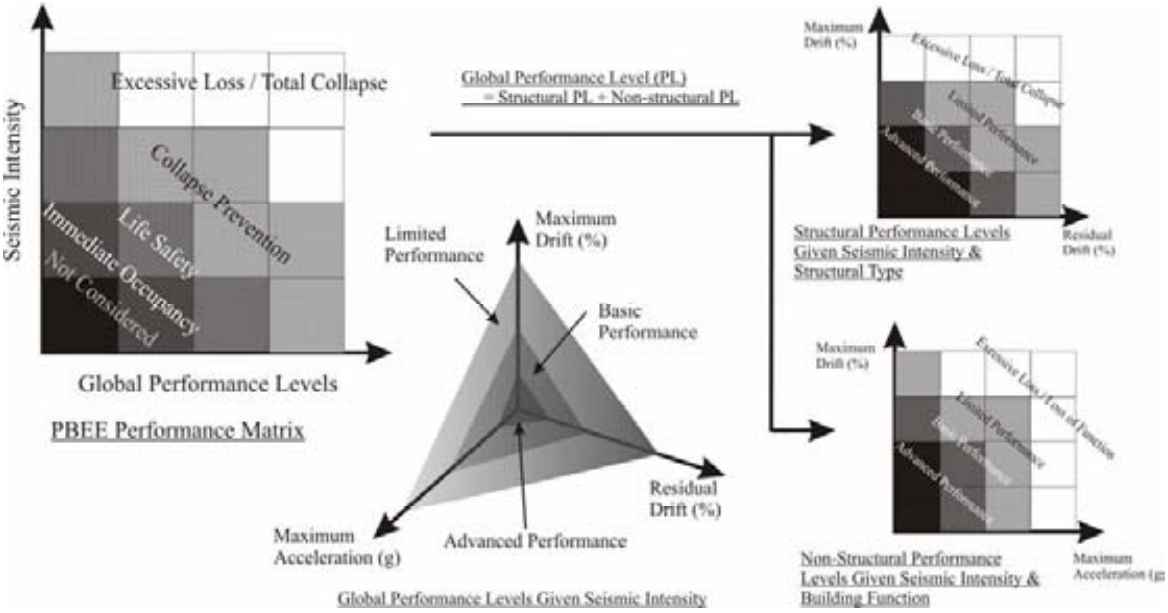

Figure 3.3: Seismic performance objective domains for new buildings and seismic retrofit [102].

3.1.2.1 Limited Performance (LP) / Limited Rehabilitation Objectives (LRO)

A *Partial retrofit* strategy preventing complete structural collapse while accepting extensive damage beyond reparability can be a valid solution for Limited Rehabilitation Objectives (LRO). Significant structural and non-structural damages are acceptable in LRO. As total collapse is prevented, human fatalities are minimised. In such a partial retrofit strategy, removal of critical structural weaknesses such as brittle columns and joint shear failures, and prevention of soft-storey collapse, may be sufficient to achieve the required performance target. LRO can result in economical implementation of partial seismic retrofit in a territorial-scale level. Compared to 'doing nothing', a partial retrofit strategy may yield a much better outcome in terms of fatalities and losses in densely populated urban cities with large stock of non-ductile buildings.

In the New Zealand Building Act 2004 [40] and the NZSEE 2006 seismic evaluation guidelines [133], the adoption of the quantifiable minimum standard of 33% of New Building Standards (NBS) is an attempt towards achieving LRO for critical earthquake-prone structures. The more widely-used ASCE-41 on the other hand, specifies LRO as non-collapse and life-safety objectives in moderate earthquakes. In particular, ASCE-41 [11] specifies the θ_{drift} limit of 4.0% for LRO of RC frames. This reflects a rational compromise with reality – that for large building

stocks, it is not possible to retrofit all vulnerable existing buildings to the modern seismic code requirements.

Nevertheless, a narrow interpretation of the 33% NBS lateral strength (base-shear) limit state may result in un-conservative seismic retrofit decision. This is schematically illustrated in Figure 3.4 below. For example, only case G) with the lateral strength < 33%NBS is considered earthquake-prone building (EPB) under current interpretation of the 2004 Building Act, within the NZSEE guidelines [133]. From a seismic performance perspective, cases E and F are seismically-vulnerable as they will be vulnerable to collapse under moderate-to-large earthquakes (with >67%NBS displacement demand). Figure 3.4 again emphasizes the importance of holistic view of the seismic performance after the retrofit interventions. Cases C and D, while do not attain 67%NBS lateral strength, are more preferably for their ductile response and sufficient deformation capacity.

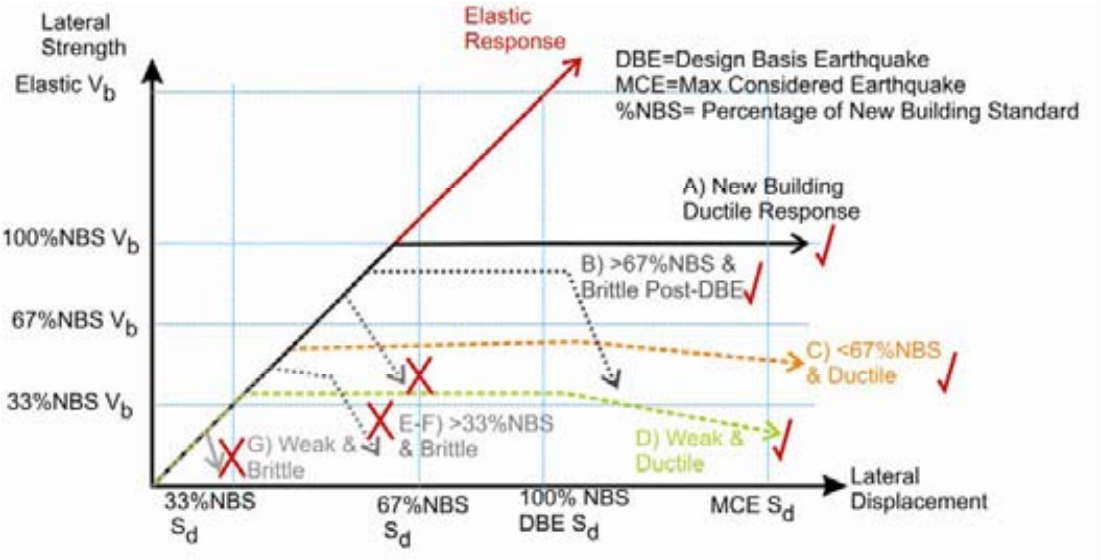

Figure 3.4: Seismic retrofit objectives versus the New Zealand %NBS (percentage of New Building Standard) requirement in terms of strength and displacement requirements. V_b = lateral strength / building base shear.

3.1.2.2 Basic Performance (BP) /Basic Safety Objective (BSO)

Basic Performance (BP) or Basic Safety Objective (BSO) within the FEMA-356/ASCE-41 framework generally corresponds to the achievement of new building design objectives (or 100% NBS in NZSEE guidelines terminology). Under design level earthquakes (10% in 50 years) and maximum credible earthquakes (MCE – 2% in 50 years), life-safety and ductile plastic mechanism are expected. Typical codes provisions, for example, the ASCE-41 and the NZS1170 [129], specify a θ_{drift} of 2.0-2.5%. Within the extension to include non-structural elements as

shown in Figure 3.3, BSO may include thresholds for floor acceleration and residual drift limits on top of θ_{drift} requirement. In BSO, some levels of structural and non-structural damages are expected.

3.1.2.3 Advanced Performance (AP) /Enhanced Rehabilitation Objectives (ERO)

Advanced Performance (AP) or Enhanced Rehabilitation Objectives (ERO) is a more recent concept, following the lessons of huge financial losses and functional downtime during the Northridge and Kobe earthquakes. The shift of societal expectation on the seismic resilience of the engineered and retrofitted structures implies a need for buildings to remain functional in moderately strong events without significant repair and functional downtime. This also implies seismic retrofit strategies must also consider structural and non-structural damage indicators such as floor acceleration and residual deformation in the conceptual stage. In ASCE-41, the recommended AP limit states for maximum θ_{drift} and residual θ_{drift} are 1.0% and negligible respectively.

The current practice to achieve ERO relies predominantly on seismic isolation retrofit or some forms of seismic strengthening with supplementary damping to achieve superior seismic performance in terms of peak displacement, floor acceleration and residual deformation. While these may be viable in many cases, it could be shown that advanced SW retrofit solutions can also provide alternative retrofit solutions to achieve advanced seismic performance.

3.1.3 Selective weakening for “strengthening” retrofit - prelude

Many seismic retrofit/rehabilitation schemes have been proposed and implemented for pre-1970s RC frames with non-ductile beam-column joints (e.g. [11, 66, 67, 133, 192]). The majority of the established methods for RC frames involve either global strengthening of the whole building or local strengthening of structural components (columns or joints). Alternatively, the seismic demand onto the structure can be reduced by supplementary damping or seismic base isolation. While most retrofit techniques can theoretically achieve a targeted PL, excessive costs, invasiveness and constructability are still the main issues for a wider implementation. Following the recent introduction of selective retrofit techniques [55, 57, 159], where strength, ductility and stiffness can be upgraded in isolation, the concept of Selective Weakening (SW) for retrofit for non-ductile RC structures was conceived [137] as an alternative retrofit approach to achieve partial and advanced retrofit performance objectives.

SW retrofit aims to improve the global inelastic mechanism and deformation capacity of the RC frames, by first weakening and then upgrading specific / critical structural (or non-structural) elements. The SW strategy can be designed to achieve different PL targets and inelastic mechanisms – from a weakened ductile flexural mechanism to a strengthened flexural-rocking mechanism. The existing foundation and other brittle elements can be protected by limiting the flexural capacities of the weakened sections. Other implementations of the SW retrofit strategy include vertical/horizontal separations of shear-deficient walls [95, 96], isolation of shear-critical precast floor systems [98, 99] and detachment of masonry infills to prevent interaction and column failures. Further treatment of the SW retrofit concept is given in §3.3.

The SW retrofit strategy fits well within a multi-level retrofit strategy for large-territorial scale implementation where the concept of full and partial retrofit was introduced by Pampanin *et al.* [80, 140, 142]. It was shown how a *partial retrofit* solution for non-ductile pre-1970s RC frames with retrofit interventions only at the exterior joints could achieve a collapse prevention PL (LRO/BSO). A partial retrofit consists of upgrading only the exterior joints to form plastic hinges in the beam framing into exterior columns, while accepting some inelastic damages in the interior joints and columns. Alternatively, a *full retrofit* solution involving a full upgrade of all beam-column joints and development of plastic hinges in the beams according to the capacity design principles can achieve a better performance objective. Similarly, Ireland *et al.* [95, 96] adopted a multi-level retrofit approach for shear-deficient structural walls using SW retrofit techniques. This will be further discussed in §3.3.2.3.

3.1.4 Chapter Outline

This chapter is divided into six sections. The first section (§3.1) will introduce the motivation underlying the SW retrofit strategy, including a brief account of performance-based seismic retrofit. In §3.2, a brief review of existing and more traditional retrofit strategies and techniques for non-ductile pre-1970s RC frames and specifically for RC beam-column joints will be presented. In §3.3, the concept of Selective Weakening retrofit will be formally presented and developed. §3.4 will present the analytical tools and retrofit design procedure for the SW retrofit for RC frames and exterior beam-column joints. The key insights and outputs of this chapter will be summarised in §3.6.

3.2 RETROFIT STRATEGIES AND TECHNIQUES FOR RC FRAMES

3.2.1 Seismic retrofit strategies and techniques

Existing performance-based seismic retrofit guidelines inherently outline various strategies to achieve the different Performance Limits (PLs) and Performance Objectives (POs) as discussed in preceding sections. Nevertheless, these strategies are generally not explicitly linked with specific retrofit strategies with the presumptions that engineering experience and structural analysis of the post-retrofit behaviour will indicate the PL achieved. In the following paragraphs, these existing retrofit strategies and techniques will be reviewed qualitatively in terms of achievable PLs.

Herein, a clear distinction is given to retrofit strategies and retrofit techniques which are often and inappropriately confused. Broadly, retrofit strategy is defined as a basic approach that is targeted to improve seismic performance to achieve overall retrofit performance objectives, such as increasing strength, increasing deformability, reducing deformation demands. Retrofit techniques, on the other hand, refer to specific technical methods/systems to achieve the strategy targets. For example, a global retrofit strategy aims at improving lateral strength and ductility modifying the hierarchy of strength in beam column joints using local retrofit techniques such as concrete or FRP (fiber reinforced polymers) jacketing.

The selection of retrofit strategies for a particular building can be complex, depending on: a) typology and as-built capacities of the existing structure, b) economic and operational consequences (cost, interruption and invasiveness requirements), and c) performance targets. Broadly, a seismic retrofit strategy can be broadly divided into a) decreasing earthquake (force or displacement) demands, and b) increasing deformation capacity. This is illustrated conceptually in Figure 3.5 for non-ductile RC frames.

Several common retrofit strategies to decrease the earthquake force or displacement demands are a) conventional strengthening (increasing lateral stiffness and strength), b) conventional supplementary damping, and c) seismic isolation retrofit. The example in Figure 3.5a shows how conventional strengthening by adding lateral stiffness and strength can effectively reduce the displacement demand in the global structure and reduce force/moment demands in the non-ductile elements. These retrofit strategies are more commonly accomplished using global retrofit techniques as to be discussed in §3.2.2, while some local retrofit techniques applied universally may result in similar retrofit outcomes.

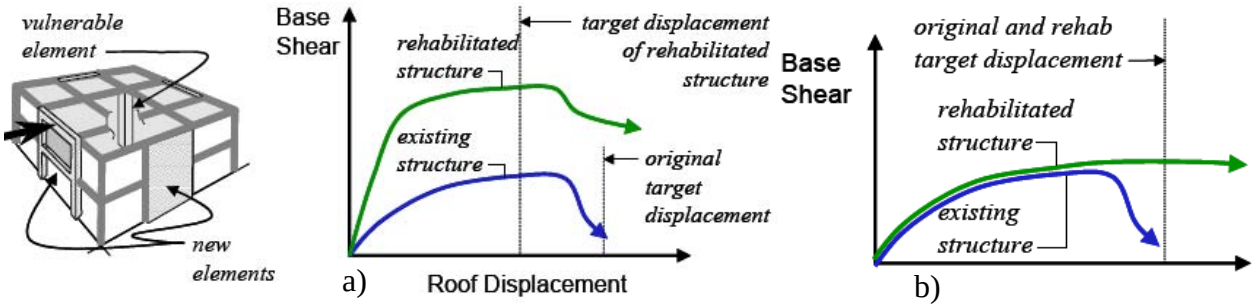

Figure 3.5: Seismic retrofit strategies – a) Decreasing earthquake (displacement) demand; b) Increasing deformation capacity (taken from [124], originally shown in [67]).

Alternatively, depending on the building structural, architectural and functional needs, it may be more appropriate to increase the deformation capacities by changing the brittle failure modes to ductile failure modes using local upgrading methods such as concrete jacketing (Figure 3.5b). Englekirk and Sabol [62], for example, presented an approach to retrofit for life-safety by concentrating on improving ductility rather than achieving required strength. Increasingly, retrofit design strategies based on controlling drift and deformations, as well as maintaining the ductility capacity-demand ratio in the inelastic hinges are preferred as building deformation (e.g. θ_{drift}) is more related to the structural damages and losses [123, 164, 167]. Pincheira [156] found that if a retrofit scheme stiffened the existing structure significantly with the primary aim to reduce drift demand, un-expectable and often un-acceptable damages may occur to un-strengthened elements. Thermou *et al.* [198] proposed a seismic retrofit methodology aiming at achieving a near-uniform distribution of inter-storey drift along the building height, eliminating local damages. Displacement-focussed retrofit strategies are consistent with the performance objectives illustrated in Figure 3.1, where PLs are associated with deformation limit states.

The effects of various retrofit strategies on the structural performance are illustrated in Figure 3.6 within an Acceleration-Displacement Response Spectrum (ADRS) domain, typical of a capacity spectrum method [29]. Within an ADRS framework, the effects of various retrofit strategies on the structural performance in terms of seismic demand and capacity spectrum can be observed. While some retrofit strategies aim at shifting the capacity spectrum, leading to either (Figure 3.6a) lower displacement demand or (Figure 3.6b) higher displacement capacity, some other strategies target at shifting the demand spectrum (Figure 3.6c and d).

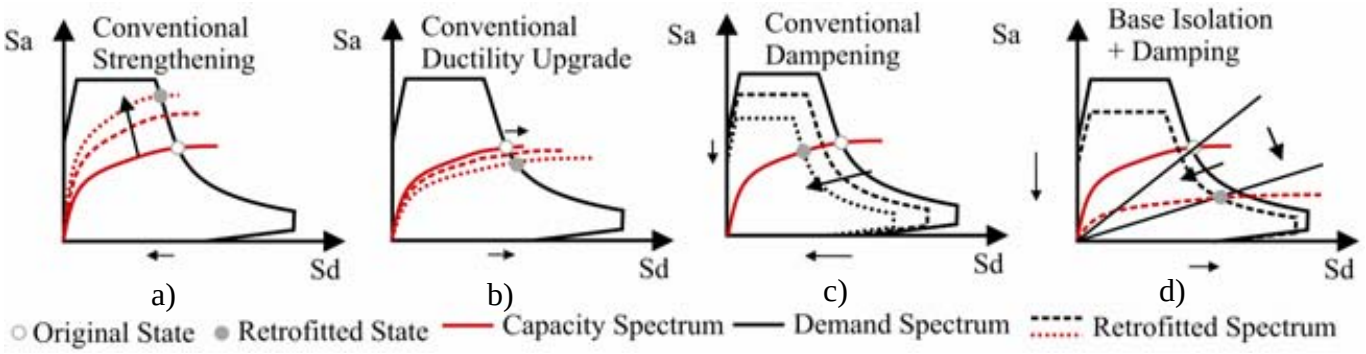

Figure 3.6: Acceleration-Displacement Response Spectrum (ADRS) illustration of different retrofit philosophies and strategies: a) conventional strengthening, b) conventional ductility upgrading, c) added damping, d) seismic base isolation.

Conventional strengthening and stiffening solutions, while reducing the deformation demand, tend to increase the inertial forces demand on the structure (Figure 3.6a). Conventional ductility upgrade would increase deformation capacity, but a non-invasive, non-labourious and effective ductility-only upgrade is presently limited (Figure 3.6b). Supplementary damping would in principle decrease the seismic demand on the structure (Figure 3.6c) but the implementation and design of these systems for seismic retrofit can be complicated [31]. Base isolation with or without supplementary damping (Figure 3.6d) would elongate the structural period, reduce seismic demand and isolate the deformation demand on the seismic isolator bearing.

Various technical guidelines provide generalised principles on the selection of retrofit strategies and techniques given a particular scenario of as-built structures (e.g. [11, 67, 133]). Considering the ever growing state-of-the-art of seismic retrofit and rehabilitation techniques for RC structures [66, 67, 133, 191, 192, 197], the following sub-section provides only a brief overview of the existing seismic retrofit strategies and techniques for non-ductile RC frames. Particular emphasis is given to the retrofit techniques of beam-column joint connections and retrofit techniques that are relevant to the SW retrofit.

3.2.2 Global strategies and techniques

Global retrofit intervention techniques may be more the cost-effective retrofit strategy than universal local elements upgrading (local retrofit) in as-built structures where existing horizontal load-path may be unavailable or grossly insufficient. Therefore, for some structures such as unreinforced masonry buildings, irregular structures and complex as-built buildings, global strategies described below may indeed be the optimal engineering retrofit solution. However, as

later briefly discussed, global retrofit strategies entail a set of complex issues to be considered, that may in effect increase their cost and decrease its effectiveness.

3.2.2.1 Global strengthening and stiffening

Global strengthening retrofit strategy and techniques were the earliest to be applied in the retrofit of seismically vulnerable RC buildings. Addition of new concrete walls for seismic retrofit has been used since the late 1970s (e.g. [88, 190]) and various variants have since been implemented, including the use of precast post-tensioned infill concrete walls/braces [69, 108], strengthened masonry infills [18] and more recently the rocking or "controlled rocking" reinforced concrete walls [117, 207]. Steel bracing systems for upgrading non-ductile RC frames have been proposed and used since the 1990s [13, 24, 158, 190, 210]. These include concentric, eccentric, K-shaped bracing systems as well as post-tensioned bracing systems [122, 158, 196, 210]. Figure 3.7 illustrates the effect of various global-level retrofit techniques in achieving global strengthening retrofit strategy objectives on the global load-displacement response [191]. Depending on the strengthening techniques, different effects on strength, stiffness and/or ductility are achievable.

The use of new lateral resisting systems in the form of new shear walls or brace-frame systems is efficient in controlling global lateral drift as well as reducing internal action demands on the existing structure. In addition to the relatively low technology intensity and simplicity in design, global strengthening using new structural walls/frames/braces along its parameter grids can be relatively non-intrusive and thus allowing continual occupancy of the building during seismic retrofit construction [67].

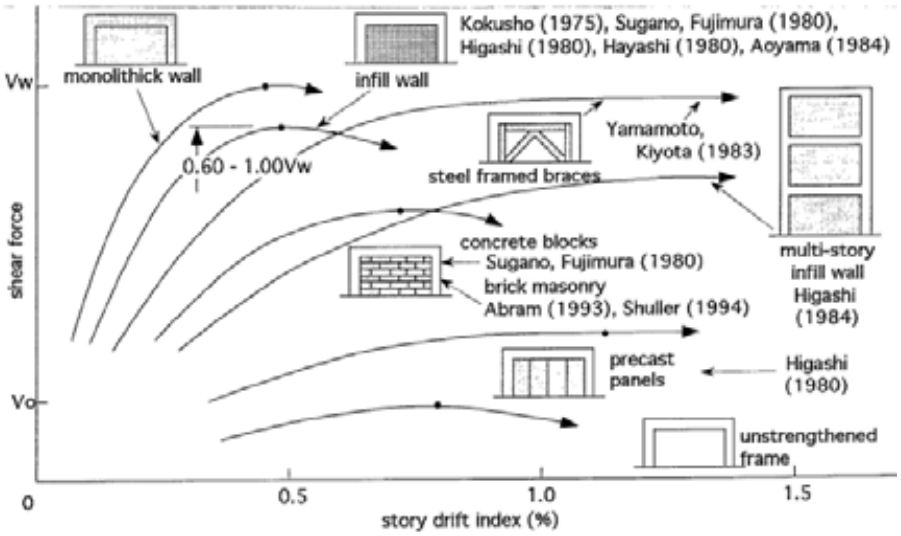

Figure 3.7: Load-displacement relationship for various typical strengthening techniques [191].

As illustrated in Figure 3.6a, conventional strengthening, while increasing the strength, stiffness and ductility capacities, also increases stiffness and strength demand on the structure. Crucial attention must also be given to the transfers of inertial forces from the existing structures to the new walls/braces as well as the actual capacity of the existing floor diagram to sustain the increased action, the distribution of walls/braces in plan and elevation, the transfer of loads to the foundations and the capacity of the existing foundations [13, 24, 69, 88, 158]. The integration of the new structural elements with the existing ones (e.g. diaphragm collectors retrofit or field-welding fitting for steel bracing) could possibly be the most costly and complex issues in the global strengthening/stiffening solutions [24, 25, 67]. The localised stress effect along the load-path (e.g. end connection of braces [108] and boundary columns in infill walls retrofit (e.g.[191])) must also be thoroughly designed.

The need to subsequently strengthen the foundation (e.g. [172]) for the increased overturning moment demand is also a major disadvantage of global strengthening strategy, in particular for added concrete shear walls. Furthermore, the difficulty in assessing and modelling the foundation-to-soil flexibility and strength gives some uncertainty over the overall effectiveness of these global strengthening approaches.

Lastly, for the global strengthening strategy, given the limitations of acceptable damage and local plastic deformability for local elements, local element ductility or strength upgrades may also be required to complement the global-scale retrofit (e.g. [176]). For example, the restrictive acceptance criteria limit for beam-column joint plastic deformation in some standards (e.g. ASCE-41) would often result in further local joint retrofit requirements. Another common example is the need for seismic force collector upgrades when a global retrofit approach such as the addition of RC shear walls is used.

3.2.2.2 Global supplementary damping and/or seismic isolation

An alternative solution to the restrictive local element deformability and foundation strength capacities is to add global supplementary damping to control the inter-storey drift and local ductility demands in the RC frames (Figure 3.6c and d). The theory and design of passive supplementary damping and/or seismic isolation for seismic retrofit of non-ductile RC frames are well established in literature [31, 181, 193]. In many parts of the world, base-isolation technology has been used for the seismic retrofit of monumental buildings (e.g. [125]) as well as non-ductile RC frames (e.g.[37, 44, 128]). Passive supplementary energy dissipation solutions are less

common for the retrofit of RC frames as the displacement required to activate the dampers is generally beyond the deformation capacities of the existing structural RC elements and non-structural components [67]. Examples of seismic retrofit with added braces with friction and fluid viscous dampers and seismic isolation are shown in Figure 3.8, while other examples are available in literature [47, 182].

Figure 3.8: Examples of global supplementary damping using: a-b) friction damped braces[107] and fluid viscous dampers [193]; and c) seismic isolation retrofit for Victoria University library [37] .

In addition to controlling the deformation demands, shaking table tests on different isolation retrofit systems have shown their ability to control the acceleration demand on the internal content of the retrofitted RC frames [44, 46]. The design limit for most seismic isolation retrofit is typically the displacement limits of the device and building. Some other issues associated with global damping or seismic isolation strategies revolve generally around cost, non-applicability in certain seismicity and building periods.

Researchers have also investigated Shape Memory Alloy (SMA) braces for seismic retrofit of non-ductile RC frames [47, 183]. SMA self-centering braces retrofit [26, 41] have shown tremendous potential in achieving high PLs under the AP retrofit objectives, in particular in controlling the peak and residual deformation demands. Lastly, while active and semi-active control retrofit solutions have been widely researched (e.g. [31, 194]), in practice, they are rarely used due to cost and complexity of design and implementation.

3.2.3 Local retrofit strategies and techniques for beam-column joints

Local retrofit strategies for RC frames are based on localised upgrade of the strength, stiffness and/or ductility capacities of structural elements using various retrofit techniques, with the intent

to improve the overall inelastic response of the global frame system. In general, local retrofit strategies can be designed for most performance objectives (LP, BP or AP). Many local retrofit techniques and solutions have been developed for non-ductile RC frames following the introduction of new seismic provisions and the availability of advanced materials (e.g. fibre-reinforced polymers, FRP, and high strength prestressing wires of steel). The following discussion is limited to local retrofit techniques for beam-column joint connections, as retrofit techniques for other structural components and failure modes (e.g. column lap-splice, beam shear, column flexural) are beyond the scope of this study.

3.2.3.1 Local elements selective retrofit – stiffness, ductility or strength retrofit

The idea of selective retrofit intervention, in which engineers separately upgrade three structural parameters: strength, stiffness and ductility, was suggested to enable control of the inelastic mechanism and failure mode of the RC structure [57]. Several practical construction methods to enhance strength, stiffness and ductility independently for non-ductile RC walls, as shown in Figure 3.9, were tested [57]. Strength-only retrofit was achieved using external unbonded boundary bars with a slotted bolt delay mechanism. Stiffness-only rehabilitation was achieved by two strips of epoxy-glued steel plates with gap to the foundation. Ductility-only retrofit was based on improvement the confinement of the concrete using U-shaped bolted steel plates.

Further analytical and parametric studies on selective retrofitting of RC elements with complete design expressions and guidelines were available [55, 67]. The design guideline was further validated with shaking-table tests of 2/3-scaled RC walls conducted at the LNEC facility at Lisbon [56]. The selective retrofit scheme was found to be economical and easy to apply. A drawback of the proposed scheme is that the current design parameters (strength, stiffness and ductility) are not directly correlated to the more important aspect of global behaviours such as θ_{drift}, floor acceleration and building base shear.

As a final verification, the selective retrofitting technique was used to repair and retrofit a full-scale four-storey three-bay non-ductile RC frame which was tested under pseudo-dynamic testing at the ELSA laboratory at Ispra [159]. The selective retrofit technique was effective in distributing the inelastic damages up the building, with stable global hysteresis behaviour. Ref [27] summarises the analytical and experimental work within the European ICONS research project which tested and compared various retrofit techniques including selective retrofit, shotcreting and added steel K-brace with shear-link dissipaters.

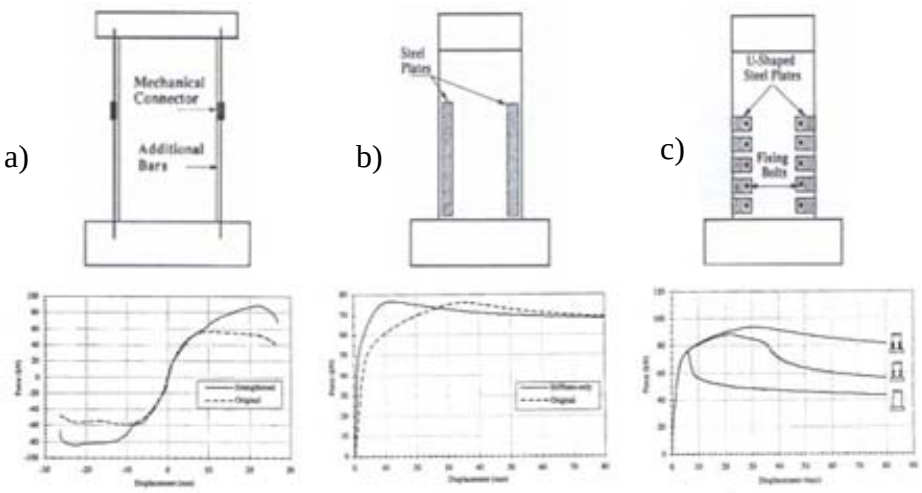

Figure 3.9: a) Selective retrofit techniques for strength-only, stiffness-only and ductility-only upgrade for structural walls [55]; b) Selective retrofit techniques implemented for non-ductile RC frames [27].

3.2.3.2 Local element retrofit via reinforced concrete and steel jacketing

The earliest form of local beam-column joint retrofit concentrated on the use of steel and reinforced concrete jackets to confine and strengthen the joint. Many of the initial researches were focused on the repair of damaged beam-column joints as local element retrofit was not widely considered until recently.

Migliacci *et al.* [121] reported the earliest set of tests on seismic behaviour of exterior beam-column joints retrofitted with steel angles and prestressed steel straps. Prestressing was achieved using preheating but it was found unreliable. They concluded that steel jacketing was effective in restoring and improving the strength and energy dissipation of the non-ductile joints. Corazao and Durrani [39] reported tests of eleven beam-column joints repaired with reinforcement concrete jacketing with steel encasement. Difficulties in in-place bending and placement of reinforcements and pinching hysteresis for retrofitted exterior joint were reported.

Alcocer and Jirsa [7] tested three different typologies of RC jacketing of interior beam-column joints with floor slab with satisfactory confinement and overall performance. Their tests were based on the experience from the post-1985 Mexico City earthquake repair and restoration. However, RC jacketing of interior beam-column joints was found to be extremely labour intensive and requiring careful detailing, as shown in Figure 3.10a. Choudhuri *et al.* [30] and Bracci *et al.* [21] tested similar RC jacketing retrofit on interior beam-column joints retrofitted with added vertical post-tensioned column reinforcements with some success. RC jacketing was shown to be effective for the repair and strengthening of exterior beam-column joints (e.g. [200]).

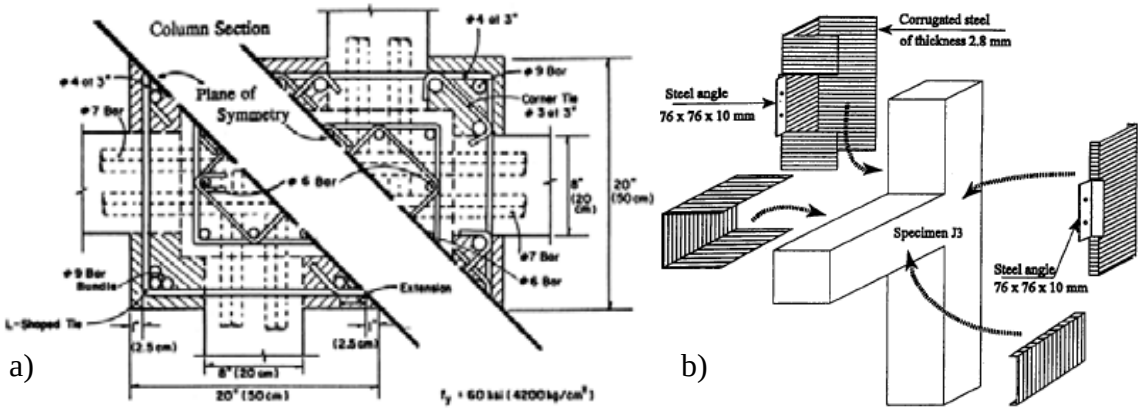

Figure 3.10: a) Reinforced concrete jacketing retrofit of interior beam-column joints [7]; b) Corrugated steel plates jacketing of exterior joints [76].

Steel jacketing provides a less laborious and faster construction retrofit option, compared to RC jacketing. Steel jacketing retrofit involves the encasement of the beam-column joint with a thin layer of steel plates, and concrete grouting filling the gap between the steel and existing concrete. Circular and rectangular steel jacketing were shown to be just as efficient in providing confinement to the beam-column joint regions [89]. Alternatively, jacketing solution with corrugated steel plates, considering the corrugated plates were considerably stiffer than flat steel plates, was also shown to be effective [17, 75, 76]. The corrugated plates were grouted upon piece-meal installation as shown in Figure 3.10b.

Without careful analysis of the hierarchy of strength, column hinging or beam shear failure might occur due to the over-strengthening from the jacketing [89]. Typically, a gap between the beam and column face is provided to minimise the flexural over-strength from the jacketing retrofit.

3.2.3.3 Composite material and FRP jacketing retrofit

Composite materials, such as FRP, are now widely adopted for structural and seismic retrofit [68, 195]. Several state-of-the-art reviews are available in literature [20, 60, 68], summarising the research and development of the use of composite materials for structural and seismic retrofit. FRP “jacketing” for seismic retrofit has some important advantages such as fast and relatively non-invasive application. Its low weight-to strength and stiffness ratio, durability and versatility offer significant advantages for applications in seismic retrofit. Figure 3.11 shows some of the possible configurations of FRP jacketing using large or small strips, various anchorage mechanisms and different design options for exterior beam-column joints.

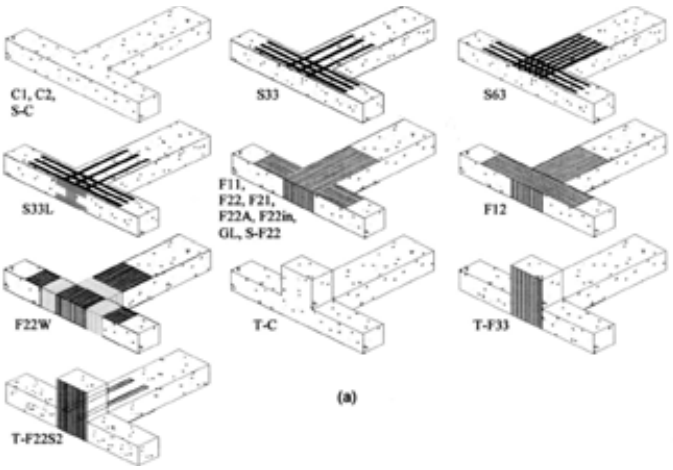

Figure 3.11: Antonopoulos and Triantafillou [10]'s comprehensive experimental test on FRP retrofit of RC exterior beam-column joint.

FRP jacketing was first used for the seismic retrofit of shear- and anchorage-deficient bridge piers and columns [167, 168]. The extension of FRP jacketing for seismic retrofit of beam-column joint aimed at improving the joint shear capacity of bridge T connections using passive confinement [73, 148]. Subsequent researches tested various configurations of FRP jacketing and anchoring (diagonal, layer, strips, U-shape, multiple layers, mechanical versus resin-bonded anchorage etc.), different FRP materials (glass, aramid, carbon etc.) and different as-built conditions (exterior versus interior joints, wide column, variation of axial load etc) (e.g.[10, 61, 74, 78, 104, 111, 139, 154, 170, 200, 202]). This was also complemented with substantial increase in the understanding of FRP bond anchorage, modelling of FRP elements and analytical design procedure for FRP-strengthened joints (e.g.[5, 8, 9, 110, 180]). Figure 3.12 illustrates the applications and tests of FRP retrofit for non-ductile RC frames: (a) pseudo-dynamic tests on the retrofitted SPEAR non-ductile RC building [42, 43] and (b) quasi-static tests on beam-column joint subassemblies [139, 140].

However, high material and labour costs as well as the need for specialist applications are some implementation issues for composite material jacketing retrofit. Another shortcoming is the possible brittle failures associated with FRP delaminating, debonding, rupture and internal shear failures [10, 61, 78, 139, 170, 202]. Some experimental tests highlighted the importance of adequate FRP anchorage to effectively strengthen the beam-column joints [51, 77, 79]. The delaminating and lateral bulging (buckling) of the FRP jacket, limited by the maximum strain sustained in the FRP composites, are also other technical complexities that needed to be considered [10, 79].

a) b) c)

Figure 3.12: a) Implementation of Glass-FRP retrofit for columns and beam-column joints in SPEAR building [43]; b-c) Improved strength and ductility capacities of FRP-retrofitted exterior joints [140].

Furthermore, some research indicated that the failure mechanism of the beam-column joints can be adversely affected if FRP retrofit was applied indiscriminately without considering the actual hierarchy of strength (e.g.[139, 149]), as discussed in the previous paragraph. As a controversial but possible outcome, a structures with joints indiscriminatingly wrapped with FRP could collapse due to the development of a soft-storey mechanism which was unlikely to occur in the as-built (thus prior to the retrofit) configuration. In some scenarios, the use of external FRP for confinement of plastic hinges can lead to lower global system ductility and displacement capacities despite an increase in overall flexural strength [23].

Recent developments in the seismic retrofit of beam-column joints with composite-materials include advanced analytical models for FRP-strengthened joint [9, 20], inclusion of 3D bi-directional excitations [6, 59], the use of cement-based composite with tensile fabric [70] and large-scale testing of FRP retrofitted non-ductile frames and beam-column joints (e.g. [42, 43, 119, 139]). In the three-storey non-ductile RC frames with FRP retrofitted beam-column joints by Pampanin *et al.* [139], improved global strength and displacement capacities were observed. Di Ludovico *et al.* [42, 43] tested glass-FRP retrofit on the 3-storey torsionally-critical non-ductile RC frames as shown Figure 3.12a. Enhancement in global seismic behaviour and local plastic rotation were observed and brittle failures in the joint were prevented.

More recently, comparative experimental studies of three (post-earthquake) retrofit strategies and techniques on ¼ scaled pre-1970s RC frames were carried out by Dolce *et al.* [44, 45, 48, 49], including a repaired and FRP-retrofitted solution. The three retrofitted frames are shown in Figure 3.13. Model 1 represents a local beam-column joint retrofit strategy using FRP jacketing technique, Model 2 represents a global seismic isolation retrofit technique using base

isolators and Model 3 represents a global strengthening strategy using prestressed steel brackets (DIS-CAM) technique.

Figure 3.13: Different retrofit strategies and techniques for non-ductile RC frames: a) Model 1: Local strengthening using FRP jacketing; b) Model 2: Base isolation retrofit; c) Model 3: prestressed steel bracket confinement and strengthening solution [45].

3.2.3.4 Added steel elements/devices – plate, bolt and haunch

Some of the early local retrofit techniques for beam-column joints involved the use of added steel elements, which were anchored onto the existing concrete using grouted bolts or clamped steel plates. However, some solutions improved the strength without significantly improving the deformation capacity or altering the damage pattern. An example of relatively unsuccessful added-steel plate retrofit technique was tested by Beres *et al.* [16], as shown in Figure 3.14. While the retrofit scheme was successful in preventing the lap-splice failure, it did not prevent the joint diagonal cracking and the brittle-nature of the force-displacement response. Joint cracks widen significantly in later stages of the test with rapid strength degradation observed after the peak strength (see Figure 3.14b).

Ghobarah and El-Amoury [77] tested several retrofit techniques for the anchorage of beam bottom longitudinal reinforcements using bolted steel plates (as per Beres *et al.* solution) and FRP jacketing solutions, with limited success in preventing brittle shear failure modes of the joints and beams. Masi *et al.* [119] tested a retrofit solution in which the 180° hook beam anchorage in the joint were restored using welded bars attached to external steel plates. FRP wrap was also applied in the columns. The anchorage restoration increased beam-column joint subassemblies capacity by 300% when compared to the as-built specimen.

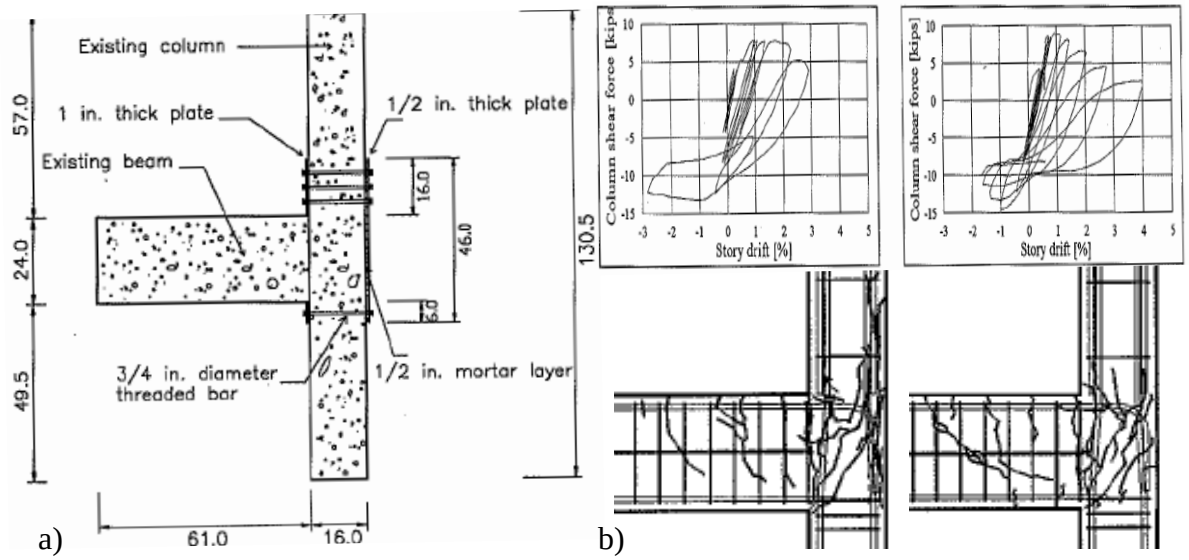

Figure 3.14: Confining steel plates retrofit as tested by Beres *et al.* [16]: a) retrofit details; b) force-displacement and damage pattern of as-built (left) and retrofitted (right) beam-column joint.

A diagonal haunch retrofit solution, first proposed for the retrofit of steel moment-resisting frame welded joints [64, 211], was extended for the retrofit of non-ductile pre-1970s RC beam-column joints [71, 142, 143]. As shown in Figure 3.15a, added steel haunches consisting of simple tubes or metallic elements could change the load path of the shear force transfer and keep the joint panel region undamaged. Stable beam hinging hysteresis behaviour was obtained (Figure 3.15b). More recently, retrofit technique using cast-in-situ concrete haunches was tested in which weak-beam strong-column retrofit outcome was achieved [28].

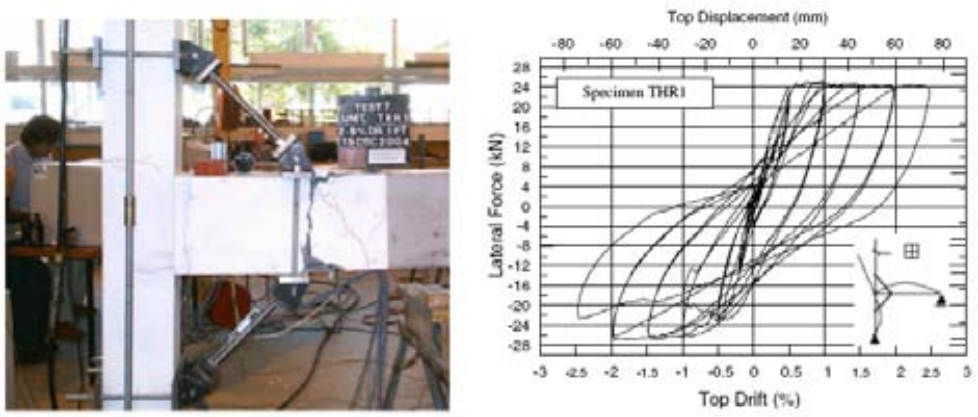

Figure 3.15: Steel haunch retrofit for exterior beam-column joints [143].

3.2.3.5 Joint prestressing and external post-tensioning for seismic retrofit

External prestressing using post-tensioning technology for the strengthening of RC and masonry structures is widely used (e.g. [1, 3, 53, 91]). In particular, external post-tensioning retrofit is used to upgrade ultimate and serviceability strengths for increased gravity loading, deficient circular/liquid retaining structures (e.g. domes and water tanks), corrosion deteriorated structures and historical structures. Figure 3.16a and b show an example of concrete-encased post-tensioned retrofit for the gravity-strengthening of a parking structure in San Francisco [1]. Considerations for external post-tensioning retrofit solutions include: a) the anchorage bearing region, b) transfer of post-tensioning force and the structure, and c) durability and fire protection [91]. Some limitations of external post-tensioning retrofit include the required access for post-tensioning jack and specialist requirement for prestressing installation.

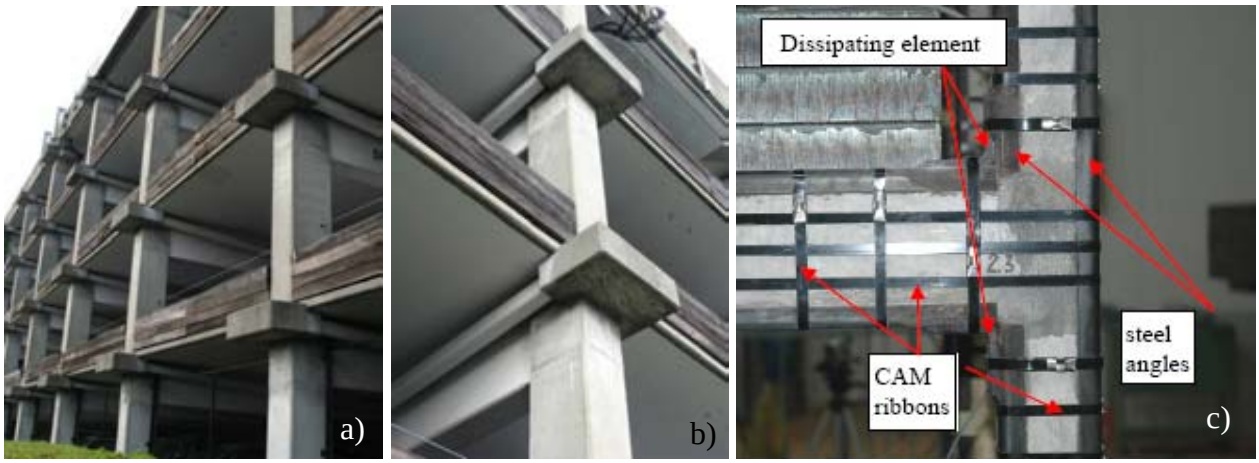

Figure 3.16: External post-tensioning retrofit solutions for RC frames: a-b) Gravity-load strengthening of parking structure (described in ref. [1]); c) DIS-CAM prestressed beam-column joint retrofit [49].

For seismic retrofit of RC structures, several external post-tensioning techniques have been proposed. External prestressing to increasing confinement for RC columns was shown to improve their shear and ductility capacities (e.g. [109, 174]). An innovative example of a prestressed confinement solution called the DIS-CAM system was tested for the retrofit of RC frames [45, 49] (Figure 3.13c and Figure 3.16c). Additional confinement was provided with prestressed steel ribbons and additional energy dissipation was achieved using mild-steel angles with weakened slot yielding in flexural. Several external post-tensioning retrofit techniques have been proposed for global strengthening of RC frames including addition of unbonded post-tensioned braces [90, 157, 196], diagonal prestressing tendons up the building [122, 179] and unbonded post-tensioned boundary infill wall elements [69]. More recently, the addition of post-tensioned rocking external structural walls (either made of precast concrete or laminated timber) have been proposed and tested for the seismic retrofit of non-ductile RC frames [117, 118, 207].

Horizontally prestressed joints have been experimentally and analytically investigated for the seismic retrofit of pre-1970s multi-bent bridges [93, 94, 114, 167, 188]. Primarily, the addition of horizontal axial force would reduce the joint principle tensile stress, p'_t, demand and increase the lateral capacity before joint diagonal cracking. In addition, external post-tensioning anchorage would provide confinement to the joint core and would reduce/delay joint crack widening, concrete wedge spalling and joint shear strength degradation. Added joint prestressing would also increase the width of the joint diagonal compression strut, thus improving the anchorage behaviour of the column longitudinal reinforcements.

Ingham *et al.* [92-94] used unbonded post-tensioned high-strength bars with a cast-in-place concrete anchorage for the knee joint retrofit (see Figure 3.17a). High prestressing force (nominal joint compressive stress, σ_{jh}=7.22MPa) was required to force the column hinging within a knee joint subassembly as part of the retrofit design. However, this resulted in premature compressive crushing and spalling of the concrete in the joint core, and ultimately the loss of lateral load capacity at structural ductility, μ = 1.5-2.0. It was suggested that the principal compression stress, p'_c, should be limited to $0.25f'_c$ (where f'_c is the most probable concrete compressive strength) to prevent the joint compressive failure. As a whole, an improved seismic behaviour was observed with column hinging activated prior to $\mu = 1.5$.

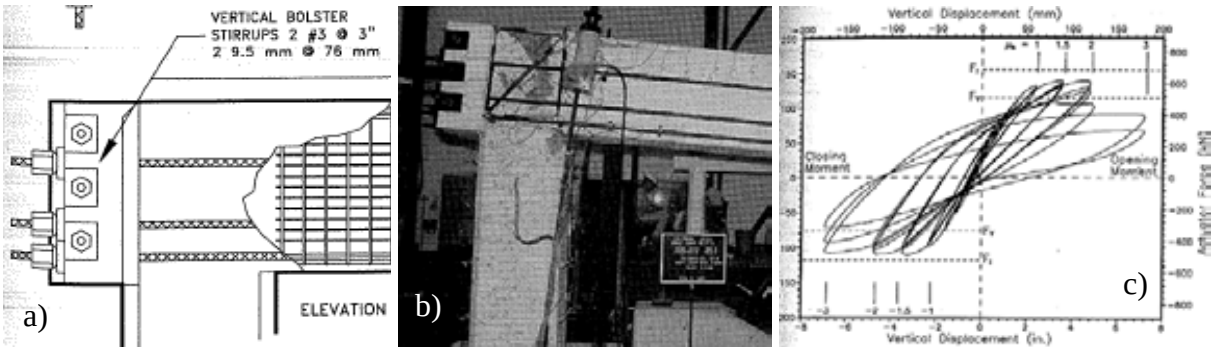

Figure 3.17: Prestressed bridge knee joint bridge joint [93]: a) Structural detail of the knee external post-tensioning; b) Joint compression crushing at structural ductility level 2; c) force-displacement hysteresis.

Following that, Lowes and Moehle [114] tested a post-tensioned joint retrofit solution where RC-encased and bonded post-tensioned tendons were added on both sides of the as-built beams and joints. RC bolsters were added to increase the joint area and to reduce the joint compressive stress. Compared to Ingham *et al.*'s test [92-94], slightly lower post-tensioning force with σ_{jh} of 2.3MPa, was applied to achieve strong cap-beam weak column response. The maximum joint shear (v_{jh}) and p'_t stresses measured were 0.40 $\sqrt{f'_c}$ (MPa) and 0.25 $\sqrt{f'_c}$ (MPa) respectively. Good ductile column flexural behaviour without joint damage was attained. The final failure mode was concrete crushing and buckling of column longitudinal reinforcement adjacent to the joint panel.

Using a strut-and-tie analysis and principal stresses limits, Sritharan *et al.* [187, 188] have demonstrated that cap beam and joint prestressing in T-bridge bent could reduce the joint shear reinforcements when compared to well-designed non-prestressed joint solutions. The idealised joint force equilibrium and the external force-transfer model proposed by Sritharan *et al.* [185, 186] is given in Figure 3.18. Two full-scale multi-column bridge bents were tested to validate the design procedure and the prestressed joint solution for new bridge construction [189].

However, the use of joint horizontal post-tensioning for seismic retrofit of RC frames is a relatively unexplored area. The use of partially and full-bonded prestressed beam-column joint for seismic resistance have been tested at the University of Canterbury [19, 150, 151, 199]. These tests form the basis of the provision 15.4.4.2 in NZS3101 [132] which allows for the reduction of horizontal joint shear reinforcement by:

$$\Delta A_{jh} = \frac{0.7F_{ps-l}}{f_{yh}} \qquad \textbf{3.1}$$

where $F_{ps\text{-}l}$ is the force after all losses in the prestressing steel that is located within the central third of the beam depth and f_{yh} is the yield strength of the horizontal joint shear reinforcement.

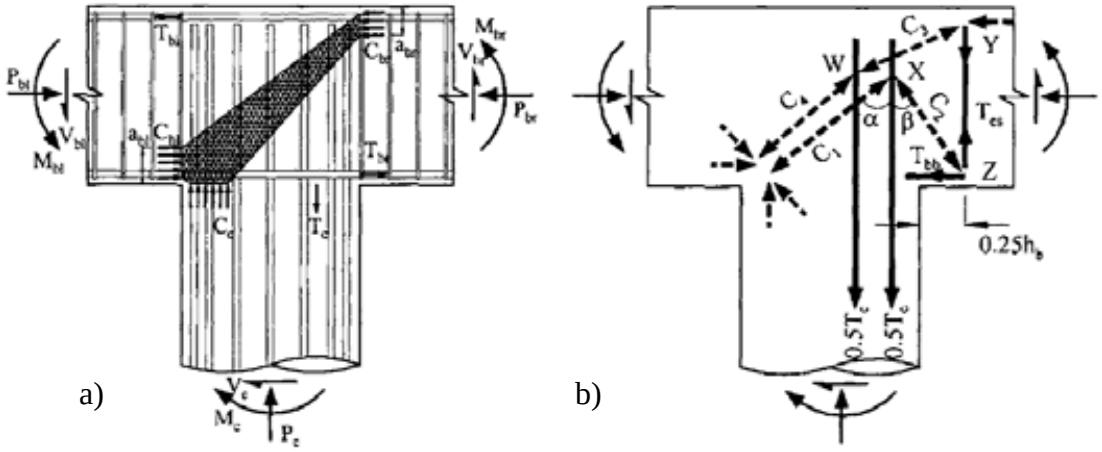

Figure 3.18: Strut-and-tie analysis for prestressed T-bridge joint : a) Idealised joint compression strut and b) external strut force transfer model [185].

Nishiyama *et al.* [127, 212] tested seven bonded prestressed exterior beam-column joint subassemblages based on the NZS3101 provision, investigating the influence of location of tendon anchorage, prestressing force level and concrete compressive strength on the joint shear strength capacity. All specimens failed in joint shear and anchorage deterioration of the post-tensioning system, as shown in Figure 3.19. It was found that joint shear cracking was not prevented in the test units with anchorage inside the joint (KPC1-2, KPC2-2, KPC2-3 and KPC3) as full prestressing force was not transferred into the joint. For specimens with anchorage outside the joint (KPC1-1 and KPC2-1), some level of shear strength improvement was attained. NZS3101 [132] and AIJ guidelines [4] overestimated the joint shear strength of all the specimens.

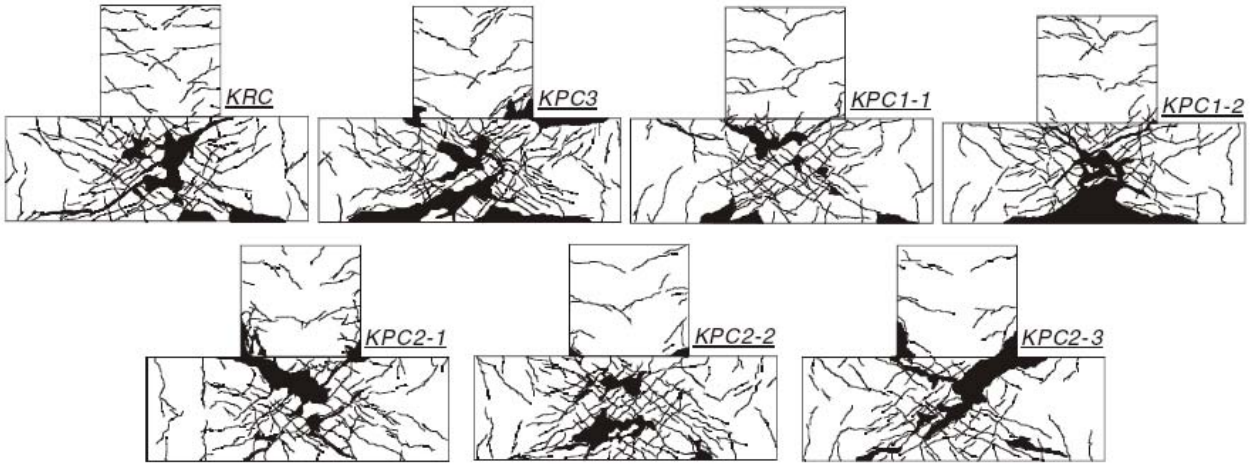

Figure 3.19: Damage pattern of prestressed exterior beam-column joint [212].

From cyclic loading test on eight prestressed and two non-prestressed concrete exterior beam-column joints, Hamahara *et al.* [82] concluded that prestressing force plays no significant part in the ultimate shear strength of beam-column joint cores. However, for two of the three exterior joints with prestressing anchorage system outside the joint core (B-PC2 VSL anchorage), the predicted nominal joint shear strengths were attained. Thus, Hamahara *et al.* and Nishiyama *et al.* both concluded that the joint prestressing forces must be anchored sufficiently outside the joint in order for full force-transfer into the joint.

The use of unbonded post-tensioning for jointed ductile ('hybrid') rocking moment-resisting connections for precast concrete (as well as steel and timber) has been growing significantly in the past two decades after the completion of the PREcast-Seismic-Structural-Systems (PRESSS) programme (e.g. [102, 131, 146, 169]). A large-scale PRESSS frames and walls building was tested at the end of the PRESSS research programme (Figure 3.20). The PRESSS programme investigated a series of solutions for precast concrete connections, including a rocking joint solution, where unbonded post-tensioning tendon through the precast concrete section provides self-centering and moment capacities to the beam-column joint. Such jointed ductile ('hybrid') rocking moment-resisting connections are capable of attaining AP objectives (§3.1.2.3) with minimal residual deformation and structural damage even after a large seismic event. The idea of rocking beam-column joint connections can also be extended to the seismic retrofit of non-ductile RC frames, under a full SW retrofit strategy [137].

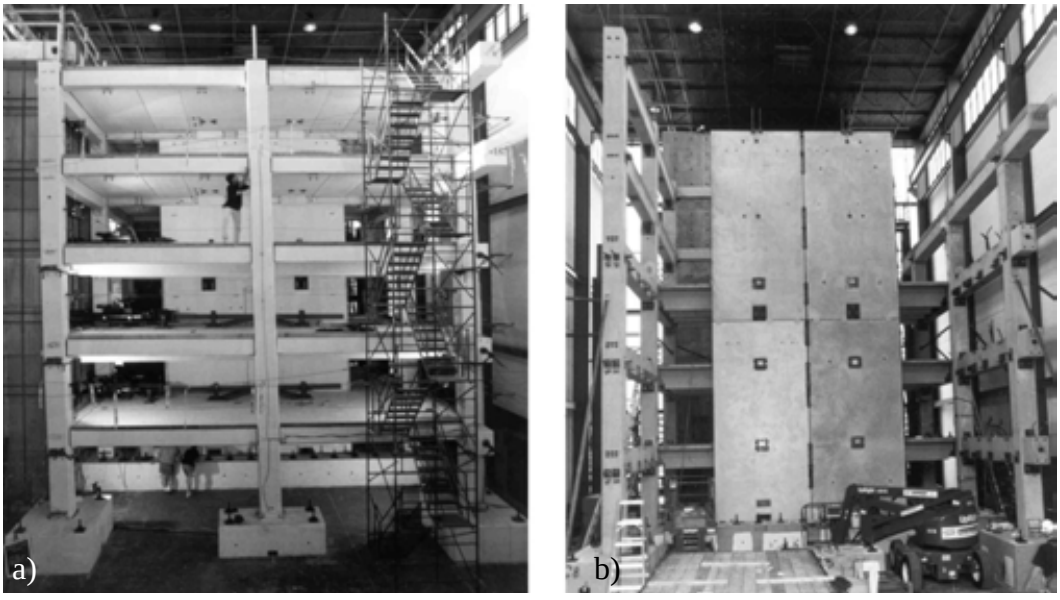

Figure 3.20: Five storey post-tensioned precast concrete building tested during the PRESSS programme [169]: a) Post-tensioned hybrid frame; b) post-tensioned coupled walls.

3.3 THE CONCEPT OF SELECTIVE WEAKENING FOR RETROFIT

3.3.1 Weakening for strengthening and retrofit

The retrofit strategies described in the previous section are predominantly focussed on increasing the strength, stiffness and/or ductility capacities through the use of various global and local retrofit techniques, as illustrated in Figure 3.6a and b. Alternative retrofit strategies to reduce the seismic demands by means of supplementary damping and/or use of base isolation systems are also shown to be effective. Instead of focussing on strengthening and by recognising the inherent strength in some of these pre-1970s RC frames, a counter intuitive "Selective Weakening (SW) for strengthening" retrofit strategy is conceived as an alternative performance-based seismic retrofit solution [137].

The Selective Weakening (SW) retrofit strategy fundamentally aims at improving the global response of the RC structure by: a) decreasing seismic demand onto brittle elements and overall structure and sub-structure via selective weakening of structural elements; and b) increasing deformation capacity of the global structure by changing both the local and global inelastic mechanisms. The required PLs of structural and non-structural elements can be designed for and achieved by combining the selective weakening of structural elements and the subsequent targeted upgrade using existing local retrofit techniques (e.g. external post-tensioning and composite jacketing). Figure 3.21 illustrates the SW retrofit concept within the ADRS domain.

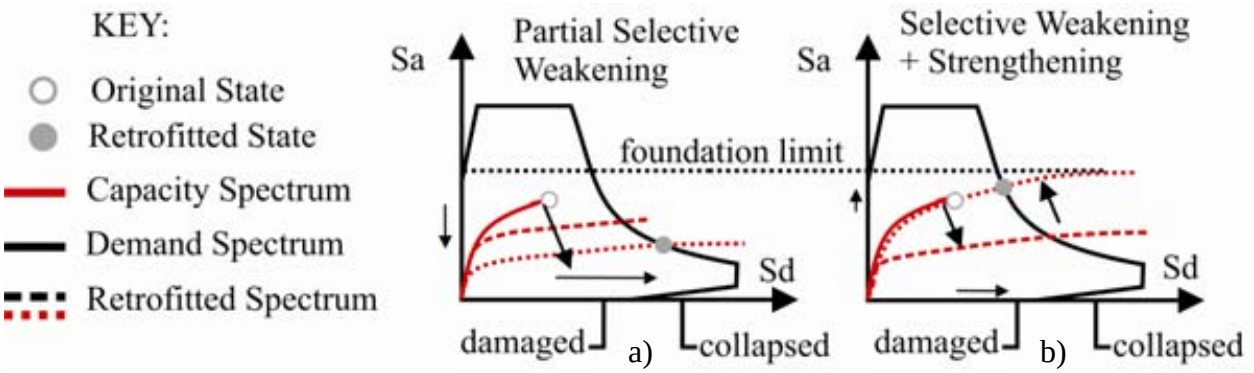

Figure 3.21: Acceleration-Displacement Response Spectrum (ADRS) illustration of Selective Weakening (SW) retrofit philosophy and strategies: a) Partial SW and b) Full SW (weakening and further enhancement).

In the *Partial SW* retrofit, selective weakening-only intervention of structural elements reduces the lateral strength and stiffness and, therefore decreases the seismic force demand, as shown in Figure 3.21a. While the reduced lateral strength will result in a higher deformation demand, the modified inelastic behaviour from a brittle to a ductile mechanism will concurrently

increase the deformation capacity of the structure (as illustrated by the longer push-over capacity spectrum). Thus, the retrofit design is limited by displacement demand-capacity and performance objectives (deformation based) – rather than by strength and force limitations.

If a higher performance level is desired, further strengthening using the local retrofit techniques discussed in §3.2 can restore/improve the lateral strength while still respecting the capacity limits of other brittle/critical connection elements such as columns and foundations. Two retrofit techniques – external post-tensioning and external composite material jacketing – are suitable for the final enhancement because of their versatility and ease of implementation. The combination of selective-weakening and post-tensioning retrofit of the beam-column joints is herein called the *Full SW* retrofit. While the full SW retrofit illustrated in Figure 3.21b seems similar to the ductility-only enhancement shown in Figure 3.6b, the Full SW retrofit would have better control of the post-retrofitted strength and clearer understanding of the ductile inelastic mechanism of the retrofitted structure.

In the following sub-section, some past researches on SW retrofit strategy will be briefly discussed. Some recent implementations of the SW retrofit strategy, including the reduced beam section of steel welded joints, vertical/horizontal separations of shear-deficient walls and isolation of shear-critical precast floor systems, will also be briefly summarised. In a broader scheme, the detachment of masonry infills to prevent frame-infill interaction or the building separation to prevent torsion or stiffness/strength irregularity can also be considered as SW retrofit techniques.

3.3.2 Past research on Selective Weakening retrofit

3.3.2.1 Weakening for strengthening of structures

The SW approach is gaining acceptance within various international seismic retrofit guidelines. In the 2003 fib seismic retrofit guidelines [67], SW retrofit strategy is considered as part of the "increasing deformation capacity" approach, in which the strength of some desired mode of failure (e.g. beam flexural hinging) can be lowered such that the desired mode of failure becomes the weakest link of the system. Example given includes the separation of spandrel beams/walls from captive short columns.

In the 1997 NERHP guidelines (FEMA-273/274) [63] and in the subsequent FEMA-356 pre-standard [65] and the ASCE-41 standard [11], "local modification of components" is given as a seismic rehabilitation method. In the ASCE-41, joint post-tensioning and selective material

removal are considered as rehabilitation measures for non-ductile RC frames. Preliminary suggestions for 'selective material removal' include a) separation of non-structural elements (e.g. infill walls) from the frame, b) weakening of beams to promote strong-column weak-beam system, and c) segmenting structural walls to change their stiffness and strength. The NZSEE seismic evaluation guidelines [133] have adopted similar wordings as per FEMA-356 [65] in its guidelines for "improvement of the structural performance", which include a mention of deliberate weakening of structural elements to remove structural irregularities. Nevertheless, these recommendations are provided in general and qualitative terms. There is no experimental or numerical research data available in literature to validate these rehabilitation measures, in particular with respect to the SW retrofit of non-ductile RC beam-column joints.

In developing retrofit solutions for acute care facilities (e.g. hospitals) with expensive non-structural elements that are acceleration-sensitive, an intentional strength reduction combined with added damping retrofit solution has been proposed by Viti *et al.* [205, 206]. The SW strategy is useful in reducing the floor acceleration demand as weakening of the structure would lengthen the building period and reduce seismic forces thus reducing floor acceleration entering the building. Via numerical fragility analysis of a prototype hospital structure, it was shown that a retrofit intervention based on weakening and dampening was better in limiting drift and acceleration sensitive damages when compared to the as-built steel frame and strengthening-only solution. Figure 3.22 shows the fragility curves generated by Viti *et al.* [205, 206] for different retrofit solutions. For instance, the "weakening and damping" frame was 2.5 times less probable to incur moderate damage for drift or acceleration sensitive non-structural components given a 500-year return period earthquake, when compared to the as-built steel frame and infill panel frames.

Based on control theory algorithm, Cimellaro *et al.* [33, 34] have developed design solutions for the distribution and placement of dampers and weakening (stiffness reduction) based on the linear-structure assumption. The procedure was then extended to an iterative optimisation procedure for inelastic structures [32]. While these studies may be useful in indicating the global dynamic behaviour of weakened and dampened structures, they are unrealistic for seismic retrofit in which the as-built pre-1970s structures generally have critical non-ductile weakness and brittle inelastic mechanism.

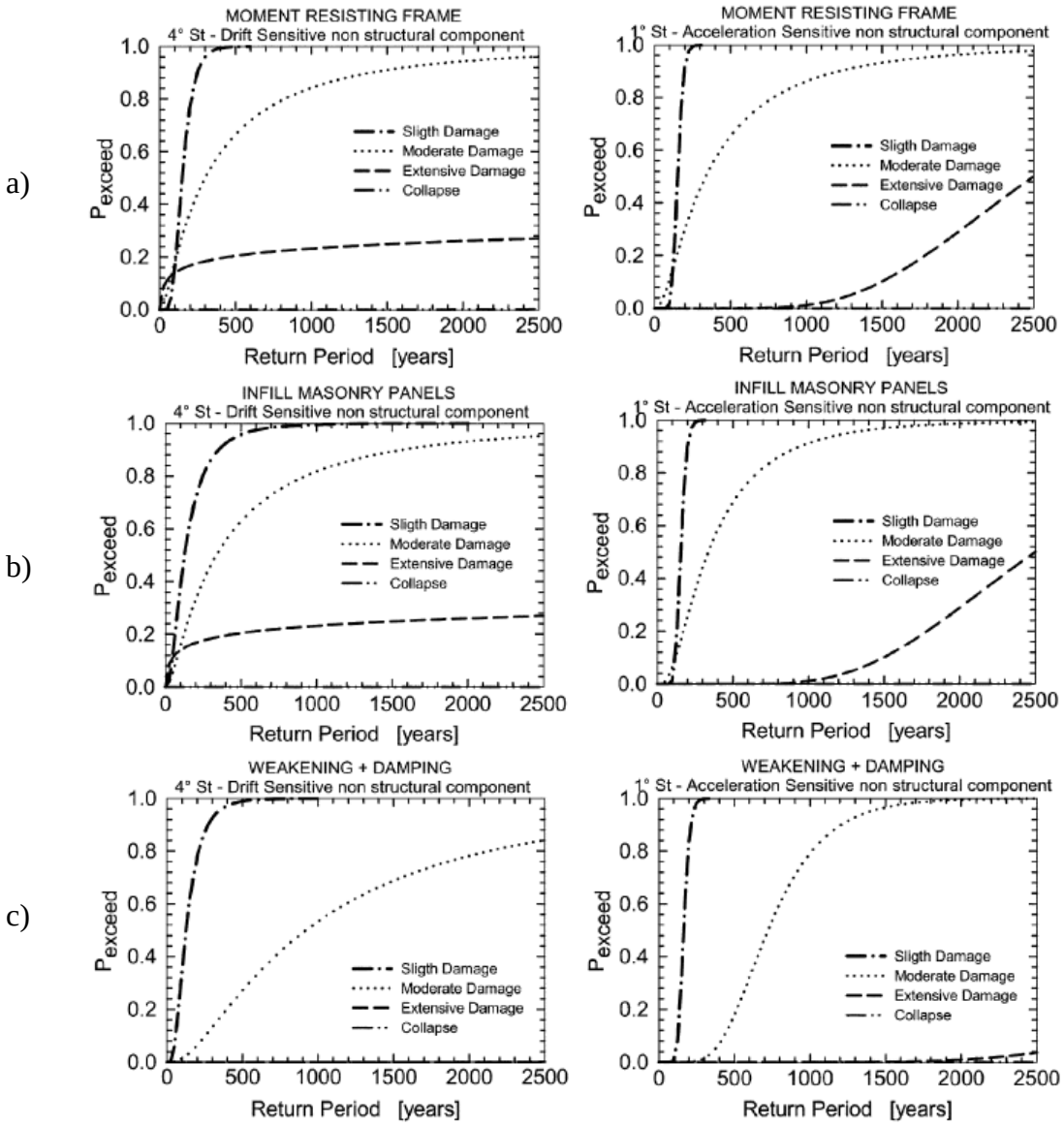

Figure 3.22: Fragility curves for drift and acceleration sensitive non-structural components: a) as-built steel moment resisting frames; b) strengthening retrofit; c) weakening-damping retrofit [205].

The concept of SW to achieve fused plastic hinges has also been investigated experimentally for bridge piers [50]. By cutting the column longitudinal reinforcements and replacing them with machined-down threaded bars, a structural fuse section can be designed at the base of the bridge pier. In a recent study, Roh *et al.* [173] investigated the use of rocking columns (through weakening) for the seismic retrofit of RC frames. It was shown that global strength reduction depended on the number of weakened rocking columns and the arrangement of those columns. However, the use of rocking column retrofit could be detrimental due to the risk of soft-storey and P-delta failures of the building.

In the course of this research, Zhang and Hu [213] have adopted the proposed SW retrofit concepts, which was presented in the 14th World Conference on Earthquake Engineering by the author [101], and explored numerically the seismic performance of a self-centering SW seismic retrofit solution for RC frame structures. It was found that a flag-shape hysteresis SW retrofitted frame performed as good as a bi-linear hysteresis buckling-restrained braced retrofitted frame in terms of peak displacement and energy dissipation demand ratio while having negligible residual displacement after an earthquake.

3.3.2.2 Retrofit of steel welded moment-resisting joints using beam-weakening

Interestingly, a similar SW retrofit strategy has been proposed for the retrofit of pre-Northridge steel welded moment-resisting frame (MRF) joints [64, 81]. In order to prevent the brittle steel weld failures in the MRF joints, a weakened flexural section is created through reducing the flange in the beam close to the column, as shown in Figure 3.23a. The reduced beam section (RBS) retrofit, was first proposed as a patented 'dogbone' connection for new seismic steel structures [97, 160]. During the post-Northridge SAC steel project, significant amount of research was carried out to validate the seismic performance of various retrofit solutions including the RBS retrofit [22, 35, 36, 58, 81, 203] and the steel haunch retrofit [64, 211].

An example of the force-displacement response of the RBS-retrofitted joint tested by Jones *et al.* [100], as shown in Figure 3.23b, demonstrated its excellent performance up to 3% inter-storey drift rotation. Composite floor slabs were shown to have detrimental effects and provided beneficial lateral stability support for the RBS-retrofitted joints[36, 100]. Final failure mode for RBS-retrofitted joint was mostly local instability/buckling of the beam web, followed by flange local buckling and lateral torsional buckling [203].

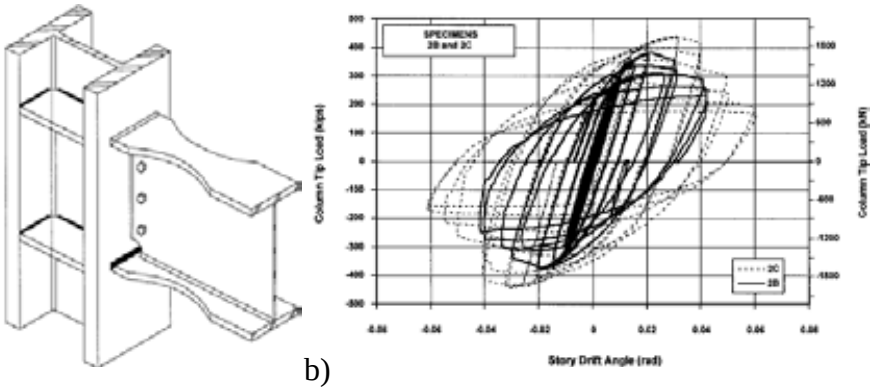

a) b)

Figure 3.23: Reduced beam section (RBS) retrofit technique for pre-Northridge steel welded moment resisting connections [100]: a) schematic sketch of the RBS connection; b) Force-displacement plot of RBS-retrofitted joint without (2B) and with composite floor slab (2C).

3.3.2.3 Selective Weakening retrofit of shear-deficient RC walls

For a shear-deficient wall, selective weakening through vertical and/or horizontal cuts reduces its strength and stiffness, which in turn reduces the spectral acceleration demand as the period elongates. The vertically cut wall also becomes more slender, in which flexural action dominates and shear-force demand decreases. This effectively changes the inelastic mechanism to a more ductile flexural hinging and therefore increases the global deformation capacity. The combined effect of lower spectral acceleration demand and higher displacement capacity is reflected in the ADRS plot for weakening-only solution shown in Figure 3.21a.

Ireland *et al.*[95, 96] have experimentally investigated the use of multi-level SW retrofit for shear-prone RC walls with poor reinforcement details (plain round bar with straight, $40d_b$ laps and minimal transverse reinforcement). Figure 3.24a shows a typical brittle shear-dominated force-displacement hysteresis curve. Figure 3.24b illustrates the two partial SW retrofit solutions considered: a) vertical segmentation to achieve weakened by flexural-dominated uncoupled walls and b) horizontal saw-cut to achieve a rocking wall solution with minimal damping and lower strength. Figure 3.24c shows the second phase of full SW retrofit which includes additional upgrading in the form of added post-tensioning with energy dissipation devices. These resulted in controlled rocking flag-shape hysteresis behaviour, similar to the hybrid self-centering seismic resisting connection (e.g. [31, 136, 169]).

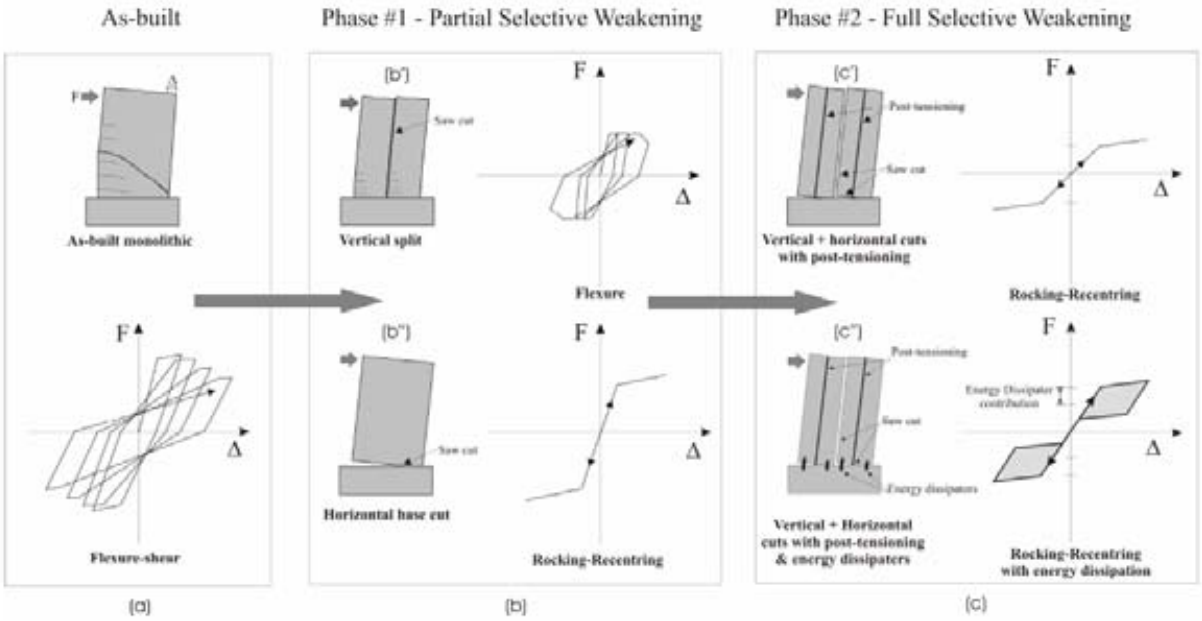

Figure 3.24: Selective Weakening (SW) retrofit shear-deficient structural wall –idealised hysteresis response before and after the retrofit interventions: a) as-built wall; b) partial SW; c) full SW retrofit [95].

a)

b)

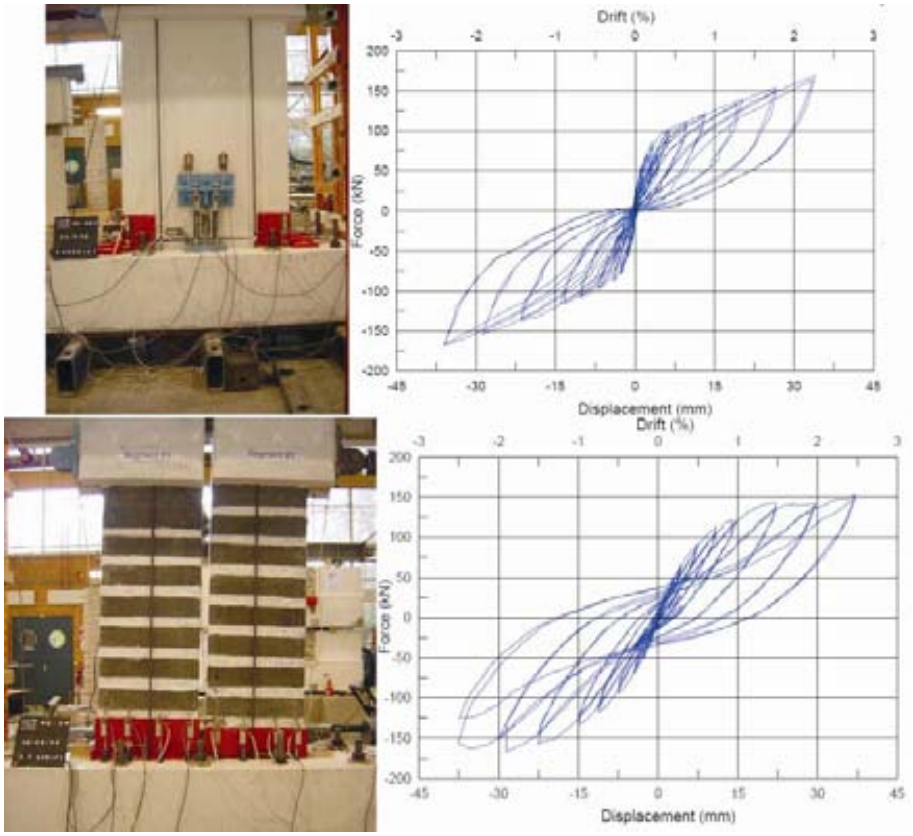

Figure 3.25: Selective Weakening retrofit shear-deficient structural wall – state of specimen at end of 2.5% drift cycles and force-displacement hysteresis curves: a) W1R specimen and b) W2R specimen [95].

Cyclic, quasi-static tests on four specimens were carried out: two benchmark walls with substandard detailing (W1 & W2), and two SW retrofit walls (W1R & W2R) [95, 96]. W1R specimen incorporates a SW at the base and the subsequent addition of post-tensioned tendons and energy dissipaters. W2R incorporates a SW with a vertical cut and subsequent confinement upgrade using FRP. For both retrofit solutions, shear-failure was averted while a ductile flexural mechanism based on rocking and dissipative motion at the base connection was activated. Figure 3.25 shows the final undamaged specimen after 2.5% drift cycles and the stable hysteresis curves for both W1R and W2R specimens.

3.3.2.4 Selective Weakening retrofit for RC flooring system

The concept of SW retrofit has also been implemented for the retrofit of precast RC hollowcore floors [98, 99]. Observed hollowcore floor units collapse during earthquakes (e.g. Northridge, 1994) and experimental investigations of precast hollowcore floors (e.g. [120]) have highlighted the vulnerability of such flooring systems in the event of strong earthquakes. Recognising that the rigidity of the monolithic seating connection could lead to undesirable and catastrophic brittle

shear-delaminating and web-splitting (as observed in HC1 in Figure 3.26) failure modes, the proposed retrofit solution [98, 99] involved drilling holes to create a weakened plane at the seating connection (as in HC4 in Figure 3.26). This effectively isolated in a controlled manner the hollowcore unit from the seating beam and reduced the flexural strength at the seating section. As seen in Figure 3.26, the selectively weakened HC4 performed well without any shear or premature unseating failures.

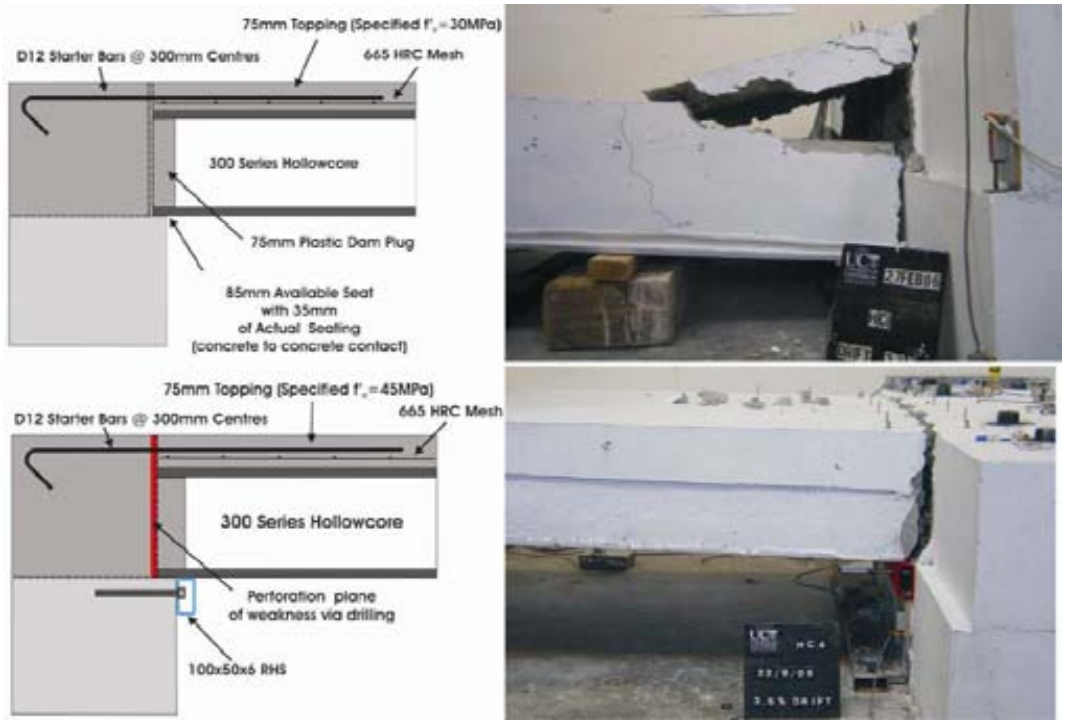

Figure 3.26: Structural detail and experimental photograph of (top): Specimen HC1 (pre-2004 New Zealand worst case representation); (bottom): Specimen HC2 (selective weakened via drilling and added seating) [99].

3.3.3 Proposed Selective Weakening retrofit for RC frames and beam-column joints

In this contribution, the extension of SW retrofit for non-ductile RC frames, in particular for the exterior beam-column joints, is proposed and developed. Principally, the SW retrofit is a capacity design-based prioritising of strengths, in which inelastic failure mode and deformations can be localised and designed to be at the weakest 'ductile' link based on the hierarchy of strength of the joint. Therefore, considering most modes of localised deformations are undesirable, the SW retrofit therefore aims to achieve beam flexural hinging by forcing the weakest link to be the beams flexural capacity with some dependable ductility. Three phases or techniques of SW retrofit for exterior beam-column joints are considered:

3.3.3.1 Beam-Weakening-only

As with the steel RBS-retrofit (§3.3.2.2) and partial SW wall retrofit (§3.3.2.3), the first phase of SW retrofit of exterior-beam column joints involves the weakening and softening of the exterior beam framing into column by saw-cutting the longitudinal reinforcements of the beams. This first phase of SW retrofit aims to change the inelastic mechanism by creating a weak-link in the form of a beam flexural hinge within the hierarchy of strength of the beam-column joints. As the weakened beam section would induce less internal force demand on both the joint and also the columns, brittle failure of the joint and column is less likely and deformation capacity of the beam-column joint subassembly is increased. Globally, the softening of the RC frames and the change of inelastic mechanism (to flexural hinging with substantially more energy dissipation), the overall seismic demand on the frame is also reduced. Conceptually, this is consistent with the ADRS response shift as shown in Figure 3.21a.

Typically, both column flexural and shear, and joint shear capacities increase in proportion to additional column axial forces. Given the effect of variation of axial load on the hierarchy of strength of a beam-column joint (see §2.4), where column and joint are stronger with increasing column axial load, it is expected that the weakening of the positive flexural strength (tension capacity of the beam soffit) alone is sufficient to induce weak-beam strong-column mechanism. Beam-weakening can be practically achieved by saw-cutting of the bottom longitudinal bars, which are generally more accessible within an existing building, using portable concrete cutter or plate-grinder. The constructability and practical issues of beam-weakening will be further explored and discussed in Chapter 4.

It has also been observed in past experimental tests of beam-column joints with shallow beams (e.g. [87, 112, 209]) where higher joint shear stress capacities were measured in joints with low beam-to-column depths ratio (i.e. the joint aspect ratio, $h_b/h_c < 2$). It was postulated that the elongated joint cores [155] and the lower shear span-to-depth ratio [86, 209] in joints with shallow beams would generate higher joint shear capacity due to the increase contributions from the column vertical reinforcements. Similarly, in a beam-weakening retrofit solution, the beam depth may be reduced by the saw-cutting of the longitudinal reinforcement, which in turn decreases the h_b/h_c ratio and increases joint shear capacity. §3.4.4 will further describe the quantitative effects of the selective beam-weakening on beam capacity, joint shear strength and the beam-column joint hierarchy of strength.

Considering a typical pre-1970s non-ductile RC frame as illustrated in Figure 3.27a, due to economical restraints particularly when dealing with a large number of buildings, the designer might decide to target a partial retrofit solution capable of guaranteeing collapse prevention (LRO or BSO) while accepting a significant level of damage. In such a scenario, a partial SW retrofit, where some (or all) bottom longitudinal rebar at the exterior beam-column joint can be severed, as shown in Figure 3.27b, is a more effective solution. The amount of weakening permissible is based on the required beam shear-capacity for gravity loading while full hinging under positive moment can be assumed for lateral loading.

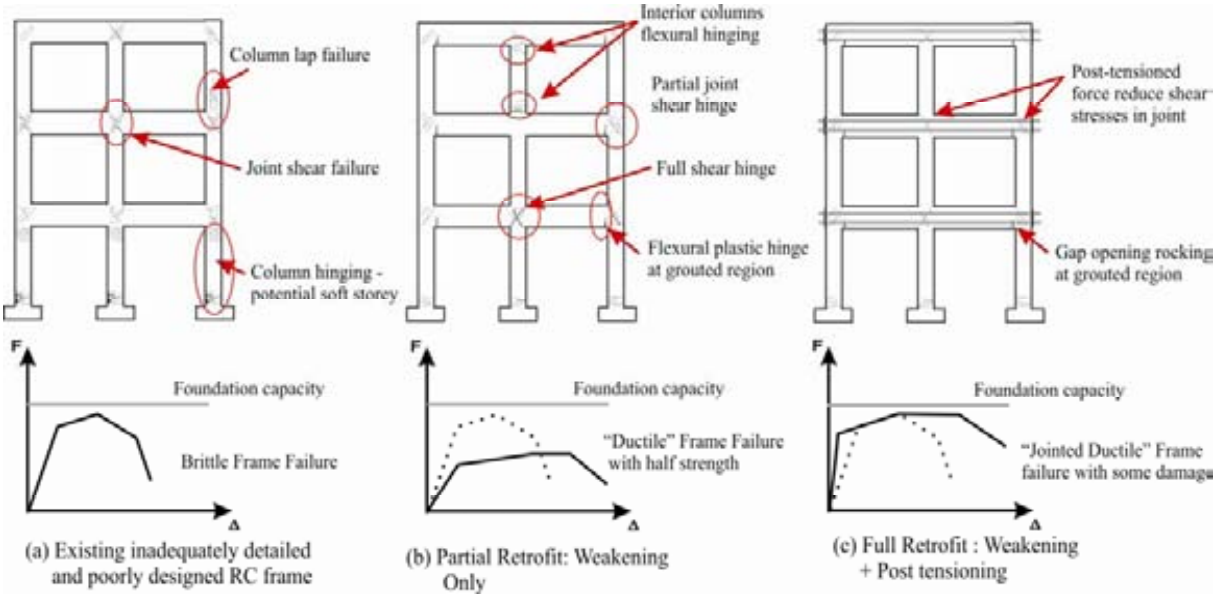

Figure 3.27: SW retrofit for RC frame – concept and expected force-displacement curves: a) existing RC frame b) partial SW retrofit: severing of bottom longitudinal beam bars; c) full SW retrofit: weakening of beam and post-tensioning joint.

The mixed inelastic mechanism, where only the exterior joints are retrofitted in non-ductile RC frames, is somehow similar to the double partial-flexural hinging as observed by El-Attar *et al*. [52]. Using analysis of gravity-dominated RC frames with pullout failures of discontinued bottom beam reinforcements, El-Attar *et al*. showed that BSO would be achieved provided the top reinforcements in the other end of the beam did not yield and no joint shear failure occurred. The lateral stiffness of the frame would be reduced but under a 'controlled' hinging action, a lower but ductile lateral force of the frame would be maintained. The lateral capacity of a pair of beam-column joint was the average negative flexural capacities of the beam at both ends of the span.

This is also similar to the recommendation for gravity-load-dominated RC frames by Paulay and Priestley [155]. Figure 3.28 represents a form of acceptable column-hinging mechanism for nominally ductile RC frames in the NZS3101 Standard [130, 132]. As long as the exterior columns in all levels are assured to remain elastic, plastic hinge development within the interior joints or columns, and exterior beam spans should spread over several or all storeys by moment-redistribution. Thus, in the SW retrofit strategy for RC frames, the exterior columns will be ensured to remain elastic via selective beam-weakening retrofit, while the interior columns will be allowed to hinge. For this type of mixed hinging mechanism, it is suggested that the structural ductility of the overall frame should be limited [155].

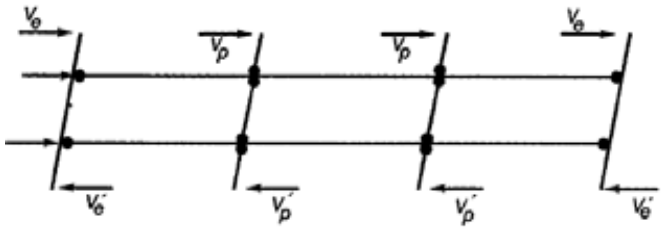

Figure 3.28: Admissible column hinging mechanism in RC frames as shown in the commentary of NZS3101:1995 [130].

3.3.3.2 Full Selective Weakening: Beam-weakening and post-tensioning solutions

The initial selective weakening of the beams and the frame as a whole might result in excessive drift and deformation demands. Therefore, in order to ensure that a higher target performance level is met, external post-tensioning and/or supplementary dissipation devices can be incorporated into a Full SW retrofit intervention. Further strengthening with external post-tensioning of the beam-column joints can improve the lateral strength capacity, while still respecting the capacities limits of other brittle/critical connection elements such as columns and foundations. By weakening first and then strengthening using post-tensioning technology, a controlled ductile 'pseudo-rocking' beam-column joint inelastic mechanism can be achieved. This is conceptually illustrated in Figure 3.21b and Figure 3.27c.

As discussed in §3.2.3.5, joint prestressing can add significant positive benefits to the unconfined concrete joint core, typical of the non-ductile beam-column joints. Joint post-tensioning would increase joint active confinement, reduce principal tensile stresses demand, mitigate joint cracking, increase joint shear capacity and reduce post-cracking strength degradation. §3.4.5 and §3.4.6 will describe the quantitative evaluation and design of beam-column joint post-tensioning retrofit.

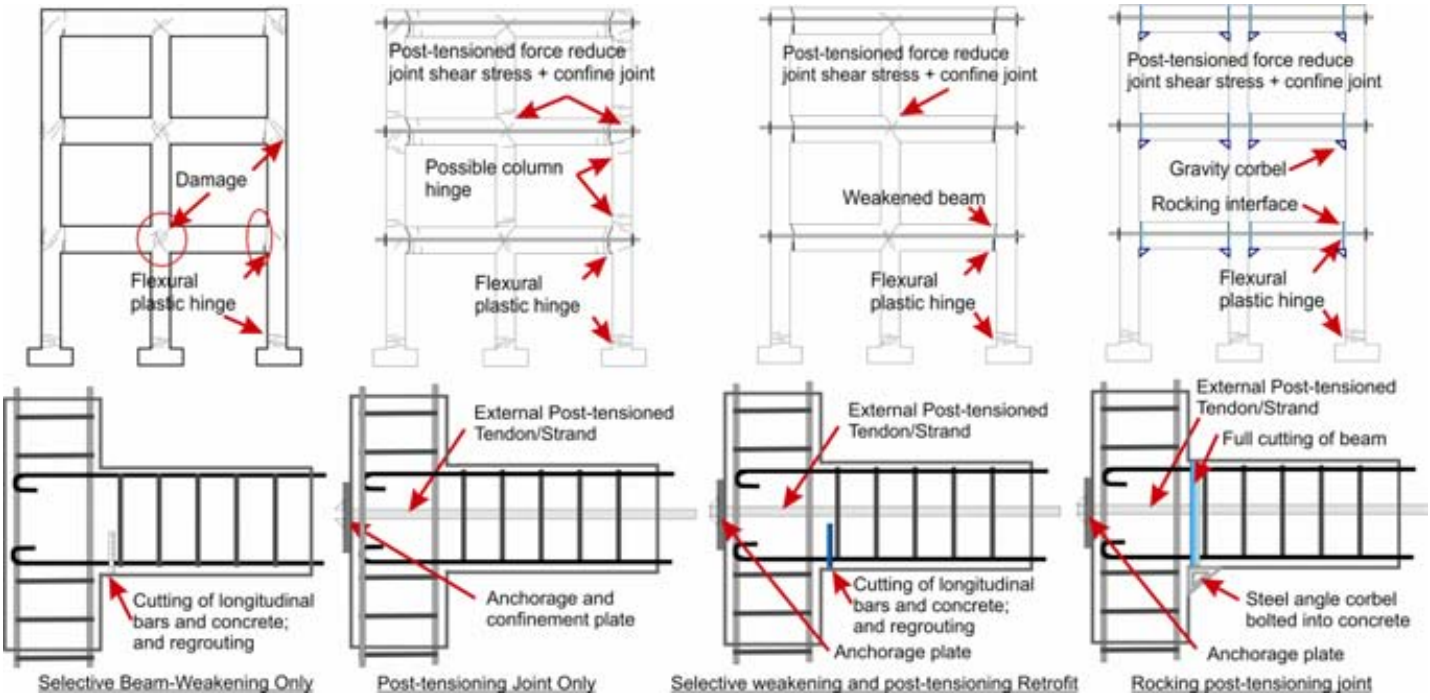

Figure 3.29: Various Selective Weakening retrofit techniques: a) Selective Beam-weakening-only; b) Joint post-tensioning-only; c) Selective beam-weakening and joint post-tensioning; d) Rocking post-tensioning joint.

It should be noted that joint post-tensioning-only retrofit is also a valid retrofit solution to strengthen the shear capacity of non-ductile beam-column joints, particularly for RC frames with reasonably strong columns (e.g. in the form of wide columns or column-walls). The latter condition is important because a post-tensioned beam-column joint connection could have high post-yield stiffness [166] that might result in the development of a strong-beam weak-column (soft storey) mechanism. Figure 3.29 gives the conceptual illustrations of the various SW retrofit techniques for RC frames: a) selective beam-weakening-only, b) joint post-tensioning-only, c) selective beam-weakening and joint post-tensioning and d) advanced controlled-rocking post-tensioning joint.

3.3.3.3 Advanced controlled-rocking joint retrofit

As per the selective-weakened and post-tensioned retrofit solution for shear-deficient walls mentioned in §3.3.2.3, a controlled rocking or hybrid rocking mechanism could also be achieved for a beam-column joint connection by fully detaching/cutting the beam from the column and adding horizontal post-tensioning, as illustrated in Figure 3.29d. Further enhancement of this rocking mechanism can be achieved using advanced energy dissipation devices (e.g. combination

hysteretic and viscous dampers in an advanced flag-shape system [102]). As per the hybrid rocking solutions for new construction and walls retrofit (e.g. [31, 131, 136, 169]), minimal structural damage can be expected in this type of connection (Figure 3.29d), in which the re-centering capacity from the post-tensioning forces will close, at the end of the seismic shaking, the rocking gap opening. As mentioned, the concept of rocking beam-column joints for seismic retrofit has been investigated using non-linear dynamics analyses [102, 213].

3.4 SELECTIVE WEAKENING RETROFIT DESIGN METHODOLOGY

3.4.1 General retrofit design philosophy

The basic retrofit design strategy is to control the hierarchy of strength of the beam-column joint to respect capacity design principles and to attain ductile flexural beam-hinging failure mode. At the local joint level, this is achieved by modifying the hierarchy of strength within the M-N (moment-axial force) performance domain of the joint. Given the hierarchy of strength of the as-built beam-column connection, depending on its typology, geometry, reinforcing details etc., SW retrofit techniques can be applied in order to modify the hierarchy of strength to achieve the targeted performance.

Figure 3.30 presents the design flowchart for the SW retrofit strategy of non-ductile RC frames. The design procedure shown herein only considers three SW retrofit techniques (selective beam-weakening, external joint post-tensioning and the combinations of both), while in reality, this design procedure can be used in conjunction with other retrofit techniques (e.g. composite jacketing of the columns). Some failure modes discussed in Chapter 2 (e.g. column shear or lap splice failures) will not be included within the retrofit design methodology to narrow the focus of the retrofit solution to the upgrading of the joint shear capacity.

The first step of the retrofit design procedure is to establish the *equivalent column moment*, M_c, versus column axial load, N_c, performance domain of the as-built beam-column joints following the same approach used for the seismic assessment (§2.4). Then, a quick retrofit design calculation, to be outlined in §3.4.3, can be used to estimate the required beam-weakening and/or joint post-tensioning to achieve the targeted and improved hierarchy of strength.

A global direct displacement-based retrofit design procedure is developed in order to derive the required local exterior beam-column joint capacity given the seismic retrofit performance objective, building typology and site seismicity. §3.4.2 will present this simplified

global retrofit design procedure and comment on the assumptions made and considerations required when implementing the SW retrofit for non-ductile RC frames.

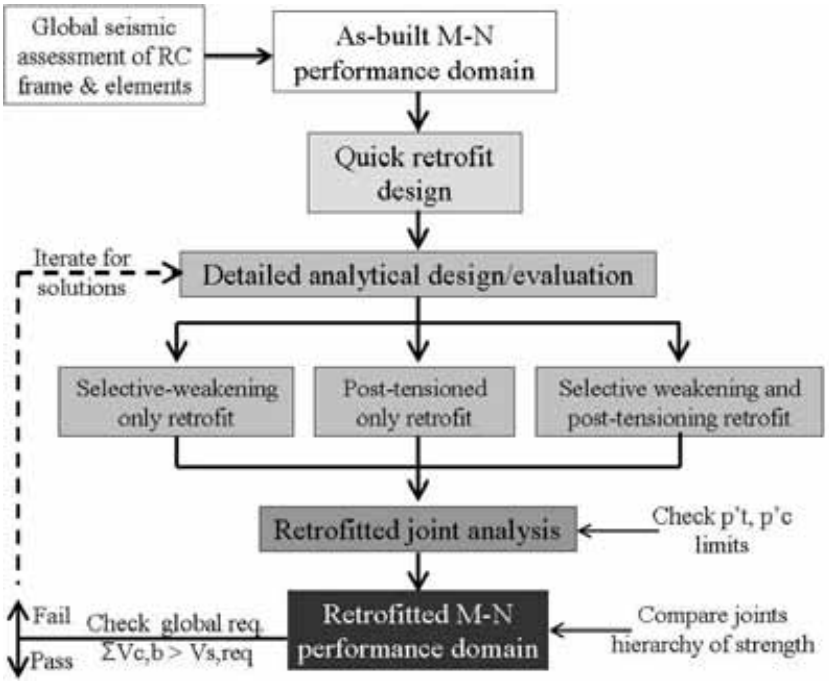

Figure 3.30: Selective Weakening retrofit design methodology.

Next, using the preliminary sizing of the SW retrofit solutions, detailed evaluation of the structural performance of the three retrofit levels/techniques is carried out using analytical tools developed in §2.4 as well as in the next two sub-sections (§3.4.4 and §3.4.5). The evaluation of beam flexural and joint shear capacity after selective-beam-weakening (§3.4.4) does not differ significantly from the evaluation of the as-built beam as discussed in §2.4. The retrofitted joint assessment will adopt modified limit states of principal stresses (p'_t and p'_c) to account for the effect of the modified joint diagonal strut on the principal stresses' capacities (§3.4.4.2).

The evaluation of the moment-rotation of externally post-tensioned beam-column joints (§3.4.5) is more complex as the section's strains incompatibility and the unbonded post-tensioning tendons require either an empirical or an iterative solution. A post-tensioning with and without beam-weakening retrofit solution would enhance the joint shear capacity by shifting the Mohr's circle into compression zone. Without experimental evidence at this stage, §3.4.6 will recommend the limit states for p'_t and p'_c in view of the assumed joint mechanics.

Lastly, converting all the component capacities of the retrofitted beam-column joint into an equivalent column moment, M_c (§2.4.1), the M-N performance domain for the retrofitted joint

can be established. The desired weak-beam strong-column/joint mechanism occurrence can be checked by analysing the hierarchy of strength of different components/failure mechanisms. §3.4.7 will briefly discuss how retrofit design actions can be selected in view of the required capacity to achieve specific retrofit global performance objectives.

3.4.2 Displacement-based global seismic retrofit of RC frame

The structural performance of the retrofitted frame depends on the structural deformation demand (e.g. inter-storey drift) for a given seismicity demand (e.g. base shear, seismic hazard spectra). Whilst the approach outlined in the previous section (§3.4.1) achieves a ductile inelastic mechanism within the retrofitted beam-column joint connection, without relating the local lateral strength and deformation capacities of the connections to the global capacities of the retrofitted frame, the retrofit design process is incomplete.

For the SW retrofit strategy, it is pertinent to assess the effect of the lateral strength of the weakened configuration (or strengthened with added post-tensioning) on the global RC frame response. Within the framework of a displacement-based design or retrofit approach [117, 163, 165], a global seismic retrofit procedure for RC frames is proposed and discussed herein. It is based on a simplification of the direct displacement based design (DDBD) procedure proposed by Priestley *et al.* [165] and on a modification of the retrofit design using post-tensioned dissipative rocking walls proposed by Marriott *et al.* [117, 145]. It seeks to answer the question: "for a selected seismic retrofit performance objective (§*3.1.2*), what is the appropriate level of beam flexural capacities in the exterior beam column joints, to be targeted through a local SW-retrofit while guaranteeing a beam-sway inelastic mechanism?" It is acknowledged that the global retrofit design discussed herein is tentative and requires further research and in-depth verification.

The proposed four-step procedure is illustrated in Figure 3.31. The following sub-sections will describe some of the key assumptions in order to adopt the DDBD design approach given in [145, 165] for the seismic retrofit design.

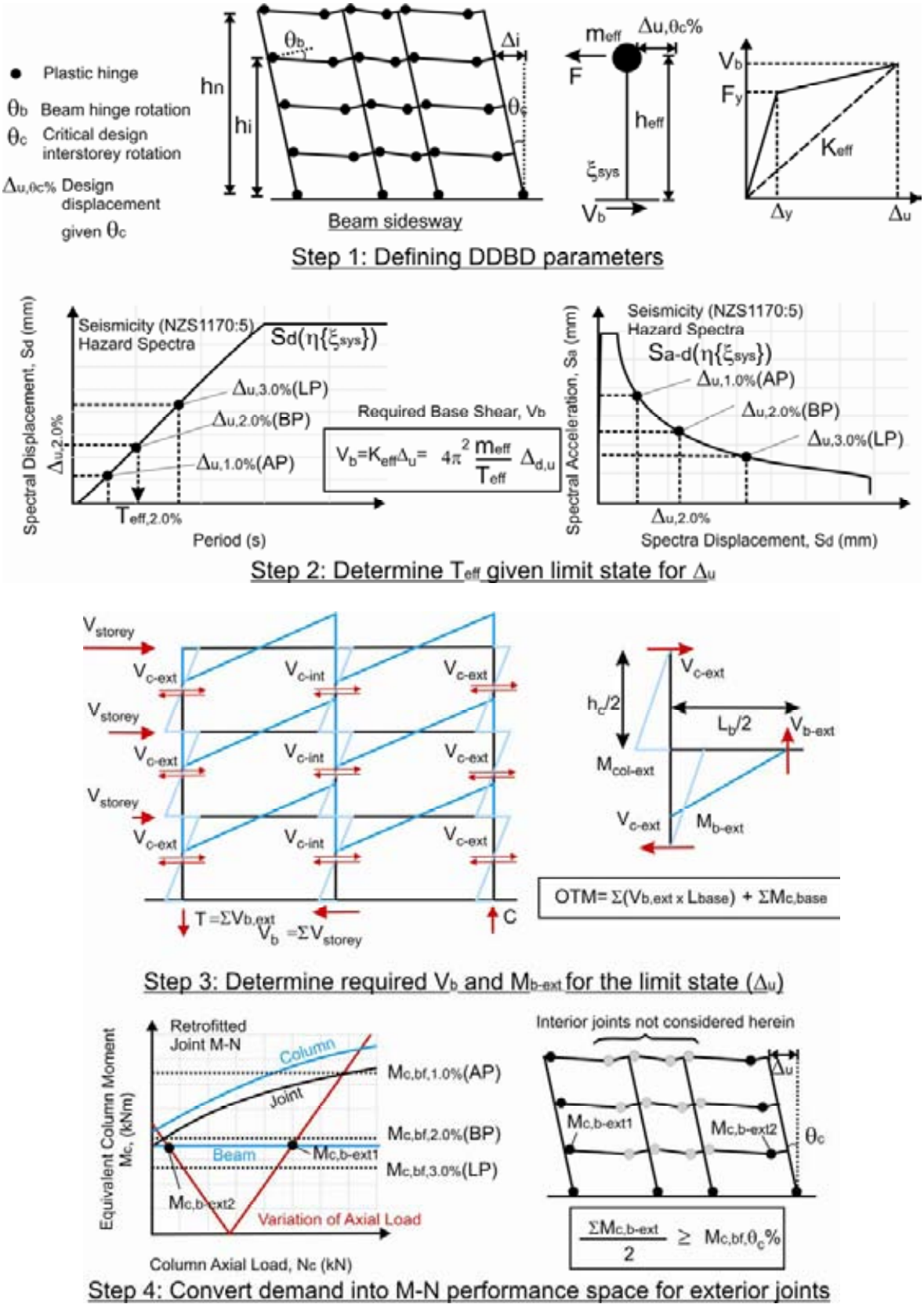

Figure 3.31: Displacement-based seismic assessment and retrofit design for RC frames.

3.4.2.1 Step 0: Define the targeted performance objectives

Within a seismic retrofit design, the definitions of targeted performance objectives for the retrofitted building in relative to a set of engineering demand parameters and performance levels are crucial. The 2004 Building Act [40] in New Zealand and the implemented earthquake-prone buildings policies in Wellington and Christchurch for example, set a retrofitted target performance of at least 33%NBS and 67%NBS respectively, in which %NBS is the percentage of new building standard [133]. In the force-based retrofit design approach, this has been taken to be building base shear, V_b. That is, the retrofitted building would have the same V_b as a new building designed at the same site for 33% or 67% of the site seismicity (as given by the seismic hazard spectra).

It is also important to recognise that the elimination of non-ductile failure mechanisms and critical structural weaknesses (e.g. irregularity) are more significant than the lateral force levels. Furthermore, the definition of seismic retrofit objectives based on V_b as a function of %NBS does not correlate well with expected damages or global seismic response. As such, the performance-based SW retrofit design described herein adopts the global deformation index - inter-storey drift, θ_c, as the design objective. For different limit states, different θ_c can be defined to match the expected damage and performance levels. For example, ASCE-41 [11] specifies θ_c for Basic Performance and Limited Performance (collapse-prevention) to be 2.0% and 4.0% drifts respectively. The definition of θ_c limit states can be based on local structural elements deformation capacities (e.g. moderate joint cracking at θ_c=1.0%) and/or non-structural elements deformation capacity (e.g. moderate cracking of clay-brick infill walls at θ_c=0.5%). The ATC-58 project [12] is currently running extensive testing programme in order to establish relevant engineering damage parameters in relation to various structural and non-structural elements.

3.4.2.2 Step 1: Define DDBD parameters for retrofitted RC frame

The DDBD parameters would define an equivalent single-degree-of-freedom (SDOF) elastic system to the retrofitted RC frame, with secant stiffness, K_{eff}, to the target displacement, $\Delta_{u,\theta c}$, at the effective height, h_{eff}, (Figure 3.31-step 1). The key assumption to define these DDBD parameters is that the inelastic mechanism of the SW-retrofitted frame is changed to beam-sway flexural hinging as postulated in the SW retrofit strategy (§3.3). As such the deformed shape, yield displacement, Δ_y and damping-ductility (ξ_{sys} -μ) formulations for a flexural hinging beam-

sway RC frame structure can be adopted with minor modifications. Other parameters such as the effective mass, m_{eff}, and effective height, h_{eff}, would be a function of the building properties. The following expressions are used to generate the DDBD parameters for a beam-hinging RC frame, but further detail is available in ref. [165]:

$$\Delta_i = \frac{\Delta_u}{H_c}\left(\frac{\delta_i}{\delta_1}\right) \quad \textbf{3.2}$$

$$\delta_i = \begin{cases} \dfrac{h_i}{h_n} & for \quad n \le 4 \\ \dfrac{4}{3}\dfrac{h_i}{h_n}\cdot\left(1-\dfrac{h_i}{4h_n}\right) & \quad n > 4 \end{cases} \quad \textbf{3.3}$$

$$\Delta_{u,\vartheta_c} = \frac{\sum m_i \Delta_i^2}{\sum m_i \Delta_i} \quad \textbf{3.4}$$

$$m_{eff} = \frac{\sum m_i \Delta_i}{\Delta_{d,u}} \quad \textbf{3.5}$$

$$h_{eff} = \frac{\sum m_i \Delta_i h_i}{\sum m_i \Delta_i} \quad \textbf{3.6}$$

where H_c is the inter-storey height at the base of the building; h_i and h_n are the height of level i and roof height; Δ_i, δ_i, and m_i, are the displacement, shape factor and mass at level i.

The estimation of the equivalent viscous damping, ξ_{sys}, for the SW-retrofitted pre-1970s frames is unknown at this stage. Tentatively, a low, constant with ductility, value of ξ_{sys} = 12.5% can be assumed. The use of constant ξ_{sys} removes the need to estimate Δ_y and μ. Δ_y may be difficult to be estimated for the SW-retrofitted pre-1970s RC frames with plain round bars because the elastic deformations of the beams, columns and joints are hugely affected by the bond capacity of the reinforcement. Alternatively, the expressions for unbonded post-tensioned precast concrete frames (ξ_{sys} ranges from 5-18%) can be used for SW retrofit solutions with external post-tensioning. References [165] and [116] give a more detailed treatment on the calculation of ξ_{sys} for unbonded post-tensioned rocking precast concrete frames.

3.4.2.3 Step 2: Determine the effective period and the required base shear.

The displacement response spectrum is used to derive the required effective period, T_{eff}, corresponding to the target design displacement, $\Delta_{u,\theta c}$, given the level of damping (ξ_{sys}). This is

illustrated in Figure 3.31-step 2, where the New Zealand NZS1170:5 [129] displacement hazard spectra is used in conjunction with three performance levels: a) Limited Performance, LP (θ_c =3.0%), b) Basic Performance, BP (θ_c =2.0%) and c) Advanced Performance, AP (θ_c =1.0%). The 5%-damped elastic hazard spectra ($S_{d,elastic}$) are reduced using a damping reduction factor, η:

$$\eta = \left(\frac{0.07}{0.02 + \xi_{sys}} \right)^{\alpha} \geq 0.7 \quad \textbf{3.7}$$

$$S_d\left(\eta\{\xi_{sys}\}\right) = S_{d,elastic} \cdot \eta \quad \textbf{3.8}$$

where α = 0.25 and 0.50 for near field and far field design ground motions respectively. Thus, the required based shear of the SW-retrofitted frame to achieve the previously defined target performance-objective (in θ_c) is calculated as $V_{b,req} = K_{eff} \cdot \Delta_{u,\theta c}$, where K_{eff} is given by:

$$K_{eff} = 4\pi^2 \frac{m_{eff}}{T_{eff}} \Delta_{u,\theta_c} \quad \textbf{3.9}$$

3.4.2.4 Step 3: Distribute the base shear and determine required members strength.

Given the $V_{b\text{-}req}$, the required flexural strength of beam hinges, $M_{b,req}$, can be determined using an equilibrium approach [165] or structural analysis with the $V_{b\text{-}req}$ distributed up the building height. The base shear is distributed in proportion to the floor mass and displacement, with an additional 10% applied to the roof level to account for higher mode effects:

$$F_{roof} = 0.1V_b + 0.9V_b \frac{m_{roof}\Delta_{roof}}{\sum m_i \Delta_i} \text{ at roof level} \quad \textbf{3.10}$$

$$F_i = 0.9V_b \frac{m_i \Delta_i}{\sum m_i \Delta_i} \text{ at other level } i \quad \textbf{3.11}$$

A close form equilibrium distribution described by Priestley *et al.* [165] is used:

$$V_{b,i} = N_e \frac{V_{storey,i}}{\Sigma V_{storey,i}} \quad \textbf{3.12}$$

where N_e is the earthquake induced tension force in the ground columns (or sum of beam shears) and $V_{storey,i}$ is the storey shear at level i. $V_{storey,i}$ is the cumulative applied distributed base shear force (F_i). N_e can be estimated using the following equation:

$$N_e = \frac{\sum(F_i h_i) - V_b(0.6H_c)}{L_{building}} \quad \textbf{3.13}$$

where $L_{building}$ is the length of the building (sum of all bay lengths, L_b). The required beam flexural capacity at each level i for the given θ_c is then given by $M_{b,i,\theta}=V_{b,i} / 2L_b$.

The internal force distribution depicted in Figure 3.31-step 3 assumes the interior joints have sufficient strength to develop $V_{c\text{-}int}$ in the interior columns. If the interior joints have insufficient strength/ductility/deformation capacities, then the interior joints will need to be retrofitted as well. In the scenario where high θ_c performance level is acceptable (e.g. LRO or BSO), then, regardless the $V_{c\text{-}int}$ capacity of the system, the interior joints and columns are checked for its ductility and deformation capacities to sustain the beam-sway (or mixed) inelastic mechanism (as previous discussed in §3.3.3.1). Alternatively, the designer may opt to iterate on the DBD retrofit procedure to allocate higher column shear demands to the exterior columns, in order to achieve a θ_c performance level.

3.4.2.5 Step 4: Conversion of demand into a M-N performance domain

Lastly, for the given $M_{b,i,\theta}$ at the exterior beam spans to sustain the beam-sway mechanism that achieves $\Delta_{u,\theta c}$ at the h_{eff} for the retrofitted RC frame for the given seismicity, $M_{b,i,\theta}$ can be converted into an equivalent column moment, $M_{c,bf,\theta}$, and thus projected into the M-N performance domain of the exterior beam-column joint as discussed in §2.4 and §3.4.1. Figure 3.31-step 4 illustrates an example of the projection of the $M_{c,bf,\theta}$ for various performance levels (AP, BP and LP) onto the M-N performance space of the hypothetical retrofitted exterior beam-column joints. For the SW retrofit design within the M-N domain, in addition to the need to satisfy the hierarchy of strength requirement, it is also necessary to satisfy the required flexural strengths of exterior spans' beams, $M_{c,b\text{-}ext}$, to achieve the required performance level (~$M_{c,bf,\theta}$):

$$\frac{\sum M_{c,b-ext}}{2} \geq M_{c,bf,\theta} \quad \textbf{3.14}$$

$$\frac{\sum M_{c,bf}}{2} \geq \frac{\sum M_{c,b-ext}}{2} \quad \textbf{3.15}$$

where $M_{c.bf}$ is the provided beam flexural capacity (in terms of M_c). As explained in §2.4.1, the following expression can be used to convert M_b into M_c (and vice-versa):

$$M_{c,bf} = M_{b,req}\left(\frac{L_b H'_c}{H_c L'_b}\right) \quad \textbf{3.16}$$

where H_c, H'_c, L_b and L'_b are geometry parameters as illustrated in Figure 2.29 (Chapter 2).

Equations 3.14 and 3.15 assume the moment demands in the flexural hinges at the exterior spans have sufficient ductility to allow moment redistribution during an earthquake. As one exterior span goes into positive moment, the other will go into negative moment. Therefore, it is not unreasonable to consider the sum of the exterior spans' beam flexural capacity in computing the total contribution from the exterior beam-column joints.

The displacement-based retrofit design procedure presented in the preceding paragraph would give a lower bound of beam flexural strength for the SW retrofit strategy as well as an estimation of the performance levels given a M-N performance domain of the retrofitted beam-column joints. §3.4.7 will revisit the comparison between the demand ($M_{b,req}$) and the provided M-N performance domain of the retrofitted beam-column joints.

3.4.3 Quick Selective-Weakening retrofit design

A quick SW retrofit design method is given herein to estimate the preliminary SW retrofit 'sizing' in terms of the levels of beam-weakening and/or external post-tensioning required for given required flexural strengths of exterior spans' beams, $M_{b,req}$, as described in the preceding section:

$$M_{b,req} \leq M_{bf} \quad \textbf{3.17}$$

The following expressions (Equations 3.18 and 3.19) can be used to estimate the M_{bf} for either a) selective beam-weakening-only b) post-tensioning-only or c) selective beam-weakening with post-tensioning retrofit solutions. As a simplification, the contributions from the non-prestressed and prestressed reinforcements are evaluated separately. Therefore, for beam-weakening-only retrofit, M_{bf} is given by $M_{b,rc}$ (Equation 3.18) while for post-tensioning with or without beam-weakening retrofit, M_{bf} is given by $M_{b,rc} + M_{b,pt}$ (Equations 3.18 and 3.19):

$$M_{b,rc} = A_s f_y (j_{rc} d) \quad \textbf{3.18}$$

$$M_{b,pt} = \phi_o T_{pt} (j_{pt} d) \quad \textbf{3.19}$$

where A_s and f_y are the total area and yield strength of the beam longitudinal reinforcements; d is the effective depth of the beam (beam depth minus the depth to the centroid of the tension reinforcement); T_{pt} is the design post-tensioning forces; j_{rc} and j_{pt} are the approximate level arm coefficients for prestressed and non-prestressed reinforcements, and are taken to be 0.85 and 0.35 respectively; and ϕ_o is the prestressing force over-strength factor (due to elongation of the tendon at beam centreline).

Tentatively for design, ϕ_o is taken to be 2 to account for the induced post-tensioning forces due to the elongation of the tendons at the design drift. The suggested values for j_{pt} and ϕ_o assume the location of the tendon to be at the centre of the beam and relatively low level of post-tensioning forces (T_{pt} < 40% of yield strength of the tendons). While ϕ_o=2 might be conservative in evaluating the capacity design hierarchy of strength, it is suggested that ϕ_o=1.5 to be used for the evaluation of allowable beam moment under dry jointed-ductile beam-column mechanism.

3.4.4 Assessment selective beam-weakening retrofit intervention

3.4.4.1 Beam flexural capacity after selective weakening retrofit

The weakening of the beam is achieved by cutting (some or all) the beam longitudinal bars. This effectively reduces the beam flexural strength adjacent to the joint and creates a weak link within the hierarchy of strength of the beam-column joint. Following the moment-curvature procedure outlined in §2.4.3 and the assessment of bond capacity discussed in §2.4.5, the upper bound and lower bound values of the beam flexural capacity can be established by assuming either perfect bond or a maximum bond capacity ($\tau_{b,max}$). Figure 3.32 gives an example of moment-curvature of a retrofitted 330mm by 230mm beam with R10 (diameter 10mm plain round bars) longitudinal reinforcements. The upper bound curves assume full steel strength development with strain hardening, while the lower bound curves assume $\tau_{b,max}=0.3\sqrt{f'_c}$ for the tension reinforcements and $\tau_{b,res}=0.15\sqrt{f'_c}$ for the compression reinforcements.

In a beam-weakening retrofit scenario, the ratio of area of tension longitudinal reinforcements-to-beam depth (A_s/h_b) is effectively reduced in proportion to the number of beam-bars severed. Lower A_s/h_b results in lower resultant compressive forces within the beam section (C_c+C_s) and therefore results in a lower bond stress demand in the compression longitudinal reinforcements (C_s). As the plain round bar 180° hooked anchorage is only effective in tension

anchorage, lower compressive bond stress demand would also improve the overall beam behaviour under cyclic loading.

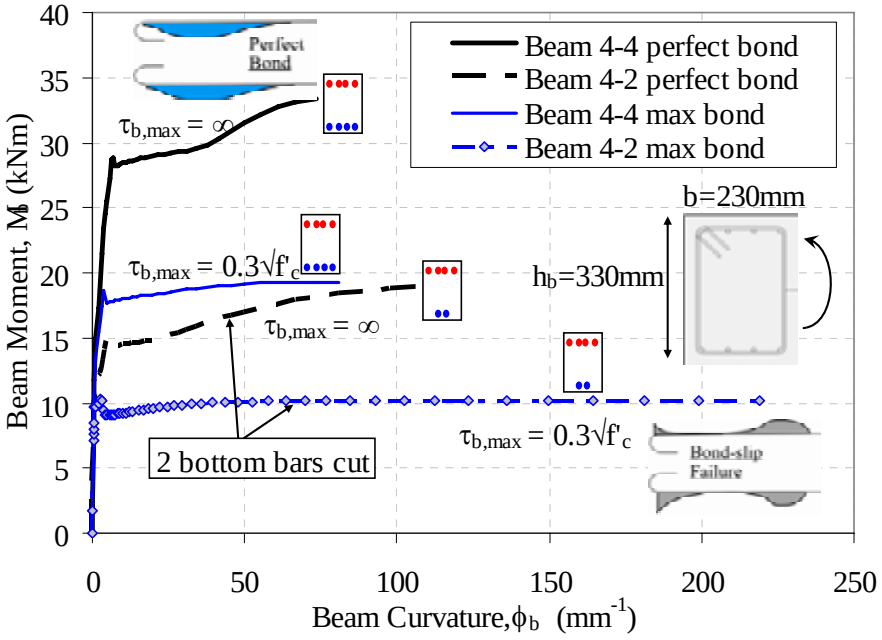

Figure 3.32: Example of beam-weakening-only moment-curvature.

3.4.4.2 Selective beam-weakening in controlling joint shear capacity-demand

Selective beam-weakening affects the joint shear behaviour in two ways. Firstly by reducing the beam flexural capacity, the joint shear stress demand is reduced. The joint shear stress demand, v_{jh}, is given by Equations 2.4 and 2.7 (from Chapter 2, reproduced below for clarity). However, within the retrofit design approach using the M-N performance domain (§3.4.1), this effect is better represented as a shift in beam capacity.

$$v_{jh} = V_{jh} / b_j h_c \qquad \textbf{3.20 (also 2.7)}$$

$$V_{jh} = T_s - V_c = \frac{M_b}{jd} - \frac{2M_c}{(H_c - h_b)} \qquad \textbf{3.21 (also 2.4)}$$

Secondly, the beam-weakening would reduce the section effective depth as the cut region would be ineffective in compression in its reduced section and pre-notched behaviour. Depending on the depth of the beam-weakening, the joint aspect ratio, h_b/h_c may change significantly, resulting in a more gradual joint diagonal compression strut as schematically illustrated by Figure 3.33. As mentioned in §3.3.3.1, past experimental tests on lightly reinforced or unreinforced beam-column joints have shown higher joint shear strength with lower h_b/h_c (e.g. [87, 112, 209]).

In literature, several available models have attempted to explain and quantify the influence of h_b/h_c on the joint shear capacity. Paulay and Priestley considered the increased joint shear capacity from shallow beam-column joints as a result of increased contributions from the column vertical reinforcements due to the elongated joint cores. [155]. Other researchers [86, 209] have considered the lower shear span-to-depth ratio in joints with shallow beams while others [14, 72, 105, 152, 175, 201] offered empirical and semi-empirical equations to capture this phenomenon.

Adopting the principal stresses approach, an alternative mechanistic model is proposed to quantify the influence of h_b/h_c on the joint shear capacity. The effects on h_b/h_c on the diagonal compression strut inclination angle, α_1, the joint panel stress states and the Mohr's circle stress states are summarised in Figure 3.33 and Figure 3.34. An "equivalent shallow beam" is assumed in the model shown in Figure 3.34 though in reality the weakened depth is partially effective in compression. During cyclic loadings, it is expected the weakened depth will crack extensively and spall off, and beam longitudinal reinforcements in compression would lose its bond capacity, thus reducing its effectiveness in compression.

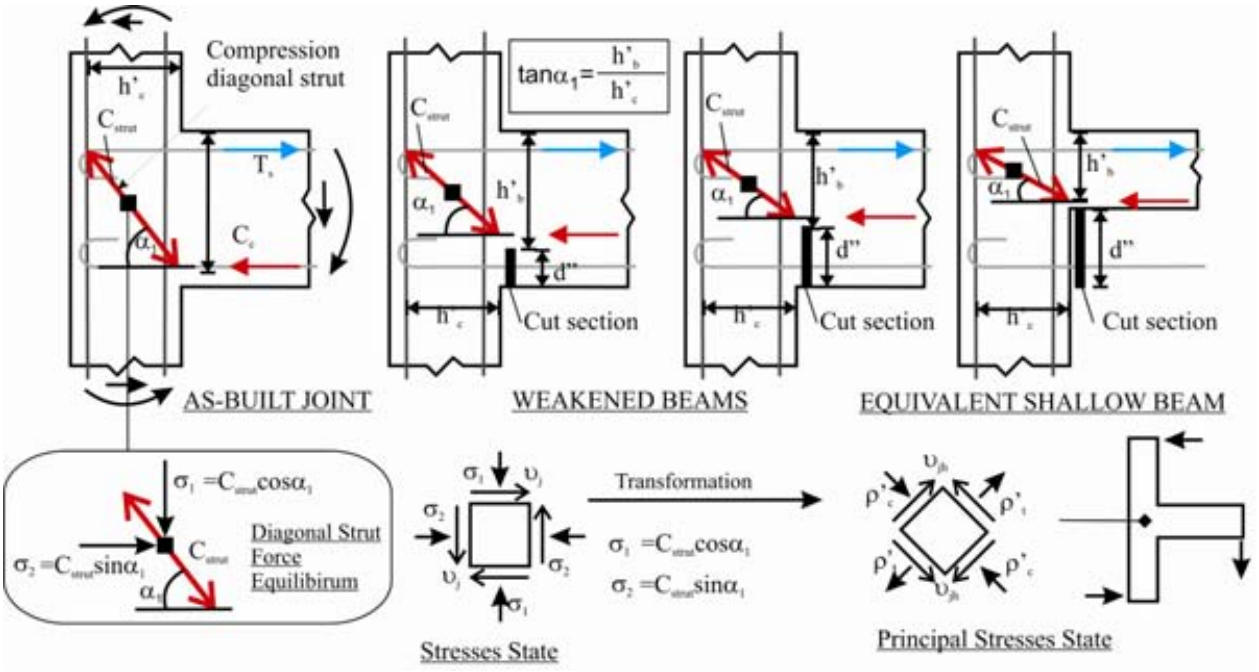

Figure 3.33: Effect on beam-weakening on the joint shear force transfer and capacity: top) Changes of compression diagonal strut inclination as the h_b/h_c decreases; bottom) Component of joint stresses given the strut inclination angle, α_1.

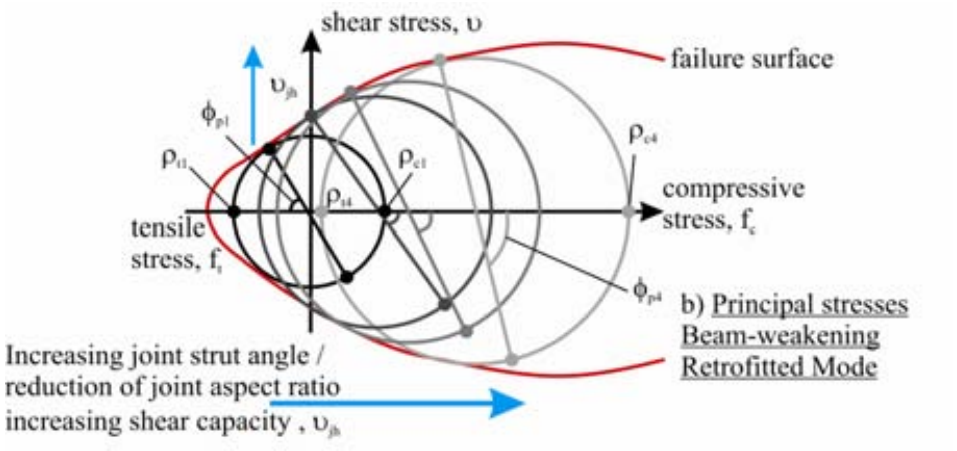

Figure 3.34: Effect on beam-weakening on the joint shear force transfer and capacity: Postulated changes in Mohr's circle due to reduction of h_b/h_c.

The model assumes a single diagonal strut resisting all the horizontal shear forces in absence of horizontal joint reinforcements, the force equilibrium equation of the joint diagonal compression strut will give the following normal stresses on a finite element of concrete within the joint core region (as shown in Figure 3.33):

$$\sigma_1 = C_{strut} \cos\alpha_1 \qquad \textbf{3.22}$$

$$\sigma_2 = C_{strut} \sin\alpha_1 \qquad \textbf{3.23}$$

The angle α_1 is the diagonal compression strut inclination angle with respect to horizontal principal plane and is given by the following equation:

$$\alpha_1 = \tan^{-1}\left(\frac{h'_b}{h'_c}\right) \qquad \textbf{3.24}$$

Therefore, as the beam-cutting depth (shown in Figure 3.33 as *d"*) increases, h_b/h_c decreases, the diagonal strut becomes less steep, α_1 decreases and the primary normal stress, σ_1, will increase and the secondary normal stress, σ_2, will decrease. For an exterior beam-column joint, σ_1 is on the horizontal plane, therefore, it can be concluded that the diagonal strut becomes more effective in resisting the horizontal shear stress.

However, to quantify the increase in joint shear strength in terms of principal stresses, a Mohr's circle analysis and postulated model is required. Figure 3.34 illustrates the assumed translation of Mohr's circles where as the h_b/h_c and α_1 decrease, the Mohr's circle shifts towards

the compressive stress limit, with an increasing principal plane angle, ϕ_p, and an increasing Mohr's circle radius and higher attainable v_{jh}.

Recalling that the maximum joint shear stress, v_{jh}, can be sustained prior to diagonal joint cracking can be calculated by solving the principal tensile stresses equation (Equation 2.10 from Chapter 2, reproduced below):

$$p'_c, p'_t = \frac{f_v + f_h}{2} \pm \sqrt{\left(\frac{f_v - f_h}{2}\right)^2 + v_{jh}^2} \qquad \textbf{3.25 (also 2.10)}$$

where p'_c and p'_t are the diagonal cracking limit states for principal compression and tensile stresses; f_v and f_h are the vertical and horizontal (post-tensioning) axial stresses. Therefore, to quantify the improvement of the joint shear strength from the beam-weakening retrofit, the limit states for p'_t and p'_c can be modified based on some semi-empirical factors to account for the expansion of the Mohr's circle.

Using a set of experimental data of lightly reinforced and unreinforced beam-column joints failing in the joint shear, Park and Mosalam [152] derived a semi-empirical equation to estimate the joint shear strength (in terms of v_{jh}):

$$v_{jh} = \frac{C\cos\alpha}{1.31 + 0.085(\frac{h_b}{h_c})} \qquad \textbf{3.26}$$

C= 1.91 for upper bound and C=0.83 for lower bound. Figure 3.35a plots the comparison of the experimental data set compiled by Park and Mosalam and their proposed joint shear equations. Various other similar empirical formulations are available in literature as mentioned, but the proposed formulation by Hegger *et al.* [86] is shown here for comparison:

$$A = 1.2 - 0.3\frac{h_b}{h_v} \qquad \textbf{3.27}$$

where A is the modification factor for v_{jh} (given in terms of $\sqrt{f'_c}$ MPa). The equation by Hegger *et al.* and the observation from finite element modelling of non-ductile beam-column joints by Eligehausen *et al.* [54] are also plotted in Figure 3.35a to further reinforce the strong correlation between h_b/h_c, α_1 and v_{jh}.

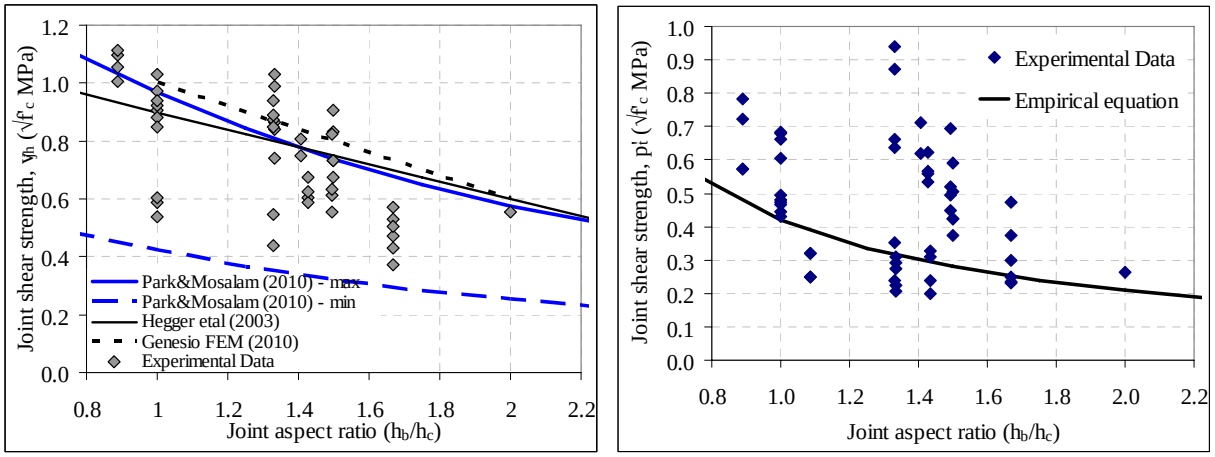

Figure 3.35: Relations of joint shear strengths and joint aspect ratio (h_b/h_c): a) nominal joint shear stress, v_{jh} ($\sqrt{f'_c}$ in MPa); b) joint principal tensile stress, p'_t ($\sqrt{f'_c}$ in MPa)

Assuming the expansion of the Mohr's circle as shown in Figure 3.34, the principal stresses limit states should increase in relation proportion to the v_{jh} with decreasing joint aspect ratio (as per Figure 3.35a). Using a truncated data set [10, 38, 59, 83, 84, 103, 134, 147, 153, 177, 204, 208] from the Park and Mosalam [152] database, with references with one or two specimens with joint failure omitted, the following empirical equation is derived to estimate the lower bound value for the p'_t given a beam-weakening retrofit induced effective joint aspect ratio (h'_b / h'_c) (as shown in Figure 3.33):

$$p'_{t-sw} = \frac{0.42}{\tan\alpha} = 0.42\frac{h'_c}{h'_b} (\text{in } \sqrt{f'_c}\text{ MPa}) \qquad \textbf{3.28}$$

where h'_c is taken to be $0.9h_c$ and h'_b is taken to be $h_b - d$". The upper coefficient of $0.42\sqrt{f'_c}$ MPa is taken from the recommendations of Priestley *et al.* [167] for peak p'_t value for T-bridge joint. The comparison between Equation 3.28 and the experimental data set is presented in Figure 3.35b. While large scatter of the p'_t versus h_b/h_c can be observed in Figure 3.35b, owing to the different beam longitudinal bar anchorage and joint reinforcement detailing in the dataset, Equation 3.28 is giving a reasonably lower bound estimation of the joint shear strength in terms of p'_t. Research by Genesio [71] has shown numerically a stronger influence of the h_b/h_c on the joint shear strength in terms of p'_t.

Lastly, it should be noted that the proposed SW beam-weakening is only cutting into the bottom face of the beam, and thus, the joint shear capacity enhancement should only be considered for the positive beam-moment. Therefore, it is possible that a flexural plastic hinge in

the beam will form under positive moments and a uni-directional joint shear hinge will form under negative moments, depending on the overall hierarchy of strength.

3.4.5 Assessment of beam capacity with unbonded post-tensioning retrofit

A section analysis procedure previously for analytical modelling of jointed ductile ('hybrid') rocking moment-resisting connections for precast concrete (e.g.[116, 131, 146, 169]) is extended for the assessment of beam-column joint capacity with unbonded post-tensioning retrofit intervention. By virtue of satisfying the capacity design requirement in the SW retrofit, flexural pseudo-rocking inelastic mechanism will be activated at the beam-column interface. The pseudo-rocking mechanism refers to the partial rocking along one large flexural crack, which is resultant of the use of plain-round bars within the connection, as shown in Figure 3.36a.

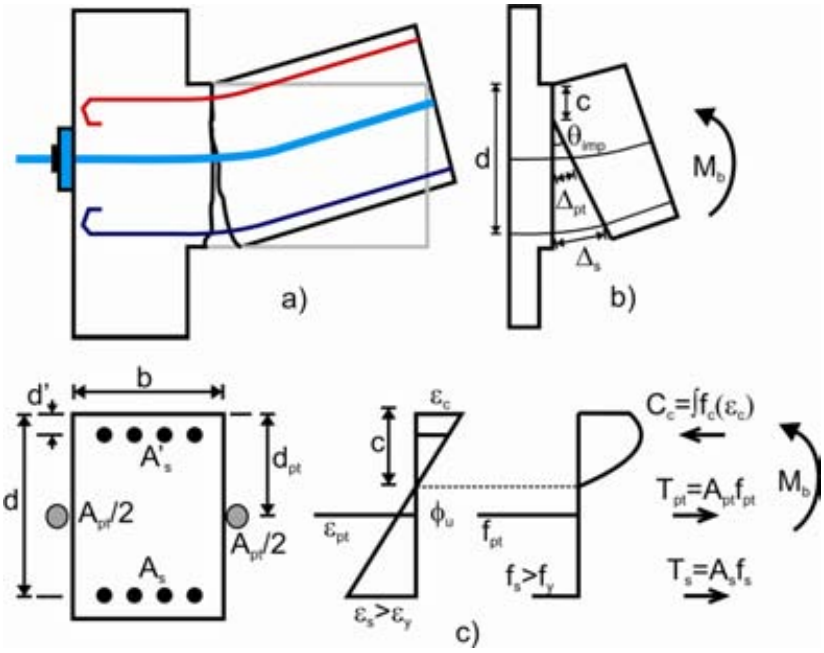

Figure 3.36: Iterative sectional analysis for post-tensioned retrofitted beam-column joints: a) Schematic of pseudo-rocking interface; b) Idealised rocking interface based on actual rocking interface; c) Sectional analysis of beam with unbonded post-tensioning tendons.

As observed in previous tests on as-built beam-column joints with plain round bars [15, 113, 141] without non-ductile joint shear failures prior to beam-yielding, flexural cracking would concentrate in one critical beam section (closest to the column-face). As with the jointed-ductile rocking connection, post-tensioned retrofitted beam-column joint with plain round bars theoretically would undergo the same strain incompatibility due to the localised bond failure of the plain round bars (as briefly discussed in §2.3.3.2 and §2.4.5). Therefore, an idealised rocking

gap opening (Figure 3.36b) with similar equivalent "strain compatibility" as in the original procedure proposed by Pampanin *et al.* [146] can be used to generate the post-tensioned retrofitted beam's moment-rotation. The procedure adopted herein is also consistent with the recommendations in the Appendix B of the 2006 NZS3101 concrete code [131].

The procedure involves an iterative analysis to solve the neutral axis, *c* that would satisfy the sectional force equilibrium under the strain/elongation equivalent compatibility assumptions (Figure 3.36c). The moment-rotation capacity curve is generated incrementally at every imposed effective rotation at the beam-column interface, θ_{imp}:

$$\theta_{imp} = \frac{\theta_{drift}}{\left(1 - \frac{h_c}{L_b}\right)} \qquad \textbf{3.29}$$

where θ_{drift} is the imposed column rotation, i.e. the inter-storey drift, L_b is the beam centre-line to centre-line span, and h_c is the column depth. The iteration for *c* requires then the evaluation of the strains and resulting forces of the unbonded post-tensioning tendons, non-prestressed beam plain round reinforcements and the concrete compressive zone. Once the section force equilibrium is satisfied, the moment capacity of the post-tensioned beam-column connection, M_b, can be evaluated (as illustrated in Figure 3.36c).

3.4.5.1 Strain and force in the unbonded post-tensioning tendons

The strain in the unbonded post-tensioning tendon is taken to be the initial strain, $\varepsilon_{pt,i}$, plus half of the elongation strain over the rocking induced gap in the idealised rocking interface, as given in Equation 3.30: the reduction factor (0.5) in the induced strain, $\Delta\varepsilon_{pt}$, is to account for the tendency to overestimate the elongation of the post-tensioning tendon, Δ_{pt}, across the cracking gap. This discrepancy arises as the selective-weakening and post-tensioned retrofitted beam-column joint does not have the same smooth 'linear' rocking interface (as per Figure 3.36b). In reality, the pseudo-rocking interface is more of a non-linear section due to uneven cracking surface and localised strain due to bond-slip as illustrated in Figure 3.36a.

$$\varepsilon_{pt} = \varepsilon_{pt,i} + \Delta\varepsilon_{pt} = \varepsilon_{pt,i} + 0.5\frac{n_{gap}\Delta_{pt}}{L_{ub,pt}} \qquad \textbf{3.30}$$

where n_{gap} is the number of gap opening along the post-tensioning tendon length and $L_{ub,pt}$ is the unbonded length of the post-tensioning tendons. Δ_{pt} is the net elongation of the post-tensioning tendons and is given by:

$$\Delta_{PT} = \theta_{imp}\left(d_{pt} - c\right) \quad \textbf{3.31}$$

where d_{pt} is the distance of the post-tensioning tendons from the extreme compression fibre. d_{pt} is equal to $h_b/2$ if the post-tensioning tendon is at mid-depth of the beam (with gross depth, h_b). A bi-linear stress-strain relationship can be used to calculate the stress and the associated tensile force in the tendons:

$$f_{pt} = \begin{cases} \varepsilon_{pt} E_s & \varepsilon_{pt} \le f_{y,pt}/E_s \\ f_{y,pt} & \varepsilon_{pt} > f_{y,pt}/E_s \end{cases} \quad \textbf{3.32}$$

$$T_{pt} = A_{pt} f_{pt} \quad \textbf{3.33}$$

where $f_{y,pt}$, E_s and A_{pt} are the yield strength, elastic modulus and total area of the post-tensioning tendons.

3.4.5.2 Strain and force in the non-prestressed beam plain round reinforcements

The non-prestressed beam longitudinal reinforcements would gradually lose the bond capacities after reaching the $\tau_{b,max}$. In particular, upon the flexural cracking in the critical beam section, localised bond-slip and concentration of steel stress would occur at the crack gap. As the bond capacity progressively decreases as the crack widens, it leads to a gradually growing length of unbonded non-prestressed reinforcements. This is similar to the jointed-ductile hybrid rocking connections in which mild-steel deformed bars are intentionally left unbonded near the critical beam-to-column section. The strain in the non-prestressed beam reinforcements, ε_s, is given by:

$$\varepsilon_s = \frac{\Delta_s - 2\Delta_{sp}}{L_{ub,s}} \approx \frac{\Delta_s + 2/3 l_{sp}\alpha\varepsilon_y}{(l'_{ub} + 2l_{sp})} \quad \textbf{3.34}$$

where Δ_s is the net elongation of the reinforcements due to the opening of the crack, Δ_{sp} is the net elongation due to the strain penetration, l'_{ub} is the unbonded length of the reinforcements and $\alpha\varepsilon_y$ is the elastic tensile strain of the reinforcement. l_{sp} is the strain penetration length and is estimated by [155, 184]:

$$l_{sp} = 0.022 f_y d_b \quad \textbf{3.35}$$

However, as it is difficult to estimate the actual unbonded length of the plain round bars at every rotation, an "approximate procedure" [146] that assumes that a negligible deformation due

to strain penetration of plain round bars, Δ_{sp} and negligible unbonded length of the non-prestressed bars, $L_{ub,s}$ is used:

$$\varepsilon_s \approx \frac{\Delta_s}{2l_{sp}} = \frac{\theta_{imp}(d-c)}{2(0.022 f_y d_b)} \quad \textbf{3.36}$$

While the mechanics of the pseudo-rocking in post-tensioning retrofitted joints and actual hybrid rocking joints is fundamentally different and the use of the strain penetration length formula derived from deformed bars is inaccurate, for the retrofitted joints, the inaccuracy in relevance to the ε_s calculation is not pertinent. This is because ε_s generally yields at early stages of the loading and due to the bond-slip of plain round bars (and thus a growing un-bonded length), the resulting f_s is limited to the yield-plateau region without really approaching the fracture strain. In absence of detailed evidence, the formulation in Equation 3.36 is used to calculate the non-prestressed reinforcement strains.

Both tension and compression beam reinforcements are considered in the section analysis. King *et al.*'s steel stress-strain model [106], described in §2.4.3, is used to calculate the stress, f_s, and resulting tensile forces, T_s, within the longitudinal reinforcements. T_s is given by $T_s=f_sA_s$ where A_s is the area of the bottom longitudinal reinforcements. In order to account for bond-slip at high level of strain, non-prestressed reinforcements' strain hardening is assumed to be limited. Within the analytical model, this is implemented using a simple bi-linear steel stress-strain model. Discussion of these parameters will be made in light of the experimental results in Chapter 6.

3.4.5.3 Strain and force in the concrete compressive zone

Pampanin *et al.* [146] proposed a formulation based on a "monolithic beam analogy" to approximate the concrete compressive strain, ε_c:

$$\varepsilon_c = \left[\frac{\left(\theta_{imp} L_{cant}\right)}{\left(L_{cant} - 0.5L_p\right)L_p} + \phi_y \right] \cdot c \quad \textbf{3.37}$$

where L_{cant} is the distance between the rocking interfaces, ϕ_y is the yield curvature and the point of contra-flexure (or half the beam span for simplicity) and L_p is the plastic hinge length. However, for RC members with plain round bars, L_p can be a very small value due to concentrated flexural cracking at the 'fixed-end beam rotation' section. As such, (L_{cant} +0.5 L_p) can be assumed to be L_{cant} while plastic hinge length to be taken as twice the strain penetration length, l_{sp}. Thus, adopting these assumptions, Equation 3.37 can be simplified to be:

$$\varepsilon_c \approx \left(\frac{\theta_{imp}}{L_p} + \phi_y \right) \cdot c \approx \left(\frac{\theta_{imp}}{2l_{sp}} \right) \cdot c \qquad \textbf{3.38}$$

For comparison, a more generic formulation for ε_c developed by Palermo [135] and Marriott [116] for jointed-ductile rocking connections with various types of energy dissipation devices (external unbonded, internal bonded etc.) is also included in the analytical programme. Contrary to Equation 3.38, the following equation does not require the calculation of l_{sp}, which is unavailable for plain round bars embedded into non-ductile beam-column joints:

$$\varepsilon_c = \left(\frac{3\theta_{imp}}{L_{cant}} + \phi_{dec} \right) \cdot c \qquad \textbf{3.39}$$

ϕ_{dec} is the curvature at decompression point. From the moment-area theorem, ϕ_{dec} is given by:

$$\phi_{dec} = \frac{2A_{pt} f_{pt,i}}{E_c b h_b^2} \qquad \textbf{3.40}$$

where $f_{pt,i}$ is the initial post-tensioning stress within the post-tensioning tendons after transfer losses and E_c is the modulus of elastic of concrete. b and h_b are the width and depth of the beam.

To determine the concrete stress, f_c and the concrete compressive resultant force, C_c, the confined concrete stress-strain model by Mander *et al.* [115, 155] can be used, as given in Equations 3.41 to 3.45. Equations 3.41 to 3.45 are essentially similar mathematical expression as the Popovic unconfined concrete model [161] for the assessment procedure presented in §2.4.3. For a given ε_c and confining over-strength factor (α_{cc} = the ratio of confined and unconfined concrete compressive strengths), the concrete stress, f_c, can be determined by the following equation:

$$f_c = \frac{\alpha_{cc} f'_c \, xr}{r - 1 + x^r} \qquad \textbf{3.41}$$

where:

$$x = \frac{\varepsilon_c}{\varepsilon_{cc}} \qquad \textbf{3.42}$$

$$\varepsilon_{cc} = \left[1 + 5(\alpha_{cc} - 1) \right] \varepsilon'_c \qquad \textbf{3.43}$$

$$r = \frac{E_c}{E_c - E_{\sec}} \qquad \textbf{3.44}$$

$$E_{\sec} = \frac{\alpha_{cc} f'_c}{\varepsilon_{cc}} \qquad \textbf{3.45}$$

where ε'_c is concrete strain at maximum concrete compressive strength (f'_c). The confining factor can be determined using the procedure set out in [115] but for pre-1970s RC beams with light transverse reinforcements, α_{cc} can be taken to be 1.1.

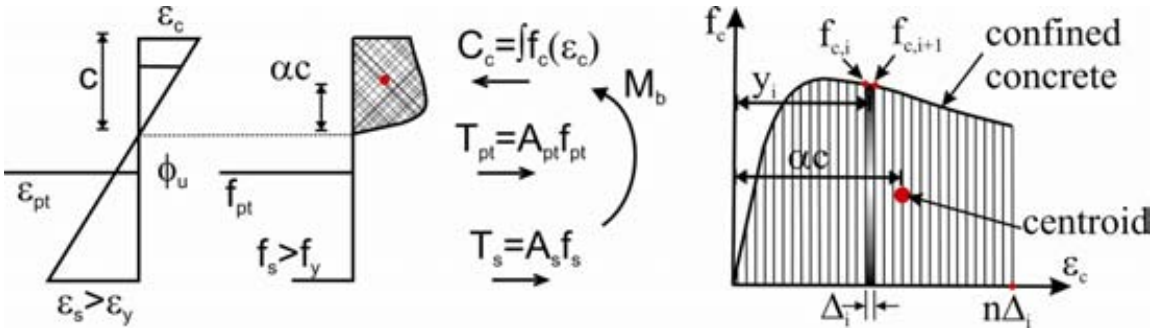

Figure 3.37: Strip integration to calculate the resultant and centroid of the concrete compression block.

With reference to Figure 3.37 above, the resultant concrete compressive force, C_c, can be calculated by numerical integration of the of the concrete stress-strain curve:

$$C_c = \sum_{i=1}^{n}\left[\left(\frac{f_{c,i} + f_{c,i+1}}{2}\right)\Delta_i\right] \qquad \textbf{3.46}$$

The centroid of which the C_c is acting can be solved by:

$$\alpha c = c - \sum_{i=1}^{n}\left[\left(\frac{f_{c,i} + f_{c,i+1}}{2}\right)\Delta_i \times \left(y_i - \frac{\Delta_i}{2}\right)\right] \Big/ C_c \qquad \textbf{3.47}$$

The flexural capacity at the given θ_{imp} is then solved by taking the moment around the centroid of C_c. The moment contribution from each component: unbonded post-tensioning, M_{pt} and non-prestressing reinforcements, M_{ms}, can be summed at every θ_{imp} to generate the complete M_b-θ_{imp} curve:

$$M_b = M_{pt} + M_{ms} \qquad \textbf{3.48}$$

$$M_b = T_{pt}\left(d_{pt} - \frac{\alpha c}{2}\right) + T_s\left(d - \frac{\alpha c}{2}\right) \qquad \textbf{3.49}$$

3.4.5.4 Comments on the proposed analytical method

Initial attempt for calculating the flexural strength of unbonded prestressing beams with unbonded post-tensioning used the existing empirical equations of the NZS3101 [132], which

were developed for simply-supported and continuous beams. Upon a review of other existing empirical and rational analytical models available in assessing the stresses and flexural capacity of unbonded post-tensioned beams (e.g. [85, 126, 171]), it was found that equations derived for beam mid-span flexural capacity often underestimate the increase in post-tensioning forces due to seismic action.

The analytical method described in the preceding sub-sections has been modified from a analytical procedure developed and validated for new beam-column joint connection using unbonded post-tensioning and mild steel non-prestressed reinforcement (either internal or external). Thus, it needs to be validated against a wide range of retrofitted beam-column joint typologies. Some inaccuracies and discrepancies with experimental results are expected due to the assumptions made. For example, in calculating the strain of the non-prestressed reinforcements (§3.4.5.2), non-compatibility of unbonded beam reinforcements' strains is assumed, while in reality, prior to the flexural cracking and debonding of the beam-reinforcement, this assumption is untrue.

Another limitation of the analytical model is the lack of consideration for the complex interaction between bond degradation and strain-hardening of the plain-round bar reinforcements at high rotation levels. Neglecting the bond degradation and including the strain-hardening would both result in over-prediction of M_b in high drift rotations and vice versa.

An anticipated consequence of the pseudo-rocking assumption is the possible over-prediction in the early stages of the loading prior to significant flexural cracking in the post-tensioned beams. This is because the pseudo-rocking assumption used to calculate the strains in the post-tensioning tendons (§3.4.5.1) assumes an instantaneous gap opening beyond the decompression point ($\phi=\phi_{dec}$). In reality, a more gradual and complex cracking sequence of the retrofitted beam would need to take place before any elongation of the tendons takes place. Naturally, if the advanced-controlled rocking SW retrofit technique as shown in Figure 3.29d is used, the actual inelastic mechanism would be very similar to rocking joints.

Figure 3.38 gives an example of analytical output for a beam-column joint retrofitted with post-tensioning and beam selective weakening when compared to the experimental test results (to be presented in Chapter 6). It can be observed that the analytical procedure adopted for the section and connection analysis gives a reasonably good analytical-experimental comparison in

predicting the global force-displacement behaviour, post-tensioning forces and neutral axis responses.

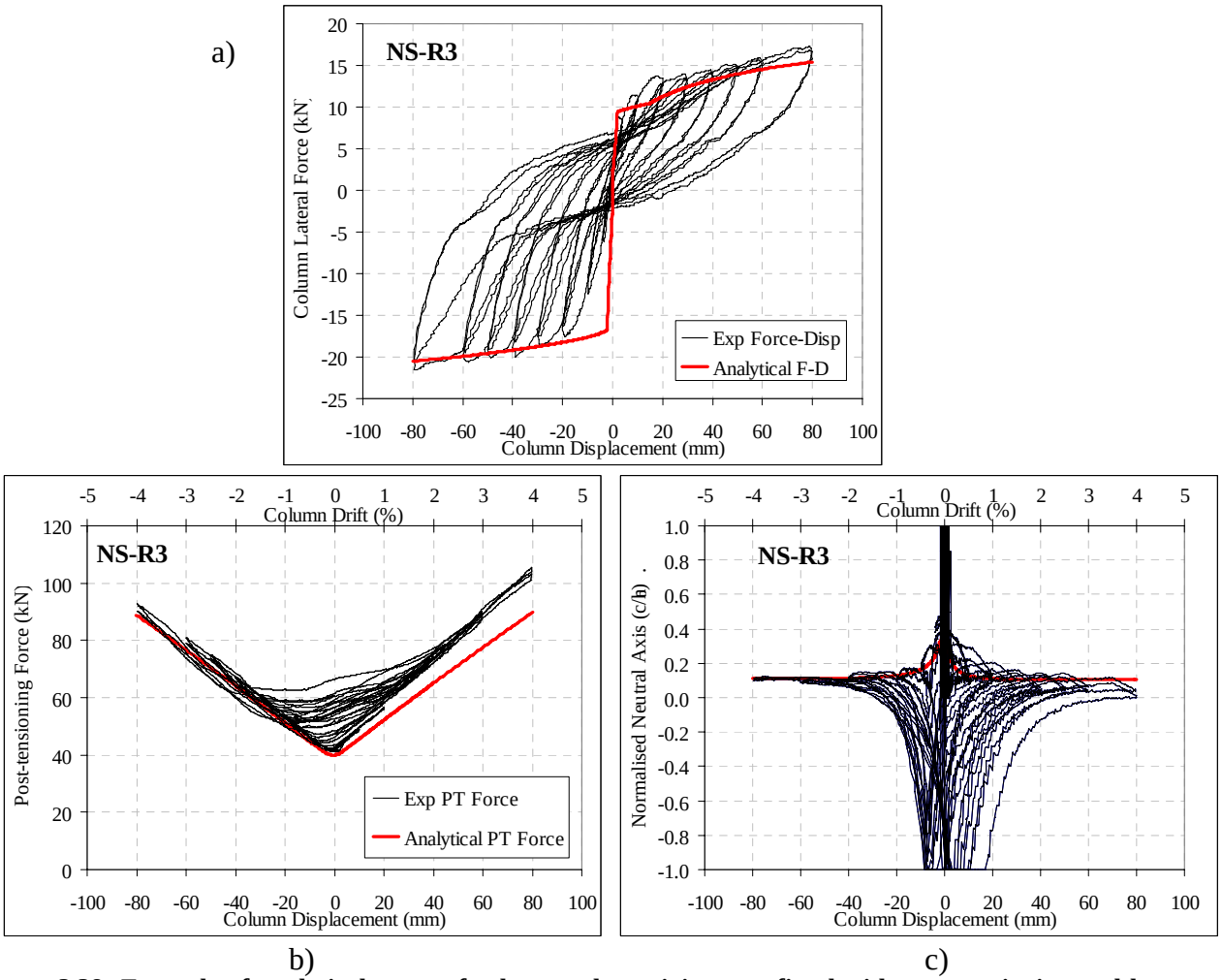

Figure 3.38: Example of analytical output for beam-column joint retrofitted with post-tensioning and beam selective weakening: a) Moment-rotation response; b) Post-tensioning tendon force c) neutral axis at the pseudo-rocking section.

3.4.6 Assessment of joint shear capacity with post-tensioning retrofit intervention

While joint external post-tensioning improves the joint shear capacity in several ways as discussed in §3.3.3, the principal tensile stress equation (given in Equation 3.25) can quantify the increase in v_{jh} prior to diagonal joint cracking. The horizontal post-tensioning forces provide the horizontal axial stress, f_h, in which a higher f_h signifies a larger Mohr's circle radius (given by the square root term in Equation 3.25). Figure 3.39 illustrates how joint post-tensioning effectively enlarges the Mohr's circle and shifts it towards the compression limit state. It is difficult to determine whether the principal angle, ϕ_p, would rotate under increasing f_h but the net effect would always be an increase in v_{jh}, slight reduction of p'_t and an increase of p'_c. Intuitively, this

may also indicate excessive joint post-tensioning forces would lead to joint diagonal compressive failure if the p'_c exceeds the crushing limit state (assumed as $0.3f'_c$ MPa [167]).

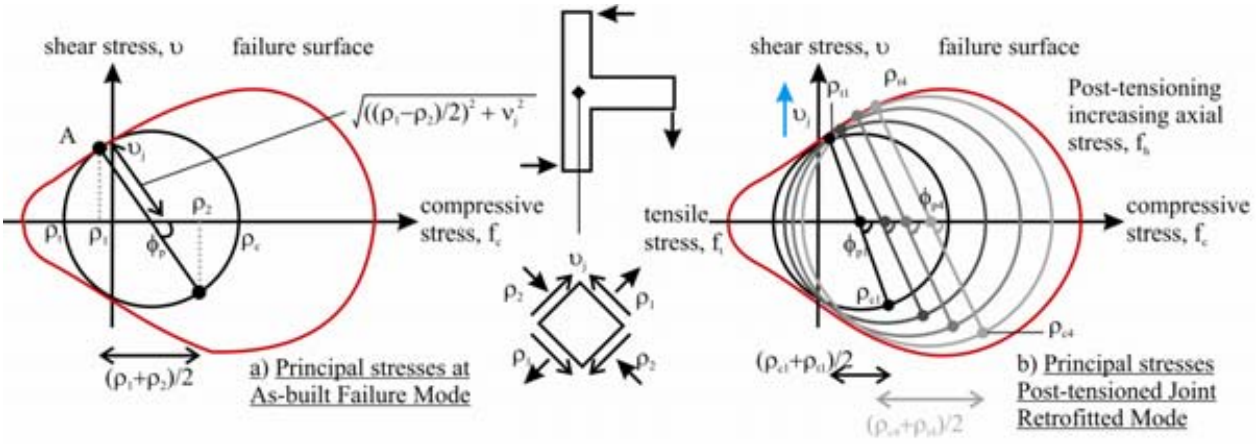

Figure 3.39: Joint post-tensioning in shifting Mohr's circle and enhancing joint shear capacity.

Depending on the configuration of the external post-tensioning anchorage, there would be some level of active confinement of the joint core region. Added confinement would prevent the cracked joint dilation and delay the loss of the interlock joint shear transfer across the cracked joint. While some concrete codes such as the NZS3101[132] and the ACI-318 [2] acknowledge the positive contribution of added confinements, there is no clear evidence of increase p'_t and p'_c limit states, unlike the joint aspect ratio in literature. Tentatively, the limit state for p'_t is suggested to be $0.25\sqrt{f'_c}$ MPa, which is about 30% higher than the value used for the as-built joint assessment ($p'_t = 0.19\sqrt{f'_c}$ MPa). If beam-weakening is used in conjunction with joint-post-tensioning, then the proposed Equation 3.28 can be adopted to conservatively estimate the joint diagonal cracking limit state for p'_t.

3.4.7 Retrofitted beam-column joint M-N performance domain

Finally, after establishing the capacities of the as-built and retrofitted elements, the hierarchy of strength of the beam-column joint can be compared within the M-N performance domain. The selective beam-weakening and the joint post-tensioning or the combination of both would affect the beam and joint capacities differently. Figure 3.40 and Figure 3.41 illustrate the effects of selective beam-weakening and joint post-tensioning on the hierarchy of strength of some examples of retrofitted pre-1970s beam-column joints with 330x230mm beam and 230x230mm column (similar to the test specimens to be described in Chapter 4).

From the beam-weakening-only retrofit example shown in Figure 3.40, the saw-cutting of the bottom longitudinal reinforcements and a depth of the concrete decreases the positive beam flexural strength (given by the beam capacities on the 'decreasing axial load' direction). On the other hand, the joint capacity increases depending on the depth of the saw-cutting. Therefore, by controlling the quantity of beam-weakening and depth of saw-cutting, the required beam-yielding inelastic mechanism can be 'designed' for both decreasing and increasing axial load directions. As will be explained further in §4.6.3, the positive beam moment corresponds to the decreasing of the column axial load in exterior beam-column joint, and vice versa, e.g. negative beam moment would correspond to the increasing of column axial load.

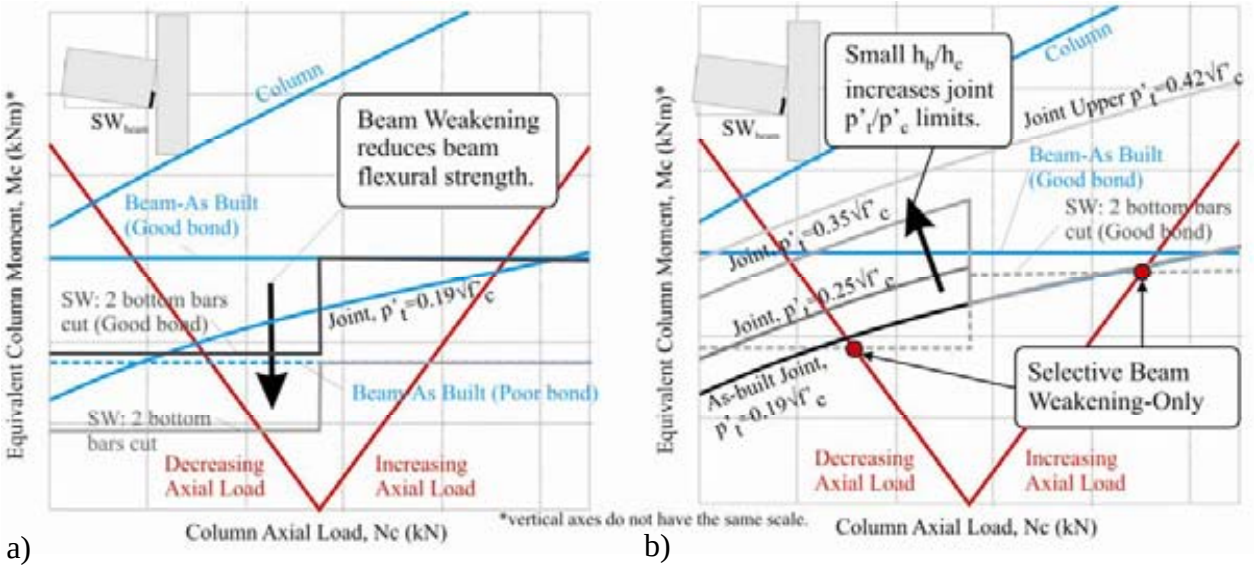

Figure 3.40: Effects of selective beam-weakening retrofit on M-N performance domain of beam-column joints: a) Reduction of positive flexural strength from bottom bars cut; b) Strengthening of joint shear capacity.

In the joint post-tensioning-only retrofit example shown in Figure 3.41, unbonded post-tensioning increases both the beam flexural and joint shear capacities. Therefore depending on the as-built column capacity, careful adjustment of the post-tensioning initial force is required in order to achieve the correct inelastic mechanism. In the example in Figure 3.41b, where 120kN joint post-tensioning retrofit is used, it can be observed that beam-hinging mechanism is hard to be obtained in a post-tensioned-only retrofit solution, without any strengthening of the column. This example here draws to the strength of SW retrofit, in which the combination of beam-weakening and joint post-tensioning would therefore yield an improved solution (or arguably joint post-tensioning in conjunction of strengthening of the columns and foundations).

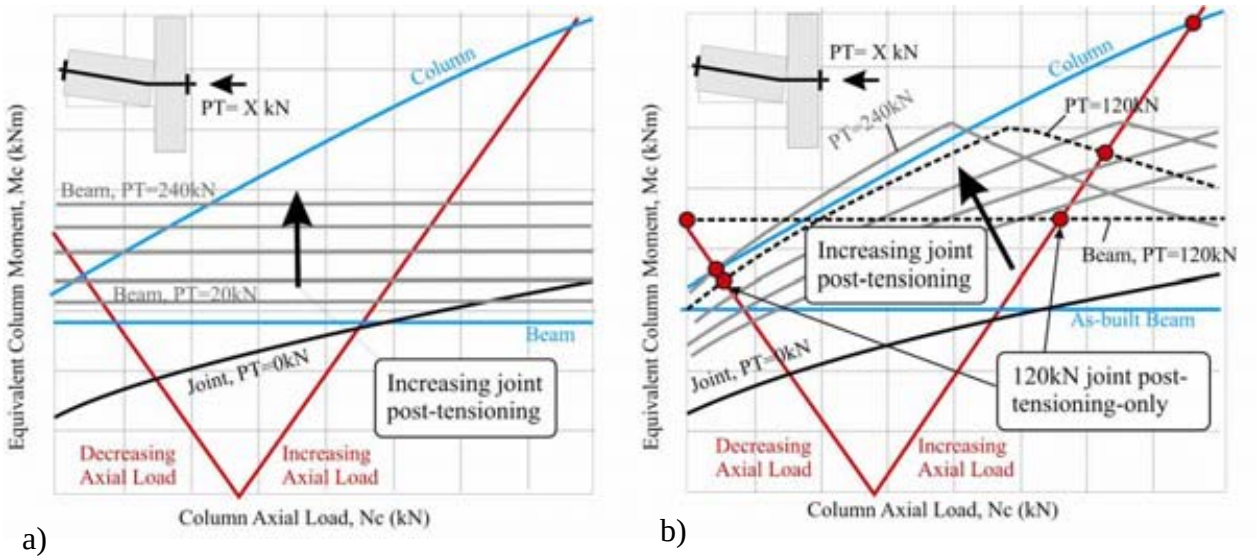

Figure 3.41: Effects of external post-tensioning of beam-column joints: a) Strengthening of beam capacity at pseudo-rocking interface; b) Strengthening of joint shear capacity.

As described in §3.4.2.5, the required flexural strengths of exterior spans' beams, $M_{c,b\text{-}ext}$, to achieve the required global performance level ($\sim M_{c,bf,\theta}$) can be included within the M-N performance domain in order to determine the post-retrofitted global frame performance. Figure 3.42 illustrates an example of a SW retrofit design within the M-N domain for a six-storey three-bay non-ductile RC frame. This case-study building is the same prototype building used for the experimental design, with further details provided in §4.2. In the example, design Equation 3.14 is satisfied for the BSO performance level at global θ_{drift} of 2.5%, which is the specification for the ultimate limit state in NZS1170:5 [129]. Of interest, the LRO performance level (collapse prevention θ_{drift} of 4.0%) is also plotted in Figure 3.42. The $M_{c,b\text{-}ext}$ values are generated using the procedure described in §3.4.2.

In generating the example in Figure 3.42, the 100%NBS of the seismic design action is used, instead of the 33%NBS or 67%NBS as currently required in the 2004 Building Act in New Zealand. If the lower seismic demand is required/expected, then the corresponding $M_{c,b\text{-}ext}$ would also be significantly lower. As alluded in §3.4.2.1, the SW design procedure outlined herein would inherently include capacity design principles and aim to achieve ductile failure modes regardless of the targeted performance levels (θ_{drift} or θ_c corresponding to the 33%NBS or 100%NBS).

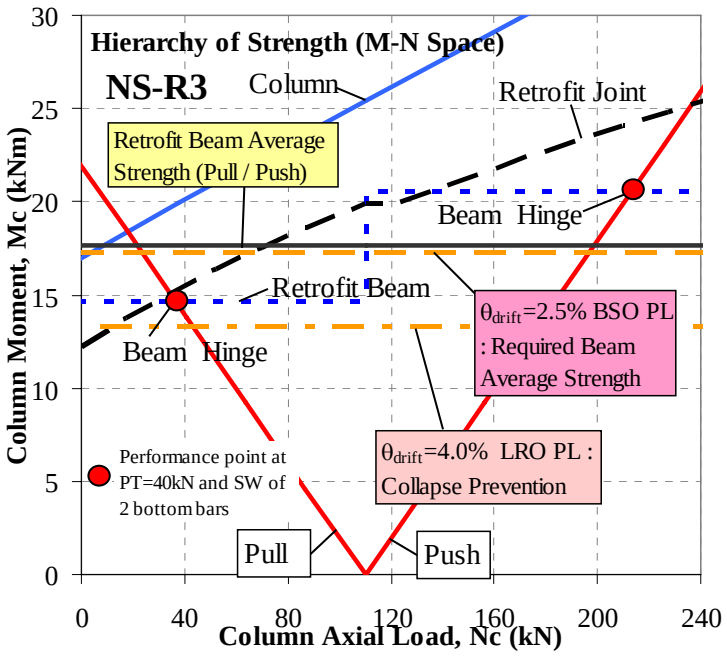

Figure 3.42: Example of retrofitted hierarchy of strength (capacity) and required beam capacities given a performance level (demand) within the M-N performance domain. The example is for a full SW retrofit with selective-weakened and post-tensioned beam-column joint.

3.5 SUMMARY AND CONCLUSIONS

1. A brief introduction of philosophy of seismic retrofit and performance-based seismic retrofit is given in §3.1. The development of performance-based seismic retrofit and the fundamental shift from a force- and strength-based towards a displacement-based seismic engineering gives an opportunity to adopt a multi-level displacement-based retrofit strategy where *partial retrofit* and *full retrofit* strategies can be developed to achieve the required performance objectives – depending on owners and designers' choice.

2. The review of existing seismic retrofit *strategies* and their implementations using various global and local seismic retrofit *techniques* in §3.2 highlights the lack of considerations for hierarchy of strength and the suitable damage parameters (e.g. θ_{drift}) in controlling the inelastic mechanisms and global structural damages. Holistic consideration of the interactions between different connection structural elements within a beam-column joint or a RC frame is also not evident in existing seismic retrofit guidelines and research.

3. *Global retrofit techniques* for RC frames (§3.2.2), while generally effective, are often intrusive and potentially costly. Integration with existing structures and continuity of local load path through existing, possible brittle elements (e.g. foundation) can be complex and expensive to be achieved.

4. *Local retrofit techniques* for beam-column joints (§3.2.3) include selective retrofit, local element jacketing using concrete, steel or composite materials, added steel elements/devices and joint prestressing. Most reviewed local retrofit techniques indicate some level of success in achieving the required structural performance objectives. However, issues of cost, constructability and effectiveness of the local retrofit on global structural behaviour are still unresolved. Many local retrofit techniques (e.g. FRP jacketing, joint prestressing) may result in excessive over-strengthening, which in turn will cause excessive damage if not failures in other parts of the structure and sub-structure (e.g. foundation).

5. From the literature of the existing local retrofit strategies and techniques for beam-column joints summarised in §3.2.3, several consistent *literature gaps* are identified:
    a. The influence of floor slab and transverse beam on the practicality and effectiveness of the retrofit solution is not widely considered, apart from several studies on FRP-retrofit of beam-column joints [59, 202].
    b. Many studies considered isolated structural deficiency (e.g. beam-column joint shear, weak-column strong-beam flexural ratio, column lap-splice, etc) with relatively few beam-column joint subassembly tests on realistic and worse-case scenarios of pre-1970s as-built beam-column joints.
    c. Plain round reinforcements, while widely used around the world from up to the 1980s, have generally been ignored in research. The influence of bond failure on the seismic performance and joint shear mechanism of pre-1970s beam-column joints is not fully understood or researched.

6. The concept of *Selective Weakening (SW) retrofit* for non-ductile RC structures has been conceived based on the need for a cheap and economical retrofit solution for non-ductile

RC frames and joints that are able to meet the required performance objectives with reasonable confidence (§3.3.1). This counter-intuitive seismic retrofit solution is developed based on the review of existing research on retrofit techniques for non-ductile RC beam-column joints, shear-dominated walls, and pre-Northridge steel moment-resisting joints (summarised in §3.3.2).

7. The SW retrofit strategy fundamentally aims at improving the global response of the RC structure by: a) *decreasing seismic demand* onto brittle elements and overall structure and sub-structure via selective weakening of structural elements; and b) *increasing deformation capacity* of the global structure by changing both the local and global inelastic mechanism. The required performance levels of structural and non-structural elements can be designed for and achieved by combining selective weakening of structural elements and subsequent targeted upgrade using existing local retrofit techniques (e.g. external post-tensioning).

8. The proposed SW retrofit *strategy* for non-ductile RC frame is formally introduced in §3.3.3 with qualitative discussions on four SW retrofit *techniques* for exterior beam-column joints: a) Beam-weakening only; b) Beam-column joint post-tensioned only; c) Full selective weakening (beam-weakening and post-tensioning) retrofit; and d) Advanced controlled-rocking hybrid retrofit.

9. A comprehensive SW retrofit design methodology is provided in §3.4, covering general retrofit design philosophy, a displacement-based global seismic retrofit design, quick SW retrofit design method and detailed analytical assessments for beam-weakening and/with post-tensioned retrofitted beam-column joints. The SW retrofit design philosophy (§3.4.1) is based on the comparison of hierarchy of strength of the beam-column joint within the M-N performance domain.

10. An innovative displacement-based retrofit design procedure is developed and presented in §3.4.2. Based on the fundamental theory of DDBD [165], a simple four-step procedure to derive the lower bound of required post-SW-retrofitted beam flexural strength as well as

to estimate the PLs given a M-N performance domain of the retrofitted beam-column joints. Further studies to understand the possible refinements of the equivalent viscous damping – ductility relationship and mixed inelastic mechanism modifications are required.

11. In §3.4.4, the effect of selective beam-weakening on the beam-flexural strength and joint shear capacity is discussed. In particular, a semi-empirical model for the increase in joint shear strength (in terms of p'_t) given a lower joint aspect ratio, which is achieved from saw-cutting of the beam, is developed using principal stresses analysis and basic mechanics.

12. Adopting the same analytical framework for controlled rocking beam-column joints based on jointed-ductile post-tensioned 'hybrid' connections (e.g. [131, 146]), an analytical tool to assess the moment-rotation of the post-tensioned beam-column joint is developed. Accurate assessment of the increase in beam-strength due to unbonded post-tensioning (of the joint) is critical in establishing the correct hierarchy of strength of the beam-column joint. Similarly, accurate assessments of the increase post-tensioning forces and its effect on the joint shear strength are critical towards a successful SW retrofit design.

13. While a brief discussion is made on the performance-based seismic retrofit (§3.1.2) and practical targeted retrofit performance level (§3.4.2.1), the SW design method outlined in §3.4 inherently includes capacity design principles and aims to achieve ductile failure modes regardless of the targeted performance levels (θ_{drift} or θ_c corresponding to the 33%NBS or 100%NBS). This reaffirms the fundamental principal of the SW retrofit: using the capacity design principles for seismic retrofit strategy to achieve ductile inelastic mechanism and adequate deformation capacities, as set out in the introduction of this chapter (§3.1).

3.6 CHAPTER 3 REFERENCES

[1] Aalami BO, Swanson DT. (1988) Innovative rehabilitation of a parking structure. *Concrete International: Design & Construction*. Feb 1988; **10**(2):30-35.

[2] ACI318-08. (2008) *Building code requirements for structural concrete and commentary*. American Concrete Inst. (ACI), Farmington Hills, MI.

[3] ACI-ICRI. (2008) *Concrete repair manual - Vol. 1 and 2*. 3rd ed. American Concrete Inst. (ACI) and Intl. Concrete Repair Inst. (ICRI), Farmington Hills, MI.

[4] AIJ-1999. (1999) *Design guidelines for earthquake resistant RC buildings based on inelastic displacement concept*. Architectural Inst. of Japan (AIJ), Tokyo, Japan.

[5] Akguzel U, Pampanin S. (2009) Analytical model for shear strengthening of RC beam-column joints using composite materials. *Proc. of NZSEE 2009 Conf*, NZSEE, Christchurch, NZ, p. 10.Paper No. 53.

[6] Akguzel U, Pampanin S. (2010) Effects of variation of axial load and bidirectional loading on seismic performance of GFRP retrofitted reinforced concrete exterior beam-column joints. *ASCE J of Composite Constr*. Jan-Feb 2010; **14**(1):94-104.

[7] Alcocer SM, Jirsa JO. (1993) Strength of reinforced concrete frame connections rehabilitated by jacketing. *ACI Structural Journal*. May-June 1993; **90**(3):249-261.

[8] Almusallam TH, Al-Salloum YA. (2007) Seismic response of interior RC beam-column joints upgraded with FRP sheets. II: Analysis and parametric study. *ASCE J of Composite Constr*. Nov-Dec 2007; **11**(6):590-600.

[9] Antonopoulos CP, Triantafillou TC. (2002) Analysis of FRP-strengthened beam-column joints. *ASCE J of Composite Constr*. Feb 2002; **6**(1):41-51.

[10] Antonopoulos CP, Triantafillou TC. (2003) Experimental investigation of FRP-strengthened RC beam-column joints. *ASCE J of Composite Constr*. **7**(1):39-49.

[11] ASCE-SEI-41-06. (2007) *Seismic rehabilitation of existing buildings. ASCE standard ASCE/SEI 41-06*. American Society of Civil Engineers (ASCE), Reston, Va.

[12] ATC-58. (2009) *Guidelines for Seismic Performance Assessment of Buildings, ATC-58 50% Draft*. Applied Technology Council (ATC), Redwood, CA.

[13] Badoux M, Jirsa JO. (1990) Steel bracing of RC frames for seismic retrofitting. *ASCE J of Struct Eng*. Jan 1990; **116**(1):55-74.

[14] Bakir PG, Boduroglu HM. (2002) A new design equation for predicting joint shear strength of monotonically loaded exterior beam-column joints. *Eng Structures*. **24**:1105-1117.

[15] Bedirhanoglu I, Ilki A, Pujol S, Kumbasar N. (2010) Behaviour of deficient joints with plain bars and low-strength concrete. *ACI Structural Journal*. May-June 2010; **107**(3):300-310.

[16] Beres A, El-Borgi S, White R, Gergely P. (1992) *Experimental results of repaired and retrofitted beam-column joint tests in lightly reinforced concrete frame buildings. Technical Report NCEER-92-0025*. National Center for Earthquake Eng. Research, SUNY, Buffalo, NY.

[17] Biddah A, Ghobarah A, Aziz T. (1999) Upgrading of nonductile reinforced concrete frame connections. *ASCE J of Struct Eng*. **123**(8):1001-1010.

[18] Billington SL, Kyriakides MA, Blackard B, Willam K, Stavridis A, Shing B. (2009) Evaluation of a sprayable, ductile-cement-based composite for the seismic retrofit of unreinforced masonry infills. *Proc. of ATC-SEI Conf, on Improving the Seismic Performance of Existing Buildings and Other Structures*, San Francisco, CA,

[19] Blakeley RWG, Park R. (1971) Seismic resistance of prestressed concrete beam-column assemblies. *ACI Structural Journal*. May 1971; **68**(9):677-692.

[20] Bousselham A. (2010) State of research on seismic retrofit of RC beam-column joints with externally bonded FRP. *ASCE J of Composite Constr*. Feb 2010; **14**(1):49-61.

[21] Bracci JM, Reinhorn AM, Mander JB. (1992) *Evaluation of seismic retrofit of reinforced concrete frame structures: Part II - Experimental performance and analytical studies of a retrofitted structural model, NCEER Report No. NCEER-92-0031*. National Center for Earthquake Eng. Research, SUNY, Buffalo, NY.

[22] Bruneau M, Engelhardt MD, Filiatrault A, Goel SC, Itani A, Hajjar J, et al. (2005) Review of selected recent research on US seismic design and retrofit strategies for steel structures. *Prog in Struct Eng Material (EESD)*. **7**:103-114.

[23] Budek A, Benzoni G. (2007) Providing external confinement to flexural members to improve ductility - the good, the bad and the ugly. In: Alkhrdahi T, Silva P, editors. *Seismic Strengthening of Concrete Buildings using FRP Composites CD-ROM, SP-258CD*. American Concrete Inst. (ACI), Farmington Hills, MI; p. SP-258-255.

[24] Bush TD, Jones EA, Jirsa JO. (1991) Behaviour of RC frame strengthened using structural steel bracing. *ASCE J of Struct Eng*. Apr 1991; **117**(4):1115-1126.

[25] Bush TD, Wyllie LAJ, Jirsa JO. (1991) Observations on two seismic strengthening schemes for concrete frames. *Earthquake Spectra*. **7**(4):511-527.

[26] Cardone D, Dolce M, Ponzo FC. (2004) Experimental behaviour of R/C frames retrofitted with dissipating and re-centering devices. *J of Earthquake Eng*. **8**(3):361-396.

[27] Carvalho EC, Coelho E. (2001) *Seismic assessment, strengthening and repair of structures*. Laboratorio Nacional de Engenharia Civil, Lisbon, Portugal.

[28] Chaimahawan P, Pimanmas A. (2009) Seismic retrofit of substandard beam-column joint by planar joint expansion. *Material and Structures (RILEM, Paris)*. **42**:443-459.

[29] Chopra AK, Goel RK. (1999) Capacity-demand-diagram methods based on inelastic design spectrum. *Earthquake Spectra*. Nov 1999; **15**(4):637-656.

[30] Choudhury D, Mander JB, Reinhorn AM. (1992) *Evaluation of seismic retrofit of reinforced concrete frame structures: Part I - Experimental performance of retrofitted subassemblages, NCEER Report No. NCEER-92-003*. National Center for Earthquake Eng. Research, SUNY, Buffalo, NY, USA.

[31] Christopoulos C, Filiatrault A. (2006) *Principles of passive supplemental damping and seismic isolation*. IUSS Press, Pavia, Italy.

[32] Cimellaro GP, Lavan O, Reinhorn AM. (2009) Design of passive systems for control of inelastic structures. *Earthquake Eng & Struct Dyn*. **38**(6):783-804.

[33] Cimellaro GP, Reinhorn AM. (2006) Sensitivity study of weakened structures with supplemental dampers. *Proc. of 4th World Conf on Struct Control and Monitoring (4WCSCM)*, Intl. Assoc. of Struct. Control (IASC), San Diego, CA.Paper No. 79.

[34] Cimellaro GP, Retamales R. (2007) Optimal softening and damping design for buildings. *J of Struct Control and Health Monitoring*. **14**(6):831-857.

[35] Civjan SA, Engelhardt MD, Gross JL. (2000) Retrofit of pre-Northridge moment-resisting connections. *ASCE J of Struct Eng*. **126**(4):445-452.

[36] Civjan SA, Engelhardt MD, Gross JL. (2001) Slab effects in SMRT retrofit connection tests. *ASCE J of Struct Eng*. Mar 2001; **127**(3):230-237.

[37] Clark WD, Mason JE. (2005) Base isolation of an existing 10-storey building to enhance earthquake resistance. *Bull of New Zealand Soc of Earthquake Eng*. Mar 2005; **38**(1):33-40.

[38] Clyde C, Pantelides CP, Reaveley LD. (2000) *Performance-based evaluation of exterior reinforced concrete building joints for seismic excitation. PEER Report 2000/05*. Pacific Earthquake Eng. Res. Center (PEER), Berkeley, CA.

[39] Corazao M, Durrani AJ. (1989) *Repair and strengthening of beam-to-column connections subjected to earthquake loading, NCEER Report No. NCEER-89-13*. National Center for Earthquake Eng. Research, Buffalo, NY.

[40] DBH. (2004) *Building Act 2004*. Dept. of Building and Housing (DBH), Wellington, NZ.

[41] Desroches R, Smith R. (2004) Shape Memory Alloys in seismic resistant design and retrofit: A critical review of their potential and limititations. *J of Earthquake Eng*. **8**(3):415-429.

[42] Di Ludovico M, Manfredi G, Mola E, Negro P, Prota A. (2008) Seismic behaviour of a full-scale RC structure retrofitted using GFRP laminates. *ASCE J of Struct Eng*. 1st May 2008; **134**(5):810-821.

[43] Di Ludovico M, Prota A, Manfredi G, Cosenza E. (2008) Seismic strengthening of an under-designed RC structure with FRP. *Earthquake Eng & Struct Dyn*. **37**(1):141-162.

[44] Dolce M, Cardone D, Moroni C, Nigro D, Palermo G, Ponzo FC, et al. (2006) TREMA Project: Experimental evaluation of the seismic performance of a R/C 1/4 scaled model upgraded with seismic isolation. *Proc. of fib 2nd Intl Congress*, Naples, Italy, p. 12.Paper ID: 9-41.

[45] Dolce M, Cardone D, Moroni C, Nigro D, Ponzo FC, Santarsiero G, et al. (2006) SICURO and TREMA Projects: the seismic performance of R/C frames seismically upgraded with different systems. *Proc. of fib 2nd Intl Congress*, Naples, Italy, p. 12.Paper ID: 9-39.

[46] Dolce M, Cardone D, Ponzo FC. (2007) Shaking-table tests on reinforced concrete frames with different isolation systems. *Earthquake Eng & Struct Dyn*. **36**(5):573-596.

[47] Dolce M, Cardone D, Ponzo FC, Valente C. (2005) Shaking table tests on reinforced concrete frames without and with passive control systems. *Earthquake Eng & Struct Dyn*. **34**(14):1687-1717.

[48] Dolce M, Moroni C, Nigro D, Ponzo FC, Goretti A, Spina D, et al. (2006) TREMA Project: Experimental evaluation of the seismic performance of a R/C 1/4 scaled model upgraded with FRP. *Proc. of fib 2nd Intl Congress*, Naples, Italy, p. 12.Paper ID: 9-42.

[49] Dolce M, Moroni C, Nigro D, Ponzo FC, Santarsiero G, Di Croce M, et al. (2006) TREMA Project: Experimental evaluation of the seismic performance of a R/C 1/4 scaled model upgraded with the DIS-CAM system. *Proc. of fib 2nd Intl Congress*, Naples, Italy, p. 13.Paper ID: 9-40.

[50] Dutta A, Mander JB, Kokorina T. (1999) Retrofit for control and repairability of damage. *Earthquake Spectra*. Nov 1999; **15**(4):657-679.

[51] El-Amoury T, Ghobarah A. (2002) Seismic rehabilitation of beam-column joints using GFRP sheets. *Eng Structures*. **24**(11):1397-1407.

[52] El-Attar AG, White R, Gergely P. (1997) Behaviour of gravity load design reinforced concrete buildings subjected to earthquakes. *ACI Structural Journal*. Mar 1997; **94**(2):133-145.

[53] Elgawady M, Lestuzzi P, Badoux M. (2004) A review of conventional seismic retrofitting techniques for URM. *Proc. of 13th Intl Brick and Block Masonry Conf*, Amsterdam, p. 10

[54] Eligehausen R, Genesio G, Ožbolt J, Pampanin S. (2008) 3D analysis of seismic response of RC beam-column exterior joints before and after retrofit. *Proc. of ICCRRR2008*, Cape Town, South Africa,

[55] Elnashai AS, Pinho R. (1998) Repair and retrofitting of RC walls using selective techniques. *J of Earthquake Eng*. **2**(4):525-568.

[56] Elnashai AS, Pinho R, Vaz CT. (2000) Experimental observations from shaking-table tests on selective techniques for repair and strengthening of RC walls. *Proc. of 12th World Conf on Earthquake Eng*, Auckland, NZ.Paper No. 2245.

[57] Elnashai AS, Salama AI. (1992) *Selective repair and retrofitting techniques for RC structures in seismic regions. Report No. ESEE/92-2*. Imperial College, London, UK.

[58] Engelhardt MD, Winneberger T, Zekany AJ, Potyraj TJ. (1998) Experimental investigation of dogbone moment connection. *Eng J*. **35**(4):128-139.

[59] Engindeniz M. (2008) Repair and strengthening of pre-1970s reinforced concrete corner beam-column joints using CFRP composites [PhD Dissertation]. Georgia Inst. of Tech., Altanta.

[60] Engindeniz M, Kahn L, Abdul-Hamid Z. (2005) Repair and strengthening of reinforced concrete beam-column joints: state-of-the-art. *ACI Structural Journal*. Mar-April 2005; **102**(2):1-14.

[61] Engindeniz M, Kahn L, Zureick A-H. (2008) Performance of an RC corner beam-column joint severely damaged under bidirectional loading and rehabilitated with FRP composite. In: Alkhrdahi T, Silva P, editors. *Seismic strengthening of concrete buildings using FRP composites, SP-258*. American Concrete Inst. (ACI), Farmington Hills, MI; p. 19-36.

[62] Englekirk RE, Sabol TA. (1991) Strengthening buildings to a life safety criterion. *Earthquake Spectra*. Feb 1991; **7**(1):81-87.

[63] FEMA-273/274. (1997) *NEHRP guidelines for the seismic rehabiliation of buildings (and commentary)*. Federal Emergency Management Agency (FEMA), Washington, D.C.

[64] FEMA-351. (2000) *Recommended seismic evaluation and upgrade criteria for existing welded steel moment-frame buildings*. Federal Emergency Management Agency (FEMA), Washington, D.C.

[65] FEMA-356. (2000) *Pre-standard and commentary for the seismic rehabilitation of buildings.* Federal Emergency Management Agency (FEMA), Washington, D.C.

[66] FEMA-547. (2006) *Techniques for the seismic rehabilitation of existing buildings*. Federal Emergency Management Agency (FEMA), Washington, D.C.

[67] fib. (2003) *Seismic assessment and retrofit of reinforced concrete buildings: State-of-the-art report, fib Bulletin no. 24*. Intl. Fed. for Struct. Concrete (fib), Lausanne, Switzerland.

[68] fib. (2006) *Retrofitting of concrete structures by externally bonded FRPs with emphasis on seismic applications, fib Bulletin no. 35*. Intl. Fed. for Struct. Concrete (fib), Lausanne, Switzerland.

[69] Frosch RJ, Wanzhi L, Jirsa JO, Kreger ME. (1996) Retrofit of non-ductile moment resisting frames using precast infill wall panels. *Earthquake Spectra*. Nov 1996; **12**(4):741-760.

[70] Gencoglu M, Mobasher B. (2008) The rehabilitation of the deficient RC exterior beam-column joints using cement based composites. *Proc. of 14th World Conf on Earthquake Eng*, Beijing, China, p. 8.Paper ID: 12-03-0024.

[71] Genesio G. (2011) Seismic assessment of RC exterior beam-column joints and retrofit with haunches using post-installed anchors (in preparation) [PhD dissertation]. Uni. of Stuttgart, Stuttgart, Germany.

[72] Genesio G, Eligehausen R, Pampanin S. (2010) Seismic assessment of pre-1970s RC beam column-joints. *Proc. of 14th European Conf on Earthquake Eng*, Ohrid, Macedonia,

[73] Gergely P, Pantelides CP, Reaveley LD. (1998) Shear strengthening of bridge joints with carbon fibre composites. *Proc. of 6th US National Conf on Earthquake Eng*, Earthquake Eng. Research Inst. (EERI), Seattle, WA,

[74] Gergely P, Pantelides CP, Reaveley LD. (2000) Shear strengthening of RC T-joints using CFRP composites. *ASCE J of Composite Constr*. **4**(2):56-64.
[75] Ghobarah A, Aziz T, Biddah A. (1996) Seismic rehabilitation of reinforced concrete beam-column connections. *Earthquake Spectra*. Nov 1996; **12**(4):761-780.
[76] Ghobarah A, Aziz T, Biddah A. (1997) Rehabilitation of reinforced concrete frame connections using corrugated steel jacketing. *ACI Structural Journal*. **94**(3):283-294.
[77] Ghobarah A, El-Amoury T. (2005) Seismic rehabilitation of deficient exterior concrete frame joints. *ASCE J of Composite Constr*. 1st Oct 2005; **9**(5):408-416.
[78] Ghobarah A, Said A. (2001) Seismic rehabilitation of beam-column joints using FRP laminates. *J of Earthquake Eng*. **5**(1):113-129.
[79] Ghobarah A, Said A. (2002) Shear strengthening of beam-column joints. *Eng Structures*. July 2002; **24**(7):881-888.
[80] Giovinazzi S, Pampanin S, Lagomarsino S. (2006) Alternative retrofit strategues for pre'70 R.C. buildings: Vulnerability models and damage scenario. *Proc. of 1st European Conf on Earthquake Eng and Seismology (1ECEES)*, Geneva, Switzerland.Paper No. 1148.
[81] Gross JL, Engelhardt MD, Uang C-M, Kasai K, Iwankiw NR. (1999) *AISC Design Guide Series No. 12: Modification of existing welded steel moment frame connections for seismic resistance*. American Inst. of Steel Construction (AISC), Chicago, IL.
[82] Hamahara M, Nishiyama M, Okamoto H, Watanabe F. (2007) Design for shear of prestressed concrete beam-column joint cores. *ASCE J of Struct Eng*. **133**(11):1520-1530.
[83] Hanson NW, Conner HW. (1967) Seismic resistance of reinforced concrete beam-column joints. *ASCE Journal of Structural Division*. **95**(5):533-560.
[84] Hanson NW, Conner HW. (1972) *Tests of reinforced concrete beam-column joints under simulated seismic loading. Report No. RDO12.01D*. Portland Cement Association.
[85] Harajli MH. (2006) On the stress in unbonded tendons at ultimate: Critical assessment and proposed changes. *ACI Structural Journal*. Nov-Dec 2006; **103**(6):803-812.
[86] Hegger J, Sherif A, Roeser W. (2003) Nonseismic design of beam-column joints. *ACI Structural Journal*. **100**(5):654-664.
[87] Hertanto E. (2006) Seismic assessment of pre-1970s reinforced concrete beam column joint subassemblies. [M.E. dissertation]. Uni. of Canterbury, Christchurch, NZ.
[88] Higashi Y, Ohkubo M, Fujimata K. (1977) Behaviour of reinforced concrete columns and frames strengthened by adding precast concrete walls. *Proc. of 6th Wolrd Conf on Earthquake Eng*, 2505-2510, New Dehli, India,
[89] Hoffschild TE, Prion HGL, Cherry S. (1993) Seismic retrofit of beam-to-column joints with grouted steel tubes. *Tom Paulay Symposium: Recent developments in lateral force transfer in buildings, (also as SP-157)*. American Concrete Inst. (ACI), La Jolla, CA; p. 403-431.
[90] Hwang SJ, Chiou T-C, Hsiao F-P, Chiou YJ, Alcocer SM. (2008) Field test of RC school building retrofitted by post-tensioned rods. *Proc. of 14th World Conf on Earthquake Eng*, Beijing, China.Paper No. S15-028.
[91] ICRI. (2006) Guide for the selection of strengthening systems for concrete structures. ICRI Technical Guidelines No. 03742. *Concrete Repair Manual, 3rd ed*. American Concrete Inst. (ACI) / Intl. Concrete Repair Inst. (ICRI), Farmington Hills, MI; p. 1243-1271.
[92] Ingham JM. (1995) Seismic performance of bridge knee joints [PhD Dissertation]. Uni. of California, San Diego La Jolla, CA.

[93] Ingham JM, Priestley MJN, Seible F. (1997) Seismic response of bridge knee joints having columns with interlocking spirals. *Bull of New Zealand Soc of Earthquake Eng*. June 1997; **30**(2):114-132.

[94] Ingham JM, Priestley MJN, Seible F. (1998) Cyclic response of bridge knee joints with circular columns. *J of Earthquake Eng*. July 1998; **2**(3):357-391.

[95] Ireland MG. (2007) Development of a selective weakening approach for the seismic retrofit of reinforced concrete structural walls . [M.E.]. Uni. of Canterbury, Christchurch, NZ.

[96] Ireland MG, Pampanin S, Bull DK. (2007) Experimental investigations of a selective weakening approach for the seismic retrofit of r.c. walls. *Proc. of NZSEE Conf 2007*, NZSEE, Palmerston North, NZ.Paper No. 16.

[97] Iwankiw NR. (2004) Seismic design enhancements and the reduced beam section detail for steel moment frames. *ASCE Prac Periodical on Struct Des and Const*. May 2004; **9**(2):87-92.

[98] Jensen J. (2006) The seismic behaviour of existing hollowcore seating connections pre and post retrofit [ME Thesis]. Uni. of Canterbury, Christchurch.

[99] Jensen J, Bull DK, Pampanin S. (2007) Experimental investigation of existing hollowcore seating connection: Seismic behaviour pre and post retrofit intervention. *Proc. of NZSEE Conf 2007*, NZSEE, Palmerston North, NZ.Paper No. 12.

[100] Jones SL, Fry GT, Engelhardt MD. (2002) Experimental evaluation of cyclically loaded reduced beam section moment connections. *ASCE J of Struct Eng*. Apr 2002; **128**(4):441-451.

[101] Kam WY, Pampanin S. (2008) Selective weakening techniques for retrofit of existing reinforced concrete structures. *Proc. of 14th World Conf on Earthquake Eng*, Beijing, China.Paper ID: 05-03-0074.

[102] Kam WY, Pampanin S, Palermo A, Carr A. (2010) Self-centering structural systems with combination of hysteretic and viscous energy dissipations. *Earthquake Eng & Struct Dyn*. Aug 2010; **39**(10):1083-1108.

[103] Karayannis CG, Chalioris CE, Sirkelis GM. (2008) Local retrofit of exterior RC beam-column joints using thin RC jackets - an experimental study. *Earthquake Eng & Struct Dyn*. **37**:727-746.

[104] Karayannis CG, Sirkelis GM. (2008) Strengthening and rehabilitation of RC beam-column joints using carbon-FRP jacketing and epoxy resin injection. *Earthquake Eng & Struct Dyn*. **37**(5):769-790.

[105] Kim J, LaFave JM. (2008) Joint shear behaviour prediction in RC beam-column connections subjected to seismic lateral loading. *Proc. of 14th World Conf on Earthquake Eng*, Beijing, China.Paper No. 05-03-0070.

[106] King DJ, Priestley MJN, Park R. (1986) *Computer programs for concrete column design. UC Research Report 86/12.* Dept of Civil Eng., Uni. of Canterbury, Christchurch, NZ.

[107] Kitajima K, Yokouchi H, Chikui H, Adachi H. (2005) Seismic retrofit method by means of external damping braces using friction dampers. *Proc. of Intl Symposium on Earthquake Eng (ISEE Kobe 2005)*, Kobe, Japan, p. C193-201.Paper ID. C22.

[108] Kono S, Katayama T. (2009) Seismic retrofit of reinforced concrete building structures using prestressed braces. *Journal of Advanced Concrete Technology (ACT)*. **7**(3):337-345.

[109] Kuroki M, Kikuchi K, Sakino K, Yamakawa T. (2008) Splitting bond strength of main steel bars in R/C columns retrofitted with prestressed external hoops. *Proc. of 14th World Conf on Earthquake Eng*, Beijing, China.Paper No. 05-03-0184.

[110] Lee WT, Chiou YJ, Shih MH. (2010) Reinforced concrete beam-column joint strengthened with carbon fiber reinforced polymer. *Composite Structures*. **92**(1):48-60.
[111] Li B, Chua GHY. (2009) Seismic performance of strengthened reinforced concrete beam-column joints using FRP composites. *ASCE J of Struct Eng*. Oct 2009; **135**(10):1177-1190.
[112] Li B, Kulkarni SA. (2010) Seismic behaviour of reinforced concrete exterior wide beam-column joints. *ASCE J of Struct Eng*. Jan 2010; **136**(1):26-36.
[113] Liu A. (2001) Seismic assessment and retrofit of pre-1970s reinforced concrete frame structures, PhD Dissertation [PhD]. Uni. of Canterbury, Christchurch, NZ.
[114] Lowes LN, Moehle JP. (1999) Evaluation and retrofit of beam-column T-joints in older reinforced concrete bridge structures. *ACI Structural Journal*. **96**(4):519-533.
[115] Mander JB, Priestley MJN, Park R. (1988) Theoretical stress-strain model for confined concrete. *ASCE J of Struct Eng*. **114**(8):1804-1826.
[116] Marriott D. (2009) The development of high-performance post-tensioned rocking systems for the seismic design of structures. [PhD dissertation]. Uni. of Canterbury, Christchurch.
[117] Marriott D, Pampanin S, Bull DK, Palermo A. (2007) Improving the seismic performance of existing reinforced concrete buildings using advanced rocking wall solutions. *Proc. of NZSEE 2007*, NZSEE, Palmerston North, NZ.Paper No. 17.
[118] Marriott D, Pampanin S, Bull DK, Palermo A. (2008) Dynamic testing of precast, post-tensioned rocking wall systems with alternative dissipating solutions. *Bull of New Zealand Soc of Earthquake Eng*. **41**(2):90-103.
[119] Masi A, Santarsiero G, Moroni C, Nigro D, Dolce M, Russo G, et al. (2008) Behaviour and strengthening of RC beam-column joints: Experimental program and first results of the research activity in the framework of DPC-RELUIS project (research line 2). *Proc. of 14th World Conf on Earthquake Eng (14WCEE)*, Beijing, China, p. 8.Paper ID: 12-02-0006.
[120] Matthews J, Bull DK, Mander JB. (2003) Hollowcore floor slab performance following a severe earthquake. *Proc. of Concrete Structures in Seismic Region: fib 2003 Symposium*, Athens,
[121] Migliacci A, Antonucci R, Maio NA, Napoli P, Ferretti AS, Via G. (1983) Repair techniques of reinforced concrete beam-column joints. *Proc. of IABSE Symp on Strengthening of Building Struct - Diagnosis and Therapy*, Intl. Assn. of Bridge and Struct. Eng. (IABSE), Zurich, Switzerland, p. 355-362
[122] Miranda E, Bertero VV. (1990) Post-tensioning technique for seismic upgrading of existing low-rise buildings. *Proc. of 4th US Natl Conf on Earthquake Eng*, Palm Springs, CA, p. 393-403
[123] Moehle JP. (1992) Displacement-based design of RC structures subjected to earthquake. *Earthquake Spectra*. **8**(3):403-428.
[124] Moehle JP. (2007) State of research on seismic retrofit of concrete buildings structures in the US. In: Sugano S, editor. *IPS-2 Seismic Rehabilitation of Concrete Structures*. American Concrete Inst. (ACI) / Japan Concrete Inst. (JCI), Farmington Hills, MI; p. Part II, R4.
[125] Mohka AS, Amin N, Constantinou MC, Zayas VA. (1996) Seismic isolation retrofit of large historic building. *ASCE J of Struct Eng*. Mar 1996; **122**(3):298-308.
[126] Naaman AE, Burns N, French CW, Gamble WL, Mattock AH. (2002) Stresses in unbonded prestressing tendons at ultimate: recommendation. *ACI Structural Journal*. July-Aug 2002; **99**(4):518-529.

[127] Nishiyama M, Wei Y. (2007) Effect of post-tensioning steel anchorage location on seismic performance of exterior beam-to-column joints for precast, prestressed concrete members. *PCI Journal*. **52**(2):18-30.

[128] Nishizawa T. (2008) Seismic isolation retrofit for major tall building. *Proc. of 14th World Conf on Earthquake Eng*, Beijing, China.Paper No. S05-01-008.

[129] NZS1170. (2004) *NZS 1170.5:2004 Structural design actions*. Standards New Zealand, Wellington, NZ.

[130] NZS3101:1995. (1995) *NZS 3101:1995 Concrete structures standard*. Standards New Zealand, Wellington, NZ.

[131] NZS3101:2006. (2006) Appendix B: Special provisions for the seismic design of ductile jointed precast concrete structural systems. *NZS3101: 2006, Concrete standards*. Standards New Zealand, Wellington, NZ.

[132] NZS3101:2006. (2006) *NZS 3101:2006 Concrete structures standard*. Standards New Zealand, Wellington, NZ.

[133] NZSEE. (2006) *Assessment and improvement of the structural performance of buildings in earthquakes*. New Zealand Soc. for Earthquake Eng. (NZSEE), Wellington, NZ.

[134] Ortiz IR. (1993) Strut-and-tie modeling of reinforced concrete short beams and beam-column joints. Uni. of Westminister, London, UK.

[135] Palermo A. (2004) The use of controlled rocking in the seismic design of bridges [PhD dissertation]. Politecnico de Milano, Milan, Italy.

[136] Pampanin S. (2005) Emerging solutions for high seismic performance of precast/prestressed concrete buildings. *Journal of Advanced Concrete Technology (ACT)*. **3**(2):202-223.

[137] Pampanin S. (2006) Controversial aspects in seismic assessment and retrofit of structures in modern times: Understanding and implementing lessons from ancient heritage. *Bull of New Zealand Soc of Earthquake Eng*. **39**(2):120-133.

[138] Pampanin S. (2009) Alternative performance-based retrofit strategies and solutions for existing RC buildings. Geotechnical, Geological and Earthquake Eng. vol. 10. In: Ilki A, Karadogan F, Pala S, Yuksel E, editors. *Seismic Risk Assessment and Retrofitting With Special Emphasis on Existing Low Rise Structures*. Springer, Netherlands; p. 267-295.

[139] Pampanin S, Bolognini D, Pavese A. (2007) Performance-based seismic retrofit strategy for existing reinforced concrete frame systems using fiber-reinforced polymer composites. *ASCE J of Composite Constr*. March/April 2007; **11**(2):211-226.

[140] Pampanin S, Bolognini D, Pavese A, Magenes G, Calvi GM. (2004) Multi-level seismic rehabilitation of existing frames and subassemblies using FRP composites. *Proc. of CICE 2004*, Adelaide, Australia,

[141] Pampanin S, Calvi GM, Moratti M. (2002) Seismic behaviour of RC beam-column joints designed for gravity loads. *Proc. of 12th European Conf on Earthquake Eng*, London, UK.Paper 726.

[142] Pampanin S, Christopoulos C. (2003) Non-invasive retrofit of existing RC frames designed for gravity loads only. *Proc. of fib2003 Symposium on Concrete Structures in Seismic Region*, Athens, Greece.Paper No. 170.

[143] Pampanin S, Christopoulos C, Chen T-H. (2006) Development and validation of a haunch metallic seismic retrofit solution for existing under-designed RC frame buildings. *Earthquake Eng & Struct Dyn*. **35**(14):1739-1766.

[144] Pampanin S, Christopoulos C, Priestley MJN. (2002) *Residual deformations in the performance-based seismic assessment of frame structures*. IUSS PRESS, Pavia, Italy,.

[145] Pampanin S, Marriott D, Palermo A, Bolognini D. (2010) *PRESSS Design Handbook*. New Zealand Concrete Society (NZCS), Auckland, New Zealand.

[146] Pampanin S, Priestley MJN, Sritharan S. (2001) Analytical modelling of the seismic behaviour of precast concrete frames designed with ductile connections. *J of Earthquake Eng*. **5**(3):329-367.

[147] Pantelides CP, Clyde C, Reaveley LD. (2002) Performance-based evaluation of reinforced concrete exterior joints for seismic excitation. *Earthquake Spectra*. Aug 2002; **18**(3):449-480.

[148] Pantelides CP, Gergely P, Reaveley LD, Volnyy VA. (1999) Retrofit of RC bridge pier with CFRP advanced composites. *ASCE J of Struct Eng*. **125**(10):1094-1099.

[149] Pantelides CP, Okahashi Y, Reaveley LD. (2008) Seismic rehabilitation of RC frame interior beam-column joints with FRP composites. *ASCE J of Composite Constr*. Aug 2008; **12**(4):435-445.

[150] Park R, Thompson KJ. (1974) *Behaviour of prestressed, partially prestressdd and reinforced concrete interior beam-column assemblies under cyclic loading: test results of units 1 to 7. UC Research Report 74-9.* Dept. of Civil Eng., Uni. of Canterbury, Christchurch, NZ.

[151] Park R, Thompson KJ. (1977) Cyclic load tests on prestressed and partially prestressed beam-column joints. *PCI Journal*. Sept-Oct 1977; **22**(5):84-100.

[152] Park S, Mosalam KM. (2009) *Shear strength models of exterior beam-column joints without transverse reinforcement. PEER Report 2009/106*. Pacific Earthquake Eng. Res. Center (PEER), Berkeley, CA.

[153] Parker DE, Bullman PJM. (1997) Shear strength within RC beam-column joints. *The Structural Engineer*. Feb 1999; **75**(4):53-57.

[154] Parvin A, Altay S, Yalcin C, Kaya O. (2010) CFRP Rehabilitation of concrete frame joints with inadequate shear and anchorage details. *ASCE J of Composite Constr*. Jan-Feb 2010; **14**(1):72-82.

[155] Paulay T, Priestley MJN. (1992) *Seismic design of reinforced concrete and masonry buildings*. John Wiley & Sons Inc., Christchurch, NZ.

[156] Pincheira JA. (1993) Design strategies for the seismic retrofit of reinforced concrete frames. *Earthquake Spectra*. **9**(4):817-842.

[157] Pincheira JA, Jirsa JO. (1992) *Seismic strengthening of reinforced concrete frames using post-tensioned bracing systems. PMSEL Report No 92-3.* Uni. of Texas at Austin, Austin, TX.

[158] Pincheira JA, Jirsa JO. (1995) Seismic response of RC frames retrofitted with steel braces or walls. *ASCE J of Struct Eng*. Aug 1995; **121**(8):1225–1235.

[159] Pinho R. (2000) Selective Retrofitting of RC Structures in Seismic Areas [PhD dissertation]. Imperial College of Science, Technology and Medicine, London, UK.

[160] Plumier A. (1990) New idea of safe structures in seismic zones. *Proc. of IABSE Symp*, Intl. Assn. of Bridge and Struct. Eng. (IABSE), Uni. of Liege, Brussels, p. 432-436

[161] Popovics S. (1973) A numerical approach to the complete stress-strain curves for concrete. *Cement and Concrete Research*. Sept 1973; **3**(5):583-599.

[162] Priestley MJN. (1995) Displacement-based seismic assessment of existing reinforced concrete buildings. *Proc. of Pacific Conf on Earthquake Eng*, Melbourne, Australia, p. 225-244

[163] Priestley MJN. (1997) Displacement-based seismic assessment of reinforced concrete buildings. *J of Earthquake Eng*. Jan 1997; **1**(1):157-192.

[164] Priestley MJN, Calvi GM. (1991) Towards a capacity design assessment procedure for reinforced concrete frames. *Earthquake Spectra*. **7**(3):413-437.
[165] Priestley MJN, Calvi GM, Kowalsky MJ. (2007) *Displacement-based seismic design of structures*. IUSS Press, Pavia, Italy.
[166] Priestley MJN, MacRae GA. (1996) Seismic tests of precast beam-to-column joint subassemblages with unbonded tendon. *PCI Journal*. Jan-Feb 1996; **40**(1):64-81.
[167] Priestley MJN, Seible F, Calvi GM. (1996) *Seismic design and retrofit of bridges*. John Wiley & Sons Inc., NY.
[168] Priestley MJN, Sieble F. (1995) Design of seismic retrofit measures for concrete and masonry structures. *Construction and Building Materials*. **9**(6):365-377.
[169] Priestley MJN, Sritharan S, Conley JR, Pampanin S. (1999) Preliminary results and conclusions from the PRESSS five-story precast concrete test building. *PCI Journal*. **44**(6):42-67.
[170] Prota A, Nanni A, Manfredi G, Cosenza E. (2004) Selective upgrade of underdesigned reinforced concrete beam-column joints using carbon fibre-reinforced polymers. *ACI Structural Journal*. Sept-Oct 2004; **101**(5):699-707.
[171] Roberts-Wollman CL, Kreger ME, Rogowsky DM, Breen JE. (2005) Stresses in external tendons at ultimate. *ACI Structural Journal*. Mar-Apr 2005; **102**(2):206-213.
[172] Roeder CW, Banerjee S, Jung DR, Smith SK. (1996) The role of building foundations in seismic retrofit. *Earthquake Spectra*. Nov 1996; **12**(4):925-942.
[173] Roh H-s. (2007) Seismic behaviour of structures using rocking columns and viscous dampers [PhD dissertation]. State Uni. of New York (SUNY), Buffalo, NY.
[174] Saatcioglu M, Yalcin C. (2003) External prestressing concrete columns for improved seismic shear resistance. *ASCE J of Struct Eng*. Sept 1992; **129**(8):1057-1070.
[175] Sarsam KF, Phillips ME. (1985) The shear design of in-situ reinforced concrete beam-column joints subjected to monotonic loading. *Magazine of Concrete Research*. Mar 1985; **37**(130):16-28.
[176] Sasani M, Bertero VV, Anderson JC. (1999) *Rehabilitation of nonductile RC frame building using encasement plates and enery-dissipating devices. PEER Report 1999/12*. Pacific Earthquake Eng. Res. Center (PEER), Berkeley, CA.
[177] Scott RH, Hamil SJ. (1998) Connection zone strain in reinforced concrete beam column connection. *Proc. of 11th Intl Conf on Exp Mechanics*, Oxford, UK, p. 65-69
[178] SEAOC. (1995) *Vision 2000 Committee Report - A framework for performance-based seismic engineering*. Structural Engineers Association of California (SEAOC), Sacramento, CA.
[179] Shalouf F, Saatcioglu M. (2006) Seismic retrofit of non-ductile reinforced concrete frames with diagonal prestressing. *Proc. of 8th US National Conf on Earthquake Eng*, San Francisco, CA, p. 10.Paper No. 439.
[180] Shrestha R, Smith ST, Samali B. (2009) Strengthening RC beam-column connections with FRP strips. *Proc of the ICE - Structures and Buildings*. **165**(5):323-334.
[181] Skinner RI, Robinson WH, McVerry GH. (1993) *An introduction to seismic isolation*. Wiley, New York.
[182] Sorace S, Terenzi G. (2008) Seismic protection of frame structures by fluid viscous damped braces. *ASCE J of Struct Eng*. Jan 2008; **134**(1):45-55.
[183] Speicher MS, Desroches R, Leon RT. (2008) Preliminary investigation on SMA-based recentering beam-column connection. *Proc. of 14th World Conf on Earthquake Eng*, Beijing, China.Paper No. 05-01-0301.

[184] Sritharan S. (1998) Analysis of concrete bridge joints subjected to seismic actions. [PhD Dissertation]. Uni. of California, San Diego La Jolla, CA.
[185] Sritharan S. (2005) Strut-and-Tie analysis of bridge tee joints subjected to seismic action. *ASCE J of Struct Eng*. **131**(9):1321-1333.
[186] Sritharan S, Ingham JM. (2003) Application of strut-and-tie concepts to concrete bridge joints in seismic region. *PCI Journal*. **48**(4):66-90.
[187] Sritharan S, Priestley MJN, Seible F. (1996) *Seismic response of column/cap beam tee connections with cap beam prestressing, SSRP Research Report No. 96/09*. Uni. of California at San Diego, La Jolla, CA.
[188] Sritharan S, Priestley MJN, Seible F. (1999) Enhancing seismic performance of cap beam-column bridge joints using prestressing. *PCI Journal*. **44**(4):74-91.
[189] Sritharan S, Priestley MJN, Seible F. (2001) Seismic design and experimental verification of concrete multiple column bridge bents. *ACI Structural Journal*. **98**(3):335-346.
[190] Sugano S. (1981) Seismic strengthening of existing reinforced concrete buildings in Japan. *Bull of New Zealand Soc of Earthquake Eng*. Dec 1981; **14**(4):209-222.
[191] Sugano S. (1996) State-of-the-art in techniques for rehabilitation of buildings. *Proc. of 11th World Conf on Earthquake Eng*, Elsevier Science Ltd, Acapulco, Mexico.Paper 2175.
[192] Sugano S. (2007) *Seismic rehabilitation of concrete structures, IPS-2*. American Concrete Inst. (ACI) / Japan Concrete Inst. (JCI), Farmington Hill, MI.
[193] Symans MD, Charney FA, Whittaker AS, Constantinou MC, Kircher CA, Johnson MW, et al. (2008) Energy dissipation systems for seismic applications: Current practice and recent developments. *ASCE J of Struct Eng*. Jan 2008; **134**(3):3-21.
[194] Symans MD, Constantinou MC. (1999) Semi-active control systems for seismic protection of structures: A state-of-the-art review. *Eng Structures*. June 1999; **21**(6):469-487.
[195] Teng JG, Chen JF, Smith ST, Lam L. (2002) *FRP strengthened RC structures*. John Wiley & Sons, West Sussex, UK.
[196] Teran-Gilmore A, Bertero VV, Youssef NFG. (1996) Seismic rehabilitation of infilled non-ductile frame buildings using post-tensioned steel braces. *Earthquake Spectra*. Nov 1996; **12**(4):863-882.
[197] Thermou GE, Elnashai AS. (2006) Seismic retrofit schemes for RC structures and local-global consequences. *Prog in Struct Eng Material (EESD)*. 19 Dec 205; **8**:1-15.
[198] Thermou GE, Pantazopoulou SJ, Elnashai AS. (2007) Design methodology for seismic upgrading of substandard reinforced concrete structures. *J of Earthquake Eng*. July 2007; **11**(4):582-606.
[199] Thompson KJ, Park R. (1980) Seismic response of partially prestressed concrete. *ASCE Journal of Structural Division*. **106**(ST8):1755-1775.
[200] Tsonos AG. (1999) Lateral load response of strengthened reinforced concrete beam-to-column joints. *ACI Structural Journal*. Jan-Feb 1999; **96**(1):46-56.
[201] Tsonos AG. (2007) Cyclic load behaviour of RC beam-column subassemblages of modern structures. *ACI Structural Journal*. July-Aug 2007; **104**(4):468-478.
[202] Tsonos AG. (2008) Effectiveness of CFRP-jackets and RC-jackets in post-earthquake and pre-earthquake retrofitting of beam-column subassemblages. *Earthquake Spectra*. Mar 2008; **30**(3):777-793.
[203] Uang C-M, Yu Q, Noel S, Gross JL. (2000) Cyclic testing of steel moment connections rehabilitated with RBS or welded haunch. *ASCE J of Struct Eng*. Jan 2000; **126**(1):57-68.

[204] Uzumeri SM. (1977) Strength and ductility of cast-in-place beam-column joints, SP-53-12. *Reinforced Concrete Structures in Seismic Zone, ACI SP-53*. American Concrete Inst. (ACI), Detroit, MI; p. 293-350.

[205] Viti S, Cimellaro GP, Reinhorn AM. (2006) Retrofit of a hospital through strength reduction and enhanced damping. *Smart Structures and Systems*. **2**(4):339-355.

[206] Viti S, Reinhorn AM, Whittaker AS. (2002) Retrofit of structures: Strength reduction with damping enhancement. KEERC-MCEER Joint Seminar on Retrofit Strategies for Critical Facilities, New York.

[207] Wada A, Qu Z, Ito H, Motoyui S, Sakata H, Kasai K. (2009) Seismic retrofitting using rocking walls and steel dampers. *Proc. of ATC-SEI Conf, on Improving the Seismic Performance of Existing Buildings and Other Structures*, San Francisco, CA, p. 1010-1021

[208] Wong HF. (2005) Shear strength and seismic performance of non-seismically designed RC beam-column joints [PhD thesis]. Hong Kong Uni. of Science and Tech., Hong Kong.

[209] Wong HF, Kuang JS. (2008) Effects of beam-column depth ratio on joint seismic behaviour. *Proc of the ICE - Structures and Buildings*. **161**(2):91-101.

[210] Yamamoto Y. (1993) Strength and ductility of frames strengthened with steel bracing. In: Okada T, editor. *Earthquake Resistance of Reinforced Concrete Structures: A Volume Honoring Hiroyuki Aoyama*. Uni. of Tokyo Press, Tokyo, Japan; p. 467-476.

[211] Yu Q-S, Uang C-M, Gross JL. (2000) Seismic rehabilitation design of steel moment connection with welded haunch. *ASCE J of Struct Eng*. Jan 2000; **126**(1):69-78.

[212] Yue W, Nishiyama M, Watanabe F. (2004) Shear strength capacity of prestressed concrete beam-column joint focusing on tendon anchorage location. *Proc. of 13th Conf on Earthquake Eng*, Vancouver, Canada,

[213] Zhang Y, Hu X. (2010) Self-centering seismic retrofit scheme for reinforced concrete frame structures: SDOF system study. *Earthquake Eng & Eng Vibration*. June 2010; **9**(2):271-283.

CHAPTER 4. EXPERIMENTAL TEST DESIGN AND PROGRAMME

"No amount of experimentation can ever prove me right; a single experiment can prove me wrong."

Albert Einstein, 1879-1955

4.1 INTRODUCTION

Building on the conceptual development and the analytical work described in the preceding chapters, this chapter describes the experimental testing programme to proof-test the concept of Selective-Weakening (SW) retrofit of reinforced concrete (RC) beam-column exterior joints. In addition, the experimental results will form the basis for the calibration and verification of the numerical and analytical models. The behaviour of the as-built and SW-retrofitted beam-column joints under simulated seismic effects will be assessed in terms of their various performance criteria: strength, displacement/ductility, energy dissipation and failure modes.

Nine 2/3-scaled exterior beam-column joint subassemblies, three as-built and six retrofitted specimens, were constructed and tested under a unidirectional lateral loading. Displacement-controlled quasi-static lateral loading was used to simulate the seismic action on these beam-column joints under severe earthquake actions. These joint subassemblies were to replicate the beam-column joint connections within a one-way non-ductile RC frame, with structural deficiencies typical of the pre-1970s New Zealand construction practice. Parameters considered in the tests included the levels of external post-tensioning forces, locations of beam weakening, the presence of column lap-splices and the presence of cast-in-situ slab and transverse beams. The nine beam-column joint subassemblies tested are as follows:

Unit NS-O1 :As-built benchmark exterior beam-column joint.
Unit NS-R1 :NS-O1 retrofitted with selective beam-weakening only.
Unit NS-R2 :NS-O1 retrofitted with external post-tensioning only.

Unit NS-R3 :NS-O1 retrofitted with Full SW retrofit - beam weakening and external post-tensioning.

Unit NS-R4 :Similar to the NS-R3 retrofit solution with a different location for the beam weakening.

Unit S-O1 :As-built NS-O1 with column lap-splices detailing.

Unit S-R3 :S-O1 retrofitted with Full SW retrofit (R3 solution) - beam weakening and external post-tensioning.

Unit SL-O1 :As-built NS-O1 with cast-in-situ slab and transverse beam stubs.

Unit SL-R3 :SL-O1 retrofitted with Full SW retrofit (R3 solution) - beam weakening and external post-tensioning.

The prefixes of NS, S and SL represent the three different configurations of as-built benchmark: a) NS: benchmark beam-column joints with standard pre-70s non-ductile RC details; b) S: as-built beam-column joints with deficient column lap-splice; and c) SL: as-built beam-column joints with floor-slab and transverse beams. Three as-built joints, used to benchmark seismic performance of un-retrofitted joints, are labelled with the suffix O1. The four Selective-Weakening retrofit solutions are labelled with the suffixes R1, R2, R3 or R4.

This chapter is divided into ten sections including this introduction section. §4.2 will discuss the rationale of the experiments, while §4.3 will describe the details of the test units, in particular the structural detailing and the retrofit solutions implemented. §4.4 will outline the construction aspects of the as-built and retrofitted units and §4.5 will give the relevant material properties. The test setup and loading protocol used for the experiment will be explained in §4.6. The final three sections will describe the instrumentation used as well as the procedure and equations to analyse the experimental data. Appendix A will present the calculations for the variation of axial loading used in the experiments and the M-N performance domains of the as-built and retrofitted beam-column joints based on the analytical framework presented in §2.4 and §3.4 respectively. Assumptions made in the calculation for the M-N performance domain will be briefly described.

4.2 EXPERIMENTAL TEST DESIGN

4.2.1 Test design and prototype of pre-1970s RC frames

The experimental programme consisted of cyclic lateral loading of nine two-third-scaled exterior beam-column joint subassemblies up to 4.0% inter-storey drift, θ_{drift}. The test subassemblies were

designed to replicate the approximate seismic behaviour of the exterior beam-column joints of the lower storey of the prototype six-storey RC frame, as shown in Figure 4.1. The prototype RC frame was designed to simulate a typical mid-rise residential/commercial multi-storey building typical of pre-1970s building stock. An exterior beam-column joint subassembly rather than one or multi-bay sub-frame was selected to save cost and to reduce the complexity of the test setup.

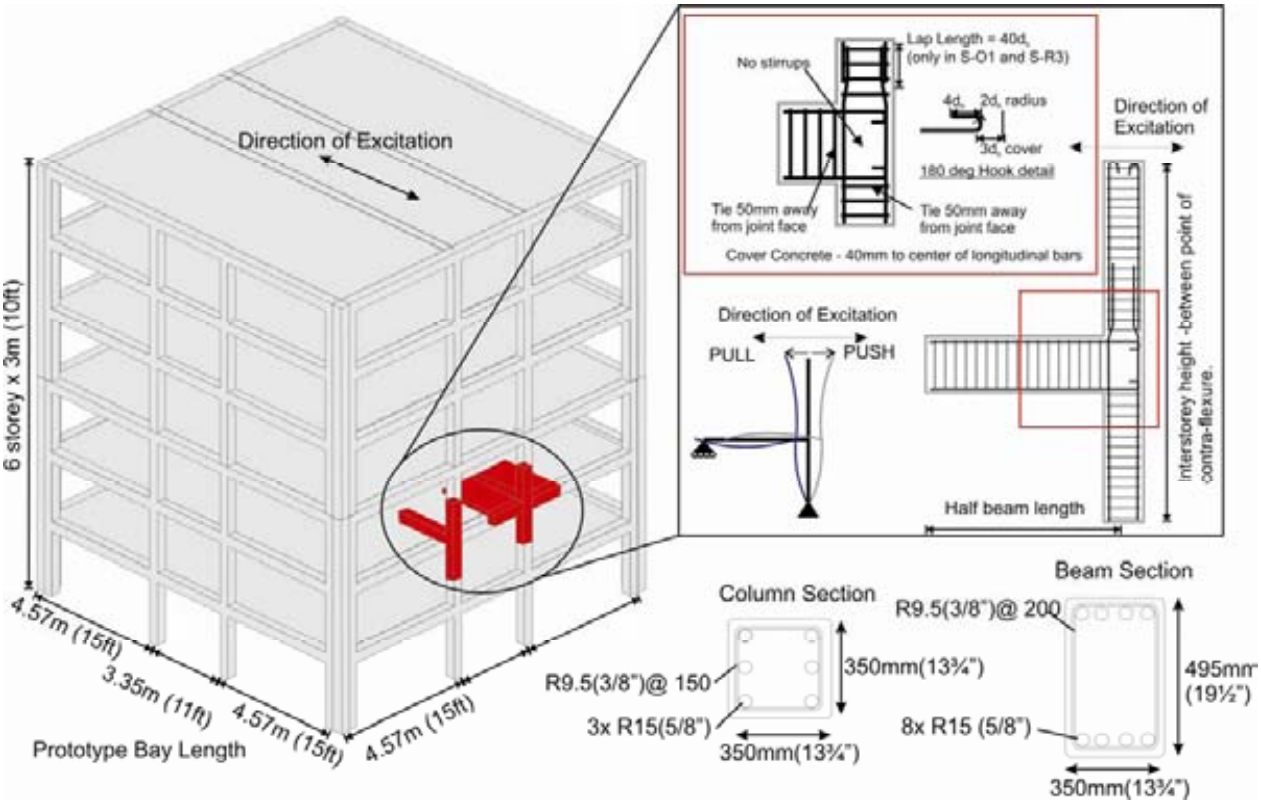

Figure 4.1: Beam-column joint test specimen as subassembly of a prototype six-storey non-ductile RC frame. Insert: beam-column joint detailing adopted for test specimens.

The material properties, deficiencies in reinforcement detailing and violation of capacity design philosophy were intently included in the prototype structure so that it could represent the worst typical case in pre-1970s construction practice worldwide (including New Zealand) while meeting the requirements of older building codes [3, 28]. The reinforcement detailing of the beam-column joints was based on older pre-1970s design codes and existing literature on non-ductile beam-column joints as reviewed in §2.3. The Seismic Retrofit Research Board (SRRB) of the FRST-funded Retrofit Solutions Project, consisting of prominent NZ practicing engineers, also provided invaluable inputs on the prototype building design [44].

The beam-column joint subassembly detailing, as shown in Figure 4.1-insert, reflected the structural inadequacies of the pre-1970s non-ductile RC frames. These structural details were

generally consequences of the gravity-loading dominated design or low lateral design force. For all the test units, the following set of structural detailing was adopted as the worst case scenario:

- No joint shear reinforcement (stirrups) in the beam-column joint regions.
- 180° standard hook anchorage for the beam longitudinal bars into the joint panel region. They were generally assumed to be tension-only anchorages in gravity-only design, in which neither moment reversal nor positive beam moment was expected.
- Lack of capacity design consideration leading to strong-beam, weak-column or brittle inelastic mechanism. The column moment capacity-to-beam moment capacity ratio for beam-column joints adopted for the as-built specimen was 1.79 for positive beam moment and 0.98 for negative beam moment.
- The use of plain round reinforcing bar with poor bond behaviour, for longitudinal and transverse reinforcement.
- Inadequate anti-buckling and confinement reinforcement within the columns, typically of gravity-only designed columns.

4.2.2 Rationale of test matrix selection

In generating the experimental test matrix, a few key criteria were considered within the conception and design stages. While cost and time limited the possibility of running a large number of tests to yield statistical distribution (randomisation), the test matrix, in particular with respect to the selection of the retrofit solutions to be experimentally tested, explicitly considered the concept of replication and blocking within the matrix, to avoid some common pitfalls of large structural tests [22].

By changing one retrofit parameter incrementally within the four retrofitted specimens (NS-R1, NS-R2, NS-R3 and NS-R4), individual retrofit variable's effects were discretised and insights from different variables could be distinguished. By implementing the retrofit solution R3 for all three as-built joint typologies (NS-R3, S-R3 and SL-R3), replication of the structural performance of R3 retrofit solution could be discerned and quantified. However, this series of nine beam-column joints test is by no means sufficient in covering all governing characteristics, particularly those in relation to the geometric and material properties. This shortcoming will be challenged using numerical modelling which as will be described in Chapter 9.

Another innovation of the test matrix design was to widen the scope of the as-built specimens and to differentiate the effects of some added as-built parameters such as column lap-splices and floor slabs/transverse beams on their seismic behaviour. As evident from the literature

review presented in Chapter 2, the existing experimental database of the seismic performance of different as-built non-ductile beam-column joints typologies was sparse. Thus, the added as-built parameters would provide variation and replication to the Full SW solution R3 as well as adding to the knowledge base of pre-1970s existing beam-column joint behaviour. As mentioned, the prefixes of NS, S and SL represent the three different configurations of as-built benchmark:

- NS-series: the standard benchmark pre-1970s RC exterior beam-column joints. The test results and analysis of this set of specimens will be presented in Chapters 5 and 6.
- S-pair: Pre-1970s beam-column joints with deficient column lap-splices. The use of column starter bars and lap-splices at the floor level was commonplace and without explicit capacity design consideration, these lap-splices within potential moment reversal plastic hinge regions were particularly vulnerable (e.g. [9, 36, 38]). Chapter 7 will further explore the influence of column lap-splices on as-built and retrofitted beam-column joints, in conjunction with the experimental results of the S-pair.
- SL-pair: Pre-1970s beam-column joints with floor-slab and transverse beams. Floor slab and transverse stubs could change the internal hierarchy strength of the beam-column joint by increasing the negative moment capacity of the beam and joint shear/deformation capacity (e.g. [11, 12, 14, 15]). The floor slab and transverse beams will also affect the constructability of the proposed SW retrofit interventions. Chapter 8 will present the experimental results of the SL-pair and discuss the implication of transverse beams and floor slab on the as-built and retrofitted beam-column joints.

4.3 TEST SPECIMENS

4.3.1 General description of test matrix and as-built benchmark NS-O1

The beam-column joint subassembly is assumed to be located between points of contra-flexure, occurring at the mid-height of columns and mid-span of the beams of the second floor beam-column joint within the one-way RC frame shown in Figure 4.1. Although the gravity loading may influence the bending moment demand along the beams for these non-ductile RC frames, for the first seven specimens without cast-in-situ slab, the point of inflection is assumed to be at the mid-span of the beam. The influence of gravity-loading and the shifted inflection point were investigated with the two specimens with cast-in-situ slab and transverse beam stubs (SL-O1 and SL-R3).

All test specimens had the same dimensions and member sizes as well as the same longitudinal and transverse reinforcement ratio within the beams and columns. Apart from the specimens with additional slabs-transverse stubs (SL-O1 and SL-R3), all other specimens shared the same reinforcing and geometry details. Two specimens (S-O1 and S-R3) included column lap-splice details. NS-O1 was the as-built benchmark beam-column joint whereas test units NS-R1, NS-R2, NS-R3 and NS-R4 were retrofitted un-tested specimens with similar reinforcing details as NS-O1. A quick summary of the test matrix is given in Table 4.1 while the reinforcing and retrofit details of all specimens are given in Table 4.2.

Table 4.1: Test matrix of the nine beam-column joint specimens.

Unit	As-built parameters			Selective Weakening Retrofit parameter	
	Benchmark Details	Column Lap-Splice	Slab & Transverse Beam Stubs	Beam Weakening	External Post-Tensioning (PT)
NS-O1	√	-	-	-	-
NS-R1	√	-	-	√	-
NS-R2	√	-	-	-	√
NS-R3	√	-	-	√	√
NS-R4	√	-	-	√	√
S-O1	√	√	-	-	-
S-R3	√	√	-	√	√
SL-O1	√	-	√	-	-
SL-R3	√	-	√	√	√

The beams were 330 x 230 mm with both top and bottom longitudinal reinforcement ratio of ρ/ρ' =0.46% (4-R10 for top and bottom reinforcement) and transverse reinforcement ratio of ρ_{sh} = 0.042% (R6 at 133mm centre-to-centre (c-c) spacing). As mentioned, the column moment capacity-to-beam moment capacity ratio for beam-column joints adopted for the as-built specimen was 1.79 for positive beam moment and 0.98 for negative beam moment. Of interest, the longitudinal beam bar diameter, $d_{b,b}$, to column dimension, h_c, was 0.04345, which was comparable to the New Zealand NZS3101:2006 code requirement limiting $d_{b,b}/h_c$ to 0.04472 (f'_c=20MPa, f_y=330MPa, α_o=1.0) and 0.04382 (f'_c=30MPa, f_y=330MPa, α_o=1.25). The longitudinal column bar diameter, $d_{b,c}$, to beam depth, h_b, was 0.0303, compared to the NZS3101:2006 requirement of a maximum $d_{b,c}/h_b$ of 0.05311 (hinging column, f'_c=30MPa, f_y=330MPa).

The columns were 230 x 230mm with a longitudinal column steel ratio, ρ_{sc}, of 0.891% (two layers of 3-R10 in the strong axis), compared to the NZS95:1955 [28] recommendation of minimum longitudinal column steel ratio, ρ_{sc} of 0.8%. The column transverse reinforcement ratio

was 0.673% (R6 at 100mm c-c spacing). In comparison, the NZS95:1955 [28] code allowed the maximum spacing for column stirrups of 120mm (12 $d_{b,c}$) (the least of 2/3h_c, 12 $d_{b,c}$ and 12inches). Both the beam and column transverse reinforcement stirrups were adequately anchored with a 135° bent as the importance of proper stirrup anchorage had long been recognised in New Zealand [19, 25, 28].

Table 4.2: Description of beam-column joint test units.

Test Unit	Description	Beam Bottom Reinforcements	Cutting Radius (mm)	Weakened section distance from column C/L (mm)	Post-tensioning (PT) Force (kN)	Concrete Strength, f'c (MPa) [1]
NS-O1	As-built joint benchmark	4-R10	-	-	-	17.3
S-O1	As-built joint with column lap-splice	4-R10	-	-	-	15.1
SL-O1	As-built joint with slab/transverse beams	4-R10	-	-	-	13.4 & 19.9 [2]
NS-R1	R1: Beam-weakening only	2-R10 [3]	80	165	-	25.6
NS-R2	R2 : Post-tensioning (PT) only	4-R10	-	-	120	28.2
NS-R3	R3: Beam-weakening and PT	2-R10 [3]	80	165	40	24.3
NS-R4	R4: Beam-weakening and PT	2-R10 [3]	80	310	24	30.3
S-R3	S-O1 with the R3 retrofit	2-R10 [3]	80	165	40	20.7
SL-R3	SL-O1 with the R3 retrofit	2-R10 [3]	80	165	40	17.0 & 23.1 [2]

Abbreviation: B-C=beam column; PT=post-tensioning; R10 = diameter 10mm plain round bars ; C/L = center line.
[1] Concrete strength at the day of testing; [2] Top half of the column and other parts were casted separately.
The first value given is the top half of the column concrete strength. [3] Selective beam weakening with two outer bottom longitudinal bars severed. [4] The manufacturer specified yield strength of the PT tendons is 1560MPa.

The joints had no transverse reinforcement and the beams' longitudinal reinforcing bars were anchored with double 180° standard hooks. The standard hook detailing met the requirements of the NZS95:1955 [28] for a) bent radius (>2$d_{b,b}$); b) straight length beyond the bent >4 $d_{b,b}$; and clear concrete cover to the hook tip >3$d_{b,b}$.

Geometry and reinforcement details of the all the test-units without floor slab and without column lap-splice (NS-O1, NS-R1, NS-R2 and NS-R3 NS-R4) are shown in Figure 4.2 while the test units with column lap-splices detailing (S-O1 and S-R3) are presented in Figure 4.3. The geometry and reinforcing details for the test units with floor slabs (SL-O1 and SL-R3) are given in Figure 4.15 and Figure 4.16. Note that these are the as-built detailing, prior to the retrofit solution implementation. Additional stirrup reinforcement was added at the end-region of the beam and columns in order to prevent local failure from concentration of stresses due to the application of load in the experiments.

The calculated flexural, shear and predicted failure modes of the as-built and retrofitted specimens are summarised in Table 4.3. The calculations of capacities for all as-built structural elements were done according to the material presented in §2.4 (Chapter 2). The evaluation of the retrofitted components was done based on the procedure described in §3.4 (Chapter 3). Appendix A presents the M-N performance domains for the test specimens as well as the assumptions made for the evaluation of the beam-columns joints.

In Table 4.3, $M_{c\text{-}bf}$ and $M_{c\text{-}cf}$ refer to the flexural capacities of the beam and column in terms of equivalent column moment (M_c). $M_{c\text{-}j}$, $M_{c\text{-}bv}$ and $M_{c\text{-}cv}$ are the shear capacities of the joint, beam and column in terms of M_c. $F_{sys\text{-}cal}$ is the predicted lateral strength capacity for the predicted failure mode.

R1 and R2 schemes represented two incremental solutions of the SW retrofit strategy – by either beam weakening-only or joint post-tensioning-only retrofit techniques. In the R1 scheme, 50% of the bottom longitudinal beam bars and 80mm radius concrete in the weakened section were cut. Aiming at reducing the joint shear demands as well as inducing the flexural hinge in the beam, the R1 retrofit scheme was designed as a collapse-prevention retrofit intervention. The R2 solution was also a partial SW solution, where the joint and the beam were post-tensioned with two externally anchored tendons with 60kN initial prestressing force. The increased axial stress in the joint and the confinement improved the joint shear behaviour while the post-tensioning also increased the flexural and shear capacities of the beam. The specimen NS-R2 was expected to hinge in the beam and column, depending on the variation of axial load in the column. This gave a further rationale to combine the two SW techniques to achieve a higher performance level.

The R3 and R4 retrofit solutions corresponded to the combination of beam weakening and joint post-tensioning to achieve the most desirable retrofit outcome. The locations of beam weakening and levels of post-tensioning force varied between the solutions R3 and R4. The R3 scheme was implemented on three different as-built scenarios (NS-R3, S-R3 and SL-R3), to replicate the results as well as to understand the influence of as-built parameters on retrofit solutions. While the following paragraphs describe qualitatively the retrofit solutions implemented, the design calculations for the retrofit solutions are summarised in Table 4.3 and further described in Appendix A. Figure 4.4 to Figure 4.7 present the retrofitting detailing for the retrofit schemes R1 to R4 respectively.

Table 4.3: Analytical capacities for various failure modes of test specimens as-built and retrofitted beam column joints.

Test Unit	$M_{c\text{-}bf}$ [1] (kNm)	$M_{c\text{-}cf}$ (kNm) at N_g axial load	$M_{c\text{-}cf}$ [2] (kNm) at varying axial load	$M_{c\text{-}cf}$ [2] / M_{bf} [1]	$M_{c\text{-}j}$ [3] (kNm)	$M_{c\text{-}bv}$ [4] (kN)	$M_{c\text{-}cv}$ [4] (kN)	$F_{sys\text{-}cal}$ [5] (kNm)	Predicted failure mode (Pull:+ and Push:-)
NS-O1	± 14.5	25.0	+19.0 -34.5	+0.59 -1.08	+8.9 - 12.4	34.5	39.1	+10.6 -14.8	Joint shear failure
S-O1	± 14.3	21.8	+15.8 -30.5	+0.50 -0.97	+8.5 - 11.9	33.6	37.1	+10.2 -14.2	Joint shear failure
SL-O1	+17.8 -23.2	24.4	+19.0 -31.5	+0.48 -0.61	+8.8 - 13.0	-[6]	36.7	+10.5 -15.6	Joint shear failure
NS-R1	+8.6 -15.1	25.8	+17.2 -38.5	+0.91 -1.15	+12.9 - 20.0	37.6	39.2	+10.3 -18.1	Beam flexural (±)
NS-R2	± 19.6	25.5	+18.3 -38.8	+0.44 -0.92	+16.7 - 29.8	42.2	39.1	+20.0 -23.4	Beam flexural (-) / column flexural (+)
NS-R3	+12.7 -17.0	25.4	+18.5 -38.7	+0.66 -1.03	+14.7 - 25.3	38.9	39	+15.2 -20.3	Beam flexural (±)
NS-R4	+12.1 -16.1	26.5	+19.1 -41.1	+0.68 -1.10	+15.1 - 25.1	40.2	40	+14.5 -19.3	Beam flexural (±)
S-R3	+13.0 -17.2	24.0	+17.0 -38.0	+0.59 -1.00	+15.3 - 26.0	38.2	39.6	+15.6 -20.6	Beam flexural (±)
SL-R3	+15.7 -23.9	25.0	+19.0 -34.0	+0.55 -0.64	+15.4 - 25.3	-[6]	37.4	+18.3 -28.6	Joint Shear / Beam (+) / Beam flexural (-)

Positive force, moment, displacement and drift correspond to PULL cycles while negative values indicate PUSH cycles. Positive beam moment is when the bottom face of the beam is in tension. [1] Calculated nominal beam flexural capacity, concrete compression strain ≥ 0.003.

[2] Calculated nominal column flexural capacity at axial load variation as per described in §4.6.3.

[3] Calculated joint shear capacity based on the analytical approach described in §2.4.1 and §3.4, normalised as equivalent column moment (M_c)

[4] Calculated beam and column shear capacities follow the §2.4.2, assuming the initial axial force values for post-tensioning and column axial load.

[5] Calculated sub-assemblage lateral force capacity and failure modes are based on the hierarchy of strength. [6] not computed.

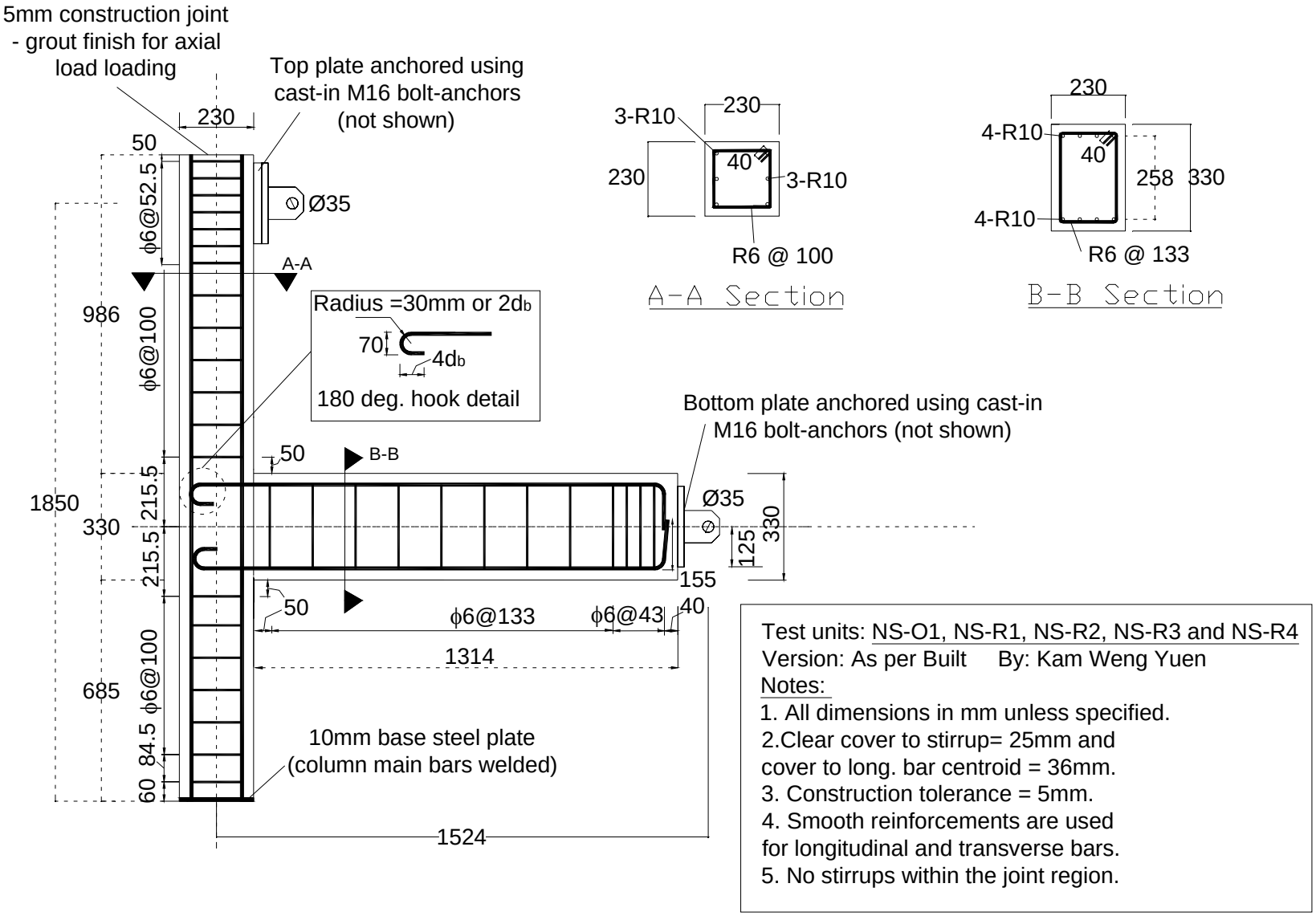

Figure 4.2: Reinforcing and geometry details for test unit NS-O1, NS-R1, NS-R2, NS-R3 and NS-R4.

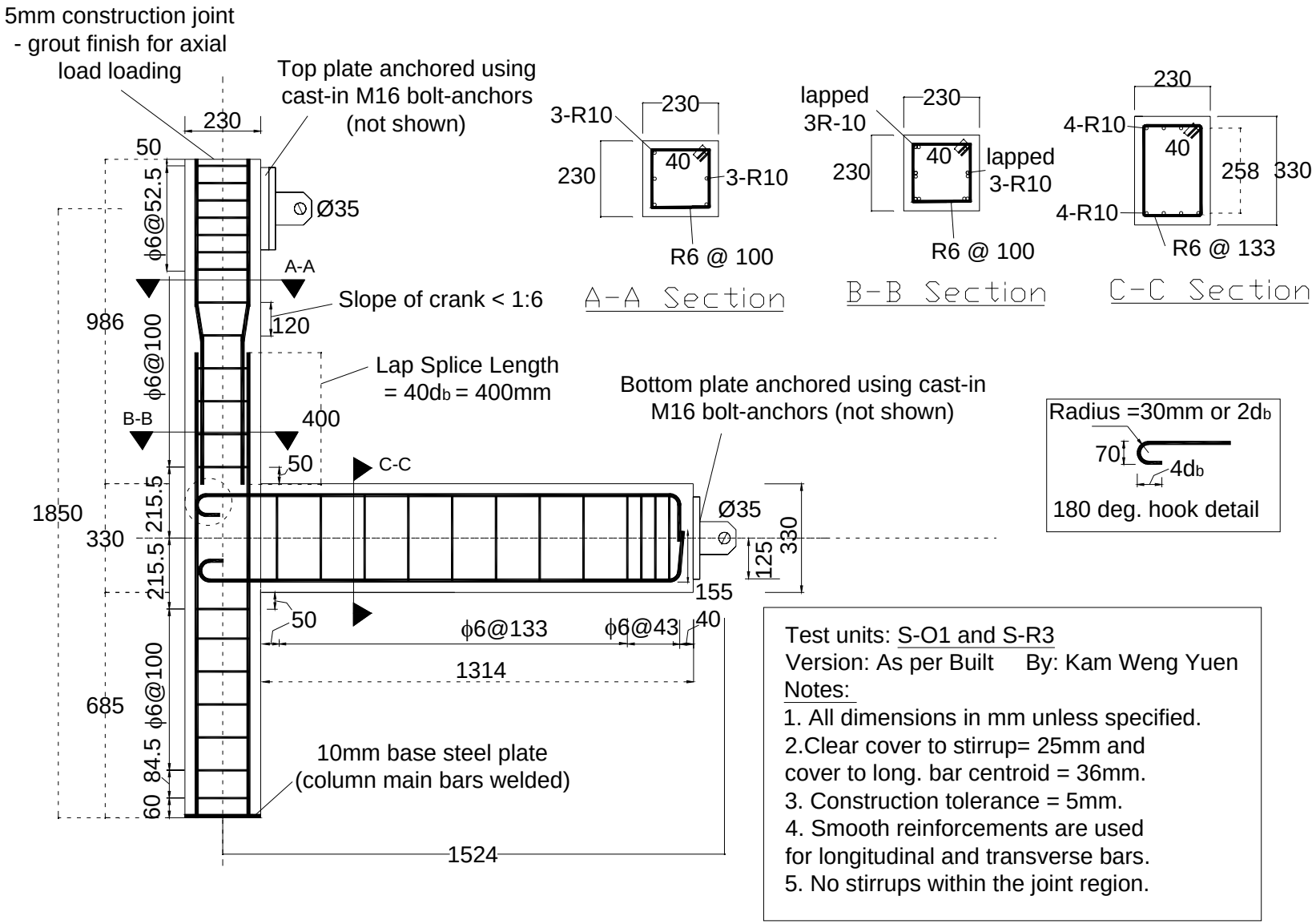

Figure 4.3: Reinforcing and geometry details for test unit S-O1 and S-R3.

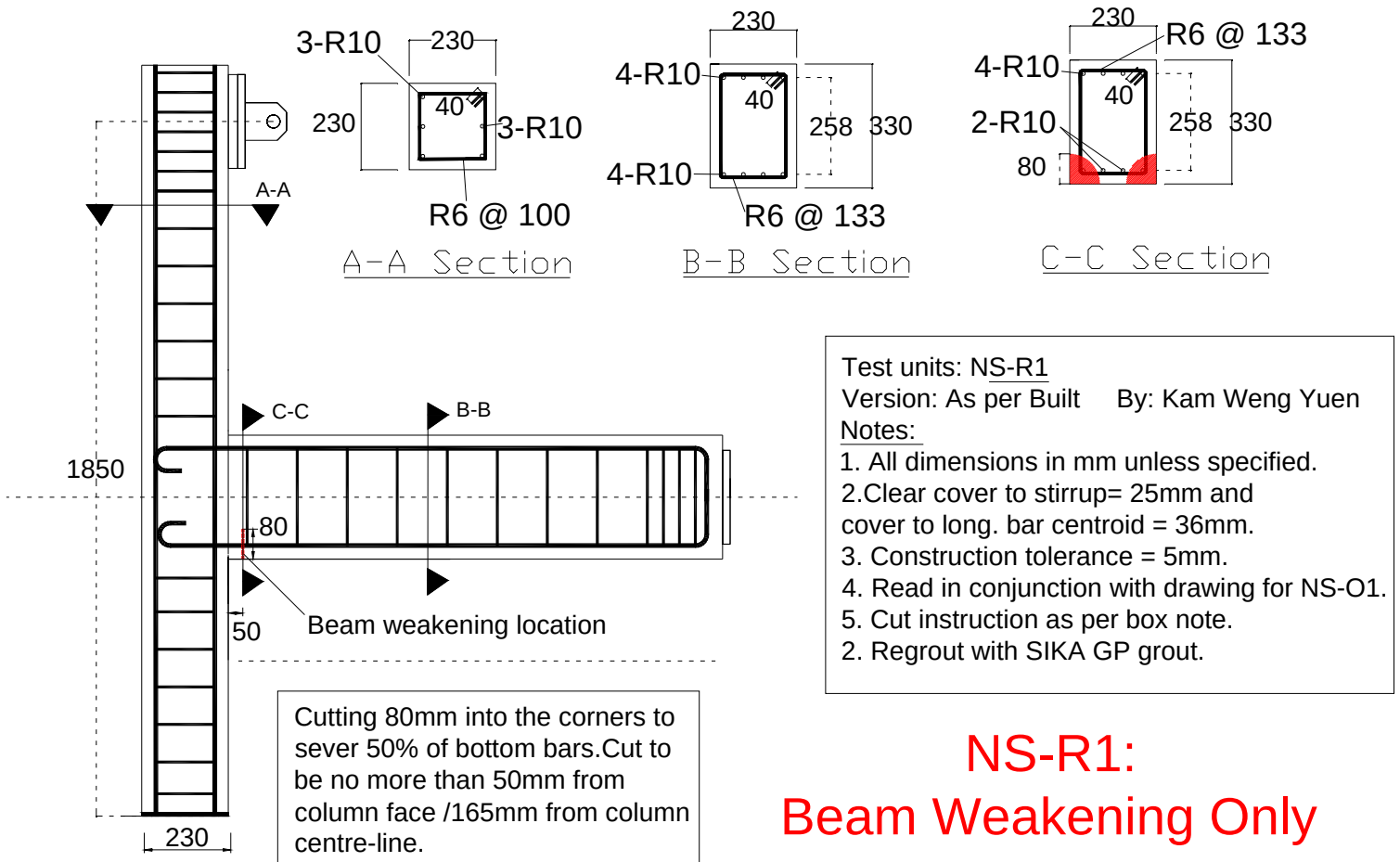

Figure 4.4: Retrofitting details for test unit NS-R1.

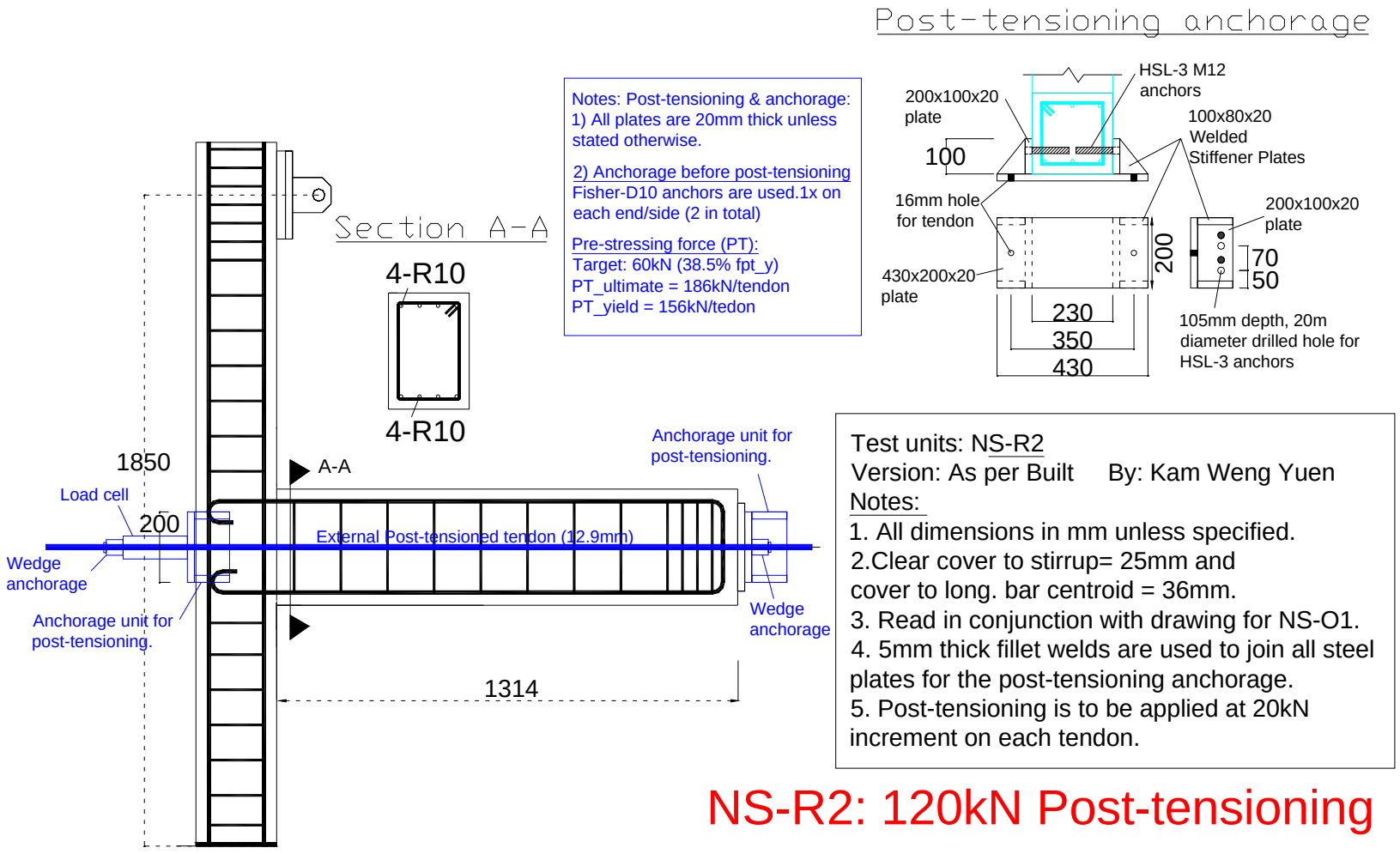

Figure 4.5: Retrofitting details for test unit NS-R2.

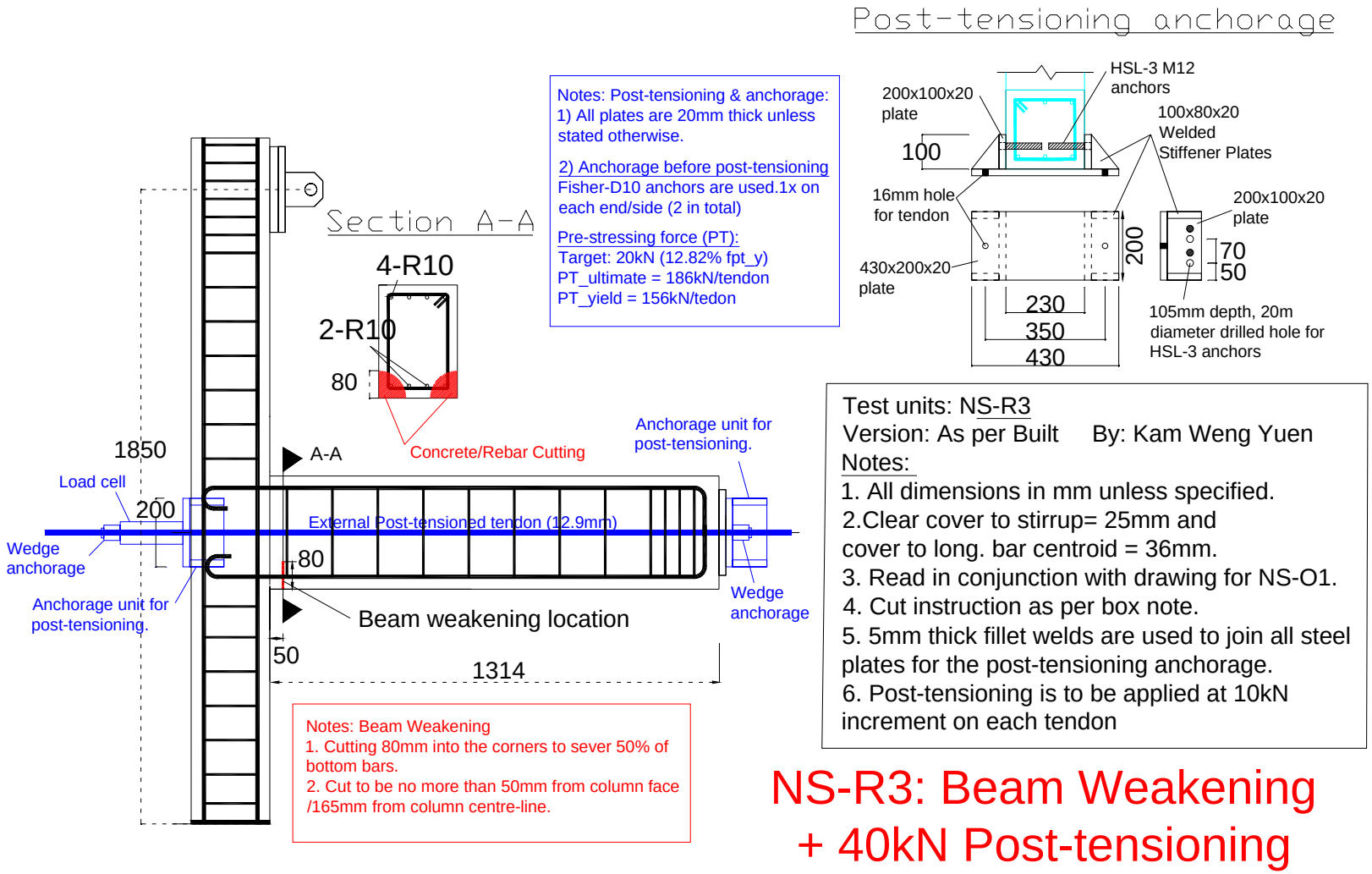

Figure 4.6: Retrofitting details for test unit NS-R3.

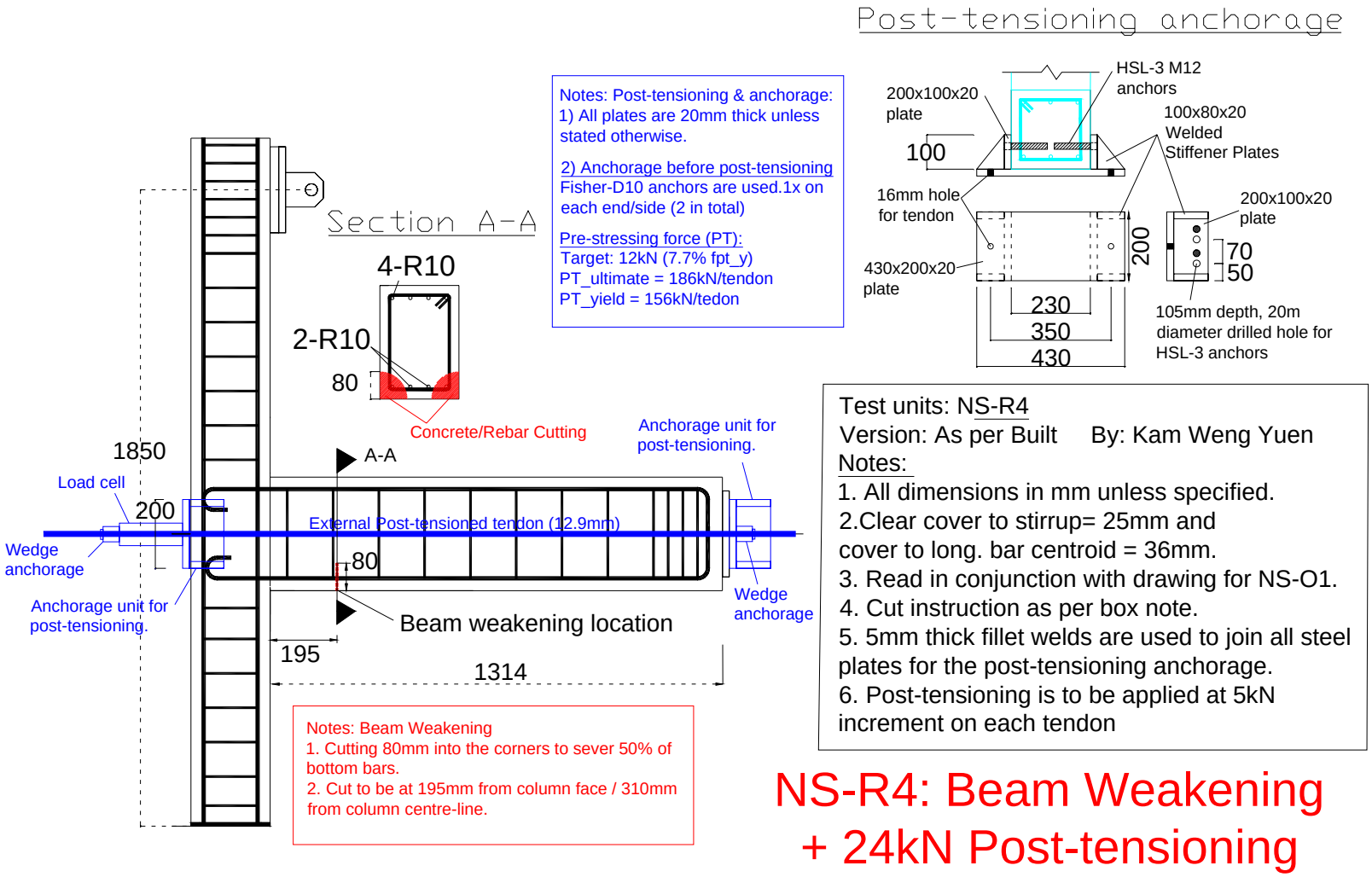

Figure 4.7: Retrofitting details for test unit NS-R4.

4.3.2 Test unit NS-R1 – beam weakening only

Test unit NS-R1 represented a partial selective-weakening retrofit in which the only retrofit intervention involved was a 50% beam flexural weakening. Physically, this comprised of cutting two of the external bottom longitudinal beam bars as well as some of the surrounding concrete. This was done in the laboratory using an 180x2.5x22.2mm masonry/concrete cutting plate on hand portable grinder (see Figure 4.8a). An 80mm cutting radius was specified and the weakened section was 165mm from the column centre-line. This corresponded with a distance of 50mm from the column face, which was the minimum distance possible due to the physical dimension of the hand grinder. There are other concrete-cutting equipments which allow for a smaller tolerance in the commercial.

The weakened slot was later re-grouted with the SIKA™ GP Grout (se Figure 4.8b). The cleaning and grouting were done according to the manufacturer's specification, including pre-moisturising the surface for better bonding. The grout had a compressive strength of 26MPa after 24 hours and 55MPa after 7 days (based on the manufacturer's specification). No grout cylinder was tested due to lack of laboratory setup for a grout cylinder compressive test. Figure 4.8 shows the final pre-testing state of the retrofitted NS-R1 beam-column joint where its minimal invasiveness was clearly demonstrated.

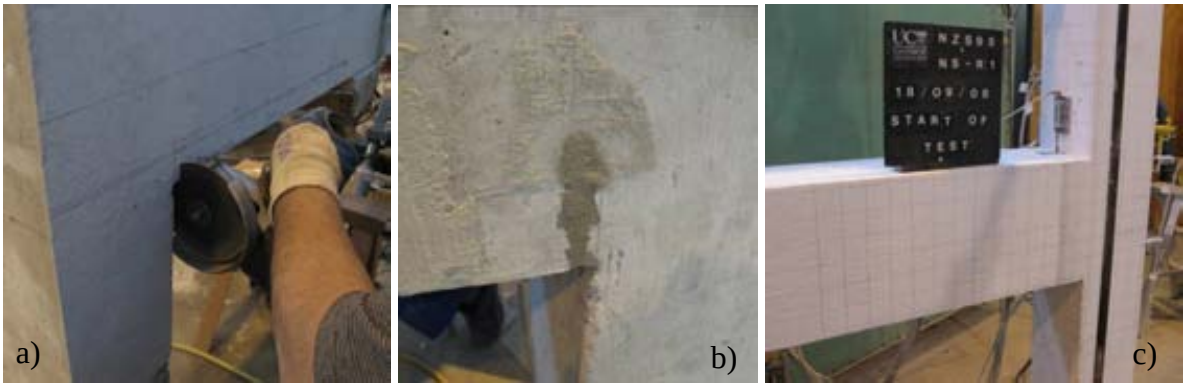

Figure 4.8: Selective beam weakening retrofit intervention on NS-R1: a) cutting of reinforcement; b) re-grouting of weakened section; c) final pre-testing state of retrofitted NS-R1.

Figure 4.8 also illustrates the laboratory methods used for implementing selective beam weakening retrofit for retrofit scheme R1, R3 and R4. Due to the limitation of the grinding plate radius, a complete 80mm clear radius cut was not achieved in some retrofitted specimens (NS-R3 and S-R3). However, as the section would crack at a lower level of loading at the weakened section, it was deemed not critical. Care was taken to visually check that the required steel

reinforcement was completely severed. It was also found that the type of grout or in fact re-grouting was not important in the global seismic response of the retrofitted beam-column joint.

4.3.3 Test unit NS-R2 – joint post-tensioning only

The R2 solution was also a Partial SW solution, in which the retrofit intervention was externally applied/anchored prestressing of the joint and beam. Test unit NS-R2 was designed to isolate and investigate the effect of external prestressing on the poorly detailed beam-column joint. Increased axial stress in the joint and the confinement effect would improve the joint shear behaviour significantly while the post-tensioning would increase the flexural and shear capacities of the beam. While NS-R2 was primarily to discretise the influence of the joint prestressing in retrofit solutions, it also alluded to the importance of the weakening for retrofit concept when adopting a local strengthening-only retrofit strategy such as adding external prestressing forces.

For NS-R2, 120kN total post-tensioning force was applied using two tendons prestressed to 60kN each, thus to 38.5% of the yield strength of the tendons, $f_{y\text{-}pt.}$ This corresponded with approximately 1.58MPa horizontal stress across the joint panel region. The selection of ~40% $f_{y\text{-}pt}$ was to ensure no yielding of the tendons in the worst case scenario of fully rigid-body rocking at the weakened section. At this level of post-tensioning force, NS-R2 was expected to hinge in the beam during the Push direction and to hinge in the column during the Pull direction.

Post-tensioning was done using a hand-pumped mono-strand prestressing jack with a self-reacting bridge unit, as shown in Figure 4.9. The setup was post-tensioned slightly beyond the required post-tensioning force to account for anchorage take-up (wedge-set) losses. Cone wedges were manually hammered in during each increment of post-tensioning. Post-tensioning was done incrementally on the left and right sides to avoid induced-eccentricity and twisting of the specimen. A 20kN force was applied on every increment. As the geometric bending would increase the force on one side while the other side was stressed up, careful consideration had to be given to ensure the correct forces were applied. For test unit NS-R2, 59.97kN and 59.72kN were applied on the tendons before the start of the test.

An over-designed steel anchorage unit was used to anchor the post-tensioned tendons on the joint column face and beam end, as shown in Figure 4.9. The anchorage unit was attached to the beam column joint, first with two Fischer™ 10mm FAZ II anchors and then with friction bearing on the joint concrete face upon post-tensioning. In the preliminary design, four 10mm mechanical anchors were designed to carry all the required shear-force transfer from the post-tensioning tendons. However, a larger bearing plate was used in the final design in order to

provide improved confinement on top of the horizontal axial forces. This was to ensure a well distributed prestressing force in the joint core, learning from the lessons of existing prestressed joint tests with internal prestressing or without confinement bearing [27, 42, 43]. The anchorage unit was manufactured in-house using welded 20mm steel plates.

Figure 4.9: External post-tensioning retrofit intervention using monostrand hand-pump hydraulic jack on external steel plate anchorages.

It is expected that commercial prestressed anchorage and systems (e.g. VSL, BBR, Freyssinet and Dywidag) can be used for practical retrofit applications. It is also noted that only a relatively low prestressing force and therefore few strands were required for a successful joint retrofit (as per NS-R3 and NS-R4). From the laboratory experience, the post-tensioning retrofit intervention was found to be not labour-intensive exercise. Admittedly, in real-life application, the plasters and other non-structural claddings all would affect the labour demand of the retrofit intervention, as with most other retrofit techniques.

4.3.4 Full SW retrofit: test units NS-R3 and NS-R4

The R3 and R4 solutions were Full SW retrofit schemes, where the beams were selectively weakened in conjunction with external prestressing of the beam-column joint. In addition to changing the inelastic mechanism by ensuring the formation of ductile plastic hinge in the beam, higher deformation and energy-dissipation capacities were targeted for the R3 and R4 retrofits.

The locations of beam weakening and levels of post-tensioning force varied between the solutions R3 and R4. The shift in beam-weakening location in the NS-R4 specimen was targeted to relocate the plastic hinge in the beam away from the joint. This would further reduce joint shear demand and provide a longer anchorage length to the beam longitudinal bars, assuming the weakest section at the weakened section. Meanwhile, the variation of post-tensioning forces between NS-R3, NS-R4 and NS-R2 was intended to give a meaningful description of the effects of the joint prestressing on the seismic performance of the retrofitted joints.

For test unit NS-R3, 50% of the bottom longitudinal reinforcement was severed at 50mm from the column internal face and the weakened slot was subsequently re-grouted, similar to the NS-R1 retrofit intervention. NS-R4, on the other hand, had 50% of the bottom longitudinal reinforcement cut at 195mm from the column internal face (Figure 4.10). This corresponded to the weakened sections being at 165mm and 310mm from the column centre-line for retrofit schemes R3 and R4 respectively. In addition, for NS-R4, no re-grouting of the cut concrete was used to check whether this laborious step was necessary to achieve successful retrofit outcome.

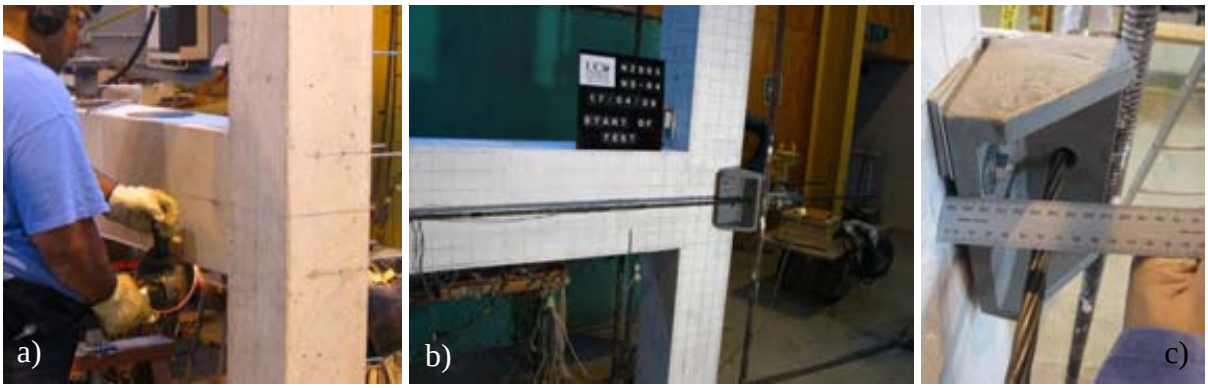

Figure 4.10: a) Beam weakening for NS-R4 was 310mm away from the column centre-line; b) NS-R4 with beam weakening and external post-tensioning retrofit interventions; c) the post-tensioning tendon was 60mm from the beam face.

The different external post-tensioning force levels applied to NS-R3 and NS-R4 were 40kN and 24kN respectively. This translated to two mono-strand tendons stressed to 12.8% of $f_{y\text{-}pt}$ and 7.7% of $f_{y\text{-}pt}$ for NS-R3 and NS-R4 respectively. This also corresponded to approximately 0.527MPa and 0.316MPa horizontal joint stresses across the joint panel region for NS-R3 and NS-R4. The post-tensioning procedure and anchorage details were similar to the NS-R2 specimen, as shown in Figure 4.9 and Figure 4.10. Post-tensioning was done incrementally on the left and right sides with approximately 5kN post-tensioning force applied on every increment. As shown in Figure 4.10c, the post-tensioning tendon was approximately 60mm from the concrete surface.

4.3.5 Specimens with column lap-splice: test units S-O1 and S-R3

Specimens S-O1 and S-R3 were designed to investigate the influence of the presence of column lap-splices on the as-built and retrofitted beam-column joints. Both S-O1 and S-R3 had the same reinforcement and geometrical details as the benchmark as-built NS-O1 specimen, with the exception of column reinforcement lap-splices above the joint region. The reinforcing details of S-O1 and S-R3 are given in Figure 4.3 and close-up photographs of the lap-splice detailing are given in Figure 4.11.

The column lapping length used was $40d_b$, consistent with the older codes [3, 28] requirements for tension lap-splices of plain round bars. The 1955 NZS95 concrete code [28] specified a minimum lap length of no less than 40 times the column longitudinal bar diameter, $d_{b,c}$, for reinforcement acting both in tension and compression. For exterior columns though, lap-splice lengths between $24d_{b,c}$ to $40d_{b,c}$ have been observed in older building drawings. Some previous international researches [6, 8] have adopted lap lengths between $20d_{b,c}$ to $36d_{b,c}$ for deformed bars specimens, based on the 1956/1963 ACI318 [2, 3] codes. For plain round bar reinforcement, the required anchorage length was double of those specified in the code for deformed bars. Therefore, the selection of lap-splice length of $40d_{b,c}$ was both realistic and conservative. A crank in the column longitudinal bars with a slope of 1:6 was included within the column lap-splice, consistent with the requirements of the 1956/1963 ACI318 [2, 3] codes. Figure 4.11b shows the chamfered ends of the longitudinal reinforcing. This was done to avoid excessive end-bearing anchorage from typical rough ends from on-site steel cutting.

Figure 4.11: Detail of column lap-splices in specimen S-O1: a) S-01 reinforcement cage; b) chamfered end of the lapped reinforcement; c) Lap-splice length of 400mm ($40d_{b,c}$).

In the assessment of the as-built and retrofitted specimens, column lap-splice capacity was checked as discussed in §2.4.6. While the column lap-splices were not expected to govern the

failure mode of the as-built S-O1, as joint shear failure would dominate the inelastic mechanism, lap-splice failure was expected in the retrofitted S-R3 specimen. The extent of the influence of the lap-splice failure on the capacity of the as-built and retrofitted specimens was to be assessed through the experimental tests. For the retrofitted specimen S-R3, no attempt was made to change the design of the R3 retrofit scheme implemented for NS-R3 and SL-R3.

4.3.6 Specimens with floor slabs and transverse beams: SL-O1 and SL-R3

SL-O1 and SL-R3 were representations of the exterior joints of an interior frame, in which two transverse gravity beams were framed into the exterior beam-column joint of the interior seismic frame, as shown in Figure 4.1. In addition to the transverse beams, SL-series specimens had a cast-in-situ one-way floor slab spanning transversely across the beam. The cast-in-situ slab had thickness of 100mm with top and bottom R6 steel mesh on 150mm c-c squares (665TrueMesh^{TM}) and a cantilevered length of 490mm from the beam centre-line. This corresponded to a typical six-inch floor slab commonly found in pre-1970s RC frames. The reinforcing and geometry details of test units SL-O1 and SL-R3 are presented in Figure 4.12, Figure 4.15 and Figure 4.16.

The reinforcement detailing of the slab onto the beam-column joint was consistent with a typical gravity-designed one-way slab. The slab was assumed to span transversely to the beam-column joint. Therefore the top mesh was continuous across the beam longitudinal bars and the bottom mesh was anchored with a 180° hook, extending 1/3rd into the longitudinal beam width. On the transverse direction of the slab, top mesh was anchored into the transverse beams with 90° bents with a $24d_b$ anchorage length. The bottom mesh was discontinued outside the transverse beam, as per typical distribution reinforcement within discontinuous edge slab boundary detailing. No torsion reinforcement was included, though in some pre-1970s constructed buildings, torsion reinforcing in the form of U-shape clip reinforcement was added to the discontinued-edge slabs.

Figure 4.12: Reinforcing cage and details for test units with slabs – SL-O1 and SL-R3.

The transverse beam stub adopted the same reinforcing detailing as the main beam, not an uncommon assumption in pre-1970s 'gravity-frames' construction. An effective flange clear width and cantilevered length of the transverse beam of 490mm ($0.5b_b + h_b$) from either side of the beam-column centre-line was adopted. In designing the cantilevered slab and transverse beam width provided in the experimental setup, there is an balance of economics/cost and whether additional slab/beam width will provide any additional information. As discussed in §2.4.3, for beam-column joint subassemblies tests, the over-strengthening factor due to diaphragm interaction and beam elongation is rarely observed. Furthermore, for beam-column joints with smooth reinforcement, it was expected that the slab participation would be lower than joints with deformed reinforcement due to premature bond failure. Therefore, the conservative lower bound value (Cl. 9.3.1.4 instead of Cl 9.4.1.6.2) for the effective flange clear width (from beam edge) from the 2006 NZS3101 [30] was adopted.

Retrofit solution R3 was implemented for the retrofitted specimen SL-R3. This included a beam weakening at 165mm from the column centre-line and joint post-tensioning of 40kN (2.8% of $f_{y\text{-}pt}$). For the external post-tensioning of the joints, 16mm diameter holes were drilled through the transverse beams in order for the post-tensioning tendons to pass through, as shown in Figure 4.13b. The post-tensioning anchorage unit for the beam-column joint with transverse beams was similar to those used in the NS- series, but was inverted as shown in Figure 4.13c.

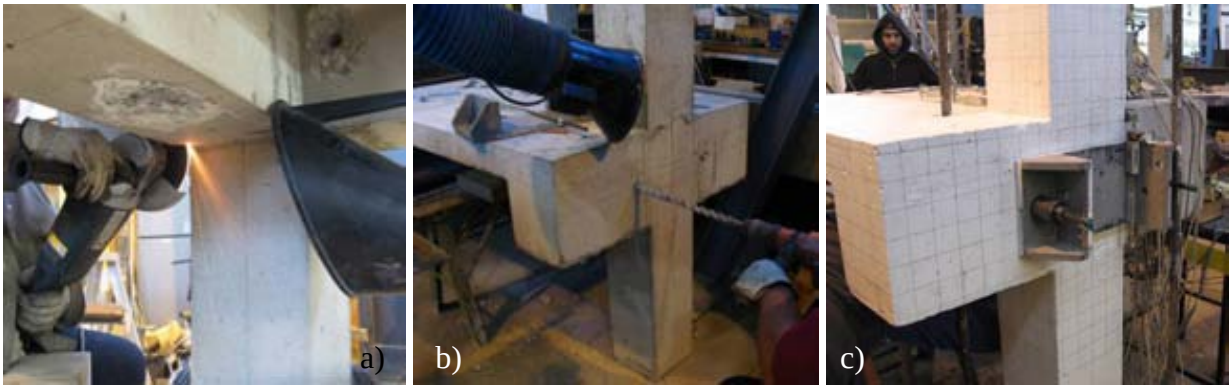

Figure 4.13: Retrofitting beam-column joint with slab, SL-R3: a) beam weakening; b) drilling through transverse beam for post-tensioning tendons; c) external post-tensioning anchorage at the external joint face.

While the beam-column joints with floor slab and transverse beams (SL-series) were meant to provide more realistic and practical validation of the SW retrofit (scheme R3), the SL-series also checked and confirmed the influence of shear demand under combined gravity and seismic loadings on the SW retrofitted beams. Expected gravity-loading and the relevant boundary conditions of internal forces were applied in the specimens with floor slab and

transverse beams (SL-O1 and SL-R3). The added gravity-loading on the slab gave a better representation of the loading and the capacity of the beam-column joints, as the added negative moment demand was compensated with the added negative beam capacity from the slab. The consequence of these combined effects was an increased shear demand on the beam and the joint. However, increased confinement and torsion resistance of the transverse beams, in turn, provided positive contribution to the joint behaviour. Further details of the gravity-loading on the SL-series beam-column joints are given in §4.6.4.

4.4 SPECIMENS CONSTRUCTION

4.4.1 Formwork and concrete casting

The formwork was manufactured from 20mm plywood sheets, reinforced with 90mm timber planks, steel angles and wood screws. The plywood sheets came with laminates of smooth surface. The formworks were oiled prior to casting to assist removal and the formwork internal edges were sealed with silicone sealants to avoid bleeding of water. In order to save material, many of the formworks were re-cycled from the available timber forms from previous tests. In saving casting time and overall cost, six beam-column joint specimens (NS-R1 to NS-R4, S-O1 and S-R3) were casted together using linked formwork as shown in Figure 4.14. For the beam-column joint with slab and transverse stub specimens (SL-O1 and SL-R3), the first set of formworks were modified in order to cast vertically in two stages, as shown in Figure 4.18.

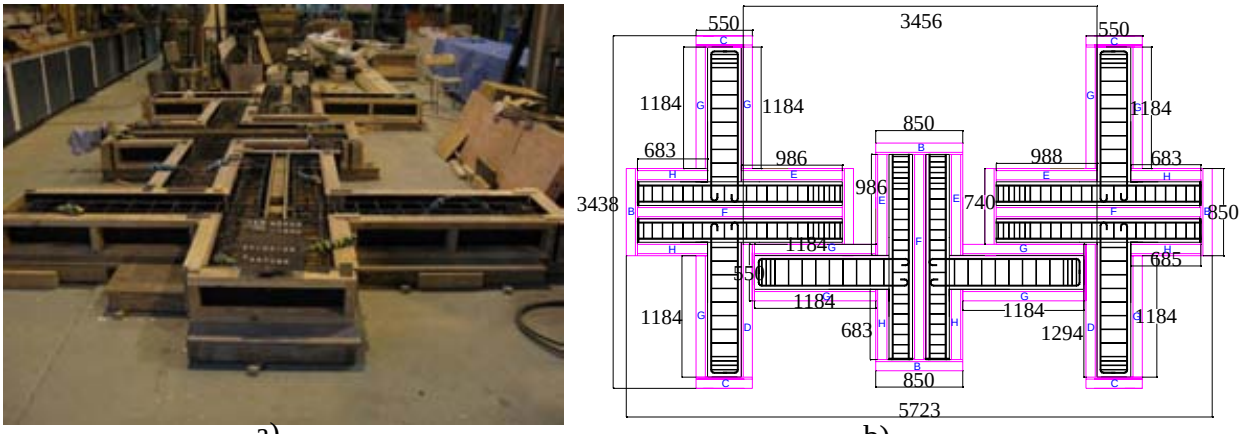

a) b)

Figure 4.14: a) 2D specimens without slab – ready for casting; b) Formworks for 2D specimens without slab.

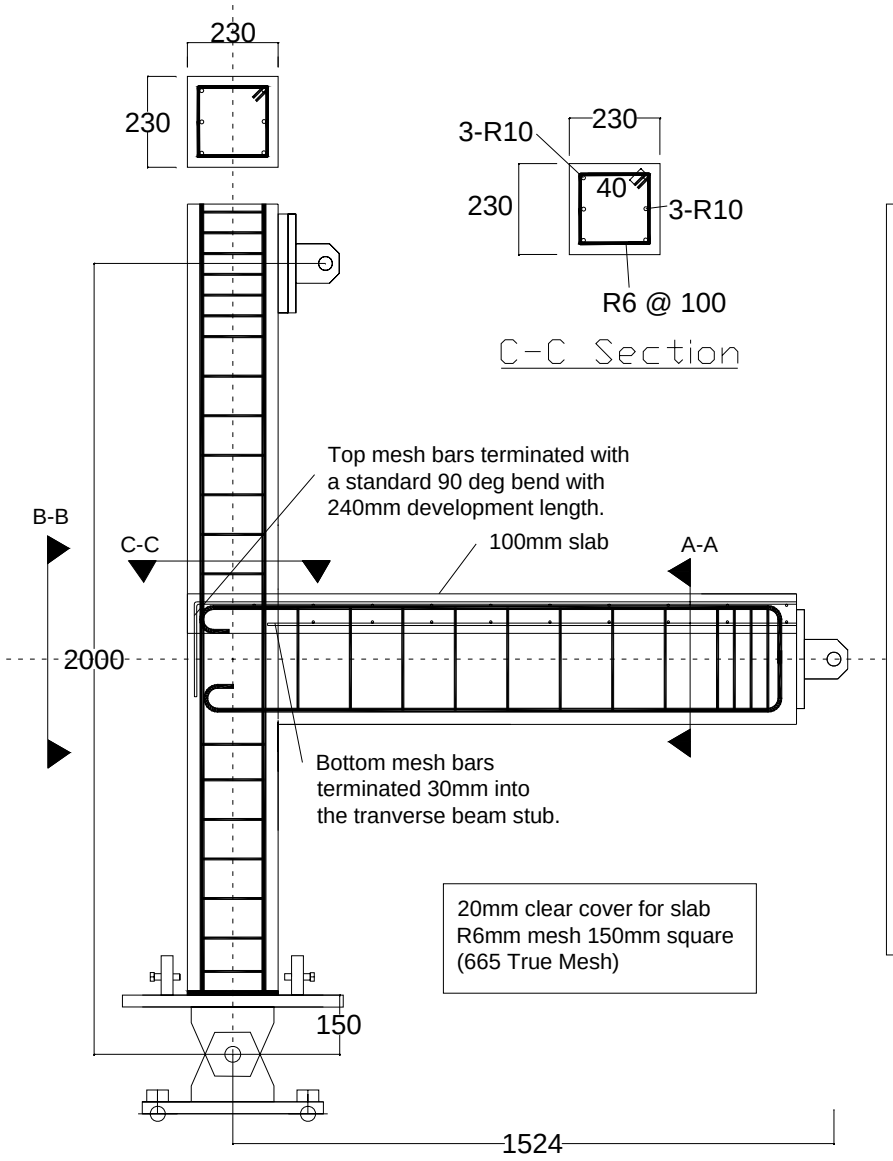

Test units: SL-O1 and SL-R3
Version: As per Built
By: Kam Weng Yuen

Notes:
1. Refer to NS-O1 drawings for reinforcing details of the columns and beams. Some details omitted in this drawing.
2. All dimensions in mm unless specified.
3.Clear cover to stirrup= 25mm, cover to long. bar centroid = 36mm and clear cover to mesh = 20mm.
4. Construction tolerance = 5mm.
5. Smooth reinforcements are used for long. and transverse bars.
6. No stirrups within the joint region.
7. Effective flange width assumed = 980mm (3 x beam depth). This is higher than NZS3101:2006 & ACI318-08 recommendation of lease of {1x beam depth, 8x slab thickness, beam length/4}.

Figure 4.15: Reinforcing and geometry details for test units with slabs – SL-O1 and SL-R3 – part 1.

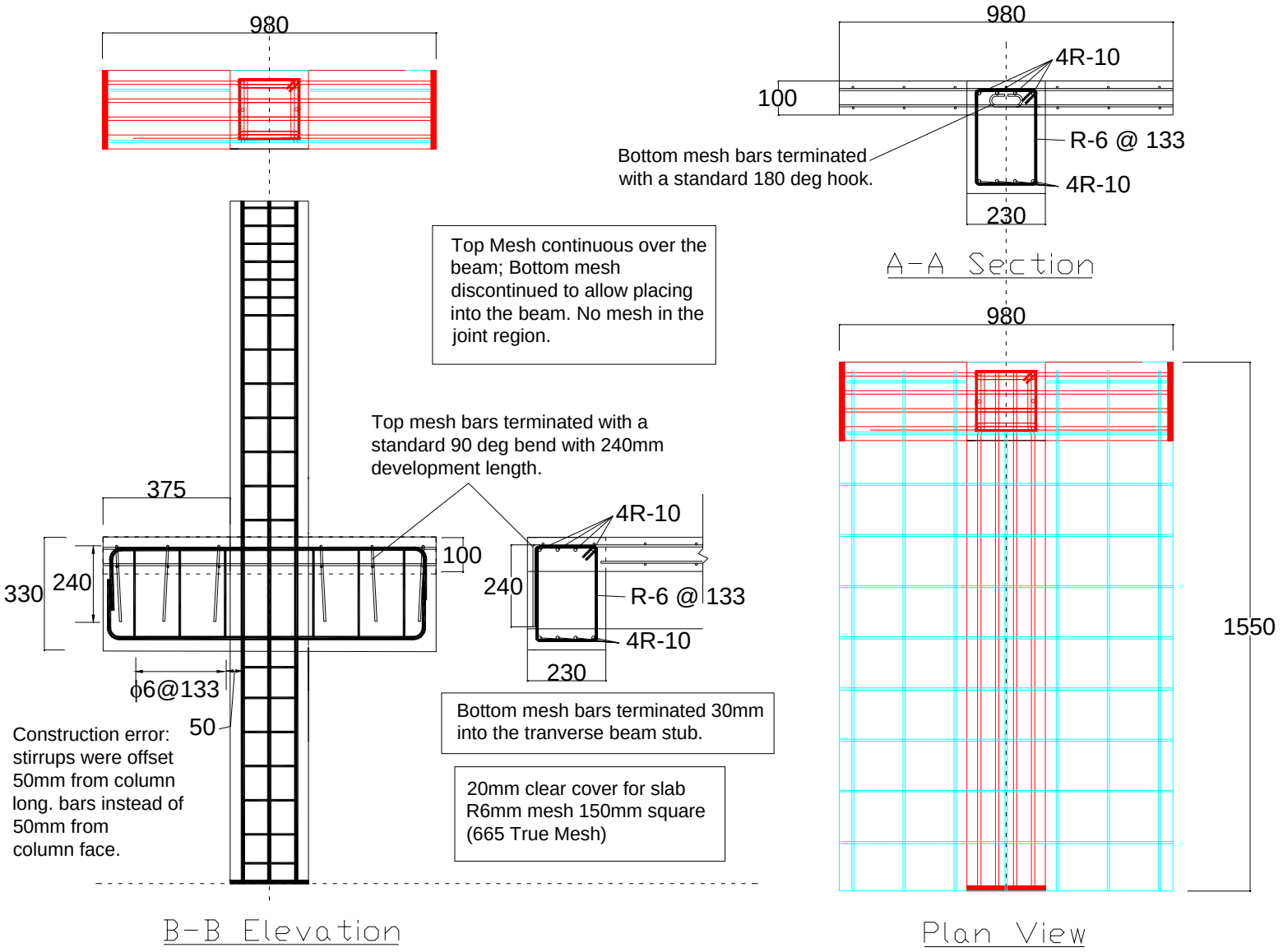

Figure 4.16: Reinforcing and geometry details for test units with slabs – SL-O1 and SL-R3 – part 2.

4.4.2 Reinforcing cages

All steel reinforcing bars were ordered to specified lengths and bents from a local steel provider. Careful steel order instruction was given to ensure correct bending of the end hooks and cranking of the column lapping reinforcement. The steel cages were tied together with 2mm tie wires with considerable care given to ensure the desired reinforcement spacing, before electrical strain gages were attached to the longitudinal and transverse reinforcement. Instrumentation will be further described later in this chapter (§4.7).

Upon the placement of the reinforcing cage in the casting mould, plastic spacers were inserted to ensure a 25mm clear cover to the stirrups reinforcement and an approximately 36mm cover to the centroid of longitudinal reinforcement of the beam and column. The 1955 NZS95 code specified an at least 1-1.5inch (25.4-38.1mm) clear cover to stirrups and a 1.5-2 inch (38.1-50.8mm) clear cover to main reinforcement, with the variation based on the assumed weather exposure. Therefore, for the 2/3-scaled beam-column joint test units, the specified concrete cover was consistent with the scaled concrete cover requirements of 25.4mm and 33.8mm for the stirrups and main bars respectively, assuming weather-exposed exterior beam-column joints. The distance between the ends of hooks of the beam longitudinal bars to the mould was checked to be at least 40mm ($4d_{b,b}$), as per the requirements for standard hooks. For specimens SL-O1 and SL-R3, the clear cover for the slab mesh was 20mm, which was comparable to the 1955 NZS95 requirement of 1.25 inch (un-scaled: 31.75mm and 2/3-scaled: 21.2mm).

The column longitudinal bars were butt-welded onto a 20mm steel base plate. The base plate was to prevent local crushing or bending at the base of the column. At the end regions of the beams and columns, additional stirrups were added to prevent localised damage due to stress concentration from the load application. Four 16mm ‘elephant foot’ internally-threaded anchors were used to provide connections between the specimen and the test setup (Figure 4.17a).

Figure 4.17: a) Anchorage for the loading plates; b) Details of the joint reinforcing; c) Steel reinforcing cages.

4.4.3 Concrete casting

Except for the specimens with slabs (SL-O1 and SL-R3) and the as-built specimen NS-O1, all other specimens were casted horizontally in one single pour (see Figure 4.18a). The concrete was supplied by a ready-mix plant, with specified 28-days f'_c and slump to be 20MPa and 150mm respectively. The maximum aggregate size was 13mm to allow for some concrete micro-structure scaling. The concrete was placed by a concrete laydown bucket and was compacted with portable electric vibrators. After casting, all test units were cured for approximately seven days with damp hessian fabrics covered with plastic sheets. Formworks were stripped off the test units after the curing period.

Figure 4.18: a) Casting of 2D-plane specimen without slabs; b) Preparation of concrete cylinder units; c) Formworks for beam-column joint with slab specimen; d) Casting of NS-O1 specimen.

For the specimens with floor slab and transverse beams, NS-O1 and NS-R3, two separate vertical castings were carried out. In the first pour, the beams, slab, joint and the bottom half of the column were casted with concrete ordered from a commercial ready-mix plant (see Figure 4.18c-d). The concrete f'_c and slump were specified to be 20MPa and 150mm respectively. In the second pour, the top half of the column was casted with concrete mixed in the laboratory. The concrete mix with a water-cement-ratio of 0.76 and a water demand of 170 litre/m^3 was designed to achieve the same specified strength and slump as the ready-mix concrete.

Slump tests were carried out before the concrete casting. For each casting session, six cylinders were prepared for the 7 and 28 days concrete compressive tests. In addition, for each specimen, three additional cylinders were prepared for the day-of-testing f'_c tests. All concrete material tests were done in accordance to the NZS3112:1986 standard [31].

4.5 MATERIAL PROPERTIES

4.5.1 Reinforcing steels

The longitudinal and transverse reinforcement used for all test specimens was mild steel Grade 300E plain round bars. At least five reinforcing steel testing samples were prepared for each batch of steel reinforcement used to construct the test units. These samples were tested on the Avery Universal Testing Machine, in accordance to NZS4617:2001 [34] with an average loading rate of 600MPa/min. The average material properties of the steel reinforcement are presented in Table 4.4. Typical stress-strain curves of the steel reinforcement are presented in Figure 4.19.

Table 4.4: Average material properties of steel reinforcement.

Test Unit	Description	A_s (mm^2)	E_0 (MPa)	f_y (MPa)	f_{ult} (MPa)	ε_{sh} (%)	ε_{ult} (%)	n
NS-O1	Beam & Column R10	78.5	195566	362	482	1.0	15	5
	Beam & Column R6	28.3	194738	400	512	0.5	10	5
NS-R1 to	Beam R10	78.5	202527	335	456	3.5	20	12
NS-R4, S-	Column R10	78.5	211825	351	475	3.5	20	14
O1, S-R3	Beam & Column R6	28.3	201195	432	528	0.2	8	14
	Beam R10	78.5	206324	347	455	4.0	18	5
SL-O1 and	Column R10	78.5	196730	489	637	2.0	15	6
SL-R3	Beam & Column R6	28.3	203163	431	539	0.5	10	5
	Mesh R6 *	28.3	200000	485	675	0.5	10	0

Note: As is the bar area, Eo is the elastic Young's modulus and n is the number of specimen tested. ε_{ult} (%) is the strain at the peak stress, f_{ult} (before necking) and is taken to be the maximum uniform elongation as defined in NZS 4671:2001 if the strain at the peak stress is not observed. ε_{sh} is the strain at the end of the yield plateau and the onset of strain-hardening. *Mesh R6 reinforcements were not tested and the most probable values specified by the manufacturers are shown.

The average measured yield strengths (f_y) were generally larger than the specified values for Grade 300E steel bars by 12% to 20% for the R6 bars and by 33% to 62% for the R10 bars. New Zealand steel suppliers still provide Grade 430 based on the older NZS3402 specification [32] for cold-formed R6 stirrup reinforcement as generally the over-strength and lower ductility for stirrup reinforcement are acceptable. Thus, it was not surprising that most supposedly Grade 300E R6 stirrups had measured f_y ranging from 400MPa to 432MPa, with nearly no yield plateau within the stress-strain relationship, as shown in Figure 4.19. For the R6 mesh steel, no reinforcing samples were tested as the tensile test apparatus was not suitable for a small sample. The properties listed in Table 4.4 for R6 mesh bars are taken from the New Zealand Steel reinforcing mesh handbook [46].

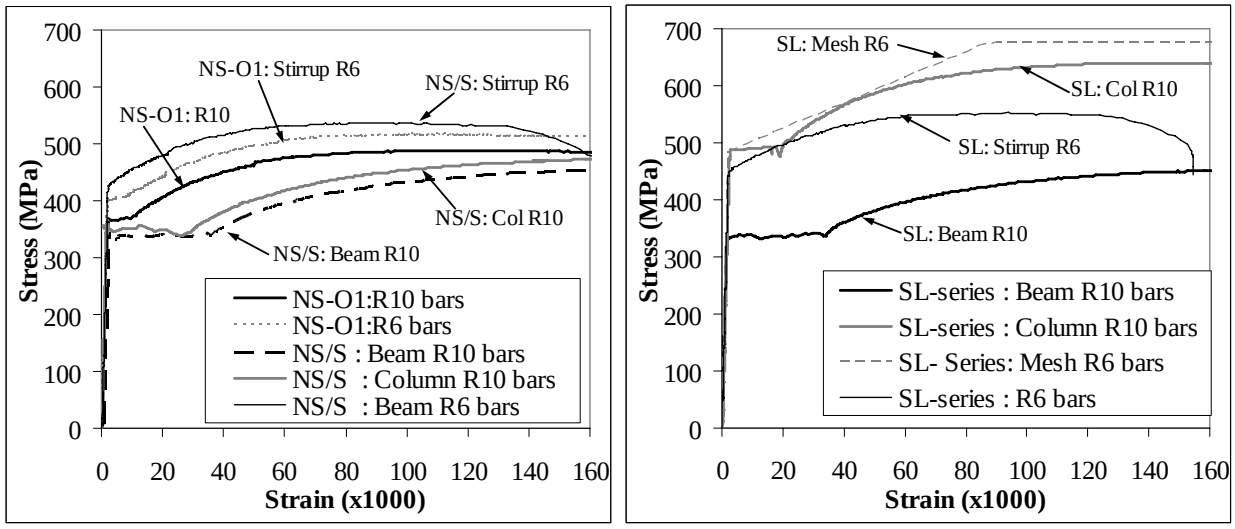

Figure 4.19: Typical stress-strain curves for the steel reinforcement.

Another anomaly in the steel test results was in the R10 column bars used for specimens SL-O1 and SL-R3. On average, the test coupons for column R10 bars used for the SL-series registered f_y of 489MPa and ultimate strength (f_{ult}) of 637MPa, which were beyond the expected characteristic values for Grade 300E mild steel. In the NZS4671:2001 standard, Grade 300E should have 5% and 95% percentile yield strengths of 380MPa and 300MPa respectively. This 62% discrepancy of steel yield strength would over-strengthen the columns and affect the hierarchy of failures of the SL-series beam-column joints. Nevertheless, for the SL-series specimens, analytical assessment has shown that the failure mode would not have changed even with the over-strength factor of 1.40 for the column reinforcement.

Historically, pre-1970s New Zealand RC structures were predominantly constructed using structural steel with minimum f_y of 33,000 psi (227MPa) as specified in the 1962 NZS1693 code [29, 35]. In the subsequent NZS1693 amendments and the newer NZS3402 code revisions [32, 33] in the mid-1970s, the minimum steel strength was increased to 275MPa. The use of Grade 300E mild steel nevertheless was justified as the relative strengths between each element within the beam-column joints would remain consistent despite the higher yield strength.

4.5.2 Concrete

The specified 28-day concrete compressive strength, f'_c, was 20MPa, to reflect the pre-1970s construction practice. NZS95:1955 [28] for example, specified 1500-4000 psi concrete (10.3-27.6MPa) for maximum allowable working stress, beyond which a special study was required. While concrete aging may result in concrete strength 1.5 times the original specified f'_c at 28 days, this was partly and implicitly accounted for by the consideration that all the beam-column

joint specimens would be tested between 100-180 days after casting, due to the constraint of laboratory testing setup availability.

Six 100mm diameter x 200mm test cylinders were prepared for 7-day and for 28-day tests for each casting batch. In addition, three test cylinders were prepared for day-of testing compressive tests. These test cylinders were cured in a fog room at 20°C temperature and near 100% humidity. The concrete cylinders were tested using the Avery Universal Testing Machine, according to NZS3112:1986 requirements [31]. Test results are summarised in Table 4.5. As noted, several different casting batches were necessary and slump tests were done prior to each casting batch. To determine the tensile strength of the concrete, a conservative empirical equation [39] of $f'_t = 0.5\sqrt{f'_c}$ was adopted.

Table 4.5: Concrete material properties including compressive strengths and casting/testing dates.

Test Unit		f'_c 7-day (MPa)	f'_c 28-day (MPa)	Day of testing strength, f'_c (MPa) [1]	Day of testing strength, f'_t (MPa) [2]	Age during testing (days)	Date of Testing	Date of Casting	Slump (mm) [3]
	NS-O1	9.8	17.5	17.3	3.2	137	22/02/2008	15/10/2007	180
	S-O1	15.1	20.6	15.1 [4]	1.9	71	6/08/2008	27/05/2008	170
	NS-R1			25.6	2.5	113	18/09/2008		
	NS-R2			25.1	2.5	105	10/09/2008		
	NS-R3			24.3	2.5	133	7/10/2008		
	NS-R4			30.3	2.8	325	17/04/2009		
	S-R3			27.5	2.6	308	31/03/2009		
SL-O1	Bottom Half	13.7	16.4	19.9	2.2	178	4/06/2009	8/12/2008	160
	Top Column	8.2	10.4	13.4	1.8	171		15/12/2008	190
SL-R3	Bottom Half	13.8	18.4	23.1	2.4	185	10/07/2009	26/01/2009	130
	Top Column	12.7	12.7	17.0	2.1	171		9/02/2009	160

[1] Tested according to the NZS3112-Part 2:1986 specifications with at least 3 samples. [2] Except for NS-O1, the tensile strength, f'_t is determined from $f'_t = 0.5\sqrt{f'_c}$. [3] Tested according to the NZS3112-Part 1:1986 specifications.

[4] There was excessive bleeding of the test cylinders due to error in cyclinder preparation.

The average 28-day f'_c for the casting for the six plane beam-column joint specimens indicated correct concrete strength was achieved. However, for test unit S-O1, which was tested in 71 days, the concrete cylinder tests were registered unexpected low values due to the excessive bleeding of the test cylinders. Two specimens: NS-R4 and S-R3, which were tested much later after the casting, at 325 and 308 days respectively, had gained some strengths but still within the most probable strength limit of 1.5 times the specified f'_c [35]. The two laboratory-mixed concrete for the top columns of SL-O1 and SL-R3 were found to be relatively weak, with 28-day strength of 10.4MPa and 12.7MPa respectively.

4.6 TEST SETUP AND PROTOCOL

4.6.1 Test setup

The beam-column joints were tested upright as per real position within a reinforced concrete frame, as shown in the experimental test setup in Figure 4.20. To simulate earthquake loading, a cyclic quasi-static lateral loading was applied from the top of the column, which represented the contra-flexural point at the mid height of an inter-storey column. The horizontal servo-controlled actuator was connected to the specimen by a 40mm diameter steel pin connection which allowed free rotation but constrained horizontal displacements. The horizontal cyclic load was applied using the servo-controlled 50kN hydraulic jack connected to an automatic hydraulic pump that was operated at 3000 psi pressure and a maximum flow rate of 130litre/min.

The top of the column was connected to the actuator with steel plates bolted into four M16 ‘elephant foot’ anchorages that were cast into the concrete (Figure 4.17a). The bottom of the column was placed on a 2D universal hinge base which allowed unidirectional free rotation. The column was prevented from slipping through a set of 16mm bolts and steel plates welded to the pin base. The end of the beam was connected to a pin-pin connection, which allowed free horizontal displacement, thus allowing beam elongation and satisfying the beam-column joint subassemblage’s boundary conditions as shown in Figure 4.1. To restrain out-of-plane movement, the Y-direction horizontal ram was connected during the testing, with pin-pin connection as per the horizontal loading setup described above.

Vertical axial load was applied using a self-equilibrating apparatus as shown in Figure 4.20. A 300kN servo-controlled actuator applied the compression axial load on the column by pushing against a 40mm steel plate that was tied back to the column hinge base by two 24mm diameter high strength MacAlloy bars. While varying axial loads were applied, the applied axial load was ensured to maintain compression loading, as the self-equilibrating loading setup could not accommodate axial tension to occur. The axial load actuator was connected to the same hydraulic pump as the horizontal load actuator.

All the specimens were thoroughly instrumented to measure: a) lateral force applied, b) displacement at the top of the column, c) local deformation components, and d) strains in the reinforcement. All instrumentations were connected through a series of four-pin serial cables and analogue-to-digital protocol convertor to a data logging computer with the Universal Data Logging programme. For the loading control, the load cell and corresponding monitoring

potentiometer for each servo-controlled hydraulic actuator were connected to a controller box via a series of RS-422 cables and were converted into a RS-232 feed into the controller computer.

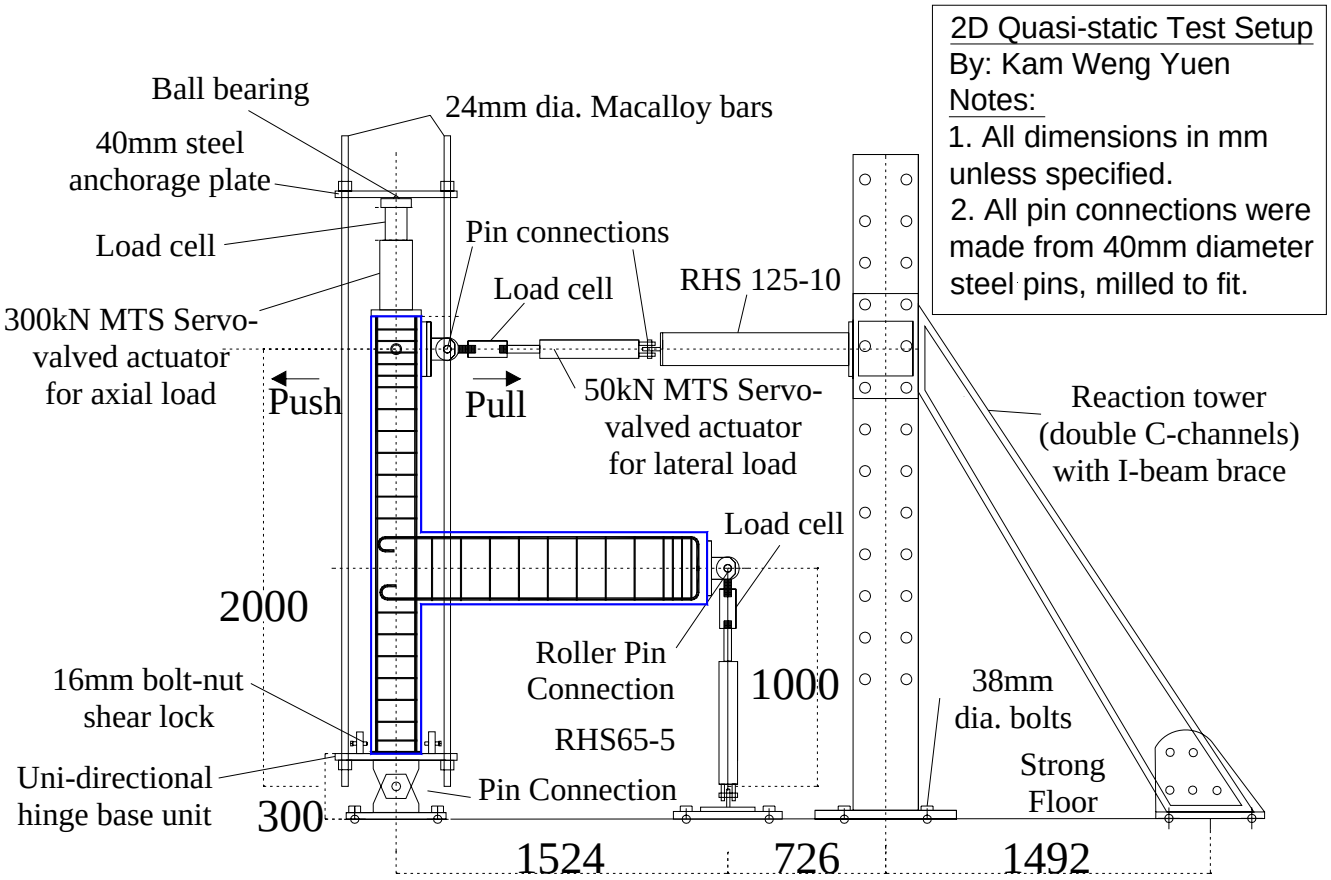

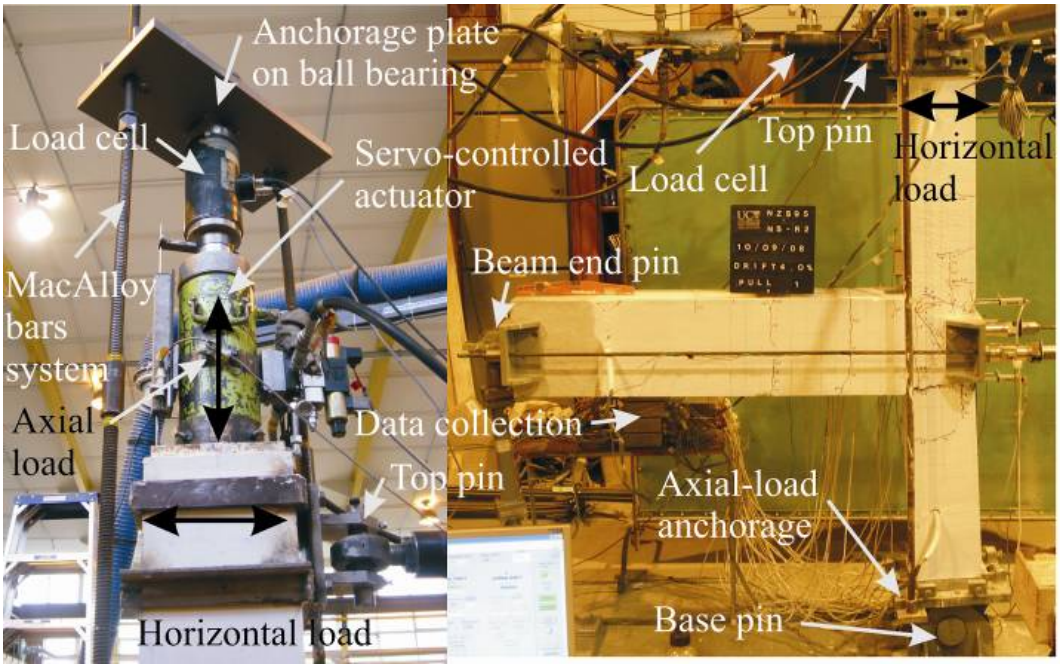

Figure 4.20: top) Experimental test setup; bottom) Photo of axial loading apparatus and test setup.

4.6.2 Lateral loading protocol

The lateral loading protocol used in this experiment consisted of two displacement-controlled cycles at increasing amplitudes: 0.1%, 0.2%, 0.5%, 1.0%, 1.5%, 2.0%, 2.5%, 3.0% and 4.0% inter-storey drift, as shown in Figure 4.21a. The quasi-static cyclic testing regime allowed a careful monitoring of the different performance limit states, which was crucial in generating mechanistic and behavioural (macro) models [22]. The lateral loading was coupled with varying axial loading, whose details will be explained in the next section. Two displacement-controlled loading cycles were preferred over the more demanding three-cycle increasing quasi-static loading typically adopted for the qualification of new structural systems [4]. Such preference in the retrofitted and as-built non-ductile beam-column joints was justified by that it may be excessively demanding to impose three cycles of peak inter-storey drift based on dynamic analyses of as-built RC frames (e.g. [18, 37]).

The loading direction sign convention adopted in this thesis is shown in Figure 4.21b. As a sign convention for the thesis, *Pull loading direction* refers to the *positive top column lateral displacement,* Δ_c, which induces *positive beam bending moment,* M_b, and *tension strain* in the bottom face of the beam. This also corresponds to *positive lateral force,* F_c, imposed on the column and *negative beam shear* force along the beam section. Therefore, *Push loading direction* refers to the *negative top column lateral displacement,* Δ_c, *negative lateral force,* F_c, *negative beam bending moment,* M_b, and *tension strain* in the top face of the beam.

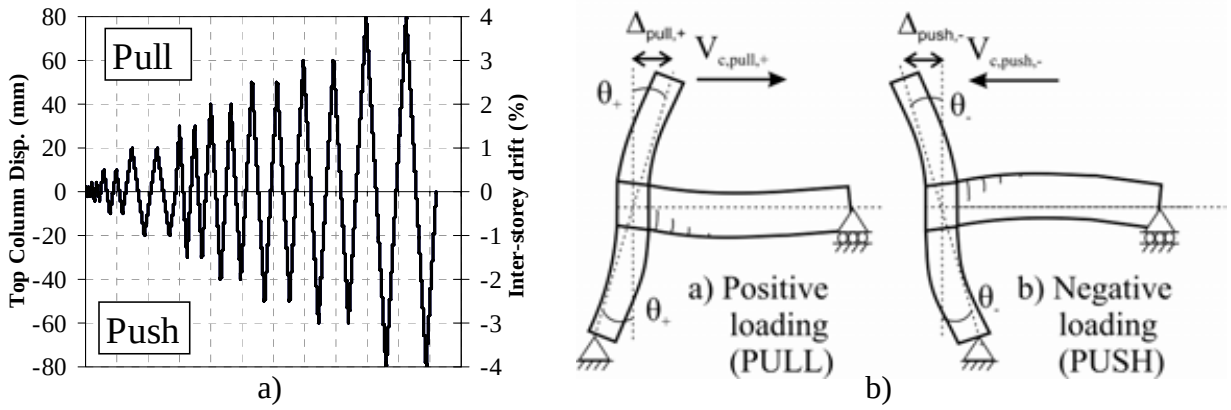

Figure 4.21: a) Quasi-static loading protocol; b) Loading direction sign convention.

Inter-storey drift was adopted as the displacement / response index because this was consistent with the growing recognition of the need to establish displacement capacity as well as force and ductility capacities. However, it was recognised that the interpretation of the imposed inter-storey drift demand needed to be related to the displacement ductility demand from inelastic dynamic analysis, which considered the inherent stiffness and energy dissipation of the structure

[37]. Furthermore, the traditional University of Canterbury ductility-cycles based approach [37] was not adopted because the yielding capacity of the beams might not be achieved in as-built non-ductile beam-column joints.

Lateral loading was imposed using a hydraulic servo-controlled actuator connected to the top of the column, as shown in Figure 4.20. An in-house LabView^{TM} programme [26] for unidirectional quasi-static loading with a variation of column axial loads was used for loading control. In order to remove the strain-rate effect and to achieve stable loading, a small displacement increment was adopted. Between 0.2% to 1.0% drift cycles, a 0.01% drift (0.2mm) step was adopted, while between 1.5% to 4.0% drift cycles, a 0.025% drift (0.5mm) step was adopted. In total, each testing protocol had 5600 step points.

4.6.3 Variation of axial loading

Variation of axial load on the exterior beam-column joints of RC frames is expected as observed in static and dynamic analyses of RC frames e.g. ref. [21]. For exterior beam-column joints, the induced variation of column axial demands due to the frame actions and vertical acceleration can be up to 100% of the axial action due to gravity loads, resulting in tensile actions in the columns [1, 13, 20, 21]. The bond behaviour and the shear capacity of the beam-column joints are significantly affected by the level of axial load presence in the joint [5, 20, 23, 45]. In addition, the variation of axial load also significantly reduces the columns' flexural and shear strength and ductility capacities [1, 7, 13, 17]. While the increase of axial load is considered to be beneficial to the beam-column joint sub-assemblies (e.g.[39]), the additional axial load might also result in the principal compression stress, p'_c, in the joint exceeding the compression strut capacity ($0.3f'_c$ MPa [40]). Furthermore, the increase in axial load in the column and joint also precipitates premature axial load failure and column longitudinal bars buckling.

Therefore, to simulate more realistically the seismic demand and capacity of the external beam-column joints, a varying axial load was imposed on the beam-column joints. As reviewed in Chapter 2, most previous experiments on beam-column joint subassemblies (for both existing capacity and retrofit solution evaluations) have used either constant or zero column axial loads. In this research, the variation of axial load is quantified as a function lateral load applied to the columns, as reflected by Equation 4.1 below, where the constant α is a geometric function of the RC frame and F_c is the lateral force applied at the top of the column:

$$N = N_g + N_e = N_g + \alpha F_c \quad \textbf{4.1}$$

For the prototype six-storey, three-bay, non-ductile RC frame described in §4.2.1, Equation 4.2 gives the function of the variation of axial load used in the experimental test. The variation of axial load was controlled directly by the LabView™ in-house controller programme and a 300kN servo-valve hydraulic actuator (as shown in Figure 4.20). Due to the limitations of the test setup, the axial load in the column must remain in compression and this provided an upper bound for the α value that can be used. The value of the varying axial load ratio, α=4.63, while unusually high, accounted for the induced axial load changes within a six-storey, three-bay RC frame as shown in Figure 4.1. The derivation for the values given in Equation 4.2 is given in Appendix A.

$$N = 110kN \pm 4.63F_c \quad \textbf{4.2}$$

To investigate the possible range of α values given the typical pre-1970s RC frame building configurations of 3-8 stories high and 3-5 bays long, a simple static analysis, where seismic inertial force was assumed to be acting at 2/3rd height of the building, H, was carried out. Referring to calculations in Appendix A, Table 4.6 below shows the possible range of α value for the exterior beam-column joints in internal frames considering the typical pre-1970s RC frame buildings, assuming the overturning moment at the base is resisted by the induced axial loads in the exterior columns. For buildings with several bays, this approximation may be incorrect as seismic axial forces would be also induced in some of the interior columns. It can be concluded that for a mid-rise RC frame, where H exceeds 9m, the variation of axial load should be explicitly considered in the assessment of the exterior columns of RC frames. The ratio of variation, α, increases in proportion to the induced overturning moment at the base of the building, and therefore to the building height.

Table 4.6: The range of α value for variation of axial load on exterior columns. An inter-storey height of 3m and a bay length of 4.5m are assumed.

α ratio	3 storeys (9m)	6 storeys (18m)	8 storeys (24m)
1 bay	2.68	5.36	7.15
3 bays	2.23	4.46	5.96
6 bays	2.12	4.24	5.68

For the corner exterior joints (of perimeter frames), the effect of variations of axial loads can be more severe as shown by experimental tests [10, 16]. While the scope of this study

excludes the corner exterior joints, designers can easily account for the corner joint amplification by multiplying the unidirectional variation of axial load by a factor of 1.414 ($\sqrt{2}$ – assuming 45° angle attack and symmetrical joint dimensions) [39].

4.6.4 Gravity-loading for SL-O1 and SL-R3

Referring to the gravity-load calculation in Appendix A, the uniformly distributed dead and live loads (G+Q) for each RC frame of the prototype building were calculated to be 19.2kN/m for typical floors and 10.0kN/m for the roof level. Linear static analysis (e.g. with SAP2000) with a cracked stiffness of $0.4I_g$ and $0.6I_g$ for the beam and column sections respectively were used to determine the bending moment and shear demands at the level 2 exterior beam-column joint. The resulting bending moment, M_b*, and shear force, V_b*, at the beam-to-column face, determined from elastic analysis of the prototype RC building, were 28.4 kNm and 43.1kN respectively. By taking the appropriate scaling factors, $(2/3)^3$ and $(2/3)^2$ for bending moment and shear force respectively, the required imposed actions due to gravity loads for the beam-column joint subassemblies model were M_b*=8.4kNm and V_b*=19.2kN. There was an incompatible region at the mid-span of the beam due to different boundary conditions. However, this was not significant as it would be far from the important beam-column connection region.

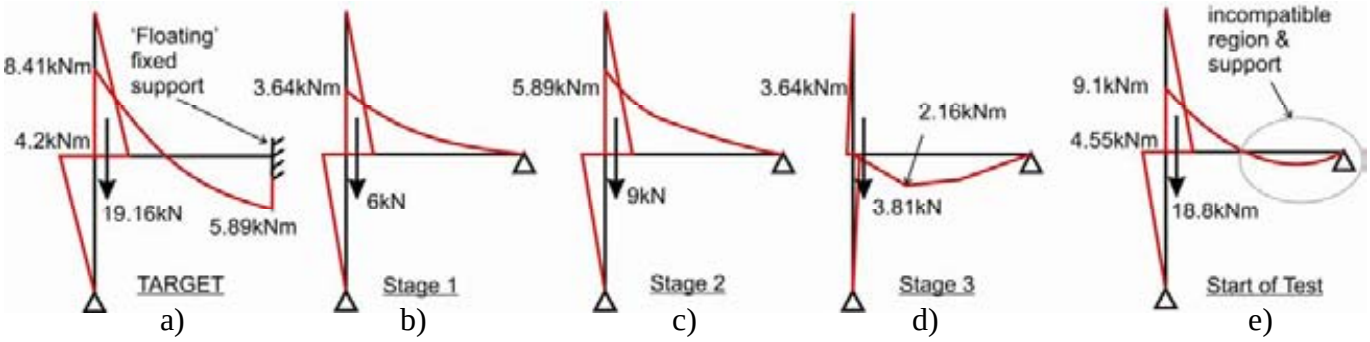

Figure 4.22: Boundary conditions for beam-column joint with slab subassembly: a) Required as calculated from static analysis; b) Imposed at stage 1; c) Imposed at stage 2; and d) Imposed at start of test.

To replicate the demand on the critical beam-to-column face section, 1608x300x20mm steel plates, weighing approximately 100kg each, were placed on the floor slab. The bending moment diagrams and the shear forces at the beam-column interface at every stage of the loading are shown in Figure 4.22. Table 4.7 summarises the imposed internal forces at every stage of the gravity loading, which was divided into three stages:

1. The beam-column joint subassembly was set up with the column levelled, all instrumentation values zeroed and the beam propped by an external screw jack. The external prop was then removed and the beam and floor slab were effectively cantilevered

off the column face. The cantilevered self-weight of the beam and slabs would induce M_b=3.64kNm and V_b=5.55kN at the beam-column critical section (Figure 4.22b).

2. With the beam cantilevered, three steel plates were placed parallel to each side of the beam. One and two additional plates were placed at 450mm and 750mm from the column face respectively. These added steel plates generated M_b=5.89kNm and V_b=9.0kN at the critical section (Figure 4.22c). The steel plate configuration is shown in Figure 4.23b.
3. The beam-end vertical pinned support was then bolted up.. A further nine steel plates were placed onto the slab at 450mm and 750mm from the column face, as shown in Figure 4.23c. Adding weight to the beam-end support pinned would induce the required V_b at the beam-column face while maintaining the negative M_b. The final internal actions on the beam-column interface section were M_b=9.1kNm and V_b=18.8kN (Figure 4.22d).

Table 4.7: Summary of imposed internal actions from added gravity load.

Stage	Description	Beam-column interface		Beam-span (maximum)		Total added weight
		Moment (kNm)	Shear (kN)	Moment (kNm)	Shear (kN)	
1	Self-weight of cantilevered beam and slab.	-3.64	5.50	0	0	0
2	Cantilevered beam: 6 plates in parallel to beam, 1 plate at 450mm from column face and 2 plates at 750mm from column face.	-5.89	9.00	0	0	900
3	Pinned beam-end: 4 plates at 450mm from column face and 3 plates at 750mm from column face.	0.44	3.81	2.1	-3.19	700
Final	At the start of tests	-9.09	18.31	2.1	-3.19	1600

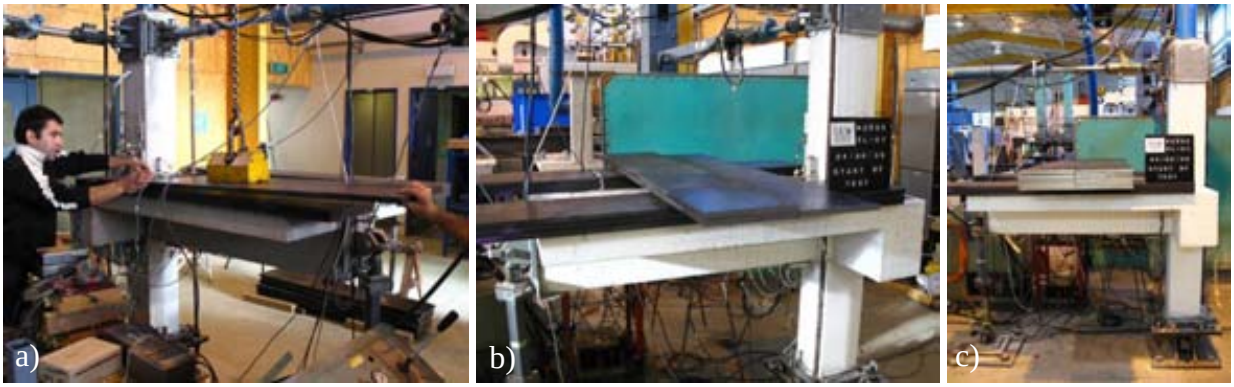

Figure 4.23: Stages of steel plates loading for gravity-load actions on SL-O1 and SL-R3: a) Parallel steel plates with cantilevered beam; b) total gravity load with cantilevered beam; c) total added steel plates (with pinned beam end) at the start of test.

4.7 INSTRUMENTATION

4.7.1 Measurements of loads

Applied loads and reactive forces were measured using load cells, which consisted of hollow cylinders machined from high strength steels and instrumented with two independent sets of full bridge circuits of 350Ω resistance strain gages. The load cells were calibrated in compression up to 125% of the expected load range using the Avery Universal Testing Machine. A 300kN capacity load cell was used to measure the varying vertical axial force on the column, while 50kN capacity load cells were used to measure the applied horizontal force and the reactive force at the beam-end. The location of the load cells is shown in the test setup in Figure 4.20.

4.7.2 Measurements of displacements

To measure the global horizontal displacements of the beam-column joints, rotary potentiometers with a 5kΩ resistance were used. The locations of these rotary potentiometers are shown in Figure 4.24a. For the top-of-column displacement measurement for both loading control and data logging, a loaded-spring rotary potentiometer with approximately 150mm travel length on each side was used. In measuring mid-depth beam net elongation, two disc potentiometers, connected to the specimen with a nylon wire through a drilled bolt and with weight on the free end were used. Inter-storey drift, θ_{drift}, was obtained by dividing the global horizontal displacement at the top of column, Δ_{drift}, with the column inter-storey height:

$$\theta_{storey} = \Delta_{drift} / h_c \qquad \textbf{4.3}$$

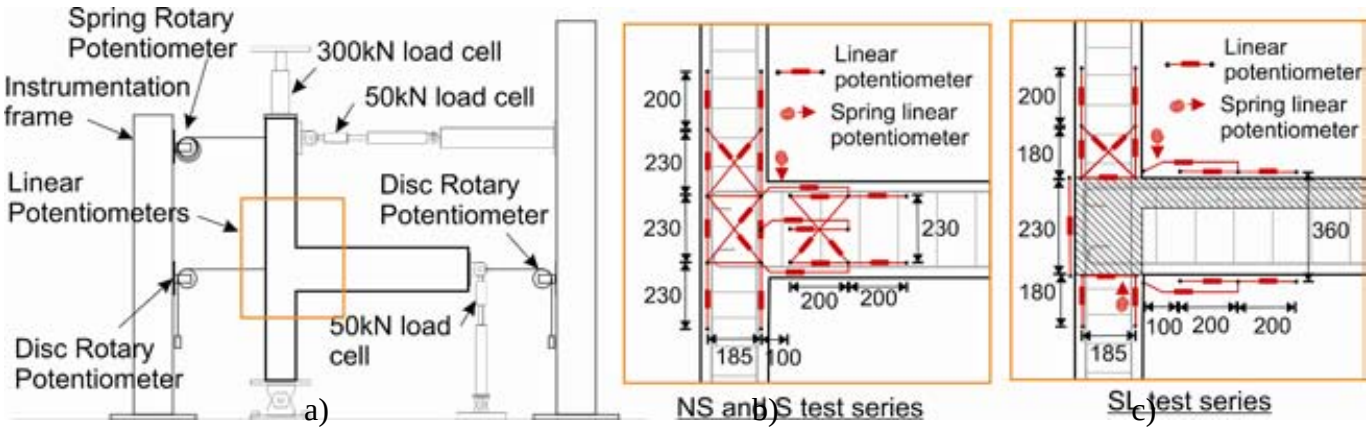

Figure 4.24: a) Load and displacement instrumentation; and b) Location of potentiometers to measure average rotation and shear distortion.

4.7.3 Measurements of average rotations and shear distortions

Linear Variable Displacement Transducers (LVDTs) or linear potentiometers were used to monitor the average rotations of the beams and columns during the test. Two pairs of LVDTs across the beam-column interface were used to determine the fixed-end rotation of the beam. In addition, three pairs of diagonally inclined LVDTs were used to measure the shear distortions within the beam-column joint region, and critical column and beam regions. The procedure to calculate the average rotations and shear distortions will be discussed in the next section (§4.8). Extensions or elongations of the potentiometers were taken to be positive values.

The position of the potentiometers is shown in Figure 4.24b. Calibrated LVDTs of 30mm and 50mm travel lengths were mounted on 6mm steel rods, which were epoxied into the pre-drilled 20mm deep holes on the specimen's concrete surface. Bostik Titan Bond^{TM} epoxy was used. For the beam-chord rotation measurement, the LVDTs were placed at the top and bottom faces of the beams (instead of the sides).

For the SL test series (beam-column joint with slabs), a slightly different configuration of potentiometers had to be used due to the presence of the floor slabs and transverse beams, as shown in Figure 4.24b and Figure 4.25. However, by measuring only the relative vertical and horizontal deformations of the joint panel zone, the estimation of joint shear distortion requires the assumption of constant relative vertical-horizontal distortion, which is not true.

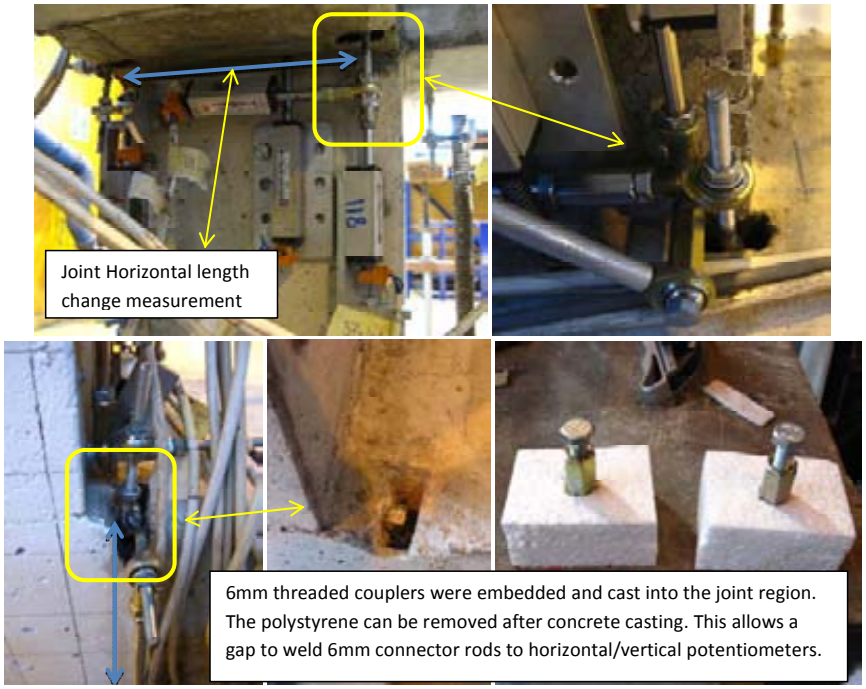

Figure 4.25: Instrumentation for measuring joint shear distortion of beam-column joints with slab and transverse beams.

4.7.4 Measurements of internal deformations

Local strains in reinforcement were continuously measured using electrical resistance wire strain gages. 5 mm long strain gages (TML FLA-5-11-3L) were used on the longitudinal bars and 3 mm long gages (TML FLA-3-11-3L) were used on the stirrups. Both types had gage resistances of 120Ω. Figure 4.26 shows the locations of the strain gages on the longitudinal and transverse reinforcement for all the specimens and Figure 4.27 shows the strain gages layout on the floor slab mesh for specimens SL-O1 and SL-R3. At each location, one strain gage was attached to the outside surface of the reinforcement. Two gages were used across most sections in order to provide redundancy against strain gage failure during concrete casting and testing.

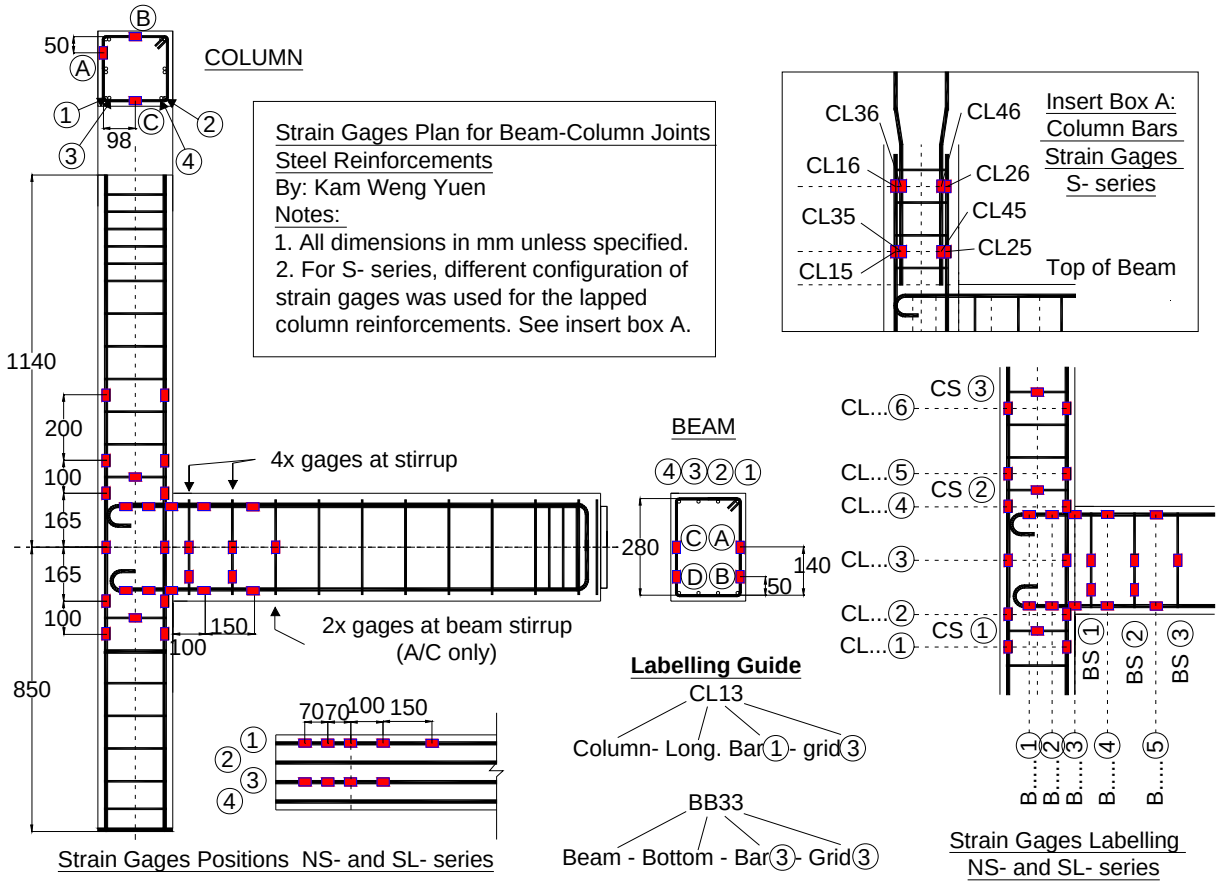

Figure 4.26: Strain gages plan and labelling guide for all beam-column joint test units.

Surface preparation was done as recommended by the strain gage manufacturer (Tokyo Sokki Kenkyujo). A small 5-7mm rectangular flat area was made on the steel reinforcement using a file or a sand grinder. The surface was then cleaned with #120 sand papers and cotton buds dipped in acetone solution. A drop of TML-CN (Cyanoacrylate) bonding adhesive was placed onto the back of the strain gage and the prepared surface before the strain gage was pressed onto the reinforcement surface with a polyethylene sheet for approximately 30 seconds of curing time.

Caution was taken to ensure the strain gage was placed at the correct marked centre-line location. Three layers of waterproofing coating paste (TML-N1) were placed within 48 hours over the strain gages and the wire terminal. Then, a 3M rubber mastic tape was used to cover the strain gages to provide protection against physical abrasion. Finally, the strain gages were tested before and after the casting of the concrete using a strain-gage resistance tester to check their connectivity. The labelled strain gages' lead wires were bundled in groups and tied along the reinforcement bars. The wires were led away from the beam-column joint regions and protected during the concrete casting.

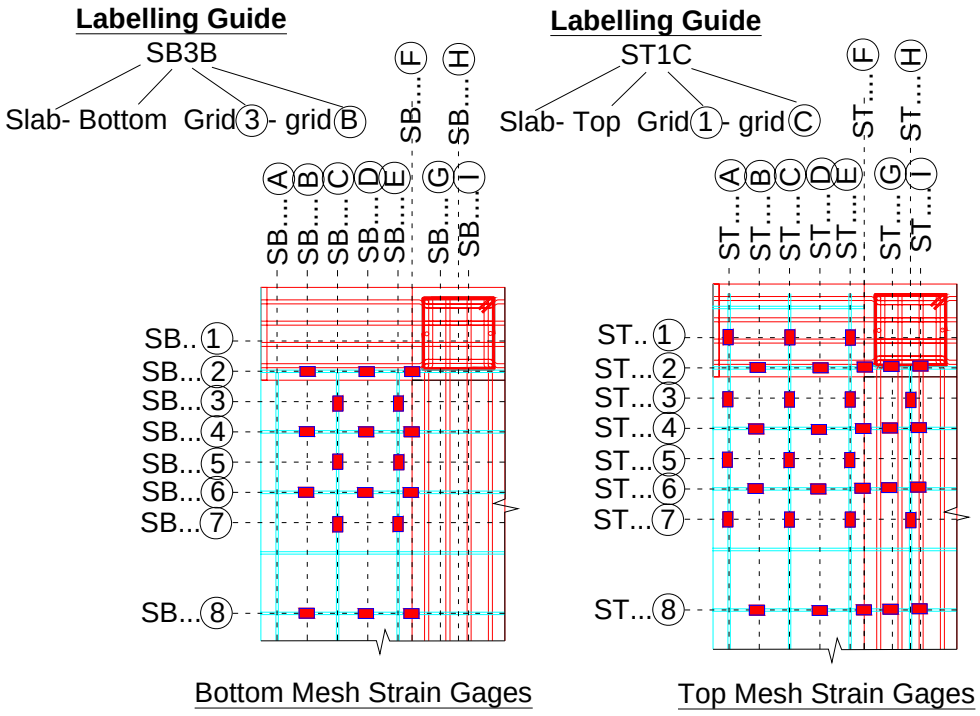

Figure 4.27: Strain Gages Plan and labelling guide for SL-O1 and SL-R3 Slab.

Of the approximately 600 strain gages used, only about 2% of them failed prior to the start of the test, which was reasonably satisfactory. However, for plain-round bars reinforced specimens, where localised stresses and bond slip failures were more common, strain gages were ineffective at high deformation levels. In particular, bond-slipping of smooth reinforcement would lead to abrasion of the strain gages and lead wires, and subsequently debonding failure of the gages. This was consistent with some localised tests [41] on smooth and abraded surfaces of strain gages, where debonding failure was observed in all specimens but more acutely for smooth surface applications. It was noted that debonded gages may still provide 'inaccurate' cyclic readings as the gages would still be held in place by the coating material.

4.7.5 Observation of cracking

The critical regions of the beam-column joints were painted white and gridded with 50mm squares to assist crack observations. Cracks in the positive (Pull) and negative (Push) displacements were marked with blue and red felt pens respectively. During testing, photographs were taken from three fixed locations at the peak of each loading cycle to provide a complete progression of damage. Crack widths, length and locations were recorded at each loading peak.

4.8 DISPLACEMENT DECOMPOSITION

4.8.1 Deformation components of exterior beam-column joints

In order to understand the distribution of damage and the contributing inelastic mechanism, the displacement components of the inter-storey displacement, Δ_{drift}, measured experimentally by the top-of-column global displacement of the beam-column joint subassembly can be disaggregated into different components. The Δ_{drift} can be expressed as a sum of the five components, as given in Equation 4.4. The procedure used to determine each component is given in the following sub-sections. For the flexural deformations, it is possible to further discretise the deformation as average rotation and average curvature per each measured region. The different deformation components for exterior beam-column joints are as illustrated in Figure 4.28.

$$\Delta_{drift} = +\Delta_{elastic(beam+col)} + \Delta_{beam,\,flexural} + \Delta_{beam,\,fixed-end} + \Delta_{col,\,flexural} + \Delta_{joint} \qquad \textbf{4.4}$$

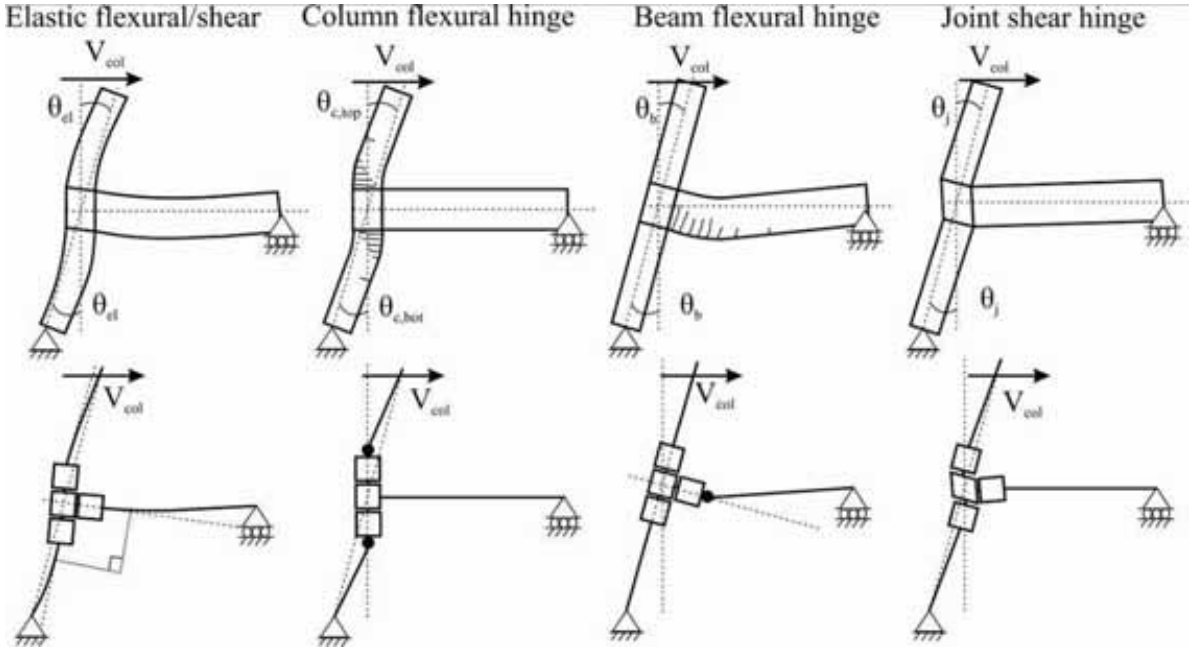

Figure 4.28: Deformation modes of exterior beam-column joints.

4.8.2 Beam and column elastic deformations

The beam elastic flexural deformations contribution to the horizontal displacement of the top column of the test specimen can be calculated using basic structural mechanics equations for the prismatic beam element, as follows:

$$\Delta_{beam,elastic} = (\delta_{b,elastic-flexural} + \delta_{b,elastic-shear})\frac{H_c}{L_b} = (\frac{F_b L'^3_b}{3E_c I_{e,b}} + \frac{qF_b L'_b}{0.2b_w h_b E_c})\frac{H_c}{L_b} \quad \textbf{4.5}$$

$$\Delta_{col,elastic} = \delta_{col,elastic-flexural} + \delta_{col,elastic-shear} = \frac{F_c H'^3_c}{3E_c I_{e,c}} + \frac{qF_c H'_c}{0.2b_c h_c E_c} \quad \textbf{4.6}$$

where $\delta_{elastic\text{-}flexural}$ and $\delta_{elastic\text{-}shear}$ are the elastic flexural and shear displacement components, q is a shape factor for the rectangular section (=1.2) and the other symbols as previously defined elsewhere. The values of the flexural stiffness of the prismatic element, E_cI_e, reflect the allowance made for the effect of cracking of the concrete. The use of upper limits of effective moment of inertia, I_e, as given by Equations 4.7 and 4.8 below, was to account for the possible double-counting of the elastic deformations in the measurement of average curvatures across the plastic hinge region from the linear potentiometers. The I_e for beam ($I_{e,b}$) and column ($I_{e,c}$) respectively are given by:

$$I_{e,b} = 0.5I_g \quad \textbf{4.7}$$

$$I_{e,c} = 0.7I_g \quad \textbf{4.8}$$

where I_g is the moment of inertia based on the uncracked gross concrete area.

4.8.3 Beam measured flexural deformations

Beam flexural deformation contributions to the global displacement of the top of column were estimated from the average curvature (and average rotation) measured within each region in the beam. A pair of top and bottom linear potentiometers was used to measure the average curvature across the region.

With reference to Figure 4.29, the flexural deformations and the average curvature of the beam can be calculated as follows:

$$\Delta_{beam,\,flexural} = \sum \theta_{beam,i}(L'_b - x_i) \quad \textbf{4.9}$$

$$\Delta_{beam,\,flexural} = \sum \frac{(\delta_{top-i} - \delta_{bottom-i})}{h_i}(L'_b - x_i) \quad \textbf{4.10}$$

$$\varphi_{beam,i} = \theta_{beam,i} / s_i \quad \textbf{4.11}$$

where $\theta_{beam,i}$ and $\varphi_{beam,i}$ are the average rotation and average curvature over region i with s_i width, $\delta_{top\text{-}i}$ and $\delta_{bottom\text{-}i}$ are the measured top and bottom displacements over region i, h_i is the vertical distance between the top and bottom potentiometers, L'_b is the distance between the column face and the centre of the beam pin and x_i is the distance from the column face to the centre of region i.

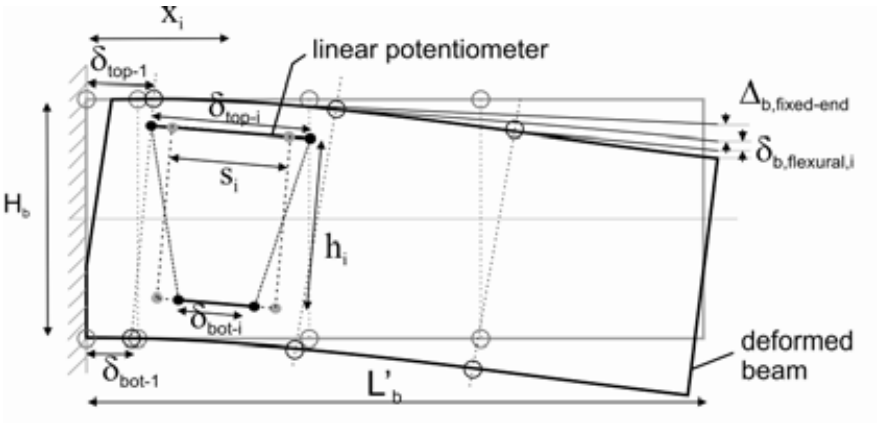

Figure 4.29: Estimation of displacement components from beam flexural and fixed-end rotation.

4.8.4 Beam fixed-end deformations and neutral axis

With the use of plain round bars in the test specimens, beam fixed-end deformations, $\Delta_{beam,fixed\text{-}end}$, were expected to be significant as bond failure along the plain round bars would eventuate in a large crack opening at the beam-column interface, as seen in previous tests [24]. Two pairs of 30mm and 50mm linear potentiometers were used to measure the beam fixed-end deformations. Due to the physical limitation of the potentiometers, the fixed-end regions were measured within a 50mm end region for all plane beam-column specimens and a 100mm end region for specimens with floor slab. For the specimen with floor slab, due to the constraint of the transverse beams framing into the joint, it was not possible to measure accurately the cracking in between the beam and column interface. The $\Delta_{beam,fixed\text{-}end}$ is calculated using the following equation:

$$\Delta_{beam,\,fixed-end} = \theta_{b,\,fixed-end}\,(L'_b - 0.5x_1) \quad \textbf{4.12}$$

$$\Delta_{beam,\,fixed-end} = \frac{\left(\delta_{top-1} - \delta_{bottom-1}\right)}{h_i}(L'_b - 0.5x_1) \quad \textbf{4.13}$$

For the beam-column joint with post-tensioning retrofit intervention, it is possible to measure the neutral axis across the beam fixed-end rotation. As described in §3.4.5, due to the localised flexural cracking at the beam-column interface and the unbonded post-tensioning, a pseudo-

rocking mechanism (Figure 4.30a) can occur. With reference to Figure 4.30b and c, the following equations are used to calculate the rotation across the pseudo-rocking interface, θ_{imp}, and the neutral axis, c:

$$\theta_{imp} = \frac{\delta_1 - \delta_2}{x_2 - x_1} \quad if\ \delta_1 > \delta_3 \quad \text{(Pull)}$$

$$\theta_{imp} = -\left(\frac{\delta_3 - \delta_2}{x_3 - x_2}\right) \quad if\ \delta_1 < \delta_3 \quad \text{(Push)} \qquad \textbf{4.14a \& b}$$

$$c = \frac{h_b(\delta_2 - 0.5\delta_1) - x_1\delta_2}{\delta_1 - \delta_2} \quad if\ \theta_{imp} > 0 \quad \text{(Pull).}$$

$$c = \frac{\delta_2 x_3 - 0.5\delta_3 h_b}{\delta_3 - \delta_2} \quad if\ \theta_{imp} < 0 \quad \text{(Push)} \qquad \textbf{4.15a \& b}$$

If the differences between the potentiometers (δ_1-δ_2) and (δ_3-δ_2) are very small (<0.001), then the θ_{imp} is taken to be zero and the neutral axis to be infinity (or the whole beam depth, h_b).

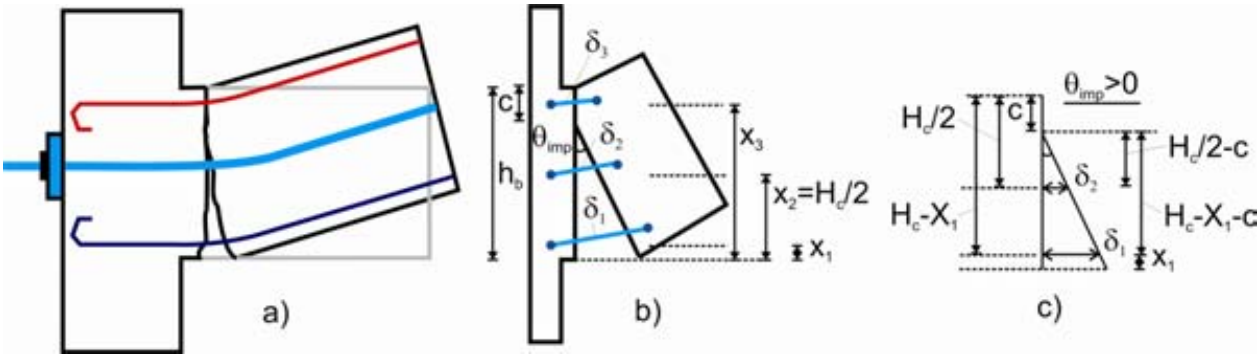

Figure 4.30: Calculation of the neutral axis of the pseudo-rocking interface in the post-tensioned beam-column joints.

4.8.5 Column measured flexural deformations

The calculation for the column measured flexural deformations, $\Delta_{col,flexural}$, is similar to the beam measured flexural deformations described in §4.8.3. With reference to Figure 4.31, the $\Delta_{col,flexural}$ is calculated by the following equations:

$$\Delta_{col,\,flexural} = \sum \theta_{col,i}(H'_c - x_i) \qquad \textbf{4.16}$$

$$\Delta_{col,\,flexural} = \sum \frac{(\delta_{c,li} - \delta_{c,ri})}{h_i}(H'_c - x_i) \qquad \textbf{4.17}$$

where $\theta_{col,i}$ is the average rotation along the region i, $\delta_{c,li}$ and $\delta_{c,ri}$ are the measured left and right displacements over the region i, h_i is the horizontal distance between the left and right potentiometers, H'_c is the distance between the beam face and the centre of the either the top pin

($H'_{c,top}$) or the base pin ($H'_{c,bottom}$) and x_i is the distance from the beam face to the centre of region i. The average column curvature across region i, $\varphi_{col,i}$ is calculated by dividing $\theta_{col,i}$ with the width, h_i, of the region i.

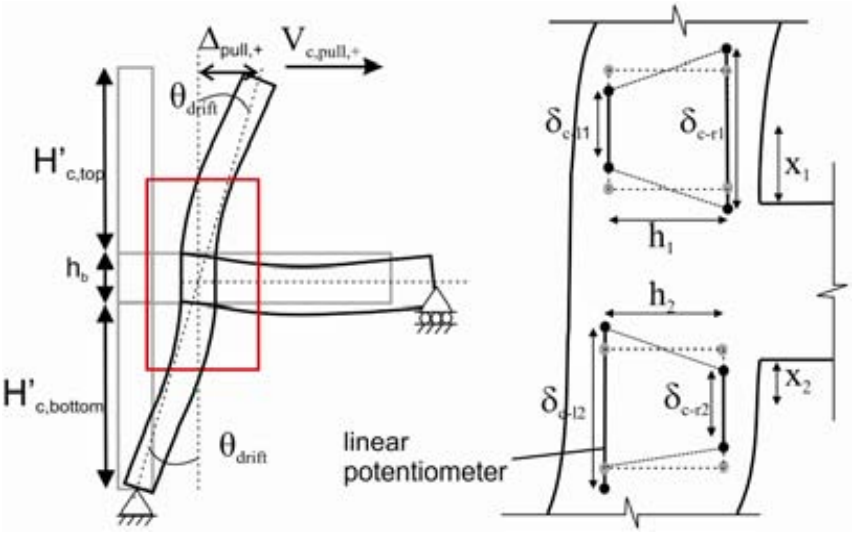

Figure 4.31: Estimation of displacement component from the measured column flexural deformation.

4.8.6 Beam and column shear deformations

While neither the beams nor columns were expected to fail in shear for the as-built and retrofitted beam-column joints, instrumentations were included in a few of the early test specimens to measure the beam and column shear deformations. A pair of diagonal potentiometers was used within the critical regions of the beams and columns. The procedure to calculate the horizontal displacement due to beam and column shear deformations is similar to those for the joint shear distortions to be presented in the next section.

4.8.7 Joint shear distortions in plane beam-column joints

For plane beam-column joint specimens, two diagonal potentiometers were used to measure the average joint shear distortion, γ_j, and the horizontal displacement at the column top due to the joint shear, Δ_{joint}. The γ_j for beam-column joints with floor slab and transverse beams could not be measured directly due to the presence of the transverse beams, thus this approach can only be used for the plane beam-column joint specimens. Based on the geometry relationship of the joint panel and assuming that all distortions were due to shear (constant flexural rotation), the average γ_j can be derived as shown in Figure 4.32. In Figure 4.32, $L_{d,o}$ is the original diagonal length of the joint panel zone, and δ_1 and δ_2 are the measured diagonal elongation and shortening, where elongation is positive.

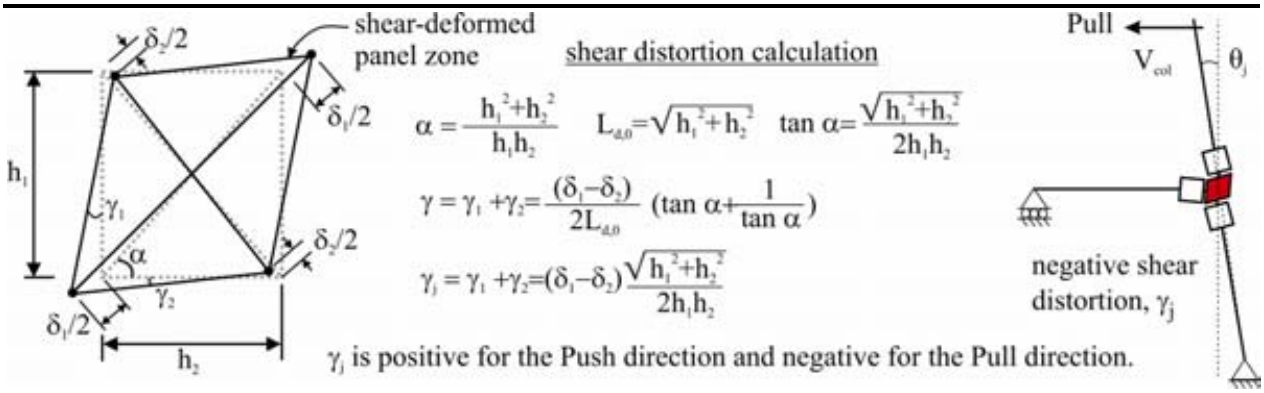

Figure 4.32: Joint shear distortion calculation and sign convention.

The horizontal displacement at the column top due to the joint shear, Δ_{joint}, can therefore be expressed by the following equations:

$$\gamma_j = (\delta_1 - \delta_2)\frac{\sqrt{h_1^2 + h_2^2}}{2h_1h_2} \qquad \textbf{4.18}$$

$$\Delta_{joint} = \gamma_j (H_c - h_b - \frac{H_c}{L_b} h_c) \qquad \textbf{4.19}$$

where H_c is the inter-storey column height or the distance between the column end pins (H_c = 2000mm), L_b is the beam span to the column centre-line or the distance between the beam end pins (L_b = 1524mm), whereas h_b and h_c are the depths of the beam and column respectively.

4.9 DATA REDUCTION AND POST-PROCESSING

4.9.1 Joint stresses

Given the measured applied lateral load and the reaction load at the beam-end, the joint stresses in terms of joint shear stress demand, v_{jh}, and the joint principal stresses (p'_t and p'_c) can be calculated. Assuming the internal forces distribution as per Figure 2.27 (of Chapter 2), the v_{jh} can be calculated using the following equations with an assumption of the internal beam moment level arm, jd:

$$v_{jh} = V_{jh} / b_j h_c \qquad \textbf{4.20 (also 2.7)}$$

$$V_{jh} = T_s - V_c = \frac{M_b}{jd} - \frac{2M_c}{(H_c - h_b)} \qquad \textbf{4.21 (also 2.4)}$$

where b_j is the effective width of the joint and jd is taken to be 0.85d and d is the effective depth of the beam (beam depth to the centroid of the tension bars). M_b and M_c can be derived directly from the load cell measurements of the beam-end reaction, V_b, and the applied lateral load, F_c:

$$M_b = V_b L'_b \quad \textbf{4.22}$$

$$M_c = F_c H'_c \quad \textbf{4.23}$$

To calculate the principal tensile stresses, the Mohr's circle stresses equation (Equation 2.10 from Chapter 2, reproduced below) can be used:

$$p'_c, p'_t = \frac{f_v + f_h}{2} \pm \sqrt{\left(\frac{f_v - f_h}{2}\right)^2 + v_{jh}^2} \quad \textbf{4.24 (also 2.10)}$$

where p'_c and p'_t are the diagonal cracking limit states for the principal compression and tensile stresses; and f_v and f_h are the average vertical and horizontal (post-tensioning) axial stresses. f_v and f_h are given by:

$$f_v = \frac{N}{h_c^2} \quad \textbf{4.25}$$

$$f_h = \frac{T_{PT}}{h_c b_j} \quad \textbf{4.26}$$

where N is the axial force measured in the column and T_{PT} is the measured post-tensioning force in the tendons.

4.9.2 Equivalent viscous damping and energy dissipation

Energy dissipation (E_d) or work done (in Joule, J) due to inelastic action within the beam-column joint subassembly was computed by summing up the area under the load-displacement hysteresis curves. Numerically, this was done through step-by-step integration of the data points, as shown in Figure 4.33. However, while E_d gives an energy dissipation index for the comparison of different test units qualitatively, it is not very useful or descriptive.

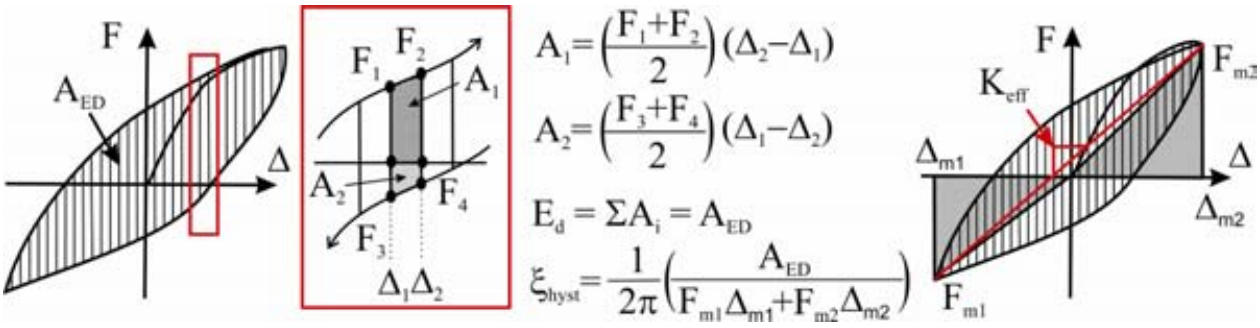

Figure 4.33: Energy dissipated, equivalent viscous damping and effective secant stiffness for hysteresis curves.

The area-based equivalent viscous damping, ξ_{hyst}, is a better representation of the inelastic energy dissipation as well as the damping capacity of the beam-column joint subassembly.

Considering the experimental quasi-static loading is similar to sinusoidal cyclic loading, the ξ_{hyst} generated is compatible with the displacement response prediction using damped displacement-spectra. Thus, the experimentally derived ξ_{hyst} values are useful for the direct-displacement-based seismic assessment and the SW retrofit design of the RC frame systems. With reference to Figure 4.33, the area-based ξ_{hyst} values can be calculated using the following expressions:

$$\xi_{hyst} = \frac{1}{4\pi}\frac{E_d}{E_{\max}} \quad \textbf{4.27}$$

$$\xi_{hyst} = \frac{1}{2\pi}\frac{A_{ED}}{\sum F_{m,i}\Delta_{m,i}} \quad \textbf{4.28}$$

where E_d is the total energy dissipated in one complete cycle, E_{max} is the equivalent strain energy at the maximum displacement ($\Delta_{m,i}$) of the cycle and $F_{m,i}$ is the corresponding lateral force applied at $\Delta_{max,i}$.

4.9.3 Average effective secant stiffness

Another response parameter of the hysteresis response curves evaluated is the average effective secant stiffness, K_{eff} (in kN/mm). K_{eff} is defined as the slope of the line connecting the peak-to-peak force-displacement points at each imposed displacement cycle, as shown in Figure 4.33. Alternatively, K_{eff} can be calculated by taking the average of the effective secant stiffness for both positive and negative displacement peaks. Equation 4.29 is used to calculate the K_{eff}:

$$K_{eff} = \frac{|F_{m1}| + |F_{m2}|}{|\Delta_{m1}| + |\Delta_{m2}|} \quad \textbf{4.29}$$

4.9.4 Strain gage data reduction

On each plane beam-column joint subassembly, approximately 50 strain gages were used while on each beam-column joint with floor slab and transverse beams, up to 107 strain gages were used. With continuous load-trigger data monitoring during the test, significant amount of strain gage readings were generated from the test. However, it was found from the experiments that the abrasion, due to bond slip and localised cracks due to smooth-reinforcement, prematurely damaged quite a number of strain gages during the test. The partial de-bonding of the strain gage from the steel surface due to the abrasion still gave cyclic readings but was no longer representative of the actual strain in the steel. Therefore it was necessary to carry out data-reduction where unrealistic strain gage readings were discarded. Based on past recommendation [41], an overall cumulative ±6000 micro-strains range was taken to be a reliable strain reading.

Beyond this range, the data was manually checked for usability and accuracy. In general, the use of strain gages for monitoring of the internal strain was found to be relatively ineffective for plain round bar reinforcement.

4.10 SUMMARY AND CONCLUSIONS

1. The chapter describes the rationale and design for the experimental test matrix nine 2/3-scaled exterior beam-column joint subassemblies incorporating pre-1970s non-ductile structural detailing. The experimental studies are aimed at investigating the seismic behaviour and effectiveness of SW retrofit techniques for non-ductile RC exterior beam-column joints with sub-standard structural details. Test parameters included levels of external post-tensioning forces, locations of beam weakening, influence of column lap-splice, and the presence of cast-in-situ slab and transverse beams. The conceptual design of the retrofit solutions is presented in §4.2 and §4.3, while the analytical prediction of the performance domain of the retrofitted beam-column joints is presented in Appendix A.

2. The construction and retrofit solutions of the three as-built and six retrofitted test specimens are provided in details in §4.3 and §4.4. From the laboratory experience, the SW retrofit – both beam-weakening and external joint post-tensioning, were relatively straight-forward and not laborious or time-consuming. The re-grouting of the weakened beam section was the most laborious part and has been found to be unnecessary in achieving similar structural performance for the retrofitted specimens. As the post-tensioning force required for a successful retrofit was relatively low, the anchorage plate and post-tensioning tendon could be further rationalised into a cheaper solution.

3. Material testing result is presented in §4.5. It has been found that most steel reinforcing, despite their Grade-300 specification, typically have much higher strength. In particular, small diameter reinforcement (R6), which was used as transverse reinforcement, had over-strength values up to 33% to 62% of the specified yield strengths. For specimens SL-O1 and SL-R3, material test results indicated that a wrong steel grade (Grade 500 instead of Grade 300) was used for the column reinforcement.

4. The test setup, loading protocol, instrumentation and procedure to post-process the test results are presented in this chapter (in §4.6 to §4.9). The justifications for the loading protocol, in particular the variation of column axial load and the gravity loading for beam-column joints with slab are also discussed in some depth. The derivation of the variation axial loading is given in Appendix A. The procedure to simulate the most appropriate way the seismic and gravity loadings imposed boundary conditions for the SL-series specimens is described in §4.6.4.

5. The use of strain gages for monitoring of the internal strain has been found to be relatively ineffective for plain round bar reinforcement, which tend to fail in bond-slip. The abrasion due to bond slip and localised cracks due to smooth-reinforcement both prematurely damaged quite a number of the strain gages during testing.

4.11 CHAPTER 4 REFERENCES

[1] Abrams DP. (1987) Influence of axial force variations of flexural behaviour of reinforced concrete columns. *ACI Structural Journal*. Nov-Dec 1987; **84**(3):246-254.

[2] ACI318-56. (1956) *Building code requirements for reinforced concrete (ACI318-56)*. American Concrete Inst. (ACI), Detroit, MI.

[3] ACI318-63. (1963) *Building code requirements for reinforced concrete (ACI318-63)*. American Concrete Inst. (ACI), Detroit, MI.

[4] ACI374-1. (2005) Acceptance criteria for moment frames based on structural testing and commentary (ACI374-1-05). *ACI Structural Journal*.

[5] Agbabian MS, Higazy EM, Abdel-Gaffar AM, El Nashai AS. (1994) Experimental observations on the seismic shear performance of RC beam-to-column connections subjected to varying axial column force. *Earthquake Eng & Struct Dyn*. **23**(8):859-876.

[6] Aycardi LE, Mander JB, Reinhorn AM. (1994) Seismic resistance of R.C. frame structures designed only for gravity loads: Experimental performance of subassemblages. *ACI Structural Journal*. **91**(5):552-563.

[7] Benzoni G, Ohtaki T, Priestley MJN, Seible F. (1996) *Seismic performance of circular reinforced concrete columns under varying axial load. SSRP - 96/04*. Uni. of California, San Diego, La Jolla, CA.

[8] Beres A, Pessiki S, White R, Gergely P. (1996) Implications of experimental on the seismic behaviour of gravity load designed RC beam-column connections. *Earthquake Spectra*. **12**(2):185-198.

[9] Bracci JM, Reinhorn AM, Mander JB. (1992) *Seismic resistance of reinforced concrete frame structures designed for gravity loads: Part I - Design and properties of a one-third scale model structures. Technical Report NCEER-92-0027*. National Center for Earthquake Eng. Research, SUNY, Buffalo, NY.

[10] Cheung PC, Paulay T, Park R. (1989) *Interior and exterior reinforced concrete beam-column joints of a prototype two-way frame with floor slab designed for earthquake*

resistance. UC Research Report 89-2. Dept. of Civil Eng., Uni. of Canterbury, Christchurch, NZ.

[11] Cheung PC, Paulay T, Park R. (1991) Mechanisms of slab contributions in beam-column subassemblages. In: Jirsa JO, editor. *Design of beam-column joints for seismic resistance, SP-123*. American Concrete Inst. (ACI), Detroit, MI; p. 259-290.

[12] Di Franco MA, Mitchell D, Paultre P. (1995) Role of spandrel beams on response of slab-beam-column connections. *ASCE J of Struct Eng*. **121**(3):408-419.

[13] Di Sarno L, El Nashai AS, Manfredi G. (2010) *Seismic response of RC members subjected to the 2009 L'Aquila (Italy) near-field earthquake ground motions. MAE Report No. 10-01*. Mid-America Earthquake (MAE) Center, Uni. of Illinois at Urbana-Champaign, Urbana, IL.

[14] Durrani AJ, Zerbe HE. (1987) Seismic resistance of R/C exterior connections with floor slab. *ACI Structural Journal*. **113**(8):1850-1864.

[15] Ehsani MR, Wight J. (1985) Effect of transverse beams and slab on behaviour of reinforced concrete beam-to-column connections. *ACI Structural Journal*. Mar-Apr 195; **82**(2):188-195.

[16] Engindeniz M. (2008) Repair and strengthening of pre-1970s reinforced concrete corner beam-column joints using CFRP composites [PhD Dissertation]. Georgia Inst. of Tech., Altanta.

[17] Esmaeily A, Xiao Y. (2004) Behaviour of reinforced concrete columns under variable axial loads. *ACI Structural Journal*. Jan-Feb 2004; **101**(1):124-132.

[18] Hakuto S, Park R, Tanaka H. (1995) *Retrofitting of reinforced concrete moment resisting frames. UC Research Report 95-4*. Dept. of Civil Eng., Uni. of Canterbury, Christchurch, NZ.

[19] Hamann CW. (1953) *Commentary on New Zealand Standard Building Code.* . N.Z. Institution of Engineers, Technical Publications LTD, Wellington, NZ.

[20] Higazy EM, Elnashai AS, Agbabian MS. (1996) Behaviour of beam-column connections under axial column tension. *ASCE J of Struct Eng*. May 1996; **122**(5):501-511.

[21] Lai S-S, Will GT. (1986) R/C space frames with column axial force and biaxial bending moment interactions. *ASCE J of Struct Eng*. July 1986; **112**(7):1553-1572.

[22] Leon RT, Deierlein GG. (1996) Considerations for the use of quasi-static testing. *Earthquake Spectra*. **12**(1):87-109.

[23] Li B, Pan T-C, Tran CTN. (2009) Effects of axial compression load and eccentricity on seismic behaviour of nonseismically detailed interior beam-wide column joints. *ASCE J of Struct Eng*. **135**(7):774-784.

[24] Liu A. (2001) Seismic assessment and retrofit of pre-1970s reinforced concrete frame structures, PhD Dissertation [PhD]. Uni. of Canterbury, Christchurch, NZ.

[25] MOW-NZ. (1950) *Ministry of Works technical memorandum*. Ministry of Works, Wellington, NZ.

[26] NI-Labview. (2003) LabView 7. National Instruments Corporation, Austin, TX; p. Data acquisition, instrument control program.

[27] Nishiyama M, Wei Y. (2007) Effect of post-tensioning steel anchorage location on seismic performance of exterior beam-to-column joints for precast, prestressed concrete members. *PCI Journal*. **52**(2):18-30.

[28] NZS95:1955. (1955) *New Zealand Standard - Model Building By-Laws: Part IV and V*. New Zealand Standard Inst., Wellington, NZ.

[29] NZS1693:1962. (1962) *Deformed steel bars of structural grade for reinfroced concrete*. Standards Assoc. of New Zealand, Wellington, NZ.

[30] NZS3101:2006. (2006) *NZS 3101:2006 Concrete structures standard*. Standards New Zealand, Wellington, NZ.
[31] NZS3112:1986. (1986) *NZS 3112:1986 Methods of test for concrete*. Standards New Zealand, Wellington, NZ.
[32] NZS3402:1989. (1989) *Steel Bars for the Reinforcement of Concrete*. Standards New Zealand, Wellington, NZ.
[33] NZS3402P:1973. (1973) *Hot rolled steel bars for reinforced concrete*. Standards Assoc. of New Zealand, Wellington, NZ.
[34] NZS4671:2001. (1989) *Steel reinforcing materials*. Standards New Zealand, Wellington, New Zealand.
[35] NZSEE. (2006) *Assessment and improvement of the structural performance of buildings in earthquakes*. New Zealand Soc. for Earthquake Eng. (NZSEE), Wellington, NZ.
[36] Orangun CO, Jirsa JO, Breen JE. (1977) A reevaluation of test data on development length and splices. *ACI Structural Journal*. Mar 1977; **74**(3):114-122.
[37] Park R. (1989) Evaluation of ductility of structures and structural assemblages from laboratory testing. *Bull of New Zealand Soc of Earthquake Eng*. **22**(3):155-166.
[38] Paulay T. (1982) Lapped-splice in earthquake-resisting columns. *ACI Structural Journal*. **74**(6):458-469.
[39] Paulay T, Priestley MJN. (1992) *Seismic design of reinforced concrete and masonry buildings*. John Wiley & Sons Inc., Christchurch, NZ.
[40] Priestley MJN, Seible F, Calvi GM. (1996) *Seismic design and retrofit of bridges*. John Wiley & Sons Inc., NY.
[41] Restrepo-Posada JI. (1993) *Seismic behaviour of connections between precast concrete elements, UC Research Report No. 93-3*. Dept. of Civil Eng., Uni. of Canterbury, Christchurch, NZ.
[42] Sritharan S, Priestley MJN, Seible F. (1996) *Seismic response of column/cap beam tee connections with cap beam prestressing, SSRP Research Report No. 96/09*. Uni. of California at San Diego, La Jolla, CA.
[43] Sritharan S, Priestley MJN, Seible F. (1999) Enhancing seismic performance of cap beam-column bridge joints using prestressing. *PCI Journal*. **44**(4):74-91.
[44] SRRB. (2005) *Research board for seismic retrofitting solutions to existing buildings: a practitioners wish list* Seismic Retrofit Research Board.
[45] Tsonos AG, Tegos IA, Penelis G. (1995) Influence of axial force variations on the seismic behaviour of exterior beam-column joints. *J of European Earthquake Eng*. **3**:51-63.
[46] Wireplus. (2009) *Wireplus reinforcing mesh handbook*. [online: http://www.wireplus.co.nz/] ed. Wireplus Ltd Auckland, Auckland, NZ.

CHAPTER 5. TESTS RESULTS OF RC BEAM-COLUMN EXTERIOR JOINTS – AS BUILT BENCHMARK SPECIMEN: NS-O1

"I personally believe that shear stress itself is a meaningless quantity. If a joint is to fail in shear, it is either going to fail in diagonal compression (because cracked concrete under reversed loading cannot sustain the diagonal compression field), or it is going to fail by diagonal tension (because stirrups yielded extensively and we got a corner-to-corner crack)."

Thomas Paulay

In Proc. of the 9th World Conference on Earthquake Engineering (Vol. VIII; pp.597)

Tokyo, Japan. 2nd-9th Aug 1988

5.1 INTRODUCTION

The test result of the as-built benchmark specimen, NS-O1, is presented in this chapter. NS-O1, as described in the previous chapter, is an exterior reinforced concrete (RC) beam-column joint representative of the pre-1970s New Zealand construction practice with non-ductile seismic deficiencies. NS-O1 had theoretical flexural beam strength of 32.0kNm with perfect bond assumption and of 16.0kNm with bond failure of longitudinal reinforcement in compression. The ratios of theoretical column-to-beam moments were 0.59 for positive beam moment and 1.08 for negative beam moment. The predicted failure mode was joint shear failure in both positive and negative displacements. Theoretical equivalent column moments due to joint diagonal cracking were 8.9kNm and -12.4kNm for positive and negative column displacement respectively. This corresponded with theoretical lateral load strength, F_c of +10.6kN and -14.8kN, respectively. The hierarchy of strength evaluation of NS-O1, following the approach presented in §2.4, is presented in Appendix A.

The NS-O1 specimen was constructed and tested in partnership with two other PhD researchers – Umut Akguzel and Giovacchino Genesio. While the raw experimental data are

common between the three researchers, the analysis and interpretation of test results presented in this chapter have been done independently. The presentation of the chapter focuses on the vulnerability characteristics of the as-built pre-1970s non-ductile exterior beam-column joint. Albeit a short chapter, the NS-O1 results will serve as the benchmark for comparison with all other test specimens presented in Chapters 6, 7 and 8. The chapter will conclude with a brief discussion on the assessment and mechanics of unreinforced exterior beam-column joints. The complete test data and photographic observations for NS-O1 will be included in Appendix B.

As a sign convention for this thesis, the *Pull loading direction* refers to the *positive top column lateral displacement, Δ_c,* which induces *positive beam bending moment, M_b,* and *tension strain* in the bottom face of the beam. This also corresponds with the *positive lateral force, F_c,* imposed on the column and *negative beam shear* force along the beam section. Vice versa, the *Push loading direction* refers to the *negative top column lateral displacement, Δ_c, negative lateral force, F_c, negative beam bending moment, M_b,* and *tension strain* in the top face of the beam. The concrete compressive strength at the day of testing, f'_c, was 17.3MPa for specimen NS-O1.

5.2 GENERAL DESCRIPTION OF BEHAVIOUR

The F_c versus Δ_c hysteresis plot for NS-O1 is given in Figure 5.1. The damage and cracking patterns observed at the end of selected peak inter-storey drift, θ_{drift} loading cycles are shown in Figure 5.2. θ_{drift} is given by Δ_c/H_c and H_c is the column height (=2000mm). NS-O1 was tested up to the 2nd cycle of the 3.0% lateral drift due to safety concerns after the significant damage of the joint and the observed loss of axial load carrying capacity.

In the Pull-Push loading cycles of ±0.1% and ±0.2% drifts cycles, hairline flexural cracks were initiated in the beam with gradual loss of stiffness of the beam-column joint. The ratio of cracked stiffness-to-uncracked stiffness, K_{cr}/K_{ini}, was 0.643 with the initial stiffness, K_{ini}, of 2730kN/m.

In the 1st Pull cycle of +0.5% drift, a crack initiated at the corner of the beam-column joint. This crack propagated horizontally along the bottom beam longitudinal reinforcement anchorage into the joint. Hairline flexural cracks on the column tension face were also observed. Further extensions of these flexural cracks in the beam and column were observed in the 2nd cycles of ±0.5% drift.

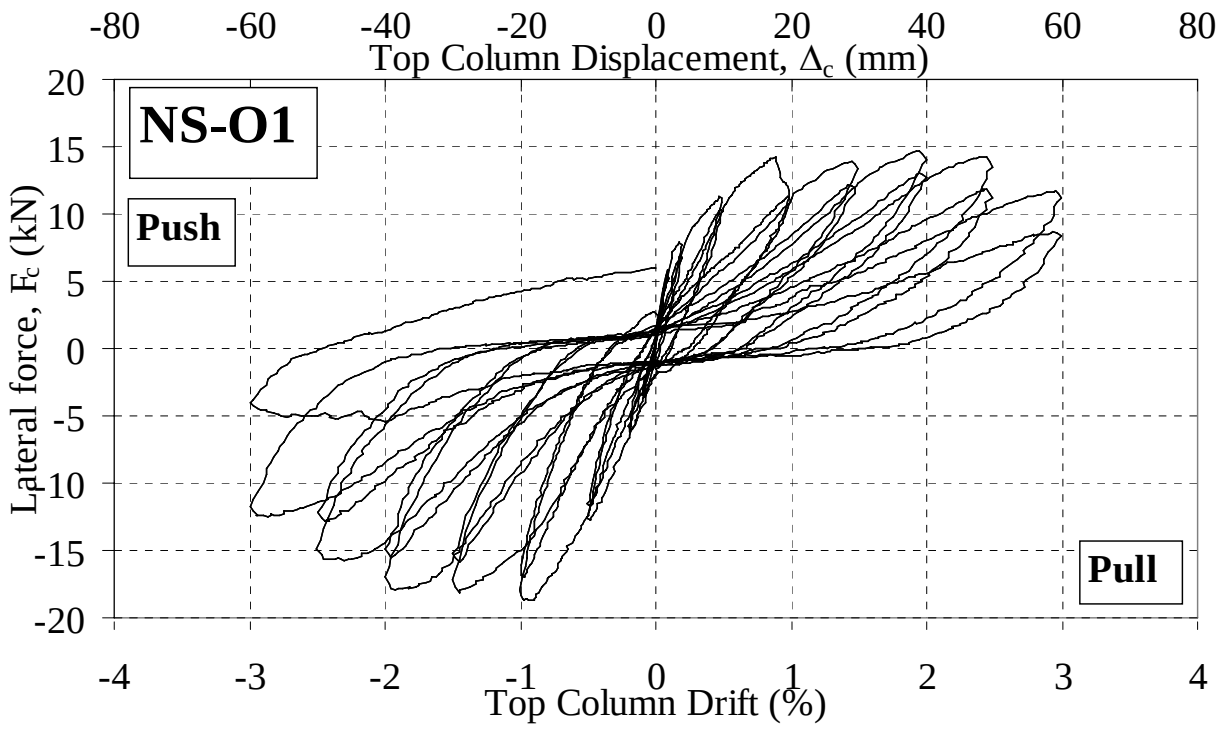

Figure 5.1: Top column lateral load, F_c, versus top column displacement, Δ_c, and drift, θ_{drift}, for NS-O1.

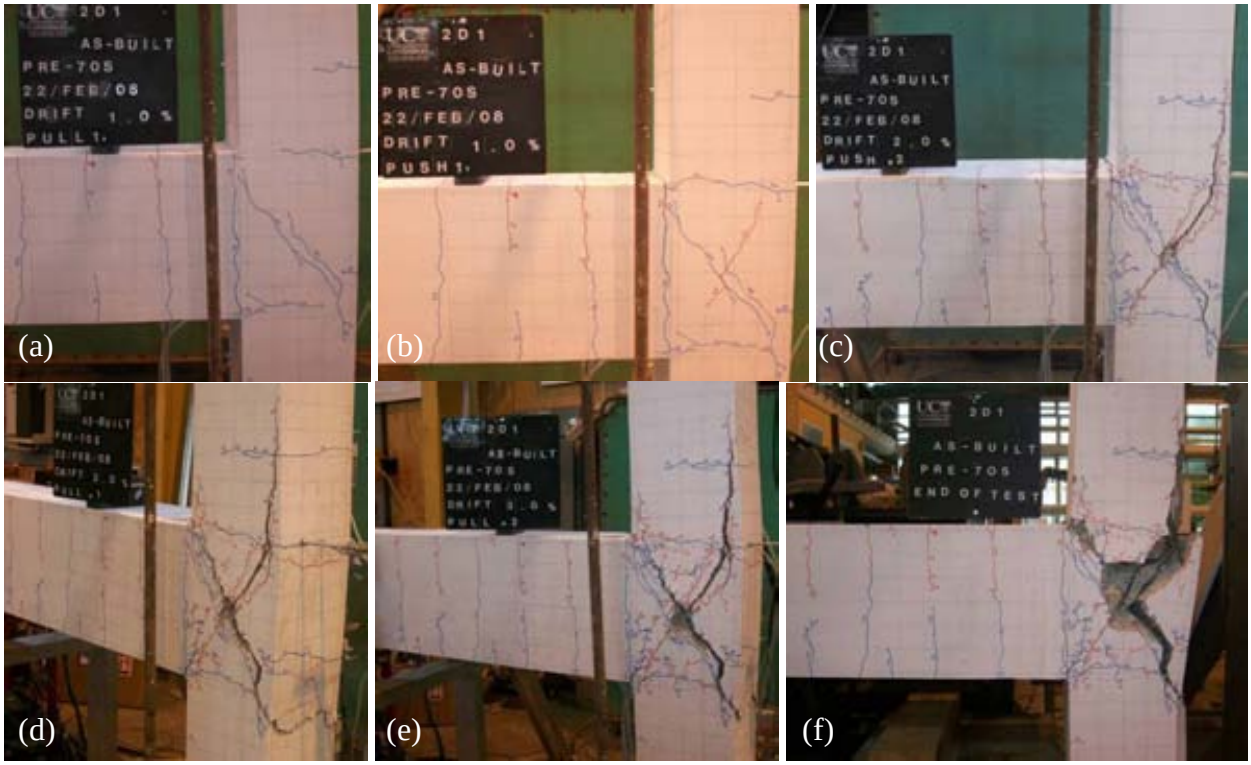

Figure 5.2: Observed cracking pattern of NS-O1: TOP: a) 1st Pull cycle of +1.0%; b) 1st Push cycle of -1.0% drift; and c) 2nd Push cycle of -2.0% drift. BOTTOM: d) 1st Pull cycle of +3.0% drift; e) 2nd Pull cycle of +3.0% drift; and f) End of test after the completion of ±3.0% drift cycles loading.

In the loading to the 1st Pull peak of the +1.0% drift cycles, a joint diagonal cracking was initiated (Figure 5.2a) between the corners of the joint panel zone. The diagonal cracking occurred at approximately +0.9% drift ratio. The joint cracking was observed with a sudden drop in the measured F_c. In the reverse loading to the 1st Push peak of -1.0% drift cycles, a diagonal crack along the concrete diagonal compression strut was observed (Figure 5.2b). The diagonal cracking in the Push direction occurred at -1.0% drift ratio. Similarly, a sudden drop of F_c was observed. The peak F_c in the Push direction of -18.7kN was observed at approximately -0.93% drift level. Figure 5.3 shows the close-up sequence of events of NS-O1 up to the ±1.0% drift.

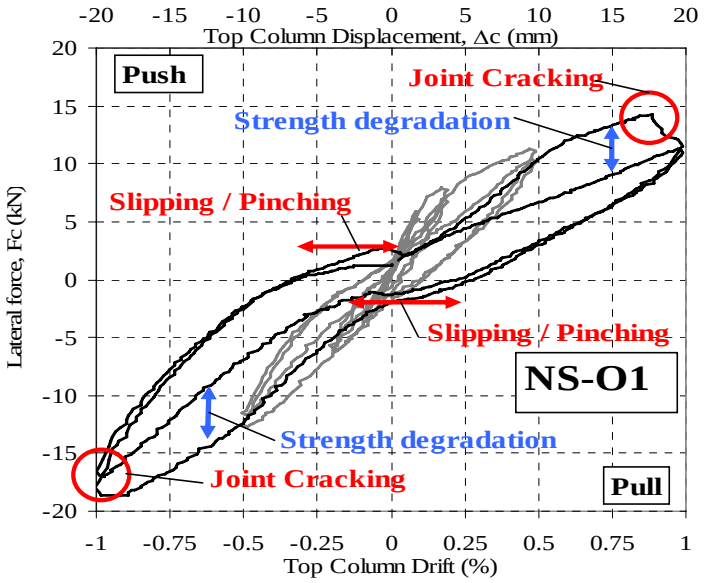

Figure 5.3: Applied lateral load, F_c, versus horizontal top-column displacement, Δ_c, up to ±1.0% drift cycles.

The measured lateral loads, F_c, at the joint cracking were +14.37kN and -18.92kN for the Pull and Push loading directions respectively. This was comparable with the predicted theoretical lateral load strength, F_c of +10.6kN and -14.8kN respectively, indicating the conservatism of the joint principal stresses assessment (described in §2.4.1 of Chapter 2) and the principal tensile stress limit, p'_t of 0.19 $\sqrt{f'_c}$ MPa.

In the 2nd cycles of the ±1.0% drift, NS-O1 exhibited significant strength degradation as more joint cracks appeared and the existing diagonal joint crack widened. The maximum widths of the joint diagonal crack were 1.2mm (Pull direction) and 1.0mm (Push direction) respectively. With widening cracks in the joint and the beam-column interface, the loss of bond in the beam longitudinal reinforcement was expected. This resulted in the thin pinched hysteresis loop with reduced energy dissipation in the 2nd cycles of the ±1.0% drift as shown in Figure 5.3. The close-

up hysteresis loop shown in Figure 5.3 also highlights the significant slipping within the F_c-Δ_c loops, in particular during the cyclic load reversal. The slipping was due to the local bond failure of the plain round bars and the closing up of cracks during the unloading and re-loading in the opposition direction.

The 'structural or ultimate failure', defined as the 20% in-cycle or peak-to-peak strength degradation, was observed at the 2nd Pull peak of the +1.0% drift. Limited ductility capacity was achieved at the structural failure at a drift of ±1.0% as the bottom beam longitudinal bars did not yield while the top longitudinal bars did just yield.

In the loading to ±1.5% drift cycles, the joint diagonal crack extended into the top and bottom halves of the column, joining with the vertical bond-split cracks along the exterior column longitudinal reinforcement. Maximum crack widths of 2.0mm (Pull direction) and 1.1mm (Push direction) were observed along the vertical edge of the joint diagonal crack near the exterior face of the joint (Figure 5.2b). Due to the minimal confinement of the concrete wedge, the unrestrained push-out force from the 180º hooked end anchorage of the longitudinal beam bars in compression further widened the joint diagonal-vertical crack. Such concrete wedge expulsion was consistent with previous tests of unreinforced or lightly reinforced exterior joint with non-ductile beam bar anchorage (e.g. [9, 12]).

In the loading to ±2.0% drift cycles, the vertical cracks along the column longitudinal bars extended approximately 150mm above and below the joint region (Figure 5.2c). New hairline cracks and the widening of the joint main diagonal cracks along the compression struts were observed. Some concrete spalled off at the centre of the joint. At this stage, the joint shear transfer mechanism was still viable despite the extensive joint cracks (up to 4mm crack width in ±2.0% drift cycles). In the Pull loading direction, a maximum F_c of +14.7kN was measured at 1.95% drift, compared to the F_c of +14.37kN at joint diagonal cracking.

Nevertheless, while peak forces were sustained in the 1st cycles of the force-displacement hysteresis, severe degradations of strength and stiffness were observed in the 2nd cycles of ±1.0%, ±1.5% and ±2.0% drifts, suggesting the severity of the bond strength and joint shear strength degradation in cyclic loading.

The column longitudinal bars began to buckle under the increasing axial load during the 1st cycle Pushing to -2.5% drift. The concrete wedge spalling was further aggravated by the buckling column longitudinal bars as joint diagonal crack widths widened to 7mm. The eventual

loss of shear transfer mechanism across the heavily damaged joint core and the buckling of the column bars led to significant strength degradation in the 2.5% drift cycles. The 1st cycle peak-to-peak strength degradations were 1.3% and 14.2% in the Pull and Push directions respectively. The in-cycle strength degradations were 19% and 17.5% in the Pull and Push directions respectively. The higher strength degradation in the Push direction, in which the axial load was increasing, was indicative that joint compressive crushing and column reinforcement buckling as the causes of the strength degradation.

In the ±3.0% drift cycles, the joint region was completely shattered and the full concrete wedge spalling was prevented merely by the concrete adhesive resistance to the column longitudinal bars. In the 1st cycles of the ±3.0% drift, joint diagonal cracks with maximum crack width of larger than 12mm were measured, thus effectively reducing the remaining friction interlock shear force transfer across the cracked joint core. As the main diagonal strut no longer carried much compression force, alternative load paths, indicated by the new hairline cracks on the joint panel zone, as shown in Figure 5.2d-e, were formed. The load-displacement hysteresis of the 3.0% cycles showed rapid strength degradation as the buckled column reinforcement no longer provided any dowel-effect confinement to the joint core concrete.

By visual observation of the friction sliding along the diagonal crack and the significant buckling of the column longitudinal reinforcement, axial load failure of the beam-column joint was detected at the 2nd cycles of the ±3.0% drift. The self-equilibrating axial load test setup meant gradual loss of axial load carrying capacity could be captured. However, for safety reasons, the NS-O1 test was terminated when the lateral load carrying capacity decay was captured and axial-load failure was initiated. Figure 5.2f shows the final state of the NS-O1 beam-column joint.

5.3 LOAD-DISPLACEMENT HYSTERESIS ANALYSIS

The maximum lateral force F_c corresponding to the joint diagonal cracking was higher in the Push direction when compared with the Pull direction. As the beam and column reinforcing were symmetrical, the difference in the lateral capacities in different loading directions can directly be attributed to the variations of column axial load. While an increase in column axial load in the negative displacement (Push) direction increased the peak and joint cracking capacities, it conversely accelerated the strength degradation upon the onset of joint cracking and buckling of column longitudinal reinforcement.

Further analysis of the NS-O1 load-displacement hysteresis, as described in §4.9, is presented in Figure 5.4. The in-cycle strength degradations due to bond degradation of the plain round bars were evident in the 40-50% reduction in the energy dissipated per cycle beyond the 0.5% drift cycles. While the peak-to-peak stiffness, K_{eff}, did not degrade significantly between the 1st and 2nd cycles, K_{eff} was softened rapidly beyond the beam flexural cracking at the 0.2% drift cycles and subsequent joint diagonal cracking at the 1.0% drift cycles. The energy dissipated plots in Figure 5.4a and the equivalent viscous damping ratios, ξ_{hys}, plots in Figure 5.4d both indicated some levels of energy dissipation in the NS-O1 connection. The pinching natural of the hysteresis loop nevertheless limited the ξ_{hys} values to approximately 11% and 7% for the 1st and 2nd cycles respectively.

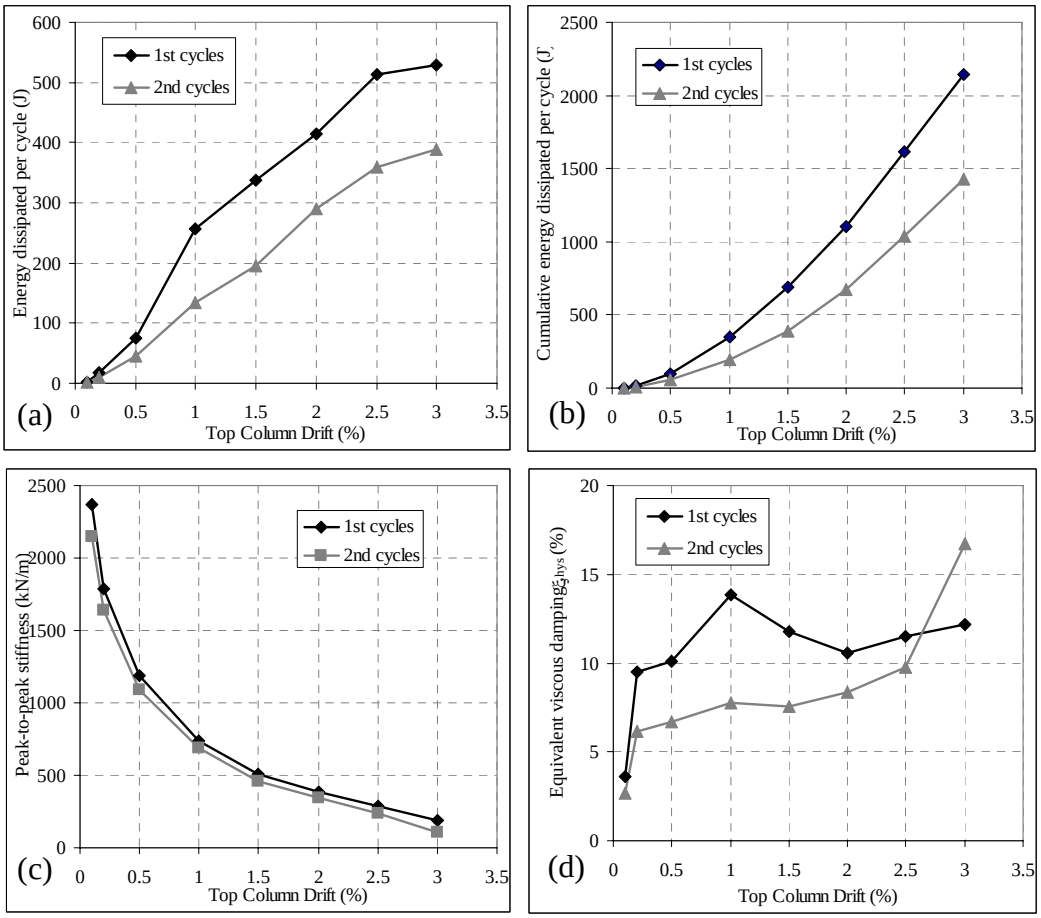

Figure 5.4: Force-displacement analysis for NS-O1: a) Energy dissipated per cycle; b) Cumulative energy dissipated per cycle; c) peak-to-peak stiffness, K_{eff}, and; d) Equivalent viscous damping, ξ_{hys}.

5.4 LOCAL DEFORMATION AND DISPLACEMENT COMPONENTS

5.4.1 Decomposition of top column horizontal displacement

The components of the top column horizontal displacement, Δ_c, or specimen drift θ_{drift} (=Δ_c /H) at the peaks of each Pull and Push loading cycles as a percentage of the total lateral displacement Δ_c or drift θ_{rift} are presented in Figure 5.5.

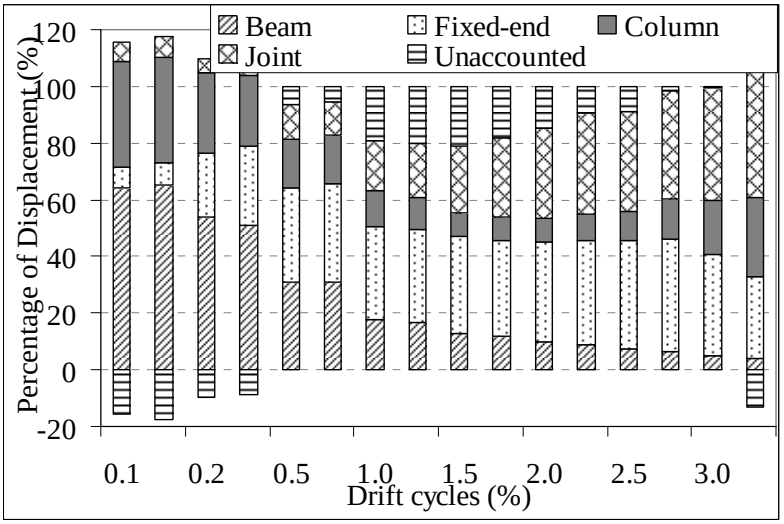

a) Pull loading direction – positive displacement.

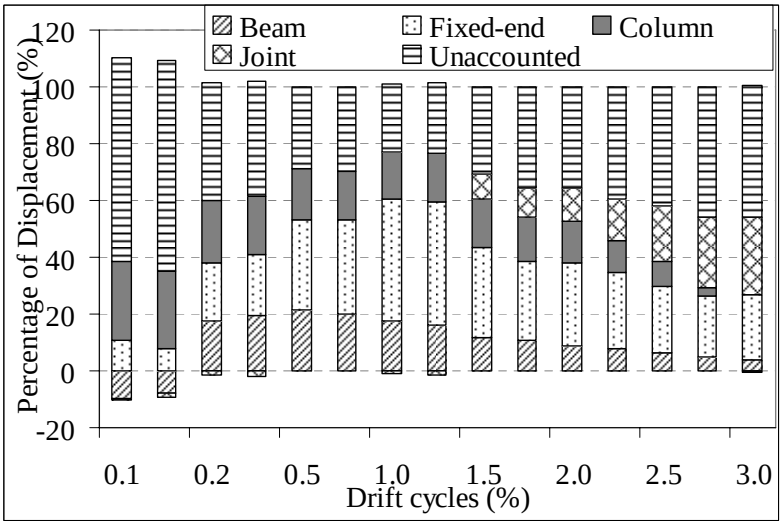

b) Push loading direction – negative displacement.

Figure 5.5: Displacement decompositions based on measured deformations for NS-O1.

In the early Pull cycles (θ_{drift} < 1.0%), beam and column flexural actions accounted for up to 80% of the lateral displacement, as confirmed by the crack observations. Interestingly, as displacement loading increased, beam fixed-end rotation components grew in proportion as a

single large flexural crack dominated the inelastic deformation in the beam. Till the end of the test, fixed-end beam rotation accounted for 30-40% of the Δ_c in the Pull cycles. With the joint diagonal cracking at the 1st cycle of the 1.0% drift, joint distortion began to grow rapidly in relative to other components. At the end of the 3.0% drift Pull cycles, joint distortion made up nearly 40-50% of the Δ_c.

A similar pattern of displacement decomposition can be observed in the Push loading cycles. Beam and column flexural deformations accounted for 40-60% of the total Δ_c components, with limited joint distortion measured prior to the 1.5% drift cycles. Beyond the 1.5% drift cycles, joint distortion increased rapidly as the percentage of the Δ_c and by the end of the 3.0% drift cycles, joint distortion accounted for nearly 30% of the Δ_c. However, in the Push cycles, there were significant 'unaccounted' components (between 24-46%) in each drift level beyond 0.1% drift, in contrast to the Pull cycles where some overestimations of the drift component were observed.

The tendency of the measured deformation components to somehow "creep" in the Pull direction was because the loading began in the Pull direction. As such, the plasticity and damage were developed first in the inelastic elements during the Pull loading cycles. In the reverse loading to the Push direction, much of the reversal displacements were still within the positive displacement range (due to the Pull loading); therefore, the displacement components in the Push direction were underestimated and unaccounted for. A consequence of this accumulation of plasticity in one loading direction can be seen as the 'beam-elongation' effect for beam-column joints under inelastic actions (e.g.[8, 16]).

While the relative deformations in each loading cycle could be measured, the net deformation due to the beam flexural cracking would be significantly under-measured if there were significant beam-elongations (un-closed beam cracks). No measurement of beam-elongation was taken for the specimen NS-R1, but from the measurements for specimens NS-R4 and S-R3, beam elongations of the retrofitted (with beam-weakening and post-tensioning) were in the range of 2mm (at θ_{drift} =±1.0%), 7mm (at θ_{drift} =±2.0%) and 27mm (at θ_{drift} =±4.0%).

Similar damage accumulation in the initial damaged direction was true for joint-shear damage. With a diagonal crack formed in the joint during the Pull direction, the diagonal crack must be closed in order to develop the diagonal compression strut force in the reverse Push loading. Globally, the joint crack closing and associated beam reinforcement's bond-slip across

the joint crack width led to the pinching lateral F_c-Δ_c hysteresis. Locally however, these actions caused residual joint cracks and accumulated joint distortions in the Pull direction, therefore shifted the measured joint distortion towards the Pull direction. This explained for the lower percentage of Δ_c measured for the joint distortion in the Push direction, despite the damage observed had indicated relatively symmetrical damage and distortion in the joint in both the Push and Pull loading directions. This is graphically illustrated in Figure 5.6.

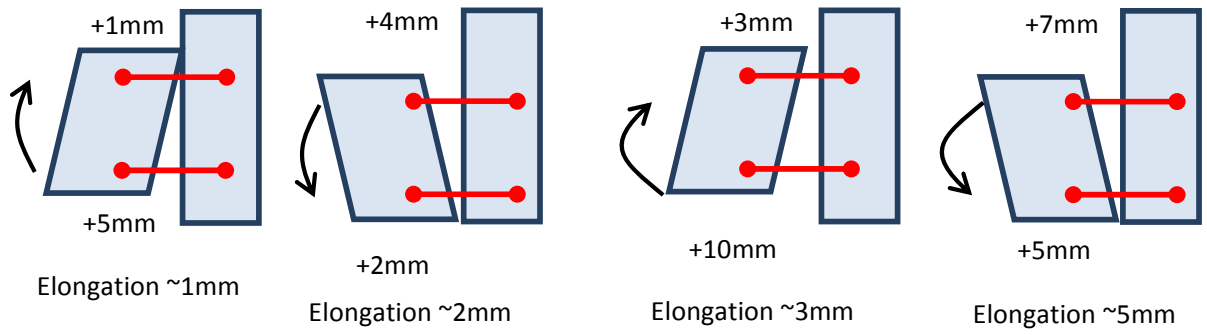

Figure 5.6: Schematic illustration of the possible under-measurement of deformation components due to beam-elongation, and cracks and damage accumulation.

5.4.2 Beam deformations

The moment-curvature plots for the beam flexural regions and beam fixed-end regions, shown in Figure 5.7 and Figure 5.8, clearly illustrate that most inelastic deformations of the beam were concentrated on the fixed-end beam-column interface. The beam flexural deformations within the 75-475 mm from the column internal face region were linear and negligible. This observation is consistent with the previous findings of Liu *et al.* [11] for beam-column joints with plain reinforcing.

In the negative beam moment (Push direction), the theoretical flexural beam strength of 32kNm (with perfect bond assumption and strain hardening) was achieved before subsequent joint shear cracking rapidly limited and degraded the available curvature ductility of the beam negative flexural hinge. Assuming the yield curvature, $\varphi_y = 2\varepsilon_y/H_b$, the curvature ductility in the negative beam moments was μ_ϕ=7.7 with φ_y = 0.011m^{-1}.and φ_u=0.085m^{-1}

In the Pull direction, premature joint failure due to lower axial load prevented the development of the theoretical beam moment and strain hardening of the bottom longitudinal reinforcement. The maximum positive beam moment developed was 26.5kNm (equivalent column moment, $M_{c,b}$ = 12.0kNm). This was lower than the prediction with perfect bond assumption ($M_{c,b}$=14.5kNm) but was also significantly higher than the prediction with maximum

bond strength, $\tau_{b,max}$ of $0.3\sqrt{f'_c}$MPa ($M_{c,b}$=7.2kNm), thus indicating that joint failure precluded the beam hinging. A relatively high average curvature of the fixed-end region, up to 0.16m^{-1}, was measured in the Pull direction. This value could be artificially inflated as the potentiometers measuring the fixed-end beam curvature were also connected to the damaged joint corner region.

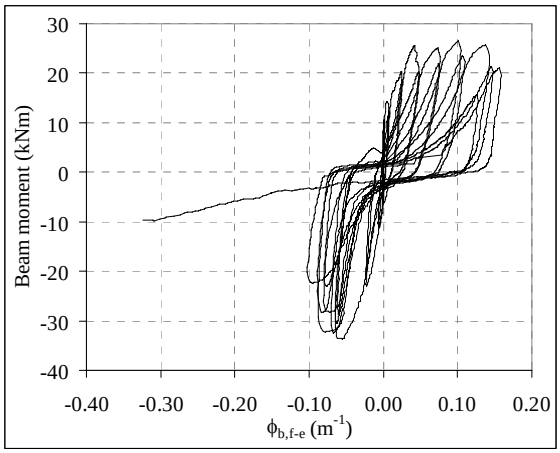

Figure 5.7: Moment-curvature plots for the fixed-end beam section.

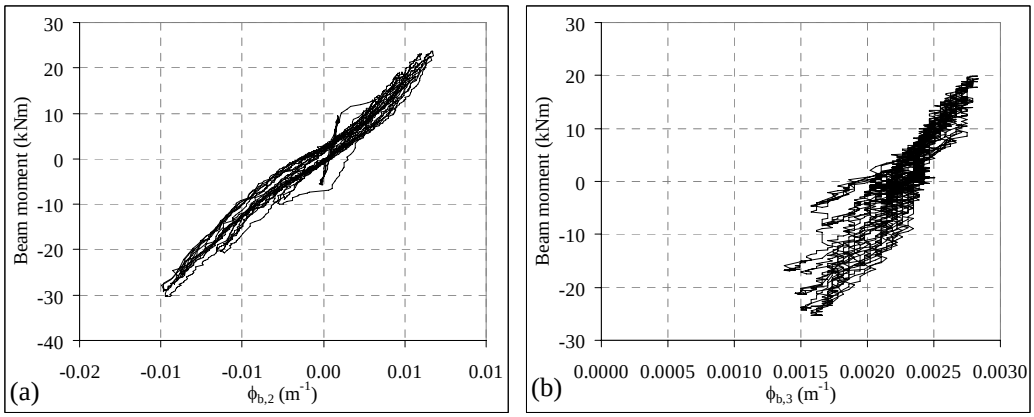

Figure 5.8: Moment-curvature plots for beam flexural sections:
a) 75-275mm from column internal face; b) 275-475mm from the column internal face.

5.4.3 Column deformations

The moment-curvature plots for the top and bottom column sections are given in Figure 5.9. The moment-curvature responses were not symmetric with higher curvature demand in the positive column moments (in the Pull direction). This corresponded to lower column moment capacity and flexural stiffness in the Pull direction as the column axial load decreased. While φ_y (0.016m^{-1}) was exceeded, the curvature ductility demand in the columns was low as the joint damage limited the moment demand in the column. The damage and strain accumulation in the Pull direction as explained §5.4.1 would also explain the creep of the moment-curvature plot towards

the positive moment direction. Similar to the beam fixed-end rotation measurement, the curvature measurement of the bottom column (Figure 5.9b) was also affected by the joint shear distortion as the linear potentiometers were connected to the damaged joint region.

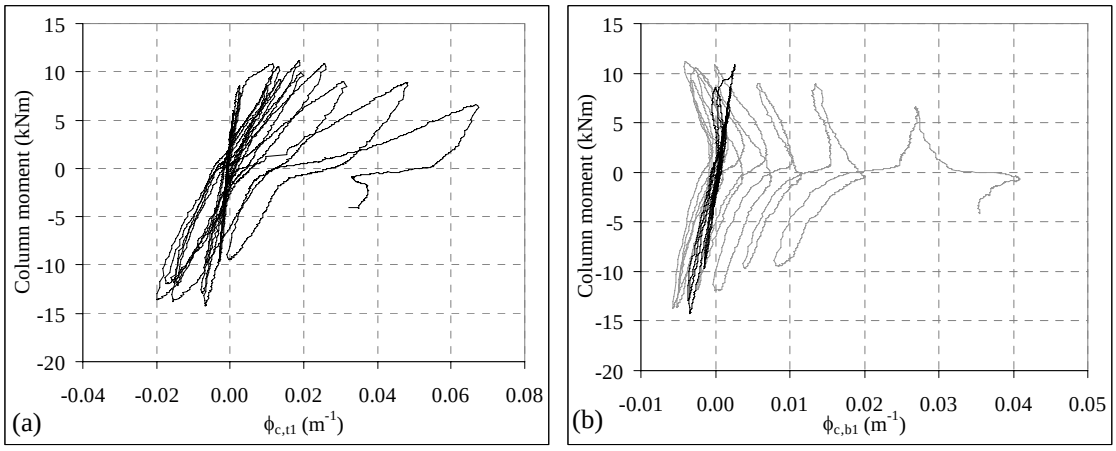

Figure 5.9: Moment-curvature plots for column flexural sections:
a) 0-200mm from beam top face; b) 0-200mm from the beam soffit.

5.5 BEAM-COLUMN JOINT BEHAVIOUR

5.5.1 Nominal joint shear stress and joint shear distortion

The nominal joint shear stress, v_{jh}, versus joint shear distortion, γ_j, and Δ_c relationships for NS-O1 are given in Figure 5.10. As with the observed joint cracks and damage, significant γ_j were measured after the joint diagonal cracking at ±1.0% drifts cycles (Δ_c ~ 20mm). v_{jh} at joint diagonal cracking were 1.65MPa (0.40 $\sqrt{f'_c}$ MPa or 0.10f'$_c$ MPa) and 2.17MPa (0.52 $\sqrt{f'_c}$ MPa or 0.13f'_c MPa) in the Pull and Push loading directions respectively. In Push direction, this also corresponded to the maximum v_{jh} measured. However, in the Pull direction, the maximum v_{jh} measured was 1.70MPa (0.41 $\sqrt{f'_c}$ MPa or 0.10f'_c MPa) at the +2.0% Pull drift.

These v_{jh} values were comparable to the Hakuto *et al.* [9] tests on lightly reinforced joints with beam anchorage of double 90° hooks bent into (0.31$\sqrt{f'_c}$ MPa) and away (0.25$\sqrt{f'_c}$ MPa) from the joint core. When compared with the recommendations of various seismic codes and assessment guidelines shown in Table 2.1 in §2.4.2.2, the NS-O1 values might indicate that the code recommendations (0.5 to 1.0 $\sqrt{f'_c}$ MPa) are not conservative. Nevertheless, as discussed in §2.3, other experiment results, in particular Beres *et al.* [3] (v_{jh} = 0.42-0.75$\sqrt{f'_c}$ MPa for various axial load and joint detailing) and Pantelides *et al.* [15] (v_{jh} ~1.0$\sqrt{f'_c}$ MPa), have demonstrated the high variability of the nominal shear stress performance limit states. The dispersion in the v_{jh} was

in fact due to the natural dispersion of the tensile strength of concrete arising from the micro-weakness points of the concrete matrix.

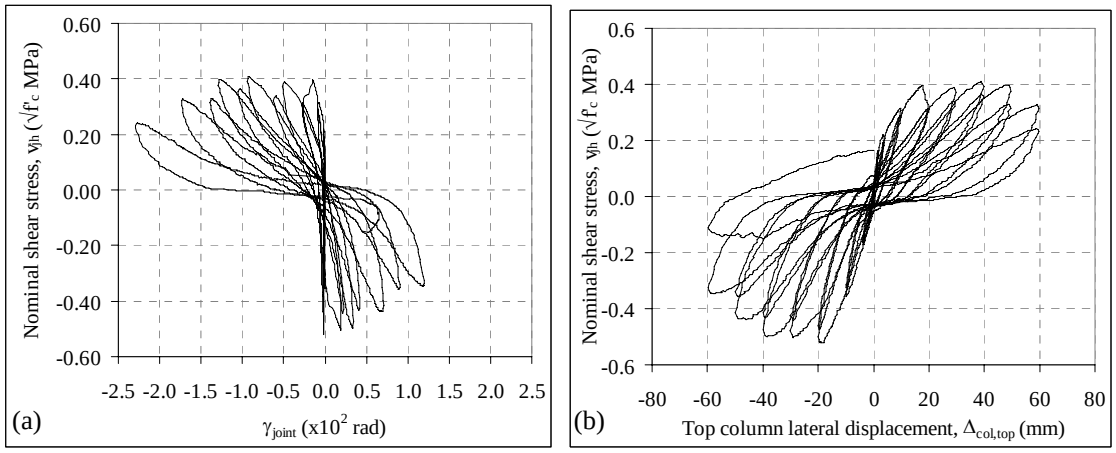

Figure 5.10: a) Nominal joint shear stress, v_{jh}, versus joint deformation, γ_j; b) Nominal joint shear stress, v_{jh}, versus top column lateral displacement, Δ_c.

5.5.2 Joint principal stresses

Figure 5.11a-b presents the relationship between the principal stresses and the column lateral displacement, Δ_c, while Figure 5.11c-d presents the relationship between the principal stresses versus joint shear deformation, γ_j.

Prior to the joint diagonal cracking, p'_t - γ_j and p'_t - Δ_c were essentially linear. The p'_t values at the joint diagonal cracking were $0.28\sqrt{f'_c}$ MPa and $0.23\sqrt{f'_c}$ MPa in the Pull and Push directions respectively. This corresponded to γ_j of -0.00150 radians and +0.00017 radians respectively. NS-O1 values were comparable to the literature values [12, 17, 18] of p'_t = 0.19 to $0.29\sqrt{f'_c}$ MPa and $0.17(f'_c)^{2/3}$[9]. For instance, Hakuto *et al.* [9] empirical equations estimated the mean and 95% confidence limit of joint cracking p'_t to be 1.14MPa ($0.27\sqrt{f'_c}$ MPa) and 0.58MPa ($0.14\sqrt{f'_c}$ MPa) respectively.

The principal compressive stresses, p'_c, at the joint diagonal cracking were $0.48\sqrt{f'_c}$ MPa and $1.12\sqrt{f'_c}$ MPa for Pull and Push respectively. As the p'_c in the Push loading direction too approached the diagonal compression cracking limits (e.g. 0.25-0.3f'_c (e.g.[18])), it was probable that the joint diagonal cracking in the Push loading direction was initiated by diagonal compressive cracking due to p'_c instead of diagonal tensile cracking. As shown in Figure 5.11d, significant p'_c - γ_j response was only observed during the Push loading cycles, as the vertical axial stress, f_v, increased. In the Pull direction, nearly constant p'_c of approximately $0.45\sqrt{f'_c}$ MPa was observed.

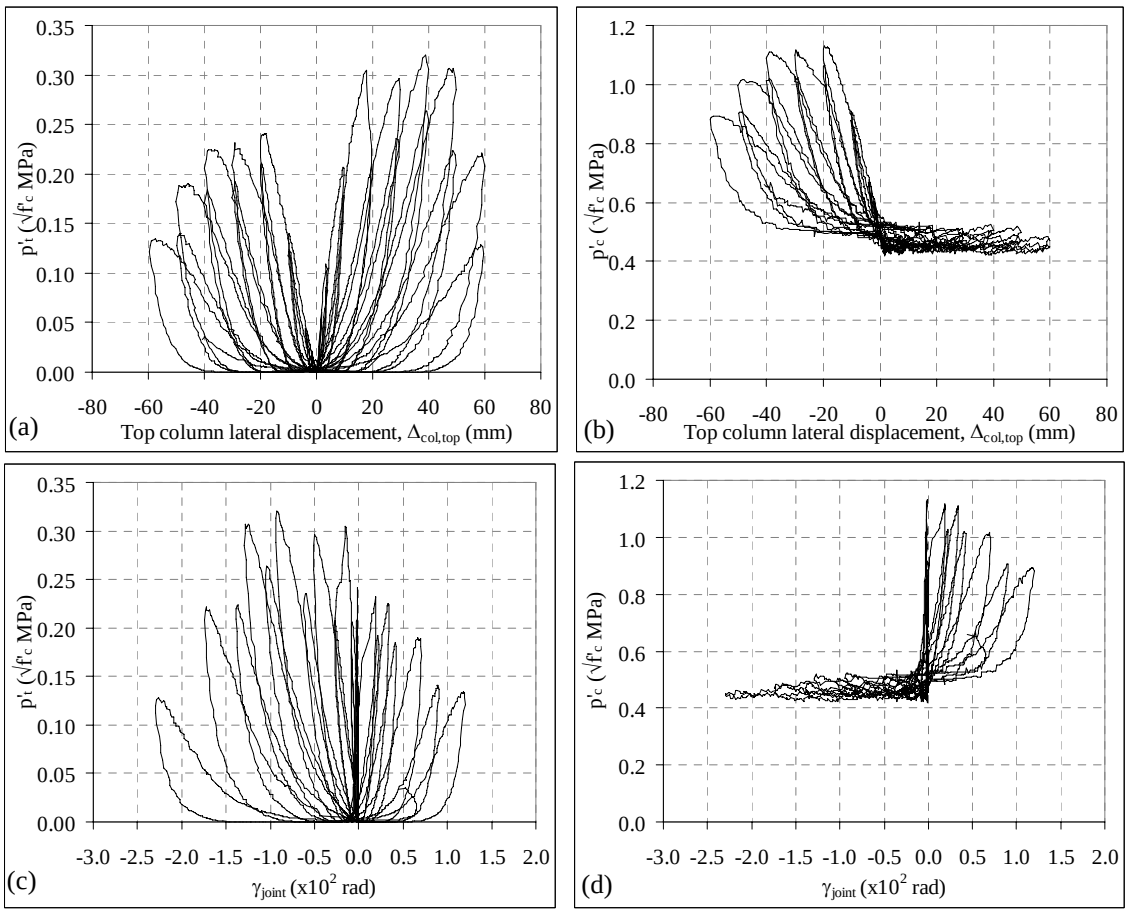

Figure 5.11: a-b) Joint principal stresses versus top column lateral displacement, Δ_c: a) principal tensile stress, p'_t; b) compressive tensile stress, p'_c; c-d) Principal stresses versus joint shear deformation, γ_j plots: c) principal tensile stress, p'_t; d) compressive tensile stress, p'_c.

Under the variation of column axial load, more severe degradations of F_c and p'_t capacities were measured when the axial load increased (in the Push direction and positive γ_j). However, the limit states of joint diagonal cracking were relatively close (18-22% difference between the two directions) despite the variation of axial load. This gave some additional insights to the unreinforced joint mechanics. While the joint cracking limit depends on the available concrete tensile strength (a function of $\sqrt{f'_c}$ MPa), joint shear strength degradation in terms of p'_t is influenced by the level of axial stress, f_v. The strength degradation will also be a function of level of confinement (or joint reinforcement), longitudinal reinforcement ratio (ρ_{cl}) and horizontal stresses (v_{jh}). Chapter 6 will look into these additional parameters with the results of the retrofitted specimens.

In terms of maximum principal stresses in the joint during the cyclic loading of NS-O1, the maximum p'_t was $0.32\sqrt{f'_c}$ MPa at γ_j =-0.009264 radians and the maximum p'_c was $1.13\sqrt{f'_c}$

MPa at γ_j =+0.00015 radians. These values are in line with the expected values (e.g. [12, 18]). Under a varying axial loadings (and column axial stress, f_v), the principal stresses are more reliable parameters for joint shear capacity compared with the v_{jh}, which only considers the horizontal shear forces. §5.7.1 will revisit these γ_j experimental limit states in comparison to the existing literature recommendations.

5.6 STEEL STRAIN PROFILES

5.6.1 Beam longitudinal reinforcement strains

Figure 5.12 and Figure 5.13 present the strain profiles of the top and bottom beam longitudinal reinforcement for the specimen NS-O1. The X-axis is the distance from the exterior column face to the location of the strain gages while the two vertical dashed lines refer to the column centre-line and the interior column face. Tensile strains are given as positive values. From the steel test, the yield strain, ε_y, for the longitudinal beam and column reinforcement was 0.00185 (1850 microstrains) and the f_y was 362MPa.

The steel strains in the top beam longitudinal bars were limited in the Pull cycles when the top reinforcing bars were under compression. Up to the 0.5% drift Pull cycles, compressive stresses up to -60MPa were developed in the beam top bars outside the joint, while compressive bond resistance along the bars was observed as the steel stress decreased linearly along the bars within the joint. Upon the bond failure in the 2nd Pull cycle of +0.5% drift, reversal of strain with tensile strains was observed on the beam reinforcement anchored into the joint and approximately zero strain was measured at the fixed-end flexural crack at the beam-to-column interface. These tensile strains were amplified beyond the +1.0% drift Pull cycles, indicating that the top beam bars were transferring joint shear force after the joint diagonal cracking.

For the top reinforcement in the Push cycles, due to the effective tension anchorage from the 180° hook in the joint, substantial steel strains were developed at the beam-to-column interface. The top steel yielded in the -1.0% drift Push cycles and continued into plastic strains at the inter-face crack in the ±1.5% drift cycles. Within the joint region, significant strain-reversal was observed beyond the -1.0% drift Push cycles, in which by the -2.5% drift Push cycles – compressive stress were measured. Many of the strain gages within the joint were damaged beyond the ±2.5% drift cycles.

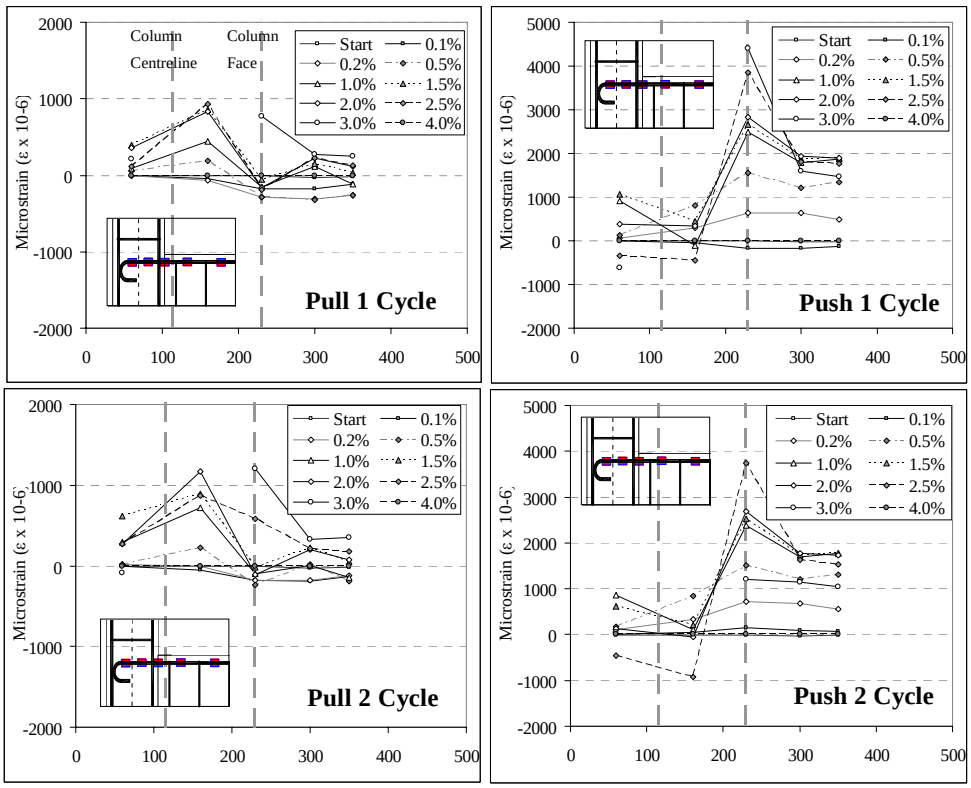

Figure 5.12: Strain profiles of beam top longitudinal bars of the specimen NS-O1.

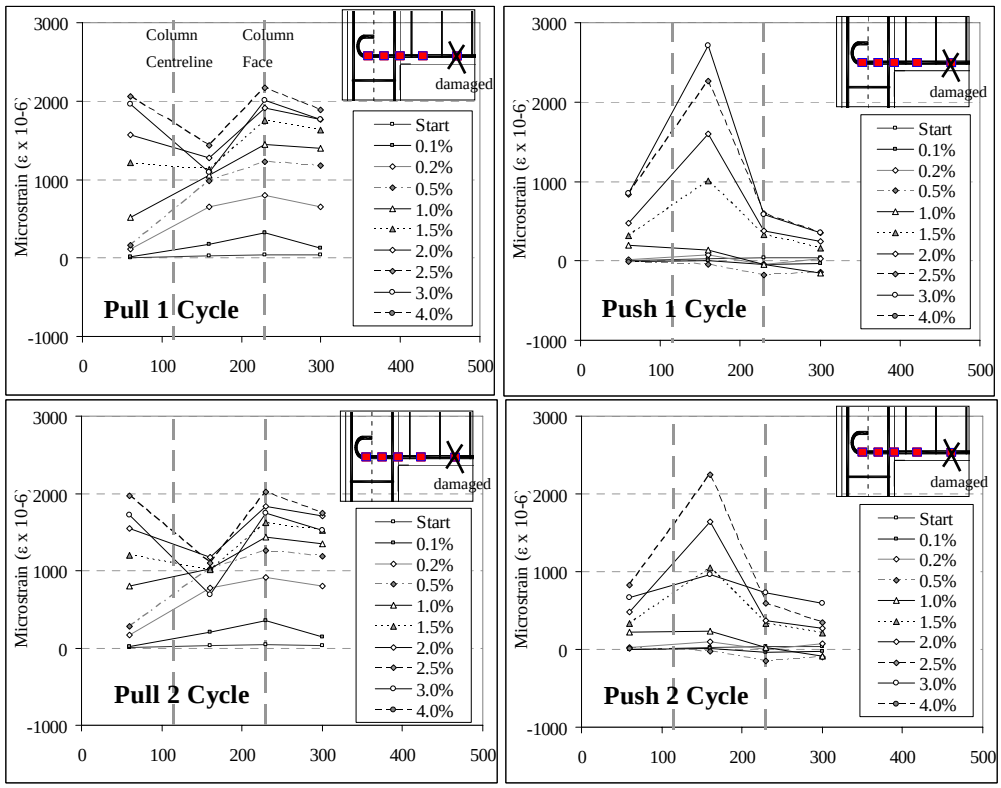

Figure 5.13: Strain profiles of beam bottom longitudinal bars of the specimen NS-O1.

The bottom reinforcement yielded in tension in the +1.0% drift Pull cycles with strain hardening was observed beyond the ±1.5% drift. Strain penetration into the joint was evident beyond the ±1.5% with strain penetration length, l_{sp}, of approximately 40mm (from the Figure 5.13). This was less than the Priestley *et al.*[18]'s recommendation of $l_{sp} = 0.022 f_y d_b$ (~65mm for NS-O1). However, the damage in the joint limited the plastic strain in the beam. Beyond the +1.5% drift Pull cycles, the strain of the steel near the hook region exceeded yield tensile strain, while the strain in the middle of the joint remained below the ε_y. This also suggested that the beam bottom longitudinal bars were carrying some joint shear after the joint diagonal cracking and the 180° hook anchorage was effective beyond joint cracking.

The strain profiles of the bottom beam bars in the Push cycles were similar to the top bars in the Pull cycles. Low compressive stresses (30~36MPa) were developed in the bottom reinforcement before the bond failure. After the joint diagonal cracks in ±1.0% drift cycles, significant tensile strains were observed on the beam reinforcement embedded into the joint, particularly the inner side of the joint core. As the loading continued, the bottom bars yielded in tensile in the joint in the +2.0% drift Push cycles. Tensile strains were measured in the bottom beam reinforcement despite the beam soffit concrete being in compression in the Push cycles. This showed the complete debonding of the steel reinforcement with the joint shear transfer dominating the strain profiles of the bottom reinforcement.

5.6.2 Column longitudinal reinforcement strains

Figure 5.14 and Figure 5.15 present the strain profiles of the exterior and interior column longitudinal reinforcement for the specimen NS-O1. In Figure 5.14 and Figure 5.15, the Y-axis is the distance from the centre-line of the beam to the strain gage location. The three horizontal dashed lines refer to the beam soffit (bottom line), beam centre-line and the beam top face (top line). As with all strain gage readings, tensile strains were measured as positive values. All column strain gages were zeroed before the axial force loading on the column at the start of the test.

Prior to the joint diagonal cracking at ±1.0% drifts in both the Pull and Push cycles, the column exterior and interior longitudinal reinforcing bars were responding elastically as expected from the bending moment demand from the lateral loading.

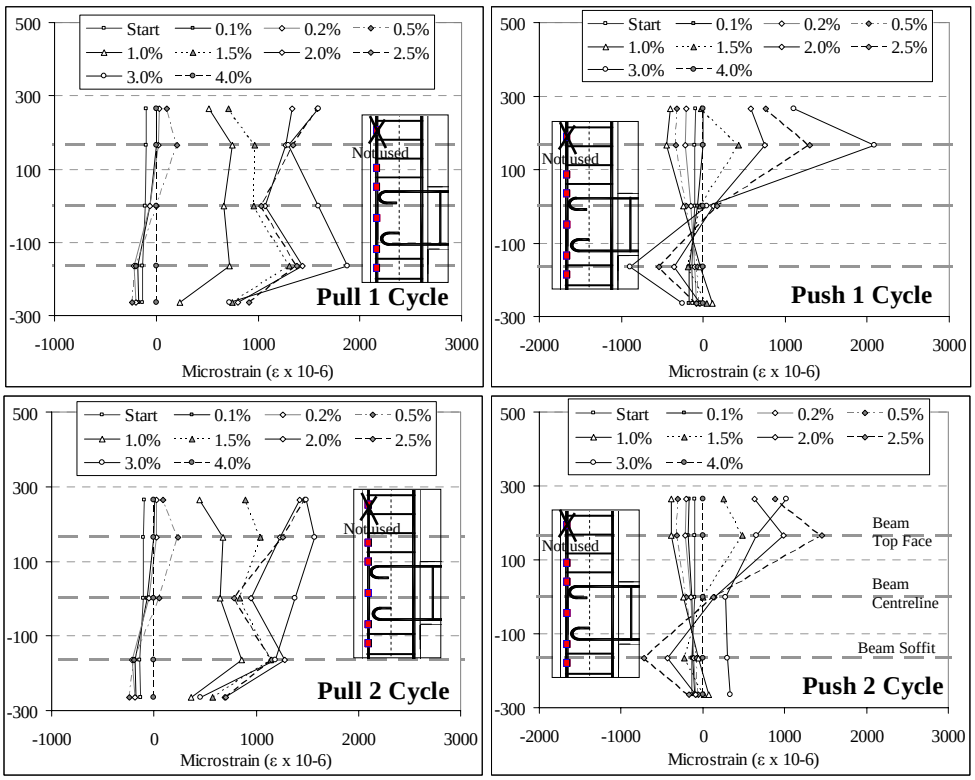

Figure 5.14: Column exterior face longitudinal reinforcement strain profiles for the specimen NS-O1.

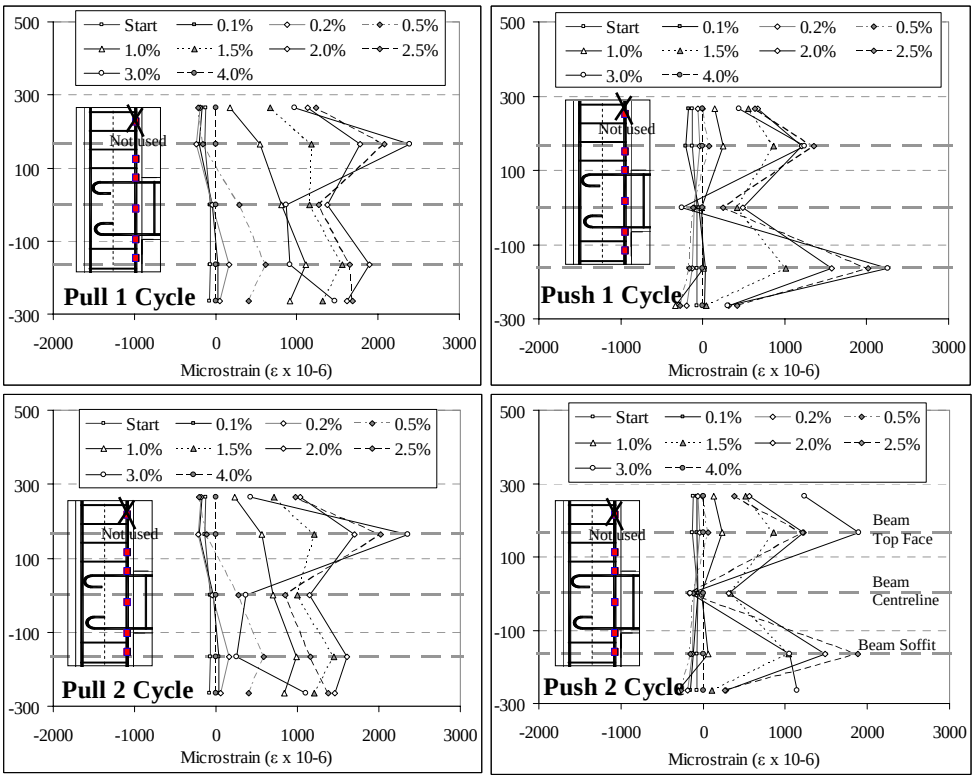

Figure 5.15: Column interior face longitudinal reinforcement strain profiles for the specimen NS-O1.

After the joint cracking, significant tensile strains were measured in both the exterior and interior column reinforcing within the joint region during the Pull cycles. With decreasing column axial load in the Pull loading cycles, the column longitudinal reinforcement played an important dual role as vertical shear and confinement reinforcement with significant dilation of the joint concrete region after joint cracking. In the Pull cycles, the column reinforcement yielded at the ±3.0% and ±2.5% drifts cycles at the exterior and interior column faces respectively. As the F_c was limited by the joint shear failure, the increase in column longitudinal tensile strains would be mostly due to γ_j and the associated shear and confinement demands from the damaged joint core.

The strain profiles of the column longitudinal bars in the Push cycles were markedly different from the strain profiles in the Pull cycles. For the column exterior bars (Figure 5.14), reversals of strains in the beam-column interface sections were observed in the Push cycles beyond the -1.0% drift cycles. In the centre of the joint core, close to zero strain was measured on the exterior column bars. The high tensile strains of the column exterior bars in the top half of the joint and high compressive strains in the bottom half could be a result of the lateral deformation of the column reinforcement as the concrete wedge gradually spalled away from the joint. At the buckling of the column exterior longitudinal bars at the -3.0% drift cycles, drops in compressive and tensile strains were observed.

For the column interior bars (Figure 5.15) in the Push cycles, the measured strains at the top and bottom column-joint interfaces increased rapidly after the joint cracking, with the interior bars yielding at the -2.5% drift. However, the strains measured at the centre of the joint were significantly lower, with the maximum tensile strain being less than 500 microstrains. The column vertical bars would not carry much joint shear forces considering the double diagonal crack patterns in the joint.

5.6.3 Stirrup reinforcement strains

The strain profiles of the stirrups in the column and the beam are shown in Figure 5.16. Only selected stirrup results are presented herein as the general trend across different measurements is similar. In generally, all stirrups responded elastically.

Strain gage CS1A, placed perpendicularly to the loading direction on the first stirrup in the bottom half of the column, approximately 50mm from the beam soffit, showed significant confining tensile stresses beyond the 1.0% drift cycles. This corresponded well with the previous deduction that the tensile yielding of the column longitudinal reinforcement was due to lateral

displacement of the column bars within the dilated joint. The stirrup with strain gage CS1A, restrained this movement and thus generating confining stresses in the perpendicular-to-loading direction in the stirrup. The maximum stress recorded in CS1A was 100MPa.

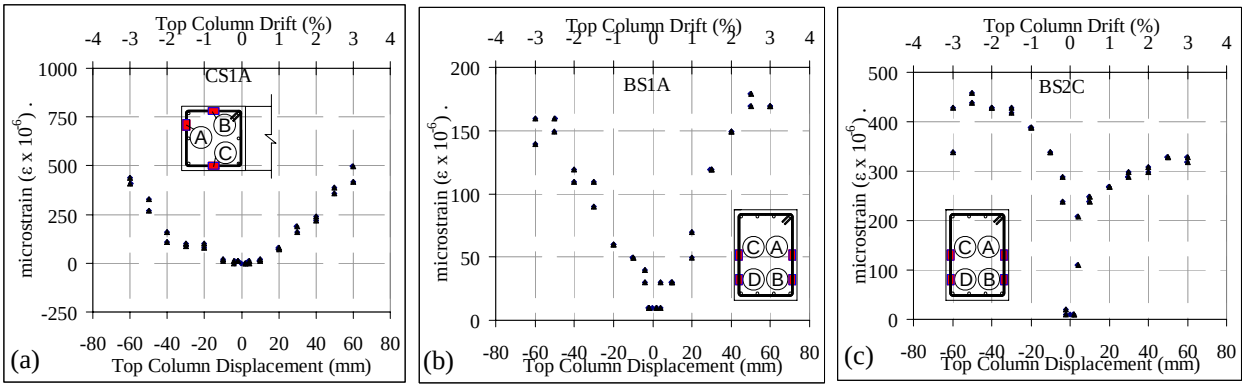

Figure 5.16: Stirrup strain profiles: a) CS1A- column stirrup 50mm from beam soffit; b) BS1A- beam 1st stirrup - 50mm from column interior face; and c) BS2C- beam 2nd stirrup - 183mm from column interior face.

The maximum stirrup stress of 98MPa was recorded on the second stirrup in the beam (see BS2C). The second stirrup, which was approximately 183mm away from the column interior face, generally had twice the steel stress when compared to the first stirrup (see BS1A), which was located 50mm away from the column interior face. The maximum nominal shear stresses within the beam section were calculated to be $0.06\sqrt{f'_c}$ MPa and $-0.08\sqrt{f'_c}$ MPa during the Pull and Push loading direction respectively.

5.7 DISCUSSIONS

5.7.1 Limit states for the joint shear distortions and principal stresses

The test results of NS-O1 suggest that the joint shear distortion γ_j limit states for joint cracking based on the Priestley *et al.* [18] may be not conservative. As mentioned in §2.4.4.1 , Priestley *et al.* [18] give γ_j at the joint diagonal tensile cracking and at the maximum p'_t to be 0.015% (0.00015 radians) and 0.07% (0.0007 radians) respectively.

As shown in §5.5.2, the measured γ_j at the joint diagonal tensile cracking in the Pull direction is -0.15%, a difference by a factor of ten. Considering the possible inaccuracies of measuring γ_j directly, the γ_j at the joint diagonal tensile cracking can be approximated from the θ_{drift} and its components. The joint cracking is at the θ_{drift} = +0.9%, and by accounting for the joint deformation component (~18% from Figure 5.5a) and the γ_j at the joint diagonal tensile cracking is about 0.16% (~18% x 0.9%).

The NS-O1 limit state for γ_j at the maximum p'_t, $\gamma_{j,peak}$, is measured to be -0.93% (Pull direction). The peak F_c and hence maximum p'_t occur approximately at the θ_{drift} of +1.95%. Similarly, referring to Figure 5.5a shown in §5.4.1, the measured joint deformation component contributes 36% to the column displacement Δ_c or subassembly drift θ_{drift} at the Pull peak of the 2% drifts; therefore, the $\gamma_{j,peak}$ is approximately 0.72% (~36% of 2%).

The NS-O1 result is consistent when compared with other tests on as-built exterior beam-column joints with no or few joint reinforcement. Table 5.1 presents the limit states from selected experimental data in which the p'_t-γ_j limit states were reported [6, 9, 12, 15]. As shown in Table 5.1, the $\gamma_{j,peak}$ limit states typically range from 0.14% to 0.72% while γ_j at the joint crack are typically low (0.01% to 0.25%). The average p'_t- γ_j limit states values listed in Table 5.1 are generally consistent with the results of NS-O1.

These observations suggests that the joint shear degradation model given in the Ref. [18] can be modified in view of more accurate representation of $\gamma_{j,peak}$ limit. Figure 5.17 shows the modified p'_t degradation curves for various joint detailing configurations that can be used to estimate the global deformation capacity of pre-1970s non-ductile beam-column joints.

Table 5.1: Joint shear distortion, γ_j, limit states from various literature sources.

Reference	Test Specimen	Joint diagonal cracking p_t ($\sqrt{f'_c}$ MPa)	Joint distortion at cracking, $\gamma_{joint,cr}$ (rad)	Maximum p_t ($\sqrt{f'_c}$ MPa)	Joint distortion at maximum p'_t, $\gamma_{joint,peak}$ (rad)
Hakuto et.al.(1995) [1]	O6 (bent in)	0.31	0.0025**	0.32	0.004**
	O7 (bent away)	0.25	0.0010**	0.25	0.004**
Pantelides et.al. (2002) [8]	Test 1 (0.1f'cAg) Up	0.72	0.0004	0.85	0.0035
	Test 1 (0.1f'cAg) down	0.79	0.0004	1.23	0.0020
	Test 2 (0.25f'cAg) Up	1.79	na	1.86	na
	Test 2 (0.25f'cAg) down	1.90	na	2.09	na
	Test 3 (0.1f'cAg) Up	0.70	0.0001	1.35	0.0072
	Test 3 (0.1f'cAg) down	0.63	0.0002	1.21	0.0043
	Test 4 (0.25f'cAg) Up	1.64	0.0003	2.13	0.0071
	Test 4 (0.25f'cAg) down	1.61	0.0003	2.05	0.0023
	Test 5 (0.1f'cAg) Up	0.88	0.0006	1.43	0.0061
	Test 5 (0.1f'cAg) down	0.79	0.0006	1.16	0.0044
	Test 6 (0.25f'cAg) Up	1.23	0.0001	1.72	0.0065
	Test 6 (0.25f'cAg) down	1.29	0.0001	1.96	0.0039
Pampanin et.al (2002)[2]	T1 positive	0.19	0.0001	na	na
	T1 negative	0.15	0.0001	na	na
	T2 positive	0.19	0.0001	na	na
	T2 negative	0.12	0.0001	na	na
Engindeniz (2008) [11]	Specimen 1 - EW	na	na	0.47	0.0014
	Specimen 1 - NS	na	na	0.40	0.0021
	Specimen 2 - EW	na	na	0.40	0.0014
	Specimen 2 - NS	na	na	0.46	0.0016
Average Values		0.84	0.0003	1.19	0.0038

na = no data available. ** approximate values from graphs.

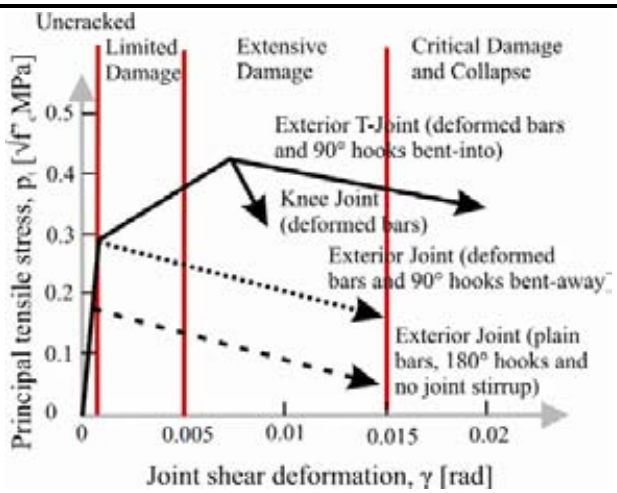

Figure 5.17: Reproduction of Figure 2.34: Revised principal tensile stress p'_t vs. joint shear deformation γ_j strength degradation curves.

5.7.2 Bond stresses along the beam reinforcement in unreinforced exterior joints

As it is not possible to differentiate the tension anchorage contributions from the 180° hook and the straight anchorage length, the bond stress in the straight length is estimated from the compression anchorage, assuming negligible compressive bearing on the concrete cover after joint cracking. Prior to joint cracking, using the strain profile values when the reinforcing are in compression in the beam-column interface section, the bond stress, τ_b, can be calculated using:

$$\tau_b = \frac{\Delta\varepsilon_s E_s A_s}{\pi d_b \Delta l_x} \qquad \textbf{5.1}$$

where $\Delta\varepsilon_s$ is the difference in the strain measured between two strain gages and Δl_x is the horizontal length between the two strain gages.

Figure 5.18 and Figure 5.19 present the bond stress distribution profiles calculated from the measured beam steel strains presented in §5.6.1. Figure 5.18 shows the maximum compressive bond stresses, $\tau_{b,max,}$, achieved in each Pull-Push cycles before bond failure, indicated by sudden reversal of strain and slipping. The maximum $\tau_{b,max}$ measured is $0.362\sqrt{f'_c}$ MPa, occurring during the 1st Pull peak in the 0.2% drift cycles. This is comparable to the recommendation of $\tau_{b,max} = 0.3\sqrt{f'_c}$ MPa (e.g. [5]), as discussed in §2.4.5. Figure 5.18 clearly illustrates in-cycles the bond strength degradation before bond failure in a particular loading direction under compressive steel stresses. The maximum bond stress prior to bond failure is at the main flexural fixed-end crack at the beam-column interface.

Figure 5.19 illustrates the identification of the bond failure with respect to the steel reinforcement in compression. Beyond the bond failure, Equation 5.1 no longer gives a correct

representation of the bond stresses as shown by the vacillating values for drift cycles after the bond failure. Figure 5.19 also indicates the bond stress distribution within the joint prior to bond failure in compression. While the bond stress distribution in the early stages is similar to other work in literature (e.g. Feldman and Barlett [7] plain bars pullout test and Hakuto *et al.* [9] interior joint deformed bars cyclic tests), the cyclic nature of plain round bars bond distribution has not been explored in literature.

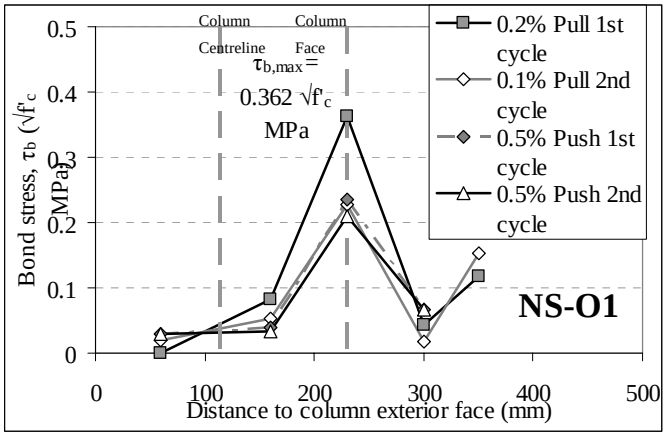

Figure 5.18: NS-O1: In-cycles bond stress degradation for maximum bond stress resisting compressive beam reinforcement stresses.

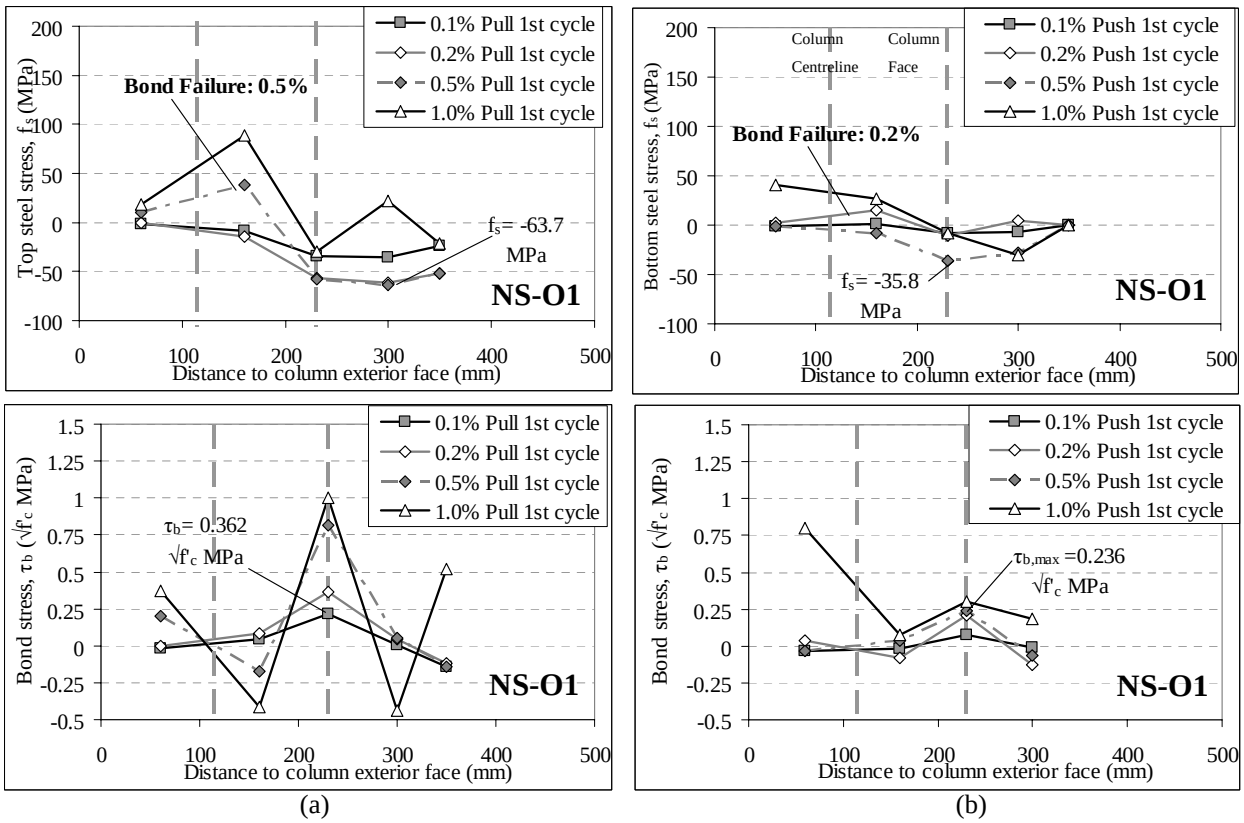

Figure 5.19: NS-O1 steel and bond stresses distribution for beam compressive anchorage into the joint at different drift levels: a) Top beam bars during Pull cycles; b) bottom beam bars during Push cycles.

The strain profiles of the beam longitudinal bars (§5.6.1) and the general relationships between the reinforcement's stress-strain and the bond's stress-slip (§2.4.5.1) can help to infer the bond stress distribution along the beam bars anchored in the unreinforced and cracked exterior beam-column joints. Figure 5.20 shows the assumed steel stress and bond stress distributions along the beam bars during the Pull loading direction with tension face at the bottom of the beam. Figure 5.20 does not consider the bearing capacity from the 180° standard hook in either compression or tension.

In the early stages of loading, the beam-column joint has minor flexural and joint cracks without complete loss of bond capacity in the critical beam section. The bond stress distribution is similar to those of straight/hooked steel reinforcement under uniaxial tension or compression as shown in Figure 5.20top. Tensile strains develop in the beam longitudinal bars within the joint region after joint cracking. As illustrated in Figure 5.19 for NS-O1, the bond failure of plain round bars can occur before the joint diagonal cracking.

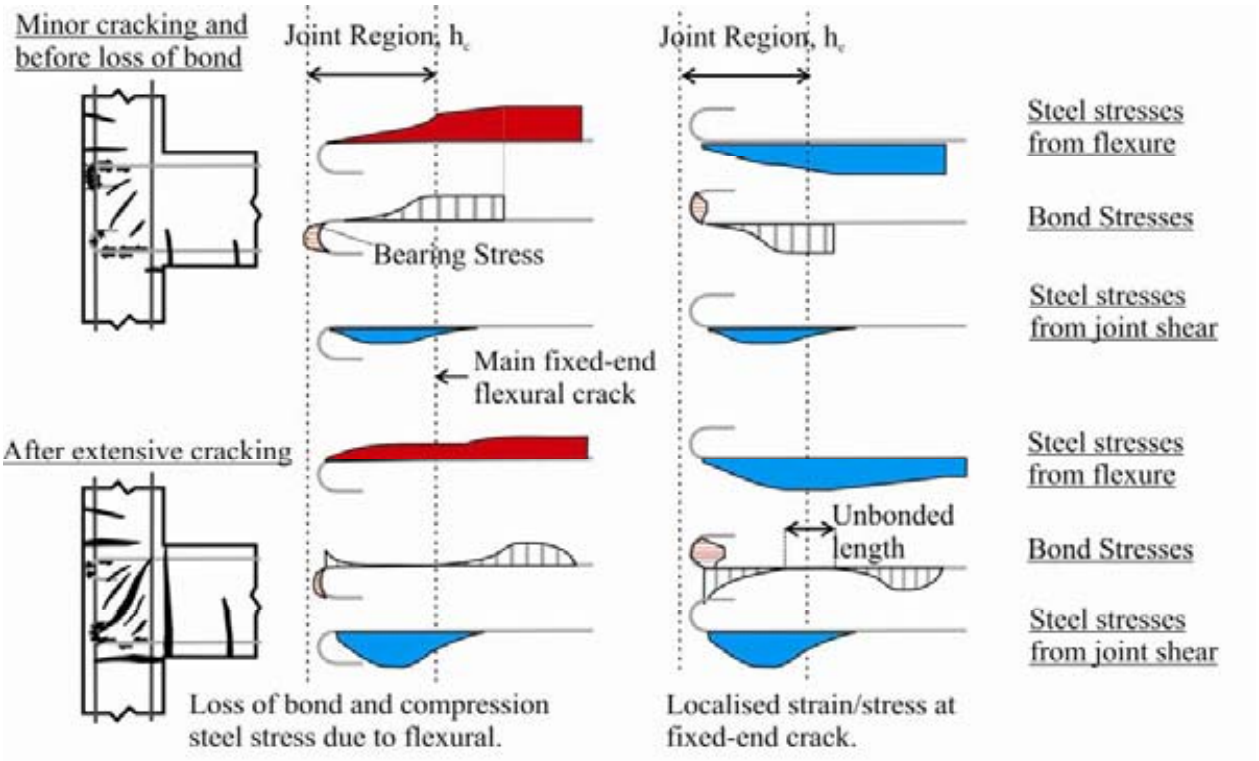

Figure 5.20: Assumed steel and bond stresses distribution along the beam longitudinal reinforcement anchored into joint with under Pull loading: top) uncracked/small crack scenario; bottom) large flexural crack scenario. Bond stresses are not drawn to scale and are exaggerated for clarity.

Bond failure limits the steel compressive stress development. As joint cracking progresses, more severe bond degradation and almost negligible residual bond strength can be expected in the compressive reinforcement as the 180° hook is not a reliable compressive anchorage. The

lack of compressive bond resistance in NS-O1 is important to be noted in the Selective Weakening (SW) retrofit design, which relies on the existing flexural strength of the weakened beam section (see §3.4.4).

For the tensile reinforcement, as the single large flexural crack at the beam-column interface grows, localised bond failure occurs at the steel reinforcement at the intermediate region of the crack. As the flexural crack widens, a length of steel reinforcement across the crack width will be unbonded with no stress transferred to the surrounding concrete. Beyond the unbonded length however, tensile stress can be developed in the steel as the 180° hook is a reliable tension anchorage. This changes the bond stress distribution along the beam longitudinal reinforcement, as shown in Figure 5.20bottom.

Within the unbonded length, the steel strain localises as the strain compatibility with the surrounding concrete is not longer applicable. This leads to a stress concentration at cracking location and which in return results in a single large flexural cracking at the beam-column interface. This results in recursive behaviour of: the widening of the flexural crack, the loss of bond at the crack location, the strain and stress concentrations and the further crack concentration/widening at the beam-column interface. As observed for NS-O1, fixed-end beam rotation accounts for 30-40% of the top column horizontal displacement till the end of test, with a large noticeable flexural crack along the beam-column interface.

Within the joint region, tensile strains develops within the reinforcement after the joint has cracked as the beam longitudinal reinforcement transfer shear forces like conventional horizontal stirrups. The widening of the joint diagonal cracks will similarly cause strain and stress localisation within the crack widths, as illustrated in Figure 5.20. The tensile strains and stresses are possible because of the effective tensile anchorage from the 180° hook. However, at advanced stages of joint damage – due to the lost of diagonal compressive struts capacity from the spalling and crushing of the concrete, joint shear strength rapidly degrades.

5.7.3 Column axial load effect on joint shear capacity

As reviewed in §2.3, the effect of column axial load on the beam-column joint capacity has been well researched in the past but sometimes with contradictory observations and conclusions from various studies (e.g.[10, 13]). The majority of the tests on non-ductile beam-column joints have indicated positive effects on the lightly reinforced joint shear strength (e.g. [4, 14]). Herein a brief discussion on the effect of the variation of the column axial load on the joint capacity, as implemented for NS-O1, is given, while further study has been carried out by Akguzel and

Pampanin [1, 2]. While it is apparent that axial load increases column flexural capacity up to the balanced point of the section, in terms of joint shear strength, a higher axial load can have both detrimental and beneficial effects.

Based on the observed principal stresses given in §5.5.2, Figure 5.21 illustrates a model of Mohr's circle stress-state as vertical axial stress, f_v, decreases and increases in the Pull and Push cycles respectively. It is assumed that the Mohr's circle generally crept to the p'_t with gradually higher theoretical rotation angle to the principal axes (principal angle), φ_p with decreasing column axial load. The p'_c plot during Pull cycles given in Figure 5.11b, suggests a rotating φ_p, pivoting about the initial p'_c value with decreasing f_v, as illustrated in Figure 5.21a. This is evident from the new diagonal joint cracks with varying angles to the horizontal plane ($\sim\varphi_p$) after the main diagonal cracking in the Pull direction, as shown Figure 5.2c.

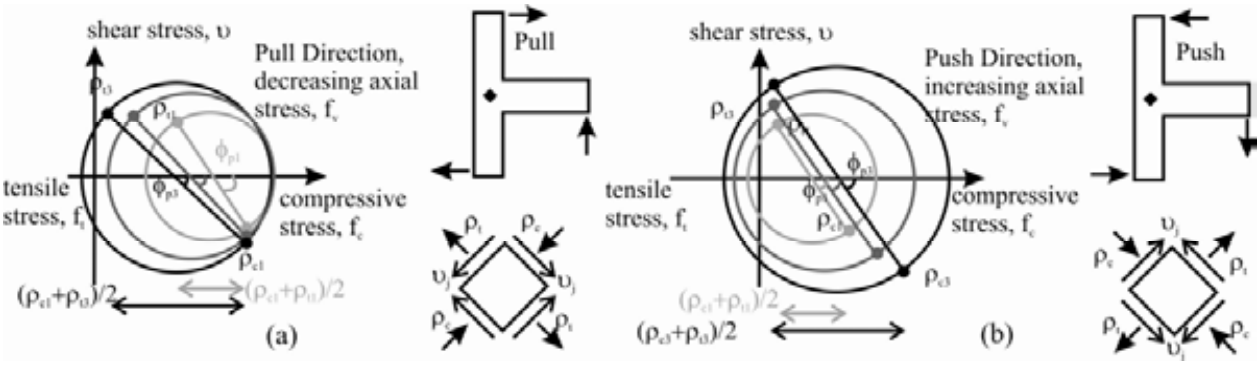

Figure 5.21: Mohr's circle model of NS-O1 joint under varying axial loads in a) Pull and b) Push loadings.

Increased axial load in the Push cycles would increase the net υ_{jh} capacity, based on the Mohr's circle stress-state analysis. However, the propensity to attain p'_c failure is also higher with increased axial stress. As illustrated in Figure 5.21 and Figure 5.11b, an increase in f_v effectively shifts and enlarges the Mohr's circle towards the compressive side. Naturally, this allows for a higher lateral capacity in the Push direction, as observed in the NS-O1 test, when compared to the Pull direction, as the p'_c cracking limit state was relatively higher than the p'_t limit. However, increased axial load and p'_c failure can lead to a more severe degradation of lateral load capacity after joint diagonal cracking, as observed in Figure 5.1. The strength degradation under increased axial load is because of the Poisson lateral dilation and subsequent degradation of interlocking friction-shear transfer capacity within the cracked joint. Higher axial load will also precipitate earlier buckling of the column reinforcement as shown in Figure 5.2f.

5.8 CONCLUSIONS

1. Specimen NS-O1, a representation of non-ductile pre-1970s exterior beam-column joints, failed in the brittle joint shear failure under cyclic seismic loading. Premature joint cracking (as observed) at the 0.9-1.0% drift cycles limited the lateral capacity of the sub-assemblage. Structural failure was attained shortly after the joint diagonal cracking and significant degradation of reinforcement bond and joint shear capacities. The force-displacement hysteresis of NS-O1 illustrated poor seismic behaviour with limited lateral force, deformation and ductility capacities, in addition to the limited energy dissipation capacity due to the pinching and slipping hysteresis loop.

2. Table 5.2 below summarises the key test results of the NS-O1, the as-built non-ductile pre-1970s beam-column joint specimen:

Table 5.2: Summary of NS-O1 test result.

Test Unit	Peak Lateral Force (kN)	Inter-storey drift at maximum force, θ_d (%)	Ultimate inter-storey drift, θ_d (rad) [1]	Lateral Force at joint cracking (kN)	Inter-storey drift at joint cracking, θ_d (rad)	Maximum column moment, $M_{sys\text{-}exp}$ (kNm)	Theoretical column moment, $M_{sys\text{-}cal}$ [2] (kNm)	$M_{sys\text{-}exp}$ / $M_{sys\text{-}cal}$
NS-O1	+14.7 -18.7	+1.95 -0.93	+1.0%-II	+14.7 -18.7	+0.9%-I -1.0%-I	+12.3 -15.6	+8.9 -12.4	+1.38 -1.26
	Failure Mode		Max / Min joint shear stress, v_{jh} (f'_c MPa)	Min / Max axial stress, f_v (MPa)	Max. principal tensile stress, p_t ($\sqrt{f'_c}$ MPa)	Max. principal compression stress, p'_c ($\sqrt{f'_c}$ MPa)	1st / 2nd cycles total energy dissipated, $E_{D,4.0\%}$ (J)	Equivalent Viscous Damping (EVD) ratio, $\xi_{hyst,2.0\%}$ [3] (%)
	Joint shear failure		+0.100 -0.125	0.82 / 3.74	0.32	1.13	2146 / 1426	10.6

Positive force, displacement and drift correspond to PULL cycles while negative values indicate PUSH cycles. I=1st cycle; II=2nd cycle. f'c =17.3MPa.
[1] Failure point defined as attained peak force was less than 80% of previous peak force. [2] Calculated maximum column moment based on the Hierarchy of Strength analysis outlined in Chapter 2. [3] $\xi_{hyst,2.0\%}$ is calculated based on hysteresis area-based equivalent viscous damping in the 1st cycle.

3. Fixed-end beam flexural and joint shear deformations were found to be critical contributors to the flexibility of the joint. In the Push direction, beam nominal flexural capacity was attained just before the joint diagonal cracking due to a principal compression stress p'_c failure, with $p'_c = 1.12\sqrt{f'_c}$ MPa. In the Pull direction, the joint diagonal cracking occurred at a principal tensile stress p'_t of $0.28\sqrt{f'_c}$ MPa. Joint shear deformation dominated the inelastic deformation of the NS-O1 beam-column joint, in particular beyond the joint diagonal cracking at 1.0% drift cycles. The maximum v_{jh} measured were $+0.1f'_c$ and $-0.13\,f'_c$ for the Pull and Push loading directions respectively.

4. In the test unit NS-O1, the ultimate loss of joint strength is because of the loss of compressive strut capacity due to concrete spalling and crushing after the diagonal joint

cracking. This suggests that if the spalling and compressive crushing within the joint core can be controlled and mitigated, the ductility capacities of the beam-column joint system can be improved.

5. Based on the NS-O1 measured joint shear deformation γ_j limit states and the re-evaluation of existing test results, a minor revision of the p'_t versus γ_j relationship is proposed for the assessment of lightly reinforced exterior beam-column joints. This is given in Figure 5.17.

6. A conceptual model of bond stress distribution based on the benchmark specimen NS-O1's strain profiles and bond stresses has been postulated. The model attempts to explain the mechanics of tensile and compressive bond capacities for plain round bars in non-ductile beam-column joints. The maximum bond stress, $\tau_{b,max}$ capacity in compression for plain round bars with 180° hook anchorage was $0.362\sqrt{f'_c}$ MPa. Limited compressive bond capacity suggests that for beam-weakening-only SW retrofit design, the compressive steel contributions can be neglected.

7. In addition, a discussion of the influence of plain round bars on the fixed-end flexural and joint shear capacities based on the mechanics of bond degradation and loss of bond at the cracking location is given in §5.7.2. An attempt to explain the concentration of stress and strain across the crack widths (joint and beam fixed-end) is given, based on strain-gage readings. The same mechanistic model can be assumed for the pseudo-rocking assumptions described in §3.4.5 for the post-tensioned beam-column joint retrofit.

8. The variability of the influence of vertical axial stresses, f_v, was discussed with a Mohr's circle stress analysis on the NS-O1 test results in §5.7.3. Under decreasing f_v in the Pull loading cycles, the Mohr's circles were creeping towards p'_t limit within a rotating φ_p about the initial p'_c value. With increasing f_v in the Push direction, the Mohr's circles shifted towards the compressive stress state with almost constant φ_p. The result suggests that added horizontal axial stress, f_h, from external post-tensioning will increase the joint shear capacity by shifting the Mohr's circles away from the principal tensile stress limit, as well as increasing the Mohr's circle radius given by $(f_h+f_v)/2$. This might conversely result in p'_c-induced diagonal cracking for the post-tensioned SW retrofit of non-ductile beam-column joints.

5.9 CHAPTER 5 REFERENCES

[1] Akguzel U. (2011) Seismic behaviour of FRP-retrofitted beam-column joints (in preparation) [PhD dissertation]. Uni. of Canterbury, Christchurch, NZ.

[2] Akguzel U, Pampanin S. (2010) Effects of variation of axial load and bidirectional loading on seismic performance of GFRP retrofitted reinforced concrete exterior beam-column joints. *ASCE J of Composite Constr*. Jan-Feb 2010; **14**(1):94-104.

[3] Beres A, Pessiki S, White R, Gergely P. (1996) Implications of experimental on the seismic behaviour of gravity load designed RC beam-column connections. *Earthquake Spectra*. **12**(2):185-198.

[4] Beres A, White R, Gergely P. (1992) *Seismic behaviour of reinforced concrete frame structures with nonductile details: Part I - Summary of experimental findings of full scale beam-column joint tests. Technical Report NCEER-92-0024*. National Center for Earthquake Eng. Research, SUNY, Buffalo, NY.

[5] CEB-Fip-MC90. (1993) *CEB-FIP Model Code 90, CEB Bulletin d'Information No. 213/214*. Thomas Telford Ltd., London.

[6] Engindeniz M. (2008) Repair and strengthening of pre-1970s reinforced concrete corner beam-column joints using CFRP composites [PhD Dissertation]. Georgia Inst. of Tech., Altanta.

[7] Feldman LR, Bartlett FM. (2007) Bond stresses along plain steel reinforcing bars in pullout specimens. *ACI Structural Journal*. Nov-Dec 2007; **104**(6):685-692.

[8] Fenwick R, Megget LM. (1993) Elongation and load deflection characteristics of reinforced concrete members containing plastic hinges. *Bull of New Zealand Soc of Earthquake Eng*. **26**(1):28-41.

[9] Hakuto S, Park R, Tanaka H. (1995) *Retrofitting of reinforced concrete moment resisting frames. UC Research Report 95-4*. Dept. of Civil Eng., Uni. of Canterbury, Christchurch, NZ.

[10] Jirsa JO, (1991) editor.^editors. *SP-123: Design of beam-column joint for seismic resistance*. American Concrete Inst. (ACI), Farmington Hills, MI.

[11] Liu A. (2001) Seismic assessment and retrofit of pre-1970s reinforced concrete frame structures, PhD Dissertation [PhD]. Uni. of Canterbury, Christchurch, NZ.

[12] Pampanin S, Calvi GM, Moratti M. (2002) Seismic behaviour of RC beam-column joints designed for gravity loads. *Proc. of 12th European Conf on Earthquake Eng*, London, UK.Paper 726.

[13] Pantazopoulou SJ, Bonacci JF. (1992) Consideration of questions about beam-column joints. *ACI Structural Journal*. **89**(1):27-36.

[14] Pantelides CP, Clyde C, Reaveley LD. (2002) Performance-based evaluation of reinforced concrete exterior joints for seismic excitation. *Earthquake Spectra*. Aug 2002; **18**(3):449-480.

[15] Pantelides CP, Hansen J, Nadauld J, Reaveley LD. (2002) *Assessment of reinforced concrete building exterior joints with substandard details. PEER Report 2002/18*. Pacific Earthquake Eng. Res. Center (PEER), Berkeley, CA.

[16] Paulay T, Priestley MJN. (1992) *Seismic design of reinforced concrete and masonry buildings*. John Wiley & Sons Inc., Christchurch, NZ.

[17] Priestley MJN, Calvi GM. (1991) Towards a capacity design assessment procedure for reinforced concrete frames. *Earthquake Spectra*. **7**(3):413-437.

[18] Priestley MJN, Seible F, Calvi GM. (1996) *Seismic design and retrofit of bridges*. John Wiley & Sons Inc., NY.

CHAPTER 6. TESTS RESULTS OF RETROFITTED RC BEAM-COLUMN EXTERIOR JOINTS: NS-R1, NS-R2, NS-R3 & NS-R4

"Science may be described as the art of systematic over-simplification."

Karl Popper, 1902-1994

6.1 INTRODUCTION

This chapter presents the experimental results for the four Selective Weakening (SW) retrofit techniques implemented on the as-built benchmark beam-column joint (NS-O1): a) Beam-weakening-only retrofit (NS-R1), b) Joint post-tensioning-only retrofit (NS-R2) c-d) Full SW retrofit with beam-weakening and joint-post-tensioning (NS-R3 and NS-R4).

As discussed in Chapter 4, the objective of these four specimens was to demonstrate the effects of the two key SW retrofit design parameters: i) the levels/locations of beam-weakening and ii) the levels of joint post-tensioning forces. In addition, the effects of the incremental SW retrofit in terms of beam-weakening-only, joint post-tensioning-only and the combinations of both interventions were also considered. The design and hierarchy of strength evaluations of the four specimens were carried out according to the procedures presented in Chapters 2 and 3. The performance-domain of the four retrofitted specimens are given in Appendix B. Table 6.1 summarises the specimens predicted theoretical strengths and failure modes.

The behaviour of the SW-retrofitted beam-column joints under simulated seismic effects will be assessed in the following performance criteria: strength, displacement/ductility, energy dissipation and failure modes. Comparison with the analytical design procedure described in Chapter 3 will also be discussed in light of the test results. The chapter will conclude with a discussion on the two retrofit design parameters and feasibility of the SW retrofit techniques. The

complete test data and photographic observations for the four specimens are given in Appendix D. All four specimens were tested until the completion of the full 2nd cycles at the 4.0% drift.

Table 6.1: Specimens NS-R1, NS-R2, NS-R3 and NS-R4: Retrofit design and description.

Test Unit	Description	Day of testing f'_c (MPa)	Beam Reinforcements: Top / Bottom	Weakened section distance from column centerline (mm)	Post-tensioning Force (kN/tendon)	Calculated lateral strength, $F_{sys\text{-}cal}$ [1] (kNm)	Predicted failure mode based on the performance domain
NS-R1	R1: Weakening-only	25.6	4-R10 / 2-R10	165	0	+10.3 -18.1 [3]	Beam Flexural
NS-R2	R2: PT-only [2]	25.1	4-R10 / 4-R10	-	60	+20.0 -23.4	Beam/Column Flexural
NS-R3	R3: Weakening & PT [2]	24.3	4-R10 / 2-R10	165	20	+15.2 -20.3	Beam Flexural
NS-R4	R4: Weakening & PT [2]	30.3	4-R10 / 2-R10	310	12	+14.5 -19.3	Beam Flexural

[1] Calculated lateral strengths were based on the design evaluation outlined in Chapter 3. Positive force, displacement and drift correspond to Pull cycles while negative values indicate PUSH cycles. [2] PT = external joint post-tensioning. [3] Perfect bond is assumed in the assessment.

The sign convention for this chapter is consistent with previous chapters in this thesis. *Pull loading direction* refers to the *positive top column lateral displacement*, Δ_c, which induces *positive beam bending moment*, M_b, and *tension strain* in the bottom face of the beam. This also corresponds to *positive lateral force*, F_c, imposed on the column and *negative beam shear* force along the beam section. Therefore *Push loading direction* refers to the *negative top column lateral displacement*, Δ_c, *negative lateral force*, F_c, *negative beam bending moment*, M_b, and *tension strain* in the top face of the beam.

6.2 NS-R1: BEAM WEAKENING-ONLY RETROFIT

6.2.1 General description of behaviour

The lateral force-displacement (F_c versus Δ_c) hysteresis plot for NS-R1 is given in Figure 6.1. The damage patterns at the selected peak inter-storey drift, θ_{drift}, loading cycles are shown in Figure 6.2 and Figure 6.3. θ_{drift} is given by Δ_c/H_c and H_c is the column height (=2000mm).

No crack was observed in the ±0.1% drift loading cycles. In the 1st Pull cycle of the +0.2% drift, a 220mm high flexural crack appeared at the weakened section (Figure 6.2a). In the 2nd Pull cycle, the maximum crack width was 0.4mm. Similarly, on the reverse Push loading to the -0.2% drift, a flexural crack initiated at the beam top face along the weakened section, resulting in a fully cracked weakened section. The ratio of cracked stiffness-to-uncracked stiffness, K_{cr}/K_{ini}, was approximately 0.77 with the initial stiffness, K_{ini}, of 2657kN/m measured in the +0.1% drift cycles.

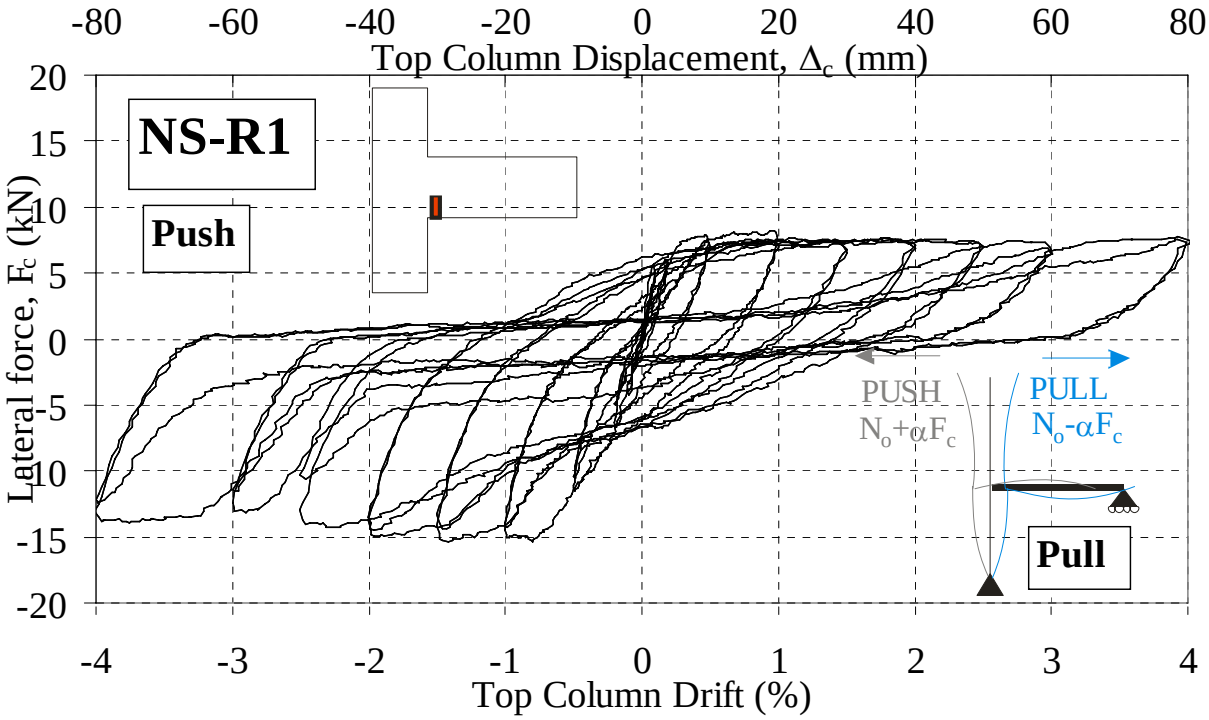

Figure 6.1: Top column lateral load, F_c, versus top column displacement, Δ_c, and drift, θ_{drift}, for NS-R1.

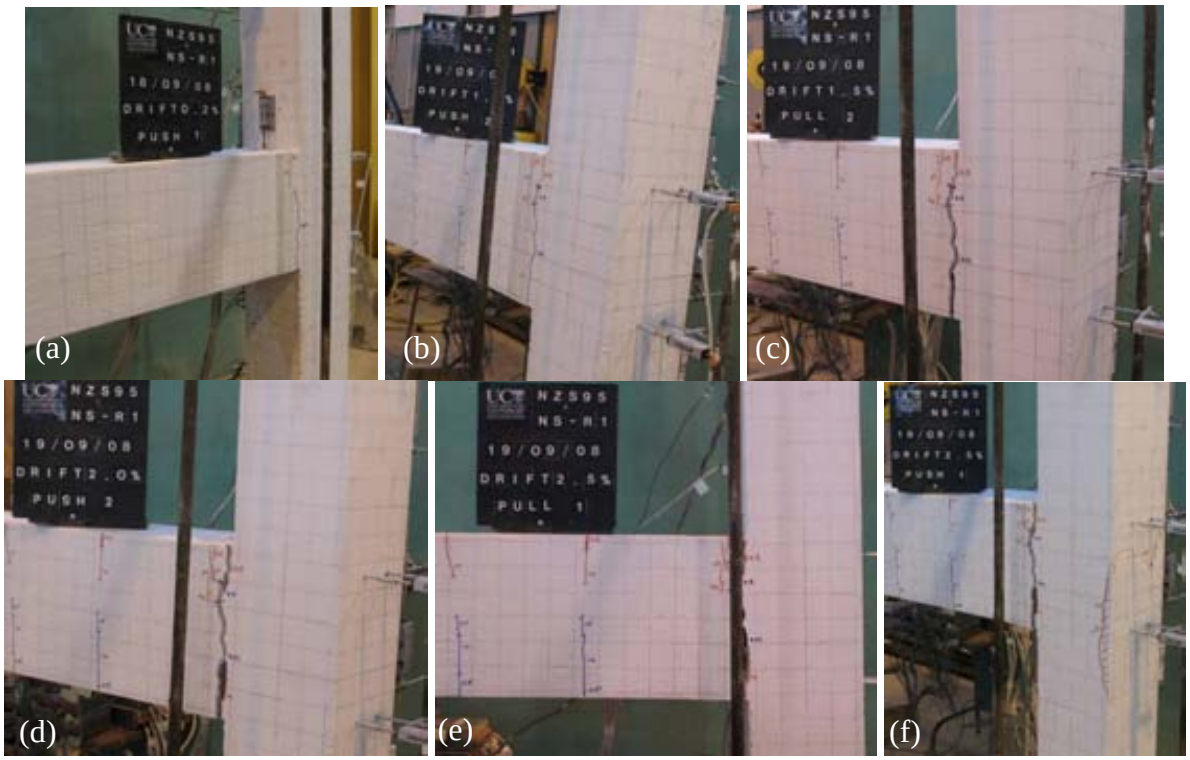

Figure 6.2: Observed cracking patterns of NS-R1: TOP: a) 1st Push cycle of the -0.2% drift; b) 2nd Push cycle of the -1.0% drift; and c) 2nd Pull cycle of the+1.5% drift. BOTTOM: d) 2nd Push cycle of the -2.0% drift; e) 1st Pull cycle of the +2.5% drift; and f) 1st Push cycle of the -2.5% drift.

In the ±0.5% drift cycles, the flexural crack at the weakened section widened to maximum crack widths of 1.6mm at the beam soffit and 0.35mm at the beam top face. Two new hairline beam flexural cracks were initiated in the 1st cycles of the ±0.5% drift. The F_c-Δ_c plot (Figure 6.1) shows evidence of bond-slip failure in the Push cycles, even in the low drift cycles (±0.1-0.2% drifts). The F_c-Δ_c hysteresis slip was more noticeable in the 2nd cycles. The beam bottom longitudinal reinforcements yielded in the Pull cycles of +0.2% drift with the F_c=+7kN, as confirmed by strain gages reading (§6.2.5).

The ±1.0% and ±1.5% drift cycles were relatively stable with no observed peak-to-peak strength degradations. Stable and relatively 'fat' hysteresis loops with significant energy dissipation capacity were achieved (see §6.2.2). Stiffness degradation and F_c-Δ_c hysteresis slip were observed in the 2nd cycles of the Push loading direction. The pinching of the F_c-Δ_c hysteresis corresponded to the slipping of the beam bottom reinforcements in the closing of the flexural crack. The beam top reinforcements yielded in the 1st Push cycles of the -1.0% drift, with the F_c=-15kN. In the ±1.5% drift cycles, the main flexural crack at the weakened section had crack widths up to 8m in the Pull direction and 1.8mm in the Push direction. Peak F_c values of +8.2kN and -15.4kN were observed at θ_{drift}=+0.95% and θ_{drift}=-0.80% respectively.

Similar cracking trend was observed in the ±2.0% drift cycles. The equivalent viscous damping, ξ_{hys}, in the ±2.0% cycles was 30.3%, indicative of a stable beam flexural plastic hinge with ample of energy dissipation. When compared to the NS-O1 specimen with joint diagonal cracks in the 1.0% drift cycles and structural failure at the 2nd cycles of the 1.0% drift, NS-R1 had achieved the retrofit objective of weak-beam strong-column behaviour and a much improved behaviour up to ±2.0% drift cycles.

In the 1st Push cycle of the -2.5% drift, a large chunk of cover concrete on the column exterior face suddenly cracked (Figure 6.2f). This was a result of the compression anchorage failure of the beam bottom bars. As the straight lengths of the bars lost their bond strengths, the 180° hooks end would consequently slip and transfer the compressive forces through bearing on the unconfined joint cover concrete. In the reversal loading to the 2nd Pull peak, the reloading stiffness decreased significantly as the beam bottom reinforcements gradually reversed the slip and re-engaged the tension anchorage of the 180° hooks. As the 180° hooks were effective in tension and the bond strengths of the beam top reinforcements were still effective in compression, the lateral loads at the peak Pull drifts were maintained. In contrast, on the 2nd Push cycle of the -

2.5% drift, the bottom bars slipped free as the spalled concrete no longer carried much compression bearing force (Figure 6.3a). Structural failure (~80% of the previous peak F_c) was detected in the 2nd Push peak of the -2.5% drift cycles.

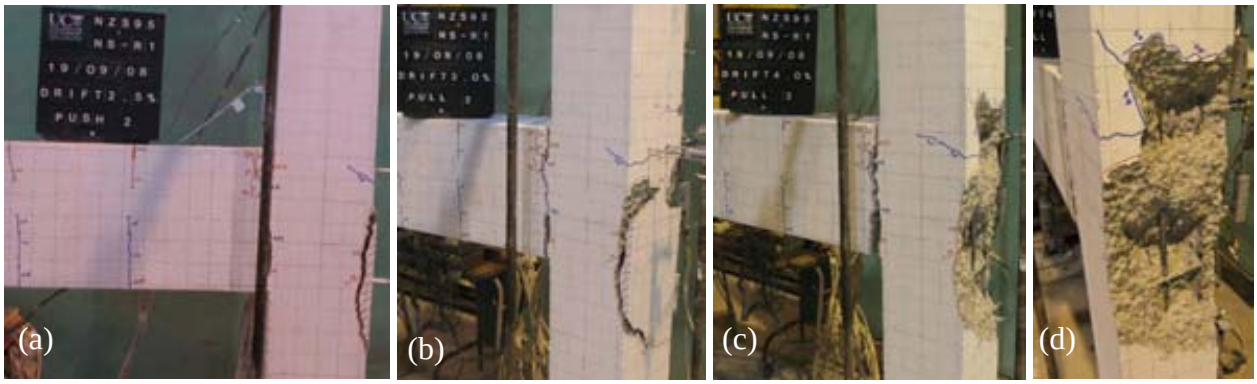

Figure 6.3: Observed cracking pattern of NS-R1: a) 2nd Push cycle of 2.5% drift; b) 2nd Pull cycle of 3.0% drift; c) 2nd Pull cycle of 4.0% drift; and d) anchorage push-out damage at the exterior joint face.

In the subsequent ±3.0% and ±4.0% drift cycles, the cracked concrete cover gradually spalled off due to the push-out of the 180° hook anchorage (Figure 6.3). In the ±3.0% drift cycles, there were bond-slip up to 20mm on both loading directions before any load-take up as the beam reinforcements were slipping through the closing of the beam main flexural crack. In the 1st cycles, as the bond strength progressively degraded, F_c was maintained though the virgin loading displacements. In the 2nd cycles however, most of the stiffness and strength were lost as the bond-capacity of plain round bars would have been lost in the 1st cycles. The limited energy dissipations in ±3.0% and ±4.0% drift cycles in NS-R1 were similar to the post-joint cracking response of NS-O1.

In the 1st Pull cycle of the +4.0% drift, the large block of concrete spalled off the column, exposing the column longitudinal bars (Figure 6.3c-d). The unrestrained column bars began to buckle in the subsequent Push cycles of -4.0% drift, leading to further lateral strength degradation.

6.2.2 Load-displacement hysteresis analysis

The standard analysis of the NS-R1 F_c-Δ_c hysteresis is presented in Figure 6.4. Significant improvements were achieved in terms of the energy dissipation capacity of the NS-R1 system, when compared to the as-built NS-O1 (see Figure 5.4). The energy dissipated per cycle for example, was about double of the NS-O1 values in between ±0.5% and ±2.5% drift cycles. The area-based equivalent viscous damping of the NS-R1 system, ξ_{hys}, was also very promising, with

ξ_{hys} up to 30% measured in the 1st cycles of ±2.0% and ±2.5% drifts. The degradation of ξ_{hys} in the 1st and 2nd cycles ranged between 12-45%, with an average of 27.7%.

Considering the design procedure described in §3.4.2 had only assumed ξ_{sys} between 10-15%, (where $\xi_{sys} = \xi_{hys} + \xi_{elastic}$), the experimental results of NS-R1 indicated the displacement demand may be lower with the increased damping from the NS-R1 connection. Nevertheless the brittle nature of the compression anchorage failure of the beam bars would suggest that further design consideration or additional retrofit interventions (as per NS-R3/R4) may be required for the complete retrofit. §6.2.6.2 will re-evaluate the compressive anchorage failure of the 180° hook anchorages in the beam-column joints.

Interestingly, the peak-to-peak stiffness, K_{eff}, did not differ significantly between the as-built NS-O1 and the retrofitted NS-R1, especially in the early drifts. In the ±0.5% and ±2.0% drifts, K_{eff} for NS-R1 were 918 and 257kN/m respectively (for the 1st cycles). In comparison, K_{eff} for NS-O1 were 1185 and 388kN/m for the 1st cycles of the ±0.5% and ±2.0% drifts.

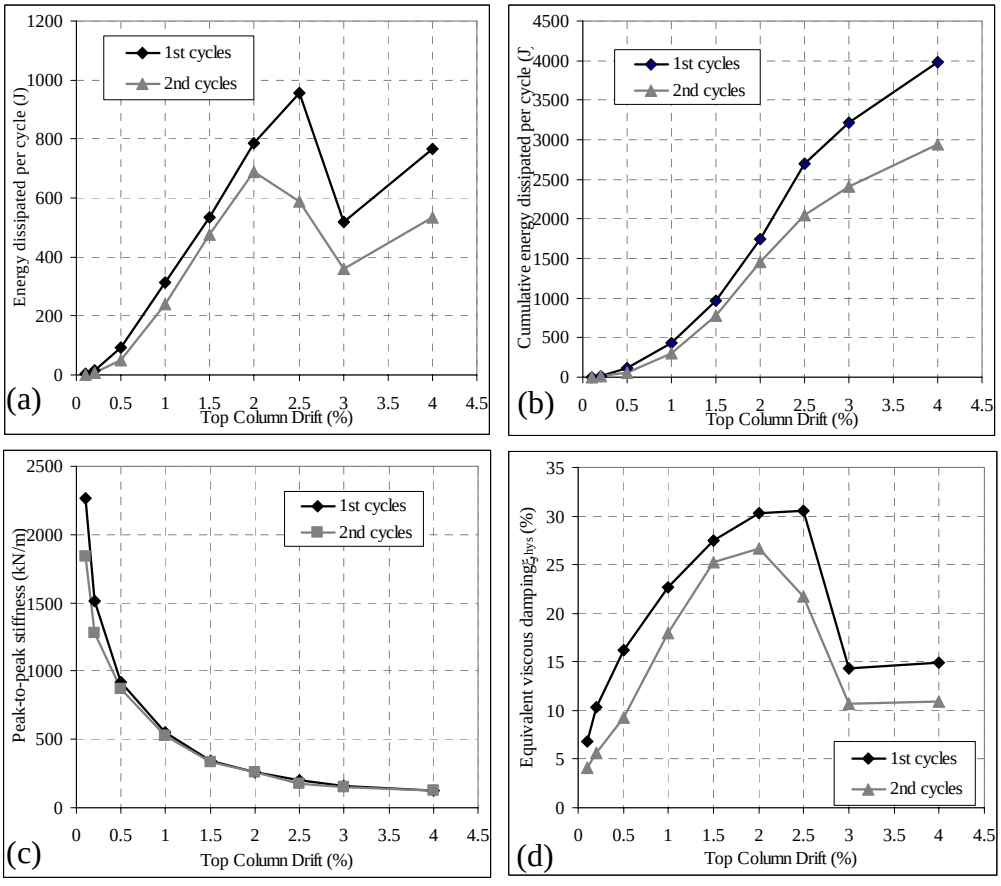

Figure 6.4: F_c-Δ_c analysis for NS-R1: a) Energy dissipated per cycle; b) Cumulative energy dissipated per cycle; c) peak-to-peak stiffness, K_{eff}, and; d) Equivalent viscous damping, ξ_{hys}.

6.2.3 Local deformations and displacement components

6.2.3.1 Decomposition of top column horizontal displacement

The components of the top column horizontal displacement, Δ_c, at the peaks of the Pull and Push loading cycles as percentages of the total Δ_c are presented in Figure 6.5. The displacement component results in Figure 6.5 were only up to ±3.0% drift cycles as many of the linear potentiometers were detached in the ±4.0% drift cycles to prevent damaging them.

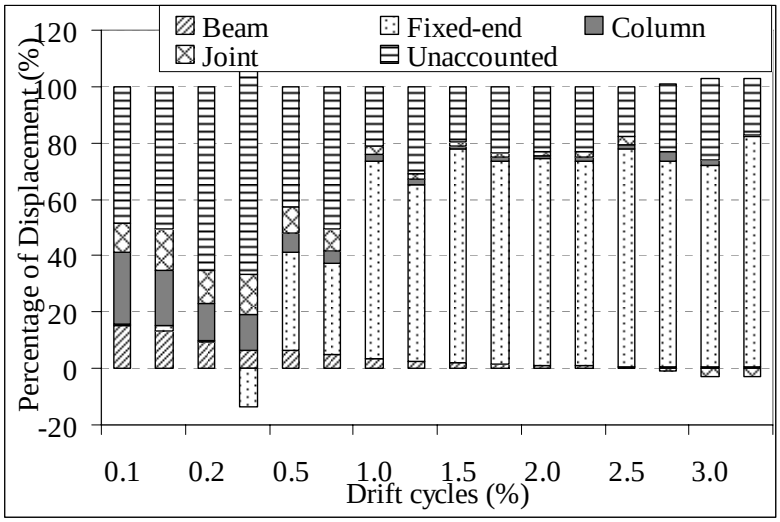

a) Pull loading direction – positive displacement.

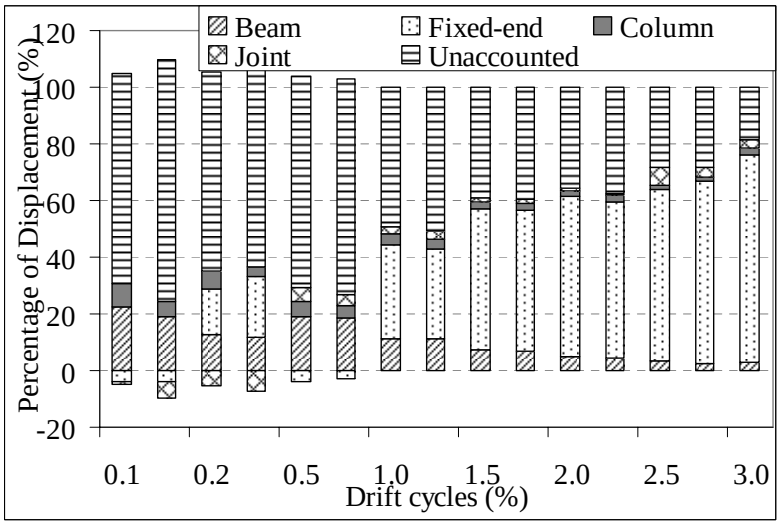

b) Push loading direction – negative displacement.

Figure 6.5: Displacement contribution decompositions based on the measured deformations for NS-R1.

It is clear from Figure 6.5 that the major source of Δ_c was the fixed-end beam displacement, $\Delta_{beam,fixed\text{-}end}$, for both the Pull and Push loading directions, indication of a

successful retrofit intervention to achieve a "weak-beam strong-column and joint". In the Pull cycles beyond +0.5% drifts, $\Delta_{beam,fixed\text{-}end}$ contributed for 20% in the +0.5% drift, and it grew to 80% in the +3.0% drift. Similarly, in the Push cycles, $\Delta_{beam,fixed\text{-}end}$ contributed between 30% (in the -1.0% drift) and 64-74% (in the -3.0% drift).

In terms of the column, beam flexural (away from fixed-end) and joint shear deformation components, the contributions to the Δ_c were relatively constant in absolute terms, with each component not exceeding more than 2mm in any drift level, except for the Δ_{joint} in the 1st Push cycles of the -2.5% drift. The beam-anchorage failure did not contribute directly to the Δ_c as the anchorage failure effectively allowed unrestrained fixed-end beam crack to widen.

As shown in Figure 6.5, there were significant unaccounted Δ_c components in the NS-R1 test, in particular in the Push direction and in the early drifts (θ_{drift} <+1.0% in the Pull cycles and θ_{drift} >-1.5% in the Push cycles). §5.4.1 (of Chapter 5) explained why the unaccounted Δ_c component tended to be more critical in the Push direction (as the damage accumulated in the initial loading direction).

The under-measurements of the Δ_c components could be attributed to an instrumentation error, in which no reliable data was attained at the low (<1mm) displacement measurements. Furthermore, while the relative deformations in each loading cycle could be measured, the net deformation due to the beam flexural cracking would be significantly under-measured if there were significant beam-elongations (un-closed beam cracks). No measurement of beam-elongation was taken for the specimen NS-R1, but from the measurements for specimens NS-R4 and S-R3, beam elongations of the retrofitted (with beam-weakening and post-tensioning) were in the range of 2mm (at θ_{drift}=±1.0%), 7mm (at θ_{drift}=±2.0%) and 27mm (at θ_{drift}=±4.0%).

6.2.3.2 Beam deformations

The moment-curvature plots for the beam flexural regions and the beam fixed-end region, shown in Figure 6.6, clearly show that nearly all of the beam inelastic deformations were concentrated on the fixed-end beam-column interface. Maximum curvatures of ±0.45m^{-1} were measured in the fixed-end beam section. Positive beam curvatures, ϕ_b, corresponded to the positive column displacement (Pull direction). The maximum beam moments developed in the Pull and Push directions were +15kNm and -27kNm respectively. With the yield curvature, $\phi_y = 2\varepsilon_y/H_b$ = 0.011m^{-1}, the curvature ductilities (at the structural failures) in the positive and negative beam

moments were 28 and 20 respectively. Structural failure occurred in the ±2.5% drift cycles, corresponding to the compression anchorage failure. As shown in Figure 6.6b-c, the beam bars did not attain φ_y in the next two flexural regions (75mm-475mm from the column internal face).

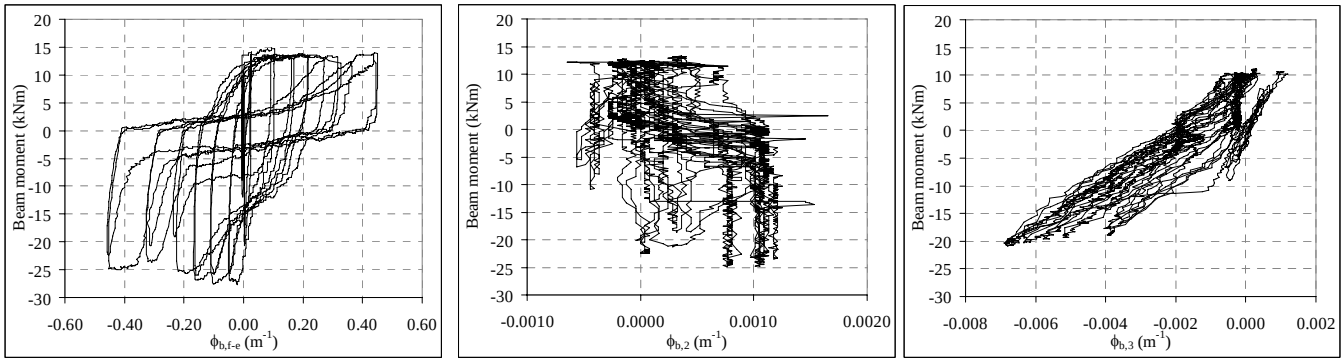

Figure 6.6: a) Moment-curvature plots for beam sections: a) fixed-end section; b) 75-275mm from the column internal face; and c) 275-475mm from the column internal face.

6.2.3.3 Column deformations

The moment-curvature plots for the top and bottom column sections are given in Figure 6.7. While the plots indicate that the column curvatures, φ_c, exceeded the φ_y (0.016m^{-1}) in the regions close to the joint, damage and crack observations suggested that the measured φ_c was affected by the expulsion of the concrete cover due to the anchorage push-out failure. The column sections would have responded elastically as the column moments measured (+6kNm and -12kNm) were much less than the column flexural capacities in both positive and negative displacements. The affected φ_c is shown as a lighter plot in Figure 6.7b-c.

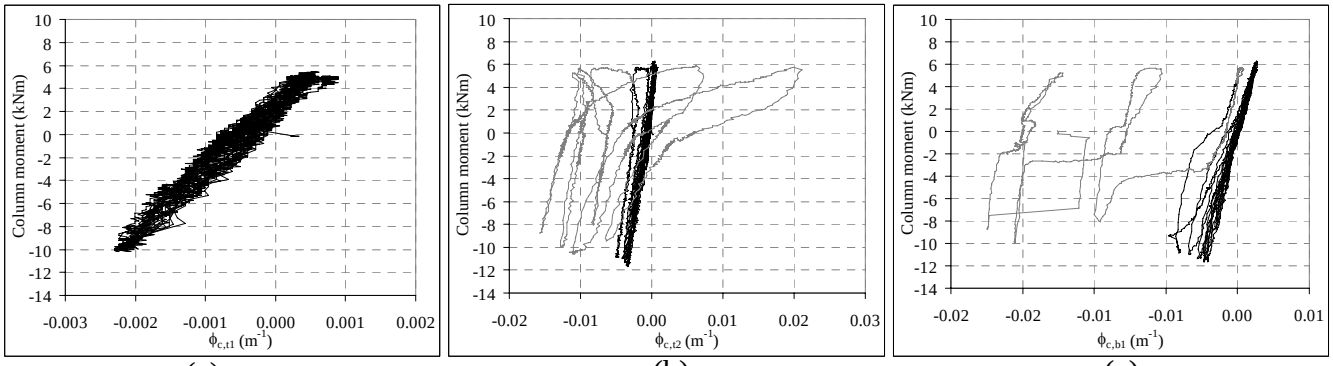

Figure 6.7: Moment-curvature plots for column flexural sections: a) 200-430mm from beam top face; b) 0-200mm from the beam top face; c) 0-200mm from the beam soffit.

6.2.4 Beam-column joint behaviour

6.2.4.1 Nominal joint shear stress and joint shear distortion

The nominal joint shear stress, v_{jh}, versus joint shear distortion, γ_j, and Δ_c relationships for NS-R1 are given in Figure 6.8. The maximum v_{jh} measured were 0.96MPa (0.19 $\sqrt{f'_c}$ MPa or 0.037f'_c MPa) in the Pull peak of the 1.0% drift and -1.78MPa (-0.35 $\sqrt{f'_c}$ MPa or -0.07f'_c MPa) in the Push peak of the 1.0% drift. Prior to the compression anchorage failure, the joint was responding linearly. No distinctive joint cracking was observed.

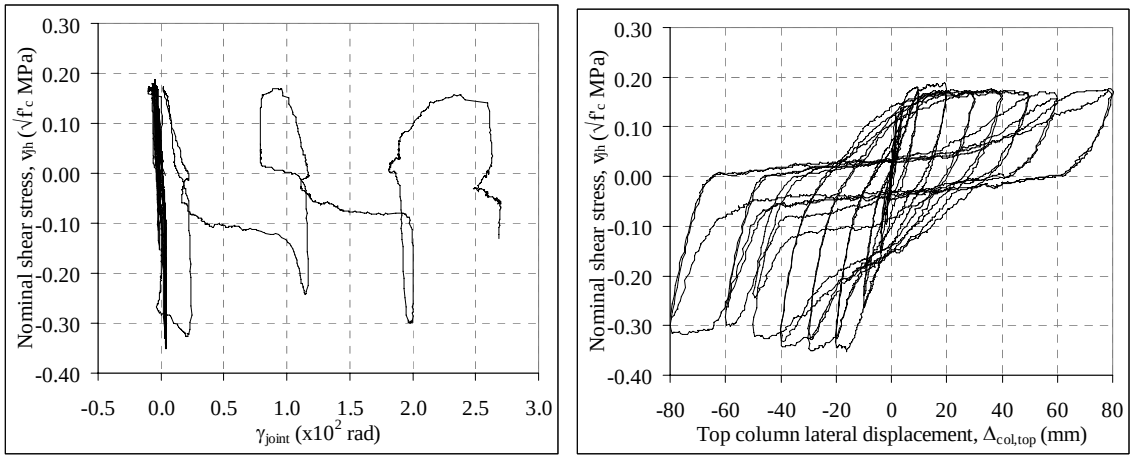

(a) (b)

Figure 6.8: a) Nominal joint shear stress, v_{jh} versus joint deformation, γ_j; b) Nominal joint shear stress, v_{jh} versus top column lateral displacement, Δ_c.

6.2.4.2 Joint principal stresses

Figure 6.9a-b presents the relationships between the principal stresses and the Δ_c while Figure 6.9c-d presents the relationship between the principal stresses versus the γ_j for NS-R1. In terms of maximum principal stresses in the joint during the cyclic loading of NS-R1, the maximum p'_t was 0.152$\sqrt{f'_c}$ MPa at γ_j =+0.00041 radians and the maximum p'_c was 0.83$\sqrt{f'_c}$ MPa at γ_j =+0.00041 radians. As there was no joint damage due to shear distortion, the measured γ_j was attributed to the anchorage failure-induced concrete spalling at the exterior face of the joint.

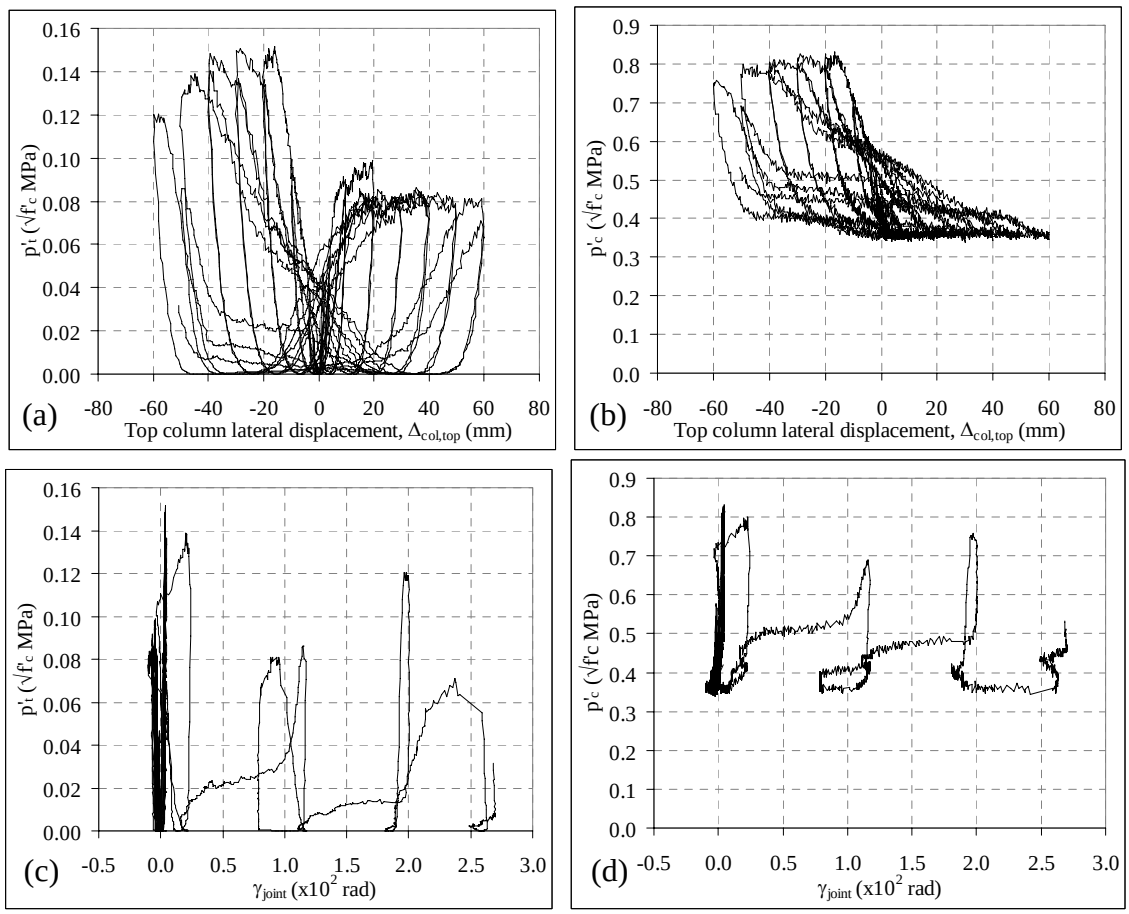

Figure 6.9: a-b) Joint principal stresses versus top column lateral displacement, Δ_c: a) principal tensile stress, p'_t; b) compressive tensile stress, p'_c; c-d) Principal stresses versus joint shear deformation, γ_j plots: c) principal tensile stress, p'_t; d) compressive tensile stress, p'_c.

6.2.5 Steel strain profiles

6.2.5.1 Beam longitudinal reinforcement strains

Figure 6.10, Figure 6.11 and Figure 6.12 present the strain profiles of the top and bottom (not weakened and weakened) beam longitudinal reinforcements for the specimen NS-R1. The X-axis is the distance from the exterior column face while the two vertical dashed lines refer to the column centre-line and the interior column face. The beam weakened section was located 50mm from the interior column face. Tensile strains are herein reported as positive values. From the steel test, the ε_y for the longitudinal beam and column reinforcements was 0.00168 (1680 microstrains) and the f_y was 335MPa.

Beam top bars (Figure 6.10) were under compressive strain up to the 1st Pull cycle in the +0.5% drift. Beyond the ±0.5% drift cycles, beam top bars were carrying tension stresses in both

the Pull and Push cycles. In the 2nd Pull cycle of the 1.0% drift, the top bars yielded in tension at the weakened section despite the beam top face being in compression in the Push loading (Figure 6.10 bottom left). The crack widths at the beam top face at this stage ranged from HL (centre) to 0.5mm (side of the beam), indicating that the neutral axis could be less than the beam top bar cover (*d'*). In the subsequent 1st Pull cycle of the +1.5% drift, the top bars again yielded in tension at the weakened section, while other strain gages along the top reinforcements were still measuring compressive strains. In the next few Pull cycles (2nd Pull of +1.5% and +2.0% Pull cycles etc.), the tensile strains extended beyond the weakened section, and the whole length of the top bars instrumented with strain gages was showing tensile strains beyond the 2nd Pull of the +2.5% drift. The yield strain penetration length into the joint region was approximately 90mm.

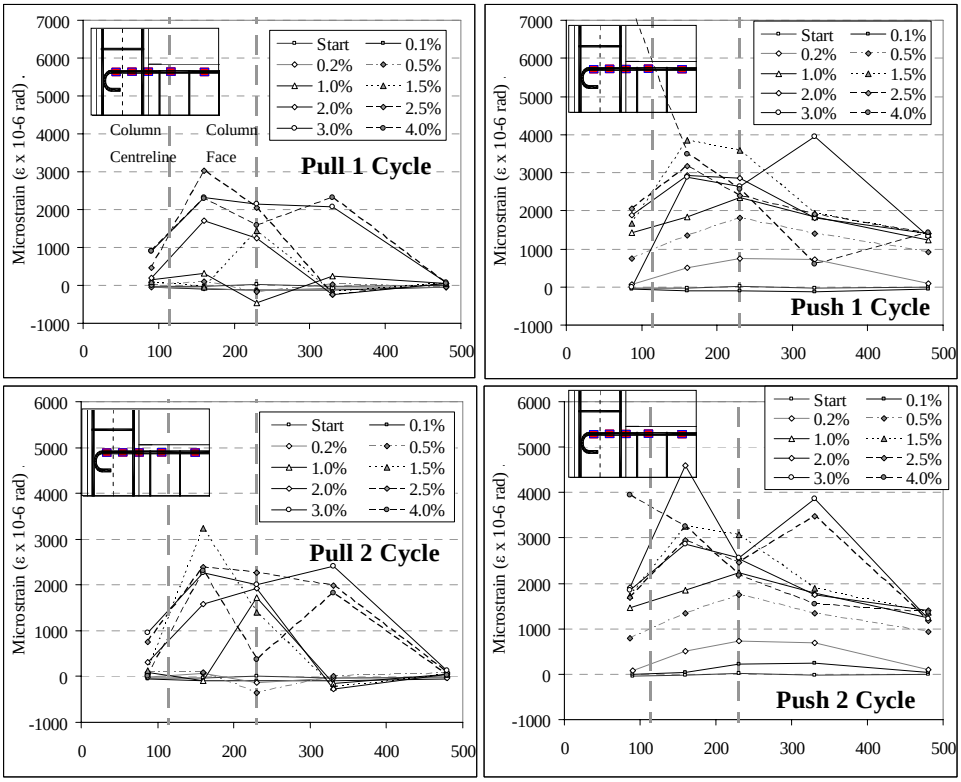

Figure 6.10: Strain profiles of beam top longitudinal bars of the specimen NS-R1.

For the beam top bars (Figure 6.10) in the Push cycles, substantial tensile strains were developed along the whole instrumented length of the top reinforcements with the maximum strain measured near the beam-to-column interface. Tensile strains peaked in the -2.5% drift Push cycles (~3500-4000 microstrains). Beyond the 2nd Push cycle of the -2.5% drift, a drop of tensile strain was measured in the weakened section. This was contrary to the localised stress

concentration at the main flexural crack, as suggested by the bond distribution model described in §5.7.2. However, recalling the compressive anchorage failure of the bottom bars in the 2nd Push cycle of the -2.5% drift, the drop in tensile strain of the beam top bars would be expected as the slipping bottom bars and the 180° hooks and the wide bottom flexural cracking would limit any compressive resultant, C_c, within the weakened section.

For the un-weakened bottom reinforcements (Figure 6.11), the strain readings in the Pull cycles show that tension yielding occurred in between +0.2 and +0.5% drifts cycles. The tensile strains peaked at the beam-column interface (near the weakened section) with maximum strain of 3700-4000 microstrains at the +0.5-1.5% drifts. Beyond the +1.5% drift, however, the measured tensile strains decreased, and in the +2.0%-3.0% drift cycles, compressive strains were measured in three of the strain gages. Careful analyses of the strain time-histories revealed that the strain gages were probably damaged during the extreme tensile strains in the +1.0-1.5% drift cycles and the bond-slip during the load-reversals.

The un-weakened beam bottom bars in the Push cycles (Figure 6.11) were carrying compressive strains up to the -2.5% drift. Compressive yielding of the bottom bars was detected in the -1.0% to -1.5% drifts. In the main flexural crack, some outlying tensile strain values were measured – owing to the possible damage of the strain gage due to localised stress-strain concentration. After the compressive anchorage failure, in which the bottom bars were slipping freely during the Push loading, most of the strain gages were damaged (therefore, there were no readings beyond the -2.5% drift).

The weakened beam bottom reinforcements (Figure 6.12), as expected, had low elastic strains (<200 microstrains for most locations) measured, as there was discontinuity along the beam-column interface (the weakened section). In the Pull cycles, after the +1.5% drift, there was a measurable increase in tensile strain in the reinforcement lengths embedded within the joint. A similar trend was observed in the Push cycles, beyond the -1.5% drifts – where the bars within the joint were measuring tensile strains up to 330 microstrains (66MPa). In the Push cycles, however, compressive strains were developed in the bars in the beam side.

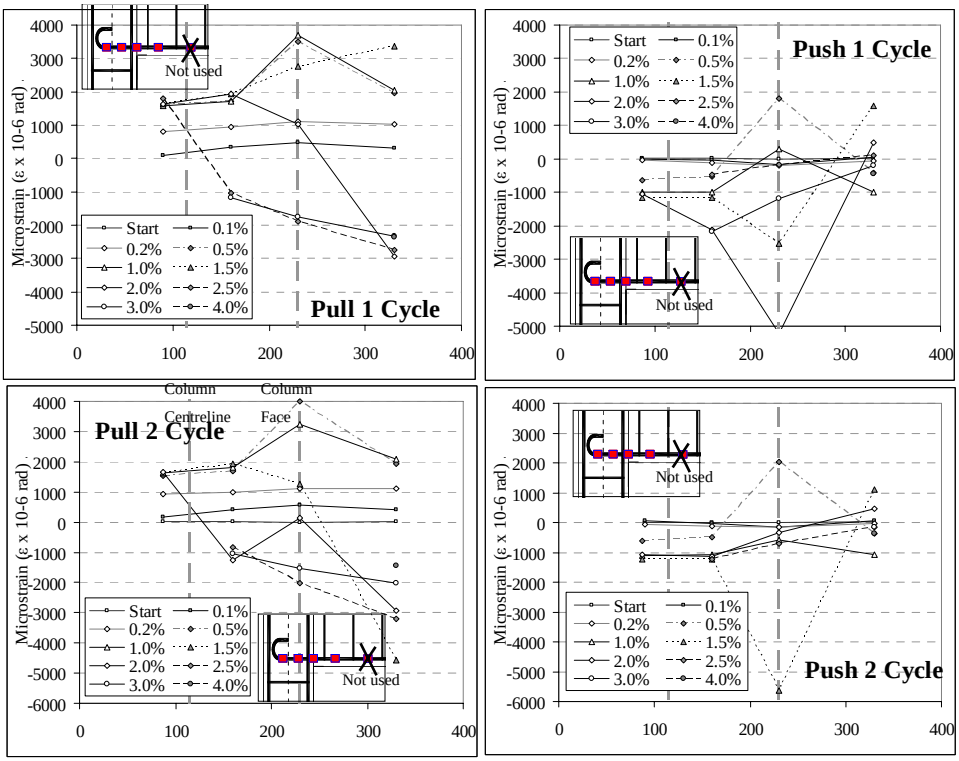

Figure 6.11: NS-R1: Strain profiles of beam bottom longitudinal bars (interior bars – not weakened).

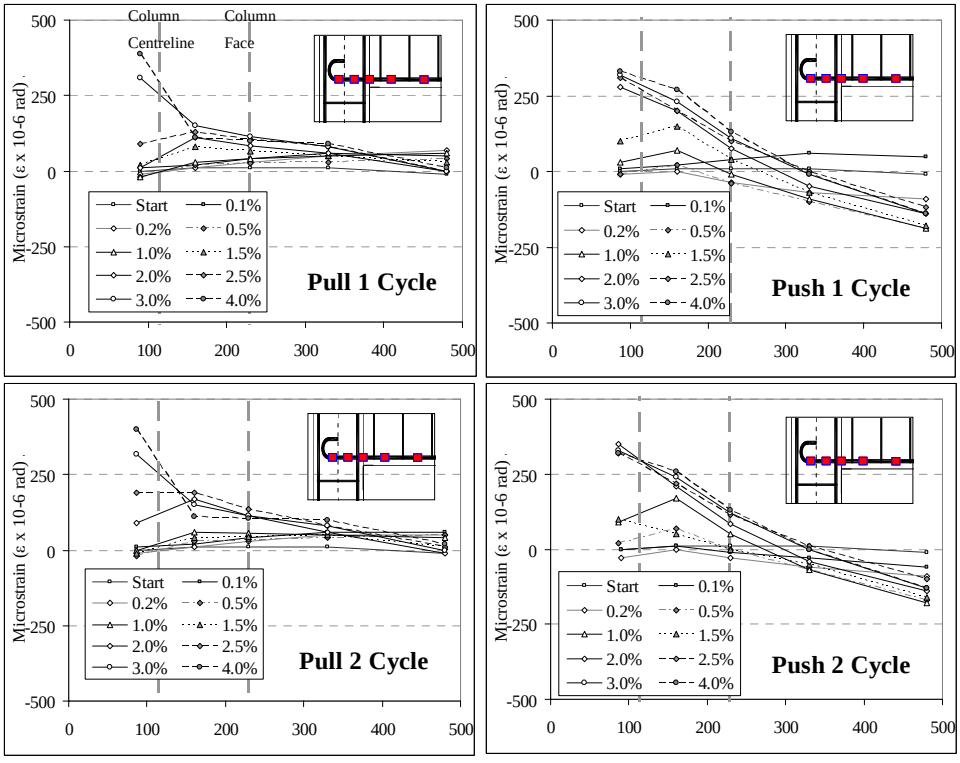

Figure 6.12: NS-R1: Strain profiles of beam bottom longitudinal bars (exterior bars –weakened).

6.2.5.2 Column longitudinal reinforcement strains

The strain profiles along the exterior and interior column bars are shown in Figure 6.13 and Figure 6.14 respectively. The Y-axis is the distance from the centre-line of the beam. The three horizontal dashed lines refer to the beam soffit (bottom line), beam centre-line and the beam top face (top line). As with all strain gages reading, tensile strains were measured as positive values. All column strain gages were zeroed before the axial force loading on the column at the start of the test. At the start of the test, the column bars were measuring -90 to -110 microstrains (-18 to -22 MPa) as a result of the initial column axial load of 110kN (~-2.08MPa uniform axial compressive stress).

The column longitudinal reinforcements were responding elastically throughout the test. The strains were increasing gradually in tension and compression for the top and bottom halves during the Pull and Push loading respectively, as expected from the column moment demands.

After the compressive anchorage failure of the beam bottom reinforcements, which resulted in the spalling of the cover concrete on the joint exterior face (~±2.5% drift), the exterior column bars showed a marked increase in tensile strains within the top half of the column in the Pull cycles. The bottom half of the exteriors column bars was also changing its strain patterns after the concrete cover spalling at the 2nd Push cycle of the -2.5% drifts.

The interior column bars did not exhibit any significant change in their strain profiles till the end of the test. In the ±3.0% and ±4.0% drifts, a marked increase in the tensile strains on the column faces in tension was observed. No cracking was observed in the interior column faces.

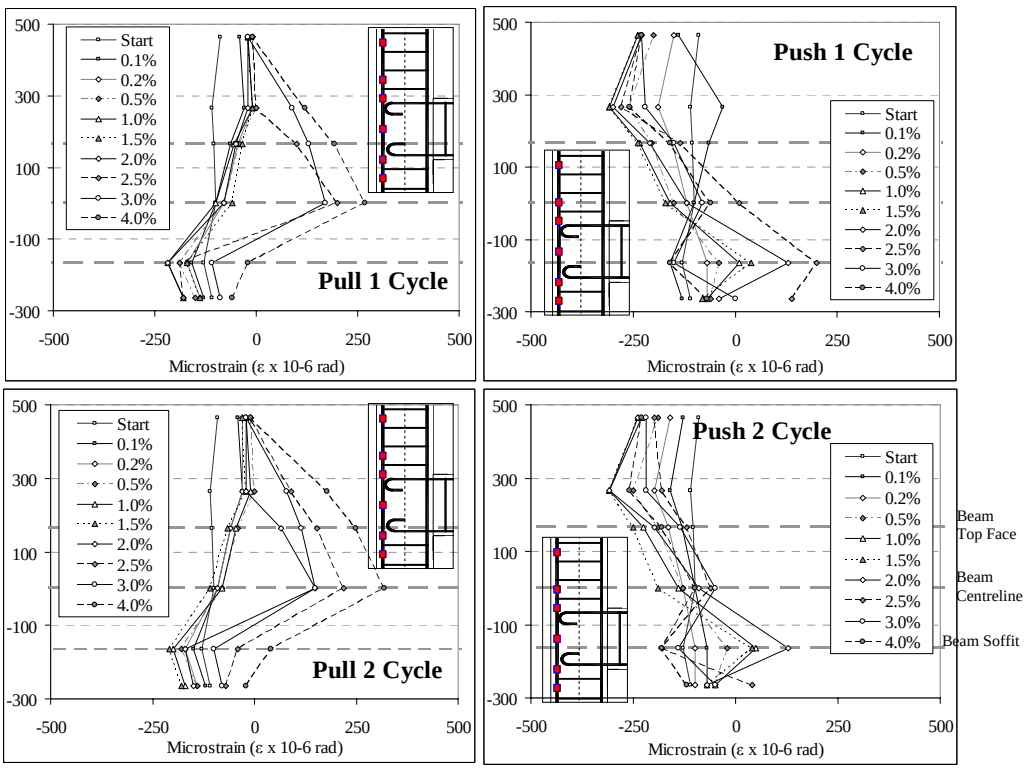

Figure 6.13: Column exterior face longitudinal reinforcements strain profiles for the specimen NS-R1.

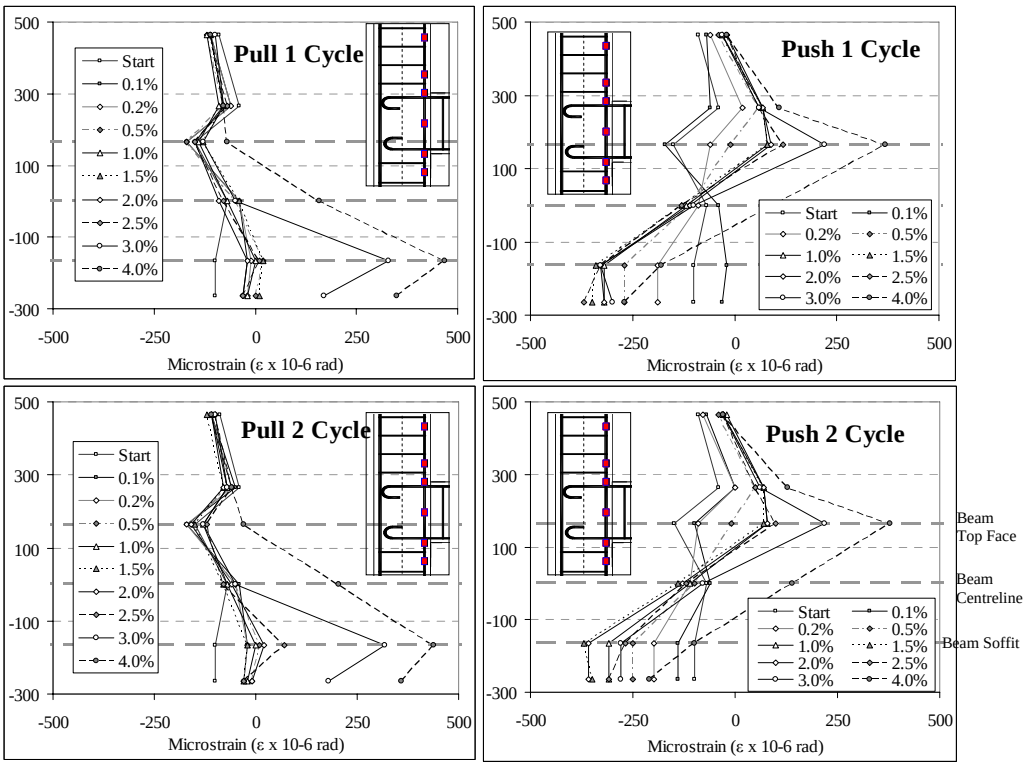

Figure 6.14: Column interior face longitudinal reinforcements strain profiles for the specimen NS-R1.

6.2.5.3 Stirrup reinforcement strains

The strain profiles of the stirrups in the column and the beam are shown in Figure 6.15. Selected stirrup results are presented herein as the general trend across different strain gages is similar. The complete dataset is given in Appendix D. In general, all the stirrups responded elastically.

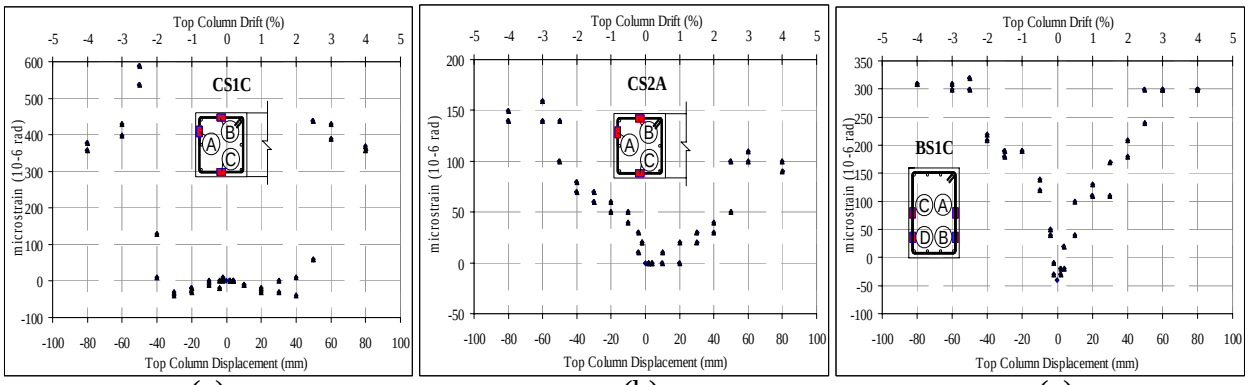

(a) (b) (c)

Figure 6.15: Stirrups strain profiles: a) CS1C - column stirrup 50mm from the beam soffit; b) CS2A - column stirrup 50mm from the beam top face; and c) BS1C -beam 1st stirrup - 50mm from the column interior face.

Strain gage CS1C, which was placed parallel to the loading direction on the 1st stirrup in the bottom half of the column, measured the column shear stress carried by the stirrup. At early stages of the test, compressive strains from the column axial loads were measured in the stirrup. At θ_{drift} =+2.5%, CS1C showed a sudden increase in tensile stresses after the joint anchorage failure and the spalling of the concrete cover due to beam bottom bars push-out. After concrete spalling (see Figure 6.3d), the stirrup restrained the column longitudinal bars from buckling. After the loss of F_c due to beam bar slip at the ±3.0% drift cycles, the measured strain in the CS1C expectedly decreased. Stirrup stresses between -8MPa to 120MPa were measured in CS1C.

Strain gage CS2A, which was placed perpendicular to the loading direction on the 1st stirrup in the top half of the column, measured limited confining stress demand on the stirrup. As observed in Figure 6.3c-d, the concrete did not completely spall off at the top half of the joint/column during the test, thus the sudden increase in tensile strain observed in the gage CS1C was not observed in the stirrup at the top half of the column. The maximum stress recorded in CS2A was 32MPa.

The maximum beam stirrup stress of 64MPa was recorded on the 1st beam stirrup (see BS1C). The maximum nominal shear stresses within the beam section were calculated to be $0.033\sqrt{f'_c}$ MPa and $-0.051\sqrt{f'_c}$ MPa during the Pull and Push loading direction respectively.

Notably, the shear capacity of the beam was not significantly affected by the beam-weakening and the concrete cutting.

6.2.6 Discussion of the NS-R1 specimen

6.2.6.1 Analytical-experimental comparison for lateral strength, F_c

The measured lateral loads, F_c, at the yielding plateau were +8.2kN and -15.4kN for the Pull and Push directions respectively. This was comparable with the predicted theoretical lateral load strength, F_c of +10.3kN and -18.1kN respectively. The 15-20% error margin can be attributed to the uncertainties in predicting the flexural capacity under the bond failure of the plain round bars. It should be noted that the 'predicted' strength for NS-R1 in Table 6.1 assumed perfect bond conditions. With poor bonds ($\tau_{b,max} = 0.3\sqrt{f'_c}$ MPa in tension), the predicted F_c values were +5.5kN and -10.4kN respectively. With this latter assumption, the analytical prediction turned to be too conservative.

From the fixed-end beam moment-curvature plot in Figure 6.6, the measured beam moments in the Pull and Push directions were +15kNm and -27kNm respectively. The theoretical flexural beam strengths, M_{bf}, were +18.8kNm and -32.0kNm with perfect bond assumption, and M_{bf} were +10.2kNm and -19.2kNm with poor bond assumption (as per §3.4.4.1). From the comparison of M_{bf} using both assumptions, it was apparent that the deficiency in the prediction was the estimation of the steel stress developed in these plain round bars under cyclic loading. Considering the 180° hook was relatively effective for tension anchorage, the use of a reduced steel strength, f_s, to represent bond failure might be under-predicting the flexural strength.

6.2.6.2 Anchorage compressive push-out failure

A critical aspect of the test specimen NS-R1 was the compressive anchorage failure of the beam bottom longitudinal reinforcements. The anchorage push-out failure of the beam bars in the 2.5% drift cycles was the structural failure mode for NS-R1. As shown in Figure 6.11, the bottom bars without weakening carried significant compressive stresses in the Push cycles prior to the anchorage failure. The top reinforcements did not sustain significant compressive strain as illustrated in Figure 6.10, due to the small neutral axis in the weakened beam section during the Pull loading.

As the bond strength of the plain-round bars is limited in compression, due to the limited straight embedded length within the joint, most of the compressive force had been carried by the

180° hook anchorage. Therefore, as the maximum push-out strength, $F_{push\text{-}out}$, exceeds the bearing capacity of the cover concrete – anchorage failure will occur. With reference to Figure 6.16, an example of the assessment of the $F_{push\text{-}out}$ is given by Fib Bulletin 24 [2] as:

$$F_{push-out} = 0.26 f'_t C\left(R_h + \frac{2C}{\tan\theta}\right)^2 \qquad \textbf{6.1}$$

where f'_t is the concrete tensile strength, C is the cover over the 180° hook and R_h is the hook radius. The inclination of the cone wedge crack θ, is given as 30° to the vertical axis.

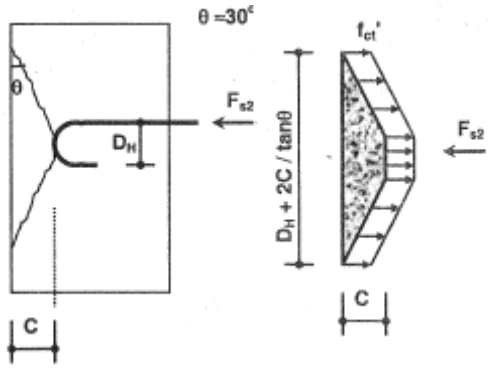

Figure 6.16: Cone splitting failure of the cover at the end of the 180° hook anchorage (taken from [2]).

For the NS-R1 specimen, where f'_t = 2.5MPa, C=40mm and R_h = 30mm, the $F_{push\text{-}out}$ is 7.97kN. For a diameter 10mm beam longitudinal bar, this corresponded to a compressive stress equal to 101.5MPa. From the strain values measured on the beam interior bottom bars during the Push cycles, the sustained stresses generally exceeded the prediction of 101.5MPa. The measured compressive stresses within the reinforcement lengths embedded in the joint ranged between 120 MPa and 240 MPa after the ±0.5% drift cycles (Figure 6.11 right).

With only the NS-R1 result, it is difficult to draw a broader conclusion except that the compressive anchorage of the 180° hook for plain round bars is unreliable particularly at higher drift levels. Collapse prevention performance objective retrofit would be successful, as significant energy dissipation and ductility was achieved prior to the anchorage push-out failure. The combination of NS-R1 with external post-tensioning of the joint (NS-R3 and NS-R4), which would overcome the compressive anchorage failure, might yield a better retrofit outcome. Furthermore, the assessment for $F_{push\text{-}out}$ (as shown in Equation 6.1) is relatively uncertain and unreliable as $F_{push\text{-}out}$ relies heavily on the tension strength of the concrete cone.

6.3 NS-R2: JOINT POST-TENSIONED ONLY RETROFIT

6.3.1 General description of behaviour

The F_c versus Δ_c hysteresis plot for NS-R2 is given in Figure 6.17. The damage and cracking patterns at the selected peak inter-storey drift, θ_{drift}, loading cycles are shown in Figure 6.18 and Figure 6.19. NS-R2 was tested up to the end of the 2nd cycles of the ±4.0% drift. Due to a testing error, no experimental data was recorded during the 1st Pull cycle of the +2.0% drifts for NS-R2.

No cracks were observed in the ±0.1% drift loading cycles. In the 1st Pull cycle of the 0.2% drift, a horizontal flexural crack appeared in the column, originated from the corner of the beam-column joint and extending 110mm into the joint (Figure 6.18a). Next, a beam hairline flexural crack appeared in the 1st Push cycle of the -0.2% drift. The ratio of cracked stiffness-to-uncracked stiffness, K_{cr}/K_{ini}, was 0.81 with the initial stiffness, K_{ini}, of 3394kN/m measured in the ±0.1% drift cycles. Both the K_{cr}/K_{ini} and K_{ini} for NS-R2 were higher than the values for NS-O1 and NS-R1, due to the beam and joint stiffening from the external post-tensioning.

In the ±0.5% drift cycles, more flexural cracks appeared in the column during the Pull loading with a maximum crack width of 0.6mm measured at the horizontal crack at the bottom half of the column. A hairline beam flexural crack also appeared in the beam-column interface during the 1st Pull of the +0.5% drift. On the reverse 1st Push loading to the -0.5% drift, more flexural cracks appeared along the beam, with a maximum crack width of 0.4mm measured at the beam-column interface. In addition, a hairline horizontal column flexural crack appeared along the beam top bars, extending into the joint panel. No new cracks or crack propagation were observed in the 2nd cycles of the ±0.5% drift.

The cracking patterns in the Pull cycles of the +1.0% drift (Figure 6.18c) indicated column hinging mechanism. The damage was concentrated at the column fixed-end rotations at the top and bottom of the joint panel. The maximum column crack widths were between 0.45mm (top half) - 1.5mm (bottom half).

On the reverse Push cycles of the -1.0% drift, beam flexural cracks at the beam-column interface dominated the inelastic deformation, with a maximum crack width of 0.85mm measured. Based on the strain gage readings (§6.3.5), the beam top longitudinal reinforcements were found to be yielding in the 1st Push cycle of the -1.0% drift with F_c=-20.1kN. The beam bottom bars did not yield throughout the test, except for the bottom reinforcements' sections close to the 180° hooks, deep within the joint.

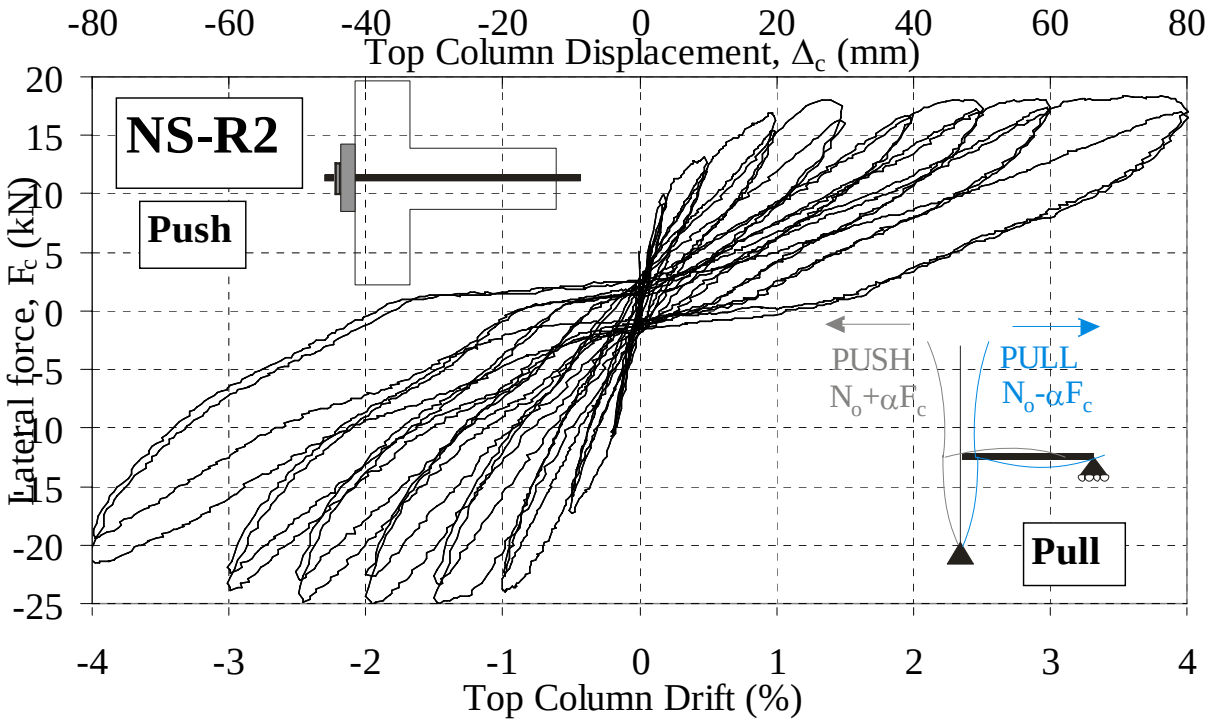

Figure 6.17: Top column lateral load, F_c versus top column displacement, Δ_c and drift, θ_{drift} for NS-R2.

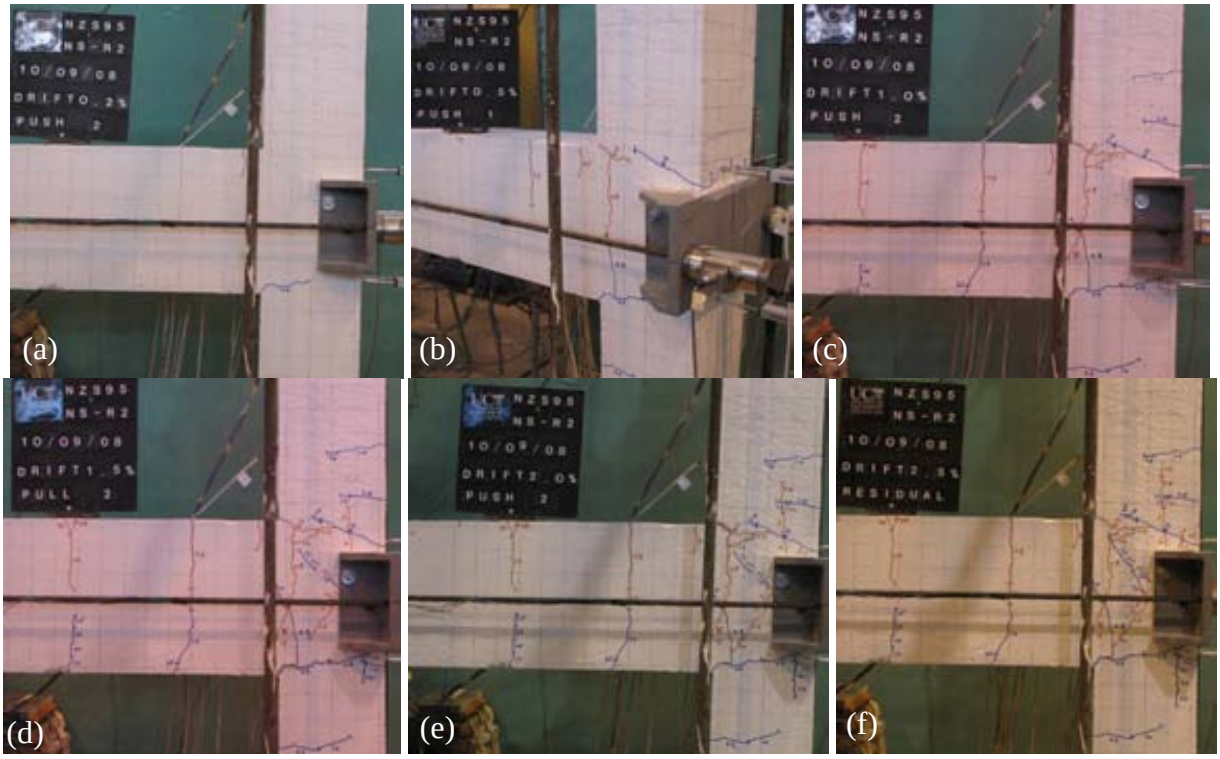

Figure 6.18: Observed cracking patterns of NS-R2: TOP: a) 2nd Push cycle of the -0.2% drift; b) 1st Push cycle of the -0.5% drift; and c) 2nd Push cycle of the -1.0% drift. BOTTOM: d) 2nd Pull cycle of the +1.5% drift; e) 2nd Push cycle of the -2.0% drift; and f) Residual crack at the completion of the ±2.5% drift cycles loadings.

In the 1st Pull cycle of the +1.5% drift, an inclined vertical crack at the bottom corner of the join, extending into the centre of the anchorage plates, was detected. This was taken to be the onset of the joint diagonal cracking in the Pull loading direction. The principal stresses at the joint cracking (positive column displacements) were $p'_t=0.245\sqrt{f'_c}$ MPa and $p'_c=0.577\sqrt{f'_c}$ MPa. The existing column flexural cracks also widened, with a maximum crack width of 2.5mm measured at the bottom corner of the column-joint interface. The column interior longitudinal reinforcements yielded in the 1st Pull cycle of the +1.5% drift with the F_c=+16.5kN, as confirmed by strain gage readings (§6.3.5). The column exterior bars did not yield until the Pull cycles of the +3.0% drift.

In the 2nd Pull cycle of the +1.5% drift, the inclined vertical crack extended diagonally across the joint panel (Figure 6.18d). Minor F_c degradation at the +1.5% Pull peak was observed. The maximum column crack width was 3 mm while the joint crack width was hairline.

In the 1st Push cycle of the -1.5% drift, similarly, a diagonal joint crack appeared in the centre of the joint panel, propagating towards the corners of the joint. The principal stresses at the joint cracking (negative column displacements) were $p'_t=0.084\sqrt{f'_c}$ MPa and $p'_c=1.2\sqrt{f'_c}$ MPa ($0.24f'_c$ MPa). The measured inclination of the diagonal crack was 54.5° to the horizontal axis. Evidently, the joint crack in the Push loading was precipitated by diagonal compression failure as the p'_c approached the cracking limit state, typically given as $0.2\text{-}0.3f'_c$ MPa [8].

Nevertheless, the major inelastic deformation and crack growths were limited to the beam fixed-end flexural crack. In the 2nd Push cycle of the -1.5% drift, the maximum beam flexural crack width was 2 mm while the joint crack width was 0.1mm. The horizontal column crack also continued to grow with a maximum crack width of 0.6mm measured.

In the ±2.0% drift cycles, all the existing cracks extended and widened, with major growth at the column flexural crack for the Pull direction, and at the beam flexural crack for the Push direction (Figure 6.18e). The maximum crack widths in the 2nd Pull cycles were 4mm at the bottom column flexural crack, 0.35mm at the joint diagonal crack and 0.6mm at the vertical crack along the exterior column reinforcements (connected to the joint diagonal crack). The maximum crack widths in the 2nd Push cycles were 2.5mm at the beam end flexural crack, 1.1mm at the top column flexural crack, 0.35mm at the joint diagonal crack.

The trend of the mixed crack growth in the column, beam and joint continued in the ±2.5% and ±3.0% drift cycles. In the Pull cycles, the crack development and widening followed

the sequence/hierarchy of: column flexural cracks → joint diagonal cracks → column vertical crack. In the Push cycles, the sequence/hierarchy of damages was in the order of: beam-end flexural → column flexural → joint diagonal crack. These differences in the inelastic damages were confirmed by the measured displacement components of NS-R2 in §6.2.3.1. The difference could be attributed to the variation of column axial loads in the two loading directions, where increased axial load in the Push direction delayed the column and joint failures. The snap-shot states of the specimen NS-R3 at the end of the ±2.5% and ±3.0% drifts are shown in Figure 6.18f and Figure 6.19a, respectively.

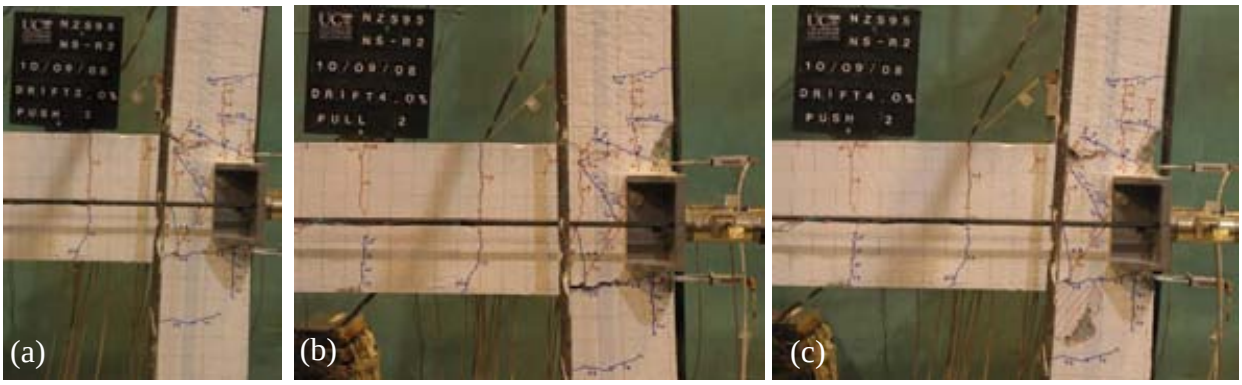

Figure 6.19: Observed cracking pattern of NS-R2: a) 2nd Push cycle of 3.0% drift; b) 2nd Pull cycle of 4.0% drift; and c) 2nd Push cycle of 4.0% drift.

The column hinging mechanism dominated the deformation in the Pull cycles of the +4.0% drift, while column and joint hinging contributed mostly to the inelastic mechanism of the Push cycles of the -4.0% drift. Spalling and crushing of the compression zones within the column were observed in both the Pull and Push directions in Figure 6.19b-c. In the Push direction, this was coupled with a marked decrease in F_c, which ultimately led to the structural failure (20% peak-to-peak strength degradation) of NS-R2.

6.3.2 Load-displacement hysteresis analysis

The F_c-Δ_c hysteresis plot for NS-R2 is shown in Figure 6.17 while the analysis of the NS-R2 F_c-Δ_c hysteresis is presented in Figure 6.20. The maximum F_c values measured were +18.4kN (at +3.56% drift) and -25.2kN (at -1.96% drift). As expected for post-tensioned beam-column joint connections, K_{eff} curve was higher for NS-R2 at all level of drift loadings, when compared to the beam-weakened solution (NS-R1) and the as-built specimen (NS-O1).

While the F_c-Δ_c envelope was sustaining the peak-to-peak lateral strength, as with other un-bonded post-tensioned connections (e.g. [7]), NS-R2 had relatively low level of energy

dissipation. Prior to the ±4.0% drift cycles, NS-R2 had about the same energy dissipation capacities (cumulative or per cycles energy dissipated - Figure 6.20a-b) as the as-built benchmark NS-O1, despite different failure modes. In fact, NS-R2 had lower ξ_{hys} when compared with the specimens NS-O1 and NS-R1. In between ±0.5-2.5% drift cycles, the average ξ_{hys} were 8.1% and 5.0% for the 1st and 2nd cycles respectively.

Nevertheless, when compared with the design procedure described in §3.4.2, where conservative values of ξ_{sys} between 10-15% were assumed, NS-R2 still had sufficient hysteretic damping. The double column hinging mechanism (soft-storey collapse) would have been a more critical design issue for the post-tensioned only retrofit solution implemented for NS-R2. For pre-1970s non-ductile beam-column joints, it is very likely that the NS-R2 retrofit solution must include a complementary column retrofit solution (FRP or column jacketing).

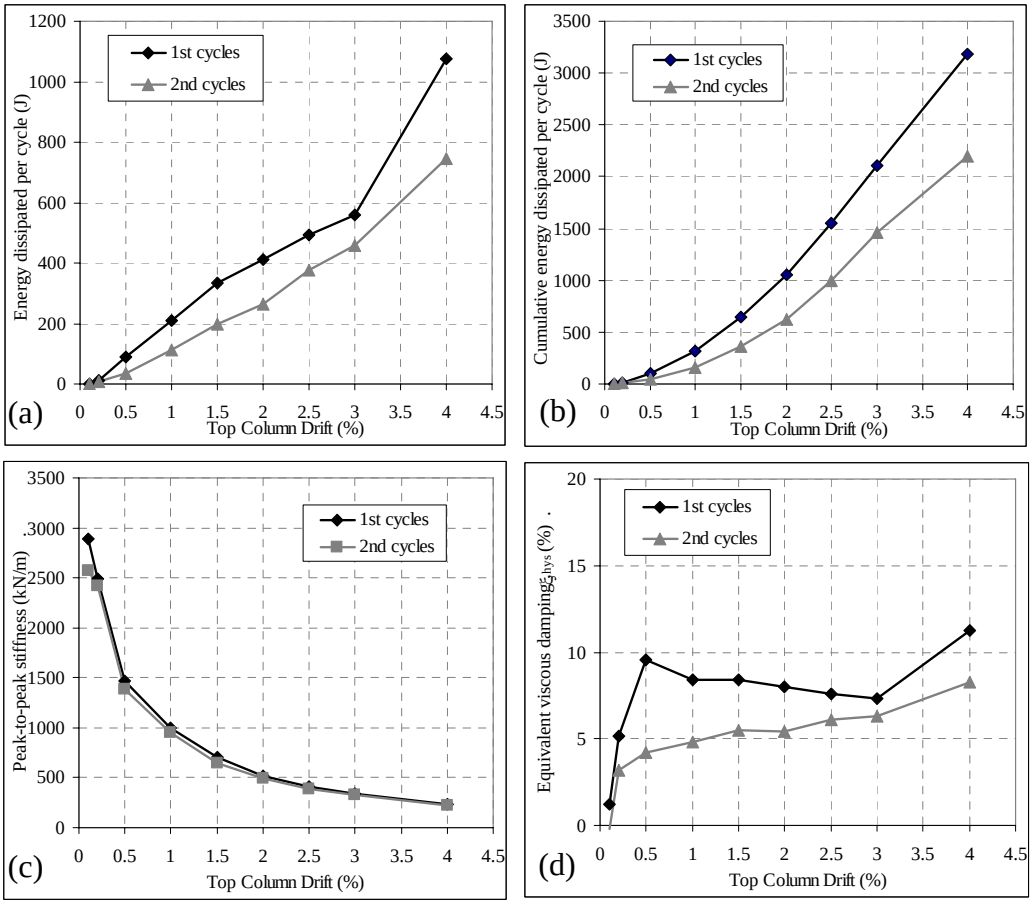

Figure 6.20: F_c-Δ_c analysis for NS-R2: a) Energy dissipated per cycle; b) Cumulative energy dissipated per cycle; c) peak-to-peak stiffness, K_{eff}, and; d) Equivalent viscous damping, ξ_{hys}.

6.3.3 Local deformations and displacement components

6.3.3.1 Decomposition of top column horizontal displacement

The contributions to the top column horizontal displacement, Δ_c at the peaks of each Pull and Push loading cycles as percentages of the total Δ_c are presented in Figure 6.21. As with NS-O1 and NS-R1, the displacement components indicated a creep of inelasticity towards the Push, leading to a significant unaccounted Δ_c component in the NS-R2 test (as explained in §5.4.1). For NS-R2, the beam yielding and joint cracking were more significant in the Push direction, leading to beam-elongation accumulation in that direction and therefore a higher unaccounted Δ_c component in the opposite Pull direction.

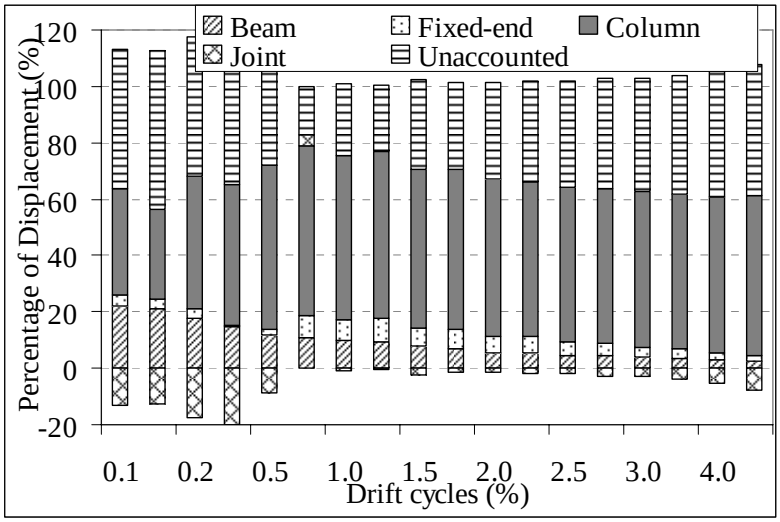

a) Pull loading direction – positive displacement.

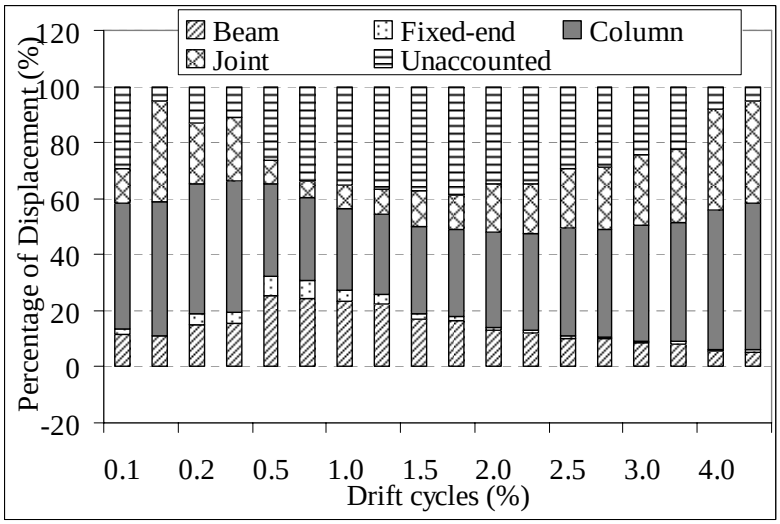

b) Push loading direction – negative displacement.

Figure 6.21: Displacement decompositions based on the measured deformations for NS-R2.

Figure 6.21 confirmed a general observation that column flexural hinging was dominating the inelastic contribution to the Δ_c in the Pull direction while a combination of beam, column and joint hinging was prevalent in the Push direction. In the Pull direction, the column flexural displacement component, $\Delta_{col,flexural}$, was relatively constant throughout the test, accounting for 50-60% of Δ_c. In the Push direction, $\Delta_{col,flexural}$ was also the dominant component, accounting for 30-50% of Δ_c with a marked increase in the final two drifts (-3.0 and -4.0%).

The beam flexural contributions ($\Delta_{beam,flexural}$) were low in both loading directions. As the beam remained elastic in the Pull direction, $\Delta_{beam,flexural}$ and $\Delta_{beam,fixed\text{-}end}$ were limited to 5-20%, with a decreasing trend as the θ_{drift} increased. In the Push direction, the beam inelastic components were increasing between -0.1% and -0.5% with a maximum contribution of 32.5%.

The post-tensioned beam had a high post-yield stiffness due the elongation of the unbonded tendon. This resulted in an increasingly higher beam flexural induced tension and compression forces into the joint as the loading increased; subsequently, the joint failed in compressive diagonal cracking at approximately -1.5% drift. Consequently, the joint contribution, Δ_{joint} increased significantly in the Push direction, accounting for 37% of Δ_c in the -4.0% drift. As a consequence of the damage accumulation (unclosed cracks) in the joint in the Push direction, negative Δ_{joint} was measured in the Pull direction.

6.3.3.2 Beam deformations

The moment-curvature plots for the beam flexural regions and beam fixed-end region are shown in Figure 6.22. The measurement of beam curvatures, ϕ_b, in the fixed-end region was interfered by the column flexural cracking, thus a larger ϕ_b than expected was measured (Figure 6.22a). The maximum M_{bf} developed in the Pull and Push directions were +32.9kNm and -45.3kNm.

The beam was responding elastically in the Pull direction (positive ϕ_b), with a maximum ϕ_b to be 0.0036 m^{-1} at the region 75-275mm away from the column face. In contrast, the beam yielded at approximately 21-22kNm in the Push direction, with the measured 'yield' curvature, ϕ_y ~ 0.0005 m^{-1}. Higher ϕ_b was measured in the Push direction as well.

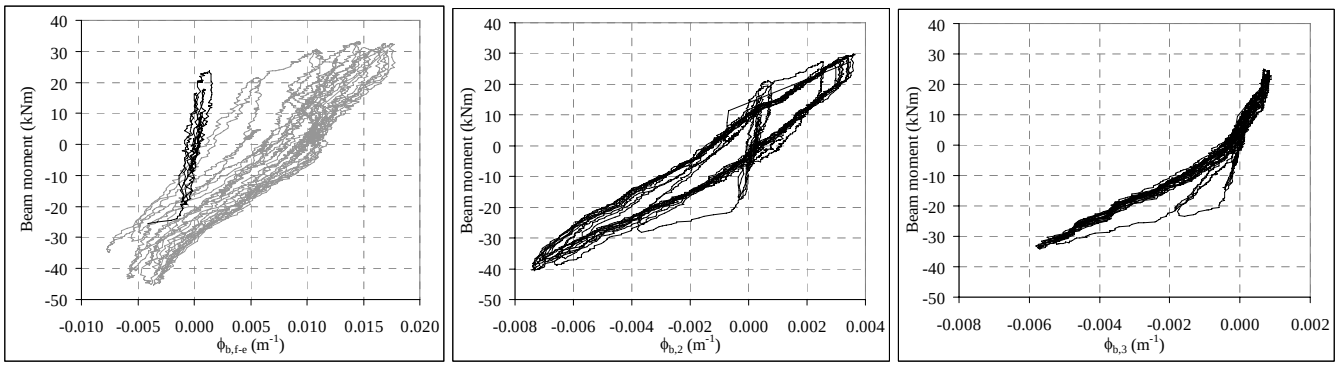

Figure 6.22: a) Moment-curvature plots for beam sections: a) fixed-end section; b) 75-275mm from the column internal face; and c) 275-475mm from the column internal face.

6.3.3.3 Column deformations

The moment-curvature plots for the top and bottom column sections are given in Figure 6.23. Column first yielded at +8.0kNm and -17.8kNm in the Pull and Push directions, with the difference as a result of the variation of the column axial loads. The observed nominal column flexural strength, $M_{c\text{-}cf}$, (taken to be the plateau moment in the hinging direction), were 13.7kNm and 19.0kNm in the Pull and Push cycles respectively.

These values were lower than the predicted $M_{c\text{-}cf}$ of +18.3knM and -38.8kNm. This highlighted the lower than expected column axial load in the Push cycles as joint failure limited the F_c and therefore limited the axial load imposed (function of F_c). At the measured nominal $M_{c\text{-}cf}$, the imposed axial loads were 26kN and 230kN for the Pull and Push loading respectively.

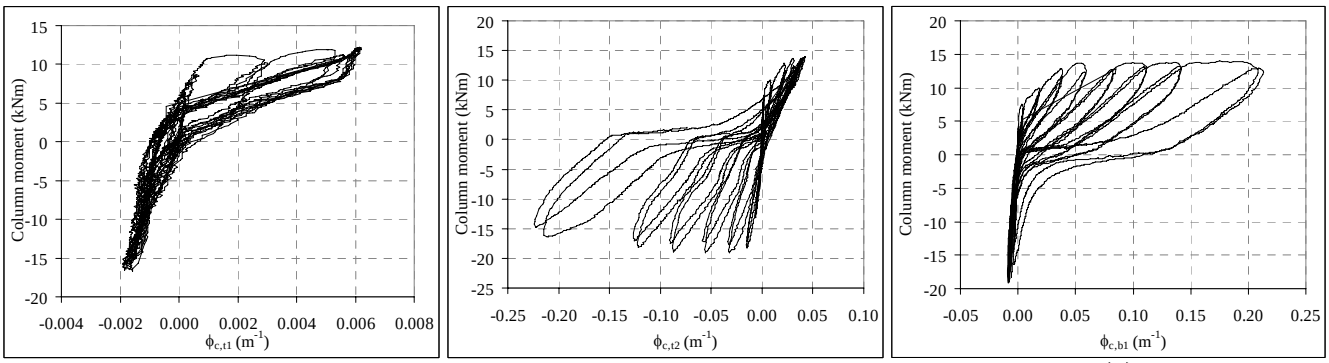

(a) (b) (c)

Figure 6.23: Moment-curvature plots for column flexural sections: a) 200-430mm from the beam top face; b) 0-200mm from the beam top face; c) 0-200mm from the beam soffit.

From Figure 6.23b-c, the column hinging mechanism in the Pull direction is evident, with maximum column curvature, ϕ_c, of +0.21m^{-1} and +0.045 m^{-1} attained in the top and bottom column halves respectively. This was confirmed by the strain gage results (§6.3.5.2), in which the

inelastic column strains (and therefore ϕ_c) in both the top and bottom sections were significantly higher in the Pull direction than the Push direction.

In the Push direction, the column hinging was concentrated at the top half, with a maximum ϕ_c of 0.22 m^{-1} (Figure 6.23b). This was confirmed by the no visible column cracks observed during the Push direction (Figure 6.19), suggesting limited column deformation that was concentrated within the horizontal crack within the top half of the joint panel.

6.3.4 Beam-column joint behaviour

6.3.4.1 Nominal joint shear stress and joint shear distortion

The nominal joint shear stress, v_{jh}, versus joint shear distortion, γ_j, and Δ_c relationships for NS-R2 are given in Figure 6.24. The maximum v_{jh} measured were 2.03MPa (0.40 $\sqrt{f'_c}$ MPa or 0.081f'_c MPa) in the 1st Pull peak of the +1.5% drift and -2.84MPa (-0.57 $\sqrt{f'_c}$ MPa or -0.113f'_c MPa) in the 1st Push peak of the -1.5% drift. The NS-R2 v_{jh} values were comparable to the ASCE-41[1] specifications of 0.5$\sqrt{f'_c}$ MPa and 0.66$\sqrt{f'_c}$ MPa for unconfined and confined exterior beam-column joints. Nevertheless, the joint shear distortion (negative γ_j) growth in the Push direction, shown in Figure 6.24a, can not be clearly explained without considering the actual principal stresses failure mechanism.

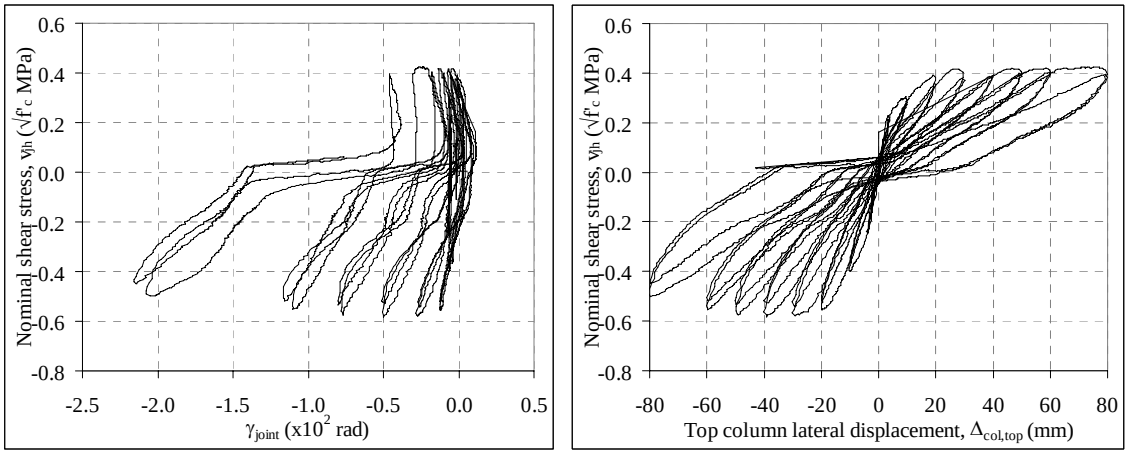

(a) (b)

Figure 6.24: a) Nominal joint shear stress, v_{jh} versus joint deformation, γ_j; b) Nominal joint shear stress, v_{jh} versus top column lateral displacement, Δ_c.

6.3.4.2 Joint principal stresses

Figure 6.25 shows the joint principal stresses responses as functions of the Δ_c and γ_j for NS-R2. In terms of maximum principal stresses in the joint during the cyclic loading of NS-R2, the

maximum p'_t was $0.264\sqrt{f'_c}$ MPa at γ_j =-0.00254 radians and the maximum p'_c was $1.21\sqrt{f'_c}$ MPa at γ_j =-0.00503 radians.

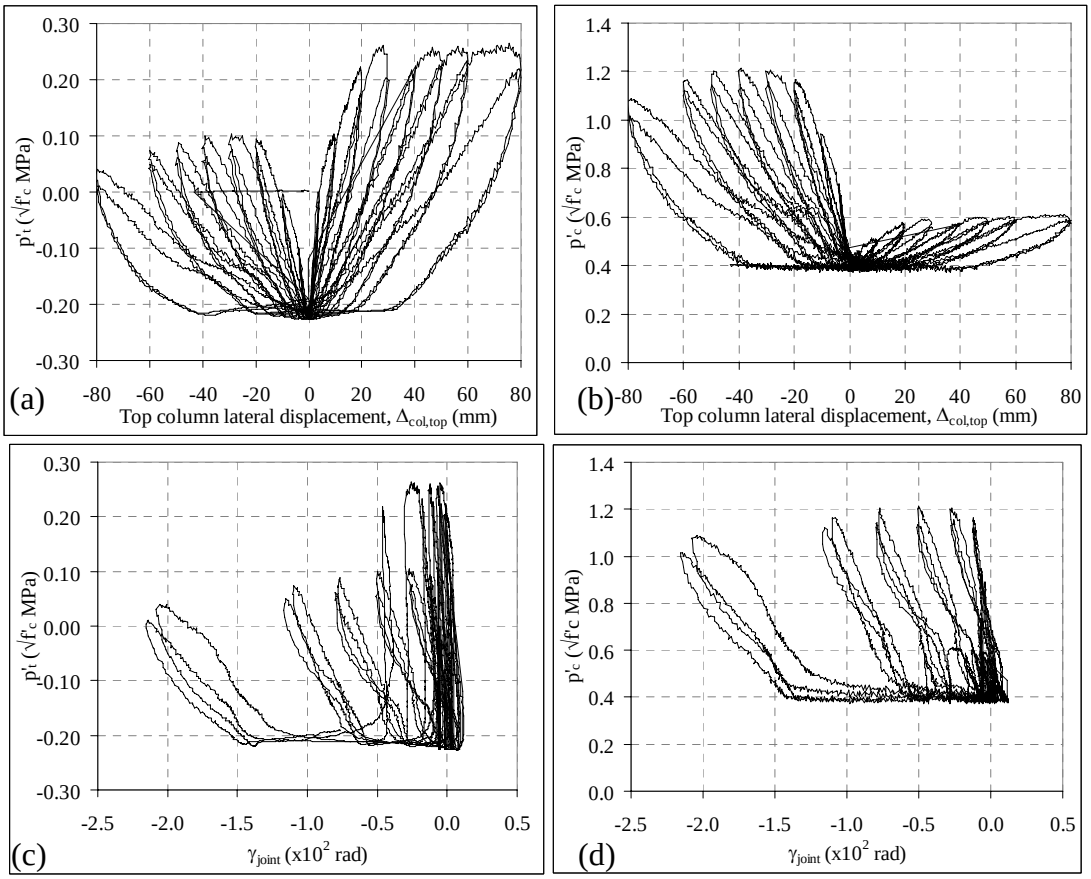

Figure 6.25: a-b) Joint principal stresses versus top column lateral displacement, Δ_c: a) principal tensile stress, p'_t; b) compressive tensile stress, p'_c; c-d) Principal stresses versus joint shear deformation, γ_j plots: c) principal tensile stress, p'_t; d) compressive tensile stress, p'_c.

Prior to the joint diagonal cracking, p'_t - γ_j and p'_c - γ_j were essentially linear. At the joint diagonal cracking at the 1st Pull cycle of +1.5% drift, the corresponding p'_t, p'_c and γ_j were $0.245\sqrt{f'_c}$ MPa, $0.577\sqrt{f'_c}$ MPa and -0.00053 radians. After the joint diagonal tensile cracking in the Pull direction, no significant degradation of p'_t was observed. The joint shear deformation (γ_j) was also limited to a maximum of -0.0012 radians in the Pull cycle, owing to the confinement effects from the post-tensioning forces.

For the joint diagonal crack in the 1st Push cycle of the -1.5% drift, the corresponding p'_t, p'_c and γ_j were $0.084\sqrt{f'_c}$ MPa, $1.20\sqrt{f'_c}$ MPa and -0.00284 radians. The p'_c - γ_j degradation of NS-R2 can be observed from Figure 6.25d. After the joint diagonal compression cracking at γ_j =-0.00284 radians, the maximum p'_c was sustained up to approximately γ_j =-0.0075 radians. After that, the p'_c gradually decreased with increasing γ_j as the joint cracks widened.

6.3.5 Steel strain profiles

6.3.5.1 Beam longitudinal reinforcement strains

Figure 6.26 and Figure 6.27 present the strain profiles of the beam top and bottom longitudinal reinforcements for the specimen NS-R2. The X-axis is the distance from the exterior column face while the two vertical dashed lines refer to the column centre-line and the interior column face. Tensile strains are given as positive values. From the steel test, the ε_y for the longitudinal beam and column reinforcements was 0.00168 (1680 microstrains) and the f_y was 335MPa.

The beam top bars (Figure 6.26) yielded in tension in the Push cycles of the -1.0% drift, with a maximum steel strain of 2140 microstrains measured at the critical section in the -1.5% drift. After the yielding, the strains in the beam top bars were stabilised around 1800-2100 microstrains, indicating a yield plateau and gradual debonding of the reinforcements. Same strain profiles were observed in both the 1st and 2nd Push cycles. After the joint cracking at the -1.5% drift, the measured tensile strain for the beam top bars within the joint decreased significantly to below yield strain in the Push cycle peaks.

The beam top bars (Figure 6.26), however, did not yield in the Pull cycles. The top bars were in compression for most of the Pull loading cycles. However, beyond the +2.5% drift, parts of the top bars were carrying tensile strains even during the Pull cycles. In particular, the section of bars within the joint increased in tensile strain as the longitudinal bars were taking some joint shear forces after the joint cracking (at the -1.5% drift).

At the critical section of the beam-column interface, the beam bottom bars (Figure 6.27) were carrying limited compressive strains up to the 1st Pull cycle of the +0.5% drift. Therefore, possibly due to a very small neutral axis depth, the top bars extended in tension strain up to +1200 microstrains (~240MPa). This localised strain/stress at the critical section was a consequence of the single concentrated flexural crack and the presence of plain-round bars (see §5.7.2). The bars within the free beam lengths were still in elastic compressive strains ~400-500 microstrains (80-100 MPa).

For the beam bottom bars (Figure 6.27), despite significant tensile strains developed during the Pull cycles, the beam reinforcements did not yield as the column flexural hinge that was governing the inelastic mechanism in the Pull direction. Within the joint panel, the bottom reinforcements yielded in tension in the +1.5% drift cycles, as a result of the joint shear crack.

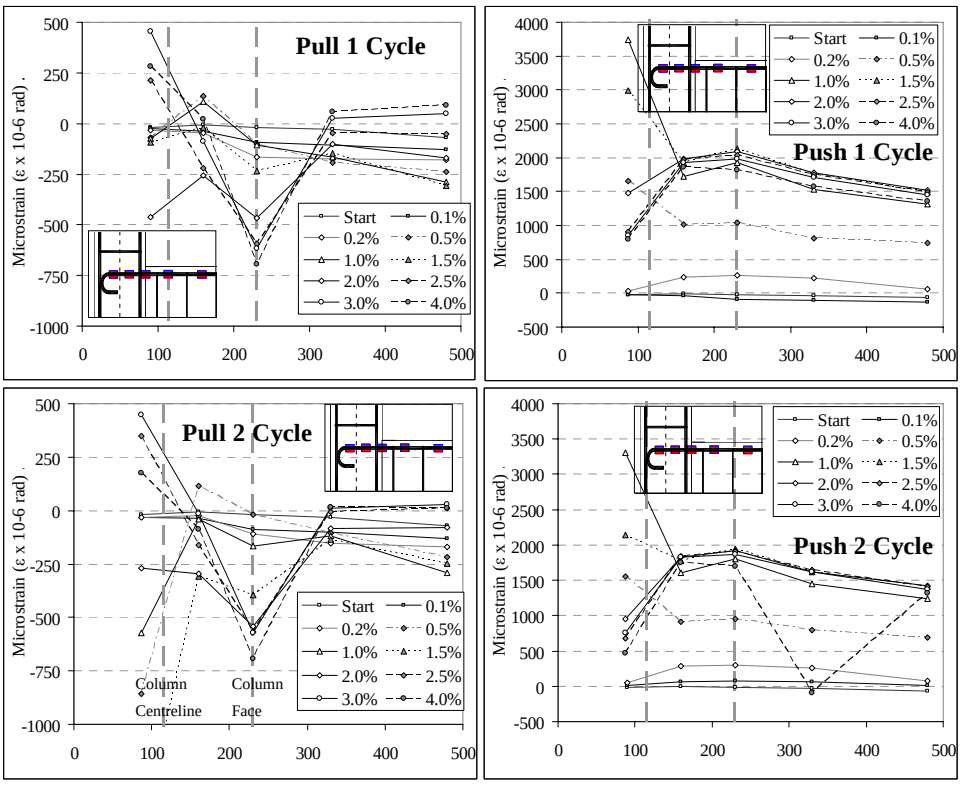

Figure 6.26: Strain profile of beam top longitudinal bars of the specimen NS-R2.

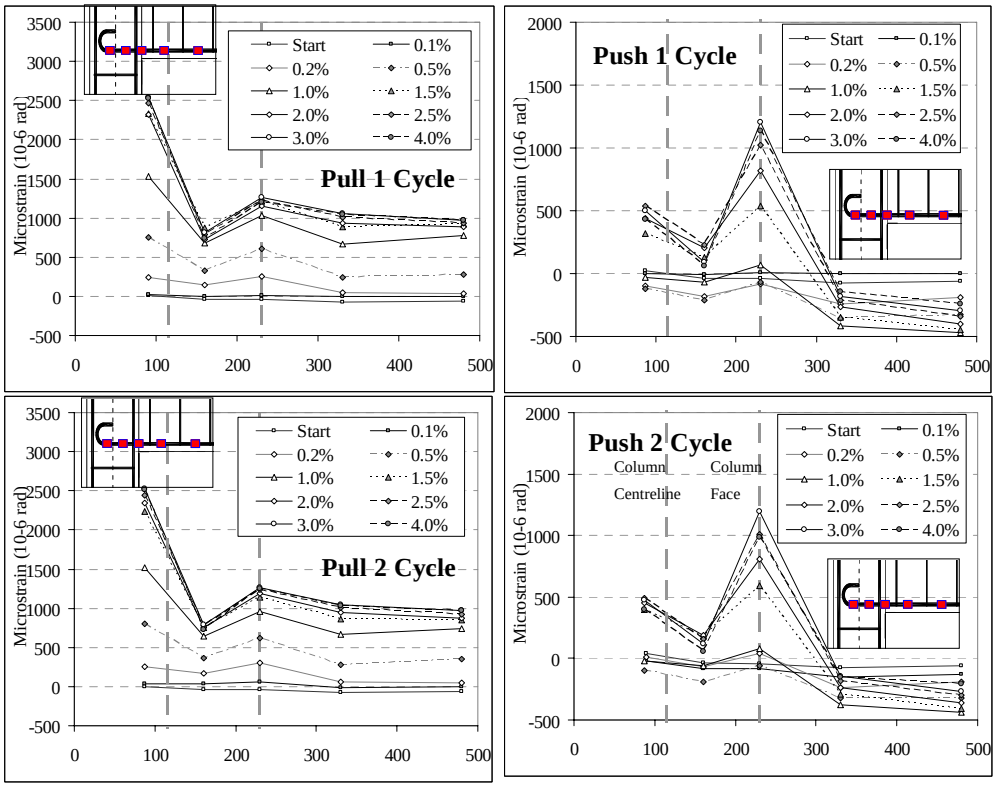

Figure 6.27: Strain profiles of bottom beam longitudinal bars of the specimen NS-R2.

6.3.5.2 Column longitudinal reinforcement strains

The strain profiles along the exterior and interior column bars are shown in Figure 6.28 and Figure 6.29 respectively. The Y-axis is the distance from the centre-line of the beam. The three horizontal dashed lines refer to the beam soffit (bottom line), beam centre-line and the beam top face (top line). As with all strain gage readings, tensile strains were measured as positive values. All column strain gages were zeroed before the axial loading on the column at the start of the test.

At the start of the test, the column bars measured -45 to -070 microstrains (-9 to -14 MPa) as a result of the initial column axial load of 110kN (~-2.08MPa uniform axial compressive stress). In general, the strain profiles of the column longitudinal reinforcements confirmed the previous observations of the top and bottom column halves flexural hinging in the Pull direction and bottom column half hinging in the Push direction (§6.3.3.3).

The column exterior face longitudinal bars (Figure 6.28) were yielding in the Pull cycles of 1.5% onwards. The yielding strain initiated at the top half of the column, but extended through the whole depth of the beam-column joint as the $+\theta_{drift}$ increased. This was an indication of bond failure of the column reinforcements, commencing at the flexural crack along the column-joint interface. This progressive bond failure prevented the yielding of the column exterior bars as the strain demands were spread across a longer unbonded length. In the Push cycles, the column exterior bars were responding elastically, as expected from the column bending moment demand. A reverse of strains was observed within the joint depth as the column strains went from compression at the top half of the column, to tension at the bottom half.

The column interior face longitudinal bars (Figure 6.29) were responding elastically up to +1.5% and -2.0% drifts in the Pull and Push cycles respectively. In the Pull cycles, column interior bars yielding commenced at the 1st Pull cycle of the +1.5% drift at the bottom column-joint interface. In the subsequent Pull cycles, the steel strain was localised along the main flexural crack in the bottom half of the column, with a maximum strain of 4700 microstrains measured before the strain gage broke. In the Push cycles, column reinforcement yielding started at the top column-joint interface at the 1st Push cycle of the -2.0% drift. However, as the θ_{drift} progressed, the column interior reinforcements within the joint depth yielded as well, with high strain localisation measured in the bottom column-joint interface crack. The joint diagonal cracking also resulted in the column bars acting as vertical shear reinforcements within the unreinforced joint (similar to NS-O1).

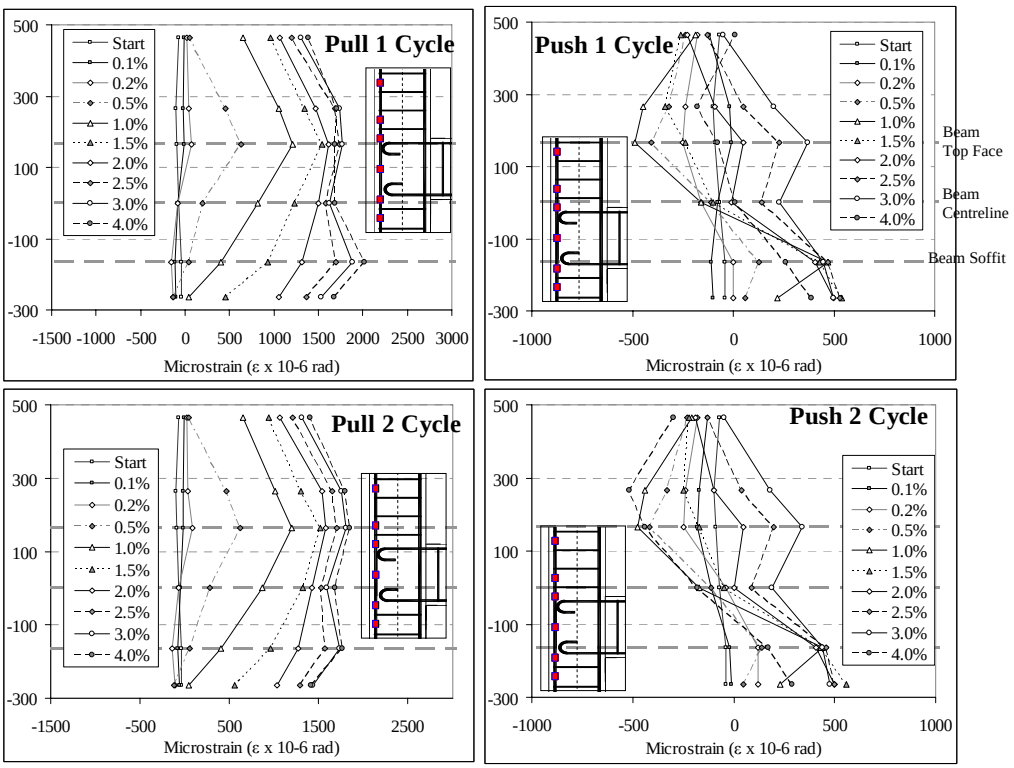

Figure 6.28: Column exterior face longitudinal reinforcements strain profiles for the specimen NS-R2.

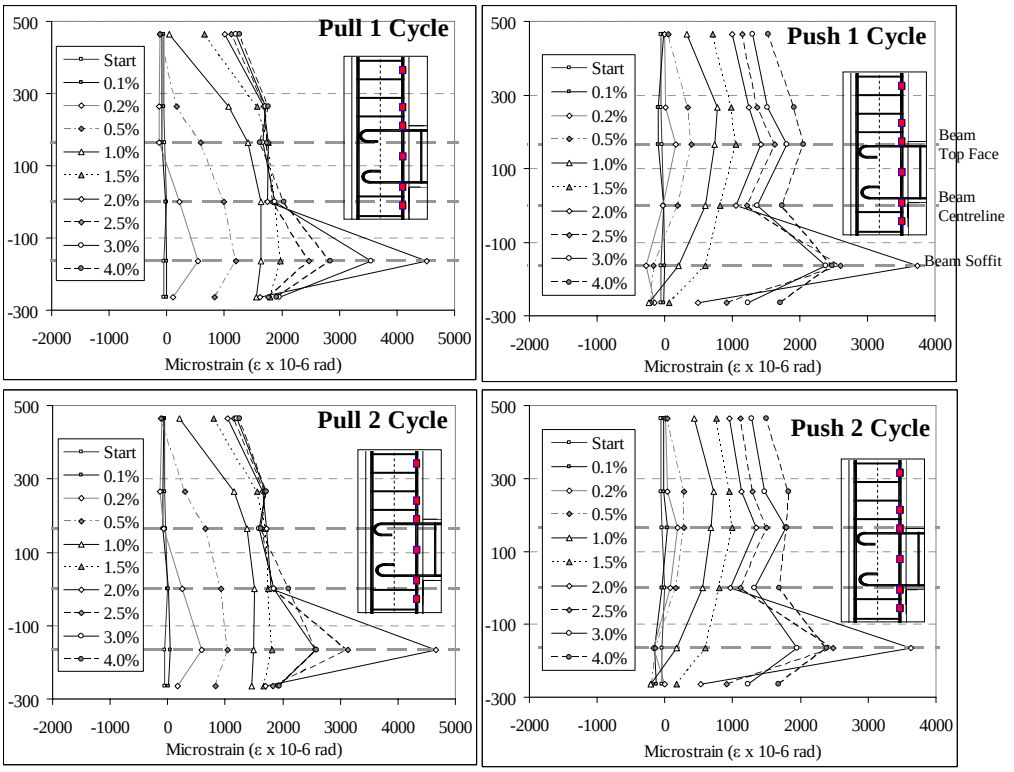

Figure 6.29: Column interior face longitudinal reinforcements strain profiles for the specimen NS-R2.

6.3.5.3 Stirrup reinforcement strains

The strain profiles of the stirrups in the column and the beam are shown in Figure 6.30. Selected stirrup results are presented herein as the general trend across the different strain gages is similar. The complete dataset is given in Appendix D. The stirrups in the column (e.g. CS1B & CS2B) were inactive up to the ±1.0% drift cycles, after which the column stirrups were picking up substantial tensile strains. This corresponded to the appearance of column flexural cracks along the tension face during the Pull cycles (Figure 6.18). The maximum stress measured in the column stirrups was ~200MPa. The stress-strain pattern in the beam stirrups (e.g. BS2A) corresponded to a linear trend up to ±1.5% drift peaks. After the yielding of the column bars in the ±1.5-2.0% drift cycles, the beam stirrup stress levelled at approximately 80-90MPa.

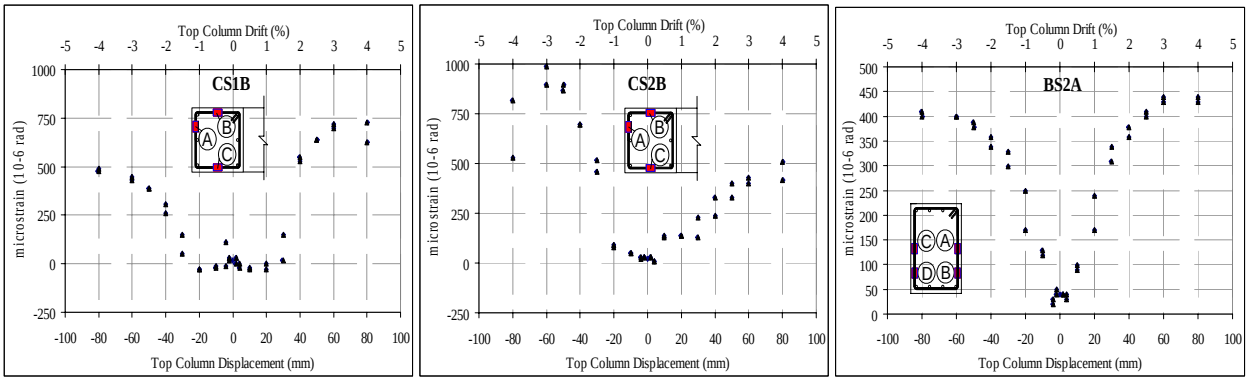

(a) (b) (c)

Figure 6.30: Stirrup reinforcement strain profiles: a) column stirrup 50mm from beam soffit; b) column stirrup 50mm from beam top face; and c) beam 2nd stirrup - 183mm from column interior face.

6.3.6 Discussion of the NS-R2 specimen

6.3.6.1 Analytical-experimental comparison for lateral strength, F_c

The F_c-Δ_c experimental-analytical comparison for specimen NS-R2 is given in Figure 6.31. The analytical procedure described in §3.4 (Chapter 3) was used to generate the predicted F_c. The maximum F_c values measured were +18.4kN (at +3.56% drift) and -25.2kN (at -1.96% drift) in the Pull and Push loading directions respectively.

For the Pull direction with decreasing column axial forces, the predicted failure mode was joint shear hinging, followed by column flexural hinging, with F_c of +20.0kN and +22.6kN for both limit states respectively. The 18.6% discrepancy in the achieved column moment, $M_{c\text{-}cf}$ (given in §6.3.3.3) could be explained by the difference in the applied axial load (N) when compared to the assumed axial load in the column flexural strength assessment. The assessment

had assumed N of 35kN at the flexural failure while the applied N was 26kN. Furthermore, the column M-N assessment did not consider the bond failure of the plain round bars, which was evident from the localised strains in the single large flexural crack in the column (§6.3.5.2).

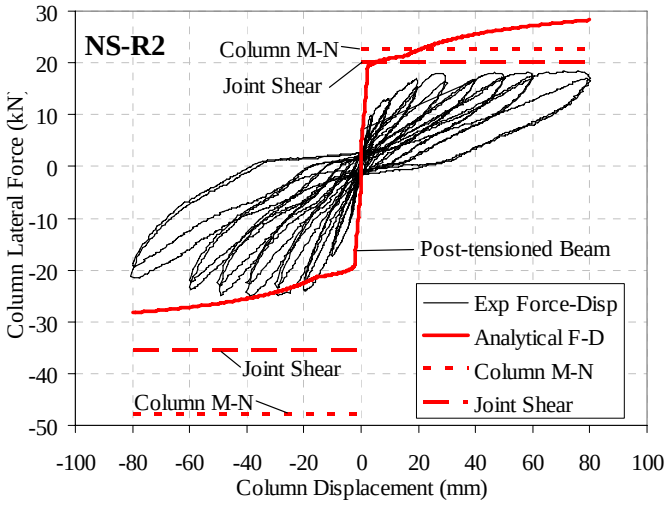

Figure 6.31: Experimental-analytical comparison of the F_c-Δ_c curves.

In the Push direction, the analytical procedure was correct in predicting the occurrence of the beam flexural hinging at a lateral force level F_c = -23.4kN. This was slightly lower than the observed peak F_c of -25.2kN. However, the analytical F_c-Δ_c envelope failed to capture the gradual stiffness decay as the bond-slips of the reinforcements were not modelled as progressive failures. The predicted F_c-Δ_c envelope did not include the degrading portion beyond the -40mm, after the joint diagonal cracking.

In both loading directions, it appeared that the assumed joint shear strength in terms of principal stresses was underestimated in the Pull direction and overestimated in the Push direction. In the Pull direction, with a reduced axial load, the p'_t of $0.25\sqrt{f'_c}$ MPa governed the joint shear strength, and this seemed to be overly conservative when compared to the poor-bond column flexural capacity. In the Push direction, the p'_c of $0.3f'_c$ MPa governed the joint shear strength. The joint diagonal cracking in θ_{drift} = -2.0% cycles suggested that with high variation of column axial load and joint post-tensioning, the p'_c limit could be exceeded. Again, this highlighted the need for accurate assessment of the column axial load at the design θ_{drift}.

6.3.6.2 Post-tensioned pseudo-rocking interface behaviour

Figure 6.32 presents the comparison between the measured and predicted post-tensioning forces and the neutral axis (normalised by the beam depth, h_b). Whilst the pseudo-rocking interface

behaviour as postulated in §3.4.5 was apparent, the predicted post-tensioned tendon forces levelled after -20mm due to the joint compressive cracking in the Push direction. In the Pull direction, the column hinging limited the lateral strength development from the pseudo-rocking mechanism, thus the predicted post-tensioned forces were lower than expected.

The measured pseudo-rocking neutral axis was erratic (Figure 6.32b) as one of the critical liner potentiometers measuring the rotation at the pseudo-rocking interface was insensitive at low displacement readings. Nevertheless, on the negative Δ_c, the neutral axis was stabilised at approximately 0.3-0.4h_b between 0 to -80mm (where pseudo-rocking behaviour was occurring). This was higher than the predicted neutral axis depth of 0.15-0.3h_b. This highlighted the error in using linear interpolation in calculating the measured neutral axis (§4.8.4) over a non-linear cracked rocking interface. Furthermore, the analytical procedure have assumed a pseudo-rocking interface where linear geometric deformation at the rocking gap was assumed, whereas in reality, the 'rocking' flexural surface was non-linear as Figure 6.19a suggested.

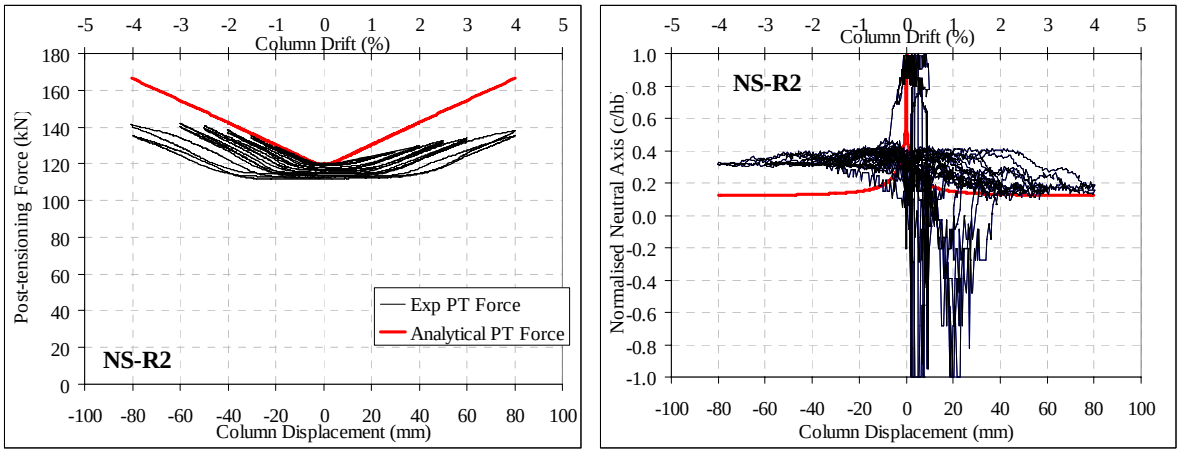

(a) (b)

Figure 6.32: Analytical prediction and experimental response at the post-tensioned pseudo-rocking interface: a) Tendon forces; and b) Neutral axis depth, normalised to the beam depth, h_b.

6.3.6.3 Influence of post-tensioning on non-ductile joint behaviour

Following the discussion of the influence of post-tensioning (§3.4.6) and of axial forces (§5.7.3) on the non-ductile joint shear capacity, the result of NS-R2 can be analysed to further confirm the previous hypotheses.

The v_{jh} results presented in §6.3.4.1 have shown the effectiveness of the added horizontal axial force in shifting the Mohr's circle and 'pre-compressing' the joint to delay/prevent the joint diagonal cracking. The initial p'_t for NS-R2 was approximately -0.2$\sqrt{f'_c}$ MPa. In terms of the

maximum v_{jh} values attained, NS-R2 was marginally higher at $+0.41\sqrt{f'_c}$ MPa and $-0.57\sqrt{f'_c}$ MPa than NS-O1 with maximum v_{jh} being $+0.40\sqrt{f'_c}$ MPa and $-0.52\sqrt{f'_c}$ MPa.

As the initial principal stresses were shifted, ultimately, a higher F_c capacity was attained in NS-R2 prior to joint diagonal cracking. As confirmed by Figure 6.25, while the joint principal stresses limit states for NS-R2 were only marginally lower or higher than those of NS-O1, the F_c at the joint cracking for NS-R2 were +17.5kN and -24.5kN, compared to +14.7 and -18.7kN for NS-O1. The maximum p'_t and p'_c attained prior to the joint diagonal cracking were $0.245\sqrt{f'_c}$ MPa and $1.2\sqrt{f'_c}$ MPa respectively for NS-R2, when compared to $0.305\sqrt{f'_c}$ MPa and $1.12\sqrt{f'_c}$ MPa for NS-O1.

In terms of design of a post-tensioned retrofit for the joint, previous recommendations [3-5] to limit p'_c to $0.25f'_c$ to prevent the joint compressive failure would be suitable. For the NS-R2 specimen, joint diagonal compressive cracking occurred at $0.24\ f'_c$ MPa ($1.2\sqrt{f'_c}$ MPa). When compared to other experimental results with joint post-tensioning by Ingham *et al.* [3-5] and Lowes and Moehle [6], the maximum observed v_{jh} , p'_t and p'_t values were interestingly comparable despite the variation in joint geometries, stirrup configuration and level of initial post-tensioning forces.

Another positive benefit of the joint post-tensioning was the added active confinement from the post-tensioning anchorage bearing plate. Despite similar bond-failure in the beam longitudinal bars as per NS-R1, the compressive anchorage failure was averted considering the availability of an alternative load path from the confinement plate. The joint shear strength degradation (at least in the Push direction) was delayed despite the high p'_c demand and the diagonal compressive cracking in the joint. The p'_c - γ_j degradation of NS-R2 can be observed from Figure 6.25d.

6.3.6.4 The need of Selective Weakening to achieve capacity design

The test results of specimen NS-R2 present a strong argument for any retrofit intervention to take a holistic capacity design or hierarchy of strength approach in terms of retrofit design. A common retrofit strategy (as reviewed in Chapter 2) is to adopt a local-element strengthening, and as illustrated in the joint post-tensioning-only retrofit solution, resolving the brittle joint failure may lead to double column flexural hinging (soft-storey mechanism). To complement a joint post-tensioning-only retrofit, the columns could alternatively be retrofitted using various retrofit techniques such as FRP and RC jacketing.

NS-R2 also alludes to the option of selective weakening of the beam (as per NS-R1) to limit the column moment demand (as well as limiting the joint shear demand). As thoroughly discussed in §3.3.3, the combination of selective beam-weakening and joint post-tensioning would yield a powerful retrofit solution.

6.4 NS-R3: FULL SELECTIVE WEAKENING – RETROFIT R3

6.4.1 General description of behaviour

The F_c versus Δ_c hysteresis plot for NS-R3 is given in Figure 6.33. The damage and cracking patterns at the selected peak inter-storey drift, θ_{drift}, loading cycles are shown in Figure 6.34. NS-R3 was tested up to the end of the 2nd cycles of the ±4.0% drift.

A stable tri-linear F_c-Δ_c envelope was observed, corresponding to three key points: a) decompression point - the neutral axis at the edge of the section with zero stress at the extreme fibre, b) yielding point c) ultimate point - corresponding to the 4.0% drift cycle peaks. Due to the bond failure of the plain round bars, particularly in the Push direction, the hysteresis loop exhibited some pinching-slip behaviour. The bond failure would have occurred on both the beam and the column longitudinal bars, particularly with significant increase of axial load and prestressing force in the Push direction.

No crack was observed in the ±0.1% drift loading cycles. However, even in the 0.1% cycles, the F_c-Δ_c plot exhibited a minor slipping on the Push direction. In the ±0.2% drift cycles (see Figure 6.34a), vertical flexural cracks appeared in the weakened section, with longer cracks in the Pull cycles. The first cracked occurring approximately at 0.11% drift was coupled with a drop in the F_c. The maximum crack width was 0.25mm in the 2nd cycle of the +0.2% drift, extending 210mm up the section depth, h_b. Hairline flexural cracks were observed in the Push cycles of -2.0% drift. From strain gages reading, the bottom longitudinal steel had not yielded at this stage. The ratio of cracked stiffness-to-uncracked stiffness, K_{cr}/K_{ini} was 0.96 with the initial stiffness, K_{ini} of 3128kN/m measured in the 1st Pull +0.1% and +0.2 drift cycles.

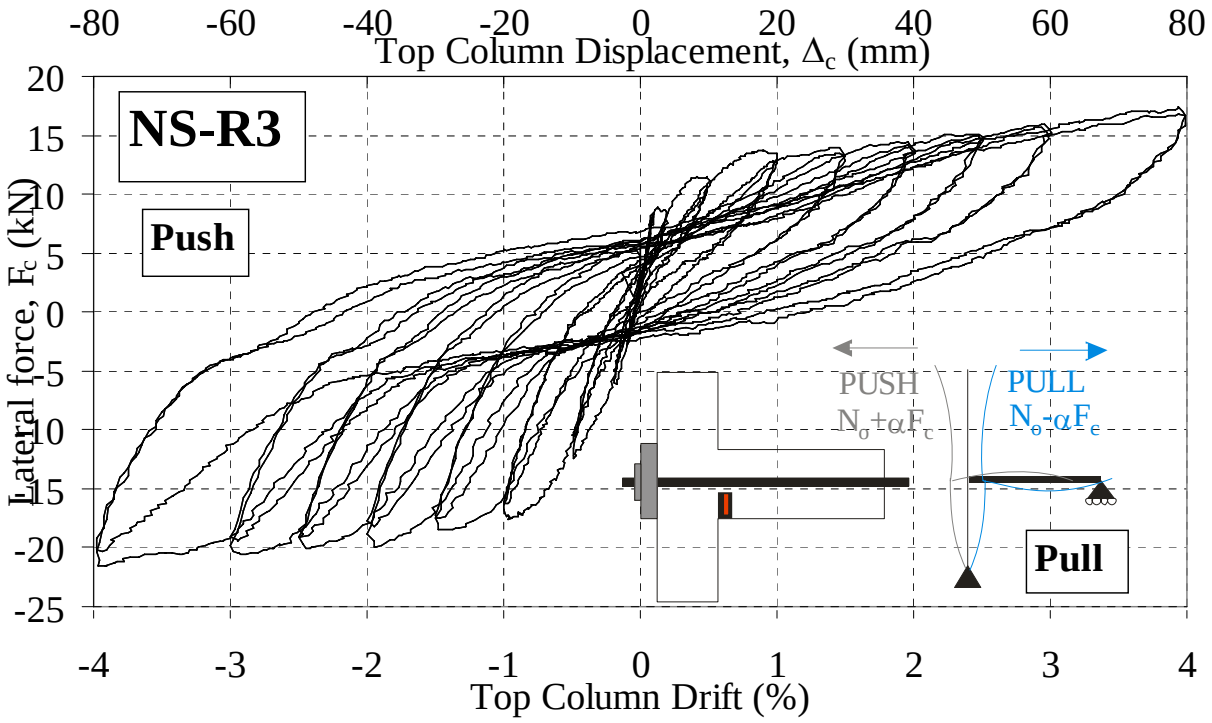

Figure 6.33: Top column lateral load, F_c, versus top column displacement, Δ_c, and drift, θ_{drift} for NS-R3.

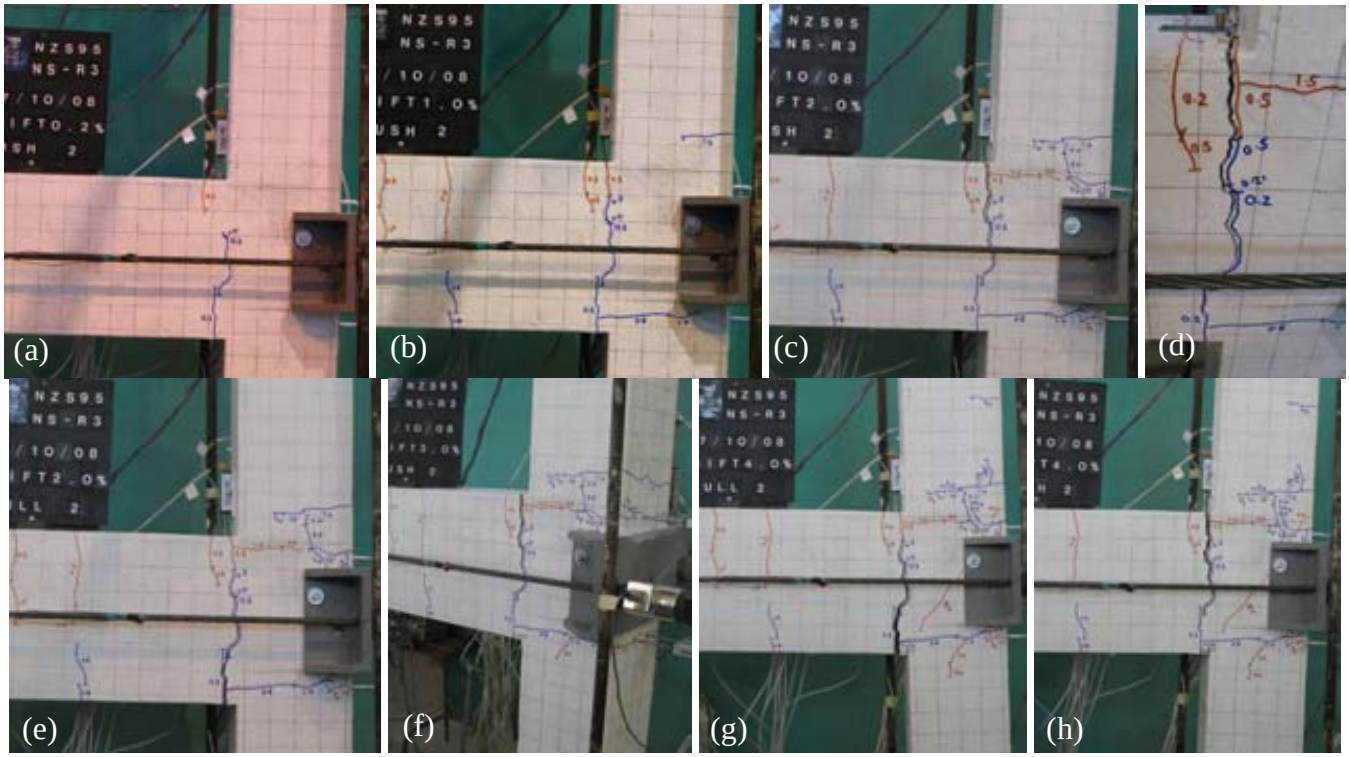

Figure 6.34: Observed cracking patterns of NS-R3: TOP: a) 2nd Push cycle of the -0.2% drift; b) 2nd Push cycle of the -1.0% drift; and c-d) 2nd Push cycle of the -2.0% drift and close-up of main crack. BOTTOM: e) 2nd Pull cycle of the +2.0% drift; f) 2nd Push cycle of the -3.0% drift; g) 2nd Pull cycle of the +4.0% drift; h) 2nd Push cycle of the -4.0% drift.

In the 1st Pull cycle of the +0.5% drift, a horizontal crack, measuring 0.15mm width, initiated from the main flexural crack at the weakened section and extended 135mm into the joint panel zone. As the crack ran along the beam bottom longitudinal bars, bond-failure-initiated split cracking was suspected. No excessive stress/strain was detected in the column longitudinal bars at this stage (§6.4.5.2). In the 1st Push cycle of the -0.5% drift, several new beam flexural cracks were observed.

In the 2nd cycles of the ±0.5% drift, no new cracks or crack extensions were observed. The maximum crack widths at the main flexural crack at the weakened section were 1.1mm (2nd Pull peak) and 0.4mm (2nd Push peak). The F_c-Δ_c hysteresis shows some stiffness and strength degradation in the 2nd cycles, leading to a thinner hysteresis loop. This further re-affirmed the loss of bond strength after the pull-out failure in the first cycles.

The 'yielding' of the NS-R3 occurred at +0.9% and -1.0% drifts in the Pull and Push directions respectively. From the strain gages data (§6.4.5.1), the beam bottom bars yielded in tension at +0.6% drift with F_c = +13.5kN. The beam top bars yielded in tension at -0.9% drift and F_c = -16.5kN, during the 1st Push cycle loading to the -1.0% drift. The maximum crack widths and cracking length at the weakened beam section were 2.5mm and 305mm up the h_b in the Pull direction, and 1.2mm and 280mm down the h_b in the Push direction. Several new hairline flexural cracks appeared in the column and the beam (Figure 6.34b).

In the 1st Pull cycle of the +1.5% drift, the horizontal crack along the beam bottom bars, extended to the exterior column face. A column flexural crack initiated in the 1st Push cycle of the -1.5% drift, linked up with the horizontal crack, which then created a section of weakness on the column longitudinal bars. Localised yielding strains were measured in this location in later loading stages. The maximum crack width of the horizontal crack was 0.85mm, while the maximum crack width at the weakened section was 4mm. In the 2nd Pull cycle of the +1.5% drift, two new column flexural cracks appeared, as the lower column axial load reduced the column flexural capacity.

In the 1st Push cycle of the -1.5% drift, a similar bond-split horizontal crack appeared along the top bars. Unlike column flexural cracks observed in NS-O1 and NS-R2 specimens – these 'bond-splitting' cracks were along the beam longitudinal bars. No new cracks were observed in the 2nd Push cycle. The maximum crack width at the weakened section was 3mm in

the 2nd Push peak of the -1.5% drift. In contrast to the Pull cycles, more severe in-cycle stiffness degradations and F_c-Δ_c hysteresis pinching behaviour were observed in the 2nd Push cycles.

In the 1st Pull cycle of the +2.0% drift, a hairline diagonally-inclined crack appeared at the top corner of the joint, along the compression strut between the compression regions from the beam/column to the centroid of the external post-tensioning. In the 2nd Pull cycle, this diagonal crack propagated vertically into the column (see Figure 6.34d). A sign of bulging as a result of the 180° hook anchorage push-out near the top of the anchorage plate was observed, suggesting the post-tensioning anchorage system should be designed to complete the load transfer of the unrestrained beam compressive anchorage.

In the Push cycles of the -2.0% drift, minor crack extensions were observed with no significant change to the damage pattern. The main inelastic mechanism remained to be the beam flexural hinging at the weakened section, with a maximum crack width measuring 5mm in both loading cycles of the ±2.0 drifts. The crack widths and the equal post-yield stiffness of the F_c-Δ_c envelope for both loading directions suggested that the behaviour was controlled by the symmetrical rocking induced by the unbonded-post tensioning of the beam-column joint. Both the beam top and bottom reinforcements were yielded in tension and compression in the ±2.0% drift cycles, as shown in the strain gage readings (§6.4.5.1).

Figure 6.35 presents the isolated cycles of the F_c-Δ_c hysteresis loops between the ±1.0% to ±3.0% drift cycles. In the Pull cycles, a stable hysteresis without in-cycle strength and stiffness degradation (i.e. modified Takeda hysteresis) was attained; it was an indication of stable beam hinging mechanism. In the Push direction however, significant degradation was observed in the 2nd cycle as a result of the bond failure along the beam reinforcements in compression. These trends were consistent between the ±1.0% and ±3.0% drift cycles.

In the ±2.5 % drift cycles, no new cracks were observed and the damage pattern was similar to the ±2.0% drift cycles. The maximum crack widths at the apparent pseudo-rocking section were 12.5mm in the Pull direction and 7.0mm in the Push direction. Limited column reinforcements yielding were observed in the Pull cycles of the +2.5% drift, where the measured steel strain just exceeded the tensile yield strain.

The damage pattern in the ±3.0% drift loading cycles was similar to those in the ±2.5% drift cycles, with minor crack extensions and continued widening of the flexural crack at the weakened section. The F_c-Δ_c hysteresis loops were also similar to the ±2.0 and ±2.5% hysteresis

loops, with slightly larger F_c-Δ_c pinching behaviour near the origin. This corresponded to the closure of the rocking gap during the loading reversal.

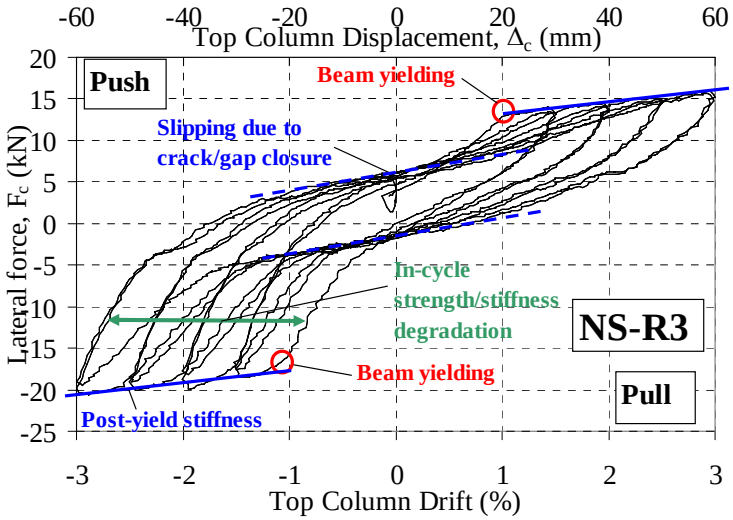

Figure 6.35: Isolated F_c versus Δ_c / θ_{drift} hysteresis loops for NS-R3 for ±1.0% to ±3.0% drifts cycles.

In the ±4.0% drift cycles, the rocking gap widths were 12mm and 10mm in the Pull and Push directions respectively. New column flexural cracks appeared in the 1st Pull cycle of the +4.0% drift, while a joint diagonal crack appeared in the 1st Push cycle of the -4.0% drift (see Figure 6.34e-f). While these cracks were insignificant to the overall behaviour of specimen NS-R3 at the ±4.0% drift, they indicated the hierarchy of strengths in the two loading directions. With a decreased axial load in Pull direction, column flexural failure will be the next failure mechanism after beam flexural hinging. In the Push direction, joint shear cracking was caused by the high p'_c within the joint panel zone, as the positive post-yield stiffness continued to increase the overall F_c. This observed hierarchy of strengths was consistent with the predicted M-N performance domain for NS-R3 given in Appendix B.

6.4.2 Load-displacement hysteresis analysis

The F_c-Δ_c hysteresis plot for NS-R3 is shown in Figure 6.33 while the analysis of the NS-R3 F_c-Δ_c hysteresis is presented in Figure 6.36. The maximum F_c values measured were +17.4kN (at +3.93% drift) and -21.6kN (at -3.91% drift).

In terms of peak-to-peak stiffness, K_{eff} (Figure 6.36a), NS-R3 curve was marginally higher than the as-built NS-O1 specimen as the beam-weakening stiffness reduction was

compensated by the post-tensioning stiffness enhancement. Except for the first two θ_{drift} levels (±0.1% and ±0.2%), the K_{eff} did not degrade significantly between the 1st and 2nd cycles.

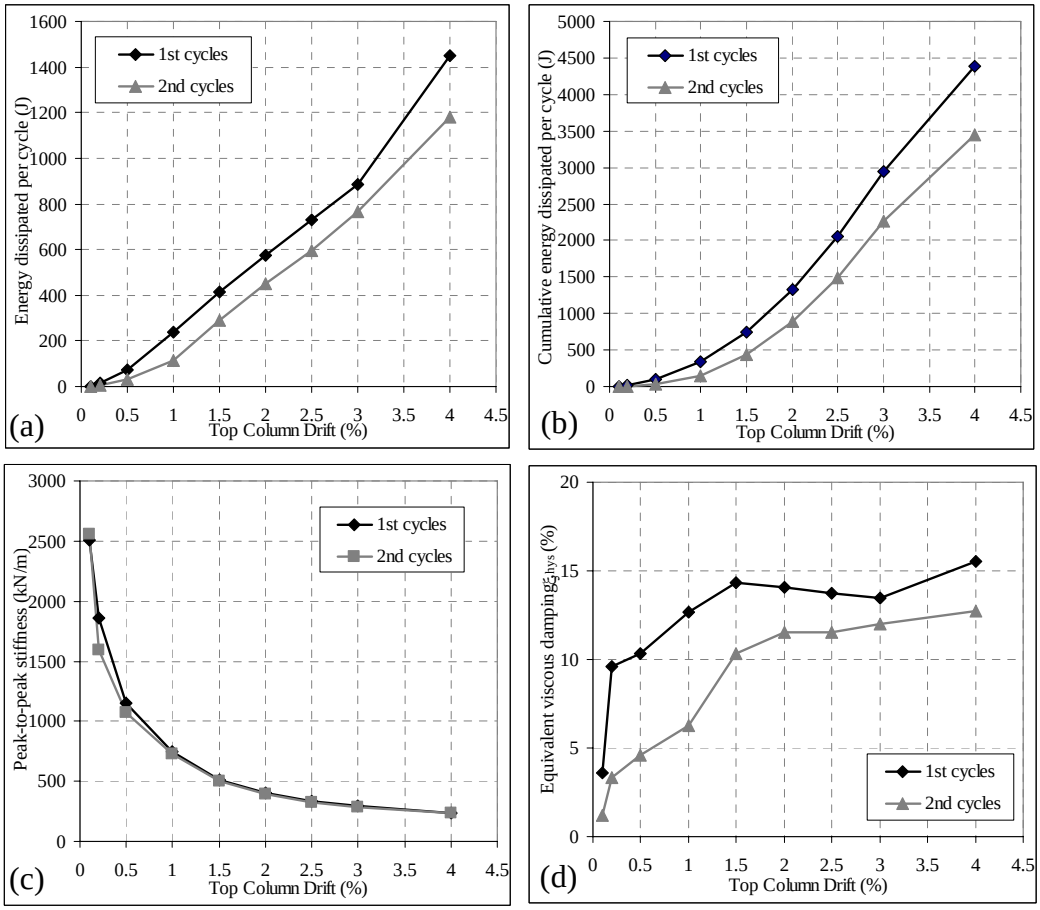

Figure 6.36: F_c-Δ_c analysis for NS-R3: a) Energy dissipated per cycle; b) Cumulative energy dissipated per cycle; c) peak-to-peak stiffness, K_{eff}, and ; d) Equivalent viscous damping, ξ_{hys}.

The energy dissipation capacity for NS-R3 was considerably improved when compared to NS-R2 and NS-O1. Between the typical design θ_{drift} (1.0%-2.5%), the ξ_{hys} were on average, 13.7% and 9.9% for the 1st and 2nd cycles respectively. Noting that the computed ξ_{hys} did not include the typical 2-5% 'elastic' contribution (ξ_{el}) to the system damping, NS-R3 achieved reasonably high damping capacities, with an average ξ_{sys} (=ξ_{hys} + ξ_{el}) of 13.8% by assuming ξ_{el}=2%. Despite the evidence of bond-slip failure in the Push cycles, the ξ_{hys} values beyond the ±1.5% drift cycles were at least 10%. The 2nd cycle values of the ξ_{hys} were typically 10-60% lesser than the 1st cycles, with more significant in-cycle degradation in the small θ_{drift}.

6.4.3 Local deformations and displacement components

6.4.3.1 Decomposition of top column horizontal displacement

The contributions to the top column horizontal displacement, Δ_c at the peaks of the Pull and Push loading cycles as percentages of the total Δ_c are presented in Figure 6.37. Fixed-end deformation, $\Delta_{beam,fixed\text{-}end}$, was the largest components of the Δ_c in both loading directions from ±0.5% onwards. $\Delta_{beam,fixed\text{-}end}$ was accounting for 60-65% of Δ_c in the Pull direction and 40-65% of Δ_c in the Push direction. In the Push direction, there was a large unaccounted component of Δ_c, particularly in the lower θ_{drift} levels.

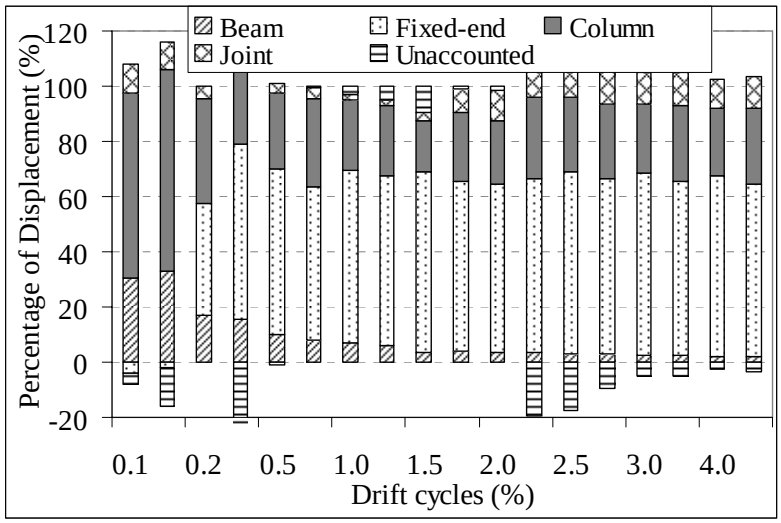

a) Pull loading direction – positive displacement.

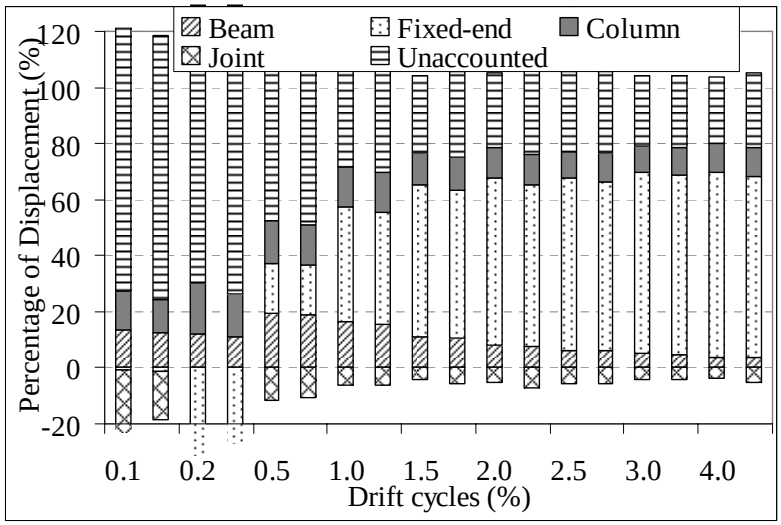

b) Push loading direction – negative displacement.

Figure 6.37: Displacement decompositions based on the measured deformations for NS-R3.

In the Pull direction, the column flexural deformation, $\Delta_{col,flexural}$, was the 2nd largest contribution to Δ_c. The $\Delta_{col,flexural}$ contribution was relatively constant, accounting for 20-30% of Δ_c in the Pull cycles and 9-15% of Δ_c in the Push cycles. In the Push direction, the beam flexural deformation, $\Delta_{beam,flexural}$, was the 2nd largest contribution to Δ_c, accounting for approximately 4-20% of Δ_c, with decreasing percentage as the θ_{drift} increased.

6.4.3.2 Beam deformations

The moment-curvature plots for the beam flexural regions and beam fixed-end regions are shown in Figure 6.38. Most of the beam crackings and inelastic deformations were concentrated on the pseudo-rocking interface along the beam fixed-end section. In both the Pull and Push loading directions, the theoretical M_{bf} capacities (+28.0kNm and -37.6kNm) were attained. The maximum M_{bf} developed in the Pull and Push directions were +31.2kNm and -38.9kNm respectively. The analytical M_{bf} considered a maximum concrete compressive strain, ε_c of 0.003, while it was harder to assess the maximum ε_c from the experimental results.

The measurement of beam curvatures, ϕ_b, in the fixed-end region would be affected by the large rocking gap opening through a non-linear interface. The maximum ϕ_b attained in the fixed-end region were +0.393m^{-1} and -0.399m^{-1} in the Pull and Push cycles respectively. These corresponded to the curvature ductility of 12 assuming ϕ_y = 0.033m^{-1} (read from the Figure 6.38a). Limited ϕ_b was measured in other beam regions, with a maximum ϕ_b of 0.0092m^{-1} measured in the region 275-475mm from the column internal face.

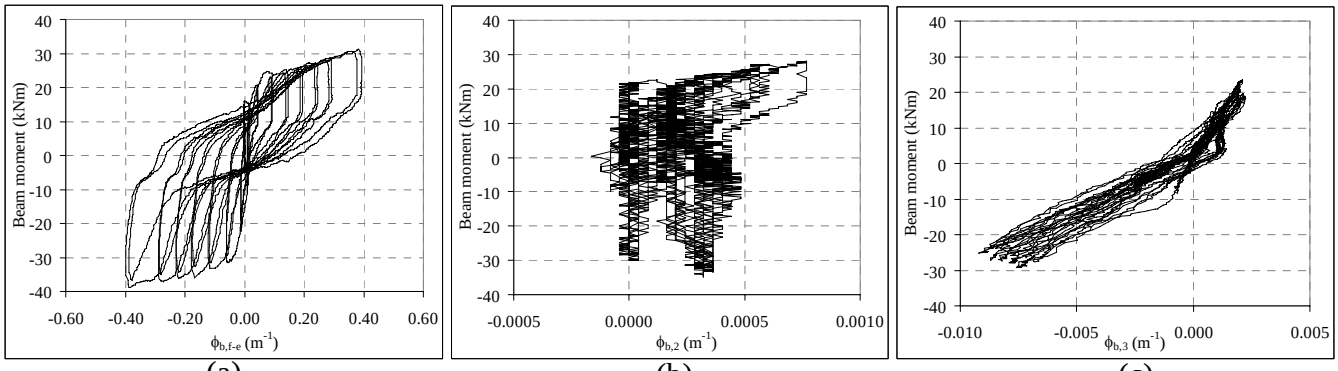

(a) (b) (c)

Figure 6.38: a) Moment-curvature plots for beam sections: a) fixed-end section; b) 75-275mm from the column internal face; and c) 275-475mm from the column internal face.

6.4.3.3 Column deformations

Figure 6.39 shows the measured moment-curvature response for the three regions of the column. The observed nominal column flexural strength, $M_{c\text{-}cf}$ (the plateau moment in the hinging direction), were +13.2kNm and -16.4kNm in the Pull and Push cycles respectively. In the Pull cycles, the $M_{c\text{-}cf}$ corresponded to the ϕ_c of 0.075m^{-1} and of 0.046m^{-1} at the top and bottom halves of the column. In the Push cycles, the $M_{c\text{-}cf}$ corresponded to the ϕ_c of -0.025m^{-1} and of -0.012m^{-1} at the top and bottom halves of the column.

These observed $M_{c\text{-}cf}$ values were lower than the predicted $M_{c\text{-}cf}$ of +18.5knM and -38.7kNm. The reason for this discrepancy was the same as NS-R2 (§6.3.3.3), in which the variation of axial load imposed in the experiment was lower than the expected column axial load used in the analytical prediction. The difficulties to establish accurate column axial load in real structures may suggest that stricter capacity design requirements (over-strength factors etc.) shall be considered for the column during the retrofit design stage (as per §3.4). This also highlights the importance of a beam-weakening as part of the retrofit intervention.

The column underwent more severe deformations (higher ϕ_c) in the Pull direction, particularly after the ±2.0% drift cycles, which corresponded closely to the yielding of the column reinforcements. The column yielding was confirmed by the strain-gages reading presented in §6.4.5.2. Curvature ductilities of 13.6 and 8.4 were developed during the Pull loading cycles in the column regions above and below the joint (assuming ϕ_y = 0.0055m^{-1}).

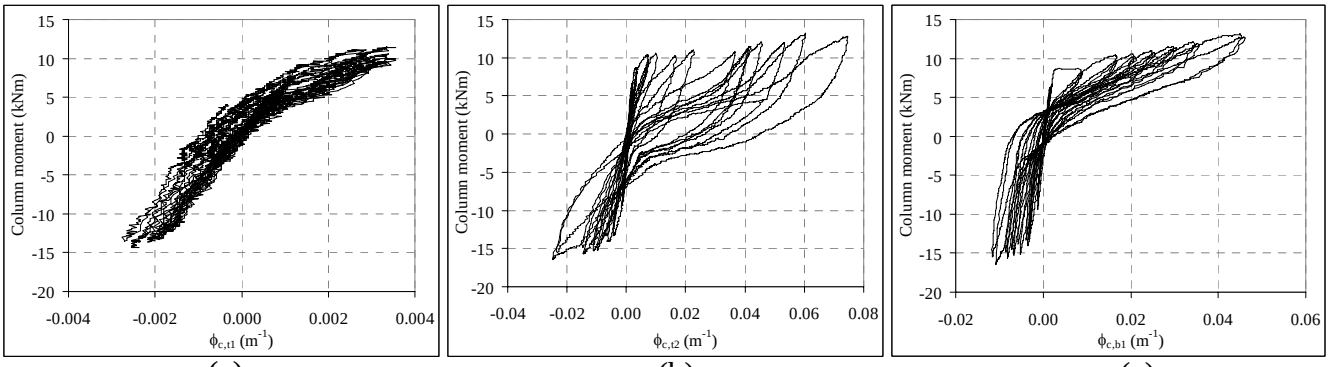

(a) (b) (c)

Figure 6.39: Moment-curvature plots for column flexural sections: a) 200-430mm from the beam top face; b) 0-200mm from the beam top face; c) 0-200mm from the beam soffit.

6.4.4 Beam-column joint behaviour

6.4.4.1 Nominal joint shear stress and joint shear distortion

The nominal joint shear stress, v_{jh}, versus joint shear distortion, γ_j, and Δ_c relationships for NS-R3 are given in Figure 6.40. The maximum v_{jh} measured were 2.01MPa (0.41 $\sqrt{f'_c}$ MPa or 0.083f'_c MPa) and -2.50MPa (-0.51 $\sqrt{f'_c}$ MPa or -0.103f'_c MPa) in the Pull and Push peaks of the ±4.0% drift. No discernable v_{jh} - γ_j trend was observable. Joint diagonal crack was only observed in the Push cycle, initiated at the 1st Push cycle of the -4.0% drift. The joint damage also corresponded to the higher v_{jh} demand in the Push direction, as the un-weakened beam top side had four longitudinal bars in tension.

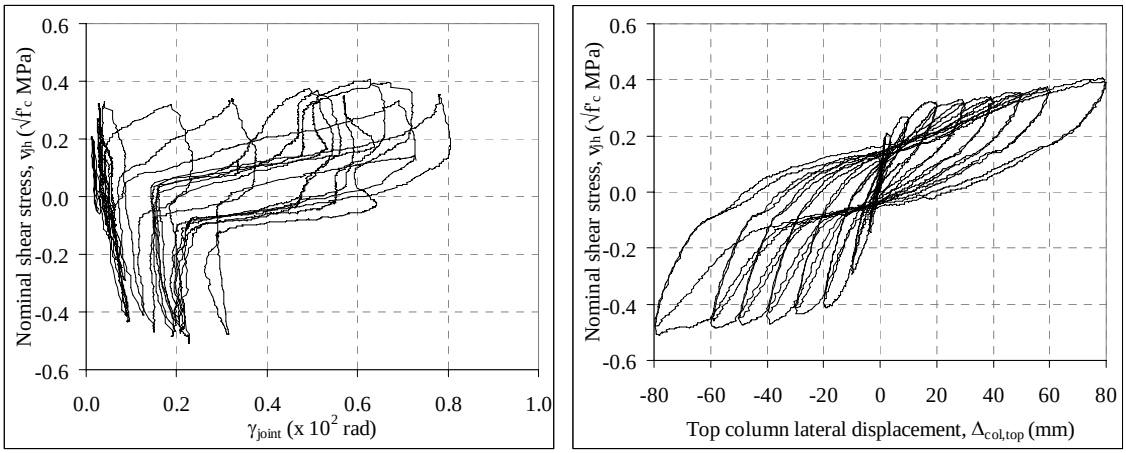

Figure 6.40: a) Nominal joint shear stress, v_{jh} versus joint deformation, γ_j; b) Nominal joint shear stress, v_{jh} versus top column lateral displacement, Δ_c.

6.4.4.2 Joint principal stresses

Figure 6.41 shows the joint principal stress responses as functions of the Δ_c and γ_j for NS-R3. In terms of maximum principal stresses in the joint during the cyclic loading of NS-R3, the maximum p'_t was 0.254$\sqrt{f'_c}$ MPa at γ_j =-0.00629 radians and the maximum p'_c was 1.087$\sqrt{f'_c}$ MPa at γ_j =-0.002268 radians. The maximum p'_c that led to joint diagonal cracking in the Push direction, was also equivalent to 0.218f'_c MPa, somewhat lower than the 0.25f'_c MPa limit discussed in §6.3.6.3.

The joint shear distortion (negative γ_j) growth in the Pull direction shown in Figure 6.41c occurred after the +2.0% drift cycle. Rather than joint shear deformation, the measured γ_j was influenced by the bulging deformation caused by the push-out of the beam 180° hook anchorage (Figure 6.34). This was confirmed by the lack of joint shear cracks in the Pull loading cycles. In

general, the selective beam weakening and external post-tensioning retrofit implemented for NS-R3 was successful in decreasing the joint principal stress demands and improving the post-cracking behaviour.

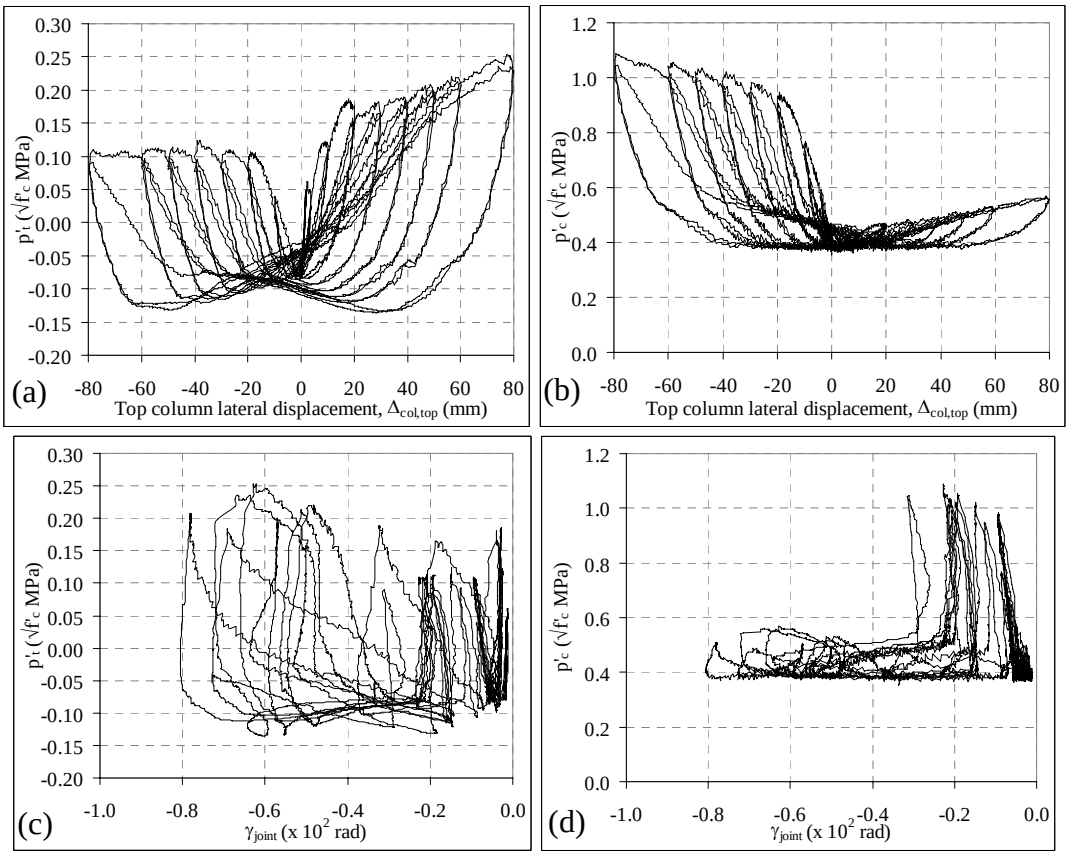

Figure 6.41: a-b) Joint principal stresses versus top column lateral displacement, Δ_c: a) p'_t - Δ_c; b) p'_c - Δ_c; c-d) Principal stresses versus joint shear deformation, γ_j plots: c) p'_t - Δ_c; d) p'_c - Δ_c.

6.4.5 Steel strain profiles

6.4.5.1 Beam longitudinal reinforcement strains

Figure 6.42 - Figure 6.44 present the strain profiles of the top and bottom (not weakened and weakened) beam longitudinal reinforcements for specimen NS-R3. The X-axis is the distance from the exterior column face to the strain gage while the two vertical dashed lines refer to the column centre-line and the interior column face. The beam weakening section was located 50mm from the interior column face. From the steel test, the ε_y for the longitudinal beam and column reinforcements was 0.00168 (1680 microstrains) and the f_y was 335MPa.

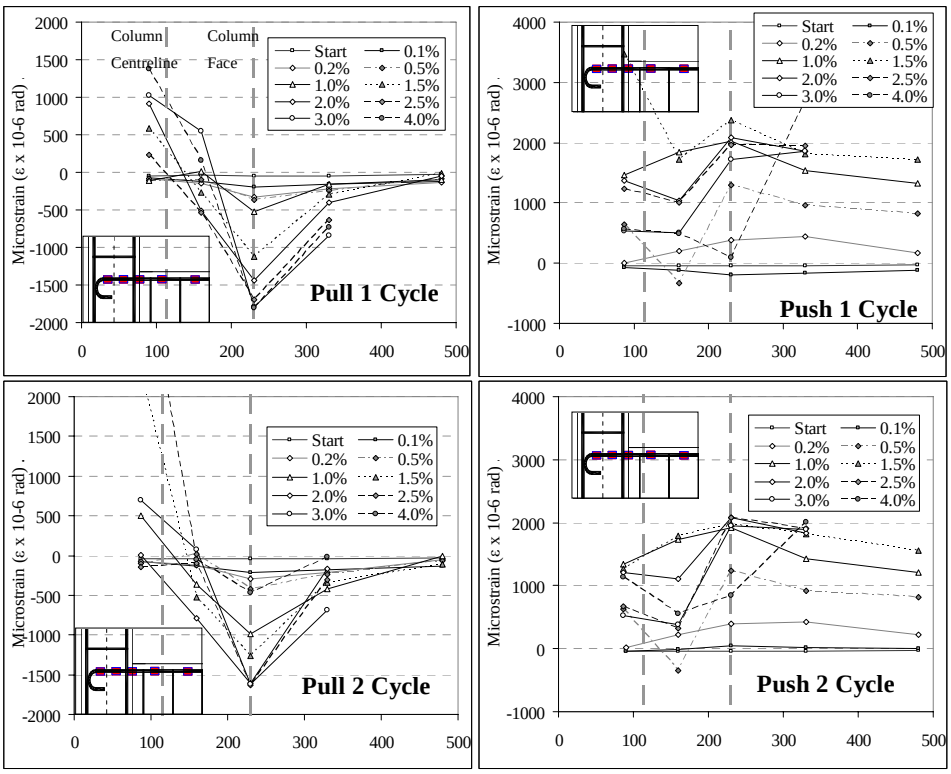

Figure 6.42: Strain profiles of beam top longitudinal bars of the specimen NS-R3.

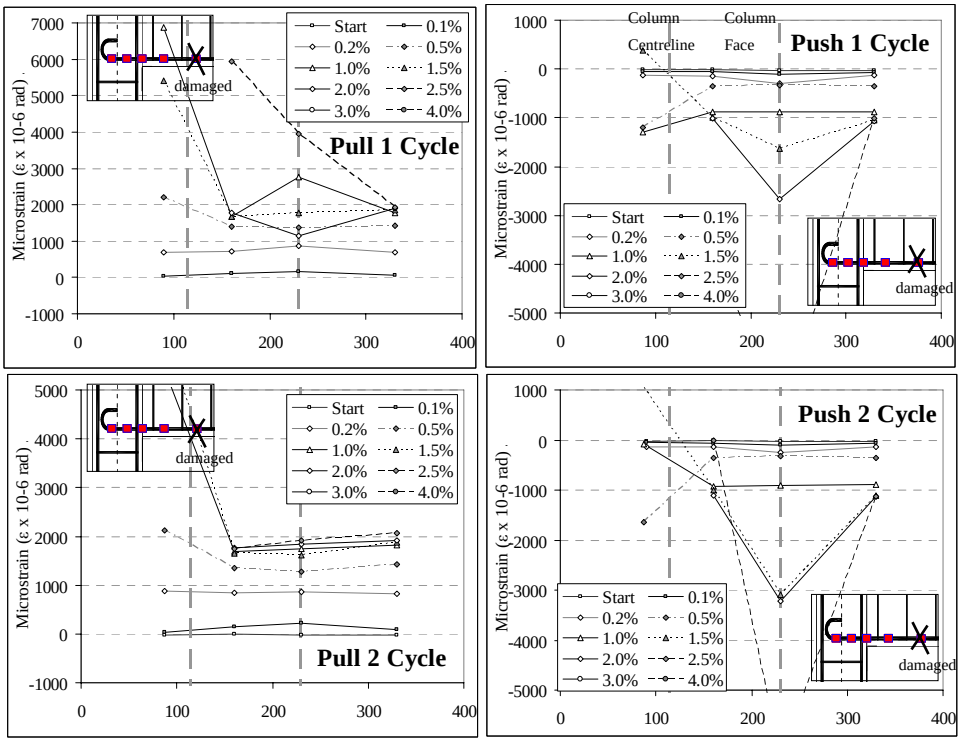

Figure 6.43: NS-R3: Strain profiles of beam bottom longitudinal bars (interior bars – not weakened).

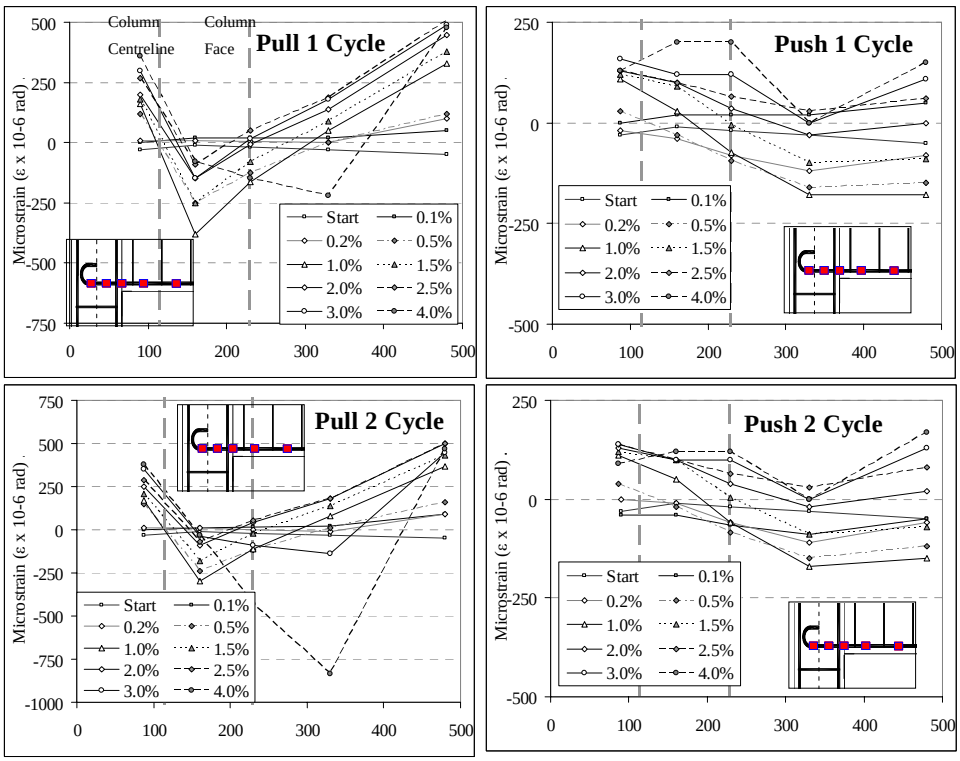

Figure 6.44: NS-R3: Strain profiles of beam bottom longitudinal bars (exterior bars – weakened).

The beam top bars (Figure 6.42) yielded in tension in the early Push cycles (-1.0% drift). At the measured peak of 2380 microstrains at the 1st Push cycle of the -1.5% drift, the yield strain penetration length was at least half the depth of the column. The progressive penetration of strains into the joint was the consequence of bond failure and subsequent debonding of the smooth reinforcements. This progressive bond failure prevented excessive strains of the beam top bars as the strain demands were spread across a longer unbonded length. The yielding strains were maintained up to -3.0% drift Push cycles, before the strain gages were ultimately broken in the 3.0%-4.0% drift cycles.

In the reverse Pull loading cycles, the beam top bars (Figure 6.42) were yielding in compression at the beam-column interface section. However, strain reversals were observed within the joint, as tensile strains were measured in the strain gages on the bars lengths within the joint. However, the quality of the strain data within the joint was low, owing to the tendency of erratic readings due to bond failure in the cyclic loading. Nevertheless, it could be concluded that the top reinforcements were yielding in tension and compression during the cyclic loading.

For the un-weakened bottom reinforcements (Figure 6.43), the strain readings in the Pull cycles show that tension yielding occurred in the +0.5% drifts cycles. The strain profiles up to the

+0.5% drift suggested that bond capacity within the joint was maintained. After the bond failure beyond the +0.5% drift, significant tensile strains were developed in the reinforcement lengths close to the 180° hook anchorage. The tensile strains were relatively uniform along the instrumented reinforcement length, suggesting debonded bottom reinforcements.

In the Push cycles, the un-weakened bottom reinforcements (Figure 6.43) were in moderate compression strains (<1500 microstrains) up to the -1.0% drift cycles. In the Push cycles of the -1.5% drift, localisation of compressive strains in the beam-column interface was observed. Within the joint region however, some strain reversals (to tension strain) were measured before most of the strain gages broke in the -2.0% drift.

The weakened beam bottom bars (Figure 6.44), as expected, had low elastic strains (<500 microstrains for most locations) measured, as there was discontinuity along the beam-column interface (the weakened section). In the Pull cycles, increases in measured strains on both sides of the weakened location were observed after the +1.0% drift cycles. In the Push cycles, low compressive strains (~35MPa) were measured in the beam, up to -1.0% drift, after which, low level of tensile strains were developed on both reinforcement lengths of the weakened location.

6.4.5.2 Column longitudinal reinforcement strains

The strain profiles along the exterior and interior column bars are shown in Figure 6.45 and Figure 6.46, respectively. The Y-axis is the distance from the centre-line of the beam. The three horizontal dashed lines refer to the beam soffit (bottom line), beam centre-line and the beam top face (top line). As with all strain gage readings, tensile strains were measured as positive values. All column strain gages were zeroed before the axial force loading on the column at the start of the test. The ε_y for the longitudinal column reinforcements was 1680 microstrains and the f_y was 335MPa.

In the Pull cycles, both the exterior face and interior face column longitudinal bars were undergoing substantial tensile strains from the +1.0% drift cycles onward. Prior to that, the column reinforcements were under low level of tensile/compressive stresses with strain reversal (approximately zero strain) observed in the middle of the joint. From the +1.0% drift peak, tensile strains increased rapidly at the column-joint interface, with tensile yielding in the +3.0%-+4.0% drifts cycles.

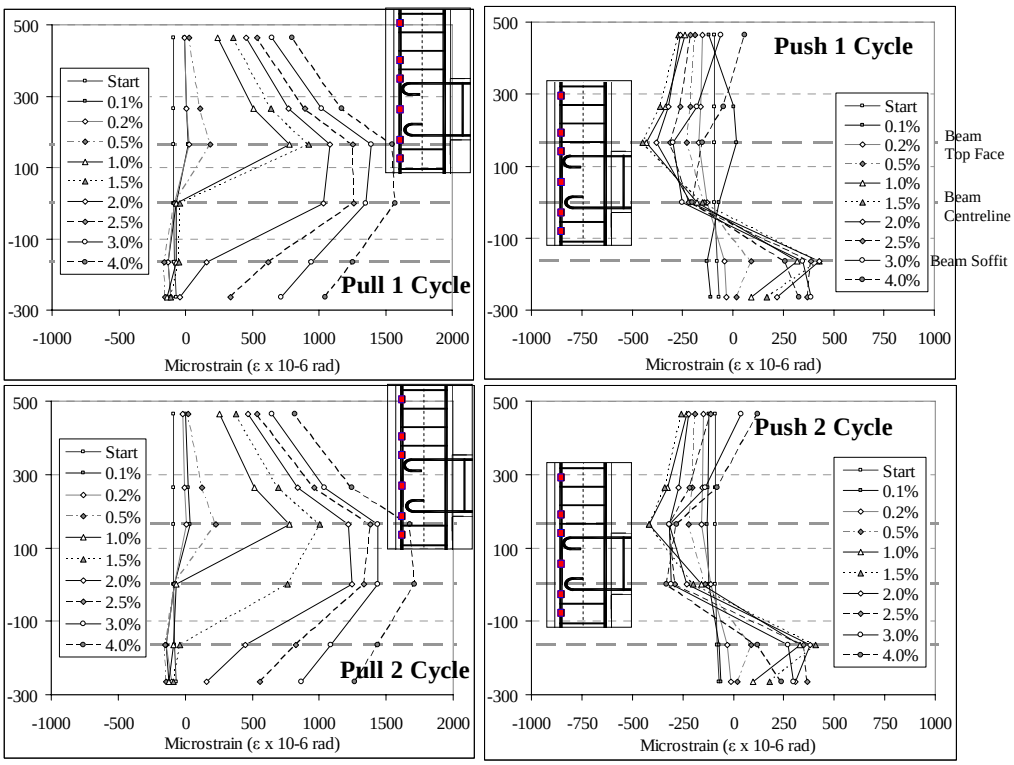

Figure 6.45: Column exterior face longitudinal reinforcements strain profiles for the specimen NS-R3.

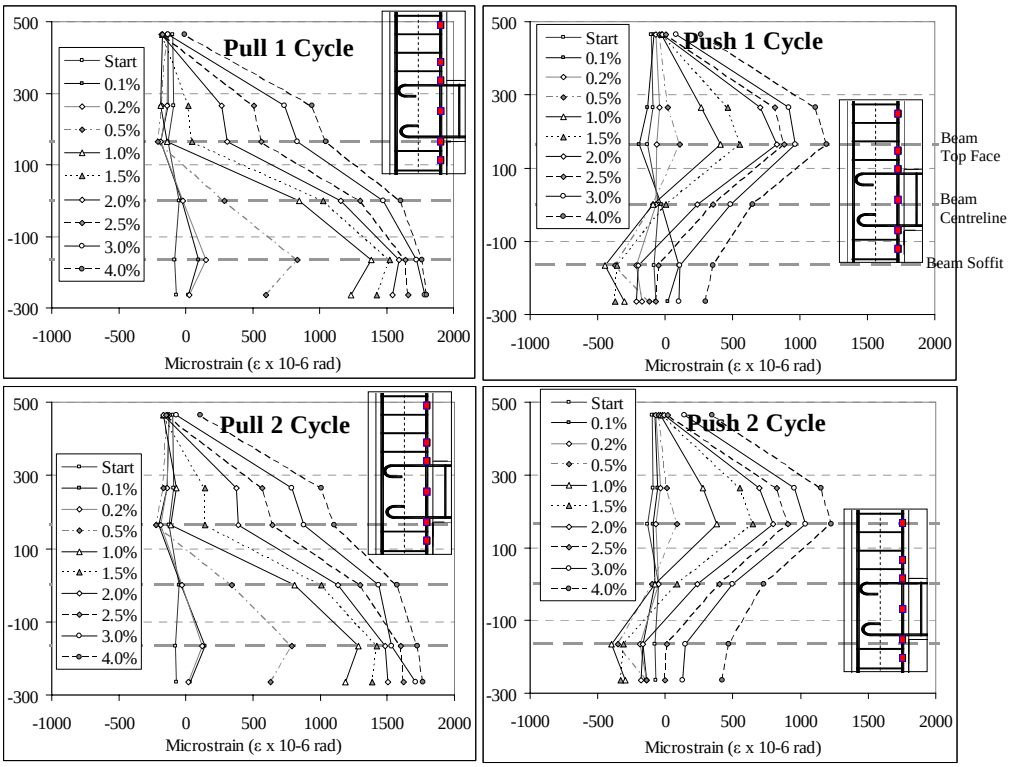

Figure 6.46: Column interior face longitudinal reinforcements strain profiles for the specimen NS-R3.

The progressive penetrations of tensile strains along both the interior and exterior column bars indicated bond failure of the column reinforcements, commencing at the flexural crack along the column-joint interface. This progressive bond failure prevented the yielding of the column bars as the strain demands were spread across a longer unbonded length. After debonding failure, the column longitudinal bars would only be effective in tension, as bar-slip would occur in the reverse loading; thus limited compressive strains were observed.

In the Push cycles, the exterior and interior column bars were responding differently. The exterior column bars in the Push cycles (Figure 6.45) were responding elastically up to the -2.0% drift. At the -2.0% drift cycles, the exterior column bars were failing in bond under compression at the top column-joint interface. After that, the compressive and tensile strains within the exterior bars decreased to less than ±200 microstrains.

Similarly, the column interior bars were responding under low strain levels up to the -1.0% drift. The development of column flexural cracks at the top column to joint interface led to strain concentration along this section (as per the column exterior bars in the Pull direction). Further Push loading cycles then degraded the bond capacity along the column bars with a progressive bond failure and strain penetration into the joint depth. It should be noted that the bond failure would have progressed into both directions (up and down) of the flexural crack. Consequently, the column strains were spread over a length of reinforcements, which was also roughly the unbonded length of the bars.

6.4.5.3 Stirrup reinforcement strains

The strain profiles of the stirrups in the column and the beam are shown in Figure 6.47. Selected stirrup results are presented herein as the general trend across different strain gages is similar. The complete dataset is given in Appendix D. Most column and beam stirrups were responding linearly to the applied F_c. The stirrups in the column parallel to the loading direction (e.g. CS1C - Figure 6.47b) however, exhibited a sharp peak of tensile strains after the ±1.5% drift. This corresponded to the appearance of column flexural cracks in the ±1.0% drift, which resulted in a higher proportion of the column shear force carried by the column stirrups.

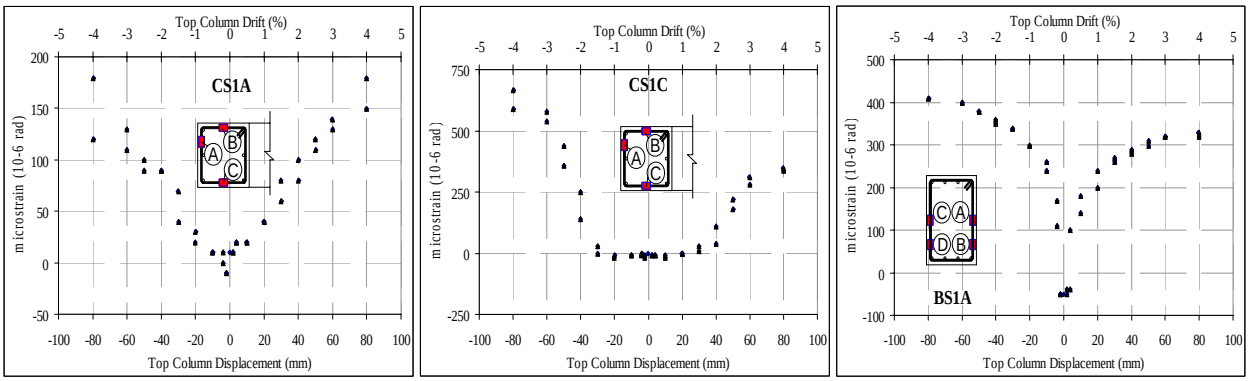

Figure 6.47: Stirrup reinforcement strain profiles: a-b) column stirrup 50mm from beam soffit – CS1A and CS1C; and c) BS1A: beam 1st stirrup - 50mm from column interior face.

6.4.6 Discussion of the NS-R3 specimen

6.4.6.1 Analytical-experimental comparison for lateral strength, F_c

The F_c-Δ_c experimental-analytical comparison for the specimen NS-R3 is given in Figure 6.48. The analytical procedure described in §3.4 (Chapter 3) was used to generate the predicted F_c-Δ_c envelope. The predicted F_c at design concrete strain (ε_c = 0.003) were +15.2kN and -20.3kN. The maximum F_c values measured in the experiment were +17.4kN (at +3.93% drift) and -21.6kN (at -3.91% drift) in the Pull and Push loading directions respectively.

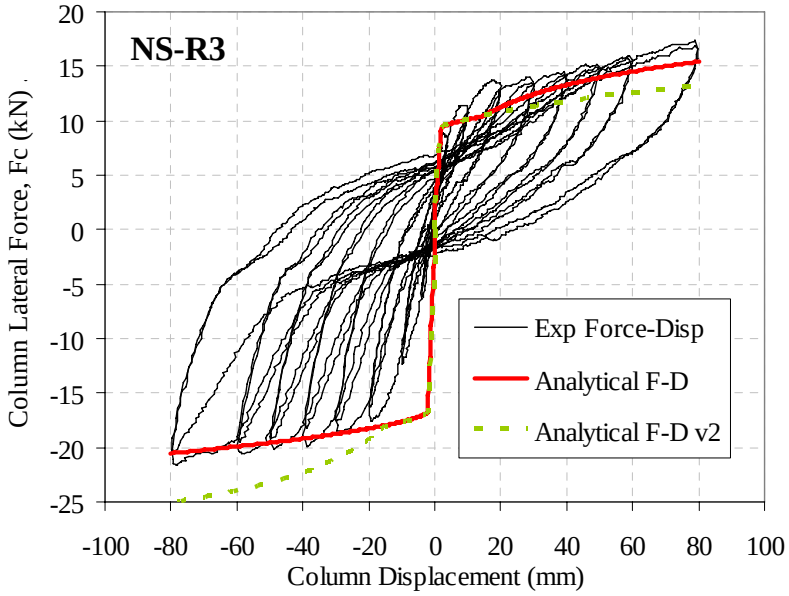

Figure 6.48: Experimental-analytical comparison of the F_c-Δ_c curves.

In general, a good analytical-experimental comparison was achieved, with approximately +15% discrepancies in the Pull direction and -7% discrepancies in the Push direction. The

predicted inelastic mechanism was beam flexural hinging in both loading directions, which was corroborated by the experimental observations. As with the NS-R2 prediction, the analytical procedure did not consider the bond failure of the column longitudinal bars, which somewhat reduced the actual flexural capacities of the column.

As explained in §3.4.5, the strain hardening of the tension reinforcement was ignored in order to account for bond failure in the non-prestressed beam bars. This bond-slip failure assumption was used for the Push (negative Δ_c) cycles. However, for the Pull cycles, the strain hardening was included as the beam-weakening was expected to result in extreme strain localisation at the weakened section. The alternative prediction (no strain hardening assumption) for the Pull cycles is shown as dotted lines in Figure 6.48, with a consistent under-prediction of F_c. Without further refinement of the existing analytical procedure to include bond-failure explicitly, the existing analytical procedure was deemed satisfactory.

6.4.6.2 Post-tensioned pseudo-rocking interface behaviour

Analytical procedure described in §3.4.5 was used to predict post-tensioning tendons' forces and neutral axis (normalised by the beam depth, h_b) at the pseudo-rocking interface for NS-R3. The analytical prediction is shown in Figure 6.49 with the measured values (as per §4.8.4). In general, a good agreement was achieved between the analytical and experimental values for both the post-tensioning forces and the normalised neutral axis.

The postulated pseudo-rocking behaviour was evident from the experiment observation shown in Figure 6.34. The rocking gap opening was up to 12mm during the testing of NS-R3 especially in the higher drift levels. As beam flexural hinging was governing the overall response of NS-R3 in both loading directions, the predicted and experimental post-tensioned tendon forces were in better match, when compared to the NS-R2 case. However, +10-14% difference between the predicted and experimental post-tensioning tendons forces was observed in the Pull cycles. This may suggest that the strain hardening assumption in the Pull cycles was incorrect and thus the improved prediction was a result of the con-current under-prediction of post-tensioning force and neutral-axis.

The predicted neutral axes were at 0.10-0.15h_b after +0.3% in the Pull direction and at 0.11-0.20h_b after -0.3% in the Push direction. These values were consistent with the stabilised measured values of the neutral axis position (Figure 6.49b). Noting that there was geometrical non-linearity at the rocking interface error as per NS-R2 (§6.3.6.2), the existing analytical

procedure could under-predict the values of the neutral axis, whereas in reality, the compression block region in the beam may be larger than the analytical calculation.

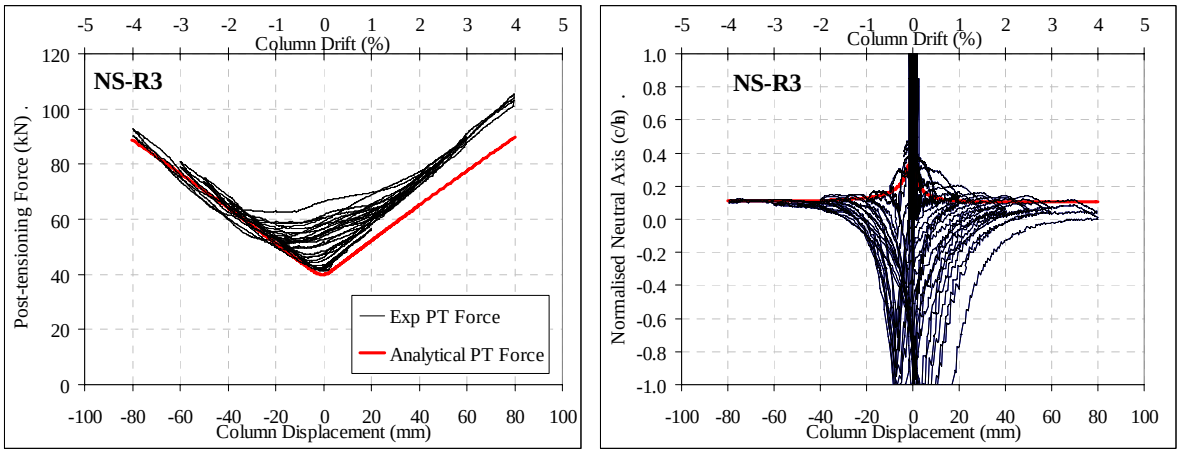

(a) (b)

Figure 6.49: Analytical prediction and experimental response at the post-tensioned pseudo-rocking interface: a) Tendon forces; and b) Neutral axis depth, normalised to the beam depth, h_b.

6.5 NS-R4: FULL SELECTIVE WEAKENING – RETROFIT R4

6.5.1 Introduction

The aims of the NS-R4 specimen were to re-affirm the retrofit solution R3 (replication) and to attempt to shift the plastic hinge further away from the column face. Shifting the weakest section away by 195mm from the column face would give a longer development length, l_d, for the beam reinforcement bars. Conversely, it may induce higher joint shear stress demand. A secondary aim was to investigate the feasibility of using a very low level of initial post-tensioning force (12kN or 7.7%f_{ypt} per tendon). Nevertheless, in many aspects, the test results of NS-R4 were similar to those of NS-R3. Therefore, the discussion of the NS-R4 results in the following sub-sections is, for brevity, only focussed on the key differences between the two specimens.

6.5.2 General description of behaviour

The F_c versus Δ_c hysteresis plot for NS-R4 is given in Figure 6.50. The damage and cracking patterns observed at the end of selected peak inter-storey drift, θ_{drift}, loading cycles are shown in Figure 6.51 and Figure 6.52. NS-R4 was tested up to the end of the 2nd cycles of the ±4.0% drift.

The overall F_c - Δ_c curves were similar for NS-R4 and NS-R3, despite some differences in the observed inelastic mechanism. The maximum F_c values measured in NS-R4 were +14.9kN (at the +4.0% drift) and -22.6kN (at the -4.0% drift), which were lower in the Pull cycles and marginally higher in the Push cycles when compared to NS-R3. The difference of F_c attained was

mostly attributed to the lower initial post-tensioning forces used and mixed inelastic mechanism observed in NS-R4.

The early stages of NS-R4 were very similar to the response of NS-R3 except for the location of the main flexural cracking as the weakened section had been shifted away from the column face. Flexural vertical cracks were observed in the weakened section in both the 1st Pull and the 1st Push cycles of the ±0.1% drift. The maximum crack width was 0.2mm. Even at the preliminary loading stage of ±0.1% drift, the F_c-Δ_c plot showed stiffness degradation and slipping in the Push direction loops (Figure 6.50).

In the ±0.2% drift cycles, the flexural crack at the weakened section, extended up to the full h_b depth. The maximum crack widths were 0.4mm and 0.3mm at the beam bottom and top faces respectively (Figure 6.51a).

In the ±0.5% drift cycles, a second set of flexural cracks appeared at the beam-column interface. The crack widths at the weakened section and the beam-column interface were 0.45mm and 0.30mm respectively. A horizontal crack was observed in the joint panel, running along the beam longitudinal reinforcements. In comparison with the NS-R3 specimen, the lower post-tensioning force in NS-R4 resulted in lower F_c in both loading directions. However, energy dissipation capacity improved in NS-R4, as fatter hysteresis loops were attained in the ±0.5% drift cycle.

The crack developments in the ±1.0% and the ±1.5% drift cycles were similar to NS-R3. While the weakened section has the largest flexural crack (up to 2.25mm wide) in the Pull cycles, the second flexural crack at the beam-column section was widening in a faster rate, especially beyond the +1.5% drift. In the Push cycle of -1.5% drift, the main inelastic deformation was concentrated at the beam fixed-end cracking with a maximum crack width of 1.9mm when compared to a crack width of 1.2mm at the weakened section. For the Push loading direction, it should be noted that NS-R4 had the same reinforcing configuration as NS-R3, only with lower post-tensioning forces.

The plastic hinge began to shift inward in the Pull cycles beyond the +1.5% cycles, from the weakened section to the beam-column interface section. The initial advantage of having a longer development length for NS-R4 was cancelled out by the growth of a flexural crack at the beam-column interface. The damage patterns at the end of the ±1.5% drift cycles were similar between the NS-R3 and NS-R4 specimens.

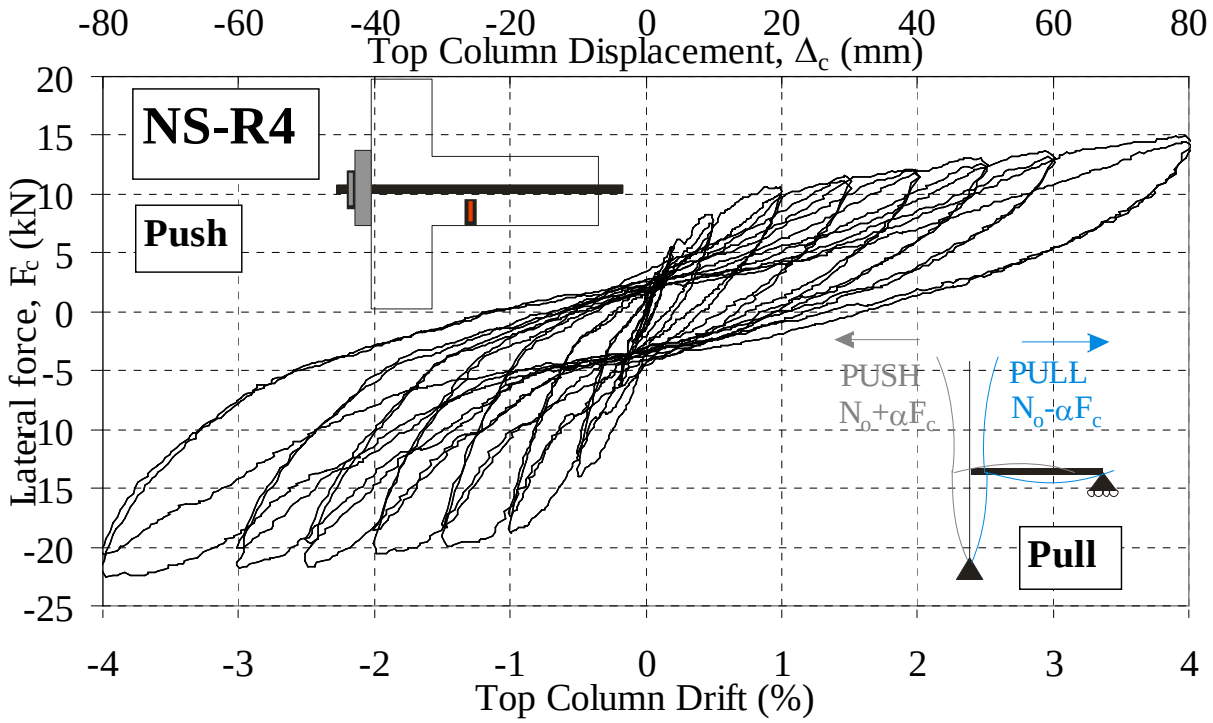

Figure 6.50: Top column lateral load, F_c versus top column displacement, Δ_c and drift, θ_{drift} for NS-R4.

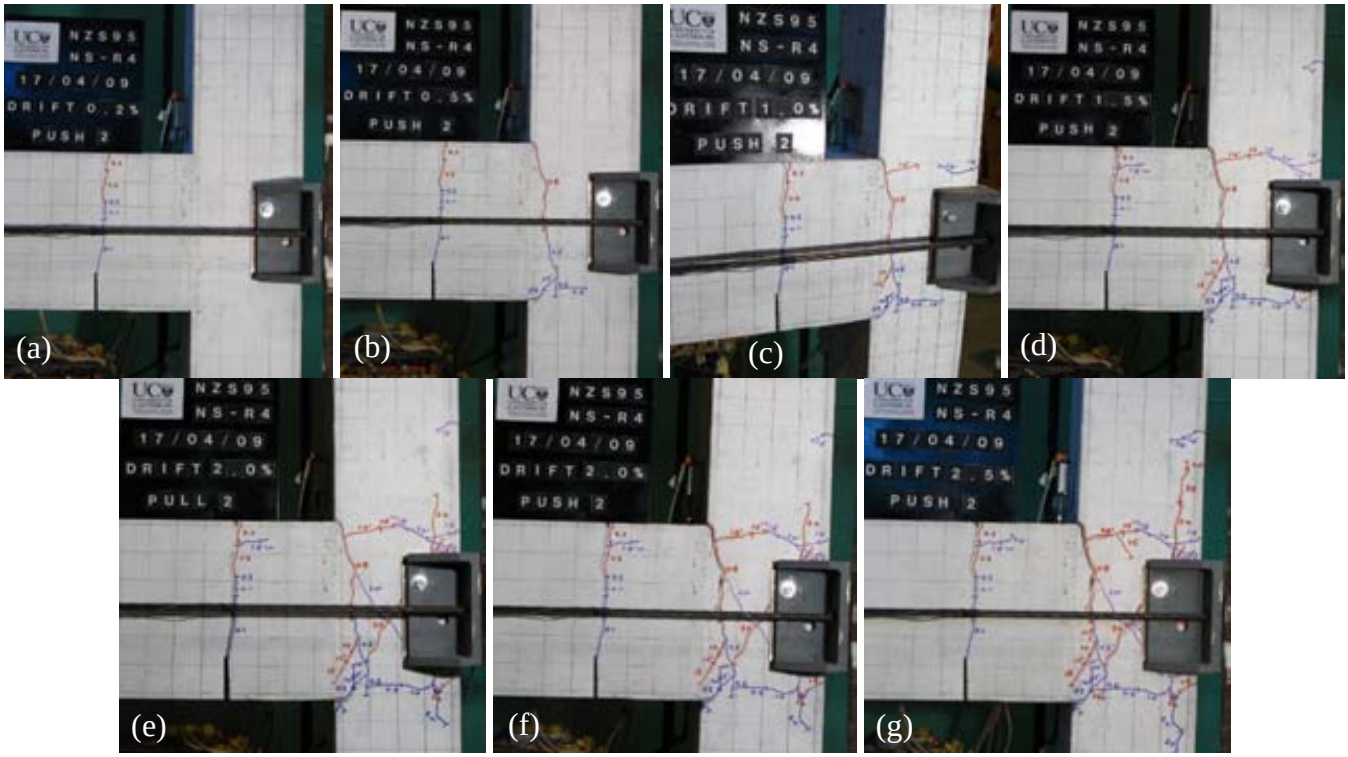

Figure 6.51: Observed cracking patterns of NS-R4: TOP: a) 2nd Push cycle of the -0.2% drift; b) 2nd Push cycle of the -0.5% drift; c) 2nd Push cycle of the -1.0% drift; and d) 2nd Push cycle of the -1.5% drift. BOTTOM: e) 2nd Pull cycle of the +2.0% drift; d) 2nd Push cycle of the -2.0% drift; and f) d) 2nd Push cycle of the -2.5% drift.

Joint diagonal cracks were observed in the 1st Push cycle of the -2.0% drift and the subsequent 2nd Pull cycle of the +2.0% drift (Figure 6.51e). However, no F_c degradation was observed as the joint post-tensioning provided an alternative joint shear force transfer mechanism while positively confining the cracked joint. For the joint cracking in the Push direction, the F_c was -19.7kN and the principal stresses p'_t and p'_c were 0.124 $\sqrt{f'_c}$ MPa and 0.910 $\sqrt{f'_c}$ MPa respectively, while for the joint cracking in the Pull direction, the F_c was +11.5kN and the principal stresses p'_t and p'_c were 0.106 $\sqrt{f'_c}$ MPa and 0.388 $\sqrt{f'_c}$ MPa respectively. Interestingly, the joint diagonal cracking in the Pull cycles occurred at lower than expected p'_t and p'_c values.

In the ±2.5% drift cycles, the joint diagonal cracks were propagating vertically into the column region and some new peripheral diagonal cracks appeared in the joint panel. The inelastic mechanism of NS-R4 gradually changed from a beam-hinging at the weakened section, to a mixture of beam and joint hinging. The crack widths at the weakened section remained constant and the cracks in the joint panel grew. The joint diagonal crack widths were 0.65-0.75mm. In terms of F_c - Δ_c loops, NS-R4 exhibited a lower bond-slip response, indicated by the less pinched hysteresis, when compared with NS-R3. However, the lateral strength degradation at the peak θ_{drift} was more pronounced in NS-R4 as the joint damages gradually reduced the beam-column joint capacity.

In the ±3.0% and ±4.0% drift cycles, further crack propagations were concentrated at the beam-column interface and the joint panel zone (Figure 6.52). At the 2nd peak of the ±4.0% drift, the maximum crack widths at the beam-column interface were 5mm and 10mm in the Pull and Push direction respectively. The maximum crack widths in the joint and column ranged between 2-3mm in the two loading directions. The cracks along the column external face longitudinal bars extended as the joint diagonal crack grew. The column longitudinal bars yielded at the first cycles of the ±3.0% drift, coupled with significant increase in the strain of the column stirrups, as indicated by the strain gages.

The damage pattern and F_c - Δ_c response indicated that beam flexural hinges at both the weakened and beam-end sections were governing up to ±1.5% drift cycles. After the joint cracking, a mixed inelastic mechanism of fixed-end beam hinging and joint shear deformation dominated the response. Despite the post-tensioning action and the selective weakening of the beam, joint shear damage increased with higher θ_{drift}. As the θ_{drift} increased, the induced elongation of the tendon, Δ_{pt}, increased and the post-yield stiffness of the F_c - Δ_c hysteresis curves

increased – and therefore the beam flexural capacity, M_b, increased, and the joint shear stress-deformation demands (i.e. V_{jh} and γ_j) increased. Nevertheless, as the joint panel was well-confined by the external post-tensioning, no significant F_c degradation was observed and the beam-column joint did not undergo 'structural failure' after the ±4.0% drift cycles.

Figure 6.52: Observed cracking patterns of NS-R4: a) 2nd Push cycle of the -3.0% drift; b) 2nd Pull cycle of the +4.0% drift; c) 2nd Push cycle of the -4.0% drift; and d) End of test after the ±4.0% drift cycles.

6.5.3 Load-displacement hysteresis analysis

The analysis of the NS-R4 F_c-Δ_c hysteresis is presented in Figure 6.53. NS-R4 response was similar to the NS-R3 F_c-Δ_c analysis (§6.4.2). Up to the ±2.0% drift, all the analysed parameters (k_{eff}, energy dissipations and ξ_{hys}) were consistent with NS-R3. Between the ±2.5 to ±4.0% drifts, energy dissipation capacities decreased by 15-20%, as joint shear damage limited the effectiveness of NS-R4. This was reflected in the narrower F_c-Δ_c hysteresis loops and larger unloading pinching behaviour. The energy dissipation capacity for NS-R4 was similar to NS-R3. Between the typical design θ_{drift} (1.0%-2.5%), the ξ_{hys} were on average, 14.1% and 10.4% for the 1st and 2nd cycles respectively. However, ξ_{hys} for the drift levels after the joint cracking (θ_{drift} = ±2.5% to ±4.0%), the average ξ_{hys} were 11.6% and 9.3% for the 1st and 2nd cycles respectively.

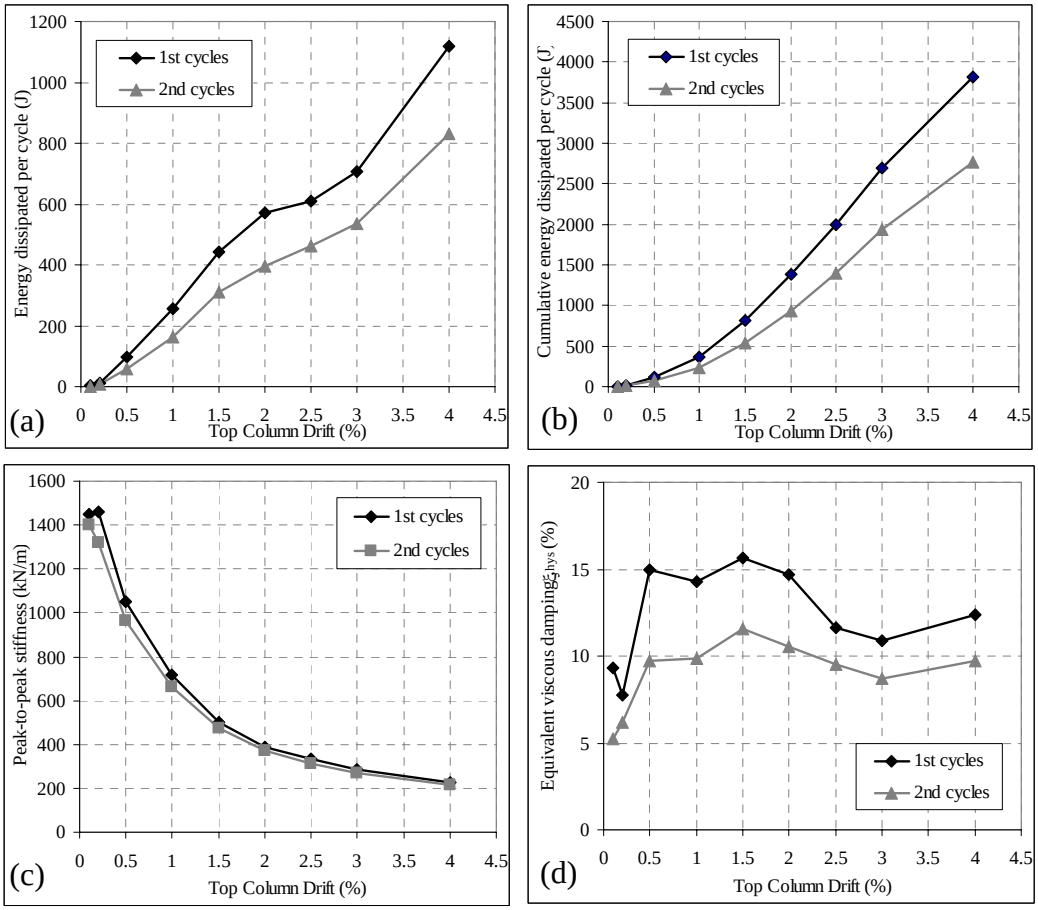

Figure 6.53: F_c-Δ_c analysis for NS-R4: a) Energy dissipated per cycle; b) Cumulative energy dissipated per cycle; c) peak-to-peak stiffness, K_{eff}, and; d) Equivalent viscous damping, ξ_{hys}.

6.5.4 Local deformations and displacement components

6.5.4.1 Decomposition of top column horizontal displacement

The components of the top column horizontal displacement, Δ_c at the peaks of the Pull and Push loading cycles as percentages of the total Δ_c are presented in Figure 6.54. The measurement for the beam fixed-end deformation, $\Delta_{beam,fixed\text{-}end}$, was blemished by the minor error within the two linear potentiometers, whereas in the shortening measuring direction, the peak displacements were truncated into plateau values. This resulted in slightly erratic $\Delta_{beam,fixed\text{-}end}$ and neutral axis (§6.5.7.2), and a large 'unaccounted' component as the θ_{drift} increased. Nevertheless, Figure 6.54 confirms the general damage observation that a mixed inelastic deformation of beam and joint was dominating the response after the ±1.5% drift, in particular in the Push loading direction.

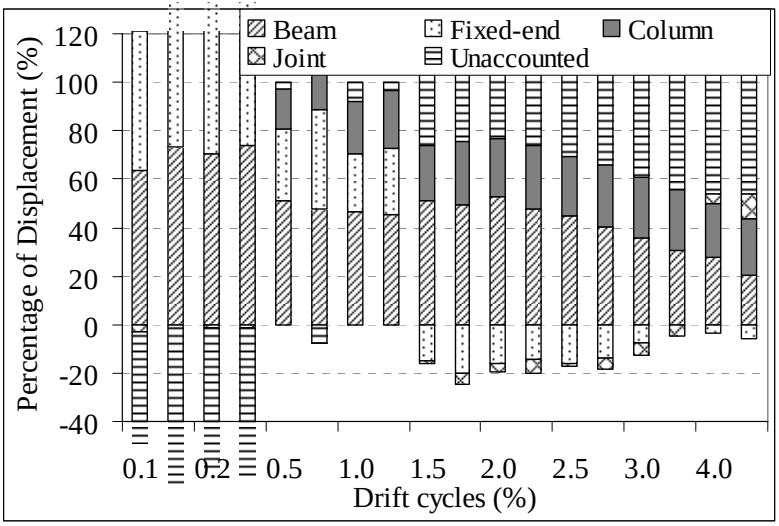

a) Pull loading direction – positive displacement.

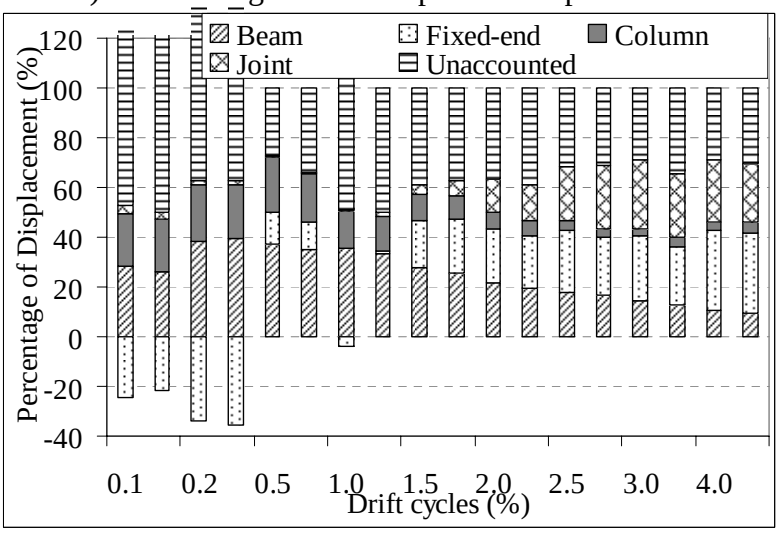

b) Push loading direction – negative displacement.

Figure 6.54: Displacement decompositions based on the measured deformations for NS-R4.

6.5.4.2 Beam deformations

The moment-curvature plots for the beam flexural regions and beam fixed-end region are shown in Figure 6.55. Most of the beam cracks and inelastic deformations were concentrated at the pseudo-rocking interface at both the weakened section (at early stages of the loading) (Figure 6.55b) and the beam fixed end section (at later stages) (Figure 6.55a).

In the Pull direction, a maximum ϕ_b of 0.066m^{-1} was measured in the flexural section with the weakened section (75-275mm from the column internal face). A maximum M_{bf} developed was 23.8kNm in the weakened section. In the Push direction, the inelastic deformation was

concentrated at the fixed-end region of the beam. A maximum ϕ_b of 0.19m^{-1} was measured at the -4.0% drift, with a maximum M_{bf} of 40.6kNm.

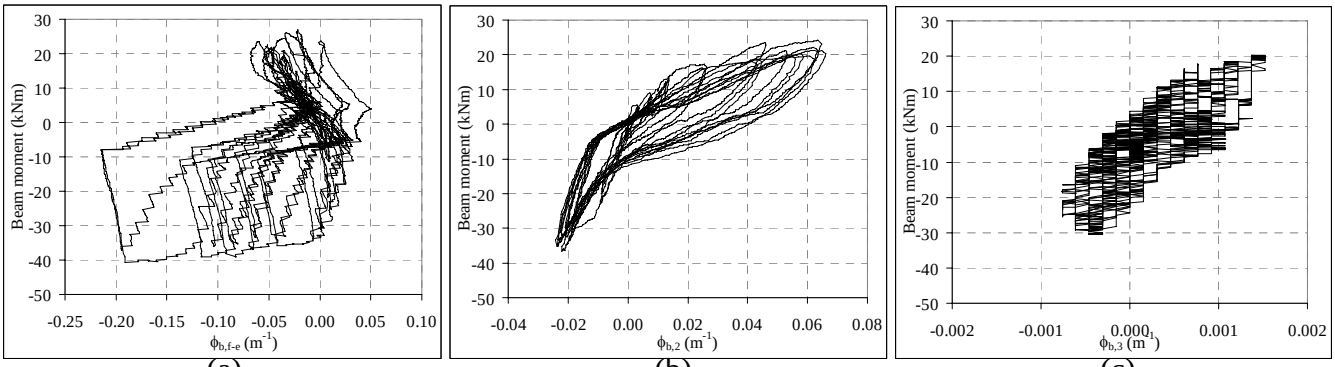

(a) (b) (c)

Figure 6.55: a) Moment-curvature plots for beam sections: a) 0-75mm from the column internal face; b) 75-275mm from the column internal face; and c) 275-475mm from the column internal face.

6.5.4.3 Column deformations

The measured moment-curvature response for the three regions of the column is shown in Figure 6.56. The observed nominal column flexural strength, $M_{c\text{-}cf}$ (the plateau moment in the hinging direction), were +10.2kNm and -16.5kNm in the Pull and Push cycles respectively. In the Pull cycles, the $M_{c\text{-}cf}$ corresponded to the ϕ_c of 0.126m^{-1} and of 0.041m^{-1} at the top and bottom halves of the column. In the Push cycles, the $M_{c\text{-}cf}$ corresponded to the ϕ_c of -0.022m^{-1} and of -0.033m^{-1} at the top and bottom halves of the column. The column response for NS-R4 was the same with the NS-R3 response except for the lower $M_{c\text{-}cf}$ in the Pull direction.

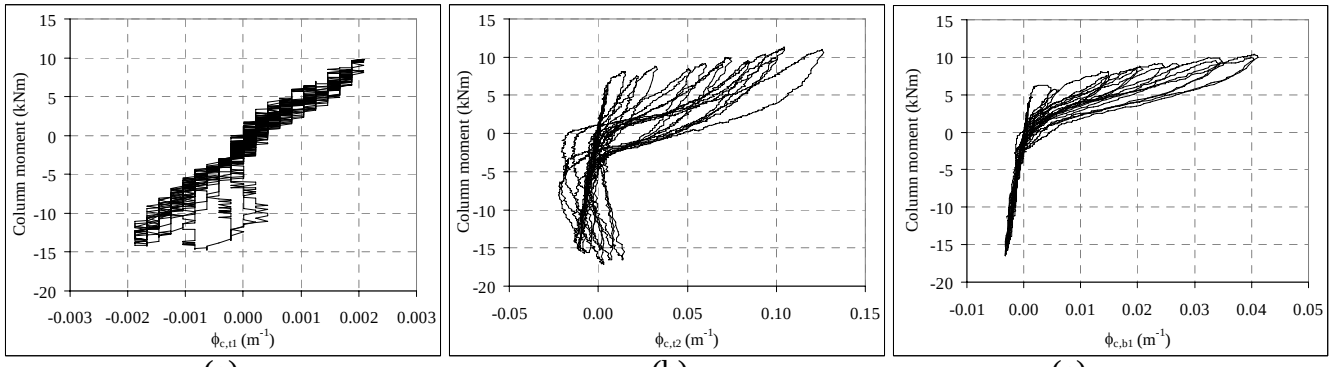

(a) (b) (c)

Figure 6.56: Moment-curvature plots for column flexural sections: a) 200-430mm from the beam top face; b) 0-200mm from the beam top face; c) 0-200mm from the beam soffit.

6.5.5 Beam-column joint behaviour

6.5.5.1 Nominal joint shear stress and joint shear distortion

The nominal joint shear stress, v_{jh}, versus joint shear distortion, γ_j, and Δ_c relationships for NS-R4 are given in Figure 6.57. The maximum v_{jh} measured were 1.73MPa (0.315 $\sqrt{f'_c}$ MPa or 0.057f'_c MPa) and -2.62MPa (-0.475 $\sqrt{f'_c}$ MPa or -0.086f'_c MPa) in the Pull and Push peaks of the ±4.0% drift. In the Pull direction (positive v_{jh}), γ_j was limited to -0.0005 radians up to the +3.0% drift cycles and γ_j grew significantly up to 0.005 radians in the two +4.0% drift cycles. The γ_j was accumulated in the Push loading direction as the first joint cracking occurred in the 1st Push cycle of the -2.0% drift. The maximum γ_j in the Push direction was 0.015 radians, indicating extensive joint damage (§2.4.2.1), without any observable degradation of v_{jh}.

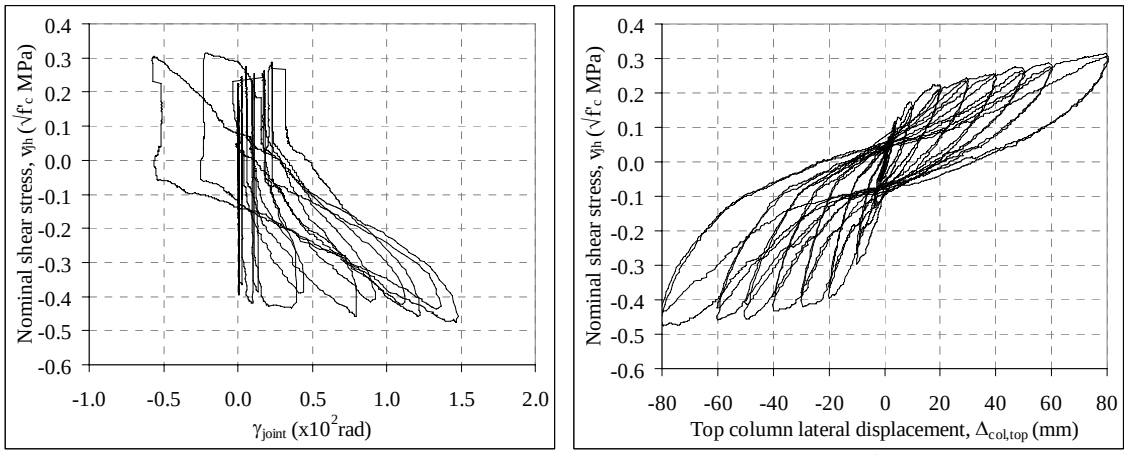

(a) (b)

Figure 6.57: a) Nominal joint shear stress, v_{jh}, versus joint deformation, γ_j; b) Nominal joint shear stress, v_{jh}, versus top column lateral displacement, Δ_c.

6.5.5.2 Joint principal stresses

Figure 6.58 shows the joint principal stress responses as functions of the Δ_c and γ_j for NS-R4. In terms of maximum principal stresses in the joint during the cyclic loading of NS-R4, the maximum p'_t was 0.169$\sqrt{f'_c}$ MPa at γ_j =-0.0022 radians and the maximum p'_c was 1.00$\sqrt{f'_c}$ MPa at γ_j =+0.015 radians. At the first joint diagonal cracking at the 1st Push cycle of -2.0% drift, the corresponding p'_t, p'_c and γ_j were 0.124$\sqrt{f'_c}$ MPa, 0.910$\sqrt{f'_c}$ MPa and -0.0039 radians. These values suggested that the joint cracking was a result of p'_c failure. However, no significant degradation of p'_c was observed after joint cracking, possibly due to the post-tensioning active confinement despite the gradual growth of joint shear deformation. For the joint diagonal crack in the 2nd Pull cycle of the +2.0% drift, the corresponding p'_t, p'_c and γ_j were 0.106$\sqrt{f'_c}$ MPa,

0.388$\sqrt{f'_c}$ MPa and -0.0017 radians. After the joint cracking, p'_t continuously rose up to 0.169$\sqrt{f'_c}$ MPa with minor growth in γ_j.

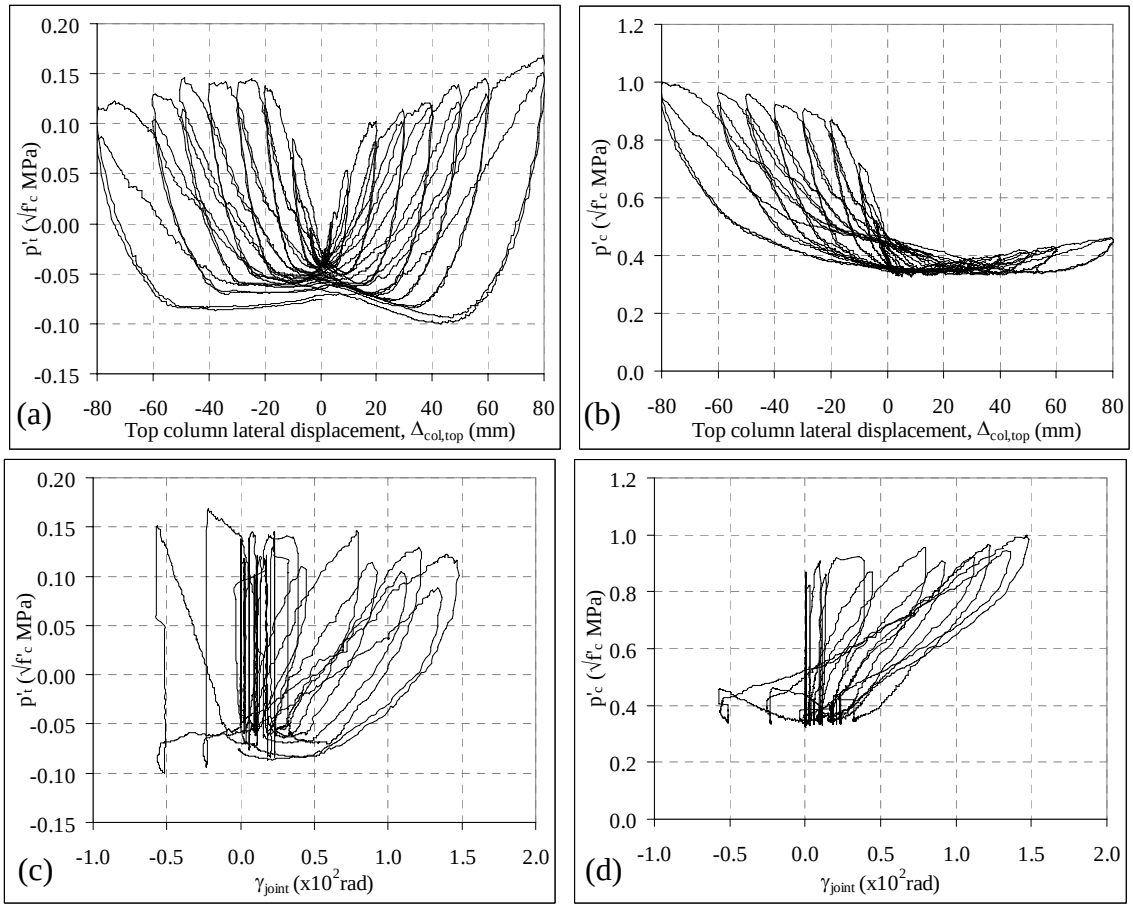

Figure 6.58: a-b) Joint principal stresses versus top column lateral displacement, Δ_c: a) principal tensile stress, p'_t; b) compressive tensile stress, p'_c; c-d) Principal stresses versus joint shear deformation, γ_j plots: c) principal tensile stress, p'_t; d) compressive tensile stress, p'_c.

6.5.6 Steel strain profiles

6.5.6.1 Beam longitudinal reinforcement strains

Figure 6.59, Figure 6.60 and Figure 6.61 present the strain profiles of the top and bottom (not weakened and weakened) beam longitudinal reinforcements for the specimen NS-R4. The X-axis is the distance from the exterior column face while the two vertical dashed lines refer to the column centre-line and the interior column face. The beam weakening section was 195mm from the interior column face and 425mm (shown on the X-axis) from the column exterior face.

Top bars strain profiles were similar as the NS-R3 responses (§6.3.5.1) except for higher tensile strains during the Push cycles. Strain concentration at the weakened section and in later

θ_{drift} levels, at the beam-column interface, was observed. Bond failure resulted in almost uniform tensile strain across a 330-350mm debonded length. Bond failure occurred after the yielding of the top bars in tension in the -0.5% drift cycles. In the reverse Pull cycles, the top bars underwent significant compression strains and yielded in the beam-column interface region at the +1.5% drift. At the weakened section, the maximum compressive strains attained was approximately 1100 microstrains, as bond failure limited the compressive strain development beyond the +1.5% drift. The top beam bars embedded within the joint region underwent high tensile strains in both Pull and Push loadings after the joint cracking at the -2.0% drift cycles.

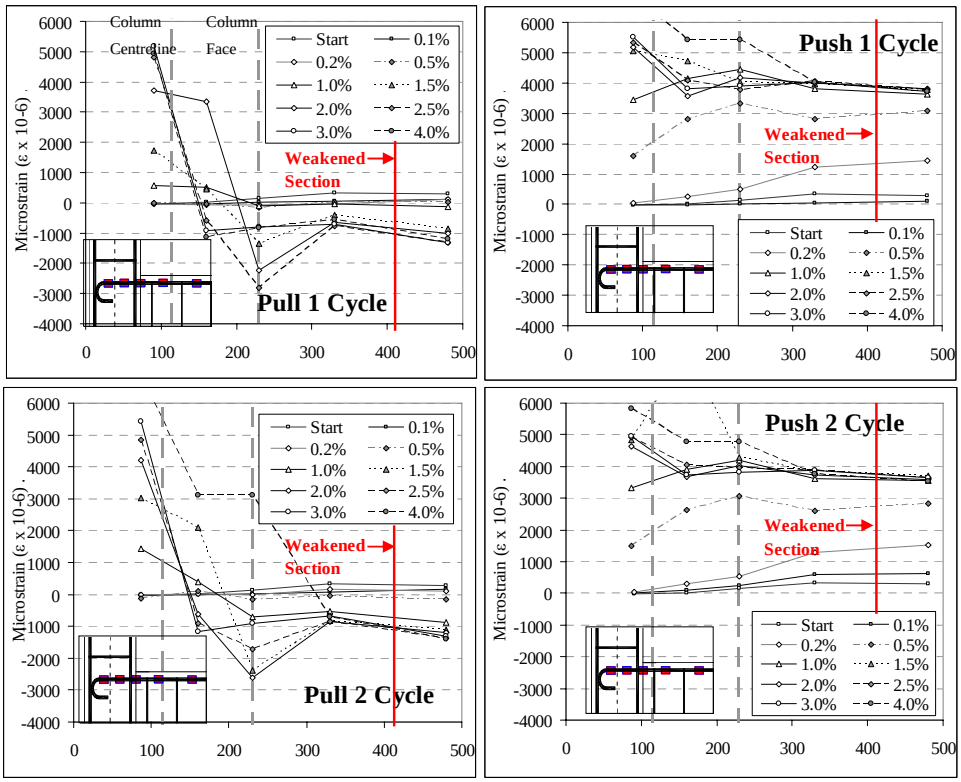

Figure 6.59: Strain profiles of beam top longitudinal bars of the specimen NS-R4.

The strains of the bottom longitudinal beam bars in the Pull loadings showed the effects of shifting the weakened section away from the beam-column interface in NS-R4. For the un-weakened beam bars (Figure 6.60), it was evident that in the Pull loading, the beam was yielding initially at the weakened section (at +0.2% drift) with subsequent yielding in the whole measured length of the beam bar by the +0.5% drift. By +1.0% drift cycles, the strains measured on the beam bars outside the joint were 4000 microstrains and did not increase with increasing drifts.

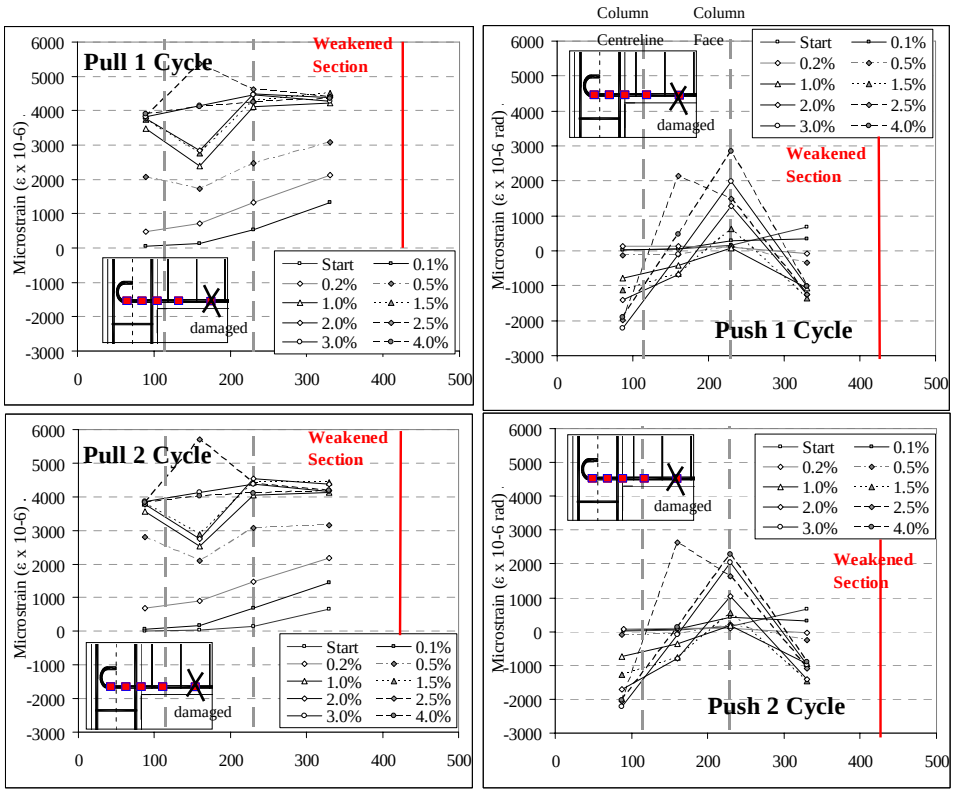

Figure 6.60: NS-R4: Strain profiles of beam bottom longitudinal bars (interior bars – not weakened).

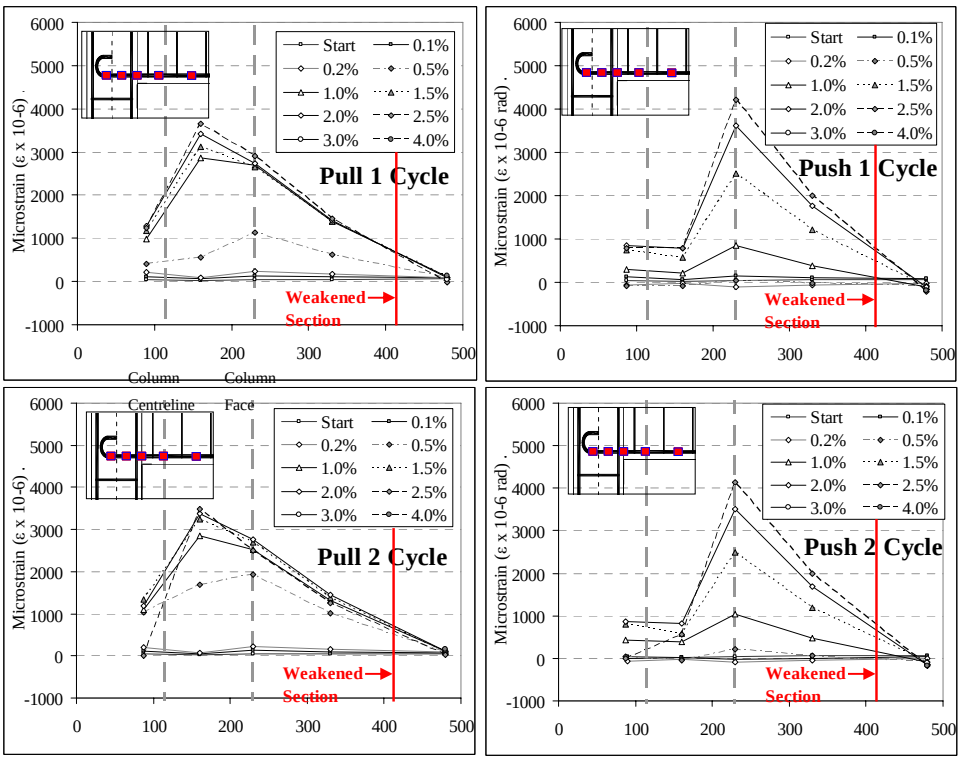

Figure 6.61: NS-R4: Strain profiles of beam bottom longitudinal bars (exterior bars – weakened).

In the Push loading direction, significant tensile strains were measured at the beam-column interface for both weakened and un-weakened bottom bars. Recalling that the crack width at the beam-column interface was as wide as 10mm, the high tensile strain was probably due to the fact that the beam reinforcements underwent considerable localised elongation as the beam elongated. For the un-weakened bar, significant compressive strains up to 2000 microstrains were measured outside the beam-end large crack.

6.5.6.2 Column longitudinal reinforcement strains

The strain profiles along the exterior and interior column bars are shown in Figure 6.62 and Figure 6.63 respectively. The Y-axis is the distance from the centre-line of the beam. The three horizontal dashed lines refer to the beam soffit (bottom line), beam centre-line and the beam top face (top line). As with all strain gage readings, tensile strains were measured as positive values. All column strain gages were zeroed before the axial force loading on the column at the start of the test. The ε_y for the longitudinal column reinforcements was 1680 microstrains and the f_y was 335MPa.

In general, the column strain profiles were similar to NS-R3 (§6.4.5.2) except for the column interior bars under the Pull loading cycles. For the column interior bars, significantly higher tensile strains were measured in NS-R4 as the joint cracking resulted in the column longitudinal bars carrying some of the joint shear forces. This was dissimilar to the NS-R2 column bars (§6.3.5.2) in which the column bars were yielding due to column flexural hinging.

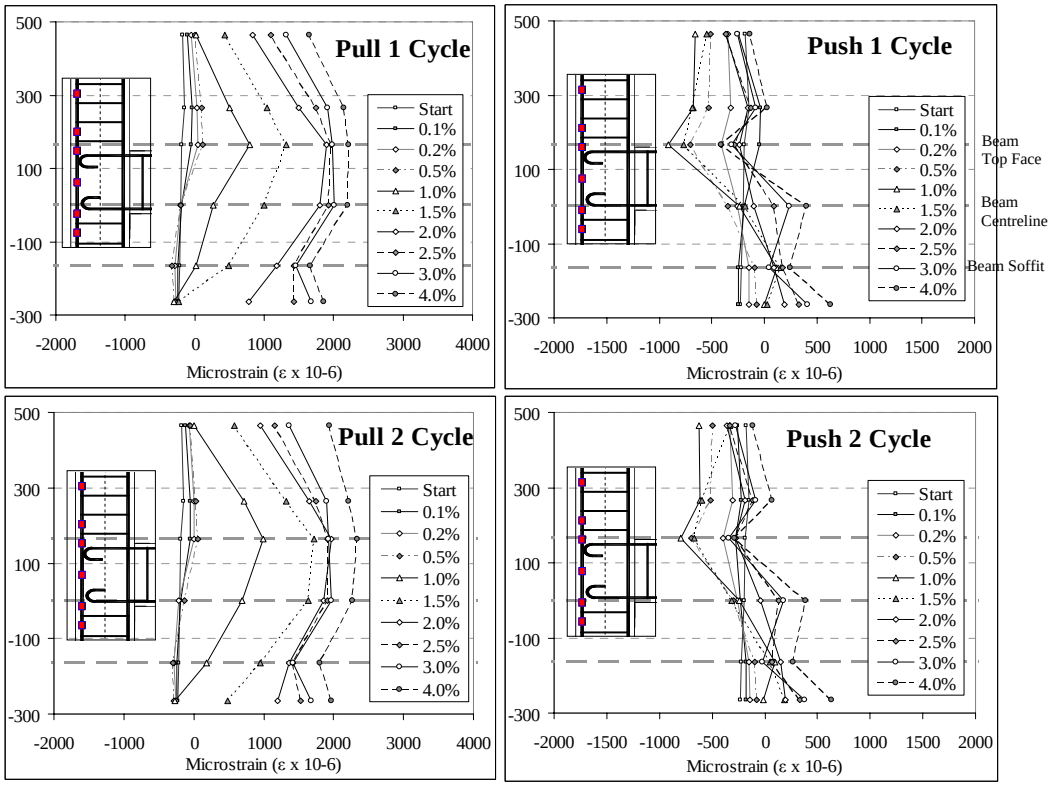

Figure 6.62: Column exterior face longitudinal reinforcements strain profiles for the specimen NS-R4.

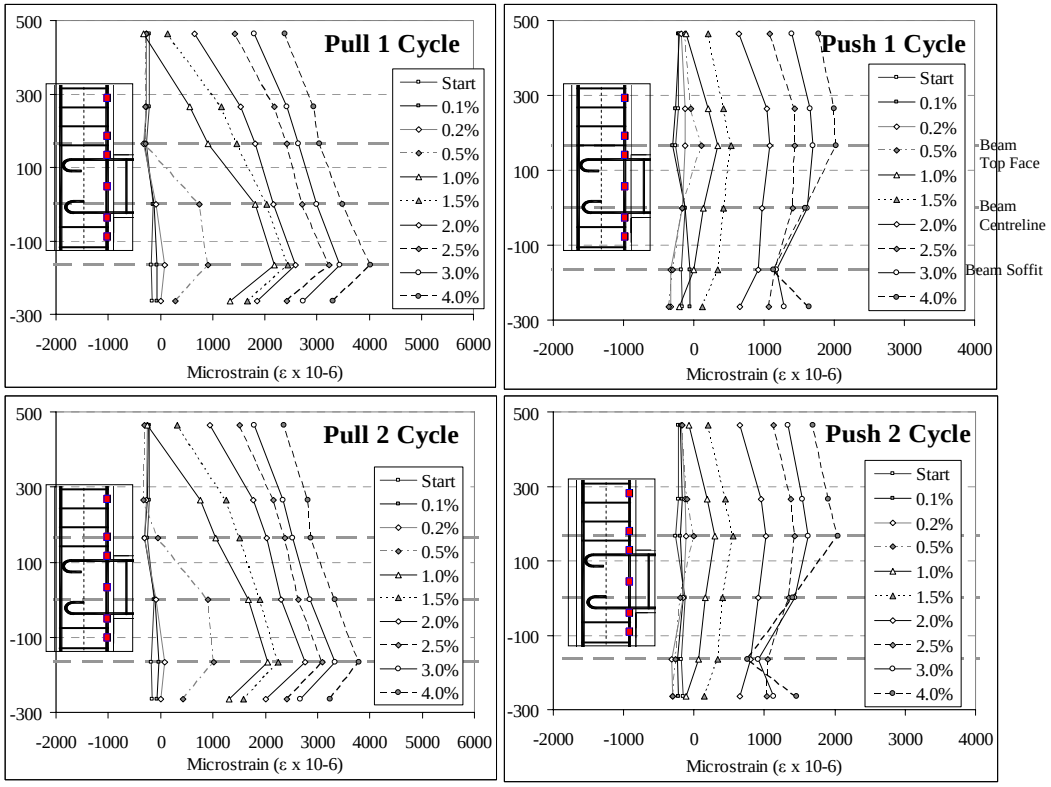

Figure 6.63: Column interior face longitudinal reinforcements strain profiles for the specimen NS-R4.

6.5.6.3 Stirrup reinforcement strains

The strain profiles of the stirrups in the column and the beam are shown in Figure 6.64. The column stirrups strain distributions were similar to the other specimens in which tensile stresses were observed after the column flexural and joint shear cracking. Figure 6.64c and d show the beam stirrup strain measurements for the stirrup before (BS1A) and after (BS2A) the beam-weakening section. It can be observed that for both loading directions, BS1A was in compression and BS2A was in tension, suggesting the conventional Mörsch truss shear mechanism [8]did not extend across the weakened section and a larger concrete diagonal compressive strut might be in effect. The high tensile strain measured in the longitudinal bars across the BS1A stirrup also suggested significant dowel force in carrying the beam shear.

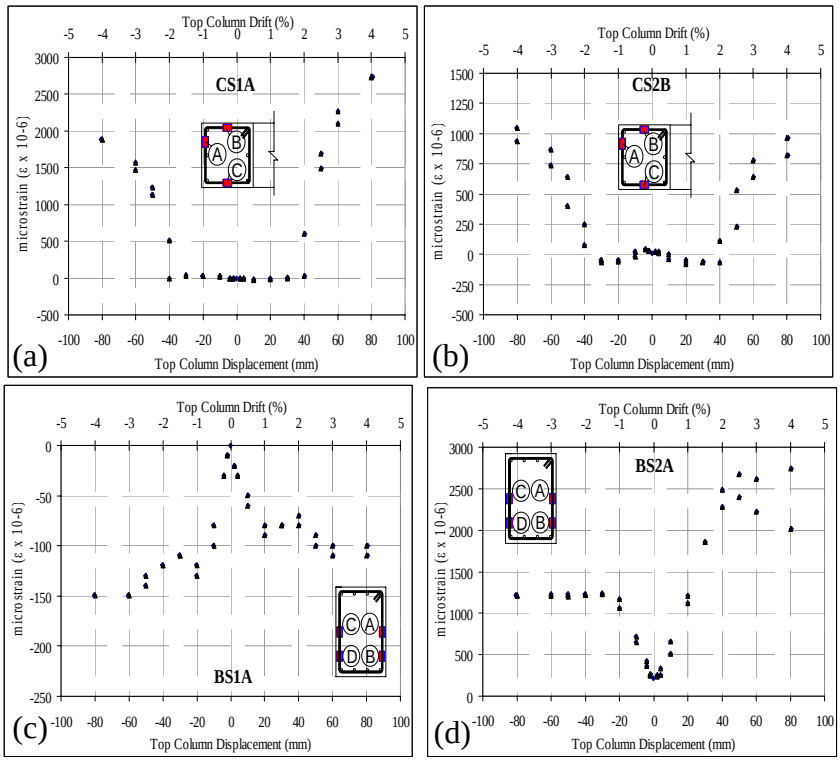

Figure 6.64: Stirrup reinforcement strain profiles: a) column stirrup 50mm from beam soffit; b) column stirrup 50mm from beam top face; c) beam 1st stirrup - 50mm from column interior face; and d) beam 2nd stirrup - 183mm from column interior face.

6.5.7 Discussion of the NS-R4 specimen

6.5.7.1 Analytical-experimental comparison for lateral strength, F_c

The F_c-Δ_c experimental-analytical comparison for the specimen NS-R4 is given in Figure 6.65. The analytical procedure described in §3.4 (Chapter 3) was used to generate the predicted F_c-Δ_c

envelope. The predicted F_c at design concrete strain (ε_c = 0.003) were +14.5kN and -19.3kN, while the maximum F_c values measured in the experiment were +14.9kN (at +4.0% drift) and -22.6kN (at -4.0% drift) in the Pull and Push loading directions respectively. The experimental-analytical comparison showed a very good agreement in terms of overall F_c-Δ_c envelope, confirming the analytical method for design.

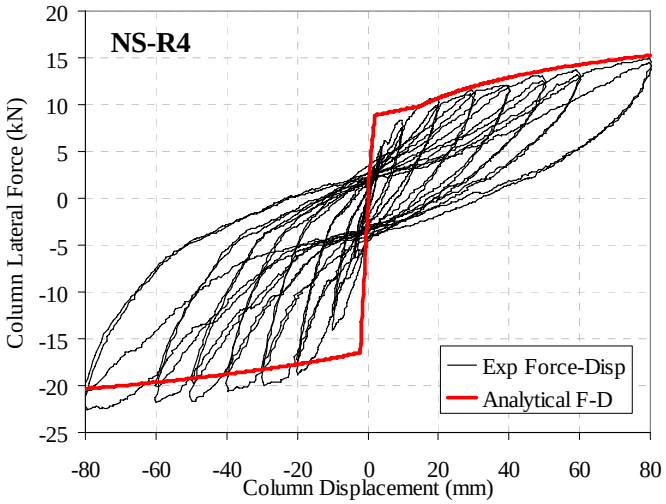

Figure 6.65: Experimental-analytical comparison of the F_c-Δ_c curves.

However, the design procedure did not predict any joint shear damage, while NS-R4 had joint shear cracking at the ±2.0% drift cycles. This discrepancy arose as the analytical evaluation underestimated the post-yield stiffness, in particular, in the Push direction as seen in Figure 6.65. The retrofit design was very sensitive to the p'_t limit state for joint cracking. For NS-R4, the differences in equivalent column moment, M_c, between a beam-hinging and a joint shear cracking performance level ranged between 5% and 20%, depending on the assumption of p'_t for joint cracking. Consequently, with reduced joint post-tensioning force and higher than expected joint shear demand from higher beam moment, NS-R4 could have joint shear cracking.

6.5.7.2 Post-tensioned pseudo-rocking interface behaviour

The predicted values of post-tensioning tendons' forces and neutral axis position at the pseudo-rocking interface are shown in Figure 6.66 and are compared with the experimental results. The prediction for the post-tensioning tendon forces was matching the experimentally observed values up to ±2.0% drift. After the joint diagonal cracks and the shifting of the beam flexural hinge to the beam-column interface section, - the analytical model was under-predicting the post-tensioning forces as it did not account for the additional elongation due to joint crack and

secondary flexural gap. As the weakening section was 195mm from the beam-column interface, the postulated pseudo-rocking interface was shifted outward. As such, the set of potentiometers measuring the 'neutral axis' across the rocking interface, as set out in §4.8.4, was no longer sufficient.

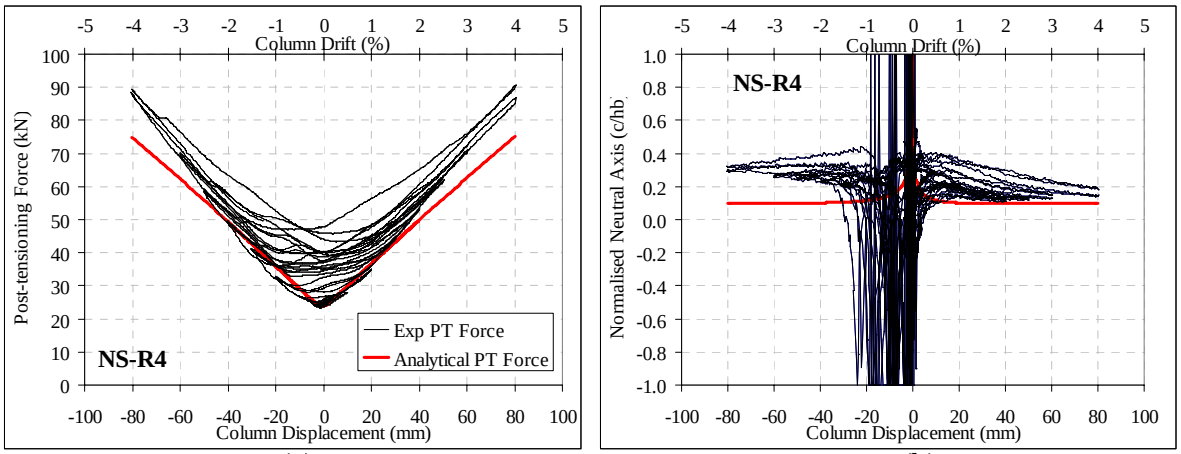

Figure 6.66: Analytical prediction and experimental response at the post-tensioned pseudo-rocking interface: a) Tendon forces; and b) Neutral axis depth, normalised to the beam depth, h_b.

6.6 DISCUSSION OF TEST RESULTS

6.6.1 Analytical prediction as per design procedures

In general, the analytical procedures outlined in Chapter 3 gave reasonably good assessment of the failure modes and lateral strengths for all the SW-retrofitted beam-column joints, as summarised in Table 6.1. Discussion for the analytical procedures for NS-R1, NS-R2, NS-R3 and NS-R4 have been given in §6.2.6.1, §6.3.6.1, §6.4.6.1 and §6.5.7.1 respectively.

The assessment of the steel stress, f_s, developed in these plain round bars under cyclic loading, is the crucial deficiency in the analytical procedure. This is mainly due to the variability of bond strength of plain round bars, which mainly relies on the adhesive and frictional bond resistance. Furthermore, progressive bond failures along the plain round bars, initiated at the cracking location, such as those discussed in §6.4.5 and §6.5.6, are highly unpredictable due to the interdependency between the bond stress-slip demand (from f_s due to beam action and the unbonded length of the bar) and the bond stress-slip capacity (which limits f_s and increases the unbonded length). Figure 5.19 and §5.7.2 of Chapter 5 have previously discussed the nature of progressive bond failure of plain round bars and the localisation of the cracking and strain over a

length of unbonded length. Nevertheless, for the purpose of practical design and assessment, the analytical procedure outlined in §3.4.4-§3.4.6 is adequate.

Table 6.2 presents the comparison between the quick design approach (§3.4.3) and the experimental results. It is found that the quick design approach is giving reasonable approximation of the F_c at the ±2.0% drift. For NS-R2, the quick design is assuming a beam-hinging mechanism while the in experiment, column hinging is observed. For NS-R4, the test result is significantly higher (39% - 44%) than the quick design approximation, while the detailed analytical procedure provides a good match with the experimental results (§6.5.7.1). As the quick design approach does not consider a possibly larger post-yield stiffness from a lower initial post-tensioning force, the quick design value for the NS-R4 specimen is expectedly inaccurate.

Table 6.2: Comparison between the quick design and the experimental results.

Test Unit	Observed Failure Mode	Experimental Peak F_c (kN)		Experimental F_c at 2.0% drift (kN)		Quick Design F_c (kN)		Ratio of Exp-to-Design Load/Capacity[1]	
		Pull (+ve)	Push (-ve)	Pull (+ve)	Push (-ve)	Pull (+ve)	Push (-ve)	Pull (+ve)	Push (-ve)
NS-R1	Beam Flexural and Bond	8.2	-15.4	7.3	-14.1	7.0	-14.0	1.04	1.01
NS-R2	Beam and Column Hinging	18.4	-25.2	16.9	-25.7	27.4	-27.4	0.62	0.94
NS-R3	Beam Flexural Hinging	17.4	-21.6	14.7	-19.5	11.5	-18.5	1.28	1.05
NS-R4	Beam Flexural Hinging	14.9	-22.6	12.2	-20.5	8.5	-14.7	1.44	1.39

Positive force, displacement and drift correspond to PULL cycles while negative values indicate PUSH cycles.

[1] When compared to the experimental F_c at the 2.0% drift.

6.6.2 Comparison between the four retrofit solutions

Figure 6.67 shows the F_c-Δ_c hysteresis comparison between the four retrofitted specimens. Figure 6.68 compares the energy dissipation capacities of the four retrofitted joint in terms of the equivalent viscous damping, ξ_{hys}. All four retrofit solutions successfully extended the displacement and ductility capacities by changing from a brittle inelastic mechanism to a ductile inelastic mechanism. As seen in Figure 6.68, at least ξ_{hys} of 10% was achieved for the typical design θ_{drift} values for all four retrofitted specimens.

While NS-R1 has lower F_c capacity compared to other solutions, it has higher energy dissipation capacity with the ξ_{hys} up to 25-30% before compressive anchorage failure in the ±3.0% drift cycles. The higher flexibility due to lower lateral strength is then compensated with the lower displacement demand from higher hysteretic damping. Therefore, as explained in the

global design methodology described in §3.4.2, the R1 retrofit solution can be designed to be a cheap and simple retrofit technique in order to achieve collapse prevention performance level.

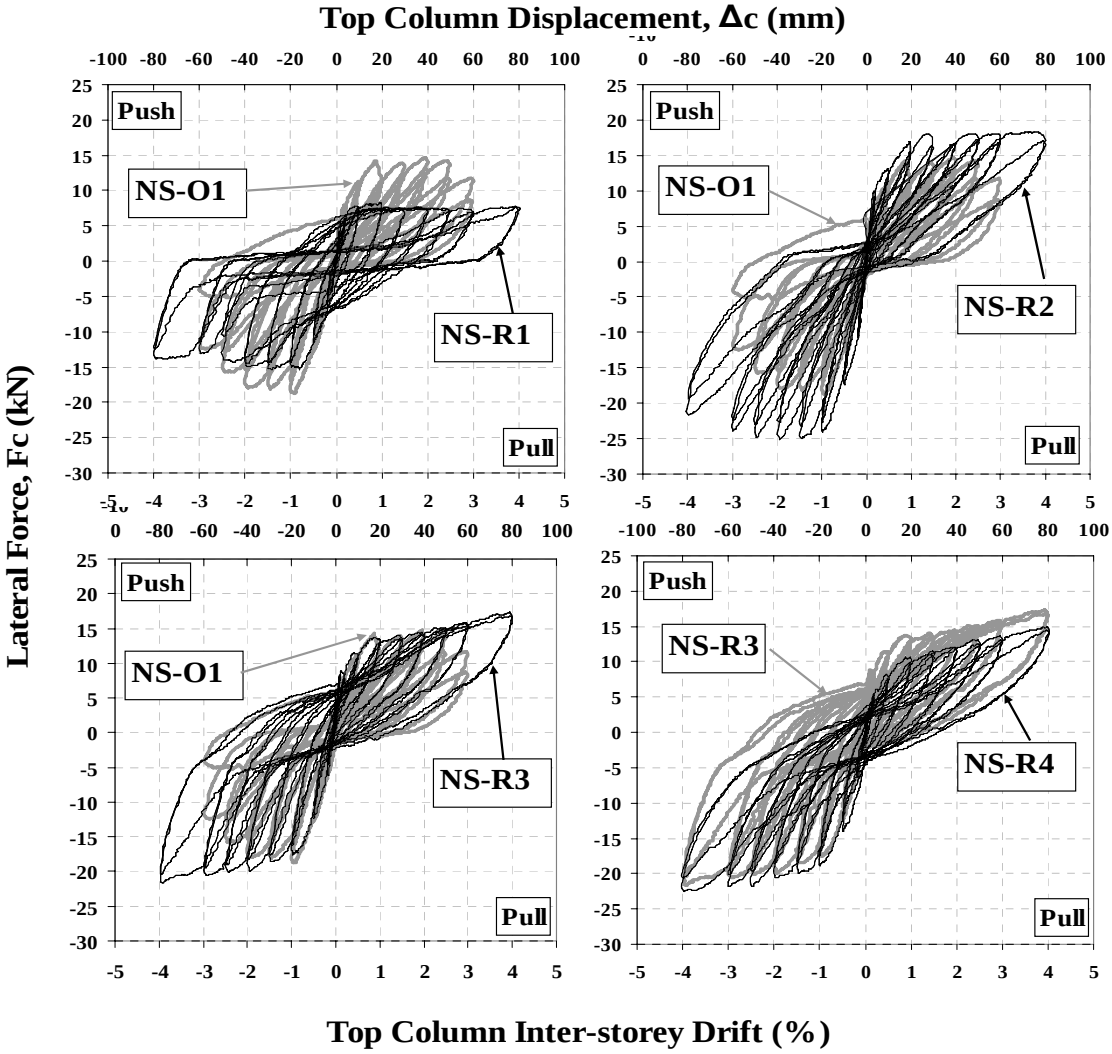

Figure 6.67: Comparison of the F_c - Δ_c and F_c - θ_{drift} hysteresis loops.

The joint post-tensioning-only retrofit solution is effective in increasing the lateral capacity of the beam-column joint subassembly. However, as illustrated in NS-R2, careful consideration for capacity design is required further retrofit interventions such as selective beam weakening, or concrete or composite jacketing on the column.

NS-R3 and NS-R4 illustrate the more ideal retrofit outcomes where the F_c is maintained or enhanced, and the inelastic mechanism and the overall seismic performance are improved. The results also confirm the versatility of the SW-retrofit techniques to achieve different performance outcome. NS-R4 result has shown that if the joint is well-confined by external post-tensioning,

some level of joint cracking can be tolerated without losing lateral strength or displacement capacity. Further considerations are required on the uncertainties in the assessment of the joint shear capacity before and after seismic retrofit.

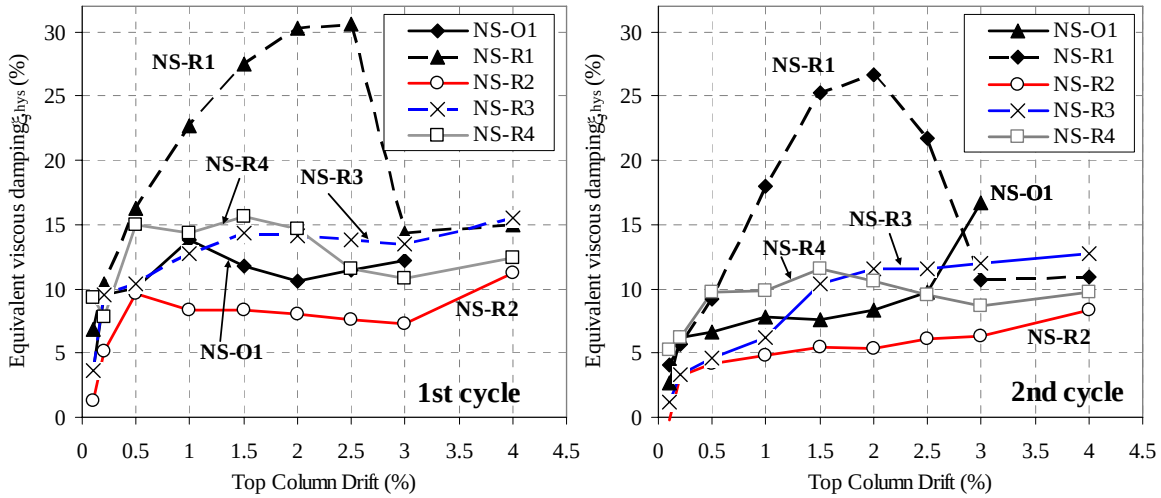

Figure 6.68: Comparison of the equivalent viscous damping, ξ_{hys} values.

6.6.3 Influence of post-tensioning forces

Three levels of post-tensioning forces are tested (NS-R2: 120kN, NS-R3: 40kN and NS-R4: 24kN) in the test specimens. These correspond to the added horizontal axial stress, f_h, of 1.581 MPa, 0.527 MPa and 0.316 MPa respectively. All three specimens have beam hinging up to ±1.5% drift, after which mixed inelastic mechanisms were observed in NS-R2 (column hinging) and NS-R4 (joint shear cracking). Thus, while higher post-tensioning force will improve the joint and beam shear behaviour via a pseudo-rocking inelastic mechanism, excessive beam-strengthening will lead to a column hinging as in NS-R2. Another drawback of excessive post-tensioning forces is the possibility of diagonal joint compressive failure, which has occurred for NS-R2 at +1.5% drift and for NS-R3 at +4.0% drift.

While from the F_c-Δ_c hysteresis envelope, it is apparent that the lower the initial post-tensioning force, the higher the post-yield stiffness of the retrofitted beam-column joint will be. The lower level of initial post-tensioning force reduces the beam moment capacity, resulting in a larger pseudo-rocking flexural crack in the beam. This in turn leads to a larger gap opening, larger tendon elongation and therefore higher post-yield stiffness of the system.

It is found that even with a low level of joint post-tensioning forces, which by itself is unable to completely prevent the joint diagonal cracking (NS-R4), and the associated active

confinement from the anchorage plate, improve the post-cracking behaviour of the joint and delay the loss of lateral strength. Figure 6.69 compares the principal stresses between the as-built NS-O1 and the two retrofitted beam-column joints NS-R3 and NS-R4.

The lower post-tensioning forces leads to the lower joint shear resistance in the NS-R4. Diagonal joint tensile cracking occurs at the ±2.0% drift cycles for NS-R4 when compared with joint tensile cracking at the +4.0% drift for NS-R3. Globally, this means lower energy dissipation and more cyclic strength degradation, when comparing NS-R4 with NS-R3. It can be seen that with higher post-tensioning forces in NS-R3, the maximum principal stresses are marginally higher (when compared with NS-R4). Furthermore, NS-R4 has more extensive joint damage and deformations.

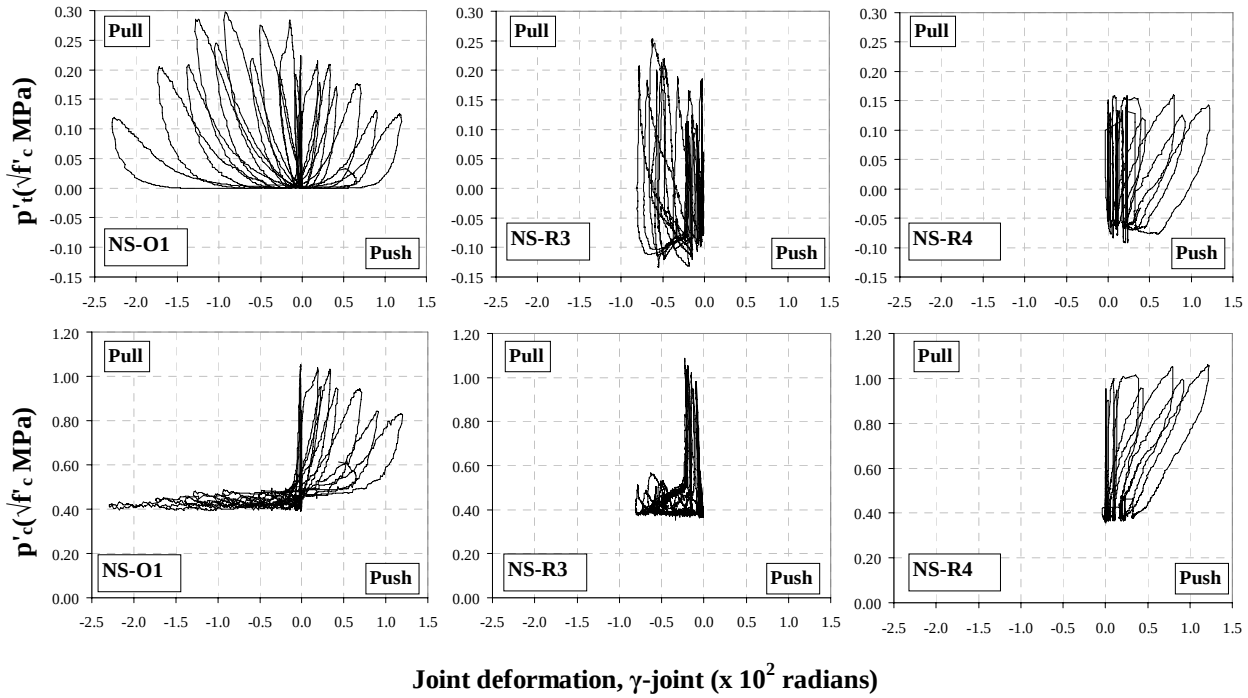

Figure 6.69: Joint shear deformation and joint principal stresses for NS-O1, NS-R3 and NS-R4.

6.6.4 Influence of beam weakening location

The shift in beam-weakening location in the NS-R4 specimen is to relocate the plastic hinge in the beam away from the joint. This will further reduce joint shear demand and will give a longer anchorage length to the beam longitudinal reinforcements, assuming the weakest section will be at the weakened section. From Figure 6.67, it is evident that NS-R3 has a higher lateral F_c in the Pull direction than NS-R4, while both specimens have similar F_c envelope in the Push direction.

The lower F_c for NS-R4 can be attributed to a) the shifted negative moment flexural hinge to the weakened section, and b) lower post-tensioning force as discussed previously.

To investigate whether the bonds of the beam reinforcements are better in NS-R4, the strain gauge readings for the top and bottom (uncut bars) during the 1st Pull peak cycles are analysed and presented in Figure 6.70. NS-R4 develops higher steel strains/stresses in both top and bottom reinforcements compared with NS-R3, thus alluding to an improved anchorage and bond performance of the NS-R4. Bond slip failure occurs in the bottom reinforcements during the Push direction, near the beam-column interface, as the steel strain decreases beyond the ±1.5% drift cycles. Similarly, in the 1st Pull cycles, steel strain decreases after the ±1.5% drift cycles in both specimens. It is believed that this strain decrease is due to bond-slip failure of the bottom reinforcements for NS-R3, while, it is due to the degradation of joint shear capacity (after diagonal tensile cracking at +2.0% drift) for NS-R4. NS-R4 also clearly illustrates the repeatability of the performance of NS-R3, albeit with lower post-tensioning forces and shifted weakened section.

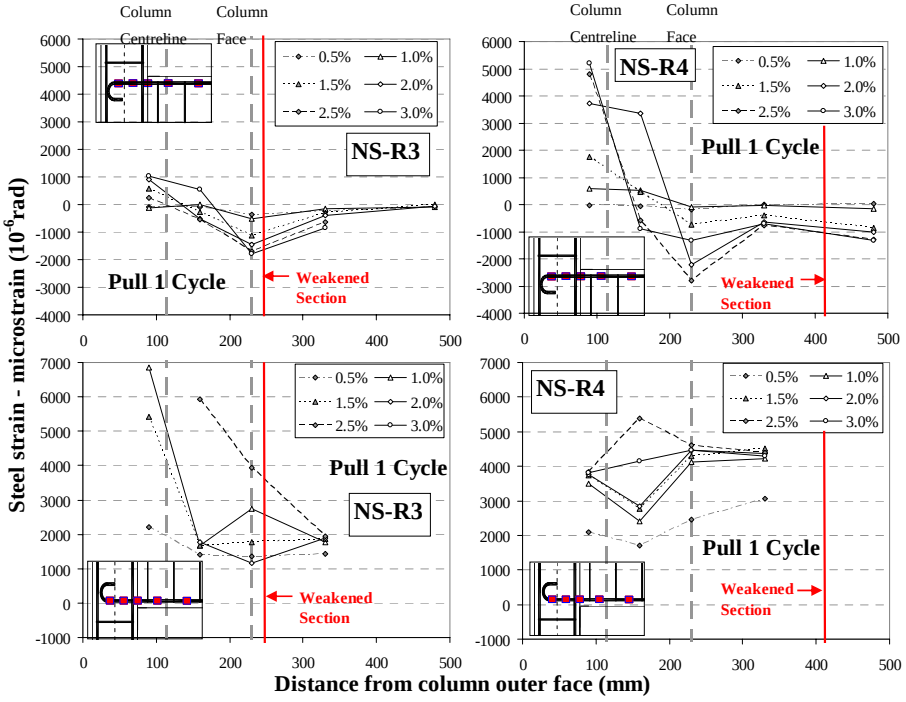

Figure 6.70: Strain gauge readings for the top and bottom longitudinal beam reinforcements for NS-R3 and NS-R4 at 1st peak at the Pull direction for different drift cycles. Grey lines are the locations for centre-line and inner column faces.

6.6.5 Trial experiments of SW retrofit for repair of beam-column joint

§3.3.3 outlined a range of proposed SW retrofit techniques for beam-column joints, from the beam-weakening only (NS-R1), the post-tensioning only (NS-R2), the Full SW retrofit (NS-R3 and NS-R4) to the advanced controlled-rocking joint retrofit (§3.3.3.3). The advanced controlled-rocking joint solution, which requires the full detachment of the beam reinforcements, was not tested on a pre-1970s non-ductile RC beam-column joint. Towards validating the SW retrofit concept, a set of trial experiments was carried out using a repaired beam-column joint designed to the NZS3101:2006 requirements. The trial tests confirmed the constructability and practicality of the external post-tensioning apparatus, while confirming the feasibility of a rocking beam-column joint retrofit. The trial experiments were also interesting confirmation that the SW retrofit can be used to repair and retrofit damaged beam-column joint. Further detail and test results of these trial experiments are available in Appendix E.

6.7 CONCLUSIONS

1. Table 6.3 below summarises the key test results of the four specimens: a) Beam-weakening-only retrofit (NS-R1), b) Joint post-tensioning-only retrofit (NS-R2) c-d) Full SW retrofit with beam-weakening and joint-post-tensioning (NS-R3 and NS-R4):

Table 6.3: Summary of NS-R1, NS-R2, NS-R3 and NS-R4 test results.

Test Unit	Peak Lateral Force (kN)	Inter-storey drift at maximum force, θ_d (%)	Ultimate inter-storey drift, θ_d (rad) [1]	Lateral Force at joint cracking (kN)	Inter-storey drift at joint cracking, θ_d (rad)	Maximum column moment, $M_{sys\text{-}exp}$ (kNm)	Theoretical column moment, $M_{sys\text{-}cal}$ [2] (kNm)	$M_{sys\text{-}exp}$ / $M_{sys\text{-}cal}$
NS-R1	+8.2 -15.4	+0.95 -0.80	-2.5%-II	na [4]	na [4]	+6.9 -12.9	+8.6 -15.1	+0.80 -0.85
NS-R2	+18.4 -25.2	+3.56 -1.96	-4.0%-II	+17.5 -24.5	+1.5%-I -1.5%-I	+15.4 -21.1	+16.7 -19.6	+0.92 -1.08
NS-R3	+17.4 -21.6	+3.93 -3.91	na [3]	-21.5	-4.0%-I	+14.6 -18.1	+12.7 -17.0	+1.15 -1.07
NS-R4	+14.9 -22.6	±4.0	na [3]	+11.5 -19.7	+2.0%-II -2.0%-I	+12.5 -18.9	+12.1 -16.1	+1.03 -1.17

Test Unit	Failure Mode	Max / Min joint shear stress, ν_{jh} (f'_c MPa)	Min / Max axial stress, f_v (MPa)	Max. principal tensile stress, p_t ($\sqrt{f'_c}$ MPa)	Max. principal compression stress, p'_c ($\sqrt{f'_c}$ MPa)	1st / 2nd cycles total energy dissipated, $E_{D,4.0\%}$ (J)	Equivalent Viscous Damping (EVD) ratio, $\xi_{hyst,2.0\%}$ [3] (%)
NS-R1	Beam Flexural and Anchorage	+0.037 -0.070	+1.29 -3.49	0.152	0.831	3987 / 2948	30.3
NS-R2	Beam/Column Flexural	+0.085 -0.116	+0.40 -4.34	0.264	1.210	3183 / 2201	8.0
NS-R3	Beam Flexural Hinging	+0.083 -0.103	+0.54 -3.97	0.254	1.087	4390 / 3439	14.1
NS-R4	Beam Flexural Hinging	+0.057 -0.086	+0.79 -4.04	0.169	1.00	3817 / 2768	14.7

Positive force, displacement and drift correspond to PULL cycles while negative values indicate PUSH cycles. I=1st cycle; II=2nd cycle. f'c =25.6MPa.

[1] Failure point defined as attained peak force was less than 80% of previous peak force. [2] Calculated maximum column moment based on the Hierarchy of Strength analysis outlined in Chapters 2 and 3. [3] $\xi_{hyst,2.0\%}$ is calculated based on hysteresis area-based equivalent viscous damping in the 1st cycle.

[4] No failure/joint cracking observed (based on the definition).

2. Specimen NS-R1 sustained inelastic beam flexural hinging up to the ±2.0% drift cycles with substantial energy dissipation capacities (ξ_{hys} = 20-30%). It failed in the ±2.5% drift cycles under compressive anchorage push-out failures due to the limited anchorage capacities of the plain round bars and 180° hook in compression. If a simple secondary upgrade to prevent anchorage failure is available, the R1 retrofit method is an efficient retrofit technique.

3. Specimen NS-R2 had a mix of beam and column hinging, as the high post-yield stiffness of the pseudo-rocking post-tensioned beam-column connection changed the hierarchy of strength in the Push direction. The experimental ξ_{hys} for NS-R2 were 5.0-8.1%. For pre-1970s beam-column joints, the NS-R2 retrofit solution almost certainly must include a complementary column retrofit solution (FRP or column jacketing). Otherwise, specimen NS-R2 highlighted the motivation to include selective beam-weakening as a part of the retrofit solution.

4. Specimen NS-R3 and NS-R4 represent the ideal SW retrofit solutions tested, in which a stable beam-hinging inelastic mechanism was attained in both cases. The joint post-tensioning increased the joint shear capacity and the beam-weakening decreased the joint shear demand. The overall effect was the prevention of joint shear failure. Furthermore, the beam-weakening reduced the beam positive moment capacity and thus encouraged beam-hinging when the column had decreasing axial load.

5. As discussed in §6.6.4, the attempt to shift the plastic hinge location by changing the beam-weakening location in NS-R4 was partially successful in the Pull direction. However, without any intervention in the negative beam moment, full relocation of the plastic hinge was not possible.

6. The influence of the initial post-tensioning forces in the SW retrofit of beam-column joint has been discussed in §6.6.3. The benefit of joint post-tensioning in reducing the principal stresses demands in the unreinforced joint was evident in all three post-tensioned specimen. Despite the joint diagonal cracking in NS-R2 and NS-R4, the active

confinement from the post-tensioning was effective in maintaining the lateral strength and deformation capacities.

7. As observed in all four retrofitted specimens, progressive penetrations of strains into the joint region for the column and beam reinforcements were the consequence of bond failure and subsequent debonding of the smooth reinforcements. This progressive bond failure prevented excessive strains of the beam top bars as the strain demands were spread across a longer unbonded length. The SW retrofit schemes discussed in this chapter did not explicitly tackle the bond weakness of the plain round bars. It is expected that the SW retrofit outcome would be improved if the as-built beam-column joint consisting of deformed bars.

8. In terms of design of post-tensioned retrofit of joint, the p'_c should be limited to $0.2f'_c$ (or $0.9\sqrt{f'_c}$) MPa to prevent the joint compressive failure, while the p'_t should be limited to $0.2\sqrt{f'_c}$ MPa if joint diagonal tensile crack is undesirable.

9. It was found that the assessment of column flexural capacities ($M_{c\text{-}cf}$) based on an assumed 'variation of axial load' might be un-conservative – particularly when an increase in the variation of column axial load was relied upon for the required $M_{c\text{-}cf}$. The considerable yielding of column reinforcements in the test specimens NS-R2 and NS-R4 suggested that a complementary column retrofit solution (FRP or column jacketing) might be necessary to achieve the capacity design principles for the retrofitted joints.

10. The accuracy and limitations of the analytical procedures described in Chapter 3 for the SW-retrofit of exterior beam-column joints were discussed in conjunction with the test results summarised in §6.6.1. In general, while there are some limitations in predicting the lateral strength of the retrofitted beam-column joints, the existing analytical procedure was deemed satisfactory for the SW retrofit design, with necessary factors of safety and capacity design considerations.

6.8 CHAPTER 6 REFERENCES

[1] ASCE-SEI-41-06. (2007) *Seismic rehabilitation of existing buildings. ASCE standard ASCE/SEI 41-06*. American Society of Civil Engineers (ASCE), Reston, Va.

[2] fib. (2003) *Seismic assessment and retrofit of reinforced concrete buildings: State-of-the-art report, fib Bulletin no. 24*. Intl. Fed. for Struct. Concrete (fib), Lausanne, Switzerland.

[3] Ingham JM. (1995) Seismic performance of bridge knee joints [PhD Dissertation]. Uni. of California, San Diego La Jolla, CA.

[4] Ingham JM, Priestley MJN, Seible F. (1997) Seismic response of bridge knee joints having columns with interlocking spirals. *Bull of New Zealand Soc of Earthquake Eng*. June 1997; **30**(2):114-132.

[5] Ingham JM, Priestley MJN, Seible F. (1998) Cyclic response of bridge knee joints with circular columns. *J of Earthquake Eng*. July 1998; **2**(3):357-391.

[6] Lowes LN, Moehle JP. (1999) Evaluation and retrofit of beam-column T-joints in older reinforced concrete bridge structures. *ACI Structural Journal*. **96**(4):519-533.

[7] Priestley MJN, Calvi GM, Kowalsky MJ. (2007) *Displacement-based seismic design of structures*. IUSS Press, Pavia, Italy.

[8] Priestley MJN, Seible F, Calvi GM. (1996) *Seismic design and retrofit of bridges*. John Wiley & Sons Inc., NY.

CHAPTER 7. INFLUENCE OF COLUMN LAP-SPLICE ON THE RETROFIT OF EXTERIOR RC BEAM-COLUMN JOINT

"Instead of looking at failure of individual columns when subjected to various axial load demands, we should perhaps look at the global response of the structure and the role of individual columns in that global response."

Thomas Paulay

In Proc. of the 9th World Conference on Earthquake Engineering (Vol. VIII; pp.595)

Tokyo, Japan. 2nd-9th Aug 1988

7.1 INTRODUCTION

7.1.1 General

While lap-splice deficiency is often studied as column deficiency, the influence of column lap-splice on the seismic performance of reinforced concrete (RC) beam-column joint can be significant. Very little research on non-ductile RC beam-column joints has included column lap-splice within its test matrix. Furthermore, very limited amount of tests [54, 57, 58] were done on columns or joint subassemblies with column lap- splice and plain round bars despite the prevalence of such configuration of construction. As some studies (e.g. [11, 15, 34]) have shown, the presence of column lap-splice just above the floor level is also a critical structural weakness that could lead to global collapse of pre-1970s RC frames. As Professor Paulay highlighted in his quote above, earthquake engineers must look beyond individual elements or failure modes but consider the interaction between the local failure modes and the global response parameters.

In the preceding chapters, the development of Selective-Weakening (SW) retrofit techniques focussed on the weakest element of the exterior beam-column joints – the unreinforced and unconfined joint panel zone. This chapter looks specifically into the influence

of column lap-splice on the seismic behaviour of as-built and SW retrofitted exterior reinforced concrete (RC) beam-column joints.

This chapter will first briefly discuss the pre-1970s building code regulations for column lap-splices and the existing research on the column lap-splice in beam-column joint connections. Then, the test results of a pair of exterior beam-column joints with inadequate lap-splice (S-O1 and S-R3) will be presented to highlight the influence of column lap-splice with plain round bars on the as-built and retrofitted joints. Lastly, the relevance of column lap-splice and extra considerations required in the SW retrofit design will be drawn from these results. This chapter will conclude by revisiting the assessment of the column lap-splice capacity in relation to the experimental results of S-O1 and S-R3.

7.1.2 Detail of test specimens with lap-splice: S-O1 and S-R3

Both S-O1 and S-R3 had the same reinforcement and geometrical details as the benchmark as-built NS-O1 specimen, with the exception of column reinforcement lap-splice above the joint region. The reinforcing details of S-O1 and S-R3 and the close-up photographs of the lap-splice detailing are given in Figure 7.1. As discussed in §4.3.5, the column lapping length used was $40d_b$, consistent with the older codes [5, 37] requirements for tension lap-splice of plain round bars. A crank in the column longitudinal bars with a slope of 1:6 was included within the column lap-splice, consistent with requirements of the 1956/1963 ACI318 [4, 5] codes. Figure 7.1b shows the chamfered ends of the longitudinal reinforcement. This was done in order to avoid excessive end-bearing anchorage from typical extruded ends from on-site steel cutting.

The second specimen, labelled as S-R3, consisted of the implementation of R3 (selective beam weakening and post-tensioning) retrofit solution (§4.3.4) on the benchmark specimen with lap-splice (i.e. S-O1). The post-tensioning force level applied was 20kN/tendon (12.8% of $f_{y\text{-}pt}$) on two mono-strand 12.9mm diameter tendons. The details of the test units S-O1 and S-R3 have been presented in Chapter 4, in particular in §4.3.5. The hierarchy of strength performance domains for both specimens are presented in Appendix B.

Figure 7.1: Detail of column lap-splice in specimen S-O1: a) S-01 reinforcement cage; b) chamfered end of the lapped reinforcement; c) Lap-splice length of 400mm ($40d_{b,c}$). (reproduced Figure 4.11 of Chapter 4)

7.2 RELEVANCE OF COLUMN LAP-SPLICE IN BEAM-COLUMN JOINTS

7.2.1 Pre 1970s building codes for column lap-splices

The historical approach to column lap-splice and anchorage of reinforcement was to consider the maximum allowable (in both maximum and average) bond stresses given the flexural bond and anchorage bond demands. This was the case for the early New Zealand Standard (NZS) concrete codes [36-38]. In the 1955 revision of the NZS building code [37], deformed and plain round bars were explicitly defined and distinguished by assigning 10% higher permissible bond stresses to deformed bars. In the region of lapping, no extra transverse reinforcement was typically provided. Figure 7.2 shows some examples of columns lap-splice detail typical of pre-1970s RC construction in New Zealand. In the absence of capacity design to prevent flexural hinges in the columns, premature failure of the lap-splice can be expected in these pre-1970s columns (e.g. [14, 42, 46]).

In NZS95:1955 [37] code, a minimum lap length of no less than 40 times the column longitudinal bar diameter, $d_{b\text{-}col}$, was specified for reinforcement acting both in tension and compression. For exterior columns though, lap-splice lengths between $24d_{b\text{-}col}$ to $40d_{b\text{-}col}$ have been observed in older building drawings. Some previous international research [11, 12] have adopted lap length between $20d_{b\text{-}col}$ to $30d_{b\text{-}col}$ for deformed bar specimens, based on the ACI 318 [4, 5] codes. As mentioned in §2.2.1, interestingly, the tension lap-splice requirement was increased in the early 1960s from $20d_{b\text{-}col}$ in the 1950s codes [4, 37] to 24, 30 and $36d_{b\text{-}col}$ for 275, 345 and 414MPa steel, respectively, in the 1960s code [5, 38]. For plain round bar reinforcement,

the required anchorage length was double of those specified in the code for deformed bars. Therefore, the selection of lap-splice length of $40d_{b\text{-}col}$ for the two test specimens was both realistic and conservative.

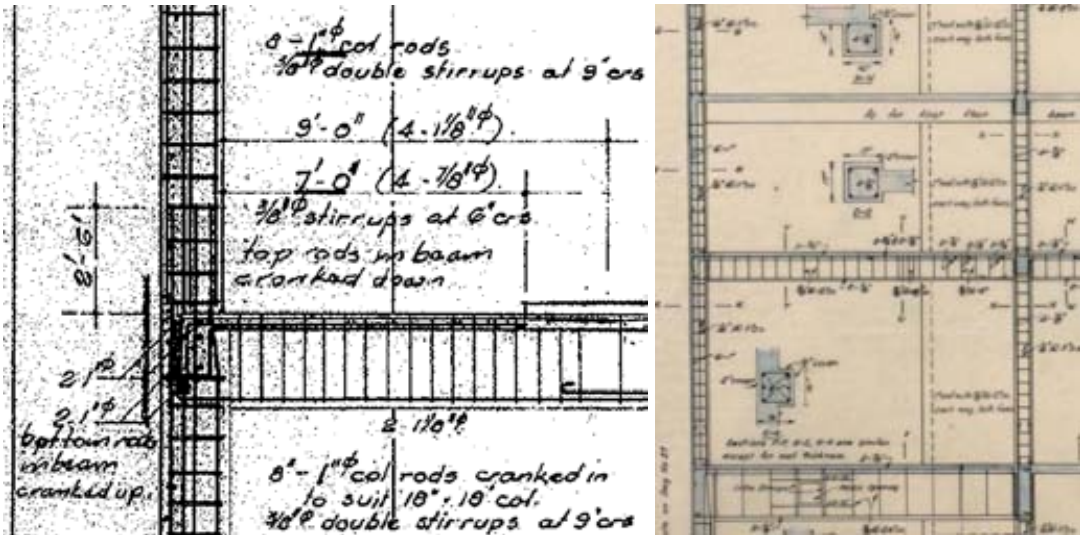

Figure 7.2: Examples column lap-splice details in pre-1970s RC buildings in New Zealand.

Only after the introduction of modern seismic design [45] and in particular the 1963 ACI 318 [5] and its 1971 revision [6] that recommendation was made to avoid lap-splices in potential plastic hinge regions. In the 1963 ACI 318, the required lap-splice length was at least $30d_{b\text{-}col}$ or 16 inches. In the 1971 ACI 318 [6], the lap-splice design emphasis was changed towards calculating a development length, l_d, given the attainable average bond resistance over l_d. This was predominantly for design convenience as well as driven by the re-evaluation of existing lap-splice/bond test data available then [6, 42]. The lap-splice bond tests showed that the uniformly distributed bond stress over a length of embedment of the reinforcement governed and the extreme variations in local bond stresses near cracks were inconsequential.

Even up to the mid-1970s and early 1980s, the seismic design of lap-splice for columns that might undergo excessive inelastic strains was contentious. Nevertheless, many researches in the 1980s have resolved many design issues in regards to achieving column lap-splice under inelastic cyclic loading with limited ductility [7, 27, 33, 39, 44, 46, 47]. The recent report of ACI 408 Committee [9] provides a good summary of the state-of-the-art of the design of lap-splice anchorage.

7.2.2 Column lap-splice failure modes and plain round bars lapping

The development of seismic code provisions for lap-splice is based on predominantly empirical equations built on test results on lap-splice connection in beams, such as works by Fagundo *et al.* [24], Orangun *et al.* [42], Sozen and Moehle [55] and more recently Canbal and Frosch [17]'s work on a mechanistic-based model with empirical verification. While essentially the behaviour of lap-splices under flexural loading is the same for beams and columns, columns in moment-resisting frames under earthquake loading typically sustain a variation of axial loads (i.e. high compression or near-tension axial loadings), high flexural and shear demands.

Thus, more recent researches on the seismic performance of lap-splice connections are focussed on the splice behaviour in column-only subassemblies (e.g. [2, 19, 20, 34, 35, 54, 57, 58]). The extensive experimental work by researchers at Cornell University (e.g. [33, 43]) and at University of Canterbury (e.g. [48]) on column/bridge piers specimens under inelastic cyclic loading confirmed the positive influence of confinement from transverse reinforcement on the strength and ductility capacity of the columns.

For lap-splice with inadequate l_d and concentrated stress-strain, the highly stressed bars tend to split thin sections of restraining concrete, creating vertical bond-split cracks along the lap-splice. These splitting cracks could also be caused by the dilation action from the ribs of deformed bars. For the lap-splice of plain round bars under cyclic loading, the bond and splice capacities would degrade rapidly after bond-split cracks as the smooth bars would lose their adhesive bond capacity. The bond degradation over the length of the lap-splice would reduce the available l_d for which force can be effective transferred from one bar to another. Figure 7.3 illustrates the different failure modes of column lap-splices, as established from extensive experimental evidences.

Essentially, the problem of non-ductile lap-splice is an issue of bond capacity and stress development of the column longitudinal bars across the lap length. Deficient lap splices are unable to develop full tensile capacity of the spliced bars. Therefore, modern lap splice design equations [3, 18] are based on providing sufficient bond stresses to develop the strains in the reinforcement and on aiming to prevent the potential splitting cracks. As such, in absence of capacity design to prevent flexural hinges in the columns, premature failure of the non-ductile column lap-splice detailing would limit the column flexural strength and ductility capacities (e.g. [14, 21, 42, 46, 49, 54]).

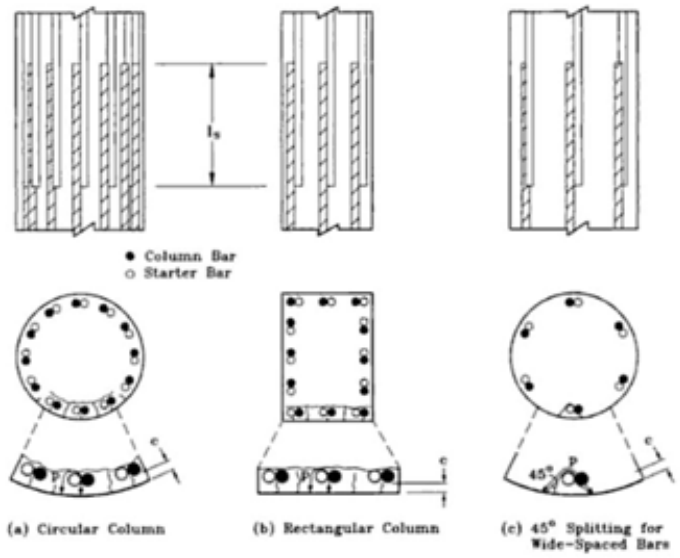

Figure 7.3 Lap-splice failure of longitudinal bars in columns [51].

Unlike deformed bars, after the bond split concrete cracks as shown in Figure 7.3, plain round bar lap-splices would lose their adhesive bond resistance quite rapidly and subsequently their lap-splice force transfer capacity. Cyclic and monotonic quasi-static tests on columns with inadequate lap-splices and plain round bars by Verderame *et al.* [57, 58] and Saunders [54] have confirmed the even poorer seismic behaviour of columns with these typologies. Figure 2.40 in Chapter 2 shows a typical example of the degrading strength and stiffness hysteresis of lap-splice and bond failures from Saunders's tests.

7.2.3 Relevance of column lap-splice on non-ductile RC joints

Within a non-ductile beam-column joint subassembly with inadequate column lap-splice however, the influence and interaction between the failure modes are not well understood at this stage. Presumably, the standard hierarchy of strength assessment described in §2.4 would be adequate to establish the weakest link and failure mode. Calvi *et al.* [16] showed that bond slip of column longitudinal reinforcement could reduce the flexural capacity by 20-30% within an interior beam-column joint, thus influencing the M-N performance domains, the hierarchy of strength and the sequence of failures. They suggested that the capacity of column lap-splice of plain round bars with 180° hooks was dependent on the frictional resistance of these bars. As such, the normal compression forces from the beam framing into the interior joint would positively contribute to the capacity of the lap-splice. This assessment procedure has been adopted by and incorporated into the fib Guidelines on seismic assessment and retrofit of RC buildings [26].

In terms of test data, inadequate lap-splice in beam-column joints subassemblages has been shown to reduce the ductility of the column flexural hinge resulting in premature failure (e.g. [11, 13, 22, 49]). Conversely, some researchers did not observe lap-splice failure in beam-column joint sub-assemblies testing due to the premature joint shear failure (e.g. [13, 49, 59]) or column axial-shear failure [61]. In analysing these conflicting results, Pessiki *et al.* concluded that when lap-splice failures occurred, they generally did not affect the maximum lateral load capacities as the joint shear failures governed the global response.

Small scale unreinforced or lightly-reinforced beam-column joints were more prone to column lap-splice failures than joint shear failure, when compared with larger scale tests. Examples of this are the 1/3 scale specimens of Aycardi *et al.* [11] and the 1/10 scale non-ductile RC frame specimens by El-Attar *et al.* [22]. Scale-comparative tests have shown that shear capacity is artificially higher , whereas lap-splice and bond capacities are relatively lower in small scale specimens [25, 30, 50]. Thus, it remains necessary to further test larger or real-size non-ductile beam-column joints with inadequate column lap-splices.

7.2.4 Retrofit of column lap-splice in non-ductile RC frame

Using the concept of shear friction, Paulay [46, 47] highlighted the importance of the amount and spacing of transverse reinforcement on the ductility of the column plastic hinged section with lap-splice. Recognising the importance of concrete confinement on the lap-splice seismic behaviour, many retrofit techniques (e.g. external steel pre-stressing, steel and reinforced concrete jacketing, and fibre-reinforced polymers jacketing) were developed to increase the confinement of the lap-splice region (e.g. [1, 2, 19, 29, 32, 52, 53, 56, 60]). More detailed discussion and review of the state-of-art of column lap-splice retrofit are available in ref. [10, 26]. Figure 7.4 presents the two commonly used retrofit techniques for inadequate lap-splices. More recently, Harries *et al.* [28] have developed a design approach for the seismic retrofit of lap-splice in non-ductile RC frames based on improving the bond capacity of the spliced reinforcement.

In modern seismic design, within the capacity design, columns of RC frames are not expected to yield; as such, it is acceptable to have column lap-splices at the floor level for the upper storeys. Likewise, if the SW retrofit could achieve a weak-beam strong-column design outcome, the flexural and inelastic strain demand on the deficient column lap-splice could be avoided. Due to the nature of the extremely poor and unreliable bond conditions of the smooth

reinforcement, such a preventive retrofit strategy might be effective when compared to the conventional confinement retrofit strategies.

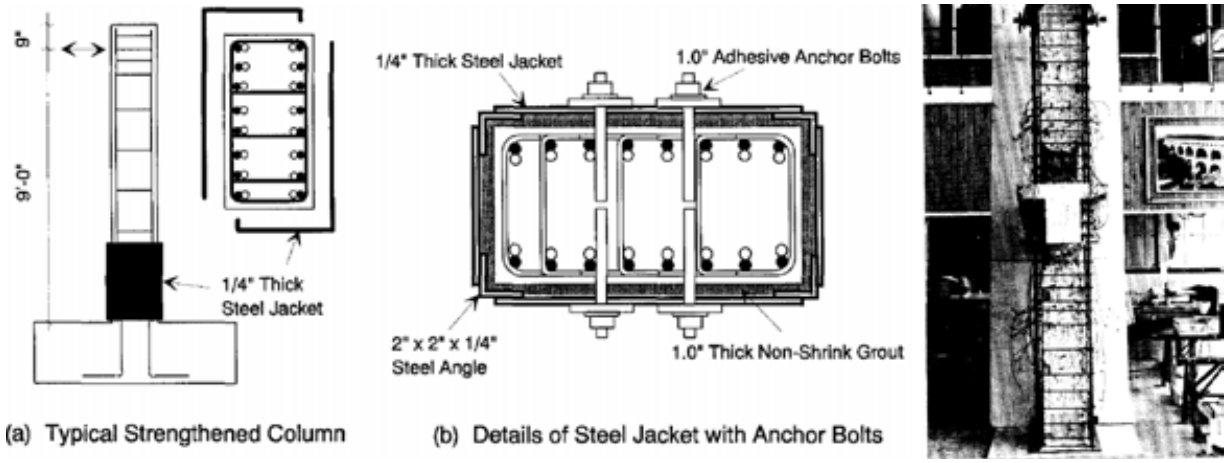

Figure 7.4: Example of seismic retrofit of columns with lap-splices: a) Steel jacketing [2] ; and b) Reinforced concrete jacketing [52].

It is nevertheless essential to assess the hierarchy of strength performance domain of the retrofitted beam-column joint in order to confirm the capacity design requirement of the weak-beam strong-column. Naturally, with retrofit solution R3 (weakening and post-tensioning), in some scenarios, there might be a need to retrofit the columns for the inadequate lap-splice and/or column shear deficiency.

7.3 TEST RESULT OF AS-BUILT JOINT WITH LAP-SPLICE: S-O1

7.3.1 General description of behaviour

The F_c versus Δ_c hysteresis plot for S-O1 is given in Figure 7.5. The damage and cracking patterns at the selected peak inter-storey drift, θ_{drift}, loading cycles are shown in Figure 7.6 and Figure 7.7. θ_{drift} is given by Δ_c/H_c and H_c is the column height (=2000mm). As described in Chapter 4, the predicted lateral force capacities, $F_{sys\text{-}cal}$, for S-O1 were +10.2kN and -14.2kN for the Pull and Push loading directions, with the expected failure to be a joint shear failure.

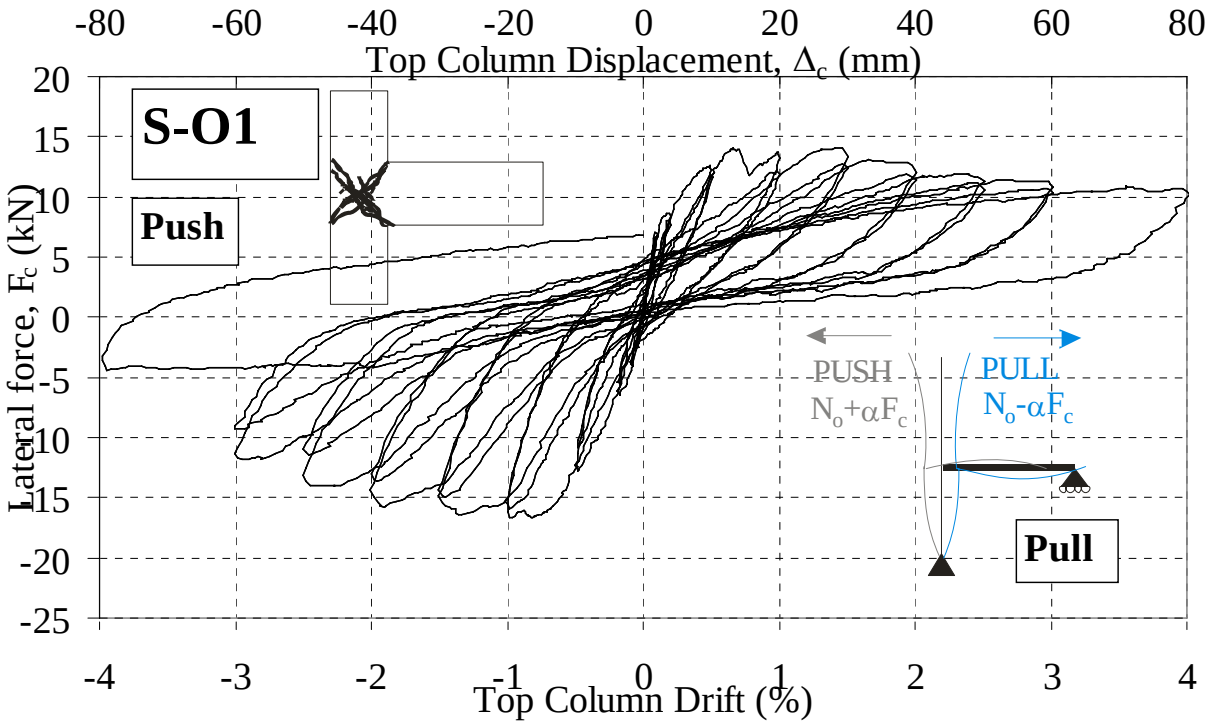

Figure 7.5: Top column lateral load, F_c, versus top column displacement, Δ_c, and drift, θ_{drift} for S-O1.

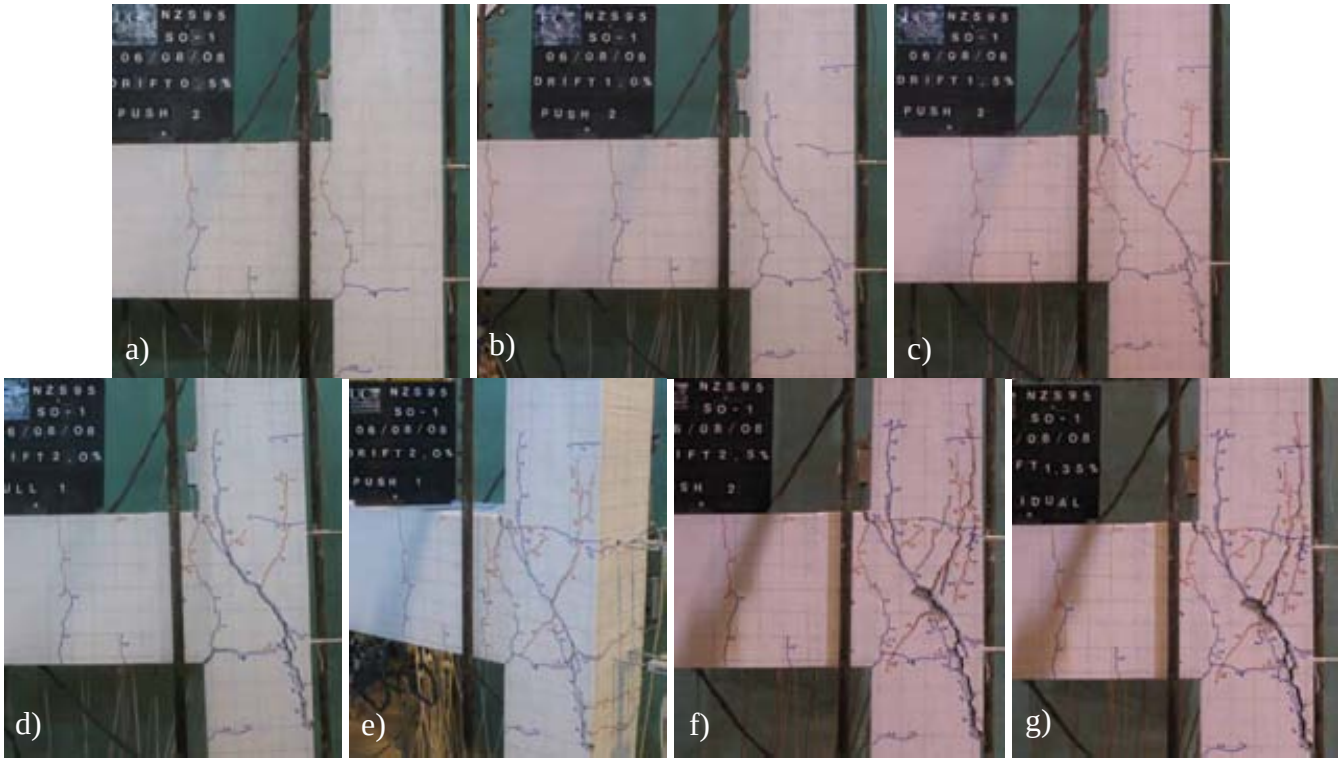

Figure 7.6: Observed cracking pattern of S-O1: TOP: a) 2nd Push cycle of the -0.5% drift; b) 2nd Push cycle of the -1.0% drift; and c) 2nd Push cycle of the -1.5% drift. BOTTOM: d) 1st Pull cycle of the +2.0% drift e) 1st Push cycle of the -2.0% drift; f) 2nd Push cycle of the -2.5% drift; and g) Residual after Pull-Push cycles of the ±2.5% drift.

No cracks were observed in the ±0.1% drift loading cycles. In the 1st Pull cycle of the +0.2% drift, two 0.15mm wide flexural cracks appeared from the bottom face of the beam. In the reverse 1st Push cycle of the +0.2% drift, two similar cracks appeared at the top face of the beam, connecting with the Pull cycle cracks, resulting in fully cracked weakened sections (Figure 7.6b). In the 2nd Pull-Push cycles of the ±0.2% drift, more beam flexural cracks were observed. The ratio of cracked stiffness-to-uncracked stiffness, K_{cr}/K_{ini}, was 0.553 with the initial stiffness, K_{ini}, of 3332kN/m measured in the +0.1% drift cycles.

In the 1st Pull peak of the +0.5% drift, a horizontal crack appeared in the joint, originated from the vertical crack at the beam-column joint interface (Figure 7.6a). No new cracks were observed in the 2nd cycles of the ±0.5% drift. The maximum crack width in the ±0.5% drift cycles was 0.35-0.45mm. At the end of the loading cycles, the residual Δ_c and flexural crack width were -2mm and 0.10mm.

In the 1st Pull cycle of the +1.0% drift, a diagonal tensile crack appeared in the joint panel and several flexural cracks appeared in the top half of the column (Figure 7.6b). The observed drop in F_c after joint shear cracking suggested the θ_{drift} at cracking was +0.7%. At the joint first crack, the principal stresses, p'_t and p'_c measured were 0.327 $\sqrt{f'_c}$ MPa and 0.554 $\sqrt{f'_c}$ MPa, with corresponding joint shear deformations, γ_j, of -0.00017 (γ_j is given in radians). The first diagonal cracking for S-O1 in the Pull loading direction was consistent with the as-built joint without lap-splice (NS-O1). In the subsequent 2nd cycles of the ±1.0% drift, the diagonal joint crack in the Pull direction was extending vertically into the column.

However, in the Push direction, no joint cracks were observed and the beam was hinging at the beam-column interface with a maximum crack width up to 2mm measured. When compared with NS-O1, S-O1 attained a similar maximum F_c (+14.1kN vs. +14.7kN (NS-O1) in the Pull loading but lower F_c (+16.7kN vs. +18.7kN (NS-O1) in the Push loading. The lower F_c in S-O1 in the Push direction, in which the column axial load was increasing, was an indication that the column lap-splice bond degradation had limited the F_c. §7.3.6 will look at the strain data for confirmation evidence of lap-splice failure in the ±1.0% drift cycles while §7.5.1 will further explore the differences between the specimens with and without column lap-splices.

In the 1st Pull peak of the +1.5% drift, the joint diagonal crack width was up to 3.5mm with the top end propagating vertically along the column interior face longitudinal bars. A joint diagonal crack appeared in the 1st Push cycle of the -1.5% drift (Figure 7.6c). The joint shear

crack occurred at the θ_{drift} ~ -1.3%. At the joint cracking in the Push direction, the principal stresses, p'_t and p'_c measured were 0.231 $\sqrt{f'_c}$ MPa and 1.148 $\sqrt{f'_c}$ MPa, with corresponding joint shear deformations, γ_j, of +0.00128. The joint diagonal and weakened beam section residual crack widths were 0.65mm and 0.25mm. The vertical crack on the internal face of the column had a residual crack width of 0.3mm.

In the ±2.0% drift cycles, further extension of the diagonal joint cracks along the lap-splice lengths along the column was observed. The vertical cracks extended up to 200mm from the beam top face. This was evident from the damage pattern photographs as shown in Figure 7.6d and e. At the end of the 2nd cycles of the ±2.0% drift, both in-cycle and peak-to-peak degradations of F_c were observed. The joint diagonal cracks and the column vertical 'lap-splice' cracks were measured 2.2-6.0mm and 1.0-2.0mm wide respectively. A lower range of the crack widths was of the Push direction. At the end of the ±2.0% drift cycles, the largest residual crack widths were the diagonal joint and vertical column cracks of the Pull direction, measuring 4mm and 1.1mm respectively.

The joint panel continued to deteriorate rapidly in the ±2.5% and ±3.0% drift cycles, as shown in Figure 7.6f and Figure 7.7a. The joint diagonal cracks were opening up and a sign of axial load failure along the diagonal cracked plane was observed. S-O1 attained structural failure in the 1st Pull cycle of the +2.5% drift, with the attained F_c less than 80% of the maximum F_c. The vertical column cracks continued to grow, in particular, in the Push direction, indicating further lap-splice bond failure. Figure 7.6g and Figure 7.7b show the residual state of the S-O1 specimen after the ±2.5% and ±3.0% drift cycles. In terms of damage state, by the end of the ±2.5% drift cycle, the S-O1 was not repairable.

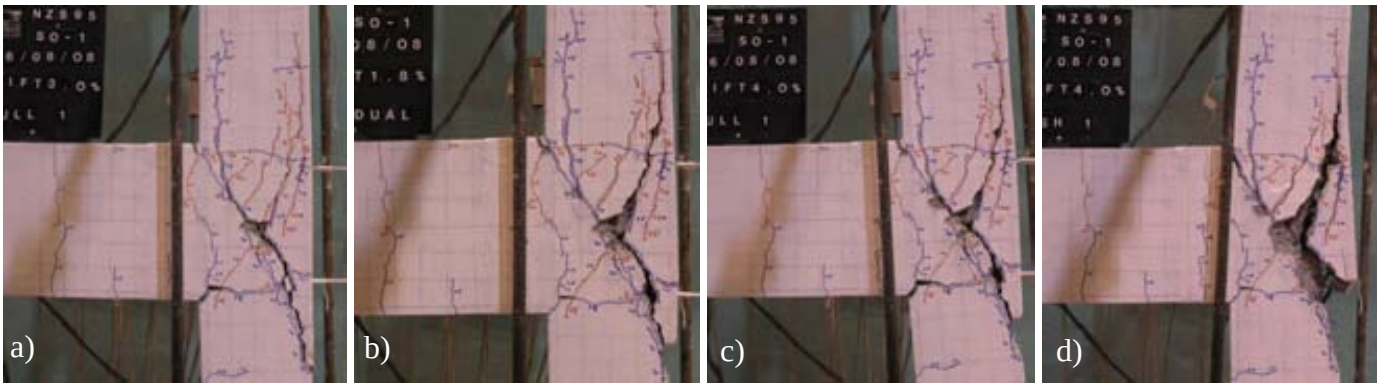

Figure 7.7: Observed cracking pattern of S-O1: a) 1st Pull cycle of +3.0% drift; b) Residual after Pull-Push cycles of ±3.0% drift; c) 1st Pull cycle of +4.0% drift; and d) 1st Push cycle of -4.0% drift.

To investigate the post-failure decay of the lateral load capacity, S-O1 was tested further for one Pull-Push cycle of the ±4.0% drift. While in the Pull direction (with decreased axial load), the joint was sustaining the lateral strength, the increasing axial load in the Push direction led to buckling of the column longitudinal bars within the damaged joint panel zone and steep F_c degradation. For safety reasons, complete 'collapse' and loss of axial load capacity were not achieved.

7.3.2 Load-displacement hysteresis analysis

The F_c-Δ_c hysteresis plot for S-O1 is shown in Figure 7.5 while the analysis of the S-O1 F_c-Δ_c hysteresis is presented in Figure 7.8. The maximum F_c values measured were +14.1kN (at +1.43% drift) and -16.7kN (at -0.98% drift). In terms of the four analysed parameters of the F_c-Δ_c hysteresis, S-O1 was giving similar curves as per specimen NS-O1. Refer to §5.4 for a more detailed discussion of the results presented in Figure 7.8.

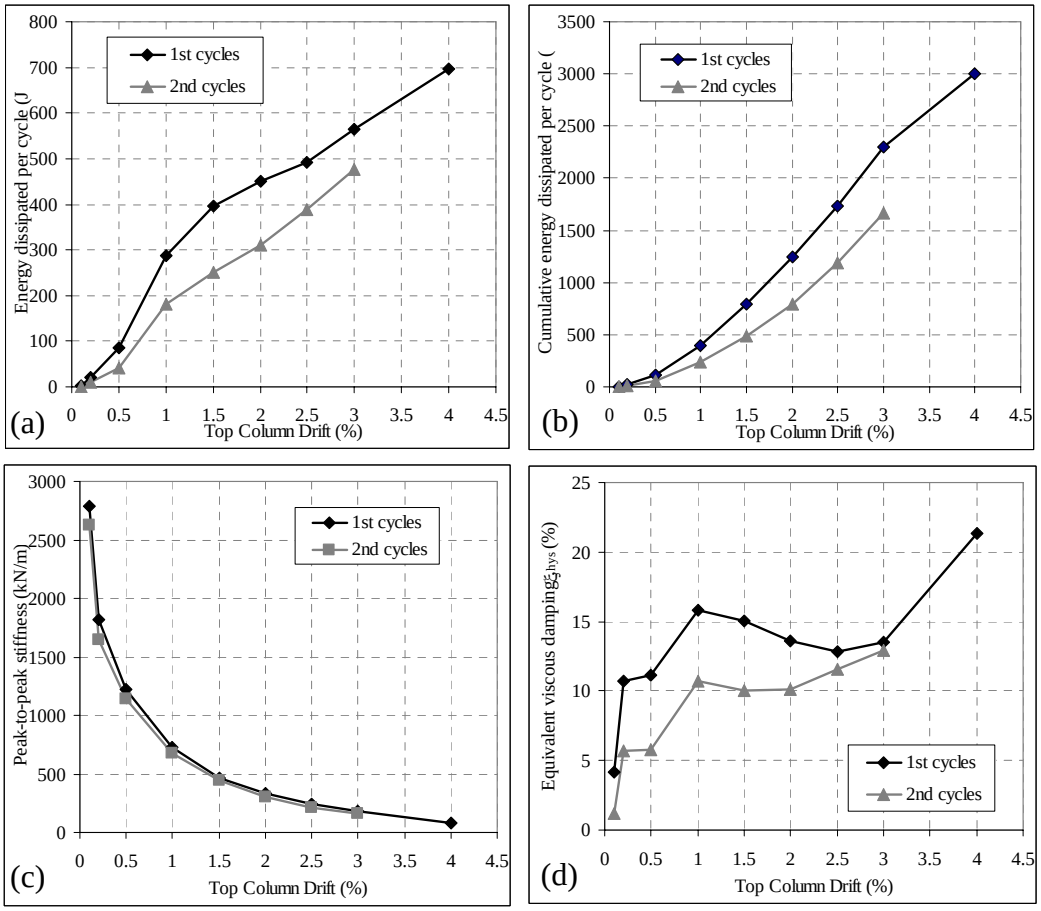

Figure 7.8: F_c-Δ_c analysis for S-O1: a) Energy dissipated per cycle; b) Cumulative energy dissipated per cycle; c) peak-to-peak stiffness, K_{eff}, and; d) Equivalent viscous damping, ξ_{hys}.

The presence of lap-splice did not seem to affect the in-cycle strength degradations, cumulative energy dissipation, energy dissipated per cycle or peak-to-peak stiffness, K_{eff}. There was minor increase (~5-15%) in the equivalent viscous damping, ξ_{hys} for S-O1 when compared with NS-O1. This increase was due to the sustained F_c in the Push cycles up to θ_{drift}=-2.5%, before axial force induced column bar buckling failure resulting significant F_c degradation.

7.3.3 Local deformations and displacement components

7.3.3.1 Decomposition of top column horizontal displacement

The components of the top column horizontal displacement, Δ_c at the peaks of the Pull and Push loading cycles as percentages of the total Δ_c are presented in Figure 7.9. Instrumentation was removed after the 1st cycles of ±3.0% drift.

In the Pull direction, the column displacement contribution, $\Delta_{col,flexural}$, to the Δ_c was also significant, ranging from 15-60% throughout the whole test. Figure 7.9a suggested that the beam flexural actions (both fixed-end and flexural) were the predominant mechanism up to the ±0.5% drift cycles. After the joint cracking in the +1.0% drift cycles, more joint contributions, Δ_{joint} were measured, but limited to less than 10% of the Δ_c. The large damage observed in the joint panel indicated that the linear potentiometer instrumentation was not capturing the Δ_{joint} accurately.

Inspection of the instrumented face showed that the joint diagonal crack was traversing between the 6mm rods at the corners of the beam-column joint panels. As the potentiometers measuring the joint shear deformation relied on the relative displacement of these corner rods, there was significant under-measurement of the joint shear deformation as the joint diagonal cracks essentially passing through the potentiometer support. In such a scenario, probably a radial external gauge could have provided a better measure of joint deformations.

In the Push direction, similar distribution of the Δ_c components was observed. However, there was a significant unaccounted displacement component, ranging between 40-60% of the Δ_c. This was a result of the damage accumulation (unclosed cracks) in the joint and apparent residual Δ_c in the Pull direction. After the joint cracking at -1.5% drift cycles, Δ_{joint} was increased significantly with Δ_{joint} accounting for nearly 50% of the Δ_c in the -3.0% drift cycle.

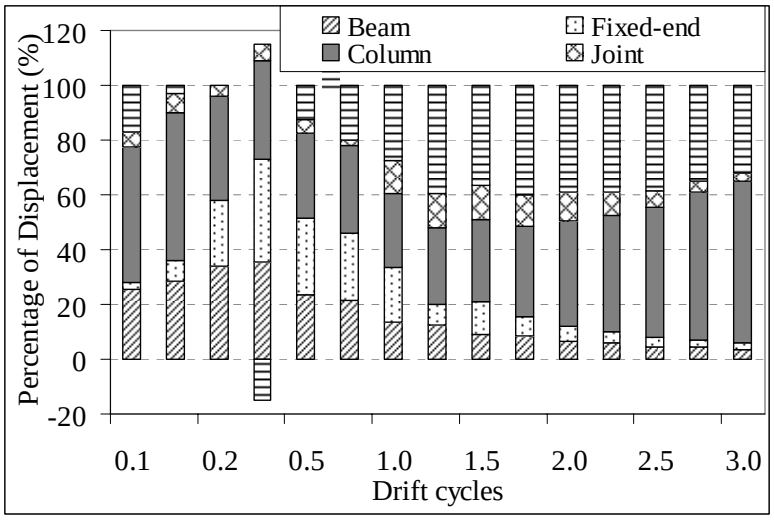

a) Pull loading direction – positive displacement.

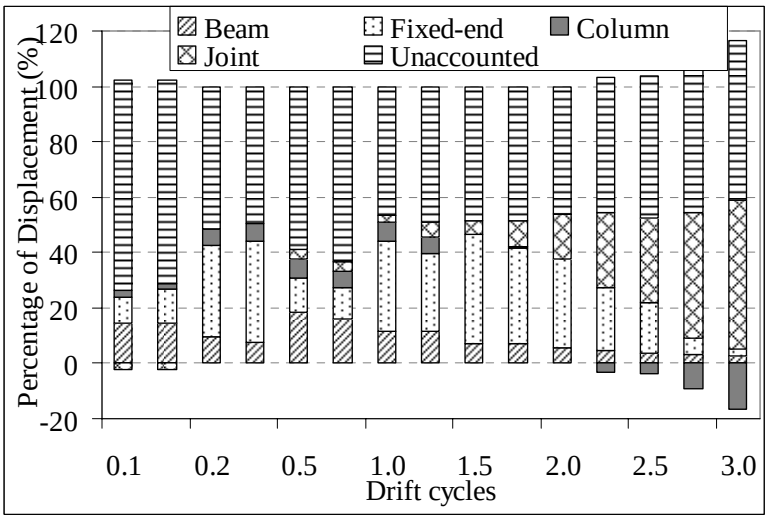

b) Push loading direction – negative displacement.

Figure 7.9: Displacement decompositions based on measured deformations for S-O1.

7.3.3.2 Beam deformations

The moment-curvature plots for the beam flexural regions and beam fixed-end region are shown in Figure 7.10. Positive beam curvatures, ϕ_b, corresponded to the positive column displacement (Pull direction) and vice versa. Figure 7.10a shows predominant beam inelastic deformations were concentrated on the fixed-end beam-column interface. The maximum beam moments developed in the Pull and Push directions were +25.9kNm and -31.1kNm respectively, and the maximum curvatures of $\pm 0.032 m^{-1}$ and $-0.110 m^{-1}$ respectively. In the negative beam moment (Push direction), it was observed that the theoretical beam flexural strength of -31.6kNm (with

perfect bond assumption and strain hardening) was achieved before joint diagonal compression failure limited the available curvature ductility. With the theoretical yield curvature, $\phi_y = 2\varepsilon_y/H_b = 0.011\text{m}^{-1}$, the curvature ductilities (at the structural failures) in the positive and negative beam moments were 3 and 10 respectively.

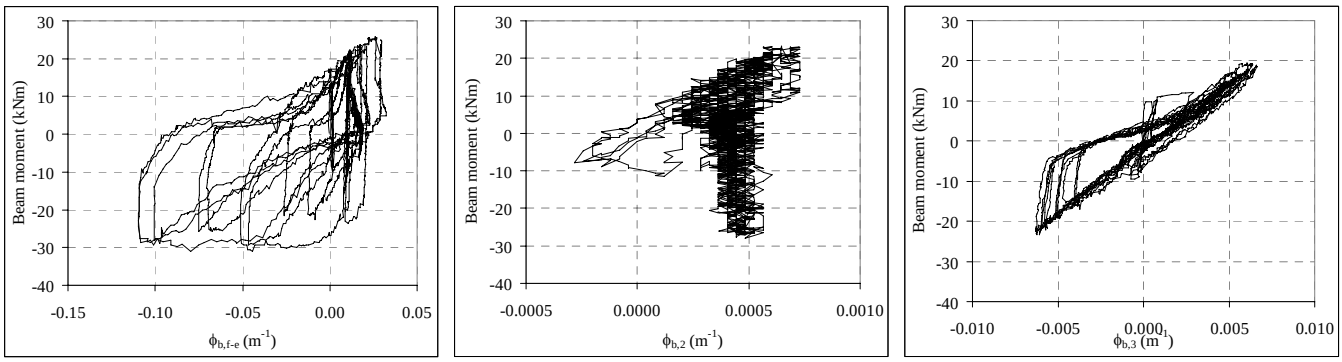

Figure 7.10: a) Moment-curvature plots for beam sections: a) fixed-end section; b) 75-275mm from the column internal face; and c) 275-475mm from the column internal face.

7.3.3.3 Column deformations

Figure 7.11 shows the measured moment-curvature response for the three regions of the column. The observed nominal column flexural strengths, $M_{c\text{-}cf}$, were +10.9kNm and -13.1kNm in the Pull and Push cycles respectively. In the Pull cycles, the $M_{c\text{-}cf}$ corresponded to the column curvatures, ϕ_c, of 0.007m^{-1} and of 0.0018m^{-1} at the top and bottom halves of the column. In the Push cycles, the $M_{c\text{-}cf}$ corresponded to the ϕ_c of -0.0084m^{-1} and of -0.0026m^{-1} at the top and bottom halves of the column. Considerable ϕ_c plasticity was developed at the bottom half of the column (in the Pull direction) while there was significant degradation of the $M_{c\text{-}cf}$ as the column ϕ_c increased in the top half of the column. This was a consequence of the lap-splice failure at higher ϕ_c ductility.

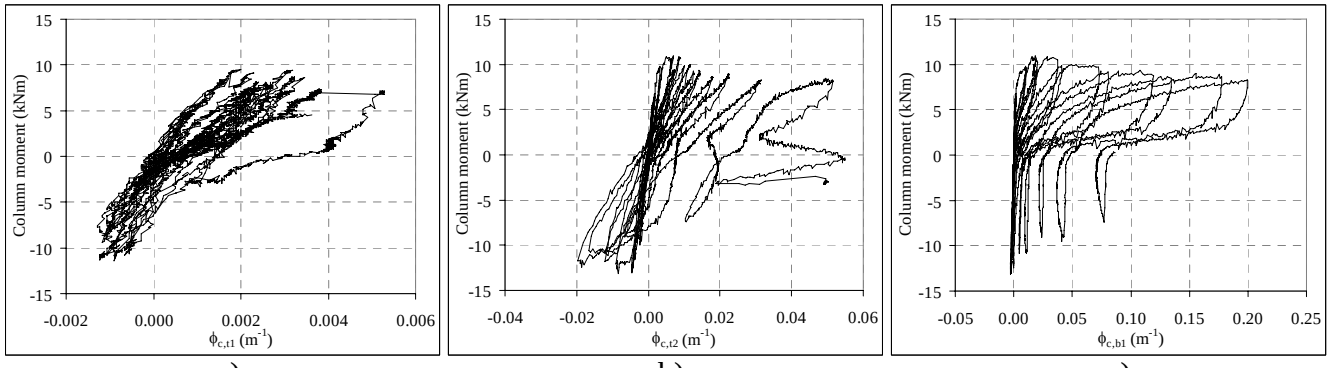

a) b) c)

Figure 7.11: Moment-curvature plots for column flexural sections: a) 200-430mm from the beam top face; b) 0-200mm from the beam top face; c) 0-200mm from the beam soffit.

7.3.4 Beam-column joint behaviour

7.3.4.1 Nominal joint shear stress and joint shear distortion

The nominal joint shear stress, v_{jh}, versus joint shear distortion, γ_j, and Δ_c relationships for S-O1 are given in Figure 7.12. As with the observed joint cracks and damage, significant γ_j were measured after the joint diagonal cracking at +1.0% (Δ_c ~ 20mm) and -1.5% (Δ_c ~ 30mm) drift cycles. v_{jh} at joint diagonal cracking were 1.67MPa (0.43 $\sqrt{f'_c}$ MPa or 0.11f'$_c$ MPa) and 2.00MPa (0.52 $\sqrt{f'_c}$ MPa or 0.13f'_c MPa) in the Pull and Push loading directions respectively. In both loading directions, this also corresponded to the maximum v_{jh} measured. These values were comparable with the NS-O1 values. The difference between the two loading directions again highlighted the influence of the variation of column axial loads.

The v_{jh} - γ_j plot shown in Figure 7.12a also illustrates the damage accumulation and creep towards the positive γ_j direction (i.e. the Push direction). Recalling the displacement component results given in Figure 7.9, the Δ_{joint} was also shown to be substantially higher in the Push direction, as a percentage of the total Δ_c. v_{jh} degraded with increasing γ_j as the diagonal cracks in the joint grew.

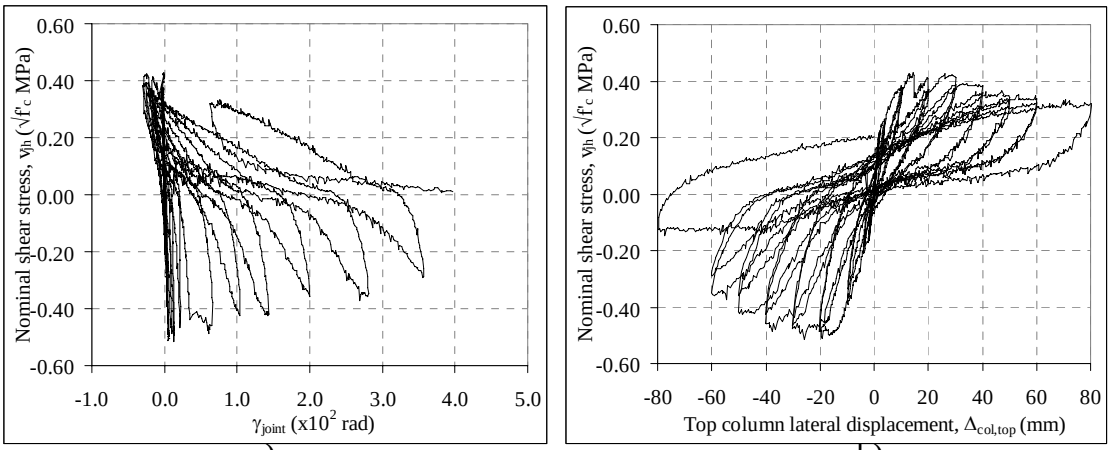

Figure 7.12: a) Nominal joint shear stress, v_{jh} versus joint deformation, γ_j; b) Nominal joint shear stress, v_{jh} versus top column lateral displacement, Δ_c.

7.3.4.2 Joint principal stresses

Figure 7.13a-b presents the relationship between the principal stresses and the column lateral displacement, Δ_c while Figure 7.13c-d presents the relationship between the principal stresses versus joint shear deformation, γ_j. In terms of the p'_t and p'_c versus Δ_c plots (Figure 7.13a-b), S-O1 responses were similar to the NS-O1 responses. However, asymmetric p'_t and p'_c versus γ_j

curves were attained for S-O1. Instead of representing the actual discrepancy of joint shear deformations between the two as-built beam-column joints, it is inferred that the measurement of γ_j could have been affected by the positions of the potentiometer anchorage rods with respect to the joint diagonal cracks (as explained in §7.3.3.1).

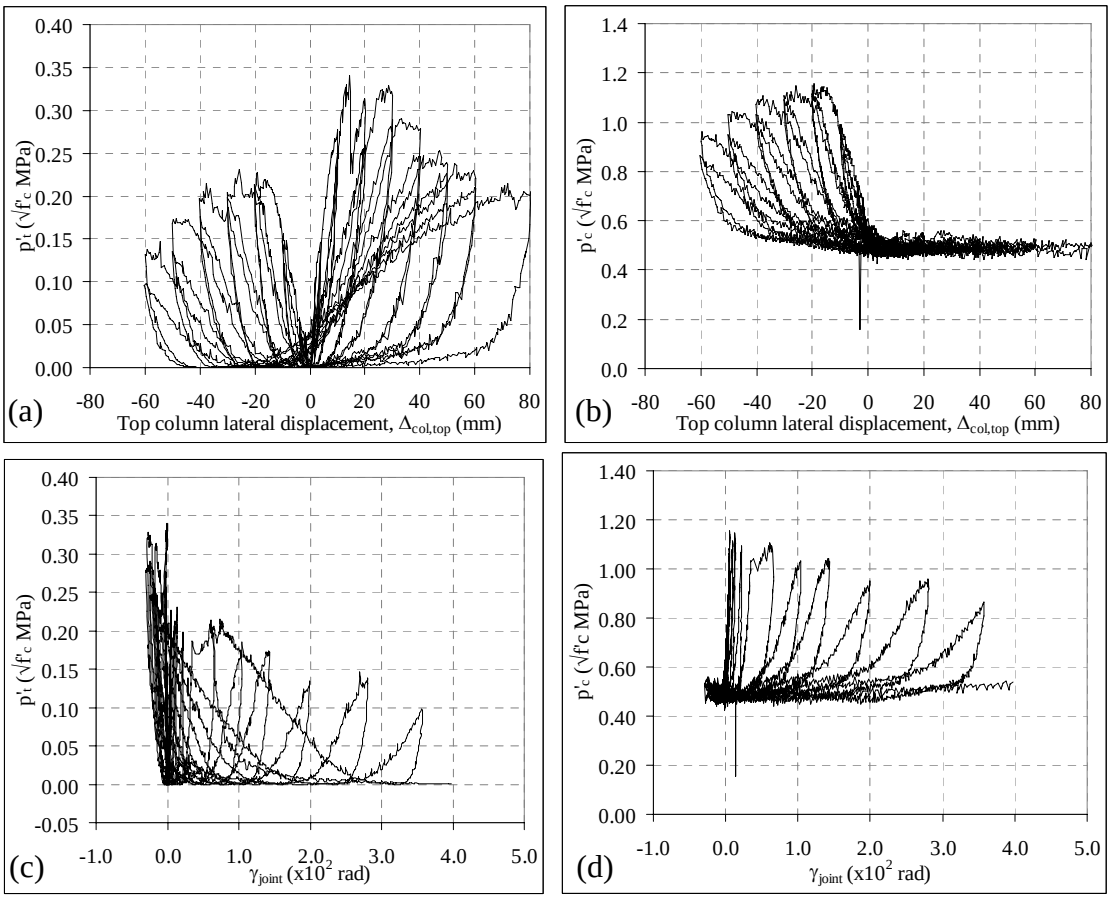

Figure 7.13: a-b) Joint principal stresses versus top column lateral displacement, Δ_c: a) principal tensile stress, p'_t; b) compressive tensile stress, p'_c; c-d) Principal stresses versus joint shear deformation, γ_j plots: c) principal tensile stress, p'_t; d) compressive tensile stress, p'_c.

At the joint shear cracking in the Pull direction at θ_{drift} = +0.7%, the principal stresses, p'_t and p'_c measured were $0.327\sqrt{f'_c}$ MPa and $0.554\sqrt{f'_c}$ MPa, with corresponding joint shear deformations, γ_j of -0.00017. A sharp drop in p'_t was also observed. This level of p'_t (>$0.3\sqrt{f'_c}$ MPa) was sustained up to approximately θ_{drift} =+1.5% before degrading rapidly to approximately $p'_t = 0.3\sqrt{f'_c}$ at θ_{drift} =+4.0%. The p'_c was relatively constant at $0.5\sqrt{f'_c}$ MPa for the Pull cycles. In the Push cycles, at the joint cracking at θ_{drift} = -1.3%, the principal stresses, p'_t and p'_c measured were 0.231 $\sqrt{f'_c}$ MPa and 1.148 $\sqrt{f'_c}$ MPa (or $0.095f'_c$ MPa), with corresponding joint shear

deformations, γ_j of +0.00128. These values suggested a concrete diagonal compressive failure in the Push direction. After joint cracking, the degradation of the p'_c curve was evident.

7.3.5 Steel strain profiles

7.3.5.1 Beam longitudinal reinforcement strains

Figure 7.14 and Figure 7.15 present the strain profiles of the top and bottom beam longitudinal reinforcement for the specimen S-O1. The X-axis is the distance from the exterior column face while the two vertical dashed lines refer to the column centre-line and the interior column face. Tensile strains are given as positive values. From the steel test, the yield strain, ε_y for the longitudinal beam and column reinforcing was 0.00168 (1680 microstrains) and the f_y was 335MPa. In general, the trends of strain profiles for both the top and bottom bars were similar for both NS-O1 and S-O1.

For the top bars, up to the 1st cycles of the ±0.5% drift, the strains measured indicated no bond degradation in both the Pull and Push cycles. A maximum compressive stress measured was 56 MPa. The top bars started yielding in the 1st Push cycle of the -0.5% drift, with localised high tensile strains measured at the beam-column interface with a maximum tensile strain up to 4300 microstrains measured. In the ±1.0% drift cycles onwards, corresponding to the joint cracking in the Pull direction, the top bars were carrying substantial tensile strains in both the Pull and Push loadings.

For the bottom bars, limited compressive resistance was available in the bottom bars in the Pull cycle, as the bars have undergone considerable tension strains in the initial Pull cycle. Before joint cracking in the Pull direction, the bottom bars were yielding in the lengths close to the 180° hook at the middle of the joint core. After joint cracking, the bar length outside the joint remained within the same tensile strains (~1500 microstrains), while the bar length embedded within the joint had increasing tensile strains.

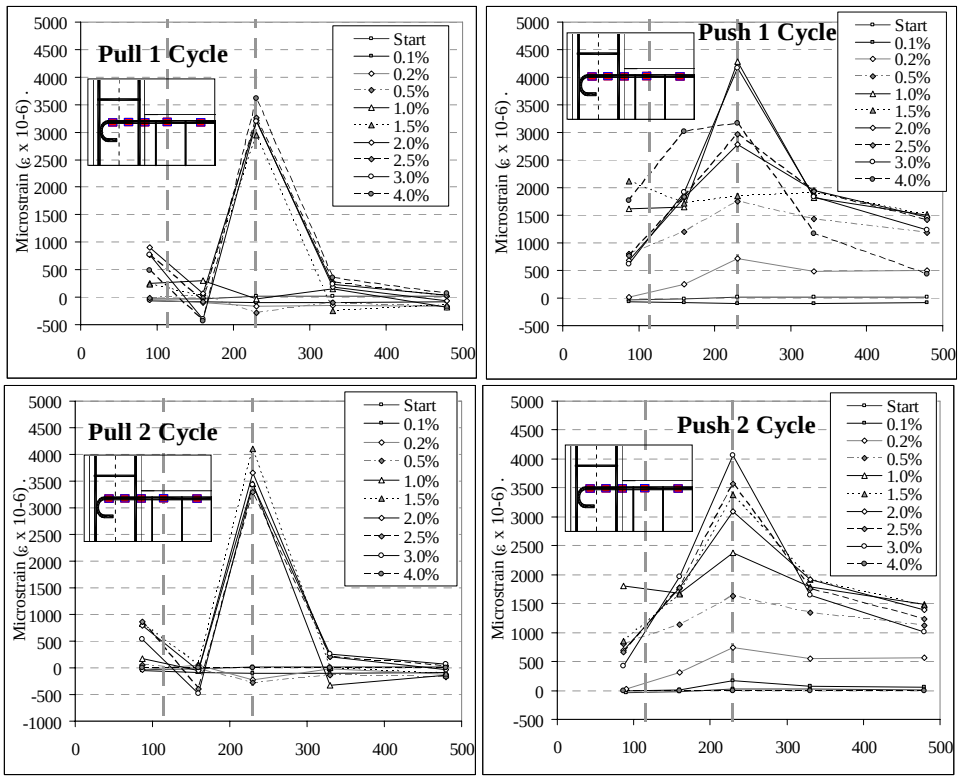

Figure 7.14: Strain profile of beam top longitudinal bars of the specimen S-O1.

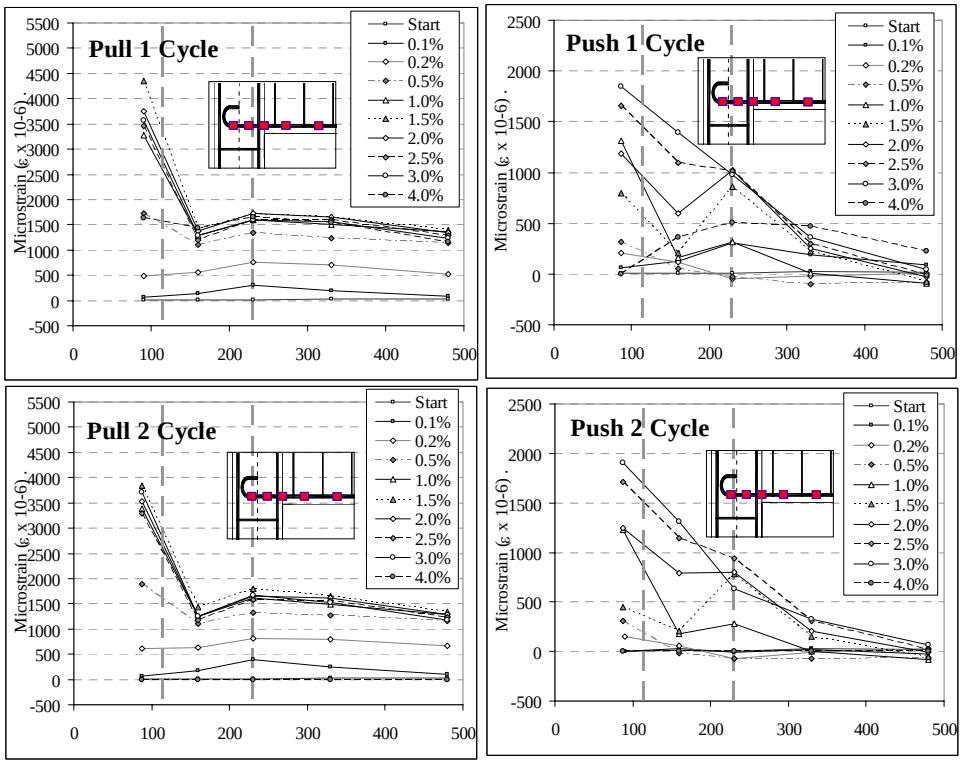

Figure 7.15: Strain profile of beam bottom longitudinal bars of the specimen S-O1.

7.3.5.2 Column longitudinal reinforcement strains

Figure 7.16 and Figure 7.17 present the strain profiles of the exterior and interior column longitudinal reinforcing for the specimen S-O1. In Figure 7.16 and Figure 7.17, the Y-axis is the distance from the centre-line of the beam. The three horizontal dashed lines refer to the beam soffit (bottom line), beam centre-line and the beam top face (top line). As with all strain gage readings, tensile strains were measured as positive values. All column strain gages were zeroed before the axial force loading on the column at the start of the test.

In general, both the exterior and interior column longitudinal bars were responding similarly to the as-built specimen without lap-splice, NS-O1. Prior to the joint diagonal cracking at +1.0% and -1.5% drifts, the column exterior and interior longitudinal reinforcing were responding elastically as expected from the bending moment demand from the lateral loading. Hence forth, the column bars within the joint region were carrying substantial strains predominantly due to the column bars carrying joint shear force transfer via dowel and shear-friction action.

However, further examination of S-O1 and NS-O1 column strain results reveals that the upper half of the column bars had lower tensile strains in the S-O1 by approximately 50% when compared with NS-O1 (§5.6.2). This could be attributed to the partial lap-splice and bond degradation/failure in S-O1. Similar observation was made in both the Push and Pull directions for both the external and internal face column bars. §7.3.6 will further examine the experimental evidence of lap-splice failure in S-O1, while §7.5.1 will discuss the influence of inadequate column lap-splice on as-built beam-column joints.

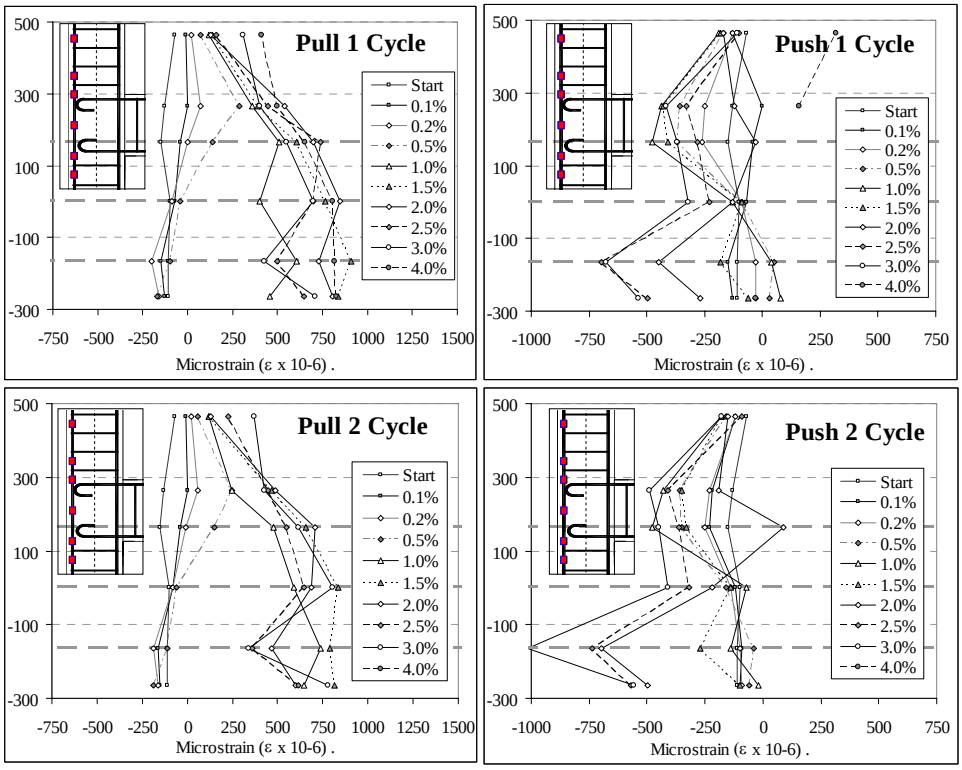

Figure 7.16: Column exterior face longitudinal reinforcement strain profiles for specimen S-O1.

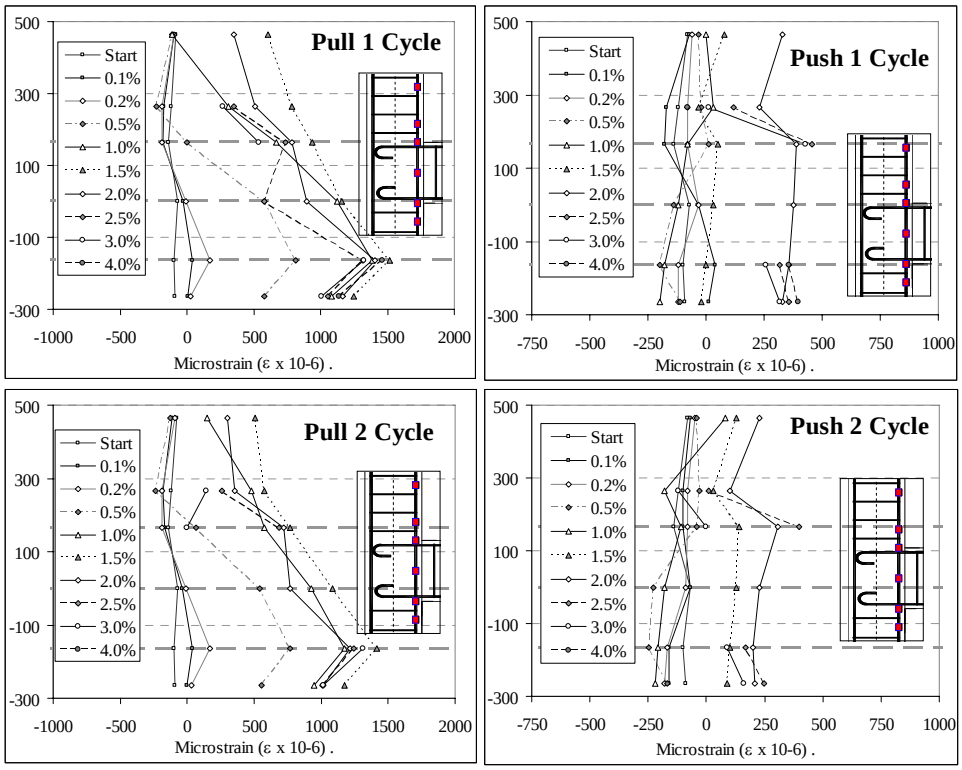

Figure 7.17: Column interior face longitudinal reinforcement strain profiles for specimen S-O1.

7.3.5.3 Stirrup reinforcement strains

The strain profiles of the stirrups in the column and the beam are shown in Figure 7.18. Only selected stirrup results are presented herein as the general trend across different measurements is similar. In generally, all the instrumented stirrups of both the beam and the column responded elastically.

Only minor increases in column stirrup strains were measured in the stirrups along the lap-splice length (CS2C and CS3A). This marginal increase in 'confining strain' in the stirrups was different from the typical observation of high increase in tensile strain after split crack of the lap-splice failure initiation in RC column with deformed bars (e.g. [33, 34, 46]). Only minor increases in column stirrup strains were measured in the stirrups along the lap-splice length (CS2C). This suggested the shear-friction mechanism for lap-splice [46], which considered the contribution of the ribs of deformed bars in the force transfer mechanics, might be inadequate to explain the behaviour of lap-splice with plain round bars. Maximum stresses measured in the column stirrups were approximately 150MPa at the stirrup CS2C.

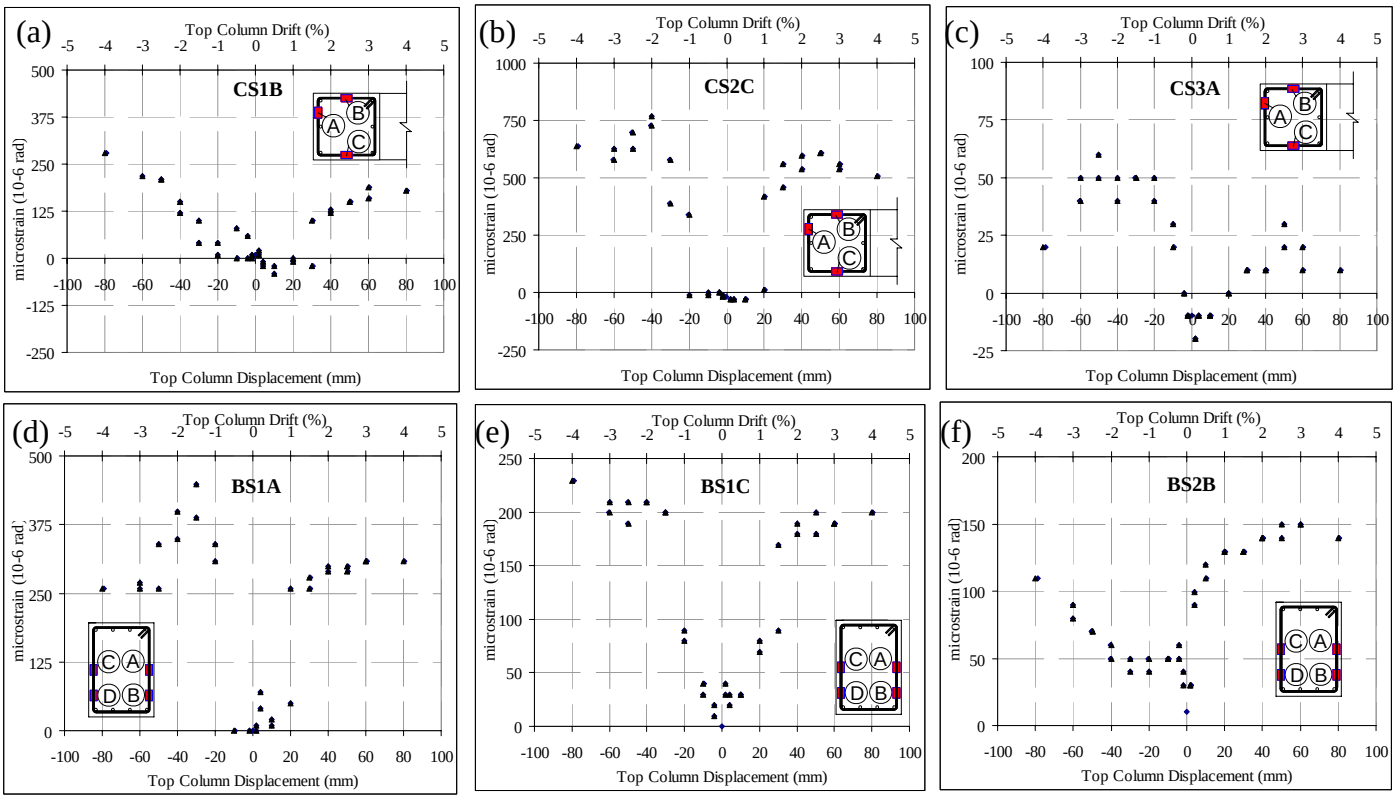

Figure 7.18: Stirrup strain profiles: TOP: a) column stirrup 50mm below the beam soffit; b) column stirrup 50mm from the beam top face; and c) column stirrup 350mm from the beam top face. BOTTOM: d-e) beam 1st stirrup 50mm from the column interior face; and f) beam 2nd stirrup 183mm from the column interior face.

7.3.6 Lap-splice strain measurements

The time history of the strain gage measurements along the lap-splice length for S-O1 is presented in Figure 7.19. The applied column top displacement, Δ_c, was also plotted on the secondary Y-axis. Four pairs of strain gages were placed on the column longitudinal bars with two pairs on the exterior face bars (CL1X and CL3X) and two pairs on the interior face bars (CL2X and CL4X). 'X' refer to the vertical location of the gages, where for X=5 and X=6, the distances are 100 mm and 300 mm from the beam top face respectively. Using the strain gages measured along the lap-splice length, the stresses on the reinforcement bars were calculated assuming linear stress-strain relationship before bond/lap-splice failure. The average bond stress, τ_{lap}, along the surface of the lap-spliced bars was calculated using the following equation:

$$\tau_{lap} = \frac{(f_{s1} - f_{s2})d_{b,col}}{4l_{d-lap}} \qquad \textbf{7.1}$$

where f_{si} = stress at the reinforcing bars at location i, $d_{b,col}$ = diameter of column longitudinal bars and $l_{d\text{-}lap}$ = the lap-splice length between location i and $i+1$.

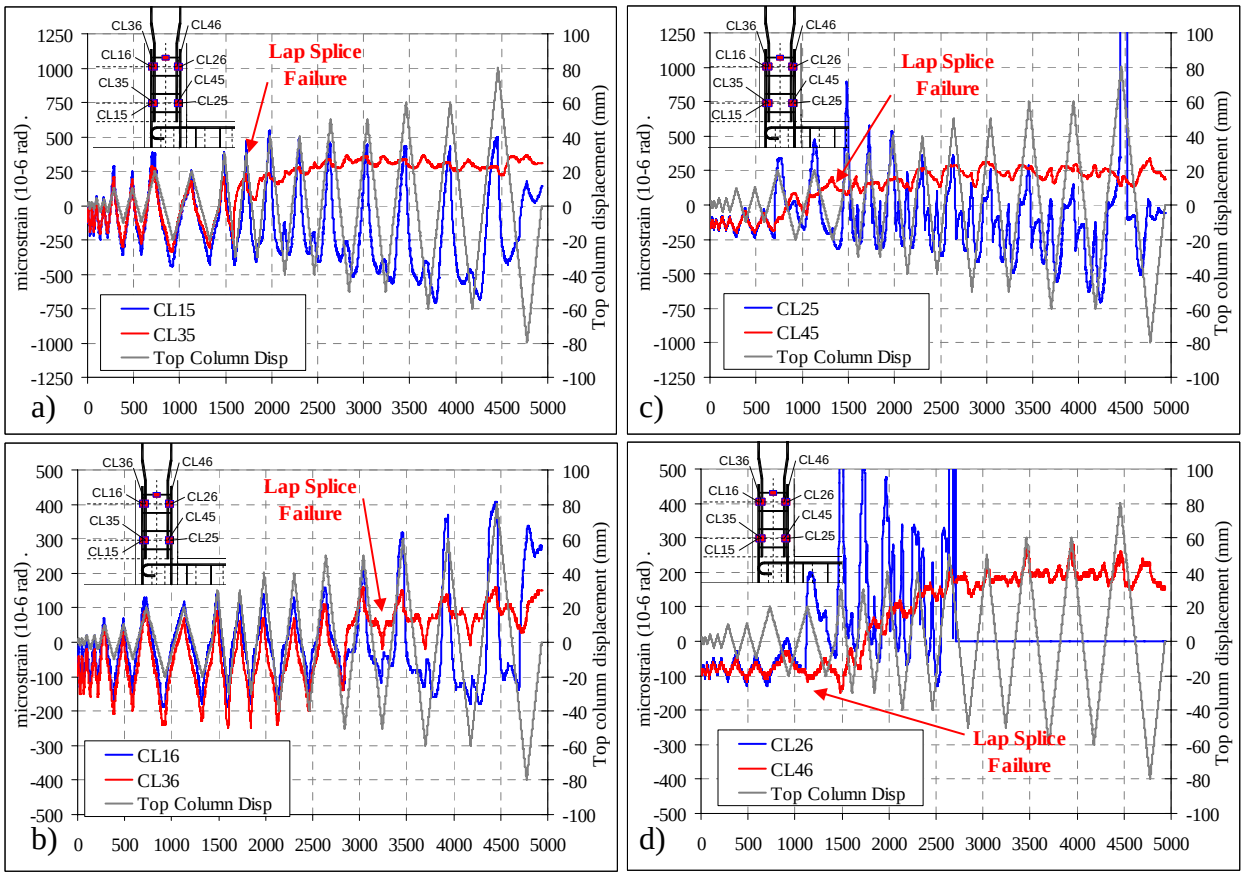

Figure 7.19: Test Unit S-O1: Strain gage readings for column longitudinal reinforcing bars lap-splice.

The lap-splice on the exterior column bars began to fail in the 2nd Pull cycle of the +1.0% drift, with total loss of force-transfer in the 2nd Push cycle of the -2.5% drift. This 'delayed' propagation of lap-splice failure was also evident from the late appearance of vertical bond-split crack in the Push direction (e.g. Figure 7.6e). The average steel stress along the measured length, $l_{d\text{-}lap}$, was approximately 52MPa and the average bond stress along $l_{d\text{-}lap}$ was 0.65MPa. Even after lap-splice failure, the bottom section of the column splice was carrying substantial tensile strains as evident from the cyclic trends of CL15 and CL16. The maximum stresses measured in the exterior bars were -150MPa (in compression) and +80MPa (in tension).

For the interior face column bars, the lap-splice failure started at the bottom end during the 2nd Push cycle of the -1.0% drift, when the spliced bars were under significant compression strains. This corresponded to the appearance of vertical split cracking on the column face, parallel to the lap-splice connection, as shown in Figure 7.6c. Then in the reverse cycle, the failure propagated to the top half of the lap-splice in the unloading branch of the 2nd Push cycle of -1.0% drift. At the initiation of lap-splice failure, the average steel stress along the measured length, $l_{d\text{-}lap}$ was approximately 38MPa and the average bond stress along $l_{d\text{-}lap}$ was 0.475MPa.

When the strain profiles of the column longitudinal and transverse reinforcement presented in the previous sub-sections are analysed in conjunction with Figure 7.19, the occurrence of lap-splice failure initiation was confirmed. As shown in Figure 7.16, after the partial lap-splice failure of the exterior bars at θ_{drift} = +1.0% and the full lap-splice failure at θ_{drift} = -2.5%, the tensile strain developed in the top half of the column exterior bars was limited before decreasing rapidly after θ_{drift} = -2.5%. Figure 7.18b also confirmed the initiation of lap-splice failure at +1.0% with a marginal increase of stirrup CS2C confining tensile strain after the vertical split cracking.

7.4 TEST RESULT OF RETROFITTED JOINT WITH LAP-SPLICE: S-R3

7.4.1 General description of behaviour

The F_c versus Δ_c hysteresis plot for S-R3 is given in Figure 7.20. The damage and cracking patterns at the selected peak inter-storey drift, θ_{drift}, loading cycles are shown in Figure 7.21 and Figure 7.22. S-R3 was tested up to the end of the 2nd cycles of the ±4.0% drift. The predicted lateral force capacities, $F_{sys\text{-}cal}$, for S-R3 were +15.6N and -20.6kN for the Pull and Push loading directions, with the expected inelastic mode to be pseudo-beam flexural rocking mechanism.

No cracks were observed in the ±0.1% drift loading cycles. In the ±0.2% drift cycles, vertical flexural cracks appeared in the weakened section, with longer cracks in the Pull cycles. The first crack initiated at the corner of the beam-column interface. In contrast to NS-R3 where the first crack was at the weakened section, the first crack in S-R3 was at the point of highest moment demand and lowest bond capacity (in terms of embedded development length, l_d). The ratio of cracked stiffness-to-uncracked stiffness, K_{cr}/K_{ini}, was 0.54 with the initial stiffness, K_{ini}, of 3198kN/m.

In the 1st Pull cycle of the +0.5% drift, a horizontal crack extended 90mm into the joint panel zone. The beam flexural crack at the beam-column interface also propagated up the section, with a maximum crack width of 1.1mm. In the remaining Pull-Push cycles of ±0.5% drift, crack growth was limited to the beam-column interface, referring to as the beam fixed-end rotation. Stiffness and strength degradations were observed in the 2nd cycles.

The beam bottom bars yielded at approximately the +0.8% drift, while pulling towards the +1.0 drift peak. The F_c at beam yielding was 13.1kN and the main flexural crack width was 2.0mm. On the reverse cycle to the -1.0% drift peak, the beam top bars yielded at approximately -0.95% drift, with F_c = -19.6kN and the maximum crack width of 0.9mm. The 'yielding' points of S-R3 were consistent with NS-R3 values (§6.4). Several new column and beam flexural cracks also appeared in the ±1.0% drift cycles (Figure 7.21 a-b). The largest residual crack at the end of the ±1.0% drift cycles was the hairline crack at the beam-column interface.

In the 1st Pull-Push cycles of the ±1.5% drift, the column cracks extended along the edge of the column-joint interface (Figure 7.21 c-d). The column horizontal flexural crack was measured 0.8mm wide. In the 1st Push cycle of the -1.5% drift, a hairline vertical crack, initiated at the anchorage bolt hole for the external post-tensioning anchorage, appeared along the exterior column bars. In addition, there was a new vertically-inclined crack on the tension face of the column. Both cracks were indications of bond-induced splitting cracks.

In the 2nd Pull-Push cycles of the ±1.5% drift, no new cracks appeared but minor extensions of the existing cracks were observed. In terms of the F_c-Δ_c hysteresis, S-R3 was responding very similarly to NS-R3 up to the ±1.5% drift cycles. As with all other retrofitted specimens, pinching and slipping of the F_c-Δ_c hysteresis loops were observed in S-R3.

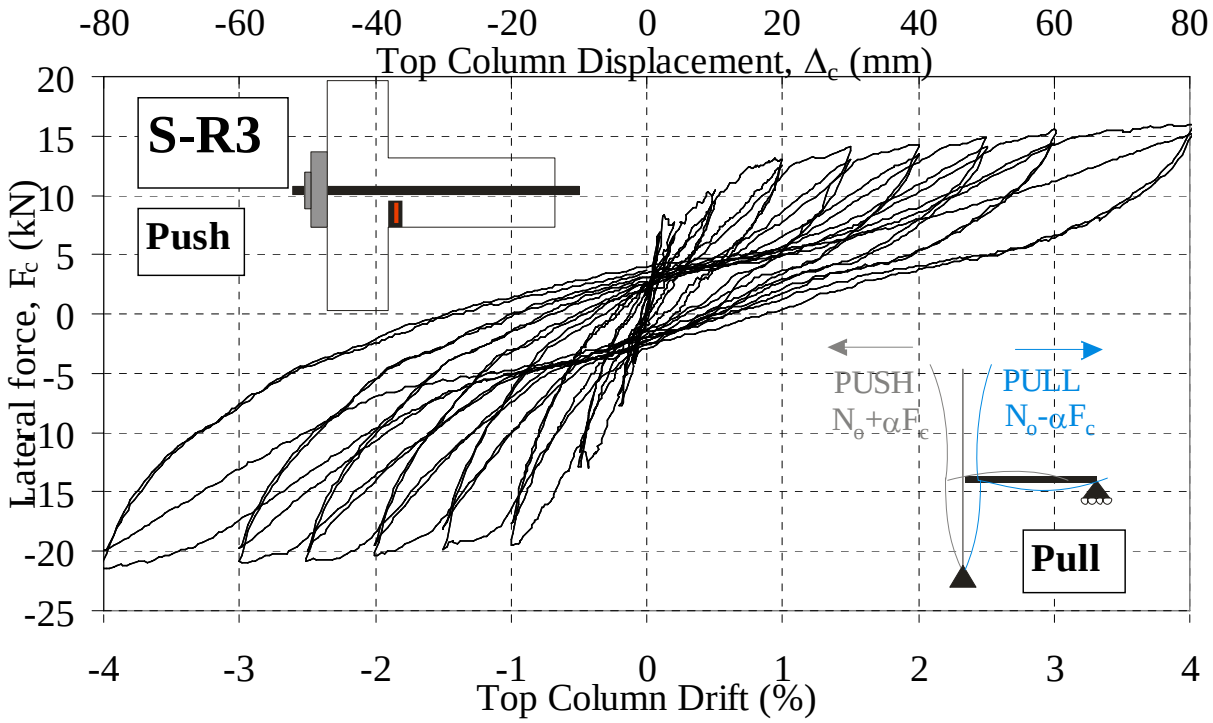

Figure 7.20: Top column lateral load, F_c, versus top column displacement, Δ_c, and drift, θ_{drift} for S-R3.

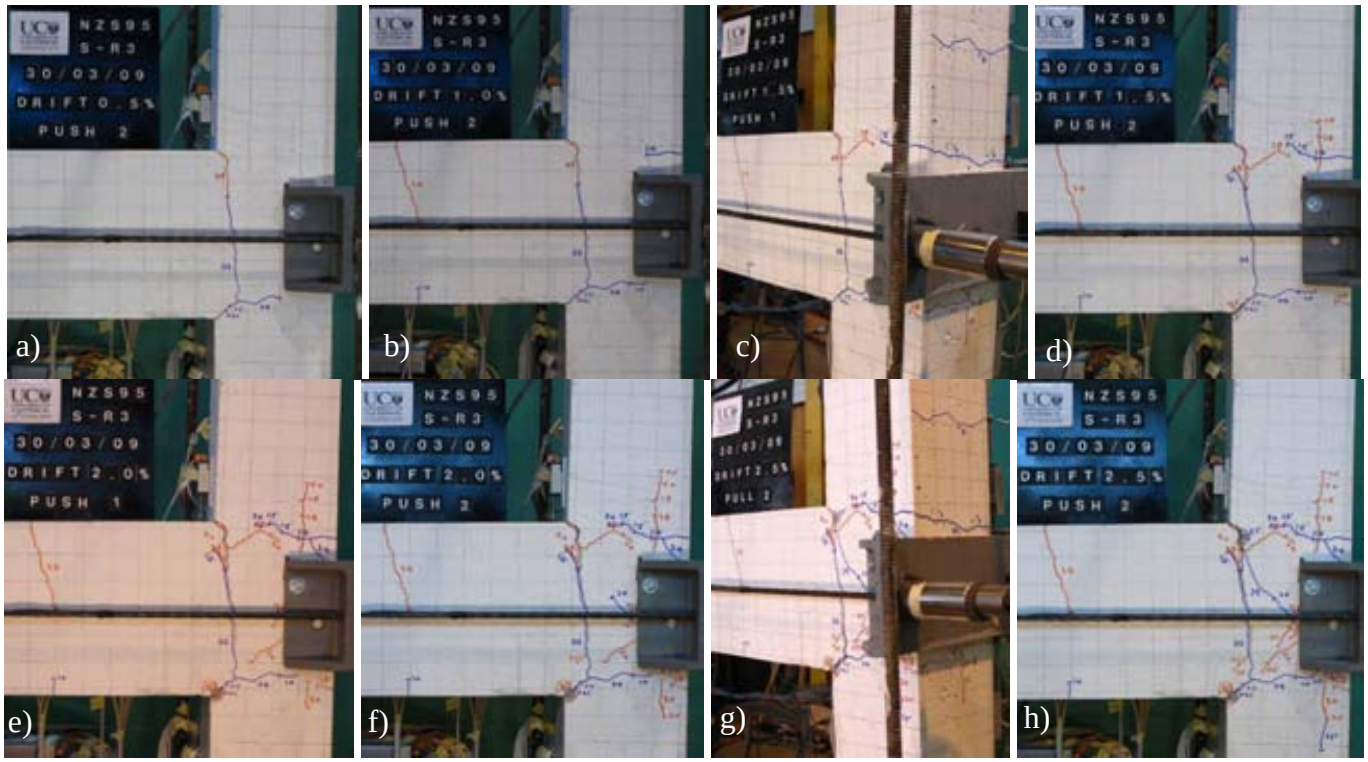

Figure 7.21: Observed cracking pattern of S-R3: TOP: a) 2nd Push cycle of the -0.5% drift; b) 2nd Push cycle of the -1.0% drift; c) 1st Push cycle of the -1.5% drift; d) 2nd Push cycle of the -1.5% drift. BOTTOM: e) 1st Push cycle of the -2.0% drift; f) 2nd Push cycle of the -2.0% drift; g) 2nd Pull cycle of the +2.5% drift; h) 2nd Push cycle of the -2.5% drift.

In the ±2.0% drift cycles, most inelastic deformation was concentrated at the beam-column interface. The largest crack width was approximately 5mm. In the 1st Push of the -2.0% drift, a hairline diagonal crack appeared in the joint. Examination of the principal stresses indicated that the joint cracking was due to p'_c failure. The joint shear crack occurred at the θ_{drift} ≈ -2.0%. At the joint cracking in the Push direction, the principal stresses, p'_t and p'_c measured were 0.112 $\sqrt{f'_c}$ MPa and 0.973$\sqrt{f'_c}$ MPa, with corresponding γ_j of +0.00355.

In the reverse loading to the 2nd Pull peak of the +2.0% drift, the diagonal joint cracking (corresponding to the Pull loading) appeared in the joint. The joint shear crack occurred at the θ_{drift} ≈ +2.0%. At the joint cracking in the Push direction, the principal stresses, p'_t and p'_c measured were 0.148 $\sqrt{f'_c}$ MPa and 0.447$\sqrt{f'_c}$ MPa, with corresponding γ_j of +0.00938. A comparison of the diagonal joint crack between the two loading directions shows that the angle of diagonal crack was higher in the Pull direction due to the lower column axial force.

In the ±2.5 % drift cycles, the joint cracks extended in both loading directions (Figure 7.21g-h) with a maximum joint crack width of 0.45mm. In addition, the joint diagonal cracks were extending upwards along the column exterior longitudinal bars. This vertical bond split crack was similarly observed in S-O1. However, no vertical cracks were observed along the column interior bars. The maximum crack widths at the apparent pseudo-rocking section were 4mm in the Pull direction and 3.0mm in the Push direction. Despite the joint and column-splice cracking, no discernable drop in F_c was observed for S-R3.

The damage pattern in the ±3.0% drift loading cycles was similar to the ±2.5% drift cycles, with minor vertical crack extensions and continued widening of the flexural crack at the weakened section (Figure 7.22a). The main flexural crack was approximately 5.0mm wide while the joint shear crack was 0.5-1.0mm wide. Minor spalling at the corner of the beam-column joint interface was observed. The vertical cracks along the column exterior face extended about 100mm above and below the joint panel. The gradual ‘unzipping’ cracking along the exterior column bars indicated progressive lap-splice failure.

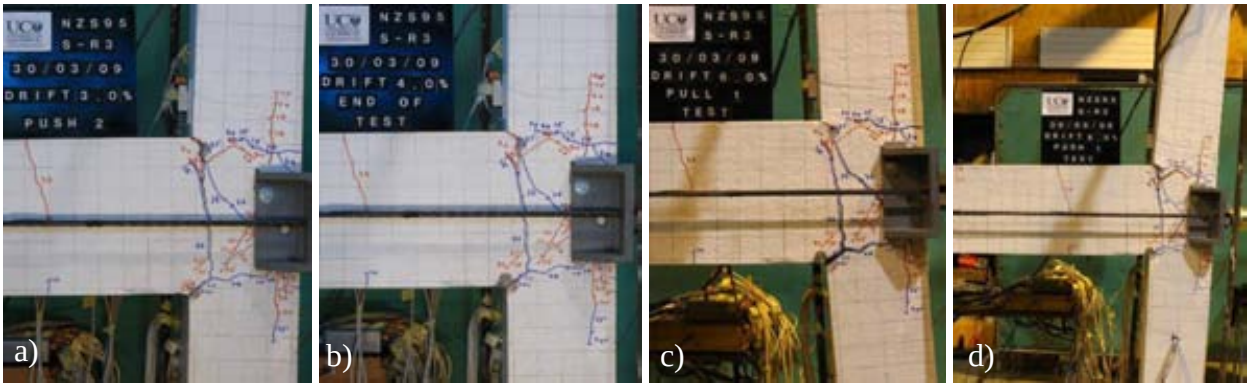

Figure 7.22: Observed cracking pattern of S-R3: a) 2nd Push cycle of the -3.0% drift; b) End of the ±4.0% drift cycles; c) 1st Pull cycle of the +6.0% drift; and d) 1st Push cycle of the -6.0% drift.

In the ±4.0% drift cycles, the dominant inelastic mechanism was still the flexural hinging at the beam-column interface. The 'rocking' gap widths were about 8mm and 6mm in the Pull and Push directions respectively. The joint diagonal cracks and column flexural and vertical cracks grew albeit at a slow rate. At the end of the ±4.0% drift cycles, the overall damage pattern was satisfactory (Figure 7.22b) as the column vertical axial and post-tensioned horizontal forces reduced the residual cracks significantly. The maximum residual crack width was 1.8mm at the beam-column interface. The joint diagonal and column flexural crack widths were approximately 0.4mm wide at the end of the test, indicating the moderate damage and repairable performance level for S-R3.

As the specimen was relatively undamaged, one Pull-Push cycle at ±5.0% and one at ±6.0% drift amplitudes were imposed on S-R3 to investigate the extreme loading damage pattern. Bulging due to the push-out of the hooked anchorage at the column face was observed, but the confinement from the post-tensioning tendons was preventing the spalling of the concrete. At the peaks of ±6.0% drift cycles, the pseudo-rocking mechanism was apparent in S-R3, with a 'rocking gap' up to 13mm measured.

7.4.2 Load-displacement hysteresis analysis

The F_c-Δ_c hysteresis plot for S-R3 is shown in Figure 7.20 while the analysis of the S-R3 F_c-Δ_c hysteresis is presented in Figure 7.23.

As with the R3-retrofitted beam-column joint without lap-splice, NS-R3, stable tri-linear F_c-Δ_c envelope was observed, corresponding to three key points: a) decompression point - the neutral axis at the edge of the section with zero stress at the extreme fibre, b) yielding point c) ultimate point - corresponded to the 4.0% drift cycle peaks. The maximum F_c values measured

were +15.9kN (at +4.0% drift) and -21.5kN (at -4.0% drift). Due to the bond failure of the plain round bars, the hysteresis loop exhibited significant pinching-slip behaviour. The experimental column moment, $M_{sys\text{-}exp}$, values (+13.3kNm and 18.0kNm) were relatively close to the theoretical column moment, $M_{sys\text{-}cal}$, values (+13.0kNm and 17.2kNm).

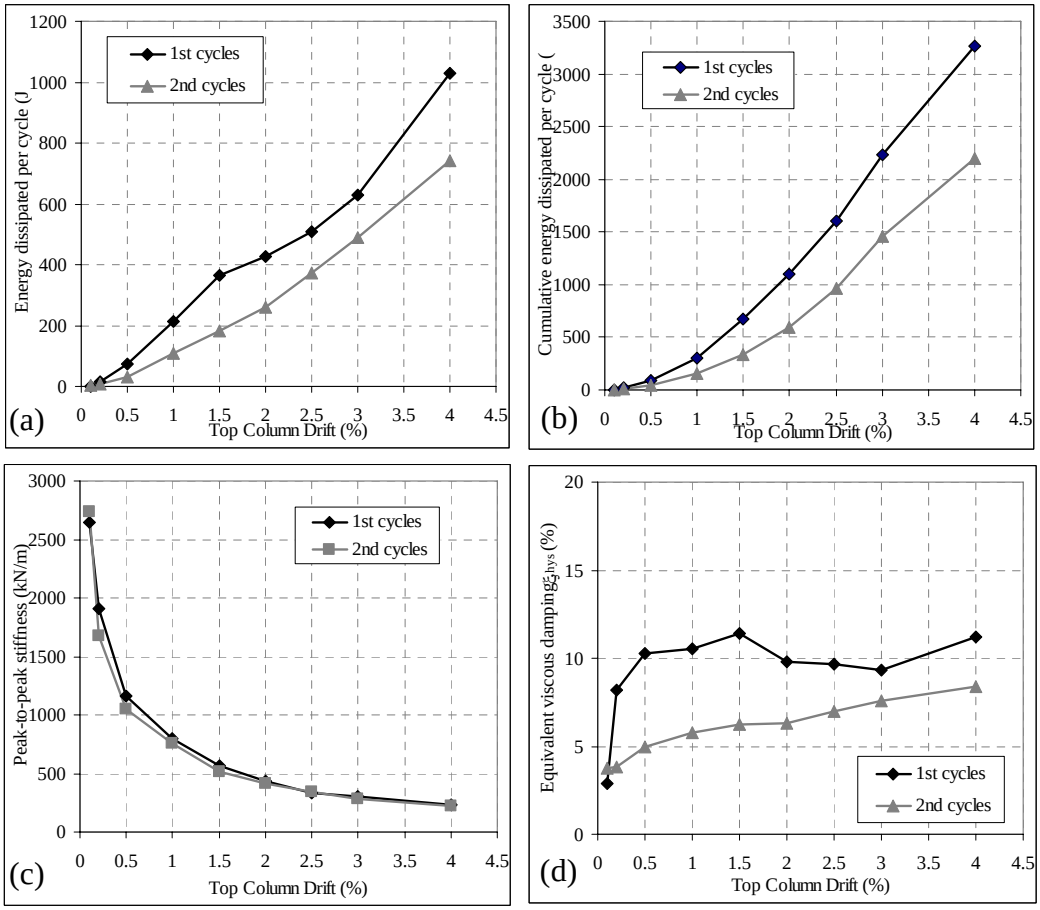

Figure 7.23: Force-displacement analysis for S-R3: a) Energy dissipated per cycle; b) Cumulative energy dissipated per cycle; c) peak-to-peak stiffness, K_{eff}, and; d) Equivalent viscous damping, ξ_{hys}.

In terms of peak-to-peak stiffness, K_{eff}, S-R3 curve was marginally higher than the as-built S-O1 specimen, especially in higher θ_{drift} levels, as the beam-weakening stiffness reduction was compensated by the post-tensioning stiffness enhancement. Except for the first two θ_{drift} (±0.1% and ±0.2%), the K_{eff} did not degrade significantly between the 1st and 2nd cycles.

However, S-R3 was only comparable if not worse in terms of energy dissipation capacities, when compared to S-O1 and NS-R3. Between the typical design θ_{drift} (1.0%-2.5%), the ξ_{hys} were on average, 10.4% and 6.3% for the 1st and 2nd cycles respectively. The in-cycle degradation of energy dissipation capacity was particularly severe for S-R3 when compared to

other specimen. This suggests the higher relative contribution of the post-tensioning tendons in terms of the overall lateral resistance, considering the F_c envelope for S-R3 and both NS-R3 and S-O1 was relatively similar. The 2nd cycle values of the ξ_{hys} were 20-55% lesser than the 1st cycles, with the in-cycle degradation more significant between θ_{drift} of ±0.2% to ±1.5%

7.4.3 Local deformations and displacement components

7.4.3.1 Decomposition of top column horizontal displacement

The components of the top column horizontal displacement, Δ_c at the peaks of the Pull and Push loading cycles as percentages of the total Δ_c are presented in Figure 7.24.

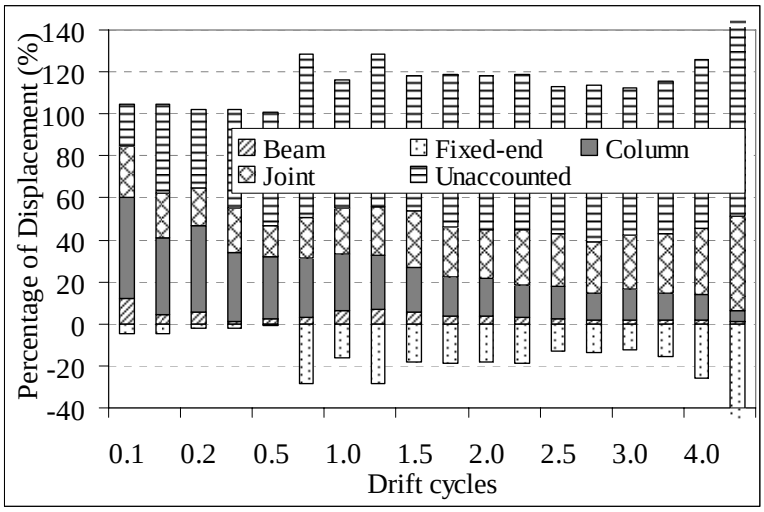

a) Pull loading direction – positive displacement.

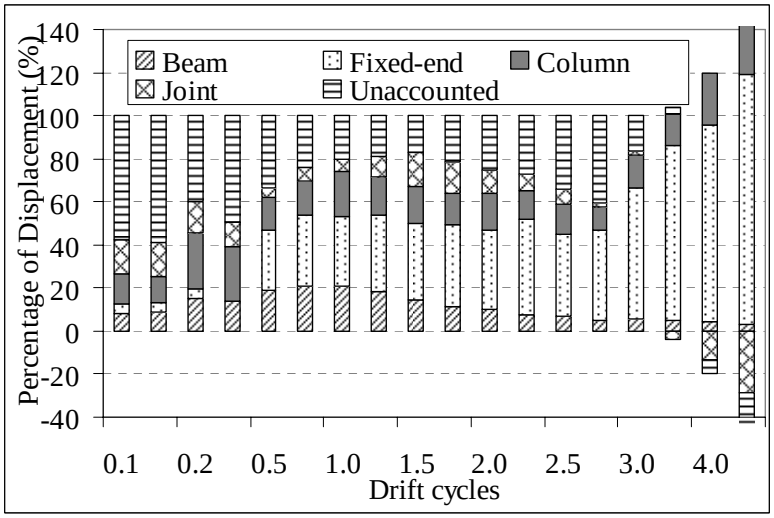

b) Push loading direction – negative displacement.

Figure 7.24: Displacement decompositions based on measured deformations for S-R3.

Fixed-end deformation, $\Delta_{beam,fixed\text{-}end}$, was the largest component of the Δ_c in the Push loading direction from -0.5% onwards, accounting for 30-75% of Δ_c in the Push direction. In the Pull direction, there was a large unaccounted component of Δ_c, predominantly because of the under-measurement and accumulation of $\Delta_{beam,fixed\text{-}end}$ in the opposite direction. The accumulation of $\Delta_{beam,fixed\text{-}end}$ was effective evidence of beam-elongation due to the plastic strain accumulation within the flexural hinge at the beam-column interface.

The column flexural deformation, $\Delta_{col,flexural}$, and joint distortion contribution, Δ_{joint}, were both relatively constant. $\Delta_{col,flexural}$ was accounting for 5-30% of Δ_c in the Pull cycles and 10-20% of Δ_c in the Push cycles. This was lower when compared to the S-O1 in which the $\Delta_{col,flexural}$ was relatively significant due to the lap-splice failure. Δ_{joint} was accounting for 5-30% of Δ_c in the Pull cycles and 10-20% of Δ_c in the Push cycles.

7.4.3.2 Beam deformations

The beam moment-curvature (M_{bf} - ϕ_b) plots for the beam flexural regions are shown in Figure 7.25. In both loading directions, the theoretical M_{bf} capacities (+28.8kNm and -38.0kNm) were attained. The maximum M_{bf} developed in the Pull and Push directions were +28.7kNm and -38.7kNm respectively. The asymmetric nature of the M_{bf} - ϕ_b plot for the fixed-end region was a consequence of the damage accumulation in the Push direction. The maximum ϕ_b attained in the fixed-end region were +0.0004m^{-1} and -0.468m^{-1} in the Pull and Push cycles respectively. These corresponded to the curvature ductility of 13.4 in the Push direction, assuming ϕ_y = 0.035m^{-1} (read from the Figure 7.25a). Limited ϕ_b was measured in other beam regions, with a maximum ϕ_b of -0.0127m^{-1} measured in the region 275-475mm from the column internal face.

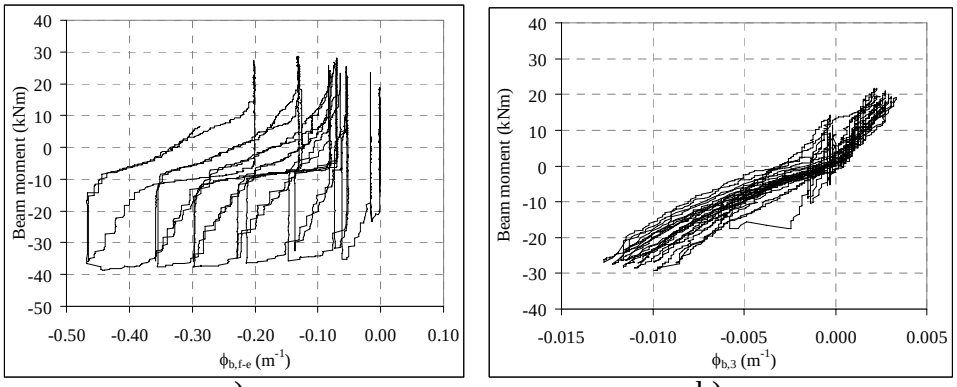

a) b)

Figure 7.25: a) Moment-curvature plots for beam sections: a) fixed-end section; and b) 275-475mm from the column internal face.

7.4.3.3 Column deformations

Figure 7.26 shows the measured moment-curvature response for the three regions of the column. The observed nominal column flexural strength, $M_{c\text{-}cf}$ (the plateau moment in the hinging direction), were +12.1kNm and -16.3kNm in the Pull and Push cycles respectively. In the Pull cycles, the $M_{c\text{-}cf}$ corresponded to the ϕ_c of 0.024m^{-1} and of 0.050m^{-1} at the top and bottom halves of the column. In the Push cycles, the $M_{c\text{-}cf}$ corresponded to the ϕ_c of -0.077m^{-1} and of -0.046m^{-1} at the top and bottom halves of the column. When compared to S-O1, the column plastic deformation was significantly lowered (about halved) in S-R3, suggesting successful retrofit intervention in limiting column lap-splice damage. Furthermore, unlike S-O1, no $M_{c\text{-}cf}$ degradation was observed despite the relatively high ϕ_c ductility demand in the first 200mm region above the beam top (Figure 7.26b). The curvature ductilities developed in this section were 4.4 and 14.0 during the Pull and Push loading cycles (assuming ϕ_y = 0.0055m^{-1}). These curvature ductility demands were similar to those observed in NS-R3 (§6.4.3.3).

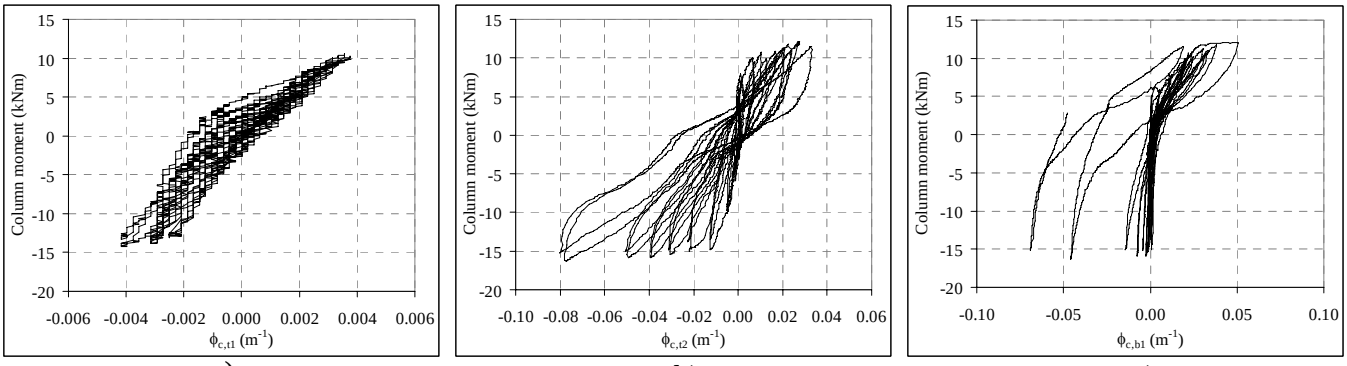

a) b) c)

Figure 7.26: Moment-curvature plots for column flexural sections: a) 230-430mm from the beam top face; b) 0-200mm from the beam top face; and c) 0-200mm from the beam soffit.

7.4.4 Beam-column joint behaviour

7.4.4.1 Nominal joint shear stress and joint shear distortion

The nominal joint shear stress, v_{jh}, versus joint shear distortion, γ_j, and γ_j versus Δ_c relationships for S-R3 are given in Figure 7.27. The maximum v_{jh} measured were 1.85MPa (0.352 $\sqrt{f'_c}$ MPa or 0.067f'_c MPa) and -2.49MPa (-0.475 $\sqrt{f'_c}$ MPa or -0.091f'_c MPa) in the Pull and Push peaks of the ±4.0% drift. The effect of beam-weakening in reducing the v_{jh} demand in the joint was apparent in the positive Δ_c direction. The maximum joint shear distortion, γ_j measured was 0.03 radians at the 2nd Pull peak of +4.0% drift.

After the joint cracking in the ±2.0% drift cycles, no discernable decrease in v_{jh} was observed. This confirmed the positive benefits of the external post-tensioning confinement in increasing the deformation capacity of cracked joint panel. Figure 7.27b shows that there was a tendency of increase in γ_j after the joint cracking at approximately ±2.0% drift cycles. At the early stages of loading, γ_j was also responding linearly as a function of Δ_c, with up to γ_j of ±0.005 radians sustained without joint diagonal cracking.

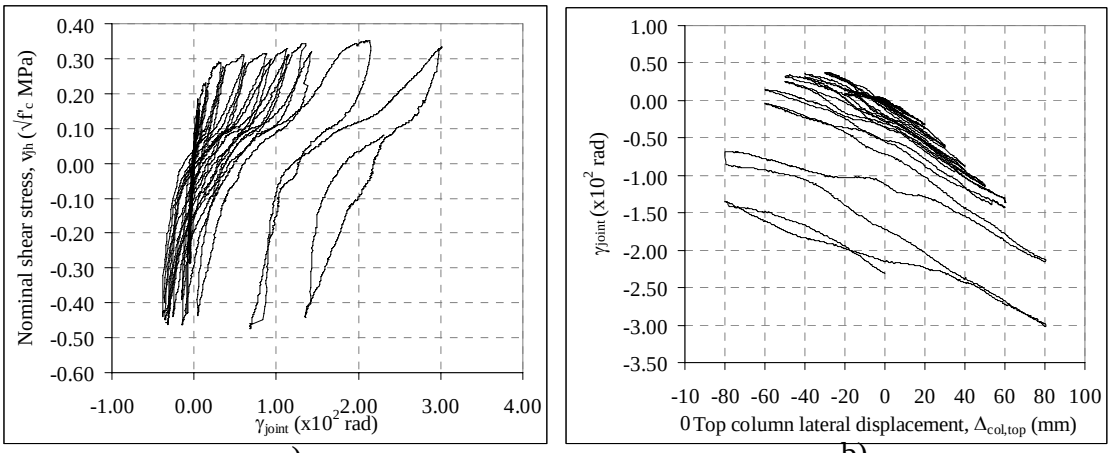

Figure 7.27: a) Nominal joint shear stress, v_{jh} versus joint deformation, γ_j; b) Joint shear deformation, γ_j versus top column lateral displacement, Δ_c.

7.4.4.2 Joint principal stresses

Figure 7.28 shows the joint principal stress responses as functions of the Δ_c and γ_j for S-R3. At the first diagonal joint cracking in the 1st Push peak of the -2.0% drift, the corresponding p'_t, p'_c and γ_j were $0.112\sqrt{f'_c}$ MPa, $0.973\sqrt{f'_c}$ MPa (or $0.186f'_c$ MPa) and 0.00355 radians. The maximum p'_c that led to joint diagonal cracking in the Push direction was somewhat lower than the $0.25f'_c$ MPa limit as discussed in §3.4. At the diagonal cracking in the 2nd Pull peak of the +2.0%, the corresponding p'_t, p'_c and γ_j were $0.148\sqrt{f'_c}$ MPa, $0.447\sqrt{f'_c}$ MPa (or $0.085f'_c$ MPa) and -0.00938 radians. In terms of maximum principal stresses in the joint during the cyclic loading of S-R3, the maximum p'_t was $0.192\sqrt{f'_c}$ MPa at γ_j =-0.0209 radians and the maximum p'_c was $1.023\sqrt{f'_c}$ MPa at γ_j =-0.0069 radians.

Similar to NS-R3, selective beam weakening and external post-tensioning retrofit implemented for S-R3 was successful in decreasing the joint principal stress demands and improving the capacity or the post-cracking behaviour. However, while the joint shear strength was maintained, γ_j would nevertheless increase significantly after joint cracking as illustrated by Figure 7.27b.

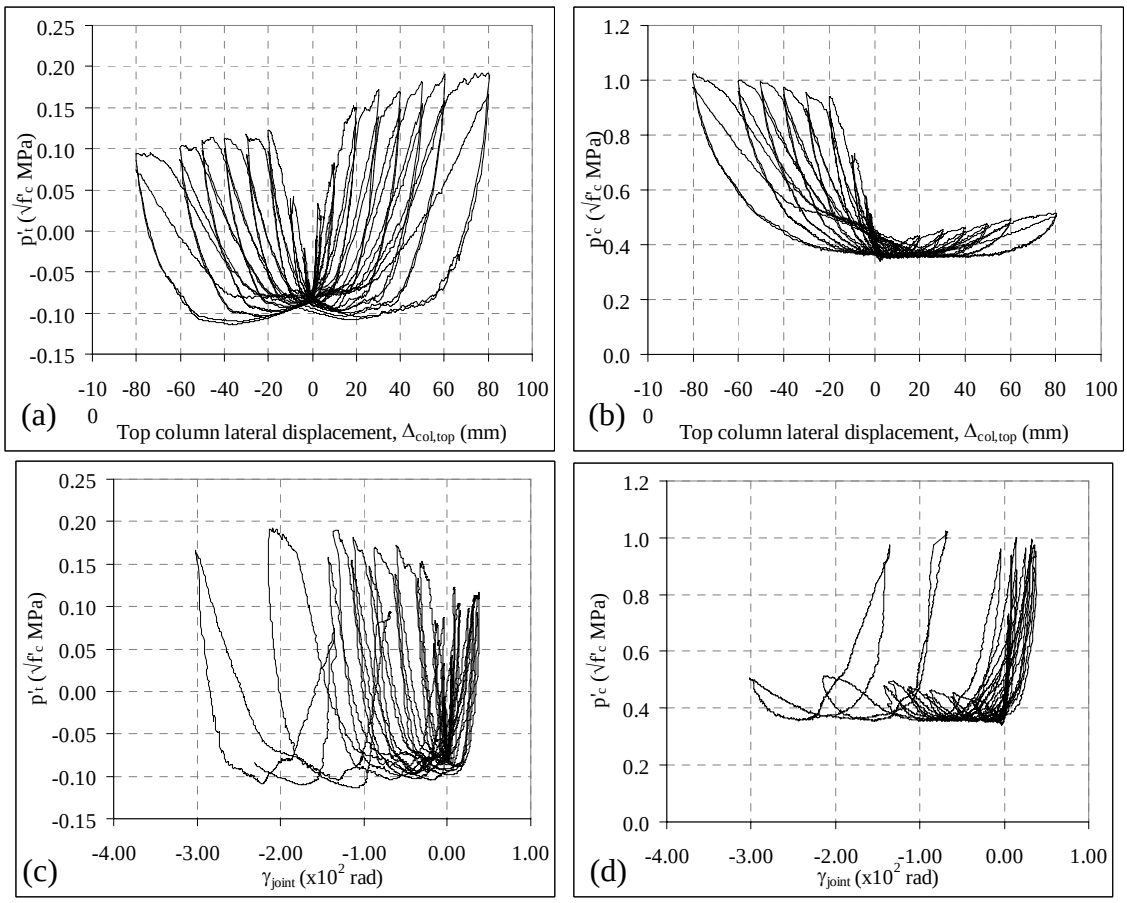

Figure 7.28: a-b) Joint principal stresses versus top column lateral displacement, Δ_c: a) principal tensile stress, p'_t; b) compressive tensile stress, p'_c; c-d) Principal stresses versus joint shear deformation, γ_j plots: c) principal tensile stress, p'_t; d) compressive tensile stress, p'_c.

7.4.5 Steel strain profiles

7.4.5.1 Beam longitudinal reinforcement strains

Figure 7.29, Figure 7.30 and Figure 7.31 present the strain profiles of the top and bottom (not weakened and weakened) beam longitudinal reinforcement for the specimen S-R3. The X-axis is the distance from the exterior column face while the two vertical dashed lines refer to the column centre-line and the interior column face. The beam weakening section was 50mm from the interior column face. Tensile strains are given as positive values. From the steel test, the ε_y for the longitudinal beam and column reinforcing was 0.00168 (1680 microstrains) and the f_y was 335MPa. Three strain gages along the bottom weakened reinforcement were damaged during the beam-weakening of S-R3, resulting in incomplete strain profiles shown in Figure 7.31.

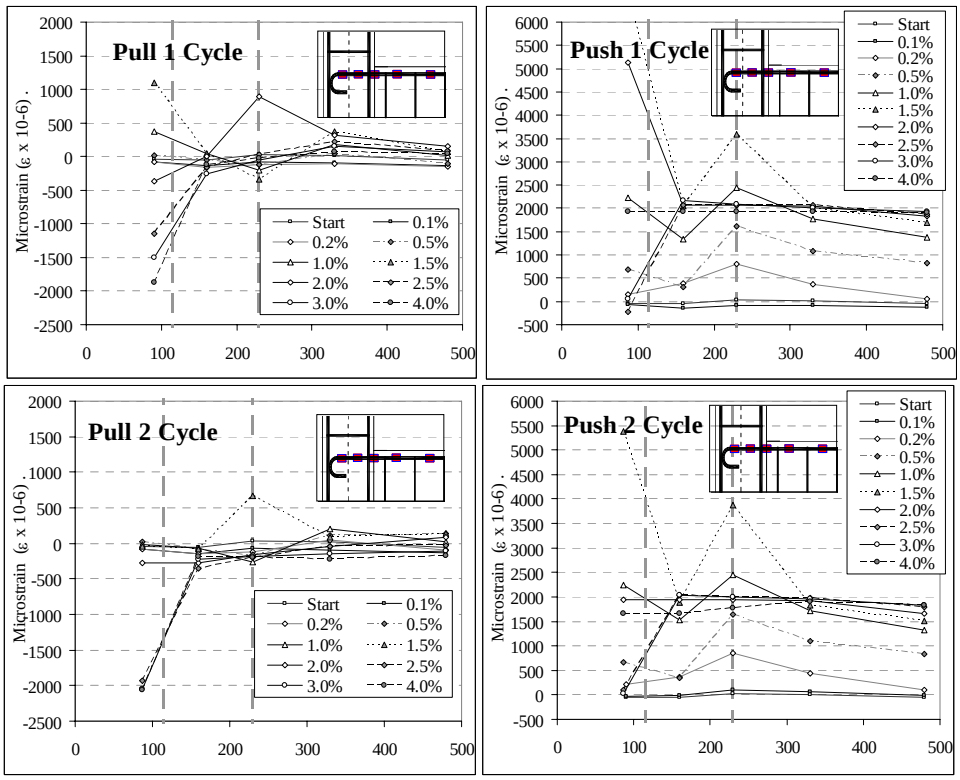

Figure 7.29: Strain profile of beam top longitudinal bars of the specimen S-R3.

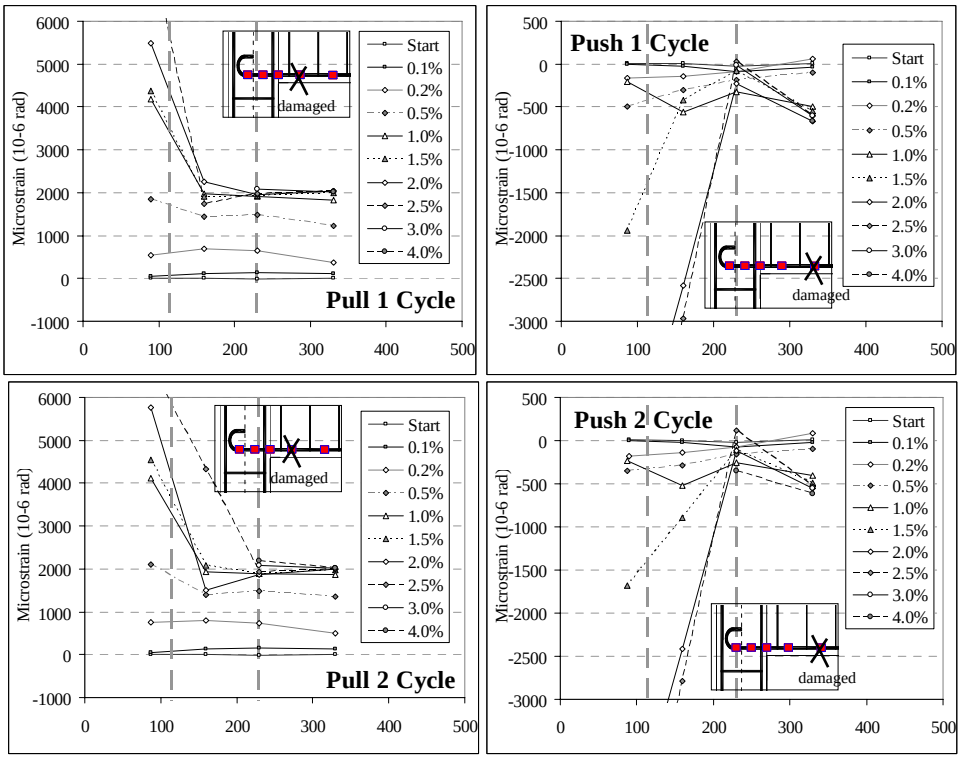

Figure 7.30: S-R3: Strain profiles of beam bottom longitudinal bars (interior bars – not weakened).

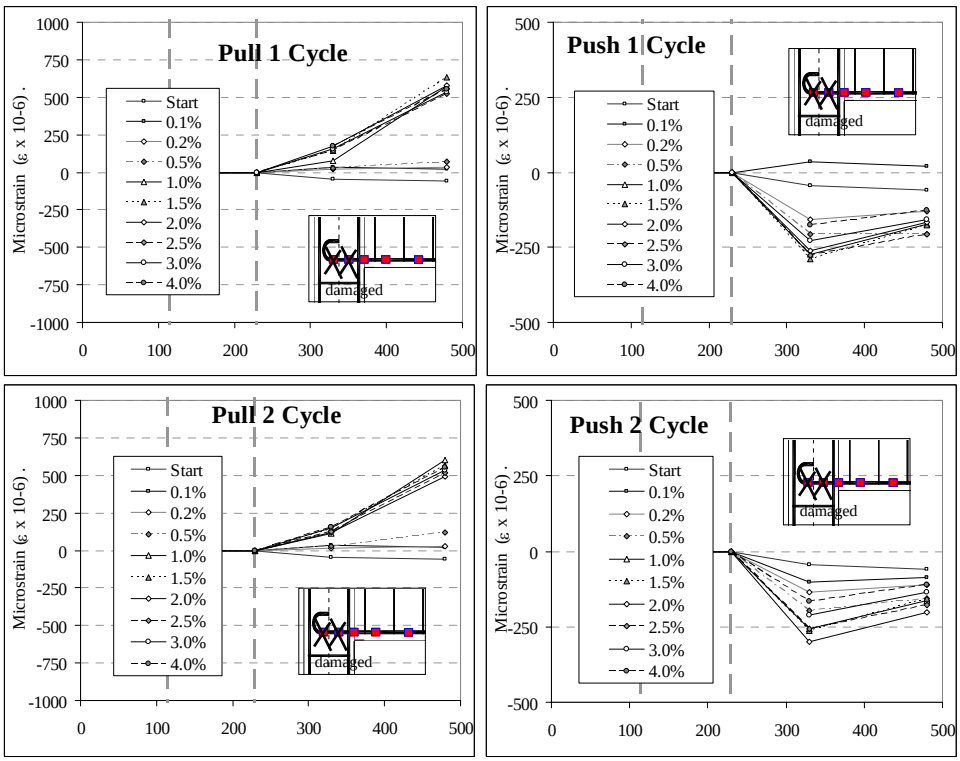

Figure 7.31: S-R3: Strain profiles of beam bottom longitudinal bars (exterior bars – weakened).

For the top bars, the strains measured indicated no bond degradation in either the Pull or the Push cycle, up to the 2nd cycles of the ±0.2% drift. The maximum compressive stress measured before the bond slip failure was 33MPa. After the bond-failure under compressive strains in the Pull cycles, the top bars had limited tensile strains (<300 microstrains) except for the length embedded within the joint core. After the joint cracking, the beam top bars embedded within the joint underwent stress reversal with yielding compressive strains measured in the +3.0% drift peaks.

The top bars started yielding in the 2nd Push cycle of the -0.5% drift, with localised high tensile strains measured at the beam-column interface with a maximum tensile strain up to 1700 microstrains. In the subsequent Push cycles, the length of the yielded bar sections was extended, and by the -2.0% drift peak, the whole instrumented length of the top bars was yielding in tension.

For the un-weakened beam bottom bars (Figure 7.30), tension yielding occurred in the +0.5% drift and compression yielding occurred in the -1.5% drift. However, unlike NS-R3, limited compressive strains were detected in the region outside the joint core, indicating bond-failure of the bars at the beam-column interface. In tension, the un-weakened bars were

responding similarly to NS-R3, with substantial yielding and strain-hardening as the Pull loading progressed.

For the weakened beam bottom bars, up to 126MPa tensile stress and 60MPa compressive stress were developed in the straight section along the beam, beyond the weakened section. The strain profiles as shown in Figure 7.31 gave an indication of the stress development of plain round bars within uncracked concrete section.

7.4.5.2 Column longitudinal reinforcement strains

The strain profiles along the exterior and interior column bars are shown in Figure 7.32 and Figure 7.33 respectively. The Y-axis is the distance from the centre-line of the beam. The three horizontal dashed lines refer to the beam soffit (bottom line), the beam centre-line and the beam top face (top line). Tensile strains were measured as positive values. All column strain gages were zeroed before the axial force loading on the column at the start of the test. The ε_y for the longitudinal column reinforcement was 1680 microstrains and the f_y was 335MPa.

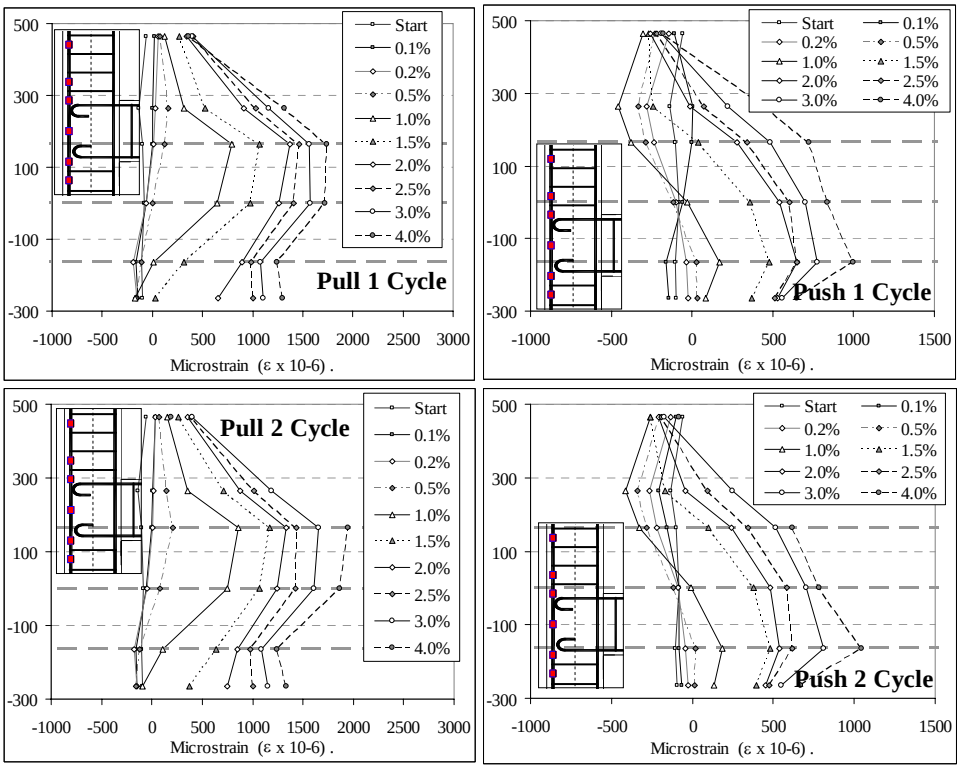

Figure 7.32: Column exterior face longitudinal reinforcement strain profiles for the specimen S-R3.

In the early loading stages up to the ±1.5% drift, the strain profiles of the column longitudinal bars of S-R3 were similar to those of NS-R3. After the lap-splice partial failure of

the exterior bars in the 2nd cycles of the ±1.5% drift, the column exterior bars lost the compression resistance during the Push cycles, and significant tensile strains were measured within the joint core region. The exterior bars yielded in tension during the Pull cycles of the +4.0% drift, as a result of the increased column moment demand from the positive post-yield stiffness of the un-bonded post-tensioned beam-column connection. The interior column bars were yielding earlier when compared to the exterior bars. The interior bars in the bottom half of the column yielded in tension in the +2.0% drift.

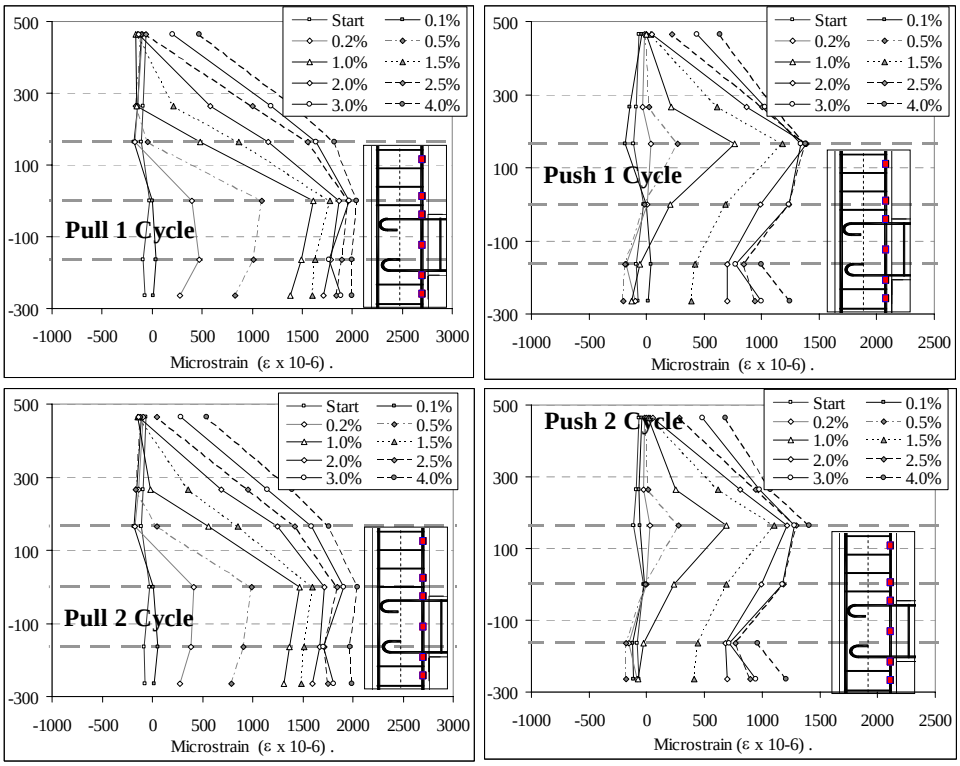

Figure 7.33: Column interior face longitudinal reinforcement strain profiles for the specimen S-R3.

7.4.5.3 Stirrup reinforcement strains

The strain profiles of the stirrups in the column and the beam are shown in Figure 7.34. Selected stirrup results are presented herein as the general trend across different strain gages is similar. The complete dataset is given in Appendix F.

Up to ±1.5% drift peaks, the stirrups in the column were not carrying substantial strains. However, after the column flexural cracking and lap-splice partial failure, a sharp increase in tensile strains was measured. For the stirrups along the lap-splice, higher tensile strain was measured in the Push direction, corresponding to the higher F_c and column flexural moment, M_{cf}.

As a result of beam-weakening, the beam stirrup closest to the column (BS1A and BS1B) was not activated for beam shear. On the other hand, higher tensile strain was observed in the third stirrup from the column interior face (BS3A). In addition, the first beam stirrup recorded compression strain in the Push direction, suggesting shallower compression strut from the bottom face of the beam into the joint core, as postulated by Figure 3.32 in §3.4.4.2.

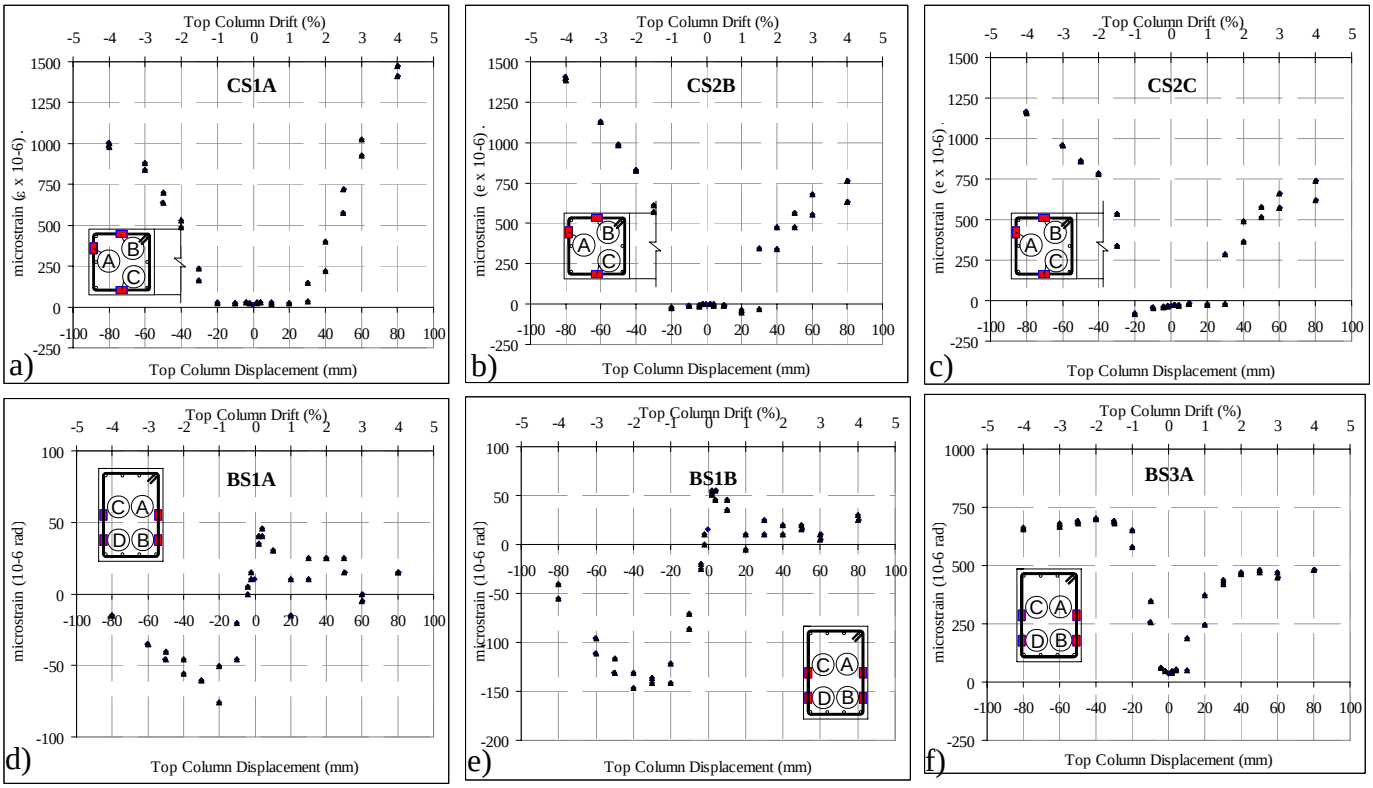

Figure 7.34: Stirrup reinforcement strain profiles: TOP: a) column stirrup 50mm from beam soffit; b-c) column stirrup 50mm from beam top face; BOTTOM: d-e) beam 1st stirrup - 50mm from column interior face; and f) beam 2nd stirrup - 183mm from column interior face.

7.4.6 Lap-splice strain measurements

The time history of the strain gages measurement along the lap-splice length for S-R3 is presented in Figure 7.35. The applied column top displacement, Δ_c is also plotted on the secondary Y-axis. Four pairs of strain gages were placed on the column longitudinal bars with two pairs on the exterior face bars (CL1X and CL3X) and two pairs on the interior face bars (CL2X and CL4X). 'X' refers to the vertical location of the gages, in which for X=5 and X=6, the locations are 100 mm and 300 mm from the beam-top face respectively. Equation 7.1 was used to calculate the average bond stress, τ_{lap}, along $l_{d\text{-}lap}$.

The lap-splice on the exterior column bars began to partially fail in the 2nd Push cycle of the -1.5% drift, with the loss of compressive force transfer at the bottom end (i.e. between CL15 and CL35). The partial failure of the exterior bar lap-splices also corresponded with the observed vertical bond-split crack in the Push loading to -1.5% drift (e.g. Figure 7.21c). At the partial failure (θ_{drift} = -1.5%), the average steel stress along the measured length, $l_{d\text{-}lap}$ was approximately 110MPa and the average bond stress along $l_{d\text{-}lap}$ was 1.38MPa. Nevertheless, a full lap-splice failure of the exterior column bars was not observed after the ±4.0% drift cycles The maximum stresses measured in the exterior bars were -80MPa (in compression) and +160MPa (in tension).

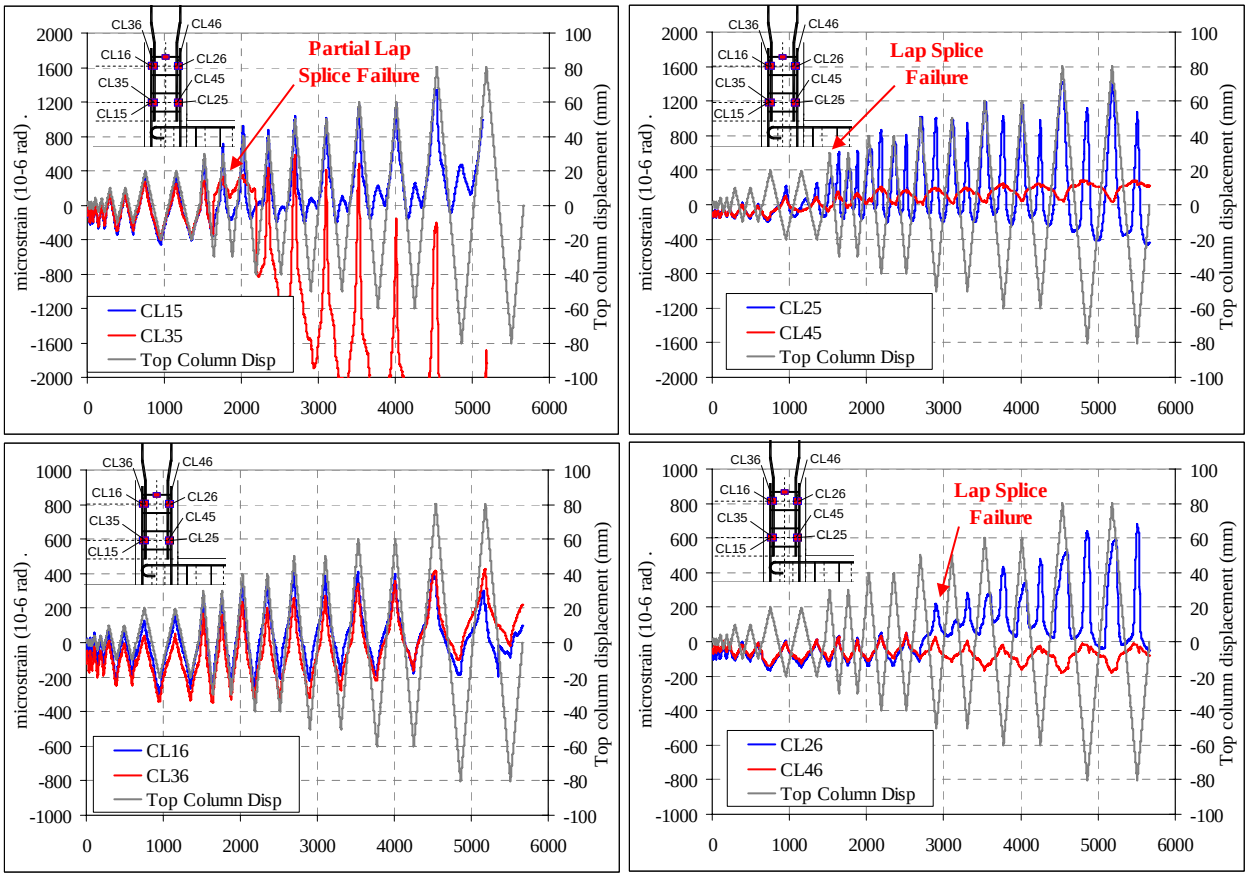

Figure 7.35: Test Unit S-R3: Strain gage readings for column longitudinal reinforcing bar lap-splices.

For the interior face column bars, the lap-splice failure started at the bottom end during the 1st Pull of the +1.5% drift, when the spliced bars were under significant tensile strains. Loss of force-transfer across the whole instrumented length of the lap-splice occurred in the 1st Push cycle of -2.5% drift. Interestingly, no vertical split cracks were observed in the column for the interior face bars, unlike S-O1. Furthermore, from the ±1.0% drift cycles onward, a reverse of strains (compression to tension) was measured within the lap-splice length. At the initiation of

lap-splice failure, the average steel stress along the measured length, $l_{d\text{-}lap}$ was approximately 40MPa and the average bond stress along $l_{d\text{-}lap}$ was 0. 50MPa.

7.5 DISCUSSION OF TEST RESULTS

7.5.1 Influence of column lap-splice on as-built and SW retrofitted joints

Comparing the test results of as-built and retrofitted beam-column joints would highlight several design issues with regards to the presence of column lap-splice in non-ductile beam-column joints. The comparisons of the F_c-Δ_c hysteresis loops and the observed damage pattern for NS-O1/S-O1 and S-O1/S-R3 are provided in Figure 7.36 and Figure 7.37 respectively.

In terms of as-built pre-1970s beam-column joints, both NS-O1 and S-O1 had similar seismic performance characteristics, in which joint shear failure led ultimately to column longitudinal bar buckling and 'structural collapse'. There was no fundamental difference between the responses of the two specimens in terms of F_c-Δ_c hysteresis response. The lap-splice failure in S-O1 did not preclude the eventual failure of joint shear hinging and the buckling of the column bars within the joint panel.

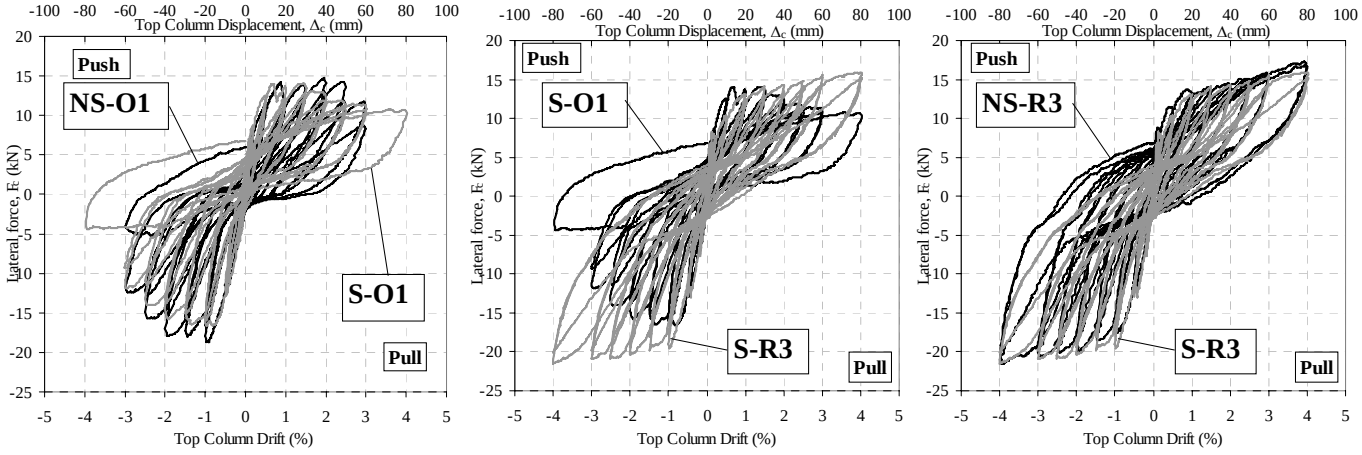

Figure 7.36: Comparison of F_c-Δ_c for as-built and SW retrofitted specimens with and without lap-splice.

The inadequate lap-splice in S-O1 and S-R3 resulted in the degradation of splice resistance with increasing ϕ_c ductility demand. However, the onset of vertical split crack did not constitute splice failure, as the transverse reinforcement provided confinement and shear-friction transfer mechanism [33, 46]. Lynn *et al.* [34] concluded that only eventual shear failure as a result of a network of vertical and inclined splitting cracks would lead to gravity axial and lateral load failures.

Furthermore, predominantly discrete flexural and bond-splitting cracks with concentrated strains dominated the inelastic deformations for the plain round bar RC joints. The discrete column cracks within S-O1 were evident in Figure 7.37. As such, lap-splice failure would only contribute significantly to the loss of stiffness and softening of the joint, without complete structural failure in terms of lateral or axial load capacities. This was also confirmed by the tests on columns with plain round bars by Verderame *et al.* [57, 58] and walls with plain round bars by Ireland *et al.* [31]. However, research (e.g. [20]) has shown that bond slip of deformed bar column lap-splice could contribute up to 45% of the Δ_c at the peak F_c.

As summarised in §7.2, there was a lack of experimental data on non-ductile beam-column joints and columns with inadequate lap-splice. The data presented in this chapter thus far have indicated that for a typical New-Zealand pre-1970s beam-column joint subassembly, joint shear failure would dominate the inelastic mechanism.

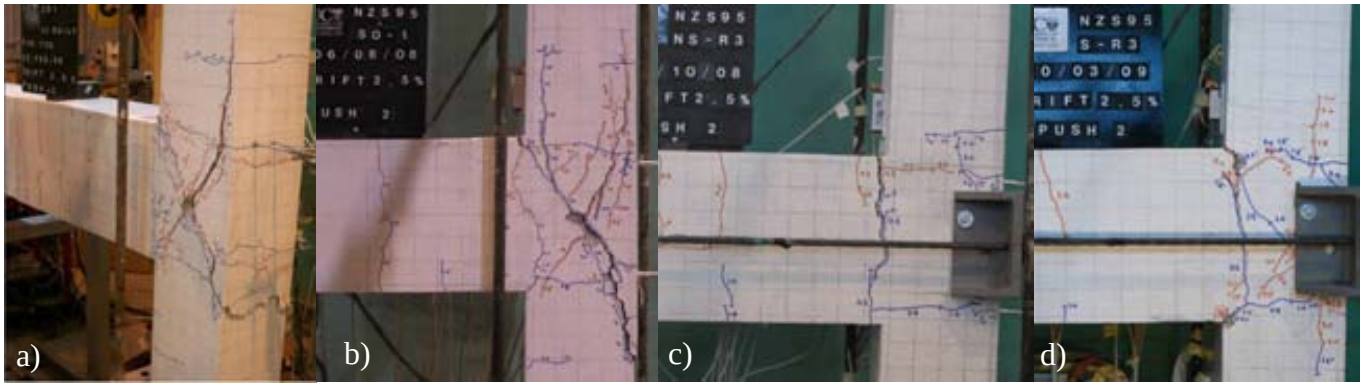

Figure 7.37: Comparison of damage pattern of as-built and SW retrofitted specimens with and without lap-splice: a) NS-O1; b) S-O1; c) NS-R3; and d) S-R3.

S-R3 has shown that inadequate lap-splice did not affect the overall seismic performance of the SW-retrofit of the exterior beam-column joint. The objectives of reducing the joint shear stresses demand as well as improving the inelastic mechanism to a beam pseudo-rocking flexural hinging were achieved in S-R3, when compared with S-O1 (Figure 7.36b). Nevertheless, while the SW retrofit in S-R3 prevented strength degradation due to joint shear crack, the beam-weakening alone was not sufficient to completely protect the column from lap-splice failure (§7.4.6). The lap-splice failure in S-R3 has led to a more pinched and thinner hysteresis loop as shown in Figure 7.36. Nevertheless, with beam-weakening, the detrimental effects of column lap-splice could be minimised, as the ϕ_c ductility demand for the column might be limited due to

lower M_{cf} demand. Further mitigation like local column jacketing might be necessary if the columns were expected to yield in the post-retrofitted frame (like the base columns).

7.5.2 Analytical and experimental comparison

The hierarchy of strength M_c-N_c performance domain and the F_c-Δ_c experimental-analytical comparison for specimen S-O1 are given in Figure 7.38. Firstly, the F_c-Δ_c comparison and the damage observed confirmed the accuracy of the joint shear assessment approach described in §2.4.2. The experimental joint shear cracking F_c values were predicted reasonably well with the joint principal stress approach. However, the evaluation procedure described in §2.4.5 and §2.4.6 for non-ductile column lap-splice details and plain round bars was found to require some modifications.

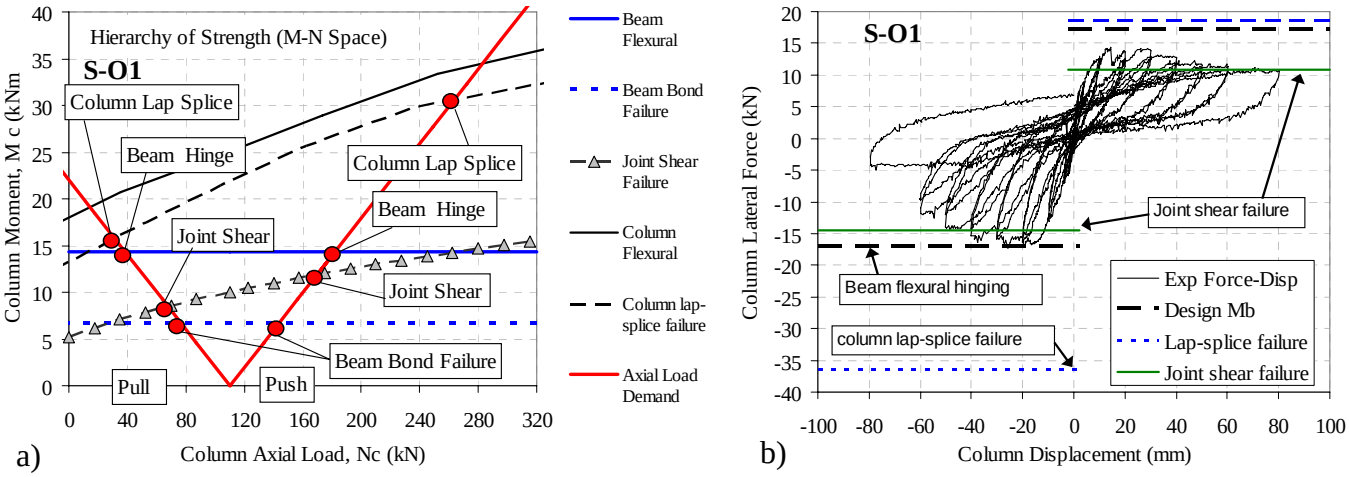

Figure 7.38: a) M-N performance domain for S-O1 (reproduced from Appendix B); b) Experimental and analytical comparison of the F_c-Δ_c for S-O1.

The F_c-Δ_c experimental-analytical comparison for specimen S-R3 is given in Figure 7.39. The maximum F_c values measured were +15.9kN (at +4.0% drift) and -21.5kN (at -4.0% drift) in the Pull and Push loading directions respectively. The analytical procedure described in §3.4 (Chapter 3) was used to generate the predicted F_c. As seen from Figure 7.39, good analytical prediction was achieved for both the Pull and Push loading directions. The predicted failure mode was beam flexural hinging, with pseudo-rocking at the beam-column interface with F_c of +15.6kN and –20.6kN. This was confirmed by the test observation with discrepancy between the experimental and analytical F_c being less than 5%.

However, the detailed analytical procedure for the SW-retrofit design (from §3.4.5) also failed to capture the degradation of stiffness in the Push direction due to the bond degradation of the beam and column longitudinal bars under reversal cyclic loading. The assessment of S-R3 did not predict joint diagonal compression cracking or partial lap-splice bond degradation. The joint diagonal compressive failure however did not affect the overall F_c-Δ_c response as the post-tensioning joint confinement and beam-weakening led to a higher ultimate γ_j (where joint shear strength began to decrease).

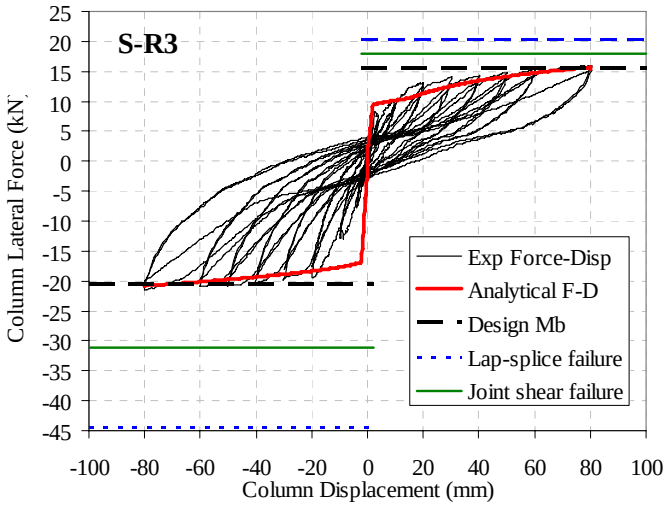

Figure 7.39: Experimental-analytical comparison of the F_c-Δ_c curves for S-R3.

Figure 7.40 presents the comparison between the measured and predicted post-tensioning forces and the neutral axis (normalised by the beam depth, h_b). Generally, the predicted post-tensioned tendon force was matching the measured forces reasonably well except for a minor under-prediction in the Pull direction. This was most probably due to the under-prediction of the pseudo-rocking induced tendon elongation and over-estimation of the non-prestressed steel reinforcement's contribution.

The measured pseudo-rocking neutral axis was erratic (Figure 7.40b) as the critical linear potentiometer at the beam-column interface mid-depth was not giving accurate reading at very low displacement readings (<1.0mm). As such, Figure 7.40b could not give a meaningful comparison with the analytical prediction.

While not discussed here, the S-R3 results also indicated the failure of the lap-splice assessment procedure to predict the partial column lap-splice failure, as discussed in §7.4.6. Therefore, for the design of SW retrofit of non-ductile beam-column joint with inadequate lap-

splice at the potential plastic hinge zone, sufficiently accurate lower-bound assessment of the column lap-splice failure capacity is required. The next sub-section (§7.5.3) will revisit the lap-splice capacity assessment in view of the test results presented in this chapter.

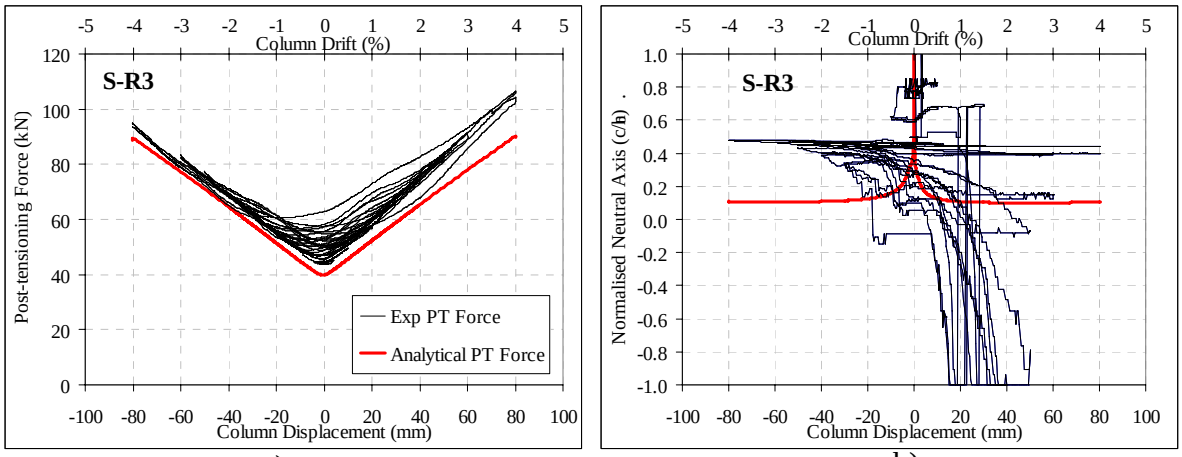

a) b)

Figure 7.40: Analytical prediction and experimental response at the post-tensioned pseudo-rocking interface: a) Tendon forces; and b) Neutral axis depth, normalised to the beam depth, h_b.

7.5.3 Assessment of column lap-splice capacity with plain round bars

It was shown in §7.3.6 and §7.4.6 that column lap-splice failure of plain-round bars had occurred for both S-O1 and S-R3. The maximum steel stresses, f_s, measured along the lapped column reinforcement, ranged from 80 to 160MPa. When compared to the limiting f_s developed in the lap-splice failure of 255MPa, there were 37% to 68% error margins. This suggests the use of 2006 NZS3101 [40] expression for the development length, l_d, within the ASCE-41 [10] approach to calculate lap-splice capacity may be unsuitable for lap-splice with plain-round bars within a non-ductile beam-column joint subassembly.

It was shown in §7.3.6 and §7.4.6 that column lap-splice failure of plain-round bars appeared to be more susceptible in tension, as expected (e.g. [23]). Both the lack of deformed ribs and the reliance on adhesive and frictional bond capacities contributed to the negligible tensile capacity of the lap-splice. τ_{lap} measured in the tests were ranging from 0.475MPa to 1.38MPa, which was the typical bond capacity of plain round bars, as summarised in §2.4.5. However, the variability of τ_{lap} and the difficulty to determine the exact point of lap-splice failure initiation means further tests are required to establish the reliable limit state of τ_{lap}.

Recalling the assessment approach adopted for the lap-splice described in §2.4.5 which was mostly developed based on empirical data using deformed bar reinforcement, it is shown from the limited data herein that such an assessment approach may be inadequate. Furthermore,

the post-peak behaviour after the initiation of lap-splice failure has not been very well understood from the two tests presented. Considering the parameter τ_{lap} seems to be more predictable when compared to f_s, a viable alternative assessment approach for inadequate column lap-splice with plain-round bars is a bond-capacity dependent model.

Harries *et al.* [28] have proposed a lap-splice capacity model based on the average bond stress capacity, which first introduced by Orangun *et al*. [42], instead of the generalised equations for development length given in ACI318-2005 [3]. For context, in the current NZSEE assessment guidelines [41], column lap-splice is evaluated based on the ratio between the provided lap length and the code-specified development length. It should be noted that the fundamental lap-splice mechanism has been acknowledged as a bond problem in the ACI 408 documents [8, 9].

Another alternative was the friction-based formulation proposed by Calvi *et al.* [16, 26], and introduced in the fib Bulletin on Seismic Assessment and Retrofit of RC Buildings [6], to account for the column longitudinal bar slipping within an interior beam-column joint with plain round bar reinforcement. The authors argued that column bars terminated at the lap-splice length for a typically low inter-storey height RC frame might lead to lower M_{cf} capacity in the range 20-50%, depending on the axial load in the column. The approach did not tackle the effect of lap-splice directly, but rather consider the effect of the bond failure of the spliced column longitudinal bars on the M_{cf}. Figure 7.41 shows an illustration of the modified column M-N capacity curves due to poor bond behaviour. A similar approach can be developed for column with inadequate lap-splice and bond capacities.

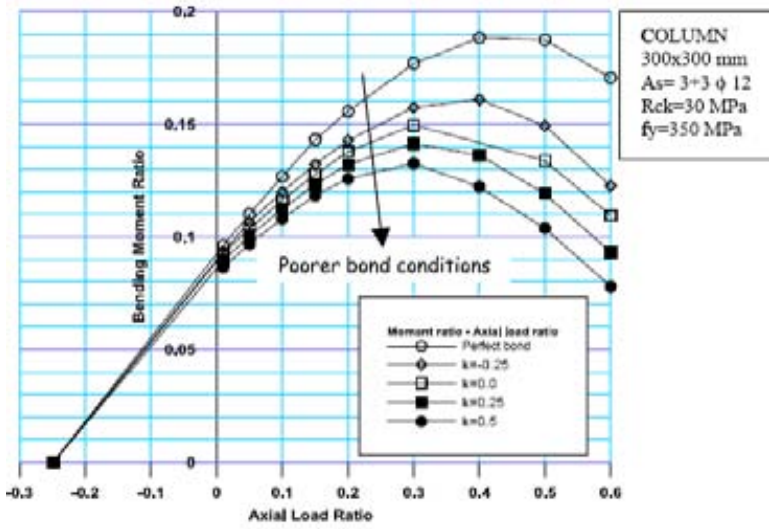

Figure 7.41: Modified column M-N capacity curves due to the influence of poor bond.

7.6 CONCLUSIONS

1. Table 7.1 below summarises the experimental results of the two specimens presented in this chapter: a) As-built beam-column joint with inadequate lap-splice (S-O1) and b) Full SW retrofit with beam-weakening and joint-post-tensioning (S-R3) on beam-column joint with lap-splice 1.

Table 7.1: Summary of S-O1 and S-R3 test results.

Test Unit	Peak Lateral Force (kN)	Inter-storey drift at maximum force, θ_d (%)	Ultimate inter-storey drift, θ_d (rad) [1]	Lateral Force at joint cracking (kN)	Inter-storey drift at joint cracking, θ_d (rad)	Maximum column moment, $M_{sys\text{-}exp}$ (kNm)	Theoretical column moment, $M_{sys\text{-}cal}$ [2] (kNm)	$M_{sys\text{-}exp}$ / $M_{sys\text{-}cal}$
S-O1	+14.1 -16.7	+1.43 -0.98	+2.5%-I	+14.3 -17.2	+0.7%-I -1.3%-I	+11.8 -14.0	+8.5 -11.9	+1.39 -1.18
	Failure Mode		Max / Min joint shear stress, v_{jh} (f'_c MPa)	Min / Max axial stress, f_v (MPa)	Max. principal tensile stress, p_t ($\sqrt{f'_c}$ MPa)	Max. principal compression stress, p'_c ($\sqrt{f'_c}$ MPa)	1st / 2nd cycles total energy dissipated, $E_{D,4.0\%}$ (J)	Equivalent Viscous Damping (EVD) ratio, $\xi_{hyst,2.0\%}$ [3] (%)
	Joint Shear & Lap Splice		+0.110 -0.133	+0.61 -3.63	0.341	1.155	2998 / 1661	13.6

Test Unit	Peak Lateral Force (kN)	Inter-storey drift at maximum force, θ_d (%)	Ultimate inter-storey drift, θ_d (rad) [1]	Lateral Force at joint cracking (kN)	Inter-storey drift at joint cracking, θ_d (rad)	Maximum column moment, $M_{sys\text{-}exp}$ (kNm)	Theoretical column moment, $M_{sys\text{-}cal}$ [2] (kNm)	$M_{sys\text{-}exp}$ / $M_{sys\text{-}cal}$
S-R3	+15.9 -21.5	±4.0	na [3]	+13.4 -20.3	+2.0%-II -2.0%-I	+13.3 -18.0	+13.0 -17.2	+1.02 -1.05
	Failure Mode		Max / Min joint shear stress, v_{jh} (f'_c MPa)	Min / Max axial stress, f_v (MPa)	Max. principal tensile stress, p_t ($\sqrt{f'_c}$ MPa)	Max. principal compression stress, p'_c ($\sqrt{f'_c}$ MPa)	1st / 2nd cycles total energy dissipated, $E_{D,4.0\%}$ (J)	Equivalent Viscous Damping (EVD) ratio, $\xi_{hyst,2.0\%}$ [3] (%)
	Beam Flexural Hinging		+0.067 -0.091	+0.71 -3.98	0.192	1.023	3261 / 2193	9.8

Positive force, displacement and drift correspond to PULL cycles while negative values indicate PUSH cycles. I=1st cycle; II=2nd cycle.

[1] Failure point defined as attained peak force was less than 80% of previous peak force. [2] Calculated maximum column moment based on the Hierarchy of Strength analysis outlined in Chapters 2 and 3. [3] $\xi_{hyst,2.0\%}$ is calculated based on hysteresis area-based equivalent viscous damping in the 1st cycle.

[4] No structural failure observed (based on the definition). f''_c for S-O1 and S-R3 are 15.1MPa and 27.5MPa respectively.

2. The as-built non-ductile beam-column joint, specimen S-O1, had both lap-splice bond failure and joint shear cracking at approximately the ±1.0% to ±1.5% drift cycles respectively. The joint panel deterioration due to the joint shear strength degradation ultimately led to structural failure at the 1st Pull cycle of +2.5%. Column longitudinal bar buckling within the heavily damaged joint core resulted in the onset of axial load failure and significant loss of F_c capacity.

3. The SW-retrofitted specimen, S-R3, has shown remarkable improvement in terms of inelastic mechanism, joint shear performance and the overall F_c-Δ_c hysteresis response. The predicted beam pseudo-rocking flexural hinging was achieved, with an average energy dissipation capacity, ξ_{hys}, of 6.3% to 10.4%. While the F_c-Δ_c of S-R3 is comparable to NS-R3, the energy dissipation capacity was lower in S-R3, presumably due to the column lap-splice partial failure.

4. The influence of column lap-splice on as-built and SW-retrofitted beam-column joints was discussed in §7.5.1. For non-ductile beam-column joints, inadequate lap-splice did not result in significant strength degradation in S-O1 due to the discrete cracking pattern of plain-round reinforcement (as discussed in earlier chapters). For retrofitted joints, while retrofit interventions prevented the joint shear failure, column lap-splice failure was not prevented completely and as a result, the lower energy dissipation capacity of S-R3 was achieved when compared to NS-R3.

5. As past research is driven more by the development of design code for *new* construction, there is a gap of experimental and analytical research on the bond and lap-splice capacities for plain round reinforcement. To ascertain the required development length and lap length for lap-splice within non-ductile RC frame buildings, further research in this area is needed.

6. The accuracy and limitations of the existing assessment procedures for inadequate plain-round bar lap-splice were discussed in §7.5.3. It is proposed that average-bond stress

capacity approaches (e.g. [8, 9, 28]) in assessing column lap-splice with plain round bars to be adopted. The development of such an analytical approach is beyond the scope of this research.

7.7 CHAPTER 7 REFERENCES

[1] Aboutaha R, Engelhardt MD, Jirsa JO, Kreger ME. (1999) Experimental investigation of seismic repair of lap splice failures in damage concrete columns. *ACI Structural Journal*. Mar-Apr 1999; **96**(2):297-307.

[2] Aboutaha RS, Engelhardt MD, Jirsa JO, Kreger ME. (1996) Retrofit of concrete columns with inadequate lap splice by the use of rectangular steel jackets. *Earthquake Spectra*. Nov 1996; **12**(4):693-714.

[3] ACI318-08. (2008) *Building code requirements for structural concrete and commentary*. American Concrete Inst. (ACI), Farmington Hills, MI.

[4] ACI318-56. (1956) *Building code requirements for reinforced concrete (ACI318-56)*. American Concrete Inst. (ACI), Detroit, MI.

[5] ACI318-63. (1963) *Building code requirements for reinforced concrete (ACI318-63)*. American Concrete Inst. (ACI), Detroit, MI.

[6] ACI318-71. (1970) Proposed revision of ACI 318-63: Building code requirements for reinforced concrete. *ACI Structural Journal*. Feb 1970; **67**(2):77-146.

[7] ACI318-77. (1977) *Building code requirements for reinforced concrete (ACI318-77)*. American Concrete Inst. (ACI), Detroit, MI.

[8] ACI-408. (1992) *State-of-the-art report on bond under cyclic loads (ACI408.2R-92)*. American Concrete Inst. (ACI), Detroit, MI.

[9] ACI-408. (2003) *Bond and development of straight reinforcing bars in tension (ACI408R-03)*. American Concrete Inst. (ACI), Farmington Hills, MI.

[10] ASCE-SEI-41-06. (2007) *Seismic rehabilitation of existing buildings. ASCE standard ASCE/SEI 41-06*. American Society of Civil Engineers (ASCE), Reston, Va.

[11] Aycardi LE, Mander JB, Reinhorn AM. (1994) Seismic resistance of R.C. frame structures designed only for gravity loads: Experimental performance of subassemblages. *ACI Structural Journal*. **91**(5):552-563.

[12] Beres A, Pessiki S, White R, Gergely P. (1996) Implications of experimental on the seismic behaviour of gravity load designed RC beam-column connections. *Earthquake Spectra*. **12**(2):185-198.

[13] Beres A, White R, Gergely P. (1992) *Seismic behaviour of reinforced concrete frame structures with nonductile details: Part I - Summary of experimental findings of full scale beam-column joint tests. Technical Report NCEER-92-0024*. National Center for Earthquake Eng. Research, SUNY, Buffalo, NY.

[14] Bracci JM, Reinhorn AM, Mander JB. (1992) *Seismic resistance of reinforced concrete frame structures designed for gravity loads: Part I - Design and properties of a one-third scale model structures. Technical Report NCEER-92-0027*. National Center for Earthquake Eng. Research, SUNY, Buffalo, NY.

[15] Bracci JM, Reinhorn AM, Mander JB. (1992) *Seismic resistance of reinforced concrete frame structures designed only for gravity loads: Part III - Experimental performance*

and analytical study of a structural model. Technical Report NCEER-92-0029. National Center for Earthquake Eng. Research, SUNY, Buffalo, NY.

[16] Calvi GM, Moratti M, Pampanin S. (2002) Relevance of beam-column damage and collapse in RC frame assessment. *J of Earthquake Eng*. **6**(1):75-100.

[17] Canbay E, Frosch RJ. (2005) Bond strength of lap-spliced bars. *ACI Structural Journal*. July 2005; **102**(4):605-614.

[18] CEB-Fip-MC90. (1993) *CEB-FIP Model Code 90, CEB Bulletin d'Information No. 213/214*. Thomas Telford Ltd., London.

[19] Chai YH, Priestley MJN, Seible F. (1991) Seismic retrofit of circular bridge column for enhanced flexural performance. *ACI Structural Journal*. Sept-Oct 1991; **88**(5):572-584.

[20] Cho J-Y, Pincheira JA. (2006) Inelastic analysis of reinforced concrete columns with short lap splices subjected to reversed cyclid loads. *ACI Structural Journal*. Mar 2006; **103**(2):280-290.

[21] Darwin D. (2005) Tension development length and lap splice design for reinforced concrete members. *Prog in Struct Eng Material (EESD)*. **7**:210-225.

[22] El-Attar AG, White R, Gergely P. (1997) Behaviour of gravity load design reinforced concrete buildings subjected to earthquakes. *ACI Structural Journal*. Mar 1997; **94**(2):133-145.

[23] Fabbrocino G, Verderame GM, Manfredi G. (2005) Experimental behaviour of anchored smooth rebars in old type reinforced concrete buildings. *Eng Structures*. **27**(10):1575-1585.

[24] Fagundo FE, Gergely P, White R. (1979) *The behaviour of lapped splices in reinforced concrete beams subjected to repeated loads. Research Report 79-7*. Dept of Structural Eng., Cornell Uni., Ithaca, NY.

[25] fib. (2000) *Bond of reinforcement in concrete: State-of-the-art report, fib Bulletin no. 10*. Intl. Fed. for Struct. Concrete (fib), Lausanne, Switzerland.

[26] fib. (2003) *Seismic assessment and retrofit of reinforced concrete buildings: State-of-the-art report, fib Bulletin no. 24*. Intl. Fed. for Struct. Concrete (fib), Lausanne, Switzerland.

[27] Gergely P, White R. (1980) Seismic design of lapped splices in reinforced concrete. *Proc. of 7th World Conf on Earthquake Eng*, Istanbul, Turkey, p. 281-288 (Vol. 284)

[28] Harries KA, Ricles JM, Pessiki S, Sause R. (2006) Seismic retrofit of lap splices in nonductile square columns using carbon fiber-reinforced jackets. *ACI Structural Journal*. Nov 2006; **103**(6):874-884.

[29] Hawkins NM, Gamble WL, Shkurti FP, Lin Y. (2000) Seismic strengthening of inadequate length lap splices. *Proc. of 12th World Conf on Earthquake Eng*, Auckland, NZ.Paper No. 1755.

[30] Ichinose T, Kanayama Y, Inoue Y, Bolander Jr. JE. (2004) Size effect on bond strength of deformed bars. *Construction and Building Materials*. Sept 2004; **18**(7):549-558.

[31] Ireland MG. (2007) Development of a selective weakening approach for the seismic retrofit of reinforced concrete structural walls . [M.E.]. Uni. of Canterbury, Christchurch, NZ.

[32] Kuroki M, Kikuchi K, Sakino K, Yamakawa T. (2008) Splitting bond strength of main steel bars in R/C columns retrofitted with prestressed external hoops. *Proc. of 14th World Conf on Earthquake Eng*, Beijing, China.Paper No. 05-03-0184.

[33] Lukose K, Gergely P, White R. (1982) Behaviour of reinforced concrete lapped splices for inelastic cyclic loading. *ACI Structural Journal*. Sept 1982; **79**(5):355-365.

[34] Lynn A, Moehle JP, Mahin SA, Holmes WT. (1996) Seismic evaluation of existing reinforced concrete building columns. *Earthquake Spectra*. Nov 1996; **12**(4):715-739.

[35] Melek M, Wallace JW. (2004) Cyclic behaviour of columns with short lap splices. *ACI Structural Journal*. Nov-Dec 2004; **101**(6):802-811.
[36] NZS95:1939. (1939) *New Zealand Standard code of buildings by-laws*. New Zealand Standards Inst., Wellington, NZ.
[37] NZS95:1955. (1955) *New Zealand Standard - Model Building By-Laws: Part IV and V*. New Zealand Standard Inst., Wellington, NZ.
[38] NZS1900.9-64. (1964) *NZS1900 - Model building bylaw: Chapter 9.3: Design and construction - Concrete*. Standards Assoc. of New Zealand, Wellington, NZ.
[39] NZS3101:1982. (1982) *Code of practice for the design of concrete structures NZS 3101:1982*. Standards Assoc. of New Zealand, Wellington, NZ.
[40] NZS3101:2006. (2006) *NZS 3101:2006 Concrete structures standard*. Standards New Zealand, Wellington, NZ.
[41] NZSEE. (2006) *Assessment and improvement of the structural performance of buildings in earthquakes*. New Zealand Soc. for Earthquake Eng. (NZSEE), Wellington, NZ.
[42] Orangun CO, Jirsa JO, Breen JE. (1977) A reevaluation of test data on development length and splices. *ACI Structural Journal*. Mar 1977; **74**(3):114-122.
[43] Panahshahi N, White R, Gergely P. (1987) *Compression and tension lap splices in reinforced concrete members subjected to inelastic cyclic loading. Research Report 87-2*. Dept of Struct. Eng., Cornell Uni., Ithaca, NY.
[44] Panahshahi N, White R, Gergely P. (1992) Reinforced concrete compression lap splices under inelastic cyclic loading. *ACI Structural Journal*. Mar-Apr 1992; **89**(2):164-175.
[45] Park R, Paulay T. (1975) *Reinforced concrete structures*. John Wiley & Sons, New York.
[46] Paulay T. (1982) Lapped-splice in earthquake-resisting columns. *ACI Structural Journal*. **74**(6):458-469.
[47] Paulay T, Priestley MJN. (1992) *Seismic design of reinforced concrete and masonry buildings*. John Wiley & Sons Inc., Christchurch, NZ.
[48] Paulay T, Zanza TM, Scarpas A. (1981) *Lapped splice in bridge piers and in columns or earthquake resisting reinforced concrete frames. UC Research Report 81-6*. Dept. of Civil Eng., Uni. of Canterbury, Christchurch, NZ.
[49] Pessiki S, Conley C, Gergely P, White R. (1990) *Seismic behaviour of lightly reinforced concrete column and beam-column joint details. Technical Report NCEER-90-0014*. National Center for Earthquake Eng. Research, SUNY, Buffalo, NY.
[50] Philleo PR, Abrams DP. (1984) *Scale relationships of concrete beam-column joints. Structural Research Series No. 8301*. Uni. of Colorado, Boulder, CO.
[51] Priestley MJN, Seible F, Calvi GM. (1996) *Seismic design and retrofit of bridges*. John Wiley & Sons Inc., NY.
[52] Rodriquez M, Park R. (1994) Seismic load tests of reinforced concrete columns strengthened by jacketing. *ACI Structural Journal*. **91**(2):150-159.
[53] Saatcioglu M, Yalcin C, inventors; United States Patent and Trademark Office (USPTO), assignee. Retrofitting existing concrete columns by external prestressing. United States of America patent US Patent 6247279. 2001 Submitted: 24 Mar 1999.
[54] Saunders DB. (2004) Seismic performance of pre 1970's non-ductile reinforced concrete waffle slab frame structures constructed with plain round reinforcing steel [PhD dissertation]. Uni. of Canterbury, Christchurch.
[55] Sozen MA, Moehle JP. (1990) *A study of experimental data on development and lap-splice lengths for deformed reinforcing bars in concrete*. S&M Partnership, Urbana, IL.

[56] Valluvan R, Kreger ME, Jirsa JO. (1993) Strengthening of column splices for seismic retrofit of nonductile reinforced concrete frames. *ACI Structural Journal*. **90**(4):432-440.
[57] Verderama GM, Fabbrocino G, Manfredi G. (2008) Seismic response of r.c columns with smooth reinforcement. Part II: Cyclic tests. *Eng Structures*. **30**(9):2289-2300.
[58] Verderama GM, Fabbrocino G, Manfredi G. (2008) Seismic response of r.c. columns with smooth reinforcement. Part I: Monotonic tests. *Eng Structures*. **30**(9).
[59] Wong HF. (2005) Shear strength and seismic performance of non-seismically designed RC beam-column joints [PhD thesis]. Hong Kong Uni. of Science and Tech., Hong Kong.
[60] Xiao Y, Ma R. (1997) Seismic retrofit of RC circular columns using prefabricated composite jacketing. *ASCE J of Struct Eng*. Oct 1997; **123**(10):1357-1364.
[61] Yavari S, Elwood K, Lin S-H, Wu C-l, Hwang S-J, Moehle JP. (2009) Experimental study of dynamic behaviour of multi-story reinforced concrete frames with non-seismic detailing. *Proc. of ATC-SEI Conf, on Improving the Seismic Performance of Existing Buildings and Other Structures*, San Francisco, CA, p. 489-499

CHAPTER 8. INFLUENCE OF FLOOR SLAB AND TRANSVERSE BEAMS ON THE EXTERIOR RC BEAM-COLUMN JOINTS

"…on membrane action in two-way concrete slabs. Their strength is very great if they can arch between the beams."

R. Park, 1933-2004

In Connections: the EERI Oral History Series (12)

Robert Park and Thomas Paulay, Robert Rietherman Interviewer

EERI, Oakland,CA, 2006

8.1 INTRODUCTION

8.1.1 General

The experimental studies in previous chapters focussed on plane 2D exterior beam-column joints without floor slabs or transverse gravity beams. In reality, few plane beam-column joints exist in existing pre-1970s reinforced concrete (RC) buildings and common configurations include the presence of cast-in-situ floor slab and transverse beams. The conventional approach for the seismic assessment and retrofit of non-ductile joints generally either ignores the slab and transverse beam contribution, or adopts modern design expressions to evaluate this interaction, such as the effective flange width and the beam torsion resistance. The following paragraphs will discuss the likelihood of such conventional approach to lead to an un-conservative assessment of the hierarchy of strength of these pre-1970s beam-column joints as illustrated in §2.4.

As the quote of Professor Park above suggests, realistic slab participation generally amplifies the beam negative moment capacity but potentially violates the capacity design requirements for strong-column weak-beam. However, the slab participation within beam-column joints with non-ductile detailing and plain round reinforcement is unclear. Furthermore, the

presence of transverse (spandrel) beams framing into the unconfined joints might lead to interesting outcomes.

In this chapter, the test results of two beam-column joint specimens with transverse beam stubs and a floor slab are presented to clarify the effects of the floor slab and transverse beam stubs on the seismic behaviour of as-built and Selective Weakening (SW) retrofitted exterior beam-column joints. The test results provide some indications for upper- and lower-bounds of slab and spandrel beam stubs participations.

For the sign convention, the *Pull loading direction* refers to the *positive column lateral displacement*, Δ_c, which induces *positive beam bending moment*, M_b, and *tension strain* in the bottom face of the beam. This also corresponds with the *positive lateral force*, F_c, imposed on the column and *negative beam shear*, V_b, force along the beam. Vice versa, the *Push loading direction* refers to the *negative column lateral displacement*, Δ_c, *negative lateral force*, F_c, *negative beam bending moment*, M_b, and *tension strain* in the top face of the beam. The displacement components analyses for SL-O1 and SL-R3 are not presented due to the significant under-measurement of the fixed-end rotations of the beams and columns. This is a result of the lack of instrumentation at the beam-column-joint interfaces due to damaged spring potentiometers.

8.1.2 Test specimen description

The first specimen, labelled as SL-O1, had the same reinforcement and geometrical details as the benchmark specimen NS-O1 with the exception of the presence of a cast-in-situ 100mm thick 1000mm wide floor slab and 380mm transverse beam stubs on both out-of-plane faces of the joint. The width of the slab was selected to satisfy the NZS 3101 recommendations [30] for effective flange width, b_{eff}. The calculated b_{eff} values for the test specimen based on various code recommendations have been presented in Table 2.2 (of §2.4.3), reproduced in Table 8.1.

The second specimen, labelled as SL-R3, consisted of the implementation of R3 (selective beam weakening and post-tensioning) retrofit solution (§4.3.4) on the benchmark specimen with a floor slab and transverse beam stubs (i.e. SL-O1). Retrofit solution R3 was implemented for the retrofitted specimen SL-R3. This included a beam weakening at 165mm from the column centre-line and joint post-tensioning of 40kN (2.8% of $f_{y\text{-}pt}$).

Table 8.1: Values of effective slab tension flange width, b_{eff} based on various international codes.

Code/Guidelines	Effective tension flange width (mm)
NZS3101:2006	890
ASCE-41 / FEMA 356	980
NZSEE 2006	1753
JBDPA-2001 / AIJ-1994	839
EC8-III (2004) [+]	630

All calculations assumed the presence of transverse beam, beam span of 3047mm, bay width of 3047mm, beam and column widths of 230mm, beam depth of 330mm, slab thickness of 100mm and provided clear slab flange width of 375mm.

Figure 8.1 shows the reinforcing detail of the transverse beam stubs and the cast-in-situ slab. The cast-in-situ slab had thickness of 100mm with R6 steel mesh on 150mm c-c squares (665TrueMesh^{TM}) and a cantilevered length of 490mm from the beam centre-line. The transverse beam stub adopted the same reinforcing detailing as the main beam, not an uncommon assumption in pre-1970s 'gravity-frames' constructions. An effective flange clear width and cantilevered length of the transverse beam of 490mm ($0.5b_b + h_b$) from either side of the beam-column centre-line was adopted.

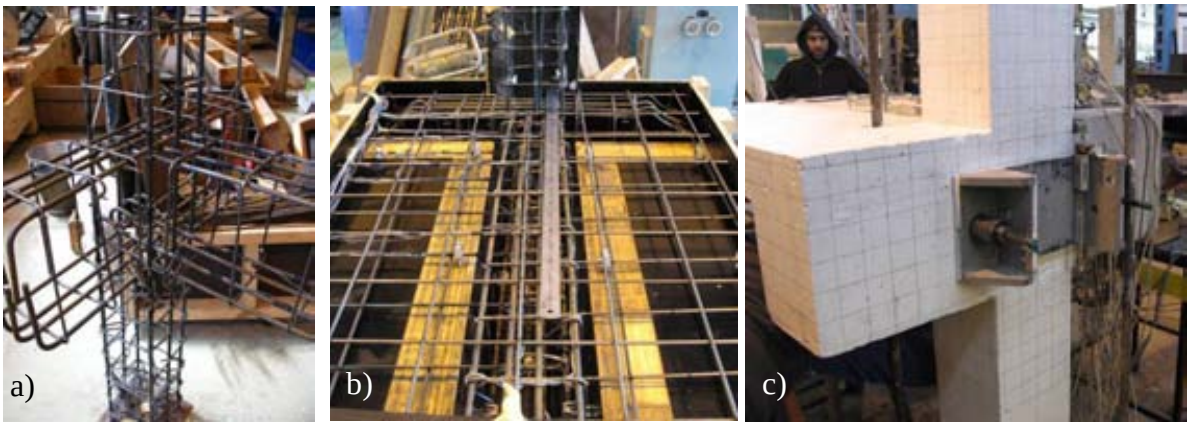

Figure 8.1: Reinforcing cage and details for test units with slabs.

Detailed description of the reinforcing and anchorage details for SL-O1 and SL-R3 are given in §4.3.5 (of Chapter 4). The hierarchy of strength performance domains for both specimens are presented in Appendix B. The day of testing concrete strengths, f'_c were 19.9MPa and 13.4MPa for the top column and bottom half of SL-O1 respectively. The f'_c for the top column and bottom half of SL-R3 were 23.1MPa and 17.0MPa.

While the beam-column joints with transverse beams and floor slab (SL-series) were meant to provide more realistic and practical validation for the SW retrofit (scheme R3), the SL-series also checked and confirmed the influence of shear demand under combined gravity and

seismic loadings on the SW retrofitted beams. Expected gravity-loading and relevant boundary conditions of the internal forces were applied in the specimens with a floor slab and transverse beams (SL-O1 and SL-R3). Further details of the gravity-loading on the SL- series beam-column joints are given in § 4.6.4.

8.1.3 Relevance of floor slab and transverse beams

As summarised in §2.3.3.4, research carried out in the 1970s-1980s, in particular international collaborative projects (e.g. [19, 22, 27, 28]), had shed much light on the behaviour of well-designed beam-column joints with floor slabs and transverse beams (e.g. [12, 14-16, 18, 24]. The amplification of beam negative moment capacity and nominal confinement effects of transverse beam under uni-directional loading were then incorporated into seismic assessment guidelines [4, 31]. Higher shear strength for joints with confining transverse beams was also incorporated into the 1976 ACI-352 guidelines [3] as well as the ACI/ASCE seismic provisions [1, 4]. However, there was an argument that in the bi-directional earthquake actions, transverse beams (seismic or gravity) would develop significant plastic hinging and would not be able to provide any positive confinement to the beam-column joint [25, 33].

Few tests (e.g. [5-8, 23, 26]) have been carried out on as-built and retrofitted pre-1970s non-ductile RC beam-column joints with floor slabs and transverse beams. Some of the early experiments on non-ductile beam-column joints did not make explicit comparison between specimens with and without floor-slabs/transverse beams [5, 6]. Beres *et al.* [8] found that the confinement from transverse beam stubs did not prevent joint shear failure but did allow for more gradual lateral strength degradations. Tests by Uzumeri *et al.* [37, 38] on unreinforced exterior RC beam-column joints with and without transverse beam stubs have shown joint shear cracking, and bond and anchorage failures before attaining the ultimate flexural capacity of the beams. The transverse beam stubs (without floor slab) were found not to influence the joint shear capacity.

Recently, Bedirhanoglu *et al.* [7] tested a series of non-ductile beam-column joints with plain round bars and a $0.7h_b$ wide floor slab and transverse beam stub on one side (i.e. corner joint specimens). In the positive beam moment direction, no effect was observed and in the negative beam moment direction, approximately 30% higher lateral load capacity was measured in the specimen with a floor slab. The floor slab and transverse beam stub also led to a smaller joint deformation, γ_j, despite a higher joint shear stress demand.

In summary, the presence of a cast-in-situ floor slab and transverse beams certainly influence the seismic behaviour of the exterior beam-column joint. The test specimens presented in this Chapter will therefore attempt to provide further evidences on their effects on the seismic behaviour of as-built and Selective-Weakening (SW) retrofitted beam-column joints.

8.2 EXPERIMENTAL RESULT OF AS-BUILT JOINT WITH SLAB: SL-O1

8.2.1 General description of behaviour

The F_c versus Δ_c hysteresis plot for SL-O1 is given in Figure 8.2. The damage and cracking patterns at the selected peak inter-storey drift, θ_{drift} loading cycles are shown in Figure 8.3 and Figure 8.5. θ_{drift} is given by Δ_c/H_c and H_c is the column height. The predicted lateral force capacities, $F_{sys\text{-}cal}$ for SL-O1, were +10.5kN and -15.6kN for the Pull and Push loading directions respectively, with expected joint shear failure. The joint shear capacity assessment did not include the confinement enhancement from the transverse beam stubs.

The gravity loads placed significant negative bending moment on the beam and resulted in a pre-compression in the bottom face of the beam. After the three stages of gravity loadings (as per §4.6.4), no visible cracks on the specimen were detected. The resulting F_c and V_b from the imposed gravity loading were -5.7kN and +2.3kN respectively.

There were no visible cracks in the ±0.1% drift cycles. Initial stiffness, K_{ini}, of 3228kN/m was measured in the +0.1% drift cycles. In the Pull cycles of the +0.2% drift, a minor crack running along the bottom beam-column corner was observed. In the 1st Push cycle of the -0.2% drift, a 0.15mm wide flexural crack appeared on the top face of the slab, extending through the whole length of the slab. The slab crack was running parallel at 150mm from the inner edge of the transverse beam. The maximum crack width grew to 0.25mm in the 2nd cycle. The ratio of cracked stiffness-to-uncracked stiffness, K_{cr}/K_{ini}, was 0.565.

Several beam flexural cracks appeared in the 1st Pull cycle of the +0.5% drift (Figure 8.3a). In addition, a 0.15mm wide crack appeared at the dry joint between the top column and the joint. In the Push cycles of the -0.5% drift, a vertical crack appeared on the outer face of the joint, possibly along the column longitudinal bars and the beam anchorages. Additionally, there was a new slab crack along the inner edge of the transverse beam. Both the transverse cracks on the slab extended through the whole thickness of the slab, with a maximum crack width of 0.45mm.

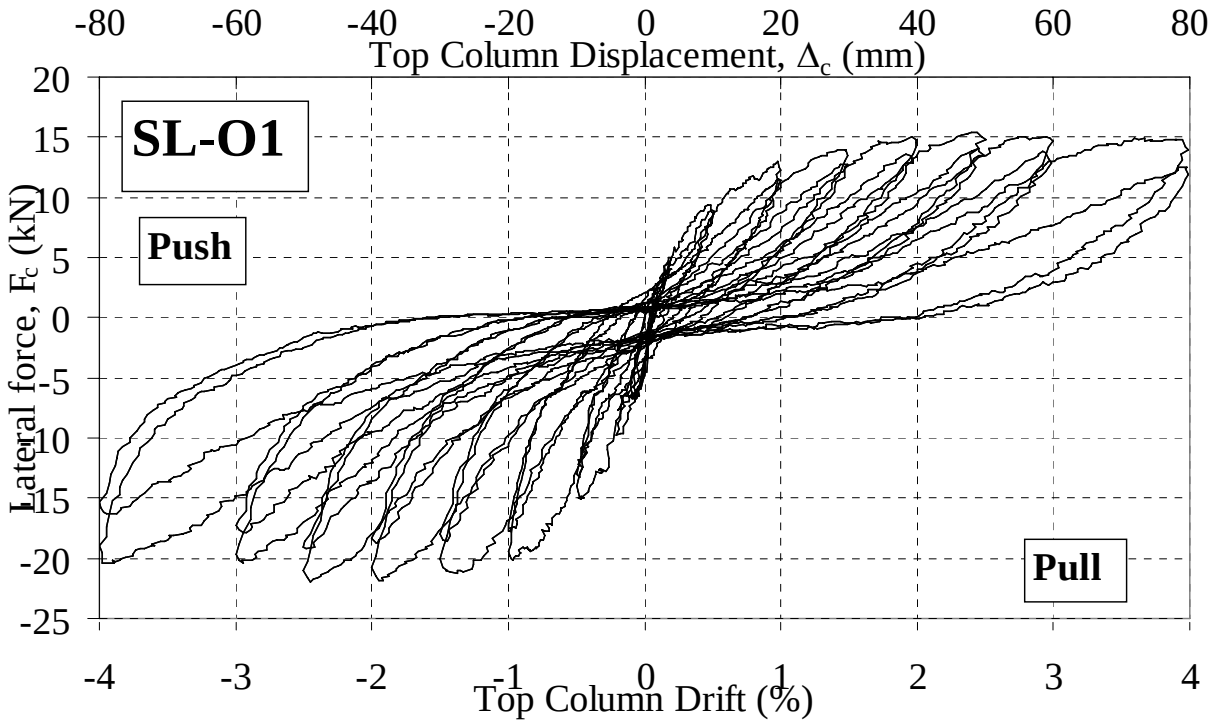

Figure 8.2: Top column lateral load, F_c, versus top column displacement, Δ_c, and drift, θ_{drift}, for SL-O1.

Figure 8.3: Observed cracking pattern of SL-O1: TOP: a) 2nd Push cycle of the -0.5% drift; and b-c) 2nd Pull cycle of the +1.0%% drift and d) 2nd Push cycle of the -1.0% drift. BOTTOM: e) 2nd Push cycle of the -1.0% drift; f) 1st Push cycle of the -1.5% drift; and g) 2nd Pull cycle of the +2.0% drift; and h) Residual after Pull-Push cycles of the ±2.0% drift.

Beam flexural cracks lengthened in the 1st Pull cycle of the +1.0% drift. The largest crack opening was at the beam-column corner, with a maximum crack width of 0.9mm. Expectedly, the beam bottom longitudinal bars yielded within the beam-column interface section, as confirmed by the strain gage data. The yield θ_{drift} was ~0.75%. The extent of cracking after the 1st Pull cycle of the +1.0% drift is shown in Figure 8.3b and c. In the 2nd Pull cycle of the +1.0% drift, minor spalling was observed at the bottom beam-column interface corner.

In the Push cycles of the -1.0% drift, another vertical crack appeared at the outer face of the joint. The vertical cracks along the joint and transverse beam boundaries, as shown in Figure 8.3d, were probably consequences of the torsion shear forces from the transverse beam into the joint core. The torsion moment on the transverse beam was induced by the torque action of the slab reinforcement acting in tension with respect to the centroid of the transverse beam. This is schematically illustrated in Figure 8.4.

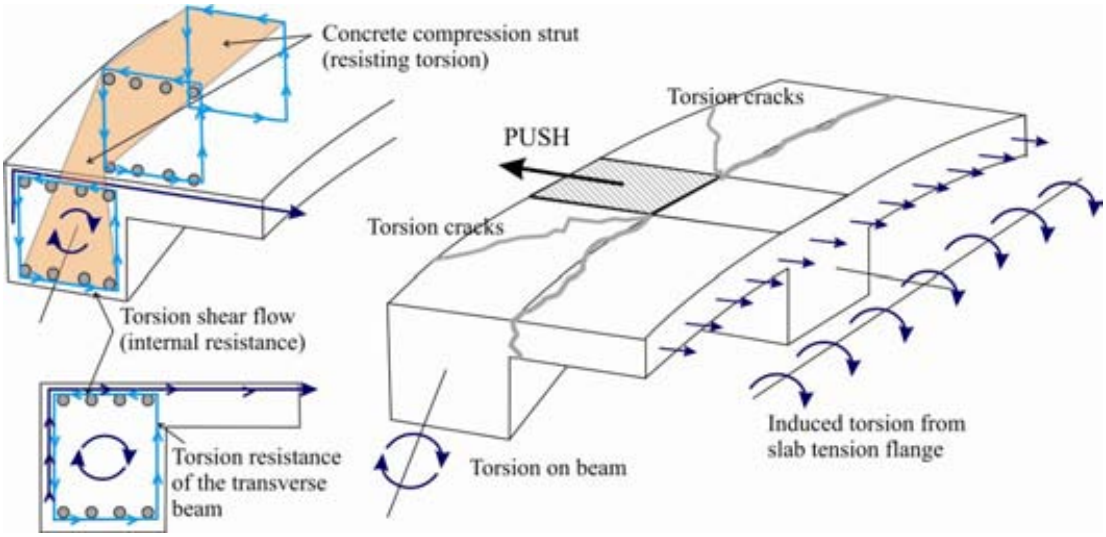

Figure 8.4: Torsion resistance and internal reactions of the transverse beam stub under lateral loading of the joint. Lighter lines are the internal resistance while the darker lines are the induced torsion demand.

The Pull-Push cycles of ±1.5% drift were dominated by the cracks growth at the corners of the beam-column joint. The maximum crack widths at the top and bottom corners of the beam-column interface were measured 1.6mm and 1.7mm respectively. Several new vertical cracks appeared in the outer face of the joint (Figure 8.3f).

Torsion diagonal cracks appeared on both transverse beam stubs in the 1st Push cycle of the -2.0% drift (Figure 8.3g). The torsion crack angle was approximately $\tan^{-1}$ (h_{bt}/b_{bt}) (~ 55°) where b_{bt} and h_{bt} were the width and depth of the transverse beam. The slab width bounded by the

torsion crack was approximately b_{bt}, which was relatively lesser when compared with test observations on well-designed beam-column joints with deformed bars. Many examples in the literature have recommended a 45° failure plane for the torsion crack (e.g. [14, 15, 19]). In the 2nd Push cycle, this crack propagated through the whole depth of the transverse beam (Figure 8.3h).

Figure 8.3h shows the residual crack pattern of the SL-O1 joint region after the ±2.0% drift cycles. The maximum residual crack width was 0.7mm, at the corner of the beam-column interface at the bottom of the beam. The torsion diagonal crack had a residual crack width of 0.15mm, suggesting significant torsion yielding of the transverse beam. Unfortunately, the lack of strain instrumentation in the transverse beam could not confirm this.

The joint region boundary cracks continued to widen and deteriorate in the ±2.5% drift cycles, as shown in Figure 8.5a and b. The torsion cracks grew in the Push direction, indicating of further torsional yielding of the transverse beam. The maximum and minimum F_c of +15.5kN and -22.0kN were achieved in the 1st cycles of the ±2.5%. The maximum and minimum F_c values were attained at θ_{drift}=+2.42% and θ_{drift}=-2.45%. The observed F_c values were significantly higher (~±5kN) when compared to the predicted F_c (+10.5kN and -15.6kN), suggesting the joint shear and transverse beam torsion cracking did not lead to the degradation of F_c.

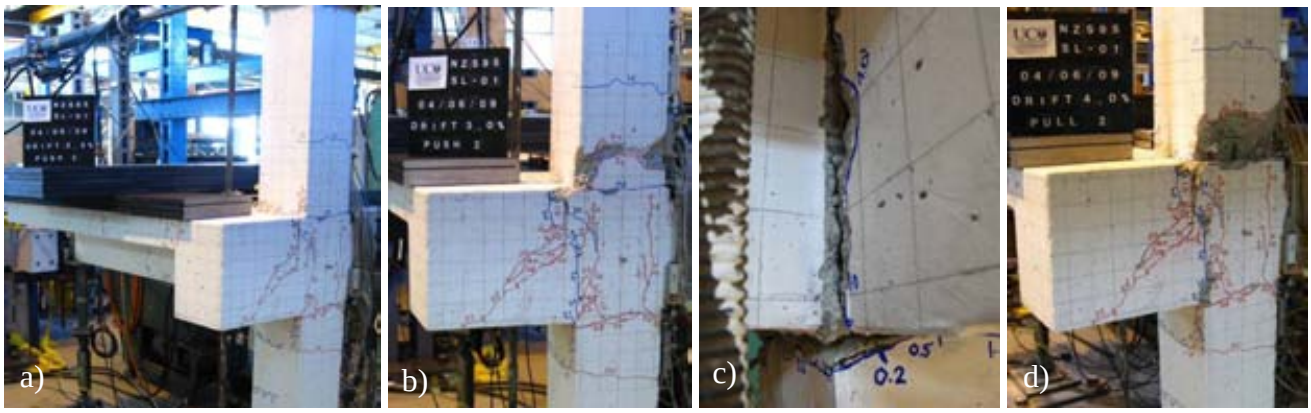

Figure 8.5: Observed cracking pattern of SL-O1: a) 2nd Push cycle of the -2.5% drift; b) 2nd Push cycle of the -3.0% drift; c) Close-up of the beam-column joint bottom corner; and d) 2nd Pull cycle of the +4.0% drift.

In the Push cycles of -3.0% drift, the column longitudinal bars started to buckle at the top column – joint interface, where the concrete had spalled off (Figure 8.5b). The concrete cover on the outer face of the joint began to spall off but was held by the transverse beam stirrups closest to the joint. The largest crack widths in the ±3.0% drift cycles were approximately 5-6mm at the joint boundary interfaces, as shown in Figure 8.5c. In the 2nd cycles of the ±3.0% drift, significant losses of strength, stiffness and energy dissipation were observed in the F_c-Δ_c of SL-O1 (Figure

8.2). Structural failure, as defined by the failure to attain 80% of the previous peak F_c, was reached at the 2nd Push peak of the -3.0% drift.

The cracking pattern up to ±3.0% drift cycles suggested a joint hinging mechanism in SL-O1. The damage was concentrated on the corners of the beam-column-joint interfaces, including a 5mm wide crack at the bottom inner corner (Figure 8.5c) and a 3mm wide crack at the dry joint between the top column and the joint (Figure 8.6a). As illustrated by Figure 8.6b, these cracking patterns could suggest either a beam-column flexural hinging or a joint shear hinging. Large opening would have been expected in the corners of the beam-column-joint interfaces with hidden corner-to-corner joint diagonal shear cracks, as observed in the test. On the other hand, the large column-joint interface crack would suggest significant column longitudinal bars stress in the scenario of column flexural hinge. However, the strains readings of the column bars (§0) indicated that up to ±2.5% drift cycles, the column bars had not yielded.

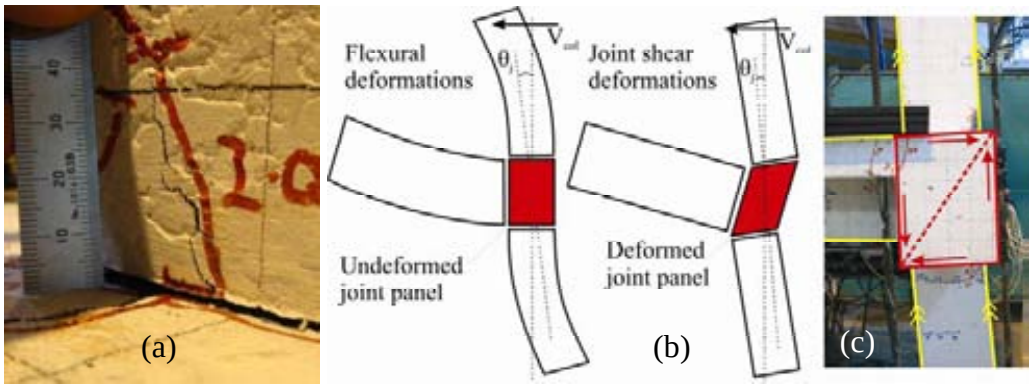

Figure 8.6: a) 4mm gap at the dry connection between top column and joint; b-c) Probable hidden joint shear deformation in the exterior joint with transverse beams.

Further spalling of the concrete around the joint panel region was observed in the ±4.0% drift cycles, as shown in Figure 8.5d. 50mm length of the column longitudinal bars were exposed at the region above the joint and on the outer face. At the end of the ±4.0% drift cycles, the outer face of the joint panel was bulging outward by approximately 5mm. The residual crack widths at the beam-column-joint interfaces and the torsion diagonal crack were 5mm and 1mm, respectively.

To investigate the post-failure decay of the lateral load capacity, SL-O1 was tested further for one Pull-Push cycle of the ±6.0% drift. At this excessively high drift demand, the postulated joint shear distortion became more evident, as shown in Figure 8.7a-c. Concrete spalling around the joint core boundaries was observed (Figure 8.7b). As instrumentation was removed from the

test specimen and data logging was stopped in the ±6.0% drift cycles, the F_c-Δ_c result was not available. The post-test forensic inspection (Figure 8.7c and d) had confirmed the presence of hidden diagonal failure planes within the joint core as previously discussed.

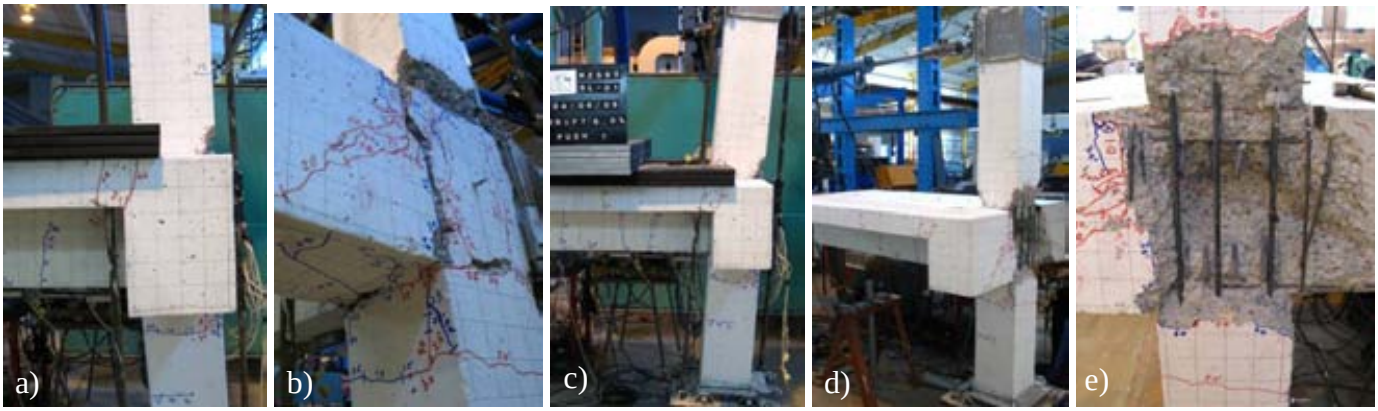

Figure 8.7: Observed cracking pattern of SL-O1: a-c) Pull-Push cycles of the ±6.0% drift; and d-e) Residual after Pull-Push cycles of the ±6.0% drift after removal of hand-loose concrete.

8.2.2 Load-displacement hysteresis analysis

The F_c-Δ_c hysteresis plot for SL-O1 is shown in Figure 8.2 while the analysis of the SL-O1 F_c-Δ_c hysteresis is presented in Figure 8.8. The maximum F_c values (+15.5kN @ +2.42% drift and -22.0kN @ -2.45%) were approximately ±5kN higher than the predicted lateral force capacities, $F_{sys\text{-}cal}$ for SL-O1 (+10.5kN and -15.6kN). This discrepancy will be further discussed in §8.4.4.

If the gravity load was not accounted for, the maximum F_c values measured were +21.2kN and -16.3kN. The peak F_c values for SL-O1 were approximately 5% and 21% higher than the NS-O1 maximum F_c values (+14.7kN -18.7kN) in the Pull and Push loading directions respectively. The 21% F_c enhancement in the Push cycles of SL-O1 was attributed to the slab flange and the transverse beam contributions. The marginally higher F_c in the Pull cycles of SL-O1 suggested a limited lateral strength and joint shear strength enhancements from the transverse beam alone, when the gravity loading effect had been discounted from the F_c-Δ_c hysteresis shown in Figure 8.2.

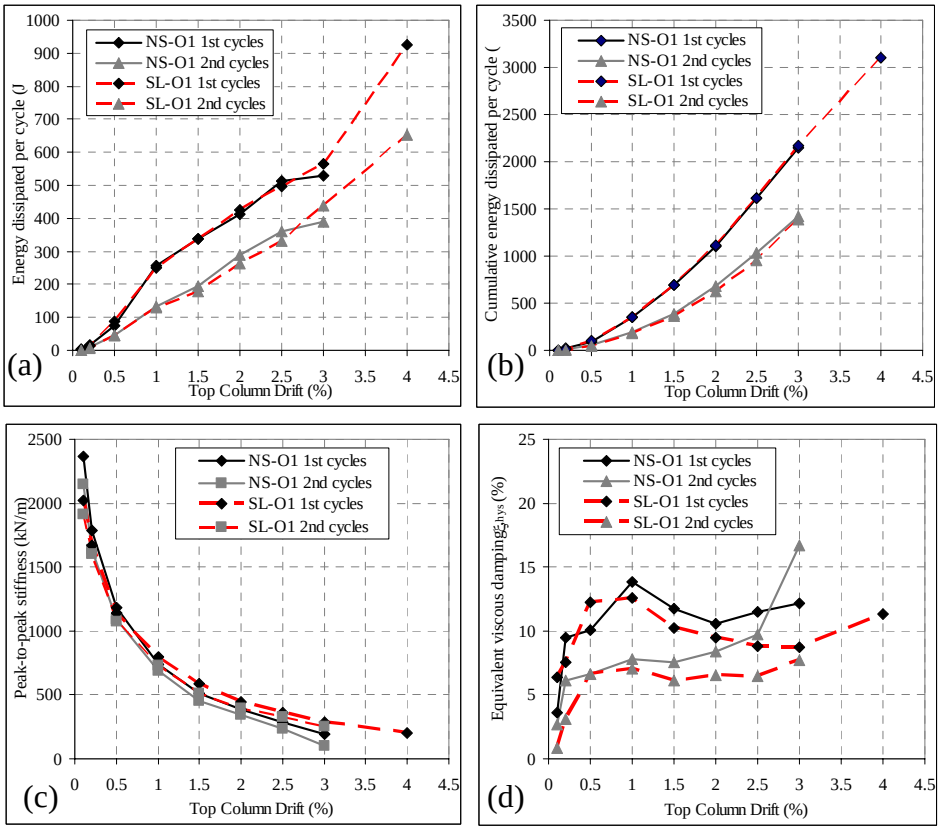

Figure 8.8: F_c-Δ_c analysis for SL-O1: a) Energy dissipated per cycle; b) Cumulative energy dissipated per cycle; c) peak-to-peak stiffness, K_{eff}, and; d) Equivalent viscous damping, ξ_{hys}.

Interestingly, in terms of the energy dissipated per cycle and the cumulative energy dissipated, SL-O1 curves were very close to the joint without slabs or transverse beams (NS-O1) curves (§5.4). This suggested that both SL-O1 and NS-O1 essentially had the same inelastic mechanism, i.e. joint shear hinging. The peak-to-peak stiffness, K_{eff} of SL-O1 was markedly higher than NS-O1, evident of the sustained F_c despite the joint shear and transverse beam torsion cracking. However, the improved envelope of F_c with limited energy dissipation capacities due to joint failure led to marginally lower (about 10%) equivalent viscous damping, ξ_{hys}, curves for SL-O1, when compared with NS-O1. As SL-O1 had higher θ_{drift} capacity, the lower ξ_{hys} would not affect the overall good performance of SL-O1.

8.2.3 Local deformations and displacement components

8.2.3.1 Beam deformations

The moment-curvature plots for the beam flexural regions and beam fixed-end regions are shown in Figure 8.9. Positive beam curvatures, ϕ_b corresponded to the positive column displacement

(Pull direction) and vice versa. Unfortunately, the $\phi_{b,f\text{-}e}$ and ϕ_b measurement was too inconsistent to give any useful data due to instrumentation errors, which effectively meant the ϕ_b ductility capacity could not be ascertained. This was because the linear potentiometers used for measuring $\phi_{b,f\text{-}e}$ did not transverse the main crack at the beam-column-joint interface.

Taking into account of the -9.1kNm beam moment boundary condition imposed by the gravity load (see §4.6.4), the theoretical components strengths as listed in Table 4.3 of §4.3.1 could be compared with the maximum beam moments. The modified theoretical beam flexural capacities were +48.5kNm and -42.2kNm in the Pull and Push loadings respectively. SL-O1 was predicted to have confined joint shear failure at the beam moments of +28.6kNm and -19.6kNm in the positive and negative loading displacements.

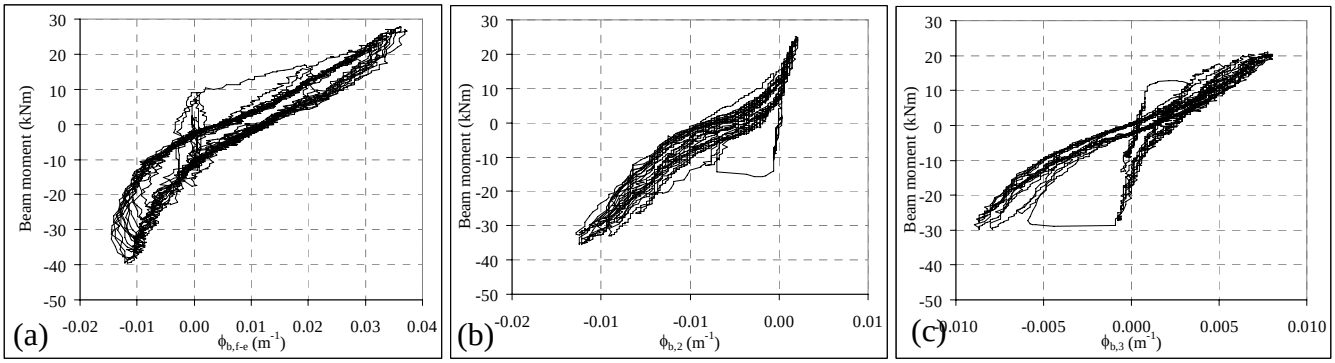

Figure 8.9: a) Moment-curvature plots for beam sections: a) fixed-end section; b) 75-275mm from the column internal face; and c) 275-475mm from the column internal face.

As shown in Figure 8.9, the maximum beam moments developed in the Pull and Push directions were +27.8kNm and -39.6kNm respectively, and the maximum curvatures of $+0.037m^{-1}$ and $-0.015m^{-1}$ respectively. Expectedly, the analytical value compared well in the Pull direction in which the floor slab was in compression and the transverse beam was not providing any torsional restraint to the beam-column joint.

On the other hand, the experimental maximum beam moment value (-39.6kNm) doubled the predicted beam moment at the joint cracking (19.6kNm). Evidently, the transverse beam torsion confinement played a role in maintaining the lateral capacity of the joint beyond the hidden joint cracking. As seen in Figure 8.9a, the flexural stiffness (slope of the moment-curvature plot) was significantly higher in the negative ϕ_b, confirming the influence of the slab tension flange and transverse beam stubs in sustaining F_c.

8.2.3.2 Column deformations

Figure 8.10 shows the measured moment-curvature response for the three regions of the column. Similar to the beam fixed end rotation measurement, the instrumentation setup did not capture the accurate ϕ_c across the beam-column-joint interfaces, as the majority of the column inelastic deformations were concentrated at these cracks (e.g. Figure 8.6a). For example, the 'yield curvature at the bottom section (Figure 8.10c) was grossly under-measured when compared to the expected yield curvature ($\sim\varphi_y = 2\varepsilon_y/H_c$).

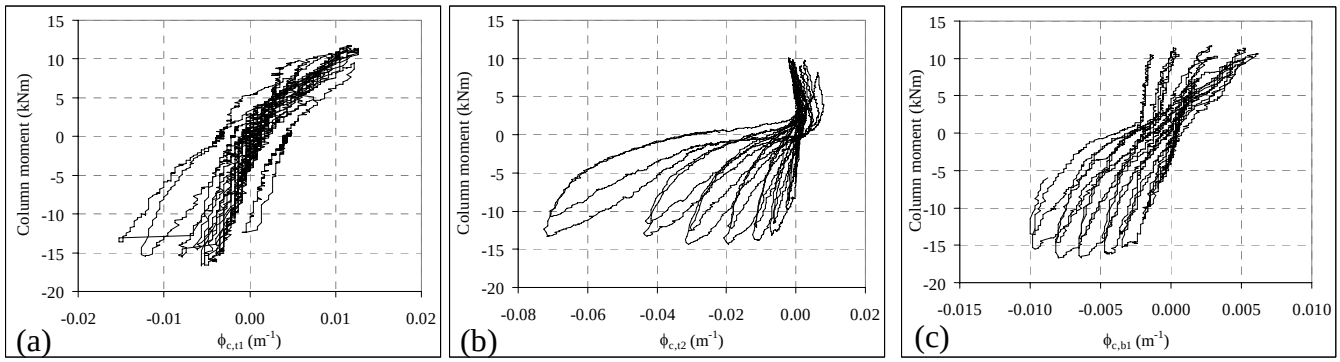

Figure 8.10: Moment-curvature plots for column flexural sections: a) 200-430mm from the beam top face; b) 0-200mm from the beam top face; c) 0-200mm from the beam soffit.

The observed nominal column flexural strengths, $M_{c\text{-}cf}$, were +11.7kNm and -16.7kNm in the Pull and Push cycles respectively. In the Pull cycles, the $M_{c\text{-}cf}$ corresponded to the column curvature, ϕ_c, of 0.0011m^{-1} and of 0.0027m^{-1} at the top and bottom halves of the column. In the Push cycles, the $M_{c\text{-}cf}$ corresponded to the ϕ_c of -0.0056m^{-1} and of -0.0080m^{-1} at the top and bottom halves of the column.

The theoretical column flexural strengths under the variation of axial loads were +19.0kNm and -31.5kNm without the gravity load contribution. Including the -4.1kNm initial condition at the beam-column interface, the theoretical $M_{c,cf}$ were +23.1kNm and -27.4kNm. The theoretical $M_{c,cf}$ was significantly higher than the test result, suggesting that column hinging did not occur in SL-O1.

8.2.4 Beam-column joint behaviour

The nominal joint shear stress, v_{jh}, and the principal stresses (p'_t and p'_c) versus the column lateral displacement, Δ_c relationships for SL-O1, are given in Figure 8.11. The joint distortion, γ_j, was not measured for SL-O1 and SL-R3. As the joint region was effectively hidden, it was not

possible to accurately determine the 'joint cracking point' despite evidence of joint shear deformation in the later stage of the test, as discussed in §8.2.1.

The maximum v_{jh} measured were 1.79MPa (0.40 $\sqrt{f'_c}$ MPa or 0.090f'_c MPa) in the 1st Pull peak of the +2.5% drift and -2.55MPa (-0.57 $\sqrt{f'_c}$ MPa or -0.128f'_c MPa) in the 1st Push peak of the -2.0% drift. These v_{jh} values in terms of $\sqrt{f'_c}$ MPa were almost the same as the NS-O1 result (0.40 $\sqrt{f'_c}$ MPa and -0.57 $\sqrt{f'_c}$ MPa), confirming the influence of concrete tensile strength (a function of $\sqrt{f'_c}$) on the v_{jh} strength. The difference between the two loading directions again highlighted the influence of the variation of column axial load.

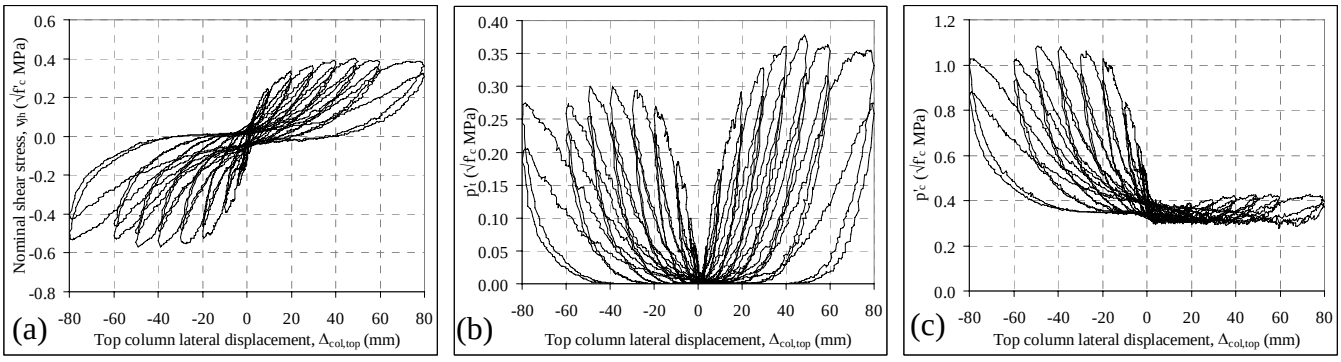

Figure 8.11: a) Nominal joint shear stress, v_{jh}, versus top column lateral displacement, Δ_c; b-c) Joint principal stresses versus top column lateral displacement, Δ_c: b) principal tensile stress, p'_t; and c) compressive tensile stress, p'_c.

In terms of maximum principal stresses in the joint during the cyclic loading of SL-O1, the maximum p'_t was 0.378$\sqrt{f'_c}$ MPa and the maximum p'_c was 1.09$\sqrt{f'_c}$ MPa. Both maximum p'_t and p'_c occurred at the 1st peak of ±2.5% drift, which coincided with the maximum and minimum F_c points. Degradation of the principal stresses occurred gradually beyond that θ_{drift} level. The degradation of principal stresses and F_c correlated to the observed bulging and gradual spalling of the concrete cover on the outer face of the joint. While the general shape of the principal stresses versus Δ_c curves in Figure 8.11 were consistent with those of NS-O1, apparent rapid degradation beyond the joint cracking was not observed in SL-O1. SL-O1 also had marginally higher p'_t values when compared to other specimens without floor slabs or transverse beams.

8.2.5 Steel strain profiles

8.2.5.1 Beam longitudinal reinforcement strains

Figure 8.12 and Figure 8.13 present the strain profiles of the top and bottom beam longitudinal reinforcing for the specimen SL-O1. The X-axis is the distance from the exterior column face

while the two vertical dashed lines refer to the column centre-line and the interior column face. Tensile strains are given as positive values. From the steel test, the yield strain, ε_y, for the longitudinal beam reinforcement was 0.00174 (1735 microstrains) and the f_y was 347MPa. `In general, the beam bars strain profiles for SL-O1 were similar to the benchmark joint NS-O1, with minor discrepancies. See §5.6.1 for a more detailed discussion in terms of the progressive failure of the bond of the plain round bars of the beam under cyclic loading.

The beam top longitudinal bars yielded in the -1.5% Push cycles at the beam-column interface section, which also corresponded to the large beam-column-joint interface crack observed during the test. From the -2.0% drift Push cycles onward, localisation of steel strains at that interface was measured. In addition, yield strain penetration occurred on both sides of the cracked interface for SL-O1, while in NS-O1, limited strain penetration was measured within the joint region due to the progressive cracking of the NS-O1 joint.

For the top reinforcement in the Pull cycles, due to the slab tension flange effect (to be discussed in §8.4.1), a spike of compression strains (up to -800 microstrains or f_s = -160MPa) was measured on the beam-column interface (also the transverse beam-slab interface). Within the joint region, the beam top bars went into tension (max f_s = +80MPa) from the +1.5% drift onwards, indicative that the top bars were carrying some joint shear forces. In NS-O1, the tensile stress measured in the top bars anchored within the joint was approximately double of that measured in SL-O1, suggesting a more extensive joint damage in NS-O1.

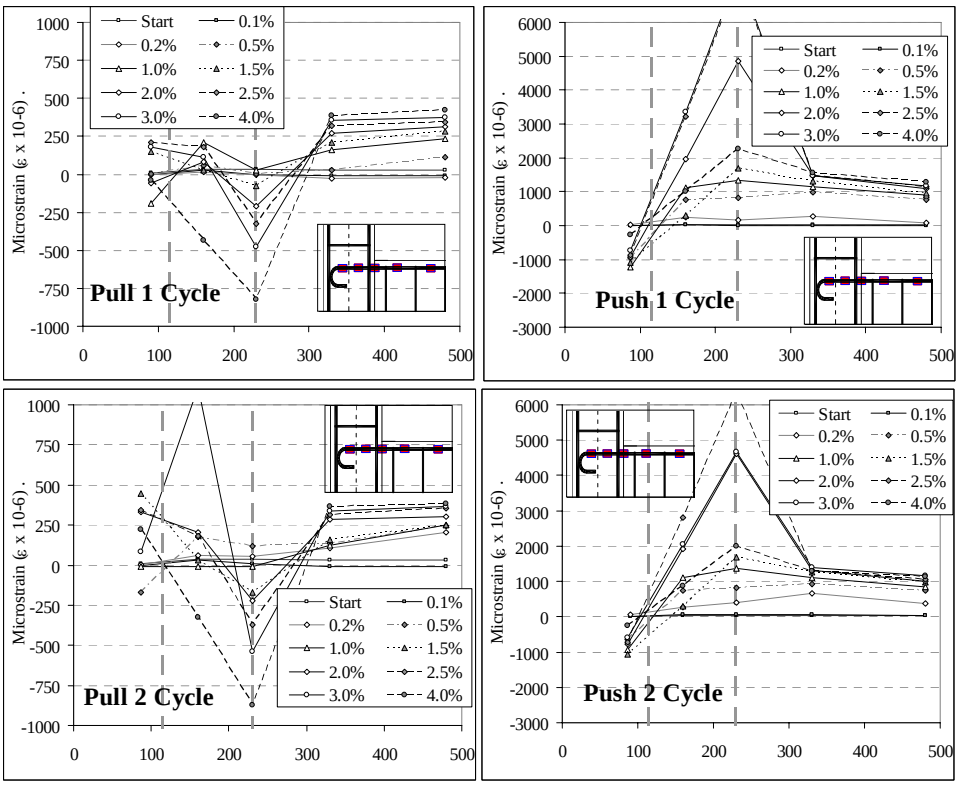

Figure 8.12: Strain profile of beam top longitudinal bars of the specimen SL-O1.

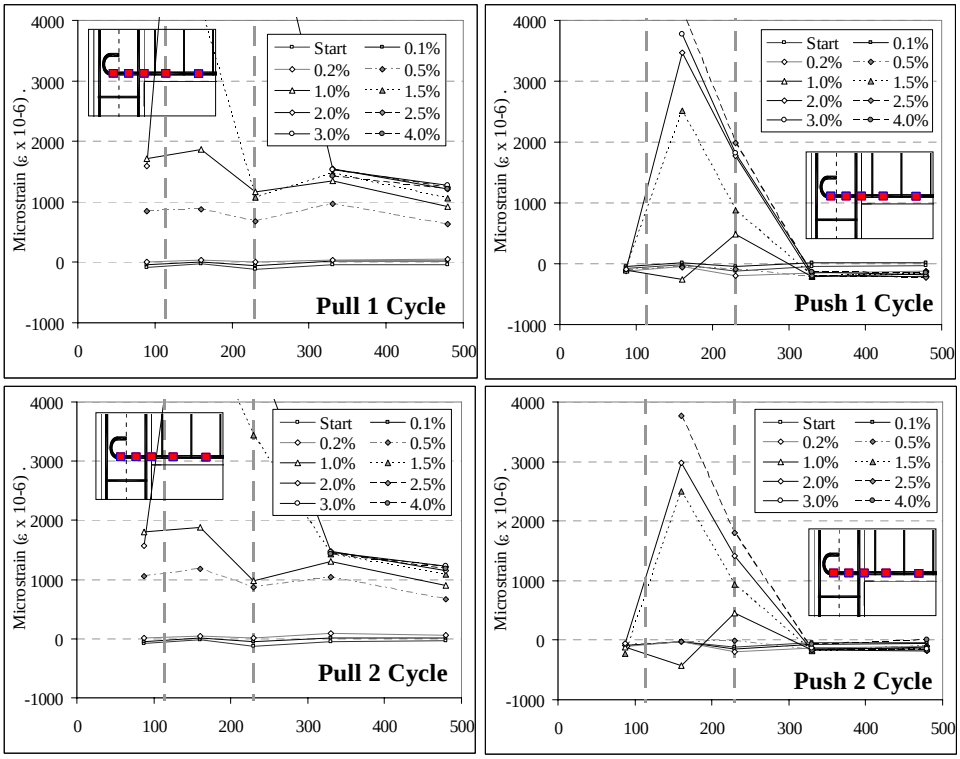

Figure 8.13: Strain profile of beam bottom longitudinal bars of the specimen SL-O1.

The strain profiles of the bottom reinforcement for SL-O1 were quite similar to those of NS-O1 in both the Pull and Push loadings. The beam bottom bars yielded in tension in the +1.0% drift Pull cycles. Interestingly, as with NS-O1, the beam bottom bars embedded within the joint was also yielding in tension in the Push cycles (from the -1.5% drift cycle onward). The sudden increase of tensile strain demand on the beam bars within the joint was evident that the joint core had cracked internally and substantial joint shear force was carried by these bars after the ±1.0% drift. Recalling from the joint diagonal cracking at ±1.0% drift in NS-O1, it could be inferred from the strain readings in Figure 8.13 that the joint had been damaged internally at the -1.5% drift.

8.2.5.2 Column longitudinal reinforcement strains

Figure 8.14 and Figure 8.15 present the strain profiles of the exterior and interior column longitudinal reinforcement for the specimen SL-O1. In both figures, the Y-axis is the distance from the centre-line of the beam. The three horizontal dashed lines refer to the beam soffit (bottom line), beam centre-line and the beam top face (top line). All column strain gages were zeroed before the axial force loading on the column at the start of the test. The yield strain, ε_y, for the longitudinal column reinforcement was 0.0024 (2400 microstrains) and the f_y was 480MPa.

The column exterior longitudinal reinforcement was responding elastically as expected from the bending moment demand from the lateral loading in both the Pull and Push drift cycles. While in NS-O1, a marked increase in tensile strains was observed after the joint shear cracking, this was not observed in SL-O1 measurements. Additionally, the maximum tensile stress measured was also relatively lower in SL-O1 when compared with the benchmark specimen NS-O1. The maximum tensile and compressive stresses measured in the SL-O1 exterior column bars were +305MPa and -174MPa respectively. It should be noted that this was considerably below the f_y as SL-O1 was built with high strength reinforcement due to the steel provider's error.

The column interior face bars were also initially responding elastically under tension and compression actions up to the +1.0% drift in the Pull cycles and -1.5% in the Push cycles. In subsequent drift cycles, the column interior bars were under increasingly higher tensile strains. Nevertheless, up to the ±2.0 % drift cycles, the column strains were below ε_y. In the ±2.5% drift peaks, up to 4500 microstrains was measured at the top column-joint interface, which corresponded to the large column-to-joint interface cracking observed in the test.

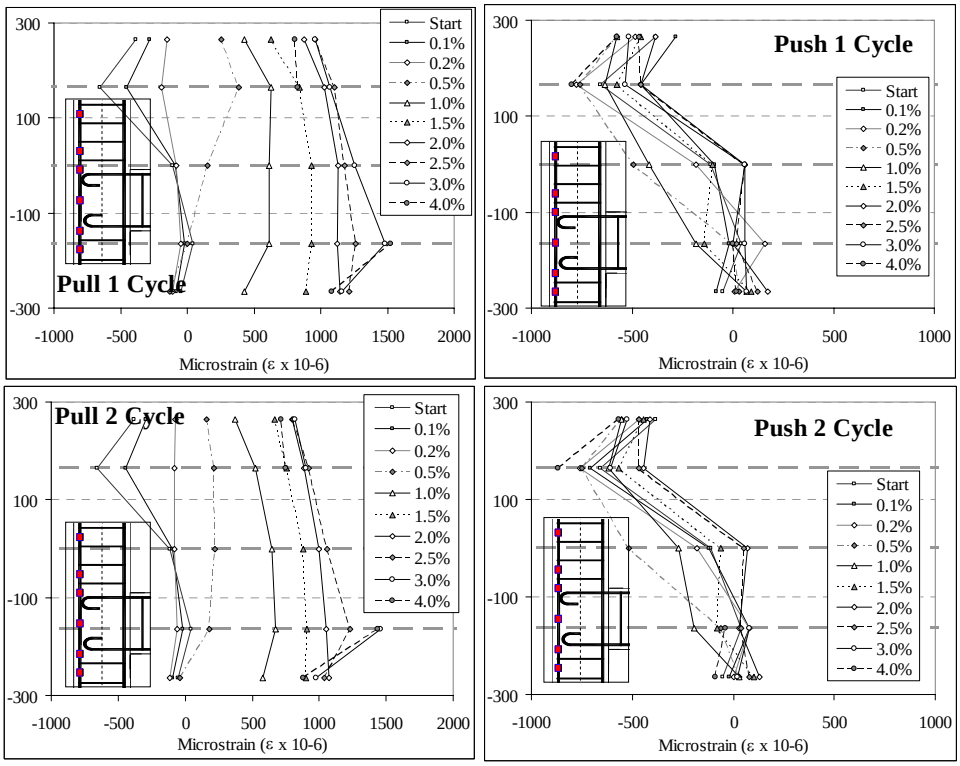

Figure 8.14: Column exterior face longitudinal reinforcement strain profiles for the specimen SL-O1.

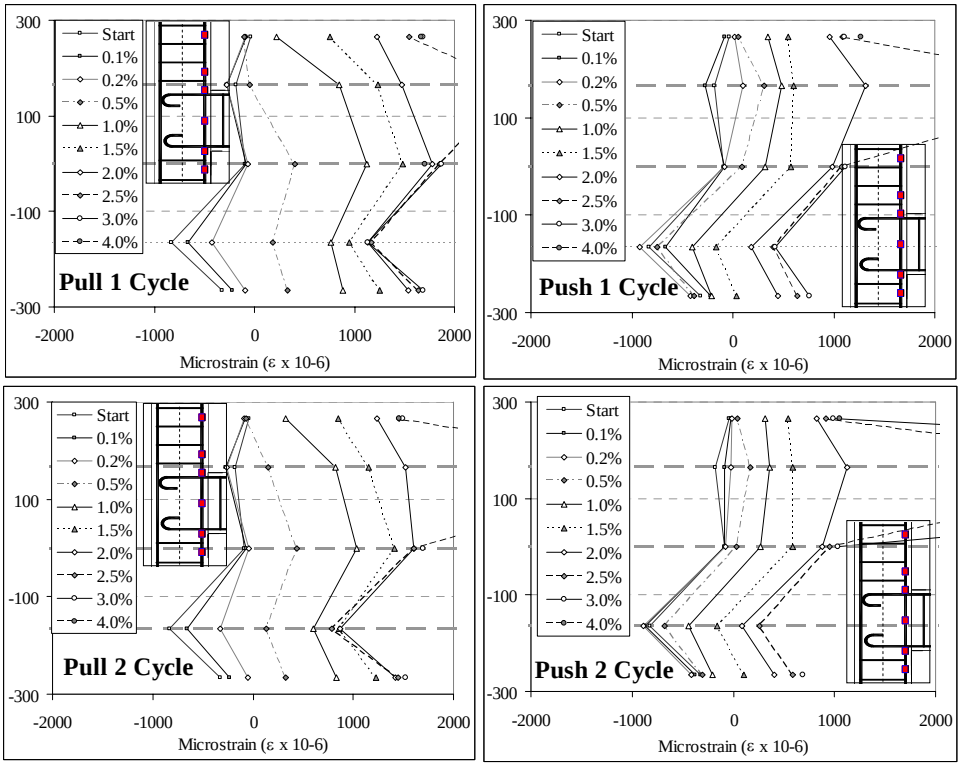

Figure 8.15: Column interior face longitudinal reinforcement strain profiles for the specimen SL-O1.

8.2.5.3 Stirrup reinforcement strains

The strain profiles of the stirrups in the column and the beam are shown in Figure 8.16. Only selected stirrup results are presented herein as the general trend across different measurements is similar. All the stirrups responded elastically. Both strain gages on the column stirrups (CS1A and CS2A) were placed perpendicular to the loading direction, thus indicating of possible confining tensile stresses. As seen in Figure 8.16a and b, these confining tensile stresses increased significantly after the ±1.5% to ±2.0% drift cycles.

Low values of strains were measured in the beam stirrups, confirming the limited flexural-shear cracking within the beam section. One notable difference in the SL-O1 when compared with NS-O1 was the measured compression in the first beam stirrups during the negative displacement cycles. This was consistent with the compression strains measured in the beam bars and slab mesh top reinforcement along this same section.

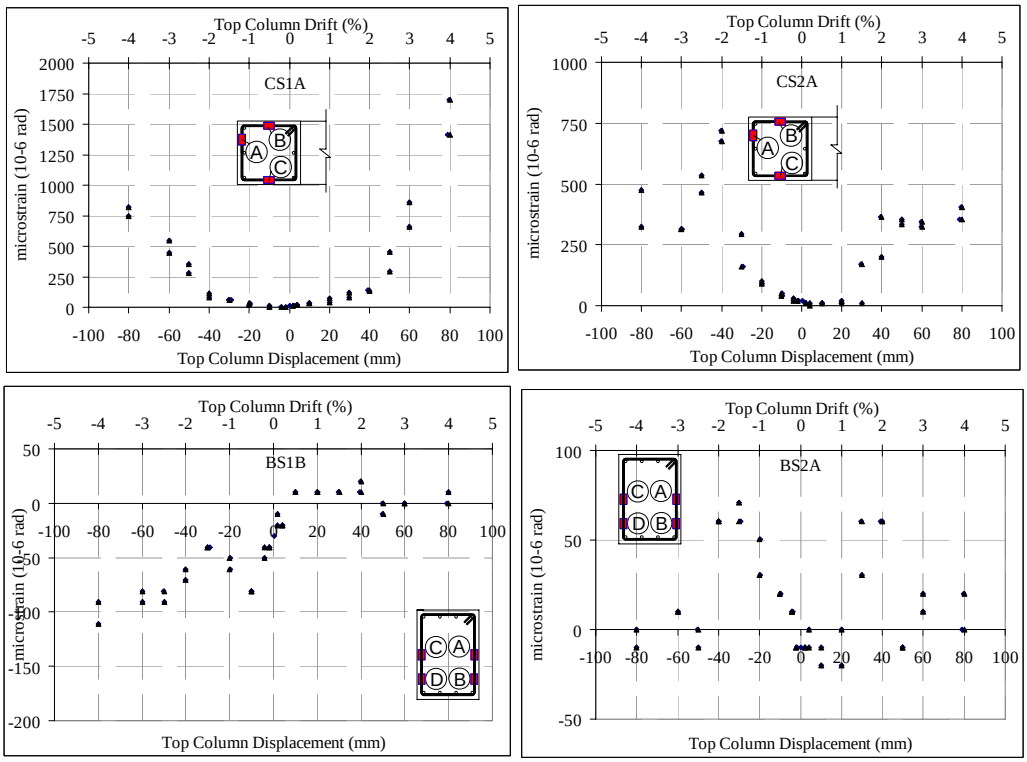

Figure 8.16: Stirrup strain profiles: TOP: a) column stirrup 50mm below the beam soffit; and b) column stirrup 50mm from the beam top face. BOTTOM: c) beam 1st stirrup - 50mm from the column interior face; and d) beam 2nd stirrup - 183mm from the column interior face.

8.2.6 Floor slab mesh strain measurements

A total of 52 strain gages were placed on the mesh reinforcement parallel and perpendicular to the loading direction. The extensive instrumentations were able to track the force distribution and pattern within the floor slab during the cyclic loading. The details of the slab mesh anchorage are given in §4.3.6. In the following paragraphs, '*x*' refers to the distance of the mesh reinforcement (instrumented) from the centreline of the column. In general, the 1st and 2nd cycles had similar strain profiles with minimal degradation of strain in the 2nd cycle. This suggested a limited bond degradation of the mesh reinforcement. Only the 2nd cycle results are shown herein for brevity.

The strain profiles for the slab top mesh reinforcement parallel to the loading direction during the Pull and Push cycles are presented in Figure 8.17 and Figure 8.18. In the Pull cycles, low tensile strains were measured in the top mesh reinforcement, ranging between 150-450 microstrains for most θ_{drift} levels. The maximum tension stress of 180MPa was measured at the slab reinforcement furthest away from the longitudinal beam, at θ_{drift}=+4.0%.

The slab top mesh in parallel to the loading direction during the Push loading would indicate of the slab tension flange effect. Up to the -1.0% drift cycles, the slab top mesh was under +1000 to +1500 microstrains (f_s = 200-300MPa) between x=0.45h_b and x=1.35h_b. Higher tension forces were measured in the slab bars closer to the transverse beam The peak of the tensile strains in the top mesh parallel reinforcement was observed in the 1st Push peak of the -1.0%, which was corresponding with the observed torsional cracks in the transverse beam stubs. This was consistent with previous observations [15, 16] which suggested that contribution of floor slab in tension was limited to the torsional capacity of the transverse beam.

The strain profiles of the slab top mesh perpendicular to the loading direction are given in Figure 8.19. As the mesh reinforcing perpendicular to the longitudinal beam were carrying mostly gravity load, it was expected to observe consistent strain profiles in both loading directions. The highest tensile strain was measured on the mesh bars along the transverse beam as the stiffer transverse beam-slab region carried more gravity weight. In the Pull cycles, a noticeable increase of tensile strains was observed in the +3.0% and 4.0% drifts.

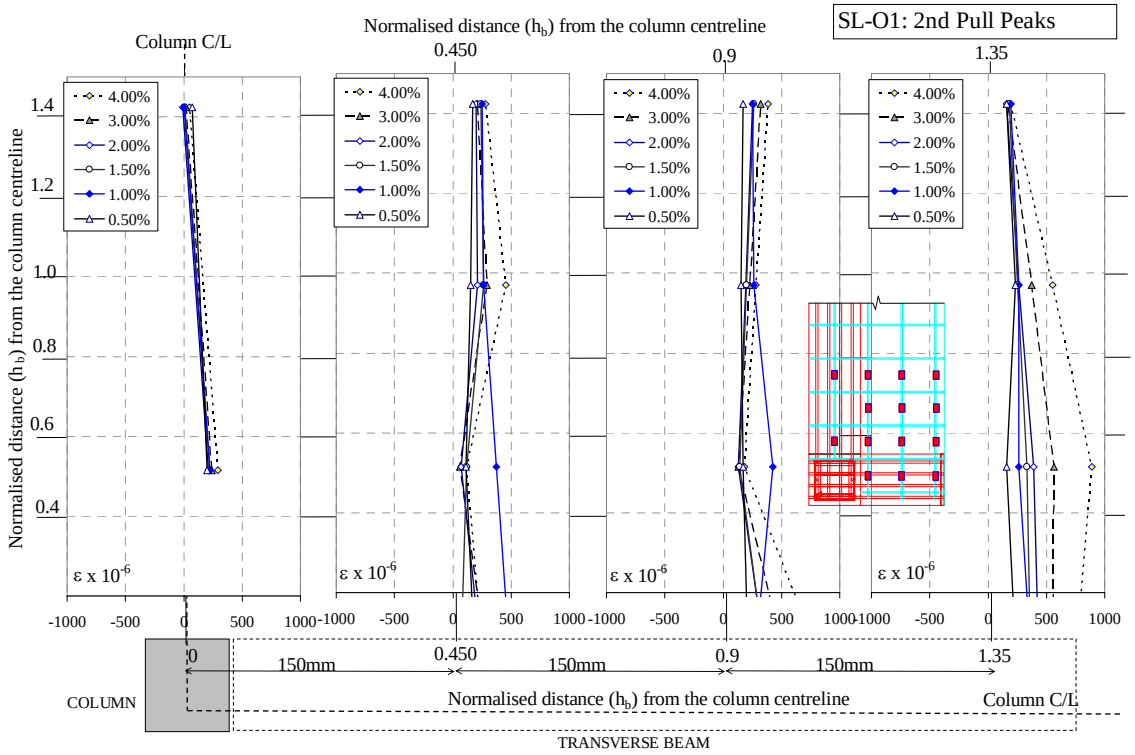

Figure 8.17: Strain profiles of slab top mesh parallel-to-loading direction for the specimen SL-O1: 2nd Pull peak cycles.

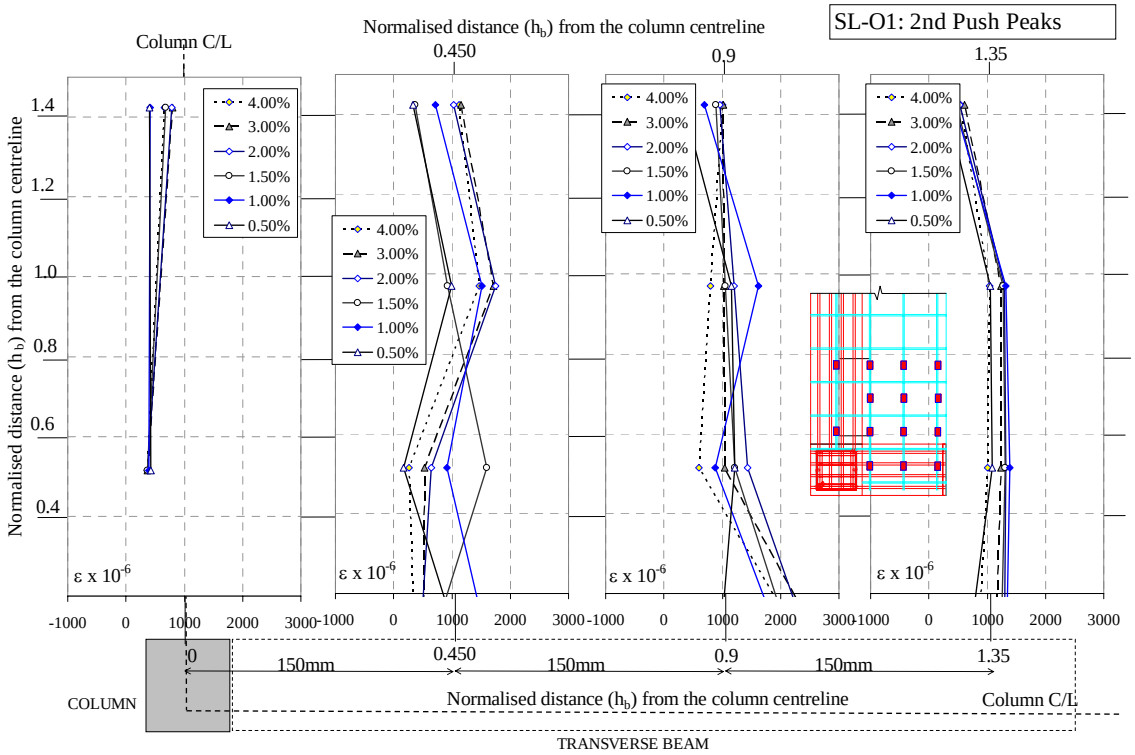

Figure 8.18: Strain profiles of slab top mesh parallel-to-loading direction for the specimen SL-O1: 2nd Push peak cycles.

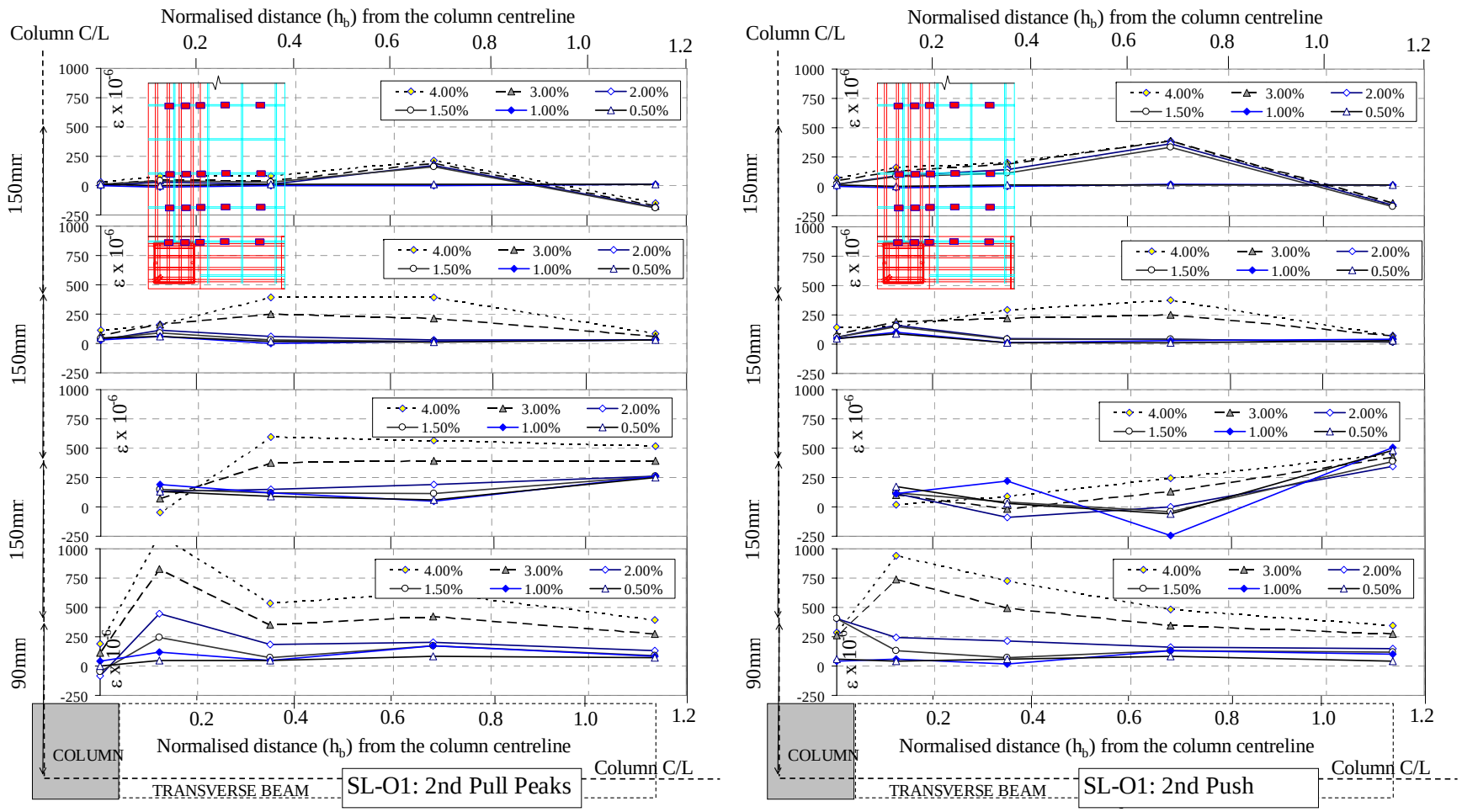

Figure 8.19: Strain profiles of slab top mesh perpendicular -to-loading direction for the specimen SL-O1: left) 2nd Pull peak cycles; right) 2nd Push peak cycles.

While the slab mesh had limited yielding, the participating slab width for the exterior beam-column joints could be determined by the portion of slab that was carrying significant tensile strains (taken to be +1000 microstrains). At the -2.0% drift, approximately $1.1h_b$ (360mm) width of the slab was participating. This was relatively lower than previous tests with deformed bars (e.g. [15, 16])– as cracking in plain-round bars specimens typically concentrated on a few discrete locations – in the SL-O1 case – just outside the transverse beam region. The torsion failure of the transverse beam nevertheless limited further development of the slab tension flange.

The strain profiles for the slab bottom mesh reinforcement parallel and perpendicular to the loading direction are plotted in Figure 8.20 and Figure 8.21. The bottom mesh reinforcement parallel to the loading was not adequately anchored into the transverse beam, as such, limited force could be developed. The maximum tensile stresses developed in the mesh bars were about +175MPa. The bottom mesh bars were showing an increase in tension strains in the Pull direction and a decrease in tension strains in the Push direction. Furthermore, the strain profiles of the bottom mesh were quite different from the top mesh at the same instrumented locations. These suggested that the neutral axis of the beam bending was in between the top mesh (d=23mm) and the bottom mesh (d=83mm).

The lateral loading did not induce much force on the bottom mesh reinforcement perpendicular to the loading direction, which was in tension due to the gravity loading. The only exception was the bottom mesh along the transverse-beam-slab-column interface. It was likely that the bottom mesh reinforcement at this section was activated by the torsional action of the transverse beam as θ_{drift} increased.

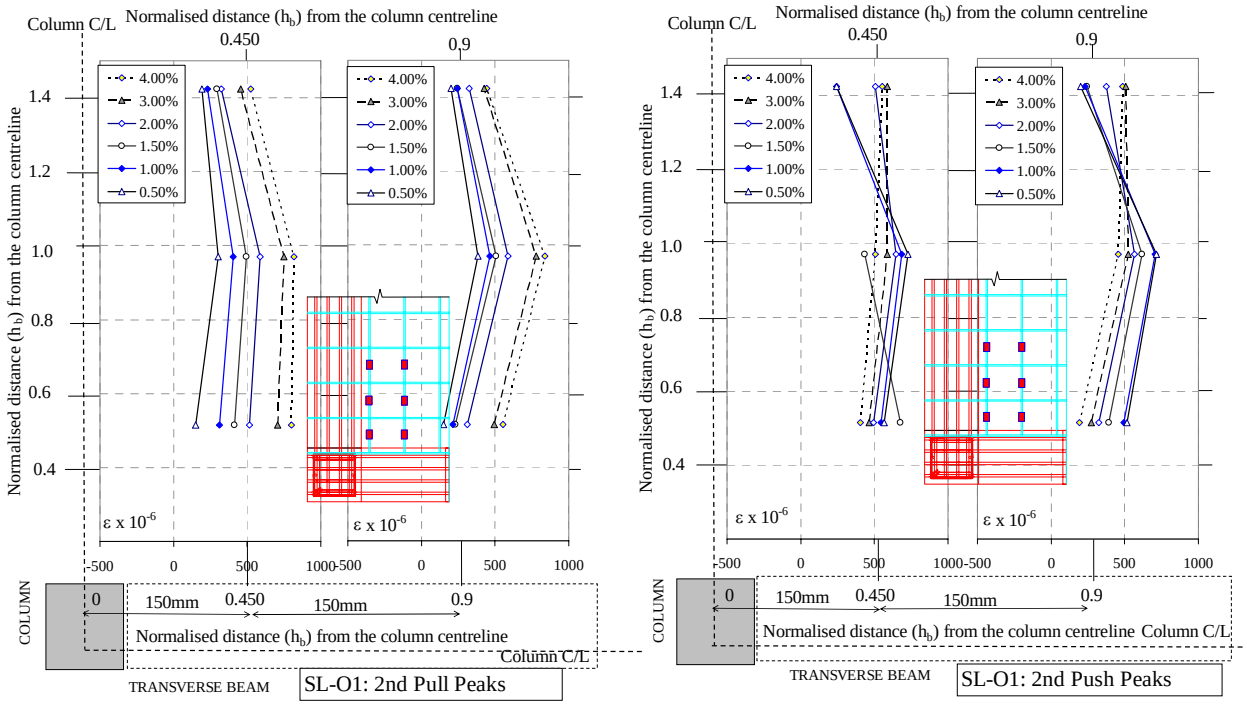

Figure 8.20: Strain profiles of slab bottom mesh parallel-to-loading direction for the specimen SL-O1.

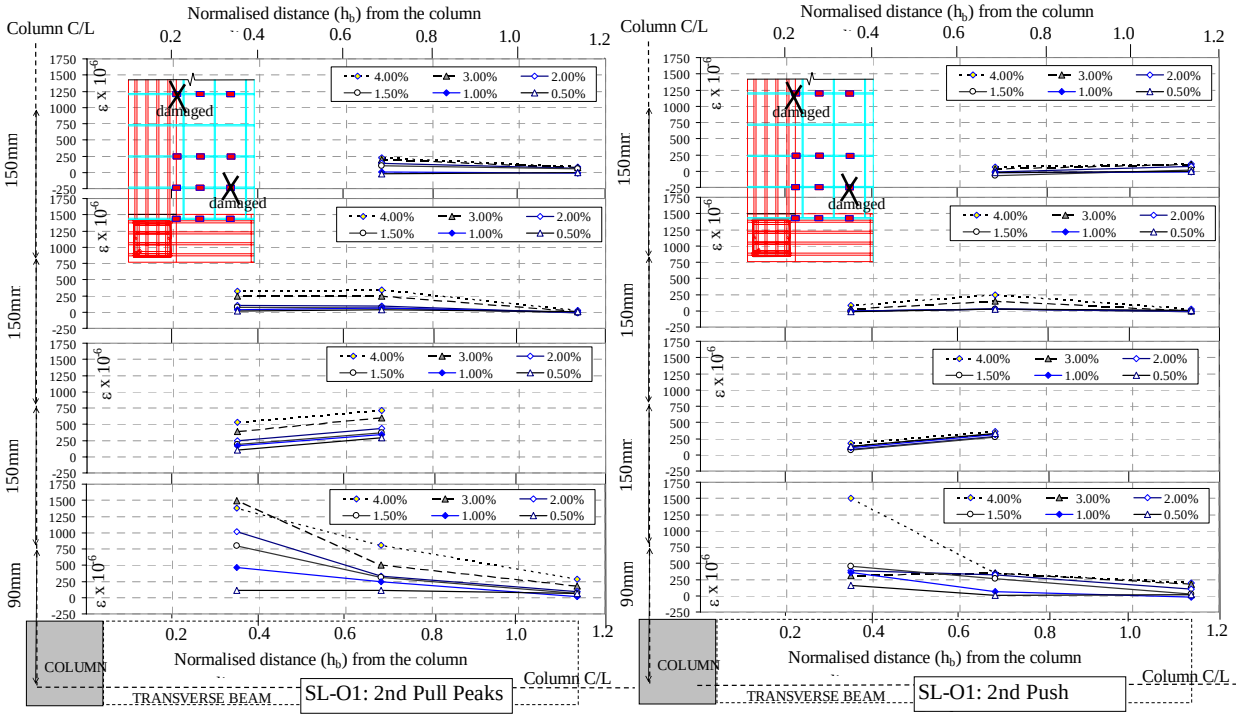

Figure 8.21: Strain profiles of slab bottom mesh perpendicular-to-loading direction for the specimen SL-O1.

8.3 EXPERIMENTAL RESULT OF RETROFITTED JOINT WITH SLAB:SL-R3

8.3.1 General description of behaviour

The F_c versus Δ_c hysteresis plot for SL-R3 is given in Figure 8.22. The damage and cracking patterns at the selected peak inter-storey drift, θ_{drift} loading cycles are shown in Figure 8.23 and Figure 8.24. The predicted lateral force capacities, $F_{sys\text{-}cal}$, for SL-R3 were +18.3kN and -28.6kN for the Pull and Push loading directions respectively, with beam flexural hinging failure mode expected. The joint shear capacity assessment did not include the confinement enhancement from the transverse beam stubs. The F_c - Δ_c hysteresis shown in Figure 8.22 includes the initial gravity load induced boundary condition (§4.6.4).

The gravity loading procedure as per §4.6.4 was applied on SL-R3. After the three stages of gravity loadings (as per §4.6.4), no visible cracks on the specimen were detected. The resulting F_c and V_b from the imposed gravity loading were -5.0kN and +3.0kN respectively.

There were no observable cracks in the ±0.1% drift cycles. Initial stiffness, K_{ini}, of 2593kN/m was measured in the +0.1% drift cycles. The measured K_{ini} was significantly lower than other specimens (typically >3000 kN/m), suggesting the specimen SL-R3 had pre-cracks from the post-tensioning intervention or the gravity loading.

In the Pull cycles of the +0.2% drift, a minor crack running along the bottom beam-column corner was observed. No other cracks were observed in the ±0.2% drift cycles. The ratio of cracked stiffness-to-uncracked stiffness, K_{cr}/K_{ini}, was 0.645.

Hairline width flexural cracks appeared on the column along the column-joint interfaces in the 1st Pull cycle of the +0.5% drift (Figure 8.23a and b). The maximum crack width at the beam bottom flexural crack during the Pull cycles was 0.3mm. In the 1st Push cycle of the -0.5% drift, a 0.5mm wide flexural crack appeared on the top face of the slab, extending through the whole length of the slab. A slab crack was also visible at the bottom face, running along the edge of the slab-transverse beam boundary. The cracking pattern so far was consistent with the SL-O1 damage.

Several hairline column flexural cracks appeared in the Pull cycles of the +1.0% drift. The largest crack opening remained at the beam-column interface, with a maximum crack width of 1.5mm. The beam bottom reinforcement yielded at approximately $\theta_{drift} \approx$+0.5% and the positive yield drift was marginally lower than SL-O1 which yielded at approximately +0.75%. At the Pull peaks of the +1.0% drift, both as-built (SL-O1) and retrofitted (SL-R3) joints have the same F_c.

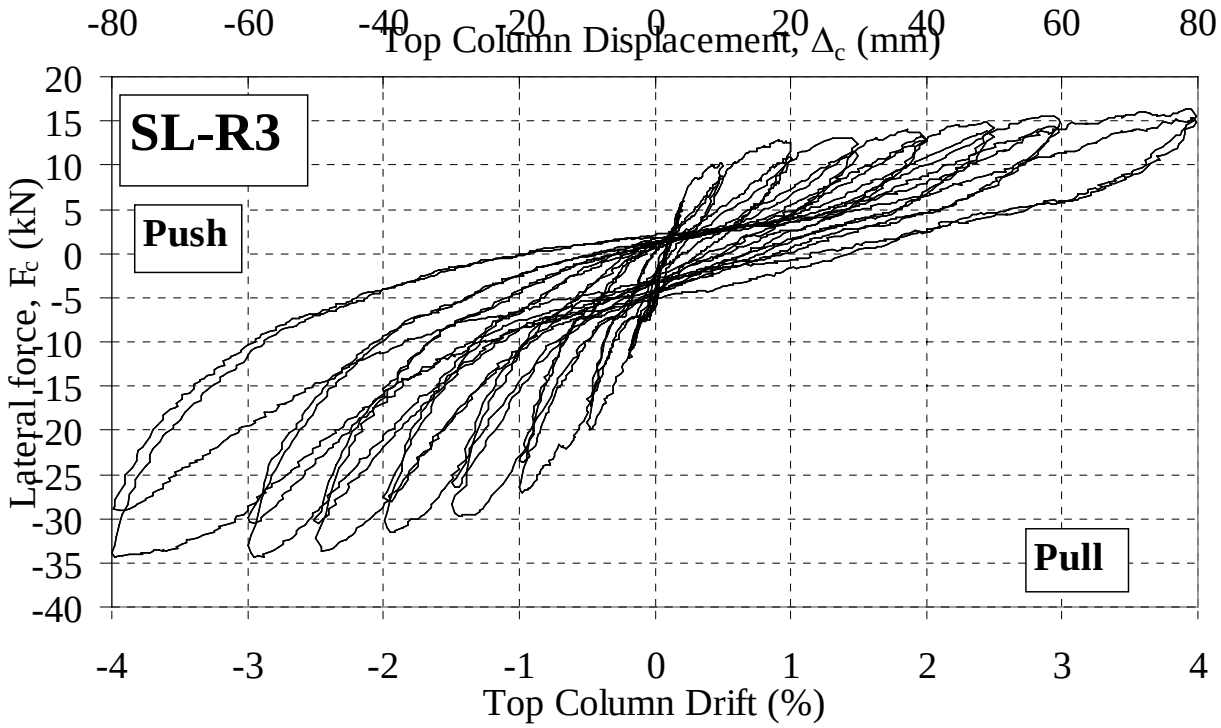

Figure 8.22: Top column lateral load, F_c, versus top column displacement, Δ_c, and drift, θ_{drift}, for SL-R3.

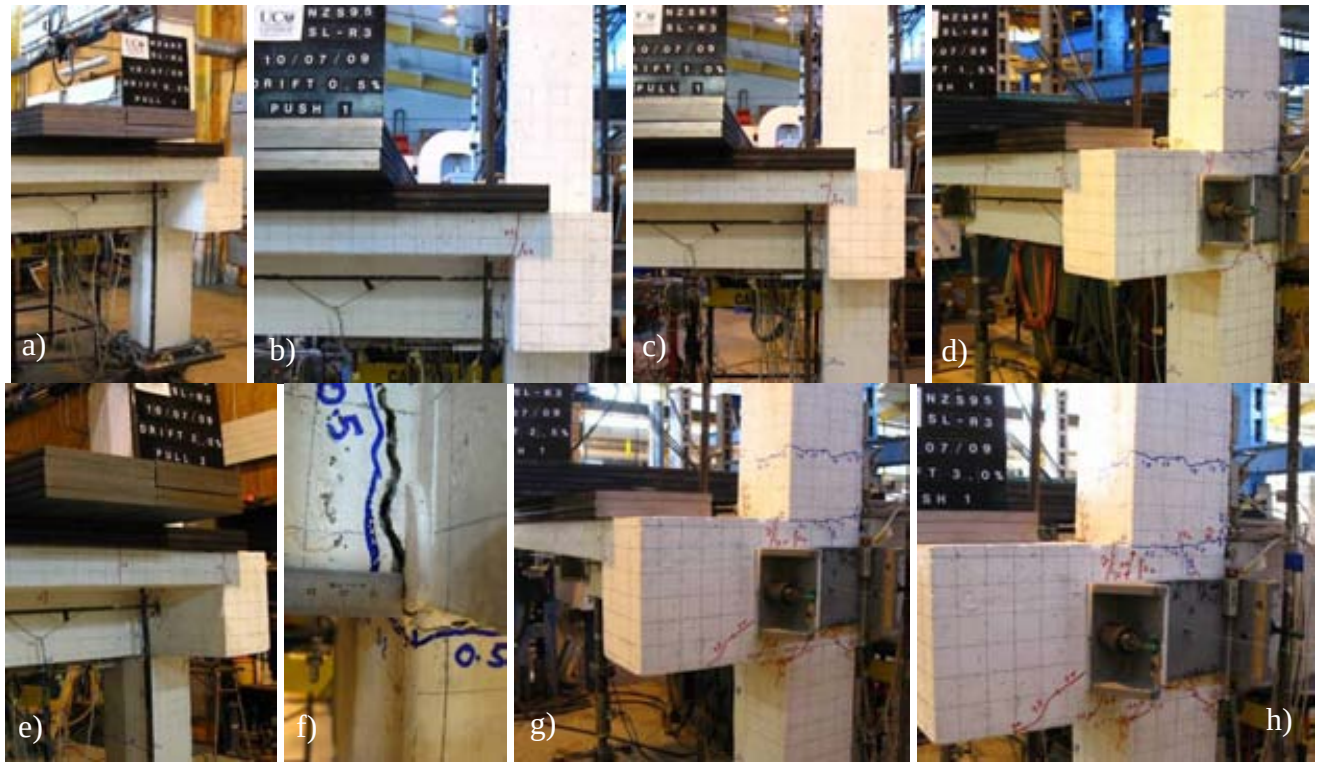

Figure 8.23: Observed cracking pattern of SL-R3: TOP: a) 1st Pull cycle of the +0.2% drift; b) 1st Push cycle of the -0.5% drift; c) 1st Pull cycle of the +1.0% drift; and d) 1st Push cycle of the -1.5% drift. BOTTOM: d-e) 2nd Pull cycle of the +2.0% drift; f) 1st Push cycle of the -2.5% drift; and g) 1st Push cycle of the -3.0% drift.

In the Push cycles of the -1.0% drift, two inclined vertical cracks appeared on the outer face of the joint, propagating between the centroid of the external post-tensioning and the corner of the joint. Considering that the principal stresses within the joint core were $p'_t = 0.175\sqrt{f'_c}$ MPa and $p'_c = 0.381\sqrt{f'_c}$ MPa, it would be unlikely that the joint crack was under shear action. The F_c-Δ_c hysteresis showed significant loss of energy dissipation within the Push cycles.

The difference and similarity between the inelastic mechanism for SL-R3 and for SL-O1 were more apparent in the Pull cycles of the +1.5%, +2.0% and +2.5% drifts (Figure 8.23d-f). The flexural crack along the beam-column interface remained the biggest source of inelastic deformation with a maximum crack width up to 5-6mm in the 2nd Pull peak of the +2.0% drift (Figure 8.23e). Unlike SL-O1, visual inspection showed that the joint remained undistorted in the Pull cycles in SL-R3. Further inspection of the strain gage data of the beam reinforcement (in §8.3.5.1) suggested more significant inelastic action within the beam for SL-R3 when compared with SL-O1. The strain profiles that suggested joint shear cracking in SL-O1 were also not observed in SL-R3. These observations confirmed the effectiveness of beam-weakening and joint post-tensioning in altering the inelastic mechanism of the beam-column joint.

In the Push direction, without beam-weakening retrofit intervention on the beam top face or the floor slab, any difference between SL-R3 and SL-O1 would be attributed to the unbonded post-tensioning of the beam-column joint. As the transverse beam was unaltered between test units SR-R3 and SL-O1, expectedly, a torsional crack was observed in SL-R3 in the -1.5% and -2.0% drift cycles. It appeared that the drilled hole in the transverse beam for the post-tensioning in SL-R3 had changed the angle of the diagonal torsion cracking, as the drilled hole became a weak point in the transverse beam. The torsional crack on the transverse beam stubs could be seen in Figure 8.23f and g. The torsion crack angle was approximately ~ 38°. The slab width bounded by the torsion crack was approximately b_{bt} and this was relatively lesser when compared with SL-O1. The maximum crack width on the floor slab by the 2nd Push peak of -2.5% was 1.7mm, along the transverse beam edge.

The maximum crack widths at the top and bottom corners of the beam-column interface were measuring 2mm and 8mm respectively (Figure 8.24a and b) in the ±3.0% drift cycles. Small hairline flexural cracks appeared in the column, while the existing column cracks along the joint-column interface grew to 1.5mm wide. The torsion cracks continued to grow in the Push direction in the -3.0% drift cycles. This was accompanied by several new vertical cracks

appearing in the outer face of the joint. The maximum crack width on the transverse beam was 1.8mm on the diagonal torsional crack. Minor spalling was observed on the top corner of the joint-transverse beam interface. There was about 10% in-cycle strength degradation in the ±3.0% drift cycles.

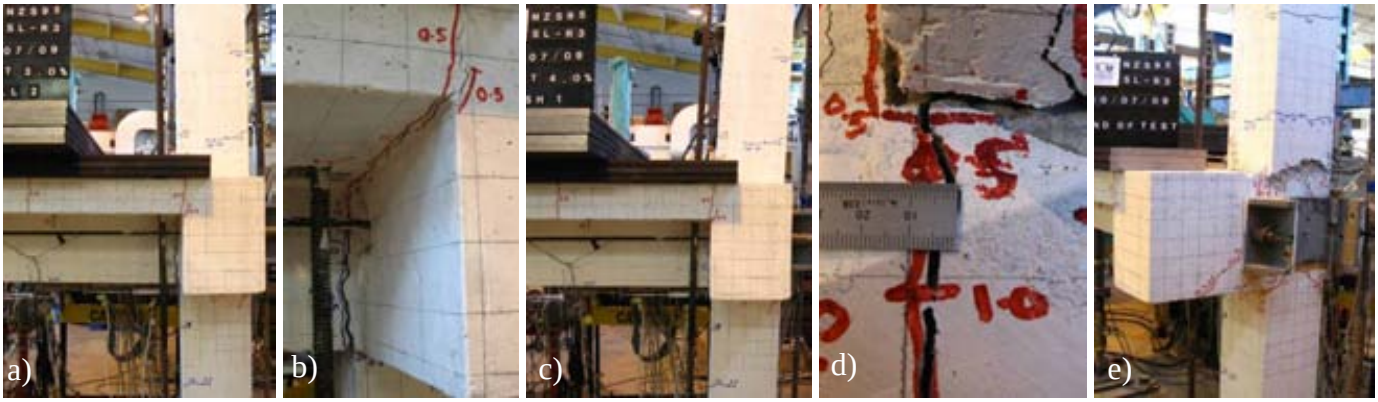

Figure 8.24: Observed cracking pattern of SL-R3: a-b) 2nd Pull cycle of +3.0% drift; c-d) 1st Push cycle of -4.0% drift; and e) End of the ±4.0% drift cycles.

In the Pull cycles of the +4.0% drift, the pseudo-rocking flexural beam hinging was the dominant inelastic deformation mode, with a maximum crack width up to 10mm measured at the beam-column interface. On the reverse loading to the -4.0%, however, a mixed inelastic mode of T-beam, column and joint hinging was observed (Figure 8.24c and d). Some spalling and delaminating of concrete were observed at the joint outer face but the joint distress was relatively smaller than SL-O1. The external post-tensioning anchorage provided active confinement on the free face of the joint, mitigating the torsional and joint shear damage.

Structural failure, as defined by the failure to attain 80% of the previous peak F_c was not reached after the ±4.0% drift cycles. The residual crack widths after the ±4.0% drift cycles (Figure 8.24e) were a) 4mm at the beam bottom flexural crack, b) 2mm at the diagonal torsional crack, c) 0.4-1.3mm at the beam top and slab, and d) 0.5-1.0mm at the column flexural cracks. The residual cracking pattern similarly suggested a mixed inelastic mechanism in the Push loading cycles and a beam flexural hinging in the Pull loading cycles. Due to the highly stressed post-tensioning tendon, SL-R3 was tested further for one Pull-Push cycle of the ±6.0% drift, as per SL-O1.

8.3.2 Load-displacement hysteresis analysis

The F_c-Δ_c hysteresis plot for SL-R3 is shown in Figure 8.22 while the analysis of the SL-R3 F_c-Δ_c hysteresis is presented in Figure 8.25. The maximum and minimum F_c of +15.7kN and -35.1kN were achieved at θ_{drift}=+3.94% and θ_{drift}=-2.95% respectively. The observed F_c value was significantly higher (~-12.8kN) when compared to the predicted F_c (+15.3kN and -23.9kN) in the Push direction, highlighting the limitation of the pseudo-rocking analytical prediction of the negative beam-moment with the presence of slab and transverse beam.

The 36.5% F_c enhancement in the Push cycles of SL-R3 was attributed to the slab flange and the transverse beam torsional restraint contributions. This result is consistent with the result by Bedirhanoglu *et al.* [7]. In their tests, an approximately 30% higher F_c for the negative beam moment was observed despite the smaller slab width, one-sided transverse beam stub and observed joint shear failures. In the absence of more advanced analysis, an over-strength factor of 30% may be adopted for the SW retrofit design.

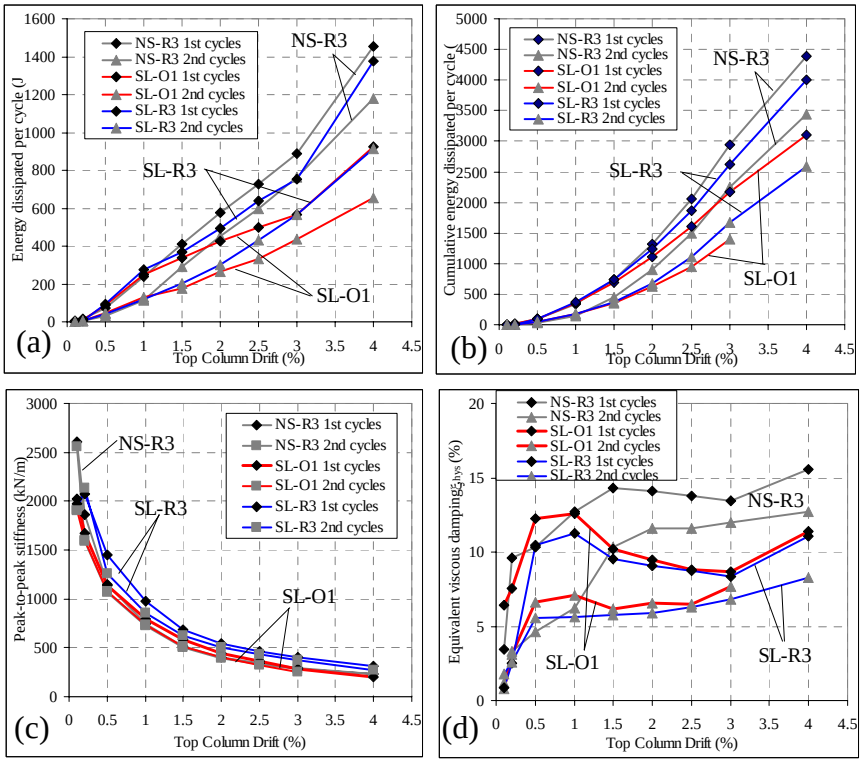

Figure 8.25: F_c-Δ_c analysis for SL-R3: a) Energy dissipated per cycle; b) Cumulative energy dissipated per cycle; c) peak-to-peak stiffness, K_{eff}, and; d) Equivalent viscous damping, ξ_{hys}.

As shown in Figure 8.25a, b and d, SL-R3 was achieving higher values in energy dissipation per cycle, cumulative energy dissipated and peak-to-peak stiffness than the as-built

specimen SL-O1. The energy dissipation capacity was improved by the beam inelastic mechanism in the Pull direction in SL-R3 when compared with the joint shear inelastic mechanism in SL-O1. Nevertheless, the additional energy dissipation did not lead to higher equivalent viscous damping, ξ_{hys} curves for SL-R3, as the maximum F_c was also higher in SL-R3.

Figure 8.25 also compared the curves for the R3 retrofitted joint with (SL-R3), and without slab or transverse beams (NS-R3). The higher F_c and thus higher column flexural and joint shear demands in the Push direction of SL-R3, which caused a partial joint-column failure mode, evidently resulted in lower energy dissipations for SL-R3 when compared with NS-R3. Furthermore, both the slab tension flange contribution to the F_c in the Push direction and to the lower energy dissipation, resulted in lower ξ_{hys} curves for SL-R3.

8.3.3 Local deformations and displacement components

8.3.3.1 Beam deformations

The moment-curvature plots for the beam flexural regions and beam fixed-end regions are shown in Figure 8.26. As with SL-O1, no accurate measurement of $\phi_{b,f\text{-}e}$ and ϕ_b was made for SL-R3 due to the instrumentation error.

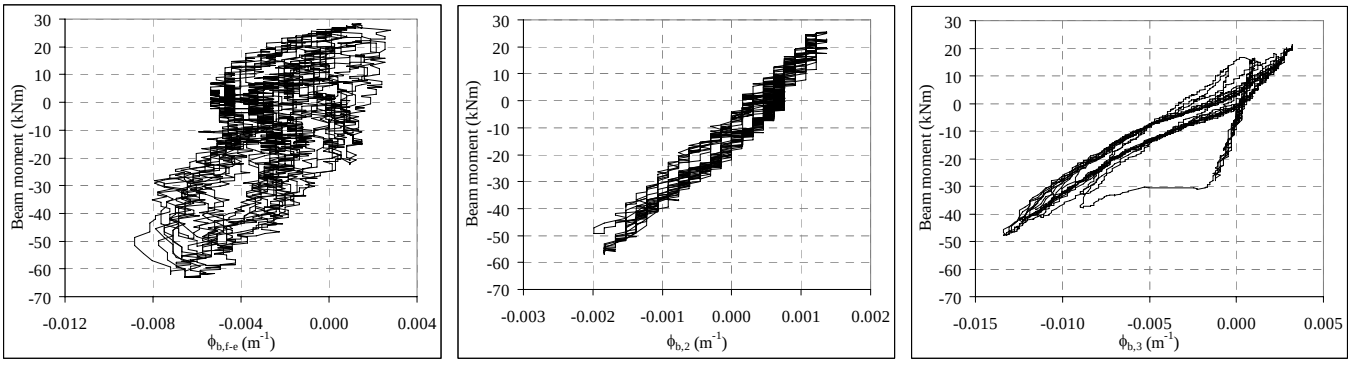

Figure 8.26: a) Moment-curvature plots for beam sections: a) fixed-end section; b) 75-275mm from the column internal face; and c) 275-475mm from the column internal face.

The maximum beam moments developed for SL-R3 in the Pull and Push directions were +28.3kNm and -63.1kNm respectively. For comparison, the predicted beam moments for SL-R3 were +34.7 kNm and -52.9kNm while the maximum experimental beam moments for NS-R3 were +31.2kNm and -38.9kNm (§6.4.3.2). The discrepancies between the predicted and the observed maximum beam moments for SL-R3 of +6.4kNm (22.6%) and -10.2kNm (16.2%) suggested that the analytical tools presented in §3.4 needed to be refined. §8.4.4 will further discuss the experimental-analytical comparison for SL-R3.

8.3.3.2 Column deformations

Figure 8.27 shows the measured moment-curvature response for the three regions of the column. The column curvature, ϕ_c measurement was inadequate without the direction measurement of the column-joint interface section. The observed nominal column flexural strengths, $M_{c\text{-}cf}$, were +12.0kNm and -26.7kNm in the Pull and Push cycles respectively. This was relatively lower than the expected column flexural capacities under the variation of axial loads: +19.0kN and -34.0kN. While significant column-joint interface cracking was observed (e.g. Figure 8.24d and e), the measured ϕ_c and the column longitudinal bars strain gage results suggested limited column inelastic deformation.

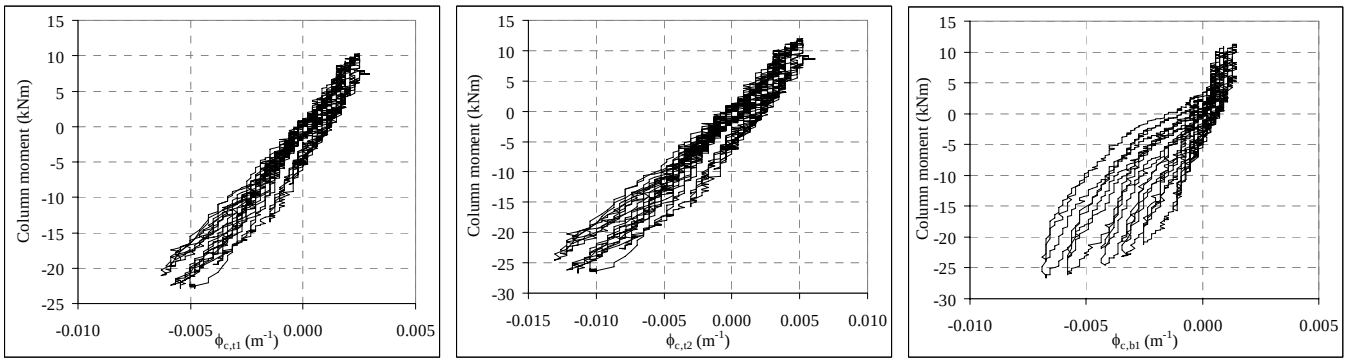

Figure 8.27: Moment-curvature plots for column flexural sections: a) 200-430mm from the beam top face; b) 0-200mm from the beam top face; c) 0-200mm from the beam soffit.

8.3.4 Beam-column joint behaviour

The nominal joint shear stress, v_{jh}, and the principal stresses (p'_t and p'_c) versus the column lateral displacement, Δ_c relationships for SL-R3 are given in Figure 8.28. No joint distortion, γ_j, was measured for SL-O1 and SL-R3.

The maximum v_{jh} measured were 1.82MPa (0.38 $\sqrt{f'_c}$ MPa or 0.079f'_c MPa) in the 1st Pull peak of the +4.0% drift and -4.07MPa (-0.85 $\sqrt{f'_c}$ MPa or -0.176f'_c MPa) in the 1st Push peak of the -4.0% drift. While the v_{jh} in the Pull direction was comparable to SL-O1's result (v_{jh} = 0.40 $\sqrt{f'_c}$ MPa and -0.57 $\sqrt{f'_c}$ MPa), the v_{jh} was significantly higher in SL-R3. This confirmed the positive effect of joint post-tensioning in increasing the joint shear strength (at least in terms of v_{jh}).

In terms of maximum principal stresses in the joint, the maximum p'_t was 0.402$\sqrt{f'_c}$ MPa and the maximum p'_c was 1.50$\sqrt{f'_c}$ MPa (or 0.312f'_c MPa). The maximum p'_t and p'_c occurred at the 1st Push peak of the -3.0% drift and 1st Push peak of the -4.0% respectively. While the p'_t

maxima for SL-R3 were similar to p'_t maxima for SL-O1, it was believed that the SW retrofit had increased the joint p'_t limit state (as described in §3.4.4 and §3.4.6) and therefore prevented joint shear failure in SL-R3. The maximum p'_c for SL-R3 was 38% higher than SL-O1's maximum p'_c of $1.09\sqrt{f'_c}$ MPa. The high maximum p'_c of $0.312f'_c$ MPa in SL-R3 indicated the high likelihood of joint diagonal crushing given the typical diagonal compression limit state (e.g. [34]).

Unlike SL-O1, no sign of degradation of the v_{jh} or the principal stresses (p'_t and p'_c) was observed for SL-R3. Furthermore, no observable drop in the principal stresses after an expected 'joint cracking' point was observed, unlike other retrofitted specimens presented in Chapter 6 (e.g. NS-R2, NS-R3 and NS-R4), despite the much higher maximum principal stress values measured in SL-R3.

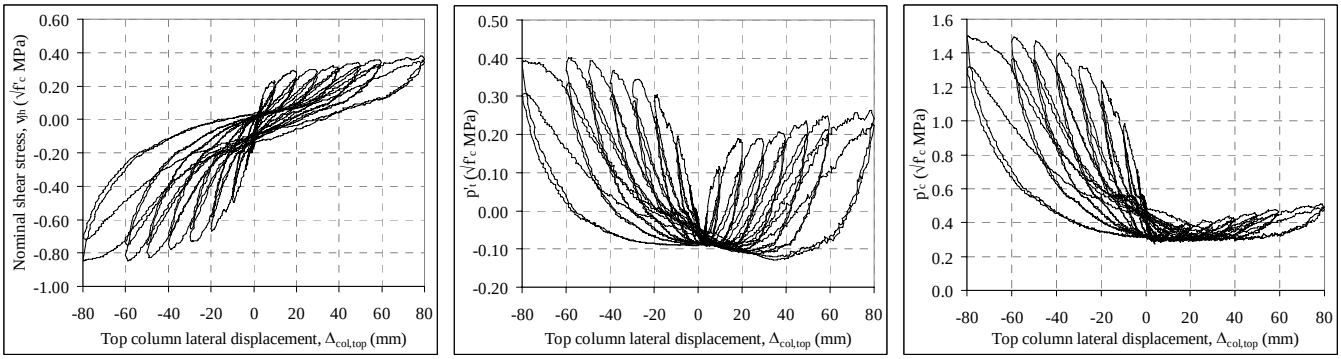

Figure 8.28: Joint shear stresses versus top column lateral displacement, Δ_c : a) Nominal joint shear stress, v_{jh} b) principal tensile stress, p'_t; and c) compressive tensile stress, p'_c.

8.3.5 Steel strain profiles

8.3.5.1 Beam longitudinal reinforcement strains

Figure 8.29 presents the strain profiles of the top beam longitudinal reinforcement while Figure 8.30 and Figure 8.31 present the strain profiles of the beam bottom un-weakened and weakened longitudinal reinforcement for SL-R3. The X-axis is the distance from the exterior column face while the two vertical dashed lines refer to the column centre-line and the interior column face. Tensile strains are given as positive values. From the steel test, the yield strain, ε_y, for the longitudinal beam reinforcement was 0.00174 (1735 microstrains) and the f_y was 347MPa. In general, the strain profiles observed in SL-R3 were similar to those of NS-R3 (§6.4.5.1)

The beam top longitudinal bars yielded in the -1.5% Push cycles at the beam-column interface section, which also corresponded to the large transverse beam-slab interface crack observed during the test. However, in subsequent cycles, progressive penetration of strains into

the joint and beam, consequence of de-bonding failure led to more uniform tensile strain demands across an approximate 160-180mm reinforcement length. In the reverse Push cycle, limited compression strains were measured in the top bars, due to the low compressive bond capacity of the plain round bars.

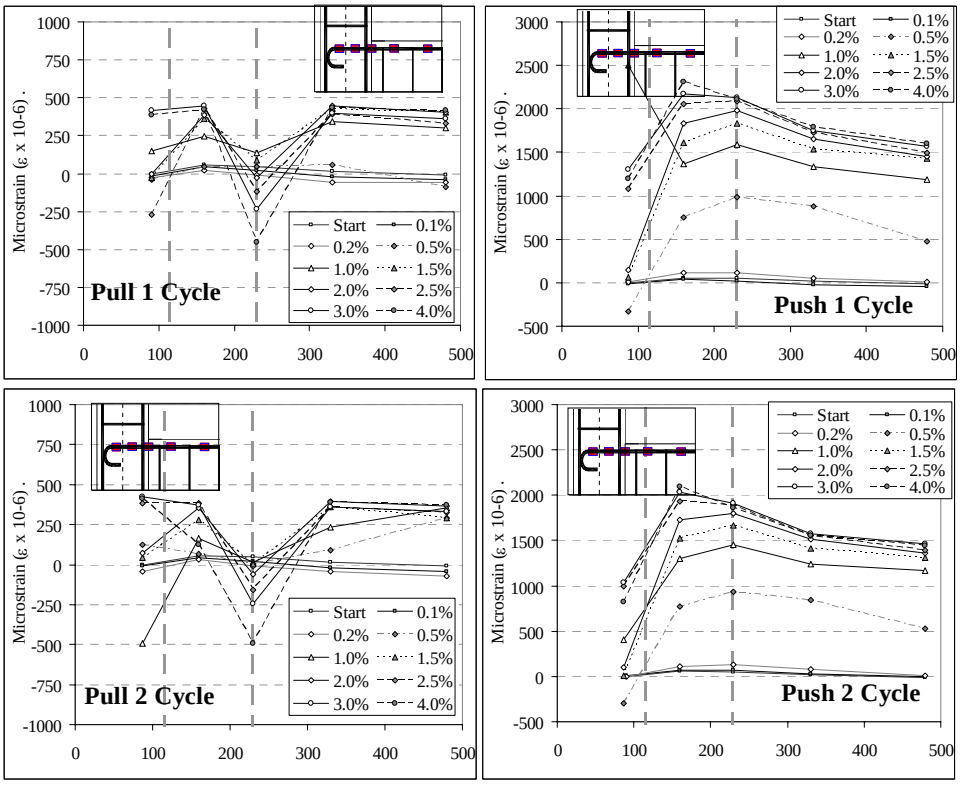

Figure 8.29: Strain profile of beam top longitudinal bars of the specimen SL-R3.

The beam un-weakened bottom reinforcement (Figure 8.30) yielded in tension in the 1st cycles of the +1.0% drift. Bond failure however limited the maximum tensile strain to 1780 microstrains. High tensile strains were measured in the un-weakened bottom bars in the Pull cycles beyond the +1.0% drift, suggesting the 180º hook was acting as an effective tension anchorage. In the Pull cycles, the beam un-weakened bottom reinforcement developed up to -180 MPa in compressive stress, again limited by the bond capacity of the plain round bars and the bearing capacity of the 180º hooks.

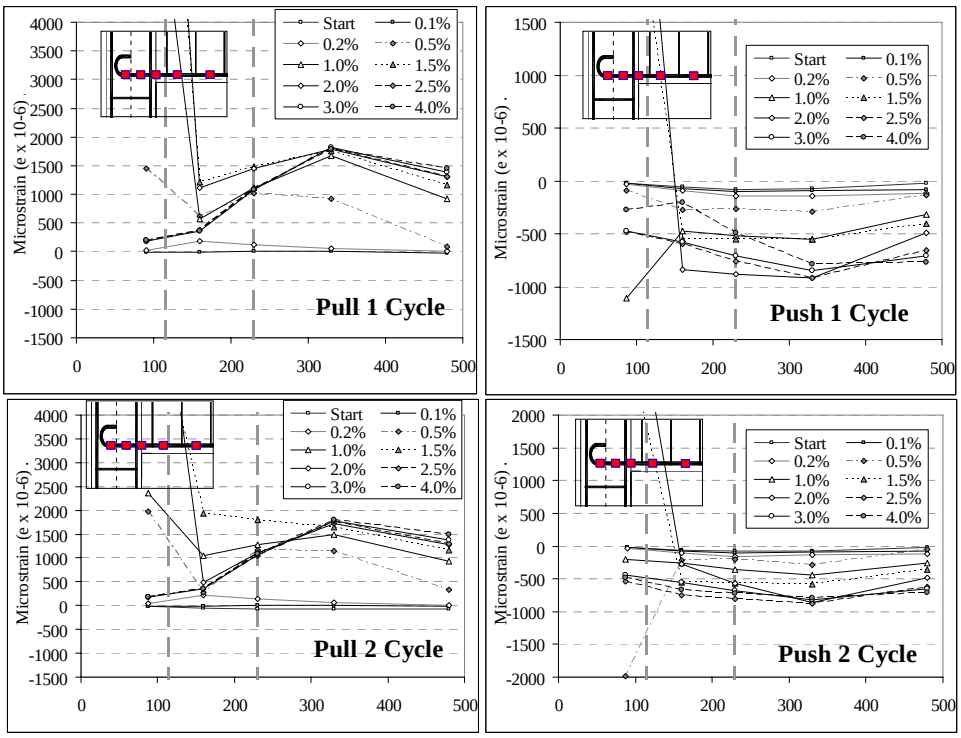

Figure 8.30: Strain profile of the un-weakened beam bottom longitudinal bars of the specimen SL-R3.

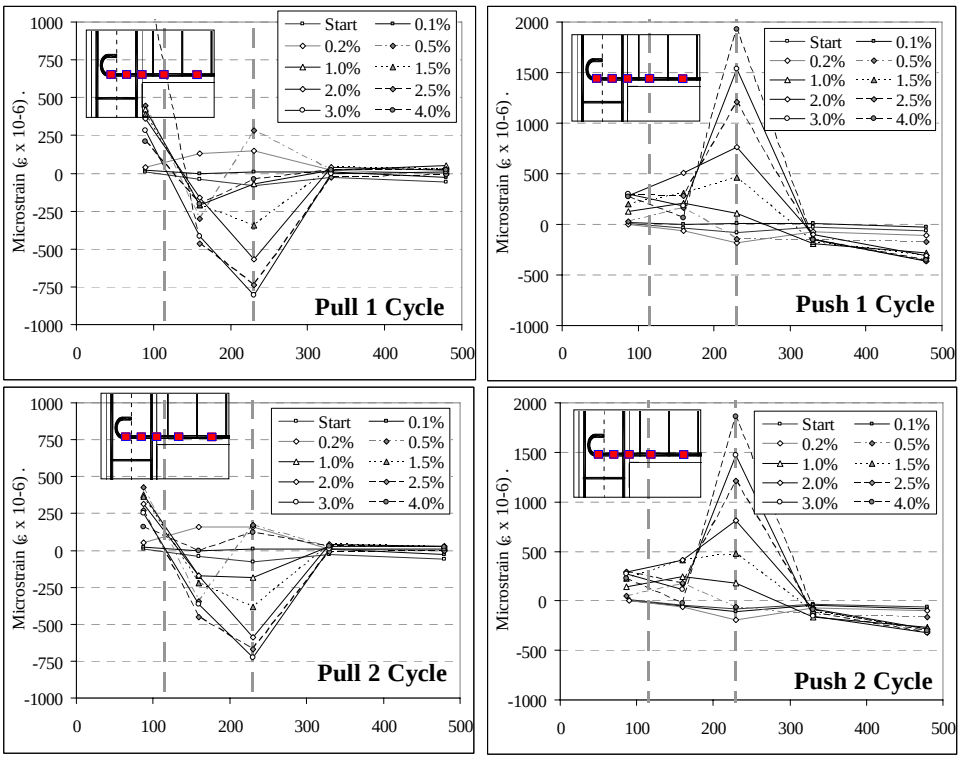

Figure 8.31: Strain profile of the weakened beam bottom longitudinal bars of the specimen SL-R3.

Interestingly, substantial strains were measured in the 'weakened' bottom beam bars in both the Pull and Push loadings. Spikes of tensile and compressive strains were measured in the beam-column interface, despite being 50mm from the selective beam-weakening section. As limited strains (< 300 microstrains) were measured in other sections of the weakened bars, it was suspected that the spikes were due to the localised damage and dowel action on the bars across the beam-column interface.

8.3.5.2 Column longitudinal reinforcement strains

Figure 8.32 and Figure 8.33 present the strain profiles of the exterior and interior column longitudinal reinforcement for the specimen SL-R3. In Figure 8.32 and Figure 8.33, the Y-axis is the distance from the centre-line of the beam. The three horizontal dashed lines refer to the beam soffit (bottom line), beam centre-line and the beam top face (top line). All column strain gages were zeroed before the axial force loading on the column at the start of the test. The ε_y for the longitudinal column reinforcement was 0.0024 (2400 microstrains) and the f_y was 480MPa.

In general, the column longitudinal reinforcement was responding elastically for most of the drift levels. The column bars strain profiles had the similar trend as the NS-R3 tests, but with approximately 30% higher tensile strains measured in the Push direction due to the higher F_c. Unfortunately, the strain gages at the critical column sections were damaged in the -3.0% and -4.0% drifts cycles, as such no direct measurement of the column bars yielding was attained. The maximum tensile and compressive stresses measured in SL-O1 column longitudinal bars were +414MPa and -174MPa respectively.

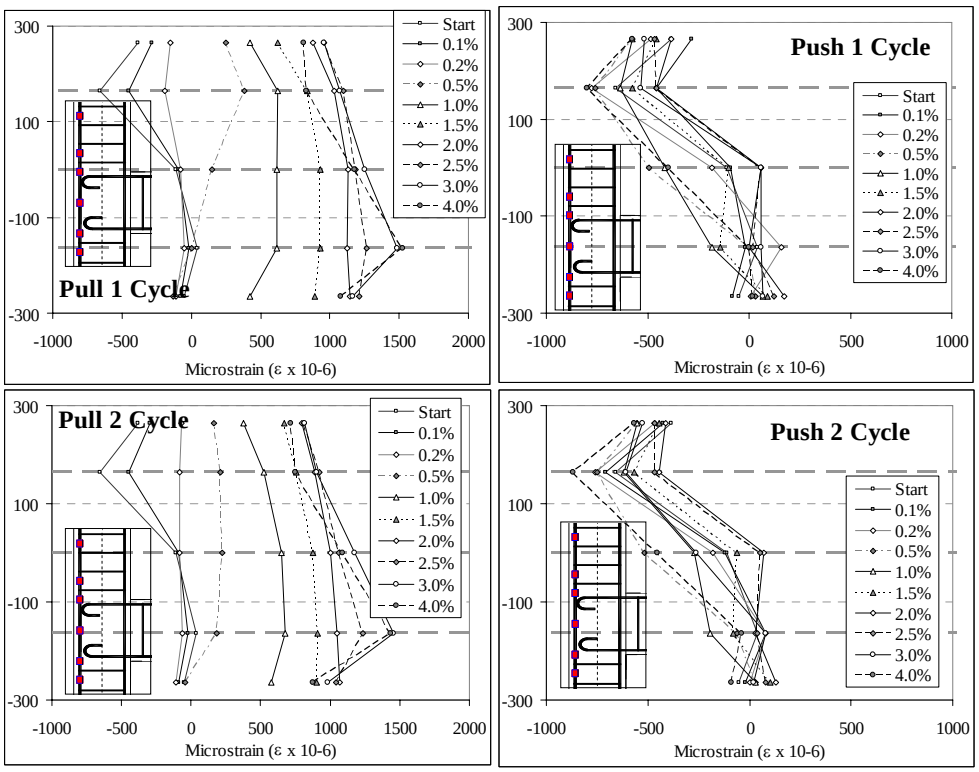

Figure 8.32: Column exterior face longitudinal reinforcement strain profiles for specimen SL-R3.

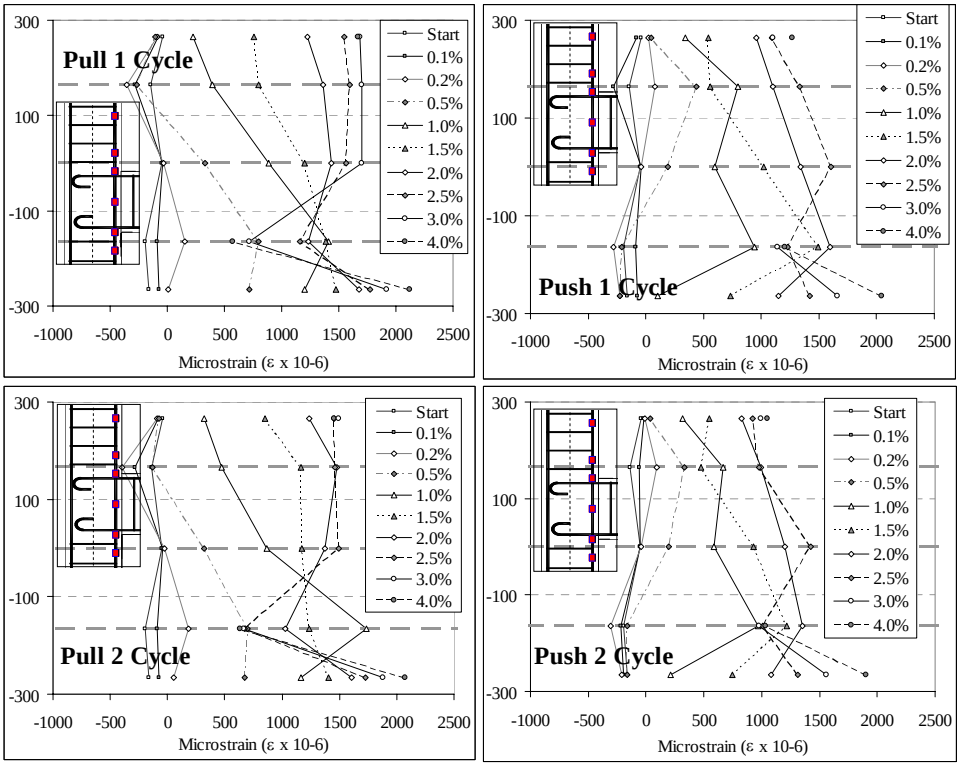

Figure 8.33: Column interior face longitudinal reinforcement strain profiles for specimen SL-R3.

8.3.5.3 Stirrup reinforcement strains

The strain profiles of the stirrups in the column and the beam are shown in Figure 8.34. Only selected stirrup results are presented herein as the general trend across different measurements is similar. In generally, all the stirrups responded elastically. The column stirrups indicated possible confining tensile stresses after the ±1.5% to ±2.0% drift cycles, which corresponded to the appearance of column flexural cracks. This was comparable to SL-O1 (§8.2.5.3) and NS-R3 (§6.4.5.3) observations. On the other hand, the beam stirrups in SL-R3 were measured tensile strains up to 450 microstrains for most drift levels, while beam stirrups in SL-O1 was indicating tensile strains about six times lesser (~75 microstrains). This confirmed previous observations that beam flexural hinging was a more dominant inelastic mechanism in SL-R3 when compared to SL-O1. Furthermore, the beam stirrups strain profiles for SL-R3 were similar to those observed in NS-R3.

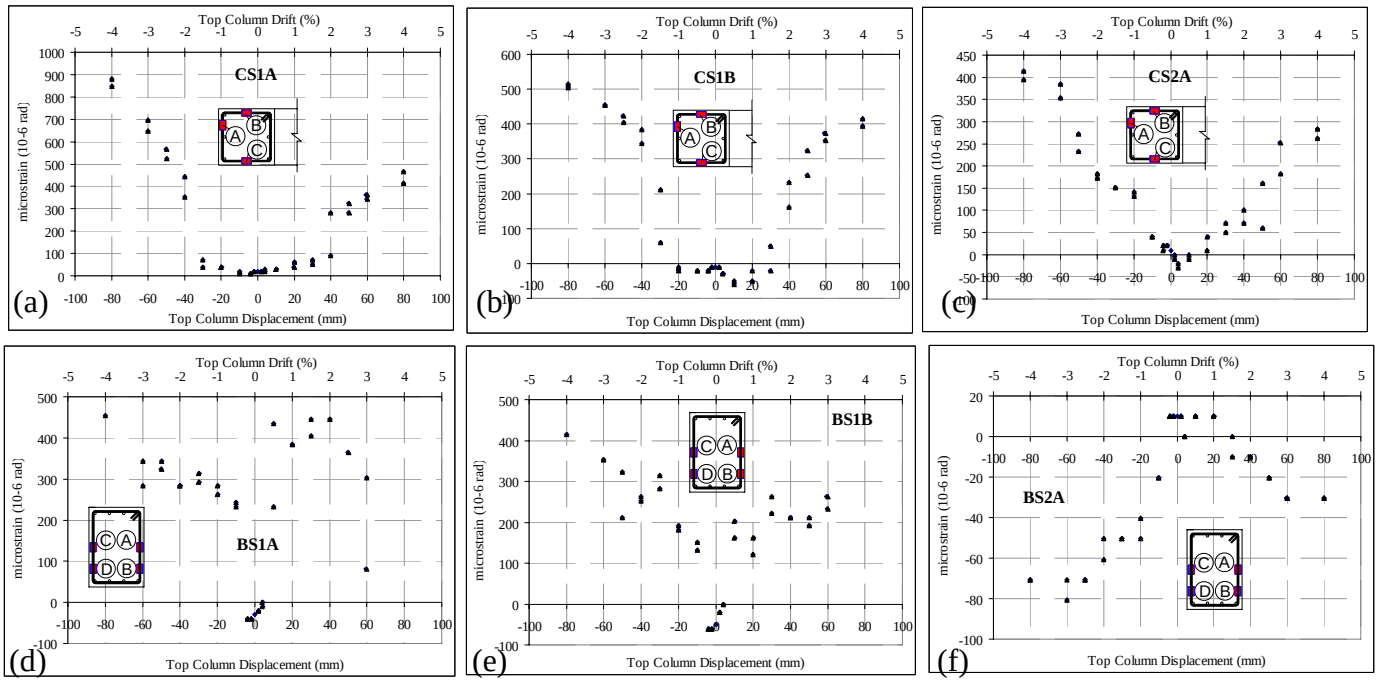

Figure 8.34: Stirrup strain profiles: TOP: a) column stirrup 50mm below the beam soffit; b) column stirrup 50mm from the beam top face; and c) column stirrup 350mm from the beam top face. BOTTOM: d-e) beam 1st stirrup 50mm from the column interior face; and f) beam 2nd stirrup 183mm from the column interior face.

8.3.6 Floor slab mesh strain measurements

A total of 46 strain gages were placed on the mesh reinforcement parallel and perpendicular to the loading direction. The details of the slab mesh anchorage are given in §4.3.6. In the following paragraphs, '*x*' refers to the distance of the mesh reinforcement (instrumented) from the

centreline of the column. In general, the 1st and 2nd cycles had similar strain profiles with minimal degradation of strain in the 2nd cycle. This suggested a limited bond degradation of the mesh reinforcement. Only the 2nd cycle results are shown herein for brevity.

The strain profiles for the slab top mesh reinforcement parallel to the loading direction during the Pull and Push cycles are presented in Figure 8.35 and Figure 8.36. The behaviour of the top mesh parallel reinforcing in the Pull loading (slab in compression) was similar to SL-O1, with minimal strains measured for most θ_{drift} levels.

The slab top mesh in parallel to the loading direction during the Push loading had showed evidence of the slab tension flange effect. In the 1st Push of the -1.0% drift, a sudden jump in strains was measured at the section x=1.4h_b. This also corresponded to the onset of torsional cracking of the transverse beam (vertical cracks along the joint outer face). It could be deduced from Figure 8.36 that at the -2.0% drift, the whole 1.35h_b (450mm) width of the slab was participating as yielding tension flange. The highest tensile strains were measured at x=0.45h_b in both transverse and longitudinal directions. These were expected as they corresponded to the location of the top slab crack along the transverse beam-slab edge, and strains localisation would be expected for the smooth mesh reinforcement.

The strain profiles of the slab top mesh perpendicular to the loading direction are given in Figure 8.37. As with SL-O1, limited strains were measured in the mesh reinforcement perpendicular to the longitudinal beam. The strain profiles in SL-R3 were consistent with those of SL-O1, but with half of the tensile strain measured. The highest mesh stresses were +156 MPa and -113MPa in the Pull and Push loading respectively. Similar to SL-O1, higher strains were observed in the regions close to the transverse beam. The lower strains measured in SL-R3 suggested a smaller torsional induced slab action when compared with SL-O1.

The strain profiles of the top mesh under the Push loading and the slab damage pattern suggested a possible force transfer model for the enhancement of lateral capacity due to the interaction of the torsion resistance of the transverse beam and the floor slab. The longitudinal reinforcement of the transverse beam carried the torsion shear flow forces (as shown in Figure 8.4) from the floor slab into the joint (and vice versa). The cantilevered free edge of the slab in the test specimen would therefore transfer these forces from the transverse beam into the longitudinal beams via a series of compressive struts and tensile ties. Figure 8.38 illustrates one possible force-transfer model for the specimen SL-R3 (also applicable to SL-O1).

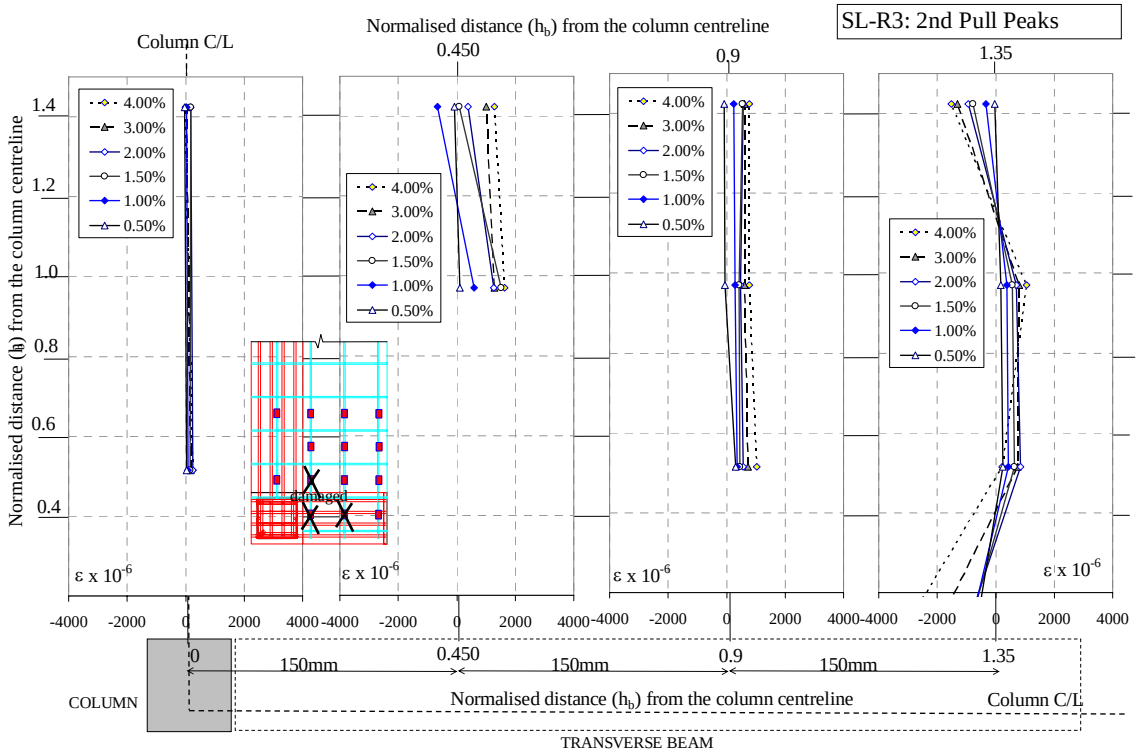

Figure 8.35: Strain profiles of slab top mesh parallel-to-loading direction for the specimen SL-R3: 2nd Pull peak cycles.

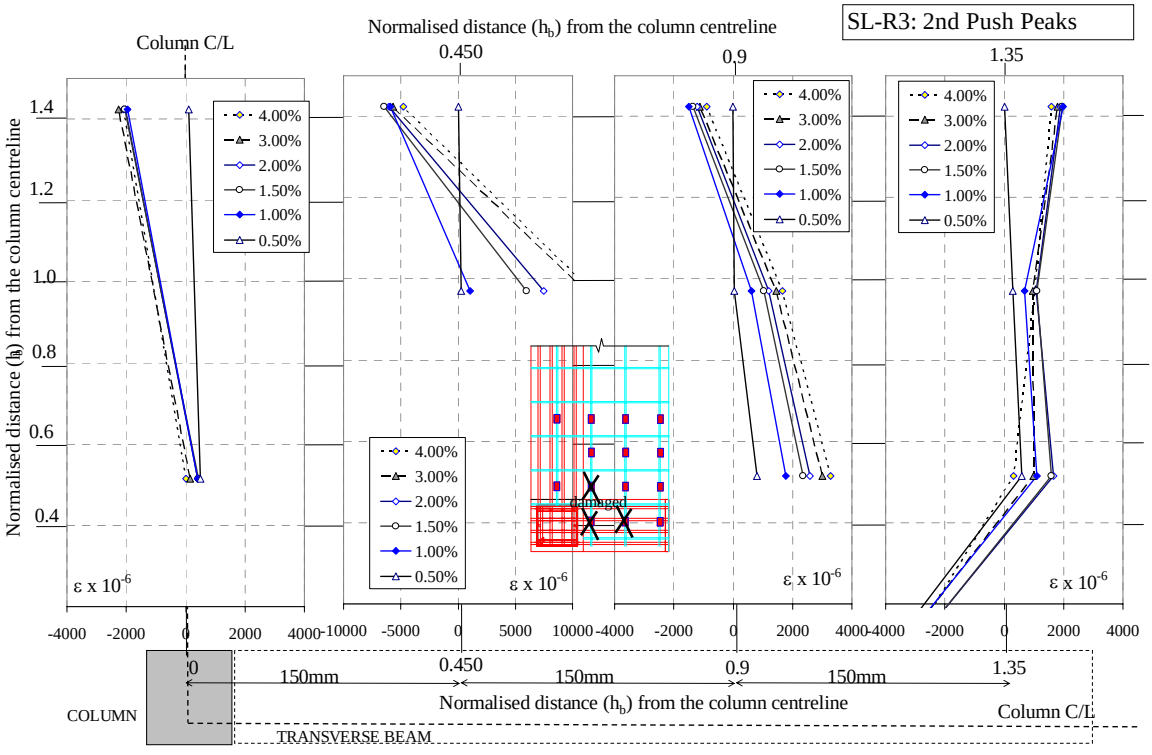

Figure 8.36: Strain profiles of slab top mesh parallel-to-loading direction for the specimen SL-R3: 2nd Push peak cycles.

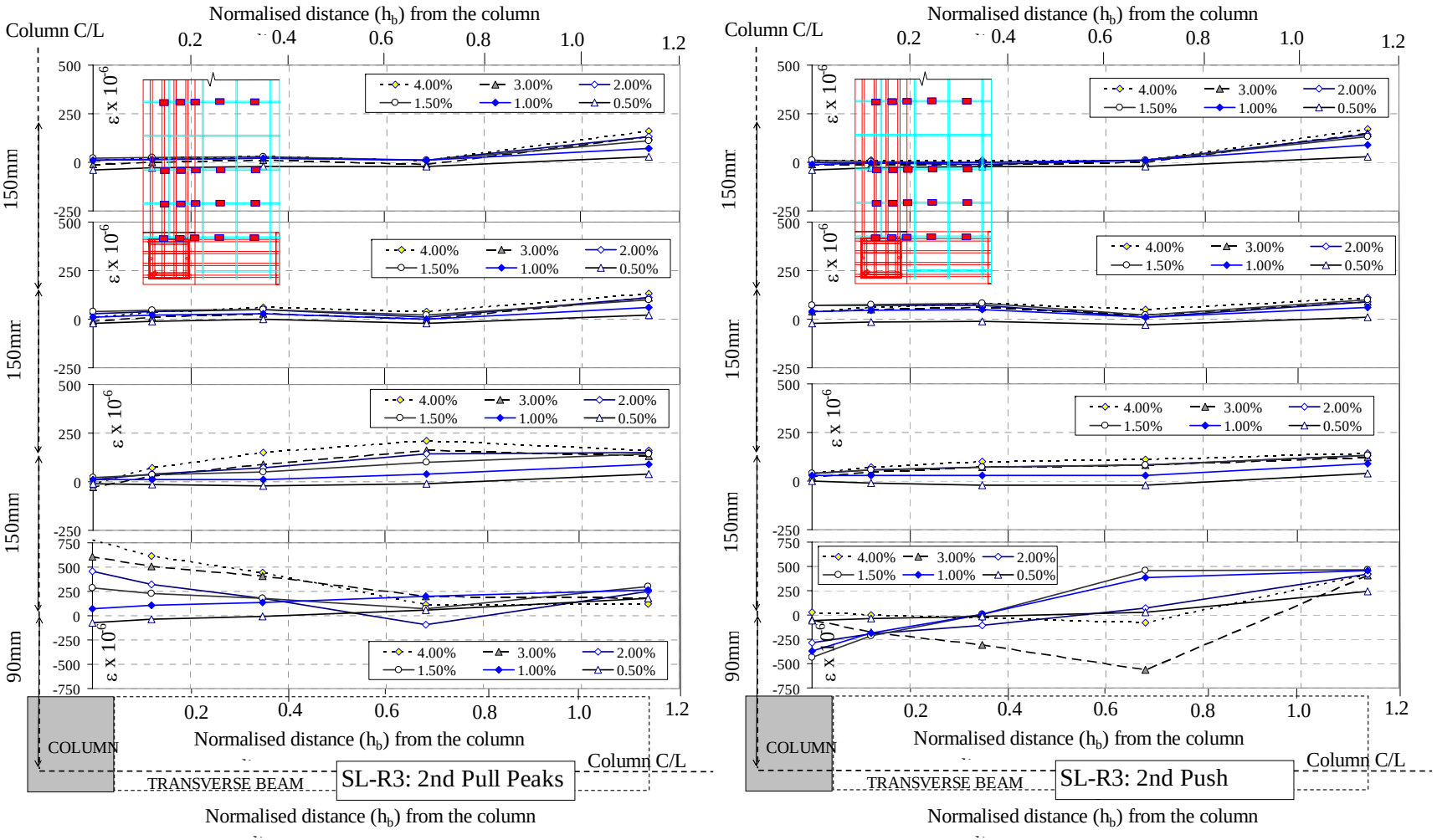

Figure 8.37: Strain profiles of slab top mesh perpendicular -to-loading direction for the specimen SL-R3: left) 2nd Pull peak cycles; right) 2nd Push peak cycles.

However, the mechanism of torsion of transverse beams is unsuitable for stable energy dissipation in reversing cyclic loadings such as earthquake action [33]. Furthermore, transverse beams under bi-directional actions may too develop plastic hinges as the beams do not recognise their roles as 'gravity-only' support (e.g. [12, 25]). For these reasons, no further consideration is given to the possible F_c enhancement as suggested by the strut-and-tie model in Figure 8.38.

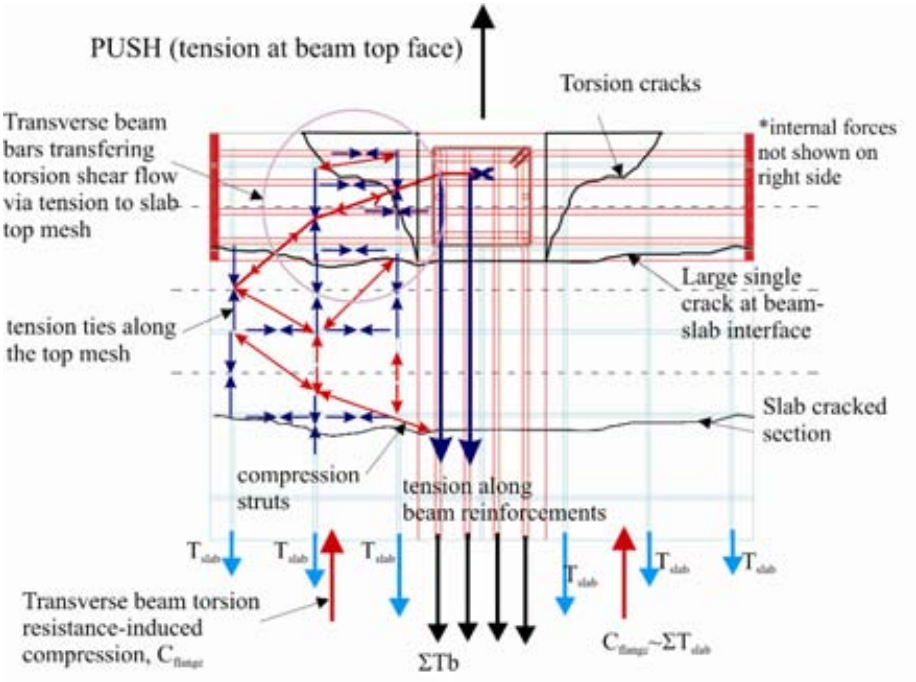

Figure 8.38: Force transfer truss model for the lateral strength enhancement due to the interaction of torsion resistance of transverse beam and the floor slab.

The strain profiles for the slab bottom mesh reinforcement parallel and perpendicular to the loading direction are plotted in Figure 8.39 and Figure 8.40. The bottom mesh reinforcement in parallel with the loading were increasing in tensile strains in both the Pull and Push cycles. In the Pull cycles, as the θ_{drift} increased, the strain increase was minimal, suggesting that the neutral axis was very close to the depth of the top mesh centroid (d = 20mm). Maximum tensile stresses developed in the mesh bars were about +175MPa. As with SL-O1, the strain profiles of the top and bottom mesh reinforcing suggested that the neutral axis of the beam bending was in between the top mesh (d=23mm) and the bottom mesh (d=83mm). It was found that the selective weakening and post-tensioning retrofit intervention did not change the response of the bottom mesh reinforcement as they were mostly effective only for gravity loading. The low tensile strains in the bottom mesh reinforcement perpendicular to the loading indicated that the

horizontal tensile ties in Figure 8.38 may be negligible (as the diagonal compression struts of the slab could form equilibrium without substantial horizontal ties.

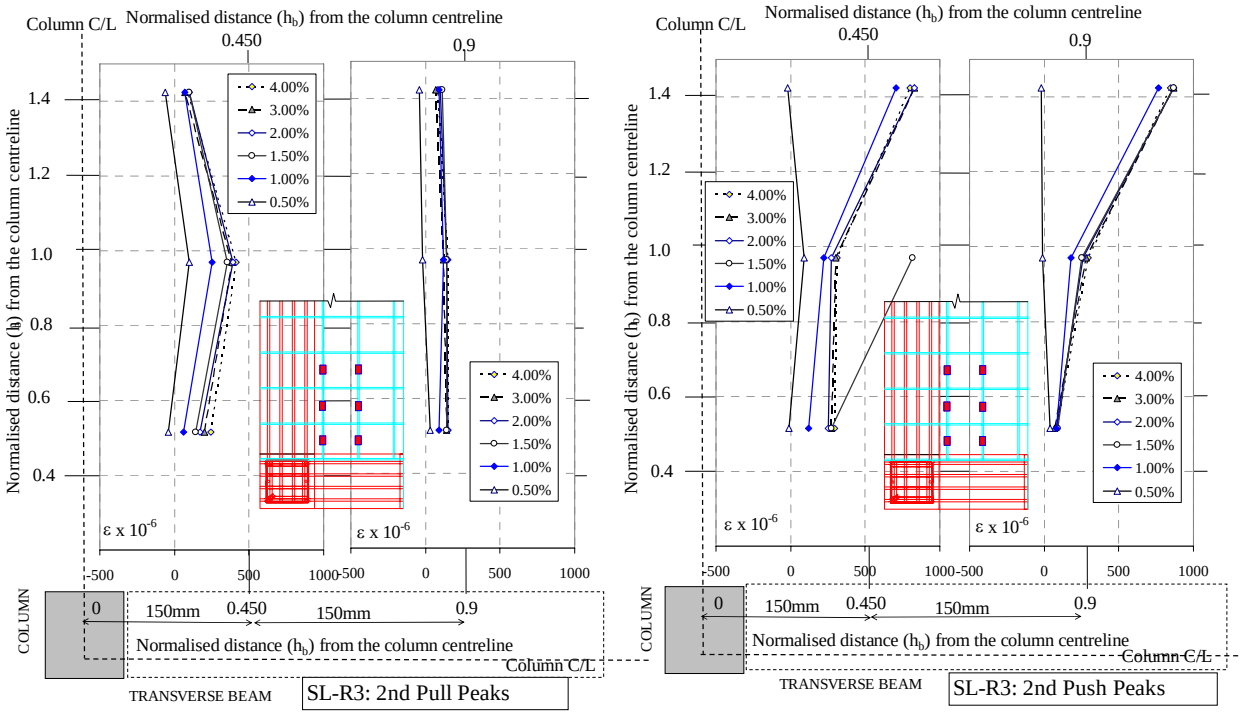

Figure 8.39: Strain profiles of slab bottom mesh parallel-to-loading direction for the specimen SL-R3.

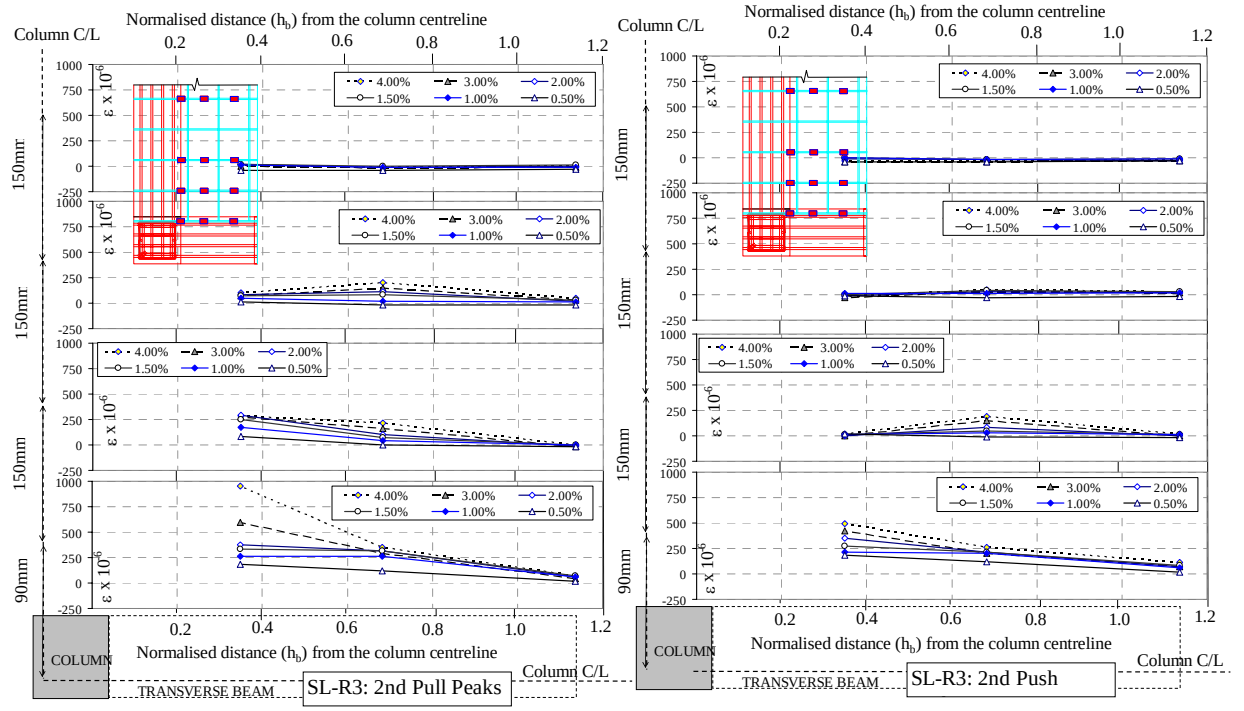

Figure 8.40: Strain profiles of slab bottom mesh for the specimen SL-R3: 2nd Push peak cycles.

8.4 DISCUSSIONS

8.4.1 Influence of floor slab and transverse beams

Transverse beam stubs, acting together under tension membrane action of the floor slab, are expected to improve the joint shear behaviour owing to the confinement transverse beams provided to the dilation of the joint concrete core [2]. As discussed in §2.4, the USA and Japanese approach (e.g. ASCE-41[4] and ACI-352 [2]) takes into account the higher joint shear capacity coefficient γ for joints with confining transverse beams. Conversely, the New Zealand and European approach (e.g. NZSEE guidelines [31] and fib bulletin [17]) considers the confining effect of transverse beams to be negligible given the hinging of transverse beams under a bi-directional excitation.

With transverse beam stubs, joint cracks could not be observed directly but could be deducted from indirect measurements (force-displacement, external distortion, potentiometers and observable cracks). As discussed in §8.2.1, evidently, the un-reinforced joint region was damaged under joint shear cracking in SL-O1. However, the transverse beams (with torsional resistance) possibly enhanced the joint shear strength via a) added confinement as postulated in ACI-352 [2], and b) an enlarged joint shear effective area. This is schematically illustrated in Figure 8.41, in which different joint shear failure planes could occur for unreinforced beam-column joints with transverse beams.

However, the amplification of the joint shear strength due to the transverse beam is not possible without the tension flange action of the slab, which explains why the presence of transverse beams alone did not induce higher joint shear capacity, as observed by Beres *et al.* [9] and Bedirhanoglu *et al.* [7].

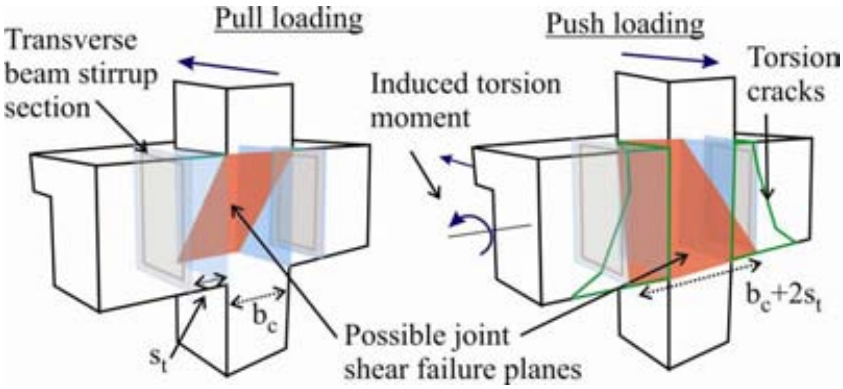

Figure 8.41: Possible hidden joint shear failure planes in exterior joint with transverse beams.

As shown in the comparison of F_c-Δ_c hystereses in Figure 8.42a, higher negative F_c and higher displacement capacities (-3% drift compared with +1% drift) were observed in SL-O1 when compared to NS-O1. The negative F_c peak was higher by about 15% in SL-O1. Torsion cracks at approximately 55° inclination were also observed on the transverse beam of SL-O1, consistent with previous test results on exterior joints with slab and transverse beams [14-16]. A possible model of force transfer to explain the contribution of the torsion resistance to the lateral strength capacity is presented in Figure 8.38 (of the previous section).

However, as the inelastic mechanism was predominantly the joint shear hinging in SL-O1, albeit a 'stable' hysteresis up to the ±3.0% drift cycles, plain-round bars bond slip and shear crack propagation resulted in a pinching low-energy-dissipation hysteresis for SL-O1. Evidently, the area-based equivalent viscous damping ratio for SL-O1 and NS-O1 were both similar, at approximately 10% in the first cycles and 6% in the 2nd cycles.

Using a truss slab-beam model, Cheung *et al.[12]* concluded that the F_c enhancement due to slab flange effect was approximately ΣT_{slab} where T_{slab} was the tensile stress of the longitudinal slab reinforcement. A similar approach was taken in postulating the truss model for force transfer from the floor slab to the beam-column joint (as shown in Figure 8.38).

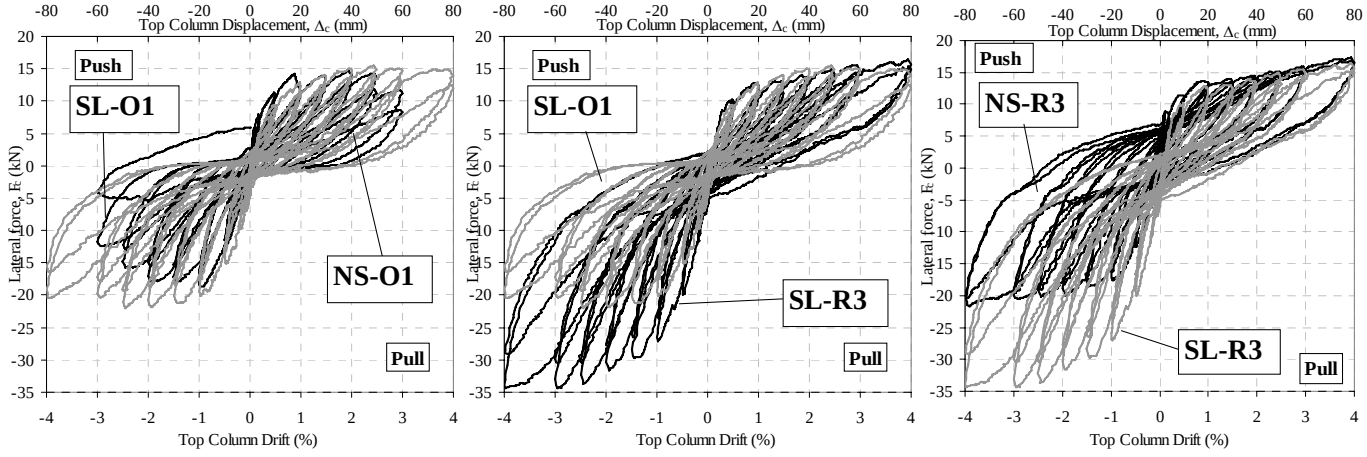

Figure 8.42: Comparison of the F_c-Δ_c hysteresis loops for as-built and R3-retrofitted beam-column joints.

Figure 8.42b and c compare SL-R3 with SL-O1 and the R3-retrofitted joint without slab. In both cases, the R3 SW retrofit intervention enhanced the peak F_c by about 37-39% in the Push direction while did not change the peak F_c in the Pull cycles significantly.

The effect of beam-column joint post tensioning was evident from Figure 8.42b and the discussion in §8.3. Given that both the specimens SL-R3 and SL-O1 had the same torsion

resistance from the transverse beam and approximately the same slab tension flange contribution, the over-strength of F_c in the Pull cycles and negative beam moment must therefore be resultants of the unbonded post-tensioning. As discussed before as well, the joint post-tensioning had also successfully changed the inelastic mechanism from a confined joint shear failure to a ductile beam inelastic mechanism.

The influence of floor slab and transverse beam on the seismic retrofit of the non-ductile beam-column joint is clearly highlighted in Figure 8.42c. As both SL-R3 and NS-R3 had the same level of post-tensioning forces and beam-weakening, the difference between the two specimens could be attributed to the presence of slab and transverse beam. If the slab-flange over-strength was not accounted for, the hierarchy of strength assessment of the retrofitted beam-column joint could be erroneous. Based on this preliminary comparison of NS-R3 and SL-R3, it is suggested that for the retrofit design of 'realistic' beam-column joint with slab, a 30% amplification factor can be taken into account when calculating the beam flexural capacity for the performance domains of the retrofitted joint (as described in §2.4.1 and §3.4.5).

It has been argued that under bi-directional loadings, the supposed confinement from the transverse beams was un-reliable for interior joint shear strength [12, 33]. Figure 8.43 shows an example of a reinforced exterior joint with transverse beams under bi-directional loadings, in which the primary beam did not develop its flexural strength due to partial joint failure. The yielding of the transverse beam possibly reduced the joint shear confinement from the transverse beams. Further testing with bi-directional loadings on non-ductile exterior joints with transverse beams stubs is required to confirm this.

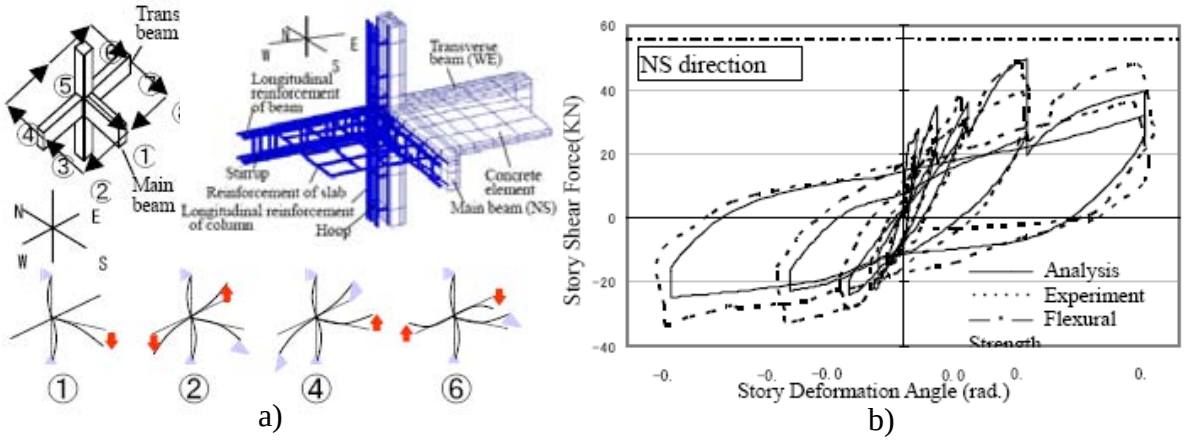

Figure 8.43: Bi-directional loadings on exterior beam-column joint with slab and transverse beam [20]: a) Test specimen and b) F_c-Δ_c in the longitudinal direction (images are adapted from [29]).

8.4.2 Quantifying the influence of transverse beam on joint shear capacity

The torsion moment demand on the transverse beam is resisted by a torsion shear flow connected by the transverse beam longitudinal and transverse reinforcing as illustrated in Figure 8.4. The transfer of the torsion shear into the joint coincides with the joint shear transfer mechanism at the first transverse beam stirrup. This suggests a possible variation of shear failure plane for the beam-column joint during the Push loading. This is schematically shown in Figure 8.41.

Following the postulated joint shear failure plane in the Push direction, the expression for the joint effective width can be modified to b_c+2s_t in the bottom edge, where b_c is the width of the column and s_t is the distance of the first transverse beam stirrups from the joint face. The effective area of the joint is therefore given as the trapezium area of Figure 8.41b which is given by ½ (b + b + 2s_t). b should be the lower value between the width of the beam, b_b and the width of the column, b_c. Thus, the effective joint width, b_j, for beam-column joint with transverse beam and slab can be calculated using the following equation:

$$b_j = \min of \begin{Bmatrix} b_b + s_t \\ b_c + s_t \end{Bmatrix} \qquad \textbf{8.1}$$

For SL-O1 and SLR3, both the ASCE-41 and NZSEE guidelines recommends the value b_j=b_c while Equation 8.1 above will yield b_j = b_c + s_t. For pre-1970s beam-column joints, s_t typically ranged between 0 to 300mm as the placement of the beam stirrups was then governed by gravity shear design. Assuming a generic s_t of 50mm (as per SL- specimens), Equation 8.1 will give 17-18% higher joint shear strength when compared with the existing equations (i.e. Equations 2.8 and 2.9). Comparing this to the 15% over-strengthening observed in the Push cycles of SL-O1 when compared with NS-O1, (both failed in joint shear), Equation 8.1 gives a good approximation of the joint shear enhancement. For comparison, ASCE-41 [4] and ACI-352 [2] expressions will give an over-strength ratio of 24% and 20% respectively for beam-column joints with confining transverse beams.

It is noted that Equation 8.1 needs to be further calibrated with more test data and existing test results on non-ductile RC exterior beam-column joints with transverse beams and slab. A preliminary comparison with the test data of Durrani and Zerbe [15] and Bedirhanoglu *et al.* [7] suggested a good agreement between the predicted over-strength ratio and the experimental finding, as given in Table 8.2.

Table 8.2: Analytical-experimental comparison for Equation 8.1 for calculating the over-strength ratio for non-ductile exterior beam-column joints with and without floor slab and transverse beams.

Test	beam width, b_b (mm)	column width, b_c (mm)	Distance of transverse beam stirrup to joint, s_t (mm)	joint effective width, b_j (mm)	b_j / b_j*	Experimental over-strength ratio (%) +
SL-O1	230	230	50	280	1.22	15.0%
Durrani and Zerbe (1986)	254	304.8	152.4	406	1.60	46.0%
Bedirhanoglu et al. (2010)	250	500	100	350	1.40	30.0%

Note: bj* is given by Equation 2.8 (NZS3101 equations). + The over-strength ratio is taken to be the ratio of the difference in the maximum lateral forces of the specimen with and without slab-transverse beams, and the maximum lateral force for the specimen with slab and transverse beam.

8.4.3 Assessment of effective flange width for non-ductile beam-column joint

An evaluation of the test results for SL-O1 and SL-R3 could indicate an effective flange width for non-ductile RC beam-column joints. The experimental values for the effective flange width were derived from the reading of the strain gages on the top mesh of the slabs (§8.2.6 for SL-O1 and §8.3.6 for SL-R3). Typically the effective width of the slab is calculated considering the portion of the slab in which the bars are beyond the yielding strain at a fixed level of drift, e.g. θ_{drift} = 2%. For SL-R3, The participating slab width for exterior beam-column joints at the -2.0% drift were 1.1h_b and at least 1.35h_b width of the slab for SL-O1 and SL-R3 respectively.

The effective width of the slab (b_{eff}) measured in both SL-O1 and SL-R3 specimens were compared with the corresponding theoretical values given in the 2007 ASCE-41 [4], NZSEE 2006 guidelines [31], 2006 NZS3101 code [30], JBDPA 2001 standard [21] and Eurocode 8 [11] as discussed in §2.4.3. Table 8.3 presents the experimental and theoretical values according to the aforementioned normative.

Table 8.3: Comparison of the effective flange width, b_{eff} between experimental results and various international codes.

Code/Guidelines	Effective tension flange width (mm)	SL-O1	SL-R3
NZS3101:2006	890 (2.70 h_b)	720 (2.2 h_b)	900** (2.7 h_b)
ASCE-41 / FEMA 356	980 (2.97 h_b)		
NZSEE 2006	1753 (5.31 h_b)		
JBDPA-2001 / AIJ-1994	890 (2.70 h_b)		
EC8-III (2004) +	839 (2.54 h_b)		

All calculations assumed the presence of transverse beam, beam span of 3047mm, bay width of 3047mm, beam and column widths of 230mm, beam depth of 330mm, slab thickness of 100mm and provided clear slab flange width of 375mm. **the whole slab width was effective.

Based on this limited experimental results, it could be proposed that for seismic assessment of non-ductile exterior joints, a minimum of approximately 2.7 times the beam depth ($2.7h_b$) is taken to be the effective flange width when calculating the beam negative moment. This would ensure a lower bound approximation for slab flange contribution when assessing the hierarchy of strength (for capacity design consideration), while giving a lower bound in terms of beam negative flexural capacity. This is contrary to the common "design" misconception where it is more conservative to adopt no flange contribution, whereas for assessment, it is more important to give an accurate representation of the beam-column joint hierarchy of strength.

This conclusion is consistent with some of the previous researches. It is suggested that the slab participation is based on the torsional resistance of the spandrel beams and therefore is proportional to the portion of slab bounded by the torsional cracks in the transverse beam [14, 15, 18]. For example, Durrani and Zerbe [15] proposed the following equation for the lower bound value effective width: $b_{eff} = b_c + 2h_{bt}$, in which b_c = column width, and h_{bt} = depth of the transverse beams. If $h_{bt} = b_c$, Durrani and Zerbe's equation would be close to $2.7h_b$.

Nevertheless, if b_{eff} is overestimated, the consequence is more uneconomical seismic retrofit, as significant investment would be required to achieve capacity design principles for the column. Therefore, a natural progression of the Selective Weakening retrofit is to cut part of the slab concrete and mesh from the longitudinal beam in order to reduce the tension flange effect. This idea was not tested in this research as the limited test matrix required a comparison between SL-R3 and NS-R3.

8.4.4 Analytical and experimental comparison

As discussed in §8.2.2, the analytical prediction for SL-O1 for the maximum F_c was approximately 5kN higher than the observed maximum F_c values, despite the correct 'failure' mode prediction. While some of the 22% -33% discrepancies in peak F_c could be attributed to the influence of the slab and transverse beams, as discussed in §8.4.1 and §8.4.2, a major source of differences was the conservatism of the p'_t limit states assumed in §2.4.2. The maximum p'_t measured in SL-O1 was $0.378\sqrt{f'_c}$ MPa, while the 'design limit' p'_t was $0.19\sqrt{f'_c}$ MPa, based on the recommendation of Pampanin *et al.* [10, 32].

The F_c-Δ_c experimental-analytical comparison for specimen SL-R3 is given in Figure 8.44. The analytical procedure described in §3.4 (Chapter 3) was used to predict F_c. The predicted failure mode was beam flexural hinging in both loading directions, as observed in the

test. Good analytical prediction for F_c-Δ_c was achieved for the Pull direction while the F_c was significantly under-estimated (~36.5%) in the Push cycles. In both loading directions, the initial stiffness was overestimated, as the analytical method could not capture the progressive bond failure and yielding of the plain bars (as described in §8.3.5.1). These results highlighted the limitations of the pseudo-rocking analytical prediction (§3.4.5) of the negative beam-moment with the presence of slab and transverse beams.

The comparison between the measured and predicted post-tensioning forces is shown in Figure 8.44b. The predicted post-tensioned tendon force was matching the measured forces reasonably well in the Pull direction while substantially overestimated the tendons forces in the Push direction. The underestimation of F_c in conjunction with the overestimation of the tendon forces suggested that the true neutral axis was smaller than the analytical neutral axis, which relied on the pseudo-rocking section to remain plane section. Nevertheless, with appropriate factors of safety, the analytical tools described in §3.4.5 should be adequate for design purposes.

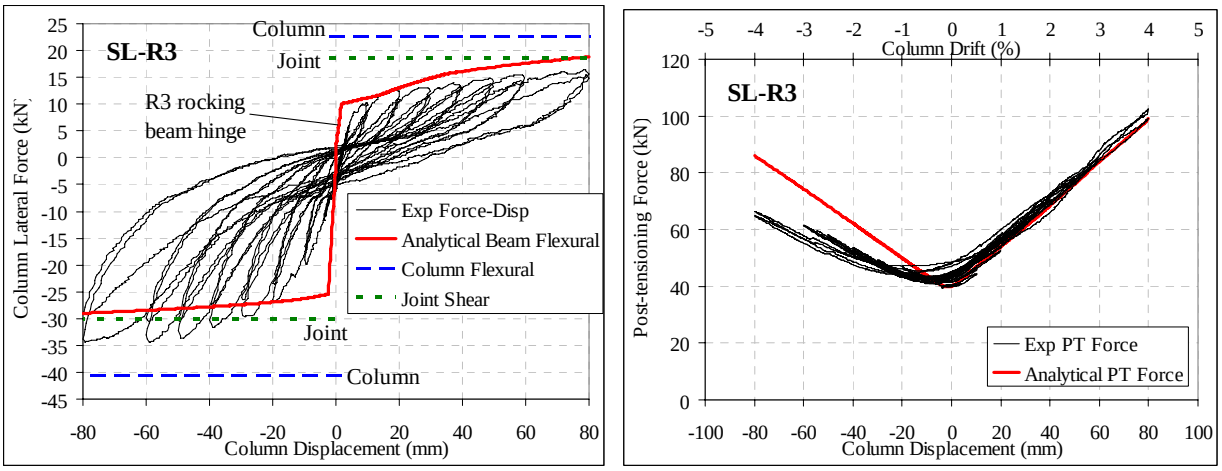

Figure 8.44: a) Experimental-analytical comparison of the F_c-Δ_c curves for SL-R3; b) Analytical prediction and experimental response of tendon forces at the pseudo-rocking interface .

8.4.5 Effect of gravity loading on SW R3 retrofit

One of the initial concerns of the selective beam-weakening of the full SW retrofit was the beam shear capacity at a high rotational demand. However, external post-tensioning would increase the beam shear capacity significantly [13]. In order to confirm the negligible impact of the gravity shear on the weakened section, realistic gravity loads boundary condition was used for SL-R3 (as described in §4.6.4). Prior to the start of the lateral loading, the bending moment(M_b) and shear force(V_b) demands at the beam-column interface were 9.1kNm and = -18.8kN respectively. At

the peak F_c loading on SL-R3, the maximum beam shear stress ($V_b/b_b h_b$) was 0.512MPa. While the conventional shear force transfer mechanism was no longer applicable in the disturbed region closed to the weakened beam section as discussed in §8.3.5.3, it could be demonstrated with a simple strut-and-tie model that significant shear capacity was available in the weakened section.

Figure 8.45 presents a schematic model of a possible shear force transfer mechanism, based on the strut-and-tie truss concept [35, 36]. The model is based on the measured strain values presented in §8.3.5. Within the 'distributed' region close to the compression block of the pseudo-rocking gap, a fan-compression strut in the form of compression diagonal field would be activated. The joint external post-tensioning on the other hand, induce a compression force which would resist significant amount of the compression strut into the joint.

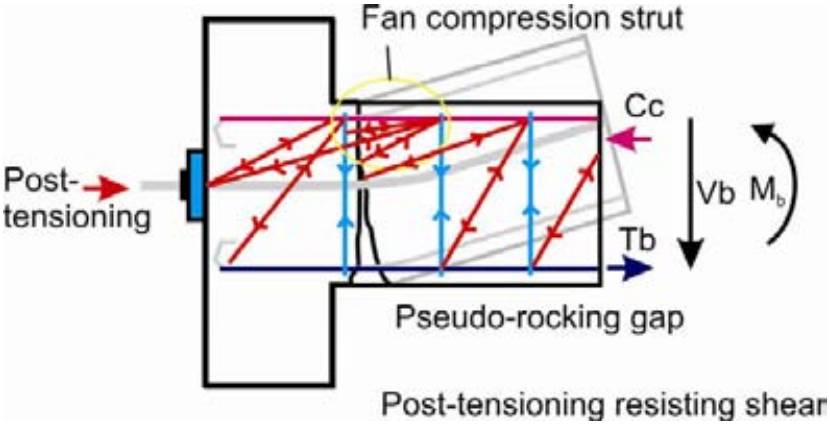

Figure 8.45: Strut-and-tie on shear force transfer in the weakened and post-tensioned beam-column joint.

8.5 CONCLUSIONS

1. Table 8.4 below summarises the experimental results of the two specimens presented in this chapter: a) As-built beam-column joint with cast-in-situ floor slab and transverse beam stubs (SL-O1) and b) Full Selective Weakening (SW) retrofit with beam-weakening and joint-post-tensioning (SL-R3) on beam-column joint with floor slab and transverse beam stubs.

Table 8.4: Summary of SL-O1 and SL-R3 test results.

Test Unit	Peak Lateral Force (kN)	Inter-storey drift at maximum force, θ_d (%)	Ultimate inter-storey drift, θ_d (rad) [1]	Peak Lateral Force (kN) without Gravity Offset [2]	Estimated Inter-storey drift at joint cracking, θ_d (rad)	Maximum column moment, $M_{sys\text{-}exp}$ (kNm)	Theoretical column moment, $M_{sys\text{-}cal}$ [3] (kNm)	$M_{sys\text{-}exp}$ / $M_{sys\text{-}cal}$ [4]
SL-O1	+15.4 -22.0	+2.42 -2.45	-3.0%-II	+21.2 -16.3	+1.0-I	+12.9 -18.4	+8.8 - 13.0	+1.46 -1.41
	Failure Mode		Max / Min joint shear stress, v_{jh} (f'_c MPa)	Min / Max axial stress, f_v (MPa)	Max. principal tensile stress, p_t ($\sqrt{f'_c}$ MPa)	Max. principal compression stress, p'_c ($\sqrt{f'_c}$ MPa)	1st / 2nd cycles total energy dissipated, $E_{D,4.0\%}$ (J)	Equivalent Viscous Damping (EVD) ratio, $\xi_{hyst,2.0\%}$ [4] (%)
	Partial-confined Joint Shear		+0.090 -0.128	+0.20 -3.54	0.378	1.085	3099 / 2042	9.6
Test Unit	Peak Lateral Force (kN)	Inter-storey drift at maximum force, θ_d (%)	Ultimate inter-storey drift, θ_d (rad) [1]	Peak Lateral Force (kN) without Gravity Offset [2]	Estimated Inter-storey drift at joint cracking, θ_d (rad)	Maximum column moment, $M_{sys\text{-}exp}$ (kNm)	Theoretical column moment, $M_{sys\text{-}cal}$ [3] (kNm)	$M_{sys\text{-}exp}$ / $M_{sys\text{-}cal}$ [4]
SL-R3	+15.7 -35.1	+3.94 -2.95	na [5]	+21.3 -29.3	na [6]	+13.1 -29.3	+15.3 -23.9	+0.86 -1.23
	Failure Mode		Max / Min joint shear stress, v_{jh} (f'_c MPa)	Min / Max axial stress, f_v (MPa)	Max. principal tensile stress, p_t ($\sqrt{f'_c}$ MPa)	Max. principal compression stress, p'_c ($\sqrt{f'_c}$ MPa)	1st / 2nd cycles total energy dissipated, $E_{D,4.0\%}$ (J)	Equivalent Viscous Damping (EVD) ratio, $\xi_{hyst,2.0\%}$ [5] (%)
	Beam Flexural Hinging		+0.079 -0.176	+0.22 -4.71	0.402	1.500	3994 / 2573	9.2

Positive force, displacement and drift correspond to PULL cycles while negative values indicate PUSH cycles. I=1st cycle; II=2nd cycle.

[1] Failure point defined as attained peak force was less than 80% of previous peak force. [2] Gravity loading resulted in -5.7kN initial lateral load on the top column.

[3] Calculated maximum column moment based on the Hierarchy of Strength analysis outlined in Chapters 2 and 3, not including the effect of gravity load - boundary conditions (M_{beam}=9.1kNm or $M_{c,b}$=4.1kNm). [5] $\xi_{hyst,2.0\%}$ is calculated based on hysteresis area-based equivalent viscous damping in the 1st cycle.

[6] No structural failure observed (based on the definition).

2. SL-O1 exhibited a joint shear inelastic mechanism as confirmed by significant cracking along the beam-column joint interface and the instrumentation data. The slab flange and the transverse beam enhanced F_c by 21% in the Push direction and a force-transfer mechanism was proposed based on the strain gages readings. The marginally higher F_c in the Pull cycles suggested a limited lateral strength and joint shear strength enhancements from the transverse beam alone. Despite the joint shear damage, SL-O1 sustained its lateral load carrying capacity up to the 2nd cycles of the -3.0% drift, which perhaps indicated the inherent strength of these types of joints.

3. To quantify the level of joint confinement from the transverse beam stub, a new failure plane and an expression for effective joint shear width, b_j, are proposed in §8.4.2 and §8.4.1. Transverse beams also improved the post-joint cracking behaviour via confinement induced by the transverse beam torsion and slab tension flange actions. Nevertheless, it is believed that bi-directional loadings on specimen SL-O1 and SL-R3 will result in significant flexural cracking in the transverse beam and thus reducing the effect of the confinement. Further testing with bi-directional loadings on non-ductile RC exterior joints with transverse beam stubs is required to confirm this.

4. The SL-R3 test illustrated how Selective Weakening retrofit could achieve a weak-beam strong column-joint mechanism within a practical constructability. Reinforcement strain measurements showed significant yielding of both the top and bottom beam bars. The presence of floor slab and transverse beam induced a 39% higher F_c in the Push direction The predicted beam pseudo-rocking flexural hinging was achieved, with an average energy dissipation capacity, ξ_{hys} of 5.9% to 9.6 %. §8.4.5 has shown the negligible effect of the beam-weakening to the beam shear capacity as the beam-column joint post-tensioning contributed significantly to the beam shear.

5. By evaluating the limited test data presented in this chapter, it was observed that the effective flange width due to interaction with the slab was lower than that observed in beam-column joint with deformed bars and ductile detailing. It is proposed that for

seismic assessment of non-ductile exterior beam-column joints, a minimum of 2.2 times beam depths ($2.2h_b$) is taken to be the effective flange width in calculating the beam negative moment. Further experimental data are required to further clarify the effective flange width for the assessment of selectively-weakened and post-tensioned joints.

6. Another retrofit solution using the Selective Weakening strategy is to sever part of the slab mesh reinforcement from the longitudinal beam in order to reduce the tension flange effect and protect the column from potential plastic hinges. Further experiments on this retrofit option are needed.

8.6 CHAPTER 8 REFERENCES

[1].ACI318-08. *Building code requirements for structural concrete and commentary*. Farmington Hills, MI: American Concrete Inst. (ACI); 2008.
[2].ACI352R-02. *Joint ACI-ASCE Committee 352: Recommendations for design of beam column joints in monolithic reinforced concrete structures*. Farmington Hills, MI: American Concrete Inst. (ACI); 2002.
[3].ACI352R-76. Joint ACI-ASCE Committee 352 - Recommendation for design of beam-column joints in monolithic reinforced concrete structures (ACI-352R-76). *ACI Structural Journal*. 1976 July 1976;**73**(7):375-393.
[4].ASCE-SEI-41-06. *Seismic rehabilitation of existing buildings. ASCE standard ASCE/SEI 41-06*. Reston, Va.: American Society of Civil Engineers (ASCE); 2007.
[5].Aycardi LE, Mander JB, Reinhorn AM. *Seismic resistance of reinforced concrete frame structures designed only for gravity loads: Part II - Experimental performance of subassemblages, NCEER-92-0028*. Buffalo, NY: National Center for Earthquake Eng. Research, SUNY at Buffalo; 1992.
[6].Aycardi LE, Mander JB, Reinhorn AM. Seismic resistance of R.C. frame structures designed only for gravity loads: Experimental performance of subassemblages. *ACI Structural Journal*. 1994;**91**(5):552-563.
[7].Bedirhanoglu I, Ilki A, Pujol S, Kumbasar N. Behaviour of deficient joints with plain bars and low-strength concrete. *ACI Structural Journal*. 2010 May-June 2010;**107**(3):300-310.
[8].Beres A, El-Borgi S, White R, Gergely P. *Experimental results of repaired and retrofitted beam-column joint tests in lightly reinforced concrete frame buildings. Technical Report NCEER-92-0025*. Buffalo, NY: National Center for Earthquake Eng. Research, SUNY; 1992.
[9].Beres A, Pessiki S, White R, Gergely P. Implications of experimental on the seismic behaviour of gravity load designed RC beam-column connections. *Earthquake Spectra*. 1996;**12**(2):185-198.
[10].Calvi GM, Moratti M, Pampanin S. Relevance of beam-column damage and collapse in RC frame assessment. *J of Earthquake Eng*. 2002;**6**(1):75-100.
[11].CEN. *European Standard EN 1998: Eurocode 8 - Design of structures for earthquake resistance - Part 3: Assessment and retrofitting of buildings*. Brussels: Comite Europeen de Normalisation; 2006.

[12].Cheung PC, Paulay T, Park R. *Seismic design of reinforced concrete beam-column joints with floor slab. UC Research Report 91-4*. Christchurch, NZ: Dept. of Civil Eng., Uni. of Canterbury; 1991.
[13].Collins MP, Mitchell D. *Prestressed concrete structures*. Toronto, Canada: Response Publications; 1997.
[14].Di Franco MA, Mitchell D, Paultre P. Role of spandrel beams on response of slab-beam-column connections. *ASCE J of Struct Eng*. 1995;**121**(3):408-419.
[15].Durrani AJ, Zerbe HE. Seismic resistance of R/C exterior connections with floor slab. *ACI Structural Journal*. 1987;**113**(8):1850-1864.
[16].Ehsani MR, Wight J. Effect of transverse beams and slab on behaviour of reinforced concrete beam-to-column connections. *ACI Structural Journal*. 1985 Mar-Apr 195;**82**(2):188-195.
[17].fib. *Seismic assessment and retrofit of reinforced concrete buildings: State-of-the-art report, fib Bulletin no. 24*. Lausanne, Switzerland: Intl. Fed. for Struct. Concrete (fib); 2003.
[18].French CW, Boroojerdi A. Contribution of R/C floor slabs in resisting lateral loads. *ASCE J of Struct Eng*. 1989;**115**(1):1-18.
[19].French CW, Moehle JP. Effect of floor-slab on behaviour of slab-beam-column connections. In: Jirsa JO, editor. *Design of beam-column joints for seismic resistance, SP-123*. Detroit, MI: American Concrete Inst. (ACI); 1991. p. 225-258.
[20].Fujii S, Morita S. Behavior of R/C exterior beam-column joint under bi-directional loading. *Proc. of Japanese Concrete Inst (JCI) Annual Convention*; 1987 Oct 1987, 1987. p. 181-186.
[21].JBDPA-2001. *Standard, Guidelines and Technical Manual for seismic evaluation and seismic retrofit of existing reinforced concrete buildings. 1st English Version. Translated by Building Research Institute.* Tokyo, Japan: Japan Building Disaster Prevention Assoc. (JBDPA); 2001.
[22].Jirsa JO, editor. *SP-123: Design of beam-column joint for seismic resistance*. Farmington Hills, MI: American Concrete Inst. (ACI); 1991.
[23].Kurose Y, Guimaraes GN, Zuhua L, Kreger ME, Jirsa JO. Evaluation of slab-beam-column connections subjected to bidirectional loading. In: Jirsa JO, editor. *Design of beam-column joints for seismic resistance, SP-123*. Detroit, MI: American Concrete Inst. (ACI); 1991. p. 39-68.
[24].Leon RT. Influence of floor members on the behaviour of reinforced concrete beam-column joints subjected to severe cyclic loading [PhD dissertation]. Austin, TX: Uni. of Texas at Austin; 1983.
[25].Leon RT, Jirsa JO. Bidirectional loading of R.C. beam-column joints. *Earthquake Spectra*. 1986;**2**(3):537-564.
[26].Li B, Tran CTN, Pan T-C. Experimental and numerical investigations on the seismic behaviour of lightly reinforced concrete beam-column joints. *ASCE J of Struct Eng*. 2009 Sept 2009;**135**(9):1007-1018.
[27].Meinheit DF, Jirsa JO. *The shear strength of reinforced concrete beam-column joints. CESRL Rep. No. 77-1*. Austin, TX: Uni. of Texas; 1977.
[28].Meinheit DF, Jirsa JO. Shear strength of R/C beam-column connections. *ASCE Journal of Structural Division*. 1981 Nov 1981;**107**(11):2227-2244.
[29].Noguchi H, Kashiwazaki T. FEM analysis of interaction effects of 3-D RC members subjected to multi-directional cyclic loading. *Proc. of ASCE Structures Congress 2009*; 2009 16-19 May, 2007; Austin, TX, 2009. p. 1209-1218.
[30].NZS3101:2006. *NZS 3101:2006 Concrete structures standard*. Wellington, NZ: Standards New Zealand; 2006.

[31].NZSEE. *Assessment and improvement of the structural performance of buildings in earthquakes*. Wellington, NZ: New Zealand Soc. for Earthquake Eng. (NZSEE); 2006.
[32].Pampanin S, Calvi GM, Moratti M. Seismic behaviour of RC beam-column joints designed for gravity loads. *Proc. of 12th European Conf on Earthquake Eng*; 2002; London, UK, Paper 726, 2002.
[33].Paulay T, Priestley MJN. *Seismic design of reinforced concrete and masonry buildings*. Christchurch, NZ: John Wiley & Sons Inc.; 1992.
[34].Priestley MJN, Seible F, Calvi GM. *Seismic design and retrofit of bridges*. NY: John Wiley & Sons Inc.; 1996.
[35].Sritharan S, Ingham JM. Application of strut-and-tie concepts to concrete bridge joints in seismic region. *PCI Journal*. 2003;**48**(4):66-90.
[36].Sritharan S, Priestley MJN, Seible F. Enhancing seismic performance of cap beam-column bridge joints using prestressing. *PCI Journal*. 1999;**44**(4):74-91.
[37].Uzumeri SM. Strength and ductility of cast-in-place beam-column joints, SP-53-12. *Reinforced Concrete Structures in Seismic Zone, ACI SP-53*. Detroit, MI: American Concrete Inst. (ACI); 1977. p. 293-350.
[38].Uzumeri SM, Seckin M. *Behaviour of reinforced concrete beam-column joints subjected to slow load reversals. Publication No. 74-05*. Toronto, Canada: Dept. of Civil Eng., Uni. of Toronto; 1974.

CHAPTER 9. NUMERICAL STUDIES OF AS-BUILT AND RETROFITTED RC FRAMES

"The object of analysis is to extend the range of experience (of designing structures), to give a correct basis of comparison between the structure that has been built and the structure that is to be built by picturing their relative distortions"

H. Cross and N.D. Morgan,
In "Continuous Frames of Reinforced Concrete", 1932

9.1 INTRODUCTION

This chapter will present two phases of numerical studies of as-built and Selective Weakening (SW) retrofitted reinforced concrete (RC) beam-column joints. As suggested by the quote of Prof. Cross and Prof. Morgan above, analytical models, validated against physical results (experiments), could provide further insights into the seismic behaviour under different test configurations.

In the first phase, fracture mechanics-based finite element (FE) models of the as-built (NS-O1) and the beam-weakening only SW-retrofitted exterior RC joints (NS-R1) are carried out. The numerical simulations are performed using the FE program MASA (MAcroscopic Space Analysis) [104], which is developed at the University of Stuttgart (Germany) specifically for 3D non-linear analysis of quasi-brittle material (such as concrete). The FE models of the as-built and retrofitted exterior RC beam-column joints are developed and verified against the experimental results.

The joint shear transfer mechanics of RC beam-column joints with inadequate joint shear reinforcement and with smooth longitudinal reinforcement can be very complex. As highlighted by the test results in the preceding chapters, both the joint shear and reinforcement bond capacities are dependent to the micro-structural behaviour of the concrete, bond and

reinforcement. The refined FE analysis will be able to provide further insights on the complex behaviour of the beam-column joints tested in this research.

In the second part of the numerical studies, non-linear dynamic analyses of as-built and retrofitted pre-1970s RC frames are carried out. The numerical simulations are performed using the FE program RUAUMOKO [25] with lumped plasticity macro-model. The beam-weakening only (R1) and beam-weakening and post-tensioning (R3) solutions are implemented for a case study pre-1970s frame building in Christchurch. The aim of this section is to confirm the viability of the SW retrofit in controlling the global response, as postulated in Chapter 3.

The first phase numerical work described in this chapter is carried out in collaboration with researchers from the University of Stuttgart, particularly in terms of the development of the as-built beam-column joint models [57]. Extensive parametric analysis on the seismic response of as-built beam-column joints using the MASA program is available in ref. [59]. Special acknowledgement is also given to a fellow postgraduate researcher, Umut Akguzel, for his assistance in the development of the retrofitted joint models.

9.2 FINITE-ELEMENT MODELLING OF RC JOINTS

9.2.1 Modelling approaches of RC beam-column joints

As reviewed in Chapter 2, the seismic response of non-ductile RC beam-column joints depends on many different parameters including the joint shear capacity, bond strength of embedded reinforcement, moment demand at adjacent elements, confinement of joint core, level of axial forces, reinforcing details and material properties. Owing to the complexity nature of RC joints and limited experimental data, numerical modelling is an attractive option to further the understanding on the underlying mechanics of beam-column joints. Many attempts on the FE modelling of RC beam-column joints are available in literature, particularly from the mid-1980s to present days. The following paragraphs will summarise and discuss the different modelling approaches.

FE modelling of RC beam-column joints can be divided into a broad spectrum, depending on the levels of discretisation and complexity. At the simplest level is the macro-models with lumped plasticity springs for the beam, column and joint [2, 39, 51, 111]. Next level up, different inelastic mechanisms of beam-column joints such as the anchorage failure, joint core shear failure, bond-slipping, and beam-joint and column-joint interfaces transfer failures can be

discretised and modelled using multiple non-linear springs macro-model [85, 86, 142]. The macro-models can also be extended to a multi-component model, in which constitutive material models are included within discrete finite elements [55]. Non-linear springs (or components) in the macro-models are experimentally calibrated [5, 51, 94, 111]. Figure 9.1 shows the typical configuration of a single-rotational spring with rigid link joint model [2, 111] and a multi-spring joint macro-model [5, 86].

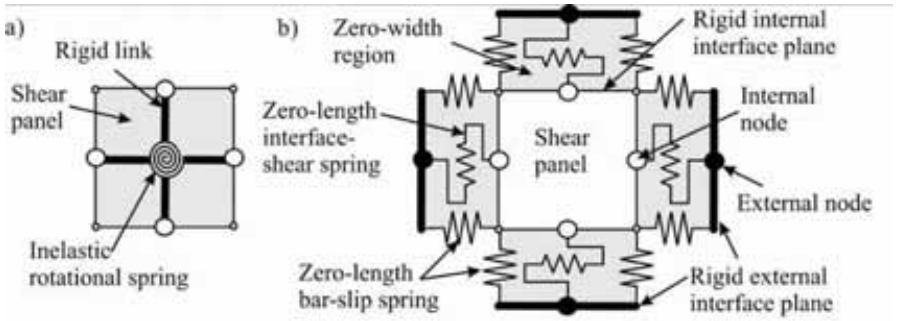

Figure 9.1:a) Single rotational spring joint model [2, 111]; b) Multi-spring macro joint model [86].

Many macro-model hysteresis rules are available in literature for RC beam-column joints but only a few models are specific for the modelling of non-ductile RC beam-column joints. Pampanin *et al.* [111] proposed a joint shear rotational spring model where the monotonic moment envelope was derived from the empirical strength degradation curve p_t-γ (principle tensile stress versus shear-deformation). Ibarra *et al.* [68] implemented a stiffness and strength degradation hysteretic model that was applicable to capture the poor joint behaviour.

With a multi-spring macro-model, Anderson *et al.* [5] calibrated constitutive models for the joint shear deformations of beam-column joints with no transverse reinforcement, subjected to a range of displacement histories and joint shear stress demand, using a limited number of experimental data [4, 139]. More recently, Favvata *et al.* [51] developed a behavioural hysteretic model (using single rotational spring) capable of describing the main characteristics of the response of RC beam-column joints under seismic loading: the initial elastic stiffness, ultimate strength, post-yield response with degrading branch/strength degradation and the special rules for a hysteretic pinching effect. Figure 9.2 shows the joint shear hysteretic models proposed by Pampanin *et al.* [111] and Ibarra *et al.* [68]. The simplicity of a macro-model with single non-linear rotational spring allows for a computationally-efficient frames dynamic analysis [23, 61, 88]. In the second phase modelling of this chapter, the macro-modelling approach will be used to investigate the dynamic behaviour of as-built and SW-retrofitted RC frames.

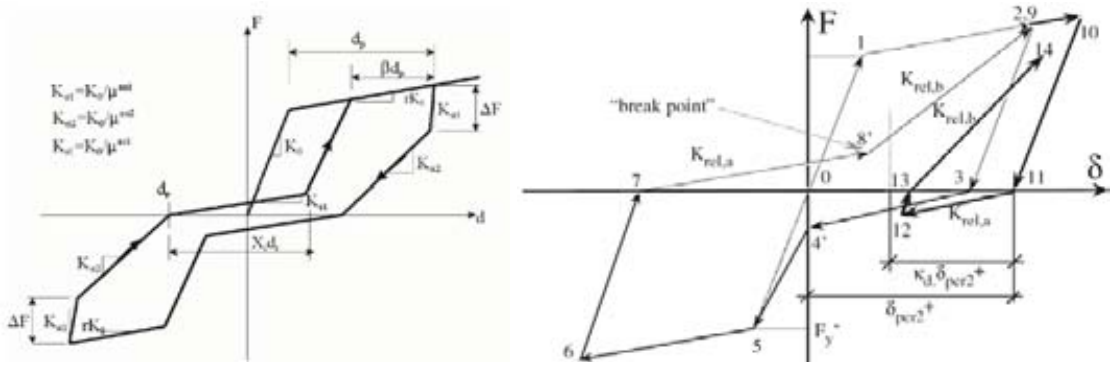

Figure 9.2: Existing hysteresis rule (constitutive model) for the modelling of poorly detailed RC beam-column joints. Left: Pampanin *et al.* [111] model; Right: Ibarra *et al.* [68] model.

An improvement from the lumped plasticity macro model is to replace the non-linear rotational spring with a smeared (distributed) non-linear zone at the location of the plastic hinges and to use fibre elements for the whole length of the element. In such an approach, termed as the fibre modelling, the force-deformation relationship of the cross-section is obtained by the integration of all the fibres across the thickness of the section [32, 70, 131]. While the fibre element modelling has been implemented into commercially available programmes e.g. OpenSees [92] and SeismoStruct [124], inelastic deformations, such as the bond-slip and joint shear distortion, are not well captured using fibre element models [28]. Recently, Cosenza *et al.* [32] have developed a fibre model capable of describing the non-linear behaviour of non-ductile beam-column joints using a hybrid fibre element with a discrete bond model and a fixed-end rotation model. Figure 9.3 shows the bond-slip and fixed end models implemented by Cosenza *et al.* [32]. However, Cosenza *et al.* model was so far limited to the monotonic push-over analysis whereas the cyclic analysis is more pertinent for earthquake-loading.

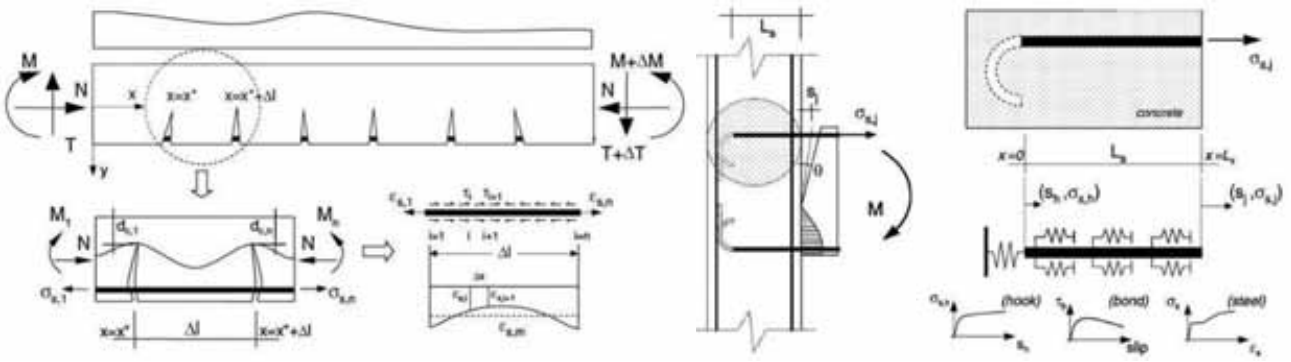

Figure 9.3: Cosenza *et al.* [32] *f*ibre element modelling with a) discrete bond-slip relationship; b) Fixed-end rotational model.

The strut-and-tie method is a promising approach to evaluate the beam-column joint shear capacity, particularly for joints with external post-tensioning. However, it requires the assumption of the stress flow pattern and the assignment of struts within the disturbed joint panel region. The strut-and-tie method is initially used for the static analysis of RC elements (e.g. [90, 123]) and within the NZS3101:2006 [102], the strut-and-tie method is specified for the design of regions of RC structures where linear strain distribution (i.e. the Bernouli's principle) does not apply. Some researchers have adopted the strut-and-tie method to model the stress flow in the RC beam-column joints under various loading conditions. Sritharan and colleagues [127-129] used the strut-and-tie approach, as shown in Figure 9.4, for the analysis and design of pre-stressed and under-reinforced precast bridge T- and knee joints. Meanwhile, Lin [80, 81] applied a simplified strut-and-tie approach based on the force equilibrium for the evaluation of stress flow in well-designed RC beam-column interior joints. Lin's method was extended the cyclic for non-seismically detailed interior beam-wide column joints [141].

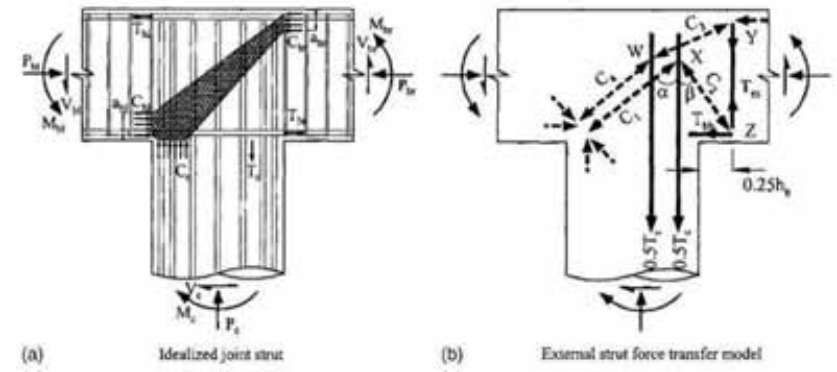

Figure 9.4: Strut-and-Tie model for pre-stressed T joints of precast concrete bridges [127].

The final category of beam-column joint modelling – the 3D continuum FE modelling requires the highest level of discretisation and complexity. Few researches have implemented continuum FE to simulate the inelastic beam-column joints due to the demanding computational needs and uncertainties with regards to the non-linear local failure mechanisms such as bond and anchorage failures. Some early attempts to model beam-column joint elements in continuum mechanics (e.g. [98, 140]) have used brittle concrete material with discrete crack, and linear steel reinforcing and bond elements.

With improved FE modelling techniques of RC elements such as the smeared cracking modelling [108, 118, 120] and the cyclic bond model [43], more sophisticated beam-column joint models have been implemented. Lowes [84] implemented steel-to-concrete bond elements in a

FE model of bridge-bent joints. Pantazapoulos and Bonacci [112] used the modified compressive field theory (MCFT) to represent the behaviour of concrete cracking and the frictional-contact theory to simulate bond-slip. Noguchi and colleagues [73, 99] investigated the bi-directional behaviour of 3D beam-column joints using 3D FEM analyses (Figure 9.5a). Ozbolt *et al.* [108] modelled interior joints using the microplanes concrete model in the FE programme MASA. Mitra [93] provided a summary of the state-of-the-art modelling of well-designed beam-column joint. Japanese researchers (e.g. [87, 125]) are very advanced in the modelling non-linear complex concrete elements such beam-column joints with irregular configurations and design requirements (e.g. super high-strength concrete).

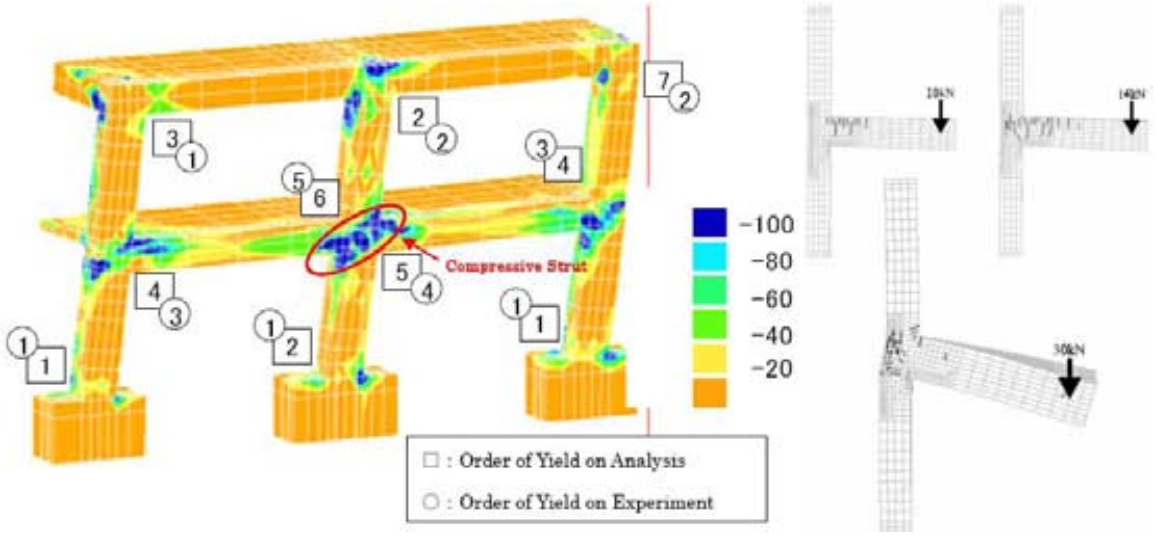

Figure 9.5: a) 3D FEM of RC frame subassembly by Noguchi and Kashiwazaki [100]; b) Monotonic FE result from Baglin and Scott [10].

In recent years, more attention was given to complementing experimental research with numerical studies for non-seismically detailed RC beam-column joints. Baglin and Scott [10] modelled RC joints with various non-ductile beam longitudinal bars anchorages (e.g. U-bar lapped with straight bars; 90 hook top bar and discontinued bottom bar) subjected to only monotonic loading (Figure 9.5b). Hegger [64] investigated the parameters of joint shear capacity of non-seismically detailed beam-column joints. Hegger confirmed the importance of concrete strength (f'_c), joint ratio (h_b/h_c), amounts of joint stirrup and beam reinforcement, and the joint detailing on the joint shear capacity. Recently, Genesio and co-authors used the MASA FE model to simulate the seismic behaviour of pre-1970s RC beam-column joints with plain round bars [41, 42].

9.2.2 Fracture mechanics-based 3D FE modelling of RC beam-column joints

The development of FE modelling of RC elements began in the late 1960s with the introduction linear plane stress analyses of RC beams by Ngo and Scordelis [95]. Nilson [96, 97] introduced the non-linear material properties and a non-linear bond-slip relationship into the FE analysis. The 1982 ASCE state-of-the-art report [9] provided a comprehensive historical summary of the subsequent pioneering research work on linear and non-linear FE analyses in the 1970s. In the 1980s, the development of FE modelling of RC elements focused on the 3D non-linear FE analysis with increasing focus on the fracture mechanics and damage theory. Discrete [65, 69], smeared [108, 118, 120] and lattice [135] cracking modelling techniques were introduced and refined to simulate the fracture and cracking of concrete elements. More complete literature review and summary on the state-of-the-art of FE analysis for RC structures is available in the fib Bulletin 45 [54] and the ACI-ASCE Joint Committee 447 report [1].

Presently, the concrete material modelling within the fracture-mechanics level can be classified into two categories: (1) Macroscopic models, in which the material properties are taken to be the average response of the complex micro-structure stress transfer mechanism and (2) microscopic models, where micro-mechanics of deformation is described by a stress-strain relationship at the micro level (i.e. modelling aggregate-cement matrix, ribs of reinforcement etc). The latter model, while philosophically more promising, is unnecessarily sophisticated for large structures such as an entire frame system.

To accurately describe the mechanics underlying the non-ductile RC beam-column joints behaviour, several complex modelling issues needed to be considered:

1. Fracture, cracking and damage phenomena - discrete or continuum (smeared) approach?
2. Constitutive law and modelling of quasi-brittle behaviour of concrete – are cracking, cumulative damage and softening of stress-strain relationship modelled adequately using the microplanes concrete model?
3. Mesh-dependent FE analysis [16] due to the use of classical smeared cracking modelling for quasi-brittle material – which of the “localization limiters” method to be use?
4. The Modelling method and generalised stress-strain relationship of reinforcement steel.
5. The bond between the reinforcement steel and concrete within RC element – which modelling technique to represent the bond behaviour of plain round bars?

The selection of the FE program MASA is an attempt to resolve some of the issues discussed above while providing complementary information and calibration for the extensive use of more manageable macro-models.

9.2.3 Non-linear dynamic investigations of non-ductile RC frames

Numerous non-linear dynamic studies on the seismic response of non-ductile and retrofitted RC frames have been carried out in various levels of complexity, as briefly discussed in §9.2.1. However, many of these studies did not consider the joint panel flexibility and inelasticity. Hakuto *et al.* [63], for example, modelled and analyzed two 1950s New Zealand RC buildings without modelling the joint. Kunnath *et al.* [74] studied the seismic response of three-, six- and nine-storey non-ductile RC frames but the joint flexibility was added manually after the analysis.

Various modelling strategies have been deployed to include various failure modes such as the joint shear, column lap-splice and the beam anchorage pull-out failures within non-linear dynamic analyses. The early work by Sause *et al.* [122], for example, used an iterative modelling approach to include the joint shear and the beam anchorage pull-out failures in the assessment of the connecting elements moment-curvature capacities. As discussed, Consenza *et al.* [31] introduced a bond-slip element and fixed-end rotation in order to capture the peculiarities of existing RC frames with plain round bars. Their analyses, which were confirmed by experimental results, clearly showed the influence of the joint deformability in the increase of the “fixed-end rotation” and the global structural response.

Stratan and Fajfar [130] found that by including a rigid offset within the joint panel and by modelling the strength degradation of columns, a much improved accuracy of the seismic response of non-ductile RC frames was achieved. The supplement to the ASCE-41 [8, 44] recognises the overestimation of the RC frame stiffness if the beam-column joints are represented as stiff or rigid zones. The document recommends an approximation for the joint shear deformations by extending the beam or column flexibility into the joint in the analytical model.

However, without explicit modelling of the joint inelasticity and bond failure (leading to pinching hysteresis), the displacement demand and fragility relationship of the non-ductile RC frames might be underestimated, as shown by the studies by Celik and Ellingwood [27] and Pampanin *et al.* [111]. The contribution by Calvi *et al.* [23] has demonstrated that such joint shear hinges may in fact prevent or delay soft-storey collapse in these very vulnerable RC frames. Coronelli *et al.* [30] have shown that bond deterioration played a significant in the global frame

deformation demands from the FE modelling of both the 'local' beam-column joint subassembly level and the 'global' RC frame.

Several University of Canterbury studies have adopted the macro-spring models for the pre-1970s beam-column joints with plain round bars and non-ductile detailing [82]. Various pinching and stiffness degradation hysteresis rules, such as the Wayne-Stewart hysteresis and the Pampanin hysteresis rules, implemented in the FE software RUAUMOKO [25], were used to capture the peculiar force-displacement hysteresis as observed in the NS-O1 specimen (in Chapter 5).

The numerical work in this chapter will only concentrate on the bare RC frames with neither any masonry infills nor any soil-structure interaction. However, many existing pre-1970s RC frames in New Zealand and elsewhere typically have one or two layers of masonry infills panels (e.g.[33, 62, 78]). Studies [24, 56, 88] have indicated the variability of the effects of masonry infills, ranging from the stiffening and strengthening the structures, to the creation of a soft-storey level due to the stiffness irregularities. A recent studies by Arefi [6] also suggested the variability of soil-structure interaction influence on the seismic response of pre-1970s RC frames.

Several studies [3, 60, 67] have noted the important role of ground motion variability and directivity effects (near-fault ground motions) in the collapse prediction of a non-ductile RC frame. The dynamic analysis presented in §9.5 and §9.6 will also consider the effects of these near-fault ground-motions on the SW-retrofitted frames.

9.3 FRACTURE MECHANICS-BASED FE MODELLING OF RC JOINTS

9.3.1 MASA – an introduction

MASA is a nonlinear 3D continuum FE code that is typically used for the analysis of concrete structures, developed by Ožbolt and colleagues [104] at the University of Stuttgart. In addition to providing a sound theoretical framework which answers some of the critical issues raised in §9.2.2, MASA is selected for its versatility in discrete bond modelling.

In MASA, the concrete is modelled using the microplanes concrete model with relaxed kinematic constraint on the smeared crack approach [107, 108]. The reinforcement steel is simulated by the uniaxial tri-linear stress-strain relationship. To account for a bond between reinforcement and concrete, a discrete bond-slip model is employed. Spatial discretisation of concrete is performed by 3D eight-node solid finite elements. The reinforcement is modelled by

1D truss finite elements. Cracking and damage of concrete are represented in a smeared way. To assure mesh objective results, a crack bond approach [18] was employed. Figure 9.6 gives an example of previous implementation of MASA for the analysis of shear-prone RC column. The following sub-sections further discuss the different modelling assumptions in MASA.

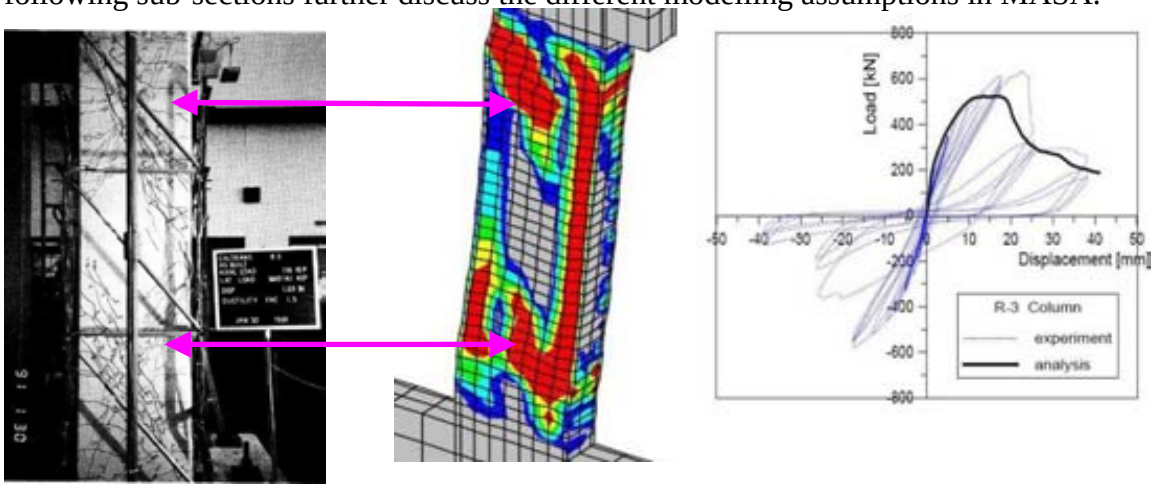

Figure 9.6: MASA 2D analysis of shear-dominated RC column – a) Observed experimental cracking pattern [117]; b) MASA simulation of diagonal shear cracking (dark area represents maximal principal strains); c) Comparison of experimental and numerical force-displacement response [adapted from [108]].

9.3.2 Microplanes concrete model with smeared concrete cracking

The concrete microplanes model, a type of smeared cracked model, was initially developed by Bažant [11] and successively refined to M2 [19, 21], M3 [22], M4 [15] and finally M5 family in Bažant and Caner [13, 14]. In MASA [104], a variant of the M2 model is implemented with relaxed kinematic constraint concept [107, 108].

Figure 9.7 succinctly summarises the key ideas behind the microplanes model for concrete. In a microplanes model, the material is characterised by uniaxial stress and strain relationship on planes of various orientations called “microplanes”. A constitutive law at a vector (uniaxial on each orientation) is conceptually simpler and easier to formulate [132]. At each finite element integration point, the microplanes can be taken to represent damage planes or weak planes of the microstructure of the material. The use of the microplanes model within a smeared cracking approach allows generic FE meshing without specifying the crack location as microplanes represent random planes of weakness and can be arbitrarily determined during the analysis. By the basis of virtual work principle, the macroscopic stress tensor is obtained by integrating contributions of all strain-stress vectors in all the microplanes orientations. In the relaxed kinematic approach [107], a discontinuity function is introduced to denote cracking

(discontinuity in macroscopic strain) and to relax the kinematic constraint (continuum assumption) in cases where the localization of strain is physically unrealistic. Only the effective microplanes stresses are used to calculate the microplanes stresses.

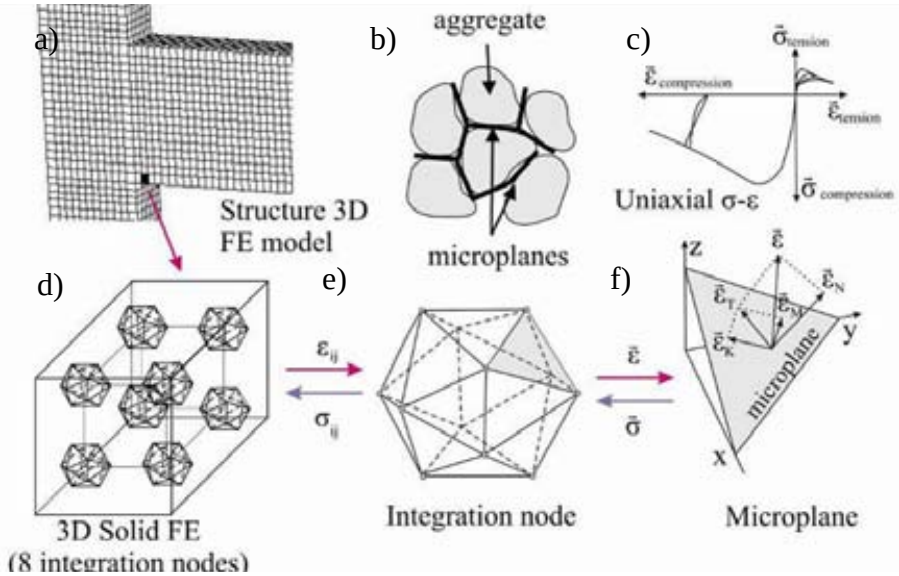

Figure 9.7: Microplanes concrete model [21, 107]: a & d) 3D solid FE for concrete with 8 integration nodes; b) Microplanes representing the weak cement matrix planes between aggregates; c) Uniaxial constitutive relationship for concrete implemented on each microplane; e) Each node consists of 21 microplanes orientations per hemisphere; f) Integration of microplanes strain components for macroscopic stress.

The advantages of microplanes model for concrete, succinctly summarised in [11, 13], outweigh the burden of significantly greater computation (in numerically integrating stress-strain in all microplanes). It should be noted that there are other approaches to model smeared cracking in concrete such as the rotating cracking model [29], multi-directional fixed cracking [37, 120], damage-plasticity approach [52], and the higher order gradient smeared cracking [35]. An alternative to the smeared cracking approach is the discrete crack approach [65, 95], but advanced re-meshing techniques [69], extremely refined mesh [91] or the prerequisite knowledge of cracking location [119] are required for the accurate modelling.

9.3.3 Mesh dependency and localization limiters for smeared cracking models

The classical smeared cracking analysis of quasi-brittle materials, such as concrete, which exhibits softening lead in its stress-strain relationship, will lead to a mesh-dependent analysis [16, 20]. This is due to the localisation of strains in a set of finite elements as the consumed fracture/compression energy within the elements would be dependent on the mesh sizes. The FE model response is then mesh dependent, in which a larger meshing FE will give higher force

response. Conversely, in an infinitely dense mesh FE model, the solution computed will have failure/fracture occurring without any energy dissipation, which is physically impossible. Therefore, to ensure mesh independent results, the total energy consumption of concrete fracture must be constant and this can be introduced using a so-called localization limiter.

There are several approaches for the localization limiter for a smeared-cracking fracture analysis: a) the cracked band method [18, 20] b) the nonlocal damage continuum approach [17, 105, 115]. c) the gradient approach [36, 75] and d) the higher-order Cosserat continuum model [34, 35]. In MASA, both the crack band method [18] and the nonlocal continuum approach (as described by Ožbolt & Bažant [105]) are implemented. In MASA however, a "Stress Relaxation Method" was developed and implemented to reduce the sensitivity to the shape of the mesh [108]. For the analysis of realistic concrete structures the crack band approach is adopted for its simplicity and numerical stability.

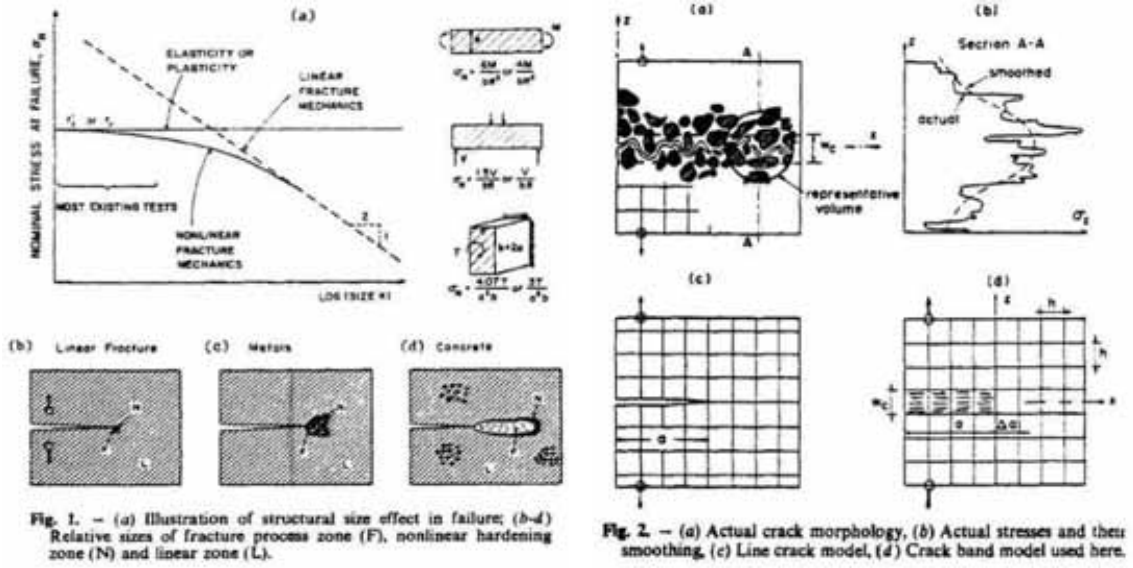

Fig. 1. – (a) Illustration of structural size effect in failure; (b-d) Relative sizes of fracture process zone (F), nonlinear hardening zone (N) and linear zone (L).

Fig. 2. – (a) Actual crack morphology, (b) Actual stresses and their smoothing, (c) Line crack model, (d) Crack band model used here.

Figure 9.8: Right: Illustration of size effect law (a) in relation to materials fracture processes; (b-d). Left: a-b) Actual concrete cracking microstructure; b) line crack model c)crank band modelling [18].

The crack band method assumes the damage (crack) is localised in a row of finite element (see Figure 9.8). To ensure the mesh independent energy consumption from cracking, the concrete constitutive law is modified such that the concrete fracture energy, $G_f = A_f h$ is constant. A_f is the area under the uniaxial stress-strain curve and h is the average element size (i.e. the width of the crack band). The same formulation is assumed for tensile fractures and compressive fractures, but the compressive fracture energy is typically 100 times larger than the tensile fracture energy. Thus, the fracture propagation of concrete depends on three parameters – fracture

energy of the material, G_f, material strength, $f'_{c,}$ and width of crack band (recommended to be three times the aggregate size). Further details of the crack band method is available in references [11, 20, 108]. The crack-band method also gives accurate modelling of "size effect" [12, 20], in addition to partially solving the mesh dependency problem as a localization limiter. The approximate energy release analysis has led to the well-known "size effect law" in quasi-brittle structures [18].

9.3.4 Reinforcing steel modelling

The reinforcing steel is modelled using uni-axial bar-truss elements in MASA. The constitutive law is a tri-linear stress-strain envelope, defined by four parameters: 1) Initial Young's modulus, E_s, 2) Strain hardened modulus, E_h, 3) yield stress, f_y, and 4) tensile/compressive plateau stress, f_{ult}. The cyclic rules for the reinforcing steel is plotted in Figure 9.9a. This constitutive relationship was adopted for all the analyses in this chapter.

MASA also includes the option to model non-linear strain-hardening and Bauschinger unloading effect, based on the Hoehler and Stanton constitutive model [66], by requiring 7 additional calibrated parameters (f_{ult}, ε_{sh}, ε_{ult}, *C1*, *R0*, *a1* and *a2*). Figure 9.9b shows the monotonic loading and unloading rules when the non-linear strain-hardening and Bauschinger unloading are included within the reinforcing steel constitutive model.

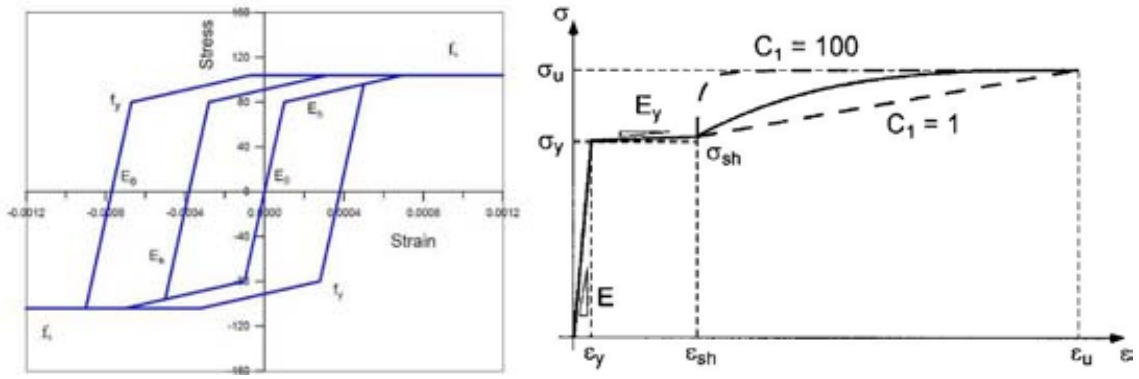

Figure 9.9: a) Uniaxial constitutive stress-strain relationship for reinforcing steel [104]; b) Raynor model for monotonic envelope [66].

9.3.5 Plain round bars discrete bond modelling

An accurate modelling of the bond between concrete and reinforcement is crucial in the modelling of RC beam-column joints, as highlighted in the preceding chapters. There are three critical issues of bond FE modelling of the beam-column joints: 1) The transfer of stress from the beam bars into the joint panel zone, 2) Progressive bond degradation and the subsequent pull-out

(or push out) failure leading to a fixed-end beam rotation, and 3) Non-linearity of the bond elements given the microscopic mechanisms (friction, interface slip, bearing action).

Principally, the numerical modelling of bond is possible at two levels: i) phenomenological modelling based on the smeared or discrete bar-concrete interface formulation ii) detailed analysis where geometry of the reinforcement (if deformed) and concrete is modelled using continuum or lattice framework. More information on the phenomenological bond models, including the theoretical and the experimental basis of the state-of-the-art bond models, are available in the fib report [53].

The discrete bond model implemented in the MASA program consists of a series of one dimensional (1D) non-linear springs (Figure 9.10) with a bond-slip constitutive relationship which depends on the state of stresses in concrete and the reinforcement bars, the type of bars, on type of loading and geometry. Only the degree of freedom along the bar direction is considered i.e. only slipping deformation is allowed for the bond elements. The bond-slip relation in the bar direction, however, depends on the radial stresses generated by surrounding concrete and transverse reinforcement. Further details of the bond model in MASA and its applications to RC structures with deformed bars can be found in Ožbolt *et al.* [106] and in Lettow [76, 77].

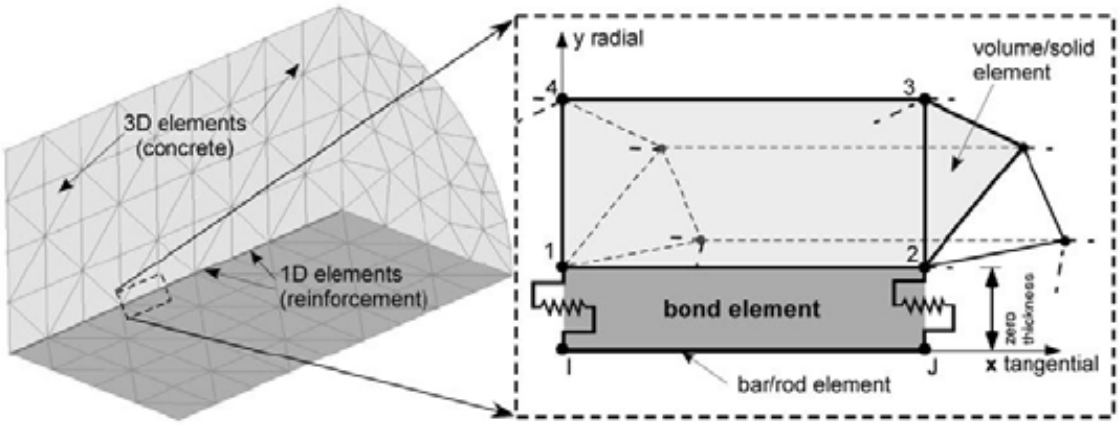

Figure 9.10: Basic assumptions of the bond model implemented in MASA (taken from [77]).

The bond model implemented in MASA evolves from the Fib-CEB Model Code 90 (MC90) [26]. The MC90 model code and the fib recommendation [40, 53] provide a simplified local bond-stress relationship akin the bond element constitutive relationships in modelling. The bond model is based on empirical data and the parameters limit states are given as statistical mean curve. The tri-part backbone of the bond-slip relationship is defined by the maximum bond

strength, τ_{max}, and three characteristics slip limits (s_1, s_2 and s_3). The τ_{max} is given by two components a) τ_m, the mechanical and adhesive (plain bar only) components, and b) τ_f , the frictional residual bond component. The three characteristic slips values depend on the state of confinement of the concrete, concrete strength and the quality of the bond strength. Table 9.1 summarises the mean values of the bond parameters given in the MC90 [26]. Figure 9.12 illustrates the bond model implemented in MASA.

Table 9.1: Reinforcing bond parameters in MC90 [26].

Reinforcement Type	Confining conditions **	Bond conditions	s1 (mm)	s2 (mm)	s3 (mm)	τ max (MPa)	τ f (MPa)	Remarks
Deformed ordinary reinforcing	Unconfined Concrete	good	0.6	0.6	1.0	$2.0\sqrt{f'_c}$	$0.3\sqrt{f'_c}$	$s_1=s_2$
		poor	0.6	0.6	2.5	$1.0\sqrt{f'_c}$	$0.15\sqrt{f'_c}$	$s_1=s_2$
	Confined Concrete	good	1.0	3.0	clear rib spacing	$2.5\sqrt{f'_c}$	$1.0\sqrt{f'_c}$	s_3 is bar dependent
		poor	1.0	3.0	clear rib spacing	$1.25\sqrt{f'_c}$	$0.5\sqrt{f'_c}$	s_3 is bar dependent
Smooth cold drawn wires	Unconfined or Confined Concrete	good	0.01	0.01	0.01	$0.1\sqrt{f'_c}$	$0.1\sqrt{f'_c}$	$s_1=s_2=s_3$; $\tau_{max}=\tau_f$
		poor	0.01	0.01	0.01	$0.05\sqrt{f'_c}$	$0.05\sqrt{f'_c}$	$s_1=s_2=s_3$; $\tau_{max}=\tau_f$
Smooth hot rolled bars	Unconfined or Confined Concrete	good	0.01	0.01	0.01	$0.3\sqrt{f'_c}$	$0.3\sqrt{f'_c}$	$s_1=s_2=s_3$; $\tau_{max}=\tau_f$
		poor	0.01	0.01	0.01	$0.15\sqrt{f'_c}$	$0.15\sqrt{f'_c}$	$s_1=s_2=s_3$; $\tau_{max}=\tau_f$

** Confined concrete is defined as having concrete cover exceeding $5d_b$ and clear spacing of transverse lreinforcement no larger than $10d_b$.

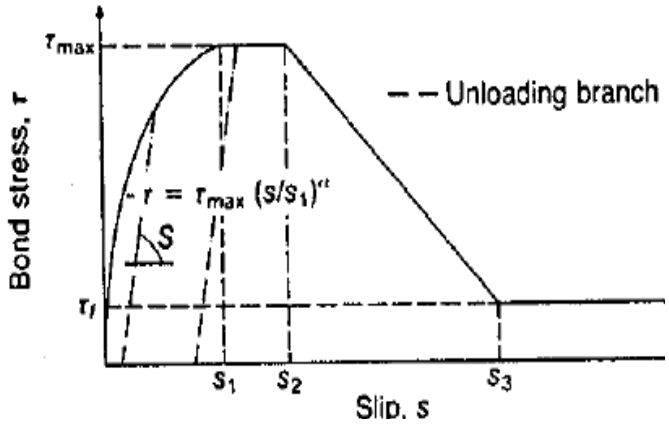

Figure 9.11: Analytical bond-slip monotonic relationship according to the CEB Model Code 1990 [26].

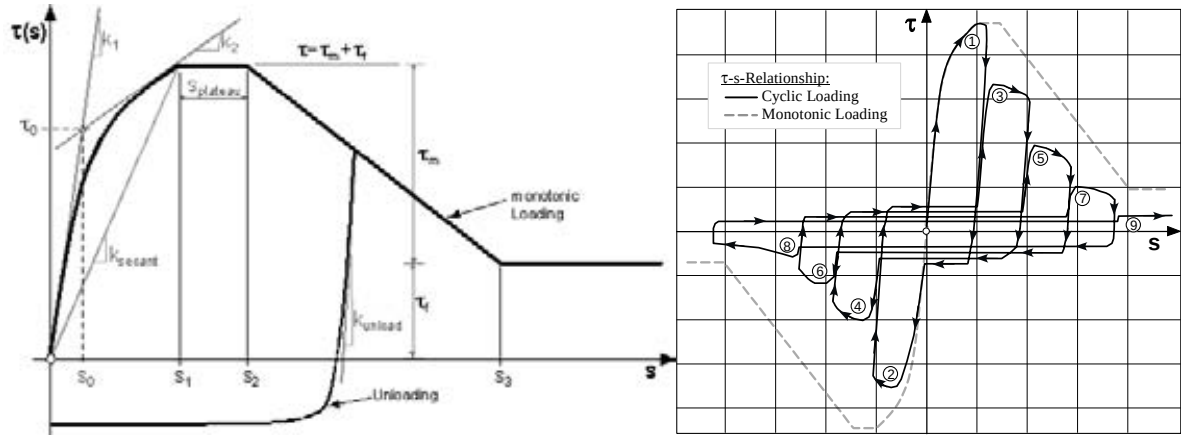

Figure 9.12: a) Bond-slip monotonic relationship and its parameters as implemented in MASA [76]; b) Bond-slip cyclic relationship for deformed bars (Eligehausen *et al.* [43]).

For the FE models in this chapter, the approach of plain round bars modelling described by Eligehausen *et al.* [41] and Genesio [58] is adopted. The bond-slip constitutive relationship of the plain round bars is calibrated to the pullout test data by Fabbrocino *et al.* [48, 49]. Table 9.2 summarises the bond parameters of plain round bars R10, as described by Eligehausen *et al.* [41], with the parameters as shown in Figure 9.12a. The cyclic bond-slip model, originally proposed for deformed bars [43] (see Figure 9.12b) is used in the FE model. Bond degradation is assumed to occur after a certain slip due to the loss of adhesive resistant of the concrete-steel interface. For deformed bars, the bond degradation occurs after the mechanical damage of the concrete-steel interface produced by the ribs of the reinforcement bars [43].

For a typical f'_c of 20MPa, the calibrated τ_f given in Table 9.2 is higher than the MC90 recommendations for smooth hot rolled bars with poor bond conditions ($\tau_{max} = \tau_f$ =0.67MPa and τ_m = 0MPa). The calibrated τ_{max} was higher by 33%, as the MC90 codes did not consider the mechanical/adhesive contribution (τ_m) to be effective for plain bars. Similar, the calibrated s_2 and s_3 values differed significantly compared to MC90.

Table 9.2: Calibrated bond parameters for plain round bars by Eligehausen *et al.* [41] and Genesio [58].

Bar Type	τ_m (MPa)	τ_f (MPa)	k_1 , k_{unload} (N/mm)	k_{sec} (N/mm)	s_2 (mm)	s_3 (mm)
R6	0.5	0.5	100	80	0.1	1
R10	0.5	0.5	100	80	0.1	1

9.3.6 As-built benchmark beam-column joint: NS-O1 model

The as-built beam-column joint model, simulating the NS-O1 test unit was developed in collaboration with two other doctoral researchers (Giovacchino Genesio and Umut Akguzel). Herein, a brief description of the FE model is given and further details of the meshing procedure and model calibration are available in ref. [58]. Asymmetric modelling technique was adopted, in which a vertical symmetry was assumed and only one-half of the beam-column joint was modelled. The out-of-plan movement at the plane of symmetry was restrained.

The 3D micro-plane concrete FE discretisation was performed by eight node solid finite elements (Figure 9.7). The concrete mesh for the NS-O1 model is given in Figure 9.13a. The average size of the hexahedral element is approximately 20 mm. To avoid local failure of the concrete solid elements at the supports and the loading points (vertical and lateral column loads), elastic material with the concrete stiffness, E_c, was used at the beam and column ends (~300mm long region). The lateral and vertical loadings were applied based on the test setup (§4.6) and nodal loads were applied across the whole line across the loading section (Figure 9.13a).

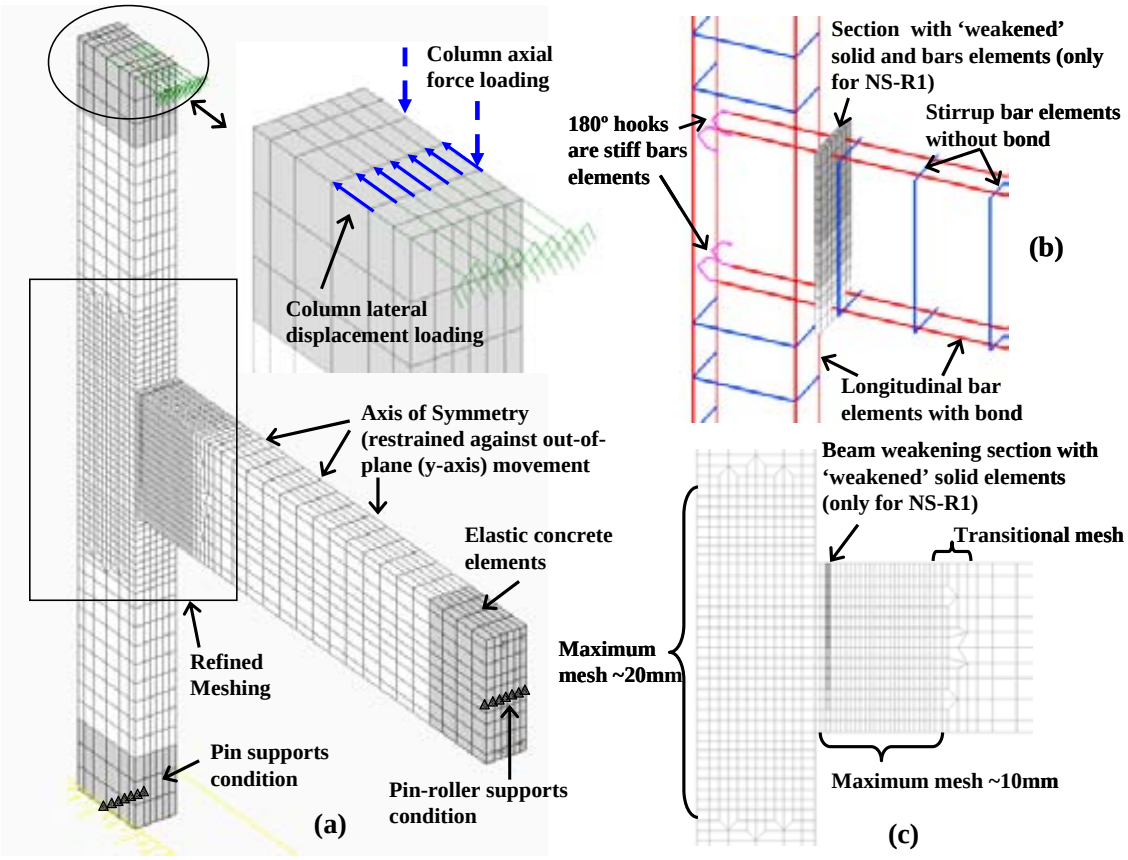

Figure 9.13: MASA model for NS-O1 and NS-R1: a) Loading and boundary conditions; b) Reinforcing elements and selective beam weakening modelling; and c) Concrete mesh configuration.

Steel reinforcement was represented by 1D truss elements with a tri-linear constitutive relationship (§9.3.4). The connection between all longitudinal reinforcement and the concrete was modelled by discrete bond elements (§9.3.5). For transverse reinforcement, a rigid connection (perfect bond) between reinforcement and concrete was assumed. This assumption neglects the influence of the relative displacement between hoops / stirrups and concrete.

Careful attention has been given to the description of the joint detailing. The 180° standard hook anchorage was modelled using stiff linear bars elements as shown in Figure 9.13b. Genesio [58] analysed the effects of different anchorage types and confirmed the extremely poor behaviour of 180° standard hook anchorage into the joint core.

9.3.7 Beam-weakening only retrofitted joint: NS-R1 model

To simulate the beam-weakening retrofit intervention, a section of material discontinuity was inserted into the weakened beam section (Figure 9.13b and c). In order to avoid any singularity issues, the weakened elements (both the concrete solid and the bar elements) were assigned a non-zero but negligible stiffness and strength. 10% of the original E_c, and nominal compressive (f'_c) and tensile (f'_t) strengths of 1.0MPa and 0.1MPa were assumed for the weakened concrete. As the cut concrete slot was expected to break in tension at very early stage of the test, a low value of fracture energy, G_f of 0.01 was assumed. In the preliminary analysis, it was found that apart from the E_c, other concrete slot parameters did not affect the joint response significantly. The material properties of the weakened slot for NS-R1 are given in Table 9.5.

9.3.8 Material and bond properties

The material and bond parameters used for the NS-O1 and NS-R1 models are summarised in Table 9.3 and Table 9.5. Table 9.4 presents the cyclic bond parameters adopted for all numerical models. The material properties are based on the tested material properties given in §4.5 (Chapter 4). In general, the material and bond properties between NS-O1 and NS-R1 are consistent, except for the bond parameters of the beam reinforcement.

The τ_f was reduced from 0.5MPa to 0.25MPa and the τ_m was reduced from 0.5MPa to 0.01MPa for NS-R1. The original calibration for the plain round bars for NS-O1 by Genesio [58] used the experimental values for τ_f and τ_m from the beam pull out test of three specimens of d_b = 12mm plain round bars with a bond length, l_d of $10d_b$ by Fabbrocino *et al.* [47, 48]. Fabbrocino *et*

al. result, as shown in Figure 9.14, was generally 33% higher than the MC90 recommendation (see §9.3.5).

Fabbrocino *et al.* results also suggested a correlation between d_b and τ_f. The beam reinforcement d_b for NS-O1 and NS-R1 was 10mm, suggesting a lower value of τ_f when compared the earlier calibration by Genesio [58]. τ_m was taken to be negligible in NS-R1 as the recommendation of the MC90 for plain round bars was preferred, considering the negligible adhesive resistance of plain round bars in reverse cyclic loading. However, a higher initial stiffness was adopted for NS-R1 to simulate the typical contribution of adhesive bond. This was simulated by the higher limits of s_1 and s_2 when compared to the deformed bars. §9.4.3 will investigate the influence of different τ_f and τ_m adopted in light of the numerical sensitivity analysis of the bond parameters.

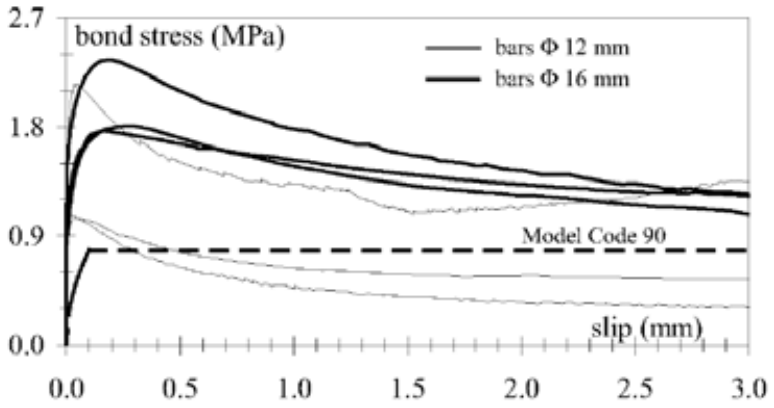

Figure 9.14: Bond stress-slip for plain round bars from beam pull-out test [48].

Table 9.3: Material parameters used for the NS-O1 numerical simulation.

Element Type	Elements	E_c (MPa)	Poisson Ratio, η	f'_c (MPa)	f'_t (MPa)	Fracture energy, G_f
3D hexahedral solid elements	Non-linear microplane* concrete	27400	0.18	17.68	1.81	0.07
	Linear concrete	27400	0.18	-	-	-

Reinforcement Type	Elements	E_s (MPa)	Eh (MPa)	Poisson Ratio, η	f_y (MPa)	f_{ult} (MPa)	A_s (mm)
1D Bar elements	R10 Column longitudinal bars	200000	1000	0.33	430	527	78.55
	R10 Beam longitudinal bars	196000	1000	0.33	330	456	78.55
	R6 Column stirrups	196000	1000	0.33	397	452	28.28
	R6 Beam stirrups	196000	1000	0.33	397	425	28.28

Reinforcement Type	Elements	τ_{max} (MPa)	τ_m (MPa)	τ_f (MPa)	s_1 (mm)	s_2 (mm)	s_3 (mm)	k_1 / k_{unload} (N/mm)	k_2 (N/mm)
Discrete bond elements **	R10 Column longitudinal bars	1.00	0.50	0.50	0.0125	0.10	1.00	100	10
	R10 Beam longitudinal bars	1.00	0.50	0.50	0.0125	0.10	1.00	100	10

* Default microplane model parameters were adopted. **Cyclic bond parameters were not changed in all specimens (See Table 9.4).

Table 9.4: Cyclic bond parameters used in the all numerical simulation.

Reinforcement Type	Elements	Radius for MP model *	Circumference of the bars	Height of the rib (mm)	Radius of the bars (mm)	Compression increment factor, a_c **	Tension reduction factor, a_t **	Cyclic Factor X **
Discrete bond elements	R10 column bars	5.00	31.40	0.10	5	0.20	0.85	0.02
	R10 beam bars	5.00	31.40	0.10	5	0.20	0.85	0.02

* Radius for the ascending branch of the bond stress-slip relationship.
** Cyclic bond parameters based on Eligehausen et al. 1983 and Lettow 2006.

Table 9.5: Material parameters used for the NS-R1 numerical simulation.

Element Type	Elements	E_c (MPa)	Poisson Ratio, η	f'_c (MPa)	f'_t (MPa)	Fracture energy, G_f
3D hexahedral solid elements	Non-linear microplane* concrete	25600	0.18	25.6	2.56	0.07
	Linear concrete	25600	0.18	-	-	-
	Weakened slot concrete	2560	0.18	1.0	0.1	0.01

Reinforcement Type	Elements	E_s (MPa)	Eh (MPa)	Poisson Ratio, η	f_y (MPa)	f_{ult} (MPa)	A_s (mm)
1D Bar elements	R10 Column longitudinal bars	200000	6850	0.33	350	475	78.55
	R10 Beam longitudinal bars	200000	6810	0.33	330	456	78.55
	R6 Column stirrups	200000	7780	0.33	430	530	28.28
	R6 Beam stirrups	200000	7780	0.33	430	530	28.28
	R10 Beam at Weakened Slot	200000	10	0.33	10	20	1.00

Reinforcement Type	Elements	τ_{max} (MPa)	τ_m (MPa)	τ_f (MPa)	s_1 (mm)	s_2 (mm)	s_3 (mm)	k_1 / k_{unload} (N/mm)	k_2 (N/mm)
Discrete bond elements **	R10 Column longitudinal bars	1.00	0.50	0.50	0.0125	0.10	1.00	100	10
	R10 Beam longitudinal bars	0.50	0.00	0.50	0.0125	0.0150	0.0200	100	5

* Default microplane model parameters were adopted. **Cyclic bond parameters were not changed in all specimens (See Table 9.4).

9.3.9 Loading protocols : lateral and varying axial load

The loading protocol applied to the numerical models was designed to simulate as closely as possible the experimental loading regime (given in §4.6). Both monotonic and cyclic loadings were displacement-controlled. The lateral top column displacement was applied at a 0.25mm step between 0 and 15mm and was applied at a 0.5mm step between 15 and 80mm. The cyclic loading pattern is shown in Figure 9.15a while the monotonic loading is a uni-directional loading towards the peak displacements of the cyclic loading pattern (i.e. 2.0mm-5.0mm-10mm-20mm-30mm-40mm-50mm-60mm and 80mm). Due to limitation in computation memory and time, only one cycle per drift level was used.

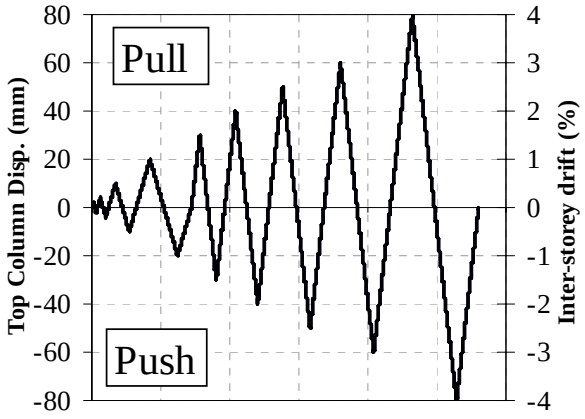

Figure 9.15: The top column lateral displacement loading protocol used in the FE cyclic analyses.

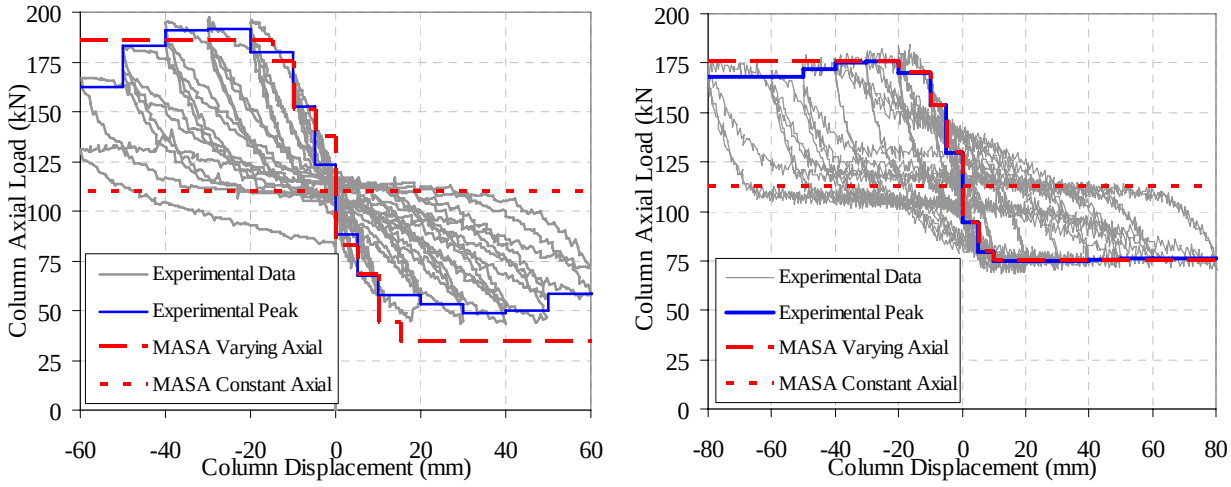

Figure 9.16: Experimental and numerical comparison of axial force loading protocol: a) NS-O1 and b) NS-R1.

The lateral load was coupled with a varying axial loading, *N*, to simulate the actual frame sway action, as per the experimental test. The loading protocol for *N* used in the numerical

analysis was back-calculated from the experimental data for the column axial load. Recalling from §4.6.3., that the variation of N was a function of the lateral load, F_c, from the experiment, it was not possible to determine the loading history of N prior to the analysis. Therefore, it was not possible to correlate and maintain the variation of axial load coefficient α (as in §4.6.3) of 4.63 as in the experiment.

9.4 RESULTS OF MASA FE MODELS

9.4.1 As-built beam-column joint NS-O1 FE analyses

In this section, a brief discussion of the monotonic and cyclic analyses results for NS-O1 will be given for the comparison with the NS-R1 FE model. The analyses and interpretation of the results presented herein are done independently by the author. The benchmark model NS-O1 was produced and calibrated by Giovacchino Genesio from the University of Stuttgart and more detailed discussion of the analyses results, included parametric analyses on various joint parameters are presented in his doctoral thesis [58].

The monotonic and cyclic FE analyses lateral force and displacement (F_c-Δ_c) results for NS-O1 are compared with the test results in Figure 9.17 and Figure 9.18. The screenshots of the principal strains and stresses of the FE model are presented in Figure 9.19. The cracking patterns observed in the test of NS-O1 are given in Figure 9.19-iv for comparison. The following discussion will draw heavily from the experimental results of NS-O1 presented in Chapter 5.

9.4.1.1 Initial stiffness

The numerical K_{ini} from the monotonic analyses were 3500 kN/m and 3775 kN/m for the Pull and Push loading respectively. These values were 22% and 49% higher than the experimental values of K_{ini}, where K_{ini}=2730 kN/m in the Pull direction and K_{ini}=1926kN/m in the Push direction. The over-estimation was also observed in the cyclic analyses. Figure 9.18 presents a close up comparison of the FE and experimental results of the initial cycles. The lateral stiffness of the beam-column joint began to soften even at early drift levels, particularly so in the Push direction (after a cycle of Pull loading). This observation suggests that the FE model did not fully capture the effect of gradual stiffness degradation due to the localised bond degradation of the plain round bars from the loading and unloading of the Pull cycles prior to the Push cycle of the -0.1% drift.

9.4.1.2 F_c-Δ_c and damage patterns

The NS-O1 FE model matches quite well with the experimental results in terms of overall F_c-Δ_c hysteresis, sequence of event and damaged pattern. The monotonic envelope matched well with the experiments in the Pull direction, capturing the peak F_c point and the post-joint cracking response.

In the numerical model, the first flexural cracks on the beam appeared at the inter-storey drift, θ_{drift} = 0.25% loading cycles. The first shear crack started at the joint region at approximately θ_{drift} = ±0.8-0.9%. In the subsequent loading cycles, the joint shear crack extended along the expected diagonal compression strut. Comparing the strain pattern shown and the NS-O1 test damage observation shown in Figure 9.19, the FE model captured the damage pattern reasonably well. At the initiation of joint shear cracks, there were sudden drops of the c F_c in the numerical analysis and this was also observed in the experimental F_c-Δ_c hysteresis.

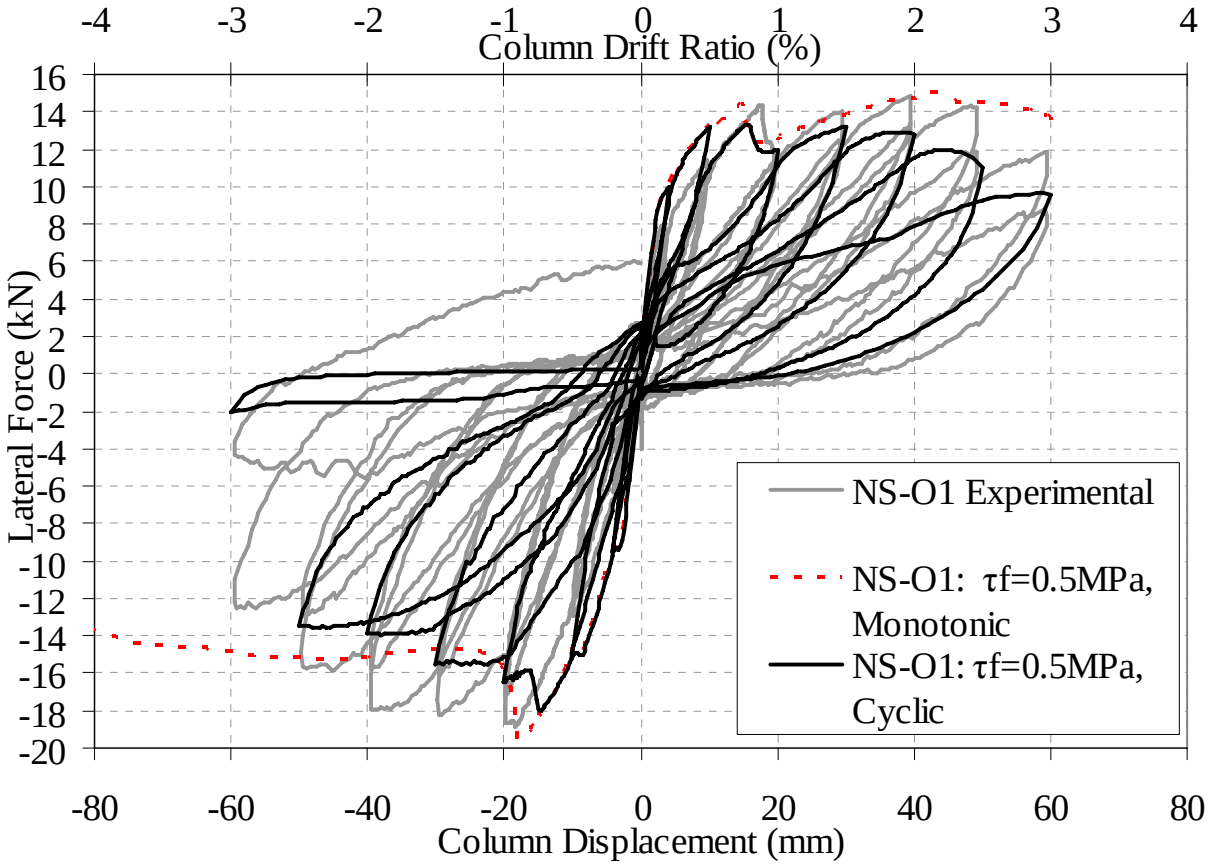

Figure 9.17: Numerical and experimental F_c-Δ_c plots for NS-O1: Monotonic and cyclic analyses with superimposed experimental results (lighter curves).

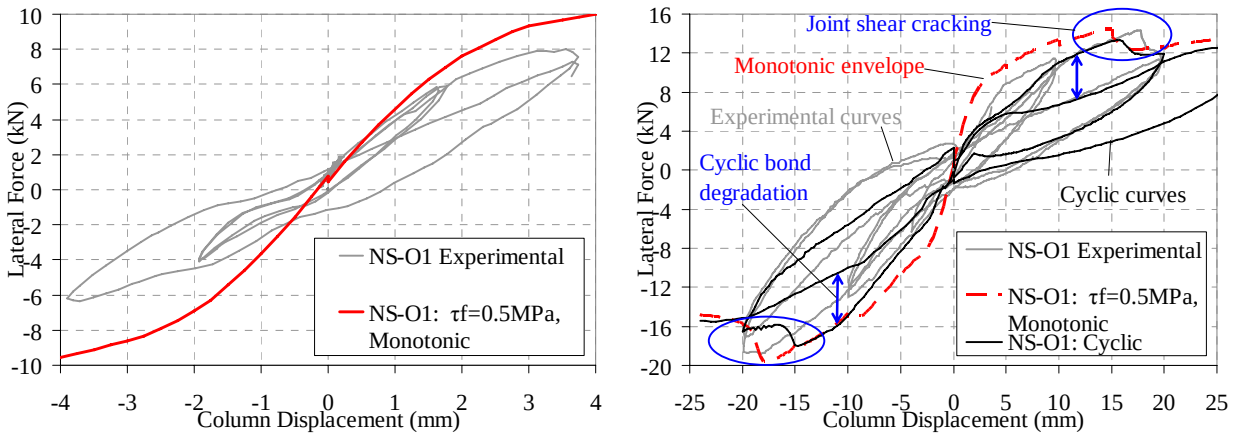

Figure 9.18: Zoom-in of the numerical and experimental F_c-Δ_c comparison for NS-O1: a) Initial stiffness; b) Joint shear cracking and cyclic degradation.

In the subsequent loading cycles, the joint shear cracks grew up (indicated by the higher principal strains) and this was coupled with a gradual reduction of F_c. The strength degradation was pronounced beyond the +1.5% drift cycles and the -1.0% drift cycle. The monotonic numerical analysis could not fully reproduce the post-peak behaviour of the F_c-Δ_c hysteresis, especially in the Push direction, where the higher axial loads were both beneficial (confining the cracked joint core) and detrimental (additional compressive force accelerating concrete spalling and bar buckling) to the joint post-cracking behaviour.

9.4.1.3 Cyclic versus monotonic analyses

The cyclic analysis was reproducing similar F_c-Δ_c envelope curve as the monotonic analysis for NS-O1. When compared to the monotonic analyses, the FE hysteresis curves were better in capturing the F_c strength degradation, especially the rapid degradation as the joint damage accumulated and the joint concrete spalled. The cyclic analysis was also able to simulate the bond degradation effects, evident from the pinching re-loading curve after one complete Pull-Push loading cycles, shown in Figure 9.18b. The damage accumulation in the cyclic analysis improved the prediction of the post-peak behaviour. However, as observed in Figure 9.17, the FE cyclic F_c-Δ_c curves degraded more rapidly than the experimental F_c-Δ_c hysteresis.

9.4.1.4 Principal stresses distribution

The principal stresses distribution given in Figure 9.19 provides some insights to the redistribution of stresses within the joint before and after the joint diagonal cracking. Figure 9.19-iv also shows the corresponding damage states of the experimental NS-O1.

From Mohr's circle stress theory, in uncracked concrete, the vector perpendicular to the principal tensile stress, p'_t, would be the principal compressive stress, p'_c. Thus, as can be seen in Figure 9.19a-i and Figure 9.19b-i, the compressive strut with the concentration of p'_c was encompassing about 60-80-% of the joint area of NS-O1.

After the joint diagonal crack and the lost of the main diagonal compressive strut, an alternative compressive strut mechanism was developed in order to maintain the joint shear strength. The softening of the concrete stress beyond the peak tensile stress was detected by the gradual decay of principal tensile stresses in the concrete elements normal to the joint crack line (given as the principal strain pattern).

The jagged dark shades (~5-10mm thick) parallel to the joint diagonal crack indicates that there was a narrow diagonal compressive strut, relying on the interface shear transfer along the joint crack. Figure 9.19a-ii provides a clear illustration of this new stress path within the joint. In the subsequent cycles (e.g. ±3.0% drift), as shown in Figure 9.19a-iii, the compression diagonal strut grew in width and in compressive (negative values) principal stress values.

In the uncracked concrete, the concrete tensile stresses balanced/resisted the compressive strut within the joint. In the cracked concrete joint, "new" compression diagonal strut appeared along the joint diagonal crack and resulted in tensile distress at the exterior face of the joint. This led to a "concrete spalling" in the FE model, as indicated by the principal strains at the exterior column-joint face. This was also consistent with the test observation.

The FE model also predicted localised spalling at the beam-to-column interface due to the growth of the flexural crack on the beam. Such high strain (cracking or concrete spalling) was not observed in the test.

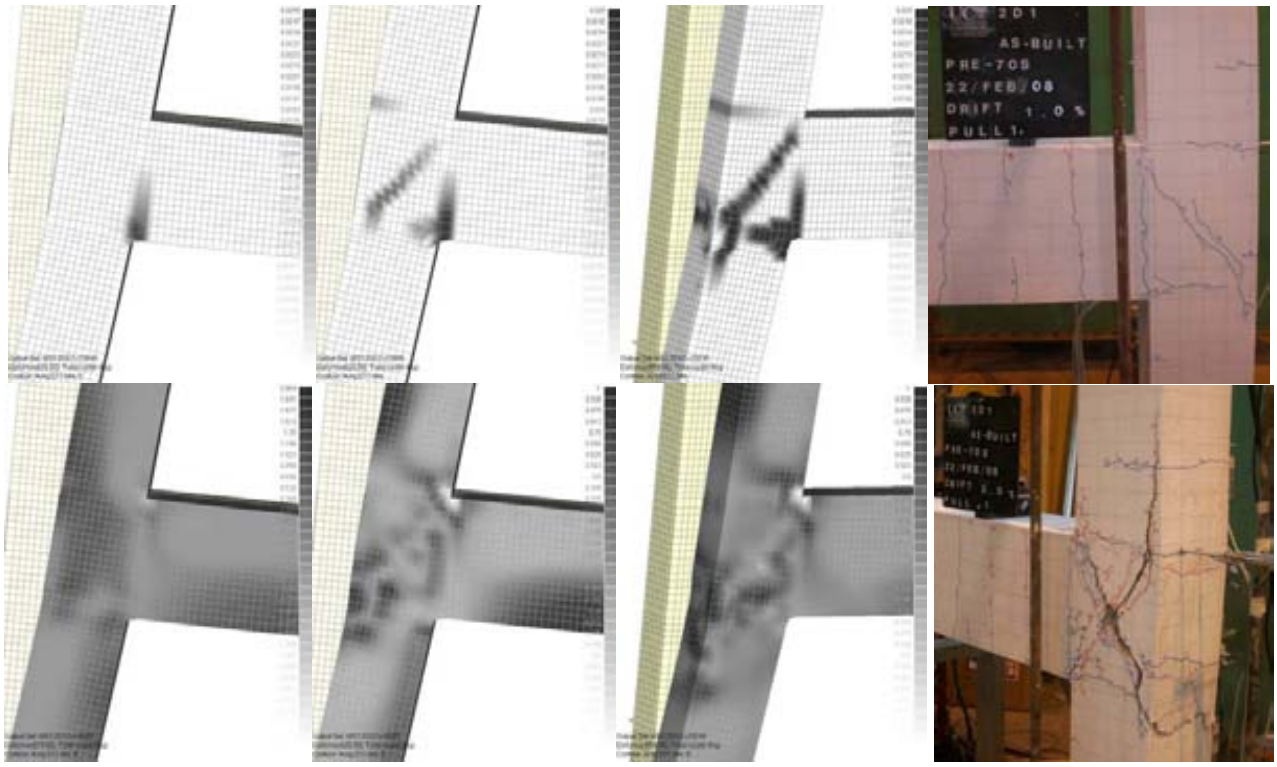

(a) Pull loading: i) +10mm (+0.5% drift), ii) +20mm (+1.0% drift) and iii) +60mm (+3.0% drift) iv) Experimental observations at +1.0% drift (top) and +3.0% drift (bottom).

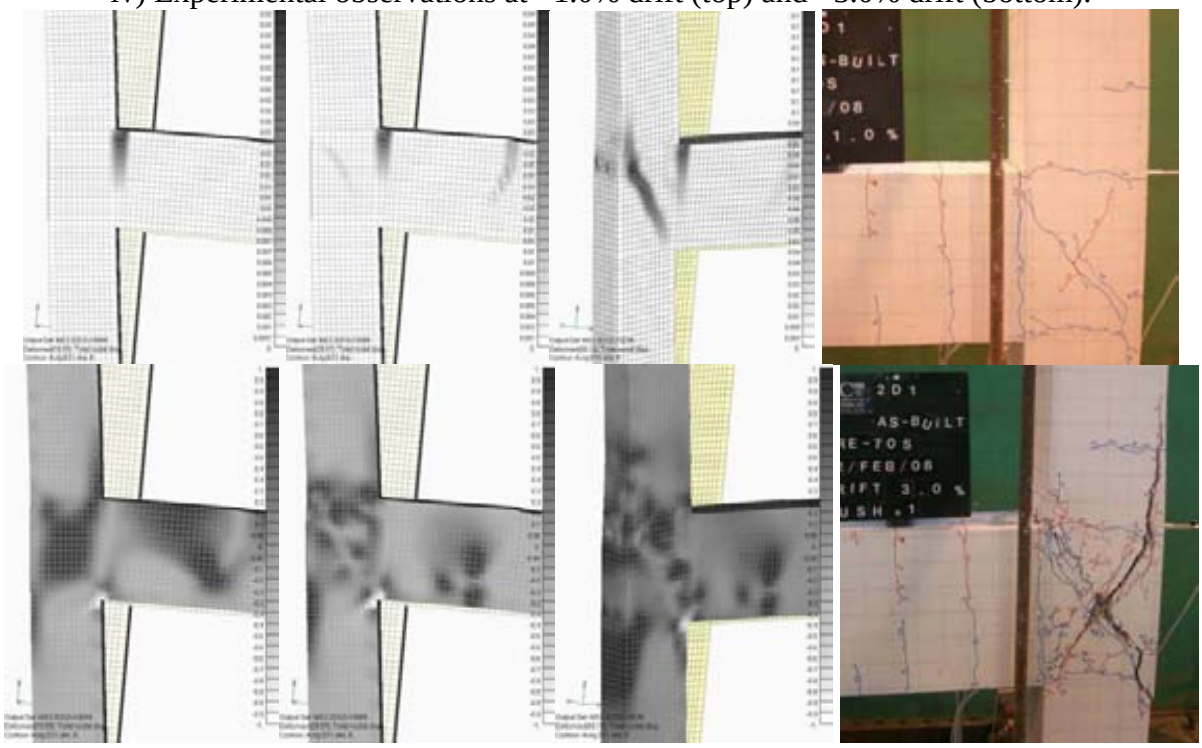

(b) Push loading: i) -10mm (-0.5% drift), ii) -20mm (-1.0% drift), iii) -60mm (-3.0% drift) and iv) Experimental observations at -1.0% drift (top) and -3.0% drift (bottom).

Figure 9.19: Screenshots of FE model NS-O1 in terms of principal strains (cracks and deformation) and principal stresses (internal force transfer). Dark strain and stress are indicative of tensile strain and stress.

9.4.2 Beam-weakening only retrofitted joint NS-R1 FE analyses

The monotonic and cyclic FE analyses lateral force and displacement (F_c-Δ_c) results for NS-R1 are compared with the experimental results in Figure 9.20. The screenshots of principal strains and stresses of the FE monotonic and cyclic models are presented in Figure 9.21 and Figure 9.23, respectively. The cracking patterns observed in the NS-O1 test are given in Figure 9.19-iv for comparison. The following discussion will draw heavily from the experimental results of NS-R1 presented in §6.2 (of Chapter 6).

9.4.2.1 Initial stiffness

The numerical K_{ini} from the monotonic analyses were 2417 kN/m and 4184 kN/m for the Pull and Push loading respectively. As observed in the comparison of the F_c-Δ_c hysteresis curves in Figure 9.22a, the predicted K_{ini} was matching with the experimental K_{ini} for the Pull direction (difference ~ 9%). However, a discrepancy up to 58.6% was observed in the Push direction.

The weakening of the beam in the FE model was simulated by the artificially weak concrete grout while in the experiment concrete grout was applied in the 'cut' region. Thus, the NS-R1 beam was effectively cracked within the weakened section in the FE model, resulting in a lower K_{ini} prediction in the Pull direction.

The overestimation of K_{ini} in the Push direction when compared with the experimental K_{ini} (of 1734kN/m) suggests that the FE model did not capture the loss of stiffness due to bond degradation of the plain round bars after the loading and unloading of the initial Pull cycle.

9.4.2.2 F_c-Δ_c and damage patterns

The NS-R1 FE model matches well with the experimental results in terms of the failure mode and the damaged pattern. However, the monotonic FE model consistently overestimated the F_c response by approximately 10-15%, particularly in the Pull direction. §9.4.3.2 will attempt to provide a rational explanation for the consistent overestimation of F_c. The dominant inelastic mechanism observed in both the NS-R1 FE model and test was the beam flexural hinging with localised strain concentration and bond failure of the plain round bars.

In the FE model, the first flexural crack on the beam appeared at the weakened section at the θ_{drift} =0.25%. In the subsequent loading cycles, the flexural crack at the weakened section grew in size (and principal strains). This was consistent with the experimental observation, as

illustrated by the comparison with principal strain plots in Figure 9.21. At the θ_{drift} = +1.0% and -1.0%, the FE model predicted crack widths (taken as the averaged principal strain multiply by the mesh element width across the crack) of 1.5mm and 1.8mm respectively. These values were comparable to the experimental observation, with the maximum beam crack widths of 4.0mm and 1.8mm in the Pull and Push directions respectively.

The principal tensile stresses decreased significantly from +2.0% drift cycles onwards, an indication of beam reinforcement' bond failure within the joint region. This did not lead to strains/cracking within the joint (unlike NS-O1) or decay of F_c. The tension anchorage was fully transferred to the 180º hooks, as also confirmed in the FE prediction of the beam bar stresses (to be discussed in §9.4.2.5). The distribution of the principal stresses will be discussed in §9.4.2.4.

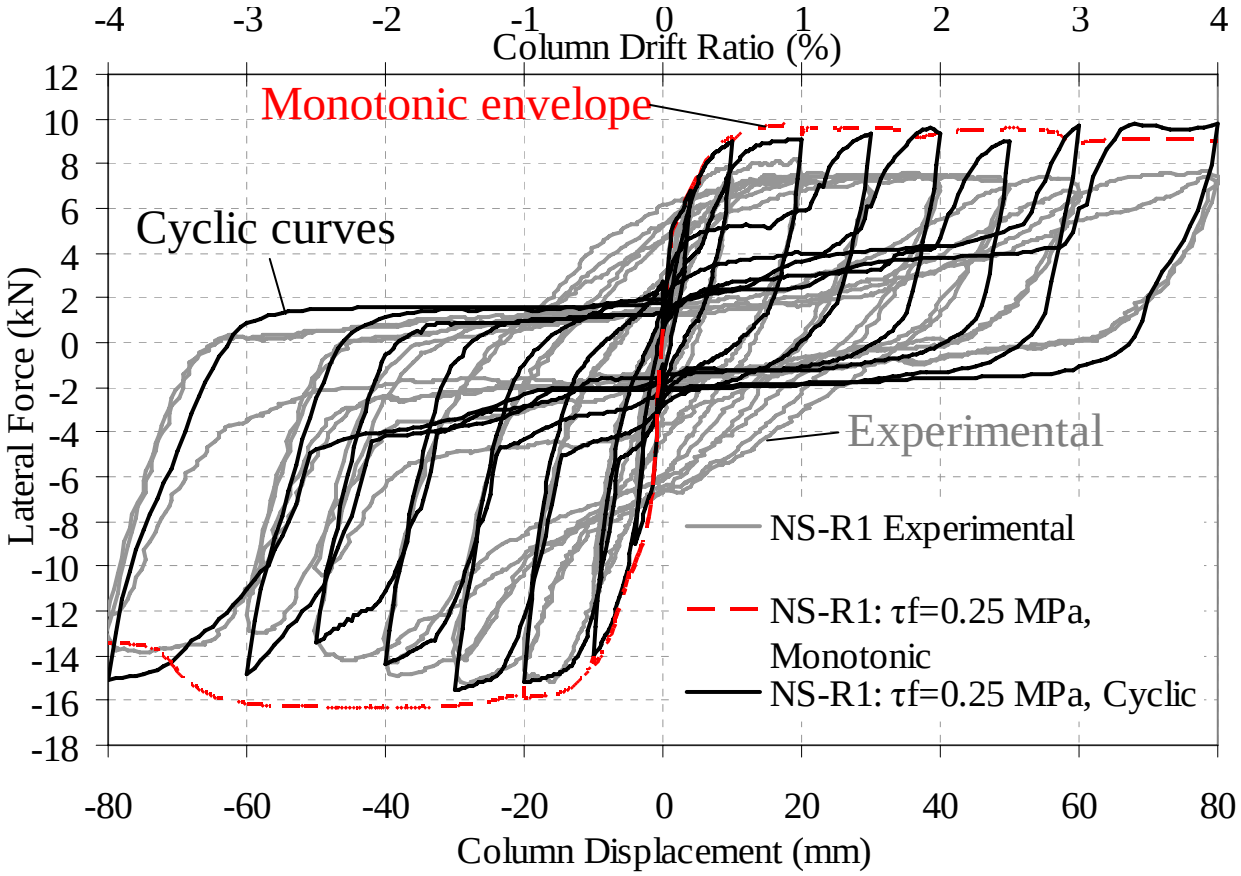

Figure 9.20: Numerical and experimental F_c-Δ_c plots for NS-R1: Monotonic and cyclic FE analyses with superimposed experimental results (lighter curves).

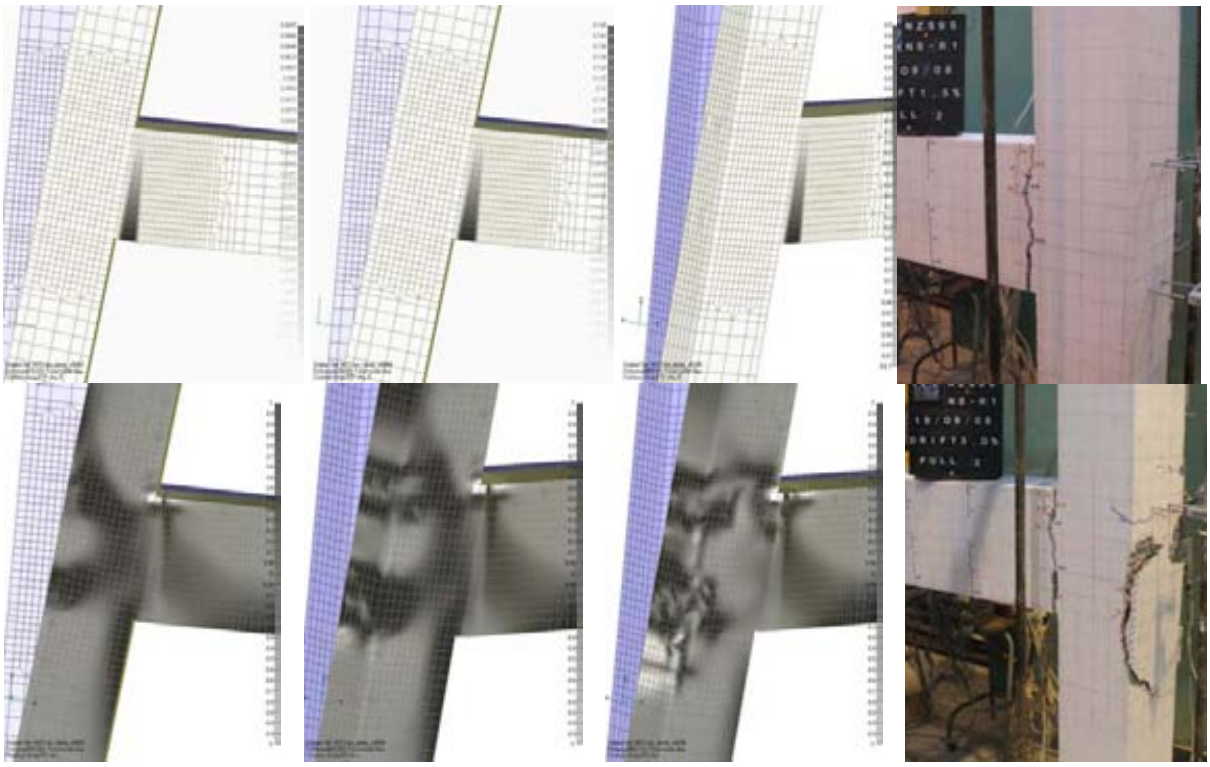

(a) Monotonic pull loading: i) +10mm (+0.5% drift), ii) +20mm (+1.0% drift), iii) +60mm (+3.0% drift) and iv) Experimental observations at +1.5% drift (top) and +3.0% drift (bottom).

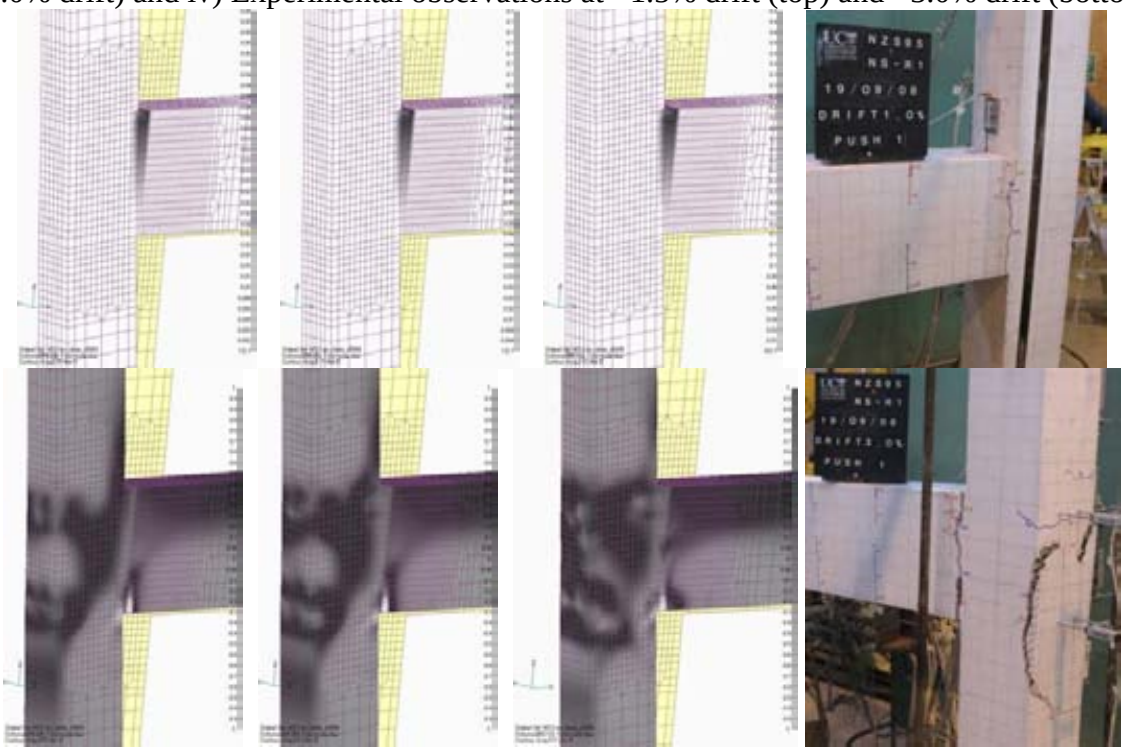

(b) Monotonic push loading: i) -10mm (-0.5% drift), ii) -20mm (-1.0% drift) iii) -60mm (-3.0% drift) and iv) Experimental observations at -1.0% drift (top) and -3.0% drift (bottom).

Figure 9.21: The principal strains (cracks and deformation) and principal stresses (internal force transfer) screenshots of FE model NS-R1: Monotonic loading. Darker contour is indicative of tensile strain and stress.

The yield drift in the Pull direction was also well captured in the FE model. However, the yield drift in the Push direction was underestimated. This difference can be attributed to the different 'yielding' mechanism of the top beam reinforcement. While in the test specimen the yielding point was defined by the steel material yielding in tension, in the FE model, the apparent 'yielding' of the beam top bars was defined by the bond failure of the steel reinforcement. This was confirmed by the comparison of beam bars stresses given in §9.4.2.5.

In later stages of the θ_{drift} (>±3.0%), the FE model showed signs of distress at the exterior joint face, due to the compressive anchorage failure of the 180º hooks. This was more evident in the cyclic analysis than the monotonic analyses, as the corresponding bond degradation was more severe. In the cyclic analysis, the column longitudinal bars on the exterior face also began to buckle at approximately -2.5% drift, as can be seen in the reinforcing stress plot in Figure 9.27. This corresponded to a gradual strength degradation in the Push cycle. This effect was not captured in the monotonic Push analysis.

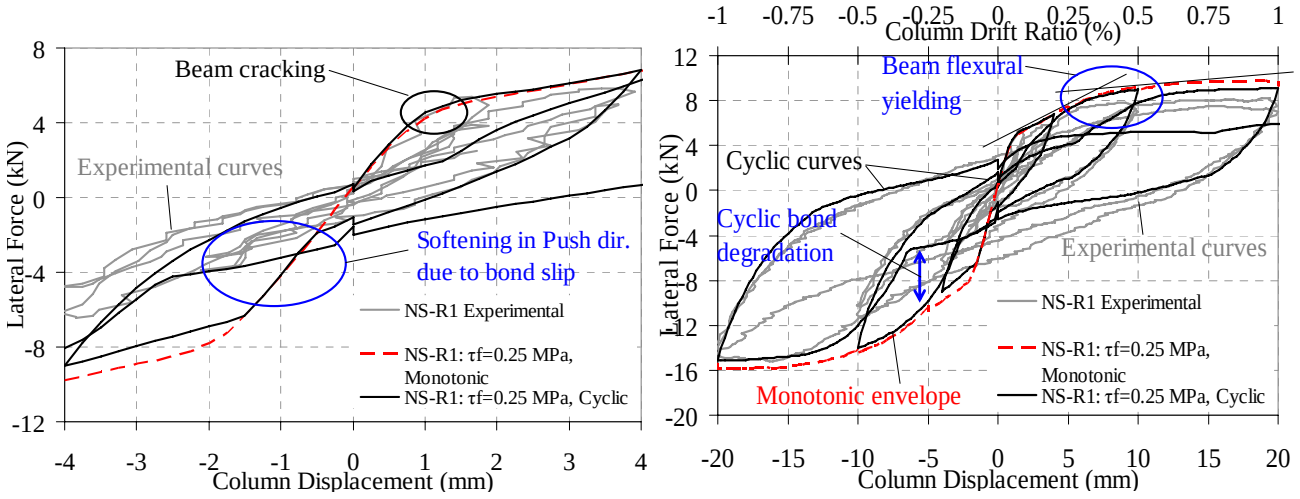

Figure 9.22: Zoom-in of the numerical and experimental F_c-Δ_c comparison for NS-R1: a) Initial stiffness; b) Joint shear cracking and cyclic degradation.

9.4.2.3 Cyclic versus monotonic analyses

As indicated by the discussion in the preceding section, the cyclic analysis for NS-R1 provided a more complete picture and improved prediction of the NS-R1 response when compared to the monotonic analyses. The cyclic analysis showed a similar F_c-Δ_c envelope curve as the monotonic analysis for NS-R1, but with a higher strength degradation in the Push direction and a significant in-cycle stiffness degradation within the hysteresis loop.

The energy dissipation capacity (the area of the F_c-Δ_c hysteresis loop) of NS-R1 was under-estimated in the FE cyclic model. The reloading stiffness in the FE model was lower than the experimental results. Furthermore, the gradual increase of reloading stiffness observed in the experiment, possibly due to frictional interlocking resistance, was not fully simulated in the FE model, as shown in Figure 9.22b.

The FE hysteresis curves were matching with the experimental result beyond the ±2.5% drift when anchorage failure and beam reinforcement bond slip dominated the inelastic response. The cyclic analysis was able to replicate the in-cycle cumulative bond degradation, as evident from the stiffness degradation in the reloading curves after one complete Pull-Push loading cycles. The stiffness degradation and pinching shape of the F_c-Δ_c hysteresis was captured very well in the FE model. Previous numerical studies [68, 79, 84, 138] have previously highlighted the difficulties in capturing the F_c-Δ_c hysteresis pinching behaviour due to the uncertainties in modelling the decay of the bond capacity. Thus, the NS-R1 result gave good indication of the potential of the MASA FE programme in this respect.

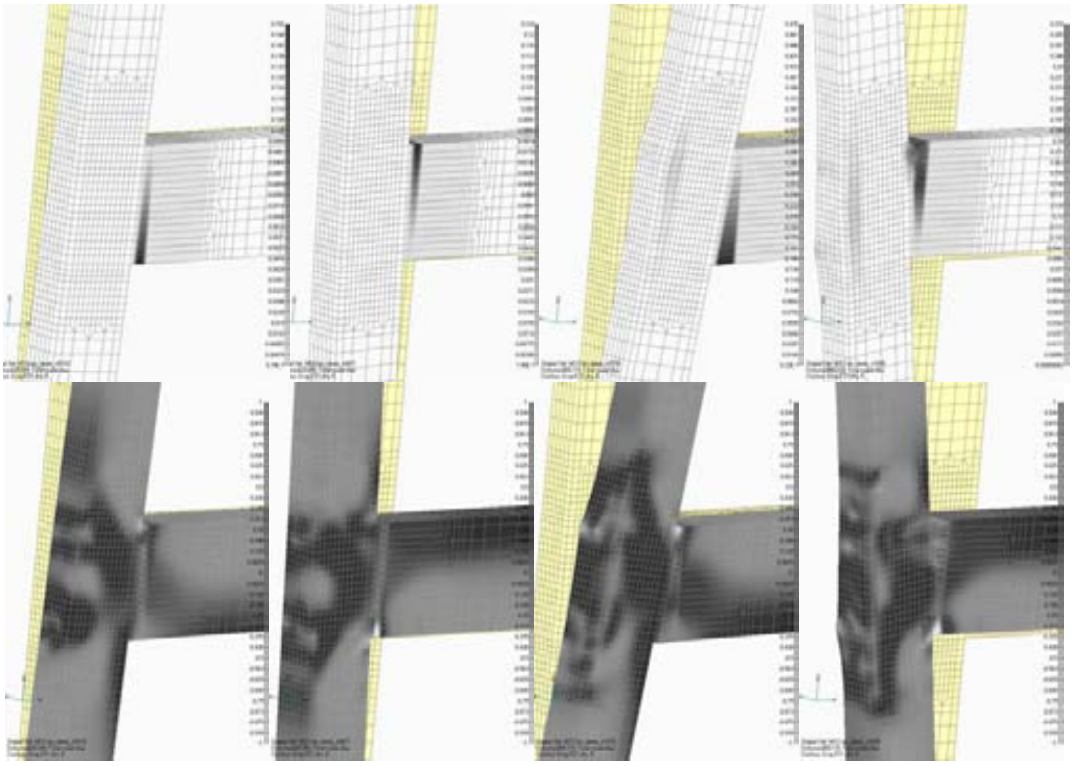

Cyclic loading: i-ii) ±20mm (±1.0% drift); and iii-iv) ±60mm (±3.0% drift).

Figure 9.23: The principal strains (cracks and deformation) and principal stresses (internal force transfer) screenshots of FE model NS-R1: Monotonic loading. Darker contour is indicative of tensile strain and stress.

9.4.2.4 Principal stresses distribution

Principal stress distributions of the joint concrete at the three different θ_{drift} levels for NS-R1 are shown in Figure 9.21 and Figure 9.23. The principal stresses distribution in the early θ_{drift} levels (±0.5% and ±1.0%) corresponded to an expected diagonal compressive strut mechanism, with a relatively wide strut. Patches of principal tensile stresses (dark shades in Figure 9.21) along the beam reinforcement within the joint reflected the bond force transferred from the reinforcement to concrete within the uncracked concrete.

The principal stress distribution changed significantly between the +2.0% and +2.5% drift cycles. The reduction of the principal tensile stress in the concrete elements along the embedded beam reinforcement indicated the loss of bond capacity of the reinforcement. The loss of bond was more peculiar in the Pull loading than the Push loading, as shown in the ±3.0% screenshots in Figure 9.21, possibly due to the lower column axial loads.

The loss of bond along the straight length of the beam bars anchorage into the joint resulted in the stiff 180º hook anchorage to work in both tension and compression. The 180º hook relied on the bearing resistance of the cover concrete on the exterior face of the joint to resist compressive forces from the beam reinforcement. This was captured in the FE model, evidently by the increase tensile stresses on the exterior face of the joint. The FE model predicted minor spalling at the ends of the 180º hook anchorages at the +4.0% cycles.

In terms of principal stress distributions, only minor difference in the Pull cycles was noted between the monotonic and cyclic analyses. While the loss of bond of the beam bars within the joint would suggest limited/no tensile stresses in the joint, the cracking and delaminating of the cover concrete the exterior face of the joint would induce similar tensile stresses as shown in Figure 9.23-iii.

The results above confirmed the interpretation of the NS-R1 experimental results in §6.2 (of Chapter 6). The compressive anchorage push-out failure in the 2nd Push cycle of the -2.5% resulted in the associated concrete spalling and lateral force strength reduction.

9.4.2.5 Reinforcement stresses profiles

Figure 9.28 to Figure 9.26 present the comparison of the experimental and numerical beam reinforcement' stresses (f_s) at the selected drift peaks for the specimen NS-R1. The FE results were taken from the cyclic analyses. A bi-linear constitutive relationship similar to the steel

model used in the FE model (Figure 9.9a) was used to convert the strain gages results of NS-R1 (given in §6.2.5) to f_s values.

In general, the FE model captures the f_s development as the early stages of the θ_{drift} levels very well. The general trends of the FE model stresses within the beam and column longitudinal bars as well as the stirrups of the beam and column were agreeable with the experimental results.

Beyond the θ_{drift} > ±2.0%, the f_s in the FE model were limited to a plateau value (~180MPa) as the bond capacity of the plain-round bars limited the f_s developed in the reinforcement. In the real specimen, with the bond failure and debonding of the beam reinforcement, effective tensile anchorage was provided by the 180º hooks and the long straight length along the beam. As such, the yield strength of the steel, f_y could still be developed in tension despite bond failure.

In the FE model, f_s did not attain f_y in tension as the 'stiff' 180º hooks anchorage could not effectively transfer the tension forces into the joint. Stiff 1D bar elements were used to model these 180º hooks anchorage, as shown in Figure 9.13. In reality, the 180º hook relied on compressive bearing resistance of the 180º hook to transfer tensile forces from the reinforcement into the concrete joint, and this effect could not be fully simulated in the FE model by the 'stiff' 1D bar elements.

The principal stress distribution diagrams in Figure 9.21 and Figure 9.23 indicated the neutral axes to be approximated 25mm in the Pull loading and 37.5mm in the Push loading. Recalling the asymmetric beam reinforcement in NS-R1 due to beam-weakening, the smaller neutral axis in the Pull direction (with two tension beam bars) was expected.

The compressive beams bars were carrying limited compressive stresses (<50MPa) in the FE model while the un-weakened bottom bars yielded in compression in the 1st Push cycles. This suggests the limitation of the 'stiff' 180º hooks anchorage in transferring the compressive forces or the effects of localised concrete compression (leading to very small neutral axis depth).

Figure 9.27 presents the stresses output for the 1D bar elements at the Pull and Push peak of ±3.0% drift. The darker shades of green to blue were indicative of tensile stresses while the lighter shades of yellow to red were indicative of compressive stresses.

Figure 9.27 also illustrates the loss of force transfer due to the bond failure of the column longitudinal bars, with uniform stresses observed along the length of column bars within the joint.

In the Push cycle, as the exterior columns bars deformed in-place under substantial compressive stresses, suggesting concrete spalling and subsequently buckling of the exterior column bars.

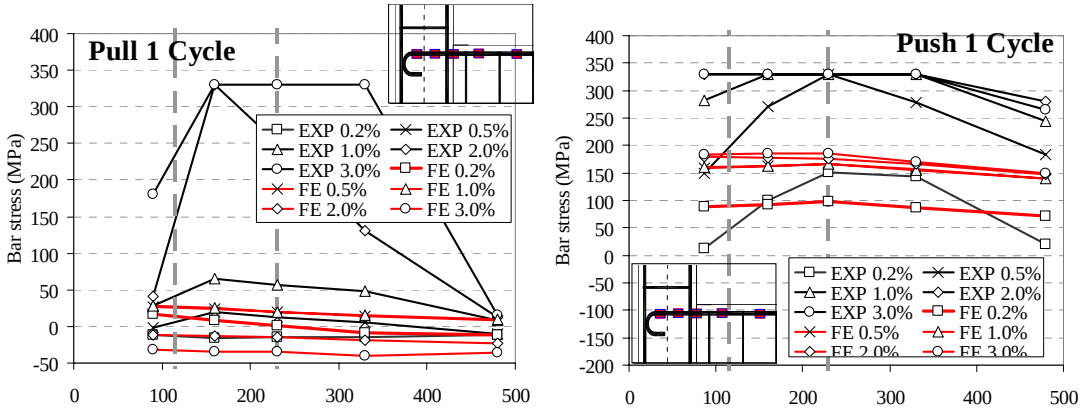

Figure 9.24: Experimental and FE beam top reinforcement stresses for NS-R1.

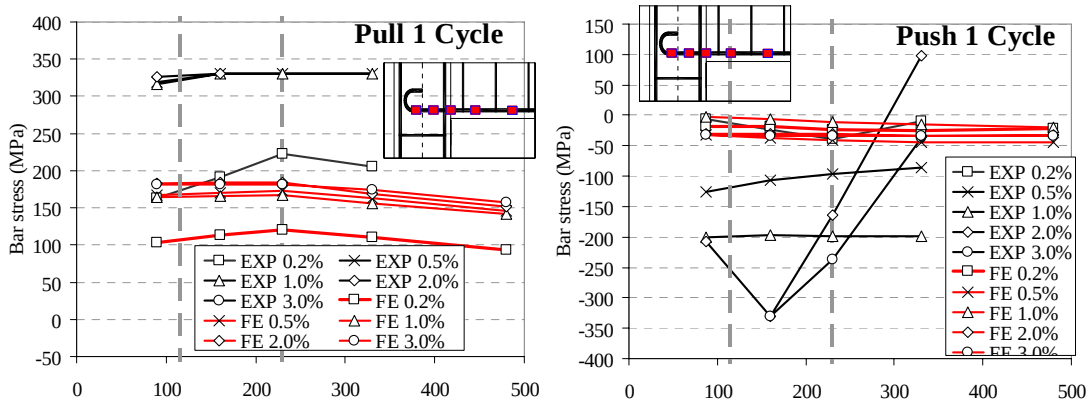

Figure 9.25: Experimental and FE beam bottom un-weakened reinforcement stresses for NS-R1.

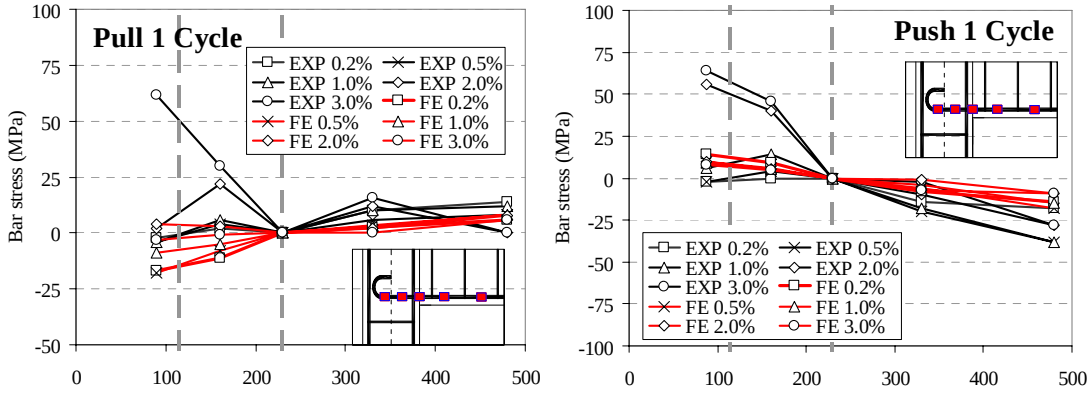

Figure 9.26: Experimental and FE beam bottom weakened reinforcement stresses for NS-R1.

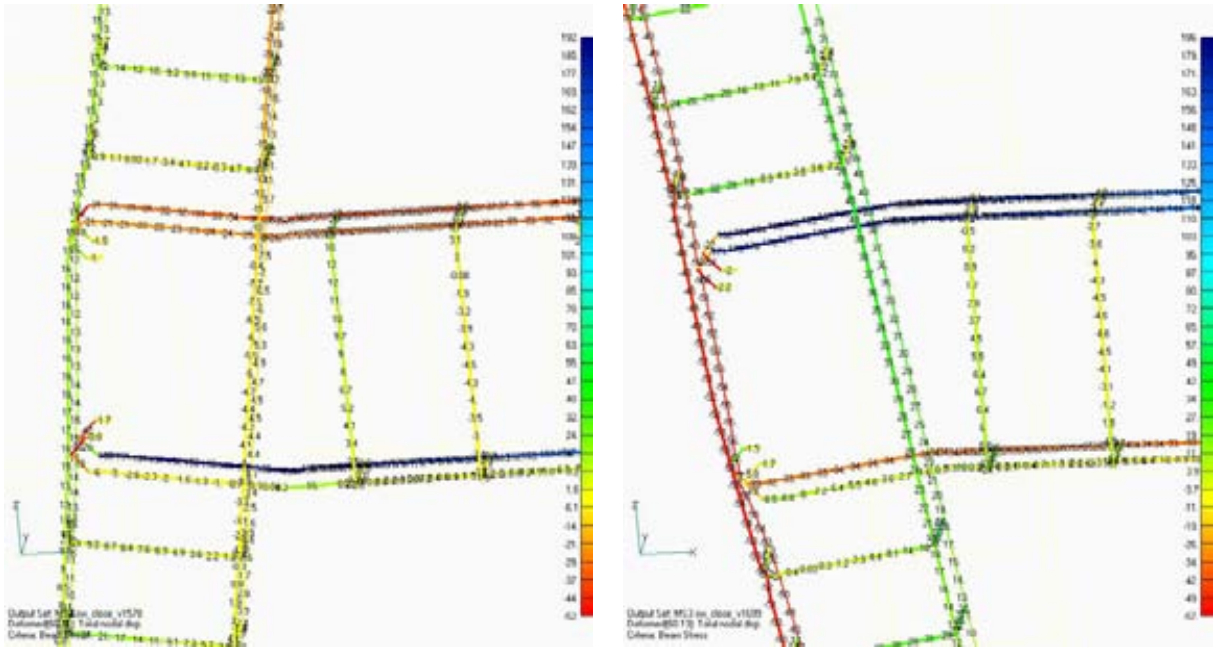

Figure 9.27: Screenshots of the FE reinforcement stresses for NS-R1 under cyclic loading at: a) +3.0% drift; and b) -3.0% drift. Positive values are tensile stresses. (Update – larger font, smaller scale)

The monotonic analyses overestimated the bond capacity, depth of the neutral axes and f_s values, when compared with the cyclic analysis. Figure 9.28 provides an experimental-analytical comparison of the un-weakened beam bottom bar stresses in the Push cycles from the cyclic and monotonic analyses. In the cyclic analysis, the bottom bar was consistently in low compressive stress, while in the monotonic analysis the bottom bar was in compression before gradually increased in tensile stress. The cyclic analysis suggested a more constant neutral axis and complete bond failure of the bars in compression. On the other hand, the monotonic analysis indicated a decreasing neutral axis with the bar acting in tension after the -1.0% Pull loading.

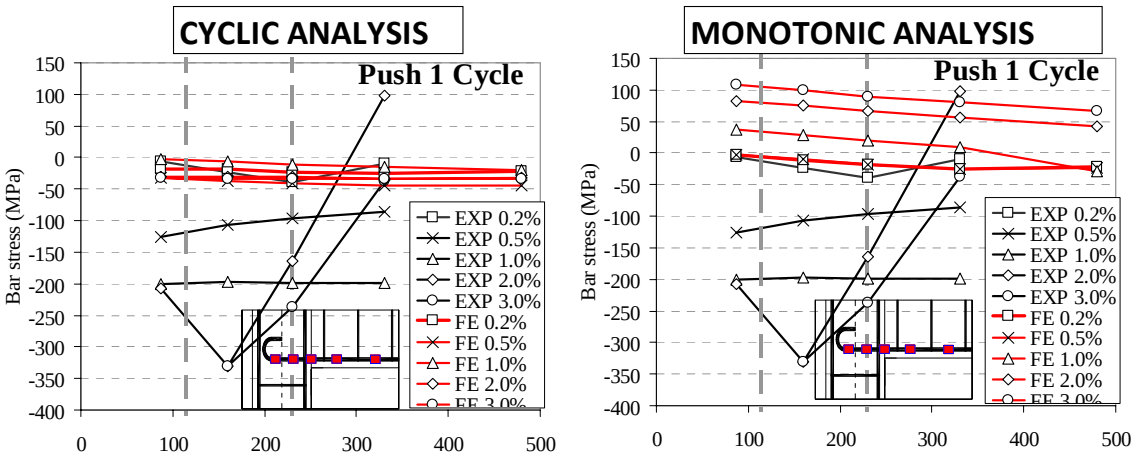

Figure 9.28: Comparison of beam bar stresses for NS-R1 under cyclic and monotonic loading.

9.4.3 Discussions and preliminary sensitivity analyses

9.4.3.1 Influence of bond parameters

As discussed in §9.3.5 and §9.3.8, the maximum bond strengths (τ_m of 0.5MPa, τ_f of 0.5MPa and τ_{max} of 1.0MPa) calibrated for the NS-O1 model were higher than the MC90 recommendations for plain round bars. The bond parameter calibration used in the NS-O1 model done by Eligehausen e *et al.* [41] and Genesio [58] was based on the limited experimental data by Fabbrocino *et al.* [48, 49]. The bond parameter calibration was done with the assumption that joint shear failure dominated the behaviour, as such the bond parameter was of a lesser influence and was not refined. For the model NS-R1, the bond parameters recommended by the CEB Model Code 90 [26] were adopted instead of the original calibration, as explained in §9.3.8.

To further understand the implications and influence of the different bond strength assumptions, three bond parameters scenarios, with the reference to Figure 9.12a, are adopted for the sensitivity analyses on NS-O1 and NS-R1 models:

a) Genesio [58] calibration based Fabbrocino *et al.* [48, 49] dataset (τ_{max} = 1.0MPa, τ_f =0.5MPa, τ_m = 0.5MPa, s_2=0.1mm, s_3=1.0mm)
b) CEB Model Code 90 smooth hot rolled bars with 'good' bond conditions (τ_{max} =1.00MPa τ_f =0.5MPa, τ_m = 0.5MPa, s_2=0.015mm, s_3=0.02mm).
c) CEB Model Code 90 smooth hot rolled bars with 'very poor' bond conditions (τ_{max} =0.25MPa τ_f =0.25MPa, τ_m = 0.0MPa, s_2=0.015mm, s_3=0.02mm).

Figure 9.29 and Figure 9.30 present the results of the sensitivity analyses of the bond parameters for NS-O1 and NS-R1 respectively. Only the Pull loading or positive displacement quadrant is analysed.

For NS-O1, both scenario (a) and (b) predicted joint shear failures at approximately 13-14kN and 20mm top column displacement, which were consistent with the experimental observations. Scenario (a) response captured the post-joint crack behaviour well for the 1st cycle peaks while scenario (b) monotonic envelope was closer to the 2nd cycle peaks. Furthermore, as bond failure subsequently dominated the response in scenario (b), the joint damage was relatively less than the joint damage of scenario (a). The comparison of scenario (a) and (b) illustrates the importance of the bond slip/displacement limits (s_2 and s_3), despite the difficulty to ascertain and variability (huge dispersion) of these parameters from local bond testing (e.g. [48, 49])

Complete bond failure and plateau-ing of the F_c-Δ_c response was observed in scenarios (b) and (c). In scenario (c), bond failure of the beam reinforcement and subsequently the anchorage failure of the 180º hooks prevented excessive joint shear stress. This highlights the fact that the bond parameters can alter and influence the hierarchy of strength and failure mechanism of pre-1970s beam-column joints. This was also previously highlighted by other studies (e.g. Calvi *et al.* [23] and Fabbrocino *et al.* [50]).

The sensitivity analyses for NS-R1 shown in Figure 9.30 also included four other bond parameter scenarios for the sensitivity analyses for NS-R1:

d) τ_{max} =0.5MPa τ_f =0.49MPa, τ_m = 0.01MPa, s_2=0.015mm, s_3=0.02mm.

e) τ_{max} =0.8MPa τ_f =0.4MPa, τ_m = 0.4MPa, s_2=0.015mm, s_3=0.02mm

f) τ_{max} =0.4MPa τ_f =0.39MPa, τ_m = 0.01MPa, s_2=0.015mm, s_3=0.02mm.

g) τ_{max} = ∞ (Perfect bond).

Apart from the scenarios (a) – Genesio/Fabbroccino calibration and (g) – Perfect bond, in all other scenarios, the beam flexural hinging and bond failures governed the response. This was as described in §9.4.2 for the benchmark FE model of NS-R1, which adopted the scenario (b) bond parameters. Several immediate conclusions can be drawn from the results shown in Figure 9.30:

a) For plain round bars, the τ_{max} and τ_m parameters do not have significant influence on the overall F_c-Δ_c response, as evident from the comparison of scenario (b) versus (d), and scenario (e) versus (f). This was true for the case of low slip capacity (s_2=0.015mm and s_3=0.02mm), as the local bond failure quickly led to debonding and re-distribution of steel strains along the debonded length (as discussed in §5.7.2).

b) The bond parameter τ_f governs the development of steel stresses, beam flexural capacity and the F_c response. The increase of τ_f in scenario (c), (f) and (d), while holding other parameters constant, corresponds to similar increase in the F_c envelope.

c) As with the NS-O1 analyses, the bond slip limits (s_2 and s_3) influences the post-peak response of the beam-column joint model significantly. In scenario (a: s_2=0.1mm and s_3=1.0mm), the bond failure and yielding of the beam bars were followed by joint shear failure and the loss F_c at approximately Δ_c = 25mm. In contrary, in scenario (b: s_2=0.015mm and s_3=0.02mm), the lack of slip capacity of the bond led to rapid debonding of the steel reinforcement and distributed steel strain. Therefore, a more stable F_c plateau beyond the initial bond failure was achieved in scenario (b).

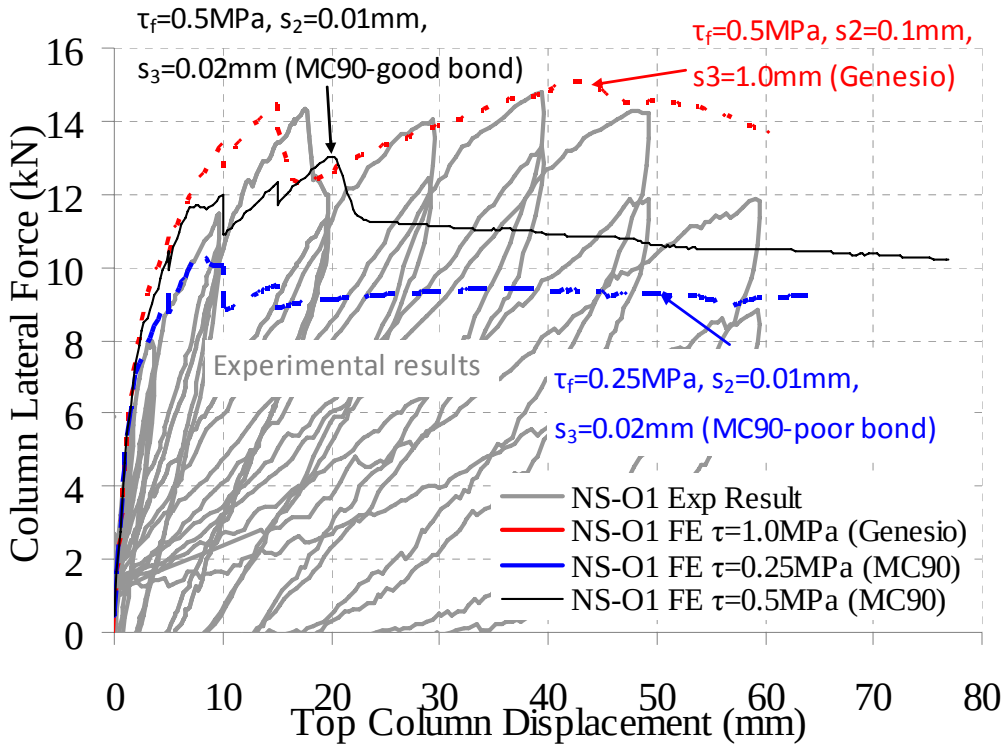

Figure 9.29: Influence of bond parameters on the monotonic Pull F_c-Δ_c response for NS-O1 model.

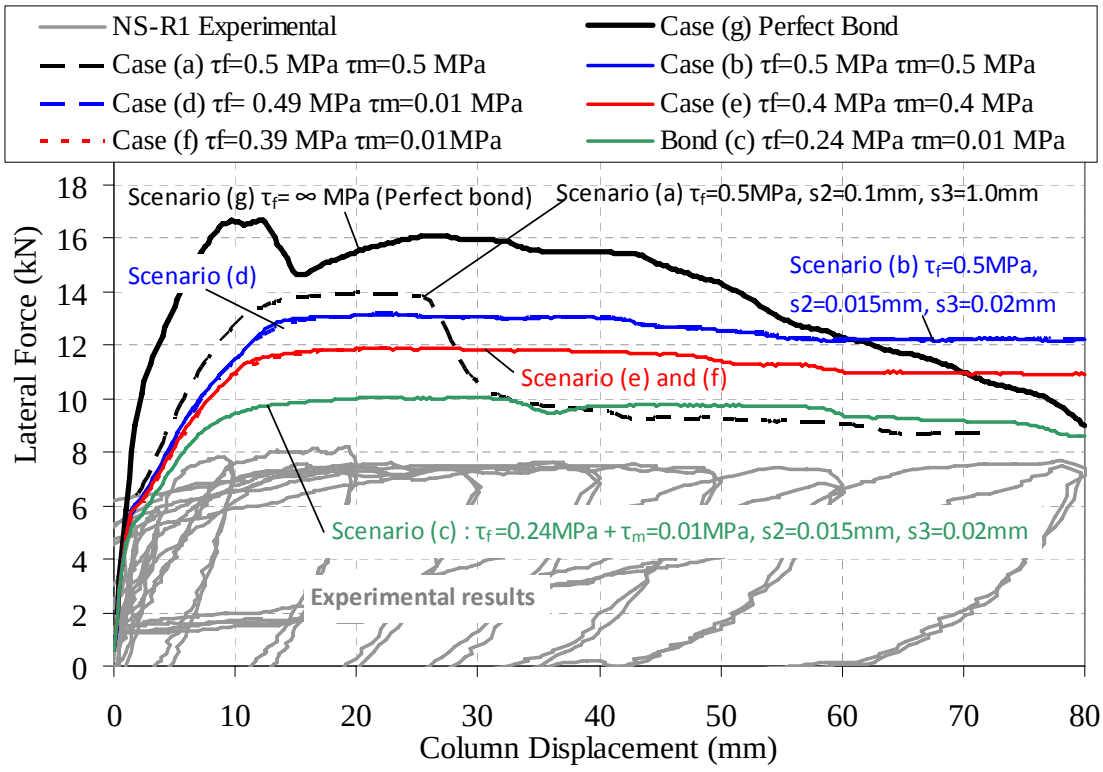

Figure 9.30: Influence of bond parameters on the monotonic Pull F_c-Δ_c response for NS-R1 model.

9.4.3.2 Possible explanation for the over-estimation of the lateral strength in NS-R1

As discussed in the preceding sections and apparent from Figure 9.30, there is a consistent over-estimation of the lateral capacity (F_c) and beam moment capacity, especially in the weakened beam direction, regardless of the bond assumption. It is believed that this over-estimation arises from the peculiarity of a single large flexural crack phenomena due to the use of the plain round reinforcement. This has been previously discussed in detail in §5.2 and §6.2.1 in light of the experimental observations of NS-O1 and NS-R1. Instead of distributed cracks along a plastic hinge length, RC members with plain round bars exhibit a large beam-end crack due to the bond failure and subsequent debonding of the plain bars within the cracked segment. This is illustrated schematically in Figure 9.31.

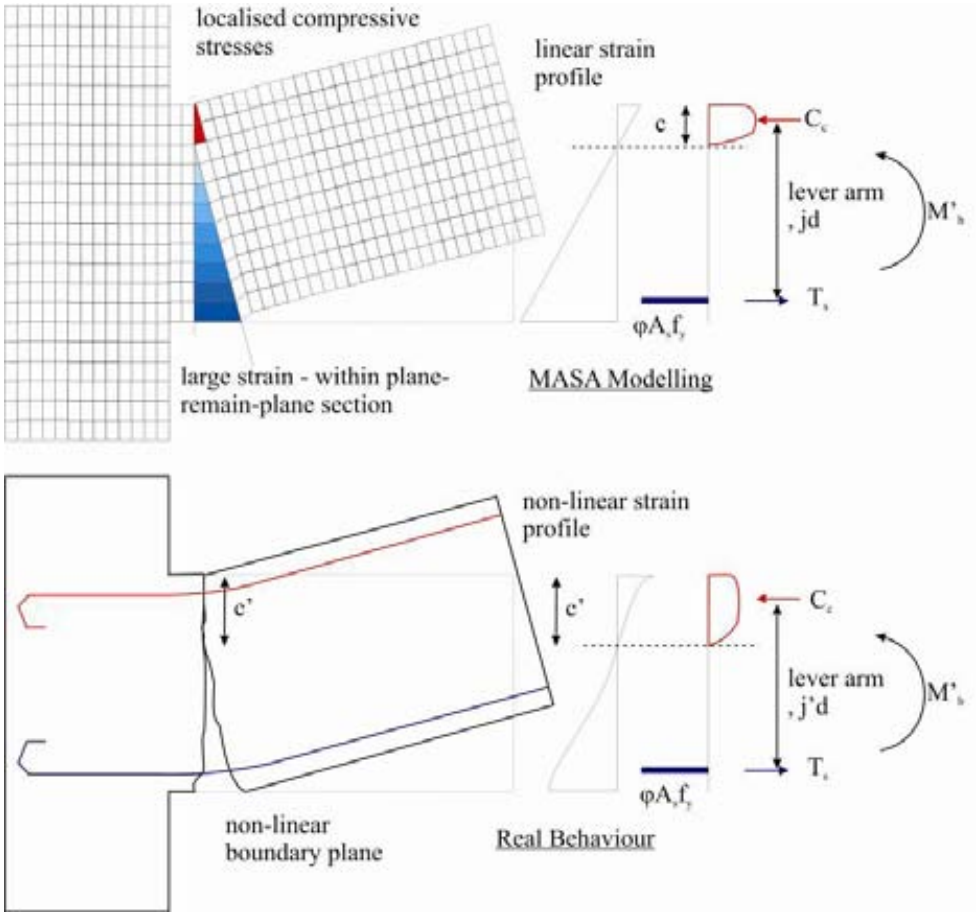

Figure 9.31: Effect of non-linear strain profile and section on the neutral axis, lever arm and flexural capacity of RC beams with plain round bars and discrete flexural crack.

While the FE analyses capture the single flexural crack and the bond failure phenomena, the section moment lever arm, neutral axis depth and concrete compressive components may be

incorrectly modelled due to the plane section assumption inherent in the FE model. In the actual RC element, the plane section assumption is significantly violated when severe bond degradation (debonding) occurs along the beam reinforcement. This was previously observed in all the test results presented in Chapters 5 to 8 as well as in existing literature (e.g. [83, 121]).

Figure 9.31 compares the postulated difference between the FE MASA model and the 'real' behaviour of the NS-R1 beam-column connection. The non-linear strain profile and the non-linear boundary plane along the beam-end crack results in larger neutral axis as larger concrete compression force, C_c is required to balance the tensile force, T_s. The larger neutral axis leads to a smaller moment lever arm and a smaller beam flexural capacity. Conversely, for the FE model, the linear strain profile (from a plane-section assumption) will result in a localised compressive region, a smaller neutral axis and a larger moment lever arm. Therefore, a higher beam flexural capacity and F_c response can be expected for the FE model.

9.4.3.3 Influence of the variation of column axial load on NS-R1

Four sets of monotonic analyses under both the Pull and Push loadings, with and without the variation of axial loads, were carried out to understand the effects of the variation of axial loads. As the dominant inelastic behaviour was beam flexural hinging and bond failure of the beam reinforcement, it was expected that the variation of column axial load would not affect the monotonic behaviour significantly. The comparisons of two pairs of analyses with and without the variation of column axial load are presented in Figure 9.32. Minor increase in F_c was observed in the Pull loading for the constant axial load case, as the higher column axial load marginally improved the bond of the embedded beam reinforcement.

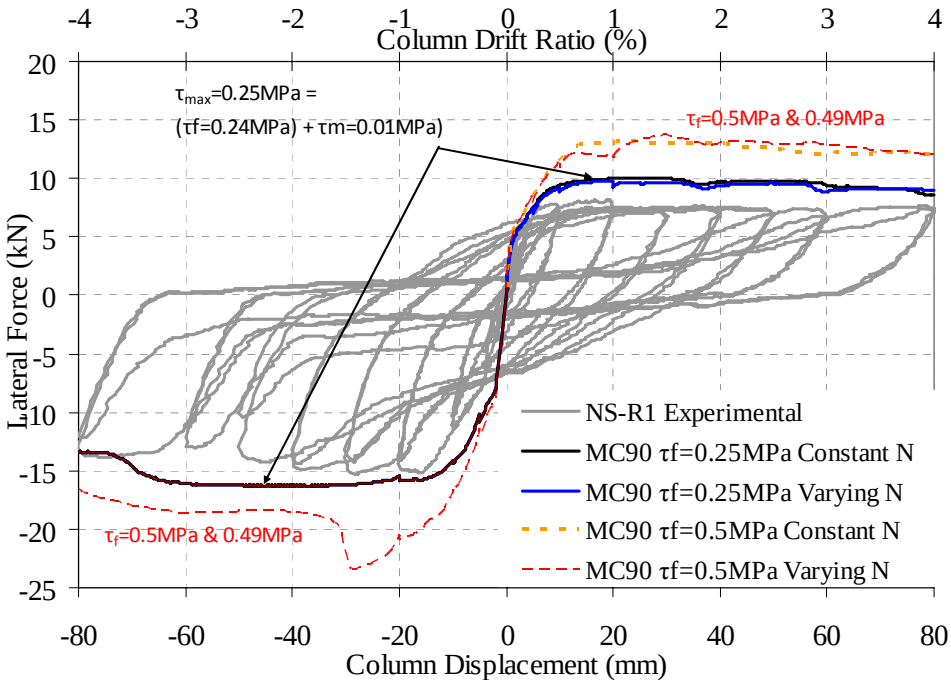

Figure 9.32: Influence of the variation of column axial load on NS-R1 beam-column joint.

9.4.3.4 Effects of different beam-weakening configurations for NS-R1

Further parametric analyses are carried out using the benchmark NS-R1 model, which is presented in §9.4.2, to study the effects of the different levels and configurations of beam-weakening in the retrofit of the beam-column joints.

Figure 9.33 summarises the monotonic responses of four different beam concrete cut depths (40mm, 80mm, 160mm and 330mm) for two different bond parameters (scenarios (c) and (b) as per §9.4.3.1). The cut depth refers to the distance from the beam soffit of which the concrete solid elements were selectively weakened within the FE model. In general, the reduction of concrete cut depths corresponds to a reduction in lateral capacity of the beam-column joint. For beam-column joint with the weaker bond (scenario c), bond failure always dominate the overall response. For joints with 'good' bond (scenario b), a scattered result is obtained, which indicates further analyses are required to confirm the behaviour.

Figure 9.34 summarises the monotonic responses of four different beam reinforcement weakening level (50% bottom bars with no re-grouting, 50% top and bottom bars with no re-grouting, 100% bottom bars and 50% bottom bars with concrete re-grouting) for two different bond parameters (scenarios (c) and (b) as per §9.4.3.1). As expected, the 100% bottom bars weakening yields a low level of lateral capacity. There is no significant difference between 50%

bottom bars weakening and 50% top and bottom bars weakening, in both bond scenarios. Re-grouting the cut-concrete with strong grout (restoring the concrete elastic properties) increases the overall lateral capacity by 15-30% for poor bond scenario, but it does not have any significant impact on the good bond scenario.

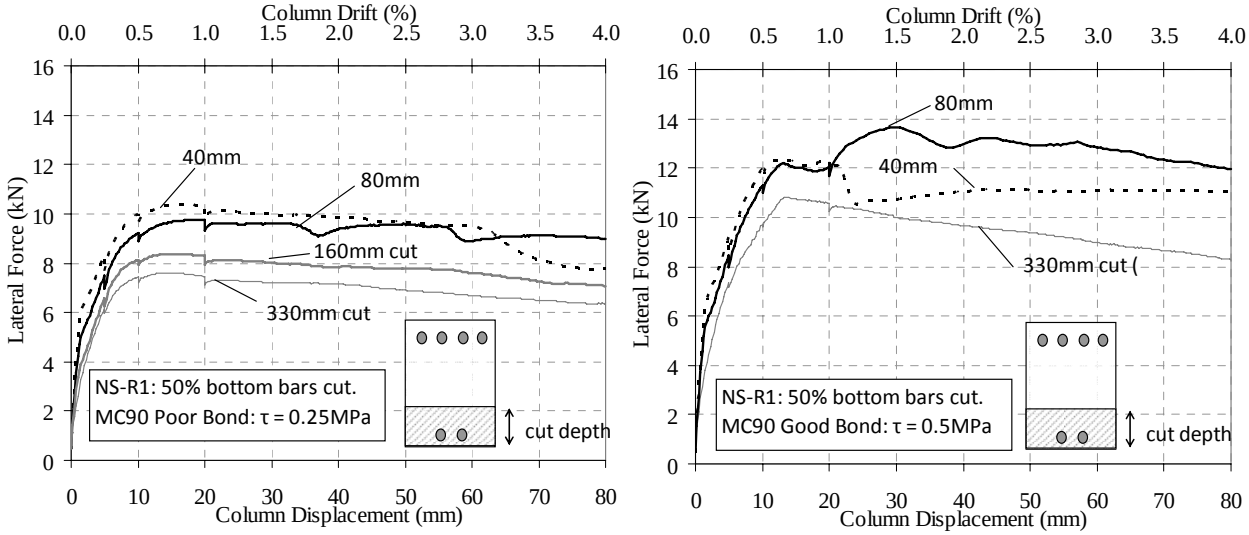

Figure 9.33: Effects of different levels of beam concrete depth weakening: i) Bond scenario (c) – τ_f=0.25MPa ; ii) Bond scenario (b) – τ_f=0.50MPa.

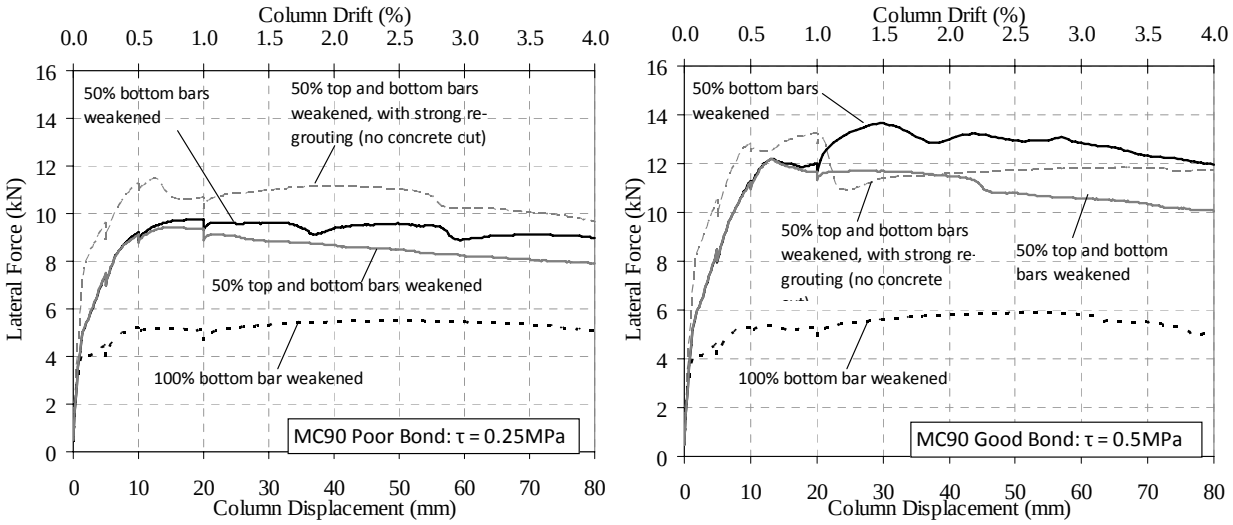

Figure 9.34: Effects of different levels of beam reinforcement weakening.

9.4.4 Modelling of external post-tensioning joint retrofit

While not presented in this chapter, preliminary work were done on the modelling of external post-tensioning of joint for seismic retrofit, as per test units NS-R2, NS-R3 and NS-R4. Figure

9.35 illustrates the modelling strategy for selective weakening and post-tensioning retrofit of beam-column joint within the MASA FE model environment.

Linear steel anchorage plate elements can be used as the anchorage of the post-tensioning forces. Post-tensioning tendon is modelled using bi-linear elastic solid material with properties reflecting the high strength prestressing steel.

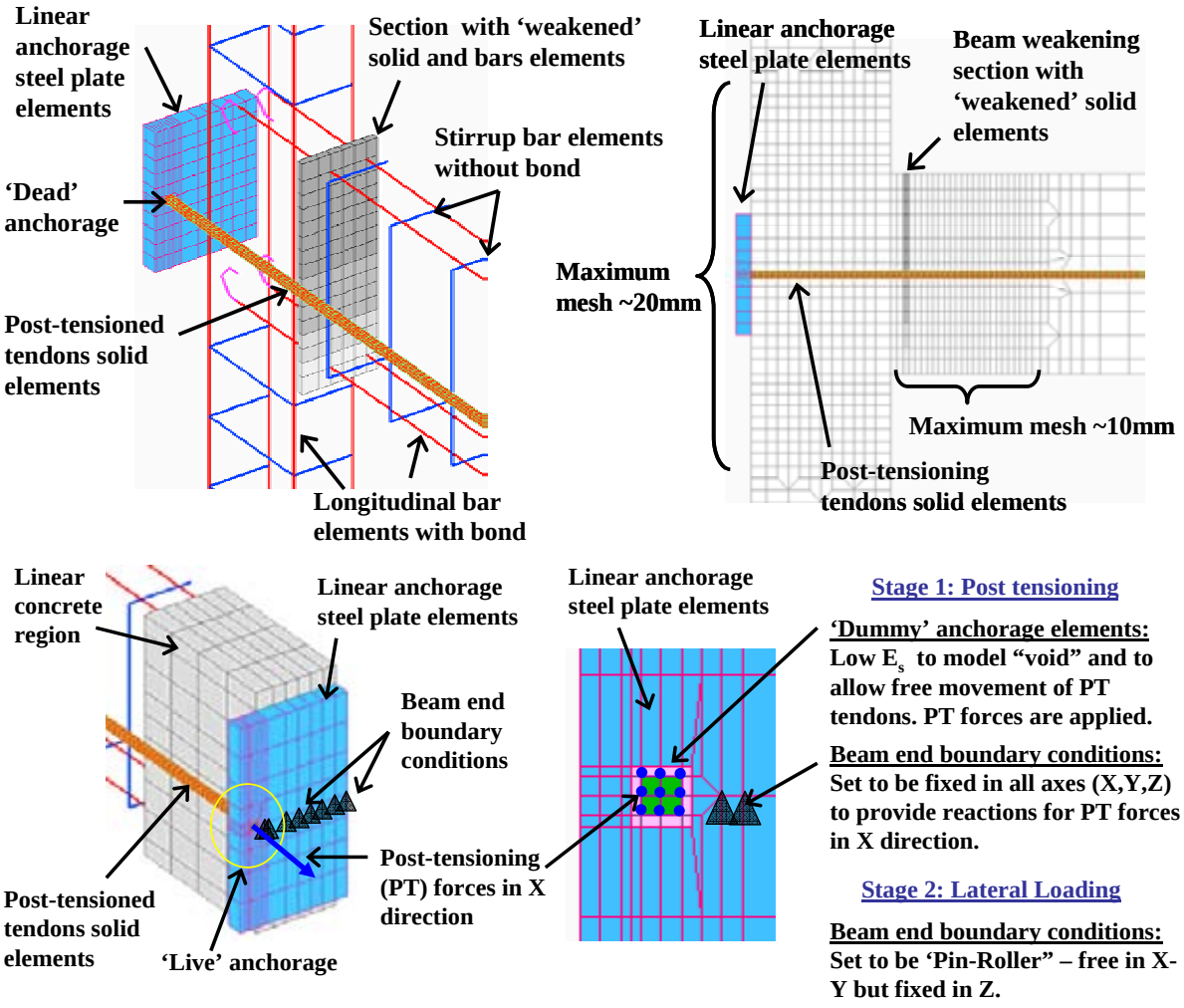

Figure 9.35: Modelling strategy of selective weakening and external post-tensioning retrofit (NS-R3).

In the 'dead' anchorage end, the post-tensioning tendon has coincidental nodes with the anchorage plates, allowing force transfer along the diameter of the tendon to the linear but very stiff anchorage plate. Realistic geometry modelling of the anchorage plates will simulate the correct bearing confinement and force transfer into the beam-column joint. In the 'live' anchorage end, a layer of dummy anchorage elements can be used in the interface layer between the post-tensioning tendon and anchorage plate.

In order to simulate post-tensioning, two phases of loading (analyses) have to be carried out, as summarised in Figure 9.35. In the first stage, the nodes along the anchorage plate on the beam-end boundary are fixed in all six degrees of freedoms. A low Young's modulus (E) is assigned to the dummy element to model 'void' between the tendon and the anchorage. Post-tensioning force is then applied on the 'free' end of the tendon. In the second phase, the dummy element's E is updated to a very high value, and therefore, effectively locking the post-tensioned tendon with the anchorage plate. The beam end boundary conditions are then changed to a roller pin, where the vertical displacement is fixed. Then, lateral load can be applied to the top of the column.

However, at the time of writing, the MASA FE programme is under the development to allow for the two-step loadings as described above. Considering the complexity of the proposed model, the MASA modelling of the full Selective Weakening retrofit (beam weakening and joint post-tensioning) is beyond the scope of this research.

9.5 DYNAMIC RESPONSE OF AS-BUILT & RETROFITTED RC FRAMES

9.5.1 Introduction

§3.4.2 outlined a simplified displacement-based seismic design procedure that relates the local lateral strength and deformation capacities of the individual elements (beams, columns and joints) to the global capacities of the retrofitted frame. To illustrate and verify the retrofit design procedure, a case-study pre-1970s RC frames building is analysed using non-linear dynamic analysis for as-built and two retrofitted scenarios.

Two retrofit outcomes are explored, using two different Selective Weakening (SW) retrofit techniques: a) beam-weakening only (R1) and b) beam-weakening and post-tensioning (R3). As measures of performance, the following response parameters are analysed, with respect to the performance-based seismic engineering discussed in Chapter 3:

a) Maximum inter-storey drift, θ_{drift}.

b) Local elements' deformation demands (in the columns, beams and joints).

Previous numerical studies of as-built non-ductile RC frames as well as retrofitted RC frames have been briefly reviewed in §9.2.3. For this study, careful attention is given to the correct representation of the beam-column joint connection, using rotational-spring macro modelling approach [5, 51, 94, 111].

9.5.2 Case study building and structural model

The case study six-storey three-bay RC frame is designed to simulate the typical mid-rise residential/commercial multi-storey building of pre-1970s building stock. It is the same prototype building, which is described in §4.2.1 and used for the design of the experimental beam-column joint sub-assemblies in Chapter 4. Poor material properties, deficiencies in reinforcement detailing and violation of capacity design philosophy are intently included in the prototype structure. The global geometry and the 2nd floor beam-column joint geometry are shown in Figure 9.36.

It is symmetrical in plan and consists of four three-bay RC frames on each direction. The columns are tapered from 15" (380mm) squares at first two floors to 14" (350mm) squares at upper stories. The beams are 19.5" (495mm) deep by 13.75" (350mm) wide. Column stirrups are typically 3/8" bars at 6" spacing (i.e. 9.5mm diameter at 150mm centres) while beam stirrups are 3/8" bars at 8" spacing (9.5mm diameter at 200mm centres). Beam-column joints are not reinforced with stirrups. The beam longitudinal bars are anchored into the exterior joints are using double 180° hooks for both the top and bottom beam reinforcement. The reinforcing details for the exterior beam-column joints are shown in Figure 9.36.

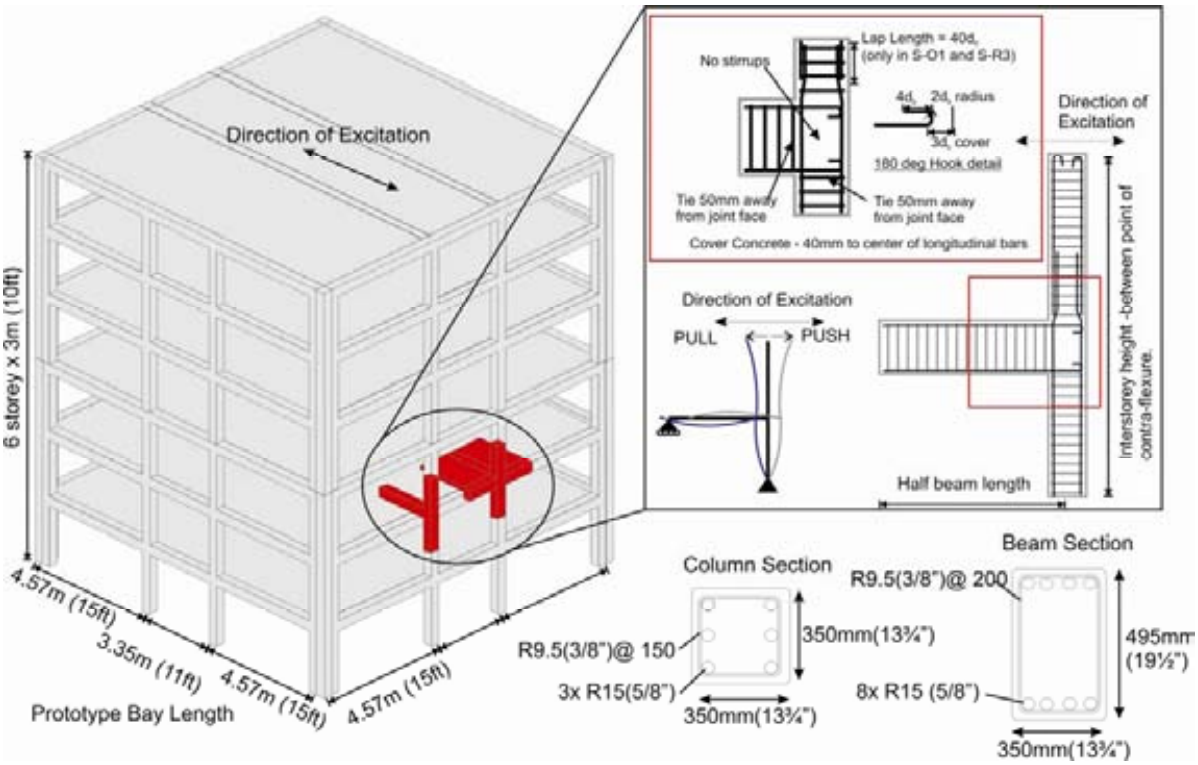

Figure 9.36: Geometry and structural detail of the case study RC frame building (reproduced Figure 4.1).

Several non-ductile structural details are omitted from this study in order to reduce the complexity of the non-linear model. Column reinforcement is spliced with $40d_b$ lapping length, but this is omitted in the numerical model in light of the experimental results presented in Chapter 7. The floor slab and transverse beam contribution to the beam negative moment and joint shear strength are not included, as with the gravity static loads. This assumption is made considering the results of Chapter 8, which suggests the higher beam negative moment will be counter-balanced by the gravity static load. §9.5.4 will describe the numerical model and assumptions, while §9.5.5 will describe beam-column joint modelling adopted in this study. §9.5.6 will discuss the assumptions made in modelling the retrofitted frames.

The seismic assessment methodology described in §2.4 is used to derive the individual elements moment-curvature capacities. Noting that the same prototype frame and connections are used, the seismic assessment of individual elements have been carried out in Chapter 4 and presented in Appendix A for the 2/3-scaled beam-column joints connections. The moment-curvature of beams, M-N interaction diagram of columns and moment-rotation of rotational joint springs are presented in Figure 9.37a-c. Figure 9.37d shows the hierarchy of strength performance domain of the 2nd floor exterior beam-column joints (which coincides with the experiment joint subassembly). The assumed material properties are: the concrete compressive strength, f'_c = 20MPa and the yield and the ultimate strengths of steel reinforcement, f_y = 300MPa and f_{ult} = 410MPa.

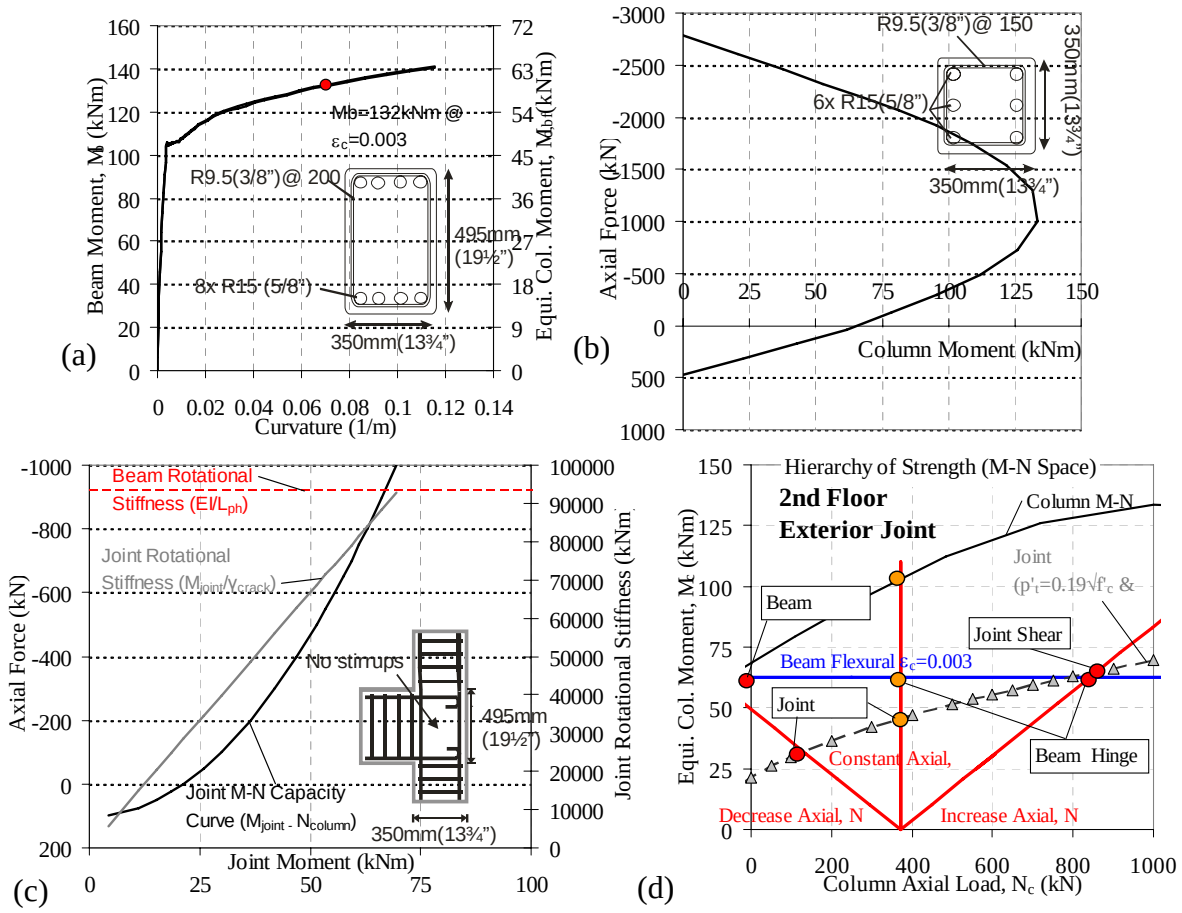

Figure 9.37: Examples of evaluation of elements capacity and hierarchy of strength: a) Moment-curvature of beam; b) M-N interaction diagram of columns; c) M-N interaction diagram of rotational joint springs; and d) Hierarchy of strength of the beam-column exterior joint at the 2nd storey.

9.5.3 Selective Weakening retrofit design

The Selective Weakening (SW) retrofit design adopts the direct displacement-based design (DDBD) procedure outlined in §3.4.2. Given the geometry and seismic mass of the building, and the seismicity of the site, the available local strength and deformation capacities of the individual elements (beams, columns and joints) are correlated to the global performance levels in terms of average maximum inter-storey drifts (assuming a beam-sway mechanism) of the retrofitted frame.

Table 9.6 summarises the DDBD parameters for the SW retrofit design of the six-storey prototype frame for a 2.0% design drift, assuming the Wellington seismicity according to the NZS1170:5 [101] with a peak ground acceleration (PGA) of 0.4g, the S_p factor of 1.0 and an assumed system equivalent viscous damping ξ_{sys} of 10%. This is but one retrofit design example and depends on different local retrofit interventions at the beam-column joints, different performance levels can be attained.

The S_p factor is defined in the NZS1170:5 to account for additional conservatism in the design, and is a function of the structural ductility, μ. The S_p factor ranges from 1.0 for μ = 1 (elastic structure) to 0.7 for $\mu \geq 2$. For the displacement-based retrofit design, it is recommended to assume a S_p of 1.0 and to directly include a more realistic ξ_{sys}. However, in order not to unnecessary penalise the displacement-based retrofit design, the S_p as a function of μ can be used with a conservative estimation of the damping ξ_{sys}.

Table 9.6: DDBD parameters for the Selective-Weakening retrofit design of the six-storey prototype RC frame for the Wellington seismicity, with Z=0.4g, S_p=1.0 and an assumed system viscous damping, ξ_{sys}=10%.

SDOF design displacement		0.105	m	SDOF design interstorey drift		2.0	%
SDOF effective height		11.820	m	SDOF equivalent viscous damping		10.00	
SDOF effective mass		494	tonnes	SDOF design base shear		475.4	kN
SDOF effective period		1.04	sec	SDOF base overturning moment		5913.3	kNm
Beam Design Moment	Level 1-2	190.5	kNm	Column Design Moment	Interior L1-3	285	kNm
	Level 3-6	94.3	kNm		Exterior L1-3	143	kNm
		Exterior Column 1	Interior Column		Interior L4-6	242	kNm
Column Axial Load	Base: N_{G+Q+E}	90.0	1620.1		Exterior L4-6	121	kNm
Column Axial Load	L3: N_{G+Q+E}	348.3	946.1				

Figure 9.38 presents a series of design curves, which relate the targeted design inter-storey drift with the exterior beam-column joint's beam flexural design moment. The curves are derived using the method outlined in §3.4.2. For example, the R1 retrofit solution, which involves 50% beam bottom bars weakening, has a beam moment capacity, M_b of 88.5kNm (or 40.1kNm in terms of the equivalent column moment, $M_{c,bf}$). This corresponds to a design inter-storey drift of 1.8% for the prototype frame, under the Wellington seismicity, a S_p factor of 1.0 and an assumed system equivalent viscous damping ξ_{sys} of 10%.

Thus, Figure 9.38 is an example how the SW retrofit strategy, by the different combinations of beam-weakening and joint post-tensioning retrofit techniques, can achieve different retrofit performance objectives. The performance limits shown in Figure 9.38 refer to the performance limit states described in §3.1.2: a) Advanced Performance (AP) / Enhanced Rehabilitation Objective (ERO); b) Basic Performance (BP) / Basic Safety Objective (BSO); and c) Limited Performance (LP) / Collapse Prevention (CP).

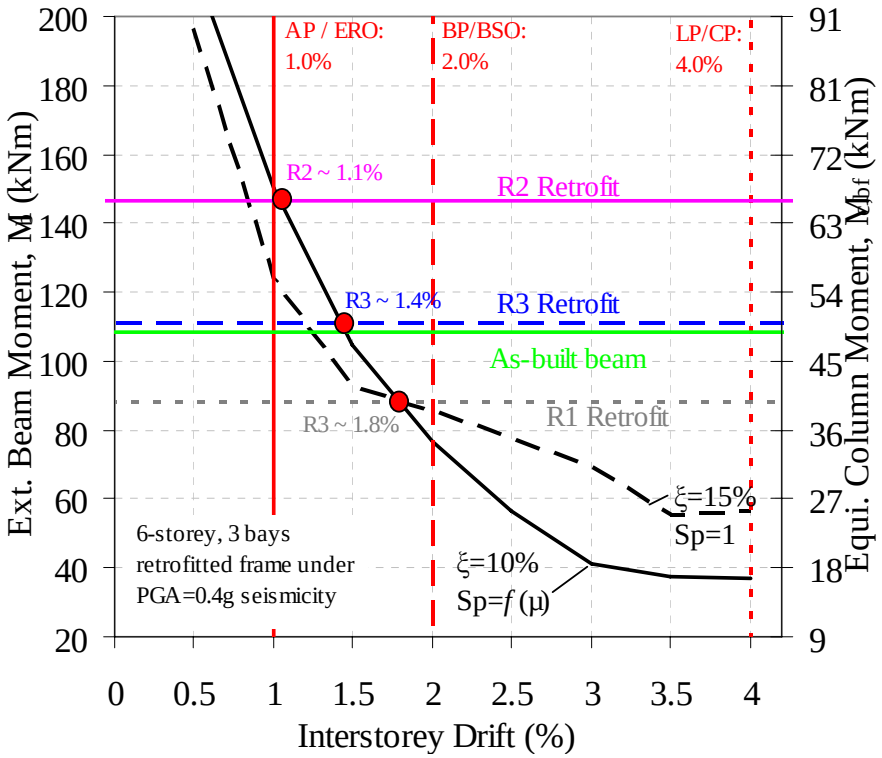

Figure 9.38: DDBD retrofit design for the prototype 6-storey 3-bay RC frame under Wellington (PGA=0.4g) seismicity. Three retrofit solutions are shown corresponding to R1, R2 and R3 designs as per §4.2.

As the prototype frame is previously adopted for the experimental beam-column joint subassemblies, thus, there is no need to re-design the retrofit solutions R1, R2 and R3 for the numerical study in this chapter. The experimental retrofit solutions, as summarised in Appendix A, are adopted as the design beam hinge flexural capacities. The hierarchy of strength performance domain for each 2/3-scaled retrofitted beam-column joints is scaled up using the following relationship for the full-scale prototype beam-column joints:

$$M_{b,prototype} = (\chi^3) M_{b,model} \quad \textbf{9.1}$$

$$V_{b,prototype} = (\chi^2) V_{b,model} \quad \textbf{9.2}$$

$$N_{prototype} = (\chi^2) N_{model} \quad \textbf{9.3}$$

where χ is the scaling factor i.e. 2/3, and M_b, V_b and N are the elements' moment, shear and axial capacities within the M-N performance domains.

The local retrofit design at the exterior beam-column joints level must first satisfy the capacity design requirements of weak beams, strong columns and joints. This is achieved by

satisfying the correct hierarchy of strength within each beam-column joint. For this thesis and the design procedure proposed in §3.4.2, there is an important underlying assumption that the (as-built or retrofitted) interior beam-column joints can sustain the necessary strength or deformation/ductility demand in order to achieve a beam-sway or a mixed inelastic mechanism (as discussed in §3.3.3.1). The seismic retrofit of the interior beam-column joints and the columns is beyond the scope of this thesis.

9.5.4 Description of analyses and numerical model assumptions

The non-linear time-history (NLTH) analyses are performed using the finite-element program RUAUMOKO [25]. As the prototype building was regular, two-dimensional (2D) frames modelling is adequate. A Newmark-beta integration scheme with a Rayleigh damping model proportional to the tangent stiffness is adopted. P-delta effects are ignored. Lumped mass and lumped plasticity modelling are adopted, where inelastic deformations are limited to discrete inelastic rotational springs in the joints, beams and columns. The numerical model of the prototype frame is illustrated in Figure 9.39.

The beams and columns are modelled using the Giberson frame elements with thin modified Takeda hysteresis (α=0.5, β=0) [103] (shown in Figure 9.41a). Cracked concrete section stiffness are used for the Giberson elements following the recommendations of Paulay and Priestley [113]. The cracked section modulus for the column was taken to be $0.6I_g$, in which I_g is the gross section modulus. This approach is used, instead of deriving the flexural stiffness from the moment-curvature plot, for simplicity as the uncertainty from the variation of axial load can affect the initial stiffness estimation. For the beam sections, the cracked section modulus is taken as the secant stiffness at the 75% of the yield moment [113].

The seismic mass, assumed static loading and the fundamental periods of models are summarised in Table 9.7. Further details are given in Appendix G. §9.5.5 will describe the beam-column joint model and §9.5.6 will briefly discuss the modelling of the retrofitted frames. The input ground motions used for the non-linear time history analyses are described in §9.5.7.

In order to simplify the analyses, the following assumptions (in addition to those mentioned) were made with respect to the numerical models used:

a) Effective diaphragm action of the cast-in-situ floor slabs was assumed to sufficiently transfer all seismic inertia forces to the lateral frame.

b) No beam elongation was modelled and the column centreline nodes remained equi-distant in relative to each other at the same floor level. Therefore, the lateral displacements of the column nodes at each level were the same. This was modelled by slaving all the column nodes within the floor level to a set of master nodes, in which the seismic masses were lumped at.

c) Small deformation assumption (no change in original member dimensions).

d) The beams and columns capacities at levels one to three, and four to six, were assumed to be equal in the retrofitted frames. This assumption relies on the corollary assumptions that plastic redistributions up the building height are possible and beam-hinging mechanism will dominate the response.

Table 9.7: Summary of global properties of numerical model.

Analysis time-step	0.005s	Seismic Masses at Level 1-5	262.4kN
Damping at 1st and 3rd modes	5%	Seismic Masses at Level 6 (roof)	125.0kN
		Column static loads	
Level 1-5 exterior columns	-338.8kN	Level 6 exterior columns	-91.5kN
Level 1-5 interior columns	-192.0kN	Level 6 interior columns	-158.6kN
		Level 6 exterior columns	-91.5kN
		Level 6 interior columns	-158.6kN

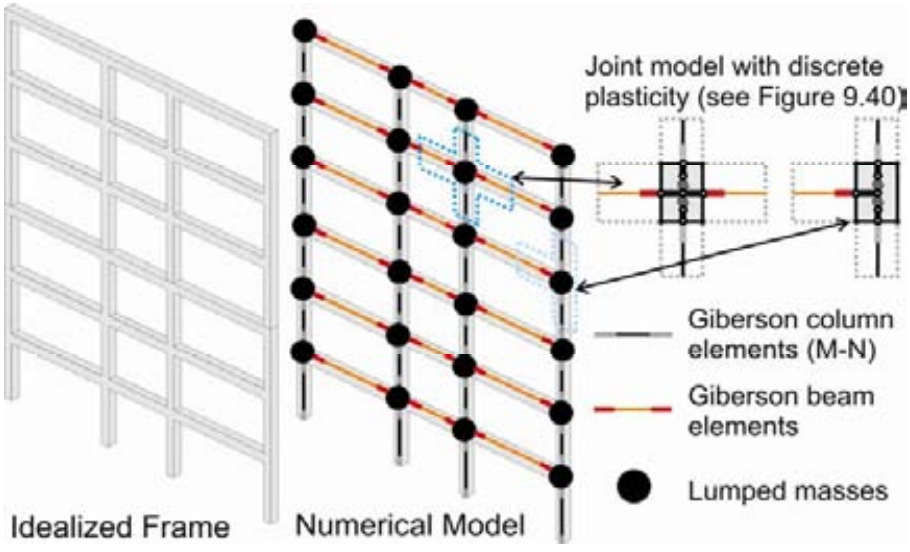

Figure 9.39: Structural model of the prototype frame.

9.5.5 Beam-column joint modelling

The beam-column joints are modelled using lumped plasticity rotational springs, connecting in series between the column nodes and the joint nodes. The beam-column joint modelling strategy

is illustrated in Figure 9.40. Realistic geometrical offset is included by offsetting the columns' and beams' end nodes from the joint centreline node with rigid links. The plastic hinge lengths (l_{ph}) are taken to be ½ of the section depth for both the beams and columns [113].

Two rotational joint springs, with the Wayne-Stewart hysteresis rule to model cyclic strength degradation, stiffness degradation and pinching hysteresis behaviour, were used for the joint panel zone for the existing RC frame. The Wayne-Stewart degrading stiffness hysteresis model [6] implemented in RUAUMOKO is shown Figure 9.41b. The Wayne-Stewart hysteresis parameters are previously calibrated against the experimental results of non-ductile beam-column joints with plain round bars [82].

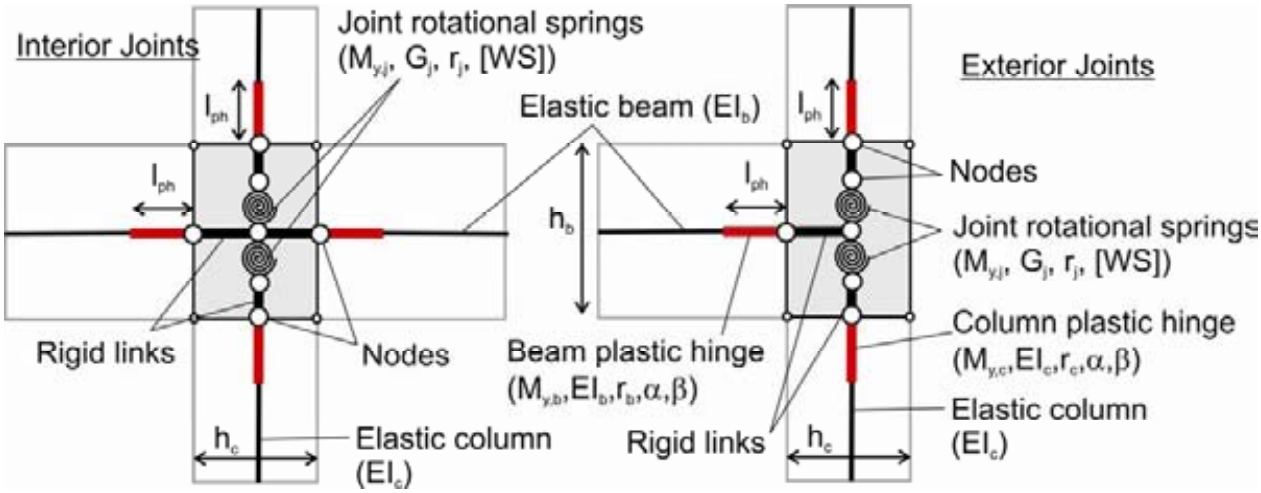

Figure 9.40: The modelling of interior and exterior beam-column joints.

As the retrofitted beam-column joints are not expected to have any joint shear failure, evident from the experimental results presented in Chapter 6, the modified Takeda hysteresis [103] was used to model the retrofitted joints. "Thin" modified Takeda hysteresis loops was used to reflect the loss of stiffness due to the bond-slip failure under cyclic loading, despite the improved backbone behaviour of the joint due to beam-weakening and/or joint post-tensioning. Table 9.8 summarises the joint hysteresis models parameters used in the analyses.

To determine the strength of the joint rotational spring, the principal stresses approach described in §2.4.2 is adopted. For the as-built joint, the ultimate capacity of the joint corresponds to the joint shear cracking p'_t of $0.19\sqrt{f'_c}$ MPa. For the retrofitted joints, the joint shear strengths are calculated using the procedure described in §3.4.4.2 and §3.4.6. The initial rotational stiffness, G_j, is taken to be M_j/γ_j, where M_j and γ_j are the ultimate joint moment capacity

and the corresponding peak joint shear distortion respectively. γ_j is taken to be 0.15% following the discussion in §5.7.1.

Interior beam-column joints are not considered in great detail in the numerical model as they are out of the scope of the research. The limit states suggested by Priestley *et al.* [116] are used to derive the equivalent moment-rotation capacity curve for the interior joints. The same modelling technique for exterior joint is used for the interior joint, as illustrated in Figure 9.40.

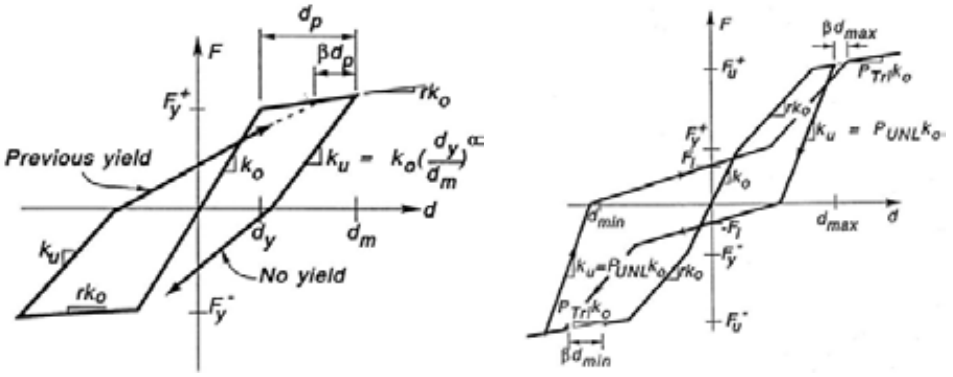

Figure 9.41: Hysteresis rules used in the numerical model: a) Modified Takeda hysteresis [103]; b) Wayne-Stewart hysteresis rule [6]. Figures are taken from ref. [25].

Table 9.8: Joint hysteresis models parameters

As-built joints: Wayne-Stewart pinching hysteresis					
Yield moment (kNm)	F_U	55.4kN	Post-yield stiffness	r	-0.001
Intercept moment (kNm)	F_I	$0.5F_U$	Unloading stiffness	PUNL	0.8
Tri-linear factor beyond FU	P_{Tri}	-0.001	Beta or Softening Factor	β	1
Positive Gap (m)	Gap+	0	Alpha or reloading/pinching factor	α	0.8
Negative gap (m)	Gap-	0	Loop type	-	1
R1 (beam-weakening only) retrofitted joints: Modified Takeda hysteresis					
Alpha or unloading stiffness	α	0.5	Beta or reloading stiffness	β	0
reloading power stiffness	NF	1	Unloading curve type	KKK	2
Post-yield stiffness	r	0			
R3 (weakened+post-tensioned) retrofitted joints: Modified Takeda hysteresis					
Alpha or unloading stiffness	α	0.3	Beta or reloading stiffness	β	0.2
reloading power stiffness	NF	1	Unloading curve type	KKK	2
Post-yield stiffness	r	0.02			

9.5.6 Selective-weakening retrofitted frames modelling

In the SW-retrofitted frames' numerical models, only the beams' and joints' inelastic properties are changed in order to account for the effects of the beam-weakening and joint post-tensioning retrofit intervention. For both retrofit interventions, the ground floor exterior columns are

assumed to be given strength and ductility retrofit (e.g. FRP or concrete jacketing) as this is necessary to achieve stable beam-sway mechanism. Table 9.9 summarizes the properties of retrofitted elements.

Table 9.9: RUAUMOKO model properties of retrofitted elements.

R1 (beam-weakening only) retrofitted joints: Modified Takeda hysteresis					
Ground floor exterior columns			Alpha or unloading stiffness	α	0.3
M-N interaction capacity	-	1.2 x M-$N_{as-built}$	Beta or reloading stiffness	β	0.2
Weakened beams					
Positive moment (kNm)	-	63	Post-yield stiffness	r	0
Negative moment (kNm)	-	unchanged	Alpha or unloading stiffness	α	0.5
Initial stiffness (kNm)	K_o	0.9 x $K_{o-as-built}$	Beta or reloading stiffness	β	0
R3 (weakened+post-tensioned) retrofitted joints: Modified Takeda hysteresis					
Ground floor exterior columns			Alpha or unloading stiffness	α	0.3
M-N interaction capacity	-	1.2 x M-$N_{as-built}$	Beta or reloading stiffness	β	0.2
Weakened beams (Level 1 to 3)					
Positive moment (kNm)	-	95 *	Post-yield stiffness	r	0.005
Negative moment (kNm)	-	-127 *	Alpha or unloading stiffness	α	0.3
Initial stiffness (kNm)	K_o	1.37 x $K_{o-as-built}$	Beta or reloading stiffness	β	0.2

* Level 4 to 6 beams have half the capacities of the lower floors.

For the R1-retrofitted frame, the beam-weakening is modelled by a reduction of the beam negative moment capacity and the beam initial stiffness. The rotational joint springs in the exterior joint panel zone are assessed using a higher p'_t (~$0.29\sqrt{f'_c}$ MPa) to account for the effect of reduced beam-depth. As the joints are not expected to crack, there will be less severe strength and stiffness degradation in the R1-retrofitted connections. Therefore, the thin modified Takeda hysteresis was used for the rotational joint springs.

For the R3-retrofitted frame, the beam-weakening and post-tensioning increase both negative and positive beam capacities, as well as the initial stiffness of the beams. The un-bonded post-tensioning of the beam-column joint also increases the post-yield stiffness of the beam. As shown in Table 9.8 and Table 9.9, slight increases in the damping capacity of the beam and joint elements are assumed for the R3-retrofit. For R3-retrofitted frame, the modified Takeda parameters, α and β, are changed to 0.4 and 0.2 respectively.

9.5.7 Far-field and near-fault input ground motions

Two suites of strong ground motion records are used, representing both far-field and near-fault events. All records are taken from the PEER online strong ground motion database [114]. The

characteristics of the both far-field and near-fault suites of scaled records are presented in Table 9.10. The earthquake characteristics of the scaled earthquake records and the scaled acceleration spectra are presented in Figure 9.42.

The first suite of earthquakes is an ensemble of seven scaled historical 'far-field' (without any directivity effect) strong ground motion records. These records are related to soil types C or D (NEHRP categories), with hypocentre depth ranging between 13 and 25km, and are generated by earthquakes of moment magnitude, M_w, ranging from 6.7 to 7.3. The second suite of earthquakes is an ensemble of seven historical near-fault earthquake records, which are selected based on its PGV/PGA ratio (at least 0.09 ms-1 / ms-2) and distance from fault (less than 10km). Records on shallow and deep soils are selected, though two records on rock site are included for near-fault suite due to their compatibility with the NZS1170:5 [101] design spectra.

The scaling of the earthquake records are done in accordance to the recommendation of the NZS1170:5 [101]. The prototype building's design site is assumed to be Wellington, with the peak ground acceleration of 0.4g and a probability of exceedance of 10% in 50 years (R=1.0). Soil class C is assumed. It is noted that there are limited number of records with directivity effects that is compatible with the NZS1170:5 hazard spectra.

The scaling of the records is done by assuming a fundamental period (T_1) of 1.45 seconds. Following the NZS1170:5, the targeted period ranges are 0.4xT_1 and 1.3xT_1. This initial T_1 is based on the preliminary as-built frame model. However, the final version of the as-built model has T_1 of 1.694sec, a minor discrepancy considering the upper bound allowance of 1.3xT_1.

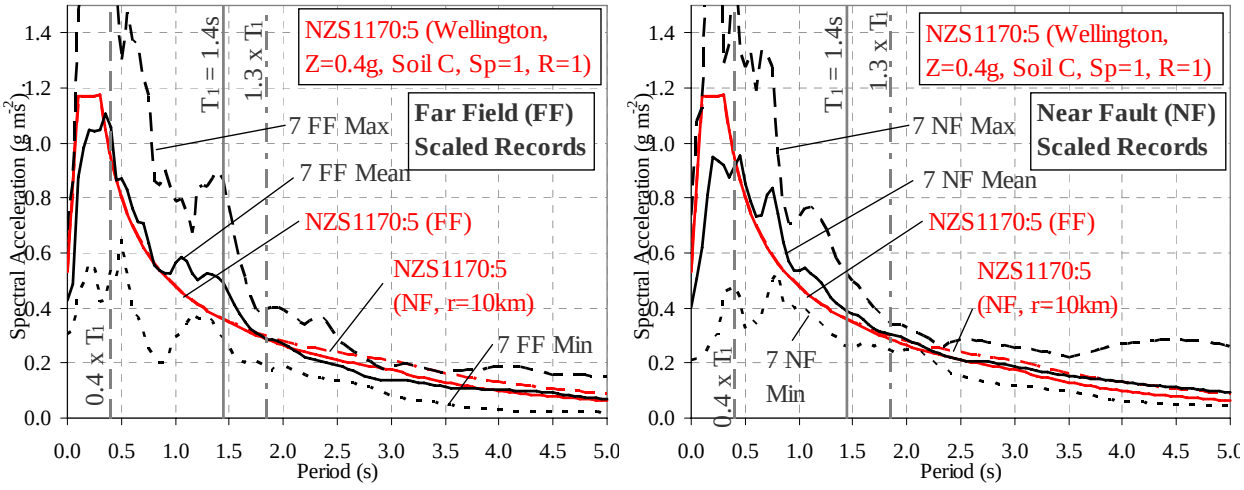

Figure 9.42: Spectral mean and maximum/minimum envelope for the scaled far-field records and near-fault records compared to the NZS1170:5 (2002) 5% damped design spectrums.

Table 9.10: Characteristics of the input ground motions. Principal horizontal direction records were used.

Name	Earthquake Event	Year	Mw	Station	Rclosest (km)	Soil Type [1]	Unscaled PGA (g)	Scaling Factor	Scaled PGA (g)	Scaled PGV (cm/s)
FAR FIELD SUITE (WITHOUT DIRECTIVITY EFFECT)										
FF1	Superstition Hills	1987	6.7	Brawley	18.2	D	0.134	3.000	0.401	51.6
FF2	Northridge	1994	6.7	Canoga Park – Topanga Clan	15.8	D	0.356	1.183	0.421	38.0
FF3	Northridge	1994	6.7	LA – Hollywood Stor FF	25.5	C	0.231	2.368	0.547	43.3
FF4	Northridge	1994	6.7	N Hollywood – Coldwater Can	14.6	C	0.271	1.653	0.448	36.7
FF5	Loma Prieta	1989	6.9	Capitola	14.5	C	0.480	1.313	0.630	47.9
FF6	Landers	1992	7.3	Desert Hot Springs	23.3	D	0.153	2.304	0.353	48.2
FF7	Landers	1992	7.3	Yemo Fire Station	24.9	D	0.210	2.010	0.421	59.7
NEAR FAULT SUITE (WITH DIRECTIVITY EFFECT)										
NF1	Northridge	1994	6.7	Newhall Fire Station	5.92	D	0.590	0.622	0.367	60.4
NF2	Northridge	1994	6.7	Sylmar - Olive view Med Ctr	5.30	D	0.843	0.485	0.408	62.8
NF3	Northridge	1994	6.7	Jensen Filter Plant	7.01	C	0.424	0.500	0.212	53.1
NF4	Imperial Valley	1979	6.5	El Centro Array# 7	0.56	D	0.463	0.616	0.285	67.3
NF5	Loma Prieta	1989	6.9	Los Gatos Pres Center	3.88	B	0.563	0.441	0.249	41.9
NF6	Tabas, Iran	1978	7.4	Tabas	2	D	0.852	0.683	0.582	82.9
NF7	San Fernando	1971	6.6	Pacoima Dam Abutment	1.81	B	1.226	0.598	0.733	67.3

[1] Soil class accordding to the NZS1170:5 (2004) classification.

Scaling the near-fault records for a uniform hazard spectra based on the recommendation of NZS1170:5 [101] has proven to be a challenging exercise. The NZS1170:5 (2004) site hazard spectra shape with its near-fault amplification at long periods is generally incompatible with the historical near-fault records (recorded in other regions around the world with a wide range of peculiar characteristics), in particular for soil class B and C. The current NZS1170:5 scaling method (NZS1170, 2004) would result in a lower excitation at the higher modes (short period) in time-history records for the near-fault suite in comparison to the far-field suite.

Several alternative approaches [126, 133] are available when dealing with near fault records to account for the higher risk and hazard resulting from the near-fault amplification and the "fling" (or velocity pulse) effect but they are not explored in this study.

9.6 RESULTS OF DYNAMIC ANALYSES

9.6.1 Dynamic properties

The dynamic characteristics of the as-built and two retrofitted frame models are given in Table 9.11. Being a pre-1970s RC frame building, in which the columns are more slender and the wall infills and partitions are heavier, the prototype RC frame has a relatively long fundamental period. For comparison, a conventional six-storey RC frame typically has fundamental period of 0.5s to 0.8s (e.g. [113]). It is noted that the prototype frame was designed to be a relatively heavy building. This is a conscious decision made during the design of the experimental test (Chapter 4), in order to induce a high variation of column axial loads on the test joint subassemblies. As such, the removal of unnecessary mass is a viable retrofit strategy that can be used in conjunction with SW retrofit of non-ductile RC frame.

Table 9.11: Dynamic characteristics of the as-built and retrofitted frame RUAUMOKO models.

Building	Period		% mass participation	
	1st mode	2nd mode	1st mode	2nd mode
As-built frame	1.694s	0.549s	83%	93%
R1 (beam-weakening only) retrofitted frame	1.734s	0.559s	84%	94%
R3 (weakened+post-tensioned) retrofitted frame	1.614s	0.524s	83%	94%

The weakening of the beam reduced the beams stiffness and therefore softened the building and lengthened the building period of R1-retrofitted building, as one would expect from the beam-weakening-only retrofit. The building stiffness was partially compensated by the

improved joint hysteresis behaviour and stiffness (recalling the joint stiffness is taken to be the ratio of joint shear capacity, M_j, and the joint cracking distortion, γ_j).

For the weakened and post-tensioned beams' flexural stiffness was approximately 35% higher than the weakening-only beams. This was expected, as the initial post-tensioning forces provided an initial decompression contribution to the initial stiffness of the connections, as observed in the experiments (presented in Chapter 6).

9.6.2 Non-linear time-history analyses

9.6.2.1 Global deformation responses

The non-linear time-history (NLTH) results are summarized in Table 9.12 and the average inter-storey drift responses are presented in Figure 9.43. The next two sub-sections will discuss the needs to analyse the local components deformation demands and the effects of near-fault ground motions in NLTH studies.

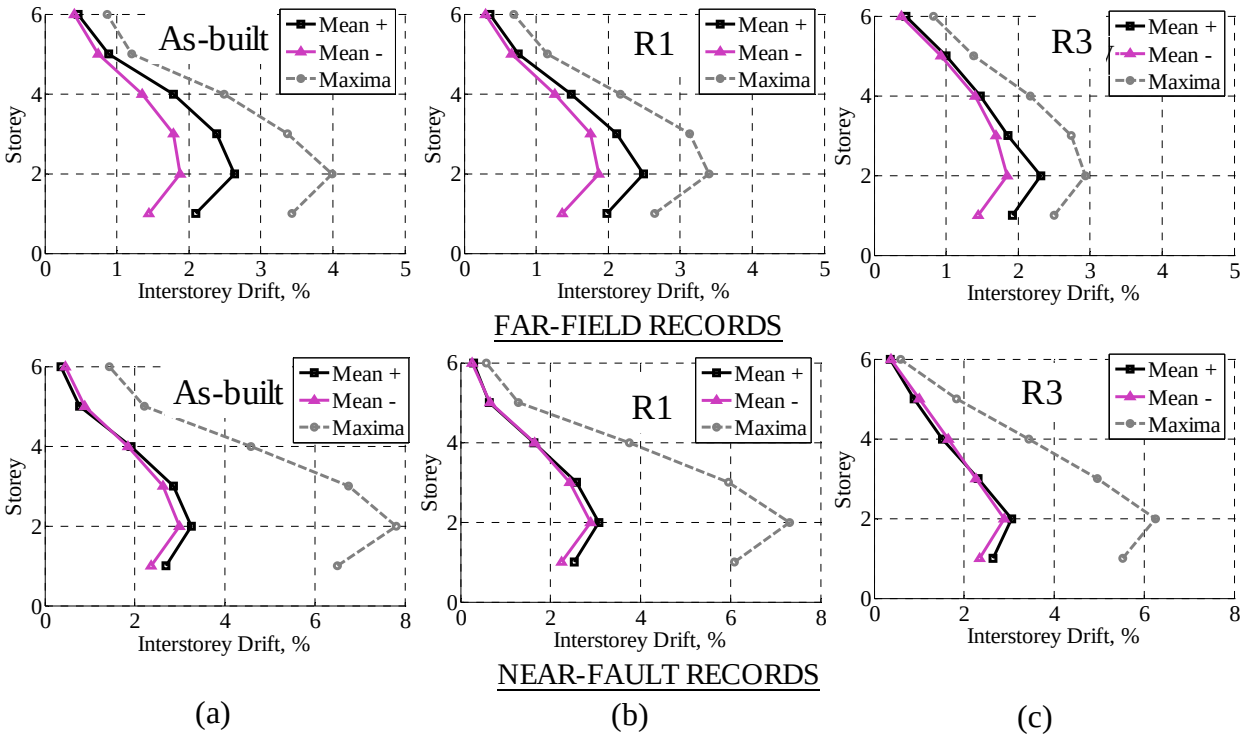

Figure 9.43: Average of peak inter-storey drift responses: Column: a) As-built frame; b) Beam-weakening only R1 retrofitted-frame; and c) Full SW R3-retrofitted frame.

The as-built frame performed poorly in both types of seismicity, with the average inter-storey drifts of 2.64% and 3.26% under the far field and near-fault events respectively. The inter-storey drifts were concentrated at the levels two and three, suggesting significant damage (and the

incipient of a soft-storey mechanism) at these levels. The average drifts at the effective height (or the lateral displacement at the effective height divided by the building effective height) for the as-built frame were 2.15% and 2.58% in the far-field and near-fault earthquakes scenarios. The maximum inter-storey drifts from 4% to 8% of the as-built frame certainly indicate the soft-storey failure in at least one of the seven input ground motions.

Table 9.12: Summary of non-linear time-history results.

Buildings	Max inter-storey drift (%)			Effective height drift (%) *		
	Design	Far-field	Near-fault	Design	Far-field	Near-fault
As-built frame	-	2.64%	3.26%	-	2.15%	2.58%
R1 retrofitted frame	~1.8%	2.49%	3.08%	~1.8%	1.96%	2.36%
R3 retrofitted frame	~1.4%	2.31%	3.06%	~1.4%	1.84%	2.31%

* Effective height of the building is 11.82m, as given in Table 9.6 and calculated based on DDBD principles.

In terms of the global inter-storey drift and the average drifts at the effective height, both retrofitted frames showed improvements when compared with the as-built frame. Under input ground motions without the directivity effects, the average drifts at the effect height were close to the DDBD design drift level for the R1 frame, but was slightly un-conservative for the R3 frame. The discrepancy between the design and the NLTH response increases further when near-fault ground motions were considered. This aspect will be further discussed in §9.6.2.3.

The inter-storey drift responses were generally higher than the average drift at the effective height, as the NLTH responses' deformed shape was not the beam-sway deformed shape assumed in the displacement-based retrofit design procedure. As illustrated by the distribution of inter-storey drifts up the building height in Figure 9.43, higher deformation demands were observed in the lower two to three storeys. One critical reason for this was the simplified design adopted for this study, in which the beams and the columns capacities were not varied up the building height. As described in §9.5.3 and §9.5.4, only two classes of beams and columns capacities (Levels 1-3 and Levels 4-6) were modelled, assuming the ductility demands on the plastic hinges could be redistributed in the retrofitted frames during the earthquakes. The discussion of the local components results in the next section will show that this assumption is incorrect for retrofitted frames, in which some elements remain critical and susceptible to over-strength of the beam flexural hinges.

9.6.2.2 Local components deformation demands

Figure 9.45 presents the mean of the peak response values of the global frame and the mean peak rotations of each modelled component (i.e. joints, beams and columns) under the seven far-field ground motions.

For the as-built frame, the joint shear deformation was the dominant inelastic mechanism, with moderate column hinging at the base and almost negligible beam plastic deformation. The test results in Chapter 5, as well as the recommendations from literature [7, 109, 110], can be used to relate the joint plastic rotation to a the limit state attained in the NLTH analyses. The as-built frame joints with the average plastic rotation demand exceeding 2.5% radians in the first two storeys suggested extensive joint damage, concrete spalling, column bars buckling and incipient structural collapse. The non-ductile base column sustained the rotational demand up to 1.2%, with a pinching hysteresis response, as the plain round bars' bond failure would prevent the brittle shear-flexural failure, as shown in the experimental tests of this type of columns [121, 136, 137]. In summary, the as-built frame building is likely to collapse under the Wellington 'far-field' event due to joint shear failures leading to joint/column axial load collapse.

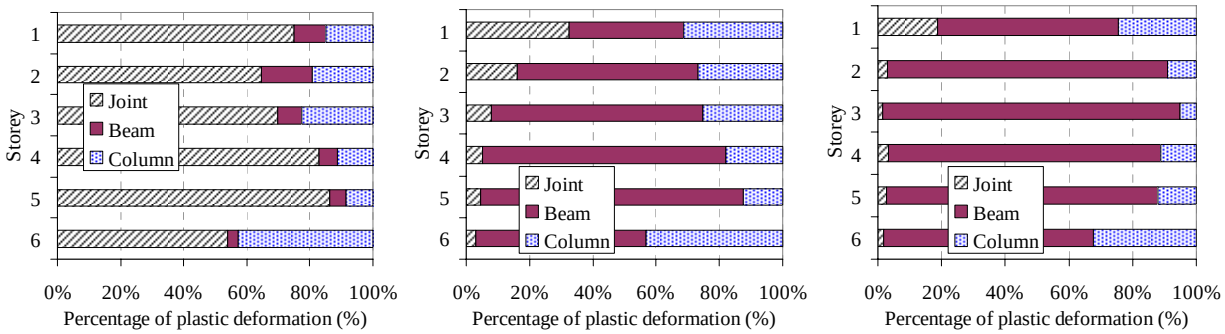

Figure 9.44: Decomposition of the plastic deformations for the three models under far-field ground motions: a) As-built; b) Beam-weakening only retrofit (R1); and c) Full Selective Weakening retrofit (R3).

While the global responses of both of the retrofitted frames were only marginally better than the as-built frame in terms of inter-storey drift response, the retrofit interventions effectively changed the dominant inelastic mechanism from a brittle joint shear failure to a relatively more ductile beam flexural hinge. This is more evident in Figure 9.44, in which the deformation components are plotted as a percentage of the total plastic deformations. While there was plastic rotation demand in the columns, this was limited to less than 1.0% radians or 20-40% of total inelastic rotation, suggesting moderate but repairable damage of these elements. As the beam-

rotation demand was less than 2.0% radians, based on the experience of NS-R1 experiment, compressive anchorage failure would have been avoided in the R1-retrofitted frame.

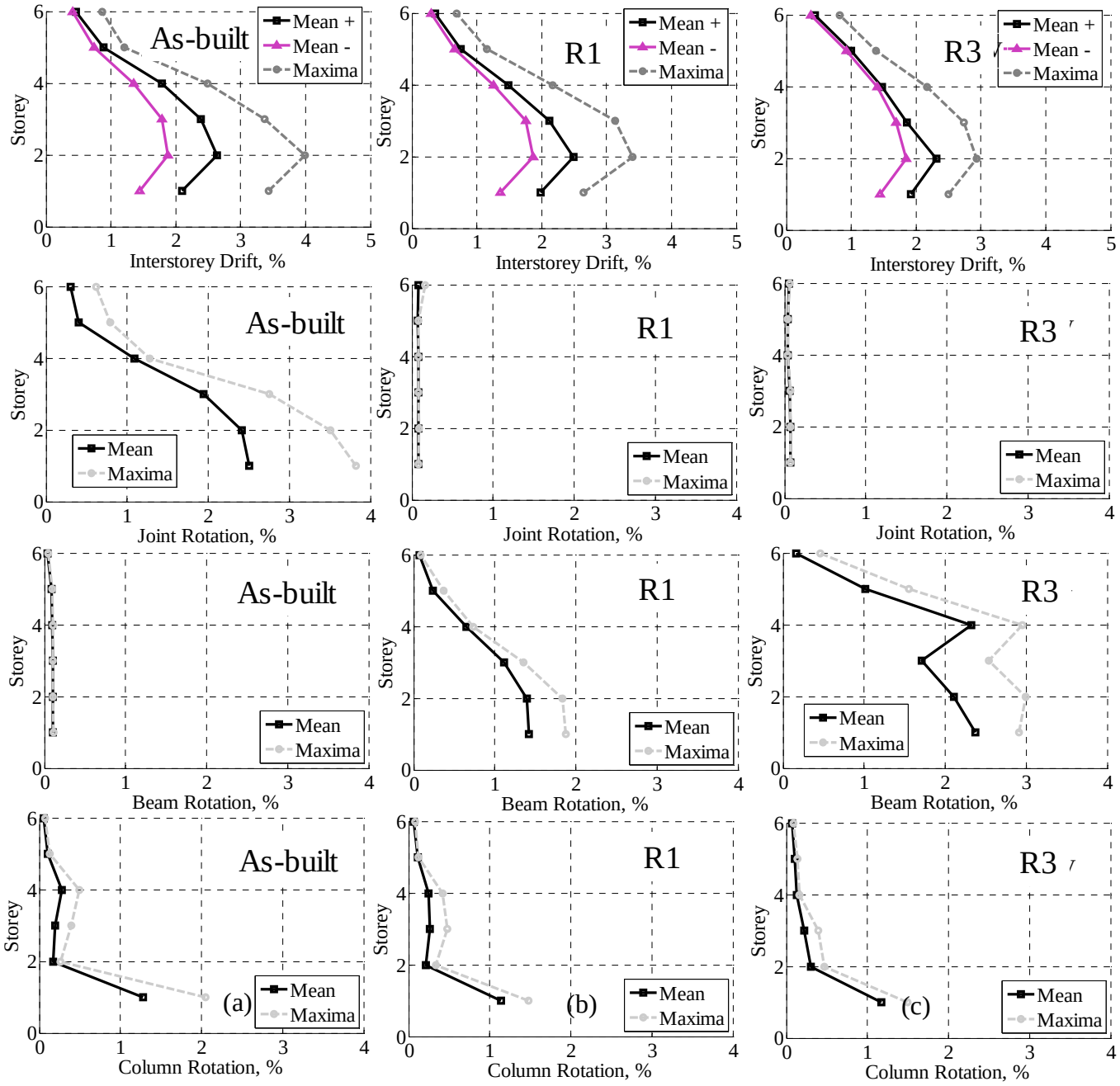

Figure 9.45: Seven far-field ground motions average of peak inter-storey drift envelopes responses and average global deformation components: Figure column: a) As-built frame; b) Beam-weakening only R1 retrofitted-frame; and c) Full SW R3-retrofitted frame.

The full SW-retrofitted (R3) frame with beam-weakening and joint post-tensioning at the exterior joints was not showing significant improvement from the R1 scenario, based on the far-field results. While the beam flexural hinging was more significant in the R3-retrofitted frame when compared with the R1-retrofitted frame, the additional damping from these flexural hinges only reduced the global inter-storey drift response marginally.

As only rudimentary hysteresis refinement was used for the modelling of the retrofitted beam and joint elements, the positive effect of the unbonded post-tensioning retrofit could not be fully appreciated. Figure 9.46 shows an example of the modified Takeda hysteretic responses of the retrofitted beams which differ quite significantly from the observed experimental hysteresis behaviour. The modelling of the weakened and post-tensioned beam would require a more sophisticated hysteretic rule than a modified Takeda hysteresis.

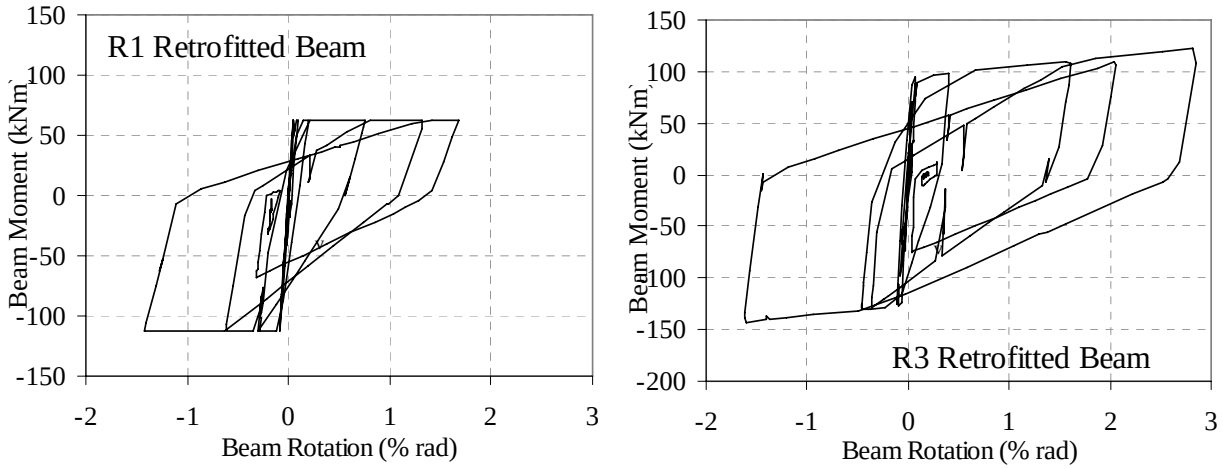

Figure 9.46: Example of beam flexural hinges hysteretic response under the FF1 excitation: a) R1 – beam-weakening only retrofit; and b) R3 – beam weakening and post-tensioning retrofit.

9.6.2.3 Effects of near-fault ground motions

Figure 9.47 presents the mean of the peak response values of the global frame and the mean peak rotations of each modelled component (i.e. joints, beams and columns) under the seven near-fault ground motions with the directivity effects.

The response spectra shown in Figure 9.42 indicated that the seismic demand in the period range of the fundamental period (1.6s) was more critical in the far-field ground motions than the near-fault ground motions. However, as shown in Table 9.12, near-fault ground motions, scaled to the same NZS1170:5 spectra as the far-field ground motions, on average, were resulting in 19-25% higher responses in terms of inter-storey drifts and 16-20% higher responses in terms

of average drifts at the effective height. This was consistent with other previous studies on well-designed RC frame structures (e.g. [3, 71]). The velocity pulse and low-cycles characteristics of the near-fault earthquakes limited the hysteretic damping of the retrofitted frames.

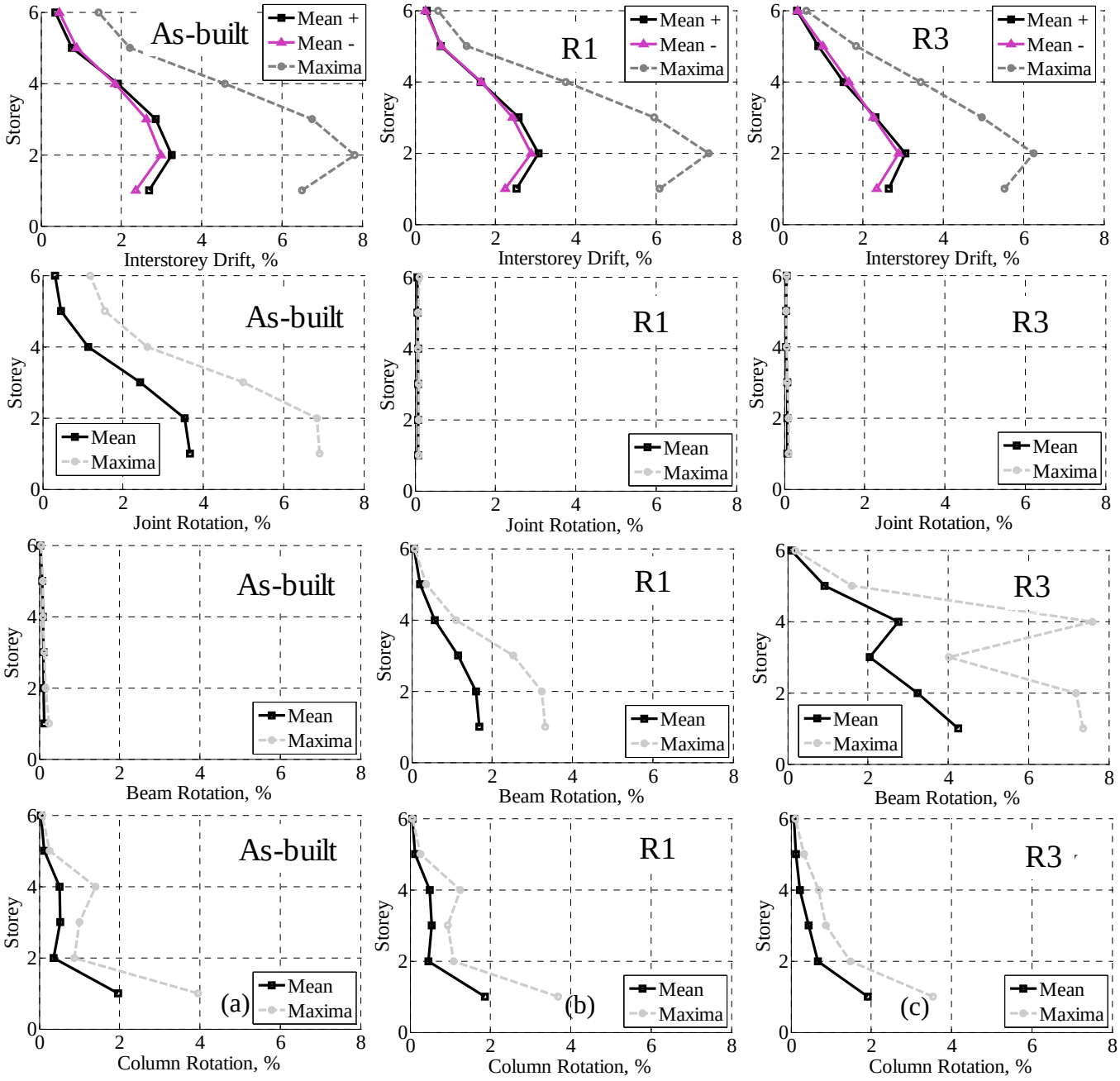

Figure 9.47: Seven near-fault ground motions average of peak inter-storey drift envelopes responses and average global deformation components: Figure column: a) As-built frame; b) Beam-weakening only R1 retrofitted-frame; and c) Full SW R3-retrofitted frame.

The distinction of having the post-tensioning of the joint and beam (with higher joint strength and positive post-yield stiffness) in the R3 retrofit was more evident in the near-fault

earthquake results. The maximum inter-storey drift response was lower in the R3-retrofitted frame when compared with the R1-retrofitted frame. The beam inelastic deformation was significantly higher in the R3-retrofit solution. Nevertheless, as both retrofitted frames relied predominantly on the hysteretic displacement-proportional damping, their efficiency in controlling the drift demand in earthquakes with directivity effects was limited.

The author and other researchers have suggested the use of advanced seismic (semi-active or passive) systems and velocity-proportional supplementary damping as means of countering the effects of the near-fault ground motions (e.g. [38, 71, 72, 89]).

9.6.3 Discussions

9.6.3.1 Modelling issues

In the course of this limited non-linear dynamic investigation, several interesting modelling issues were discovered. As the objective of the dynamic analyses was to make qualitative comparison of the as-built and SW-retrofitted frame buildings, limited attention was given to resolving these modelling issues.

The modelling of the joint shear capacity within a flexural-axial interaction surface (M-N interaction diagram) is currently limited, as the flexural-axial interacting element in the RUAUMOKO programme [25], is tailored to model column elements. The improved joint behaviour under s higher compressive column load (in the Push direction) during the earthquake is not modelled adequately. Previous attempts to include variation of axial loads in the joint capacity have been made by Galli [56] and Trowland [134] with limited success. The use of principal stresses in calculating the joint shear strength, used in this study, is nevertheless an improvement from the conventional nominal shear stress approach, which ignores the axial load contribution.

The definition of the different damping models was found to alter the results significantly for the as-built and retrofitted frame models. This arose from the limited hysteretic damping within the modelled inelastic components and the relative importance of damping from secondary elements (that were not modelled). It was found that the use of the tangent stiffness Rayleigh damping (ICTYPE=1) and the Rayleigh damping with tangent stiffness matrix as the secant damping matrix (ICTYPE=6) models implemented within the RUAUMOKO codes [25] were giving numerical instability due to the configuration of the beam-column joint models as

presented in Figure 9.40. To simplify the analyses, constant Rayleigh damping (based on initial stiffness matrix) was used.

Another limitation of the numerical model was the lack of explicit modelling of the axial and lateral collapse mechanisms and the associated strength degradation. The approach used in the preceding section is to compare the local elements' responses to empirical limit states in order to determine damage and collapse. Recent research has developed adequately accurate expressions for calculating the collapse drift, which can be incorporated within the numerical analysis in order not to over-estimate the drift capacity [45, 46]. RUAUMOKO has various options to represent lateral strength degradation [25]; however, the options were mostly based on number of cycles and/or ductility demands.

9.6.3.2 Considerations for the SW retrofit design

The NLTH results reveals several 'grey' areas that require further consideration and study in terms of the Selective Weakening (SW) retrofit design. While the aim of attaining ductile beam flexural failure mode, as per the capacity design philosophy was successful, evident from the results shown in Figure 9.45 and Figure 9.47, the global inter-storey drift responses exceeded the design expectations. This suggests that some of the assumptions made in the simplified displacement-based retrofit design procedure presented in §3.4.2, may be invalid for this prototype building. It should be noted that the retrofit design framework given in §3.4.2, is at the conceptual stage. It requires further refinement and verification to account for the following considerations:

a) The deformed shape of the building depends heavily on the assumptions of the distribution of the inelastic mechanisms. As discussed in §9.6.2, the use of a constant beam flexural strength up the building elevation and the reliance on possible moment redistribution, may not be suitable for the seismic retrofit design of non-ductile RC frames. As shown in Figure 9.45 and Figure 9.47, this design configuration leads to significantly higher inelastic demand at the lower storeys and limited inelasticity at the upper storeys. This results in a less-than-expected flexural inelastic action and damping, and therefore, higher global responses in terms of displacements and drifts.
b) The local beam-column joint hierarchy of strength design procedure have considered the positive post-yield stiffness of the beam-column joint retrofitted with unbonded post-tensioning. However, under the dynamic action, the high post-yield stiffness may lead to

the undesirable column hinging. As such, more stringent capacity-design requirements and dynamic amplification conservatism, possibly similar to those used for the design of new RC buildings (e.g. Paulay and Priestley [113]), should be included within the global design procedure.

c) The period shift of the R1-retrofitted frame is about 10% increase (§9.6.1). The current design framework (in §3.4.2) does not explicitly consider this aspect. The lengthening of the building period is generally considered a positive effect, as it leads to lower seismic demand in terms of the code-specified seismic hazard. However, in light of the near-fault ground motions results, in which the long-period spectral demand can be significantly higher, the reduction (or increase) of building stiffness due to the local SW retrofit intervention should perhaps be quantified and included in the global design procedure.

9.7 CONCLUSIONS AND FUTURE WORK

1. The chapter describes and presents two numerical studies aiming to further the understanding of as-built and Selective Weakening (SW) retrofitted beam-column joints and RC frame buildings. In general, the fracture-mechanics based FE modelling using the MASA package highlights the complexity as well as the potential of refined 3D numerical simulation in extending experimental results. On the other hand, the non-linear dynamic analyses of the as-built and SW-retrofitted RC frame buildings provide a bigger picture and seismic global responses confirmation of the SW retrofit strategy and design.

2. The abilities to model accurately the quasi-brittle behaviour of lightly RC joint and the complex behaviour of discrete bond elements in the MASA programme were demonstrated to be important in capturing and replicating the seismic responses of the as-built (NS-O1) and the SW-retrofitted (NS-R1) beam-column joint.

3. The FE model of NS-O1 suggested the redistribution of stresses along new narrower compressive strut after the joint diagonal cracking. It also predicted accurately the formation and spalling of the concrete wedge of the exterior face of the joint, for the as-built joint NS-O1 model as well as the NS-R1 retrofitted model.

4. The FE models of NS-R1 confirmed previous experiment insights (in Chapter 6) that the bond-failure of the bottom beam reinforcement results in compressive anchorage failure of the 180º hooks. While the FE models predicted accurately the location of possible concrete spalling, it did not reproduce the same level of concrete spalling as the experiment test.

5. The cyclic analysis of the NS-R1 model highlighted the failure of monotonic analyses to account for cumulative damage effects and the lack of energy dissipation results. In addition, the cyclic analysis was giving a much improved prediction on the reinforcement stresses and the concrete spalling on the exterior joint face, when compared with monotonic analyses.

6. The cyclic FE models of NS-O1 and NS-R1 captured the cyclic strength degradation due to the joint shear failure (NS-O1) and the cumulative bond failures (NS-O1 and NS-R1) very well. Due to limited computational and time resources, only limited parametric and sensitivity analyses were done on these models. Further research is needed on this area, to further the understanding of cyclic and post-peak behaviour of non-ductile RC elements with shear and/or bond failures.

7. The frictional/residual bond strength (τ_f) and the bond slip parameters (s_2 and s_3) were found to be important bond parameters on the overall response of the NS-O1 and NS-R1 FE models. The influence of the variation of column axial load on NS-R1 model was found to be limited, due to the dominant beam-flexural hinging inelastic mechanism. The influence of the variation of axial load on as-built joint has been carried out in ref. [58].

8. Preliminary recommendations were made for the MASA FE modelling of the post-tensioning retrofit (R2 and R3 solutions) of exterior beam-column joints. Further research on this area can highlight other critical SW-retrofit design parameters that have not been tested in this research.

9. The non-linear time history (NLTH) analyses confirmed the SW seismic retrofit concepts for non-ductile pre-1970s RC frame presented in Chapter 3. Using a case-study building, two suites of strong ground motions and three retrofit configurations (as-built, beam-weakening only, and weakening and joint-post tensioning retrofit), the SW retrofit strategy and techniques were shown to be relatively effective in controlling the global inter-storey drift and local members' ductility/deformation demands.

10. The simplified displacement-based retrofit design (§3.4.2) was found to be reasonably accurate for retrofit design. However, the NLTH results have shown the limitations of the some of the assumptions including the deformed shape profile, moment redistribution and building period shift (due to beam-weakening).

11. Furthermore, the design should consider for near-fault effects, long-period motions and high post-yield behaviour of post-tensioning retrofitted frames. Further parametric analyses on different building configurations and scenarios are required to improve the robustness of the simple design approach.

12. The limited NLTH studies also highlighted some modelling issues, including the effect of variation of axial load on beam-column joint capacity, the definition of damping model, and the explicit modelling of structural collapse.

9.8 CHAPTER 9 REFERENCES

[1] ACI-447. (2006) *Finite Element Analysis of Reinforced Concrete Structures (CD-ROM), SP-237CD*. American Concrete Inst. (ACI), Farmington Hills, MI.
[2] Alath S, Kunnath SK. (1995) Modelling inelastic shear deformation in RC beam-column joints. *Proc. of 10th Conf on Eng Mechanics*, Uni. of Colorado at Boulder, Boulder, CO, p. 822-825
[3] Alavi B, Krawinkler H. (2004) Behavior of moment-resisting frame structures subjected to near-fault ground motions. *Earthquake Eng & Struct Dyn.* **33**(6):687-706.
[4] Alire D. (2002) Seismic evaluation of existing unconfined reinforced concrete beam-column joints [M.Sc. thesis]. Uni. of Washington, Seattle, WA.
[5] Anderson M, Lehman DE, Stanton J. (2008) A cyclic shear stress-strain model for joints without transverse reinforcement. *Eng Structures*. **30**:941-954.

[6] Arefi MJ, Pampanin S, Cubrinovski M. (2009) Effects of SSI on the seismic response of older structures before and after retrofit. *Proc. of NZSEE 2009 Conf*, NZSEE, Christchurch, NZ.Paper No. 43.
[7] ASCE-SEI-41-06. (2007) *Seismic rehabilitation of existing buildings. ASCE standard ASCE/SEI 41-06*. American Society of Civil Engineers (ASCE), Reston, Va.
[8] ASCE-SEI-41-06. (2007) *Seismic rehabilitation of existing buildings. Supplement 1 to ASCE-41*. American Society of Civil Engineers (ASCE), Reston, Va.
[9] ASCE. (1982) *State-of-the-art report on finite element analysis on reinforced concrete*. ASCE Publication, New York.
[10] Baglin PS, Scott RH. (2000) Finite element modeling of reinforced concrete beam-column connections. *ACI Structural Journal*. Nov 2000; **97**(6):886-894.
[11] Bažant ZP. (1984) Size effects in blunt fracture: concrete, rock, metal. *ASCE Journal of Eng Mechanics*. **110**:518-535.
[12] Bažant ZP. (2000) Size effect. *International Journal of Solid and Structures*. **37**:69-80.
[13] Bažant ZP, Caner FC. (2005) Microplane model m5 with kinematic and static constraints for concrete fracture and anelasticity I: Theory. *ASCE Journal of Eng Mechanics*. **131**(1):31-40.
[14] Bažant ZP, Caner FC. (2005) Microplane model m5 with kinematic and static constraints for concrete fracture and anelasticity II: Computation. *ASCE Journal of Eng Mechanics*. **131**(1):41-47.
[15] Bažant ZP, Caner FC, Carol I, Adley MD, Akers SA. (2000) Microplane model m4 for concrete I: Formulation with work conjugate deviatoric stress. *ASCE Journal of Eng Mechanics*. **126**(9):944-953.
[16] Bažant ZP, Cedolin L. (1979) Blunt crack band propagation in finite element analysis. *ASCE Journal of Eng Mechanics*. **105**:297-315.
[17] Bažant ZP, Jirásek M. (1994) Damage nonlocality due to microcrack interactions: Statistical determination of crack influence function. In: Bažant ZP, Bittnar Z, Jirásek M, Mazars J, editors. *Fracture and damage in quasibrittle structures: Experiment, modelling and computer analysis*. 1st ed. E & FN Spon, London, UK; p. 3-17.
[18] Bažant ZP, Oh B-H. (1983) Crack band theory for fracture of concrete. *Material and Structures (RILEM, Paris)*. **16**(93):155-177.
[19] Bažant ZP, Ožbolt J. (1990) Nonlocal microplane model for fracture, damage and size effect in structures. *ASCE Journal of Eng Mechanics*. **116**(11):2484-2504.
[20] Bažant ZP, Planas J. (1998) *Fracture and size effect in concrete and other quasibrittle materials*. CRC Press, Boca Raton and London.
[21] Bažant ZP, Prat PC. (1988) Microplane model for brittle plastic material I: Theory. *ASCE Journal of Eng Mechanics*. **114**(10):1672-1688.
[22] Bažant ZP, Xiang Y, Prat PC. (1996) Microplane model for concrete I: Stress-strain boundaries and finite strain. *ASCE Journal of Eng Mechanics*. **122**(3):245-254.
[23] Calvi GM, Moratti M, Pampanin S. (2002) Relevance of beam-column damage and collapse in RC frame assessment. *J of Earthquake Eng*. **6**(1):75-100.
[24] Canbay E, Ersoy U, Ozcebe G. (2003) Contributions of RC infills to the seismic behaviour of structural systems. *ACI Structural Journal*. Sept-Oct 2003; **100**(5):637-643.
[25] Carr A. (2008) RUAUMOKO2D - The Maori God of Volcanoes and Earthquakes. Uni. of Canterbury, Christchurch, NZ; p. Inelastic Analysis Finite Element program.
[26] CEB-Fip-MC90. (1993) *CEB-FIP Model Code 90, CEB Bulletin d'Information No. 213/214*. Thomas Telford Ltd., London.

[27] Celik OC, Ellingwood BR. (2008) Modeling beam-column joints in fragility assessment of gravity load designed reinforced concrete frames. *J of Earthquake Eng*. Mar 2008; **12**(3):357-381.

[28] Ceresa P, Petrini L, Pinho R. (2007) Flexural-shear fibre beam-column elements for modelling frame structures under seismic loading - state of the art. *J of Earthquake Eng*. **11**(S1):46-88.

[29] Cope RJ, Rao PV, Clark LA, Norris P. (1980) Modelling of reinforced concrete behaviour for finite element analysis of bridge slabs. *Numerical Methods for Non-Linear Problems*. Pineridge Press, Swansea, UK; p. 457-470.

[30] Coronelli D, Mulas MG. (2001) Local-global approach in the seismic analysis of R/C frames including bond slip effects. *Eng Structures*. Aug 2001; **23**(8):911-925.

[31] Cosenza E, Manfredi G, Verderama GM. (2002) Seismic assessment of gravity load designed r.c. frames: critical issues in structural modelling. *J of Earthquake Eng*. **6**(S1).

[32] Cosenza E, Manfredi G, Verderama GM. (2006) A fibre model for push-over analysis of underdesign reinforced concrete frames. *Computers and Structures*. **84**(13-14):904-916.

[33] Crisafulli FJ, Carr A, Park R. (2000) Analytical modelling of infilled frame structures: A general review. *Bull of New Zealand Soc of Earthquake Eng*. **33**(1):30-47.

[34] de Borst R. (1991) Simulation of strain localisation: A reappraisal of the Cosserat continuum. *Eng Computations*. **8**(317-332).

[35] de Borst R, Muhlhaus HB. (1991) Continuum models for discontinuous media. In: van Mier JGM, Rots J, Bakker A, editors. *Fracture processes in concrete, rock and ceramics*. RILEM, E. & F.N. Spon, London.

[36] de Borst R, Muhlhaus HB. (1992) Gradient-dependent plasticity: Formulation and algorithmic aspects. *Intl J for Numerical Methods in Eng*. **35**:521-539.

[37] de Borst R, Nauta P. (1985) Non-orthogonal cracks in a smeared finite element model. *Eng Computations*. **2**:35-46.

[38] Dolce M, Ponzo FC, Di Cesare A, Ditommaso R, Moroni C, Nigro D, et al. (2008) JET-PACS Project: Joint experimental testing on passive and semiactive control systems. *Proc. of 14th World Conf on Earthquake Eng*, Beijing, China, p. 8.Paper ID: 12-01-0183.

[39] El-Metwally SE, Chen WF. (1988) Moment-rotation modeling of reinforced concrete beam-column connections. *ACI Structural Journal*. July-Aug 1988; **85**(4):384-394.

[40] Eligehausen R, Bigaj-van Vliet A. (1999) Bond behaviours and model. *Structural concrete - textbook on behaviour, design and performance - Vol 1 - fib Bulletin no 2*. International Federation for Structural Concrete (fib), Lausanne, Switzerland; p. 161-187.

[41] Eligehausen R, Genesio G, Ožbolt J, Pampanin S. (2008) 3D analysis of seismic response of RC beam-column exterior joints before and after retrofit. *Proc. of ICCRRR2008*, Cape Town, South Africa,

[42] Eligehausen R, Ozbolt J, Genesio G, Hoehler MS. (2006) Three-dimensional modelling of poorly detailed rc frame joints. *Proc. of NZSEE 2006 Conf*, NZSEE, Napier, NZ,

[43] Eligehausen R, Popov EP, Bertero VV. (1983) *Local bond-stress relationships of deformed bars under general excitation, Report No. UCB/EERC:83-23*. Uni. of California, Berkeley, Berkeley, CA.

[44] Elwood K, Matamoros A, Wallace JW, Lehman DE, Heintz JA, Mitchell A, et al. (2007) Update of ASCE/SEI 41 concrete provisions. *Earthquake Spectra*. Aug 2007; **23**(3):493-523.

[45] Elwood K, Moehle JP. (2005) Axial capacity model for shear-damaged columns. *ACI Structural Journal*. **102**:578-587.

[46] Elwood K, Moehle JP. (2008) Dynamic collapse analysis for a reinforced concrete frame sustaining shear and axial failures. *Earthquake Eng & Struct Dyn*. **37**:991-1012.
[47] Fabbrocino G, Verderama GM, Manfredi G, Cosenza E. (2002) Experimental behaviour of smooth bars anchorages in existing RC buildings. *Proc. of 1st fib Congress*, Osaka, Japan, p. 259-268
[48] Fabbrocino G, Verderame GM, Manfredi G. (2002) Experimental behaviour of straight and hooked smooth bars anchorage in existing r.c. buildings *Proc. of 12th European Conf on Earthquake Eng*, Elsevier, London, UK,
[49] Fabbrocino G, Verderame GM, Manfredi G. (2005) Experimental behaviour of anchored smooth rebars in old type reinforced concrete buildings. *Eng Structures*. **27**(10):1575-1585.
[50] Fabbrocino G, Verderame GM, Manfredi G, Cosenza E. (2004) Structural models of critical regions in old-type r.c. frames with smooth rebars. *Eng Structures*. **26**(14):2137-2148.
[51] Favvata MJ, Izzuddin BA, Karayannis CG. (2008) Modelling exterior beam-column joints for seismic analysis of RC frame structures. *Earthquake Eng & Struct Dyn*. **37**:1527-1548.
[52] Feenstra PH, de Borst R. (1995) A plasticity model for mode-I cracking in concrete. *Intl J for Numerical Methods in Eng* **38**:2509-2529.
[53] fib. (2000) *Bond of reinforcement in concrete: State-of-the-art report, fib Bulletin no. 10*. Intl. Fed. for Struct. Concrete (fib), Lausanne, Switzerland.
[54] fib. (2008) *Practitioners' guide to finite element modelling of reinforced concrete structures: State-of-art report. Bulletin No. 45*. Intl. Fed. for Struct. Concrete (fib), Lausanne, Switzerland.
[55] Fleury F, Reynouard JM, Merabet O. (2000) Multicomponent model of reinforced concrete joints for cyclic loading. *ASCE Journal of Eng Mechanics*. **126**(8):804-811.
[56] Galli M. (2007) Evaluation of the seismic response of existing r.c. frame buildings with masonry infills [M.E.E.]. Istituto Universitario di Studi Superiori, Pavia, Italy.
[57] Genesio G. (2009) Pers Comm: MASA3 model of as-built pre-1970s exterior beam-column joints. Stuttgart, Germany; p. Electronic files.
[58] Genesio G. (2011) Seismic assessment of RC exterior beam-column joints and retrofit with haunches using post-installed anchors (in preparation) [PhD dissertation]. Uni. of Stuttgart, Stuttgart, Germany.
[59] Genesio G, Eligehausen R, Pampanin S. (2010) Seismic assessment of pre-1970s RC beam column-joints. *Proc. of 14th European Conf on Earthquake Eng*, Ohrid, Macedonia,
[60] Ghannoum WM. (2007) Experimental and analytical dynamic collapse study of reinforced concrete frame with light transverse reinforcement [PhD dissertation]. Uni. of California, Berkeley, Berkeley, CA.
[61] Ghobarah A, Biddah A. (1999) Dynamic analysis of reinforced concrete frames including joint shear deformation. *Eng Structures*. **21**:971-987.
[62] Glogau OA. (1974) Masonry performance in earthquakes. *Bull of New Zealand Soc of Earthquake Eng*. Dec 1974; **7**(4):149-166.
[63] Hakuto S, Park R, Tanaka H. (1995) *Retrofitting of reinforced concrete moment resisting frames. UC Research Report 95-4*. Dept. of Civil Eng., Uni. of Canterbury, Christchurch, NZ.
[64] Hegger J, Sherif A, Roeser W. (2004) Nonlinear finite element analysis of reinforced concrete beam-column joints. *ACI Structural Journal*. **101**(5):604-614.

[65] Hillerborg A, Modéer M, Petersson PE. (1976) Analysis of crack formation and crack growth in concrete by means of fracture mechanics and finite elements. *Cement and Concrete Research*. **7**:773-782.

[66] Hoehler MS, Stanton J. (2006) Simple phenomenological model for reinforcing steel under arbitrary load. *ASCE J of Struct Eng*. July 2006; **132**(7):1061-1069.

[67] Ibarra LF, Krawinkler H. (2005) *Global Collapse of Frame Structures Under Seismic Excitations, John A. Blume Earthquake Engineering Center Report No. TR 152*. Dept. of Civil Eng., Stanford Uni., Stanford, CA.

[68] Ibarra LF, Medina RA, Krawinkler H. (2005) Hysteretic models that incorporate strength and stiffness deterioration. *Earthquake Eng & Struct Dyn*. **34**(12):1489-1511.

[69] Ingraffea AR, Saouma V. (1985) Numerical modeling of discrete crack propagation in reinforced and plain concrete. In: Meyer C, Okamura H, editors. *Fracture mechanics of concrete*. Martinus Nijhoff Publishers, Dordrecht; p. 171-255.

[70] Kaba S, Mahin SA. (1984) *Refined modeling of reinforced concrete columns for seismic analysis, EERC Report 84/03*. Earthquake Eng. Research Center, Uni. of California, Berkeley, CA.

[71] Kam WY, Pampanin S, Palermo A, Carr A. (2007) Advanced Flag-Shape systems for design and retrofit for near-fault structures. *Proc. of NZSEE 2007 Conf*, NZSEE, Palmerston North, NZ.Paper No. 21.

[72] Kam WY, Pampanin S, Palermo A, Carr A. (2010) Self-centering structural systems with combination of hysteretic and viscous energy dissipations. *Earthquake Eng & Struct Dyn*. Aug 2010; **39**(10):1083-1108.

[73] Kashiwazaki T, Noguchi H. (2008) Blind analysis of RC beam-column joints subjected to multi-axial combined loadings using 3D nonlinear FEM. *Proc. of 14th World Conf on Earthquake Eng*, Beijing, China.Paper No. 05-03-0131.

[74] Kunnath SK, Hoffmann GW, Reinhorn AM, Mander JB. (1995) Gravity-load-designed reinforced concrete buildings — Part I: Seismic evaluation of existing construction. *ACI Structural Journal*. **92**(3):343-354.

[75] Lasry D, Belytschko TB. (1988) Localization limiters in transient problems. *International Journal of Solid and Structures*. **24**:581-597.

[76] Lettow S. (2006) Ein Verbundelement für nichtlineare Finite Elemente Analysen - Anwendung auf Übergreifungsstöße (in German) [PhD dissertation]. Universität Stuttgart, Stuttgart, Germany.

[77] Lettow S, Eligehausen R, Ožbolt J. (2004) The simulation of bond between concrete and reinforcement in nonlinear three-dimensional Finite Element analysis. *Proc. of 5th International PhD Symposium in Civil Eng*, Delft, Netherlands,

[78] Li B, Wang Z, Mosalam KM, Xie H. (2008) Wenchuan earthquake field reconnassance on reinforced concrete framed buidlings with and without masonry infill walls. *Proc. of 14th World Conf of Earthquake Eng*, Beijing, China.S31-035.

[79] Li B, Wu Y, Pan T-C. (2003) Seismic behaviour of non-seismically detailed interior beam-wide column joints - Part II: Discussion and Theoretical Comparisons. *ACI Structural Journal*. Jan-Feb 2003; **100**(1):56-65.

[80] Lin C-M. (2000) *Seismic behaviour and design of reinforced concrete interior beam-column joints, UC Research Report 2000-1*. Dept. of Civil Eng., Uni. of Canterbury, Christchurch, NZ.

[81] Lin C-M, Restrepo J. (2002) Seismic behaviour and design of reinforced concrete interior beam-column joints. *Bull of New Zealand Soc of Earthquake Eng*. **35**(2):108-128.

[82] Liu A. (2001) Seismic assessment and retrofit of pre-1970s reinforced concrete frame structures, PhD Dissertation [PhD]. Uni. of Canterbury, Christchurch, NZ.
[83] Liu A, Carr A, Park R. (2003) A proper member model for member flexural behaviour at fixed-ends. *Proc. of Pacific Conf on Earthquake Eng*, Christchurch, NZ.Paper No. 47.
[84] Lowes LN. (1999) Finite Element Modeling of Reinforced Concrete Beam-Column Bridge Connections [PhD dissertation]. Uni. of California, Berkeley, Berkeley, CA.
[85] Lowes LN, Altoontash A. (2003) Modeling reinforced-concrete beam-column joints subjected to cyclic loading. *ASCE J of Struct Eng*. **129**(12):1686-1697.
[86] Lowes LN, Mitra N, Altoontash A. (2004) *A beam-column joint model for simulating the earthquake response of reinforced concrete frames. PEER Report 2003/10*. Pacific Earthquake Eng. Res. Center (PEER), Berkeley, CA.
[87] Maekawa K, Pimanmas A, Okamura H. (2003) *Nonlinear mechanics of reinforced concrete*. Digital Print 2009 ed. Spon Press, New York City, NY.
[88] Magenes G, Pampanin S. (2004) Seismic response of gravity-load design frames with masonary infills. *Proc. of 13th World Conf on Earthquake Eng*, Vancouver, Canada.Paper No. 4004.
[89] Marriott D, Pampanin S, Bull DK, Palermo A. (2007) Improving the seismic performance of existing reinforced concrete buildings using advanced rocking wall solutions. *Proc. of NZSEE 2007*, NZSEE, Palmerston North, NZ.Paper No. 17.
[90] Marti P. (1985) Basic tools of reinforced concrete beam design. *ACI Structural Journal*. **82**(4):46-56.
[91] Mazars J, Pijaudier-Cabot G. (1989) Continuum damage theory: application to concrete. *ASCE Journal of Eng Mechanics*. **115**(2):345-365.
[92] McKenna F, Fenves GL, Scott MH. (2004) OpenSees: Open system for earthquake engineering simulation. Pacific Earthquake Eng. Res. Center, Uni. of California, Berkeley, CA; p. Inelastic Analysis Finite Element program.
[93] Mitra N. (2007) An analytical study of reinforced concrete beam-column joint behavior under seismic loading [PhD dissertation]. Uni. of Washington, Seattle, WA.
[94] Mitra N, Lowes LN. (2007) Evaluation, calibration and verification of a reinforced concrete beam-column joint model. *ASCE J of Struct Eng*. **133**(1):105-120.
[95] Ngo D, Scordelis AC. (1967) Finite element analysis of reinforced concrete beams. *ACI Structural Journal*. **64**(3):152-163.
[96] Nilson AH. (1967) Finite element analysis of reinforced concrete [PhD dissertation]. Uni. of California, Berkeley, CA.
[97] Nilson AH. (1968) Nonlinear analysis of reinforced concrete by the finite element method. *ACI Structural Journal*. **65**(9):757-766.
[98] Noguchi H. (1981) Nonlinear finite element analysis of reinforced concrete beam-column joints. *Proc. of IABSE Colloquium*, Delft, the Netherlands, p. 639-653
[99] Noguchi H. (2006) Three-Dimensional FEM analysis of RC beam-column joints subjected to two-directional loads. In: Lowes LN, Filippou FC, editors. *Finite Element Analysis of Reinforced Concrete Structures, SP-237*. American Concrete Inst. (ACI), Farmington Hills, MI; p. 149-164.
[100] Noguchi H, Kashiwazaki T. (2009) FEM analysis of interaction effects of 3-D RC members subjected to multi-directional cyclic loading. *Proc. of ASCE Structures Congress 2009*, Austin, TX, p. 1209-1218
[101] NZS1170. (2004) *NZS 1170.5:2004 Structural design actions*. Standards New Zealand, Wellington, NZ.

[102] NZS3101:2006. (2006) *NZS 3101:2006 Concrete structures standard*. Standards New Zealand, Wellington, NZ.
[103] Otani S. (1974) Inelastic analysis of reinforced-concrete frame structures. *ASCE Journal of Structural Division*. **100**(ST7):1422-1449.
[104] Ožbolt J. (2008) MASA3 - Finite element program for 3D nonlinear analysis of concrete and reinforced concrete structures Institut fur Werkstoffe im Bauwesen, Uni. of Stuttgart, Stuttgart, Germany; p. 53 pp.
[105] Ožbolt J, Bažant ZP. (1996) Numerical smeared fracture analysis: nonlocal microcrack interaction approach. *Intl J for Numerical Methods in Eng*. **39**(4):635-661.
[106] Ožbolt J, Lettow S, Kožar I. (2002) Discrete bond element for 3D finite element analysis of reinforced concrete structures. *Proc. of fib International Symposium: Bond in concrete - from research to standards*, Budapest, 2002, p. 11
[107] Ožbolt J, Li Y, Kožar I. (2001) Microplane model for concrete with relaxed kinematic constraint. *International Journal of Solid and Structures*. **38**(16):2683-2711.
[108] Ožbolt J, Mayer U, Vocke H. (1999) Smeared fracture FE-analysis of reinforced concrete structures - theory and examples. *Proc. of Seminar on Post-Peak Behaviour of RC Structures subjected to Seismic Loads - Recent Advances and Challenges on Analysis and Design*, Japan Concrete Inst. (JCI), Tokyo, Japan, p. 23-41
[109] Pagni C, Lowes LN. (2006) Fragility functions for older reinforced concrete beam-column joints. *Earthquake Spectra*. Feb 2006; **22**(1):215-238.
[110] Pampanin S, Calvi GM, Moratti M. (2002) Seismic behaviour of RC beam-column joints designed for gravity loads. *Proc. of 12th European Conf on Earthquake Eng*, London, UK.Paper 726.
[111] Pampanin S, Magenes G, Carr A. (2003) Modelling of shear hinge mechanism in poorly detailed RC beam-column joints. *Proc. of Concrete Structures in Seismic Region: fib 2003 Symposium*, Federation International du Beton, Athens,
[112] Pantazopoulou SJ, Bonacci JF. (1994) On earthquake-resistant reinforced concrete frame connections. *Canadian Journal of Civil Eng*. **21**:307-328.
[113] Paulay T, Priestley MJN. (1992) *Seismic design of reinforced concrete and masonry buildings*. John Wiley & Sons Inc., Christchurch, NZ.
[114] PEER. (2007) PEER strong motion database. [cited; Available from: http://peer.berkeley.edu/smcat/
[115] Pijaudier-Cabot G, Bažant ZP. (1987) Nonlocal damage theory. *ASCE Journal of Eng Mechanics*. **113**:1512-1533.
[116] Priestley MJN, Seible F, Calvi GM. (1996) *Seismic design and retrofit of bridges*. John Wiley & Sons Inc., NY.
[117] Priestley MJN, Seible F, Xiao Y, Verma R. (1994) Steel jacket retrofitting of reinforced concrete bridge columns for enhanced shear strength, Part II: Test results and comparison with theory. *ACI Structural Journal*. Sept/Oct 1994; **91**(5):537-551.
[118] Rashid YR. (1968) Ultimate strenght analysis of prestressed concrete pressure vessles. *Nuclear Eng and Design*. **7**:334-344.
[119] Rots J. (1988) Computational modeling of concrete fracture [PhD dissertation]. Delft Uni. of Technology, Delft, the Netherlands.
[120] Rots J, Blaauwendraad J. (1989) Crack models for concrete: Discrete or smeared? fixed, multidirectional or rotating? . *Heron, Concrete Mechanics*. **34**(1):1-59.

[121] Saunders DB. (2004) Seismic performance of pre 1970's non-ductile reinforced concrete waffle slab frame structures constructed with plain round reinforcing steel [PhD dissertation]. Uni. of Canterbury, Christchurch.

[122] Sause R, Pessiki S, Wu S, Kurama YC. (1996) Modeling and seismic behaviour of nonductile concrete frame structures and retrofit implications. In: Sabnis GM, Shroff AC, Kahn L, editors. *Seismic rehabilitation of concrete structures, SP-160*. American Concrete Inst. (ACI), Detroit, MI; p. 231-253.

[123] Schaich J, Schaefer K, Jennewein M. (1987) Toward a consistent design of structural concrete. *PCI Journal*. May-June 1987; **32**(3):75-149.

[124] SeismoSoft. (2003) SeismoStruct - A computer program for static and dynamic nonlinear analysis of framed structures 3.0 ed. SeismoSoft, [online]. Available from URL: http://www.seismosoft.com.

[125] Shirai N. (2006) Evaluation of cyclic deterioration and post-peak behaviour of RC beam-column joints assemblages by 3-D FE analysis. In: Lowes LN, Filippou FC, editors. *Finite Element Analysis of Reinforced Concrete Structures, SP-237*. American Concrete Inst. (ACI), Farmington Hills, MI; p. 129-148.

[126] Somerville P. (2003) Magnitude scaling of the near-fault rupture directivity pulse. *Physics of the Earth and Planetary Interiors*. **137**(1):201-212.

[127] Sritharan S. (2005) Strut-and-Tie analysis of bridge tee joints subjected to seismic action. *ASCE J of Struct Eng*. **131**(9):1321-1333.

[128] Sritharan S, Ingham JM. (2003) Application of strut-and-tie concepts to concrete bridge joints in seismic region. *PCI Journal*. **48**(4):66-90.

[129] Sritharan S, Priestley MJN, Seible F. (2000) Nonlinear finite element analysis of concrete bridge joint systems subjected to seismic actions. *Finite Element in Analysis and Design*. **36**(3-4):215-233.

[130] Stratan A, Fajfar P. (2002) *Influence of modelling assumptions and analysis procedure on the seismic evaluation of reinforced concrete GLD frames*. IKPIR, Uni. of Ljubljana, Ljubljana, Slovenia.

[131] Taucer FF, Spacone E, Filippou FC. (1991) *A fiber beam-column element for seismic response analysis of reinforced concrete structures, EERC Report 91/17*. Earthquake Eng. Research Center, Uni. of California, Berkeley, CA.

[132] Taylor GI. (1938) Plastic strain in metals. *J of the Inst of Metals*. **62**:307-324.

[133] Tothong P, Cornell A, Baker JW. (2007) Explicit directivity-pulse inclusion in probabilistic seismic hazard analysis. *Earthquake Spectra*. **23**(4):867-891.

[134] Trowland M. (2004) Modelling the shear higne in beam-column joints [B.Eng (Hons)]. Uni. of Canterbury, Christchurch, NZ.

[135] van Mier JGM, Vervuurt A, Schlangen E. (1994) Boundary and size effects in uniaxial tensile tests: a numerical and experimental study. *Fracture and Damage in Quasibrittle Structures*. E. & F.N. Spon Publisher, London, UK; p. 289-302.

[136] Verderame GM, Fabbrocino G, Manfredi G. (2008) Seismic response of r.c columns with smooth reinforcement. Part II: Cyclic tests. *Eng Structures*. **30**(9):2289-2300.

[137] Verderame GM, Fabbrocino G, Manfredi G. (2008) Seismic response of r.c. columns with smooth reinforcement. Part I: Monotonic tests. *Eng Structures*. **30**(9).

[138] Verderame GM, Ricci P, De Carlo G, Manfredi G. (2009) Cyclic bond behaviour of plain bars. Part II: Analytical investigation. *Construction and Building Materials*. **23**(12):3512-3522.

[139] Walker SG. (2001) Seismic performance of existing reinforced concrete beam-column joints [M.Sc. thesis]. Uni. of Washington, Seattle, WA.

[140] Will GT, Uzumeri SM, Sinha SK. (1972) Application of finite element method to analysis of reinforced concrete beam-column joints. *Proc. of Specialty Conf on Finite Element Method in Civil Eng*, Canadian Soc. of Civil Engineers / Eng. Inst. of Canada, p. 745-766

[141] Wu Y. (2002) Experimental and analytical study of reinforced concrete interior beam-wide column joints for seismic performance [M.Eng thesis]. Nanyang Technogical Uni., Singapore.

[142] Yousseff M, Ghobarah A. (2001) Modelling of RC beam-column joints and structural walls. *J of Earthquake Eng*. **5**(1):93-111.

CHAPTER 10. CONCLUSIONS AND FUTURE RESEARCH

"The myth, then, was that refinement of the analysis process improved the end result."

M.J. Nigel Priestley, 2003

(Myths and Fallacies in Earthquake Engineering, Revisited,

The 9th Mallet Milne Lecture 2003)

(IUSS Press, Pavia pp. 121)

10.1 THESIS KEY CONTRIBUTIONS AND LIMITATIONS

This research has introduced and developed an alternative seismic retrofit strategy for pre-1970s reinforced concrete (RC) frames called "Selective Weakening" (SW). Fundamentally, the SW retrofit approach aims at changing the local inelastic mechanism to attain improved global lateral displacement, strength and energy dissipation capacities. For this research, two SW retrofit interventions such as selective weakening of the beams and/or external post-tensioning of the joints were implemented and tested. This was achieved with extensive experimental and numerical studies.

This dissertation began by outlining two hypotheses that it intended to answer, using a series of research questions. In the following two sub-sections (§10.1.1 and §10.1.2), the key findings of this thesis will be summarised and restated, with the intention of answering the research questions outlined in §1.3 (of Chapter 1). The following sub-section §10.1.3 will summarize other auxiliary key findings from this research.

10.1.1 Hypothesis 1: Selective Weakening *retrofit strategy* for pre-1970s RC frames

The first hypothesis challenges the conventional thinking of seismic retrofit with the counter-intuitive idea that a Selective Weakening (SW) strategy can improve both the local and global ductility/displacement capacities of pre-1970s RC frames. To test and confirm that hypothesis, several aspects of seismic vulnerability, assessment and retrofit of pre-1970s RC frames are

investigated in the first three Chapters of the thesis. These form the basis of the conceptual development and the analytical design tools for the SW retrofit techniques proposed for the RC frame and the exterior beam-column joints.

10.1.1.1 Seismic vulnerability of pre-1970s RC frames and joints in NZ

Chapter 2 has established the state-of-knowledge of the seismic vulnerability of pre-1970s RC frames and beam-column joints. Reviews of historical literature, building codes and building drawing archives have established the structural peculiarity of these pre-1970s RC frame buildings built in New Zealand. It confirms the presence of common deficiencies in beam-column joints such as the lack of joint stirrups, inadequate column capacity, the absence of capacity design consideration, the use of plain-round bars, the presence of non-ductile column lap-splice and the use of non-ductile beam anchorages such as 180º hooks. Previous studies on non-ductile beam-column joints highlight the key deficiencies that any joint seismic retrofit must overcome.

10.1.1.2 Seismic assessment procedure for non-ductile beam-column joints

State-of-the-art seismic assessment tools and procedures for RC beam-column joints are summarised in Chapter 2. Current practice of seismic assessment often fails to consider the interacting demand-capacity of various structural elements connected to the beam-column joint. A seismic assessment procedure for non-ductile beam-column joints based on the capacity design philosophy and hierarchy of strength evaluation has been presented with the necessary analytical tools to evaluate the specific failure mechanisms. The inelastic mechanism of the beam-column joint is determined by comparing realistic failure mechanisms (e.g. joint shear failure, beam hinging, bond slip etc.) using a common denominator (equivalent column moment, M_c). Careful attention was given to the assessment of unreinforced beam-column joint shear capacity and the evaluation of bond capacity of plain round reinforcements. Possible improvements to the current NZSEE guidelines for seismic evaluation [9] can be made by adopting some of the suggested procedures in §2.4.

10.1.1.3 Seismic retrofit strategies and techniques for RC frames and joints

Chapter 3 reviews the state-of-the-art of seismic retrofit *strategies* and their implementations using various global and local seismic retrofit *techniques*. Global and local retrofit techniques are identified and critically discussed. Literature review has shown that many studies considered only

isolated structural deficiency, and there are consistent omissions of the floor slab and transverse beam, column lap-splices, plain-round bars and possible bond failure, in the research on seismic retrofit of non-ductile beam-column joints.

The integration of global retrofit techniques with the existing structures often implies the needs of local improvement of possibly brittle elements (e.g. foundation) to ensure the continuity of load paths. The SW-retrofit approach may avoid such integration improvement and extensive foundation retrofit. The risk of over-strengthening with local retrofit techniques leading to a brittle failure mode suggests the possibility of a selective-weakening approach. Furthermore, by adopting a performance-based seismic retrofit approach, a multi-level displacement-based retrofit strategy such as the SW retrofit can be developed to achieve the required performance objectives.

10.1.1.4 The concepts of Selective Weakening (SW) retrofit

The conceptual development of the SW retrofit strategy and techniques is presented in Chapter 3. The SW retrofit strategy fundamentally aims at improving the global response of the RC structure by: a) *decreasing the seismic demand* onto brittle elements, overall structure and sub-structure via selective weakening of structural elements (similar to period elongation effects); and b) *increasing the deformation capacity* of the global structure by changing both the local and global inelastic mechanisms. The SW retrofit strategy for a RC frame aims at achieving a ductile inelastic mechanism and adequate deformation capacities by local SW retrofit techniques on the beam-column joint connections. SW retrofit techniques involve the selective weakening of structural elements and/or subsequent targeted upgrade using existing techniques (e.g. external joint post-tensioning). Four SW retrofit *techniques* for exterior beam-column joints are proposed and developed in this study: a) Beam-weakening only; b) Beam-column joint post-tensioned only; c) Full selective weakening (beam-weakening and post-tensioning) retrofit; and d) Advanced controlled-rocking hybrid retrofit. The first three SW techniques are tested within the experimental programme

10.1.1.5 Selective Weakening retrofit design procedure and tools

An extensive SW retrofit design methodology is provided in §3.4, covering general retrofit design philosophy, a displacement-based global seismic retrofit design, a quick SW retrofit design method and a detailed analytical assessments for beam-weakening and post-tensioned retrofitted beam-column joints. The SW retrofit design philosophy is based on the comparison of

the hierarchy of strengths of the beam-column joint individual elements within a M_c-N_c performance domain. An innovative displacement-based retrofit design procedure to derive the required post-SW-retrofitted beam flexural strength and to estimate the performance level given the M_c-N_c performance domain of the retrofitted beam-column joints is developed in §3.4.2.

Several analytical tools for the SW-retrofit design were developed in Chapter 3. A semi-empirical model for the increase in joint shear strength (in terms of p'_t) given a lower joint aspect ratio, which is achieved from selective beam-weakening, is developed using principal stresses analysis and basic mechanics. An analytical tool to assess the beam moment-rotation of the external un-bonded post-tensioned beam-column joint based on the idea of pseudo-rocking of the joint is developed. The effect of joint post-tensioning on the joint shear strength is evaluated using the principal stress approach. The analytical tools and procedure compare well with the experimental results presented in Chapters 6 to 8.

10.1.2 Hypothesis 2: Selective Weakening and post-tensioning *retrofit techniques*

The second hypothesis requires the experimental and numerical validation of the feasibility of the proposed selective beam weakening and/or post-tensioning retrofit techniques for pre-1970s RC exterior beam-column joints, in the context of the Selective Weakening retrofit strategy. Chapters 4 to Chapter 8 present in detail the experimental programme and test results of the nine 2/3-scale as-built and retrofitted beam-column joints. Test parameters included levels of external post-tensioning forces, locations of beam weakening, influence of column lap-splice, and the presence of cast-in-situ slab and transverse beams.

10.1.2.1 Effects of selective-weakening and post-tensioning on pre-1970s joints

The selective beam weakening was effective in limiting the joint shear stress demand and in inducing the plastic hinges in the beam. The beam-weakening-only retrofitted specimen (NS-R1) sustained inelastic beam flexural hinging up to the ±2.0% drift cycles with substantial energy dissipation capacities (ξ_{hys} = 20-30%). NS-R1 ultimately failed under compressive anchorage push-out failure. For a collapse prevent performance level, the beam-weakening-only is a viable SW technique. However, extra precaution must be given to the brittle anchorage failure and further testing is required before implementation of the beam-weakening only intervention.

The post-tensioning-only solution (NS-R2) showed a mix of beam and column hinging, as per the experiment's design. Specimen NS-R2 highlighted the motivation to include selective

beam-weakening as a part of the retrofit solution. The benefit of joint post-tensioning in reducing the principal stress demands in the unreinforced joint was evident in all three post-tensioned specimens. The joint confinement from the post-tensioning anchorage turns out to be important, as it delays the complete joint failure and reduces the likelihood of significant strength degradation, after the joint cracking. In terms of design of post-tensioned retrofit of joint, the p'_c should be limited to $0.2f'_c$ (or $0.9\sqrt{f'_c}$) MPa to prevent the joint compressive failure, while the p'_t should be limited to $0.2\sqrt{f'_c}$ MPa if joint diagonal tensile crack is undesirable.

The combination of selective beam-weakening and external post-tensioning tested in specimens NS-R3 and NS-R4 was successful in achieving stable beam-hinging inelastic mechanism. No structural failure was achieved in either specimen as the post-tensioned beam-column joint maintained the lateral capacity up to the end of the 2nd cycles of ±4.0% drift. The attempt to shift the plastic hinge location by changing the beam-weakening location in NS-R4 was only partially successful due to the inevitable hinging close to the beam-column interface in the negative beam moment.

R1 and R2 retrofit techniques were tested to discretize the effects of each retrofit technique. In the opinion of the author, the combination of selective beam-weakening and joint post-tensioning (R3 and R4) is considered the more desirable retrofit solutions for it is more robust, flexible and effective in mitigating damage.

10.1.2.2 Influence of column lap-splice, and floor slab and transverse beams

Four beam-column joint specimens (S-O1, S-R3, SL-O1 and SL-R3) were tested to investigate the influence of column lap-splice, floor slab and transverse beams, on the as-built and SW-retrofitted joints. Partial failure of the column lap-splice reduced the energy dissipation capacity ξ_{hys} in the SW-retrofitted specimen (S-R3). However, the combination of beam-weakening and the peculiarity of plain-round bars lap-splice averted the complete shear-flexural-axial failure of the lap-splice. While deformed bars lap-splice will improve the anchorage capacity, it might in turn result in a more severe lap-splice failure. This aspect needs to be further investigated.

The presence of floor slab and transverse beams provided additional torsional resistance from the transverse beams in the loading direction with tension slab flange (Push direction). For the as-built joint, the presence of floor slab and transverse beams did not prevent joint diagonal cracking but it improved the post-cracking joint behaviour by confinement induced by the transverse beams' torsional actions. To quantify the level of joint confinement from the

transverse beam stub, a new failure plane and an expression for effective joint shear width, b_j, are proposed in Chapter 8. Further tests with bi-directional loadings on non-ductile RC exterior joints with transverse beam stubs are needed to check whether the torsional confinement persists with extensive flexural cracking on the transverse beams. The SL-R3 test also confirmed the practical constructability of selective beam weakening and external post-tensioning retrofit intervention.

10.1.2.3 Realistic modelling of the as-built and SW-retrofitted joints

Chapter 9 describes and presents two numerical studies aiming to further the understanding of as-built and SW-retrofitted beam-column joints and RC frame buildings. The fracture-mechanics based finite element (FE) modelling using the MASA FE package highlights the complexity as well as the potential of refined 3D numerical simulation in extending experimental results. The microplanes concrete model could simulate the lightly reinforced joint region realistically. The modelling of discrete bond elements in the MASA gives a much improved prediction of the reinforcement stresses. The cyclic models of NS-O1 and NS-R1 also captured the cyclic strength degradation due to joint shear failure (NS-O1) or cumulative bond failures (NS-R1) well. The frictional/residual bond strength (τ_f) and the bond slip parameters (s_2 and s_3) were found to be important bond parameters.

10.1.2.4 Global performance of the SW-retrofitted frames

The non-linear time history (NLTH) analyses in Chapter 9 provide a bigger picture and seismic global response confirmation of the SW retrofit strategy for non-ductile RC frames. The SW retrofit of the pre-1970s frame was shown to be effective in controlling the global inter-storey drift and local members' ductility/deformation demands. The simplified displacement-based retrofit design (developed in Chapter 3) was found to be reasonably accurate for the retrofit design. However, the NLTH results have shown the limitations of the some of the assumptions including the deformed shape profile, moment redistribution and building period shift (due to beam-weakening). The NLTH results highlighted the importance of the considerations for near-fault effects, long-period motions and high post-yield behaviour of post-tensioning retrofitted frames. Further parametric analyses on different building configurations and scenarios are required to improve the robustness of the simple design approach.

10.1.3 Additional key findings from experiments

10.1.3.1 Beam-column joint testing

Two peculiarities in the beam-column joint testing were the realistic simulation of the variation of column axial load and the improved simulation of the seismic and gravity loadings imposed boundary conditions. This has been discussed in some depths in Chapter 4 and Appendix A. The strain gages were found to be ineffective for plain round bars where large discrete cracking is expected to result in premature bond-slip and failure of the strain gages.

10.1.3.2 Seismic performance of as-built pre-1970s beam-column joints

Three as-built pre-1970s beam-column joints were tested as part of the overall testing matrix. In addition to a plane benchmark pre-1970s exterior beam-column joint (NS-O1), the two other specimens illustrated the influence of column lap-splice (S-O1), and the presence of floor slab and transverse beams (SL-O1) on the seismic performance of pre-1970s joints. All three as-built specimens had joint shear failure under cyclic loading. Damage limit states in terms of principal stresses, joint shear distortions, inter-storey drifts, cracking pattern and crack widths are presented.

Based on the NS-O1 result, a minor revision of the p'_t versus joint shear deformation, γ_j, relationship has been proposed for the assessment of lightly reinforced exterior beam-column joints in Chapter 5. For specimen S-O1, the inadequate lap-splice did not result in significant strength degradation due to the concentrated cracking pattern of the plain-round bar reinforcement. The column lap-splice failure in S-O1 also delayed the joint cracking and ultimate structural failure in the Push direction (with increasing axial loads).

The presence of transverse beams did not prevent the joint shear cracking but it delayed the lateral strength degradation due to the joint failure in SL-O1. A method to account for the increase in joint shear capacity due to the presence of slab and transverse beam is proposed in Chapter 8. The slab flange and the transverse beam enhanced F_c by 21% in the Push direction and a force-transfer mechanism was proposed based on the strain gage readings. The effective flange width due to interaction with the slab was lower than that observed in the joint with deformed bars and ductile detailing. It is proposed that for seismic assessment of non-ductile exterior beam-column joints, a minimum of 2.2 times beam depths ($2.2h_b$) is taken to be the effective flange width in calculating the beam negative moment.

10.1.3.3 Influence of bond in beam-column joints with plain bars

Existing literature on plain-round bar reinforcement has been thoroughly reviewed. A conceptual model of bond stress distribution based on the benchmark specimen NS-O1's strain profiles and bond stresses has been postulated. In addition, a discussion of the influence of plain round bars on the fixed-end flexural and joint shear capacities based on the mechanics of bond degradation and loss of bond at the cracking location is given in Chapter 5. The same mechanistic model can be assumed for the pseudo-rocking assumptions described in Chapter 5 for the post-tensioned beam-column joint retrofit.

10.1.3.4 Influence of the variation of column axial load

The assessment of joint shear strength using principal stresses approach accounts for the variation of vertical axial stresses, f_v. The same approach was taken in analysing the effects of added horizontal axial stress, f_h, from external post-tensioning of the joint. A Mohr's circle stress-state model on the effects of the variation of column axial load on joint shear strength was described in Chapter 5. It was found that the assessment of column flexural capacities ($M_{c\text{-}cf}$) based on an assumed 'variation of axial load' might be un-conservative – particularly when an increase in the column axial load was relied upon for the column moment capacity.

10.2 RECOMMENDATIONS FOR FUTURE RESEARCH

Several topics are identified for future research in the course of this research:

10.2.1 Database and inventory of as-built and retrofitted buildings

A lack of complete database of as-built and retrofitted pre-1970s multi-storey buildings stock in New Zealand is notable, despite the availability of such information within local territories, city councils and heritage trusts. It is suggested that future research to complete the relatively sparse database on seismically vulnerable and retrofitted buildings within major New Zealand cities be performed.

10.2.2 Refinement and validation of the displacement-based seismic retrofit

The displacement-based seismic retrofit design procedure developed in Chapter 3 is preliminary and is based on a significant number of assumptions. As the numerical analyses in Chapter 9 has shown, further studies are necessary to refine the deformed shape profiles and the equivalent viscous damping versus ductility relationship. For the partial retrofit or possibly seismic retrofit

targeting a lower performance level, the effect of a mixed inelastic mechanism (beam hinging with interior columns hinging etc.) on the overall design and seismic response needs to be further studied.

10.2.3 Analytical tools development and validation

Further considerations are required on the uncertainties in the assessment of the joint shear capacity before and after seismic retrofit. In addition, as the experimental-analytical comparison in Chapter 6 has shown, a limitation of the analytical procedures developed in this thesis is related to the uncertainties in the assessment of the bond capacity of plain round bars. The existing assessment procedure for inadequate plain-round bar lap-splice was also found to be inadequate in Chapter 7. The average-bond stress capacity approach is suggested for the assessment of column lap-splices with plain round bars. Most importantly, the analytical tools developed in this research have only been compared with one set of experimental results, and further validation and refinement is required before they can be implemented in practice.

10.2.4 Plain round bars bond testing

As observed in all the retrofitted specimens, progressive bond failure, debonding and strain penetration resulting from the poor bond resistance of plain round bars have limited the energy dissipation capacity in the 2^{nd} load cycles. However, it is also apparent that the plain bar reinforcement provides some positive effects such as the localising flexural cracks and preventing complete lap-splice failure. Nevertheless, limited test data on the bond capacity (as listed in Chapter 2) prevented reliable assessment of the anchorage capacities of the plain bar bonds. Further experimental research along the approach of Fabbrocino *et al.* [1] and Feldman and Barlett [2] would be valuable in the development of the analytical and assessment tools.

10.2.5 Further SW-retrofitted beam-column joints tests

Due to limited time and resources, several configurations of SW-retrofitted beam-column joints were not included within the scope of the research. It is expected that the SW retrofit outcome would be improved if the as-built beam-column joint consisted of deformed bars. While the cyclic bond degradation might decrease, deformed bars might introduce different sets of issues such as distribution hinging and increase joint shear demand. Another un-tested retrofit option is to sever part of the slab mesh reinforcement from the longitudinal beam in order to reduce the tension flange effect and protect the column from potential plastic hinges.

10.2.6 FE model parametric analysis of SW retrofit of beam-column joints

Due to limited computational and time resources, only limited parametric and sensitivity analyses were done on the FE models developed in this research. Further research is needed to further the understanding of cyclic and post-peak behaviour of non-ductile RC elements with shear and/or bond failures. The influence of the variation of column axial load and different loading patterns can be further investigated using FE models.

10.2.7 Advanced controlled-rocking joint retrofit solutions

The development of advanced self-centering systems using un-bonded post-tensioning or shape memory alloy technology for new 'minimal damage' seismic resisting systems (e.g. [4, 7]) suggests the opportunity to develop similar advanced controlled-rocking retrofit solutions as described in §3.3.3.3. Numerical results of 'conventional' self-centering systems (e.g. [5-7]) and retrofitted systems [8, 11], as well as the positive experimental results presented in Chapters 6 to 8 for SW retrofit, have indicated the feasibility of this advanced retrofit solution. Actual application of self-centering retrofit strategy using new additional re-centering shear walls in Japan [10] have also illustrated the cost feasibility of such a seismic retrofit solution.

10.2.8 Large-scale and multi-bay frames experimental testing

A major assumption of this investigation is that the seismic retrofit of the exterior beam-column joints alone or in conjunction with other retrofit interventions can lead to a more ductile global behaviour. This was partially confirmed in the limited dynamic studies presented in Chapter 9. Nevertheless, the "true" validation of the SW retrofit concept can only be achieved with large-scale experimental testing of either a full-scale sub-frame (e.g. double-bay two-storey frame specimen) or a reduced-scale complete frame prototype. Multi-bay frames will allow better representation of the plasticity distribution between the exterior and interior beam-column joints. Multi-bay frames, with the appropriate boundary conditions, can reveal further information regarding the effect of inelastic beam elongation and the possible horizontal in-plane restraints from the induced beam axial load. Lastly, dynamic shaking table tests or fast pseudo-dynamic tests on large-scale specimens can check the conventional numerical modelling strategy (e.g. Chapter 9).

10.2.9 Economic and constructability of SW retrofit

The governing issues in deciding a retrofit strategy or techniques are often the economics (cost) and constructability. Cost and constructability are some of the most common questions encountered by the author in the course of this research, when discussing seismic retrofit with practicing engineers. While the structural feasibility of SW retrofit has been demonstrated in this thesis, other important issues as on-site constructability, reliable post-tensioning confining anchorage, application on irregular 'real' structures and economic need to be further understood. This can only be achieved via research-to-industry implementation and careful case-study applications of the SW retrofit technology.

10.3 CLOSING REMARKS

In the final months of the write-up of this dissertation, an earthquake of magnitude (M_w) 7.1 occurred on 4 September 2010 with an epicentre located at Darfield, a town about 40 km west of the city of Christchurch [3]. The earthquake has a focal depth of 10 km and the maximum intensity felt was 8 based on MMI scale. Fortunately, the RC buildings in the city centre, both the pre-1970s and post-1970s construction, performed relatively well compared to other building classes such as unreinforced masonry and residential houses on liquefied ground. Nevertheless, signs of incipient brittle failures such as joint shear and column shear cracking were consistent with those observed in test specimens NS-O1, S-O1 and SL-O1 [3].

Considering the earthquake has only resulted in low-to-moderate damage in non-retrofitted RC structures, it is hard to quantitatively evaluate the possible higher performance or seismic resilience provided by the seismic retrofit interventions. Without a doubt, a ground motion of different characteristics (including longer duration or different frequency-energy contents) than the Darfield (Canterbury) earthquake may impose a higher deformation demands on these buildings. In the absence of ductile failure modes, these pre-1970s non-retrofitted RC buildings may fail in a catastrophic manner. The large floor space and high density nature of multi-storey RC building will result in significant fatalities in an event of a non-ductile collapse. This earthquake nevertheless serves as a timely reminder to New Zealand and the rest of the world of the importance of seismic retrofit work, such as that presented in this thesis.

The quote from Professor Priestley at the start of this chapter too reminds the earthquake engineering profession that refinement of our analysis and design process with sophisticated

computer software may not necessarily improve the end results. Without a good understanding and design of load paths, hierarchy of strengths and capacity design principles, the seismic retrofit myth, then, is that the strengthening and certainly not the weakening of a building, would improve the end result.

Addendum after the PhD Examination (17th May 2011):

A few months after the submission of the thesis and approximately 6 months after the 4th September 2010 earthquake, an earthquake of magnitude (M_w) 6.3 occurred on 22nd Feb 2011 with an epicentre located at Heathcote Valley, about 10 km east of the Christchurch central business district (CBD). The second earthquake generated significantly stronger ground shaking in the Christchurch CBD with peak ground acceleration (PGA) ranging from 0.361g ms^{-2} to 0.714g ms^{-2} recorded in the CBD recording stations. With ground shaking approximately 1.5 to 2.5 times the design level seismicity (PGA~0.22g), many RC buildings had moderate-to-severe structural damage. In particular, two six-storey RC buildings (Canterbury Television, CTV building and Pyne Gould Corporation, PGC building) collapsed resulting in multiple fatalities. There were 115 and 16 deaths in the CTV and PGC buildings respectively, accounting for 72% of the total 182 fatalities in the earthquake. The author's firsthand experience in the emergency building safety evaluation process, including close-up inspection of the collapsed 1960-built PGC building with unreinforced beam-column joint, further reaffirms the urgent need for effective seismic retrofit of these buildings. The future of the city remains unclear and a Royal Commission inquiry has commenced to investigate the causes of these buildings collapses.

10.4 CHAPTER 10 REFERENCES

[1] Fabbrocino G, Verderame GM, Manfredi G. (2005) Experimental behaviour of anchored smooth rebars in old type reinforced concrete buildings. *Eng Structures*. **27**(10):1575-1585.

[2] Feldman LR, Bartlett FM. (2007) Bond stresses along plain steel reinforcing bars in pullout specimens. *ACI Structural Journal*. Nov-Dec 2007; **104**(6):685-692.

[3] Kam WY, Pampanin S, Dhakal RP, Gavin H, Roeder CW. (2010) Seismic performance of reinforced concrete buildings in the September 2010 Darfield (Canterbury) earthquakes. *Bull of New Zealand Soc of Earthquake Eng*. Dec 2010; **43**(4):340-350.

[4] Kam WY, Pampanin S, Palermo A, Carr A. (2006) Advanced Flag-Shaped systems for high seismic performance. *Proc. of 1st European Conf on Earthquake Eng and Seismology (1ECEES)*, Geneva, Switzerland.Paper No. 991.

[5] Kam WY, Pampanin S, Palermo A, Carr A. (2007) Advanced Flag-Shape systems for design and retrofit for near-fault structures. *Proc. of NZSEE 2007 Conf*, NZSEE, Palmerston North, NZ.Paper No. 21.

[6] Kam WY, Pampanin S, Palermo A, Carr A. (2008) Implementation of advanced flag-shape (AFS) systems for moment-resisting frame structures. *Proc. of 14th World Conf on Earthquake Eng (14WCEE)*, Beijing, China, p. 8.Paper ID: 05-06-0129.

[7] Kam WY, Pampanin S, Palermo A, Carr A. (2010) Self-centering structural systems with combination of hysteretic and viscous energy dissipations. *Earthquake Eng & Struct Dyn*. Aug 2010; **39**(10):1083-1108.

[8] Marriott D, Pampanin S, Bull DK, Palermo A. (2007) Improving the seismic performance of existing reinforced concrete buildings using advanced rocking wall solutions. *Proc. of NZSEE 2007*, NZSEE, Palmerston North, NZ.Paper No. 17.

[9] NZSEE. (2006) *Assessment and improvement of the structural performance of buildings in earthquakes*. New Zealand Soc. for Earthquake Eng. (NZSEE), Wellington, NZ.

[10] Wada A, Qu Z, Ito H, Motoyui S, Sakata H, Kasai K. (2009) Seismic retrofitting using rocking walls and steel dampers. *Proc. of ATC-SEI Conf, on Improving the Seismic Performance of Existing Buildings and Other Structures*, San Francisco, CA, p. 1010-1021

[11] Zhang Y, Hu X. (2010) Self-centering seismic retrofit scheme for reinforced concrete frame structures: SDOF system study. *Earthquake Eng & Eng Vibration*. June 2010; **9**(2):271-283.

Al Nisbet (Tuesday, 19th October 2010), Opinion A14, The Press.

SELECTIVE WEAKENING AND POST-TENSIONING FOR THE SEISMIC RETROFIT OF NON-DUCTILE RC FRAMES

WENG YUEN, KAM

NOV 2010

VOLUME II: APPENDICES

A thesis submitted in partial fulfilment of the requirements
for the Degree of
Doctor of Philosophy in Civil Engineering

Under the supervision of by:
Associate Professor Stefano Pampanin
Professor Athol Carr
Adjunct Professor Des Bull
Dr. Alessandro Palermo

Department of Civil and Natural Resources Engineering
College of Engineering
UNIVERSITY OF CANTERBURY
Christchurch, New Zealand.

APPENDICES TABLE OF CONTENT

APPENDIX A. CALCULATION FOR VARIATION OF AXIAL LOAD AND M-N PERFORMANCE DOMAINS OF TEST UNIT BEAM-COLUMN JOINTS

A.1 AXIAL LOAD CALCULATIONS

A.1.1 Gravity-only axial load takedown

With reference to the prototype reinforced concrete (RC) frame shown in Figure 4.1, the gravity-only axial loads, N_g on the exterior beam-column joint specimens are calculated herein. The following assumptions are made: a) concrete density of 23.5kN/m^3, b) columns and beams dimensions of 300x300 mm and 450x300 mm respectively, c) slab thickness of 150mm, d) superimposed dead load, G of 0.5kPa and basic live load, Q of 3kPa (corresponding to 60psf specified for offices in NZS95:1955 [3]). The tributary area for the exterior beam-column joints of an internal frame is given by = [(4.57+3.35)/2]^2, which is 5.8% of the total gross floor area. Table A.1 summarises the axial load takedown calculation. For simplicity, the N_g adopted for the experiment was 110kN. For the 2/3-scaled test specimens, the axial load force is scaled down by the following equation:

$$N_{g-2/3} = N_g \times (2/3)^2 \qquad \textbf{A.1}$$

Table A.1: Average material properties of steel reinforcements.

Dead Weight	Floor	Roof	**Live Load**	Floor	Roof
Column D/L per floor (kN)	138.2	0.0	Q (basic - Office)	3	
Beam D/L per floor (kN)	180.6	180.6	ψ-c	0.4	0
Slab D/L per floor (kN)	481.4	320.9	ψ-a	0.54	0
Superimposed D/L (kPa)	0.5	0.0	**Q-uls per floor (kN)**	88.52	0.00
SDL per floor (kN)	68.3	0.0	**Total Gravity Load per floor (kN)**	956.9	501.5
Exterior Beam-Column Joint Tributary Area				5.80%	
Unscaled 1st-2ndFloor beam-column joint Axial Load, Ng (kN)				251.1	
2/3rd-scaled 1st-2nd Floor beam-column joint Axial Load, Ng (kN)				**111.61**	

A.1.2 Variation of axial load due to seismic action for prototype RC frame

With reference to Figure A.1, the variation of axial load, ΔN at the exterior columns can be approximated by assuming an equivalent lateral loading, F acting at an effective height of 2/3 of the total building height, H, will induce an overturning moment that will be resisted by ΔN times the total bay length, B. It is assumed that no induced axial loads in the interior columns:

$$\frac{2}{3}FH = \Delta NB \qquad \textbf{A.2}$$

$$\Delta N = \alpha V_c = \frac{2H}{3B}\frac{F}{F_c} \qquad \textbf{A.3}$$

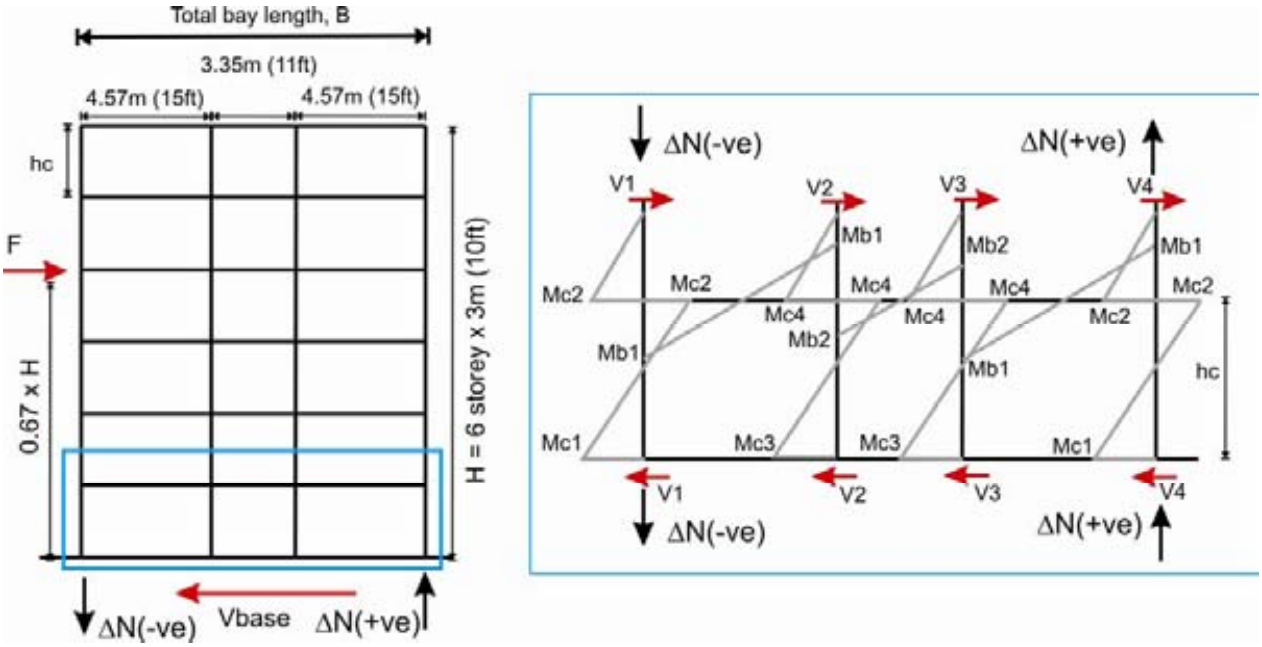

Figure A.1: Static analysis of RC frame to calculate the variation of axial load.

Considering a simplified equilibrium condition of the first two storeys of the prototype six-storey three-bay frame as shown in Figure A.1, the ratio of F to the lateral force at the column inflection point, F_c, can be derived by the following equations assuming an inflection point at 0.6 of the column height, h_c:

$$M_{c2} = 2/3M_{c1} \text{ and } M_{c4} = 2/3M_{c3} \qquad \textbf{A.4a \& b}$$

$$V_1, V_4 = \frac{M_{c1} + M_{c2}}{h_c} = \frac{5}{2}\frac{M_{c2}}{h_c} \qquad \textbf{A.5}$$

$$V_2, V_3 = \frac{M_{c3} + M_{c4}}{h_c} = \frac{5}{2}\frac{M_{c4}}{h_c} \quad \textbf{A.6}$$

Hereon, two failure mechanisms leading to two forms of column shear distributions can be assumed. If the lateral capacity of the RC frame is governed by the inelastic mechanism of the exterior beam-column joints – be it the joint shear failure, column flexural or shear failure or beams in the exterior span failure, without further moment redistribution, the base column shear and moments between the exterior and interior columns are equal. That is $M_{c1} = M_{c3}$ and therefore $V_{1,4} = V_{2,3}$. This is reasonable as typical pre-1970s gravity-based RC frames had columns and beams with similar dimensions and moment-capacities as well as non-engineered beam-column joint connections. Furthermore, the shorter internal span of the prototype frame would have resulted in lower flexural demand in the internal beams. Based on this assumption, the ratio of F/F_c is given by:

$$F = \Sigma V = 10\frac{M_{c2}}{h_c} = 5\frac{M_{b1}}{h_c} \quad \textbf{A.7}$$

$$\frac{F}{F_c} = \frac{\Sigma V}{V_{1,4}} = 10 \bullet \frac{2}{5} = 4 \quad \textbf{A.8}$$

In the 2nd scenario, where the interior beam-column joint connections or beam-hinging govern the lateral capacity of the RC frames, the base column shear distribution can be approximated by $2V_{1,4} = V_{2,3}$ and $2M_{c1} = M_{c3}$. This is based directly on the assumptions that the plastic flexural hinges in all the beams are activated, i.e. the moment redistribution along the beams hinges is possible ($M_{b1} = M_{b2}$). Therefore, the bending moment in the columns can be approximated by $M_{c2} = 0.5M_{b1}$ and $M_{c4} = (M_{b1} +. M_{b2})/2$ Thus, the ratio of F/F_c is given by:

$$F = \Sigma V = 5\frac{M_{c2}}{h_c} + 5\frac{M_{c4}}{h_c} = 15\frac{M_{c2}}{h_c} = \frac{15}{2}\frac{M_{b1}}{h_c} \quad \textbf{A.9}$$

$$\frac{F}{F_c} = \frac{\Sigma V}{V_{1,4}} = 15 \bullet \frac{2}{5} = 6 \quad \textbf{A.10}$$

For experiment on as-built and retrofitted beam-column joints where both assumptions were applicable depending on the hierarchy strength of the beam-column joints, an average value of F/F_c =5 was adopted. Therefore, for an exterior beam-column joint, the variation of axial load, ΔN at the column top is given by:

$$\Delta N = \alpha F_c = \frac{2H}{3B}\frac{F}{F_c}F_c = 3.33\frac{H}{B}F_c \qquad \textbf{A.11}$$

For the prototype building shown in §4.2.1 and Figure A-2, where H=18m and B=12.497m (41ft), α is 4.63. Therefore, the following relationship was used for the experiments:

$$N = N_g \pm \alpha F_c = 110kN \pm 4.63F_c \qquad \textbf{A.12}$$

Extending the calculation above, α values for various building aspect ratios (H/B) and number of bays can be calculated. Table A.2 below shows the possible range of α values for exterior beam-column joints in internal frames considering the typical pre-1970s RC frame buildings to be of 3-8 stories high, and 3-5 bays long. It can be concluded that for a mid-rise RC frame, where the building height, H, exceeds 9m, the variation of axial load should be explicitly considered in the assessment of the exterior columns of RC frames. Expectedly, the variation of axial load is more critical for slender buildings (higher H/B) as implied by Equation A.11.

Table A.2: The range of α values for variation of axial load on exterior columns. Inter-storey height of 3m and bay length of 4.5m are assumed.

α ratio	3 storeys (9m)	6 storeys (18m)	8 storeys (24m)
1 bay	2.68	5.36	7.15
3 bays	2.23	4.46	5.96
6 bays	2.12	4.24	5.68

A.2 M-N PERFORMANCE DOMAIN OF AS-BUILT BEAM-COLUMN JOINTS

The seismic assessment methodology described in §2.4 is used to derive the M-N performance domains for all the as-built beam-column joint specimens. The assumptions of the prototype building and the specimen details are given in §4.2.1 and §4.3 respectively. The following sub-sections will describe some of the assumptions used in the calculations.

A.2.1 NS-O1

Two limit states for beam flexural failures are considered: a) with perfect bonds, therefore full strength development in the reinforcements; b) beam bars bond failures. In evaluating the beam bars bond failure, the maximum and residual bond stress capacities, $\tau_{b,max}$ and $\tau_{b,res}$ are taken to be $0.3\sqrt{f'_c}$ MPa and $0.15\sqrt{f'_c}$ MPa respectively. These results in limiting beam bars f_s are 171MPa and 85MPa respectively. The f'_c value is taken from the day-of-testing compressive strength (f'_c =

17.3MPa) while the reinforcing steel properties are taken from the steel test results (§4.5.1). In evaluating the joint shear capacity, the limit states for the principal stresses are taken to be p'_t = $0.19\sqrt{f'_c}$ MPa and $p'_c = 0.3f'_c$ MPa. The M-N performance domain for NS-O1 is shown in Figure A.2.

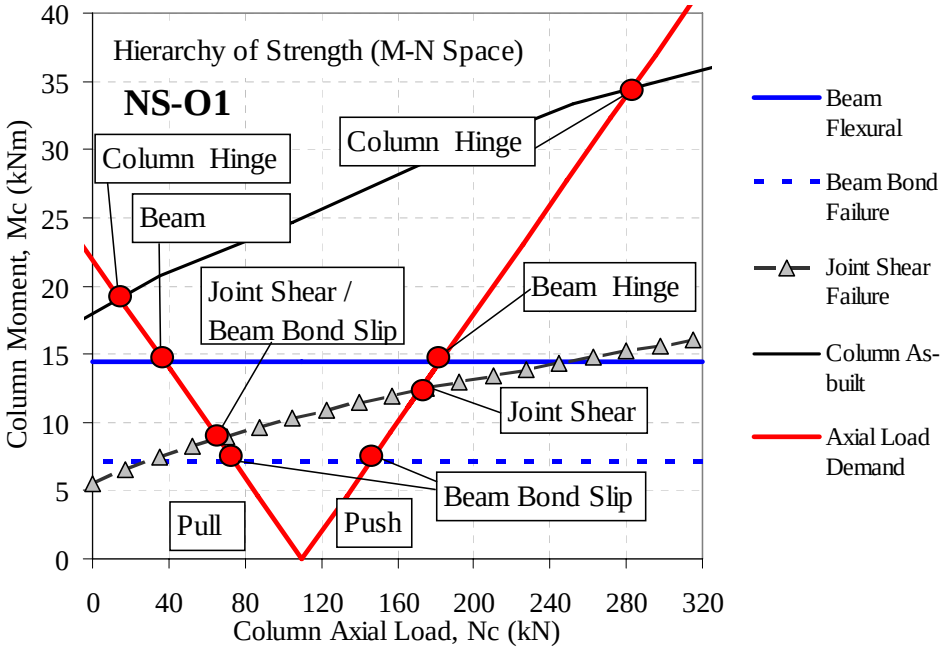

Figure A.2: M-N performance domain and hierarchy of strength analysis for NS-O1.

A.2.2 S-O1

Five limit states for column flexural failures are considered: a) flexural with perfect bond, b) column lap-splice failure, limiting f_s developed in the tension, c) residual lap-splice strength, d-e) two levels of column shear capacities, depending on the flexural ductilies. Figure A.3 shows the column hierarchy of strength of test unit S-O1, considering the above five failure modes. The shear capacities are noticeably high as the column transverse reinforcement content is relatively high in the specimen design. In evaluating the column lap-splice failures, the ASCE-41 [2] approach with the development lengths calculated with the NZS3101 [4] expressions, is adopted in calculating the limiting f_s of the column longitudinal bars. f_s at the lap-splice onset failure and residual strength are 255MPa and 51MPa. If the ACI318 [1] development length equations are adopted, the f_s at lap-splice failure is calculated to be 352MPa.

Similar to NS-O1, the beam bars' maximum and residual bond stress capacities, $\tau_{b,max}$ and $\tau_{b,res}$, are taken to be $0.3\sqrt{f'_c}$ MPa and $0.15\sqrt{f'_c}$ MPa respectively. These result in limiting beam

bars f_s to be 161MPa and 80MPa respectively. The f'_c value is taken from the day-of-testing compressive strength (f'_c = 15.1MPa) while the reinforcing steel properties are taken from the steel test results (§4.5.1). In evaluating the joint shear capacity, the limit states for the principal stresses are taken to be $p'_t = 0.19\sqrt{f'_c}$ MPa and $p'_c = 0.3f'_c$ MPa. The M-N performance domain for S-O1 is shown in Figure A.4.

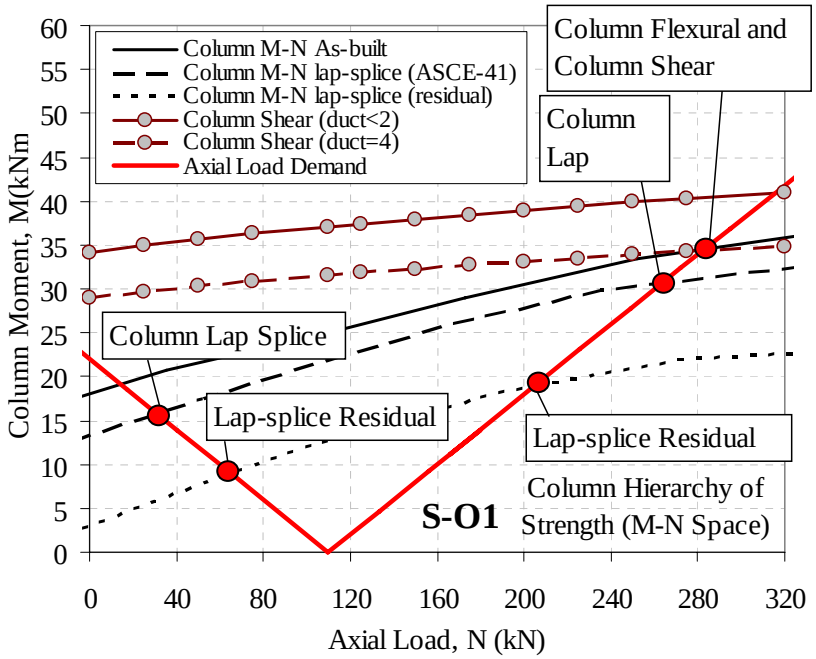

Figure A.3: S-O1 Column hierarchy of strength for various failure mechanism.

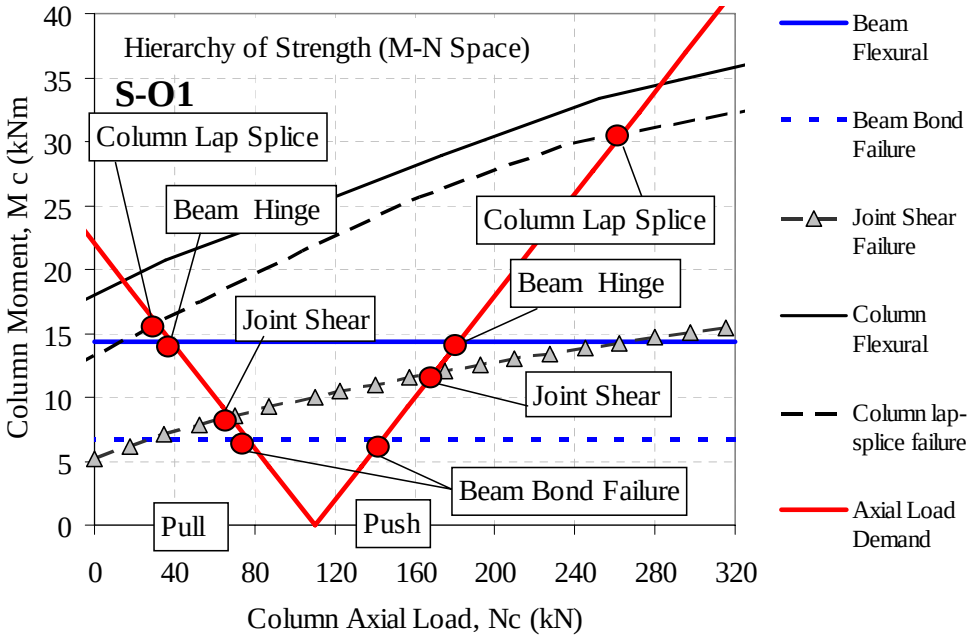

Figure A.4: M-N performance domain and hierarchy of strength analysis for S-O1.

A.2.3 SL-O1

The assessment of the slab effective flange width, b_{eff} will be further discussed in Chapter 8. For the M-N performance domain evaluation, b_{eff} is taken to be 890mm. Table A.3 summarises the range of b_{eff} calculated with the different provisions from various international codes and the geometry of test unit SL-O1:

Table A.3: The range of slab effective flange width, b_{eff}, for test specimens SL-O1 and SL-R3.

Code/Guidelines	Effective tension flange width (mm)
NZS3101:2006	890
ASCE-41 / FEMA 356	980
NZSEE 2006	1753
JBDPA-2001 / AIJ-1994	839
EC8-III (2004) [+]	630

All calculations assumed the presence of transverse beam, beam span of 3047mm, bay width of 3047mm, beam and column widths of 230mm, beam depth of 330mm, slab thickness of 100mm and provided clear slab flange width of 375mm.

Similar to NS-O1, $\tau_{b,max}$ and $\tau_{b,res}$ are taken to be $0.3\sqrt{f'_c}$ MPa and $0.15\sqrt{f'_c}$ MPa respectively. These result in limiting beam bars f_s to be 168MPa and 84MPa respectively. The f'_c value is taken from the day-of-testing compressive strength (f'_c = 16.4MPa for the lower half of the specimen) while the reinforcing steel properties are taken from the steel test results (§4.5.1). In evaluating the joint shear capacity, the limit states for the principal stresses are taken to be $p'_t = 0.19\sqrt{f'_c}$ MPa and $p'_c = 0.3f'_c$ MPa. As per the discussion in Chapter 2, no enhancement of joint shear strength is assumed for the transverse beam confinement effect. The M-N performance domain for SL-O1 is shown in Figure A.5.

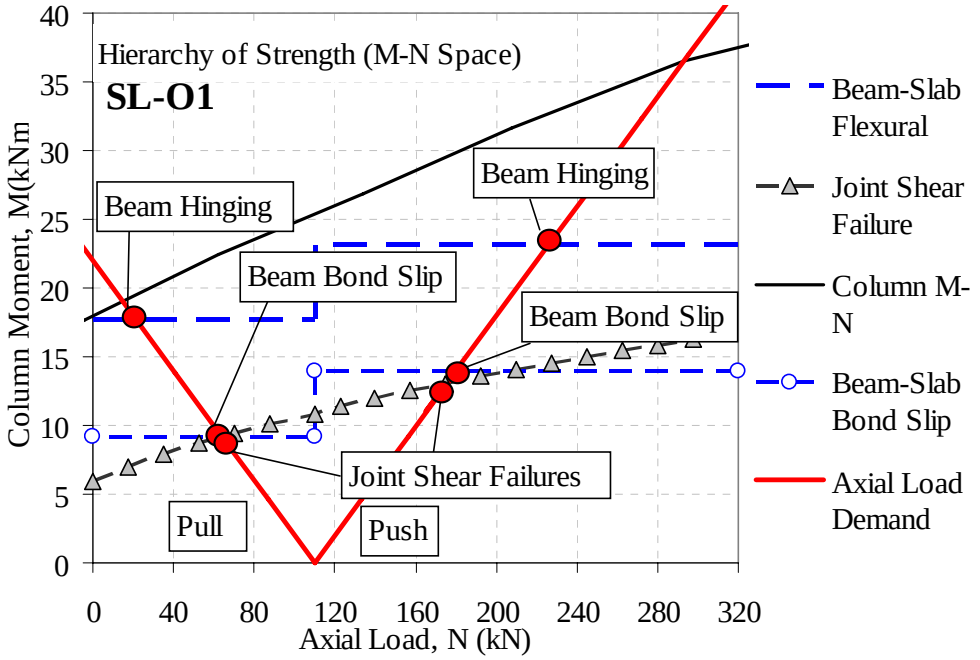

Figure A.5: M-N performance domain and hierarchy of strength analysis for SL-O1.

A.3 M-N PERFORMANCE DOMAIN OF RETROFITTED JOINTS

The analytical tools and methodology described in §2.4 and §3.4 are used to derive the M-N performance domains for all the retrofitted beam-column joint specimens. The assumptions of the prototype building and the specimens retrofitting details are given in §4.2.1 and §4.3 respectively.

A.3.1 NS-R1

The M-N performance domain for NS-R1 is shown in Figure A.6. The f'_c value is taken from the day-of-testing compressive strength (f'_c = 25.6MPa). In evaluating the retrofitted joint shear capacity, the joint aspect ratio, h'_b/h'_c, is taken to be (0.9*230mm)/(330mm-36mm) = 0.704. Thus, the modified limit state for the p'_t is $0.296\sqrt{f'_c}$ MPa and the limit $p'_c = 0.3f'_c$ MPa still applies. For the beam flexural failure, two limit states have been considered: a) with perfect bond; and b) limit bond capacity, where $\tau_{b,max}$ and $\tau_{b,res}$ are taken to be $0.3\sqrt{f'_c}$ MPa and $0.15\sqrt{f'_c}$ MPa respectively. These results in limiting beam bars f_s to be 210MPa and 105MPa respectively.

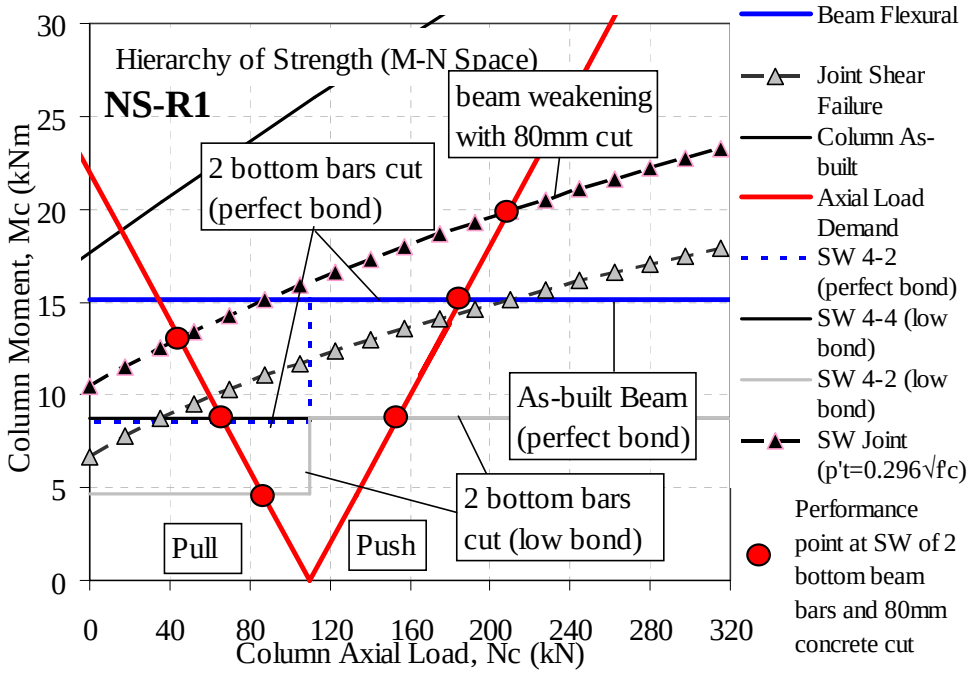

Figure A.6: M-N performance domain and hierarchy of strength analysis for NS-R1.

A.3.2 NS-R2

The M-N performance domain for NS-R2 is shown in Figure A.7. The f'_c value is taken from the day-of-testing compressive strength (f'_c = 25.1MPa). The post-tensioning force applied is 120kN. At the post-tensioned beam flexural failure limit state (ε_c = 0.003), the tendon force is about 157kN (just yielding). Concrete confinement factor of 1.1 is assumed. For the nonprestressed reinforcements, no strain hardening is assumed as it is expected that bond-slip of the plain rebars will limit the strain hardening. In evaluating the joint shear capacity, the limit states for the principal stresses are taken to be $p'_t = 0.25\sqrt{f'_c}$ MPa and $p'_c = 0.3f'_c$ MPa. The higher p'_t limit state is to account for the increase in confinement and decrease in the h'_b/h'_c ratio.

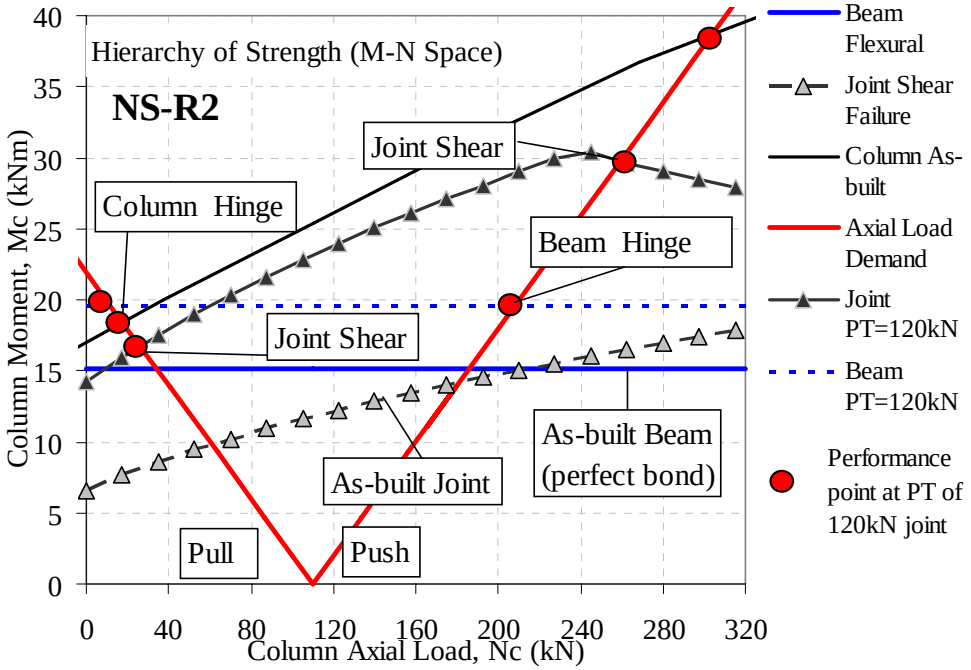

Figure A.7: M-N performance domain and hierarchy of strength analysis for NS-R2.

A.3.3 NS-R3

The M-N performance domain for NS-R3 is shown in Figure A.8. The f'_c value is taken from the day-of-testing compressive strength (f'_c = 24.3MPa). The post-tensioning force applied is 40kN. At the post-tensioned beam flexural failure limit state (ε_c = 0.003), the tendon force is about 83.5kN. Concrete confinement factor of 1.1 is assumed. For the nonprestressed reinforcements, strain hardening in tension is assumed for the reinforcements in the weakened beam face (bottom beam bars) while no strain-hardening is assumed for the top beam bars (in both tension and compression). In evaluating the joint shear capacity, the limit states for the principal stresses are taken to be $p'_t = 0.25\sqrt{f'_c}$ MPa and $p'_c = 0.3f'_c$ MPa.

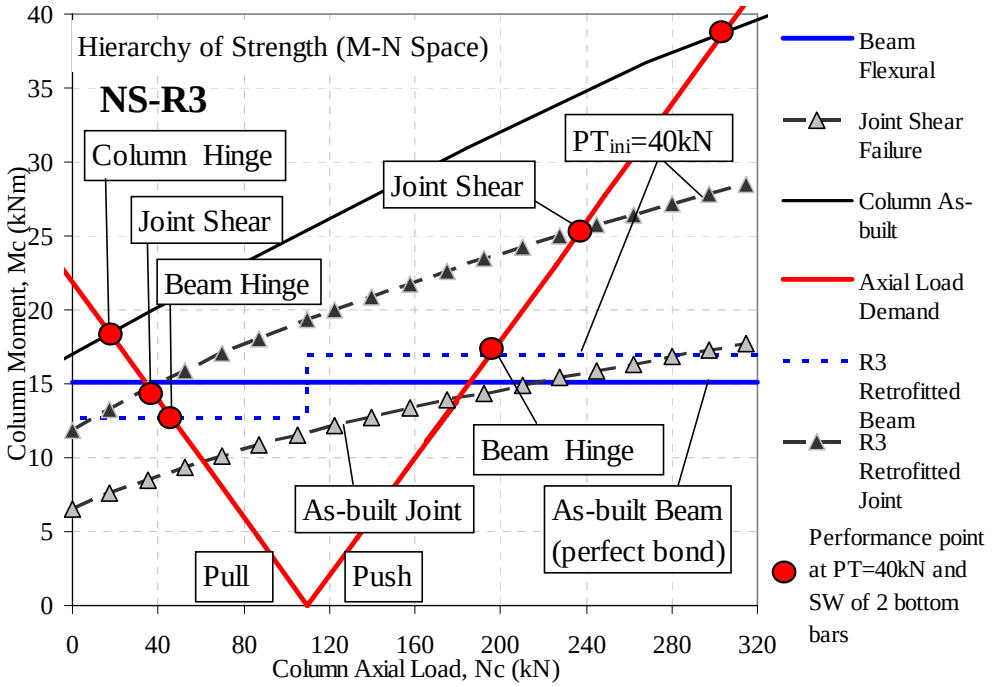

Figure A.8: M-N performance domain and hierarchy of strength analysis for NS-R3.

A.3.4 NS-R4

The M-N performance domain for NS-R4 is shown in Figure A.9. Similar assumptions for the evaluation of the post-tensioned beam flexural and the joint shear capacities as per NS-R3 were adopted. The f'_c value was taken from the day-of-testing compressive strength (f'_c = 30.3MPa).

In evaluating the joint shear capacity, the limit states for the principal stresses are taken to be $p'_t = 0.25\sqrt{f'_c}$ MPa and $p'_c = 0.3f'_c$ MPa. Due to the shift of the weakening location, the beam-hinging flexural capacity was decreased in accordance to the reduction of beam moment along the beam (approximately 95% of the beam moment at the beam-column interface).

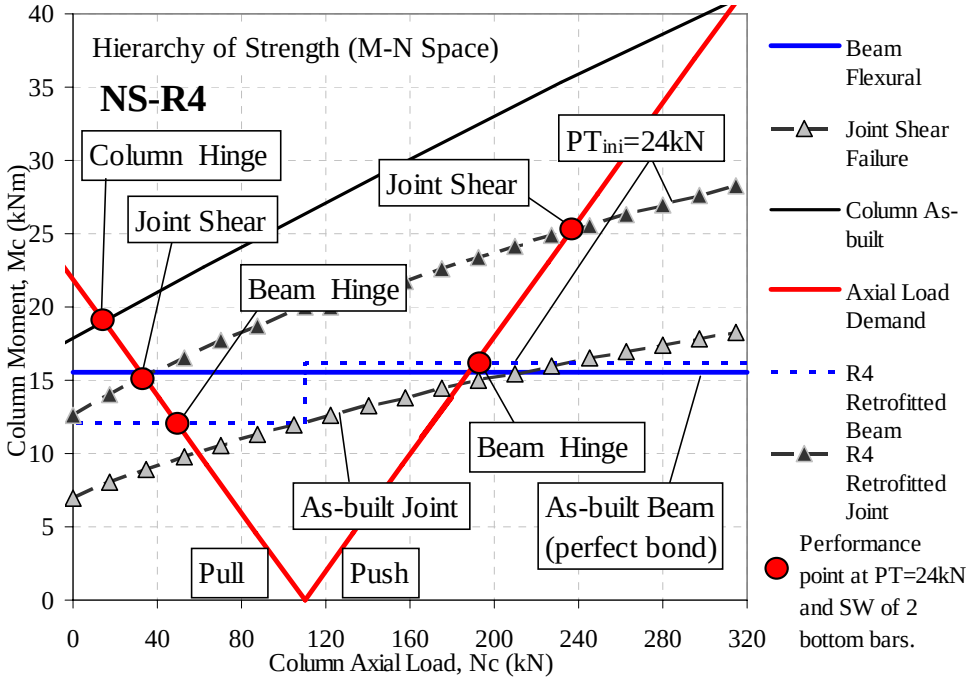

Figure A.9: M-N performance domain and hierarchy of strength analysis for NS-R4.

A.3.5 S-R3

The M-N performance domain for S-R3 is shown in Figure A.10. Similar assumptions for the evaluation of the post-tensioned beam flexural and the joint shear capacities as per NS-R3 are adopted. The f'_c value is taken from the day-of-testing compressive strength (f'_c = 27.5MPa). Similar assumptions as per S-O1 is made in evaluating the column lap-splice failures, as no retrofit intervention is used for the column. The f_s at the lap-splice onset failure and residual strength are 311MPa and 62MPa.

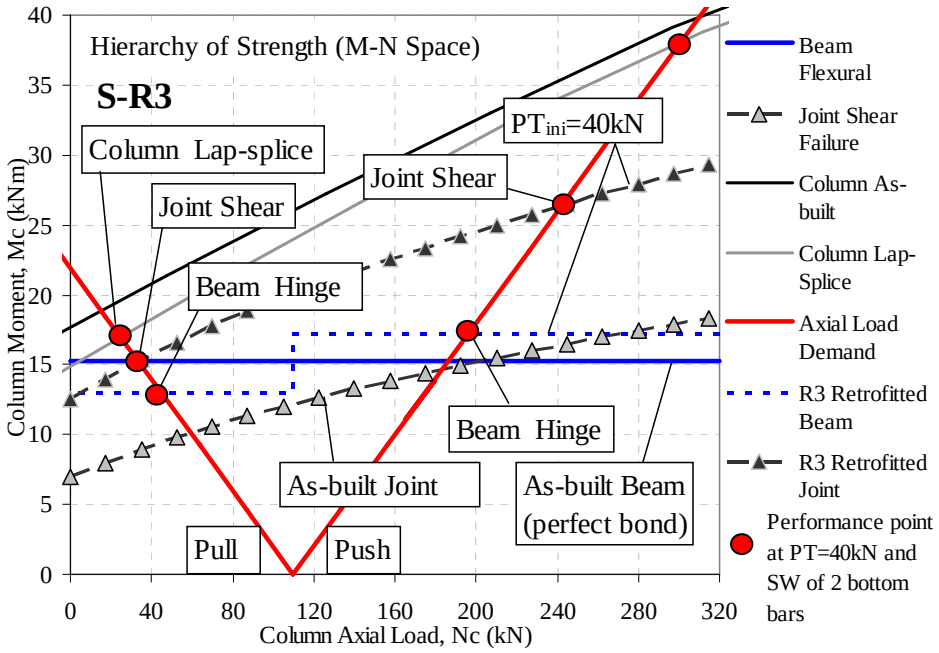

Figure A.10: M-N performance domain and hierarchy of strength analysis for S-R3.

A.3.6 SL-R3

The M-N performance domain for SL-R3 is shown in Figure A.11. The f'_c value is taken from the day-of-testing compressive strength (f'_c = 23.1MPa for the beam and joint and f'_c =17.0MPa for the upper column). Similar to SL-O1, the b_{eff} is taken to be 890mm and all the mesh reinforcements within b_{eff} are assumed to be effective in tension. For simplicity, the additional b_{eff} is not considered in the post-tensioned beam evaluation when the slab was in tension. Concrete confinement factor of 1.1 is assumed. For the nonprestressed reinforcements, strain hardening in

tension is assumed for the reinforcements in the weakened beam face (bottom beam bars) while no strain-hardening is assumed for the top beam bars (in both tension and compression). At the post-tensioned beam flexural failure limit state (ε_c = 0.003), the tendon force is about 99kN and 76kN in the Pull and Push cycles respectively. In evaluating the joint shear capacity, the limit states for the principal stresses are taken to be $p'_t = 0.25\sqrt{f'_c}$ MPa and $p'_c = 0.3f'_c$ MPa.

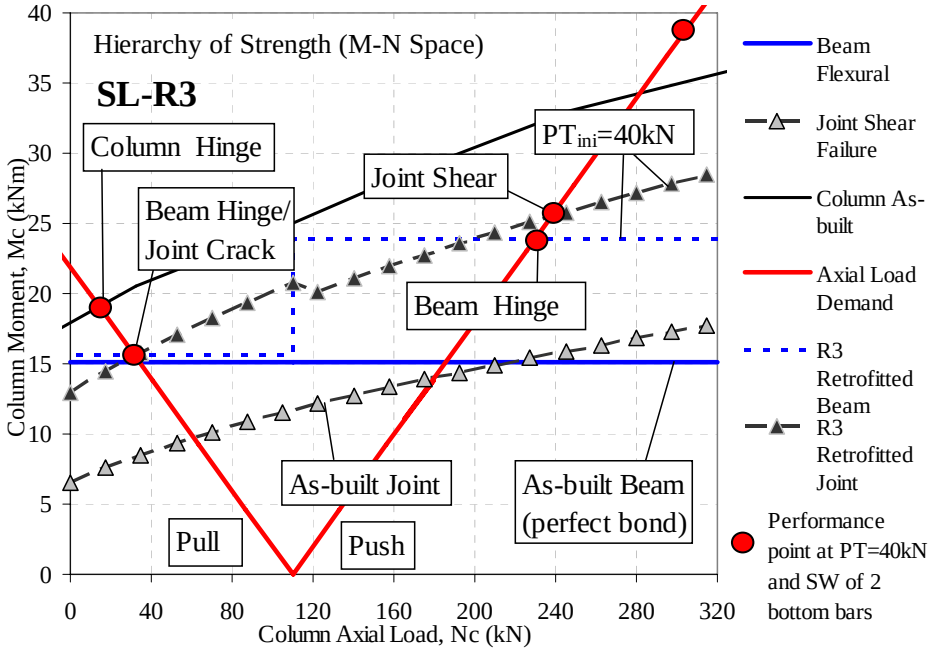

Figure A.11: M-N performance domain and hierarchy of strength analysis for SL-R3.

A.4 APPENDIX A REFERENCES

[1] ACI318-08. (2008) *Building code requirements for structural concrete and commentary*. American Concrete Inst. (ACI), Farmington Hills, MI.

[2] ASCE-SEI-41-06. (2007) *Seismic rehabilitation of existing buildings. ASCE standard ASCE/SEI 41-06*. American Society of Civil Engineers (ASCE), Reston, Va.

[3] NZS95:1955. (1955) *New Zealand Standard - Model Building By-Laws: Part IV and V*. New Zealand Standard Inst., Wellington, NZ.

[4] NZS3101:2006. (2006) *NZS 3101:2006 Concrete structures standard*. Standards New Zealand, Wellington, NZ.

APPENDIX B. EXPERIMENTAL TEST DATA AND LOG OF NS-O1

B.1 NS-O1 – AS-BUILT B-C JOINT BENCHMARK

B.1.1 Force-displacement hysteresis

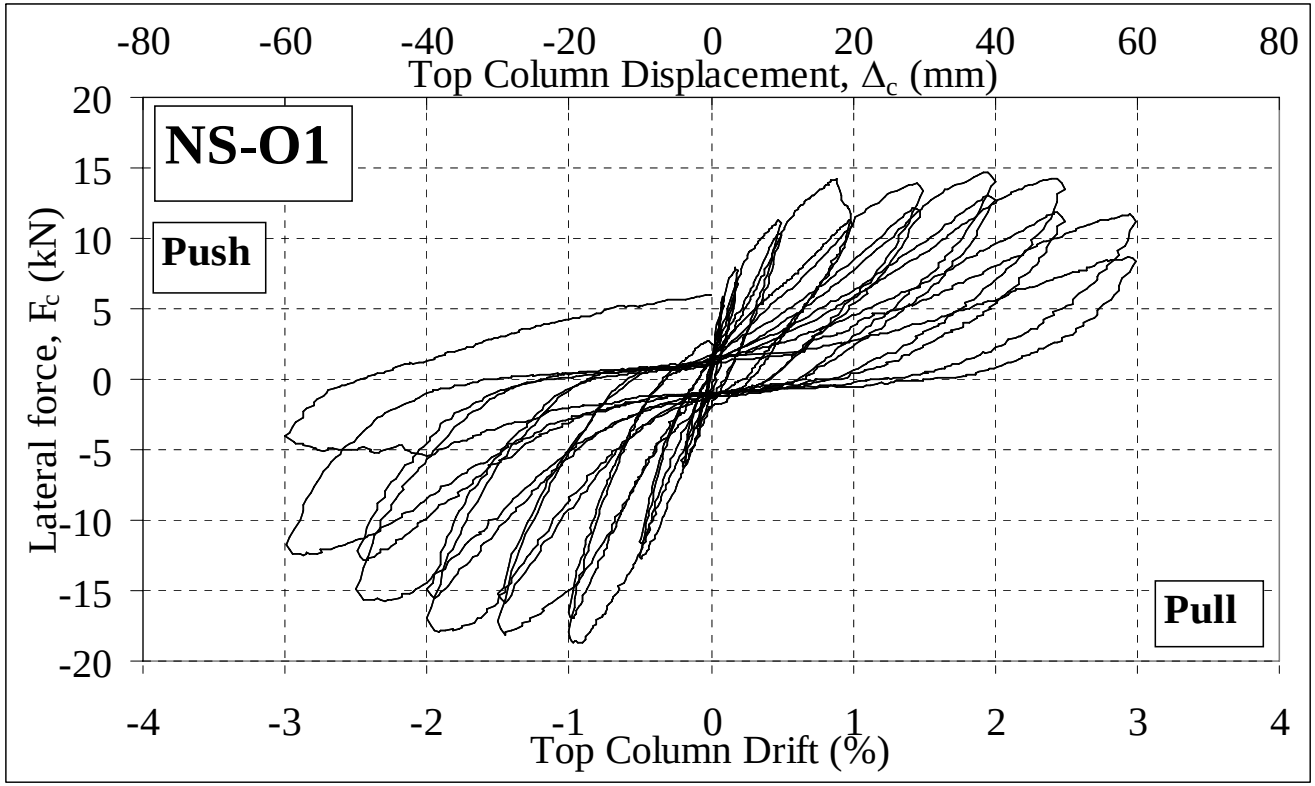

Figure B.1: Test Unit NS-O1: Top column lateral load, F_c versus top column displacement, Δ_c and drift, θ_{drift}.

B.1.2 Photographic observations

Figure B.2 General observation photographs for test unit NS-O1 at: Start, ±0.2%, ±0.5%, and ±1.0% drifts.

Figure B.3 General observation photographs for test unit NS-O1 at: ±1.0%, ±1.5% and ±2.0% drifts.

Figure B.4 General observation photographs for test unit NS-O1 at: ±2.0%. ±2.5%, ±3.0% drifts and the end-of-test.

B.1.3 Column strain gage readings

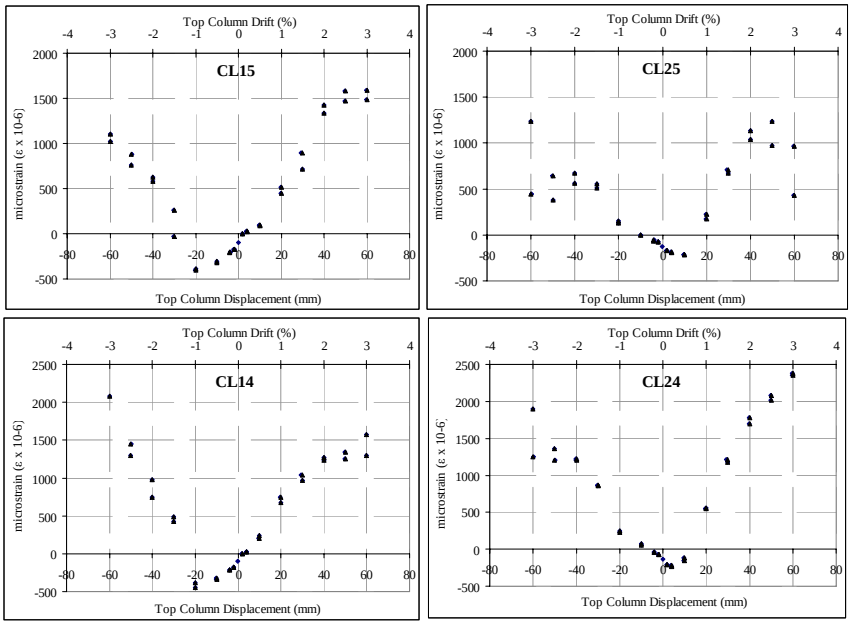

Figure B.5: Test Unit NS-O1: Column longitudinal bars strain gage readings: Top half.

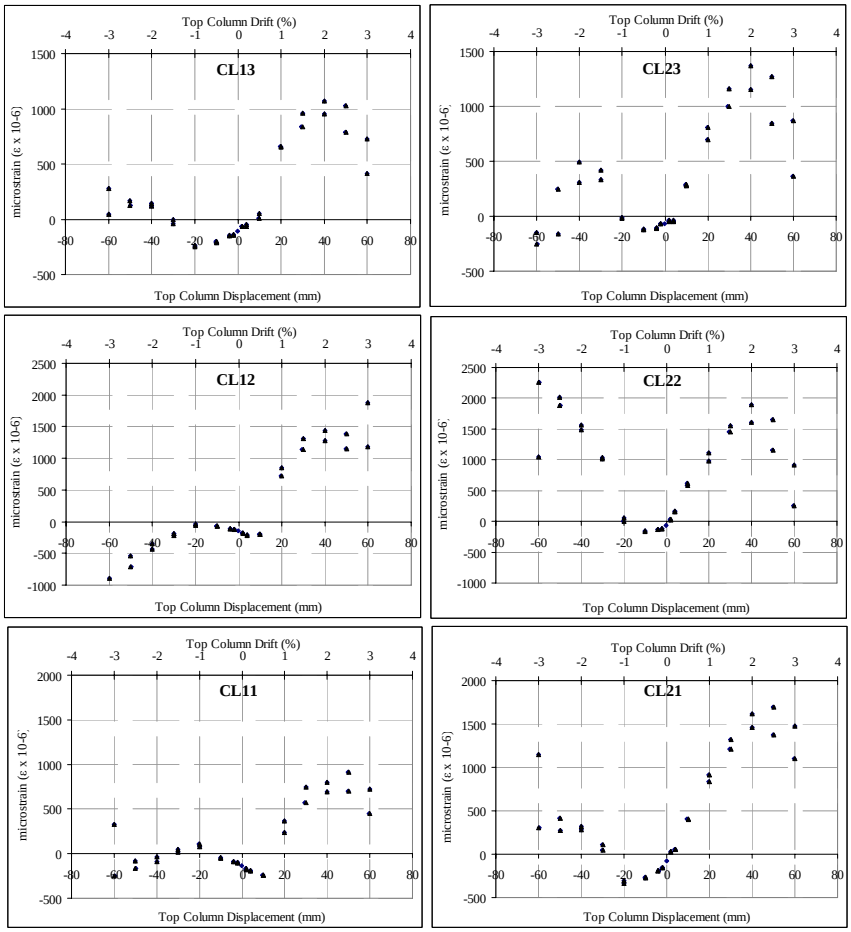

Figure B.6: Test Unit NS-O1: Column longitudinal bars strain gage readings: Bottom half.

B.1.4 Beam strain gage readings

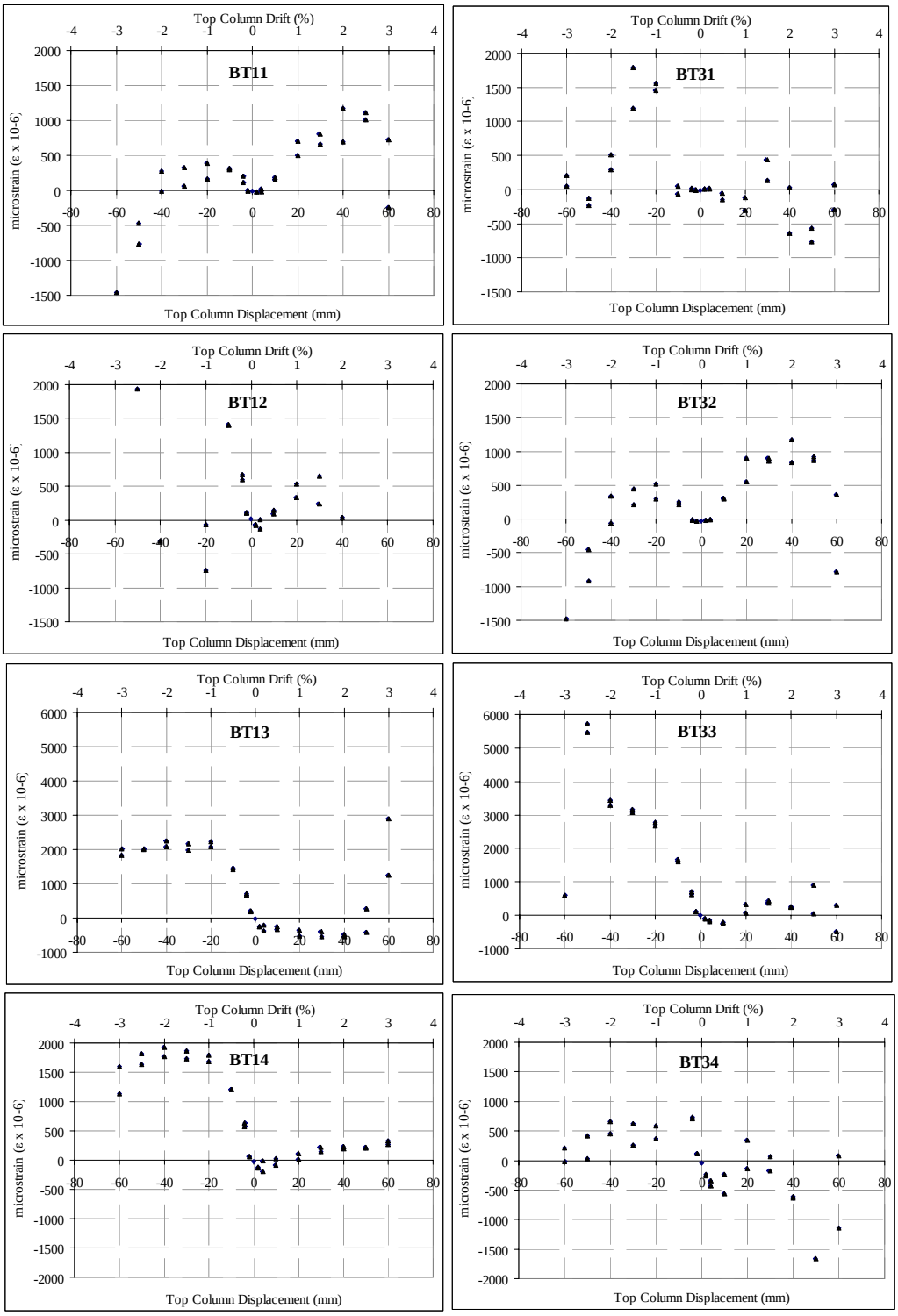

Figure B.7: Test Unit NS-O1: Beam longitudinal bars strain gage readings: Top bars.

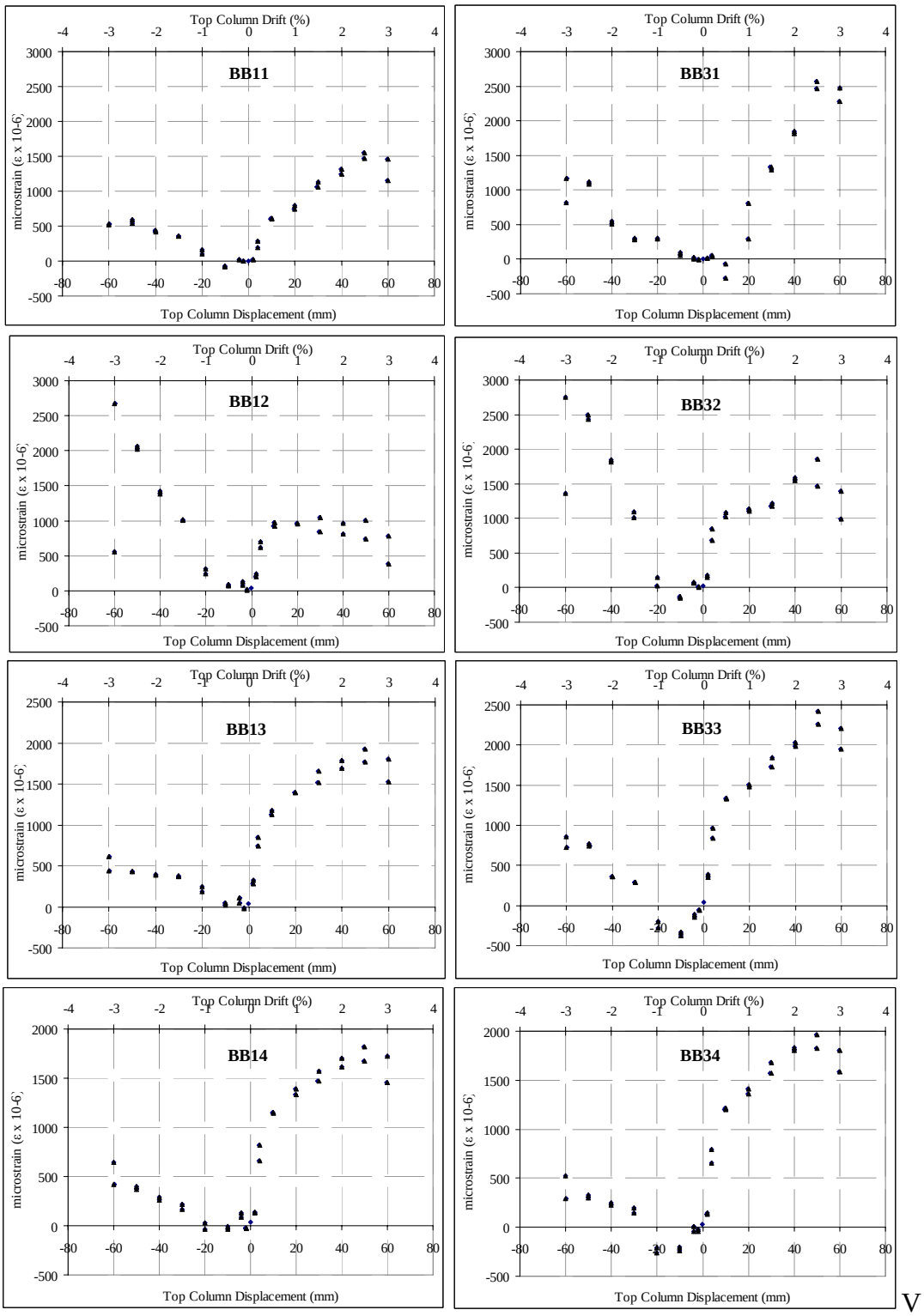

V

Figure B.8: Test Unit NS-O1: Beam longitudinal bars strain gage readings: Bottom bars.

B.1.5 Stirrups (column and beam) strain gage readings

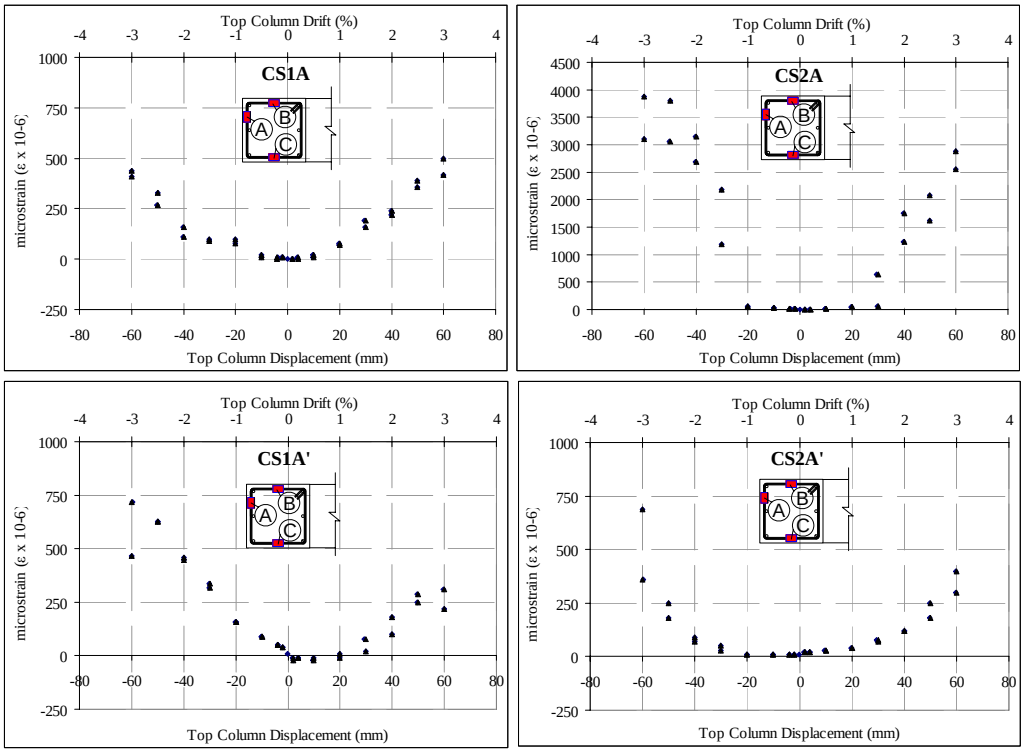

Figure B.9: Test Unit NS-O1: Column stirrups bars strain gage readings.

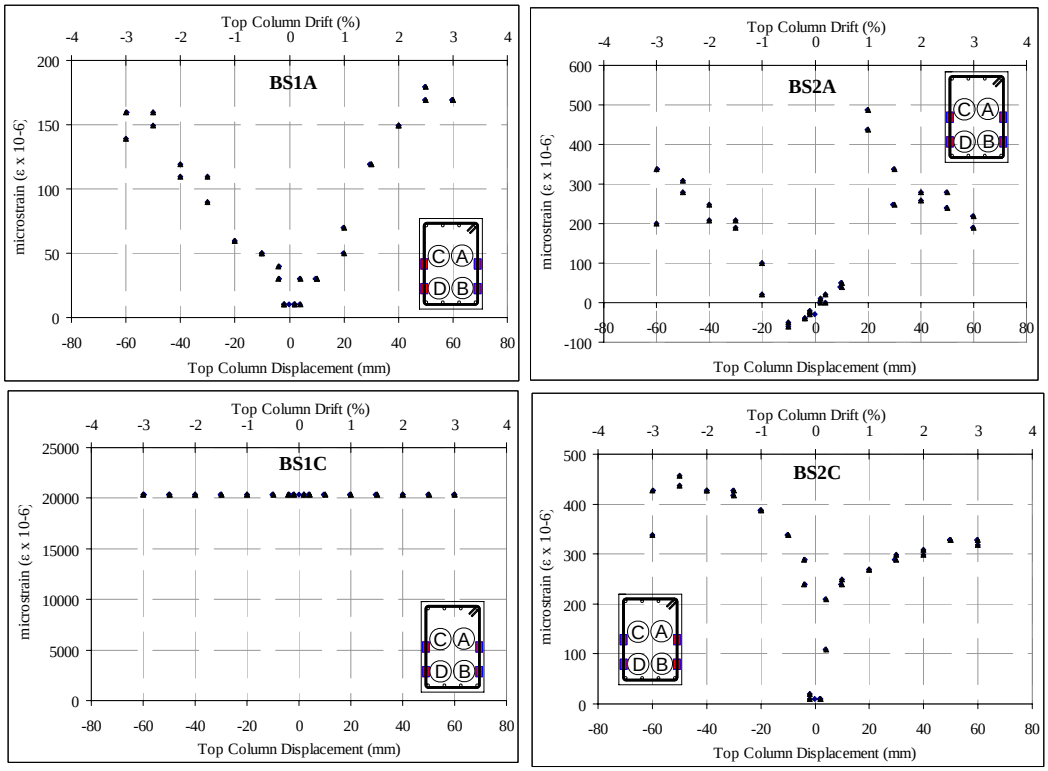

Figure B.10: Test Unit NS-O1: Beam stirrups bars strain gage readings.

APPENDIX C. EXPERIMENTAL TEST DATA AND LOG FOR NS-R1, NS-R2, NS-R3 AND NS-R4

C.1 NS-R1 –RETROFITTED B-C JOINT WITH BEAM-WEAKENING -ONLY

C.1.1 Force-displacement hysteresis

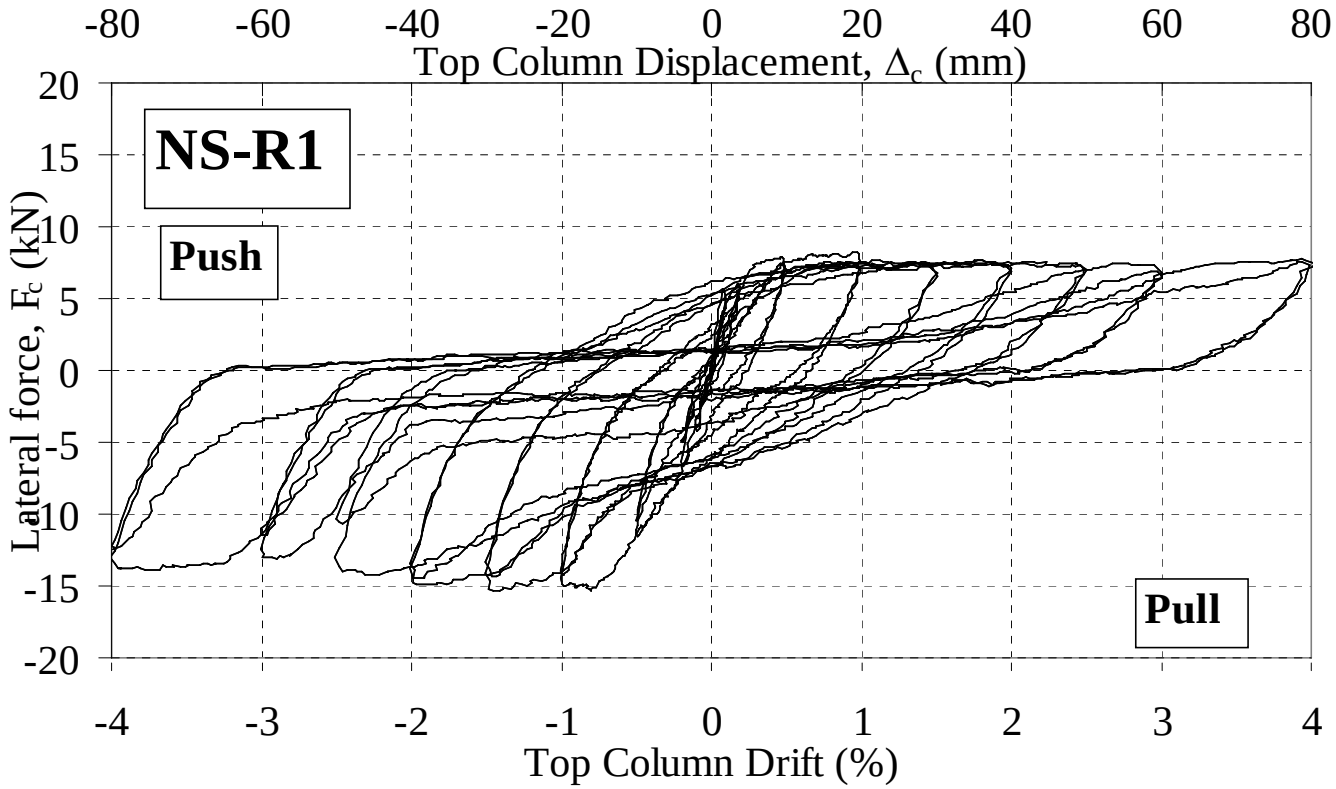

Figure C.1: Test Unit NS-R1: Top column lateral load, F_c, versus top column displacement, Δ_c, and drift, θ_{drift}.

C.1.2 Photographic observations

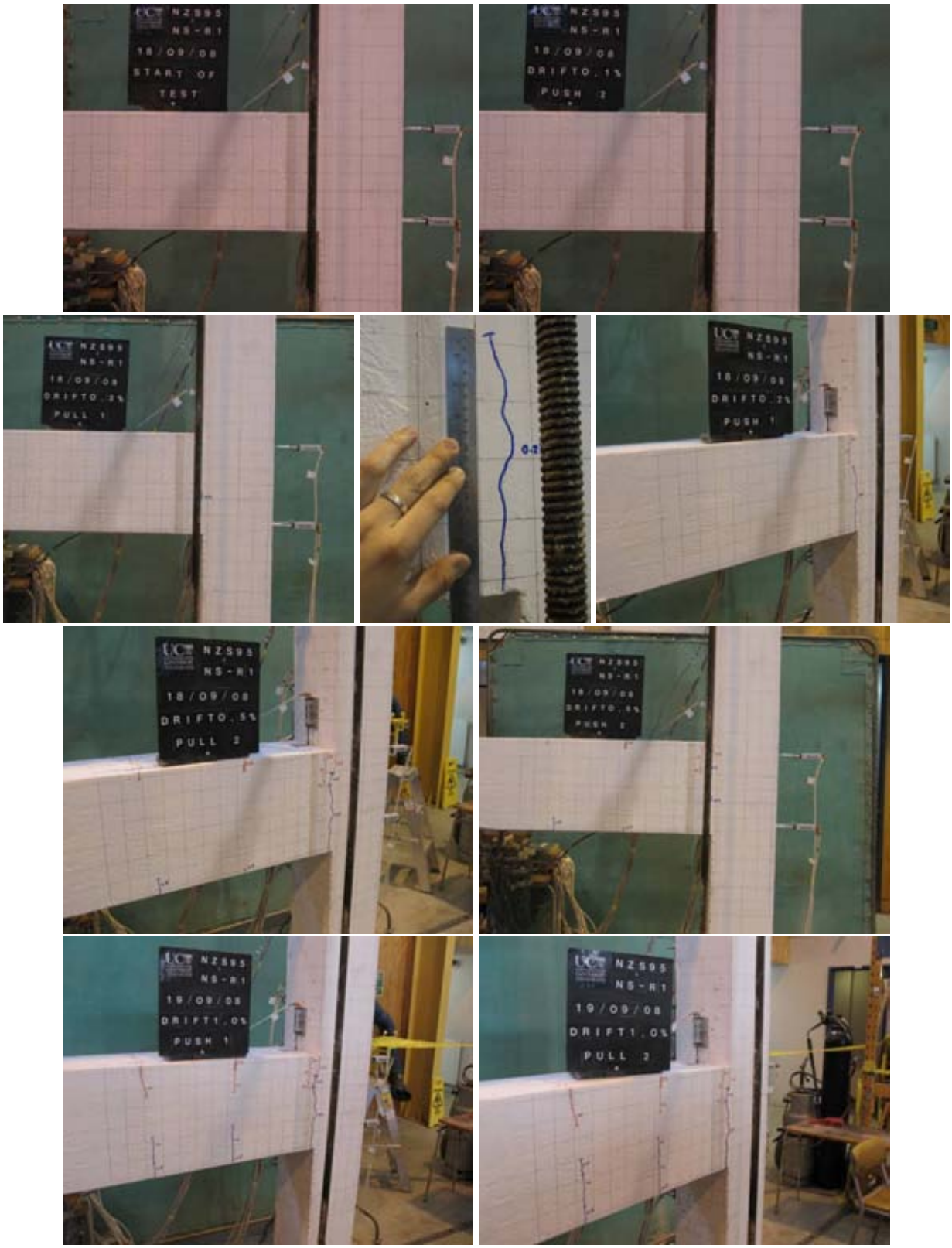

Figure C.2: General observation photographs for test unit NS-R1 at: Start, ±0.2%, ±0.5% and ±1.0% drifts.

Figure C.3: General observation photographs for test unit NS-R1 at: ±1.0%, ±1.5% and ±2.0% drifts.

Figure C.4: General observation photographs for test unit NS-R1 at: ±2.0% and ±2.5% drifts.

Figure C.5: General observation photographs for test unit NS-R1 at: ±3.0% and ±4.0% drifts.

Figure C.6: General observation photographs for test unit NS-R1 at the end-of-test.

C.1.3 Column strain gage readings

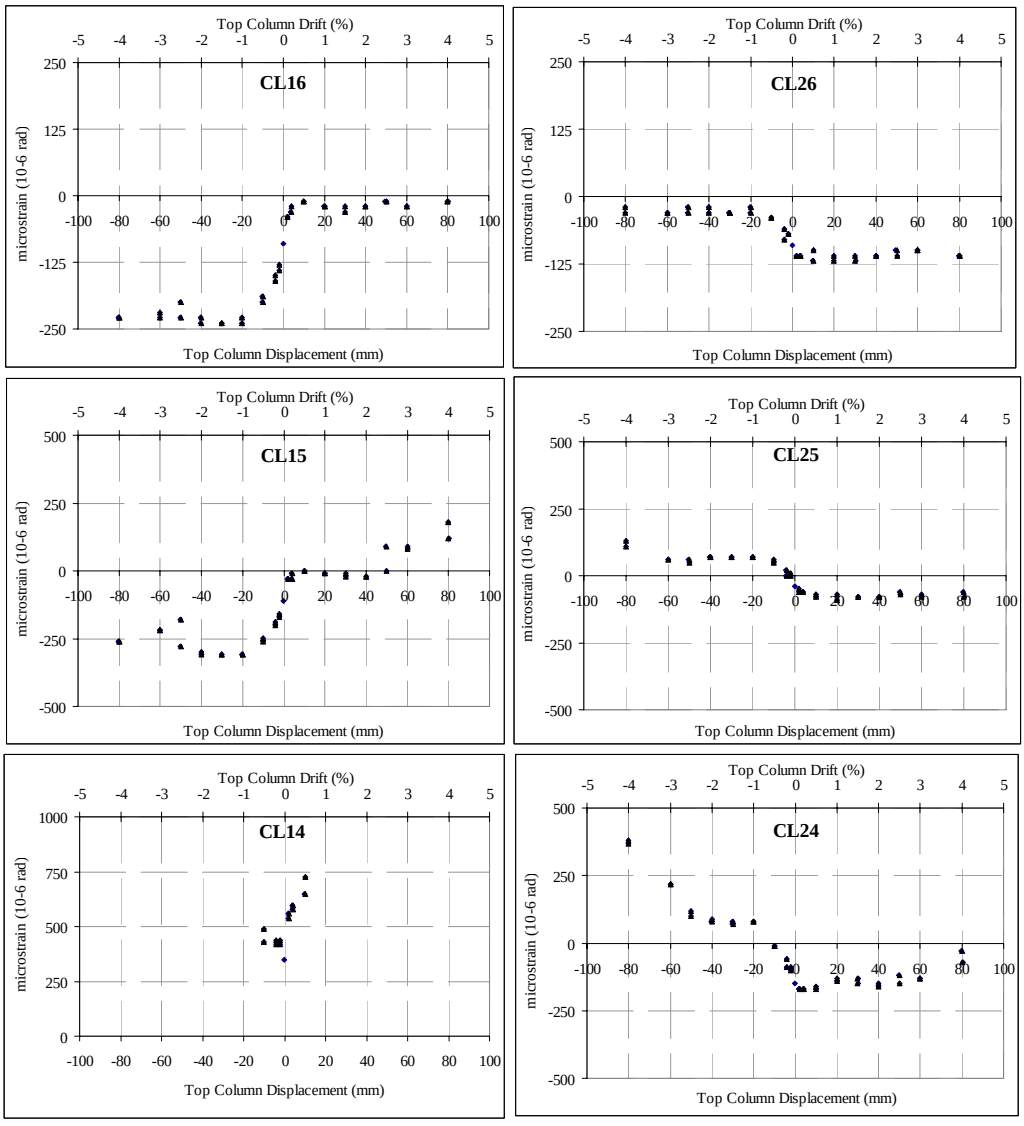

Figure C.7: Test Unit NS-R1: Column longitudinal bars strain gage readings: Top half.

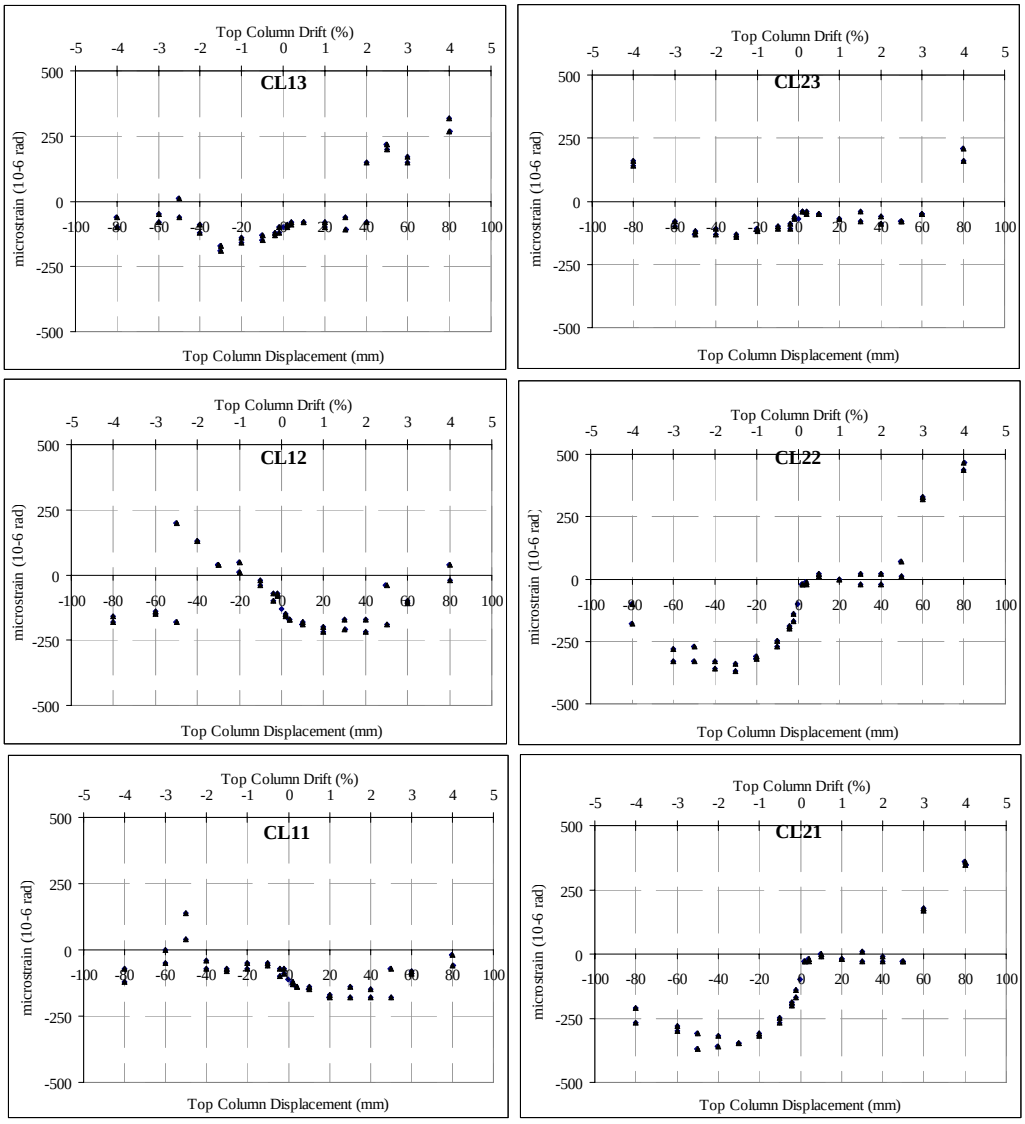

Figure C.8: Test Unit NS-R1: Column longitudinal bars strain gage readings: Bottom half.

C.1.4 Beam strain gage readings

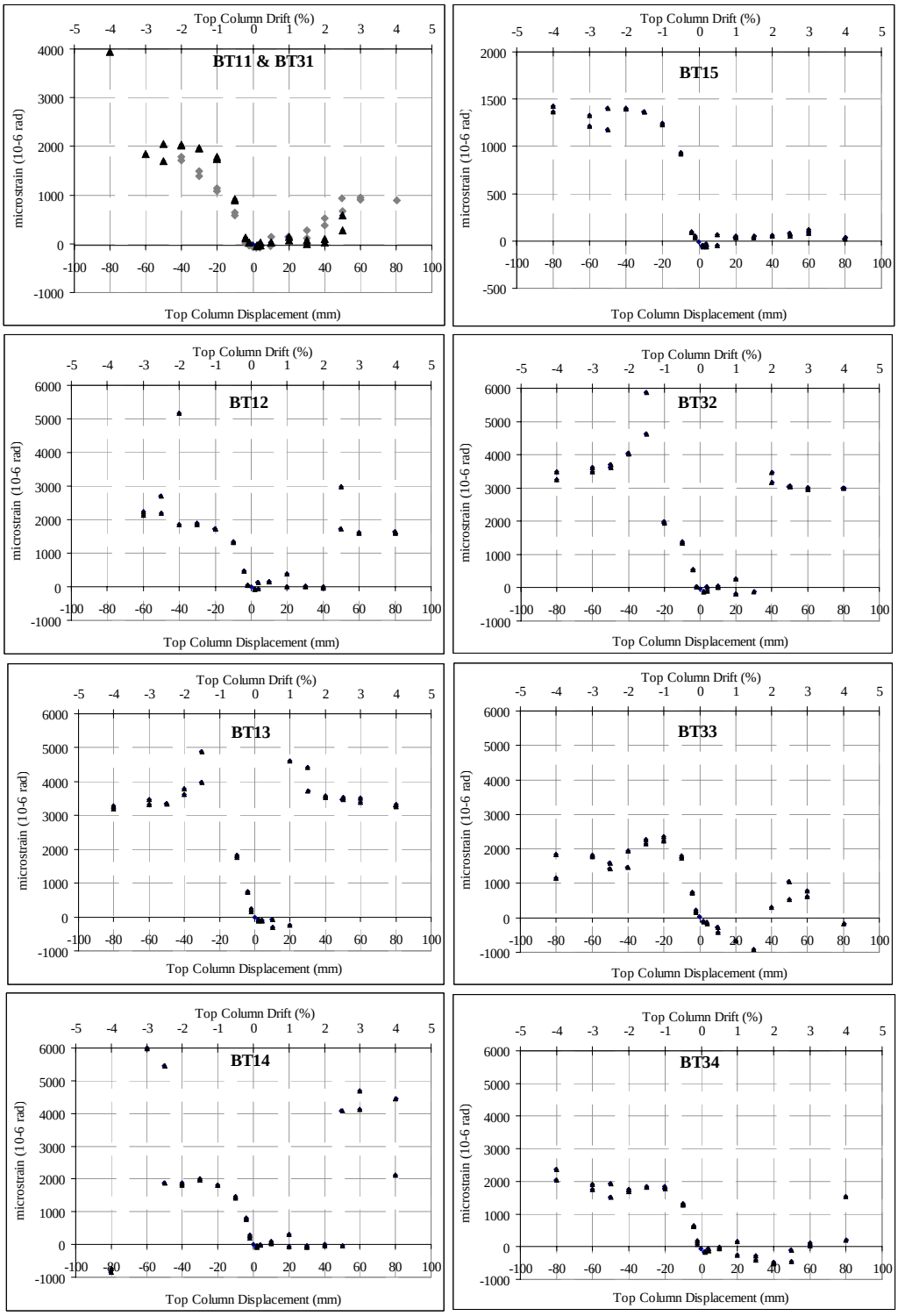

Figure C.9: Test Unit NS-R1: Beam longitudinal bars strain gage readings: Top bars.

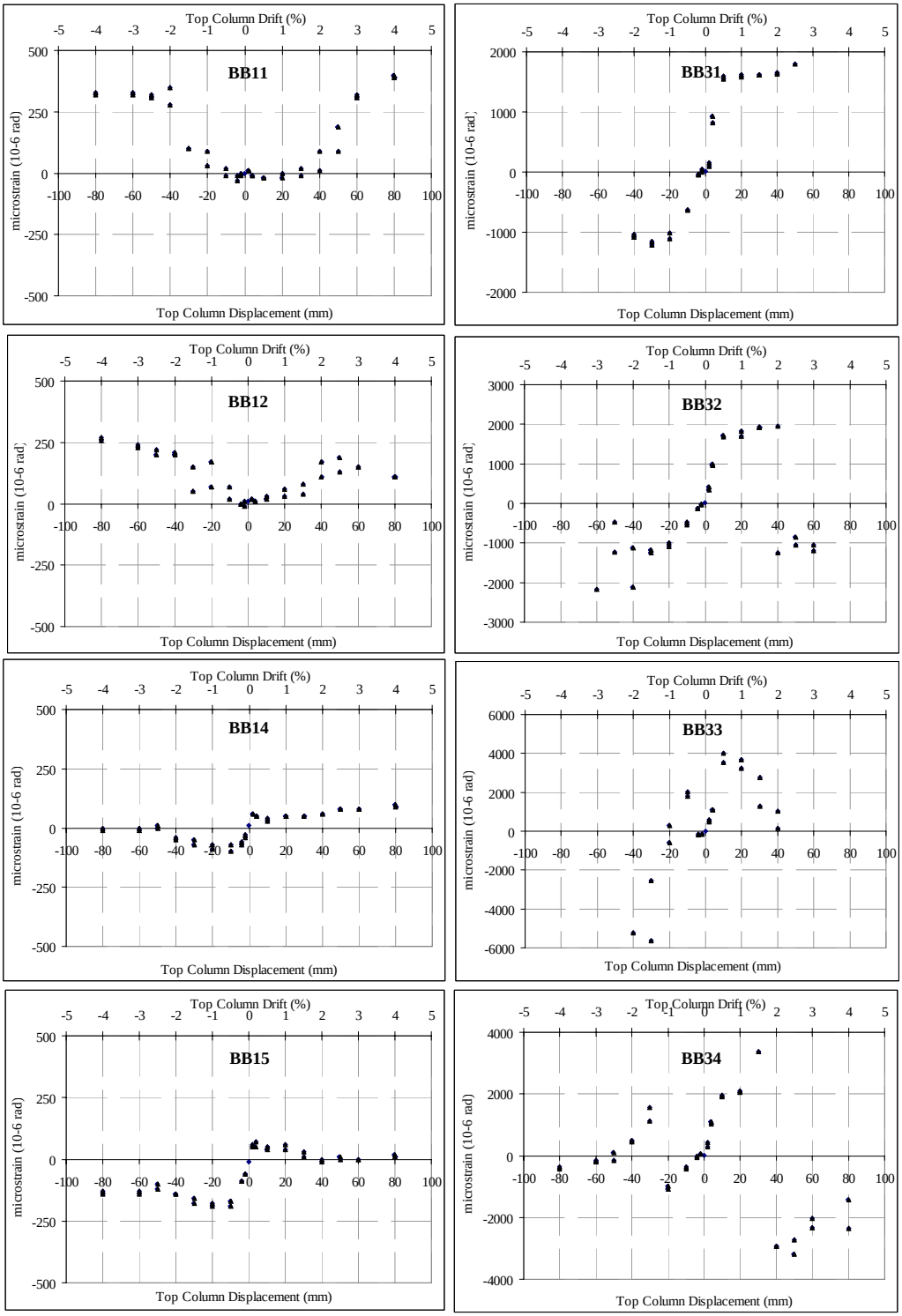

Figure C.10: Test Unit NS-R1: Beam longitudinal bars strain gage readings: Bottom bars: BB1X-severed beam bar and BB3X – uncut beam bar. (BB13 was damaged at installation. BB3 gages were broken at ±2% drift cycles.)

C.1.5 Stirrups (column and beam) strain gage readings

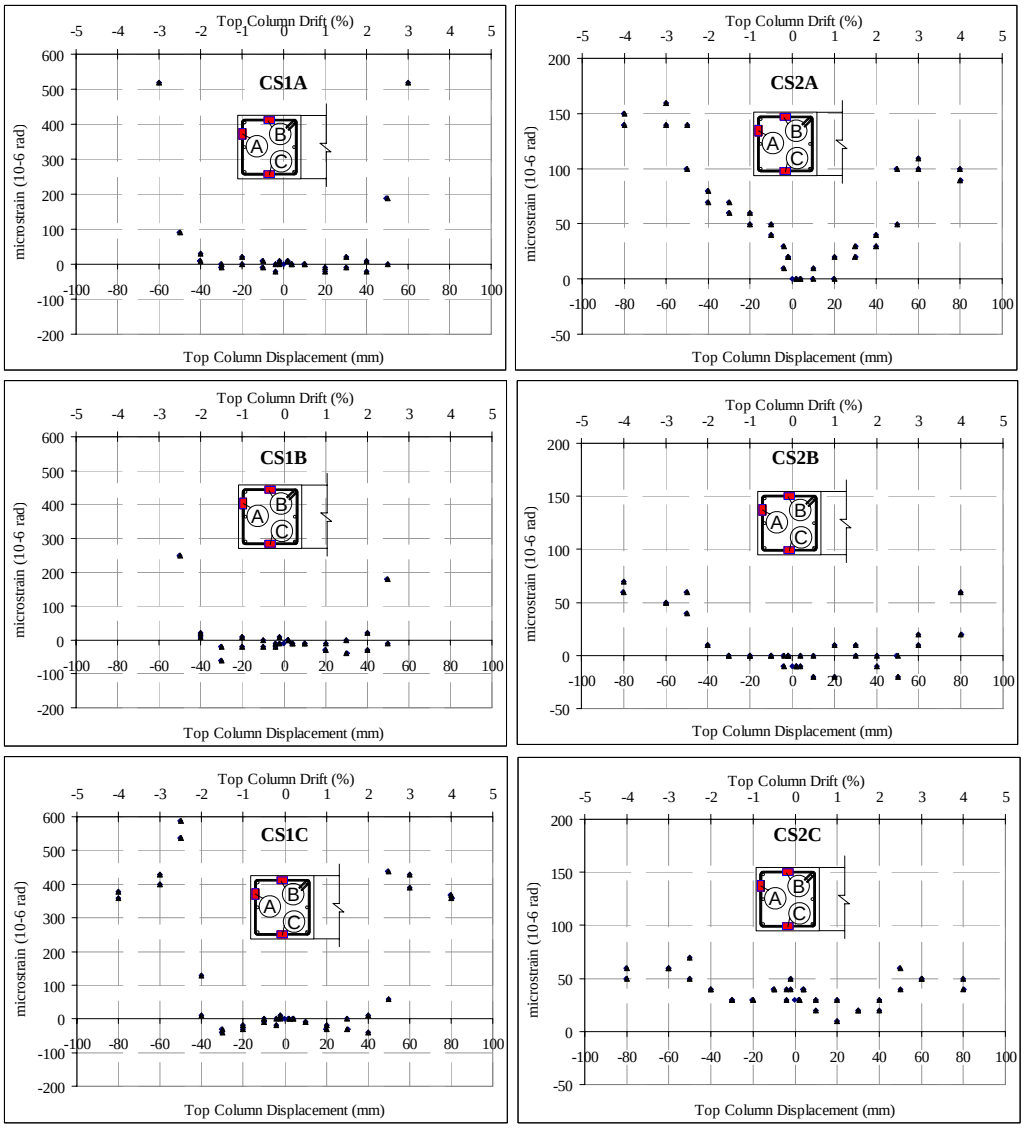

Figure C.11: Test Unit NS-R1: Column stirrups bars strain gage readings.

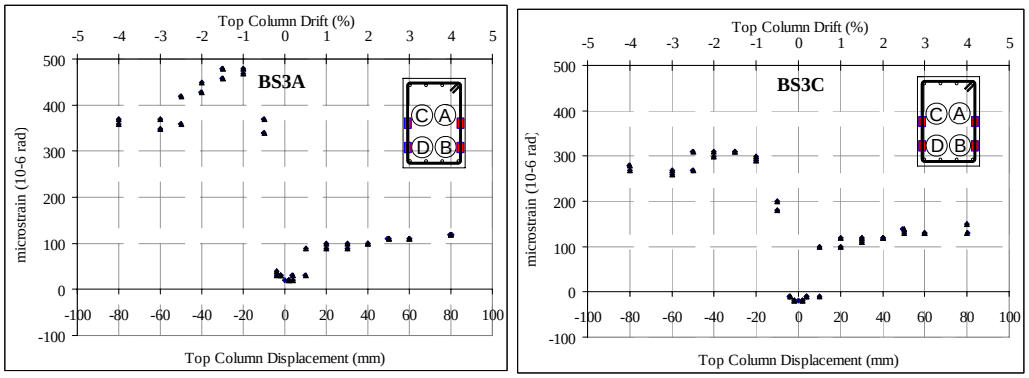

Figure C.12: Test Unit NS-R1: Beam stirrups bars strain gage readings (BS3C was damaged).

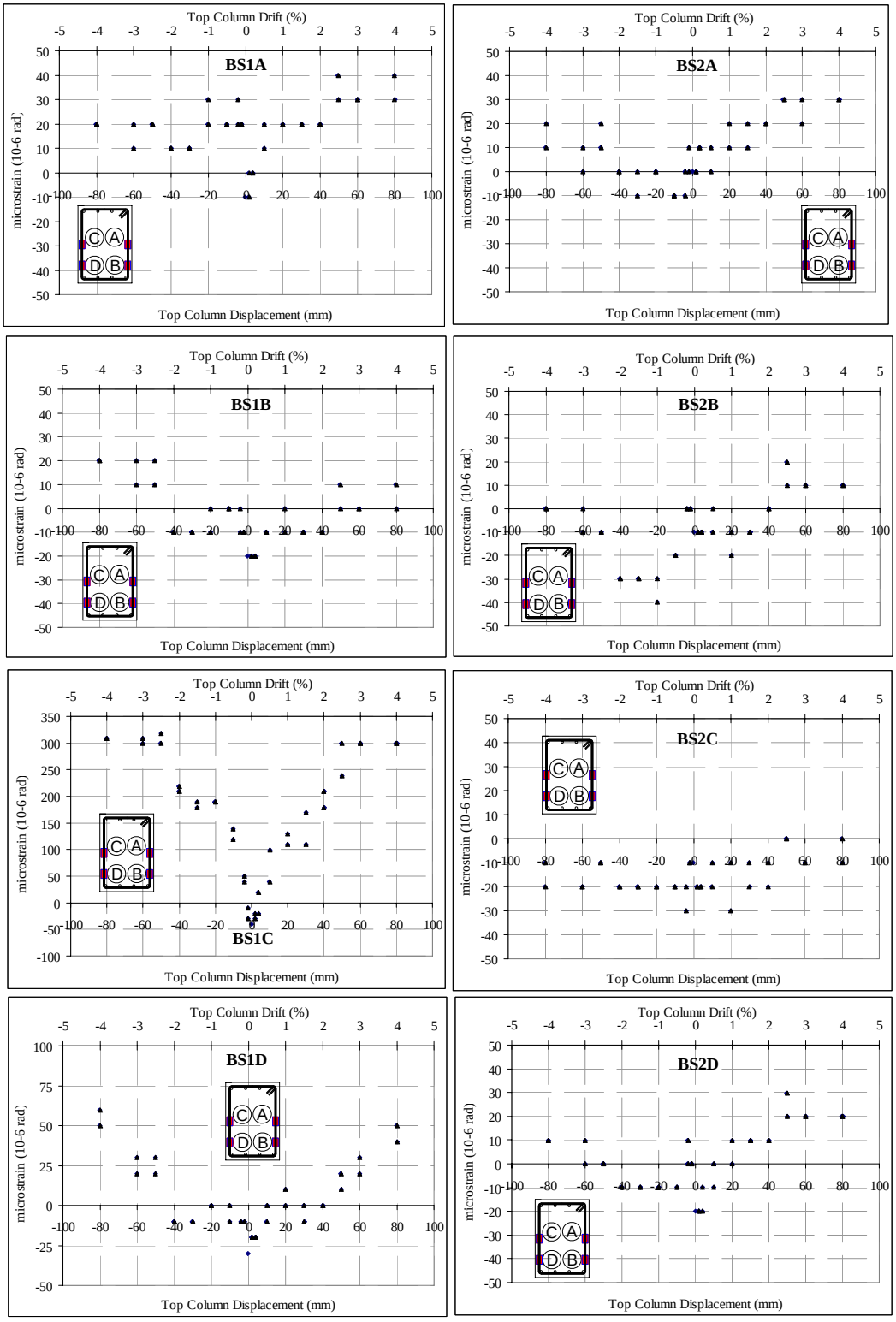

Figure C.13: Test Unit NS-R1: Beam stirrups bars strain gages reading.

C.2 NS-R2 –RETROFITTED B-C JOINT WITH POST-TENSIONING-ONLY

C.2.1 Force-displacement hysteresis

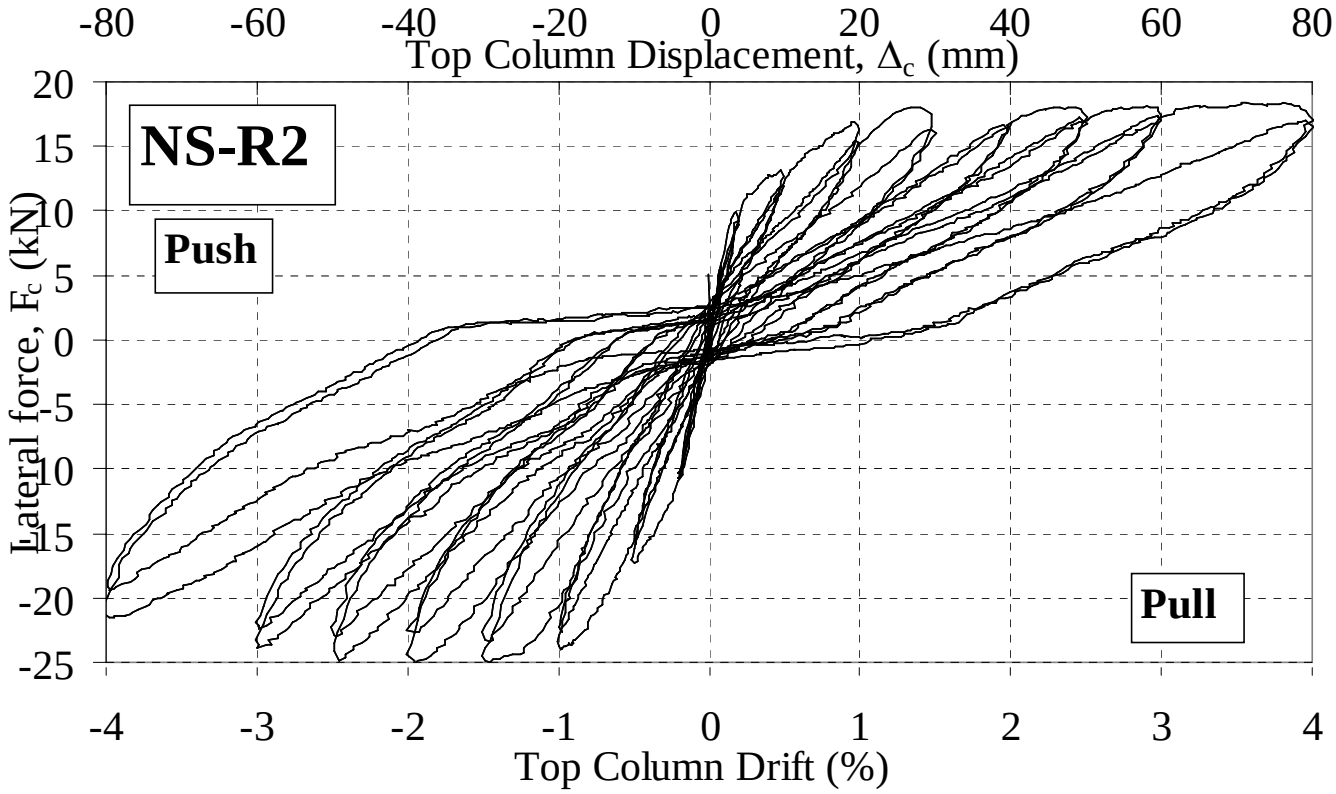

Figure C.14: Test Unit NS-R2: Top column lateral load, F_c, versus top column displacement, Δ_c, and drift, θ_{drift}.

C.2.2 Photographic observations

Figure C.15: General observation photographs for test unit NS-R2 at: Start, ±0.2% and ±0.5% drifts.

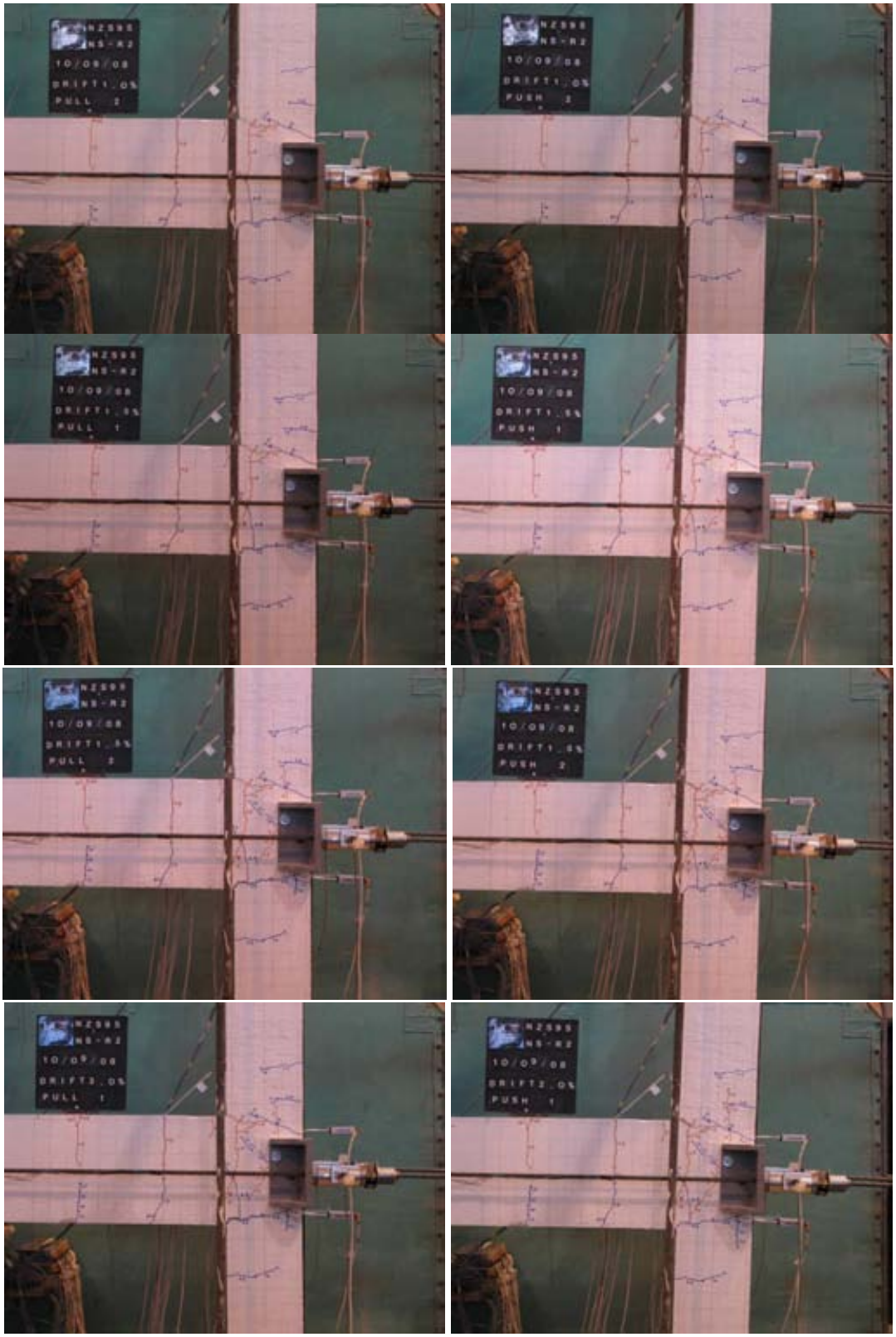

Figure C.16: General observation photographs for test unit NS-R2 at: ±1.0%, ±1.5% and ±2.0% drifts.

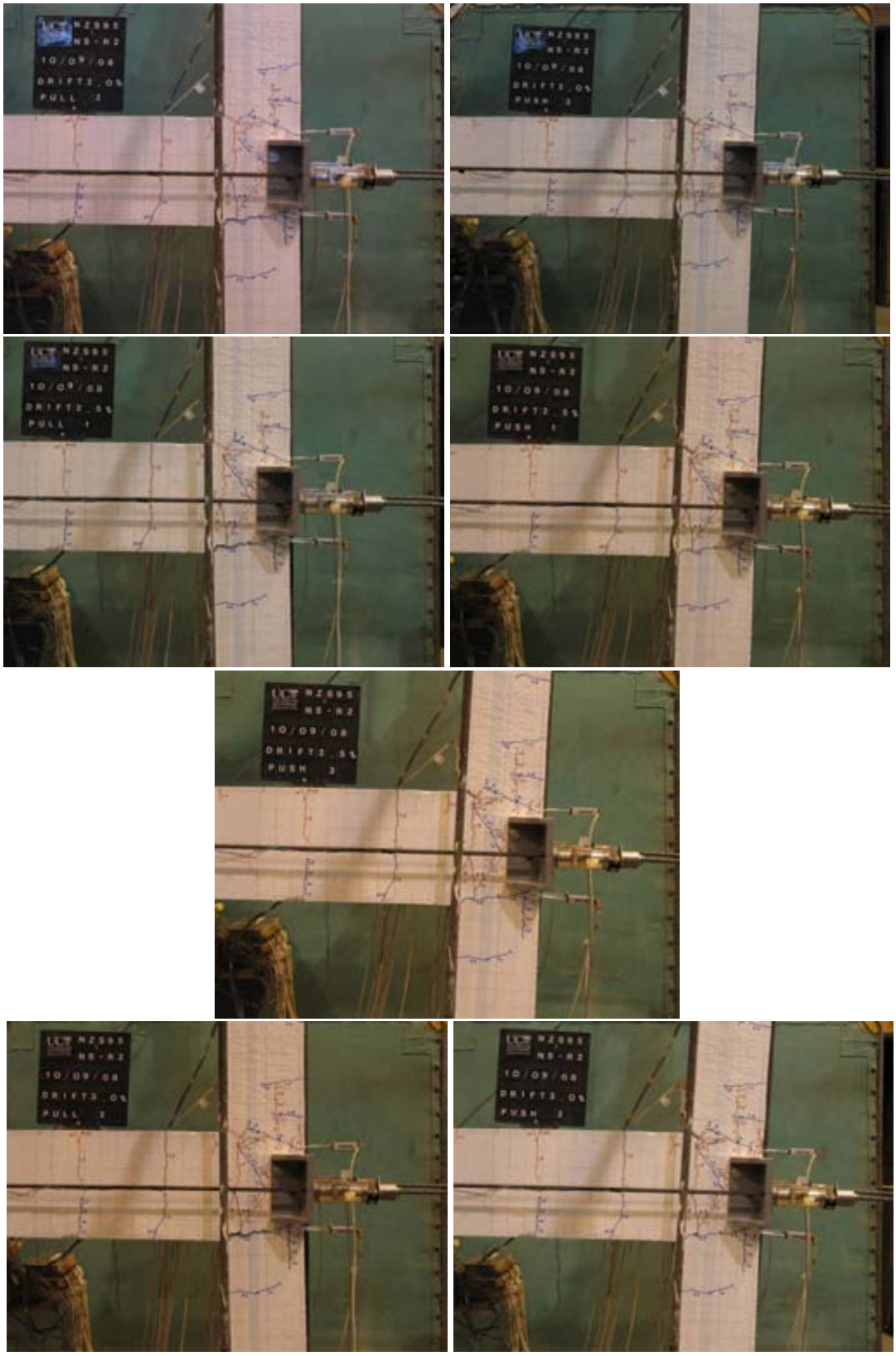

Figure C.17: General observation photographs for test unit NS-R2 at: ±2.0%, ±2.5% and ±3.0% drifts.

Figure C.18: General observation photographs for test unit NS-R2 at: ±4.0% drift and the end-of-test.

C.2.3 Column strain gage readings

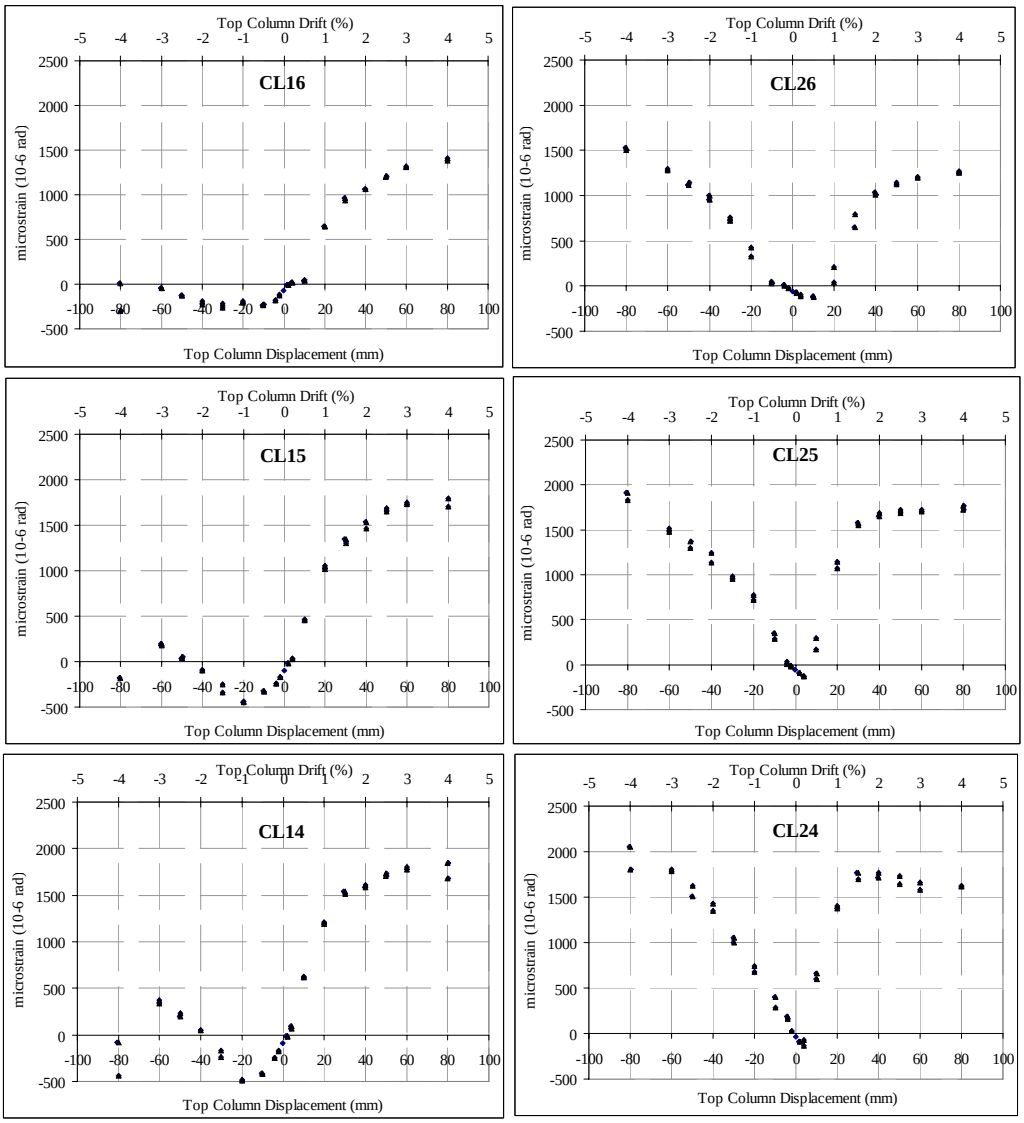

Figure C.19: Test Unit NS-R2: Column longitudinal bars strain gage readings: Top half.

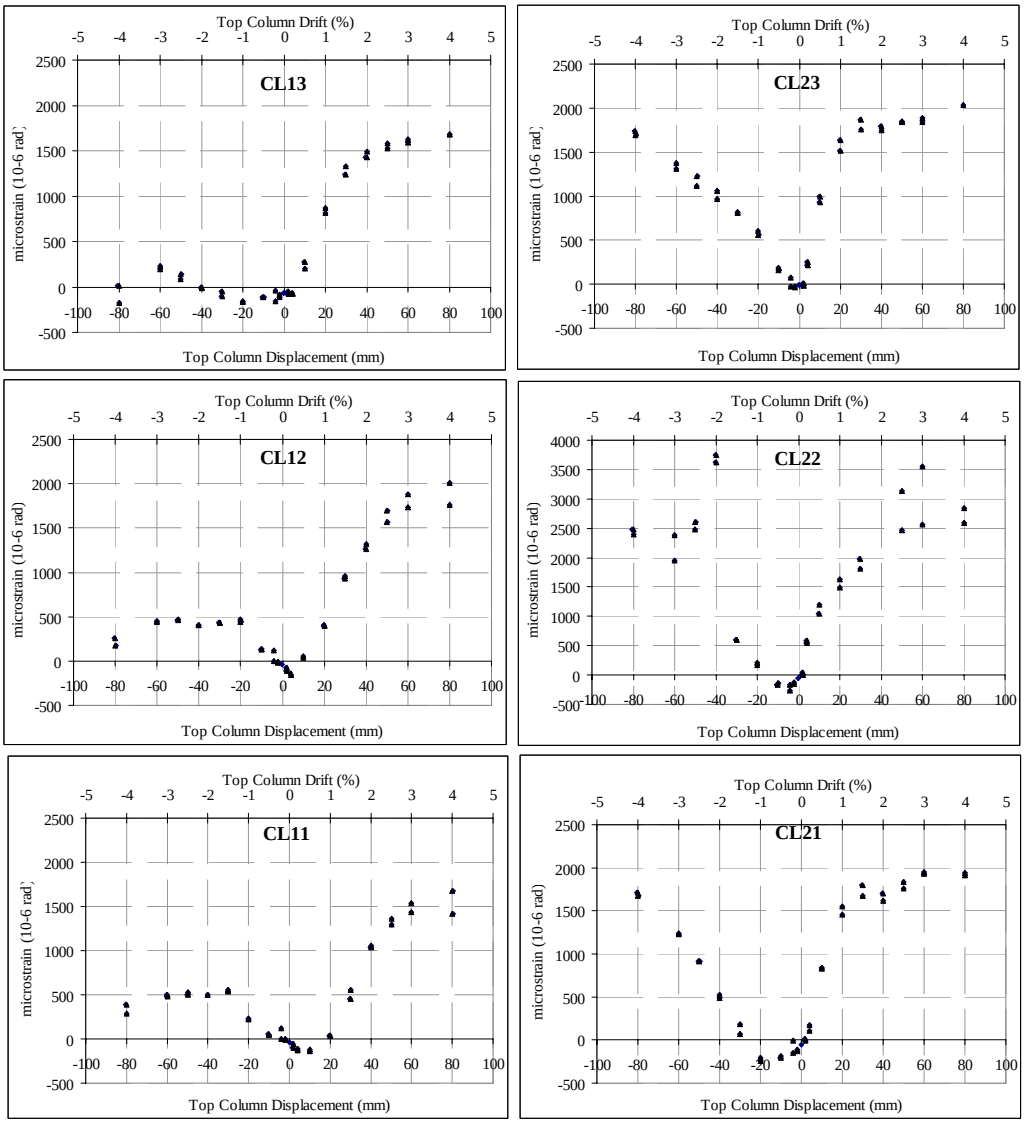

Figure C.20: Test Unit NS-R2: Column longitudinal bars strain gage readings: Bottom half.

C.2.4 Beam strain gage readings

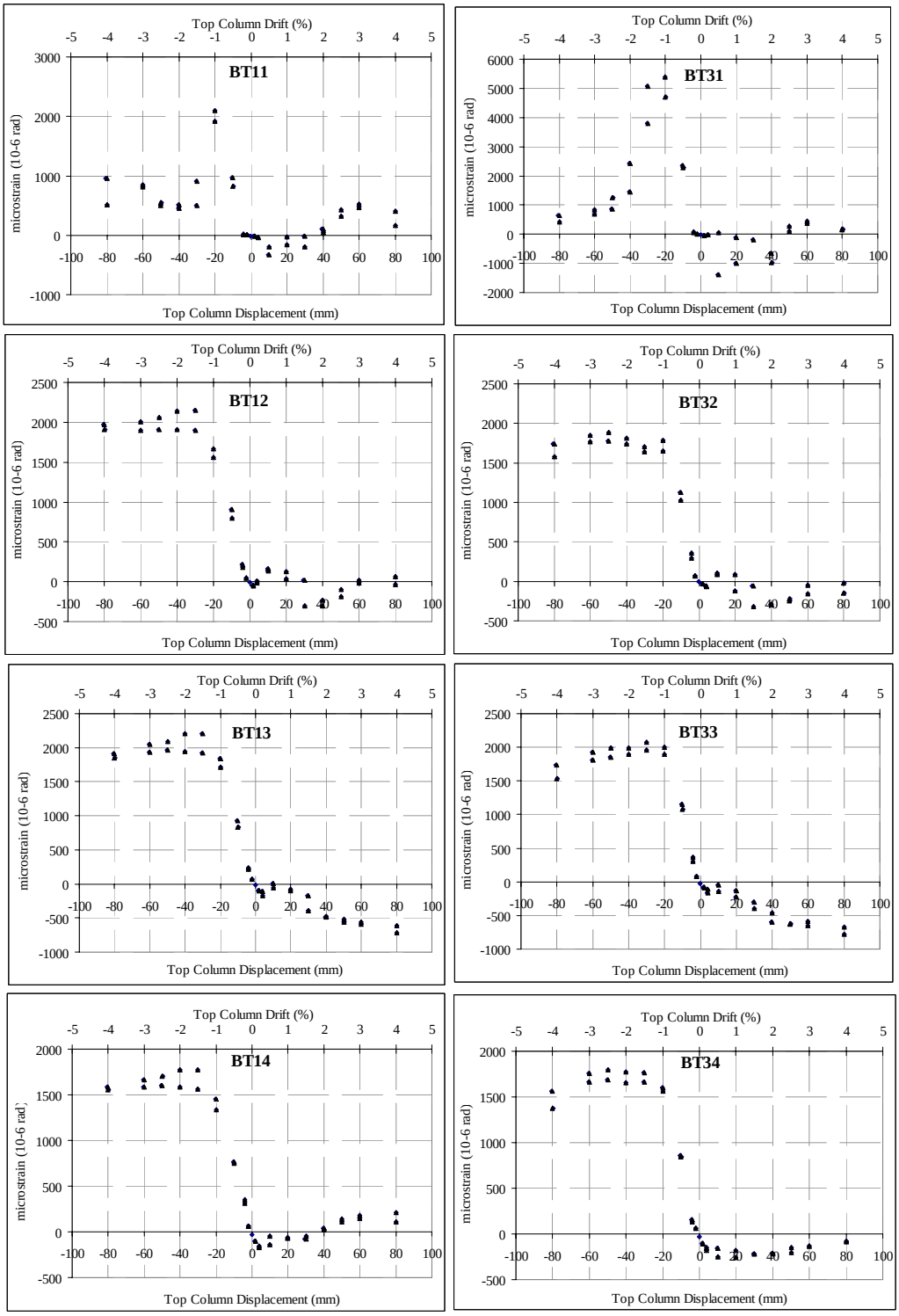

Figure C.21: Test Unit NS-R2: Beam longitudinal bars strain gage readings: Top bars.

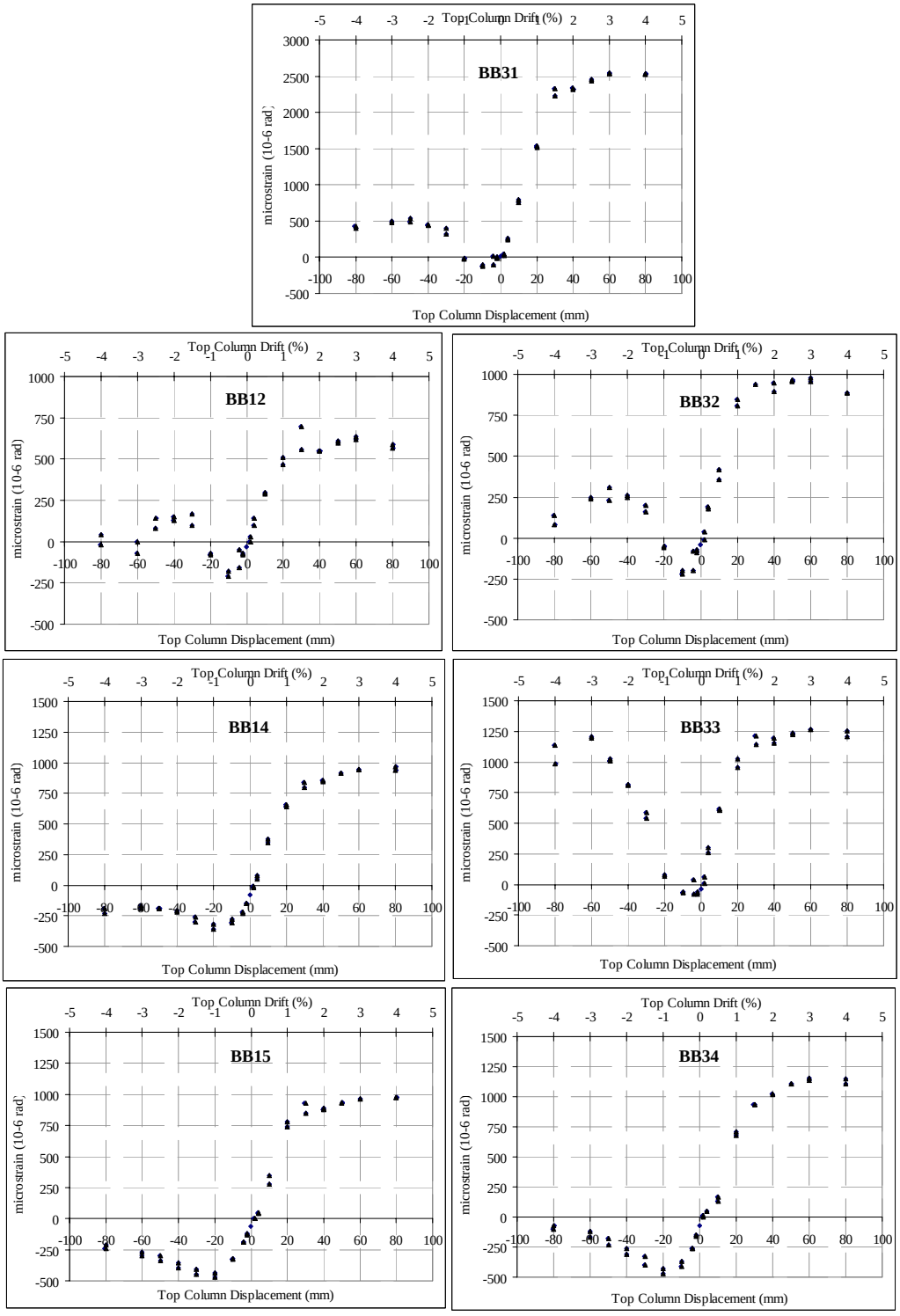

Figure C.22: Test Unit NS-R2: Beam longitudinal bars strain gage readings: Bottom bars. (BB11 and BB13 were damaged during construction.)

C.2.5 Stirrups (column and beam) strain gage readings

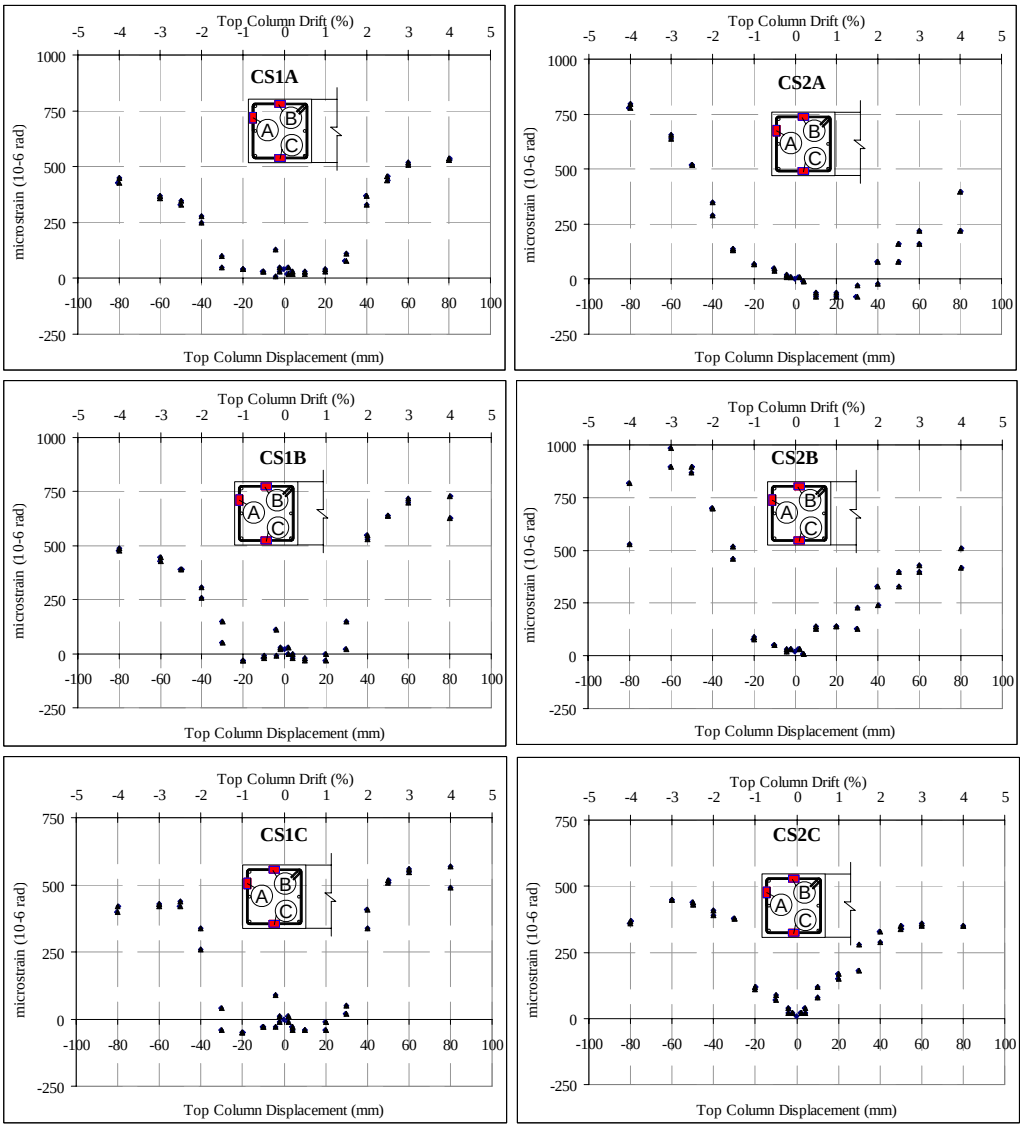

Figure C.23: Test Unit NS-R2: Column stirrups bars strain gage readings.

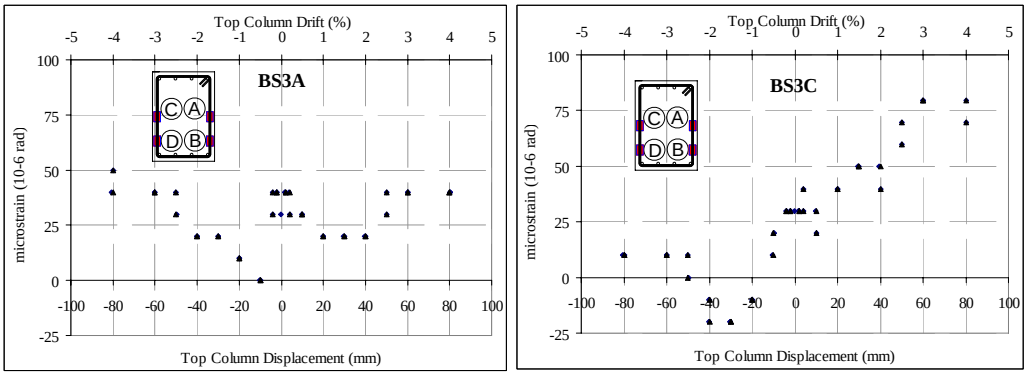

Figure C.24: Test Unit NS-R2: Beam stirrups bars strain gage readings (BS3C was damaged).

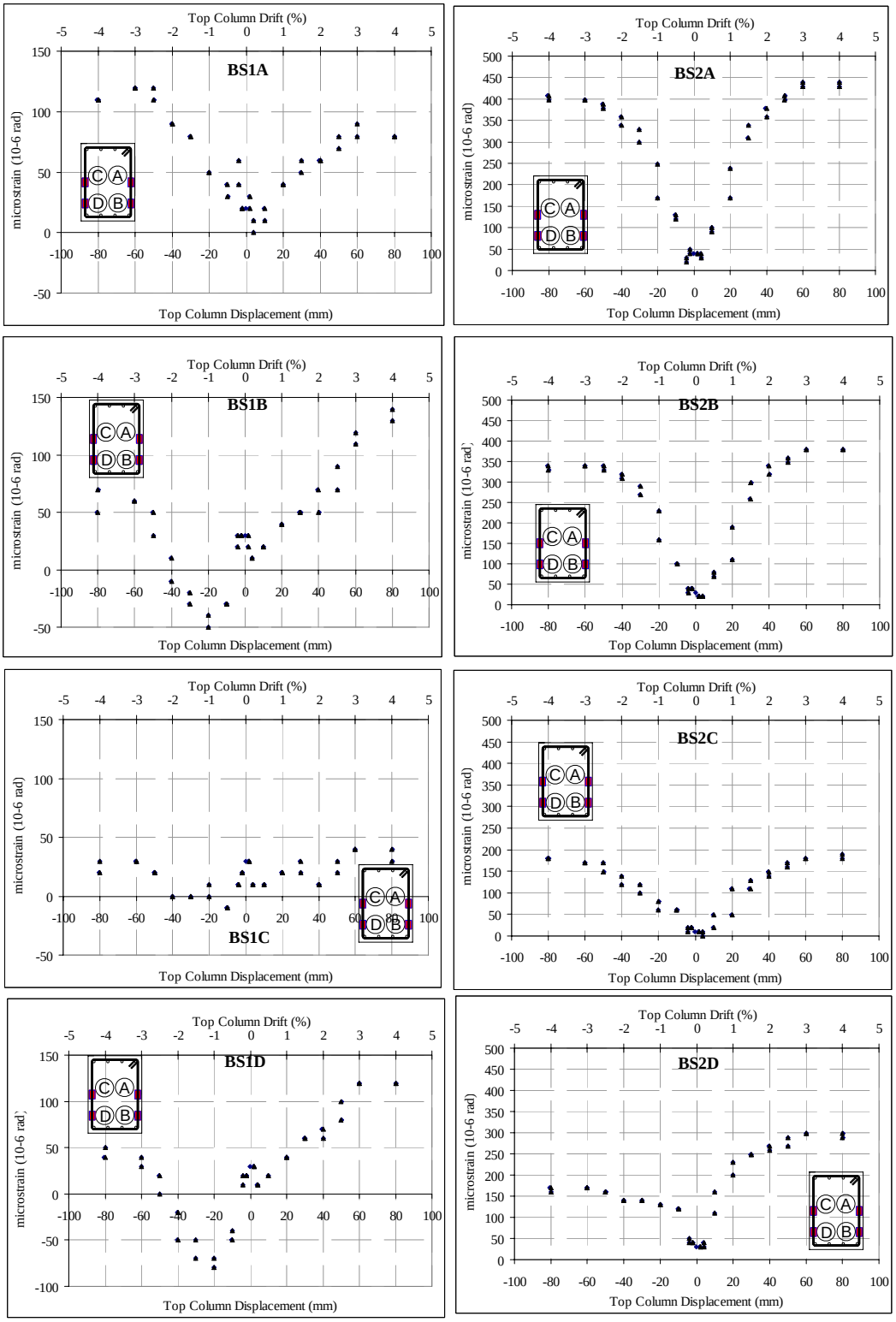

Figure C.25: Test Unit NS-R2: Beam stirrups bars strain gages reading.

C.3 NS-R3 –RETROFITTED B-C JOINT WITH WEAKENING & POST-TENSIONING

C.3.1 Force-displacement hysteresis

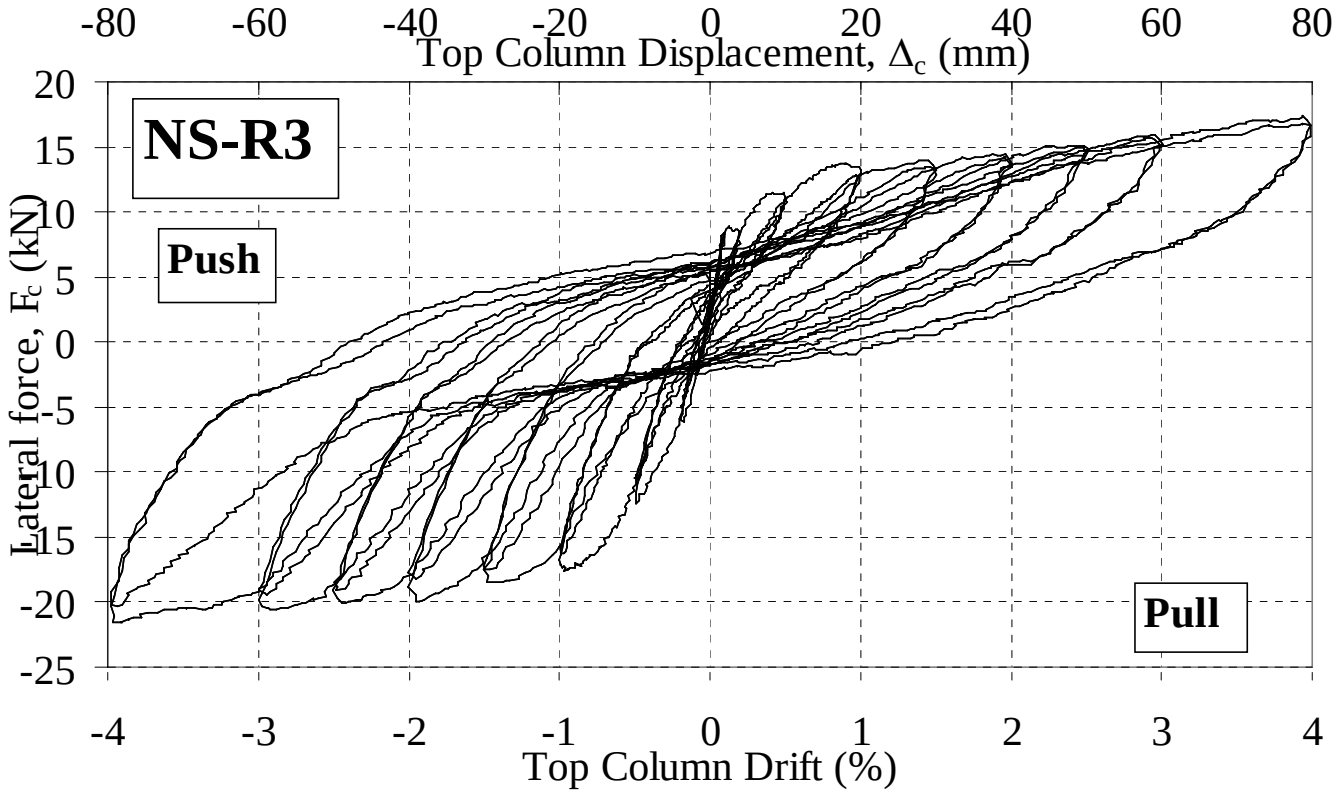

Figure C.26: Test Unit NS-R3: Top column lateral load, F_c, versus top column displacement, Δ_c, and drift, θ_{drift}.

C.3.2 Photographic observations

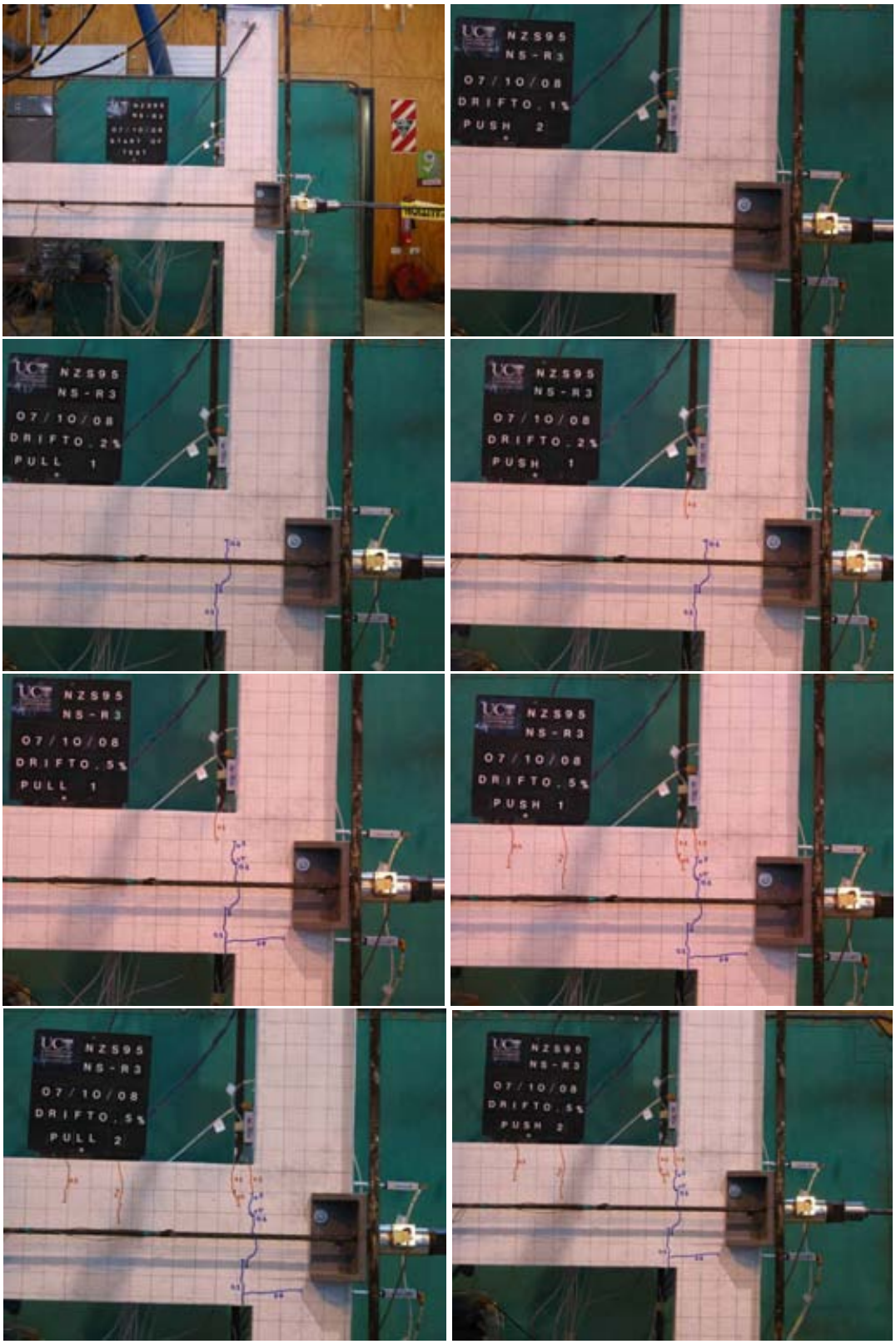

Figure C.27: General observation photographs for test unit NS-R3 at: Start, ±0.2% and ±0.5% drifts.

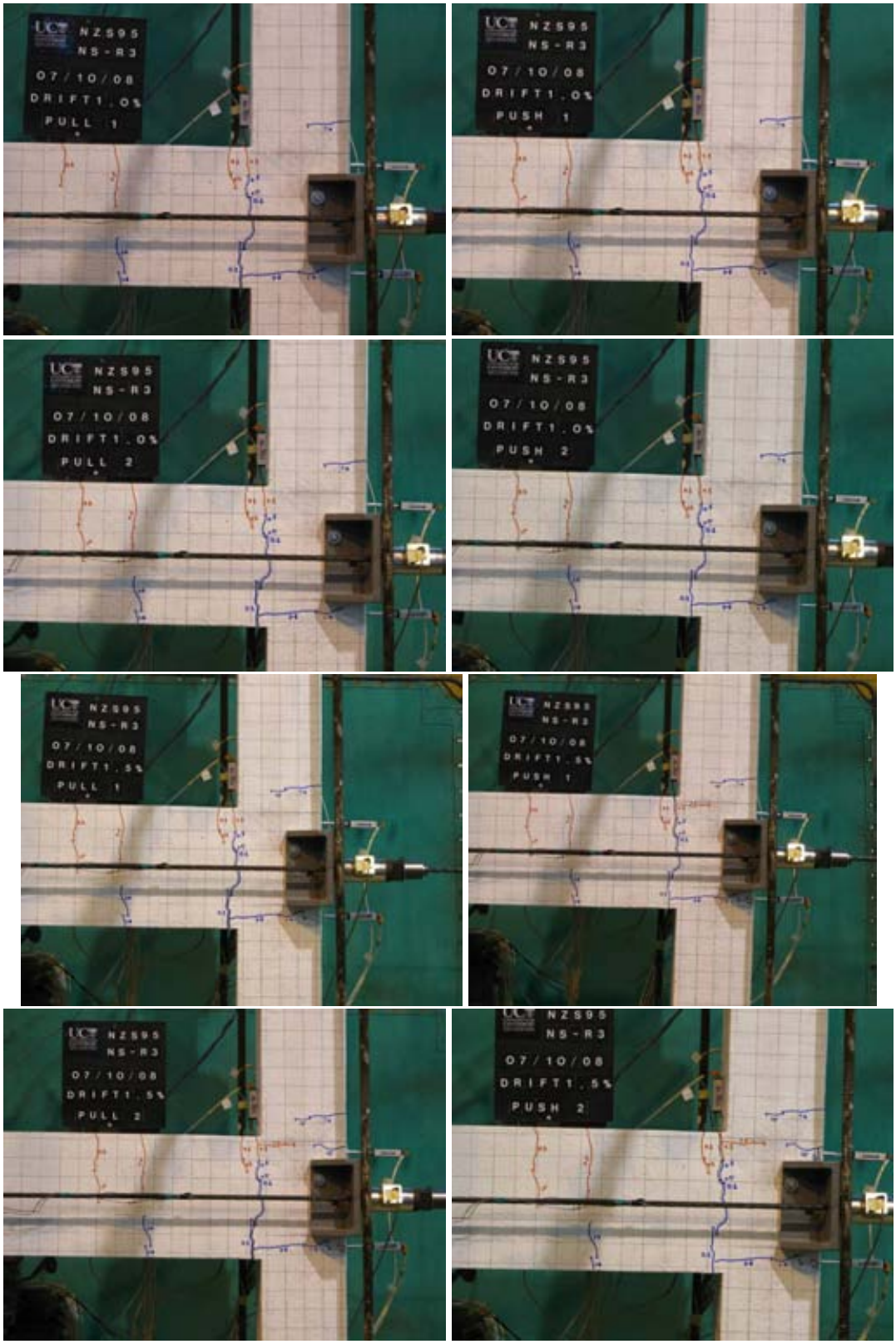

Figure C.28: General observation photographs for test unit NS-R3 at: ±1.0% and ±1.5% drifts.

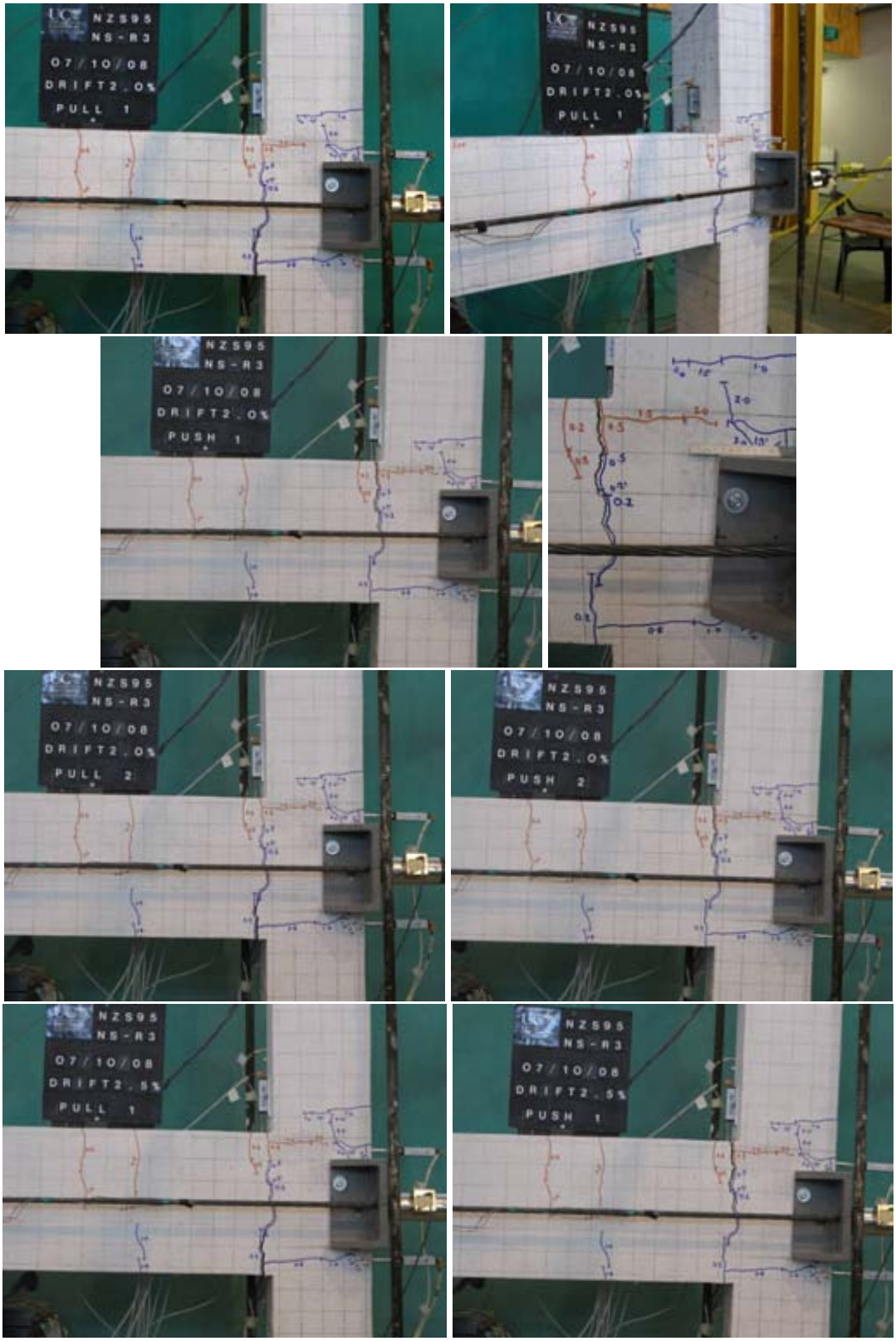

Figure C.29: General observation photographs for test unit NS-R3 at: ±1.5%, ±2.0% and ±2.5% drifts.

Figure C.30: General observation photographs for test unit NS-R3 at: ±2.5%, ±3.0% and ±4.0% drifts.

Figure C.31: General observation photographs for test unit NS-R3 at: ±4.0% drift and the end-of-test.

C.3.3 Column strain gage readings

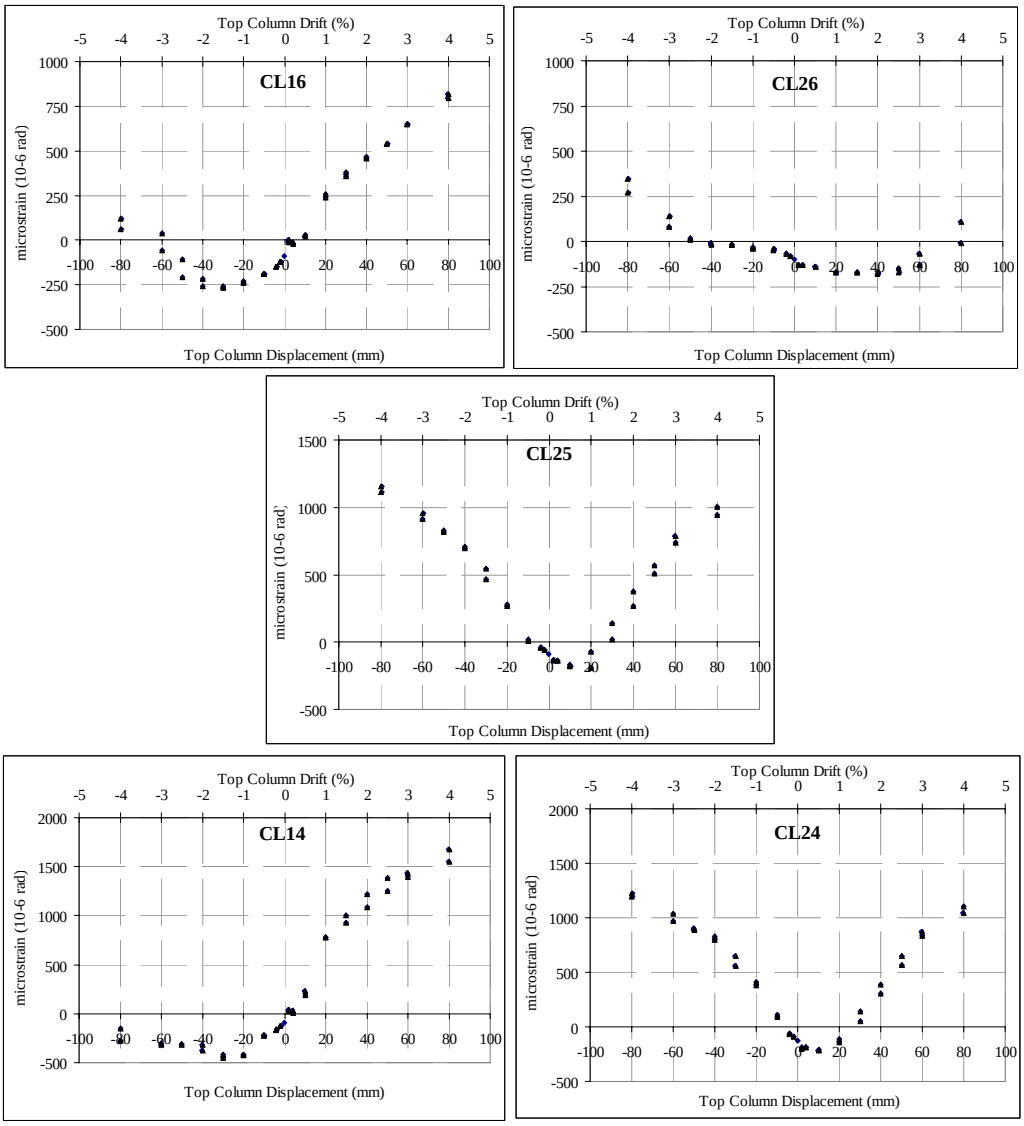

Figure C.32: Test Unit NS-R3: Column longitudinal bars strain gage readings: Top half.

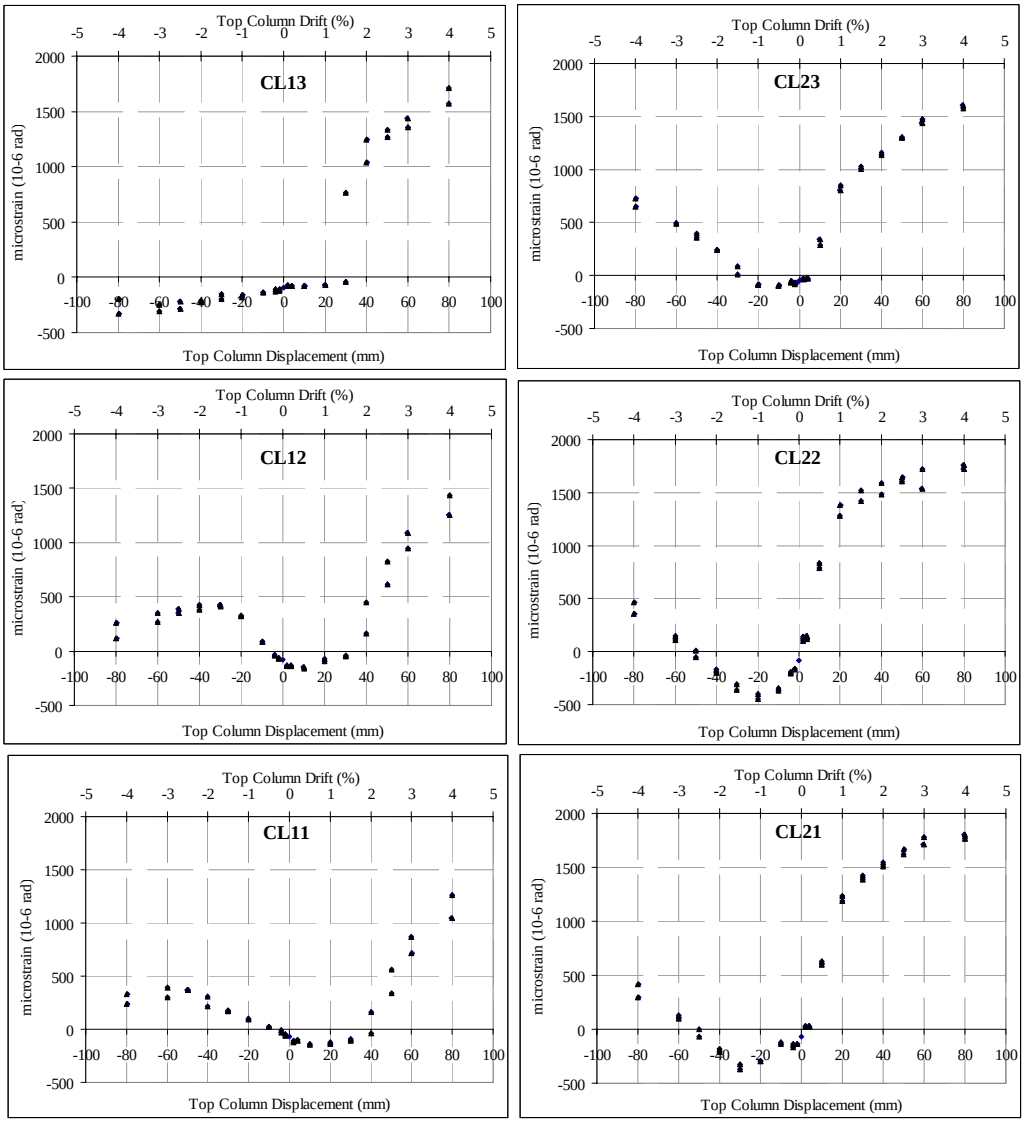

Figure C.33: Test Unit NS-R3: Column longitudinal bars strain gage readings: Bottom half.

C.3.4 Beam strain gage readings

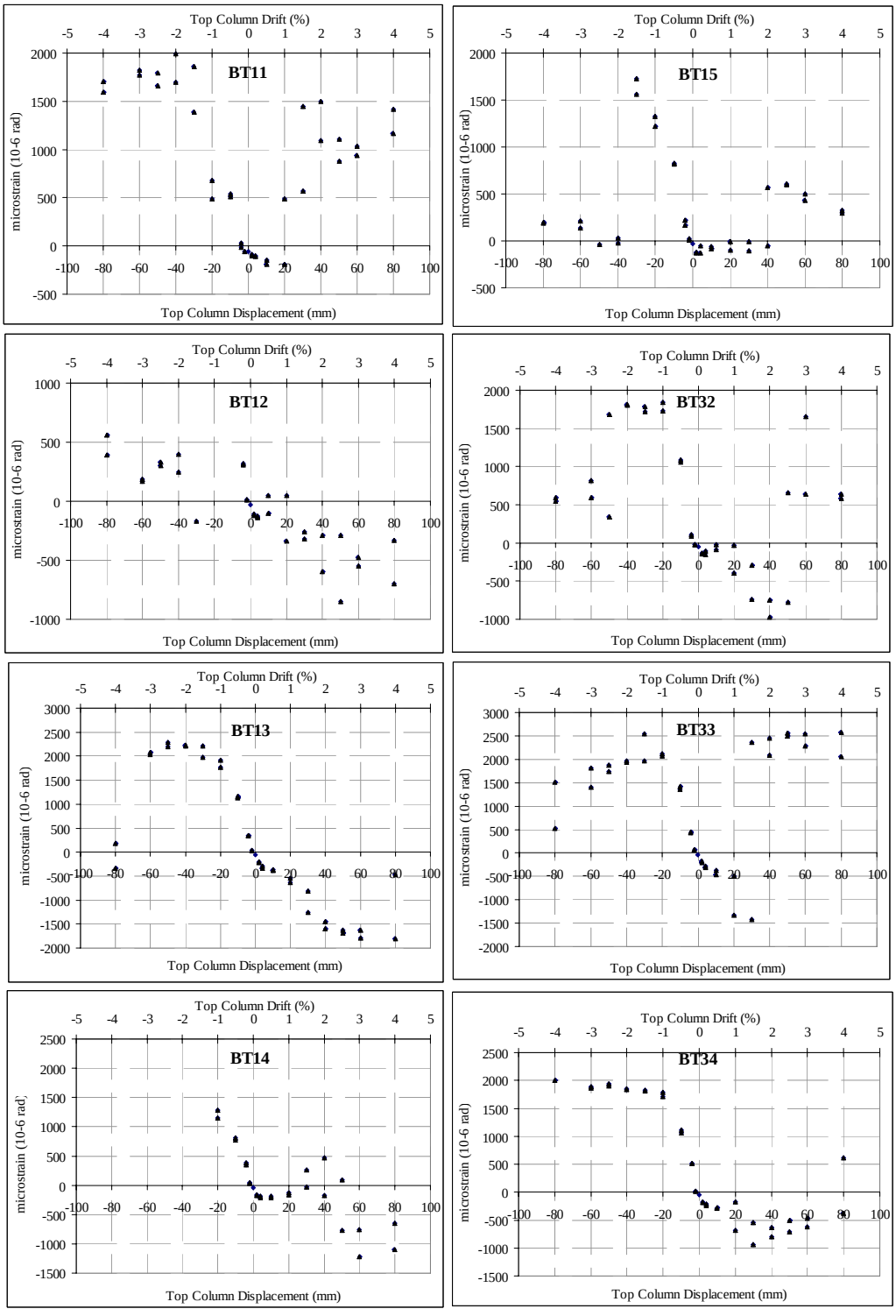

Figure C.34: Test Unit NS-R3: Beam longitudinal bars strain gage readings: Top bars. (some gages were damaged beyond 1.5% drift cycles & BB31 was damaged before testing).

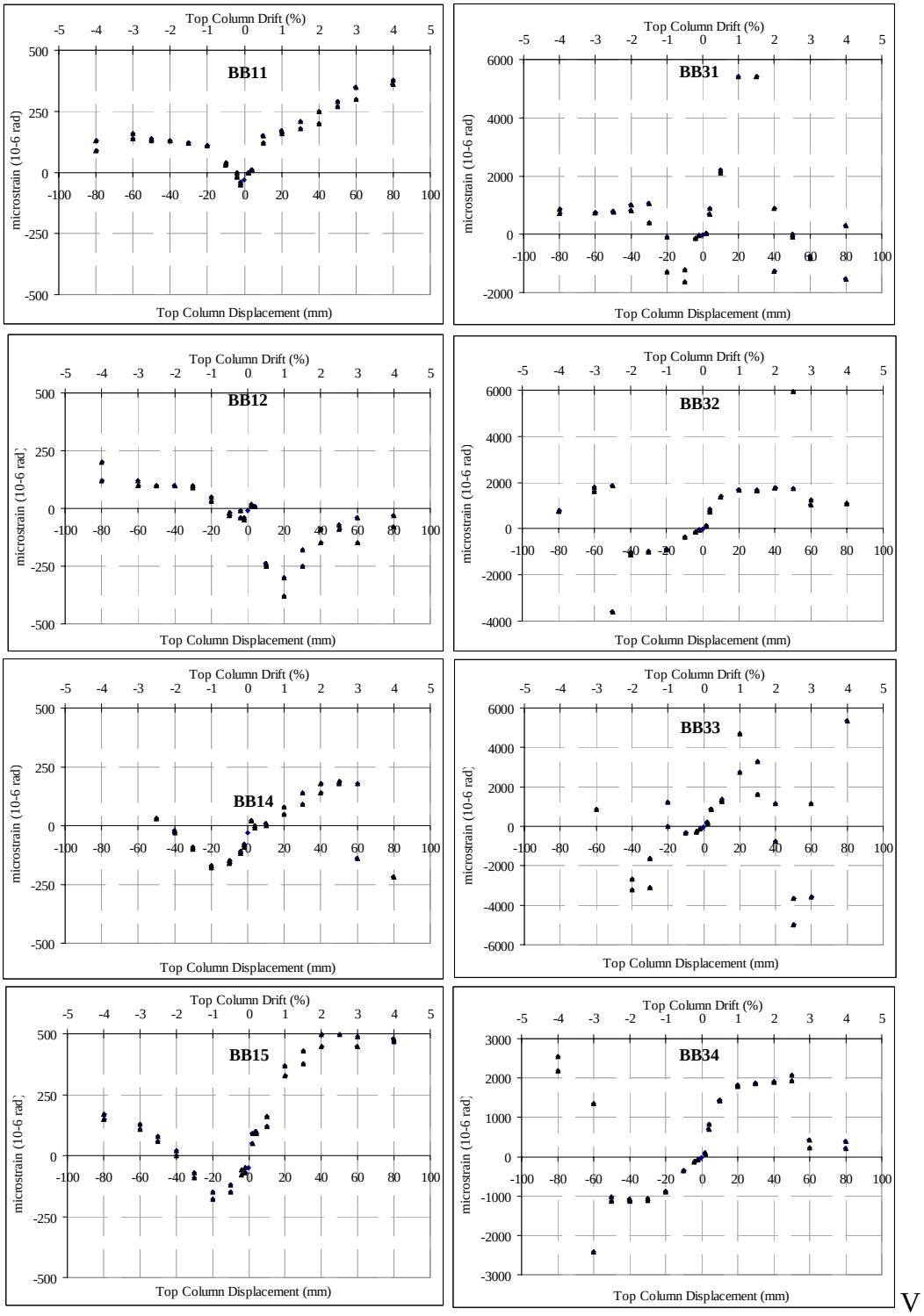

V

Figure C.35: Test Unit NS-R3: Beam longitudinal bars strain gage readings: Bottom bars. BB1X-severed beam bar and BB3X – uncut beam bar.(BB13 was damaged before testing.)

C.3.5 Stirrups (column and beam) strain gage readings

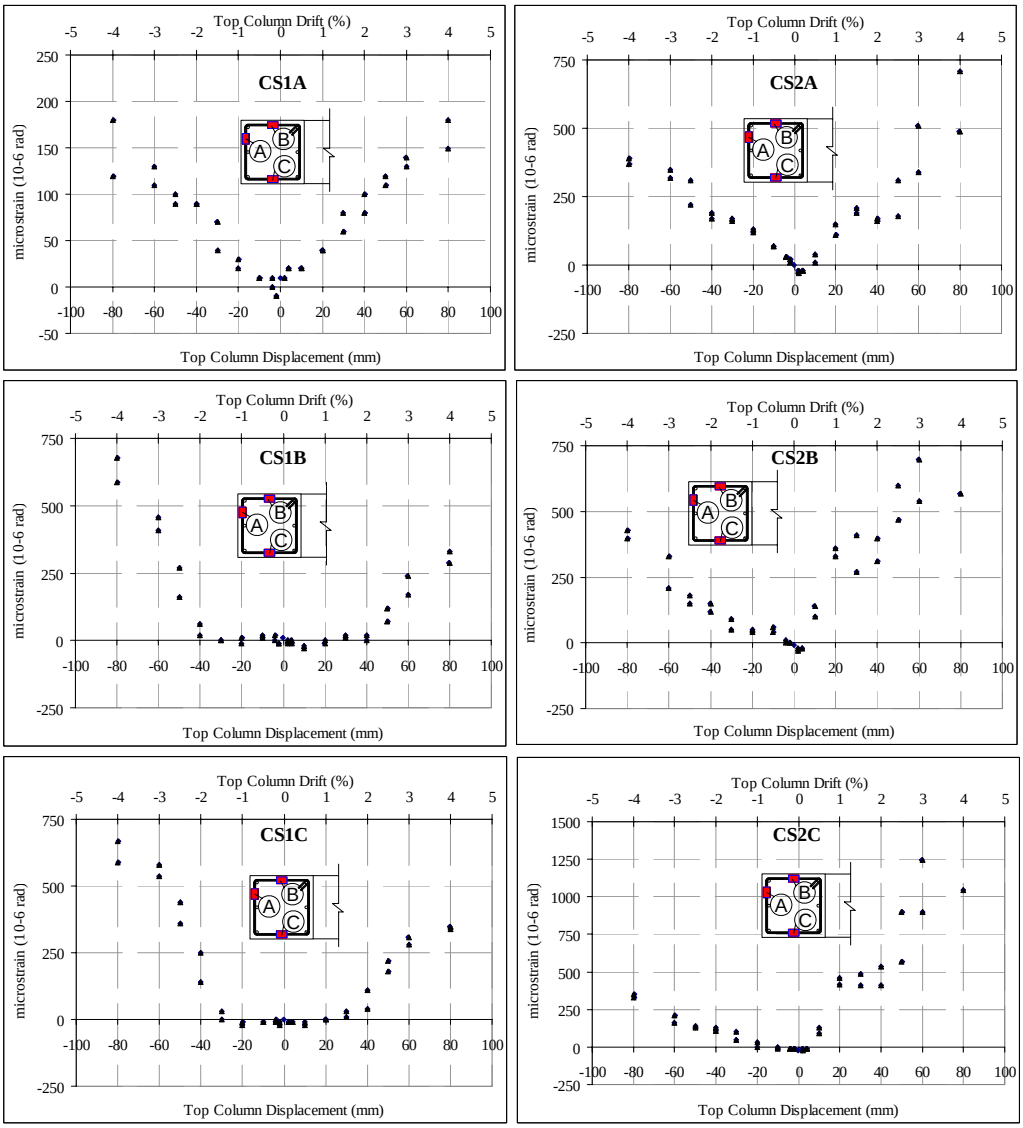

Figure C.36: Test Unit NS-R3: Column stirrups bars strain gage readings.

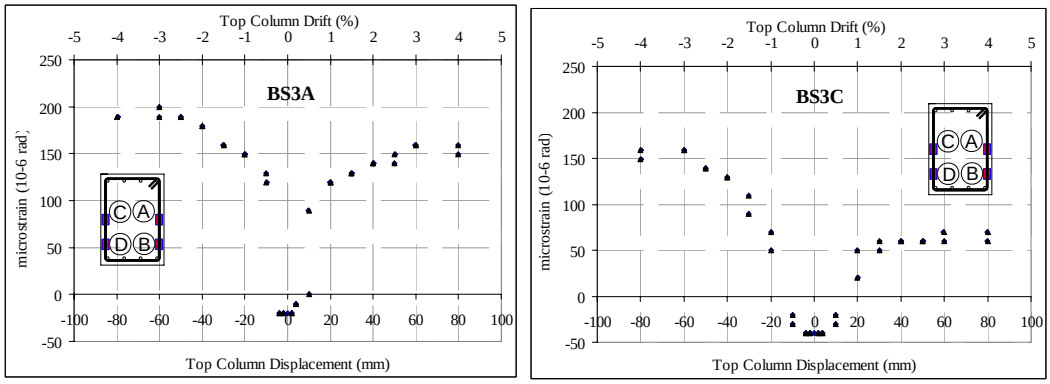

Figure C.37: Test Unit NS-R3: Beam stirrups bars strain gage readings.

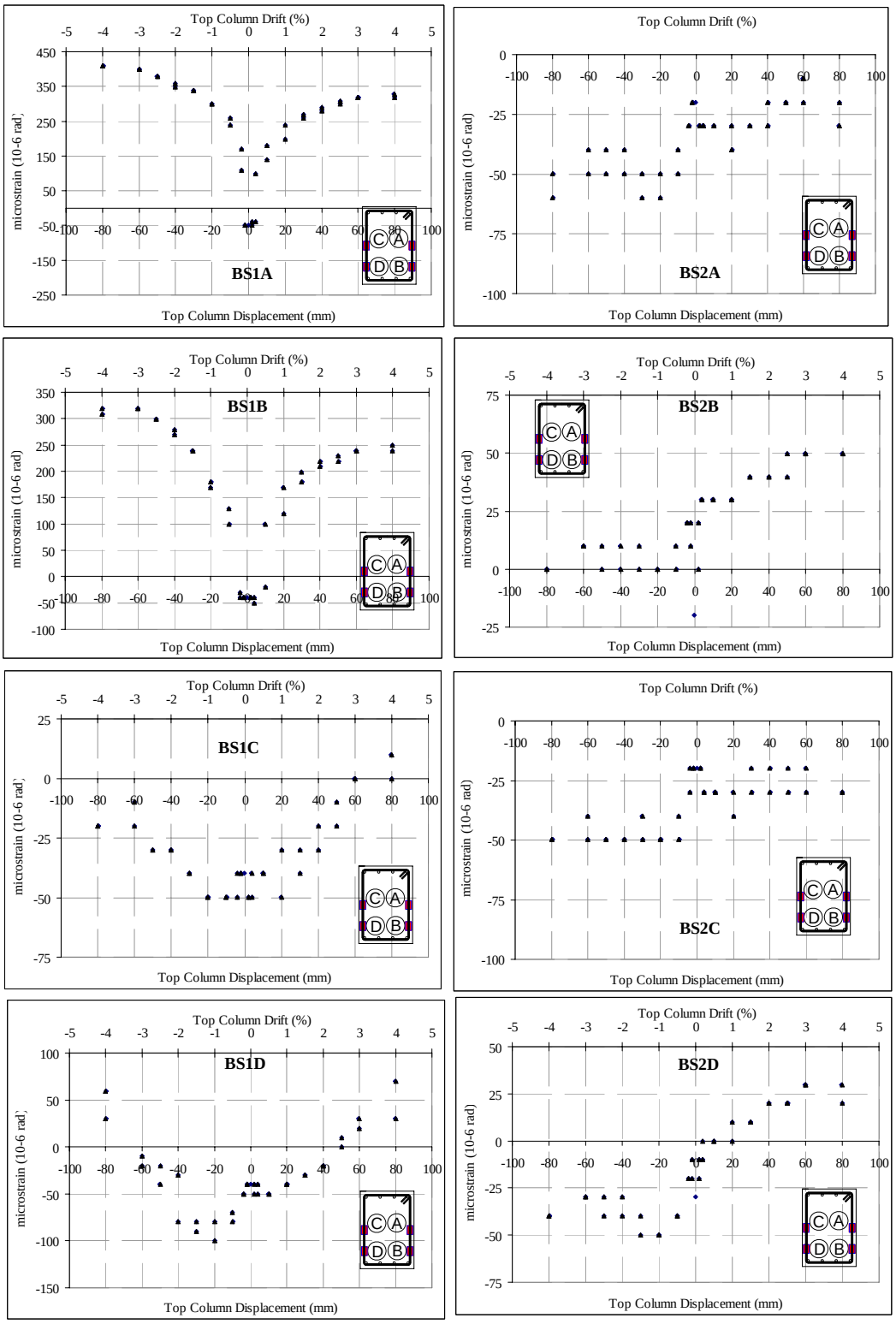

Figure C.38: Test Unit NS-R3: Beam stirrups bars strain gages reading.

C.4 NS-R4 –RETROFITTED B-C JOINT WITH WEAKENING & POST-TENSIONING

C.4.1 Force-displacement hysteresis

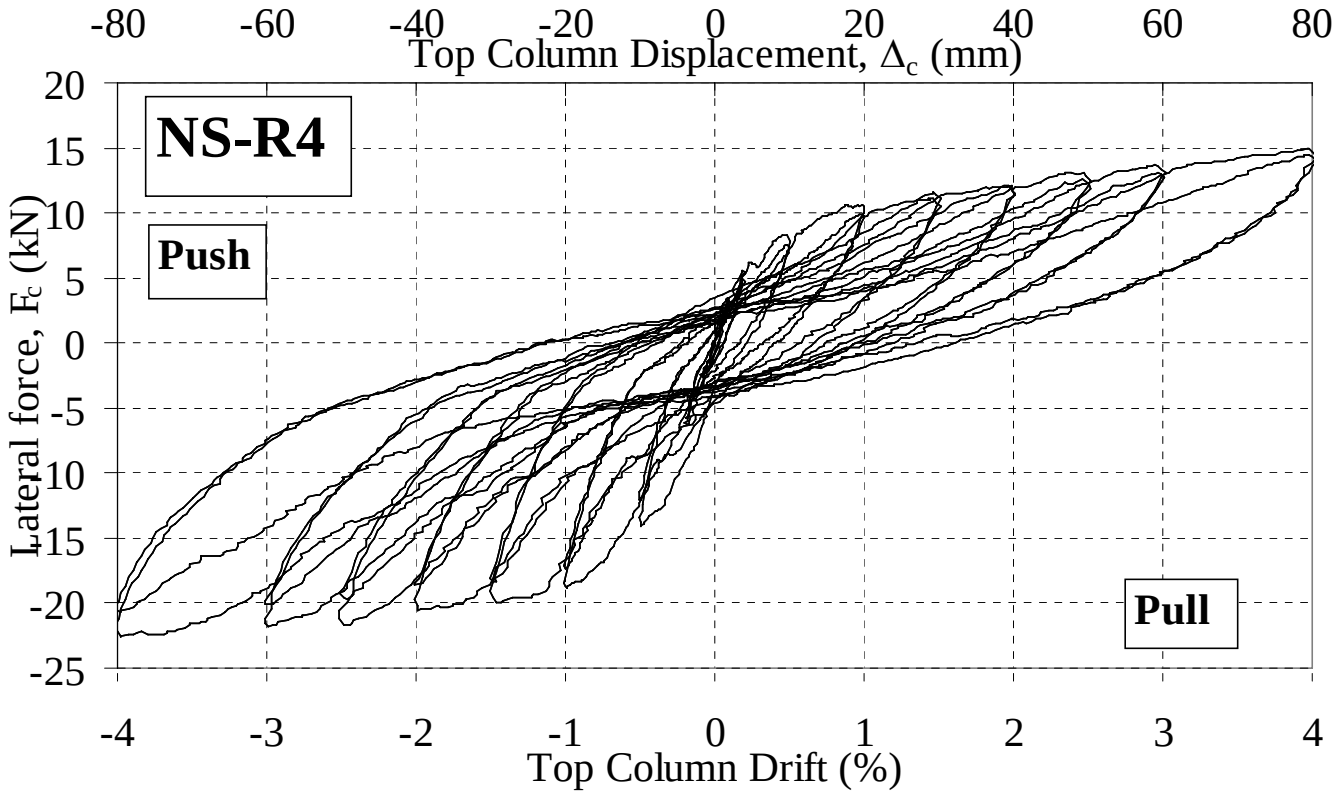

Figure C.39: Test Unit NS-R4: Top column lateral load, F_c, versus top column displacement, Δ_c, and drift, θ_{drift}.

C.4.2 Photographic observations

Figure C.40: General observation photographs for test unit NS-R4 at: Start, ±0.2% and ±0.5% drifts.

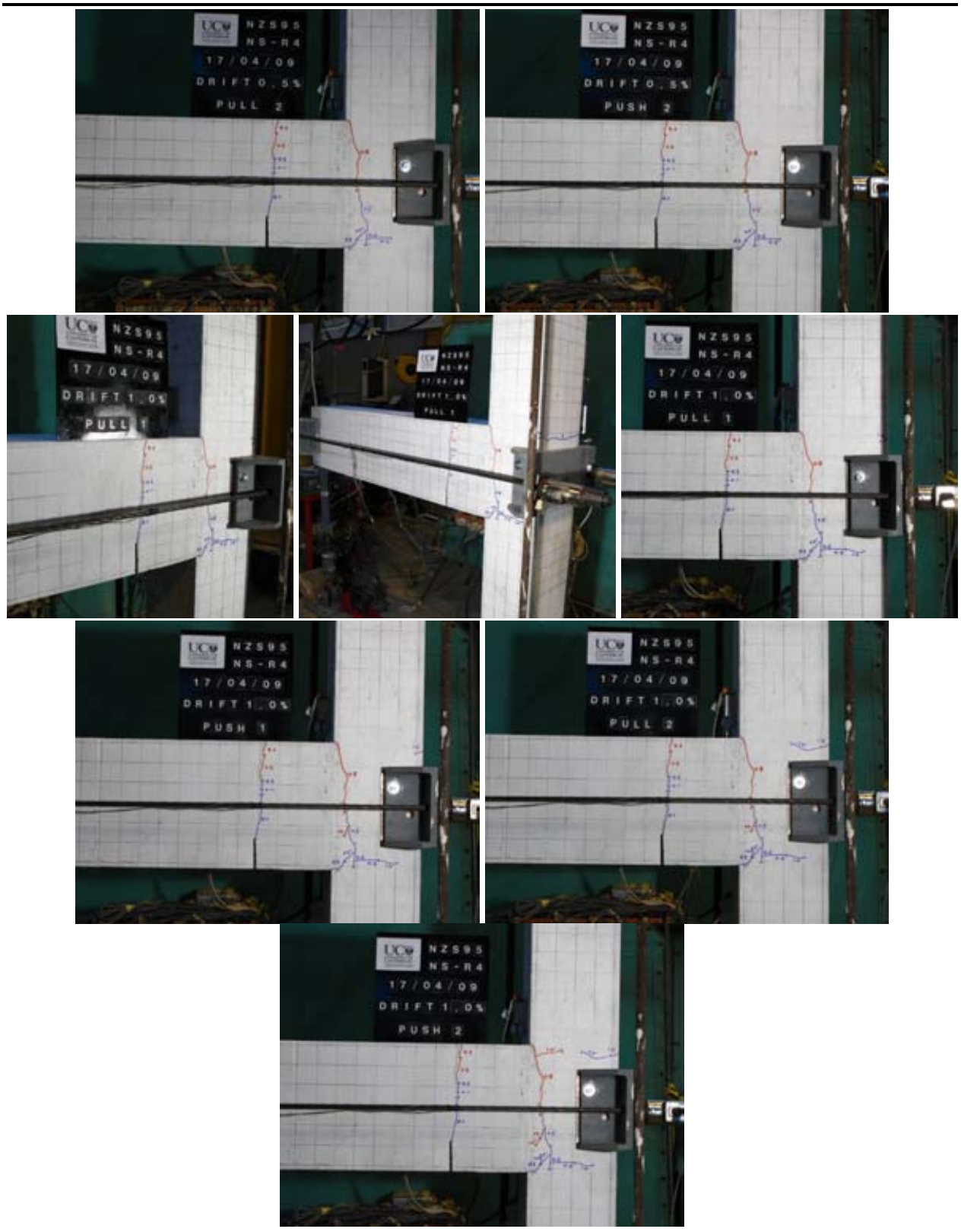

Figure C.41: General observation photographs for test unit NS-R4 at: ±0.5% and ±1.0% drifts.

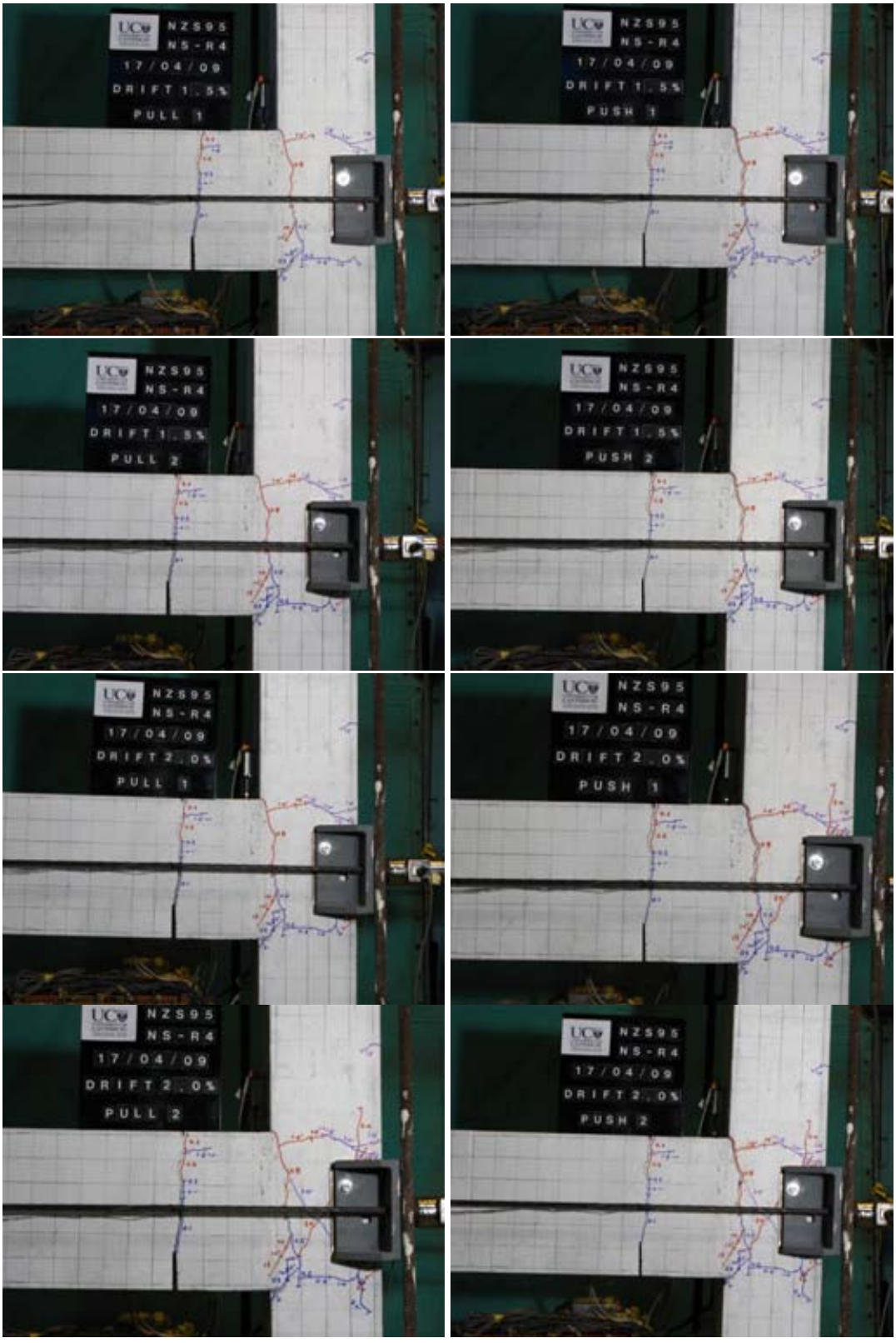

Figure C.42: General observation photographs for test unit NS-R4 at: ±1.5% and ±2.0% drifts.

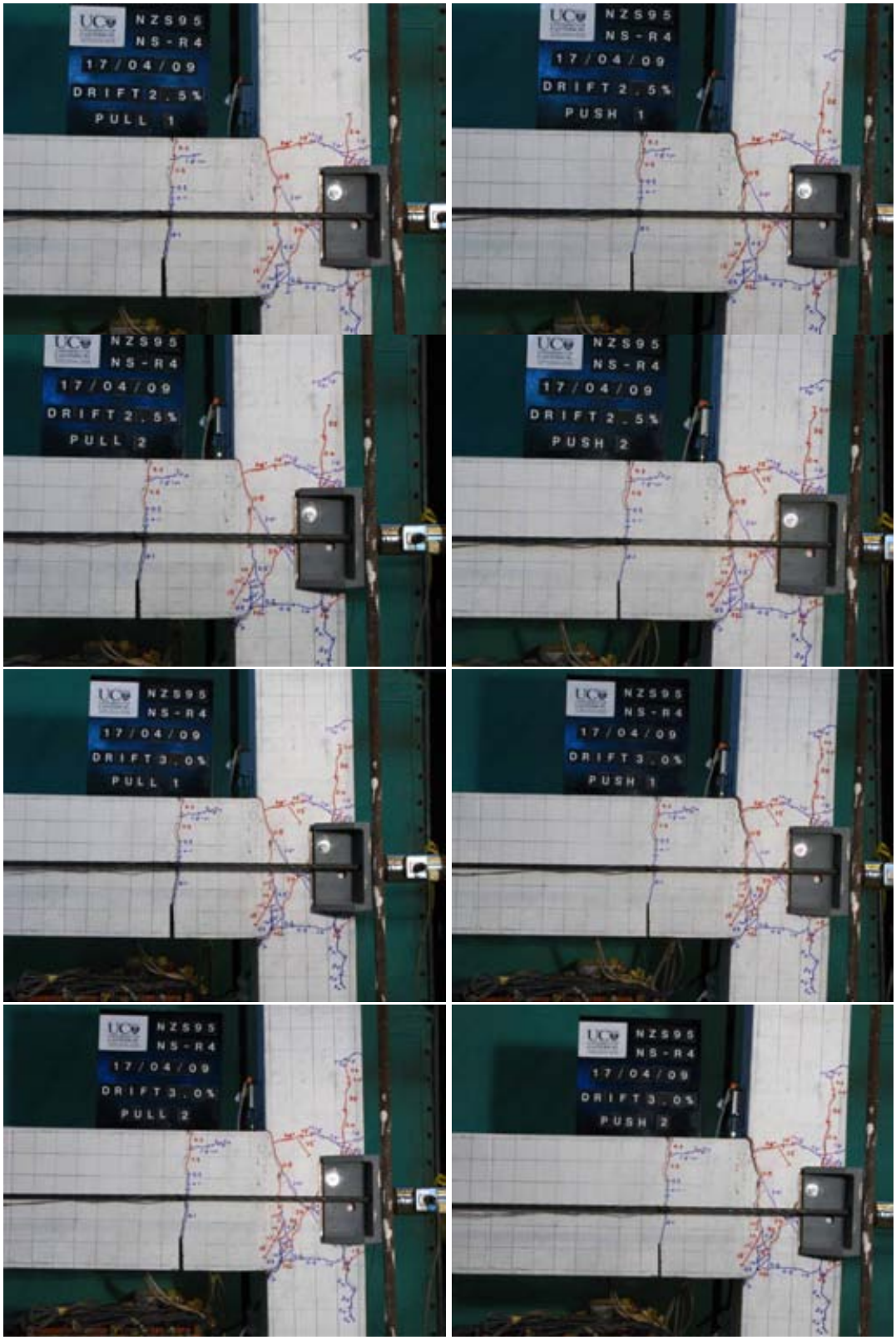

Figure C.43: General observation photographs for test unit NS-R4 at: ±2.5% and ±3.0% drifts.

Figure C.44: General observation photographs for test unit NS-R4 at: ±4.0% drift and the end-of-test.

C.4.3 Column strain gage readings

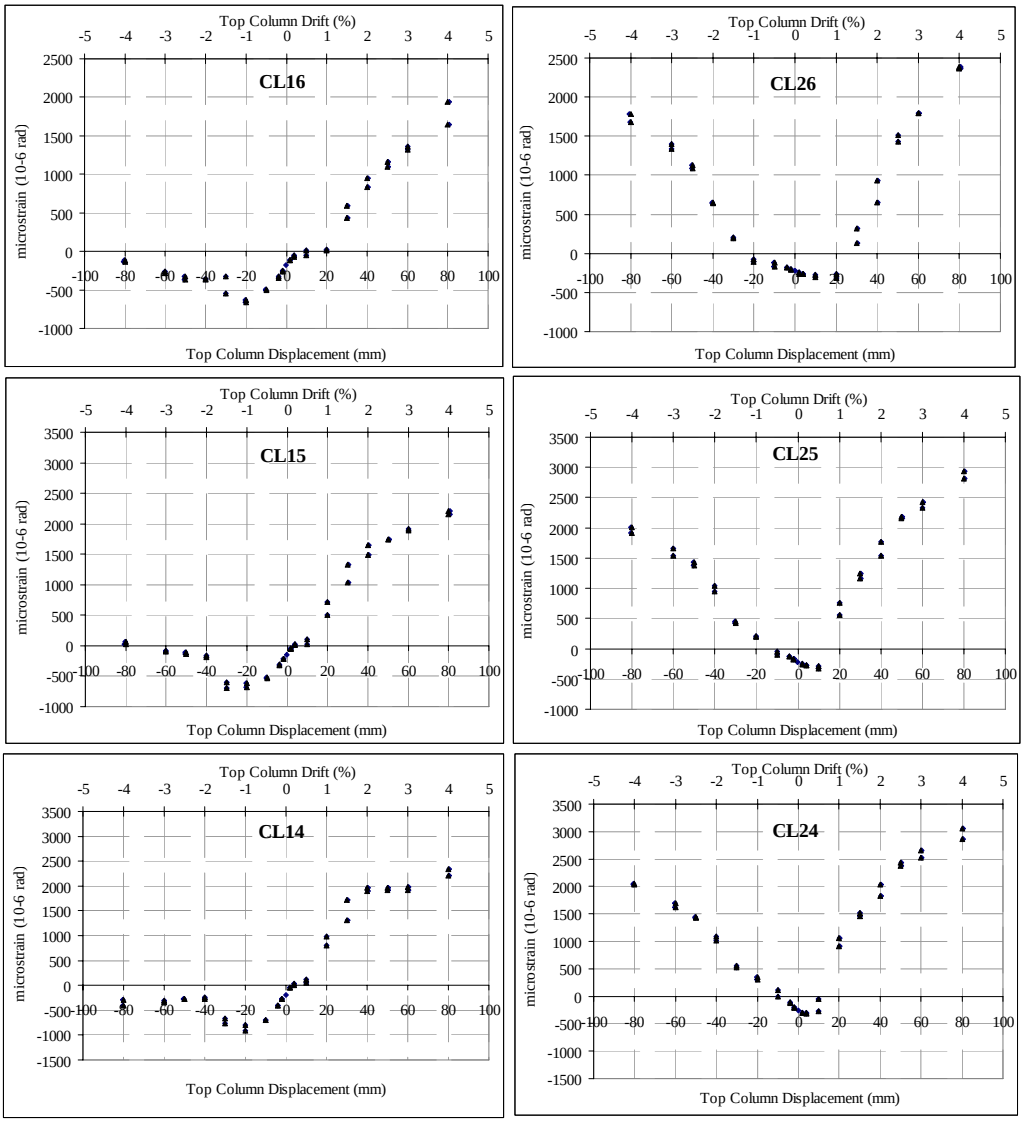

Figure C.45: Test Unit NS-R4: Column longitudinal bars strain gage readings: Top half.

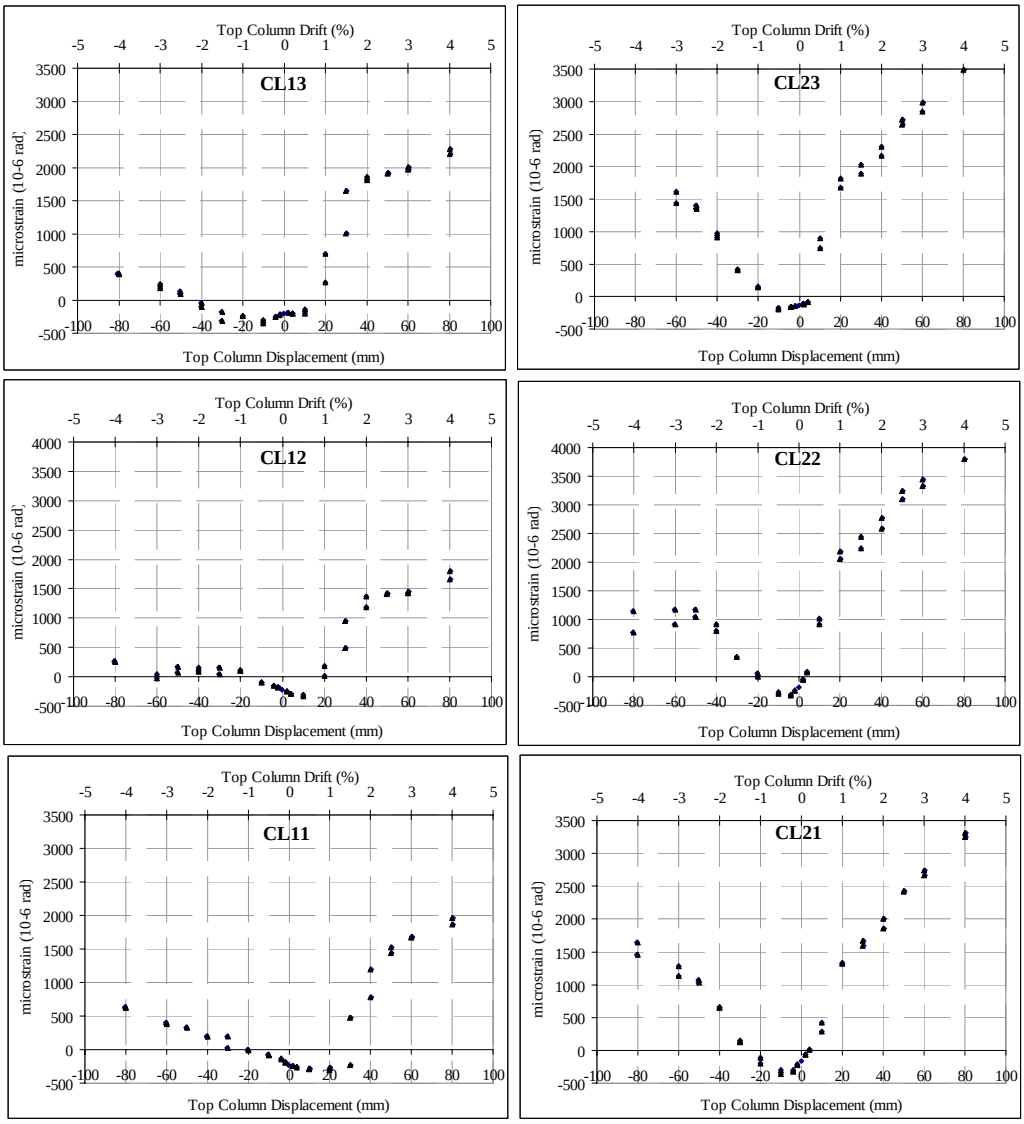

Figure C.46: Test Unit NS-R4: Column longitudinal bars strain gage readings: Bottom half.

C.4.4 Beam strain gage readings

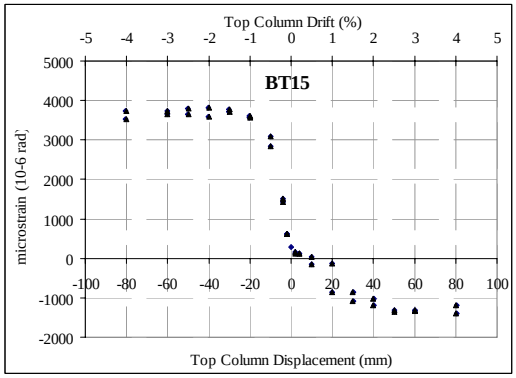

Figure C.47: Test Unit NS-R4: Beam longitudinal bars strain gage readings: Top bars (BT15).

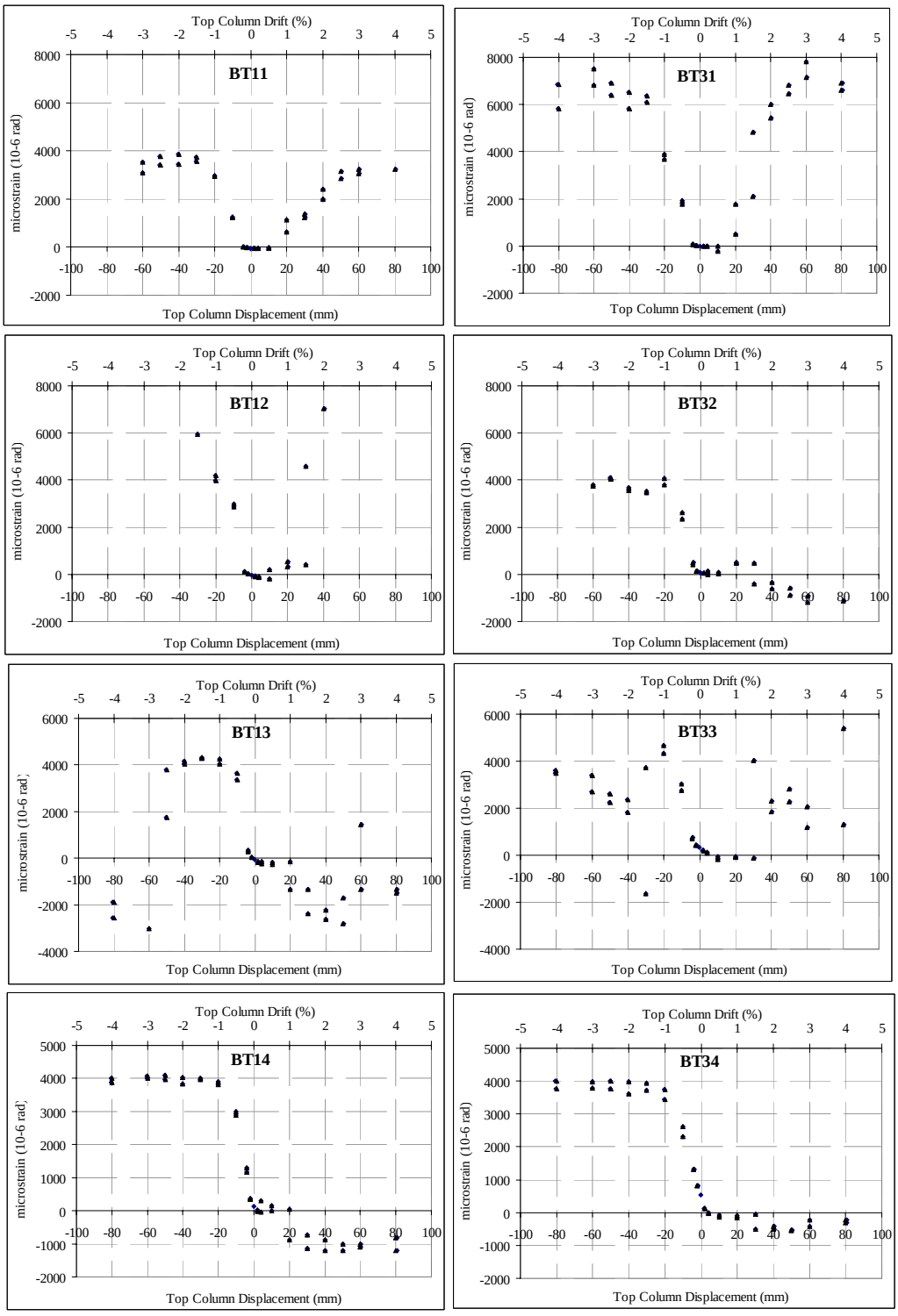

Figure C.48: Test Unit NS-R4: Beam longitudinal bars strain gage readings: Top bars (BT12 and BT33 were damaged at drifts > ±1.5%).

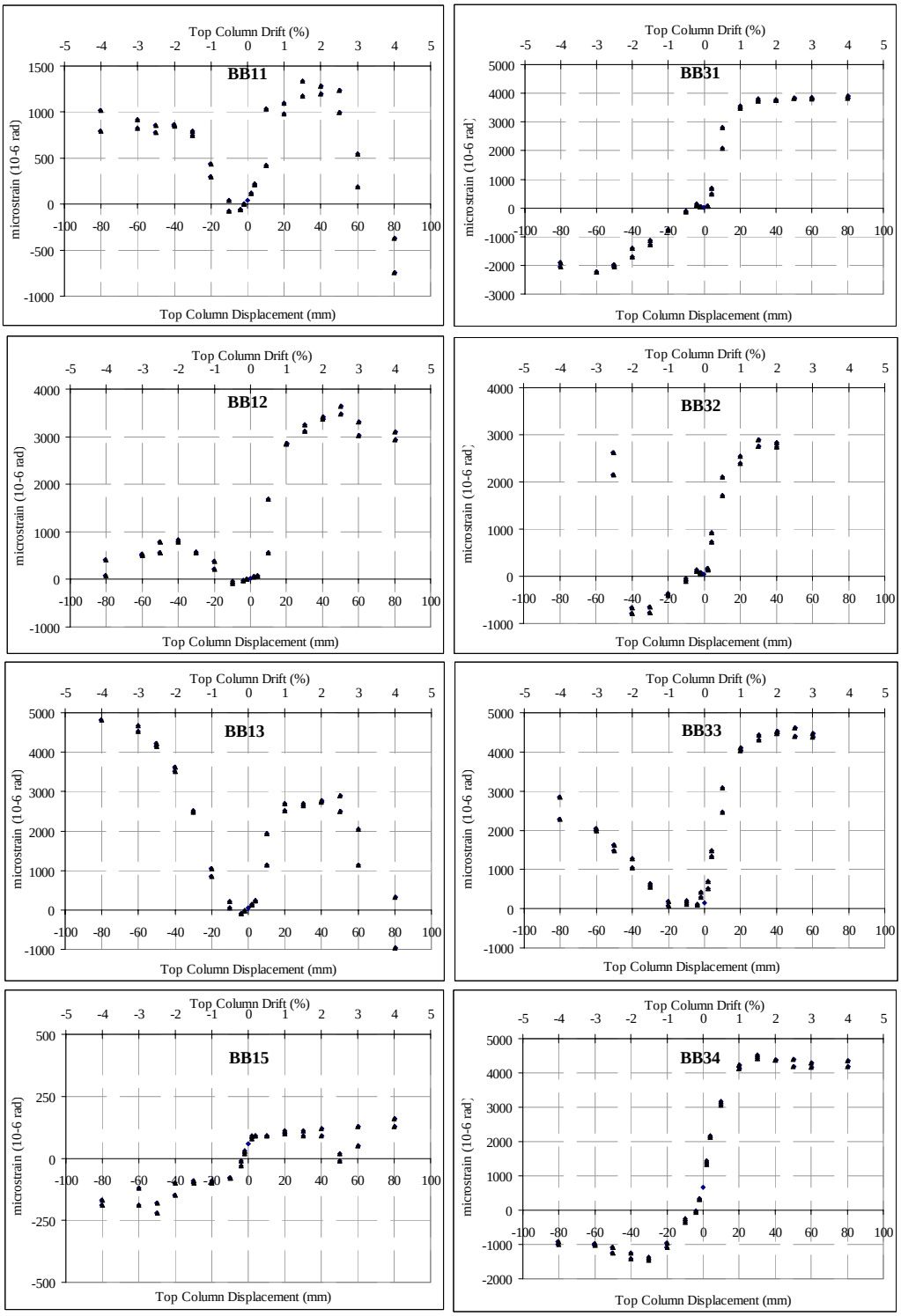

Figure C.49: Test Unit NS-R4: Beam longitudinal bars strain gage readings: Bottom bars. (BB14 was damaged.)

C.4.5 Stirrups (column and beam) strain gage readings

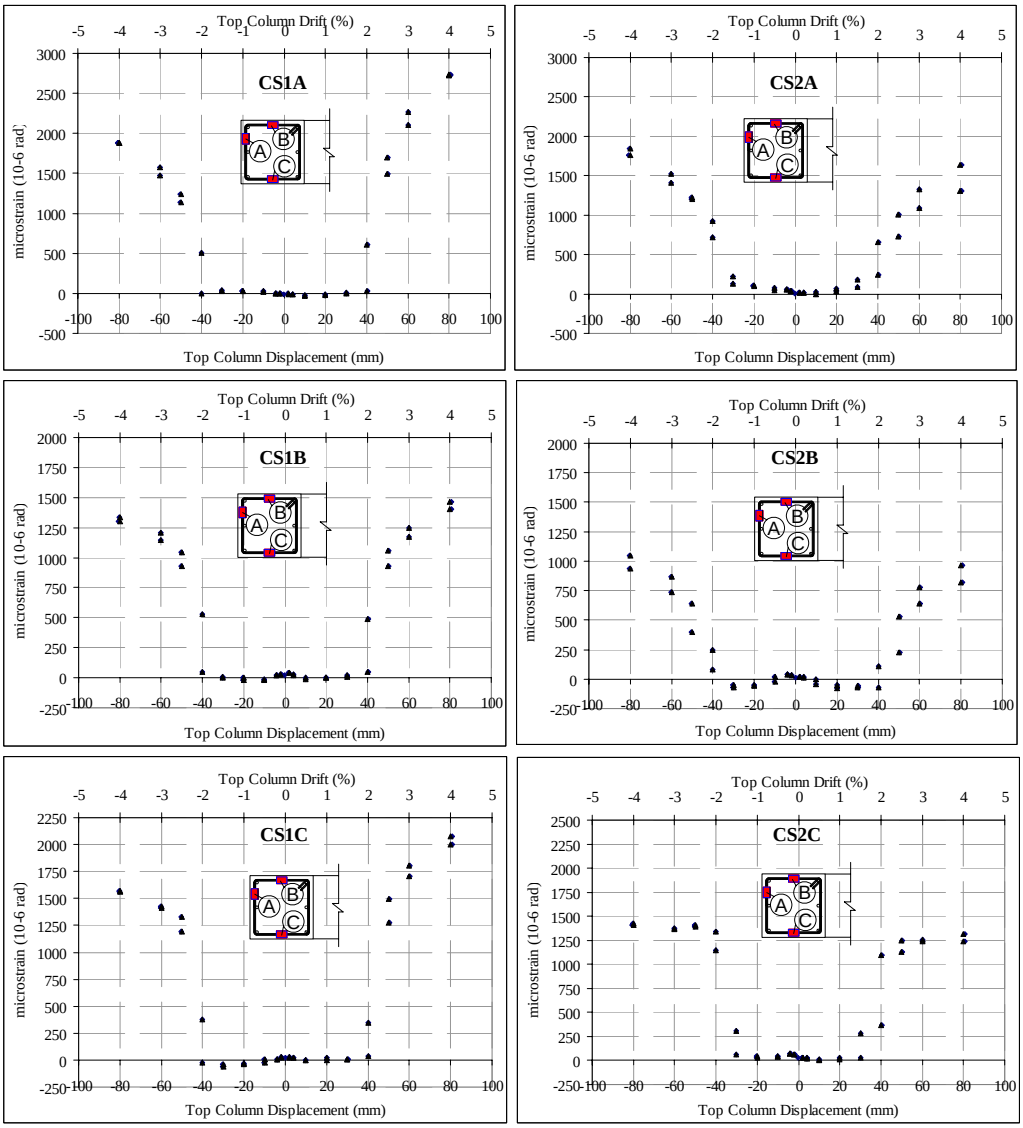

Figure C.50: Test Unit NS-R4: Column stirrups bars strain gage readings.

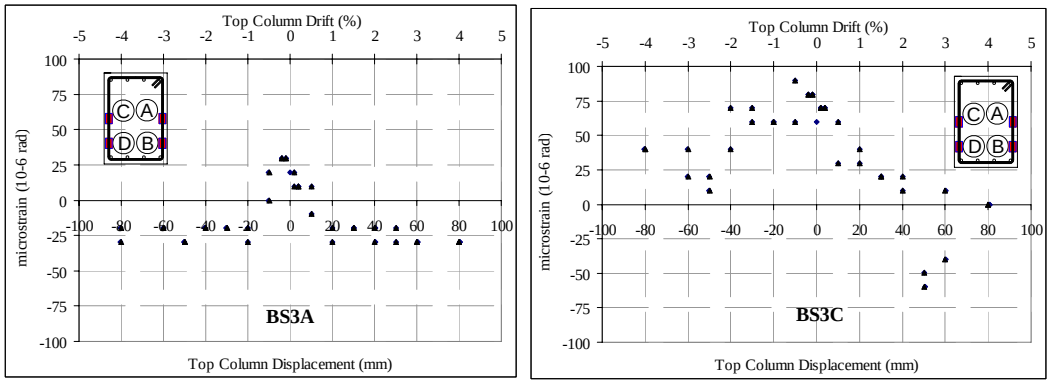

Figure C.51: Test Unit NS-R4: Beam stirrups bars strain gage readings.

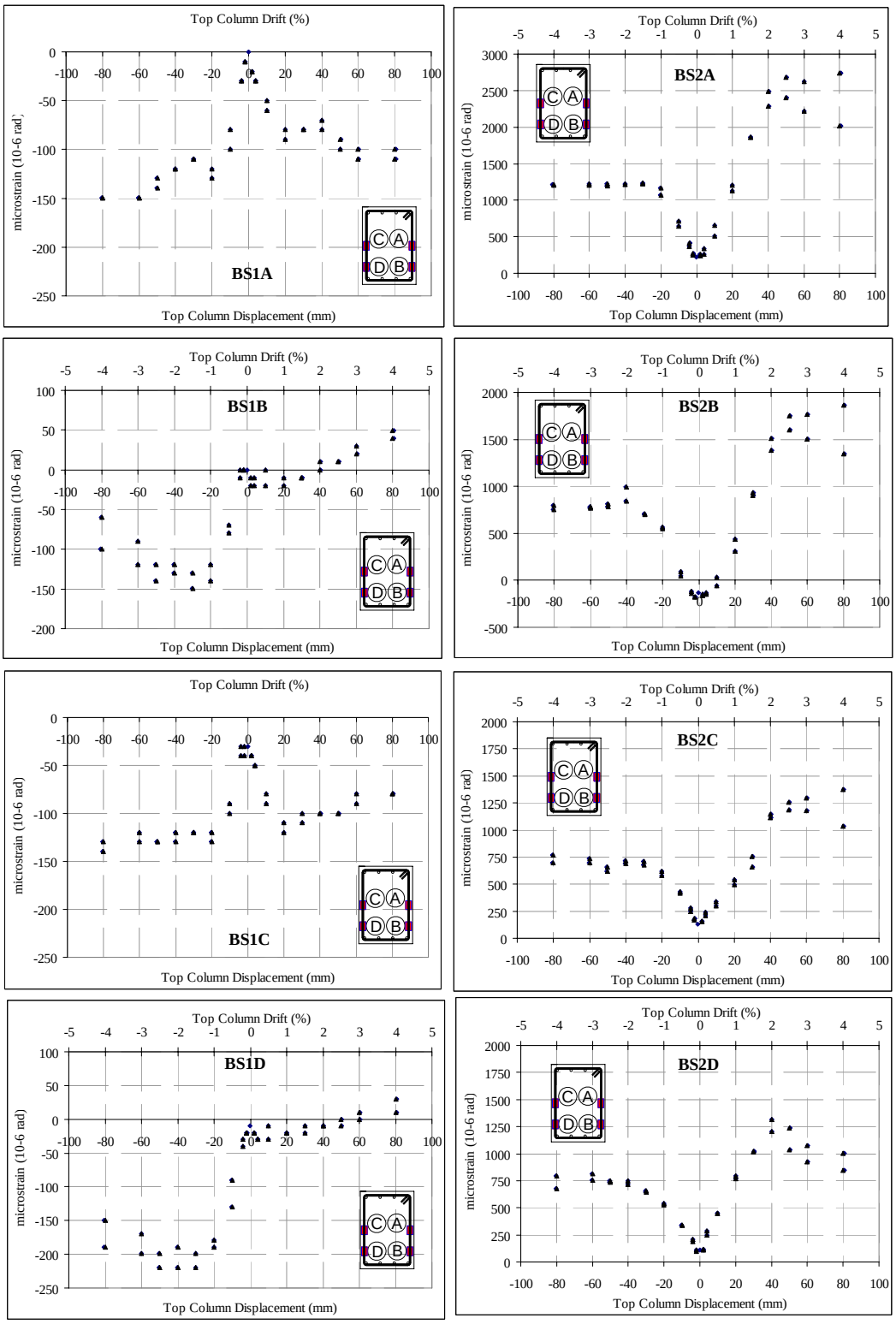

Figure C.52: Test Unit NS-R4: Beam stirrups bars strain gage readings.

APPENDIX D. TRIAL EXPERIMENTS ON SELECTIVE WEAKENING RETROFIT AND REPAIR ON EXTERIOR BEAM-COLUMN JOINT

D.1 SPECIMENS DETAIL AND TEST SUMMARY

D.1.1 Test specimens, testing setup and loading protocol

This appendix describes three tests on a 2/3-scaled exterior beam-column joint specimen, designed to the NZS3101:2006 requirements, in order to test several preliminary assumptions and ideas:

1. Advanced controlled-rocking joint retrofit, described in §3.3.3.3 was not tested on a pre-1970s non-ductile RC beam-column joint specimen. The advanced-rocking retrofit solution requires full detachment of the beam reinforcements in order to achieve a controlled rocking interface between the column and the beam.
2. The feasibility and practicality of external post-tensioning of the joint, using in-house laboratory-constructed anchorage and pre-stressing equipments.
3. The effectiveness of two repairing solutions for an earthquake-damaged plastic hinge region: a) full concrete replacement, and b) concrete replacement and post-tensioning.

The trial experiments were carried out using the same test setup as described in §4.6.1. The lateral loading protocol consisted of three displacement-controlled cycles at increasing amplitudes: 0.1%, 0.2%, 0.5%, 0.75%, 1.0%, 1.5%, 2.0%, 2.5%, 3.0% and 4.5% inter-storey drift with a small amplitude cycle in between the large drifts, as shown in Figure D.1. The as-built specimen NZS3101-O1's reinforcing detail is shown in Figure D.2 and Figure D.3. The geometry of the trial specimen was chosen to be close to the pre-1970s non-ductile RC beam-column joint benchmark (NS-O1). Deformed mild steel reinforcements were used and commercial pre-mix concrete compression strength of 30MPa was used.

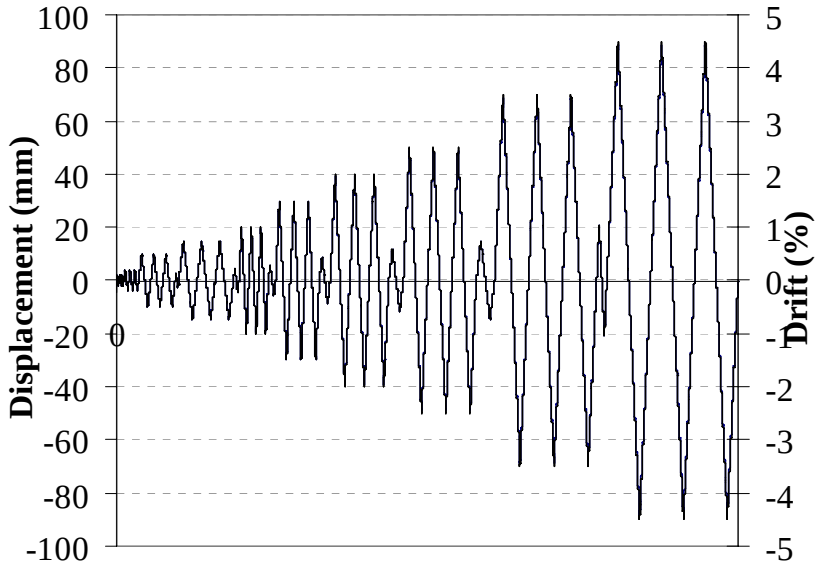

Figure D.1: Lateral load protocol for the trial experiments.

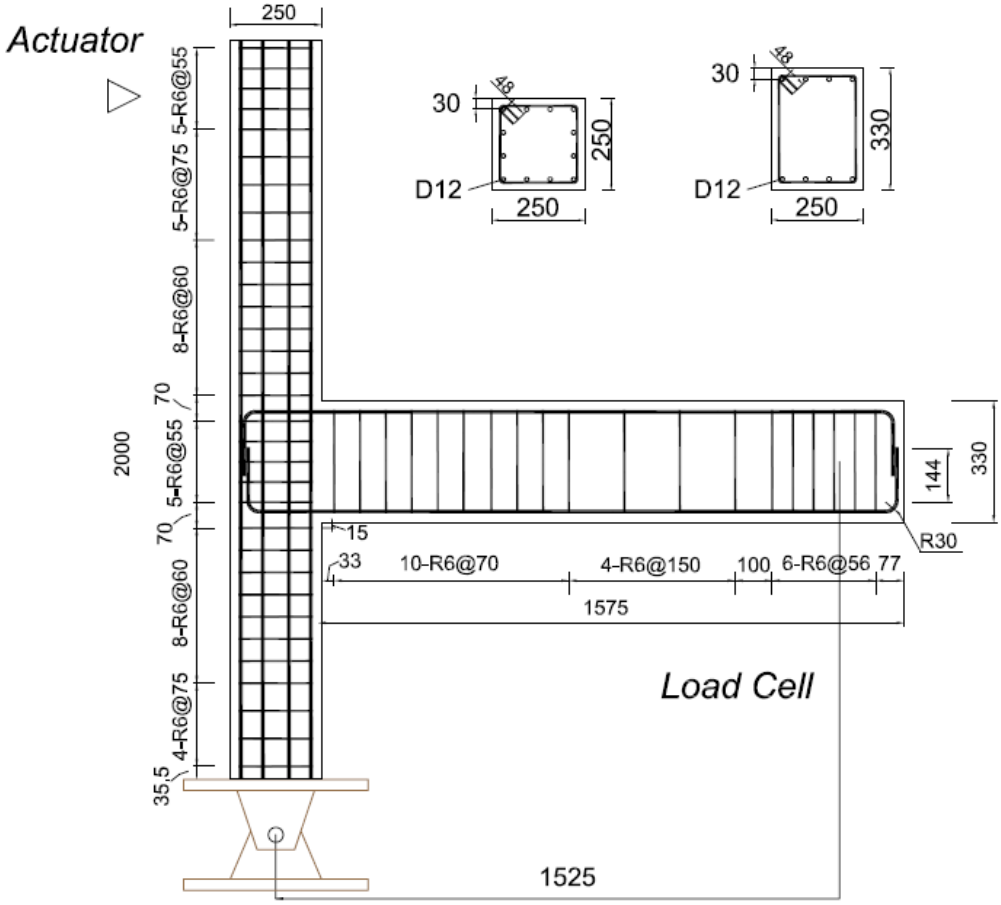

Figure D.2: As-built specimen NZS3101-O1 reinforcing detail.

Figure D.3: Reinforcing detail and formwork of the test unit NZS3101-O1.

D.1.2 Repair and retrofit details

After the first test (NZS3101-O1), the plastic hinge region at the beam was repaired using concrete replacement technique. Sika® MonoTop® 634 flowable micro-concrete with characteristic compressive strength, f'_c of 50MPa, was used to re-concrete the damaged region. Figure D.4a and b show the state of the plastic hinge region after the first test and prior to the re-concrete of the first repair (R1) respectively. The first repaired specimen is called herein NZS3101-R1.

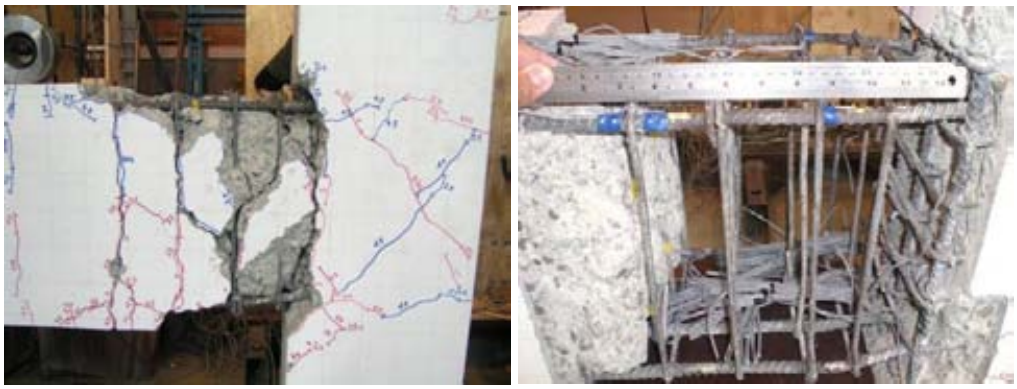

Figure D.4: a) Beam-column joint NZS3101-O1 after the 1st Test (as-built); b) The repaired region before the first repair (R1) re-casting.

After the second test, the damaged specimen was repaired for the second time using the combination of re-concrete and external joint post-tensioning repair (R2). In the R2 repair, all the bottom reinforcements in the beam were severed, 50mm off the column face, after the removal of the damaged concrete. The stirrup spacing was increased from 70mm to 120mm, with some additional stirrups removed, in order to reduce the shear capacity in the beam. Similar to the R1 repair, Sika Monotop634 was used to re-concrete the damaged zone. The external post-tensioning

was anchored using anchorage steel plates (see Figure D.5b-d). Initial post-tensioning force of 45% f_{ypt} (70kN) was used on the two high-strength prestressing 12.9mm diameter tendons.

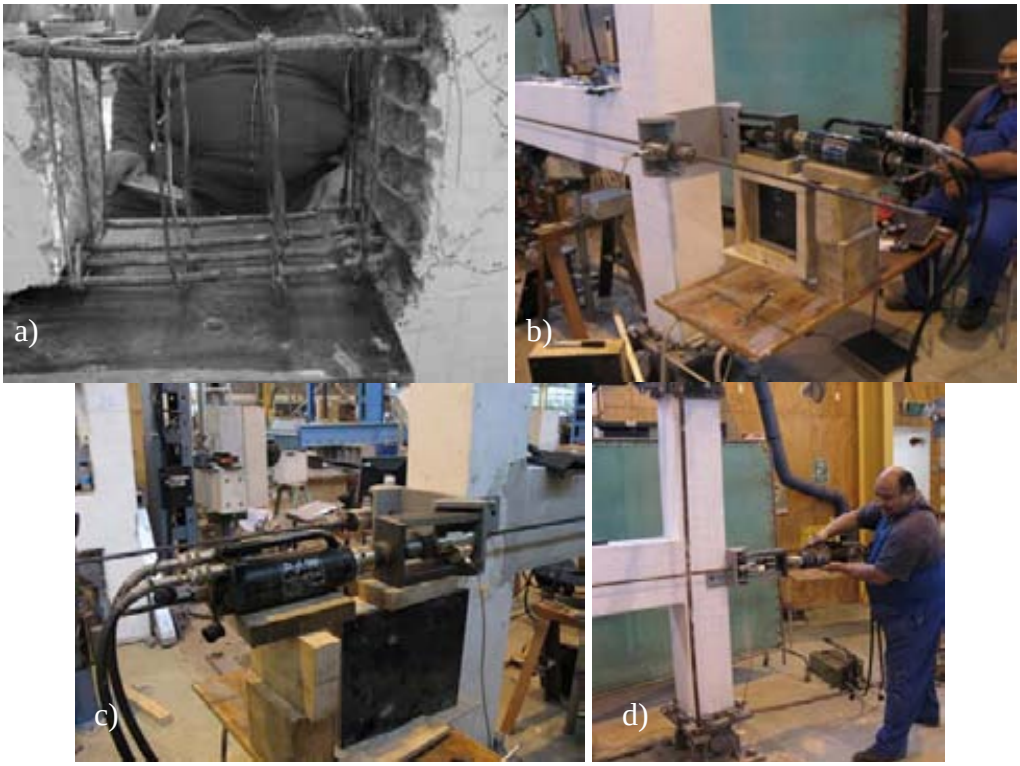

Figure D.5: a) The repaired region before the 2nd repair (R2) prior to recasting. Notice the increased stirrup spacing and severed bottom longitudinal bars; b-d) External post-tensioning with initial force of 40% f_{ypt}.

D.1.3 Summary and comparison between the trial specimens

Figure D.6 and Figure D.7 present the comparison of the applied lateral force, F_c versus column top displacement/drift (Δ_c / θ_{drift}) for both the repaired specimens (NZS3101-R1 and NZS3101-R2) and the as-built specimen (NZS3101-O1).

The benchmark beam-column joint NZS3101-O1 behaved expectedly with a ductile beam hinging behaviour without any notable damage to the column or joint. The beam theoretical moment capacity was attained and maintained up to the end of the ±4.5% drift cycles. Fat hysteresis loops with significant energy dissipation were achieved.

The first repair (R1) method was successful in restoring the lateral force and displacement capacities as well as the energy dissipation capacity. The high strength repair concrete (f'_c = 50MPa) shifted the plastic hinge towards the old and new concrete interface, resulting in a higher lateral load, F_c in both loading directions.

The second repair (2) illustrated the feasibility and constructability of the external post-tensioning of the beam-column joint. An upper bound of prestressing force (75% f_{ypt}) was used to

test the reliability of the anchoraging and prestressing system. The test has also demonstrated the expected post-yield stiffness of the 'pseudo-rocking' beam-column joint. From Figure D.7, it was evident that the beam-weakening and post-tensioning successfully replicated the advanced controlled-rocking behaviour, as envisioned in §3.3.3.3.

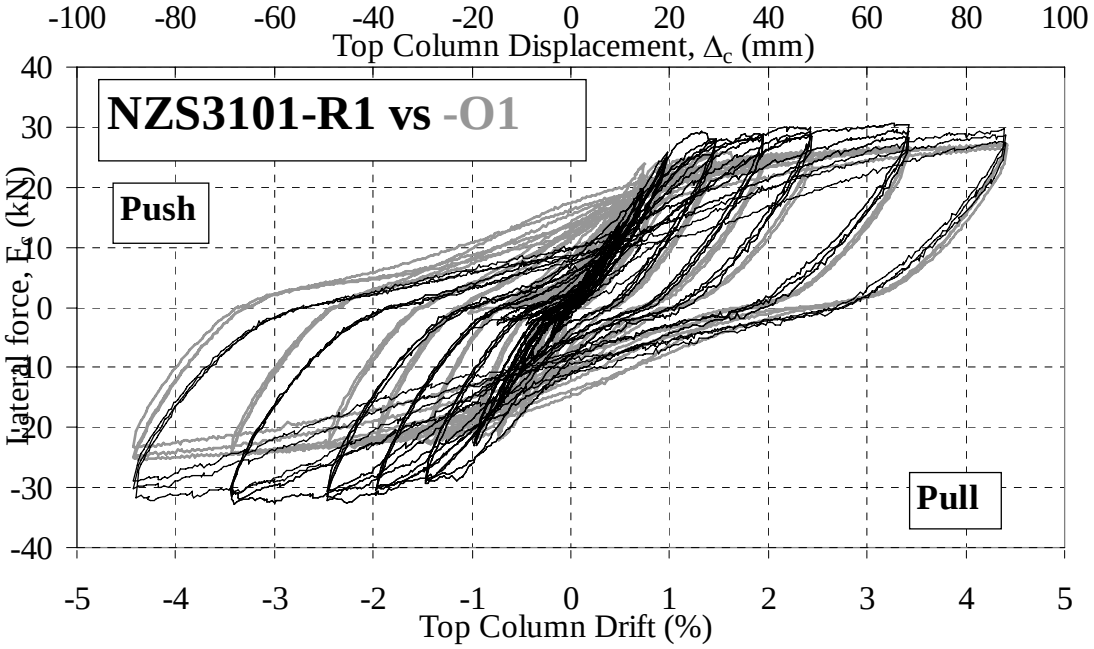

Figure D.6: Top column lateral load, F_c versus top column displacement, Δ_c and drift, θ_{drift} for test Unit NZS3101-R1 and NZS3101-O1.

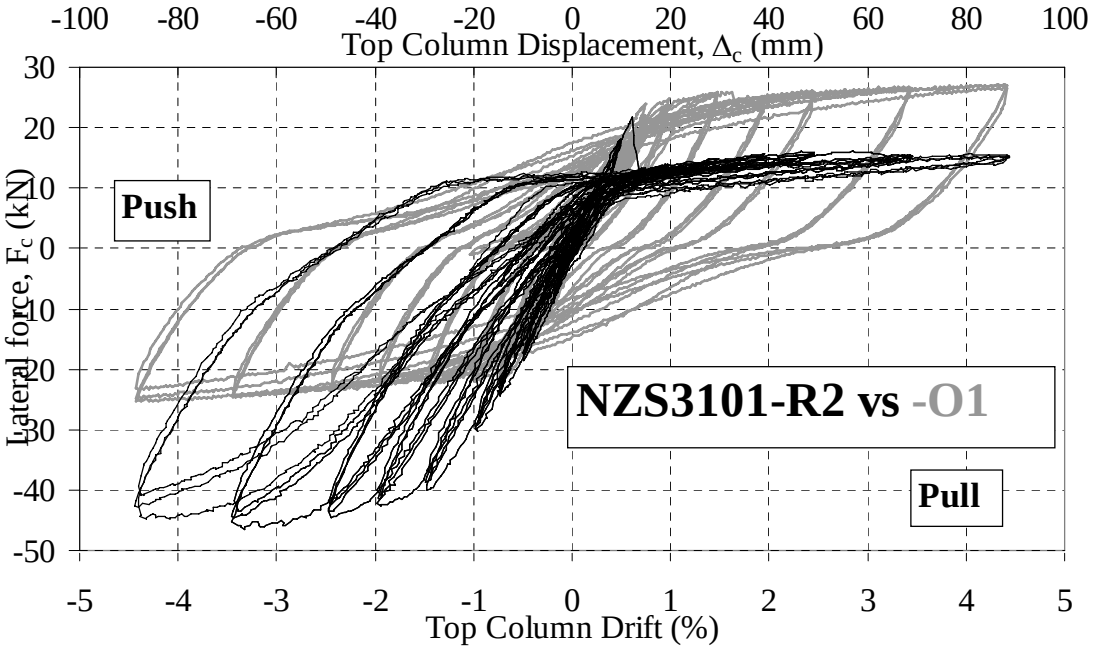

Figure D.7: Top column lateral load, F_c versus top column displacement, Δ_c and drift, θ_{drift} for test Unit NZS3101-R2 and NZS3101-O1.

D.2 NZS3101-O1 : AS-BUILT WELL-DESIGNED JOINT

D.2.1 Lateral force displacement hysteresis

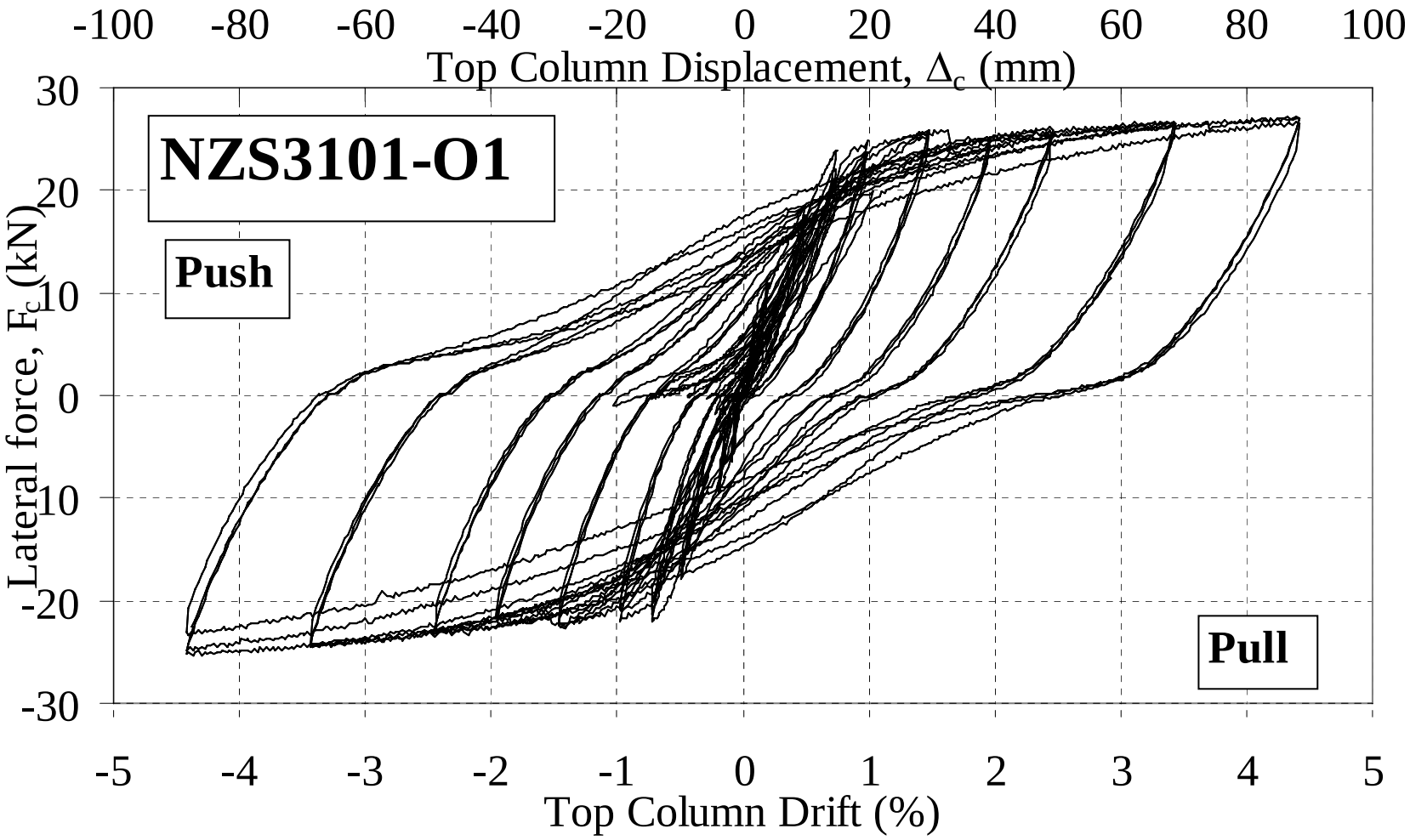

Figure D.8: Test Unit NZS3101-O1: Top column lateral load, F_c versus top column displacement, Δ_c and drift, θ_{drift} .

D.2.2 Description of selected loading cycles

Start:. The as-built NZS3101-O1 beam-column joint was a representative of a well-designed beam-column connection, designed to the NZS3101:2006 requirements. A ductile response was expected.

0.5% Push 3- Distributed flexural cracks along the beam top and bottom faces were observed.

0.75% Pull 1- Hairline diagonal joint cracks were observed.

1.0% Pull 3 – New minor flexural cracks appeared in the columns and the beam.

2.0% Push 3 – A well-developed flexural plastic hinge was formed in the beam. From observation, the plastic hinge length was approximately the beam depth, h_b. A flexural-shear crack pattern was observed at the region close to the beam-column interface.

3.5% Pull 3 – At the bottom face of the beam, fragments of unconfined concrete spalled off, exposing the beam bottom bars.

4.5% Pull & Push cycles - In the 4.5% loading cycles, flexural beam deformation continued to govern the inelastic mechanism. Due to the spalling of the cover concrete, lateral strength degradation was observed.

Conclusions – The as-built NZS3101-O1 developed a weak-beam strong column-joint behaviour as expected. Beam flexural deformation governed the inelastic mechanism. The structural ductility of the NZS3101-O1 joint attained was six without strength degradation.

D.2.3 Photographic observations

Figure D.9: General observation photographs for test unit NZS3101-O1.

D.3 NZS3101-R1 : RE-CONCRETING REPAIR JOINT

D.3.1 Lateral force displacement hysteresis

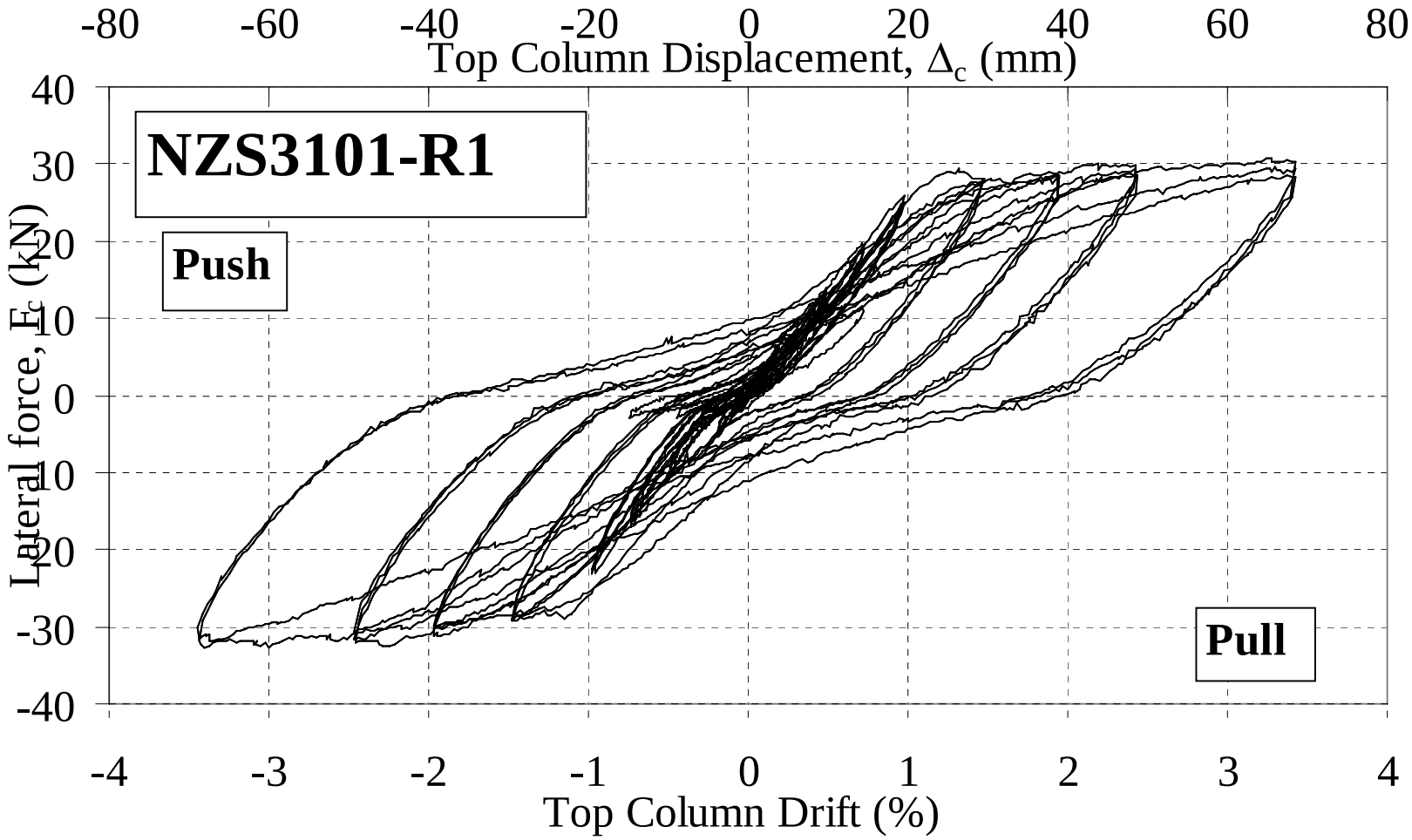

Figure D.10: Test Unit NZS3101-R1: Top column lateral load, F_c versus top column displacement, Δ_c and drift, θ_{drift}.

D.3.2 Description of selected loading cycles

Start:. Sika monotop 634 flowable micro concrete was used to repair the damaged section.

0.5% Pull 1 - First visible flexural crack was observed at the bottom face along the repaired interface.

0.75% Pull 1 - More hairline cracks appeared at the repaired beam zone and some old cracks re-surfaced in the joint panel zone.

1.0% Pull-Push cycles - The F_c-Δ_c hysteresis was exhibiting low energy dissipation.

1.5% Pull-Push 1 - Diagonal cracks appeared on the repaired concrete-old concrete interface, with a maximum crack width of 1.2mm.

2.0% Pull 1 - More new flexural cracks appeared within and outside the repaired zone. The diagonally-inclined flexural crack at the repaired section was approximately 1.6mm wide.

2.0% Pull 3 – By the end of the 2.0% drift cycles, the vertical flexural crack outside the repaired zone outgrew the diagonal crack on the repaired interface, indicating shifting of the plastic hinge.

2.5% Pull 3 – A flexural-shear cracking pattern was formed at the repaired interface region. Some concrete spalling at the interface section was observed, coupled with some stiffness degradation in the F_c-Δ_c plot. The shear deformation and cracking along the interface zone was significant.

3.5% Pull-Push 3 - Concrete spalled off at the top and bottom faces of the beam, exposing the beam longitudinal bars. No buckling of the beam bars was observed. The major crack was the vertical flexural crack outside the repaired region.

4.5% Pull 1 - Progressive spalling of concrete at the plastic hinge region was observed. New flexural cracks appeared within the repaired region.

4.5% Pull-Push 3 - Minor buckling of the longitudinal bars was observed at the compression face of the beam. Nevertheless, the F_c-Δ_c hysteresis behaviour of the specimen was very stable.

Conclusions – The repair of the damaged plastic hinge region using re-concreting technique was a success. The strength and stiffness of the as-built NZS3101-O1 were restored with minor loss of energy dissipation capacity. Despite the rigorous three-cycles loading protocol up to 4.5% inter-storey drift, no low cycle fatigue or buckling of the beam longitudinal bars was observed.

D.3.3 Photographic observations

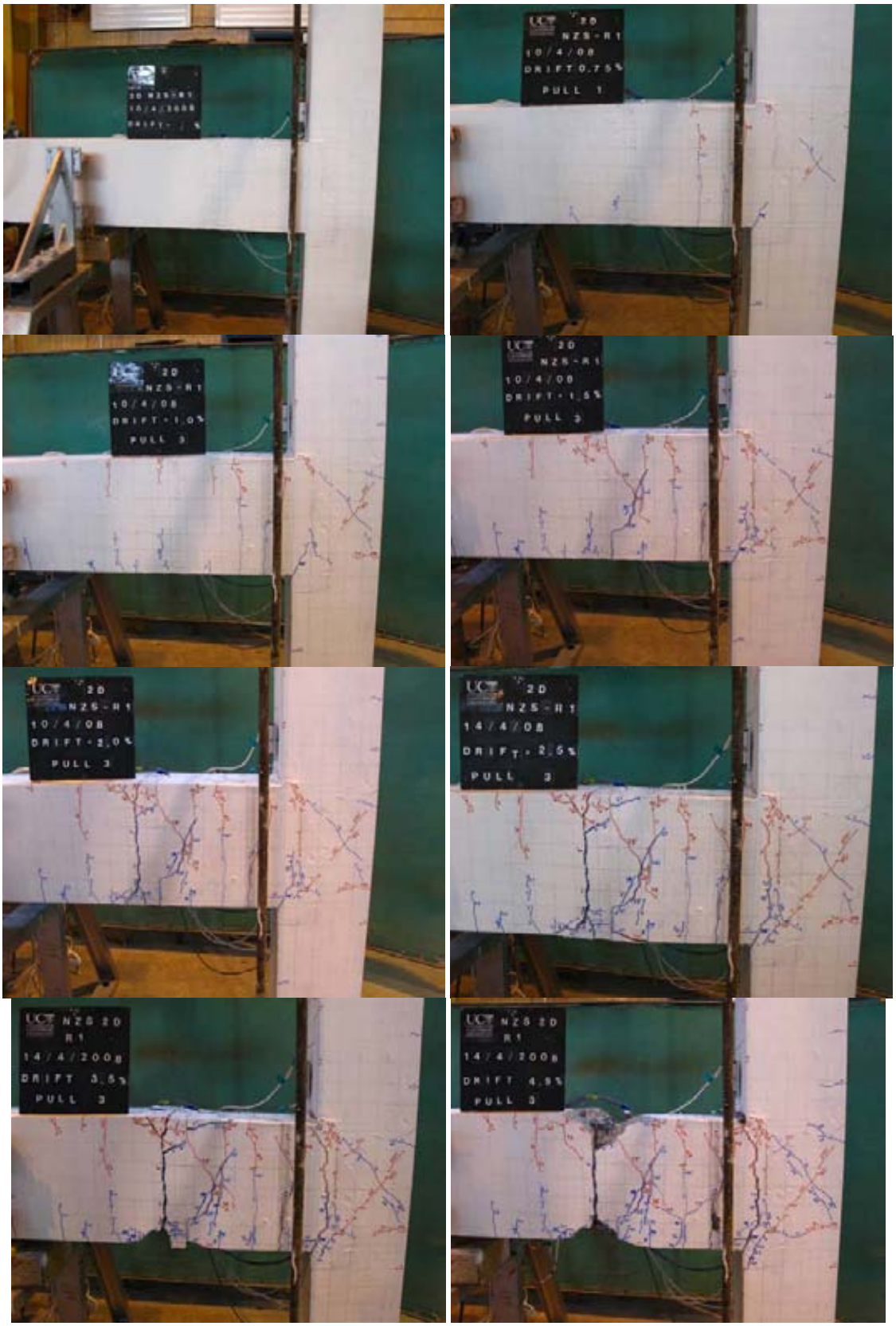

Figure D.11: General observation photographs for test unit NZS3101-R1.

D.4 NZS3101-R2 : SELECTIVE WEAKENING RETROFIT AND REPAIR JOINT

D.4.1 Lateral force displacement hysteresis

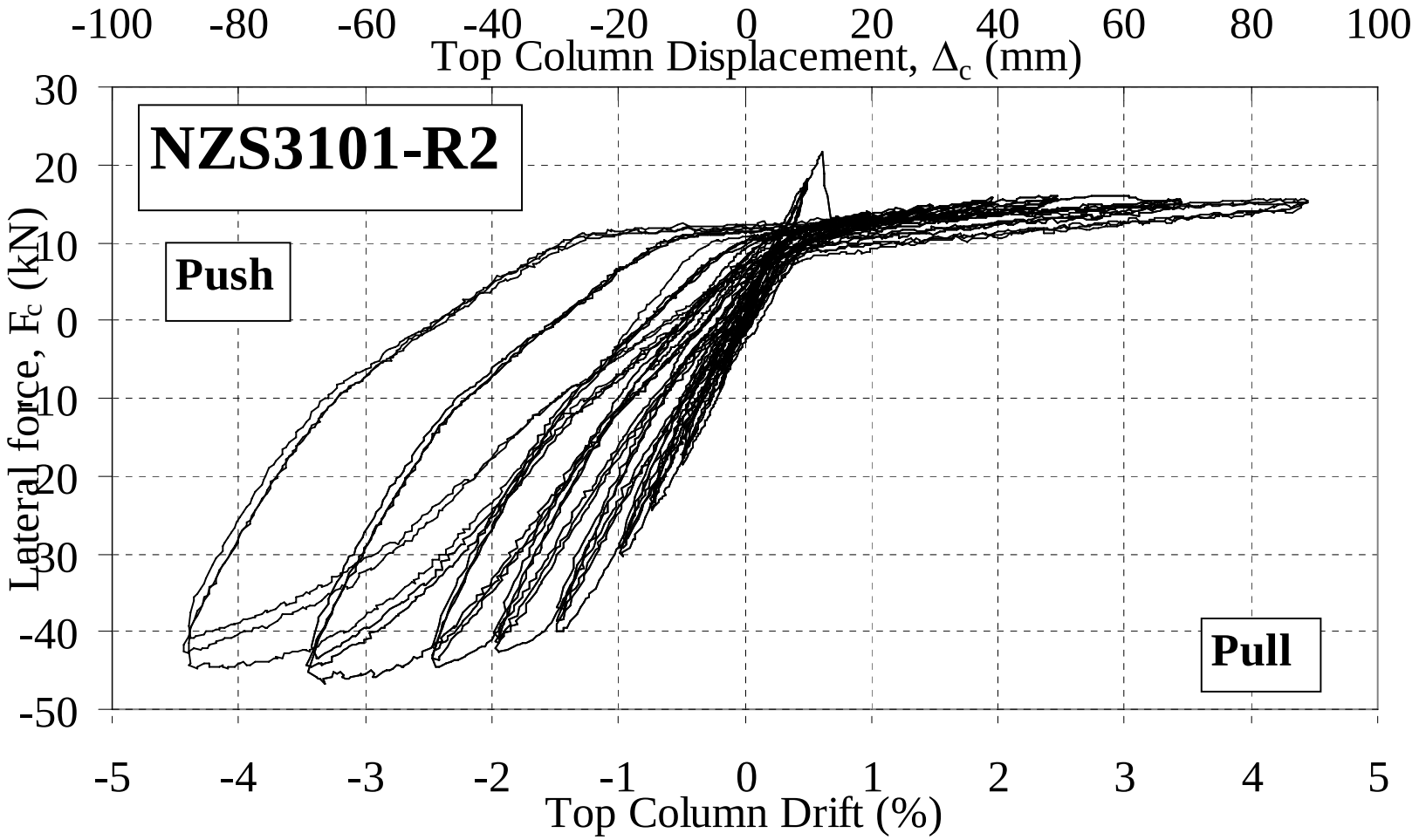

Figure D.12: Test Unit NZS3101-R2: Top column lateral load, F_c versus top column displacement, Δ_c and drift, θ_{drift}.

D.4.2 Description of selected loading cycles

Start: Initial post-tensioning (PT) forces applied were 70kN (45% f_{tpy}). Sika monotop grout was used to repair the damaged section.

0.5% Push 3- Minor hairline flexural cracks at the old-new concrete interface were observed.

0.75% Pull 1- A sudden crack opening (with a bang), starting at the location where bars were cut, propagated towards the stirrup. The flexural crack was 290mm from beam bottom with 40mm uncracked section. Reduced section and neutral axis was coupled with a sudden drop F_c was observed. This weakened plane became the pseudo-rocking interface at the Pull direction.

1.0% Pull 3 -All inelastic deformations concentrated at the rocking gap opening.

1.5% Push 3 -While the beam rocked on the Pull direction, the beam had a well developed flexural plastic hinge in the Push direction. Flexural cracking interaction with the PT force decreased the direction/angle of the cracks. F_c-Δ_c plot indicated that top bars yielded approximately at the 1.5% Push-3.

2.0% Push 3 -Appearance of diagonally inclined cracks at the top face (tension) of the beam. These diagonal cracks were probably caused by bond-splitting failure of the beam top bars.

2.5% Pull 3- Inelastic deformation concentrated at the weakened section, with a gap opening up to 9mm. Concrete crushing at the top face of the beam was observed, with minor F_c degradation.

2.5% Push 3 – In the Push direction, more horizontal/diagonal bond-splitting cracks appeared at the top face of the beam. These cracks were concentrated along the longitudinal bars depth.

3.5% Push 3 – Significant energy dissipation (fat hysteresis loops) was observed in the F_c-Δ_c plot. At the top face of the beam, a large chunk of unconfined concrete spalled off, exposing the beam top bars.

4.5% Pull & Push cycles - In the 4.5% Pull direction, no further damage was observed as the stable rocking gap mechanism was governing. Spalling at the top face of the beam during the Push cycles however reduced the overall F_c.

Conclusions – Repair and retrofit with external post-tensioning and re-concrete worked reasonably well in restoring the strength and stiffness of the beam-column joint. There was no shear failure observed despite the reduced number of stirrups. External post-tensioning of the beam-column joint was feasible and practical in the laboratory implementation.

D.4.3 Photographic observations

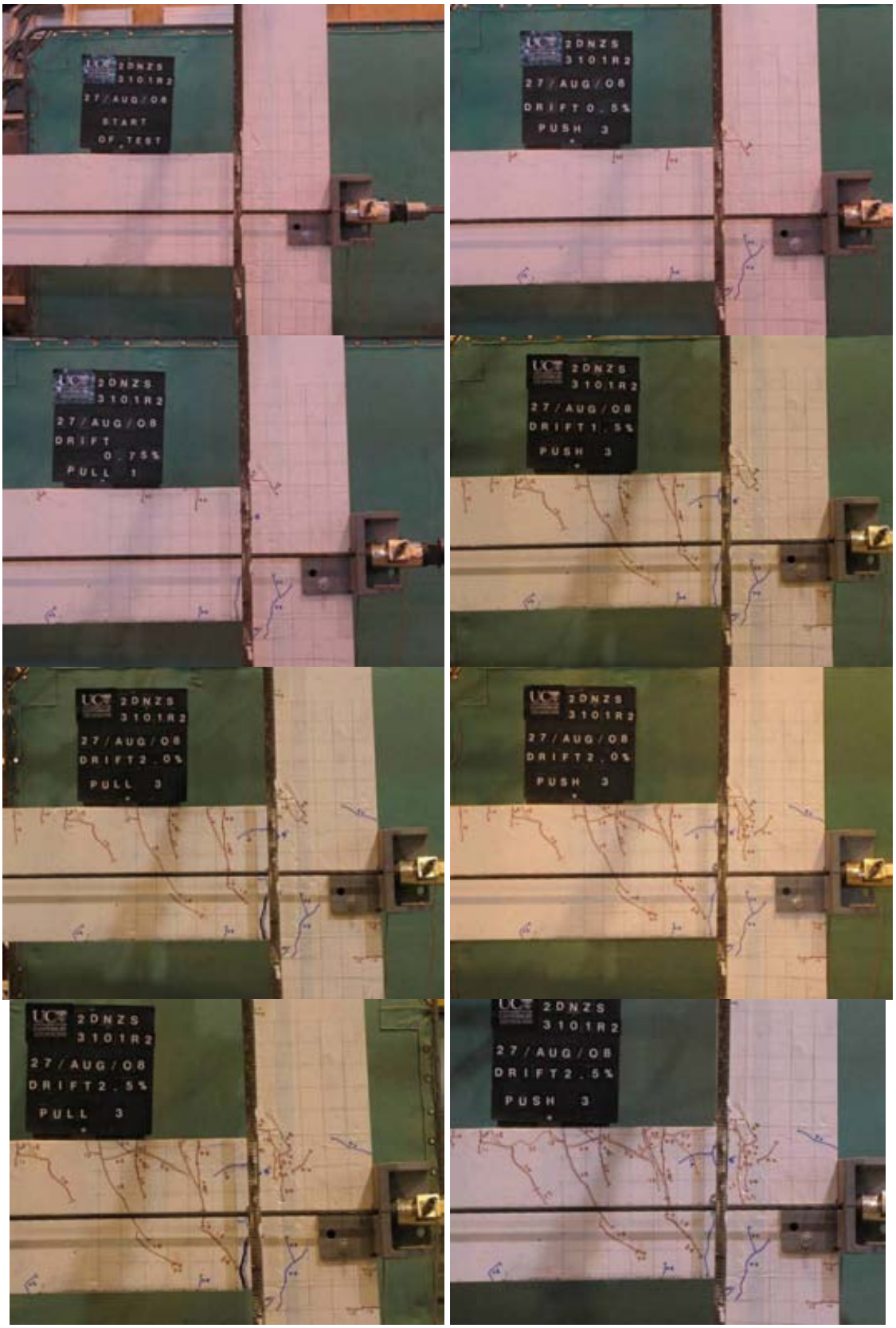

Figure D.13: General observation photographs for test unit NZS3101-R2.

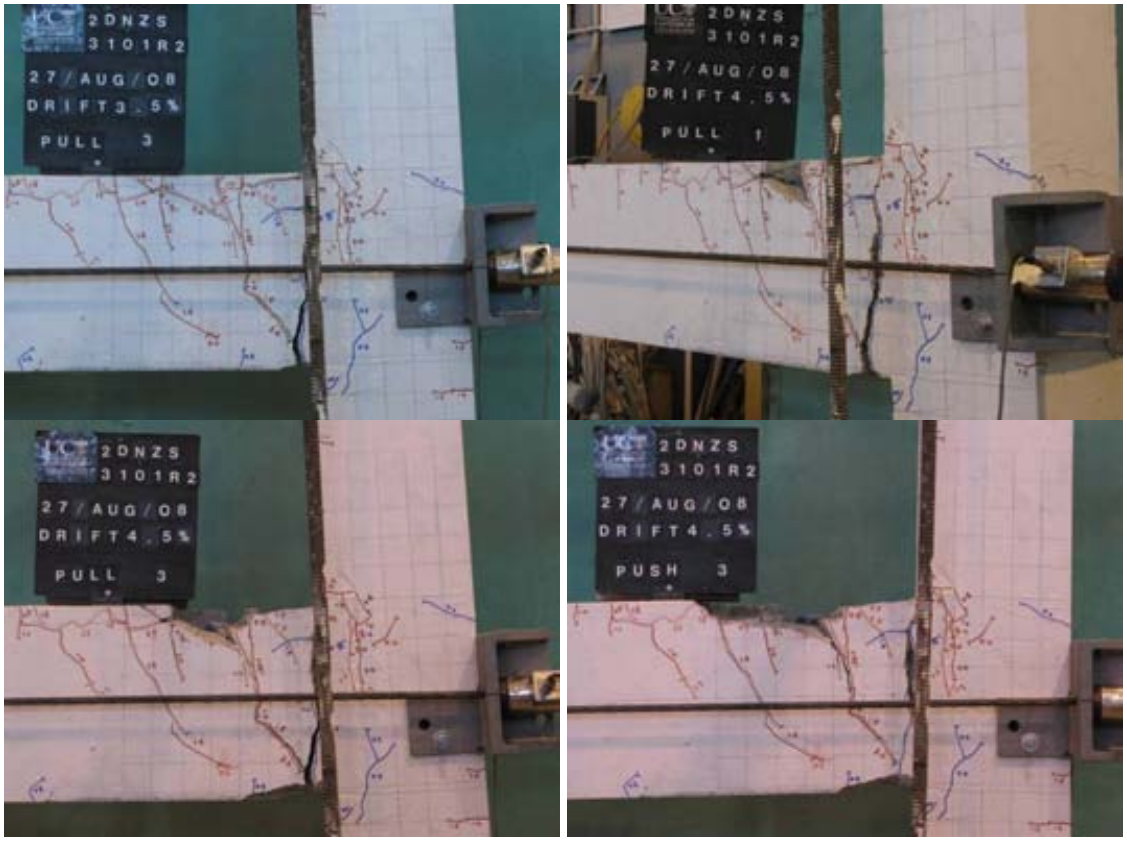

Figure D.14: General observation photographs for test unit NZS3101-R2.

APPENDIX E. EXPERIMENTAL TEST DATA AND LOG FOR S-O1 AND S-R3

E.1 S-O1 – AS-BUILT B-C JOINT WITH COLUMN LAP SPLICE

E.1.1 Force-displacement

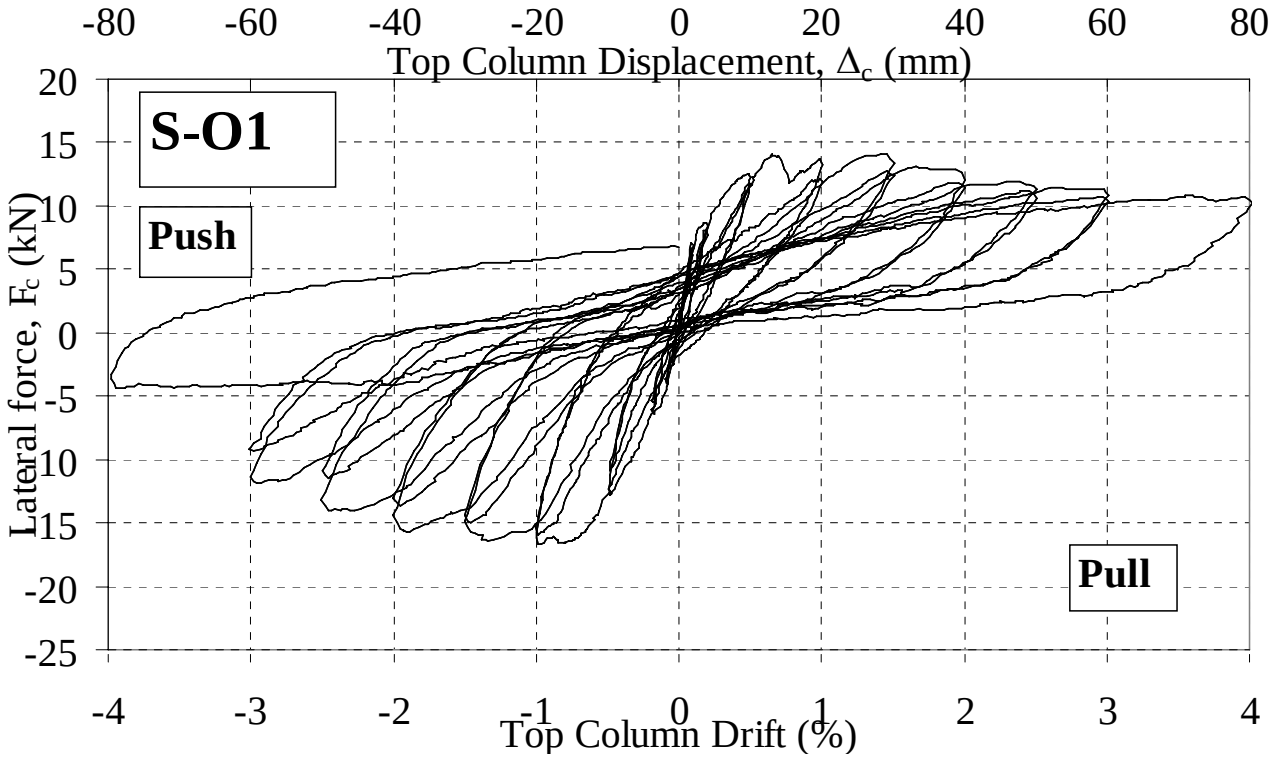

Figure E.1: Test Unit S-O1: Top column lateral load, F_c versus top column displacement, Δ_c and drift, θ_{drift}.

E.1.2 Photographic observations

Figure E.2 General observation photographs for test unit S-O1 at: Start, ±0.2%, ±0.5%, and ±1.0% drifts.

Figure E.3 General observation photographs for test unit S-O1 at: ±1.0%, ±1.5%, ±2.0% and ±2.5% drifts.

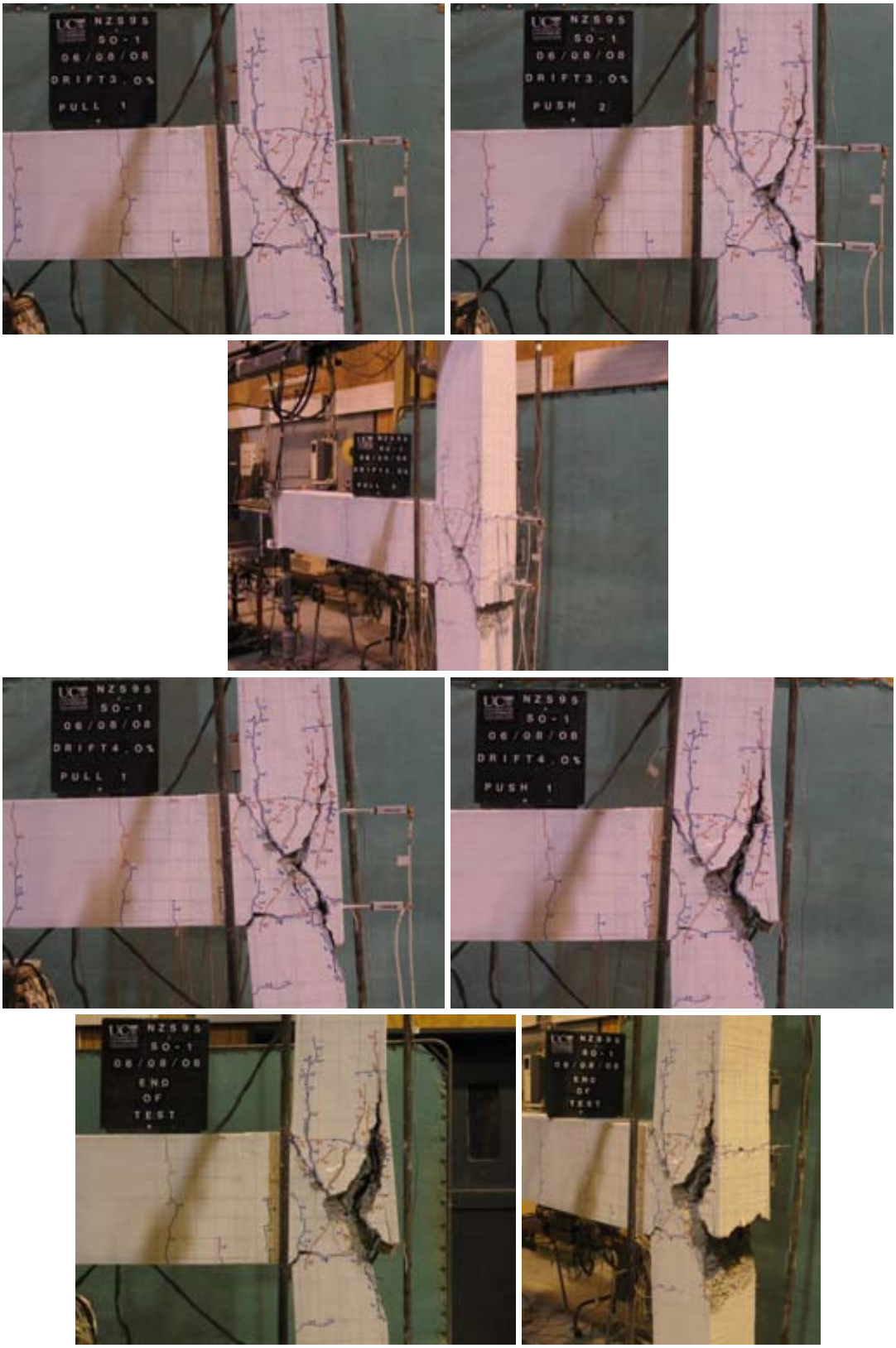

Figure E.4 General observation photographs for test unit S-O1 at: ±3.0%, ±4.0% drifts and the end-of-test.

E.1.3 Column strain gage readings

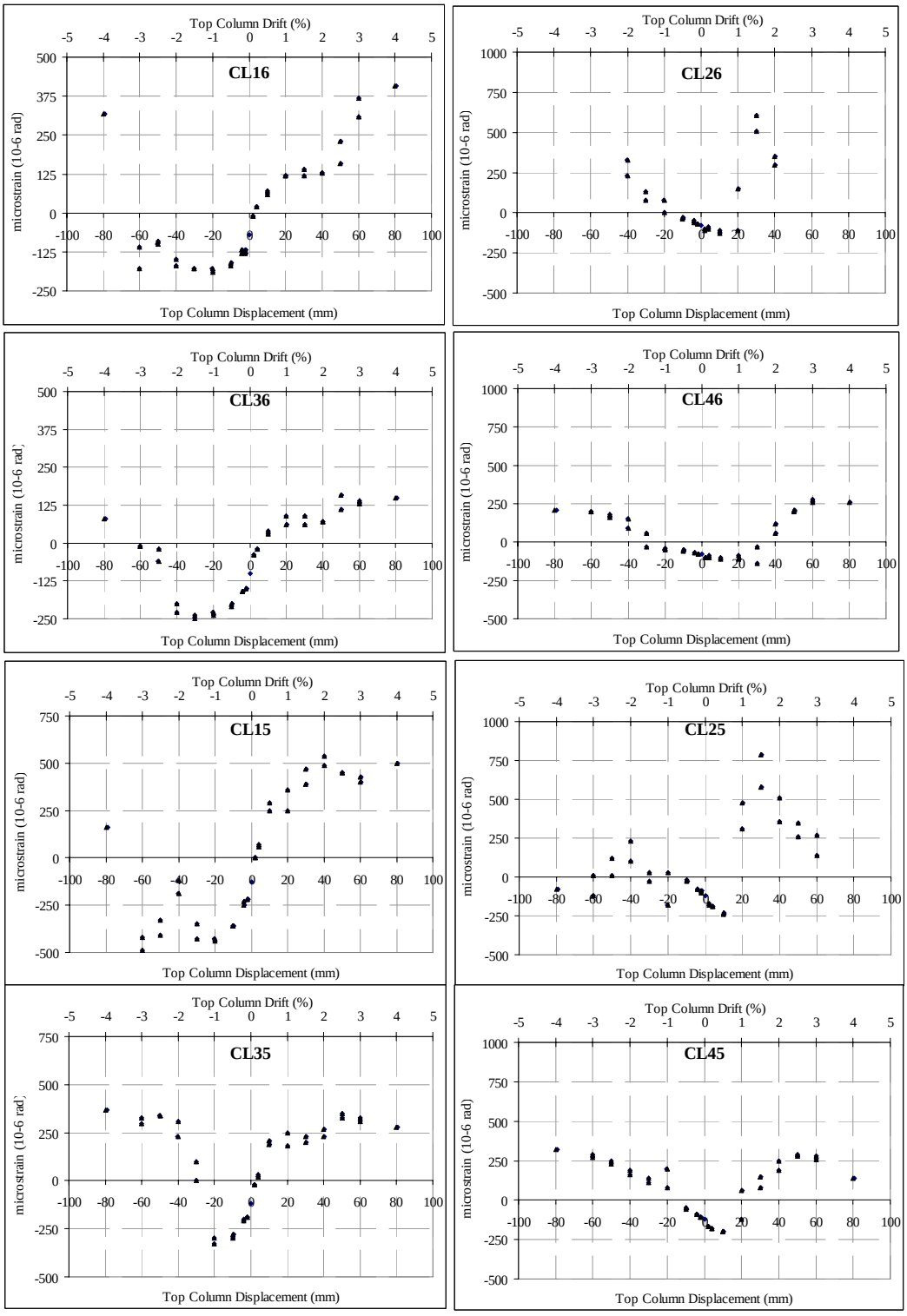

Figure E.5: Test Unit S-O1: Column longitudinal bars strain gage readings: Top half.

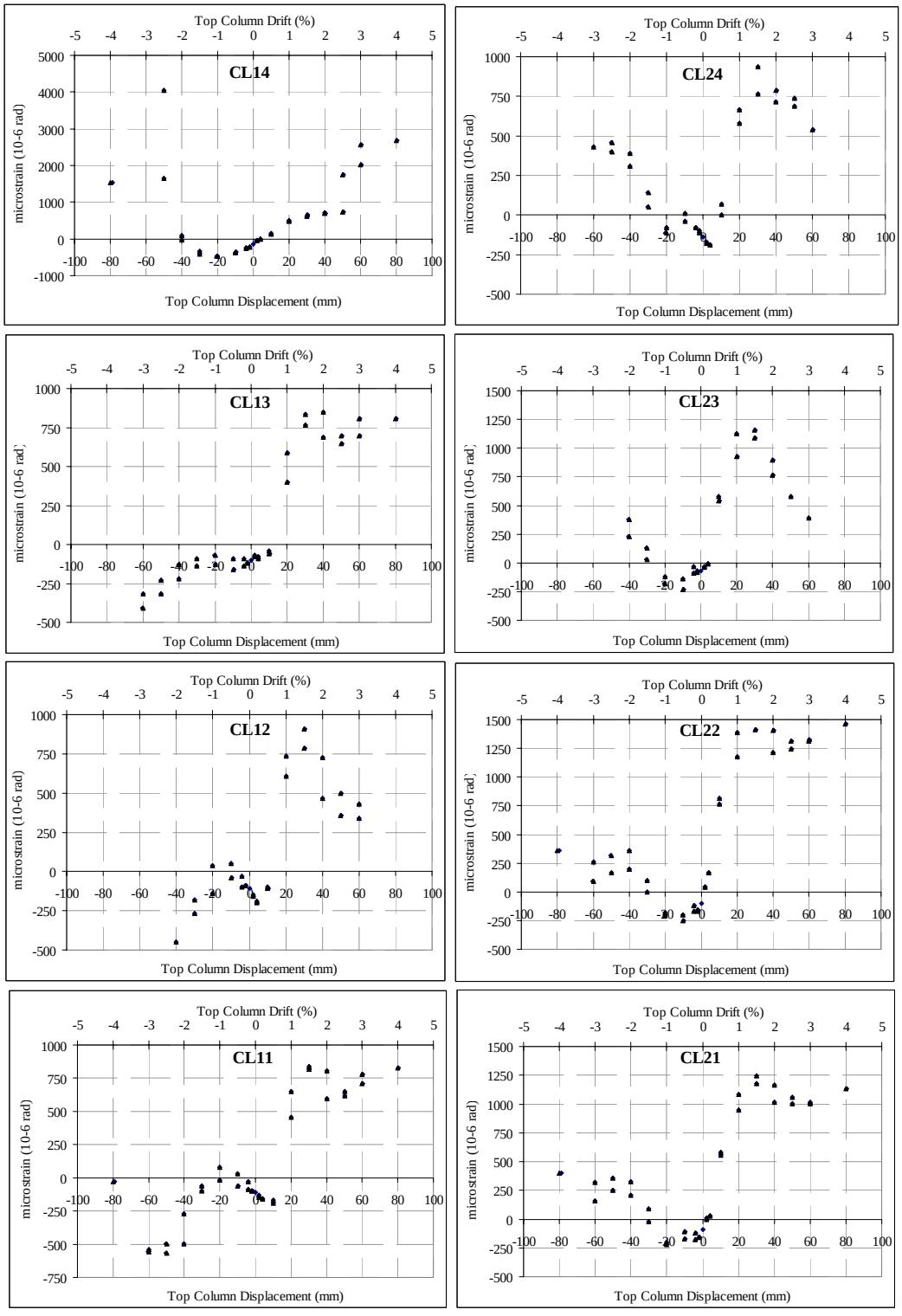

Figure E.6: Test Unit S-O1: Column longitudinal bars strain gage readings: Bottom half.

E.1.4 Beam strain gage readings

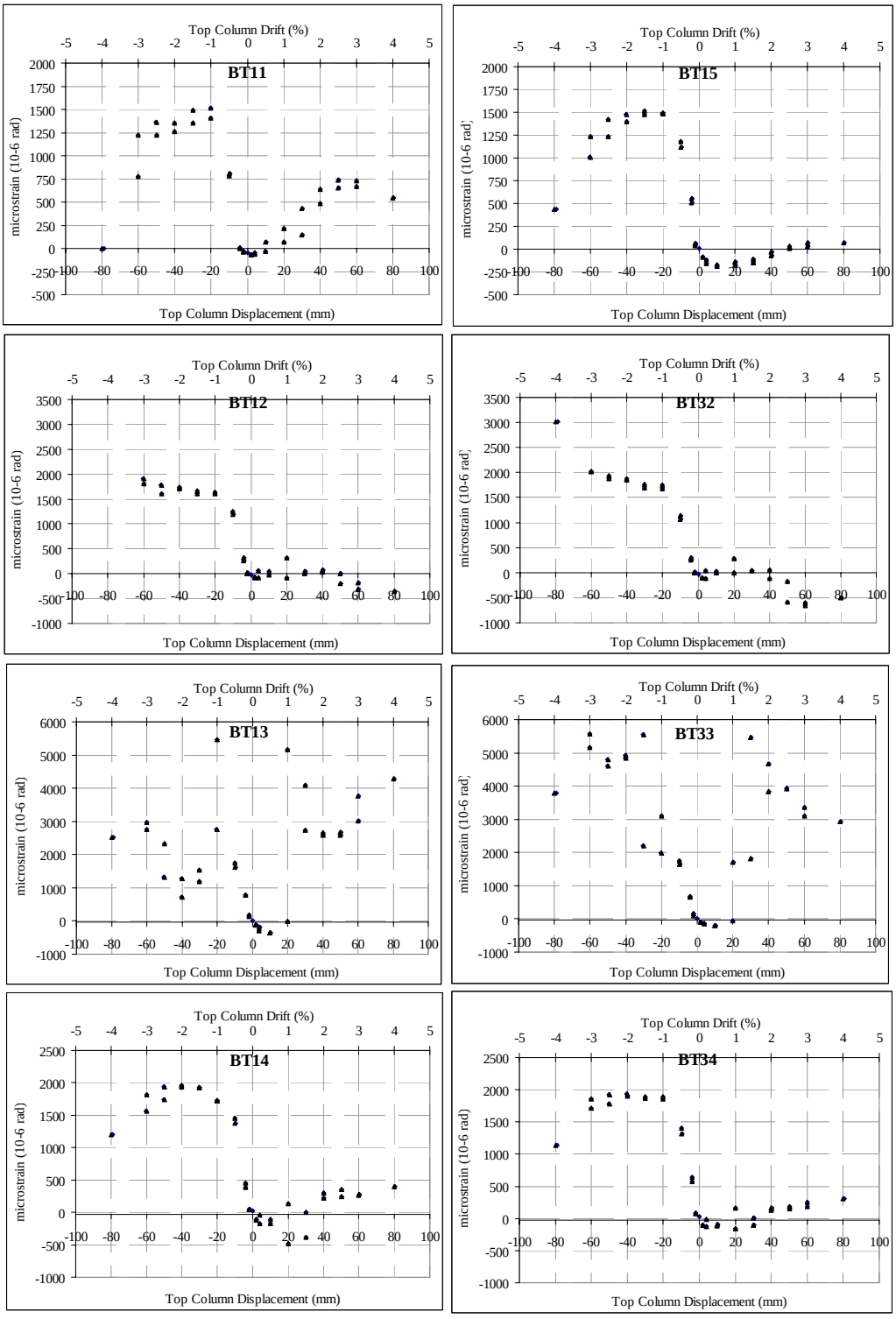

Figure E.7: Test Unit S-O1: Beam longitudinal bars strain gage readings: Top bars (BT31 was damaged).

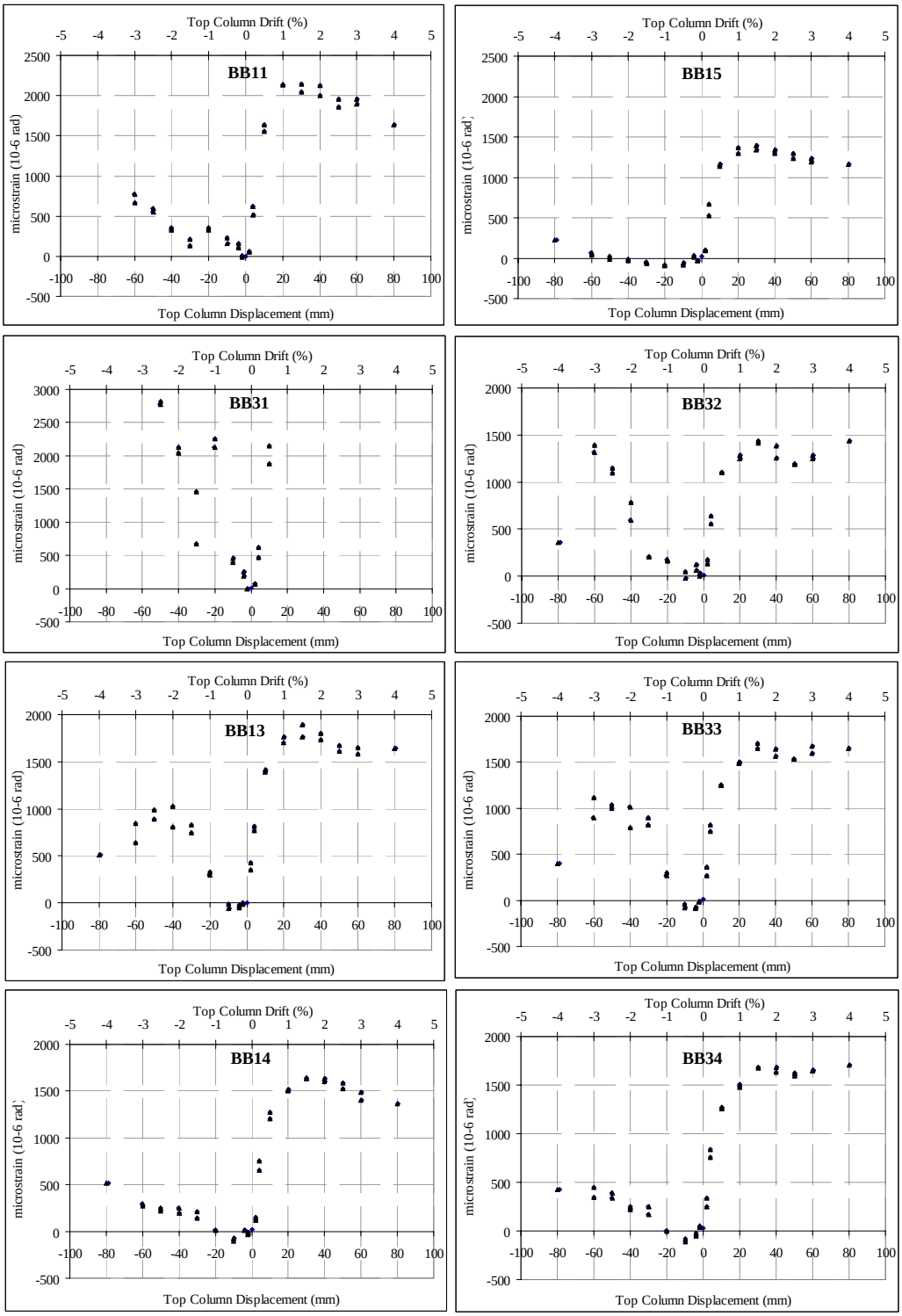

Figure E.8: Test Unit S-O1: Beam longitudinal bars strain gage readings: Bottom bars (BB12 was damaged).

E.1.5 Stirrups (column and beam) strain gage readings

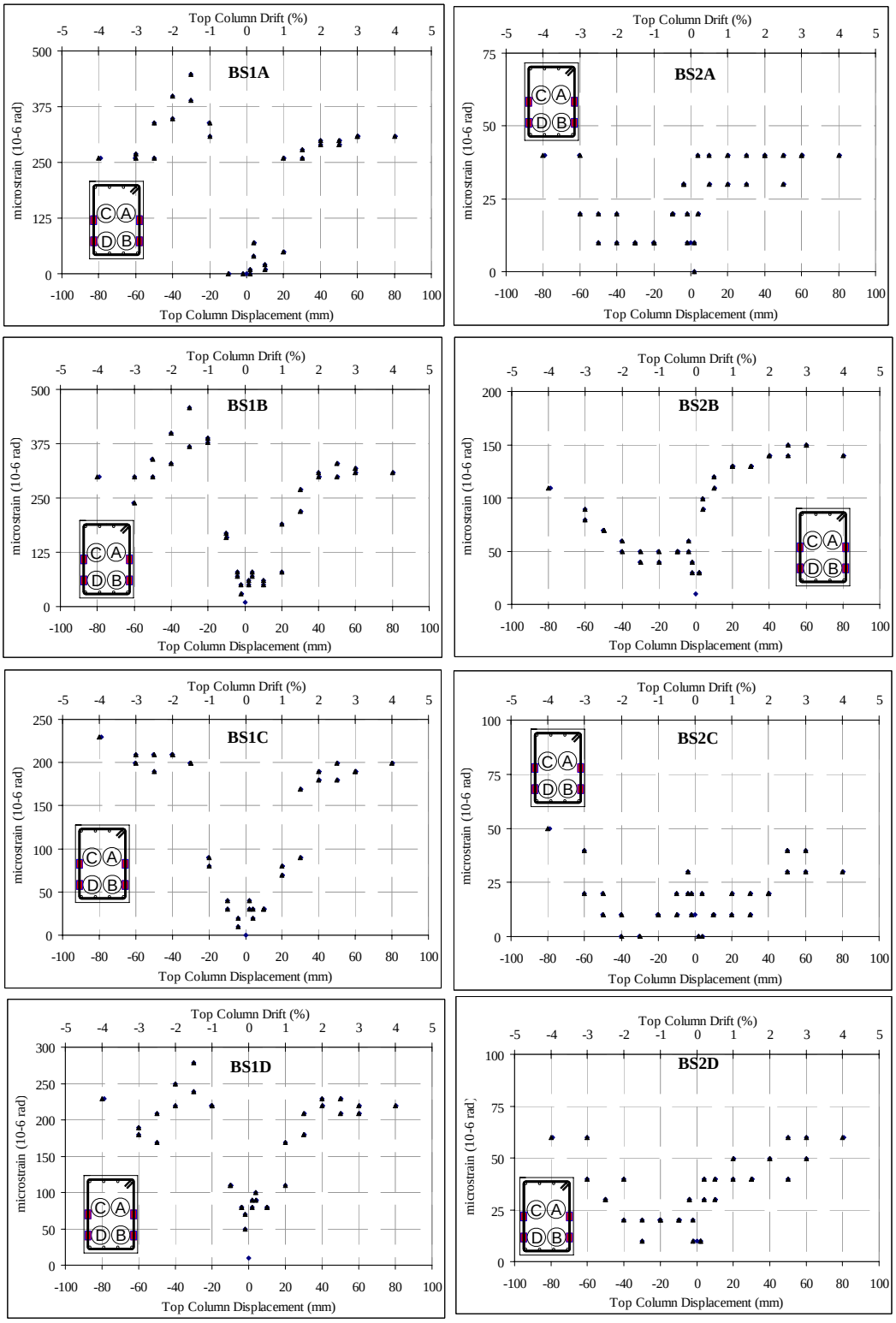

Figure E.9: Test Unit S-O1: Beam stirrups bars strain gage readings.

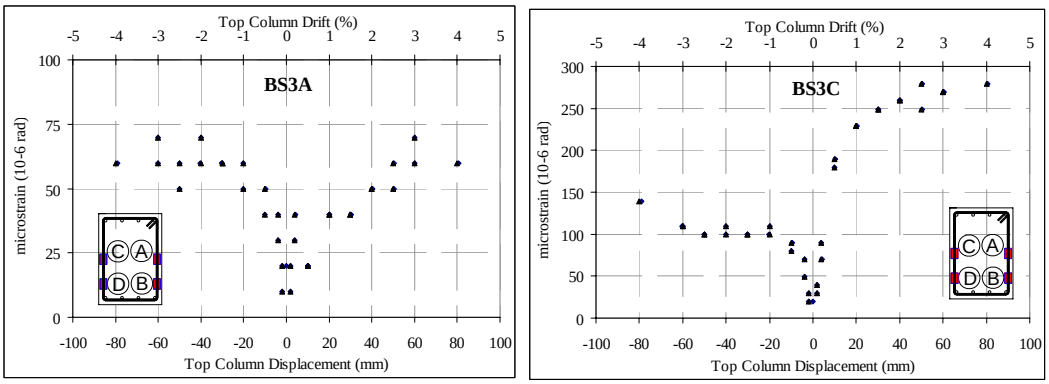

Figure E.10: Test Unit S-O1: Beam stirrups bars strain gage readings.

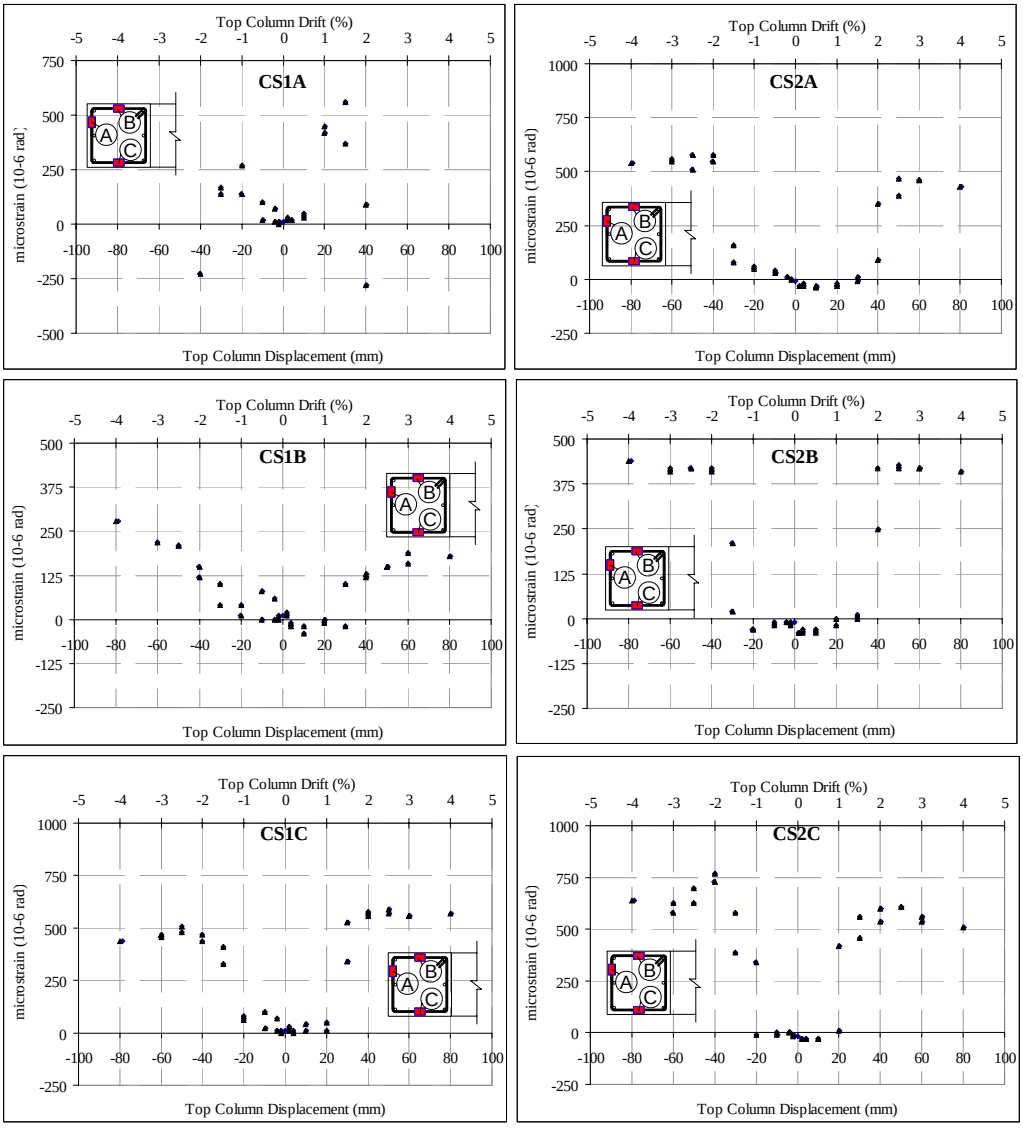

Figure E.11: Test Unit S-O1: Column stirrups bars strain gage readings.

E.2 S-R3 –SELECTIVE-WEAKENING RETROFIT JOINT WITH LAP SPLICE

E.2.1 Force-displacement

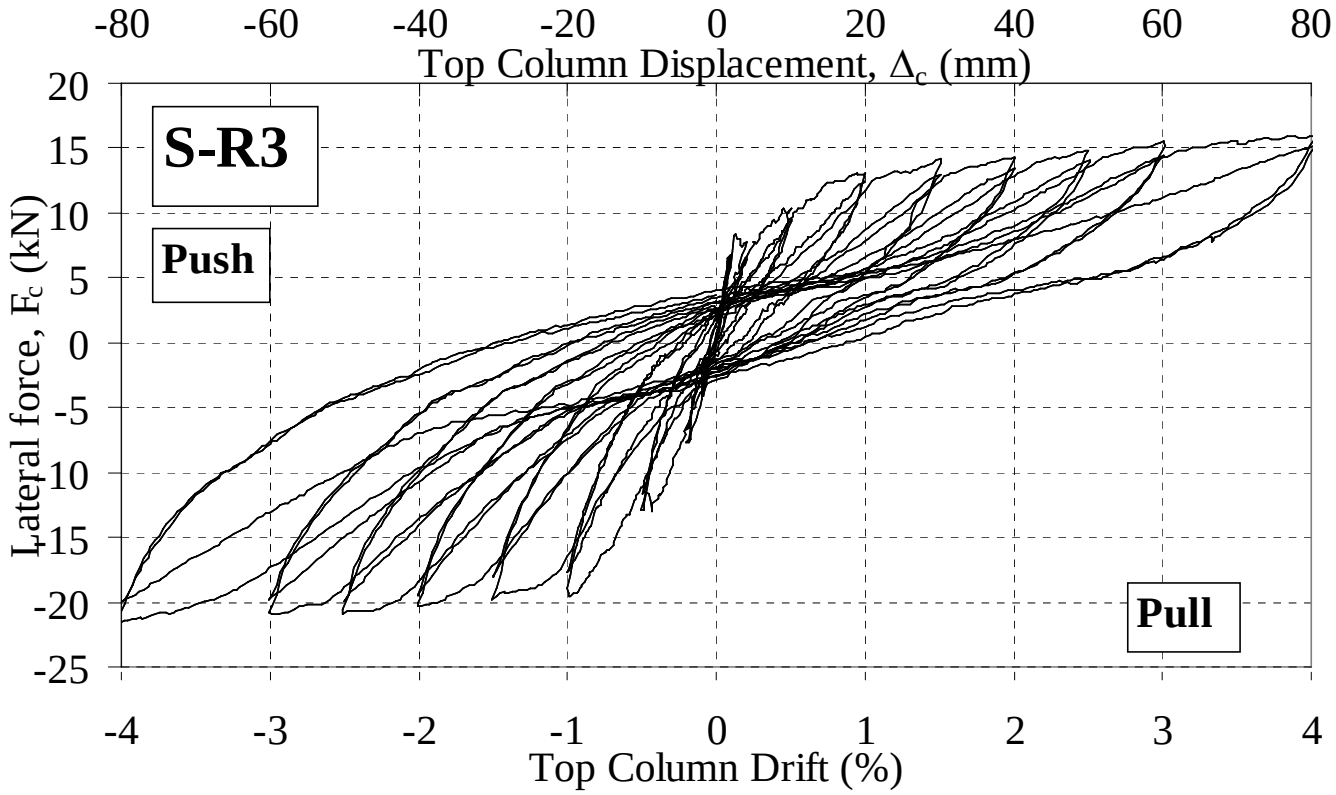

Figure E.12: Test Unit S-R3: Top column lateral load, F_c versus top column displacement, Δ_c and drift, θ_{drift}.

E.2.2 Photographic observations

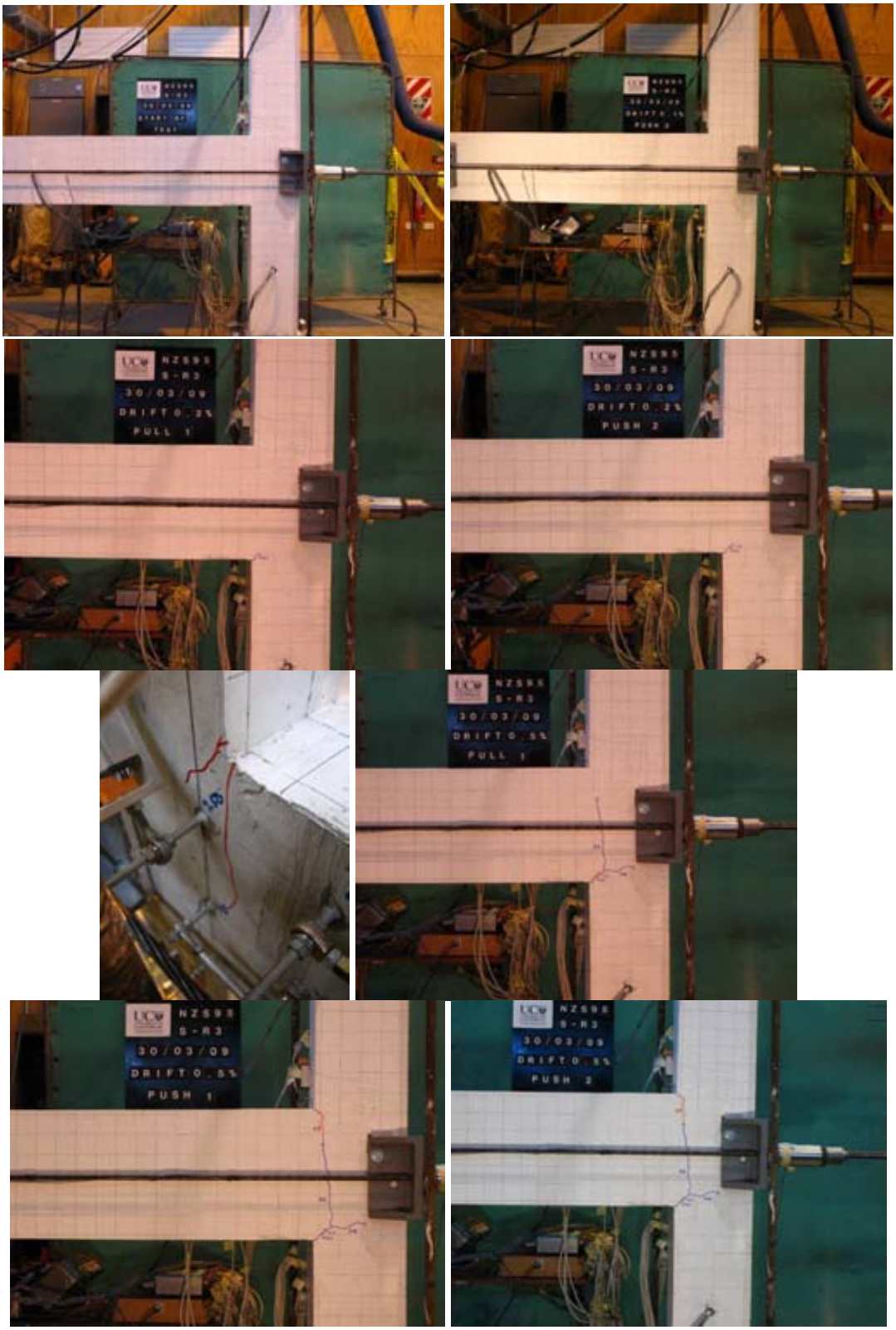

Figure E.13 General observation photographs for test unit S-R3 at: Start, ±0.2% and ±0.5% drifts.

Figure E.14 General observation photographs for test unit S-R3 at: ±1.0% and ±1.5% drifts.

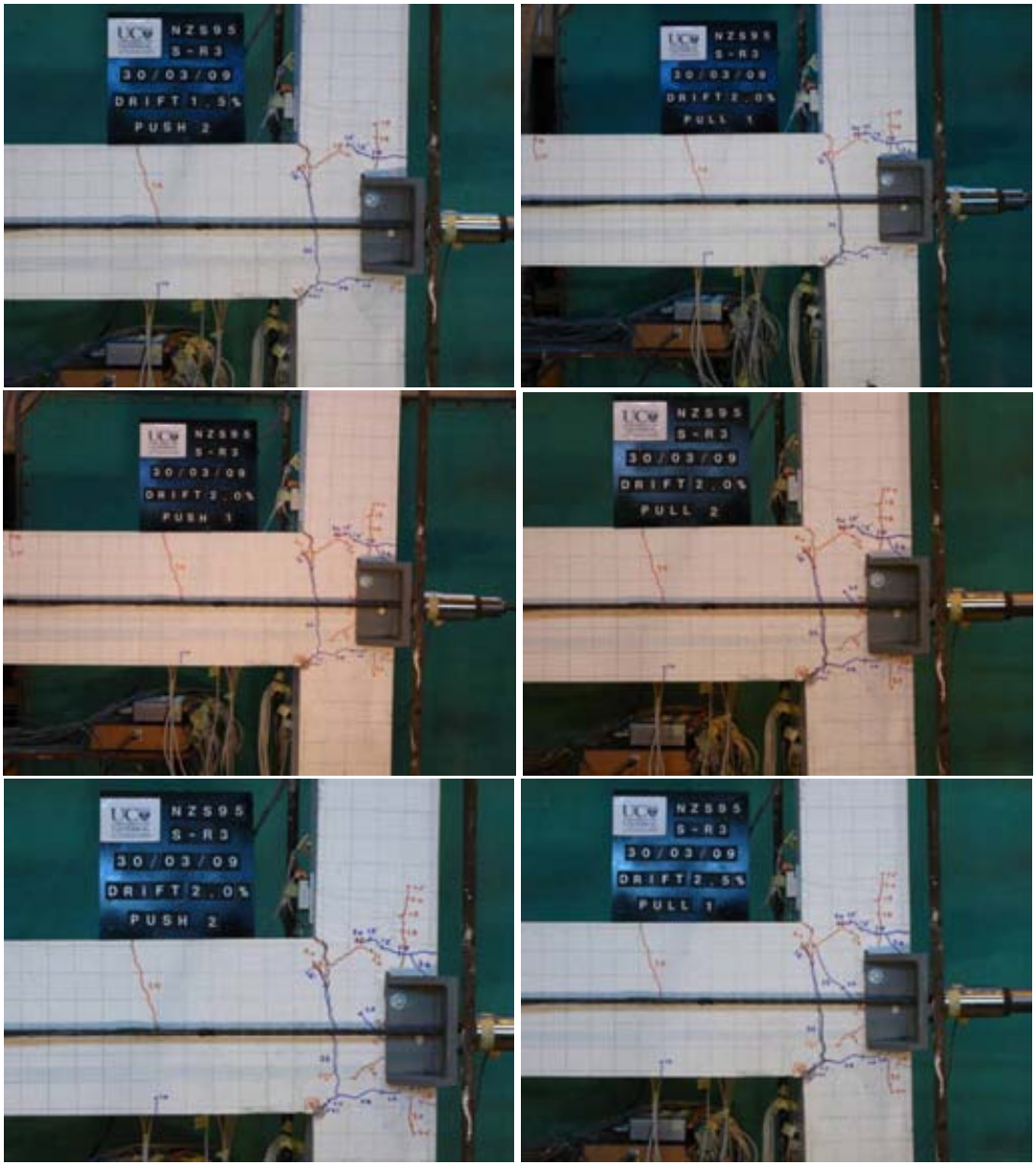

Figure E.15 General observation photographs for test unit S-R3 at: ±1.5%, ±2.0% and ±2.5% drifts.

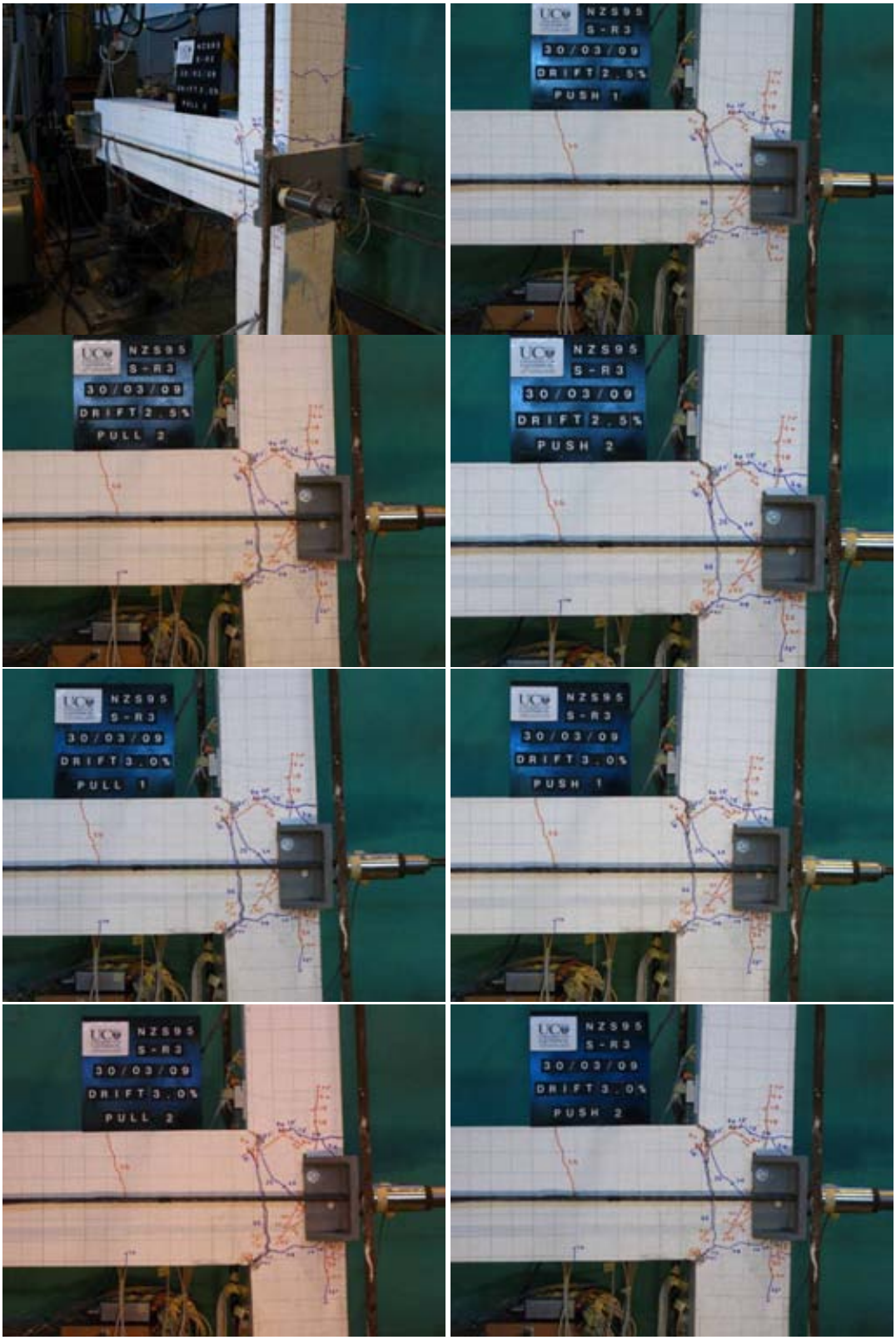

Figure E.16 General observation photographs for test unit S-R3 at: ±2.5% and ±3.0% drifts.

Figure E.17 General observation photographs for test unit S-R3 at: ±4.0% drift and the end-of-test.

E.2.3 Column strain gage readings

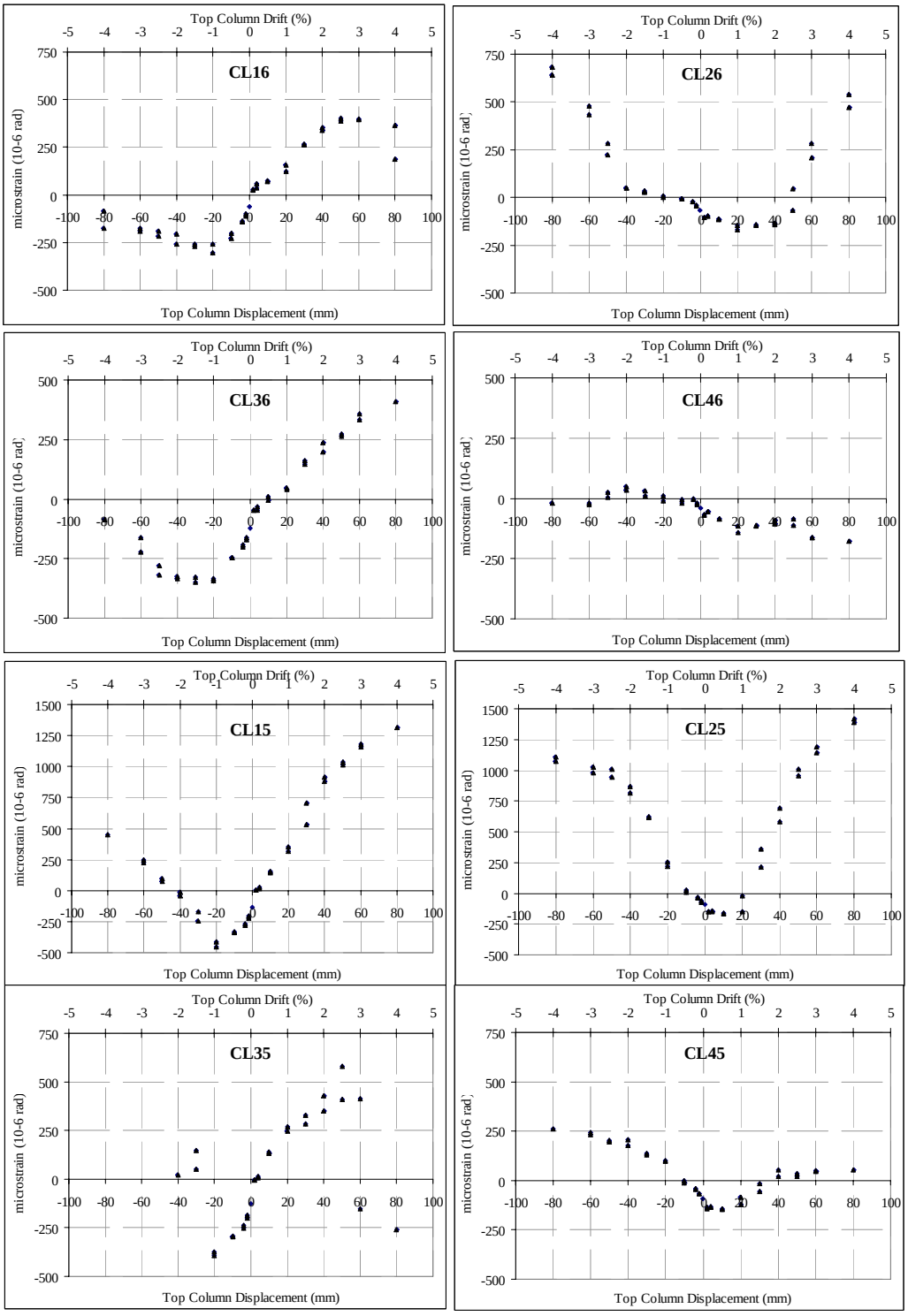

Figure E.18: Test Unit S-R3: Column longitudinal bars strain gage readings: Top half.

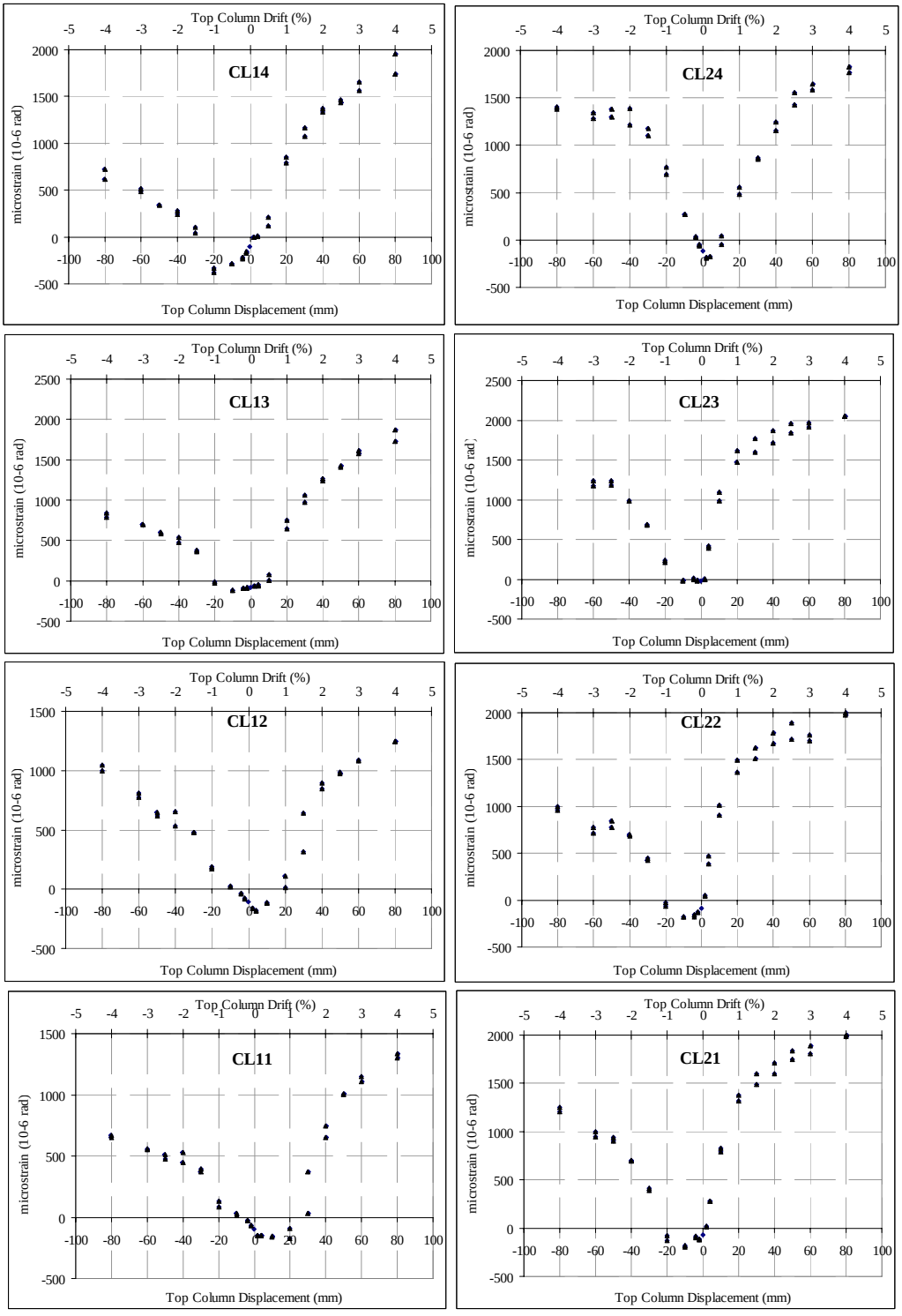

Figure E.19: Test Unit S-R3: Column longitudinal bars strain gage readings: Bottom half.

E.2.4 Beam strain gage readings

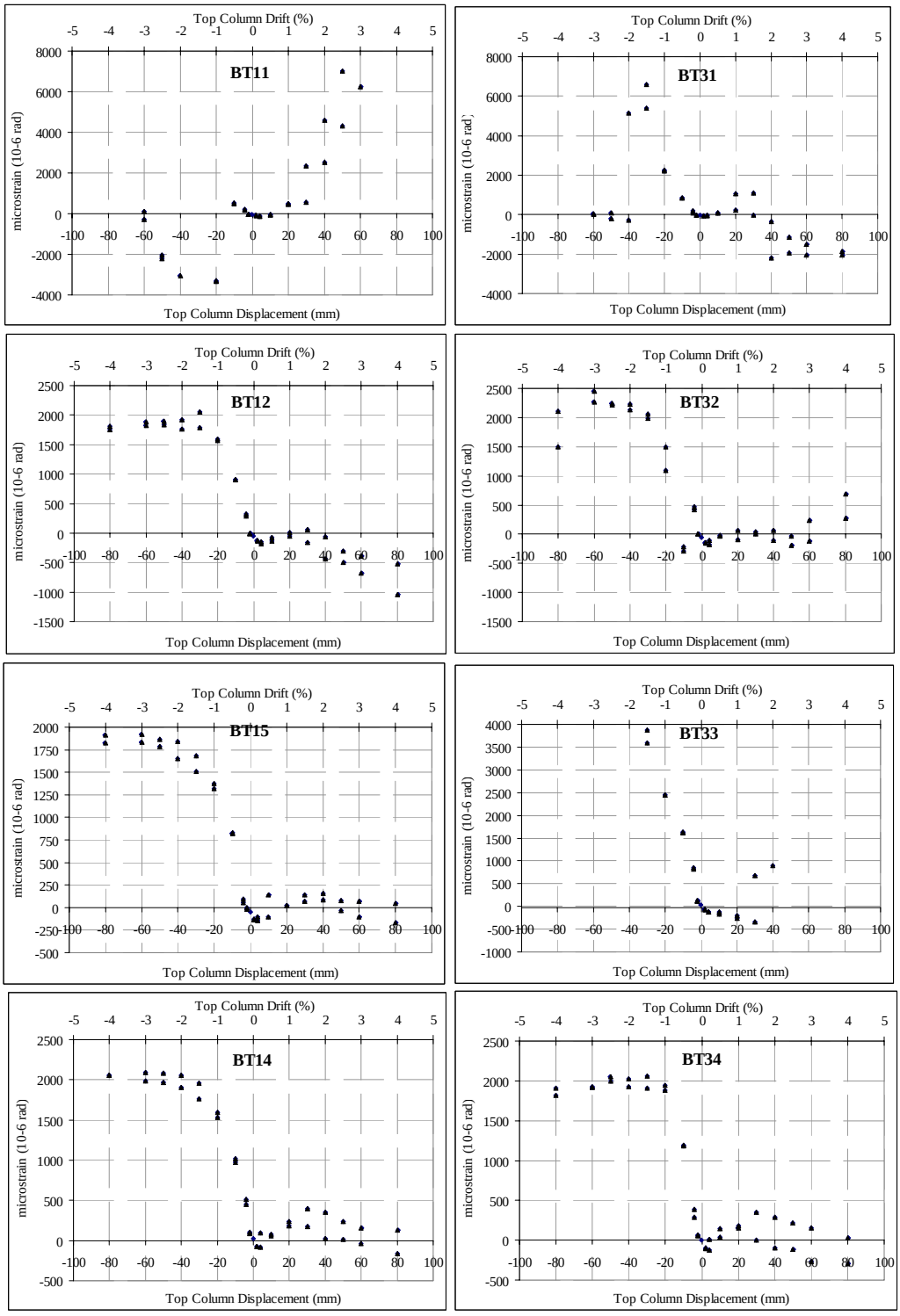

Figure E.20: Test Unit S-R3: Beam longitudinal bars strain gage readings: Top bars (BT13 was damaged).

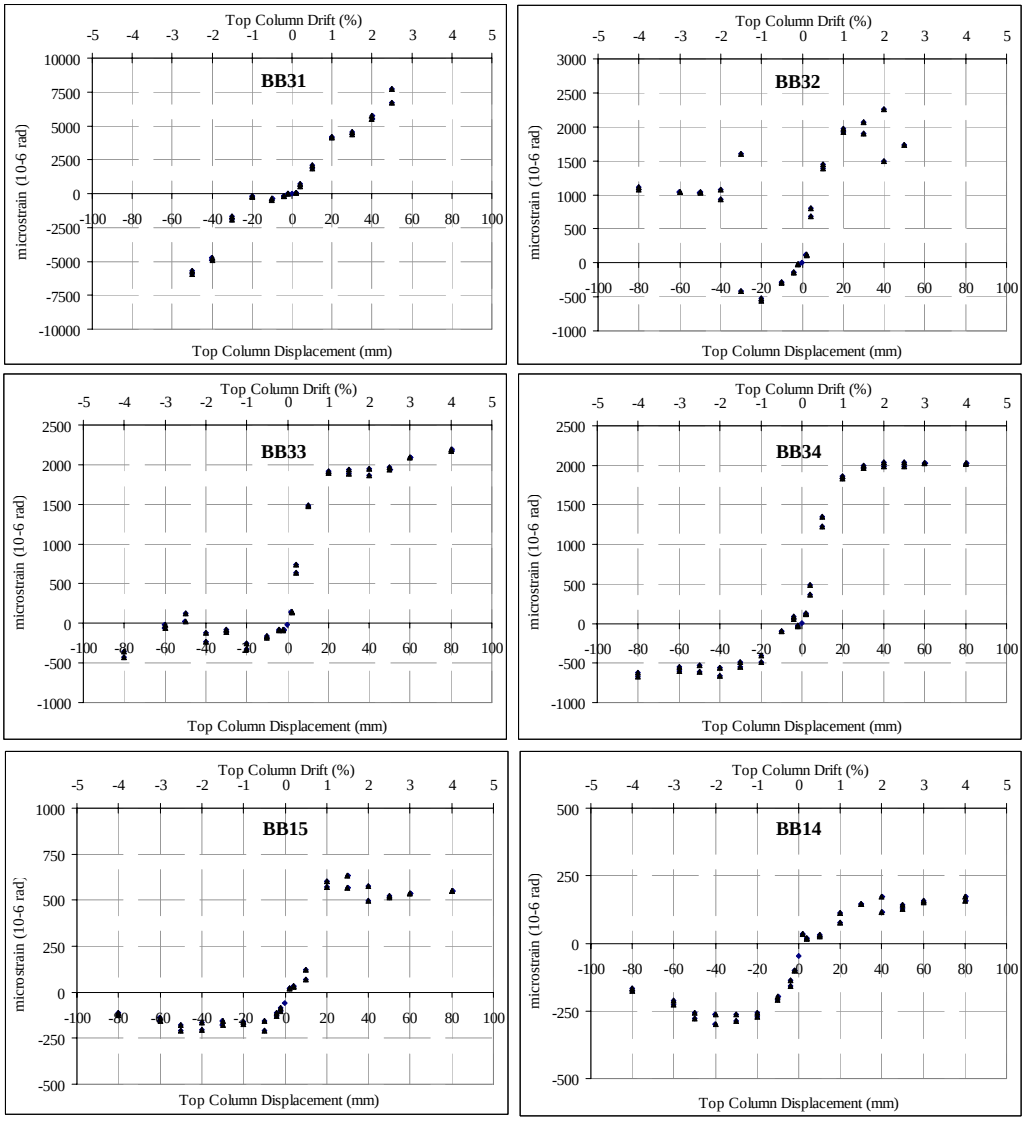

Figure E.21: Test Unit S-R3: Beam longitudinal bars strain gage readings: Bottom bars (BB11, BB12 and BB13 were damaged).

E.2.5 Stirrups (column and beam) strain gage readings

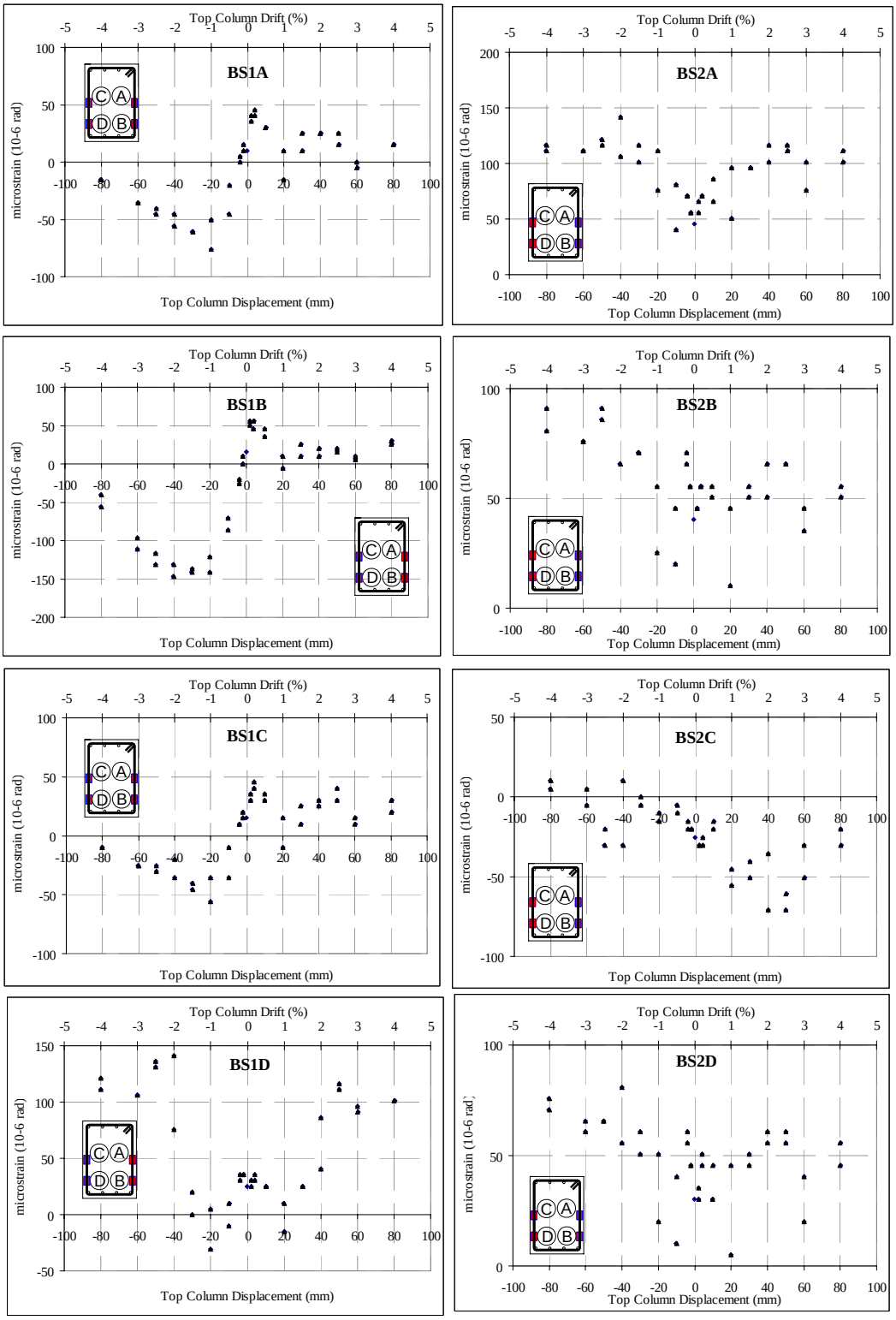

Figure E.22: Test Unit S-R3: Beam stirrups bars strain gage readings.

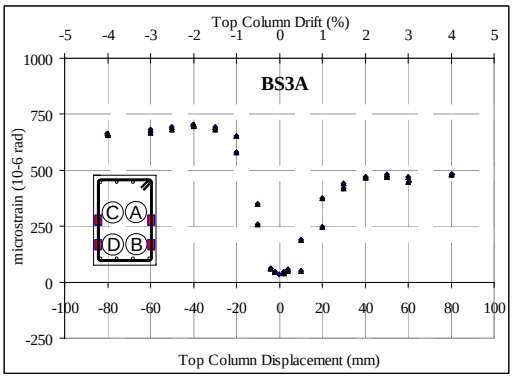

Figure E.23: Test Unit S-R3: Beam stirrups bars strain gage readings (BS3C was damaged).

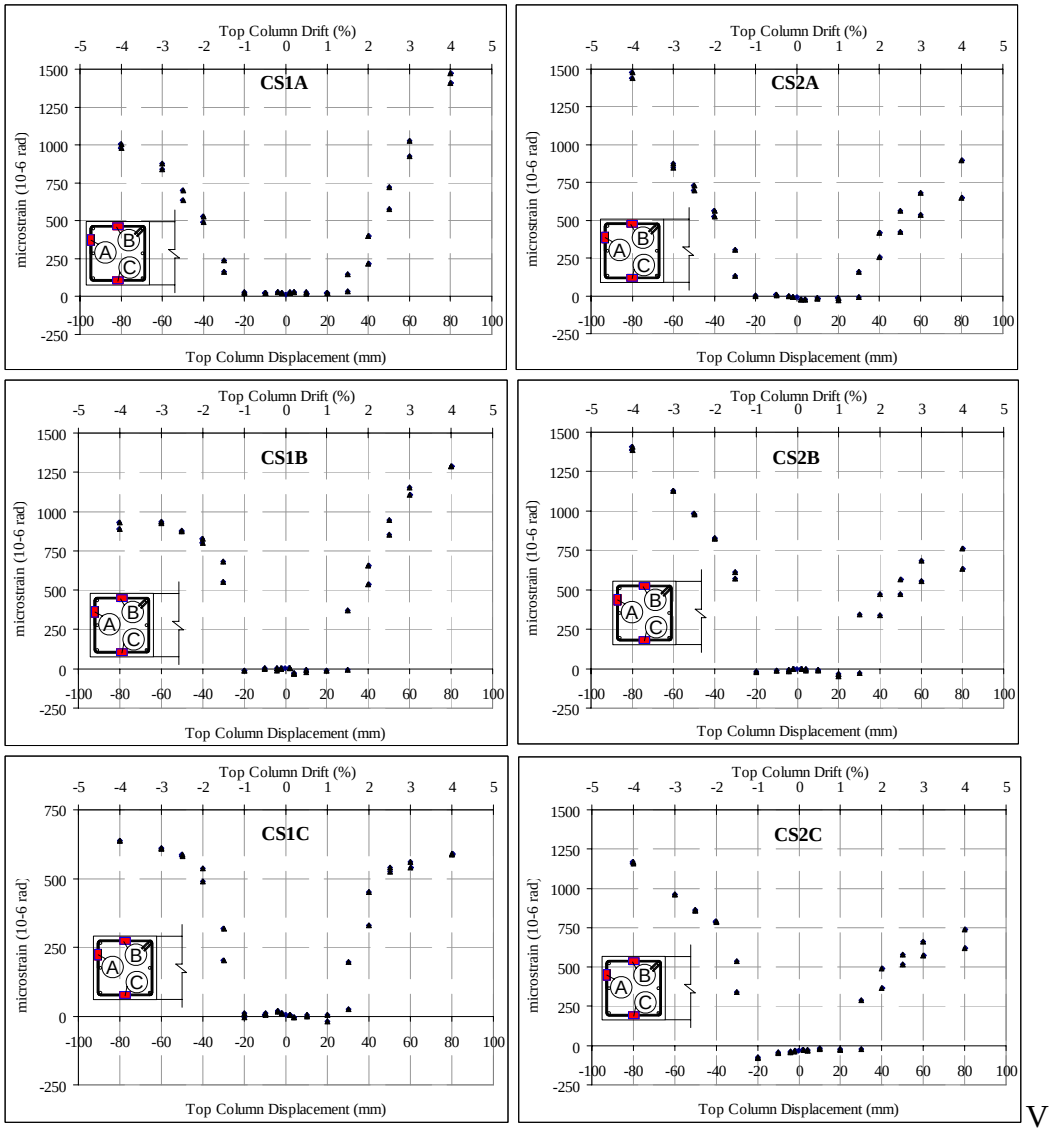

Figure E.24: Test Unit S-R3: Column stirrups bars strain gage readings.

APPENDIX F. EXPERIMENTAL TEST DATA AND LOG FOR SL-O1 & SL-R3

F.1 SL-O1 – AS-BUILT B-C JOINT WITH SLAB

F.1.1 Force-displacement

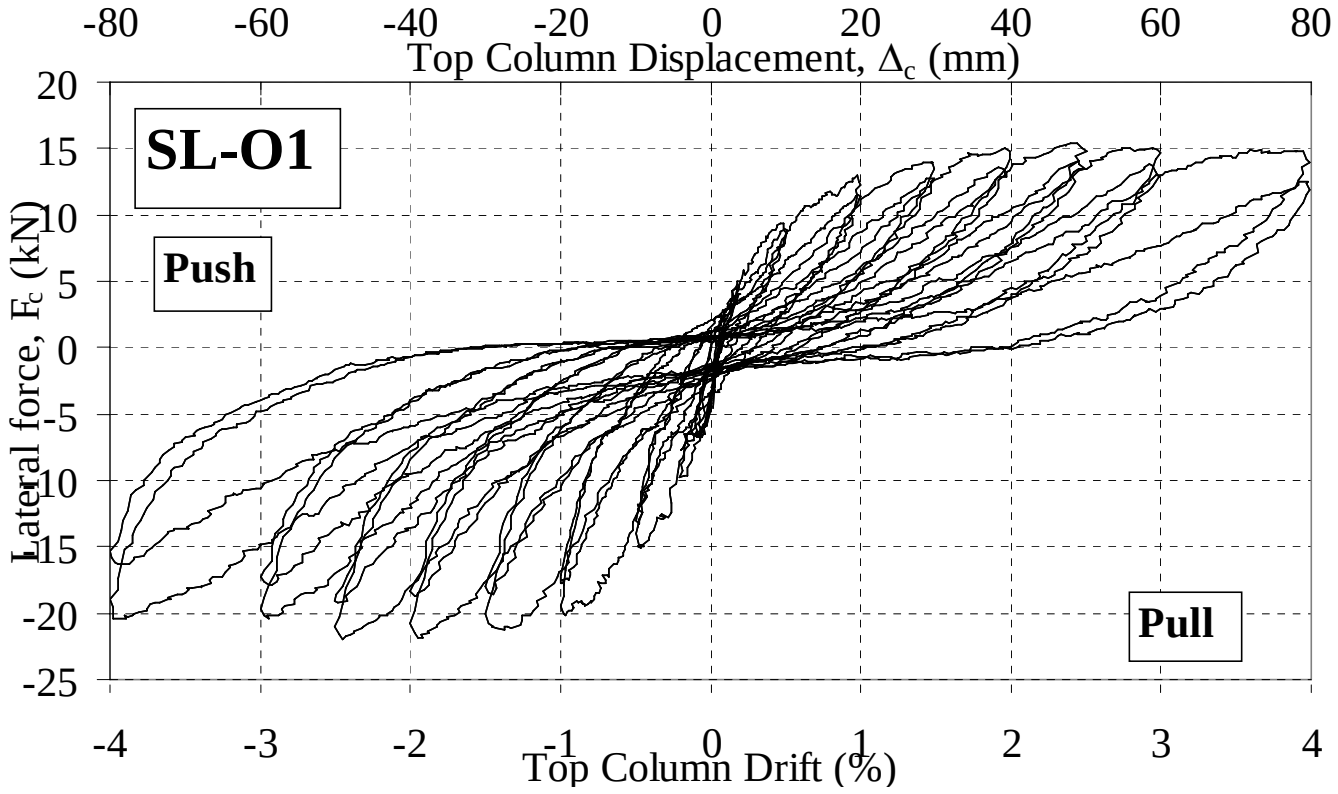

Figure F.1: Test Unit SL-O1: Top column lateral force-displacement hysteresis plot.

F.1.2 Photographic observations

Figure F.2 General observation photographs for SL-O1 at: Gravity loading, start of test and ±0.2% drifts.

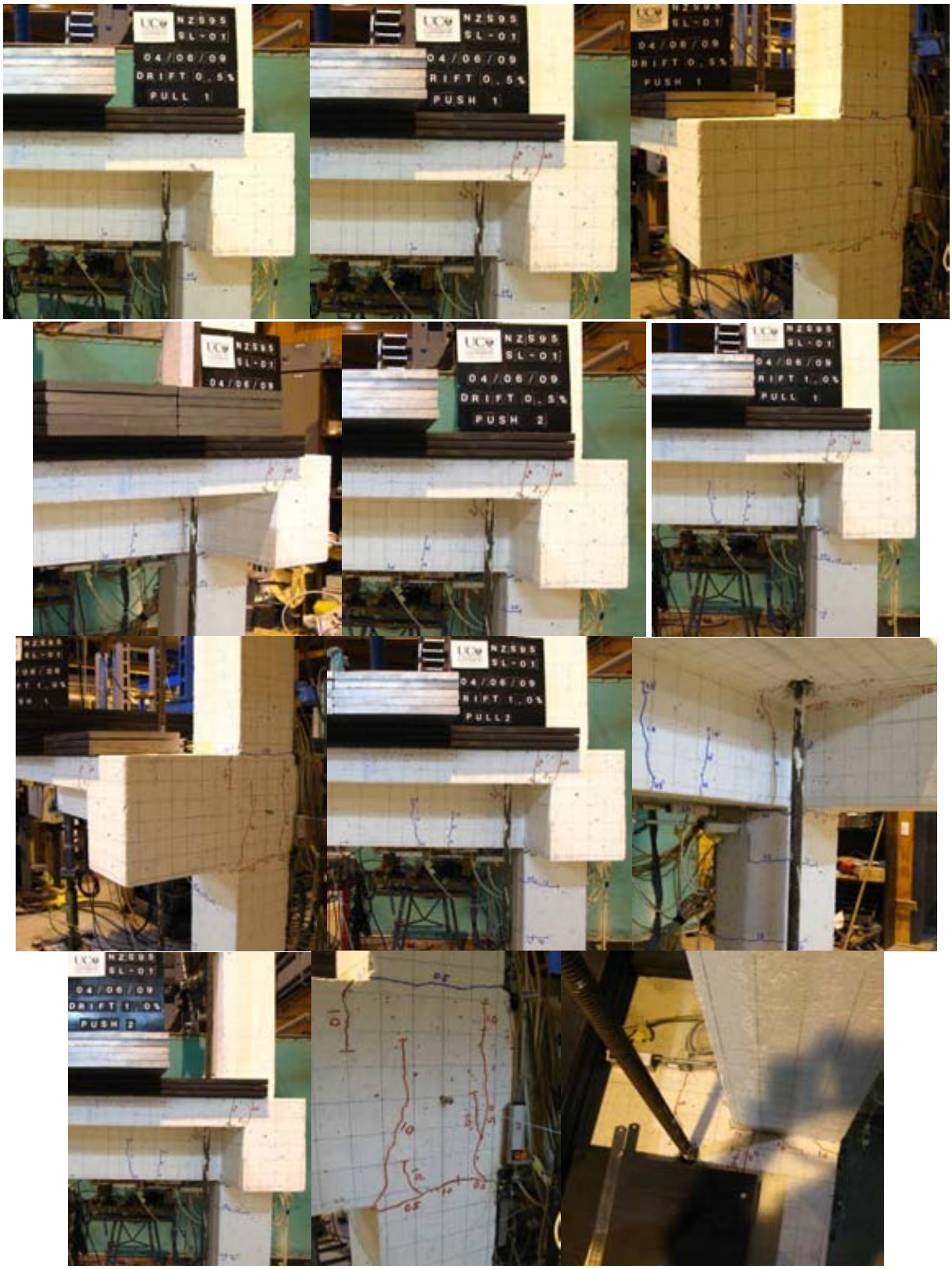

Figure F.3 General observation photographs for test unit SL-O1 at: ±0.5% and ±1.0% drifts.

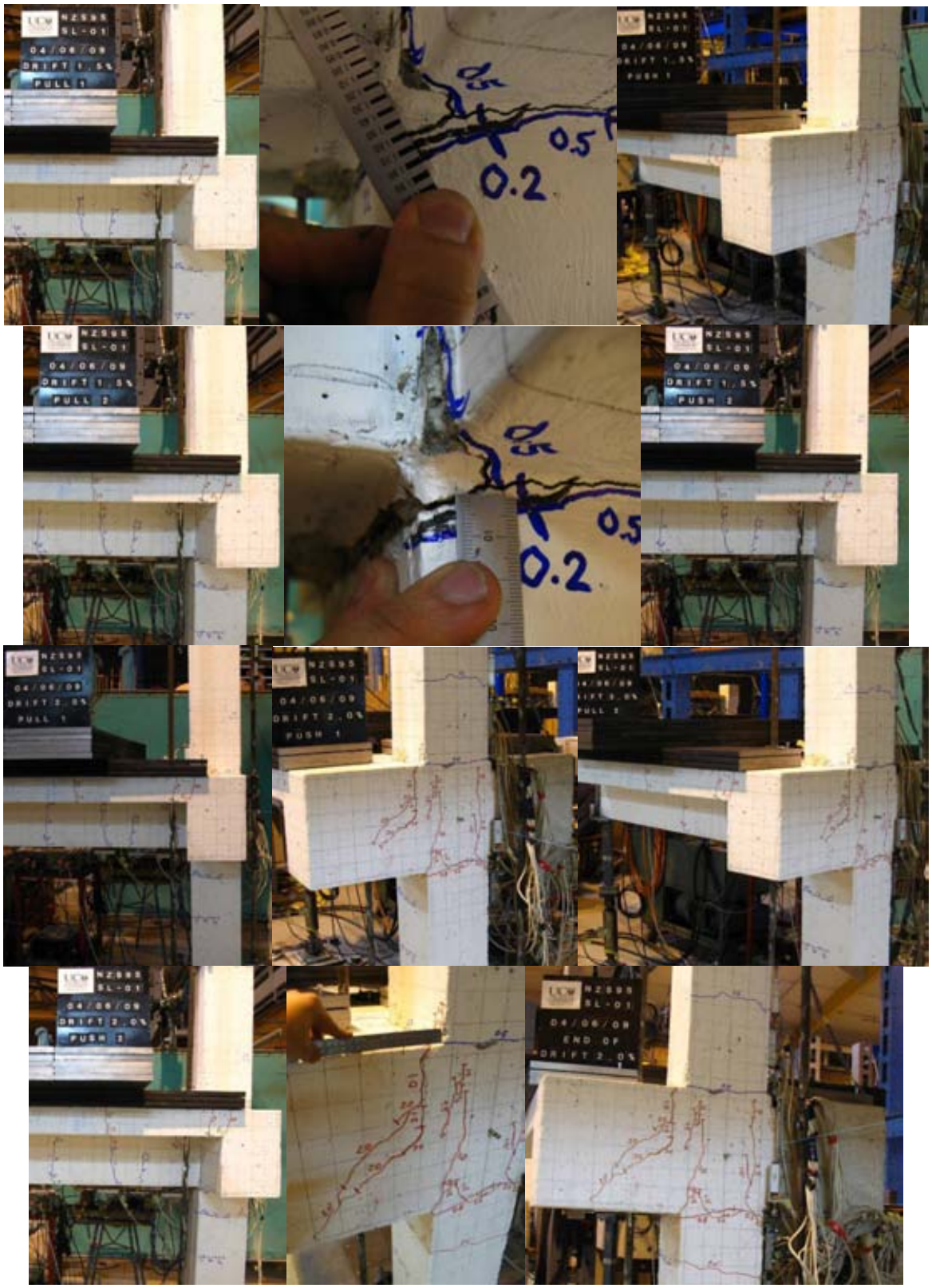

Figure F.4 General observation photographs for test unit SL-O1 at: ±1.5% and ±2.0% drifts.

Figure F.5 General observation photographs for test unit SL-O1 at: ±2.5% and ±3.0% drifts.

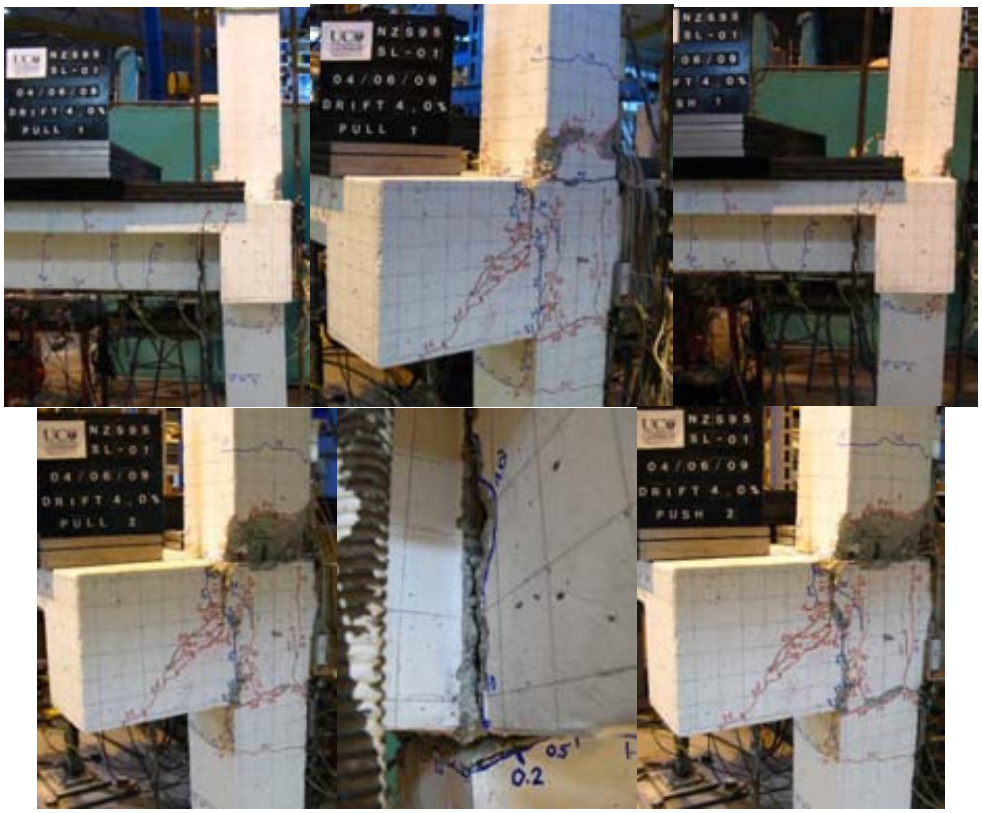

Figure F.6 General observation photographs for test unit SL-O1 at: ±4.0% drift.

Figure F.7 General observation photographs for test unit SL-O1 at: ±6.0% drift and the end-of-test forensic inspection.

F.1.3 Column strain gage readings

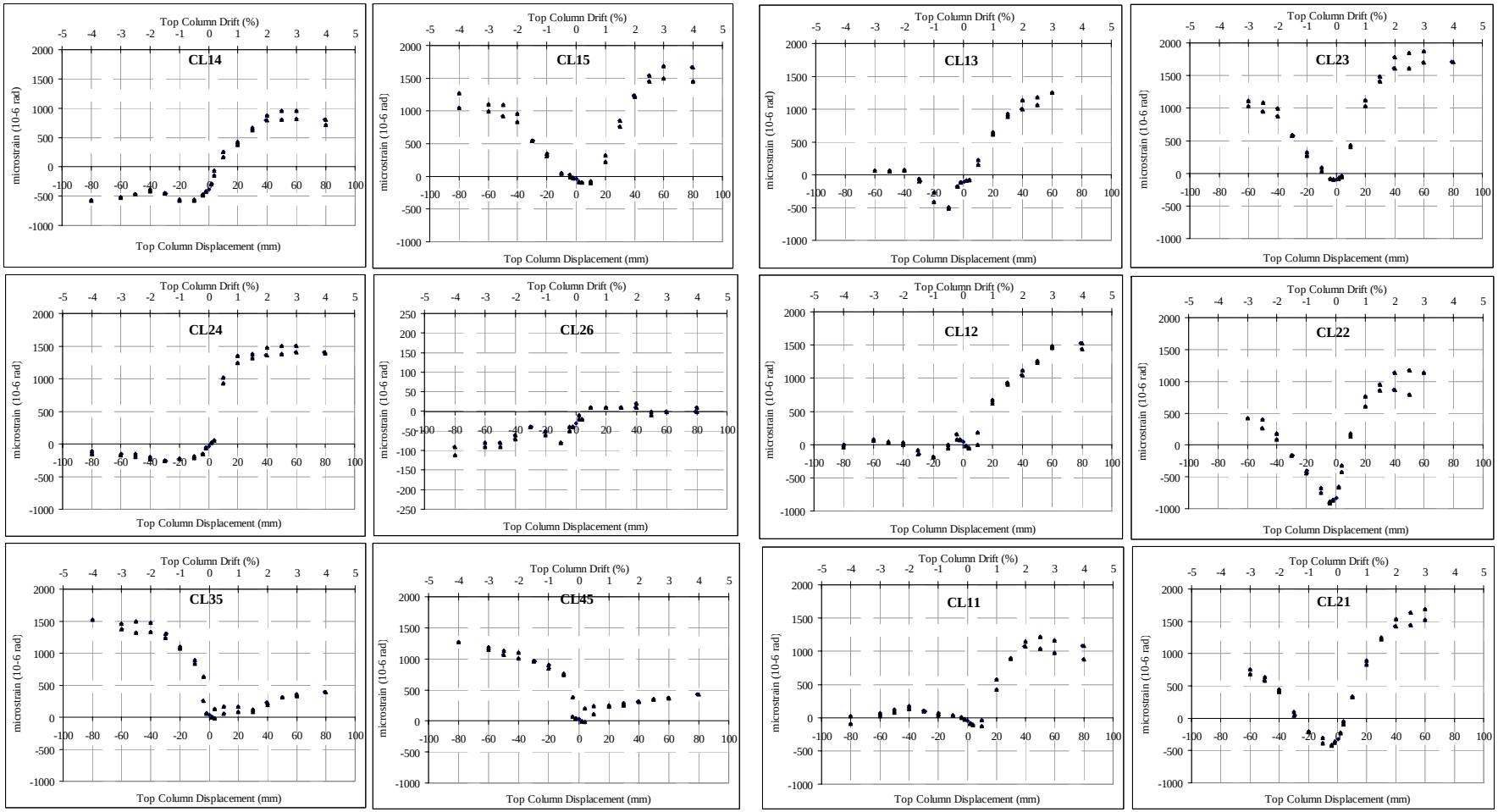

Figure F.8: Test Unit SL-O1: Column longitudinal bars strain gage readings : LEFT: Top half; RIGHT: Bottom half. .

F.1.4 Beam strain gage readings

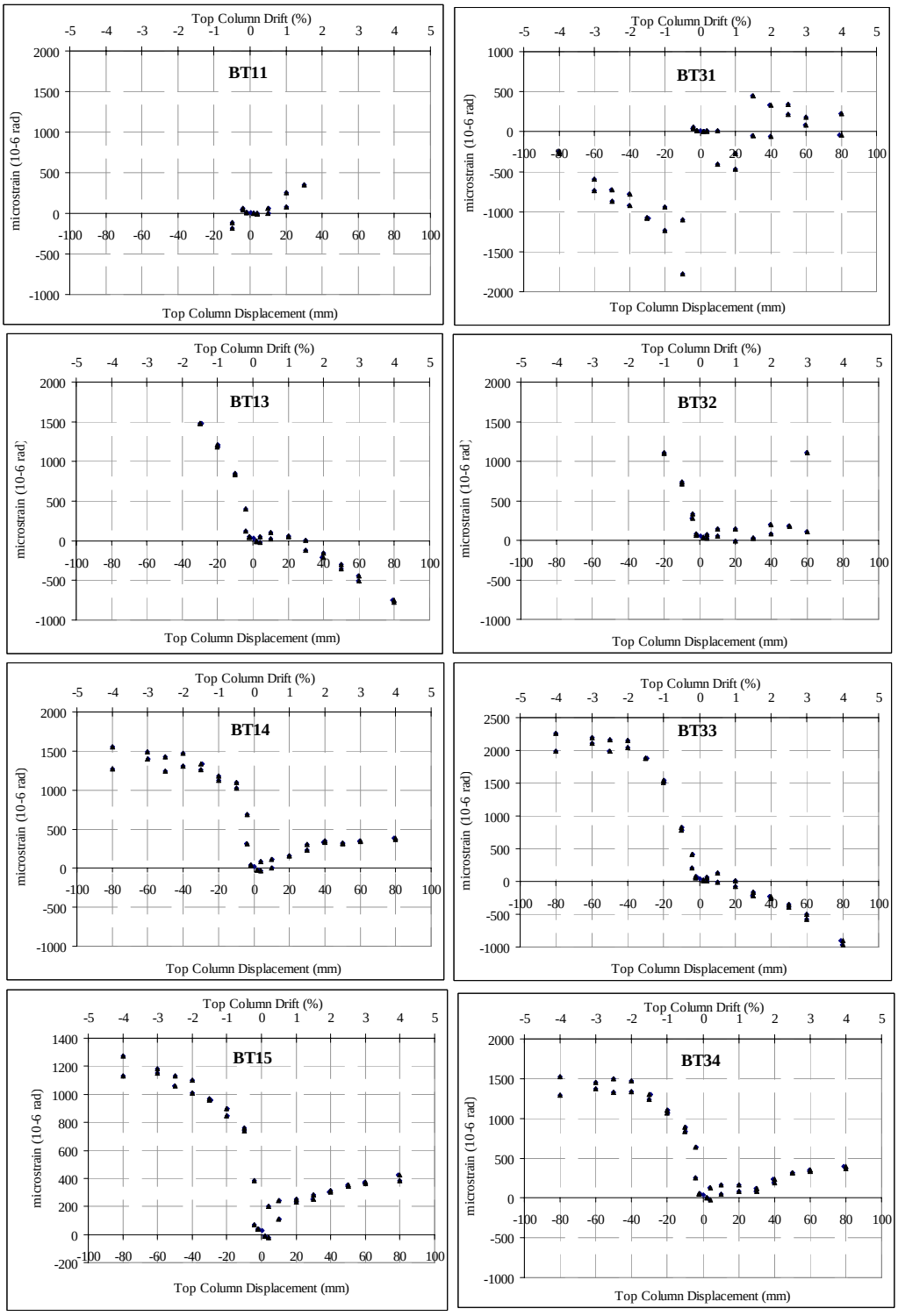

Figure F.9: Test Unit SL-O1: Beam longitudinal bars strain gage readings : Top bars (BT12 was damaged).

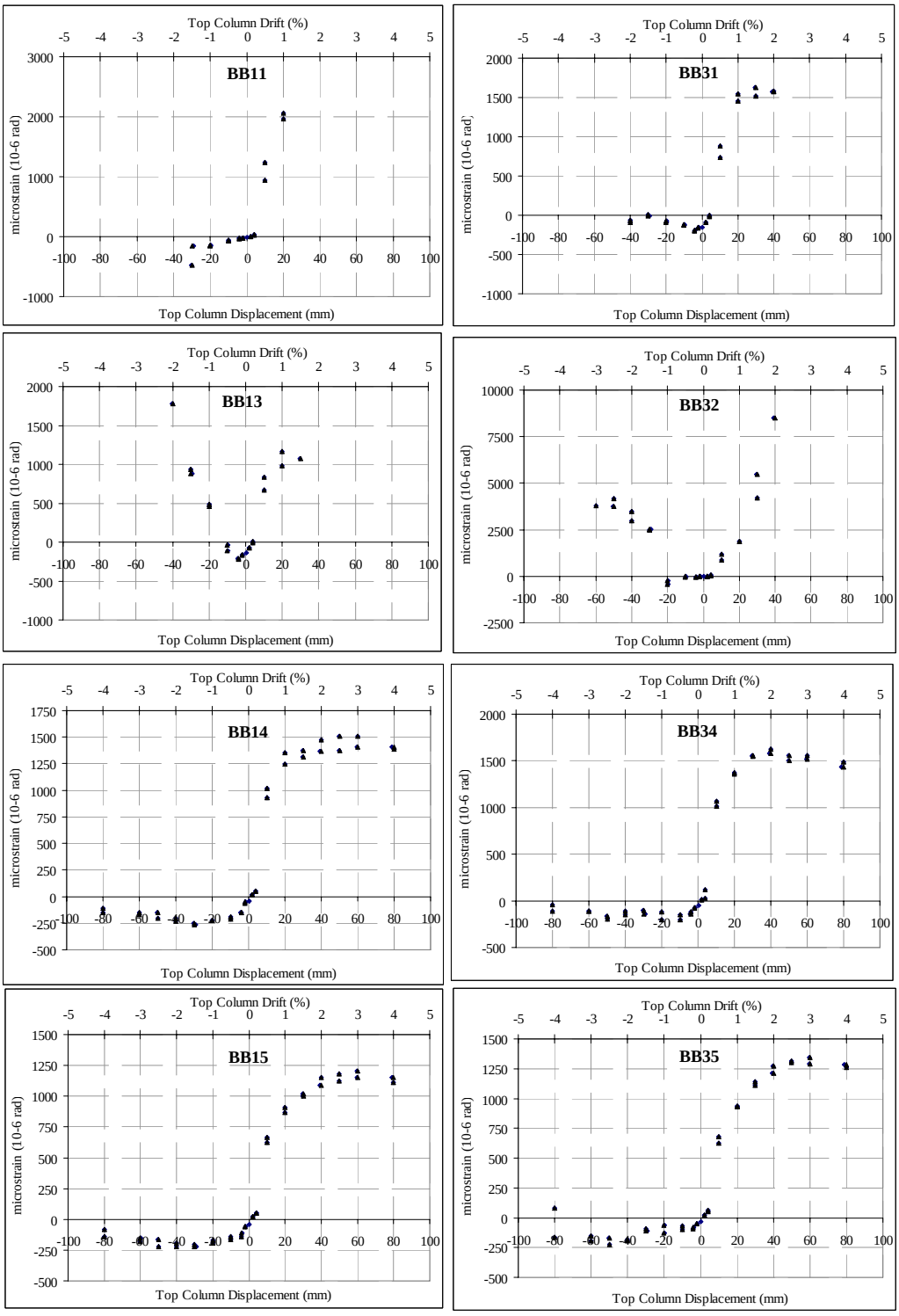

Figure F.10: Test Unit SL-O1: Beam longitudinal bars strain gage readings : Bottom bars (BB12 and BB33 were damaged).

F.1.5 Stirrups (column and beam) strain gage readings

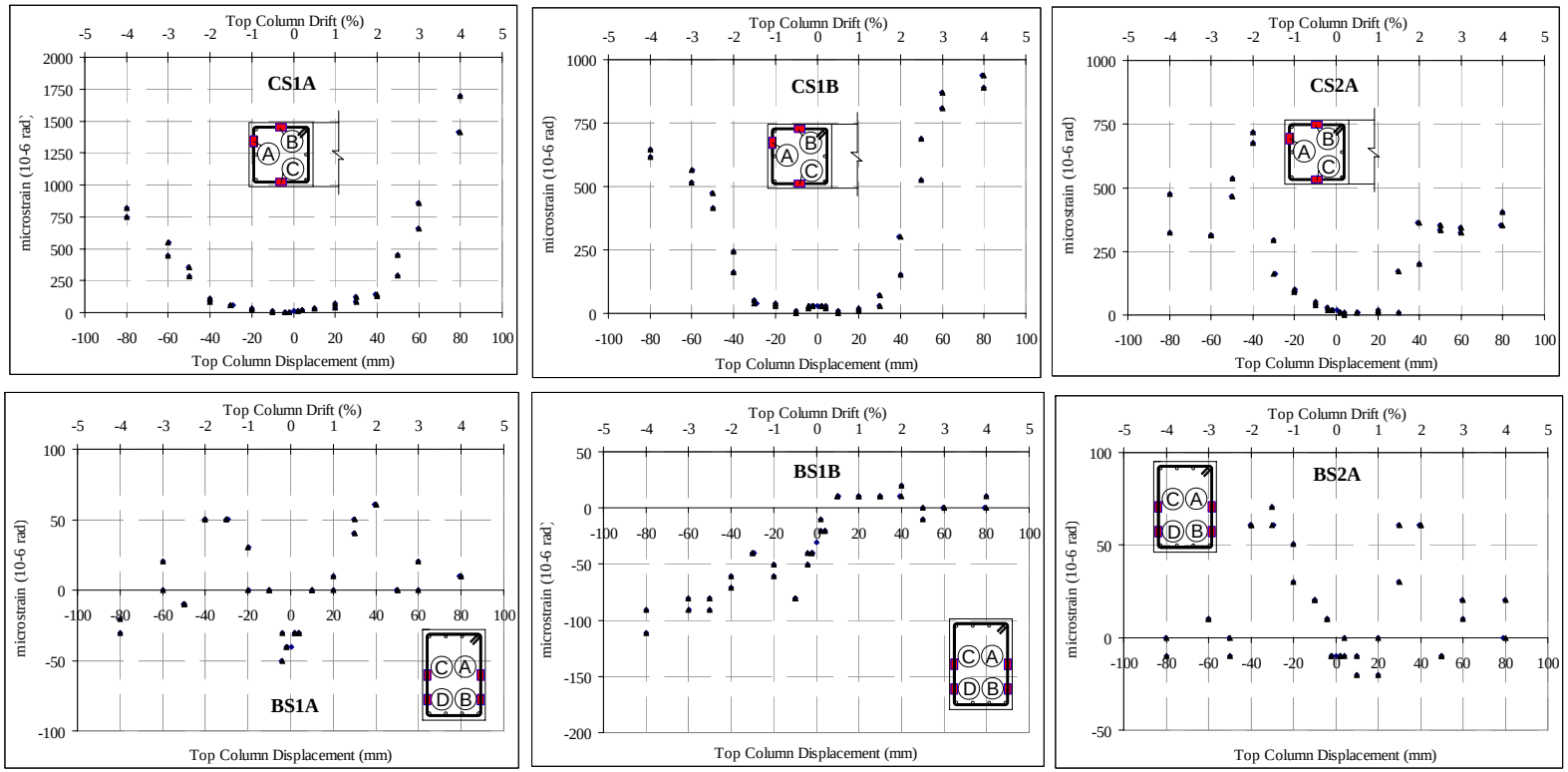

Figure F.11: Test Unit SL-O1: Column and beam stirrups bars strain gage readings.

F.1.6 Slab mesh reinforcements strain gage readings

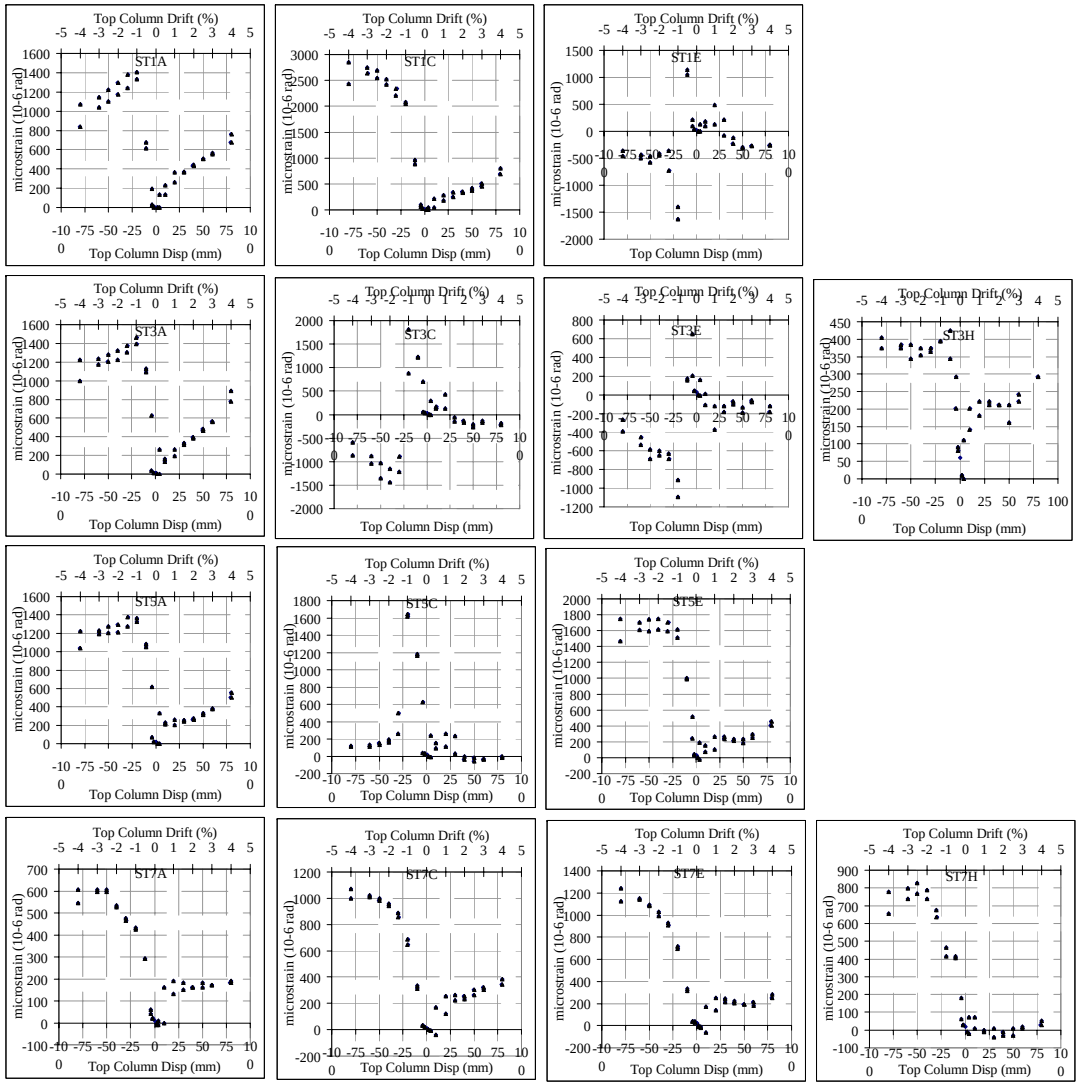

Figure F.12: Test Unit SL-O1: Slab top mesh parallel to loading direction strain gage readings.

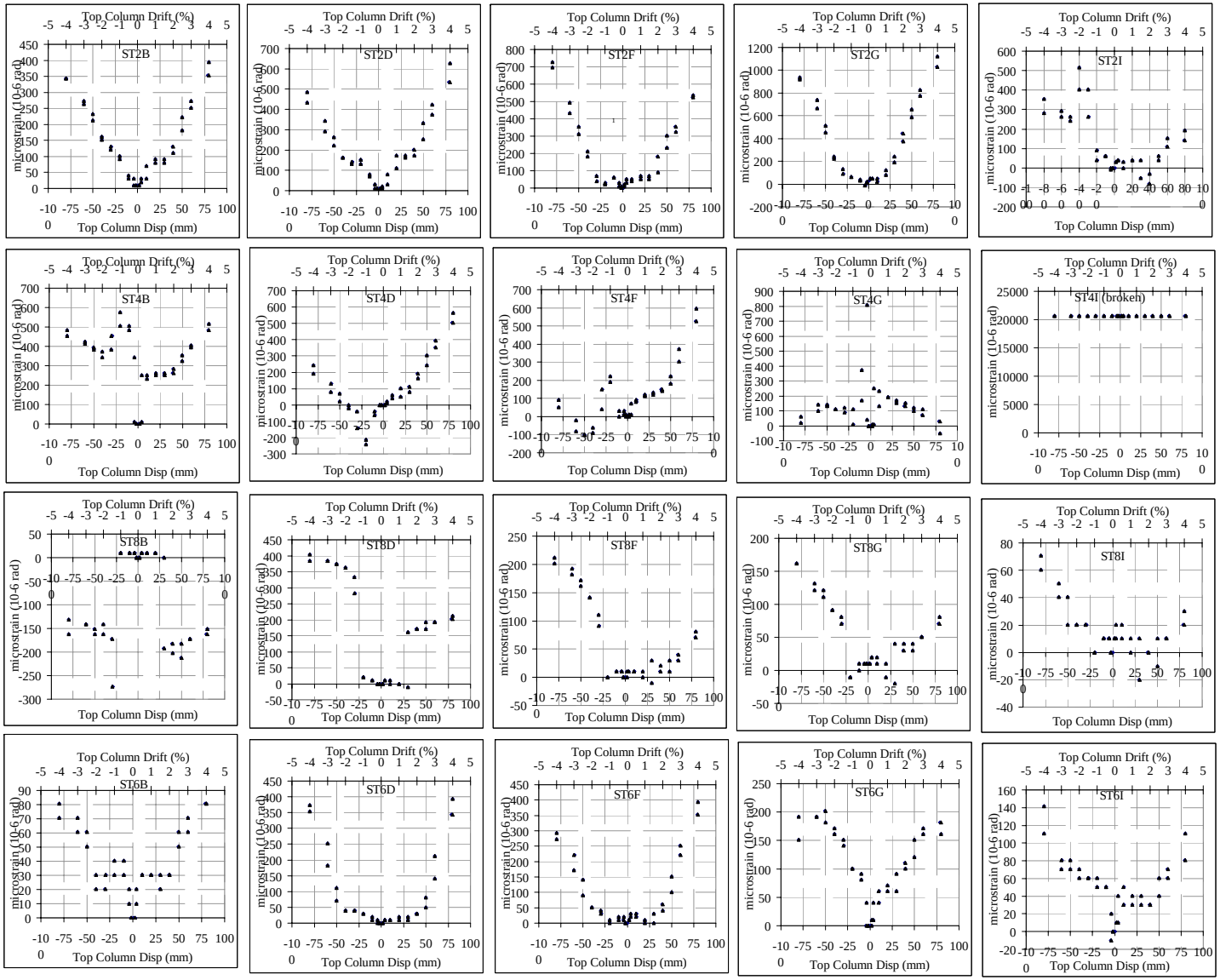

Figure F.13: Test Unit SL-O1: Slab top mesh perpendicular to loading direction strain gage readings.

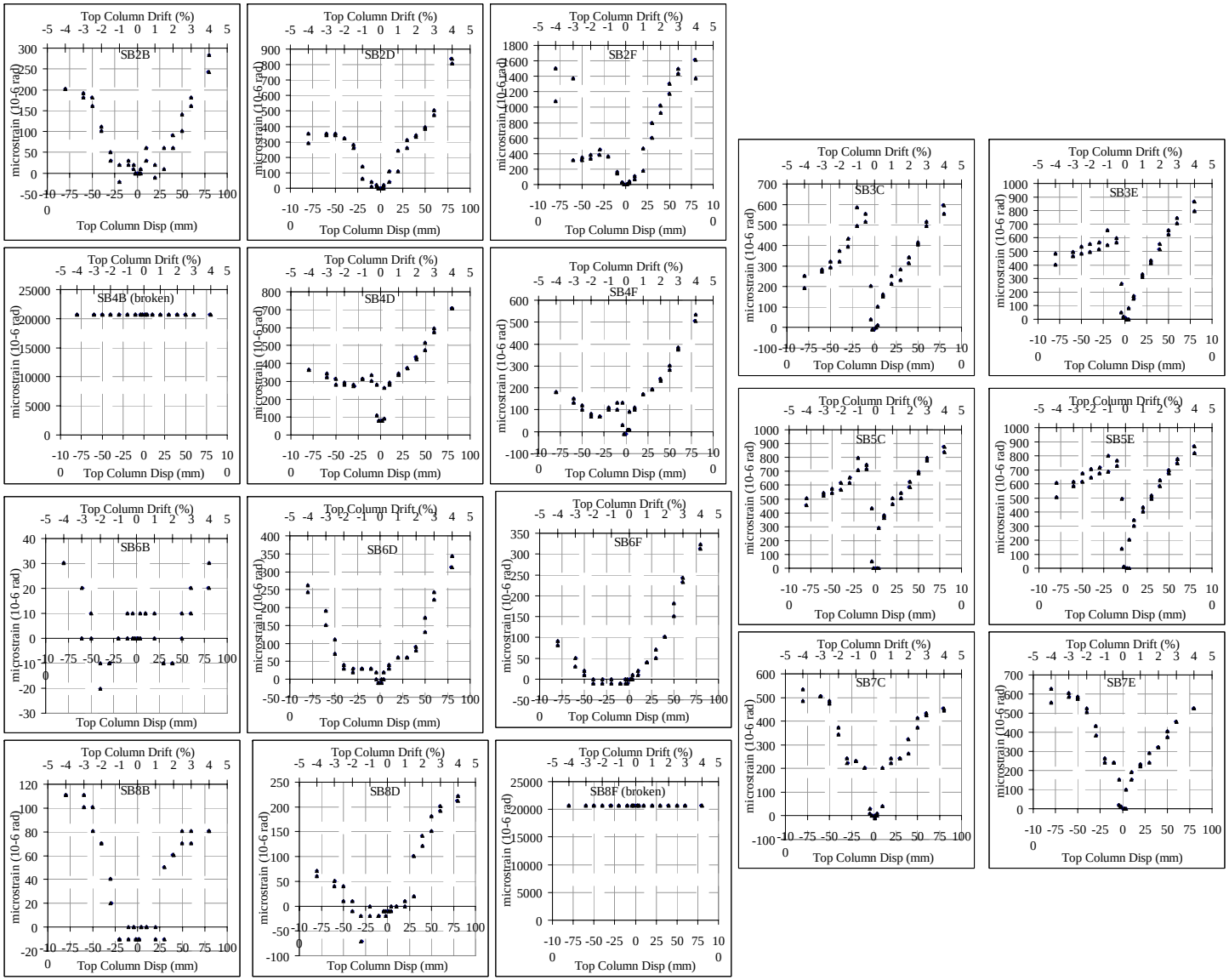

Figure F.14: Test Unit SL-O1: Slab bottom mesh parallel and perpendicular to loading direction strain gage readings.

F.2 SL-R3 –R3 SELECTIVE-WEAKENING RETROFIT JOINT WITH SLAB

F.2.1 Force-displacement

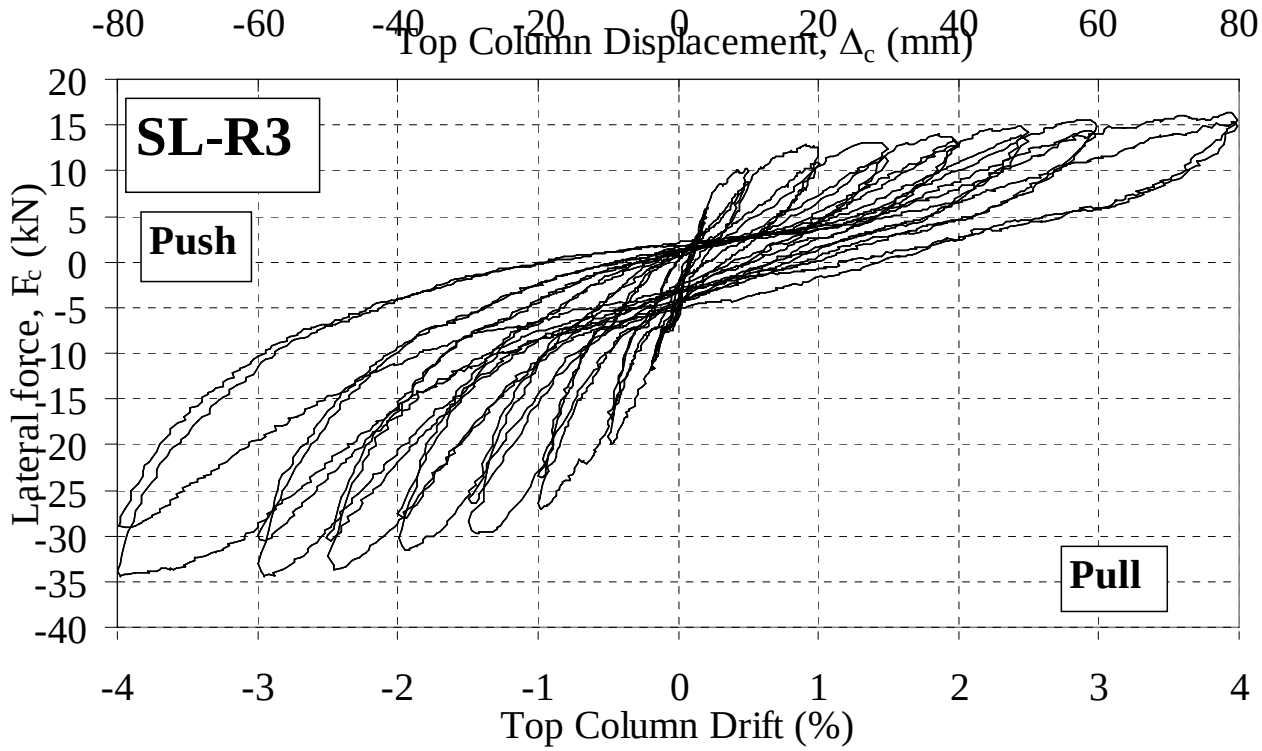

Figure F.15: Test unit SL-R3: Top column lateral force-displacement hysteresis plot.

F.2.2 Photographic observations

Figure F.16 General observation photographs for test unit SL-R3 at: Retrofitting, gravity loading, start of test, ±0.1% and ±0.2% drifts.

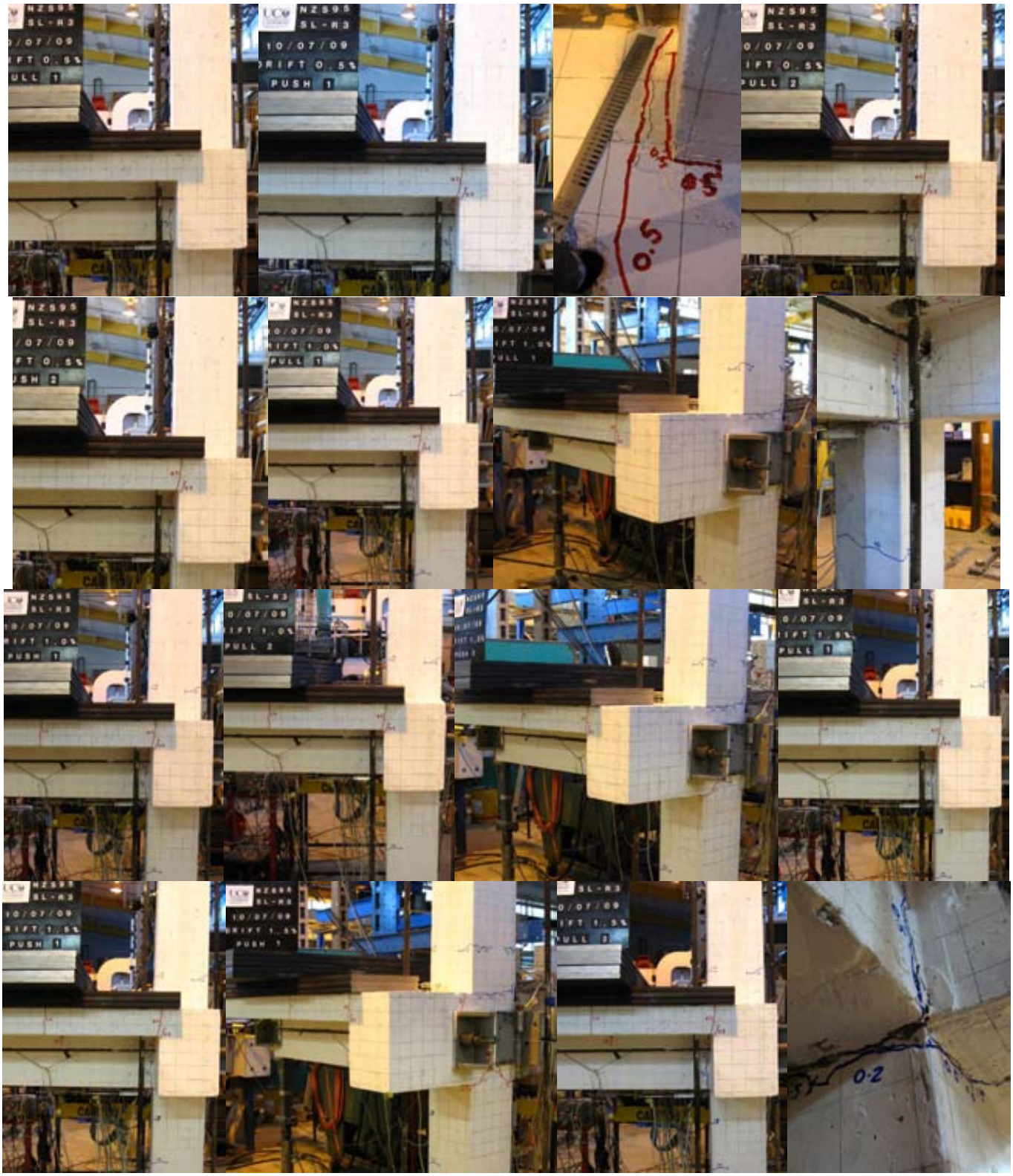

Figure F.17 General observation photographs for test unit SL-R3 at: ±0.5%, ±1.0% and ±1.5% drifts.

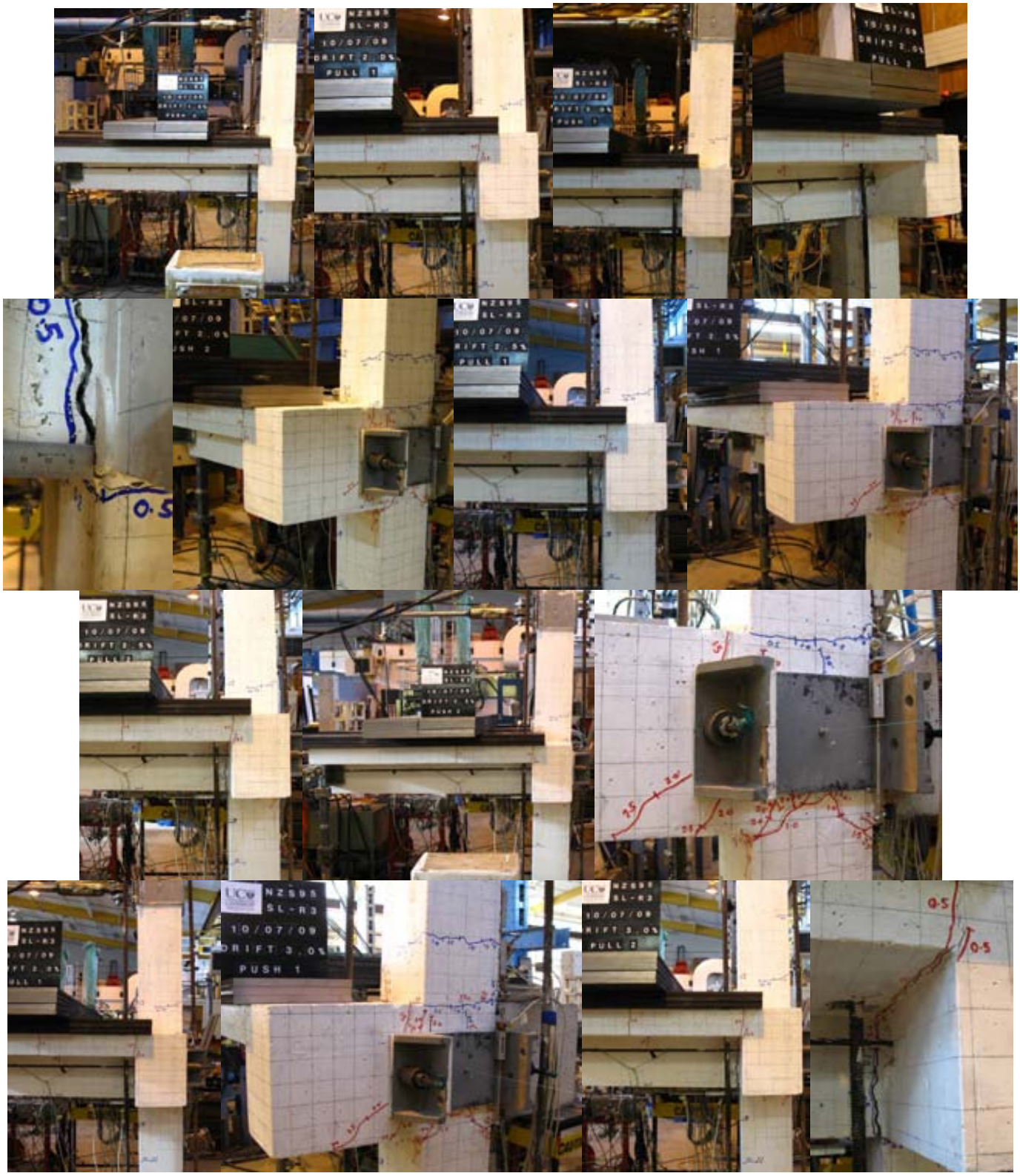

Figure F.18 General observation photographs for test unit SL-R3 at: -1.5%, ±2.0%, ±2.5% and ±3.0% drifts.

Figure F.19 General observation photographs for test unit SL-R3 at: ±3.0%, ±4.0% drifts and the end of test.

F.2.3 Column strain gage readings

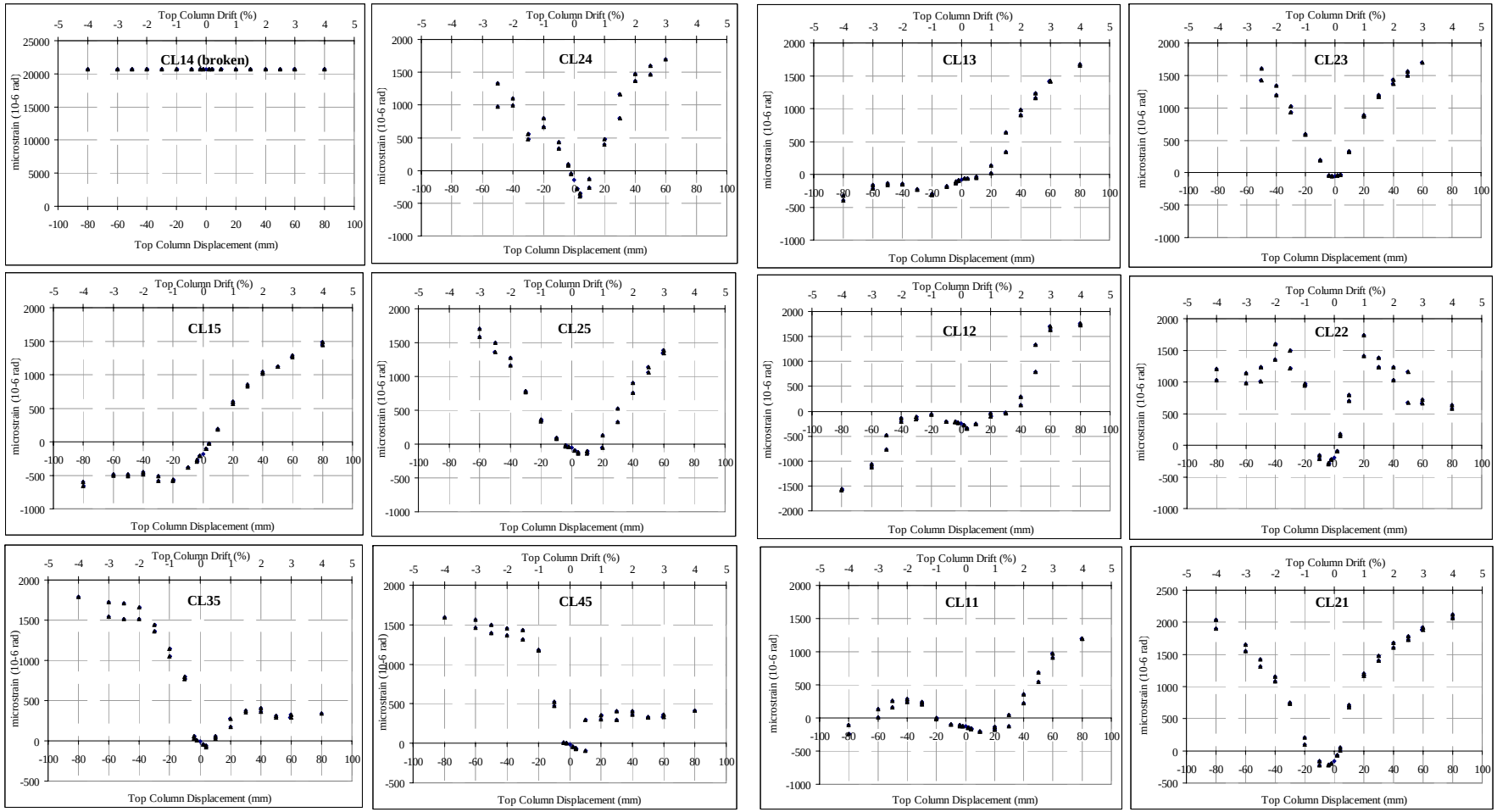

Figure F.20: Test Unit SL-R3: Column longitudinal bars strain gage readings : LEFT: Top half; RIGHT: Bottom half. .

F.2.4 Beam strain gage readings

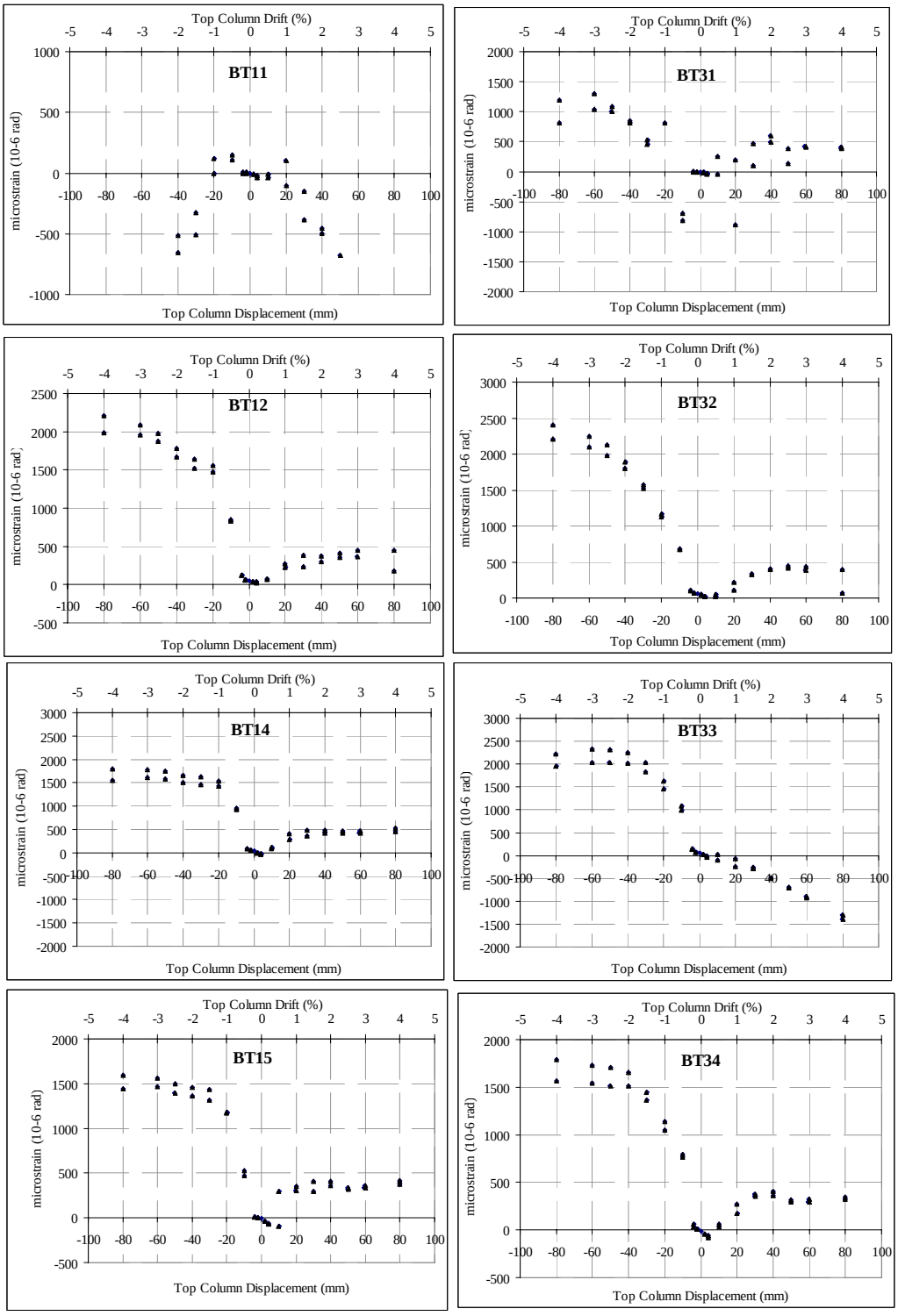

Figure F.21: Test Unit SL-R3: Beam longitudinal bars strain gage readings : Top bars (BT13 was damaged).

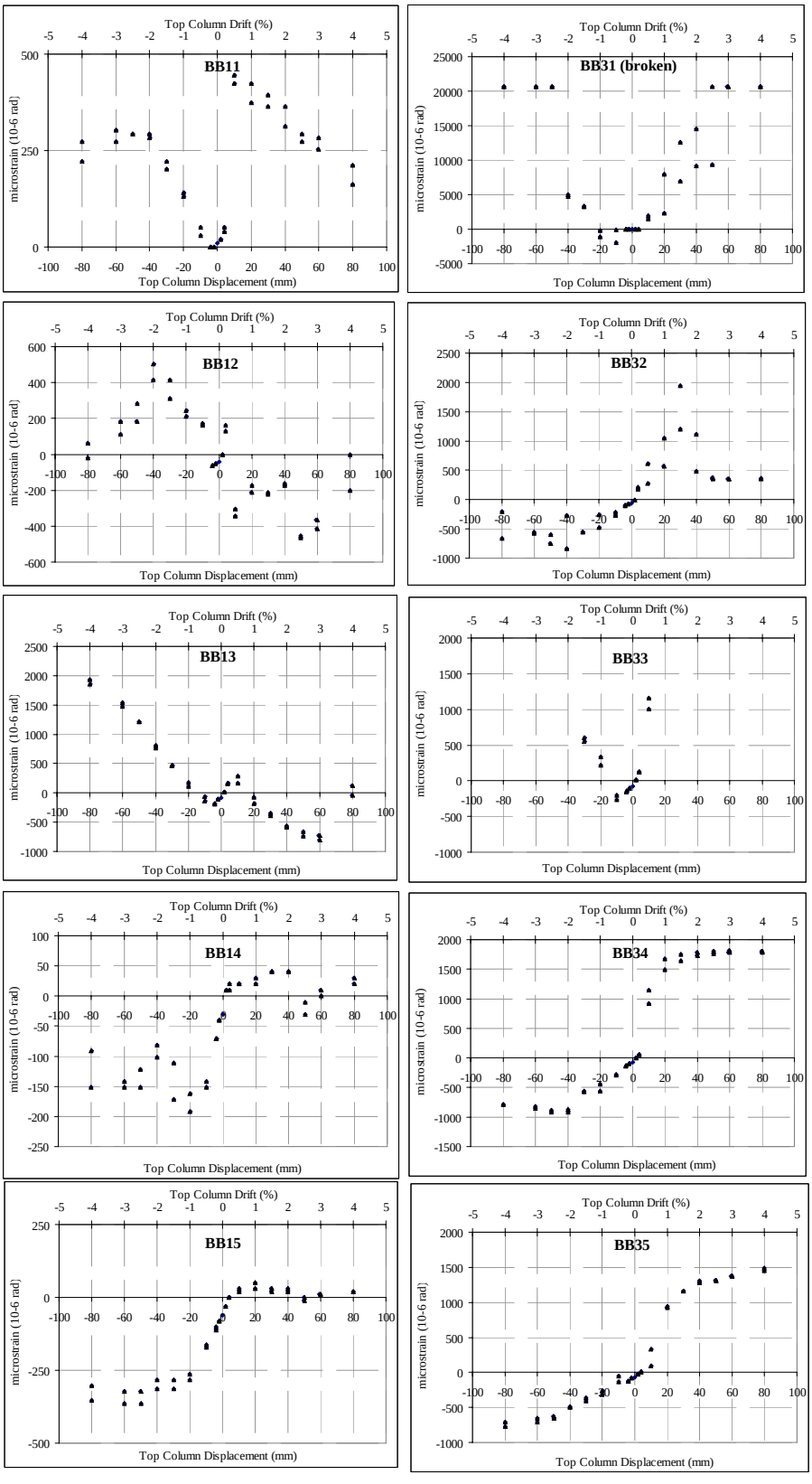

Figure F.22: Test Unit SL-R3: Beam longitudinal bars strain gage readings.

F.2.5 Stirrups (column and beam) strain gage readings

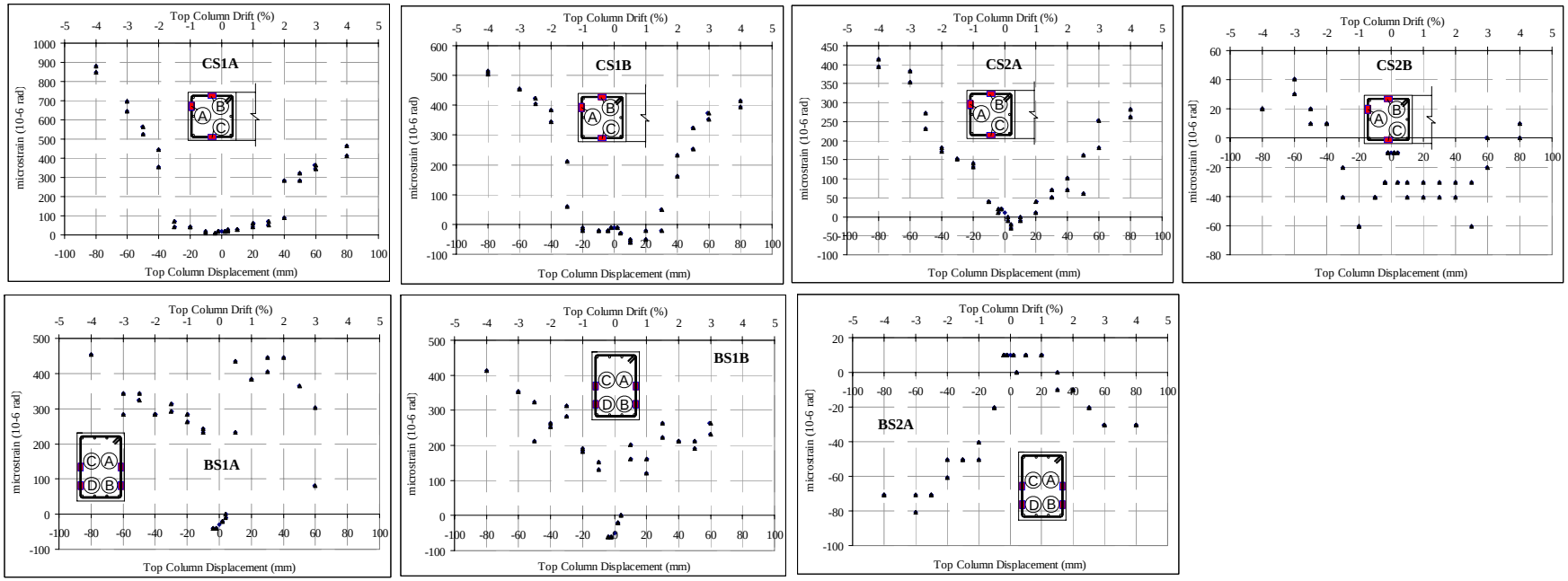

Figure F.23: Test Unit SL-R3: Column and beam stirrups bars strain gage readings.

F.2.6 Slab mesh reinforcements strain gage readings

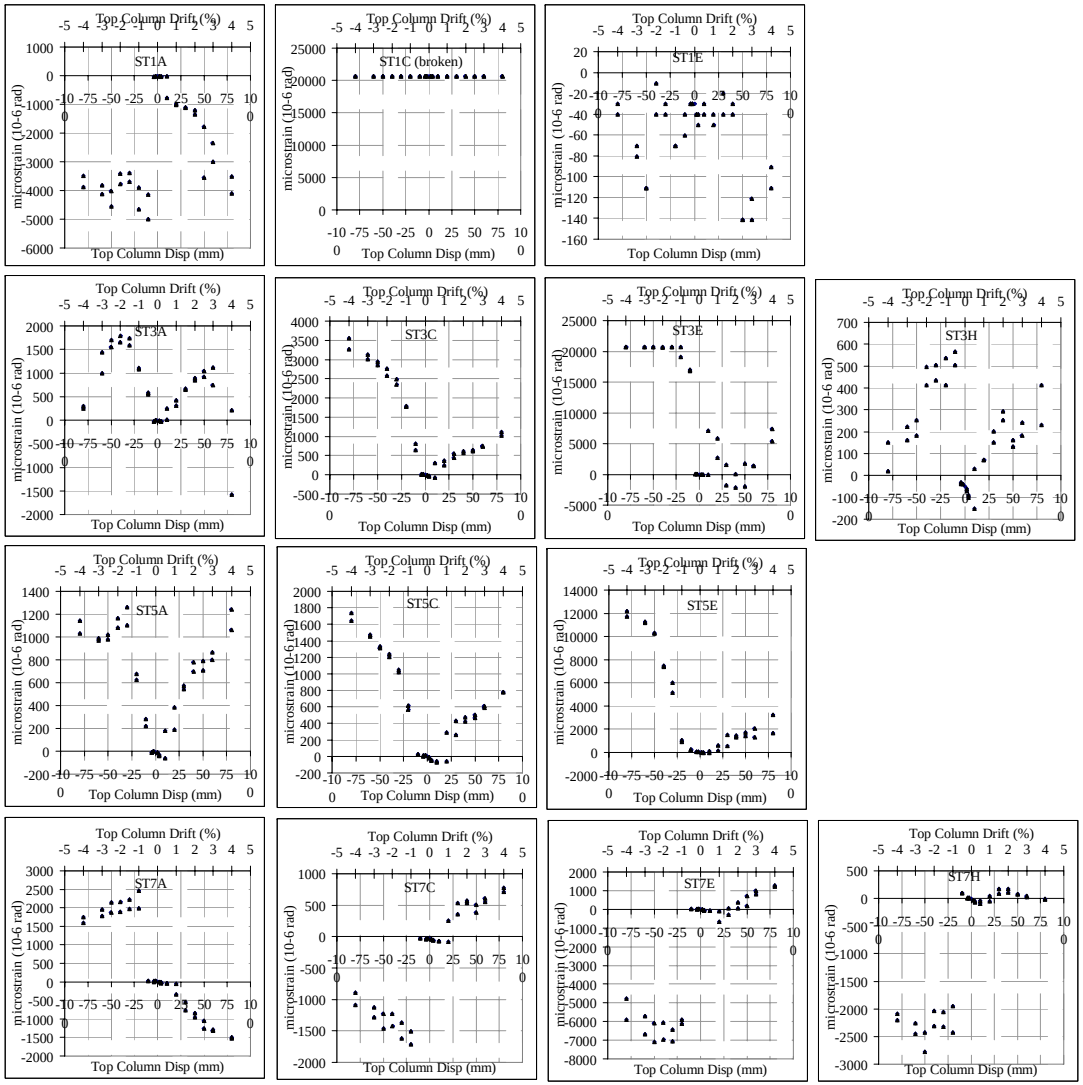

Figure F.24: Test Unit SL-R3: Slab top mesh parallel to loading direction strain gage readings.

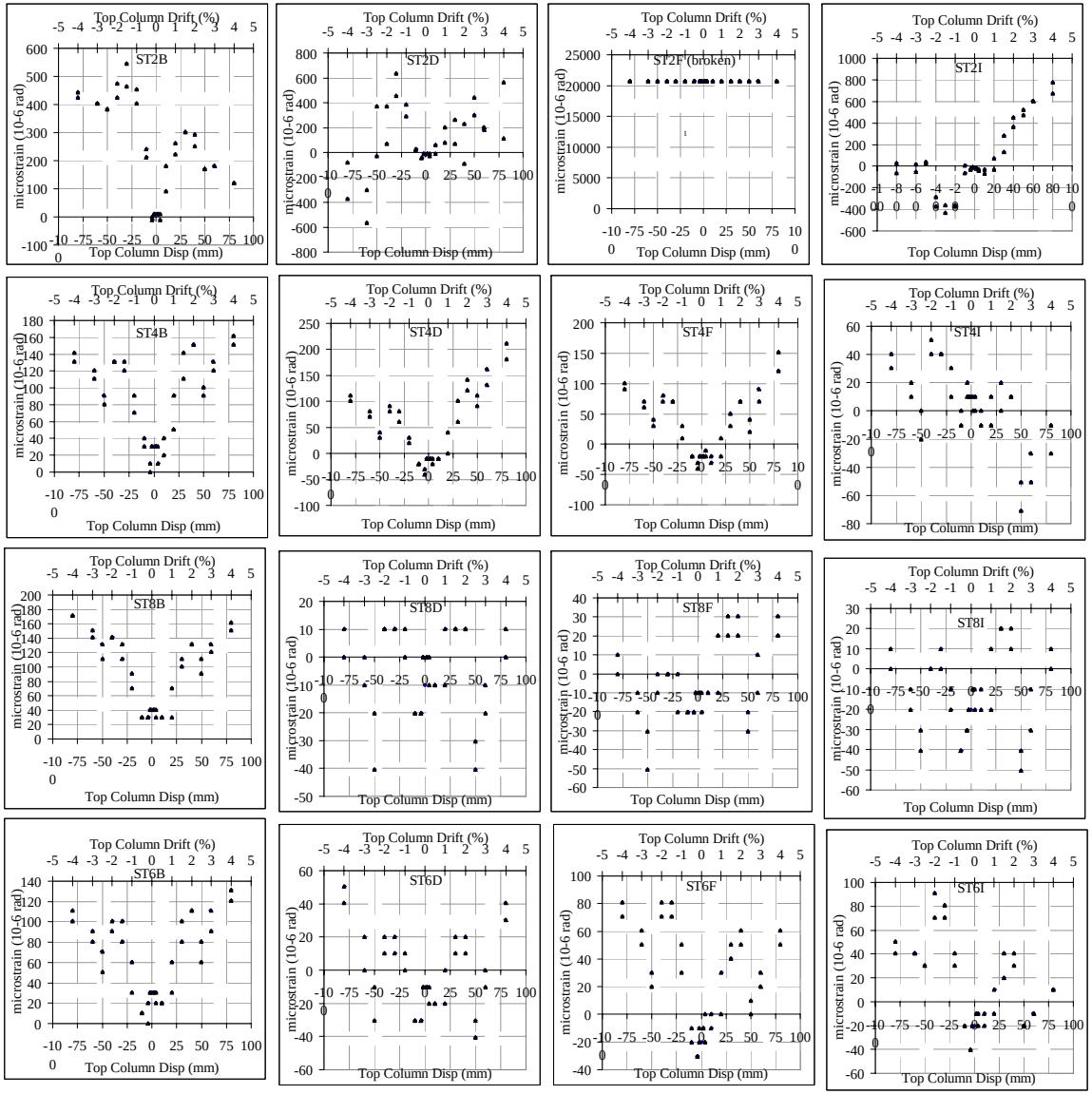

Figure F.25: Test Unit SL-R3: Slab top mesh perpendicular to loading direction strain gage readings.

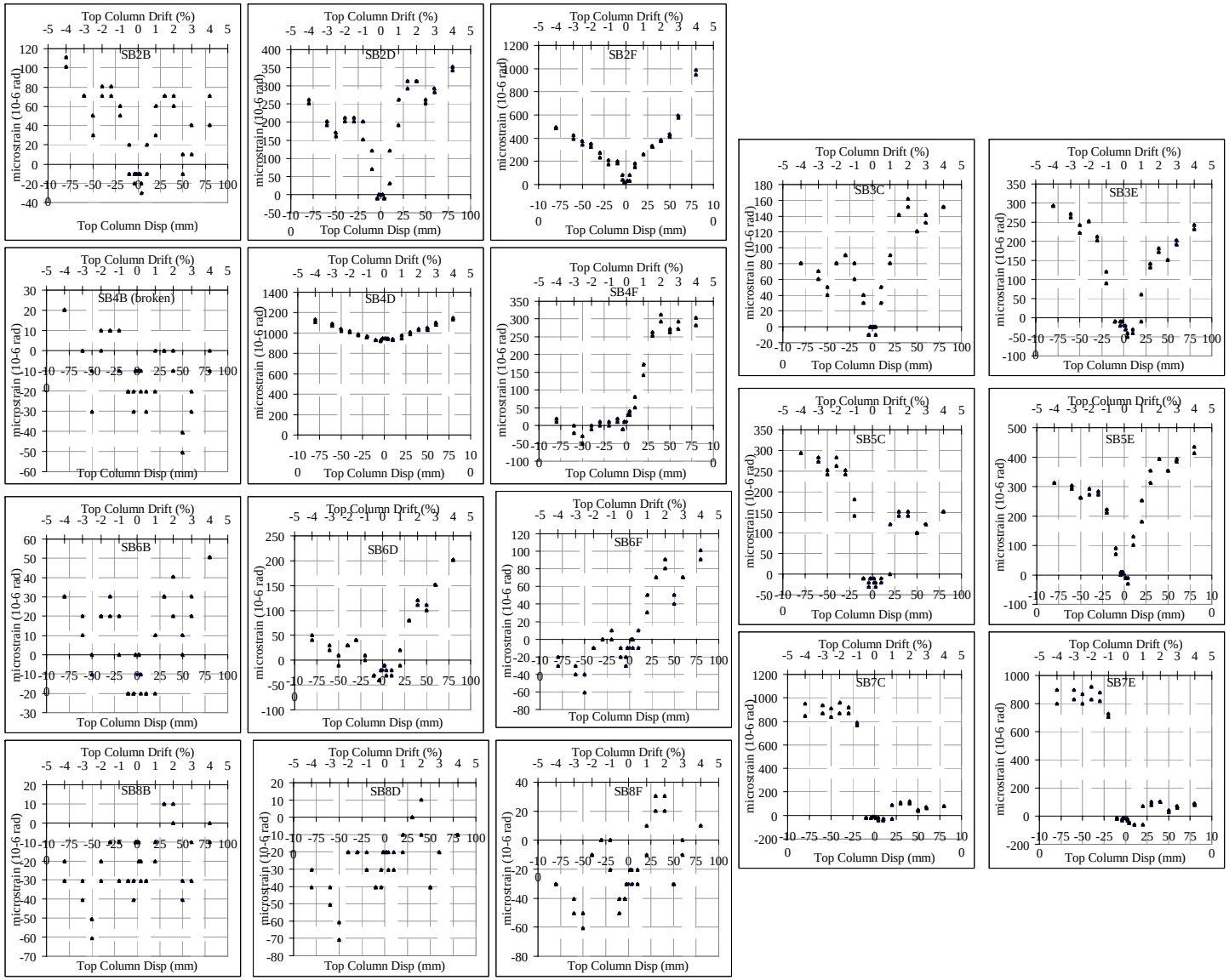

Figure F.26: Test Unit SL-R3: Slab bottom mesh parallel and perpendicular to loading direction strain gage readings.

APPENDIX G. SUPPLEMENTARY DATA TO CHAPTER 9 NUMERICAL ANALYSES

G.1 NON-LINEAR TIME-HISTORY ANALYSES INPUT DATA

G.1.1 Ground motions response spectra and time history

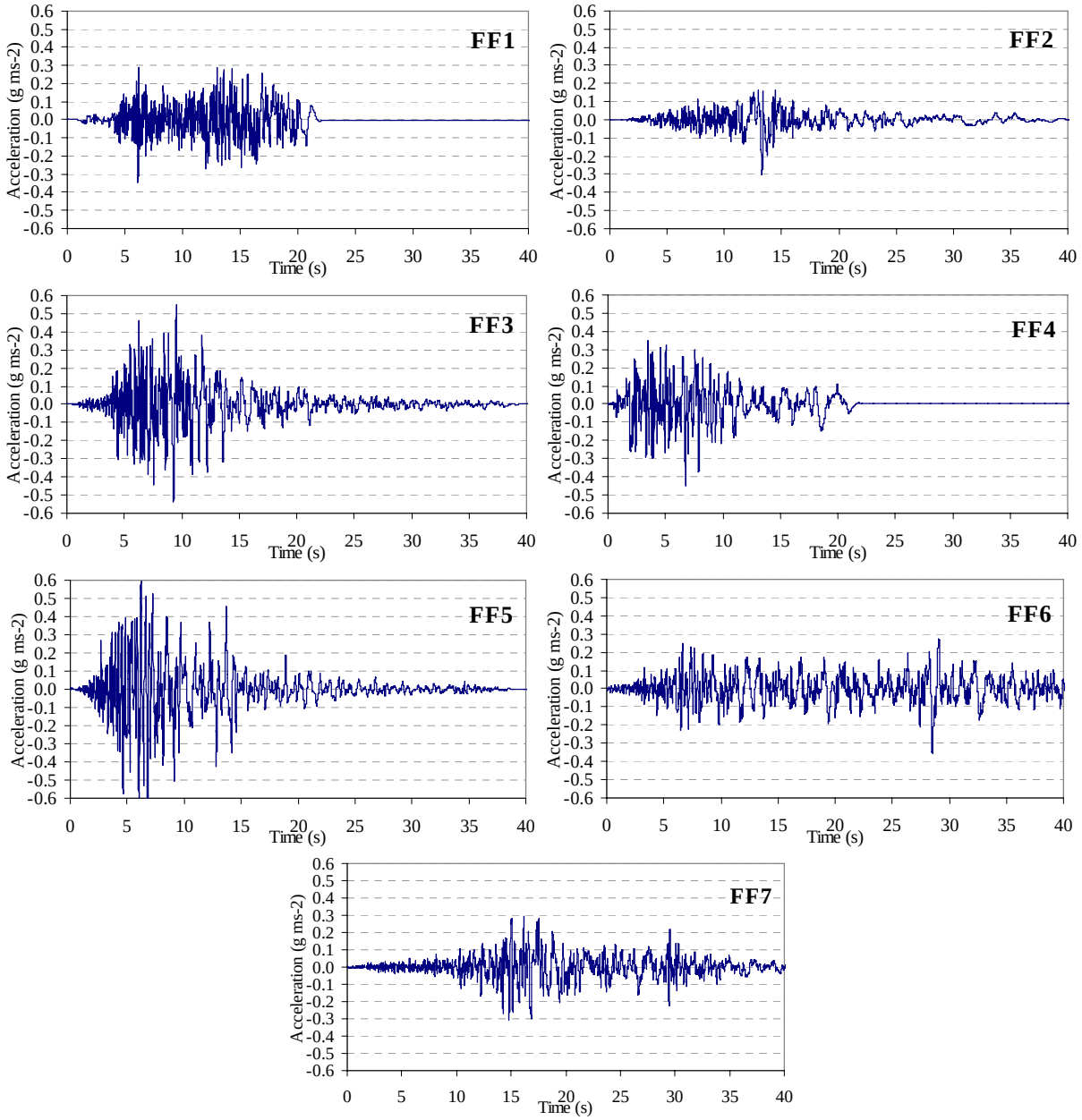

Figure G.1: Scaled far-field suites of earthquake: Response spectra and acceleration time-history.

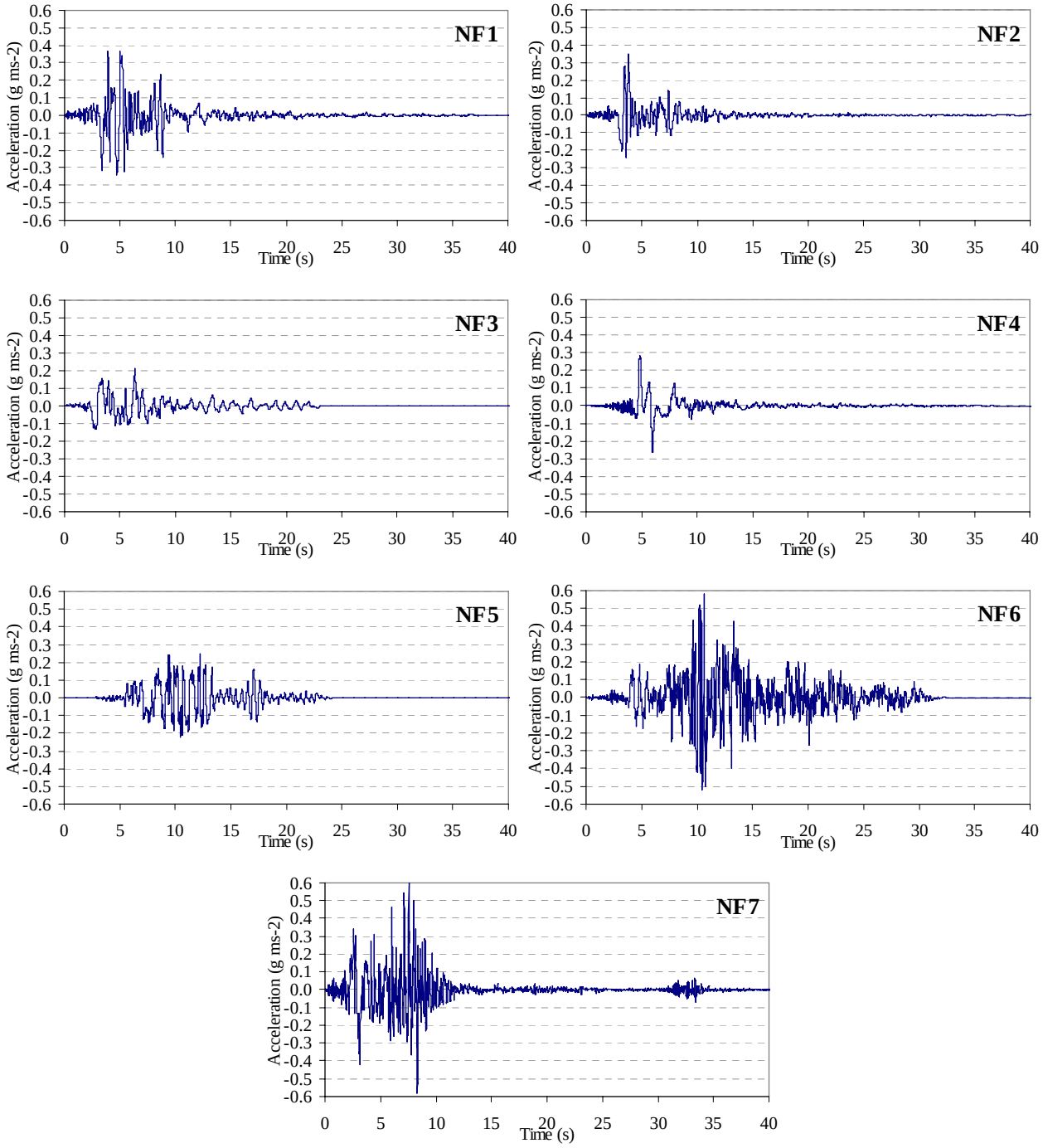

Figure G.2: Scaled near-fault suites of earthquake: Response spectra and acceleration time-history.

G.1.2 Non-linear dynamic analyses elements properties

Table G.1: Ruaumoko model members properties: As-built frame.

As-built frame			
General Material Properties			
Young's Modulus, Ec (kPa)	3.00E+07	Shear Modulus, G (kPa)	1.25E+07
Column C1 (Exterior columns at Level 1). PROP 1			
PYC (kN)	-2785.7	Hysteresis Rule	Modified Takeda
PB (kN)	-999.7	Takeda alpha	0.5
MB (kNm)	133.8	Takeda beta	0
M1B (kNm)	103.8	post-yield stiffness	0.03
M2B (kNm)	131.0	Section area	0.1225
M0 (kNm)	61.5	Section modulus, I (m^4)	0.00075
PYT (kN)	469.6	Plastic hinge length (m)	0.175
Column C2 (Interior columns). PROP 2			
PYC (kN)	-2898.0	Hysteresis Rule	Takeda
PB (kN)	-987.1	Takeda alpha	0.5
MB (kNm)	148.2	Takeda beta	0
M1B (kNm)	113.9	post-yield stiffness	0.03
M2B (kNm)	144.1	Section area	0.1225
M0 (kNm)	87.3	Section modulus, I (m^4)	0.00075
PYT (kN)	622.6	Plastic hinge length (m)	0.175
Column C3 (Exterior columns at upper levels). PROP 3			
PYC (kN)	-2785.7	Hysteresis Rule	Takeda
PB (kN)	-999.7	Takeda alpha	0.5
MB (kNm)	133.8	Takeda beta	0
M1B (kNm)	103.8	post-yield stiffness	0.03
M2B (kNm)	131.0	Section area	0.1225
M0 (kNm)	61.5	Section modulus, I (m^4)	0.00075
PYT (kN)	469.6	Plastic hinge length (m)	0.175
All beams. PROP 4-7			
Section area	0.17325	Hysteresis Rule	Modified Takeda
Section modulus, I (m^4)	0.00141502	Takeda alpha	0.5
Positive yield momemt (kNm)	105.0	Takeda beta	0
Negative yield momemt (kNm)	-105.0	post-yield stiffness	0
		Plastic hinge length (m)	0.2475
Exterior Joints. PROP 8 and 10.			
Rotational Stiffness	56000	Hysteresis Rule	Wayne-Stewart
Positive ultimate momemt (kNm)	42	Yield moment, F_U	36.5kN
Negative ultimate momemt (kNm)	-42	Intercept Moment, Fi	$0.5F_U$
post-yield stiffness	-0.001	** other Wayne-Stewart parameters listed below	
Interior Joints. PROP 9.			
Rotational Stiffness	74000	Hysteresis Rule	Wayne-Stewart
Positive ultimate momemt (kNm)	71.6	Yield moment, F_U	55.4kN
Negative ultimate momemt (kNm)	-71.6	Intercept Moment, Fi	$0.5F_U$
post-yield stiffness	-0.001	** other Wayne-Stewart parameters listed below	

Table G.2: Ruaumoko model members properties: R1-retrofitted frame.

R1-retrofitted Frame			
General Material Properties			
Young's Modulus, Ec (kPa)	3.00E+07	Shear Modulus, G (kPa)	1.25E+07
Column C1 (Exterior columns at Level 1). PROP 1			
PYC (kN)	-2785.7	Hysteresis Rule	Modified Takeda
PB (kN)	-999.7	Takeda alpha	0.3
MB (kNm)	160.5	Takeda beta	0.2
M1B (kNm)	124.6	post-yield stiffness	0.03
M2B (kNm)	157.2	Section area	0.1225
M0 (kNm)	73.8	Section modulus, I (m^4)	0.00075
PYT (kN)	469.6	Plastic hinge length (m)	0.175
Column C2 (Interior columns). PROP 2			
PYC (kN)	-2898.0	Hysteresis Rule	Takeda
PB (kN)	-987.1	Takeda alpha	0.5
MB (kNm)	148.2	Takeda beta	0
M1B (kNm)	113.9	post-yield stiffness	0.03
M2B (kNm)	144.1	Section area	0.1225
M0 (kNm)	87.3	Section modulus, I (m^4)	0.00075
PYT (kN)	622.6	Plastic hinge length (m)	0.175
Column C3 (Exterior columns at upper levels). PROP 3			
PYC (kN)	-2785.7	Hysteresis Rule	Takeda
PB (kN)	-999.7	Takeda alpha	0.5
MB (kNm)	133.8	Takeda beta	0
M1B (kNm)	103.8	post-yield stiffness	0.03
M2B (kNm)	131.0	Section area	0.1225
M0 (kNm)	61.5	Section modulus, I (m^4)	0.00075
PYT (kN)	469.6	Plastic hinge length (m)	0.175
All beams. PROP 4-7			
Section area	0.15925	Hysteresis Rule	Modified Takeda
Section modulus, I (m^4)	0.001099	Takeda alpha	0.5
Positive yield momemt (kNm)	63.0	Takeda beta	0
Negative yield momemt (kNm)	-112.0	post-yield stiffness	0
		Plastic hinge length (m)	0.2475
Exterior Joints. PROP 8 and 10.			
Rotational Stiffness	86666.667	Hysteresis Rule	Modified Takeda
Positive ultimate momemt (kNm)	65	Takeda alpha	0.5
Negative ultimate momemt (kNm)	-97.5	Takeda beta	0
post-yield stiffness	0		
Interior Joints. PROP 9.			
Rotational Stiffness	74000	Hysteresis Rule	Wayne-Stewart
Positive ultimate momemt (kNm)	90	Yield moment, F_U	55.4kN
Negative ultimate momemt (kNm)	-135	Intercept Moment, Fi	$0.5F_U$
post-yield stiffness	-0.001	** other Wayne-Stewart parameters listed below	

Table G.3: Ruaumoko model members properties: R3-retrofitted frame.

R3-retrofitted Frame			
General Material Properties			
Young's Modulus, Ec (kPa)	3.00E+07	Shear Modulus, G (kPa)	1.25E+07
Column C1 (Exterior columns at Level 1). PROP 1			
PYC (kN)	-2785.7	Hysteresis Rule	Modified Takeda
PB (kN)	-999.7	Takeda alpha	0.3
MB (kNm)	160.5	Takeda beta	0.2
M1B (kNm)	124.6	post-yield stiffness	0.03
M2B (kNm)	157.2	Section area	0.1225
M0 (kNm)	73.8	Section modulus, I (m^4)	0.00075
PYT (kN)	469.6	Plastic hinge length (m)	0.175
Column C2 (Interior columns). PROP 2			
PYC (kN)	-2898.0	Hysteresis Rule	Takeda
PB (kN)	-987.1	Takeda alpha	0.5
MB (kNm)	148.2	Takeda beta	0
M1B (kNm)	113.9	post-yield stiffness	0.03
M2B (kNm)	144.1	Section area	0.1225
M0 (kNm)	87.3	Section modulus, I (m^4)	0.00075
PYT (kN)	622.6	Plastic hinge length (m)	0.175
Column C3 (Exterior columns at upper levels). PROP 3			
PYC (kN)	-2785.7	Hysteresis Rule	Takeda
PB (kN)	-999.7	Takeda alpha	0.5
MB (kNm)	133.8	Takeda beta	0
M1B (kNm)	103.8	post-yield stiffness	0.03
M2B (kNm)	131.0	Section area	0.1225
M0 (kNm)	61.5	Section modulus, I (m^4)	0.00075
PYT (kN)	469.6	Plastic hinge length (m)	0.175
Beams at level 1-3. PROP 4-5			
Section area	0.17325	Hysteresis Rule	Modified Takeda
Section modulus, I (m^4)	0.0016484	Takeda alpha	0.3
Positive yield momemt (kNm)	94.8	Takeda beta	0.2
Negative yield momemt (kNm)	-127.0	post-yield stiffness	0.005
		Plastic hinge length (m)	0.2475
Beams at level 4-6. PROP 6-7			
Section area	0.17325	Hysteresis Rule	Modified Takeda
Section modulus, I (m^4)	0.0016484	Takeda alpha	0.3
Positive yield momemt (kNm)	47.4	Takeda beta	0.2
Negative yield momemt (kNm)	-63.5	post-yield stiffness	0.005
		Plastic hinge length (m)	0.2475
Exterior Joints. PROP 8 and 10.			
Rotational Stiffness	120000	Hysteresis Rule	Modified Takeda
Positive ultimate momemt (kNm)	90	Yield moment, F_U	36.5kN
Negative ultimate momemt (kNm)	-135	Intercept Moment, Fi	$0.5F_U$
post-yield stiffness	0.02		
Interior Joints. PROP 9.			
Rotational Stiffness	74000	Hysteresis Rule	Wayne-Stewart
Positive ultimate momemt (kNm)	90	Yield moment, F_U	55.4kN
Negative ultimate momemt (kNm)	-135	Intercept Moment, Fi	$0.5F_U$
post-yield stiffness	0.02	** other Wayne-Stewart parameters listed below	

G.2 RUAUMOKO INPUT FILES

G.2.1 As-built frame

```
Line 1  !   BL Model (file name)
2       !   Kam WY - Chapter 9 Dynamic Analysis of As-built and Retrofitted Frames
3       !   Units: KN, m                    !           Date Oct 2010
4       6 storey as - built frame   ! Chapter 9 prototype RC frame
5       !   IPANAL   IFMT    IPLAS    IPCONM   ICTYPE   IPVERT   INLGEO  IPNF     IZERO     ORTHO IMODE
6                2       0        1        0        0        0        0        0        0
7       !   NNP      NMEM     NTYPE    M        MODE1    MODE2    GRAV     C1       C2        DT       TIME     FACTOR
8                72       106      11       5        1        3        9.81     5        5    0.005    50       1
9       !   KP       KPA      KPLOT    JOUT     DSTORT   DFACT    XMAX     YMAX     NLEVEL    NUP      IRESID   KDUMP
10               0        20       100      0        1        5        1        1        7         2        1        0
11      !   MAXIT    MAXCIT   FTEST    WAVEX    WAVEY    THETA    DXMAX    DYMAX    D         OMEGA F
12               5        0        0.001
13
14      NODES  ! Coordinate X Y Z, Constraint x y z , Slaving x y z
15      !   N        X(N)     Y(N)     NF1      NF2      NF3      KUP1     KUP2     KUP3      IOUT
16               1        0        0        1        1        1        0        0        0 ! Principal nodes, Base
17               2        4.57     0        1        1        1        0        0        0
18               3        7.92     0        1        1        1        0        0        0
19               4        12.49    0        1        1        1        0        0        0
20               5        0        3        0        0        0        0        0        0 ! 1F
21               6        4.57     3        0        0        0        5        0        0
22               7        7.92     3        0        0        0        5        0        0
23               8        12.49    3        0        0        0        5        0        0
24               9        0        6        0        0        0        0        0        0 ! 2F
25               10       4.57     6        0        0        0        9        0        0
26               11       7.92     6        0        0        0        9        0        0
27               12       12.49    6        0        0        0        9        0        0
28               13       0        9        0        0        0        0        0        0 ! 3F
29               14       4.57     9        0        0        0        13       0        0
30               15       7.92     9        0        0        0        13       0        0
31               16       12.49    9        0        0        0        13       0        0
32               17       0        12       0        0        0        0        0        0 ! 4F
33               18       4.57     12       0        0        0        17       0        0
34               19       7.92     12       0        0        0        17       0        0
35               20       12.49    12       0        0        0        17       0        0
36               21       0        15       0        0        0        0        0        0 ! 5F
37               22       4.57     15       0        0        0        21       0        0
38               23       7.92     15       0        0        0        21       0        0
39               24       12.49    15       0        0        0        21       0        0
40               25       0        18       0        0        0        0        0        0 ! 6F
41               26       4.57     18       0        0        0        25       0        0
42               27       7.92     18       0        0        0        25       0        0
43               28       12.49    18       0        0        0        25       0        0
44               29       0        2.999    0        0        0        0        5        0 ! Joint spring joints
45               30       0        3.001    0        0        0        0        5        0
46               31       4.57     2.999    0        0        0        0        6        0
47               32       4.57     3.001    0        0        0        0        6        0
48               33       7.92     2.999    0        0        0        0        7        0
49               34       7.92     3.001    0        0        0        0        7        0
50               35       12.49    2.999    0        0        0        0        8        0
51               36       12.49    3.001    0        0        0        0        8        0
52               37       0        5.999    0        0        0        0        9        0 ! Joint spring joints
53               38       0        6.001    0        0        0        0        9        0
54               39       4.57     5.999    0        0        0        0        10       0
55               40       4.57     6.001    0        0        0        0        10       0
56               41       7.92     5.999    0        0        0        0        11       0
57               42       7.92     6.001    0        0        0        0        11       0
58               43       12.49    5.999    0        0        0        0        12       0
59               44       12.49    6.001    0        0        0        0        12       0
60               45       0        8.999    0        0        0        0        13       0 ! Joint spring joints
61               46       0        9.001    0        0        0        0        13       0
62               47       4.57     8.999    0        0        0        0        14       0
63               48       4.57     9.001    0        0        0        0        14       0
64               49       7.92     8.999    0        0        0        0        15       0
65               50       7.92     9.001    0        0        0        0        15       0
66               51       12.49    8.999    0        0        0        0        16       0
67               52       12.49    9.001    0        0        0        0        16       0
68               53       0        11.999   0        0        0        0        17       0 ! Joint spring joints
69               54       0        12.001   0        0        0        0        17       0
70               55       4.57     11.999   0        0        0        0        18       0
71               56       4.57     12.001   0        0        0        0        18       0
72               57       7.92     11.999   0        0        0        0        19       0
73               58       7.92     12.001   0        0        0        0        19       0
74               59       12.49    11.999   0        0        0        0        20       0
75               60       12.49    12.001   0        0        0        0        20       0
76               61       0        14.999   0        0        0        0        21       0 ! Joint spring joints
77               62       0        15.001   0        0        0        0        21       0
78               63       4.57     14.999   0        0        0        0        22       0
79               64       4.57     15.001   0        0        0        0        22       0
80               65       7.92     14.999   0        0        0        0        23       0
81               66       7.92     15.001   0        0        0        0        23       0
82               67       12.49    14.999   0        0        0        0        24       0
83               68       12.49    15.001   0        0        0        0        24       0
84               69       0        17.999   0        0        0        0        25       0 ! Joint spring joints
85               70       4.57     17.999   0        0        0        0        26       0
86               71       7.92     17.999   0        0        0        0        27       0
87               72       12.49    17.999   0        0        0        0        28       0
```

```
88
89      DRIFT
90      1 5 9 13 17 21 25
91
92      ELEMENTS
93        1         1         1        29         0         0 ! Columns  ! Monitored in DYNAPLOT batch
94        2         2         2        31         0         0
95        3         2         3        33         0         0
96        4         1         4        35         0         0
97        5         3        30        37         0         0              ! Monitored in DYNAPLOT batch
98        6         2        32        39         0         0
99        7         2        34        41         0         0
100       8         3        36        43         0         0
101       9         3        38        45         0         0              ! Monitored in DYNAPLOT batch
102      10         2        40        47         0         0
103      11         2        42        49         0         0
104      12         3        44        51         0         0
105      13         3        46        53         0         0              ! Monitored in DYNAPLOT batch
106      14         3        48        55         0         0
107      15         3        50        57         0         0
108      16         3        52        59         0         0
109      17         3        54        61         0         0              ! Monitored in DYNAPLOT batch
110      18         3        56        63         0         0
111      19         3        58        65         0         0
112      20         3        60        67         0         0
113      21         3        62        69         0         0              ! Monitored in DYNAPLOT batch
114      22         3        64        70         0         0
115      23         3        66        71         0         0
116      24         3        68        72         0         0
117      25         4         5         6         0         0 ! Beams    ! Monitored in DYNAPLOT batch
118      26         5         6         7         0         0              ! Monitored in DYNAPLOT batch
119      27         4         7         8         0         0
120      28         4         9        10         0         0              ! Monitored in DYNAPLOT batch
121      29         5        10        11         0         0              ! Monitored in DYNAPLOT batch
122      30         4        11        12         0         0
123      31         4        13        14         0         0              ! Monitored in DYNAPLOT batch
124      32         5        14        15         0         0              ! Monitored in DYNAPLOT batch
125      33         4        15        16         0         0
126      34         4        17        18         0         0              ! Monitored in DYNAPLOT batch
127      35         5        18        19         0         0              ! Monitored in DYNAPLOT batch
128      36         4        19        20         0         0
129      37         4        21        22         0         0              ! Monitored in DYNAPLOT batch
130      38         5        22        23         0         0              ! Monitored in DYNAPLOT batch
131      39         4        23        24         0         0
132      40         6        25        26         0         0              ! Monitored in DYNAPLOT batch
133      41         7        26        27         0         0              ! Monitored in DYNAPLOT batch
134      42         6        27        28         0         0
135      43         8        29         5         0         0 ! Joint sprir ! Monitored in DYNAPLOT batch
136      44         8         5        30         0         0
137      45         9        31         6         0         0
138      46         9         6        32         0         0
139      47         9        33         7         0         0
140      48         9         7        34         0         0
141      49         8        35         8         0         0
142      50         8         8        36         0         0
143      51         8        37         9         0         0              ! Monitored in DYNAPLOT batch
144      52         8         9        38         0         0
145      53         9        39        10         0         0
146      54         9        10        40         0         0
147      55         9        41        11         0         0
148      56         9        11        42         0         0
149      57         8        43        12         0         0
150      58         8        12        44         0         0
151      59         8        45        13         0         0              ! Monitored in DYNAPLOT batch
152      60         8        13        46         0         0
153      61         9        47        14         0         0
154      62         9        14        48         0         0
155      63         9        49        15         0         0
156      64         9        15        50         0         0
157      65         8        51        16         0         0
158      66         8        16        52         0         0
159      67         8        53        17         0         0              ! Monitored in DYNAPLOT batch
160      68         8        17        54         0         0
161      69         9        55        18         0         0
```

```
199
200  PROPS
201    1 FRAME    ! Column C1 350 x 350 - Thin Takeda parameters - first floor exterior columns
202            2         0         0         4         0         0                    ! General info
203     3.00E+07  1.25E+07    0.1225    0.1225   0.00075         0     0.175     0.175 ! Elastic prop
204            0      0.03     0.175     0.175                                        ! Plastic hinge
205       -2785.7    -999.7     133.8     103.8     131.0      61.5     469.6         0  ! Yield Beam-Column Surface M-N intera
206          0.5         0         1         2                                        ! Takeda parameter
207
208    2 FRAME    ! Column C2 350 x 350 - Thin Takeda parameters - interior columns
209            2         0         0         4         0         0                    ! General info
210     3.00E+07  1.25E+07    0.1225    0.1225   0.00075         0     0.175     0.175 ! Elastic prop
211            0      0.03     0.175     0.175                                        ! Plastic hinge
212       -2898.0    -987.1     148.2     113.9     144.1      87.3     622.6         0  ! Yield Beam-Column Surface M-N intera
213          0.5         0         1         2                                        ! Takeda parameter
214
215    3 FRAME    ! Column C3 350 x 350 - Thin Takeda parameters - Same as C1 - upper floors exterior columns
216            2         0         0         4         0         0                    ! General info
217     3.00E+07  1.25E+07    0.1225    0.1225   0.00075         0     0.175     0.175 ! Elastic prop
218            0      0.03     0.175     0.175                                        ! Plastic hinge
219       -2785.7    -999.7     133.8     103.8     131.0      61.5     469.6         0  ! Yield Beam-Column Surface M-N intera
220          0.5         0         1         2                                        ! Takeda parameter
221
222    4 FRAME    ! Beam B2/B3 - Takeda parameters Span 1 (long) Level 1-5
223            1         0         0         4         0         0                    ! General info
224     3.00E+07  1.25E+07   0.17325   0.17325  0.001415         0    0.2475    0.2475 ! Elastic prop
225            0         0    0.2475    0.2475                                        ! Plastic hinge
226            0         0       105      -105       105      -105                    ! Yield moments
227          0.5         0         1                                                  ! Takeda parameter
228
229    5 FRAME    ! Beam B3 - Takeda parameters - Span 2 (short) Level 1-5
230            1         0         0         4         0         0                    ! General info
231     3.00E+07  1.25E+07   0.17325   0.17325  0.001415         0    0.2475    0.2475 ! Elastic prop
232            0         0    0.2475    0.2475                                        ! Plastic hinge
233            0         0       105      -105       105      -105                    ! Yield moments
234          0.5         0         1         2                                        ! Takeda parameter
235
236    6 FRAME    ! Beam B4 - Takeda parameters (long span, level 6)
237            1         0         0         4         0         0                    ! General info
238     3.00E+07  1.25E+07   0.17325   0.17325  0.001415         0    0.2475    0.2475 ! Elastic prop
239            0         0    0.2475    0.2475                                        ! Plastic hinge
240            0         0       105      -105       105      -105                    ! Yield moments
241          0.5         0         1         2                                        ! Takeda parameter
242
243    7 FRAME    ! Beam B4 - Takeda parameters (short span, level 6)
244            1         0         0         4         0         0                    ! General info
245     3.00E+07  1.25E+07   0.17325   0.17325  0.001415         0    0.2475    0.2475 ! Elastic prop
246            0         0    0.2475    0.2475                                        ! Plastic hinge
247            0         0       105      -105       105      -105                    ! Yield moments
248          0.5         0         1         2                                        ! Takeda parameter
249
250    8 SPRING   !              Exterior Joint J1
251            1         9         0         0  1.00E+07  1.00E+07     56000         0         0    -0.001         0         0         0
252         5000     -5000      5000     -5000        42       -42
253         36.5     18.25    -0.001       0.8         0         0         1       0.8         1
254
255    9 SPRING   !              Interior Joint J2
256            1         9         0         0  1.00E+07  1.00E+07     74000         0         0    -0.001         0         0         0
257         5000     -5000      5000     -5000      71.6     -71.6
258         55.4      27.7    -0.001       0.8         0         0         1       0.8         1
259
260   10 SPRING   !              Roof Joint J3
261            1         9         0         0  1.00E+07  1.00E+07     56000         0         0    -0.001         0         0         0
262         5000     -5000      5000     -5000        42       -42
263         36.5     18.25    -0.001       0.8         0         0         1       0.8         1
264
265   11 FRAME    ! Elastic Rigid Links 5x beam stiffness
266            1         0         0         0         0         0         0
267     3.00E+07  1.25E+07   0.93025    1.1163      0.05         0         0         0 ! Elastic Properties
268
```

```
272  WEIGHTS 0 ! in KN
273    5   262.4
274    6   262.4
275    7   262.4
276    8   262.4
277    9   262.4
278   10   262.4
279   11   262.4
280   12   262.4
281   13   262.4
282   14   262.4
283   15   262.4
284   16   262.4
285   17   262.4
286   18   262.4
287   19   262.4
288   20   262.4
289   21   262.4
290   22   262.4
291   23   262.4
292   24   262.4
293   25     125
294   26     125
295   27     125
296   28     125
297
298  LOADS
299    5     0     -192     0
300    6     0   -332.8     0
301    7     0   -333.8     0
302    8     0     -192     0
303    9     0     -192     0
304   10     0   -332.8     0
305   11     0   -333.8     0
306   12     0     -192     0
307   13     0     -192     0
308   14     0   -332.8     0
309   15     0   -333.8     0
310   16     0     -192     0
311   17     0     -192     0
312   18     0   -332.8     0
313   19     0   -333.8     0
314   20     0     -192     0
315   21     0     -192     0
316   22     0   -332.8     0
317   23     0   -333.8     0
318   24     0     -192     0
319   25     0     -91.5     0
320   26     0   -158.6     0
321   27     0   -158.6     0
322   28     0     -91.5     0
323
324  EQUAKE
325  !  IBERG   ISTART   DELTAT   ASCALE   END   VEL   DIS   TSCALE
326          3       1    0.005        1    -1     0     0       1
```

G.2.2 Beam-weakening only (R1) retrofitted frame

Only the material properties section (PROP) is presented as other sections are the same as the as-built model (G.2.1).

```
PROPS
  1 FRAME    ! Column C1 350 x 350 - Thin Takeda parameters
            2         0         0         4         0         0                    ! General info
 3.00E+07  1.25E+07    0.1225    0.1225   0.00075         0     0.175     0.175 ! Elastic prop
            0      0.03     0.175     0.175                                       ! Plastic hinge
      -2785.7    -999.7     160.5     124.6     157.2      73.8     469.6         0  ! Yield Beam-Column Surface M-N intera
          0.3       0.2         1         2                                       ! Takeda parameter

  2 FRAME    ! Column C2 350 x 350 - Thin Takeda parameters
            2         0         0         4         0         0                    ! General info
 3.00E+07  1.25E+07    0.1225    0.1225   0.00075         0     0.175     0.175 ! Elastic prop
            0      0.03     0.175     0.175                                       ! Plastic hinge
      -2898.0    -987.1     148.2     113.9     144.1      87.3     622.6         0  ! Yield Beam-Column Surface M-N intera
          0.5         0         1         2                                       ! Takeda parameter

  3 FRAME    ! Column C3 350 x 350 - Thin Takeda parameters - Same as C1 for now
            2         0         0         4         0         0                    ! General info
 3.00E+07  1.25E+07    0.1225    0.1225   0.00075         0     0.175     0.175 ! Elastic prop
            0      0.03     0.175     0.175                                       ! Plastic hinge
      -2785.7    -999.7     133.8     103.8     131.0      61.5     469.6         0  ! Yield Beam-Column Surface M-N intera
          0.5         0         1         2                                       ! Takeda parameter

  4 FRAME    ! Beam B2/B3 - Takeda parameters Span 1 (long) Level 1-5          Retrofitted R1 BCJ
            1         0         0         4         0         0                    ! General info
 3.00E+07  1.25E+07    0.17325   0.17325  0.001099         0    0.2475    0.2475 ! Elastic prop
            0         0    0.2475    0.2475                                       ! Plastic hinge
            0         0        63      -112        63      -112                    ! Yield moments
          0.5         0         1         2                                       ! Takeda parameter

  5 FRAME    ! Beam B3 - Takeda parameters - Span 2 (short) Level 1-5          ! Interior Span not retrofitted
            1         0         0         4         0         0                    ! General info
 3.00E+07  1.25E+07    0.17325   0.17325  0.001099         0    0.2475    0.2475 ! Elastic prop
            0         0    0.2475    0.2475                                       ! Plastic hinge
            0         0        63      -112        63      -112                    ! Yield moments
          0.5         0         1         2                                       ! Takeda parameter

  6 FRAME    ! Beam B4 - Takeda parameters (long span, level 6)                Retrofitted R1 BCJ
            1         0         0         4         0         0                    ! General info
 3.00E+07  1.25E+07    0.17325   0.17325  0.001099         0    0.2475    0.2475 ! Elastic prop
            0         0    0.2475    0.2475                                       ! Plastic hinge
            0         0        63      -112        63      -112                    ! Yield moments
          0.5         0         1         2                                       ! Takeda parameter

  7 FRAME    ! Beam B4 - Takeda parameters (short span, level 6)               ! Interior Span not retrofitted
            1         0         0         4         0         0                    ! General info
 3.00E+07  1.25E+07    0.17325   0.17325  0.001099         0    0.2475    0.2475 ! Elastic prop
            0         0    0.2475    0.2475                                       ! Plastic hinge
            0         0        63      -112        63      -112                    ! Yield moments
          0.5         0         1         2                                       ! Takeda parameter

  8 SPRING   !            Retrofitted R1 BCJ
            1         4         0         0 1.00E+07 1.00E+07  86666.67         0         0         0         0     0     0
         5000     -5000      5000     -5000        65     -97.5
          0.5         0         1         2                                       ! Takeda Parameter

  9 SPRING   !            Interior Joint J2
            1         9         0         0 1.00E+07 1.00E+07     74000         0         0    -0.001         0     0     0
         5000     -5000      5000     -5000        90      -135
         55.4      27.7    -0.001       0.8         0         0         1       0.8         1

 10 SPRING   !            Roof Joint J3
            1         4         0         0 1.00E+07 1.00E+07  86666.67         0         0         0         0     0     0
         5000     -5000      5000     -5000        65     -97.5
          0.5         0         1         2                                       ! Takeda Parameter

 11 FRAME    ! Elastic Rigid Links 5x beam stiffness
            1         0         0         0         0         0         0
 3.00E+07  1.25E+07    0.93025   1.1163      0.05         0         0         0 ! Elastic Properties
```

G.2.3 Full selective-weakening (R3) retrofitted frame

Only the material properties section (PROP) is presented as other sections are the same as the as-built model (G.2.1).

```
PROPS
1 FRAME    ! Column C1 350 x 350 - Thin Takeda parameters
2 0 0 4 0 0 ! General info
3.00E+07 1.25E+07 0.1225 0.1225 0.00075 0 0.175 0.175 ! Elastic prop
0 0.03 0.175 0.175 ! Plastic hinge
-2785.7 -999.7 160.5 124.6 157.2 73.8 469.6 0 ! Yield Beam-Column Surface M-N interaction
0.3 0.2 1 2 ! Takeda parameter

2 FRAME    ! Column C2 350 x 350 - Thin Takeda parameters
2 0 0 4 0 0 ! General info
3.00E+07 1.25E+07 0.1225 0.1225 0.00075 0 0.175 0.175 ! Elastic prop
0 0.03 0.175 0.175 ! Plastic hinge
-2898.0 -987.1 148.2 113.9 144.1 87.3 622.6 0 ! Yield Beam-Column Surface M-N interaction
0.5 0 1 2 ! Takeda parameter

3 FRAME    ! Column C3 350 x 350 - Thin Takeda parameters - Same as C1 for now
2 0 0 4 0 0 ! General info
3.00E+07 1.25E+07 0.1225 0.1225 0.00075 0 0.175 0.175 ! Elastic prop
0 0.03 0.175 0.175 ! Plastic hinge
-2785.7 -999.7 133.8 103.8 131.0 61.5 469.6 0 ! Yield Beam-Column Surface M-N interaction
0.5 0 1 2 ! Takeda parameter

4 FRAME    ! Beam B2/B3 - Takeda parameters Span 1 (long) Level 1-5 Retrofitted R1 BCJ
1 0 0 4 0 0 ! General info
3.00E+07 1.25E+07 0.17325 0.17325 0.001648 0 0.2475 0.2475 ! Elastic prop
0 0.005 0.2475 0.2475 ! Plastic hinge
0 0 94.8 -127 94.8 -127 ! Yield moments
0.3 0.2 1 2 ! Takeda parameter

5 FRAME    ! Beam B3 - Takeda parameters - Span 2 (short) Level 1-5 ! Interior Span not retrofitted
1 0 0 4 0 0 ! General info
3.00E+07 1.25E+07 0.17325 0.17325 0.001648 0 0.2475 0.2475 ! Elastic prop
0 0.005 0.2475 0.2475 ! Plastic hinge
0 0 94.8 -127 94.8 -127 ! Yield moments
0.3 0.2 1 2 ! Takeda parameter

6 FRAME    ! Beam B4 - Takeda parameters (long span, level 6) Retrofitted R1 BCJ
1 0 0 4 0 0 ! General info
3.00E+07 1.25E+07 0.17325 0.17325 0.001648 0 0.2475 0.2475 ! Elastic prop
0 0.005 0.2475 0.2475 ! Plastic hinge
0 0 47.4 -63.5 47.4 -63.5 ! Yield moments
0.3 0.2 1 2 ! Takeda parameter

7 FRAME    ! Beam B4 - Takeda parameters (short span, level 6) ! Interior Span not retrofitted
1 0 0 4 0 0 ! General info
3.00E+07 1.25E+07 0.17325 0.17325 0.001648 0 0.2475 0.2475 ! Elastic prop
0 0.005 0.2475 0.2475 ! Plastic hinge
0 0 47.4 -63.5 47.4 -63.5 ! Yield moments
0.3 0.2 1 2 ! Takeda parameter

8 SPRING   !          Retrofitted R1 BCJ
1 4 0 0 1.00E+07 1.00E+07 120000 0 0 0.02 0 0 0
5000 -5000 5000 -5000 90 -135
0.3 0.2 1 2 ! Takeda Parameter


9 SPRING   !          Interior Joint J2
1 9 0 0 1.00E+07 1.00E+07 74000 0 0 0.02 0 0 0
5000 -5000 5000 -5000 90 -135
55.4 27.7 0.02 0.8 0 0 1 0.8 1


10 SPRING   !          Roof Joint J3
1 4 0 0 1.00E+07 1.00E+07 120000 0 0 0.02 0 0 0
5000 -5000 5000 -5000 90 -135
0.3 0.2 1 2 ! Takeda Parameter

11 FRAME    ! Elastic Rigid Links 5x beam stiffness
1 0 0 0 0 0 0
3.00E+07 1.25E+07 0.93025 1.1163 0.05 0 0 0 ! Elastic Properties
```